



UWMAK-I - A Wisconsin Toroidal Fusion Reactor Design

B. Badger, M.A. Abdou, R.W. Boom, R.G. Brown, E.T. Cheng, R.W. Conn,
J.M. Donhowe, L.A. El-Guebaly, G.A. Emmert, G.R. Hopkins,
W.A. Houlberg, A.B. Johnson, J.H. Kamperschroer, D. Klein, G.L. Kulcinski,
R.G. Lott, D.G. McAlees, C.W. Maynard, A.T. Mense, G.R. Neil, E. Normand,
P.A. Sanger, W.E. Stewart, T. Sung, I.N. Sviatoslavsky, D.K. Sze,
W.F. Vogelsang, L.J. Wittenberg, T.F. Yang, and W.D. Young

**November 20, 1973
(revised March 15, 1974)**

UWFDM-68

***FUSION TECHNOLOGY INSTITUTE
UNIVERSITY OF WISCONSIN
MADISON WISCONSIN***

DISCLAIMER

This report was prepared as an account of work sponsored by an agency of the United States Government. Neither the United States Government, nor any agency thereof, nor any of their employees, makes any warranty, express or implied, or assumes any legal liability or responsibility for the accuracy, completeness, or usefulness of any information, apparatus, product, or process disclosed, or represents that its use would not infringe privately owned rights. Reference herein to any specific commercial product, process, or service by trade name, trademark, manufacturer, or otherwise, does not necessarily constitute or imply its endorsement, recommendation, or favoring by the United States Government or any agency thereof. The views and opinions of authors expressed herein do not necessarily state or reflect those of the United States Government or any agency thereof.

UWMAK-I - A Wisconsin Toroidal Fusion Reactor Design

B. Badger, M.A. Abdou, R.W. Boom, R.G. Brown, E.T. Cheng, R.W. Conn, J.M. Donhowe, L.A. El-Guebaly, G.A. Emmert, G.R. Hopkins, W.A. Houlberg, A.B. Johnson, J.H. Kamperschroer, D. Klein, G.L. Kulcinski, R.G. Lott, D.G. McAlees, C.W. Maynard, A.T. Mense, G.R. Neil, E. Normand, P.A. Sanger, W.E. Stewart, T. Sung, I.N. Sviatoslavsky, D.K. Sze, W.F. Vogelsang, L.J. Wittenberg, T.F. Yang, and W.D. Young

Fusion Technology Institute
University of Wisconsin
1500 Engineering Drive
Madison, WI 53706

<http://fti.neep.wisc.edu>

November 20, 1973 (revised March 15, 1974)

UWFDM-68

UWMAK-I

A WISCONSIN TOROIDAL FUSION REACTOR DESIGN

BY

The University of Wisconsin Fusion Feasibility Study Group

B. Badger	R. G. Lott
M. A. Abdou	D. G. McAlees
R. W. Boom	C. W. Maynard
a) R. G. Brown	A. T. Mense
T. E. Cheng	G. R. Neil
R. W. Conn	d) E. Normand
J. M. Donhowe	P. A. Sanger
L. A. El-Guebaly	W. E. Stewart
G. A. Emmert	T. Sung
b) G. R. Hopkins	I. Sviatoslavsky
W. A. Houlberg	D. K. Sze
c) A. B. Johnson	W. F. Vogelsang
J. H. Kamperschroer	e) L. J. Wittenberg
a) D. Klein	T. F. Yang
G. L. Kulcinski	W. D. Young

November 20, 1973

Revised: March 15, 1974

University of Wisconsin

UWFDM - 68

- a) Westinghouse Corp.
- b) Gulf General Atomic Corp.
- c) Battelle Northwest Laboratories
- d) Sargent and Lundy Corp.
- e) Monsanto Chemical Corp.

Summary

The design details of a low- β , D-T fusion reactor based on the Tokamak confinement concept is described. Included in the report are technological problems that have been assessed or uncovered, whether or not detailed solutions are presented. The thermal power output of the plant is 5000 MW. The basic structural material is 316 stainless steel and the heat transfer medium is lithium. Materials compatibility limits the maximum temperature to 500°C implying an electrical output of $\sim 1500 \text{ MW}_e$ is to be expected.

The plasma is characterized by an average toroidal beta of .052 and an average poloidal beta of 1.08. The nominal plasma radius is 5 meters and the torus radius is 13 meters, giving an aspect ratio of 2.6. The ion and electron temperatures are 11.1 KeV and 11 KeV, respectively, and the average ion density is 0.8×10^{14} (D+T) ions/cm³. The mean particle confinement time is 14.2 seconds and the fractional burnup is 7.2%, and the burn time is 5400 seconds.

The plasma is designed to operate with a double null point, poloidal field divertor that is consistent with the small aspect ratio of 2.6 suggested by optimization studies. The field topology is created by superconducting divertor coils outside the main toroidal field magnets.

The magnetic field at the plasma axis is 3.82 Tesla. The maximum field at the superconductor of the toroidal field magnets is 8.66 Tesla. This low maximum field is possible because the double-null, poloidal divertor allows the toroidal magnets to be reasonably close to the plasma. The maximum magnet bore diameter is 20.5 meters. The 8.66 Tesla maximum field also allows the use of NbTi as the superconductor, a present-day technology choice. The magnets are fully stabilized with copper and have a large, 2 cm x 2 cm conductor design. The support material is stainless steel and detailed stress calculations have been made to guide the magnet design.

The neutron flux to the first wall gives a neutron wall loading of 1.25 MW/m^2 . Radiation induced embrittlement has forced the first wall to be designed such that it can be changed every two years. This decision is made to ensure against costly brittle failures during operation. Liquid lithium is used to cool the UWMAK-I blanket, which is constructed of 316 stainless steel and operated at a maximum temperature of 500°C. The pumping power associated with the lithium coolant is 22 MW, a completely reasonable value because of the unique flow design employed.

Neutron and photon transport calculations indicate the breeding ratio in UWMAK-I is 1.49 and the doubling time will be as low as 2-3 months. The energy attenuation through the blanket and shield is $\sim 10^{-6}$. Detailed heating calculations, based on kerma factors from the MACK program

(recently developed at Wisconsin), were performed and reveal that the energy amplification of the blanket is ~17%. It is found that 16.55 MeV of energy is produced per 14.06 MeV neutron incident on the blanket. Thus, the total energy per fusion reaction, including the 3.52 MeV alpha energy is ~20 MeV. This is in contrast to values of 22-27 MeV which have commonly been used in computing power output for fusion plants. The shield behind the blanket is composed of Pb, and B₄C with stainless steel structure. Helium gas is used for cooling the shield.

It is shown that radioactive stainless steel corrosion products, in large amounts up to 2500 Kg/year, must be removed from the coolant to avoid maintenance problems. Tritium is separated from the lithium coolant via yttrium traps. The afterheat and radioactivity at shutdown after ten years of operation are 32 MW_T and 1.6 x 10⁹ curies, respectively. These values drop to < 1 kW_T and < 10³ curies after 100 years of storage.

Detailed power cycle, safety, environmental impact, architectural and economic studies of UWMAK-I are not included here and will be described in a subsequent report.

Preface

The purpose of this report is to present a comprehensive view of the University of Wisconsin Tokamak Reactor Design, UWMAK-I. This report does not, and cannot, contain all of the detailed thoughts and calculations that are behind this reactor concept. Such details appear in UWFDM's (University of Wisconsin Fusion Design Memos) which are liberally referenced throughout the text.

It is quite possible that some of the numbers or ideas expressed here may have to be changed in the first few months after this issue. Therefore, we have tried to make each chapter as self-consistent as possible so that pages can be removed and inserted without disrupting an orderly numbering sequence of tables, figures, references, etc. in other chapters. The reader will note that each copy of this report is numbered and periodically replacement pages will be sent to the owner to update this report.

Four parts of the UWMAK-I analysis were not completed by the printing of this report; power cycle, building design, economics and environmental impact. These sections should be finished by the middle of 1974 and will be the subject of another report. (Vol. II, UWFDM-68)

Several of our colleagues must be acknowledged for their support, stimulation and encouragement in the writing of this document. We wish to express our appreciation to Professors Kerst and Symon of the University of Wisconsin Physics Department, Dr. H. K. Forsen of Exxon Nuclear Company and Professor M. W. Carbon, Chairman of the Nuclear Engineering Department of the University of Wisconsin.

The preparation of this report represented no small task and we must commend several people for their skill, patience and dedication in the assembly of this document. Mrs. Connie Linehan did a remarkable job of typing the report and coordinating the secretarial activities. She was ably assisted by Mrs. Suzan Steindorf. Mr. Ralph Brittelli, the project administrative assistant, and Chi-Kin Lin provided invaluable support for the final assembly and presentation of the ideas in this design. Other graduate students which in one way or another contributed to this project include Mr. Max Sherman, Mr. William Weber and Mr. Bruce Yeazell.

We enthusiastically acknowledge the financial support received from the Wisconsin Electric Utilities Research Foundation and the USAEC Division of Controlled Thermonuclear Research. Without their help and encouragement we would not have been able to pursue this very important study.

G. L. Kulcinski, Director
Fusion Feasibility Study Project

R. W. Conn, Associate Director
Fusion Feasibility Study Project

TABLE OF CONTENTS

	<u>Page</u>
Preface	
Summary	
I. Overview of UWMAK-I	I-1
II. Plasma	
Summary	II-1
A. Principles of Tokamak Operation	II-A-1
B. Optimization	II-B-1
C. Start-Up	II-C-1
D. Neutral Beam Plasma Heating to Ignition	II-D-1
1. Introduction	II-D-1
2. The Computational Model for Plasma Simulation	II-D-1
3. Plasma Heating by Neutral Beam Injection	II-D-11
4. Impact of Results on Other Machines	II-D-24
5. Summary of Beam Heating Analysis	II-D-24
E. Neutral Injector Design	II-E-1
1. Neutral Injector Design	II-E-1
2. Fueling	II-E-10
F. Plasma Operating Conditions	II-F-1
1. Introduction	II-F-1
2. Transport Equations and the β Limit	II-F-1
3. Radial Profiles for n, T, j , and q	II-F-6
4. Point Kinetics and Steady State Equations	II-F-12
5. Energy Balance Studies and Plasma Operating Conditions	II-F-16
G. Control and Economics	II-G-1
H. Recycle and Shutdown	II-H-1
I. Alternate Plasma Assumptions and Economic Implications	II-I-1
1. Optimization	II-I-1
2. Start-Up, Transformer Design, and Energy Storage	II-I-1
3. Neutral Beam Heating	II-I-4
4. Plasma Operation, Thermal Stability and Limits on β and q	II-I-4
III. Divertor	
A. General Considerations	III-A-1
B. Magnetic Field Design	III-B-1
C. Particle Dynamics and Transport in the Divertor	III-C-1
D. Divertor Particle Collectors and Vacuum System	III-D-1
IV. Blanket and Shield	
A. General Design Features	IV-A-1
1. Requirements	IV-A-1
2. Choice of Coolant	IV-A-3
3. Choice of Structural Material	IV-A-6
4. Choice of Moderator-Reflector	IV-A-12
5. System Description	IV-A-13
a. Blanket	IV-A-13
b. Shield	IV-A-13
6. Summary of Blanket and Shield Dimensions and Masses	IV-A-19

	<u>Page</u>
B. Heat Transfer	IV-B-1
1. General Discussion	IV-B-1
2. MHD Pressure Drop	IV-B-2
3. Design Strategy	IV-B-4
4. System Description	IV-B-7
a. Pressure Drop	IV-B-10a
b. Temperature Distribution	IV-B-13
c. Cooling of the Shield	IV-B-13
C. Corrosion and Corrosion Product Transport in Lithium-Cooled Stainless Steel Fusion Reactor Circuits	IV-C-1
1. General Discussion	IV-C-1
2. Lithium-Stainless Steel Compatibility	IV-C-3
a. Lithium Chemical Corrosion	IV-C-3
b. Irradiation Effects on Corrosion	IV-C-8
c. Solubilities of Selected Elements in Lithium	IV-C-9
d. Corrosion Mechanisms	IV-C-11
e. Summary of Thermochemical Relationships for Carbides, Nitrides and Oxides	IV-C-12
f. Mechanical Property Effects	IV-C-13
g. Lithium Purity	IV-C-14
3. Corrosion in Auxiliary Systems	IV-C-18
a. Lithium Cleanup System	IV-C-18
b. Tritium Extraction System	IV-C-19
c. Helium Circuit for Cooling the Shield	IV-C-19
d. Heat Exchanger Corrosion	IV-C-19
4. Corrosion Product Transport	IV-C-20
5. Problems Associated with Radioactive Crud	IV-C-22
6. Summary of Corrosion Product Transport Considerations	IV-C-23
D. Thermal and Mechanical Stresses in the Heat Removal Cells	IV-D-1
1. Thermal Stresses	IV-D-1
2. Pressure Stresses	IV-D-3
3. Mechanical Stresses	IV-D-8
E. First Wall Replacement	IV-E-1
1. Reasons for Consideration	IV-E-1
2. Proposed Removal Scheme	IV-E-1
3. Impact on Reactor Efficiency	IV-E-10
F. Support for Blanket and Shield Structures	IV-F-1
1. Blanket	IV-F-1
2. Shield	IV-F-1
G. Summary Progress Report for the Period Oct. 1, 1972 to Sept. 30, 1973.	IV-G-2
1. Introduction	IV-G-2
2. Design Considerations	IV-G-2
3. The Model	IV-G-9
4. Results and Discussion	IV-G-9
5. Conclusions	IV-G-10
H. Insulator Requirements in the Blanket	IV-H-1

	<u>Page</u>
V. Neutronics and Photonics	
A. Blanket and Shield Responses	V-A-1
1. Tritium Production	V-A-2
2. Radiation Damage Responses	V-A-2
3. Energy Deposition and Gamma Production	V-A-4
4. Energy Attenuation	V-A-4
5. Energy Production and Economics	V-B-1
B. Results and Conclusions of Neutronics and Photonics	V-B-1
Design Studies of the Blanket and Shield	V-B-1
1. Introduction	V-B-1
2. First Wall and Structural Materials	V-B-2
3. Blanket Region	V-B-2
4. Reflector Region	V-B-12
5. Magnet Shield	V-B-15
a. Introduction	V-B-15
b. Shield Composition	V-B-18
c. Optimum Shield Thickness	V-B-24
6. Monte Carlo Calculations	V-B-29
7. Variational Sensitivity Study	V-B-39
8. Details of Present U.W. Design	V-B-39
9. Conclusions	V-B-52
C. Nuclear Data Requirements	V-C-1
1. Introduction	V-C-1
2. Multigroup Neutron Cross Sections	V-C-1
3. Multigroup Gamma Cross Sections	V-C-7
4. Photon Production Cross Sections	V-C-7
5. Response Functions	V-C-10
6. Kerma Factors	V-C-10
7. Comparison and Analysis of Neutron Kerma	V-C-17
Factors for CTR Materials	
8. Conclusions	V-C-30
D. Flux Calculations	V-D-1
1. Introduction	V-D-1
2. Neutron Source Distribution	V-D-3
3. Neutron Source Geometry Effects and Cylinder	
Slab Calculations	V-D-3
4. Effects of Scattering Anisotropy	V-D-8
5. Order of S_n	V-D-8
6. Gamma Computational Model	V-D-10
7. Variational Procedures	V-D-13
8. Conclusions	V-D-15
VI. Radiation Damage	
A. Potential Radiation Effects in D-T Fusion Reactors	VI-A-1
B. Damage Units	VI-B-1
1. General Considerations	VI-B-1
2. Displacement Cross Sections for Potential	
CTR Materials	VI-B-3
3. Typical dpa Values for Fission Reactors	VI-B-7

	<u>Page</u>
C. Potential Radiation Effects in D-T Fueled Fusion Reactors	VI-C-1
1. Void Induced Swelling	VI-C-1
a. Development of General Swelling Equation	VI-C-1
b. Observations on the General Swelling Formula	VI-C-4
c. Experimental Data on Swelling in 316 SS	VI-C-5
d. Design Equations for Swelling in 316 SS	VI-C-12
2. Bubble Induced Swelling	VI-C-18
a. General Considerations	VI-C-18
b. Gas Induced Swelling in Boron Carbide	VI-C-19
3. Effect of Irradiation on the Mechanical Properties of Steel	VI-C-23
4. Transmutation Effects in 316 SS	VI-C-39
5. Surface Effects	VI-C-47
a. Sputtering	VI-C-47
b. Blistering	VI-C-70
D. Specific Effects in UWMAK-I Blanket	VI-D-1
1. Swelling	VI-D-1
a. Void Swelling in 316 SS	VI-D-1
b. Gas Bubble Swelling in 316 SS	VI-D-11
2. Mechanical Property Changes in 316 SS	VI-D-13
a. Changes in Yield Strength	VI-D-13
b. Loss of Ductility in UWMAK-I Heat Removal Cells	VI-D-18
3. Transmutation Effects in 316 SS for UWMAK-I First Wall	VI-D-20
4. Surface Effects - UWMAK-I First Wall	VI-D-21
E. Specific Swelling Effects in B_4C for UWMAK-I Shield	VI-E-1
F. Radiation Damage to Magnet Components	VI-F-1
1. The Magnet Conductor	VI-F-1
a. Superconducting Materials	VI-F-1
b. Stabilizing Material	VI-F-6
c. Modifications to Conductor Design	VI-F-10
d. Heat Deposition from Irradiation	VI-F-15
2. Polymeric Materials	VI-F-15
a. General Considerations	VI-F-15
b. Limitations in UWMAK-I	VI-F-16
3. Conclusion	VI-F-20
G. Summary of Limitations on UWMAK-I Power Levels Due to Radiation Damage	VI-G-1
VII. Magnets	
A. Toroidal Field Magnet	VII-A-1
1. Specifications and Description of the Magnet Design	VII-A-1
a. Specifications	VII-A-1
b. Description of Components	VII-A-1
c. Materials Required for 12 Magnets	VII-A-2
2. Construction Techniques	VII-A-6
a. Conductor	VII-A-6
b. Discs	VII-A-6
c. Assembly of discs	VII-A-7
d. Structural assembly	VII-A-7

	<u>Page</u>
3. General Restraints and Design Factors	VII-A-7
a. Introduction	VII-A-7
b. Stress Analysis and Design Procedure for Magnet Windings and Reinforcement	VII-A-8
c. Conductor Thermal, Mechanical and Electrical Design	VII-A-20
4. Magnetic Field Calculation	VII-A-27
a. Computer Code MAFCO-W	VII-A-27
b. The Magnetic Field Structure for UWMAK-I	VII-A-36
5. Magnet Support and Handling System	VII-A-36
B. Transformer and Divertor Coil Design	VII-B-1
C. Refrigeration Systems	VII-C-1
1. Description	VII-C-1
2. Losses	VII-C-1
3. Costs	VII-C-3
D. Power Supplies	VII-D-1
1. Toroidal Field Magnets	VII-D-1
2. Divertor and Transformer Magnets	VII-D-1
E. Cost Estimate	VII-E-1
1. Toroidal Field Magnets	VII-E-1
2. Divertor and Transformer Magnets	VII-E-1
3. Refrigeration System	VII-E-2
4. Power Supplies	VII-E-3
5. Total Cost	VII-E-3
VIII. Tritium	
A. Release Rates	VIII-A-1
1. Factors Affecting Release Rates	VIII-A-1
2. Basis for Selecting Tritium Release Rates	VIII-A-4
3. Tritium Release Rates	VIII-A-5
B. Breeding Ratio and Inventory	VIII-B-1
1. Summary of Heat Exchanger Design	VIII-B-1
2. Inventory in the Primary System	
3. Inventory, Breeding Ratio and Doubling Time	VIII-B-5
C. Tritium Extraction	VIII-C-1
1. Comparison of Hydride (Tritide) Stabilities	VIII-C-1
2. Isotope Effects on Hydrogen Reactions and Hydride Properties	VIII-C-4
3. Discussion of Alternative Tritium Extraction Methods	VIII-C-4
4. Tritium Extraction in the UWMAK-I System	VIII-C-5
a. Assessment of Yttrium as a Tritium Extraction Bed Material	VIII-C-5
b. Effect of Radioactivity on Yttrium Hydride	VIII-C-8
c. Yttrium Hydride Ignition Characteristics	VIII-C-8
5. Tritium Extractions Systems	VIII-C-8
a. Primary Lithium System	VIII-C-8
b. Secondary Sodium System	VIII-C-11
c. The Divertor Lithium Coolant	VIII-C-13
d. Helium Circuit	VIII-C-15
e. Divertor Vacuum Pumps	VIII-C-16

	<u>Page</u>
IX. Safety	
A. Magnet Failure	IX-A-1
B. Radioactivity	IX-B-1
1. Radioactivity Build-up in a SS Blanket	IX-B-1
a. Method of Calculation	IX-B-1
b. Time Dependence of Radioisotope Generation	IX-B-3
c. Time Dependence of Radioisotope Decay	IX-B-3
d. Nature of Activity	IX-B-8
2. Radioactivity of Alternate Blanket Structure	IX-B-10
C. Afterheat	
1. Afterheat from a SS Blanket	IX-C-1
a. Afterheat from a SS Blanket	IX-C-1
b. Time Dependence of Afterheat Generation	
c. Time Dependence of the Afterheat Following Shutdown	IX-C-3
d. Spatial Dependence of the Afterheat	IX-C-3
2. Afterheat in the Shield and Magnet Region	IX-C-5
3. Temperature Rise Following Loss of Coolant Flow	IX-C-5
4. Afterheat from Alternate Blanket Structures	IX-C-5
D. Lithium Fires	IX-D-1
1. Conditions to Ignite Lithium in Air	IX-D-1
2. Conditions to Ignite Sodium in Water	IX-D-2
3. Measures to Prevent Lithium Fires	IX-D-2
4. Measures to Control Lithium Fires	IX-D-3
X. Power Cycle	X-1
XI. Overall Containment	To be published in Volume 2
XII. Economics	"
XIII. Environmental Impact	"
XIV. Conclusions	
A. Plasma	XIV-A-1
B. Divertor	XIV-B-1
C. Magnets	XIV-C-1
D. Neutronics and Photonics	XIV-D-1
E. Blanket and Shield	XIV-F-1
F. Radiation Damage	XIV-F-1
G. Tritium	XIV-H-1
H. Safety	XIV-H-1
XV. Recommendations	XV-A-1
XVI. Appendices	XVI-A-1

I. Introduction

The recent advances in magnetic confinement of hot plasmas have generated considerable optimism regarding the prospects of generating electrical power from the controlled fusion process. Much of this optimism is based on the success of the Tokamak confinement concept. Given these steps forward, it is proper and timely to begin serious studies of the technological aspects of power generation from the fusion process. In 1972, a group of scientists and engineers at the University of Wisconsin initiated a design study of a large electrical power generating station based on the Tokamak concept and fueled with deuterium and tritium. The goal has been to develop a self consistent study from the standpoint of plasma physics, neutronics, materials, magnets, power cycle, environment, resources, and cost. In this paper, we summarize the design features of a 5000 MW_{th} D-T Tokamak conceptual power reactor called UWMAK-I (University of Wisconsin Tokamak). A much more detailed description of this study is described in a University of Wisconsin report.⁽¹⁾

II. Details of the Conceptual Design

The UWMAK-I is based on the Tokamak confinement concept⁽²⁾ and has been designed with the philosophy that decisions should be made, whenever possible, on present-day technology capabilities. This means invoking as little extrapolation of present-day capabilities as is possible. The goal has been to perform a scoping study in sufficient detail to uncover potential technological problems that may be important as the CTR effort increases and the goal of fusion power comes closer.

The basic power parameters of UWMAK-I are summarized in Table 1. The reactor operates with a D-T plasma and has a double-null, axisymmetric poloidal divertor. Overall views of the plant are shown in Figures 1 & 2 and a detailed cross section view of the reactor is shown in Figure 3.

The reactor has been sized by optimizing the cost per unit power in a β -limited system, where the costs are assumed to scale as the magnet costs. Constraints imposed by an air-core transformer with superconducting windings have been included. From these studies, the power output from UWMAK-I is set at 5000 MW_T. The aspect ratio is 2.6 with the wall loading limited to 1.25 MW/m² by radiation damage. The minor radius is determined to be 5 meters and the torus major radius, 13 meters.

Reactor startup makes use of an air-core transformer with superconducting windings, a configuration most consistent with the small aspect ratio demands of cost optimization. The transformer and divertor coil currents are programmed to rise with the plasma current producing a time changing flux through the plane of the plasma. For UWMAK-I, the divertor actually provides 60% of the flux needed to energize the plasma current so that the transformer proper need provide only 40%. The current in the plasma rises in

UWMAK - I OPERATING CHARACTERISTICS	
POWER	5000 MW _f 1500 MW _e
FUEL CYCLE	(D-T) , Li
DIMENSIONS	R=13m, a=5m
DIVERTOR	POLOIDAL, DOUBLE-NULL
COOLANT	LITHIUM
STRUCTURAL MATERIAL	316 SS
NEUTRON WALL LOADING	1.25 MW/m ²
MAGNETIC FIELD	B _f ^o = 3.82 T B _f ^{max} = 8.66 T
MAGNETS (SUPERCONDUCTING)	NbTi + Cu CRYOGENICALLY STABILIZED
POWER CYCLE	Li-Na-STEAM

Table 1

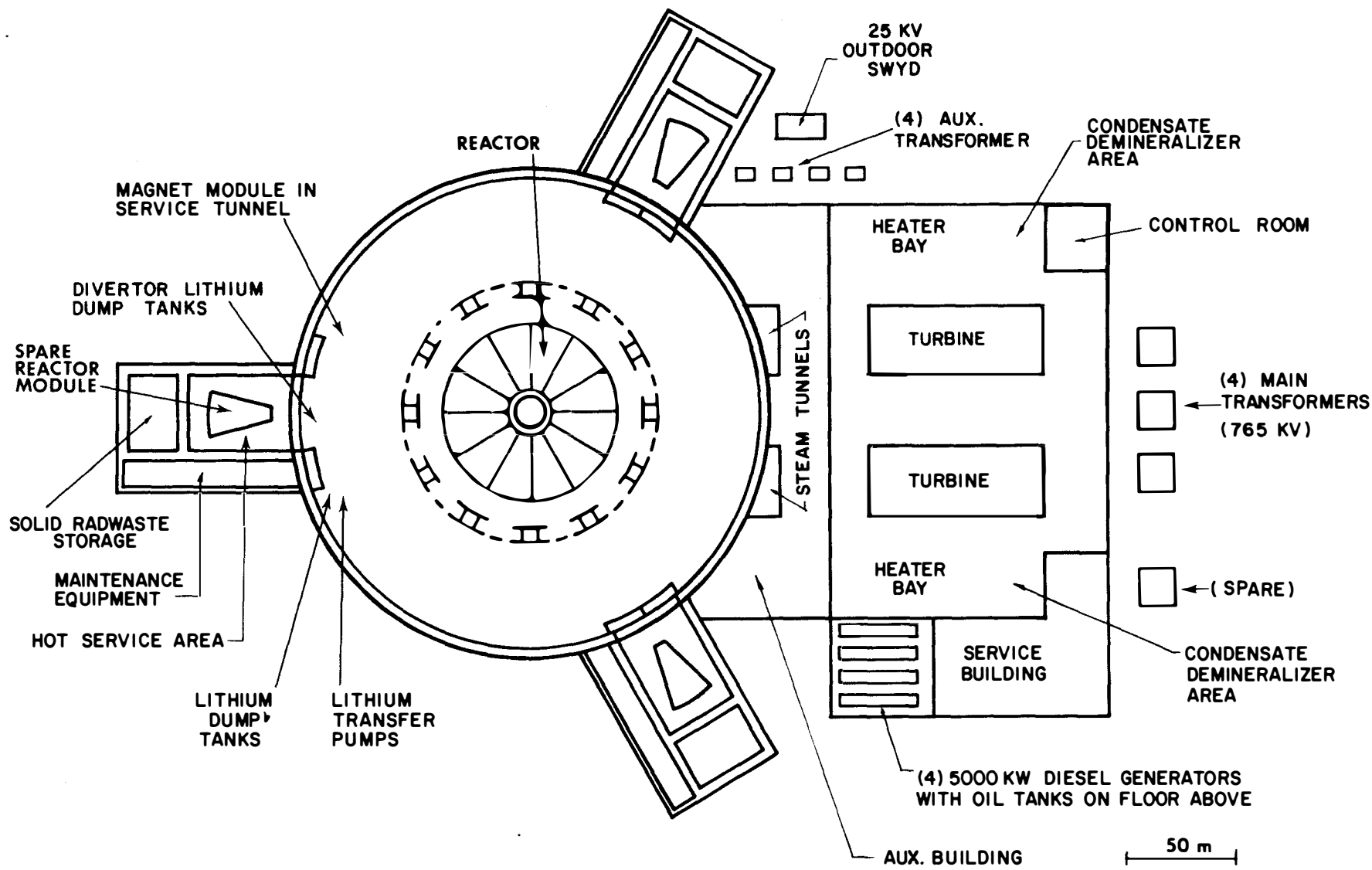


FIGURE 1 - Top View of UMAK-I Reactor Building

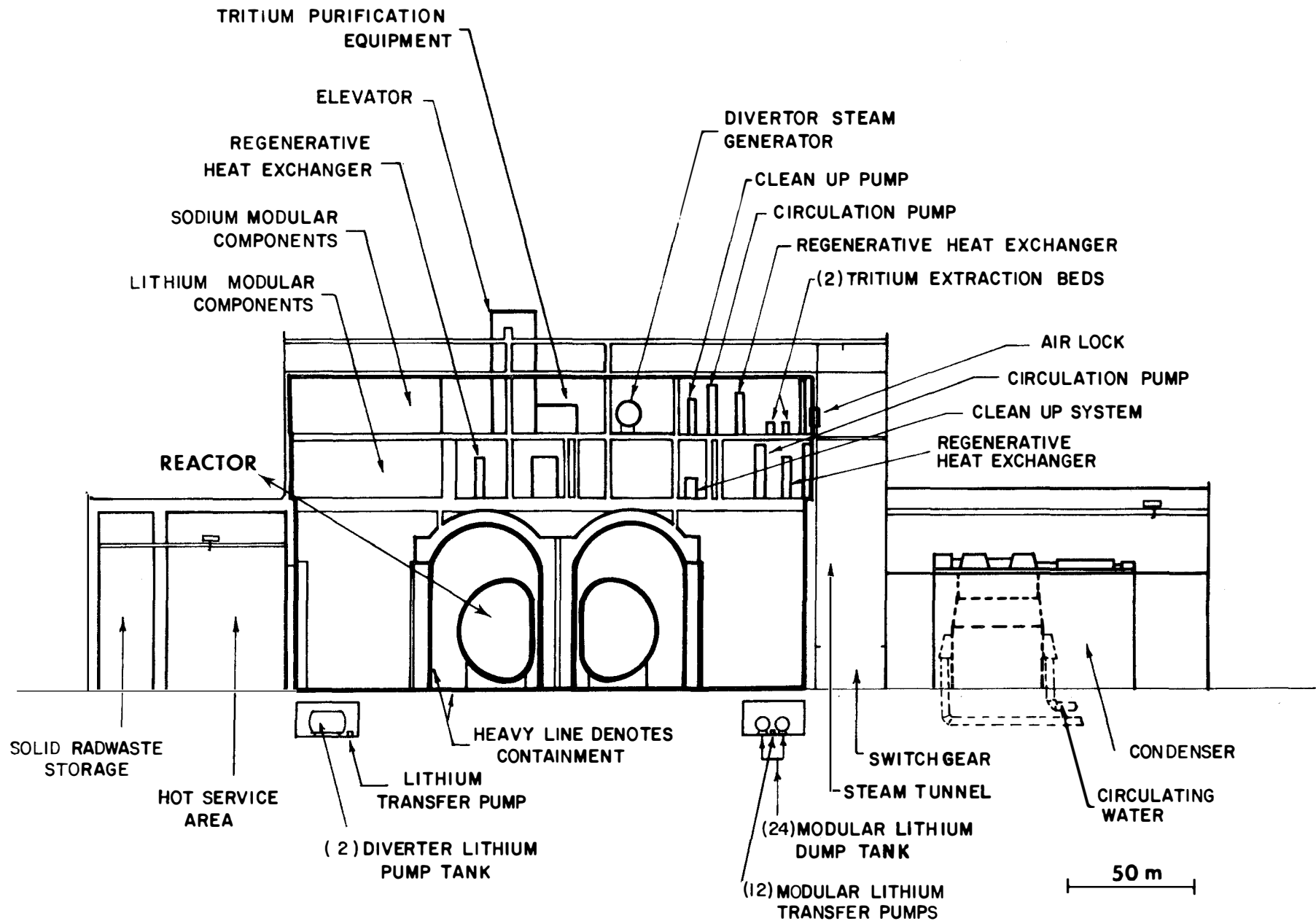
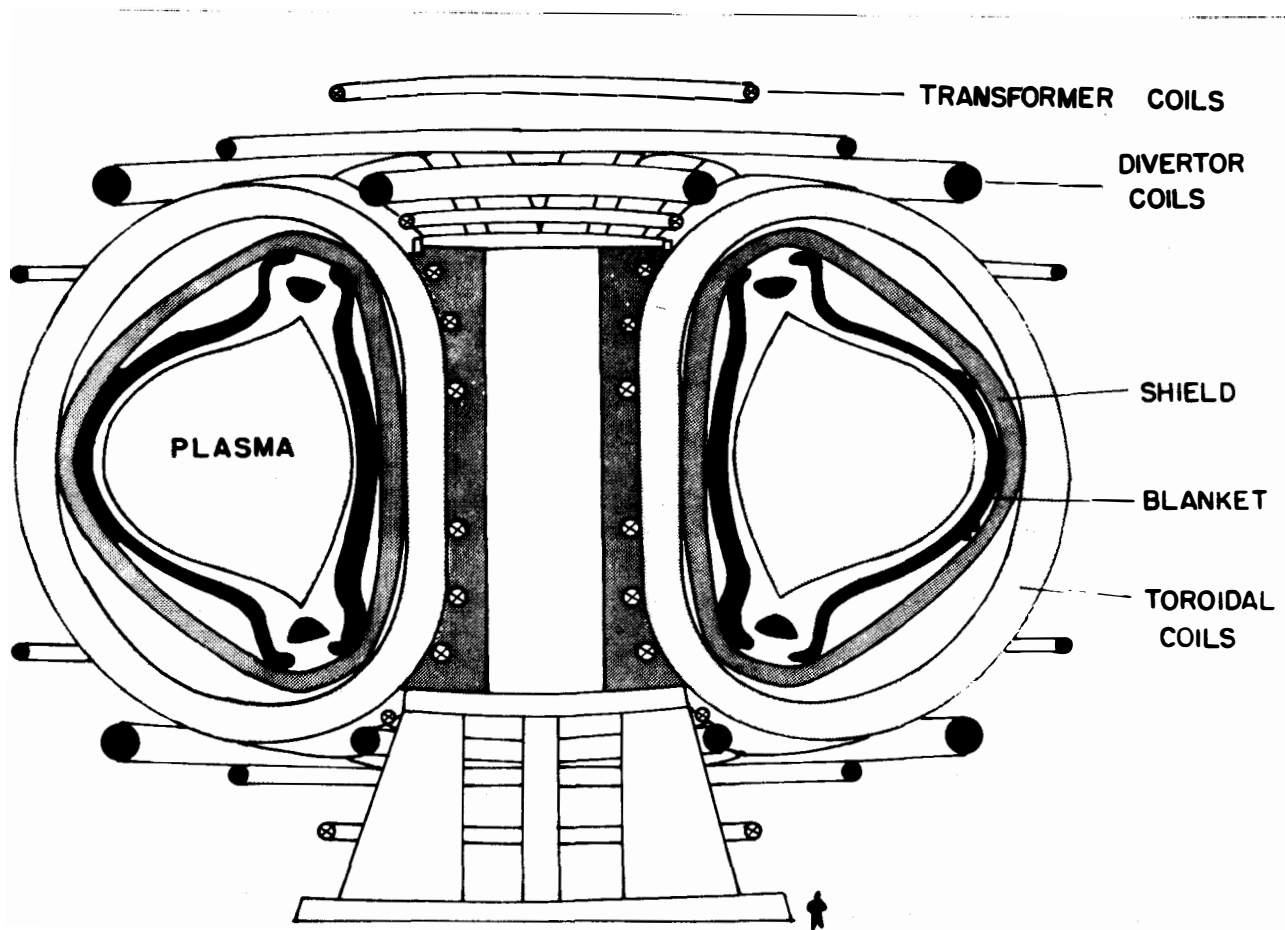


FIGURE 2. . Cross Section of UWMAK-I Reactor Building

FIGURE 3
Cross Section View of UWMAK-I Fusion Reactor



a controlled manner to its operating value of 20.7 Mamps in 100 seconds. A total of 430 volt-seconds are required to energize the plasma current. After the poloidal field of the plasma current soaks through the surrounding structure, the core flux is held constant if there is a bootstrap current⁽³⁾. However, this has not been assumed. Rather, the resistivity has been assumed to be anomalously high by a factor of 3.5 relative to the Spitzer resistivity. This implies an extra 330 volt-seconds for a 90 minute burn time and a total volt-second requirement of 760.

The operating cycle of UWMAK-I is given in Table 2. The burn time of 5400 seconds (90 min.) compares with a total recharge time of 390 seconds (6.5 min.). This gives a duty factor of 93.3% for the operating cycle. However, the plant factor is closer to 80% when scheduled outages are included. This is discussed shortly.

Plasma heating to ignition is via the use of neutral beams. Ohmic heating alone is insufficient. Neutral beams of 500 KeV injected tangent to the magnetic axis, penetrate the UWMAK-I plasma when a low density startup is used. (Initial ion density on axis is $3 \times 10^{13}/\text{cm}^3$.) With tangential injection, all ionized neutrals are on circulating orbits. The profile of power deposition per plasma particle is peaked on axis. The beams are turned on immediately after the plasma current has risen to its final value. Using 500 KeV beams and 15 MW of power, the plasma ignites in 11 seconds. Faster startups can be achieved by using more power but this is not advantageous in UWMAK-I. In the 500 KeV beam case, 99.5% of the beam is trapped in the plasma. Thus, neutral beam heating appears to be an effective way to ignite a large, power producing reactor such as UWMAK-I. The injection geometry and a graph of power deposited per plasma particle by a 500 KeV beam versus radius is shown in Figure 4. A table of beam power and associated times to ignition are given in this figure.

The neutral beam heating is to be accomplished using 10 deuterium atom beams and 10 tritium atom beams. The 500 KeV D^0 beam is produced by starting with a 1.5 KeV D^+ beam produced in a scaled version of the duopigatron. To produce the 1.5 amperes equivalent of deuterium atoms, a 2.14 ampere negative deuterium ion beam is required. This beam is produced by passing a 1.5 KeV deuterium beam through a series of cesium gas cells and accelerating D^- in this way. The 500 kV acceleration requires five electrodes with 2125 aligned 3 mm holes on 19.5 cm diameter electrodes. The sources discussed in reference 1 represent an extrapolation of existing technology, especially as far as beam power and pulse length are concerned. Also, the area of negative ion sources is still in its infancy and the 19.5 cm size of the electrodes is a considerable increase of existing sources.

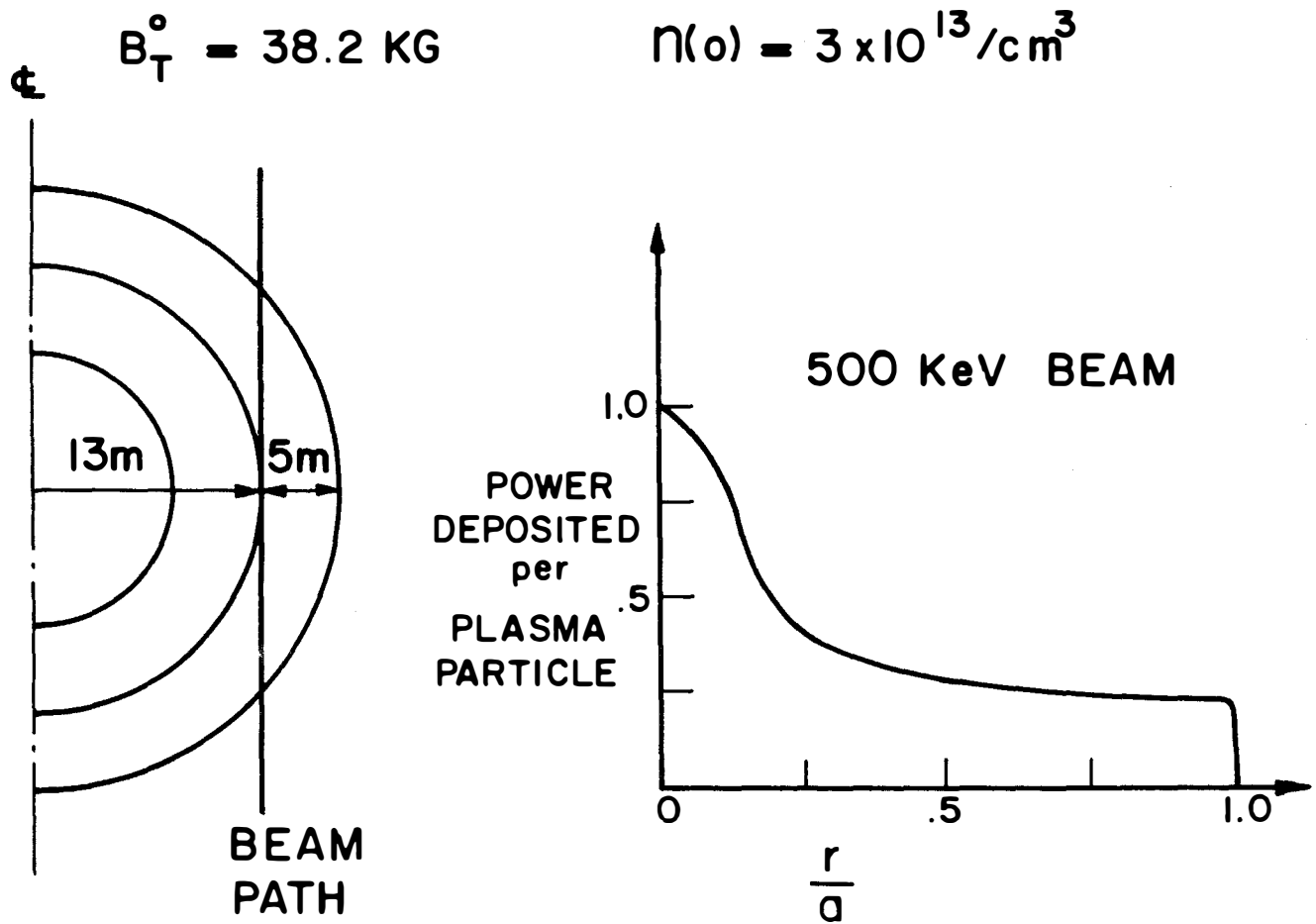
Once ignited, the plasma is assumed to rise in ~10 seconds to the operating conditions listed in Table 3. If the scaling is quasi-classical (that is, the diffusivity varies as $T^{-1/2}$ but contains an

TABLE 2

START UP, BURN, AND SHUT DOWN
SEQUENCE FOR UWMAK-I

<u>TIME-SEC.</u>	<u>EVENT</u>
0-100	GAS BREAKDOWN, CURRENT RISE PHASE OHMIC HEATING
100-111	HEATING BY NEUTRAL BEAM INJECTION TO IGNITION
111-120	INCREASE TO FULL POWER FROM IGNITION
120-5520	THERMONUCLEAR BURN, PELLETT FUELING
5520-5530	PLASMA COOL DOWN BY IMPURITY INJECTION
5530-5630	SHUTDOWN PLASMA CURRENT AND REVERSE TRANSFORMER AND DIVERTOR COILS
5630-5680	EXHAUST CHAMBER
5680-5780	COMPLETE CURRENT REVERSAL IN TRANSFORMER
5780-5790	PURGE RESIDUAL GAS - REFILL WITH FRESH (D+T) FUEL

LOW-DENSITY STARTUP WITH NEUTRAL BEAMS



EXAMPLES:

POWER (MW)	TIME TO IGNITION (sec)
15	11.0
30	5.3
50	3.6
75	2.2

Figure 4

PLASMA PARAMETERS
(Unstable Equilibrium Point)

$$T_{\text{ions}} = 11.1 \text{ KeV}$$

$$q(a) = 1.75$$

$$T_{\text{el}} = 11.0 \text{ KeV}$$

$$a = 5 \text{ m}$$

$$\bar{n}_{\text{D+T}} = 0.8 \times 10^{14} / \text{cm}^3$$

$$R = 13 \text{ m}$$

$$\bar{n}_{\alpha} = .0295 \times 10^{14} / \text{cm}^3$$

$$r_w = 5.5$$

$$\bar{\tau}_c = 14.2 \text{ sec}$$

$$A = 2.6$$

Confinement Spoiling

$$B_{\phi}^0 = 38.2 \text{ KG}$$

Factor = 450

$$B_{\theta}(a) = 8.4 \text{ KG}$$

$Z_{\text{eff}} = 3.5$

$$f_b = 7.2 \%$$

Plasma Vol. = 6400 m^3 (nominal)

$$n \tau_c = 11.35 \times 10^{14} \text{ sec} - \text{cm}^{-3}$$

Chamber Vol. = 7750 m^3 (nominal)

$$\bar{\beta}_{\theta} = 1.07$$

Wall Area = 2830 m^2 (nominal)

$$\bar{\beta}_{\phi} = .052$$

$$I_{\phi} = 21 \times 10^6 \text{ Amps.}$$

Table - 3

anomalous multiplicative coefficient relative to the classical value of the diffusivity,) then plasma operation under these conditions (2) is thermally unstable and requires feedback control. Pseudoclassical and neoclassical (5) diffusivities are cases in point. The anomalous factor, $S = 450$, in Table 3 is relative to the neoclassical value (5) of D_1 at the plasma conditions listed. The confinement time has been obtained from $\tau = a^2/4D_1$. We have suggested this operating mode because the cost of the transformer, divertor and main toroidal field coils are 55% less than for operation at a thermally stable equilibrium. (A comparison of selected parameters between thermally stable and unstable equilibria are given in Table 4.) The main toroidal magnets are estimated to cost \$83 million and the transformer and divertor coils \$70 million. The power supply for the transformer and divertor coils is ~\$66 million. Thus, a 55% increase in these costs would imply an additional 120 million dollars. It is argued that this is more than sufficient incentive to consider operation in a thermally unstable condition using feedback control, should some form of quasi-classical scaling prevail.

The UWMAK-I design imposes a conservative limit on $\bar{\beta}_\theta$ of one. Present experiments achieve a $\bar{\beta}_\theta$ of about one-half and the recent, low-aspect ratio, MHD equilibrium studies of Callen and Dory (4) give, as a best case, $\bar{\beta}_\phi \sim .1$ and $\bar{\beta}_\theta \sim 2$. For UWMAK-I, we have chosen values intermediate between these and set $\bar{\beta}_\theta \sim 1$ and $\bar{\beta}_\phi \sim .05$.

To achieve favorable operating conditions with quasi-classical scaling, energy losses from the plasma have to be increased via the addition of 0.95% argon impurity atoms. Further, as noted above, the average confinement time of ~15 sec is 2 orders of magnitude shorter than is predicted by neoclassical theory. Such reduction in confinement time, relative to neoclassical scaling, is required to both achieve a favorable power balance at $T_i = 11.1$ KeV, as listed, and to remove spent fuel (α -particles) so that a respectable (D+T) ion density can be maintained. For these operating conditions, the plasma is a low β ($\bar{\beta}_\phi = 0.052$, $\bar{\beta}_\theta = 1.07$), low field ($B_\phi = 3.82$ Tesla) reactor producing 5000 MW_T, based on a total of 20 MeV per fusion event. If the bootstrap current exists, the plasma is assumed to operate at these conditions until impurity buildup from wall erosion (because the divertor is not 100% efficient), causes excessive losses and requires shutdown and restart. Otherwise, the burn time, determined by available core flux, is 90 minutes.

The method for producing the desired operating confinement time, density, and temperature remains an unsolved problem. Recently, we have analysed plasma operation in UWMAK-I assuming the dissipative trapped ion instability (6) governs the transport. It is possible to produce thermally stable plasma equilibria in the optimal, 12-16 KeV, ion temperature range at plasma currents of about 15 M amps and confinement times of approximately 2 seconds. This short τ_c will place a significant burden on the system divertor and on the fueling requirements. These possibilities will be discussed in a future paper.

PLASMA PARAMETERS for UWMAK-I

$$\bar{\beta}_\theta = 1.08 \quad \bar{\beta}_\phi = .052$$

$$A = 2.6 \quad ; \quad q(a) = 1.75$$

THERMALLY UNSTABLE
EQUILIBRIUM

THERMALLY STABLE
EQUILIBRIUM

(Based on Anomalous Classical Scaling)

T_i (KeV)	11	28
\bar{n}_i (cm ⁻³)	$.8 \times 10^{14}$	$.367 \times 10^{14}$
f_b	7.2%	42%
τ_c (sec)	14.2	61
B_T^0 (Tesla)	3.82	4.73
RELATIVE MAGNET COST FACTORS	1.0	1.55

BURN TIME – 90 minutes

Table 4

The plasma characterized in Table 3 is assumed to be fueled during operation by injecting solid (D+T) pellets to make up for losses due to fusion and diffusion. The use of neutral beams for this purpose is highly questionable. Beam penetration is more difficult at the peak operating density of $1.2 \times 10^{14}/\text{cm}^3$ and further, the leakage rate of 3.6×10^{22} (D+T) ions/sec means that $\sim 3000 \text{ MW}_e$ of power are required when 500 KeV beams are used. Higher energy beams imply even larger power requirements and are clearly not economical. Fueling is therefore assumed to be via pellet injection, using either 20 micron radius pellets at the rate of 20×10^6 pellets per second or, if larger pellets are feasible, 2 mm radius pellets at 20 pellets per second injection rate. The former requirements are closer to current technology, assuming the plasma can withstand pellet injection in the first place.

The method for injecting such pellets to speeds sufficient for penetration of the plasma is a difficult, and essentially unsolved problem. The reason is that, based on ablation rates for single pellets, millions of volts of accelerating potential appear to be required to achieve the required pellet velocities. Given the inherently large power requirements of neutral beams for fueling purposes, the area of pellet acceleration and injection requires much further study. If it is possible to inject pellets in the 10-100 micron size and achieve penetration, then the fueling picture changes. In this case, the technology of pellet manufacture and acceleration may be at hand. Experiments to be performed by Hendricks⁽⁷⁾ on ATC should indicate, first, if the penetration depths required can be achieved and, second, whether pellet injection and the ablation process has a detrimental effect on plasma confinement.

We note that if Tokamaks have confinement times of ~ 10 seconds, they will require fueling for economical operation. The main reason for this is the relatively long start-up times required by Tokamaks to reduce the stored energy requirements to acceptable levels. For example, a 100 second start-up time in UWMAK-I requires an energy storage unit of $\sim 20 \text{ MW-hr}$ and a peak power requirement of $\sim 1000 \text{ MW}_e$ during that phase of the cycle.

UWMAK-I utilizes a double neutral point poloidal divertor generated by superconducting coils outside the toroidal D-magnets. The coil locations, currents, and separatrix (plasma boundary) are shown in Figure 5. The particles diffusing from the plasma are collected by a flowing lithium surface with a trapping efficiency of 96%. The lithium flows down the face of a stainless steel plate, under gravity alone, and the flow rate of 10 kg/sec is such that no additional cooling of the backing plate is required. This is shown in Figure 6.

The use of a double null divertor is consistent with the low aspect ratio design suggested by optimization studies. It also allows the magnets to be closer to the plasma so that the maximum field at the superconductor of the main toroidal field magnets is 8.66T for 3.82T on axis. This means one can choose NbTi as the superconductor, a present-day technology choice. The difference between a double null and single null divertor in plasma shape is shown in Figure 7. The single null requires the magnets to be further from the magnetic axis and thus require a higher maximum field to produce the same field on axis. It also requires more core space so that it may require a larger aspect ratio.

UWMAK-1 DOUBLE NULL, POLOIDAL DIVERTOR

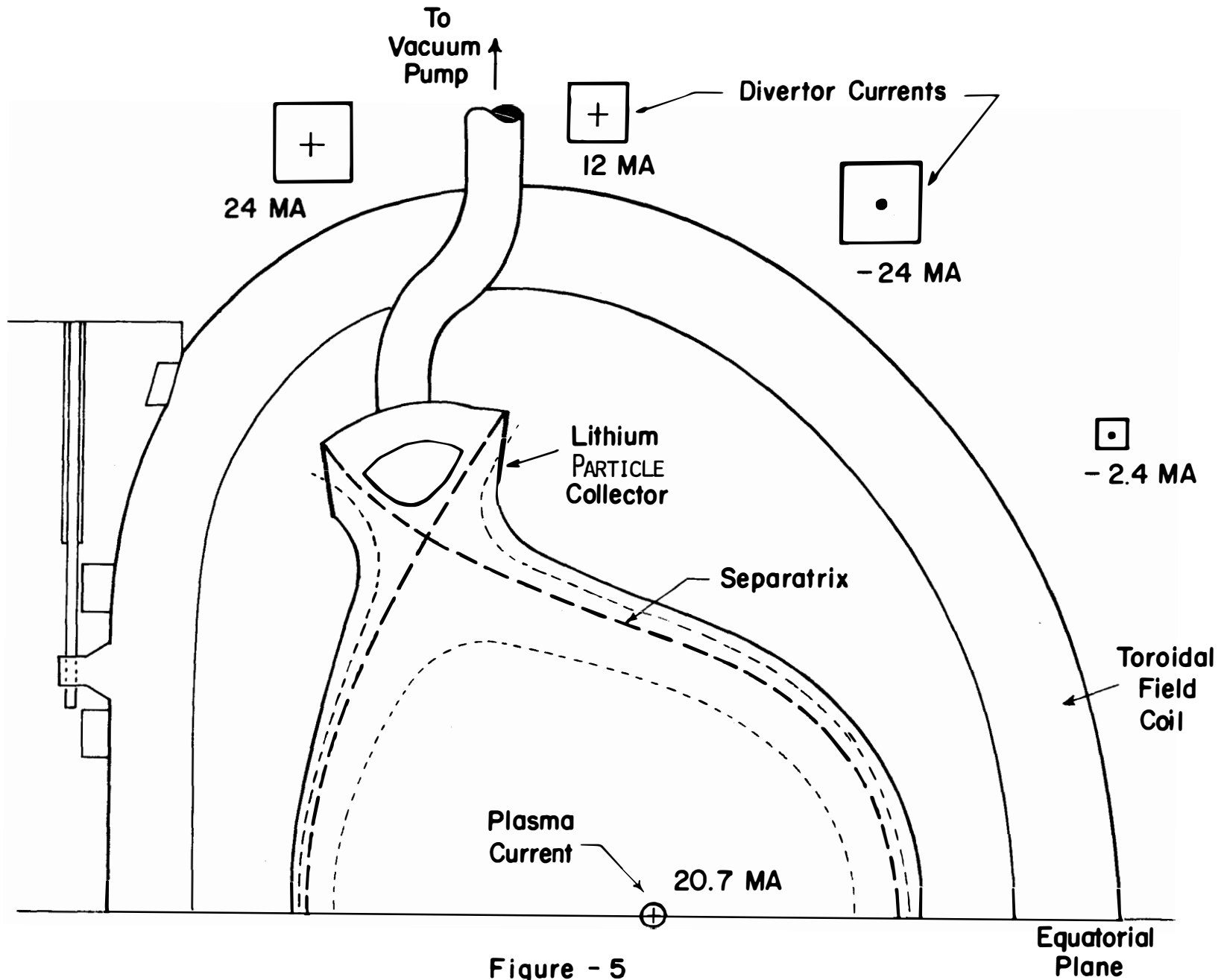


Figure - 5

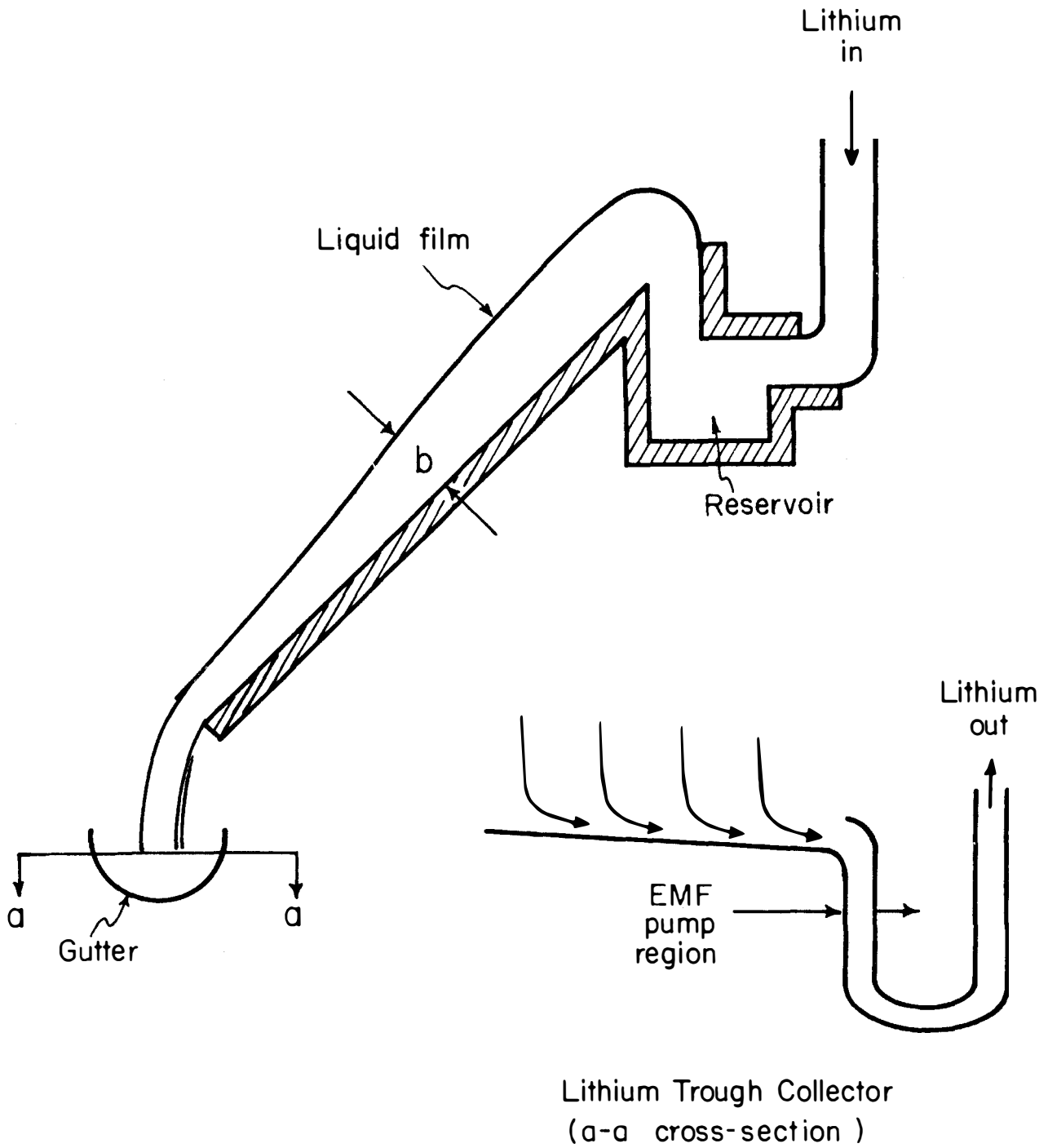


Figure 6

Schematic of One Diverter Liquid Lithium Collector Plate.

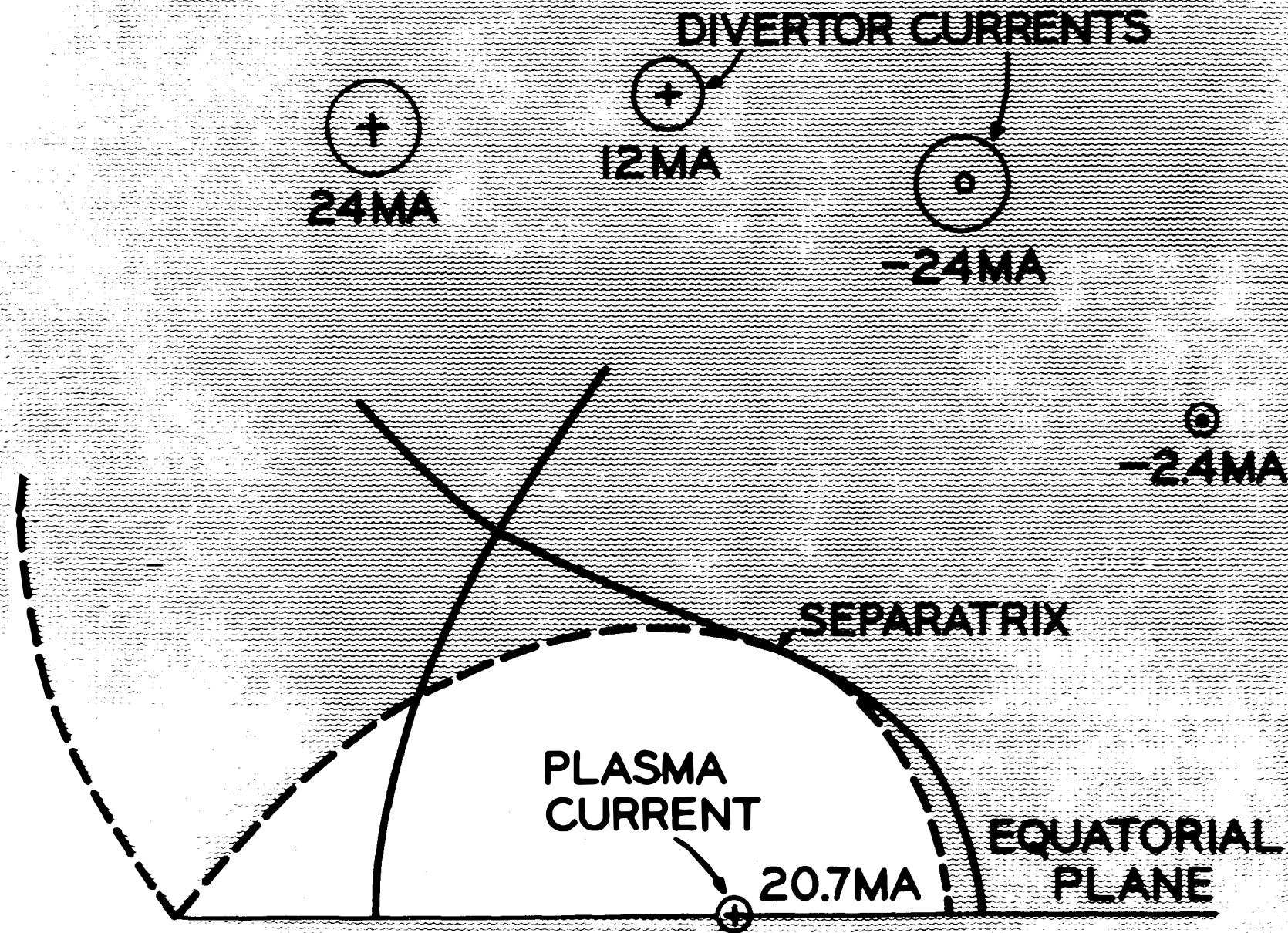


FIG. 7 COMPARISON BETWEEN SINGLE AND DOUBLE NULL POLOIDAL DIVERTORS

Each sector of the torus is to contain a complete vacuum system composed of eight 75 cm aperture mercury diffusion pumps and sixteen cryopumps. Half of the cryopumps are in operation at any given time, the other half are free for degassing. This system is backed by Roots blowers and a mechanical forepump and, in conjunction with the lithium collector surfaces, provides a pumping speed of 2.6×10^8 l/sec and a base pressure of 10^{-5} torr.

The main toroidal field magnets are superconducting using NbTi cryogenically stabilized with copper. We have concluded that such fully stabilized magnets are the most feasible and that there is no need for unstabilized magnets. The NbTi filaments are contained in a large 2 cm x 2 cm conductor and the conductor is mechanically mounted, not loosely wound. Winding with wire or tape is impossible for such large bore magnets. A list of the magnet characteristics are given in Table 5 and some of the unique features of the UWMAK-I magnets are summarized in Table 6. It is concluded that gross current densities of ~ 1000 Amps/cm² are high enough for at least 24T and that there is therefore no reason for the magnets to be unstable. Unstable magnets save only on the copper and would require a more expensive filament design.

The maximum attainable field at 4.2°K is 8.66T. By pumping on the helium, it is possible to get 10.7T at 1.8°K, still with NbTi superconductor. Thus, even operation at the plasma point requiring 4.73T on axis (as would be the case for the thermally stable plasma point in UWMAK-I) does not require new superconductor development. It is felt, however, that new conductor fabrication technology is required since wire and tape, which are now available, are unsuitable for large bore magnets such as will be required in CTR plants. To date, no large conductor production lines are known to exist.

The magnet support material is stainless steel and detailed stress calculations, such as those shown in Figure 8, have been made to guide the magnet design. An adjustable shape, constant tension design has been evolved which has a characteristic "D" shape with a high average stress in the structure. A disc design is employed which uses cooling on both sides (the conductors are embedded on both sides of the disc). The "D" shaped discs provide a solid mounting skeleton for the conductor, and provides the best structure since steel is as close as possible to the conductor.

Radiation effects in the copper can be readily countered by adding more stabilizer material so that shielding design is governed by heat deposition and refrigeration costs in the magnets. The latter costs are low, \sim \$9 million.

The supply of helium is a potential problem area. The magnet system requires 250,000 liters with 200,000 liters in storage to allow for 24 hours of operation during a refrigerator malfunction.

UWMAK-I MAGNET CHARACTERISTICS

MINIMUM BORE DIAMETER	14.8 meters
MAXIMUM FIELD AT SUPERCONDUCTOR	8.66T
SUPERCONDUCTOR	Nb Ti
STABILIZER	Cu
SUPPORT MATERIAL	S.S.
MAXIMUM STRESS IN STEEL	4220 $\frac{\text{kgf}}{\text{cm}^2}$ (60,000 psi) at 4.2°K
MAXIMUM STRAIN IN COPPER	.002
TOTAL AMPS PER CONDUCTOR	10212 AMPS
CONDUCTORS PER DISC	60
DISCS PER MAGNET	34
NUMBER OF MAGNETS	12
GROSS CURRENT DENSITY	1318 AMPS /cm ²

Table 5

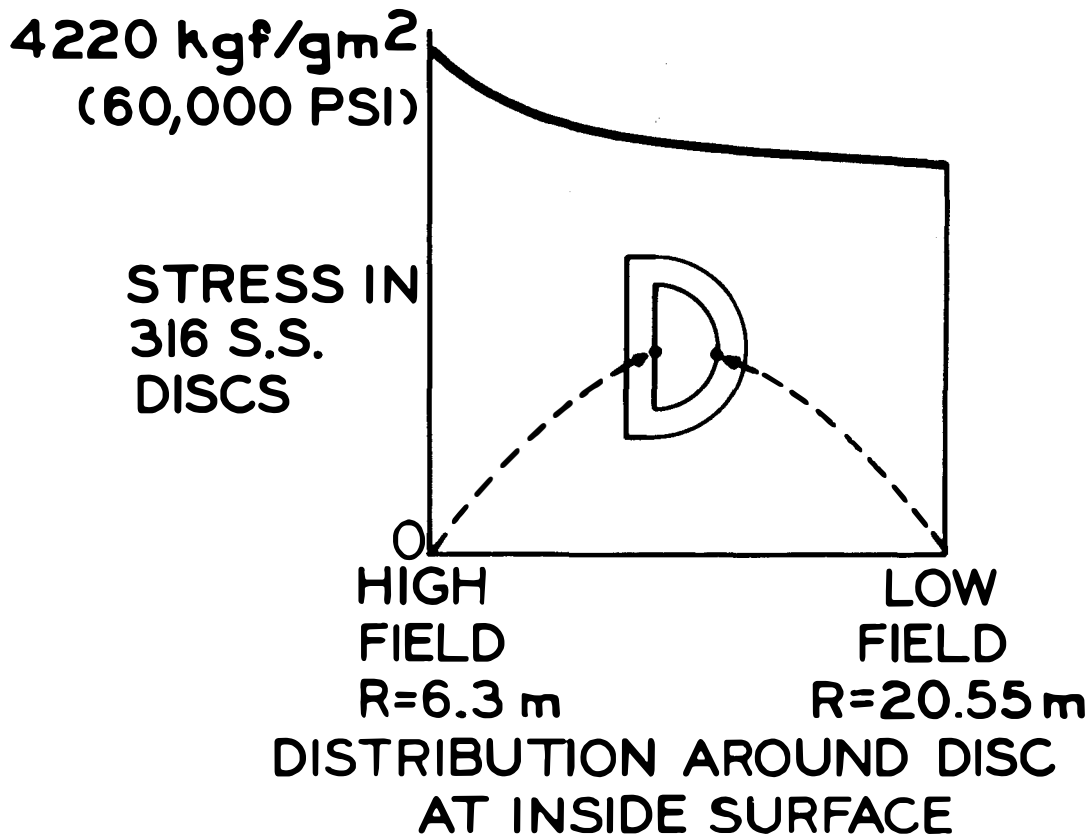
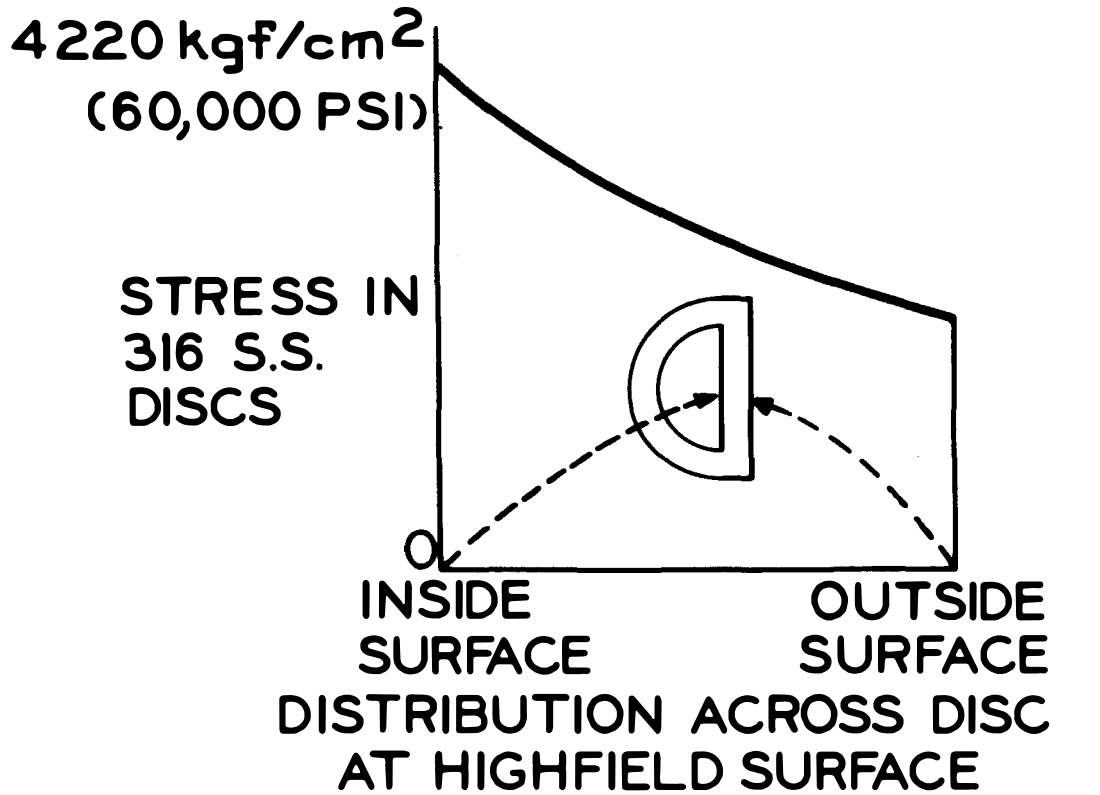
UNIQUE UWMAK-I MAGNET FEATURES

1. FULLY STABILIZED MAGNET (COPPER)
2. Nb Ti SUPERCONDUCTOR FILAMENTS IN
LARGE 2 cm x 2 cm CONDUCTOR
3. FORGED, PANCAKE DESIGN
4. DESIGNED TO $\frac{2}{3}$ YIELD POINT of ST. STEEL AFTER
DETAILED STRESS ANALYSIS
5. ADJUSTABLE SHAPE, CONSTANT TENSION DESIGN
6. MATERIALS AND MAGNET CONSTRUCTION COSTS

a. Nb Ti	5%	d. Fabrication & Assembly	41%
b. Copper	22%	e. Refrigeration	4%
c. St. Steel	28%		

Table 6

FIG. 8
STRESSES IN UWMAK-I MAGNETS



The power supply for the transformer and divertor coils is a major cost item and has not yet been designed in detail. However, energy storage for 100 second pulses will probably be via superconducting magnets. Preliminary estimates reveal that a 18 MW-hr unit coupled with a Graetz Bridge would be required.

The blanket of UWMAK-I is shown schematically in Figure 9 and the operating characteristics are listed in Table 7. It is 73.5 cm thick and separated from the 77 cm thick magnet shield by a 1 cm vacuum gap to allow for thermal insulation.

The coolant, moderator, and breeding material is lithium. The general flow pattern of the Li in the heat removal cells is shown in Figure 10. The lithium enters the reactor at 283°C and leaves at 483°C. This relatively low temperature is dictated by the corrosion rate of Li on the structure material, 316 stainless steel (SS). The maximum operating temperature of the 316 SS is limited to <500°C and this means that 1500-2500 kg of metallic corrosion product must be removed from the primary lithium circuit per year. The coolant cleanup is necessary to avoid plugging the primary heat exchanger and high radioactivity levels in the maintenance areas. The maximum pressure in the Li coolant is 28 kgf/cm² at the reactor inlet and drops to 21 kgf/cm² at the first wall of the blanket. The total power required to pump the Li is 22 MW_e, or ~1.5% of the plant output. This number is quite low due to the present design which reduces the average coolant velocity and avoids excessive eddy current losses.

The structural material chosen for UWMAK-I is 316 SS. This choice is consistent with our design philosophy to use present day technology whenever possible. The steel industry has a long established record of providing large quantities of high quality fabricated components. Recently, the quality assurance procedures of the industry have been upgraded further to produce nuclear grade components for the LMFBR program. There is a wealth of thermal, mechanical, chemical, neutronic, physical and economic data on 316 SS both in liquid metal and irradiation environments. No such data exists for refractory metals nor is there an established industry for these metals at the present time or in the foreseeable future. The choice of 316 SS does limit the operating temperature to 500°C because of corrosion, but if that were not the case, a maximum temperature of 650°C could not be exceeded because of excessive creep. Hence, our design philosophy has been to limit the 316 SS temperature to <500°C at all points in the reactor. Such a decision means that the efficiency of the reactor will probably be limited to ~30%. The maximum stress in the 316 SS is calculated to be about 914 kgf/cm² at the first wall.

The first wall of the UWMAK-I blanket has been designed to be replaced every two years because of radiation induced embrittlement. The first 20 cm has been arranged in sections such as shown in Figure 11. These sections have been designed so that they are easily removed and a new section replaced in suitable hot cell facilities. The decision to replace

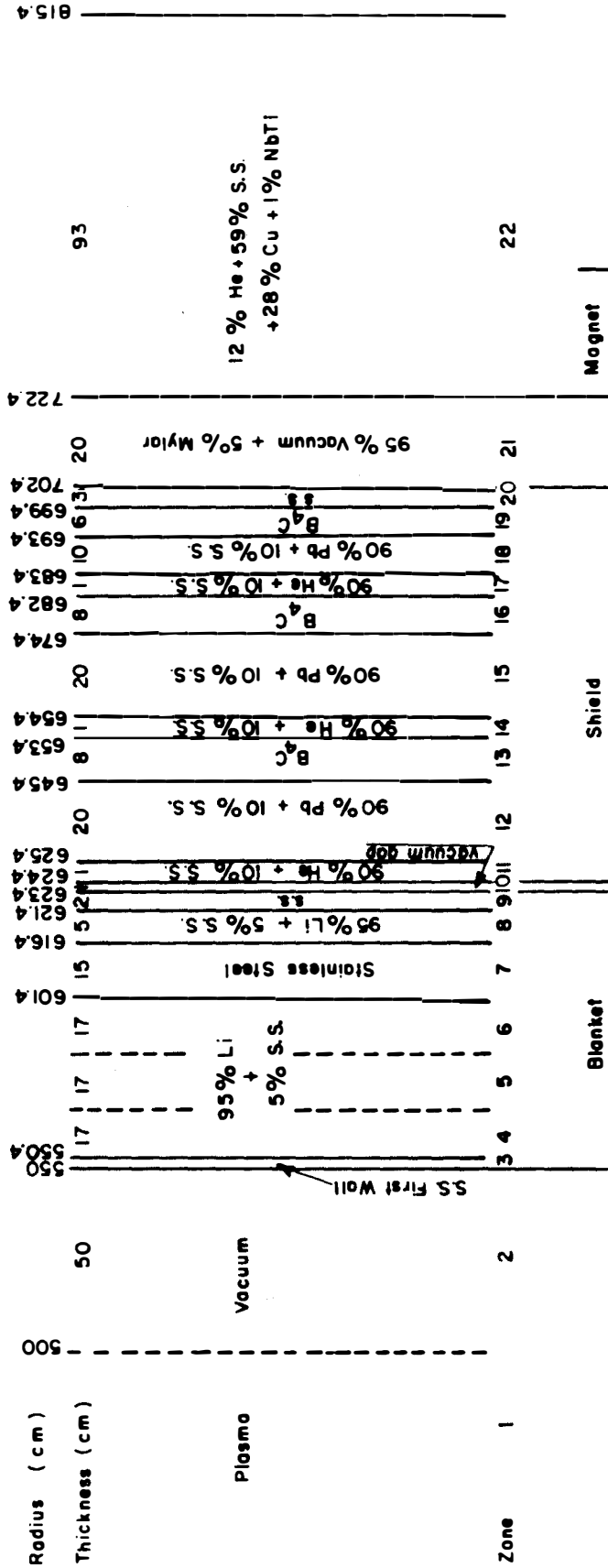
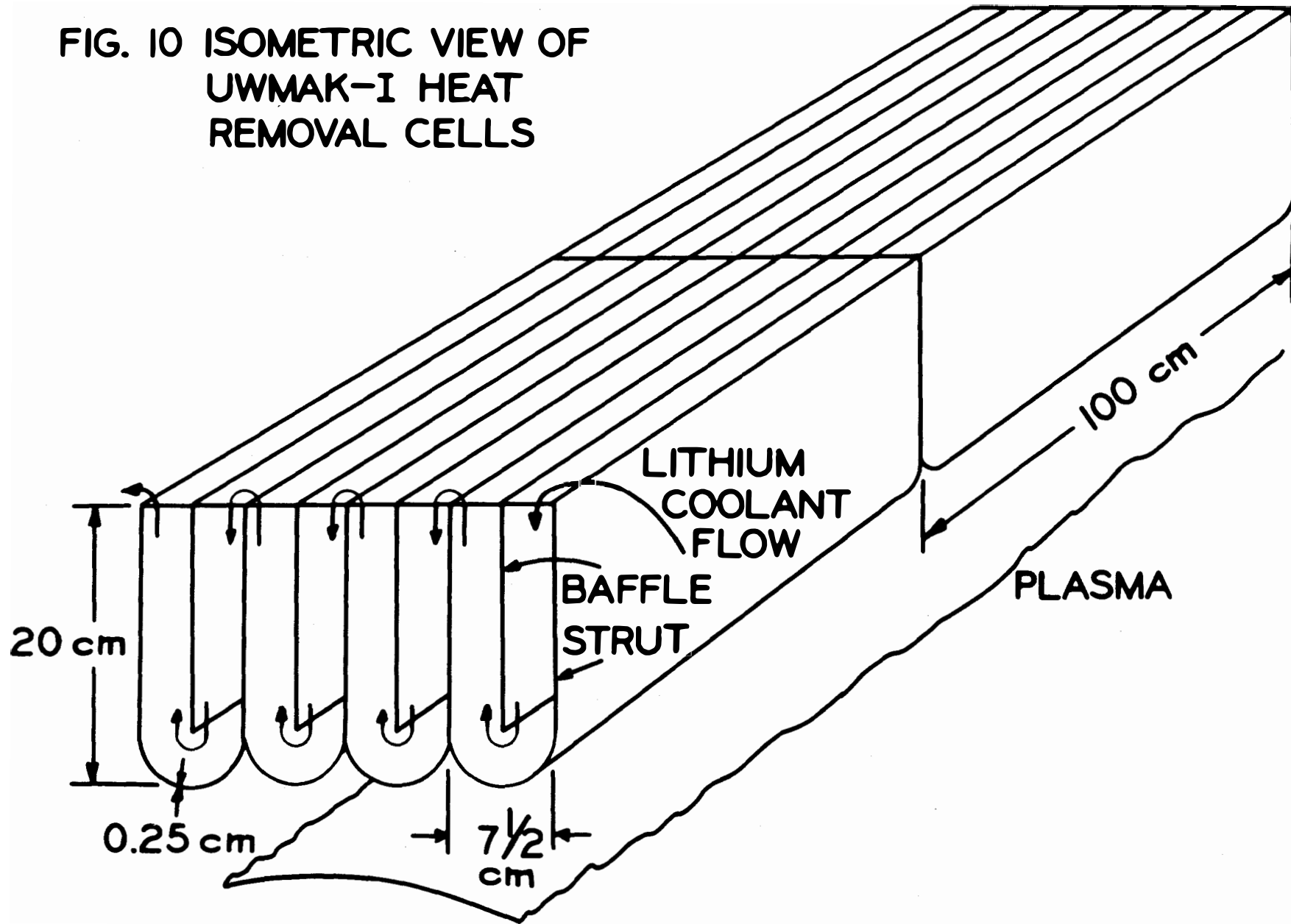


FIGURE 9 -- Schematic of UWMK-I Blanket, Shield and Magnet

BLANKET AND SHIELD CHARACTERISTICS	
DIMENSIONS -	
BLANKET	73.4 cm
VACUUM GAP	1.0 cm
SHIELD	77.0 cm
BLANKET COOLANT -	LITHIUM
PRESSURE	$28.1 \frac{\text{kgf}}{\text{cm}^2}$ (400 psig)
T_{in}	283° C
T_{out}	483° C
PUMPING POWER	22 MW _e
STRUCTURE -	316 STAINLESS STEEL
T_{max}	500° C
MAXIMUM STRESS	$914 \frac{\text{kgf}}{\text{cm}^2}$ (13,000 psi)
CORROSION RATE	1500-2500 Kg/yr
FIRST WALL -	
LIFETIME	2 years
NEUTRON WALL LOADING	1.25 MW/m ²
HEAT LOAD	12.5 watts/cm ³
SHIELD -	
COMPOSITION	B ₄ C, Pb, 316 SS
COOLANT	He, 50 atm, 200° C

Table 7

FIG. 10 ISOMETRIC VIEW OF
UWMAK-I HEAT
REMOVAL CELLS



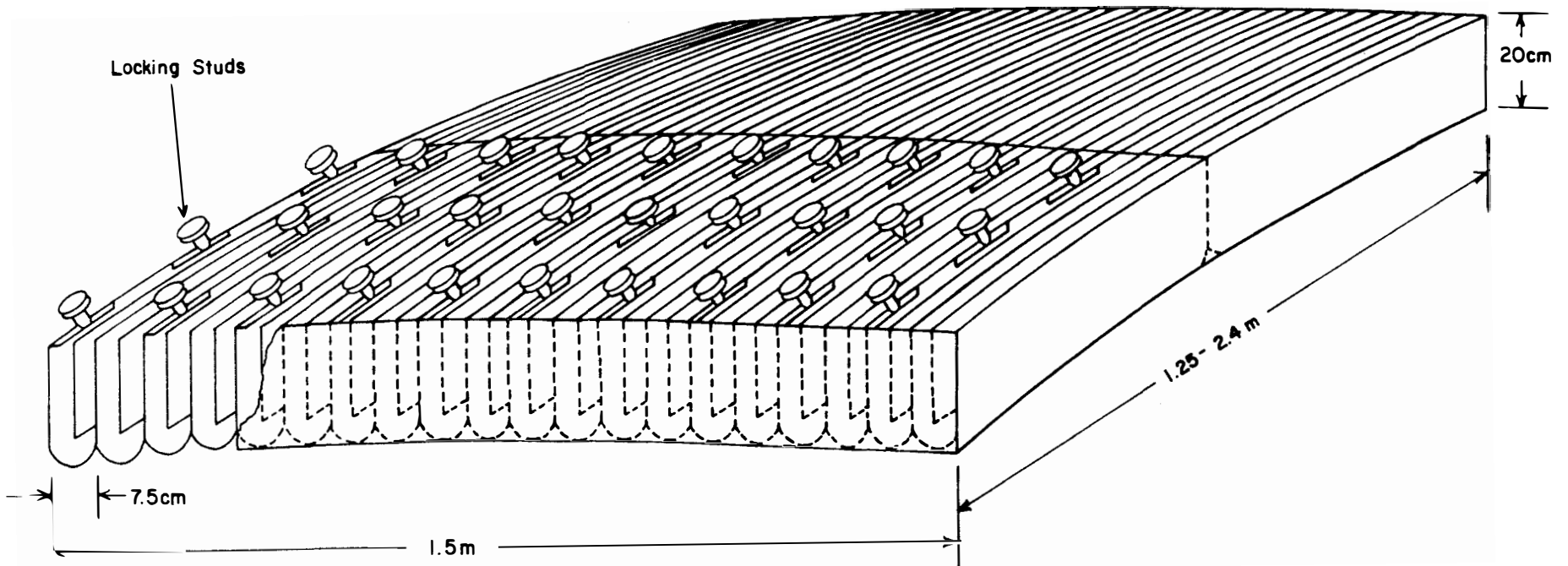


Figure 11. ISOMETRIC VIEW OF A COMPLETE SECTION OF HEAT REMOVAL CELLS
(Locking studs are shown on one half of the section only)

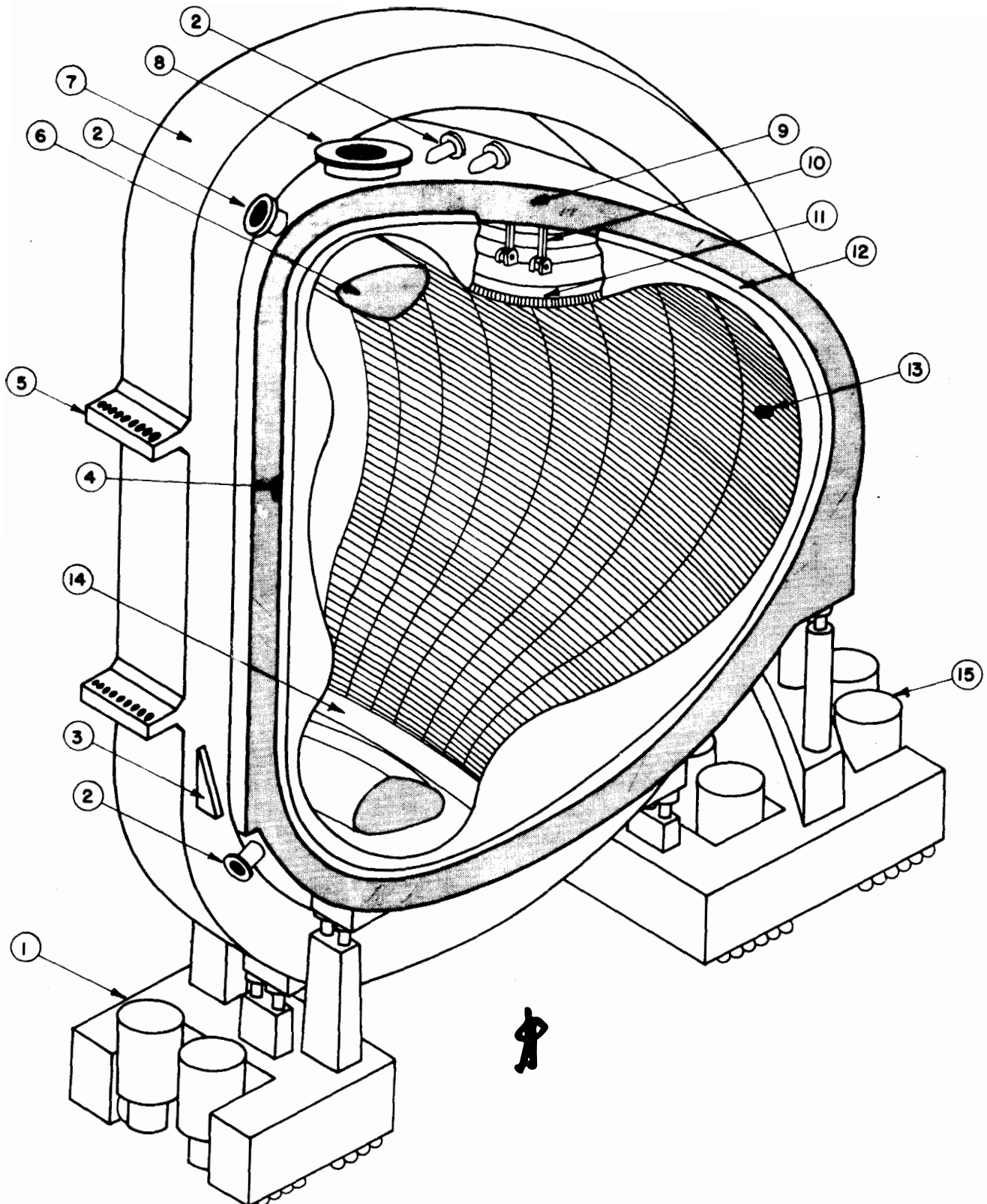
this wall every two years causes a ~6% reduction in the plant factor. Approximately 500,000 kg of 316 SS must be removed and disposed of each time the entire heat removal cells are replaced.

A complete plan for reactor disassembly has been developed and included in the overall plant layout. The reactor torus has been divided into 12 modules which can be disassembled and withdrawn into the module repair track (Figure 2,3). Figure 12 shows an isometric view of one module on its motorised vehicle. This module will be transported to a hot cell where the heat removal section (including the first wall) can be safely removed and replaced. The details on the blanket and shield disassembly can be found in Reference 1.

Finally, the shield composed of layers of B_4C and Pb and cooled with helium gas.(Figure 9) The former materials are used to slow down and absorb thermal neutrons, and absorb the high gamma fluxes from the blanket. The total heat generated in the shield is $50 MW_T$.

Neutron and photon transport calculations give a breeding ratio in UWMAK-I of 1.49 with a doubling time on the order of 2-3 months. (Table 8) The tritium breeding is likely to be adequate for all uncertainties in nuclear data or design. The energy attenuation through the blanket and shield is $\sim 4 \times 10^{-6}$. Detailed heating calculations, based on kerma factors from the MACK program⁽⁸⁾, were performed and reveal that the energy amplification of the blanket is ~17%. Figure 13 outlines the steps in performing the heating calculations and indicates the computer programs utilized. It is emphasized that with MACK and LINK, a self-consistent analysis has been performed that accurately conserves energy. It is found that 16.55 MeV of the energy are produced per 14.06 MeV neutron incident on the blanket. Thus, the total energy per fusion reaction, including the 3.52 MeV alpha energy, is 20.08 MeV. This is in contrast to values of 22-27 MeV which have been used in computing power output for fusion plants. The physical reason for this relatively low energy amplifications can be seen in Table 9. Here, an integral energy balance test which uses Q-values and reaction rates only, gives 19.92 MeV per fusion. Comparing with the 20.08 obtained by integrating over the spatial distribution of the heating shows the reliability of the calculational approach outlined in Figure 13. The presence of endoergic reactions with high Q-values has a significant impact. For example, in iron the $Fe(n,\gamma)$ reactions give 0.452 MeV but $(n,2n)$ reactions with a high threshold energy contributes negatively to the energy balance an amount, $-.585$ MeV. Thus, the energy gain expected from captures in Fe is offset by the endoergic reactions, such as $(n,2n)$ and (n,p) .

The blanket design shown in Figure 9 contains a stainless steel rather than a graphite, reflecting zone. It has been found that the steel yields higher attenuation and greater energy amplification than graphite. The shield design also shown in Figure 9 has been optimized via parametric studies with respect to composition and to thickness. The



- 1- Front motorised caterpillar
- 2- Lithium inlet or outlet
- 3- Front magnet dewar support
- 4- Front blanket support bar
- 5- Magnet support shear beam
- 6- Vacuum port shield
- 7- Toroidal magnet in its dewar
- 8- Vacuum connection
- 9- Shield

- 10- Rear blanket support rods
- 11- Heat removal cells
- 12- Blanket seal flange
- 13- Neutral beam injection port
- 14- Particle collection plate
- 15- Rear motorised caterpillar

FIGURE 12

NEUTRONIC CHARACTERISTICS OF UWMAK - I BLANKET AND SHIELD	
TOTAL ENERGY PER NEUTRON	20.08 Mev
BREEDING RATIO	1.49
DOUBLING TIME	2-3 MONTHS
ENERGY AMPLIFICATION	17.8 %
ENERGY LEAKAGE TO MAGNETS PER Mev TO FIRST WALL	4.17×10^{-6} Mev
HEAT TO FIRST WALL	1.77 MW / m ²

Table 8

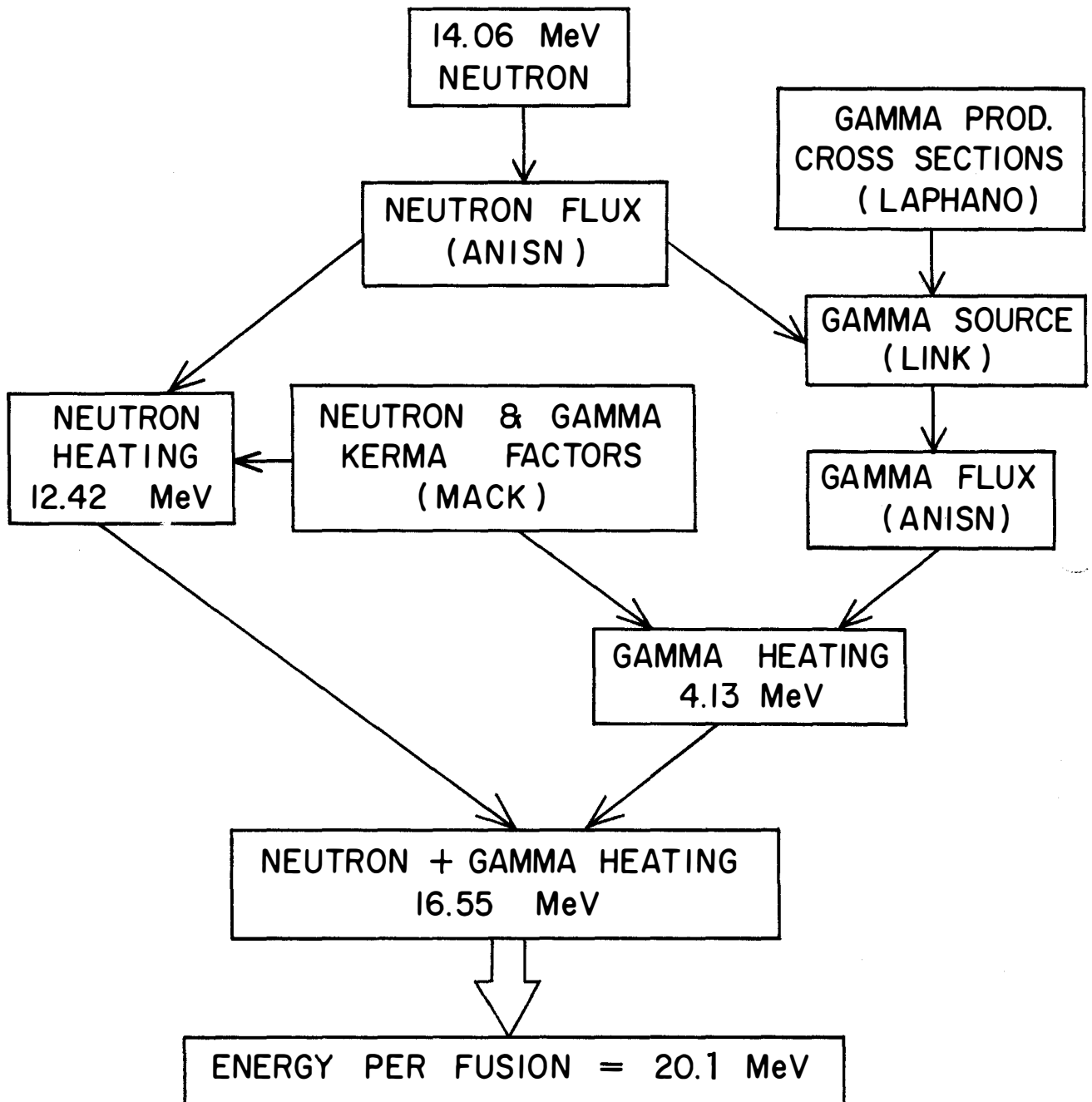
NEUTRON & GAMMA HEATING IN UWMAK-I

Figure 13

TABLE 9

MAJOR ENERGY - MASS CONVERSIONS IN UWMAK-I

$Q(\text{MeV}) \times (\text{Reaction Rate}) ; (\text{MeV} / \text{neutron incident})$

$Q = Q\text{-Value} + \text{Decay Energy}$

	(n, 2n)	(n, γ)	(n, p)	(n, d)	(n, α)	(n, n'x)	SUM
⁶ Li	-.022	.00025	-0.0019	—	4.228	-.111	+4.094
⁷ Li	-.455	0.0055	—	-0.062	—	-1.489	-2.00
Fe	-.585	.452	-0.0482	—	.0051	—	-0.1751
Cr	-.075	.206	-0.0099	—	-.0226	-.0051	+0.0931
Ni	-.0047	.1257	-.0072	—	.0031	-.0664	.051
Other materials							+0.278
Total							2.341

TOTAL ENERGY PER FUSION = (14.06 + 2.34) + 3.52 = 19.92 MeV

blanket and shield are thinner than in most previous designs and the blanket could be made thinner yet, from a neutronics viewpoint. Its size is presently limited by the requirements of blanket heat transfer. The effects of ${}^6\text{Li}$ enrichment have been investigated and found not to help the energy production. However, 4 cm of beryllium could raise energy production by ~9%.

Radiation damage studies of the UWMAK-I blanket-shield-magnet combination revealed several severe problems. Table 10 lists the major information from the present work. The most severe problem stems from the fact that the uniform ductility of the 316 SS first wall will be reduced below 1% in 2 years or less at a neutron wall loading of 1.25 MW/m^2 . This reduction in ductility extends back into the Li header and reflector region, which are 20-50 and 50-65 cm, respectively, from the first wall. (See Figure 4). It appears that the headers will have to be changed every 10 years and the reflectors every 15-20 years if one wishes to avoid costly failures during reactor operation. Such a conclusion stems from the displacement damage above and does not account for the effect of 298 atomic parts per million per year of helium nor the 636 appm per year of hydrogen generated in the 316 SS.

Swelling in the solution treated 316 SS first wall of UWMAK-I due to the production of voids was calculated to be a maximum of 7.9% after two years of irradiation. If 20% cold worked 316 SS were used, the maximum swelling value drops to 0.25%. Hence, we have decided to use the 20% CW 316 SS in the UWMAK-I design. Detailed calculations through the heat removal cells, the headers and the blanket reflector reveal that even with the use of cold worked steel, swelling values of >20% could be experienced in 30 years at 30 cm from the first wall. (see Figure 15) The coolant headers may have to be changed every 10 years and the reflectors every 15 years due to swelling as well as embrittlement.

Sputtering and blistering effects on the UWMAK-I first wall reveal that operation at the thermally unstable plasma point should not cause any severe problems due to wall erosion if the first wall is replaced every 2 years. (Figure 16) The total wall removal rates should not exceed ~0.44 mm in this time period. The major contribution to wall erosion is from the 14 MeV neutron sputtering that has been recently reported by Kaminsky(9).

Investigation of radiation induced swelling in the B_4C , transmutation of the structural alloy, degradation of thermal and electrical insulating material and reduction in superconducting properties of NbTi reveal minimal effects. Some concern arose about increased resistance in the Cu stabilizer, but proper design and periodic annealing at room temperatures can alleviate those problems.

A summary of the major integral wall loading limitations is given in Table 11. As stated above, the most limiting feature is the embrittlement

MAJOR RADIATION DAMAGE INFORMATION FOR UWMAK-I

316 SS FIRST WALL	- NEUTRON WALL LOADING 1.25 MW/m ² MAX. DISPLACEMENT RATE 18.2 yr ⁻¹ MAX. HE PRODUCTION RATE 298 appm yr ⁻¹ MAX. H PRODUCTION RATE 636 appm yr ⁻¹ T _{max.} -500°C, T -283°C UNIFORM DUCTILITY AFTER 2 YEARS-<.5% MAX. SWELLING FOR 2 YEARS 7.9% (ST 316 SS) 0.25% (20% CW 316 SS) MAX. WALL EROSION RATE 0.22 mm-yr ⁻¹ MAX. BORON ATOM BURN UP 3.2x10 ¹⁹ cm ⁻³ yr ⁻¹
B ₄ C	
Cu STABILIZER	6x10 ⁻⁵ dpa yr ⁻¹
Nb - Ti SUPERCONDUCTOR	MAX. CHANGE T _C <1°K (30 years with periodic warm up) MAX. CHANGE J _C <5% (30 years with periodic warm up)
MYLAR	MAX. EXPOSURE 2.8x10 ⁴ RAD yr ⁻¹

Table 10

FIGURE 14

ANTICIPATED UNIFORM ELONGATION REMAINING
IN 316 SS AFTER IRRADIATION IN UWMAK-1

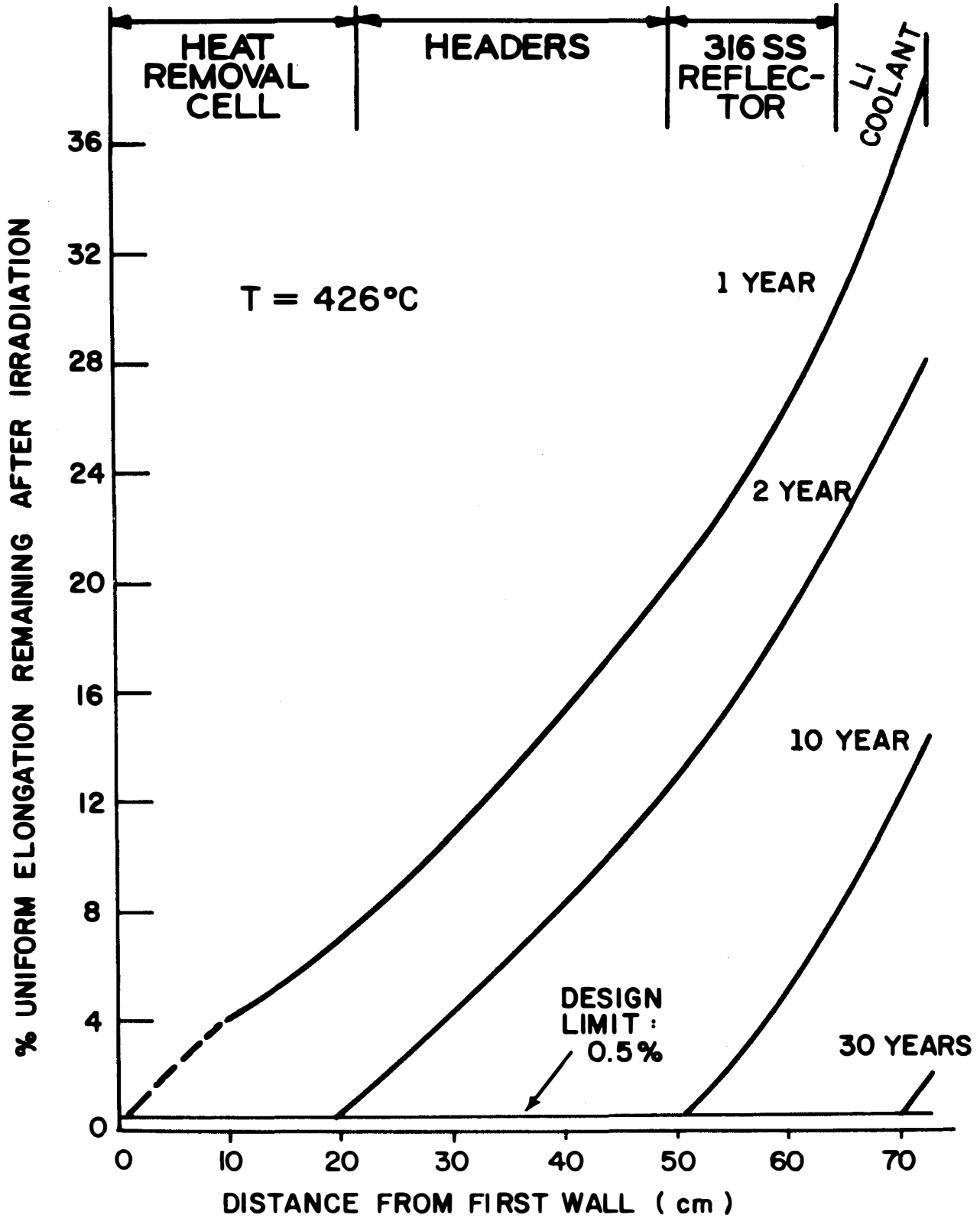
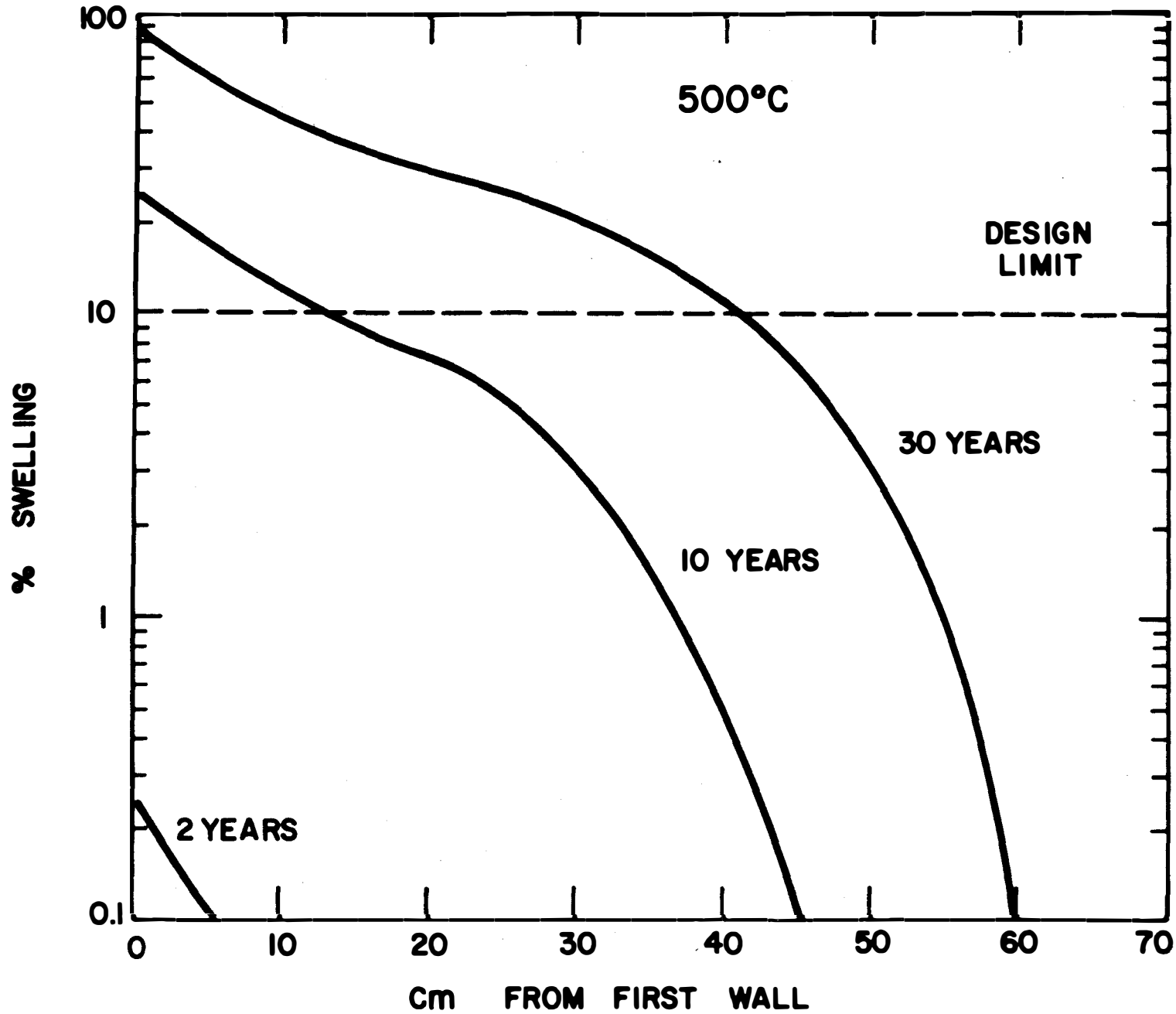


FIGURE 15

ANTICIPATED MAXIMUM SWELLING FOR 20% CW 316SS IN UWMAK-1 BLANKET



WALL EROSION OF UWMAK-I 316 SS FIRST WALL

FIGURE 16

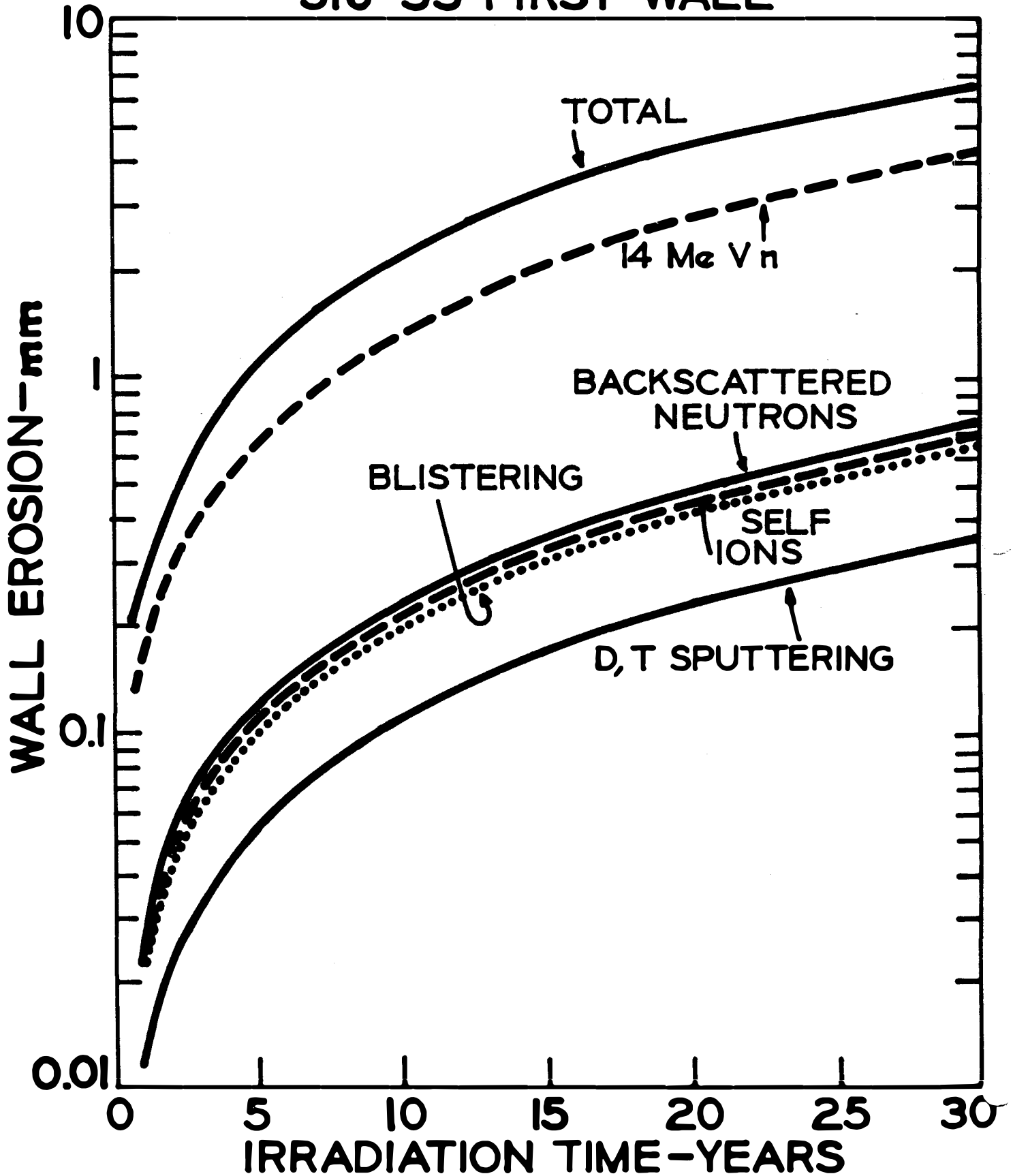


TABLE II

SUMMARY OF MATERIALS LIMITATIONS
DUE TO RADIATION DAMAGE

<u>PHENOMENA</u>	<u>INTEGRAL WALL LOADING LIMIT MW-YEARS/m²</u>
DUCTILITY (UNIFORM ELONGATION > 0.5 %)	2
SWELLING ($\Delta V/V_0 < 10\%$)	6
WALL EROSION (< 1 mm)	6

of the 316 SS which limits the lifetime to $\sim 2 \text{ MW-yr/m}^2$. This means the wall could run for 2 years at 1 MW/m^2 or 1 year at 2 MW/m^2 , etc. It is also evident that swelling and surface problems could limit the UWMAK-I first wall life to ~ 4 years if the ductility problem could be solved.

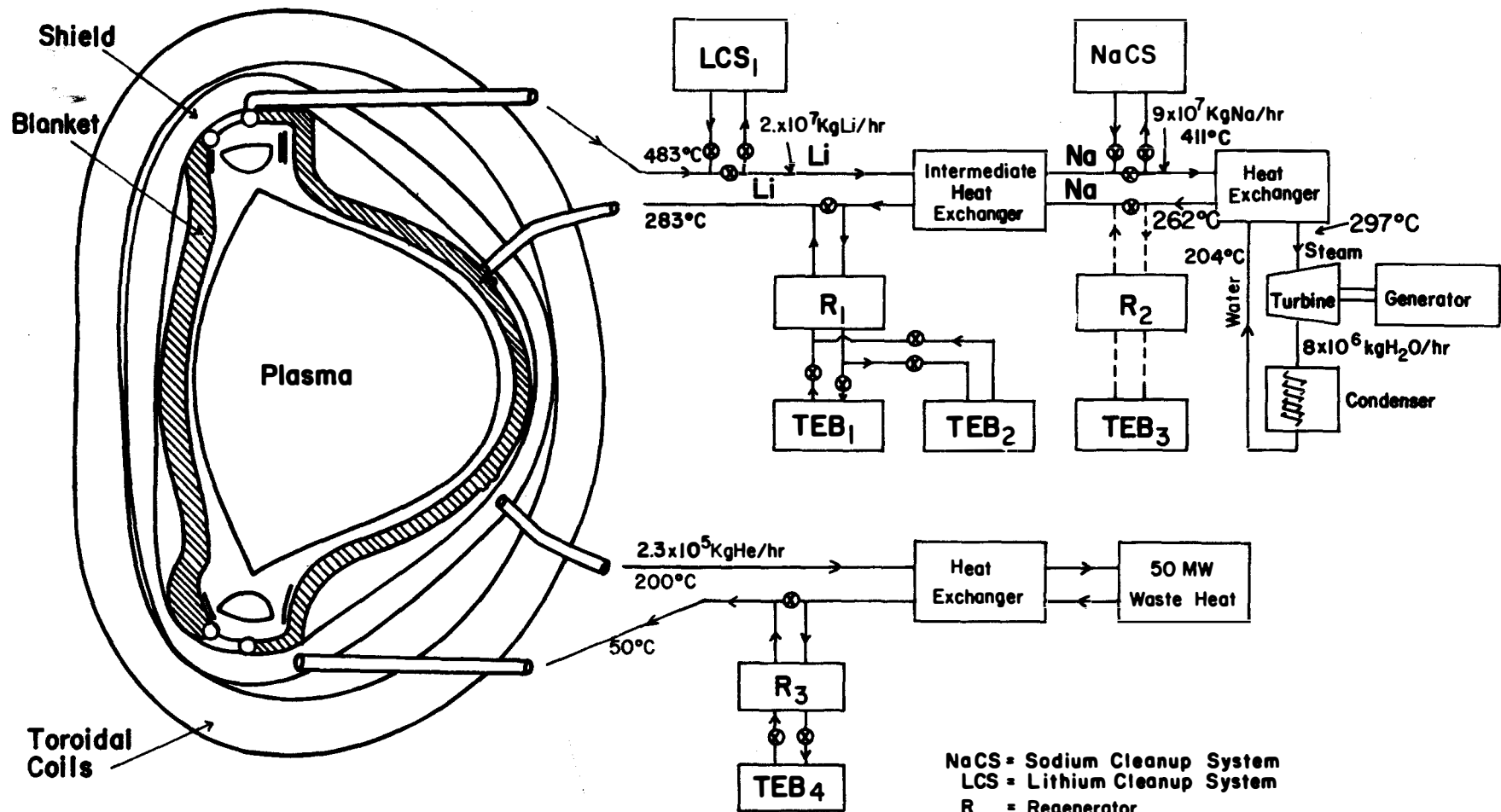
The extraction of tritium from the Li coolant is accomplished with Y traps. The breeding ratio of 1.49 is so high that doubling times of 3 to 4 months are indicated. However, when fueling, heating and vacuum ports are included in the design, it is expected that the breeding ratio may drop to a lower level. It still may be desirable to "spoil" breeding in UWMAK-I and breed more energy. Such possibilities are being investigated.

A diagram of the tritium removal scheme is shown in Figure 17 with appropriate liquid metal flow rates and temperatures. It is noted that a small amount of lithium is removed from the primary coolant loop, the temperature lowered to $\sim 300^\circ\text{C}$ and the lithium passed over a yttrium extractor bed. There are two extractors for the primary loop such that the tritium can be extracted from one unit while the other is in service. Only one extraction unit is required for the sodium secondary loop. The pertinent parameters for the tritium system are listed in Table 12.

The formation of radioisotopes in the blanket represents two potential hazards, radioactivity and afterheat. Table 13 summarizes the important radioisotopes produced per kW_{th} in UWMAK-I and their maximum permissible concentration (MPC) in km^3 of air per curie. A biological hazards potential (BHP) was calculated by dividing the activity by the MPC. The BHP's for 316 SS are also included in Table 13 and compared to alternate materials for CTR blankets. It can be seen that 316 SS is considerably better than Nb-1Zr from the standpoint of BHP but that a V-20Ti system would be even more desirable. Detailed analysis of the specific radioisotopes and their half lives are examined in Reference 1.

The decay of the radioisotopes mentioned above generated heat that must be dissipated to avoid severe temperature problems in the event that the reactor loses coolant. Pertinent information on afterheat in UWMAK-I with heat removal cells of three different materials is shown in Figure 18. The afterheat after 10 years of operation at 5000 MW_T is $\sim 31 \text{ MW}$ for 316 SS, $\sim 30 \text{ MW}$ for Nb-1Zr, and 23 MW for V-20Ti at shutdown. This radioactivity drops off quite rapidly for the vanadium system but remains rather stationary in 316 SS and Nb-1Zr for 1-2 years. Both of these latter systems show a considerable drop in the 2-20 year period decaying to less than 50 kW in 100 years. Calculations of the maximum temperature rise rate under adiabatic conditions reveal values on the order of $\sim 0.1^\circ\text{C sec}^{-1}$. More realistic approximations of the rate of heat leakage indicate the maximum value is unlikely to exceed $0.01^\circ\text{C sec}^{-1}$ indicating that emergency cooling requirements are minimal.

At this point, the areas which have not been covered in this paper should be enumerated. The details of the steam cycle and overall plant efficiency are currently under study and will be reported elsewhere⁽⁷⁾. The design of the containment structures and auxillary systems (cooling towers, transformer yards, etc.) has also begun. Economic analysis as well as safety and environmental impact studies are also underway.



NaCS = Sodium Cleanup System
 LCS = Lithium Cleanup System
 R = Regenerator
 TEB = Tritium Extraction Bed
 Flow Rates are for Whole Reactor

**Coolant Loops for
 Wisconsin Toroidal Fusion Reactor - UWMAK-1**

Figure 17

Table 12

Summary of Tritium Extraction System Characteristics^(a)

<u>Coolant System</u>	<u>Temp. Range °C</u>	<u>Extraction Method</u>	<u>Tritium Accumulation per Day (kg)</u>	<u>Tritium Leakage Ci/day</u>	<u>Total Na or Li (kg)</u>	<u>Tritium Concentration in Li or Na ppm (wt.)</u>	<u>Tritium Inventory (kg)</u>
Primary Lithium	283-483	Yttrium Metal Bed	1.05(b)	10.1	1.73×10^6	5	in Li 8.7 in beds 1.0
Secondary Sodium	261-411	Yttrium Metal Bed	~0		7.6×10^5	3.3×10^{-4}	in Na 2.5×10^{-4} in beds ~0
Divertor Lithium Sodium	200-325 190-265	Yttrium Metal Bed	7.4 T + 5.0D	2×10^{-4}	3.4×10^4 6×10^4	0.24 3×10^{-4}	in Li 8×10^{-3} in beds 3.5×10^{-5} in Na 2×10^{-5}
Divertor Vacuum	25	Charcoal-cooled with liq. He	0.3 T + 0.2D	1×10^{-4}		Not applicable	0.3
Helium	50-200	Metal getter	1.1×10^{-6}	low		Not applicable	low
			Total	10.1		Total	13.5

(a) Based upon thermodynamic calculations; no kinetic considerations

(b) At maximum breeding ratio of 1.49

Table 13
 Major Radioactive Isotopes in UWMAK-I First Wall
 With Various Blanket Materials^(a)

<u>System</u>	<u>Isotope</u>	<u>t_{1/2}</u>	<u>Activity Ci/kW⁽¹⁾</u>	<u>Maximum Permissible Concentration $\mu\text{Ci}/\text{cm}^3$</u>	<u>Biological Hazard Potential km^3 of air/kW^(t)</u>
Fusion-all	H ³	12.3y	60	2×10^{-7}	0.30
	V ⁴⁹	331d	0.67	1×10^{-10}	6.7
316 Structure only	Fe ⁵⁵	2.94y	140	3×10^{-8}	4.6
	Co ⁵⁸	27d	29	2×10^{-9}	14.5
	Ni ⁵⁷	1.5d	1.1	1×10^{-10}	11
	Mn ⁵⁴	313d	24	1×10^{-9}	24
	Co ⁶⁰	5.25y	<u>4.7</u>	3×10^{-10}	<u>15.6</u>
Total ^(c)			~310		~80
Nb-1Zr Structure	Nb ^{92m}	10.2d	152	1×10^{-10}	1,520
	Nb ^{95m}	3.75d	50	1×10^{-10}	500
	Nb ⁹⁵	35d	42	3×10^{-9}	14
	Sr ⁸⁹	54d	<u>38</u>	3×10^{-10}	<u>126</u>
Total ^(c)			~300		~2,200
V-20Ti	Sc ⁴⁸	1.83d	12.1	5×10^{-9}	2.5
	Ca ⁴⁵	152d	2.6	1×10^{-9}	2.6
	Sc ⁴⁶	85d	1.87	8×10^{-10}	2.3
	Sc ⁴⁷	3.4d	<u>1.58</u>	2×10^{-8}	<u>0.079</u>
Total ^(c)			~56		~9

(a) Neglect all isotopes with $t_{1/2} < 1$ day.

(b) 10 year exposure

(c) Including isotopes not listed.

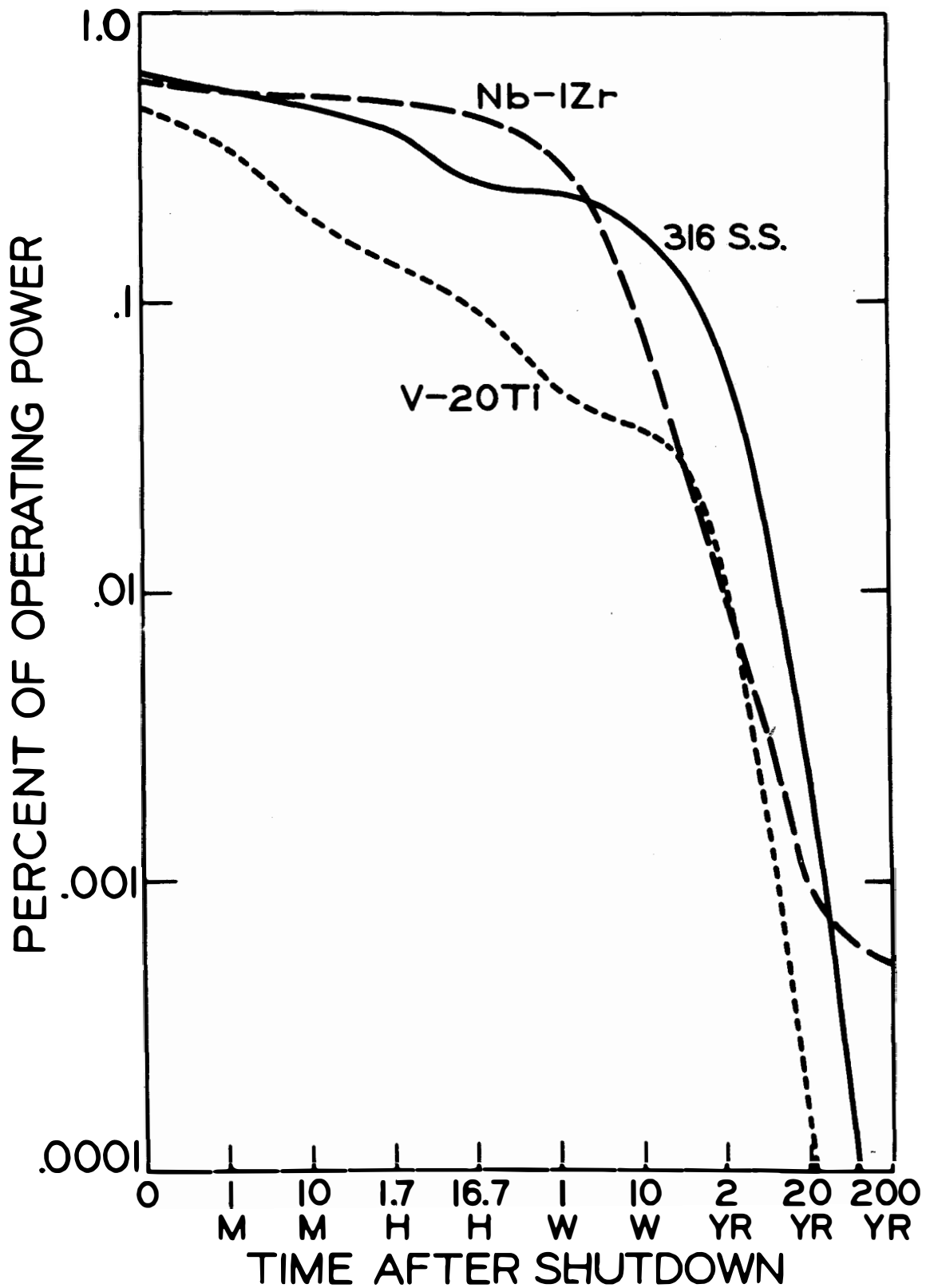


FIG. 18 DECAY HEAT IN UWMak-I BLANKET
AFTER 10 YEARS OF OPERATION

As a final point, it should be noted that the real usefulness of such a design effort lies not with the hope that such a system will actually be built, but rather in focussing attention on areas of technology that require further work before meaningful reactor studies can be completed. We fully expect that some features of UWMAK-I design will be changed as new discoveries are made in plasma physics, material behavior, and reactor technology in general. Hopefully, other laboratories will also complete detailed studies, and by noting the best features from many systems, we will be able to begin the design of the first real fusion power plant in the 1980's.

References

- 1.) B. Badger, M. A. Abdou, R. W. Boom, R. G. Brown, T. E. Cheng, R. W. Conn, J. M. Donhowe, L. A. El-Guebaly, G. A. Emmert, G. R. Hopkins, W. A. Houlberg, A. B. Johnson, J. H. Kamperschroer, D. Klein, G. L. Kulcinski, R. G. Lott, D. G. McAlees, C. W. Maynard, A. T. Mense, G. R. Neil, P. A. Sanger, W. E. Stewart, T. Sung, I. Sviatoslavsky, D. K. Sze, W. F. Vogelsang, L. Wittenberg, T. F. Yang, W. D. Young, UWFD-68, Volume 1, (March 1974).
- 2.) L. A. Artsimovich, Nucl. Fusion 12, (1972) 215.
- 3.) R. J. Bickerton, J. W. Connor, and J. B. Taylor, Nature 229 (1972) 110.
- 4.) J. D. Callen & R. A. Dory, Phys. Fluids, 15, 1523 (1972).
- 5.) M. N. Rosenbluth, R. Hazeltine, and F. L. Hinton, Phys. Fluids, 15, (1972) 116.
- 6.) B. B. Kadomtsev and O. P. Poqutse, Nucl. Fusion 11, (1971) 605.
- 7.) C. Hendricks, Private Communication.
- 8.) M. A. Abdou, C. W. Maynard, and R. Q. Wright, ORNL-TM-3994,(1973).
- 9.) M. Kaminsky and S. K. Das, To be published, J. Nucl. Materials.
- 10.) UWFD-68 Volume 2, To be published, (May 1974).

II. Plasma

The design of the fusion reactor UWMAK-I presented in this report is based upon the Tokamak concept of plasma confinement. In this chapter, the analyses relating to the operation of the plasma are presented in individual sections to allow separate presentations for the various important questions involved. The sections are ordered to roughly follow the chronology of events one expects in Tokamak operation. The first section presents a general overview of the principles of the Tokamak confinement concept and includes a discussion of the general philosophy we have followed in performing the plasma analyses. The second section contains an examination of the problem of sizing a Tokamak reactor. The scaling laws for the power of the reactor with a pressure-limited plasma (low- β plasma) are analyzed. This leads to an optimization analysis that allows one to intelligently size the reactor. Subsequent sections deal with the transformer and start-up phase of operation, the problem of plasma heating to ignition using energetic neutral beams, and the question of fueling the plasma during operation. This is followed by sections on the analysis of the possible operating conditions in a CTR Tokamak and the problem of plasma control during operation. We examine in detail the question of thermally stable versus thermally unstable operating conditions, and the problems of plasma control, which is especially important if the plasma operates in a thermally unstable condition. Also discussed here are additional points relating to system optimization and the role of the diffusion-driven bootstrap current, which can allow steady-state operation.

Each section in this chapter is reasonably self-contained so that the reader can separately examine the analysis of each problem area. However, there is much cross referencing to other sections and other chapters since all the topics covered in this report are, to one extent or another, inter-related.

Before turning to the various sections, we summarize here the essential results, including some of the problem areas that have been identified. The detailed reasoning behind the results are given in the sections that follow.

UWMAK-I operates with a D-T plasma at a poloidal beta limit of $\bar{\beta}_\theta \sim 1$, (the over bar indicates average) and has a double null, poloidal field divertor. The reactor has been sized by optimizing the cost per unit power in a β -limited system, where the costs are assumed to scale as the magnet costs. Constraints imposed by an air-core transformer with superconducting windings have been included. From these studies, the power output from UWMAK-I is set at 5000 MW_T. The aspect ratio is 2.6 with the wall loading limited to 1.25 MW/m² by radiation damage (see Chapter VI). The minor radius is determined to be 5 meters and the torus

major radius, 13 meters. Reactor startup makes use of an air-core transformer with superconducting windings, a setup most consistent with the small aspect ratio demands of cost optimization. The divertor coils are programmed to rise with the plasma current and produce a time changing flux through the plane of the plasma. For UWMAK-I, the divertor actually provides 60% of the flux needed to energize the plasma current so that the transformer proper need provide only 40%. After the initial soak phase has terminated, the core flux is held constant if the bootstrap current ($\beta_{\theta}^0 = \sqrt{A}$ limit) is present. β_{θ}^0 denotes the peak, rather than average, beta. If no bootstrap current materializes, the core flux is increased slowly to make up for the resistive drop. The burn time is determined to be 5400sec, or 90 min., and the total change in core flux is 760 webers.

Plasma heating to ignition is via the use of neutral beams. Ohmic heating alone is insufficient. Neutral beams of 350-500 KeV injected tangent to the magnetic axis, penetrate the UWMAK-I plasma when a low density startup is used. (Initial density on axis is $3 \times 10^{13}/\text{cm}^3$.) The profile of power deposition per plasma particle is peaked on axis. The beams are turned on immediately after the plasma current has risen to its final value. Using 500 KeV beams and 15 MW of power, the plasma ignites in 11 seconds. Faster startups can be achieved by using more power but this is not advantageous in UWMAK-I. In the 500 KeV beam case, 99.5% of the beam is trapped in the plasma. Thus, neutral beam heating appears to be an effective way of igniting a large, power producing reactor such as UWMAK-I.

The neutral beam heating is to be accomplished using 10 deuterium atom beams and 10 tritium atom beams. The 500 KeV D^0 beam is produced by starting with a 1.5 KeV D^+ beam produced in a scaled version of the duopigatron. To produce the 1.5 amperes equivalent of deuterium atoms for each beam, a 2.14 ampere negative deuterium ion beam is required. This beam is produced by passing a 1.5 KeV deuteron beam through a series of cesium gas cells and further accelerating the D^- obtained in this way. The 500 kV acceleration requires five electrodes with 2125 aligned 3 mm holes on 19.5 cm. diameter electrodes. The sources discussed here represent an extrapolation of existing technology, especially as far as beam power and pulse length are concerned. Also, the area of negative ion sources is still in its infancy and the 19.5 cm. size of the electrodes is a considerable increase over existing sources.

Once ignited, the plasma is assumed to rise in temperature in a controlled manner to the operating conditions given in Tables II-F-1 to II-F-3. Assuming the transport coefficients show classical scaling with density and temperature, albeit with altered or anomalous coefficients, plasma operation is in a thermally unstable state and requires control. We have suggested this operating mode because the cost of the transformer, divertor and main toroidal field coils are 50% less than

for operation in a thermally stable condition. To achieve favorable operating conditions, energy losses from the plasma had to be increased via the addition of .95% argon impurity atoms relative to the ion density. However, this is not essential. Without any bremsstrahlung enhancement, the power output drops by only about 8%. Further, the average confinement time of ~15 seconds is three orders of magnitude shorter than is predicted by neoclassical theory. Such reduction in confinement time, relative to neoclassical scaling, is required to both achieve a power balance at $T_i = 11.1$ KeV, as listed, and to remove spent fuel (α -particles) so that a respectable (D+T) ion density can be maintained. In terms of Bohm times, the confinement time of 14.2 seconds is ~~~100 Bohm times~~. For these operating conditions, the plasma is a low β ($\beta = .052$), low field ($\beta^0 = 38.2$ K Gauss) reactor producing 5000 MW_T , based on a total of 20 MeV per fusion event. If the bootstrap current exists, the plasma is assumed to operate at these conditions until impurity buildup from wall erosion (because the divertor is not 100% efficient), causes excessive losses and requires shutdown and restart. Otherwise, the burn time, determined by available core flux, is 90 minutes. Thus, this design is not predicated in the existence of a bootstrap current.

The method for producing the desired plasma operating conditions at a desired value of confinement time is an unsolved problem, as is the method of plasma control. Some preliminary ideas on these questions are included in the sections which follow. The control system, however, should have a response time on the order of .1 seconds or less to stabilize temperature excursions.

The plasma is assumed to be fueled during operation by injecting solid (D+T) pellets to make up for losses due to fusion and diffusion. The use of neutral beams for this purpose is highly questionable. Beam penetration is more difficult at the peak operating density of $1.2 \times 10^{14} / \text{cm}^3$ and further, the leakage rate of 3.6×10^{22} (D+T) ions/sec means that ~3000 MW of power are required, when 500 KeV beams are used. Higher energy beams imply even larger power requirements, which are clearly too large as is. Fueling is therefore assumed to be via pellet injection, using either 25 micron radius pellets at the rate of 10^6 pellets per second or, if larger pellets are feasible, 2 mm radius pellets at 20 pellets per second injection rate. The former requirements are within current technology, assuming the plasma can withstand pellet injection in the first place.

The method for injecting 2mm pellets to speeds sufficient for penetration of the plasma is a difficult, and essentially unsolved, problem. The reason is that, based on ablation rates for single pellets, millions of volts of accelerating potential appear to be required to achieve the required pellet velocities. Given the inherently large power requirements of neutral beams for fueling purposes, the area of pellet acceleration and injection requires much further study.

If it is possible to inject pellets in the 10-100 micron size and achieve penetration, then the fueling picture changes dramatically. In this case, the technology of pellet manufacture and acceleration is at hand. Experiments to be performed by Hendricks on ORMAK and ATC in the next several months should indicate, first, if the penetration depths required can be achieved and, second, whether pellet injection and the ablation process has a detrimental effect on plasma confinement.

This summarizes the essential results of this chapter. The reasoning and analysis behind these results are presented in the sections which follow.

II-A. Principles of Tokamak Operation

A Tokamak⁽¹⁻³⁾ is a diffuse toroidal z-pinch in which the nested set of flux surfaces is generated by the current that is induced to flow in the plasma itself. It is characteristically a low- β device, where $\bar{\beta}$ is the ratio of the average plasma pressure to the magnetic field pressure,

$$\bar{\beta} = \frac{\langle p \rangle}{B^2 / 2\mu_0} \quad (1)$$

The plasma in a Tokamak is confined by the poloidal magnetic field, B_θ , generated by a current carried in the plasma itself, and by the toroidal field, B_ϕ . The basis for the equilibrium analysis of such a system is

$$\vec{j} \times \vec{B} - \nabla p = 0 \quad (2)$$

where \vec{j} is the plasma current density. The basic coordinates of this geometry are shown in Figure II-A-1 along with the fundamental dimensions of a torus. An externally applied electric field drives the toroidal component of the plasma current, \vec{j} , which in turn generates the poloidal field.

A main characteristic of a Tokamak is the use of a strong toroidal magnetic field to suppress MHD instabilities.^(4,5) In particular, a strong B_ϕ will suppress the helical kink instability if the MHD stability factor,

$$q(r) = \frac{r}{R} \frac{B_\phi}{B_\theta(r)} \quad (3)$$

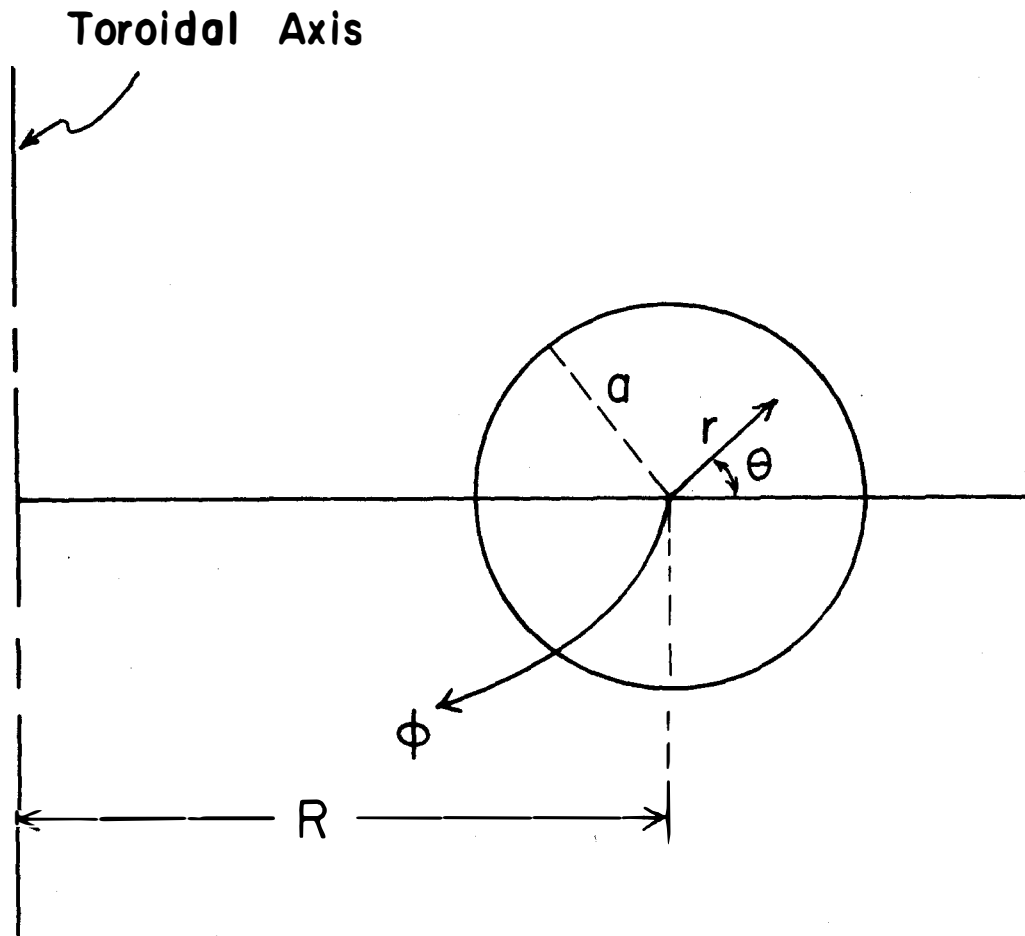
is greater than one throughout the plasma and the vacuum region. Further, the plasma current which produces B_θ provides the rotational transform required to suppress the flute instabilities⁽⁶⁾ and to counteract the grad B_ϕ drifts. For a current density which decreases in r ($j_\phi(r)$ decreases from the plasma center to the edge), the criterion to suppress local flute perturbations is the Kruskal-Shafranov limit,

$$q(r) > 1. \quad 0 \leq r \leq a \quad (4)$$

In addition to this limitation on the stability factor, q , there is an additional limitation on the plasma β , namely, that^(2,7)

$$\bar{\beta}_\theta < A \quad (5)$$

where $\bar{\beta}_\theta$ is the ratio of the average plasma pressure to the pressure of the poloidal magnetic field and A is the plasma aspect ratio.⁽²⁾ At $\bar{\beta}_\theta \sim A$, the last closed, nested flux surface has shrunk down to the plasma surface itself. Further increase of $\bar{\beta}_\theta$ causes a splitting of the magnetic surfaces inside the plasma boundary with a resultant deleterious effect on plasma confinement. The two criteria stated by equations (4) and (5) are fundamental to Tokamak operation and will be



MAJOR RADIUS, R
MINOR RADIUS, a
ASPECT RATIO, $A = R/a$

TOROIDAL COORDINATE SYSTEM

FIGURE II-A-1

met in all the plasma analysis to be reported.

In a Tokamak, therefore, the plasma current plays the dual role of generating the pinch field to trap the plasma and the rotational transform required for stability. To drive this current, the plasma itself is treated as a single turn secondary of a transformer. Energizing the primary side produces a toroidal electric field, E_ϕ , which causes gas breakdown and plasma formation and drives the toroidal plasma current. The transformer may have an iron or an air core and can have either normal or superconducting windings. An air-core transformer with superconducting windings allows for the smallest aspect ratio and this type of transformer is used in UWMAK-I. Its design is discussed in Section II-C.

The plasma has a finite resistivity that varies with electron temperature as $T_e^{-3/2}$. Therefore, plasma heating will be associated with the plasma current, although this Joule heating is insufficient to ignite a fusion reactor plasma. Additional heating in Tokamak devices has been obtained by compression of the plasma in the major radius (the ATC experiment)⁽⁹⁾ and by the injection into the plasma of high energy neutral particle beams.⁽¹⁰⁾ Because it requires an externally produced E_ϕ , the Tokamak is inherently a pulsed device. However, at high temperatures and low collision frequency (in the banana regime of neoclassical theory), trapped particle effects have led to the prediction that there will exist a diffusion driven current (a current proportional to a density gradient) which can provide the required rotational transform and trapping magnetic field, even without an externally produced electric field.^(11,12) This is the so-called "bootstrap current" and is predicted to exist with $E_\phi = 0$ when $\beta_\theta \approx \sqrt{A}$. β_θ is the ratio of the peak plasma pressure to poloidal magnetic field pressure at the plasma boundary. Under these circumstances, plasma operation could be truly steady state unless other factors, such as impurity buildup, limit the burn time. If steady state operation is not possible, long burn should be feasible if the impurity problem can be controlled using divertors.

The basic ideas regarding equilibrium of a plasma in a Tokamak⁽²⁾ can also be understood by examining Figure II-A-2. If the plasma were a straight cylinder, the poloidal magnetic pressure would be equal around the plasma boundary. However, because of the toroidal curvature, the poloidal field is stronger on the inside of the plasma loop than on the outside. Without additional fields, the loop would tend to expand in major radius. Therefore, it is necessary for plasma equilibrium to have an additional, vertical field produced by external windings, which subtracts from the poloidal field on the inside of the loop and adds to it on the outside, thus producing an equilibrium

TOKAMAK PLASMA CONFINEMENT

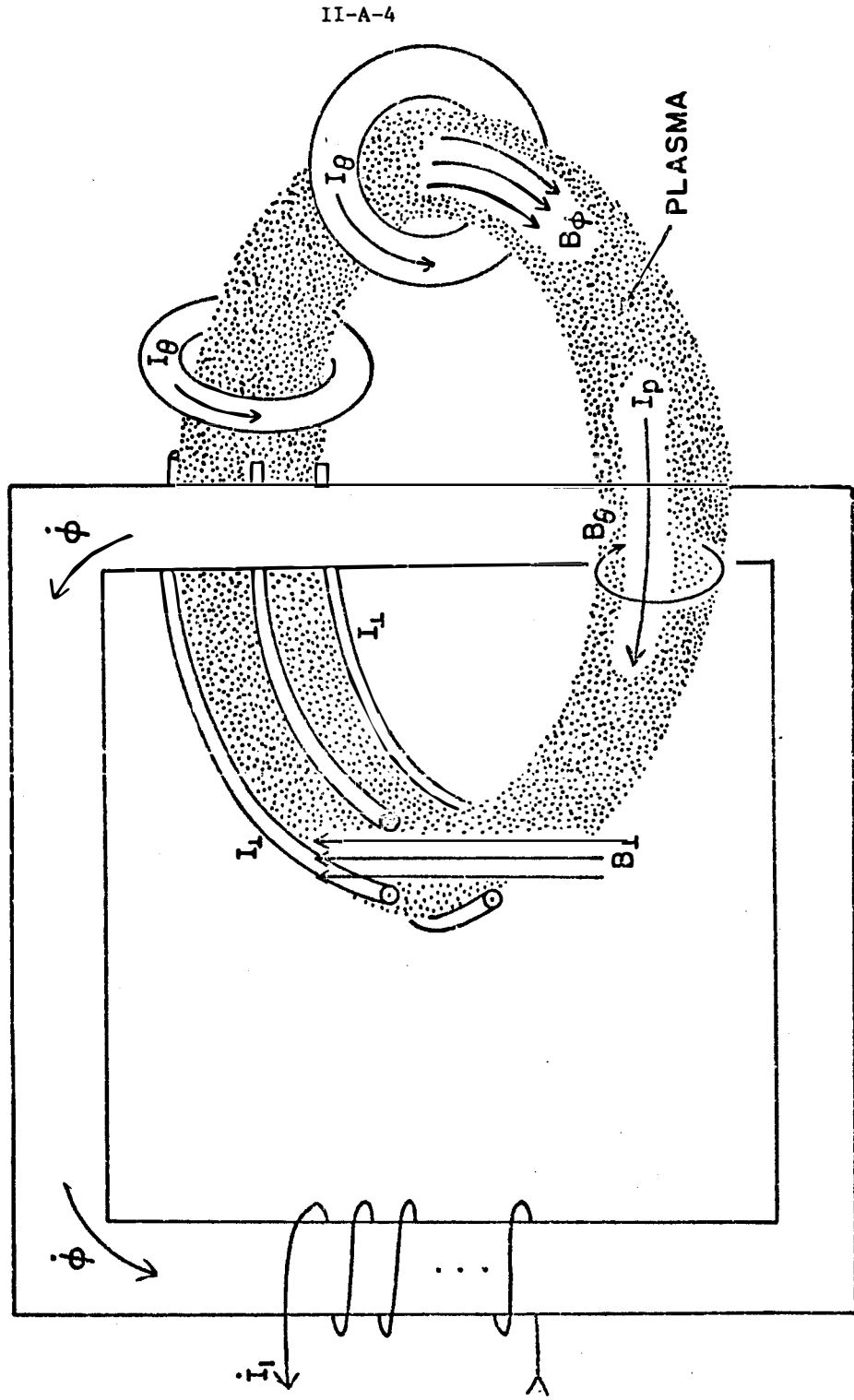


FIGURE II-A-2

configuration. Of course, in many present day experiments, eddy currents driven in a conducting shell surrounding the plasma generate the vertical field required to maintain the discharge in equilibrium⁽¹⁾ but in reactors, it seems clear that an externally produced vertical field will be required. Indeed, this vertical field, added to the poloidal field generated by the plasma current, produces a resultant magnetic field topology that leads naturally to a poloidal field divertor. A separatrix can be produced in this way which becomes a natural plasma boundary. Two such configurations are shown in Figure II-A-3. Magnetic surfaces inside the separatrix remain closed in the plasma volume. However, particles on field lines outside the separatrix are carried away from the plasma surface and can be collected. The details of the vertical field design and magnetic field topology are discussed in Chapter III, which deals with the divertor for UWMAK-I.

If the vertical field, B_z , is absolutely uniform, then the plasma loop has no restoring force in case of vertical displacements. To stabilize the loop against such displacements, the vertical field must have some curvature characterized by a decay index⁽⁸⁾

$$n = - \frac{R}{B} \frac{\partial B_z}{\partial R} \quad (5)$$

For stability against vertical displacements, one requires $n > 0$, and for stability against horizontal displacements, n must be less than .42. The vertical field produced by the divertor coils, as discussed in Chapter III, is characterized by a decay index in the interval $[0, .42]$.

As discussed, the poloidal field generated by the plasma current provides a rotational transform. When this poloidal field is superimposed on the strong toroidal field, B_ϕ , the resultant field lines are helical, as shown in Figure II-A-4.^φ The rotation generated by the poloidal field compensates for the outward drift of particles caused by the gradient in the toroidal field. The toroidal field is stronger on the inside of the torus, varying as $1/R$ from the inside to the outside of the loop.

This gradient in B_ϕ can also produce a class of particles which cannot reach the inside^φ of the plasma loop. Since effects associated with these trapped particles are most important in the reactor regime of plasma parameters (high temperature, low collision frequency), we mention briefly the basic effects of particle trapping on diffusion and conduction phenomena in Tokamaks. Only the physical aspects are discussed as they relate to the work in this report. The theoretical work of the past several years,⁽¹³⁻¹⁷⁾ which has led to our understanding of Tokamak plasmas and yielded both transport coefficients⁽¹³⁻¹⁶⁾ and a complete set of transport equations,^(17a, 17b) will not be reviewed. The transport equations are discussed in Section II-F, where plasma temperature and density profiles are discussed and the equations for fusion reactor plasma energy balance studies are derived.

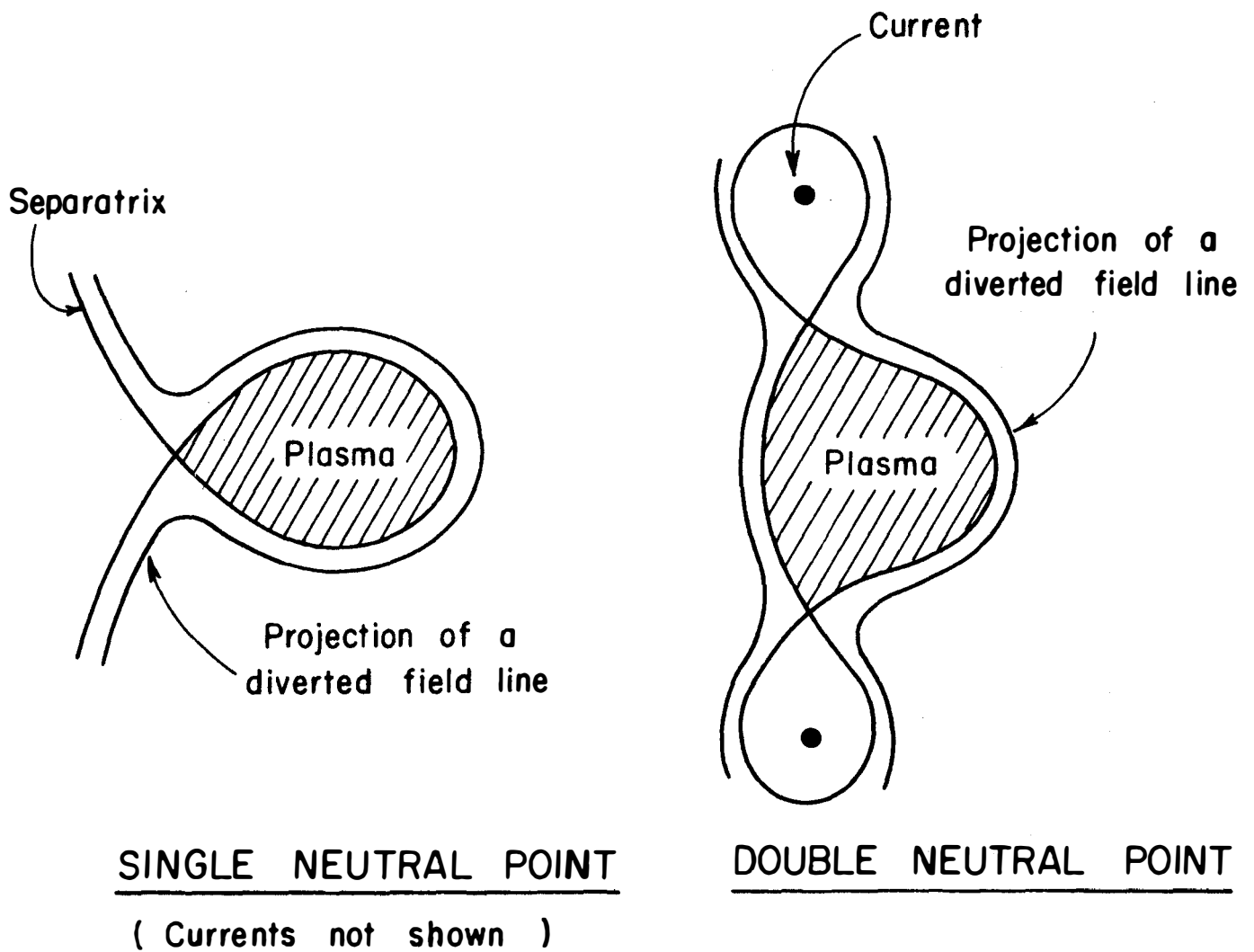


FIGURE II-A-3

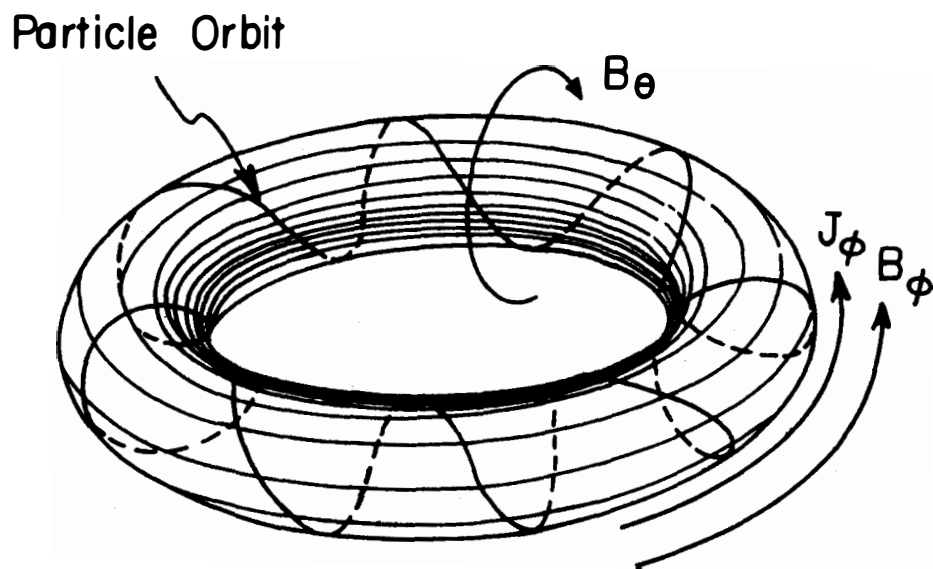


FIGURE II-A-4

The gradient in B_ϕ is illustrated in Figure II-A-5 and can be described by the equation

$$B_\phi = \frac{B_\phi^\circ}{\left(1 + \frac{r}{R} \cos\theta\right)} \quad (6)$$

where B_ϕ° is the toroidal field at R . When $A = R/r \gg 1$, this can be approximated as

$$B_\phi \sim B_\phi^\circ \left(1 - \frac{r}{R} \cos\theta\right). \quad (7)$$

The field is stronger on the inside of the torus and a particle following a helical field line as shown in Figure II-A-4 enters zones of higher magnetic induction as it moves to the inside of the torus. Conservation of the total energy leads to the equation

$$m \frac{v_{||}^2}{2} + \mu B = \text{constant} \quad (8)$$

where $v_{||}$ is the parallel velocity of the guiding center, m is the particle mass, and μ the magnetic moment derived from the gyro motion of the particle. μ is given by

$$\mu = \frac{m v_\perp^2}{2B} \quad (9)$$

where v_\perp is particle velocity perpendicular to the field.

From equation (8), it is clear that if the maximum of $v_{||}$ is small enough, or if the variation of B_ϕ can be large enough, the particles can have $v_{||} = 0$ at some point prior to reaching the inside of the torus. Such a particle is mirrored back from this turning point and is thus trapped. In the absence of drift effects, the trapped particles follow an arc between the turning points, as shown in Figure II-A-6. Drift effects displace these arcs such that the resulting orbits, projected onto the (r, θ) -plane, have the banana shape also shown in Figure II-A-6. The width for electrons of the banana orbit at the midplane is given by Δr ,

$$\Delta r = \frac{m v_{||}}{e B_\theta} \approx \frac{1}{\sqrt{A}} \rho_\theta^e \quad (10)$$

where ρ_θ^e is the gyro radius of an electron in the poloidal magnetic field. This is the important result because it means the step size which enters into the diffusion coefficient is the gyro radius in the weak magnetic field, B_θ . This leads to an enhanced diffusion in high temperature, toroidal plasmas compared with diffusion in a straight system. Nevertheless, the results yield basically classical scaling laws for the particle and energy confinement times, which is the most

encouraging aspect of the recent Tokamak research.

In the high temperature regime where CTR plasmas will operate, the plasma is essentially collisionless. In particular, the electron-ion collision frequency, ν_{ei} , which scales like $T^{-3/2}$, is less than the frequency of oscillation between turning points, called the bounce frequency,

$$\omega_{\text{bounce}} = \frac{v_{\text{th}}^e}{q R A^{3/2}} \quad (11)$$

v_{th}^e is the electron thermal velocity. The diffusion coefficient in this regime is given by

$$D_{\perp}^e = 1.12 \left(1 + \frac{T_i}{T_e}\right) q^2 A^{3/2} \nu_{ei} \rho_{e\phi}^2 ; \nu_{ei} < \omega_{\text{bounce}} \quad (12)$$

where T_i and T_e are the ion and electron temperatures and ν_{ei} is the electron-ion collision frequency. Since the classical diffusion coefficient is $\nu_{ei} \rho_{e\phi}^2$, there is considerable enhancement of the diffusion coefficient due to trapped particle effects.

The heuristic explanation for the form of the neoclassical diffusion coefficient, equation (12), is explained by recalling that the fraction of particles trapped⁽³⁾ is the order of $1/\sqrt{A}$. Also, trapped (untrapped) particles that make a transition to being untrapped (trapped) because of collision with other particles have a step size for diffusion equal to Δr . The diffusion coefficient will be obtained from an expression like

$$D_{\perp}^e \sim \frac{(\text{step size})^2}{\text{characteristic time}} \quad (13)$$

The characteristic time is the collision time for a particle to scatter from trapped to untrapped and vice-versa. This collision time is shorter than the 90° collision time because it involves smaller scattering angles to make the trapped-untrapped transition. Thus, the characteristic time becomes

$$\tau_{\text{eff}} \approx \frac{\tau_{90^\circ}}{A} \quad (14)$$

Further, the characteristic step size can be written in terms of ρ_{ϕ}^e as

$$\Delta r = \sqrt{A} q \rho_{\phi}^e \quad (15)$$

Noting that the particle flux, Γ , is proportional to $\frac{\partial n_t}{\partial r}$, where n_t is the number of trapped particles, and that

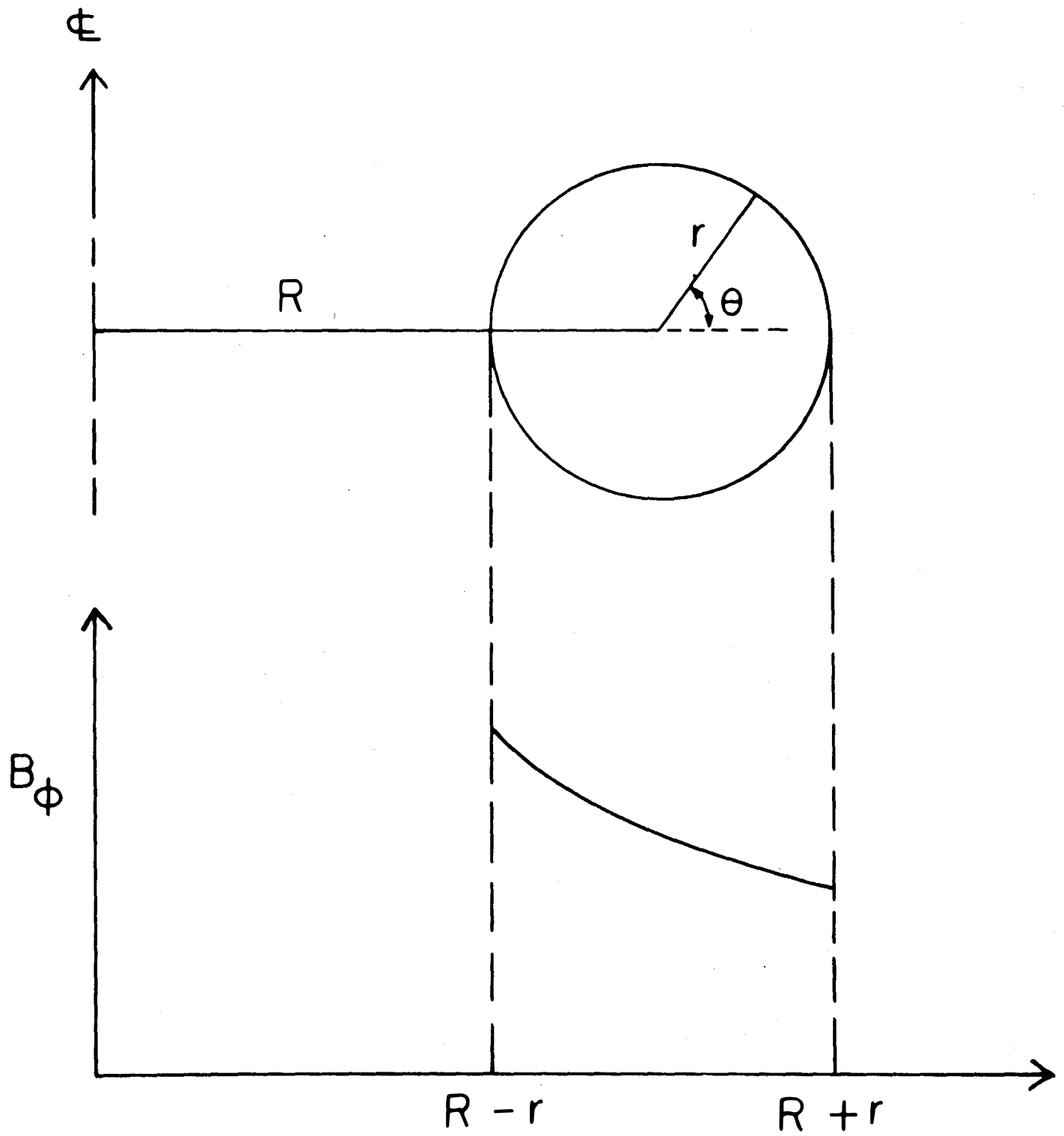
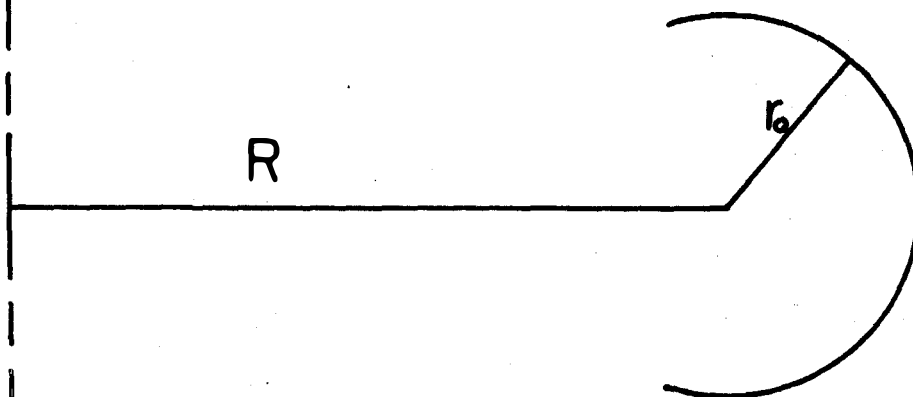
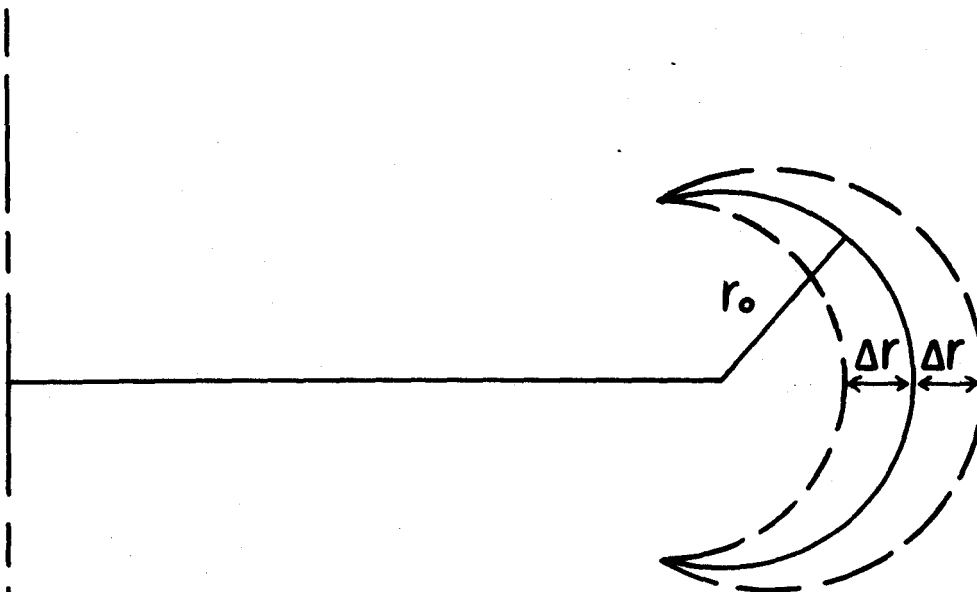


FIGURE II-A-5

II-A-11



TRAPPED PARTICLE ORBIT
(NO GRAD(B) DRIFT)



TRAPPED PARTICLE ORBIT
(WITH GRAD(B) DRIFT)

$n_t \sim \frac{1}{\sqrt{A}} n$, we have

$$D_{\perp}^{ee} \sim q^2 A^{3/2} v_{ei} (\rho_{\phi}^e)^2 \quad (16a)$$

$$D_{\perp}^e \sim q^2 A^{3/2} D_{\perp}^{\text{classical}} \quad (16b)$$

A similar analysis can be performed for the thermal conductivity and the results show the importance of including neoclassical effects in the analysis of Tokamak reactors.

This introduction has been a brief overview of the principles of the Tokamak confinement process and an indication of some specific effects important to understanding transport phenomena in a Tokamak. It is not our intent here to completely review the status of present Tokamak research. However, it is worthwhile to comment on the philosophy we have tried to follow in performing the plasma studies for UWMK-I.

We have made reasonable extrapolations based on present day understanding of Tokamak operation and have tried to use present theory wherever possible. When it has been necessary to introduce anomalous factors, such as the spoiling factor to reduce confinement time as discussed in Section II-F, these factors are noted explicitly and discussed fully. Limitations on $\bar{\beta}_{\theta}$ and q have been adhered to and, in fact, we have been conservative in the choice of $\bar{\beta}_{\theta}$. Plasma operation, from startup and heating through shutdown and recycle, has been treated in a consistent manner. The system has been designed assuming steady-state operation with $E_{\phi} = 0$ and J_{ϕ} driven by the density gradient but this is not essential. If no bootstrap current exists, the plasma will operate for a burn time of 5400 sec, during which it can be considered quasi-steady-state. These two alternative modes of operation are included and analyzed.

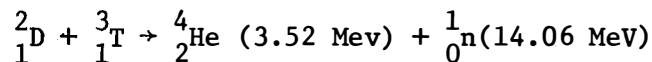
II-B. Optimization

In carrying out the various plasma analyses, and indeed in sizing the reactor itself, it is first necessary to decide on the fuel cycle and on the values of the plasma minor radius, a , and the torus major radius, R . In particular, one wants to optimize both the power and, more importantly, the cost per unit power. The analysis presented in this section addresses these questions for a Tokamak reactor. The peak plasma beta poloidal, β_{θ}^0 , is limited to \sqrt{A} (see section II-F), $A = R/a$, and the constraints of fixed power and limits on torus core space relating to transformer performance are considered. It will be shown that the core constraint makes the cost relatively independent of the maximum magnetic field strength for reactor powers greater than 5000 megawatts thermal and that the cost actually increases with magnetic field strength for reactor powers less than 5000 MW. As a result, the maximum magnetic field strength should be determined by the desired neutron wall loading.

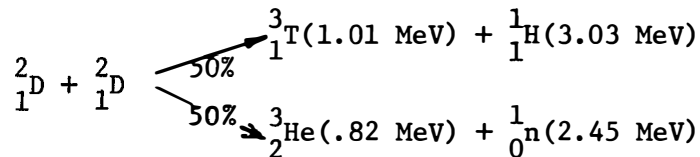
To summarize the results of this section, the D-T fuel cycle is used and the reactor size is $5000\text{MW}_{\text{th}}$, $a = 5$ meters and $R = 13$ meters. We turn now to the details explaining how these conclusions were reached.

For a near-term reactor, there are three fuel cycles which could be used and the question here is the choice among these. As will be clear, for a near-term, low- β reactor such as UWMAK-I, the deuterium-tritium (D-T) cycle is the most feasible. The basic fuel cycles are:

- 1) Deuterium - Tritium (D-T) cycle:



- 2) Deuterium - Deuterium (D-D) cycle:



- 3) Deuterium - Helium -3 (D- ${}^3\text{He}$) cycle:



Of course, within each of these cycles, reactions from other cycles take place. For example, the tritium produced in D-D reactions can be burned in situ resulting in D-T neutrons. Other reactions, such as ${}^6\text{Li}(p, {}^3\text{He}){}^4\text{He}$, ${}^6\text{Li}(d, T){}^3\text{Li}$, ${}^7\text{Li}(p, \gamma){}^8\text{Be}$, etc, could be the basis for long-term CTR fuel cycles. However, the Coulomb barrier is so large in all these reactions that plasma temperatures in excess of 1 MeV are required before a net power output can be expected. Thus, we limit the discussion here to the D-T, D-D, and D- ${}^3\text{He}$ cycles most likely to be used in the near-term future.

The choice between these cycles becomes clear for a low- β reactor when one examines the fusion cross sections for the various reactions. The cross section for the ${}^3\text{T}(d, n){}^4\text{He}$ reaction has a larger maximum value peaking at lower energies than any of the other reactions. More important from a reactor standpoint is the fusion reaction rate, $\langle\sigma v\rangle$, where $\langle \rangle$ indicates an average over a Maxwellian distribution of target nuclei. The variation of $\langle\sigma v\rangle$ with plasma ion temperature is shown in figure II-B-1. The reaction rate for the ${}^3\text{T}(d, n){}^4\text{He}$ reaction has a higher maximum occurring at lower temperatures than the other reaction types. The importance of this is that one can ignite a D-T plasma at lower temperatures (~ 5 KeV for T_i). Further, Tokamaks have β -limited plasmas so that, as we show shortly, the expression for the power in such a system is proportional to $\beta^2 B^4 \langle\sigma v\rangle / T^2$. For a given magnetic field strength and fixed β , we need only $\langle\sigma v\rangle / T^2$, which is plotted in figure II-B-2 for the three cycles under discussion. Again, the D-T cycle parameter has a larger maximum value and it occurs in the temperature range 10-15 KeV. Thus, a D-T plasma makes better use, in a β -limited system, of a given magnetic field strength. As noted, this low optimum temperature range (10-15 KeV) translates into lower ignition and operating temperatures. For these reasons, UWMAK-I is assumed to operate on the D-T cycle using a 50-50 mixture of ${}^2\text{D}$ and ${}^3\text{T}$ in the plasma.

We turn now to the question of the optimum size for UWMAK-I. To begin, consider first the question of optimization with respect to the plasma radius, assuming the major radius, R , is fixed. The expression for the power is

$$P = f \frac{n^2 \langle\sigma v\rangle}{4} E_{\text{fus}} 2\pi^2 a^2 R \quad (17)$$

where n is the ion density, $\langle\sigma v\rangle$ the fusion reaction rate, E_{fus} is the amount of energy per fusion event, and f is a factor to account for the ion spatial profile in temperature and density. For a β - limited reactor,

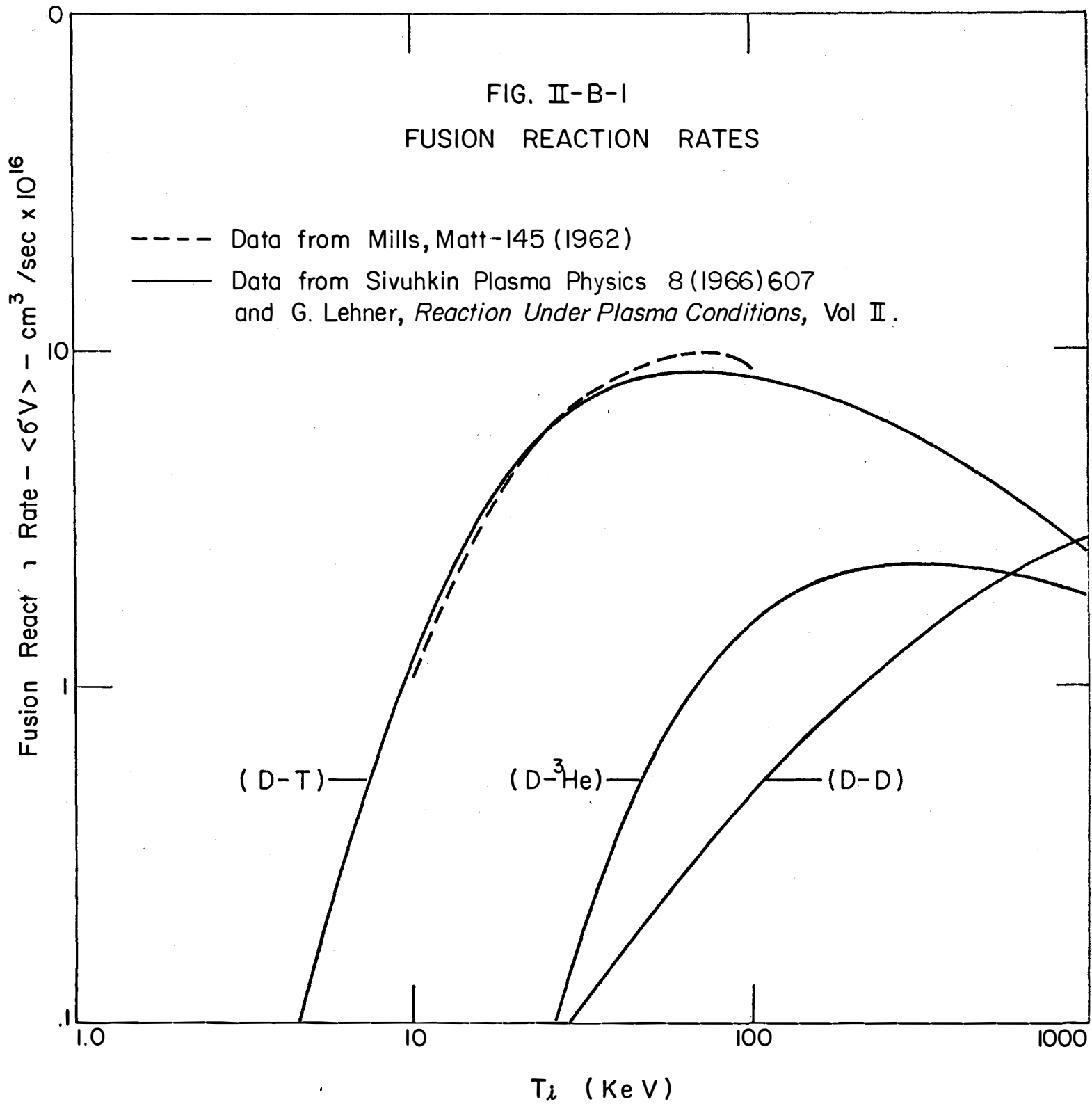
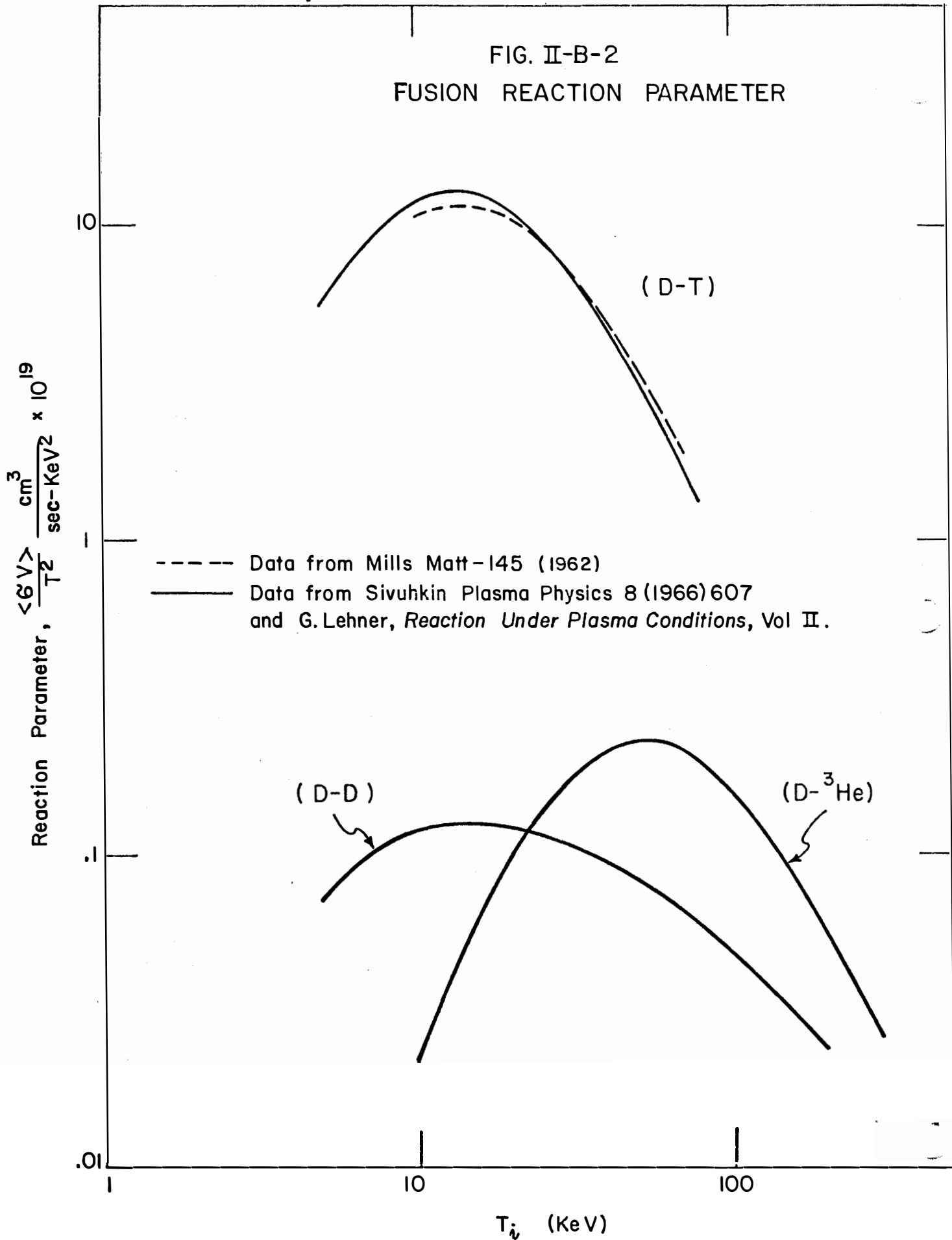


FIG. II-B-2
FUSION REACTION PARAMETER



this expression becomes

$$P = \frac{C_0 \beta_\theta^2 (B_\phi^0)^4 a^2 R}{q^4 A^4} \quad (18)$$

Using the relationship $B_\phi R = \text{constant}$ and the assumption that $\beta_\theta^0 = \sqrt{A}$,

$$P = C_0 \frac{B_m^4}{q^4} \left(1 - \frac{\tau_b}{R} - \frac{a}{R}\right)^4 \frac{a^5}{R^2} \quad (19)$$

With

$$C_0 = \frac{\pi^2 f \langle \sigma v \rangle E_{\text{fus}}}{32 \mu_0^2 k T^2} \quad ,$$

B_ϕ^0 is the toroidal magnetic field at the plasma axis, B_m is the maximum field value at the superconductor, τ_b is the vacuum gap plus blanket and shield thickness, and q is the MHD stability factor. The geometry is shown in Figure II-B-3. We note later that the assumed β -limit has little effect on the basic results reported here.

The analysis here assumes a fixed value for the plasma temperature, T , implying the temperature is independent of variations in the other parameters or that the other parameters can be varied to maintain the temperature at the desired value. Conn et al, (18), in studying steady-state solutions for Tokamak systems using self consistent energy balance and diffusion equations, has found the temperature to be very insensitive to variations in the plasma radius for operating temperatures of 10-15 keV. (Also, see section II-F.) While the fixed temperature assumption is no longer valid for operating temperatures above about 25 keV, the conclusions presented here are still found to be qualitatively correct.

By maximizing the power in equation (19) with respect to the plasma radius, a , the maximum power is found to occur at $a = \frac{5}{9}R(1 - \frac{\tau_b}{R})$. The maximum power is given by

$$P^{\text{max}} = C_0 \frac{B_m^4}{q^4} \left(1 - \frac{\tau_b}{R}\right)^9 \left(\frac{4}{9}\right)^4 \left(\frac{5}{9}\right)^5 R^3 \quad (20)$$

TOKAMAK GEOMETRY

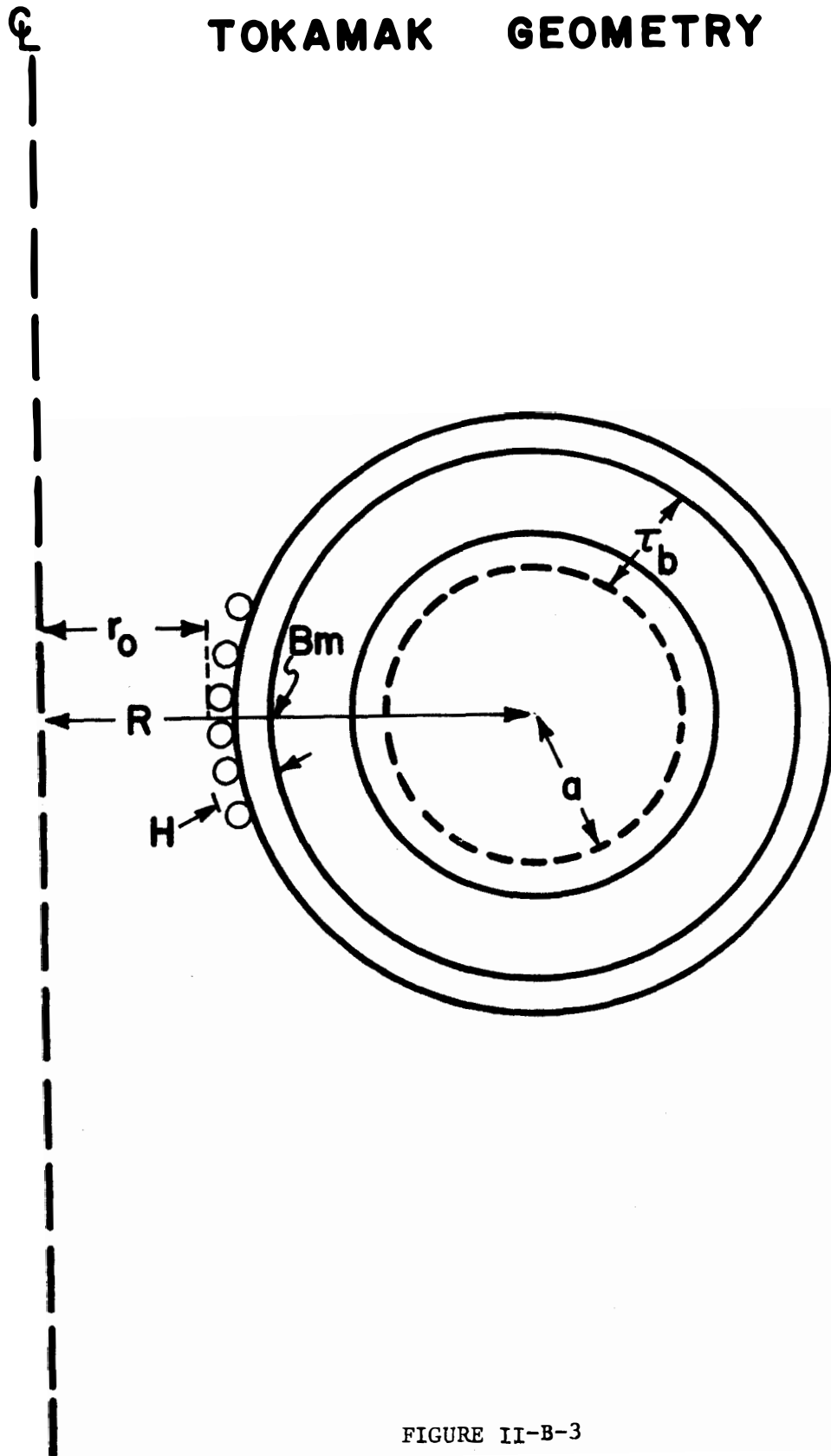


FIGURE II-B-3

The relative power as a function of plasma radius is shown in Figure II-B-4 which is a plot for a reactor having $R = 12.5\text{m}$ and $\tau_b = 2.5\text{m}$, parameters from Reference 19. As will be shown later, core space limitations as well as neutron wall loadings may limit the plasma radius to values less than the unconstrained optimum.

To minimize the relative cost/power, the following assumptions appear justified:

- (1) the cost of the reactor scales as the magnet cost
- (2) the magnet cost is proportional to the energy stored in the magnetic field, E_s .

Lubell⁽²⁰⁾ has shown that the magnet cost is proportional to $E_s^{0.8}$ and Boom⁽²¹⁾ has shown, for more limited cases, that the cost is proportional to $E_s^{1.2}$. (see also chapter VII which given the details regarding the scaling of magnet costs.) The stored magnetic energy can be expressed as

$$E_s \sim B_\phi^2 R^3 \left[1 - \sqrt{1 - \left(\frac{r_m}{R}\right)^2} \right] \quad (21)$$

and approximated by

$$E_s \sim B_\phi^2 R r_m^2 = B_m^2 [R - r_m]^2 \frac{r_m^2}{R} \quad (22)$$

where r_m is the magnet inner radius and is equal to $(a + \tau_b)$. The approximate expression is accurate to 10% for r_m/R ratios less than 0.7.

Combining (22) with (19), the cost per unit power can be expressed as

$$\text{Cost/Power} = K = \frac{C_o r_m^2 R^5}{B_m^2 q^4 (R - r_m)^2 a^5} \quad (23)$$

This expression can be minimized with respect to the plasma radius, a , and a minimum found at

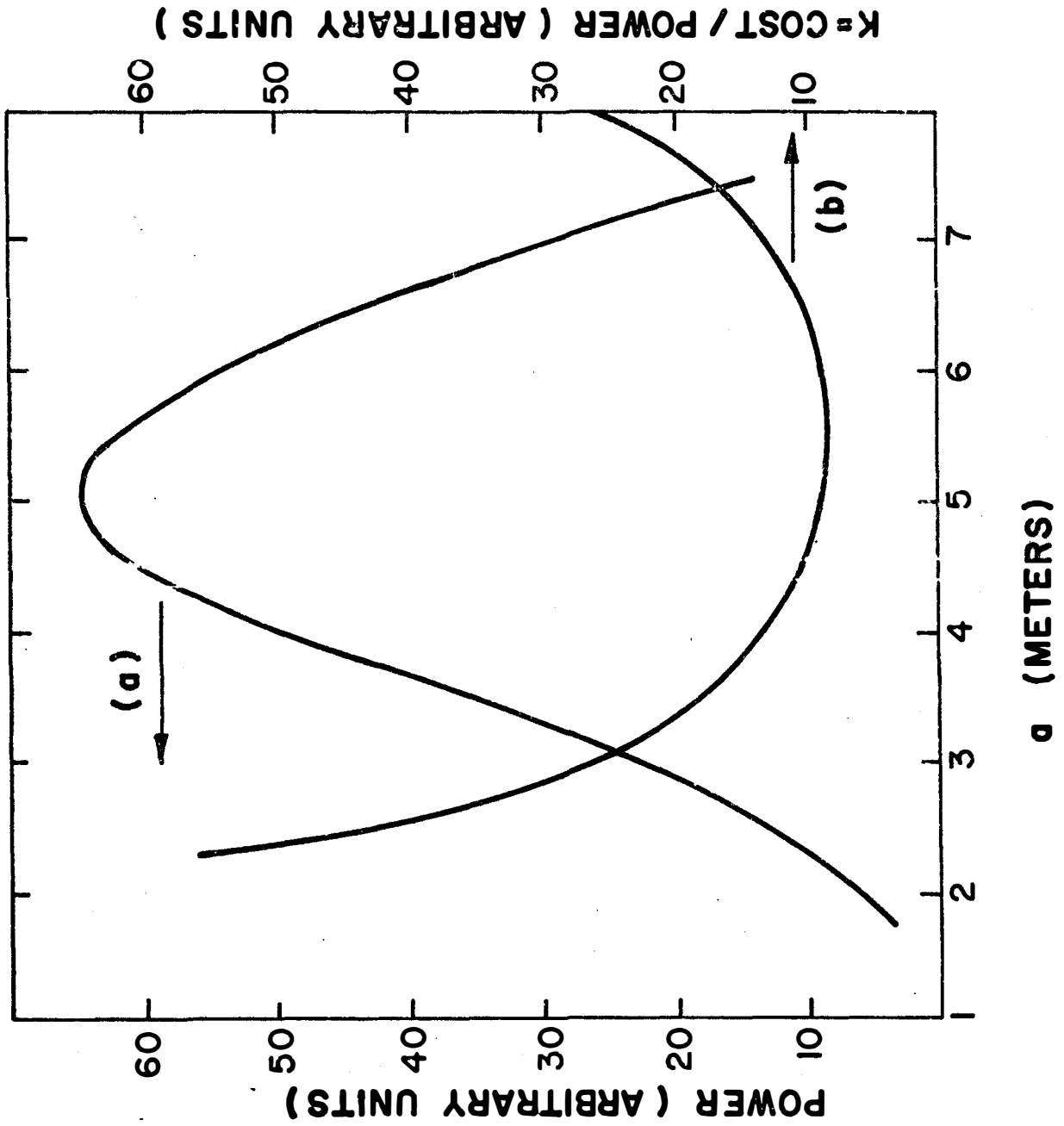


FIGURE I , -4

$$a^{\min} = \frac{3R}{10} \left[+ \sqrt{1 + \frac{40\tau_b}{9R}} \right] - \tau_b \quad . \quad (24)$$

Figure II-B-4b shows the variation of cost per unit power with minor radius, a . These studies have indicated that the optimum aspect ratios are found to have values between 1.7 to 2.5.

The variation of power and cost per power as a function of the major radius, R , is shown in Figure II-B-5. It can be seen that while the power increases by a factor of eight in going from $R = 10\text{m.}$ to $R = 15\text{m.}$, in accordance with equation (20), the cost per unit power decreased by only a factor of two. Therefore, there is little economic gain in building Tokamak reactors with $R > 15\text{m.}$ The same analysis has been done for the limit $\beta_\theta = A$ with similar conclusions.

Let us look now for a set of reactor parameters (R, a) that minimizes the cost (the stored magnetic energy) subject to the constraint of fixed power. We choose a major radius $R = aA$, solve the power equation (19) for the plasma radius, a , and then calculate the stored magnetic energy, E_s , given by equation (22). We can repeat the procedure, generating a locus of constant power points in the (R, a) plane and look for a minimum in E_s . Figures II-B-6, 7 and 8 show the variation of Cost/Power vs. Aspect Ratio at a fixed power of 5000 MW_T for different values of τ_b , the blanket and shield thickness; B_T , the maximum magnetic field at the superconductors; and, q , the MHD stability factor. A minimum can be found and as shown in the figures, occurs at aspect ratios 1.6 to 1.7. This minimum in the aspect ratio has been found to be independent of the power (1-10 GW), maximum magnetic field strength (6-20 T), and thickness of blanket and shield (1.5m.-2.5m.). The use of the more accurate expression for E_s makes the minimum more pronounced.

A plot of the minimum cost/power at three power levels, as a function of maximum magnetic field strength at the superconductors is shown in Figure II-B-9. The cost decreases monotonically with magnetic field. This behavior is altered dramatically when a core constraint is imposed.

Since all Tokamaks require an air or iron core transformer to create the toroidal plasma current, space must be provided for this transformer, its windings and the toroidal magnet windings. (The transformer is described in detail in section II-C.) The following constraint must be satisfied;

$$r_0 + H + \tau_b + a \leq R \quad (25)$$

POWER AND COST/POWER vs. MAJOR RADIUS

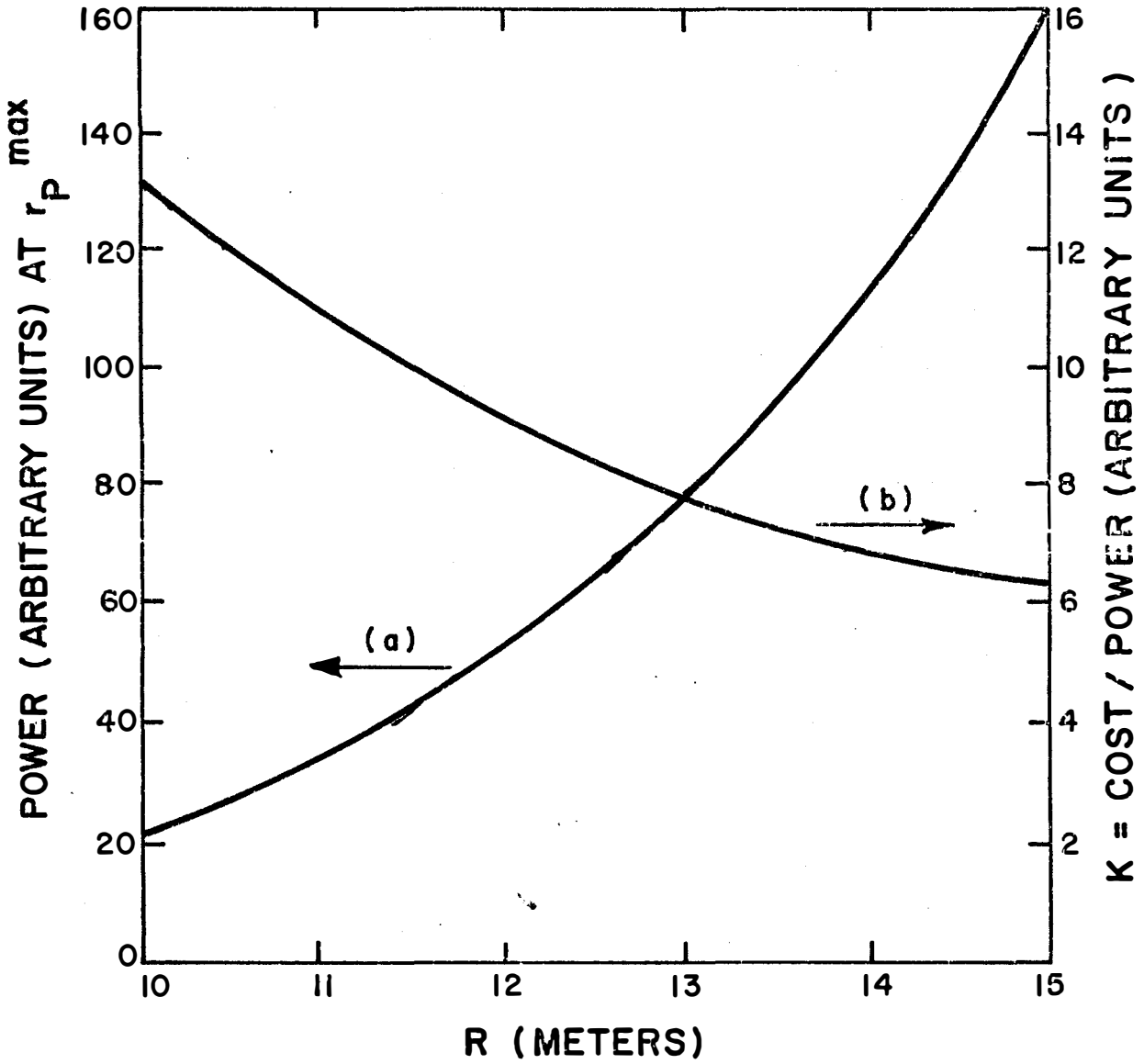


FIGURE II-B-5

COST / POWER vs. ASPECT RATIO

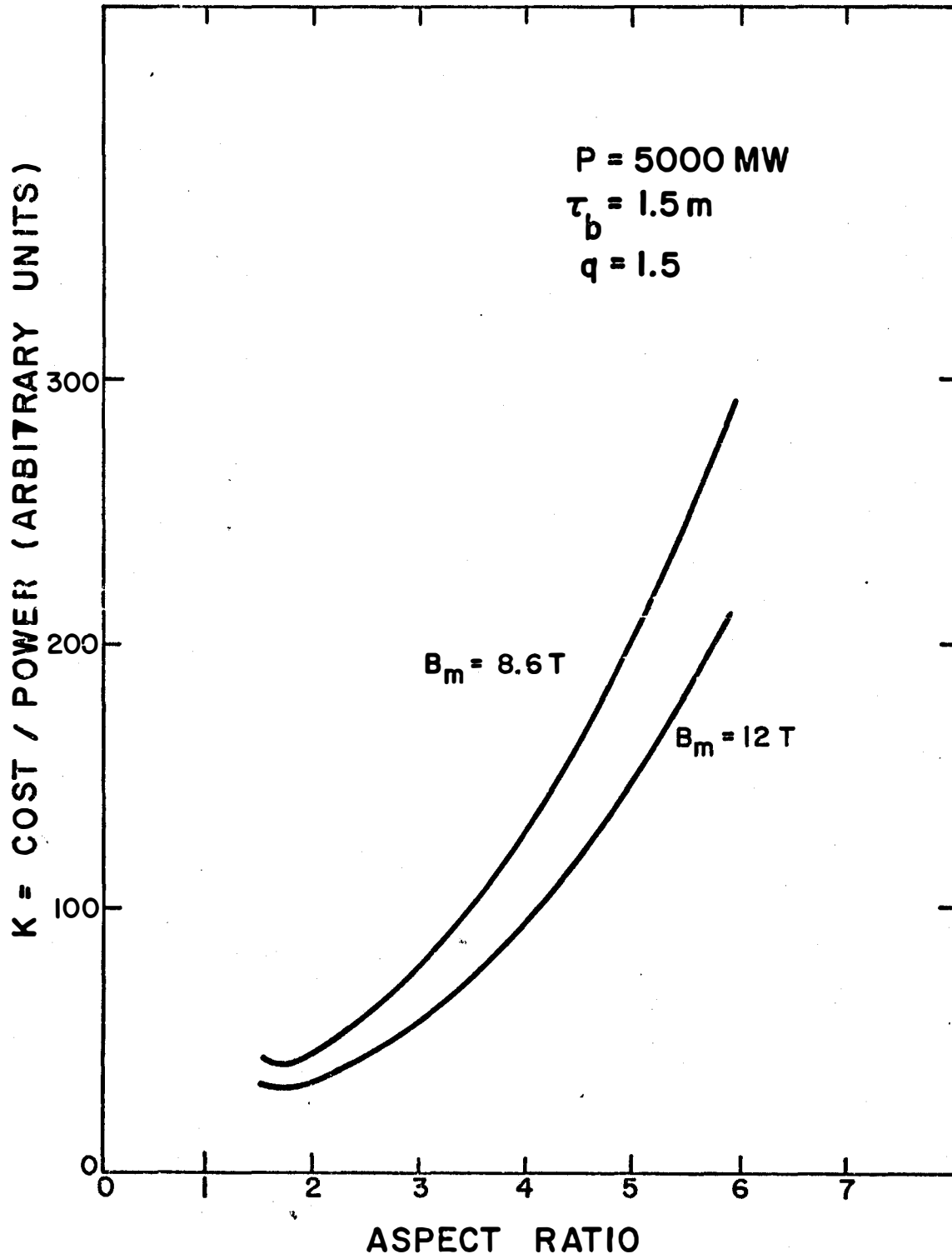


FIGURE II-B-6

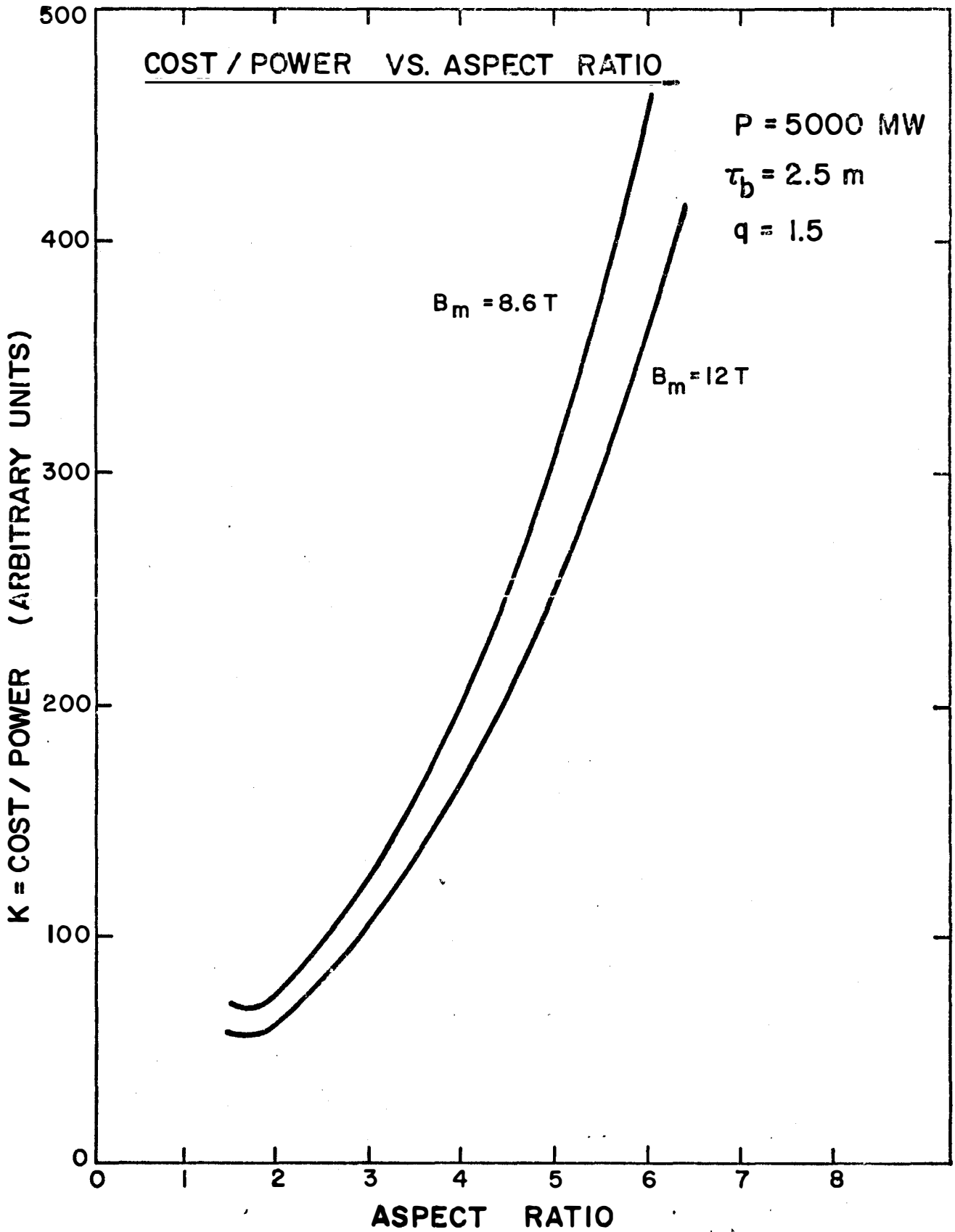


FIGURE II-B-7

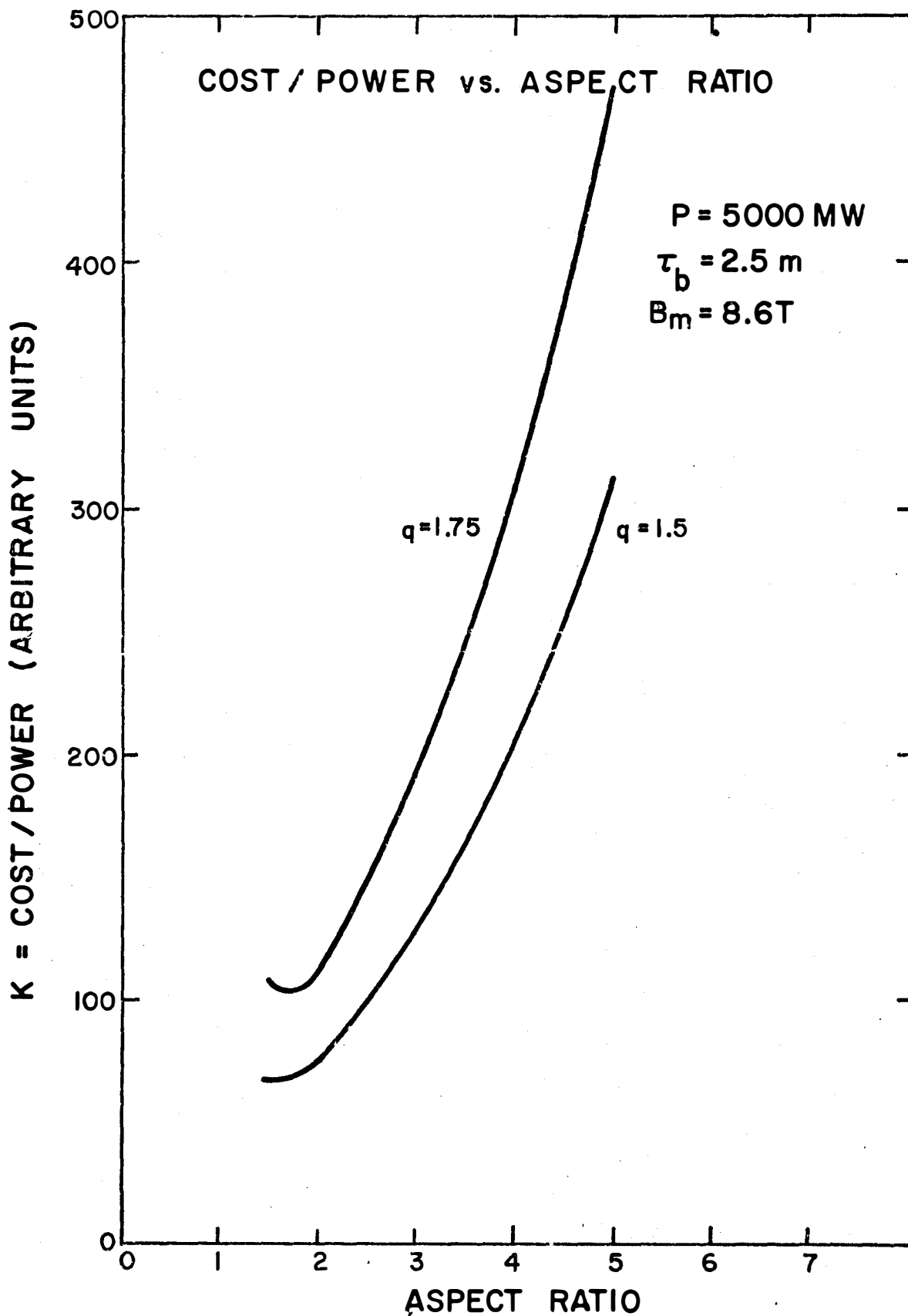


FIGURE II-B-8

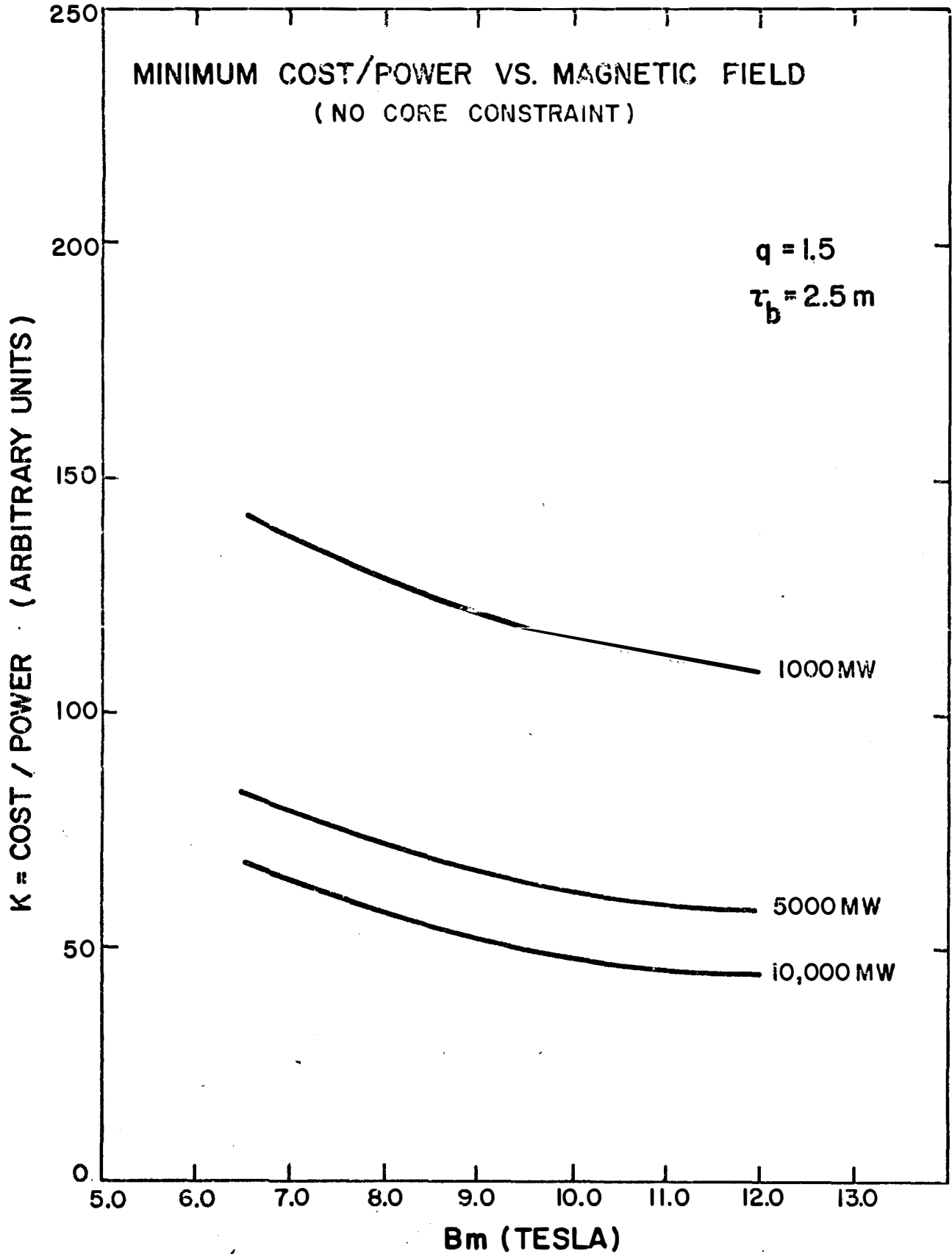


FIGURE II-B-9

where r_0 is the radius of the transformer windings, H is the combined thickness of the primary and toroidal magnet windings, τ_b is the vacuum gap plus blanket and shield thickness, and "a" the plasma radius (see Figure II-B-3.) For an air-core transformer with superconducting windings, r_0 can be computed as follows (22)

$$\pi r_0^2 B_{sp} = \phi_c = 1/2 L_p I_\phi \quad (26)$$

where B_{sp} is the superconducting primary field and L_p and I_ϕ are the plasma ring inductance and current, respectively. Since

$$B_\theta = \frac{\mu_0 I_\phi}{2\pi a} = \frac{B_\phi}{qA} \quad (27)$$

and

$$L_p \approx \mu_0 R(\ln 8A - 1.75), \quad (28)$$

it follows that

$$r_0 = \left[\frac{B_m (R-r_m) a}{q B_{sp} A} (\ln 8A - 1.75) \right]^{1/2}. \quad (29)$$

This equation is only an approximation and is conservative because of the transformer action of the divertor coils (Section II-C). For the family of (R,a) generated in the previous section, the (R,a) minimum is chosen that satisfies the constraint expressed by Equation (25). The effect of the core constraint is to increase the minimum cost, move the minimum cost reactor to higher aspect ratios and to introduce an aspect ratio dependence on magnetic field strength. The larger the magnetic field, the larger the aspect ratio for minimum cost. Figure II-B-10 shows these trends. For power levels less than 5000 Mw(th), the cost/power actually increases with magnetic field strength. By comparing Figure II-B-10 with Figure II-B-9, it can be seen that the cost of a 1000 MW reactor is a factor of three higher and the 10,000 Mw(th) reactor, 50% higher at 12T, because of the core constraint. Physically, the larger magnetic field strength requires smaller major and plasma radii to satisfy the power constraint. In order to satisfy the core constraint, a set of (R,a) values must be chosen that is far from optimum. A similar plot for a larger stability value, $q = 1.75$ used in UWMAK-I, is shown in Figure II-B-11. The same qualitative behavior exists but is not as severe as for the $q = 1.5$ case. However, when $q = 2.5$, the core constraint has only a

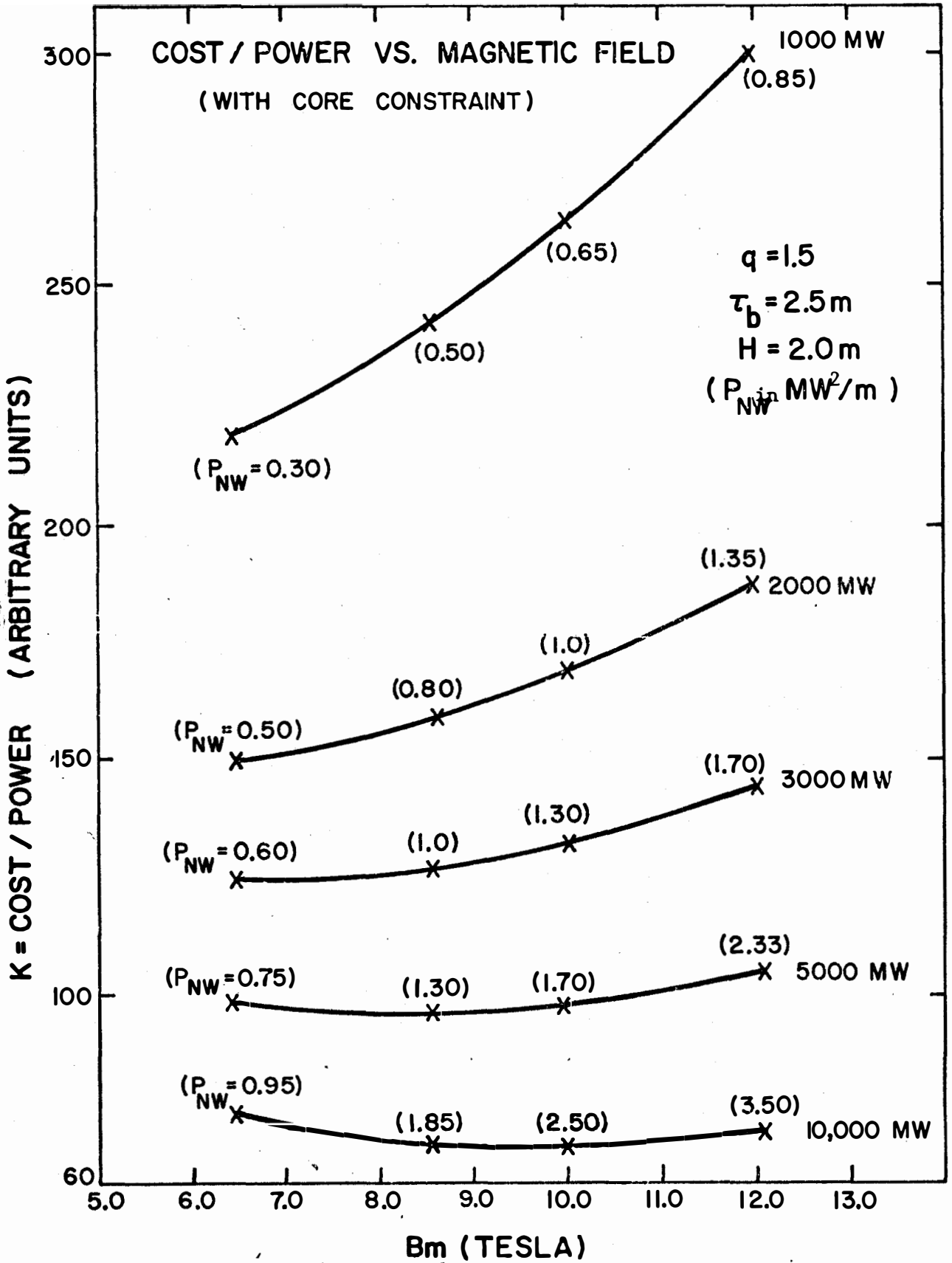


FIGURE II-B-10

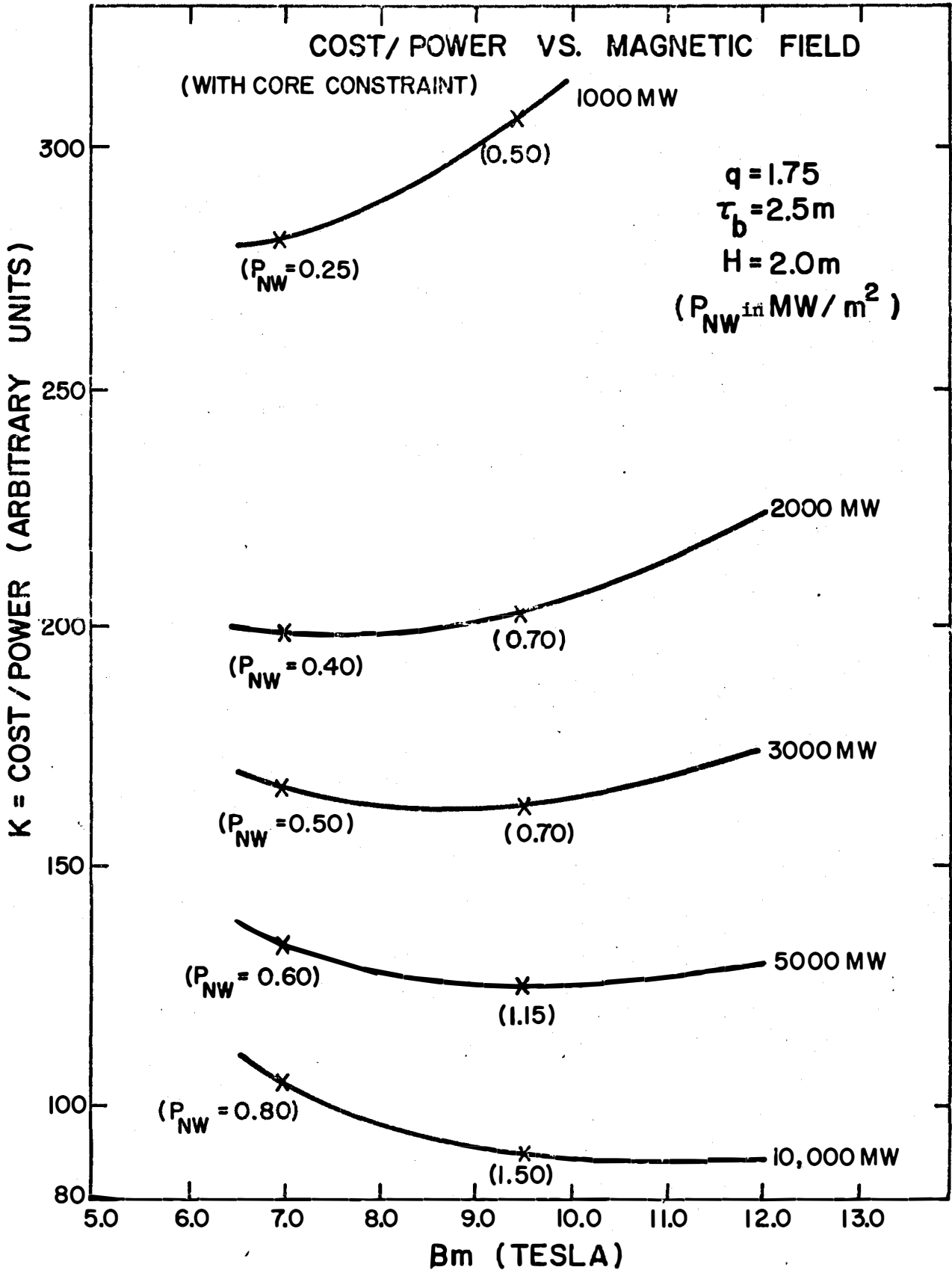


FIGURE II-B-11

small effect. In this case, since the power is inversely proportional to q^4 , larger major and plasma radii must be chosen to satisfy the power constraint. This larger (R,a) more easily satisfies the core constraint but the cost/power is more than twice the $q = 1.5$ case.

The core constraint has also moved the minimum cost reactor to higher neutron wall loadings. Materials studies as discussed in chapter VI, have indicated that the neutron wall loading may be the limiting constraint in the design of a power reactor. In both Figures II-B-10 and II-B-11, the neutron wall loadings (P_{nw}) are given in parenthesis.

Figure II-B-12 and Figure II-B-13 show the sensitivity of the results to variations in the blanket-shield thickness and primary toroidal windings, respectively. The absolute cost/power is very sensitive to these variations because the smaller thickness allows the same magnetic field on axis for a lower field at the magnet and consequently, a lower cost. Also, the same behavior with magnetic field exists as in Figure II-B-10. For the 2000 MW_T reactor, an increase in magnetic field yields an increase in cost whereas the cost of the 5000 MW_T reactor is almost independent of the field. Since it is unreasonable to expect blanket-shield plus vacuum gap plus insulation thickness to be less than 1.5m, and since the toroidal plus primary winding thickness will be at least 1 m., these results are realistic.

In summary, it has been found that the core constraint significantly increases the cost for CTR Tokamak reactors under 5000MW_T. Actually, the cost increases with increasing field for reactors smaller than 5000 MW_T. The size of UWMAK-I was therefore determined as follows. For the reasons just mentioned, the system power was set at 5000 MW_T. From a materials viewpoint (see chapter VI), a maximum allowable neutron wall loading is considered to be 1.25 MW/m² for a two-year wall life. The wall loading was therefore set at this value. When the total energy per fusion reaction, E_{fus} , is set, there is then only a single allowed value of $r_w R$, where $r_w = a + \delta$ and δ is the distance from the plasma boundary to the first wall. This relationship between neutron wall loading and $r_w R$ is given in Figure II-B-14 for various reactor powers. To obtain the wall loading for any given r_w and reactor power, one simply multiplies the value of the ordinate by $\frac{14.06}{E_{fus}}$, with E_{fus} in MeV. As discussed in Chapter V,

UWMAK-I produces 20MeV per fusion event. Thus, for a 5000MW_T plant with a neutron wall loading of 1.25 MW/m², the product $r_w R$ is 71.5 m². The distance, δ , is chosen as 50 cm such that a 3.5 MeV α -particle, born at the edge of the plasma (at $r=a$) on a weakly trapped banana orbit, will not contact the first wall. Further the optimization studies just discussed indicates that an aspect ratio of 2.6 is nearly optimal and is consistent with the core constraint. With $A=2.6$ and the other parameters fixed as described, the plasma radius must be 5 meters and the major radius 13 meters. The geometry and size of UWMAK-I is now set. The remaining sizes, such as blanket and shield thicknesses and magnet bore, are discussed in the chapters on those topics.

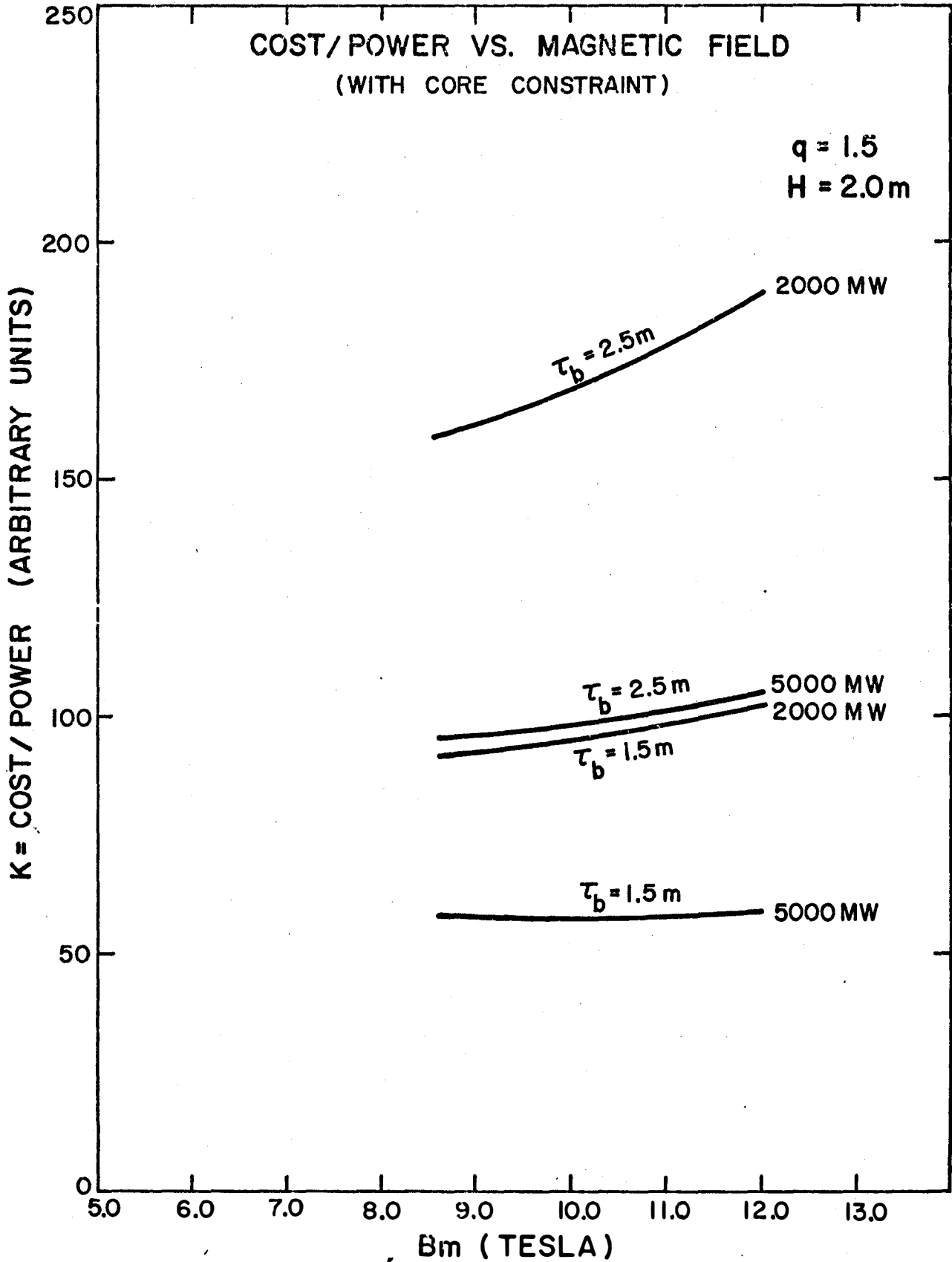


FIGURE II-B-12

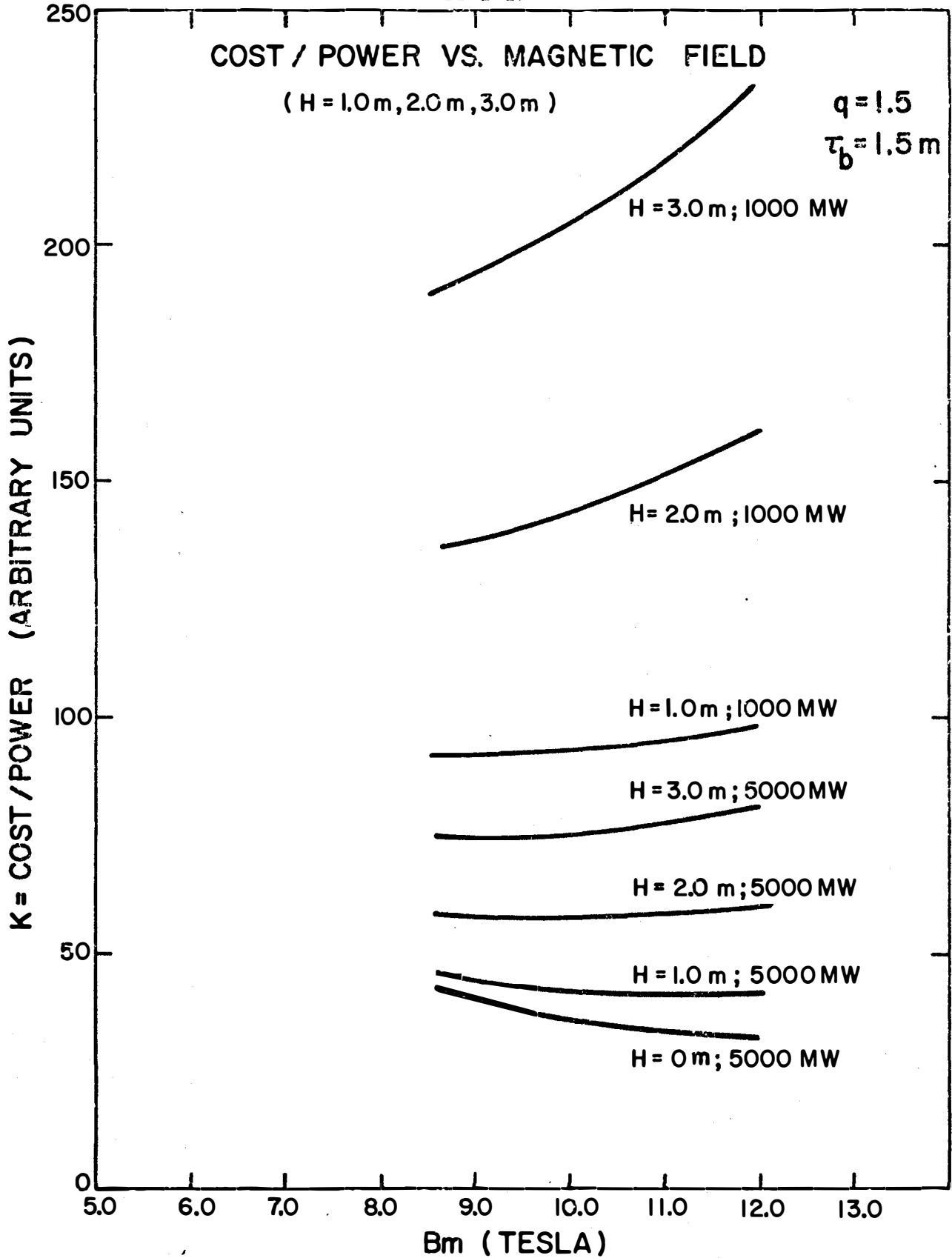


FIGURE II-B-13

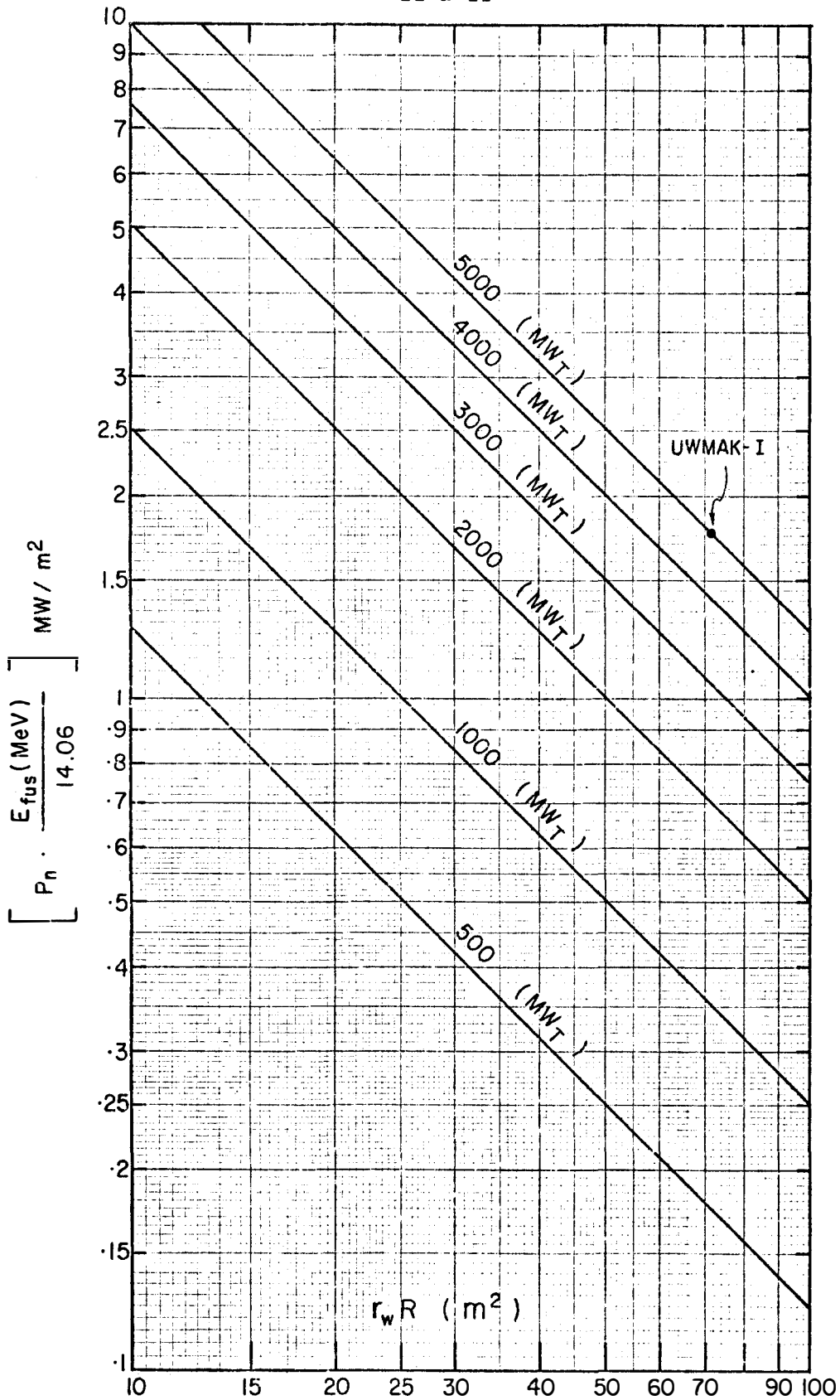


FIGURE II-B-14

II-C. Start-Up

At the start of each burn cycle, the plasma current required for Tokamak operation is generated by having the plasma act as a single turn secondary of a transformer. Energizing the primary side of the transformer produces an electric field that causes gas breakdown and plasma formation in the torus (the plasma could be preionized by other means) and drives the plasma current. Once the desired operating condition is attained and the diffusion-driven current (bootstrap current) is sufficient, according to neoclassical theory, (12,13); no electric field is required. Operation could then be truly steady-state unless other factors, such as impurity buildup, limit the burn time. If the bootstrap current is nonexistent, then the necessary electric field to maintain the plasma current is small and can be obtained by a slowly rising primary current in the transformer. In this case, the Tokamak reactor is a pulsed device but the burn time per pulse can conceivably be quite long. The reactor can thus be considered steady-state during the burn. (For the design in this report, the burn time is approximately 5400 sec or 90 minutes.)

In this section, we discuss the design and operation of the transformer. The primary is assumed to be superconducting and the coupling to the plasma is via an air-core. The transformer currents are assumed to vary from some positive value to some negative value giving a total change in the transformer current of $2I_T$. This procedure gives the smallest core size. The exact limits for the transformer currents are determined by minimizing the required magnetic poloidal field energy. This then minimizes the maximum required power. The determination of these values is discussed shortly. Alternatives to the above approach include using a normal conducting primary programmed to vary from some maximum current to 0 with an air-core or using a superconducting primary programmed the same way with an iron core. Both these possibilities were studied and were found to require larger core sizes than the design chosen. (23) The smallest possible core size is required to allow the smallest possible aspect ratio (see Section II-B, Optimization).

During the burn, the plasma current $I_\phi(t)$ is constant at the design value, I_ϕ . For simplicity, we assume that $I_\phi(t)$ rises linearly in time during the startup as shown in Figure II-C-1. The time, T_1 , has been chosen as 100 seconds to keep dB/dt on the superconducting coils low (maximum $\dot{B} = .6kG/sec$, thus keeping the heat load small). In addition, $T_1 = 100$ seconds keeps the maximum power requirements during startup to about 1000 MW_e .

The plasma resistance is shown in Table I for various values of the electron temperature. For $T_1=100$ sec, the inductive reactance during the current rise is $\omega L \sim 10^{-6}$ ohm. Thus for $T_e < 50eV$, the plasma acts like a resistive load whereas for $T_e > 50eV$, the plasma is an inductive load. To a first approximation, we will neglect the resistive phase and assume that over the entire time

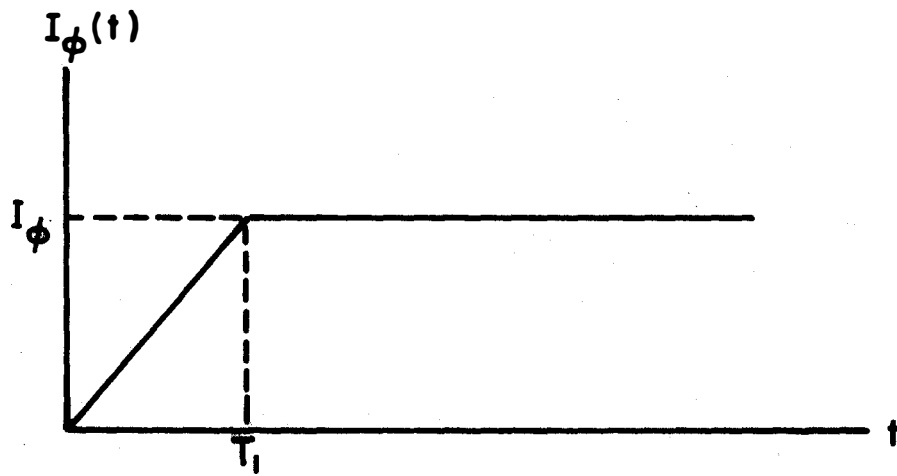


Figure II-C-1

Table I

Electron Temperature (KeV)	Resistivity* (ohm-cm)	Resistivity**	Resistivity†
.01	2×10^{-3}	7.3×10^{-3}	7×10^{-3}
.1	8×10^{-5}	2.9×10^{-4}	2.8×10^{-4}
1.0	3×10^{-6}	1.1×10^{-5}	1.05×10^{-5}
10	1×10^{-7}	3.65×10^{-7}	3.5×10^{-7}

* based on Spitzer resistivity

** based on neoclassical resistivity assuming a flat temperature profile.
The conductivity is assumed to vary as.

$$\sigma = \sigma_{sp} \left[\left(1 - 1.95 \left(\frac{r}{R}\right)^{1/2} + .95 \left(\frac{r}{R}\right)\right) \right]$$

where σ_{sp} is the Spitzer conductivity. The values in the table are obtained^{sp} by averaging over the minor cross section.

† based on $\sigma = \frac{\sigma_{Spitzer}}{Z_{eff}}$, assuming a nominal value of $Z_{eff} = 3.5$.

of current rise, the plasma acts like a perfect conductor with "frozen" poloidal flux.

The inductance of the plasma increases as the poloidal field of the plasma soaks into the blanket. This process will continue for a few seconds after T_1 and means that an increase in the core flux is required to maintain the plasma current constant at I_ϕ . Thus, the required waveform for the core flux is that shown in Figure II-C-2.

After the soak phase has terminated, the core flux is held constant if the bootstrap current is present or is increased slowly to make up for the resistive drop if the bootstrap current does not appear. The value of the plasma resistivity has been anomalously high relative to the Spitzer value. Neoclassical theory predicts a reduction in conductivity in the banana regime due to trapped electron effects. The predicted variation is

$$\sigma(r) = \sigma_{sp} \left(1 - 1.95 \left(\frac{r}{R} \right) + .95 \left(\frac{r}{R} \right)^2 \right)$$

where σ_{sp} is the Spitzer conductivity. Assuming a flat temperature profile, we can average $\sigma(r)$ over the minor radius and obtain, for UWMAK-I parameters, $\langle \sigma \rangle = (\sigma_{sp}/3.65)$. In addition, the conductivity can be reduced due to impurities by the effective Z of the plasma. For Z_{eff} defined as

$$Z_{eff} = \frac{1}{n_e} \sum_j n_j Z_j^2,$$

we have

$$\langle \sigma \rangle = \frac{\sigma_{sp}}{3.65 Z_{eff}}$$

or, for the resistivity, η ,

$$\eta = \eta_{sp} (3.65) Z_{eff}.$$

Thus, for $Z_{eff} \sim 3$, the resistivity can be anomalous by a factor of 10. However, it is not clear yet that these effects are multiplicative as indicated and for the remaining analysis, we will use the Spitzer resistivity at 11 KeV (the temperature during the burn, see section II-F) as a benchmark case and consider other cases relative to it.

For a 90 minute burn time, the volt-second requirement is 94.7 for the Spitzer resistivity case. Therefore, using the neoclassical resistivity implies 345.7 volt-seconds are required and if the resistivity is anomalous by a factor of 10, the volt-second requirement becomes as high as 1000.

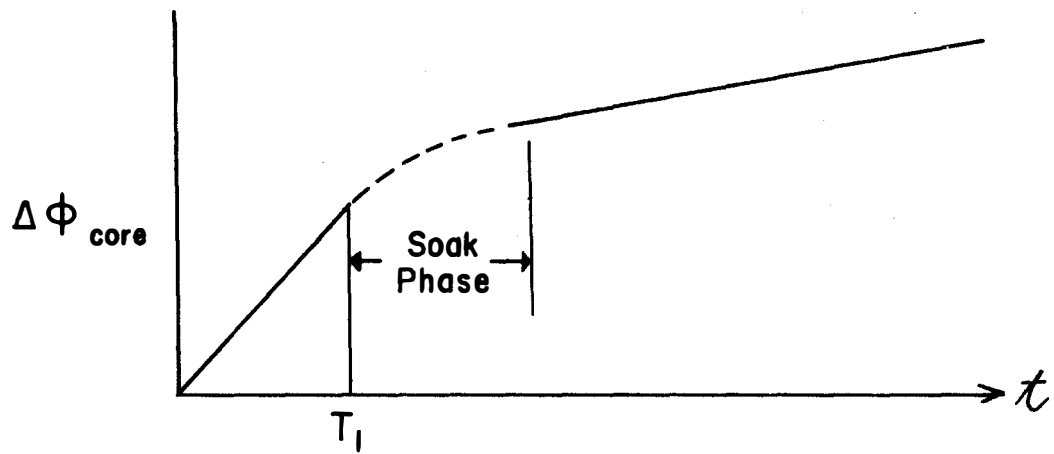


Figure II-C-2

The divertor coils (see Chapter III) are programmed to rise with the plasma. They produce a time changing flux through the plane of the plasma and hence, must be considered in designing the transformer primary. For UWMAK-I, the divertor provides 60% of the flux needed to energize the plasma current so that the transformer proper need only provide 40%. The mutual inductances of the plasma with the transformer and divertor coils has been calculated using the plasma magnetic major radius of 14 meters as opposed to the geometric plasma radius of 13 meters. The choice has been made based on the fact that the plasma currents are displaced toward the outside to obtain radial equilibrium. A more detailed justification is given in Section III. The mutual inductances were determined in terms of complete elliptical integrals. The currents were considered to be single filaments at the coil locations. The finite size of the coils has not been neglected in the self-inductance calculations, where expressions from Grover⁽⁵⁶⁾ were used. The divertor coil currents must be off at $t=0$ in order to prevent particles from going to the wall during breakdown and plasma formation. The currents in the divertor coils then rise to $+I_D$ and generate the necessary vertical field and the appropriate divertor geometry. The magnetic flux which will be stored in the blanket as the eddy currents decay is provided by the transformer primary windings, not by the divertor coils. Likewise, if a constant electric field is required to maintain the plasma current, this field must be supplied by the transformer primary only and not the divertor currents (since they are fixed in relation to the plasma current.)

The transformer coil currents have been determined in the following manner. The flux through the circle inscribed by the magnetic axis due to the divertor currents and the plasma current is calculated using a computer code described in Section III-B, Divertor Magnetic Field Design. The radius r_T of the transformer at the midplane (see Fig. II-C-3) is chosen consistent with the size of the D-windings and the anticipated size of the coils. A field line generated only by the plasma current and passing through r_T is calculated. This field $I = H\Delta$ is placed at the center of each segment by the plasma current. This procedure gives the location and relative magnitudes of a set of currents which produce flux through the center but negligible magnetic field in the vicinity of the plasma. The transformer currents determined above are then scaled (maintaining relative magnitudes) to satisfy the "frozen" poloidal flux condition,

$$\Phi(R, t=0) = \Phi(R, t > T_1), \quad (32)$$

where $\Phi(R,t)$ is the poloidal flux through the circle enclosed by the magnetic axis at time t . The final divertor currents and the transformer current change in the initial startup phase are given in Figure II-C-4. The transformer currents have been divided into 5 finite coils at the positions indicated. Since all the transformer currents are proportional, more detailed analysis of the current wave shape will be described in terms of the transformer coil T_1 .

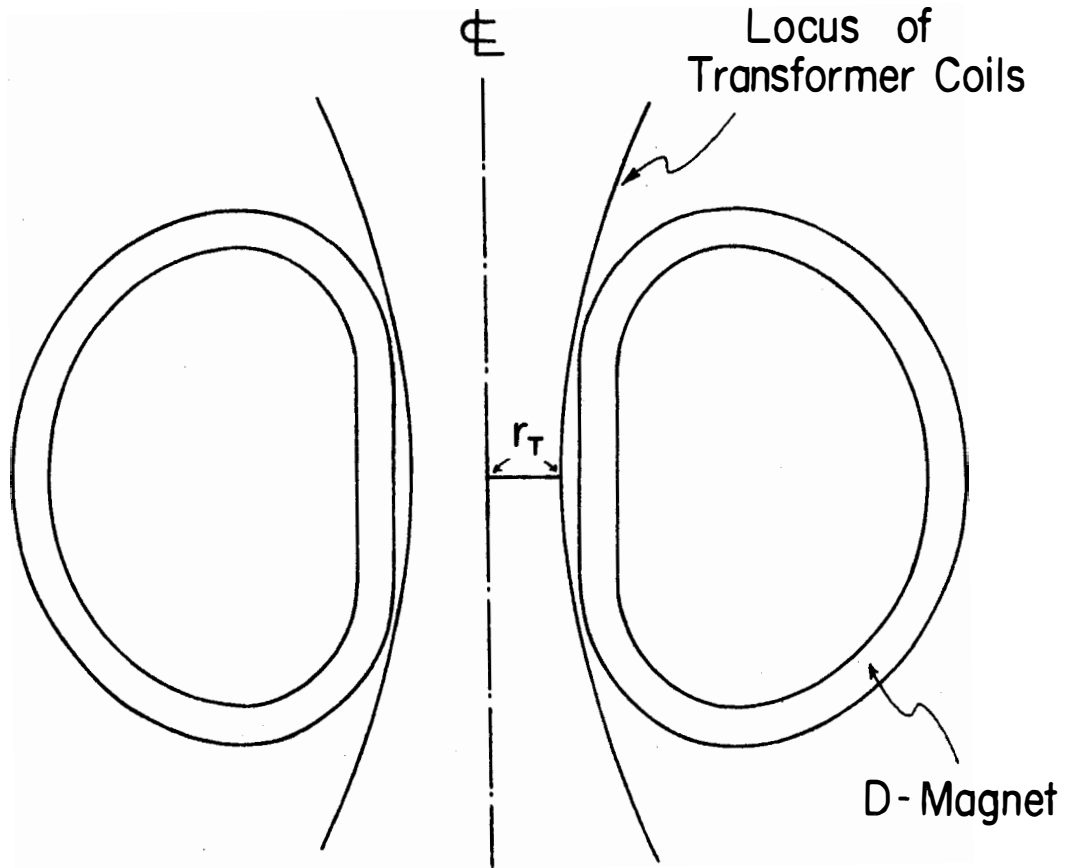
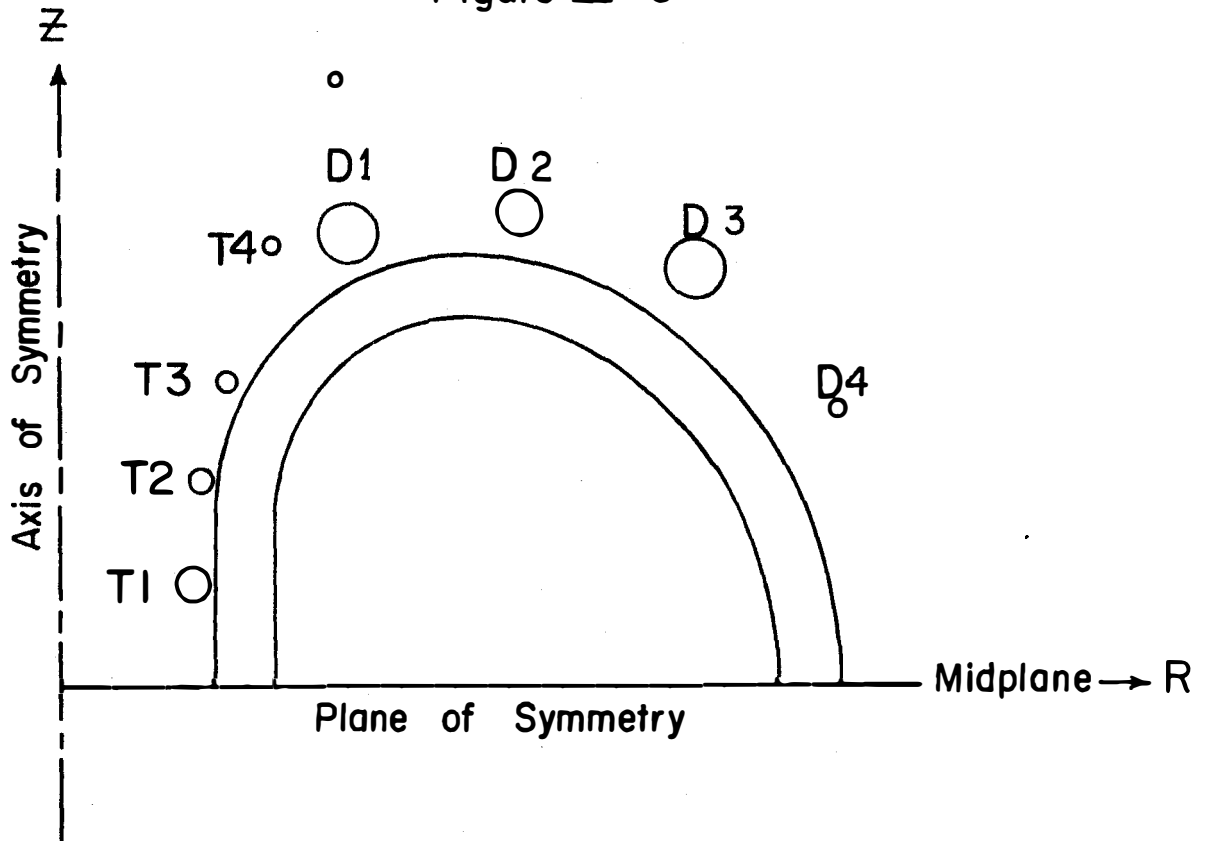


Figure II-C-3

Figure II-C-4



Coil No.	R(m)	Z (m)	I (10 ⁶ amp)	
Divertor	D 1	8	+ 24.0	
	D 2	13	+ 12.0	
	D 3	18	- 24.0	
	D 4	22	- 2.4	
Transformer			ΔI (10 ⁶ amp)	
	T 1	3.9	3.0	- 10.47
	T 2	4.3	6.0	- 9.07
	T 3	4.9	8.9	- 7.07
	T 4	6.1	12.7	- 6.55
	T 5	8.0	17.3	- 4.97

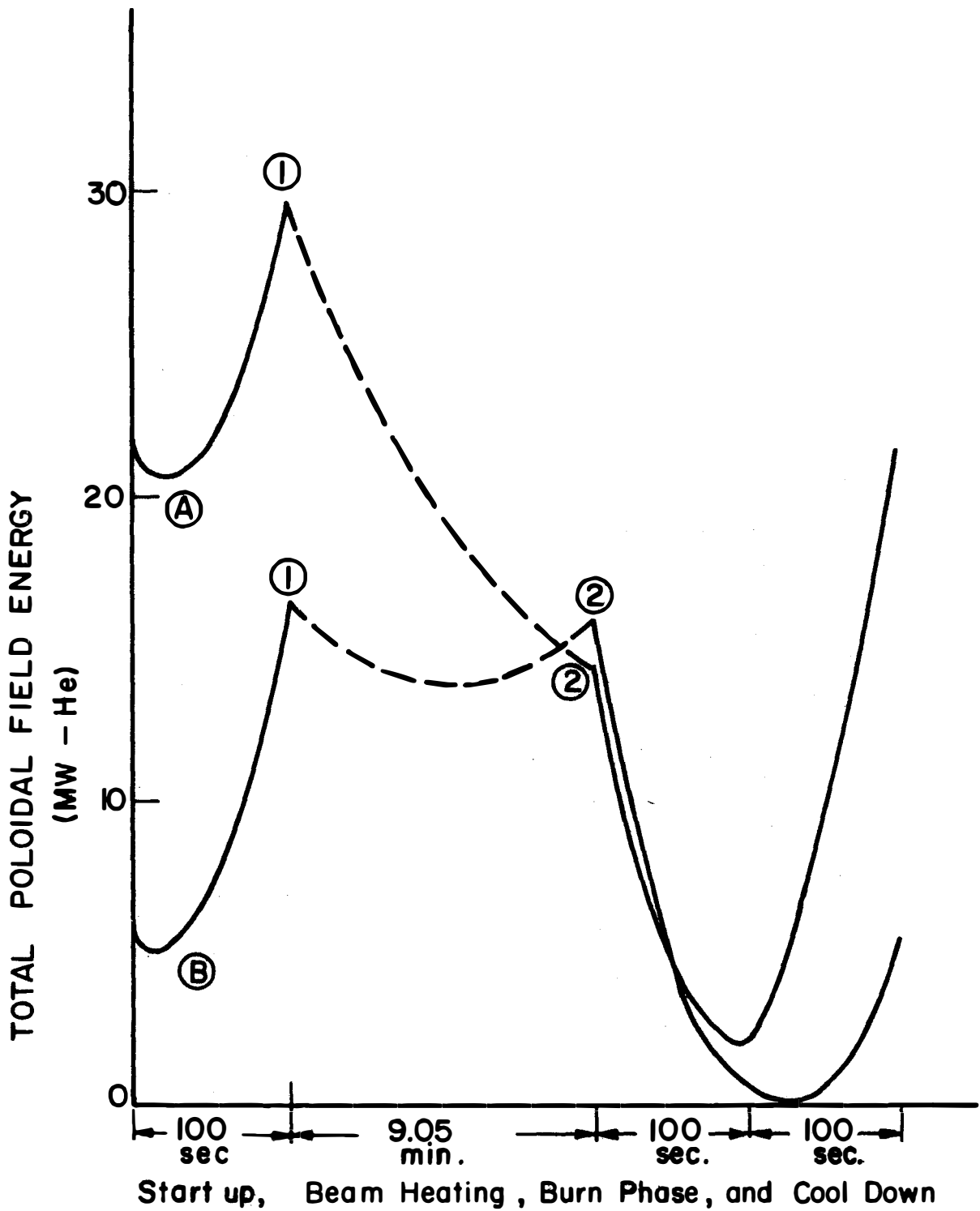
We have previously indicated that the divertor current as a function of time is determined by the plasma current. The transformer coils have been placed such that the field contributions at the plasma is small. Therefore, the magnitude and sign of I_1 at any time is arbitrary by design and other considerations determine its value. In particular, the required flux change and the desire to minimize both the magnetic energy and the power determine the current in coil T_1 . The latter conditions will also determine the size of the magnetic energy storage unit and the power rating of the SCR bridge required.

One can see the importance of correctly choosing the range of transformer currents by examining Figure II-C-5. The total poloidal magnetic energy which is used in the analysis is the only measure of energy that has a clear meaning. Due to the mutual coupling of the plasma, divertor coils and transformer coils, it is impossible to associate a certain fraction of the energy to the plasma, another fraction to the divertor, etc. Curve A plots this total poloidal energy as a fraction of time for transformer currents ranging from $2I_T \rightarrow 0$. The range in curve B is $+I/2 \rightarrow -I/2$ and results in a dramatic decrease in the maximum required energy at point 1. The optimum condition occurs when the poloidal magnetic field energy is equal at the beginning (point 1) and at the end (point 2) of the burn phase. A logical range would be $+I/2$ to $-I/2$, which assumes that the minimum energy occurs at $I(T_1) = 0$. In our system, this is not the case. As indicated in Figure II-C-6, the minimum total energy occurs at $I(T_1) = -6.35 \times 10^6$ Amps and this dictates a transformer current of $\Delta I/2 - 6.35$ at the beginning of the burn. The location of the minimum depends on the self inductance of the transformer coils, itself a function of $|I_{T_{max}}|$ and the particulars of the design determining the coil cross section. This shift, however, has proved to be small and easily corrected. At $t=0$, T_1 has a current of $(\Delta I/2 - 6.35 + 10.47) \times 10^6$ Amp, where 10.47×10^6 is the current change necessary to bring the plasma current to its operating value of 20.7 MAmps.

It is important to note that the value of ΔI is directly proportional to the plasma resistivity. As the $\Delta\phi$ required increases, the minimum energy previously described also increases, as shown in Figure II-C-7. For small resistivity values, little extra energy need be provided. However, this required energy rapidly increases and reaches 30% for $\eta = 5\eta$ Spitzer.

The present design can accommodate up to $\eta = 8\eta$ Spitzer before the critical field of 8.6 tesla is seen by the coil T_4 , the position of maximum field. A limited amount of additional flux change can be obtained by subdividing the transformer current beyond the five discrete coils already provided.

The instantaneous power required by the system has also been calculated using the inductance matrix previously computed in the calculation of the energy. The power can be written as



TIME INTERVALS WITHIN A COMPLETE BURN CYCLE

Figure II - C - 5

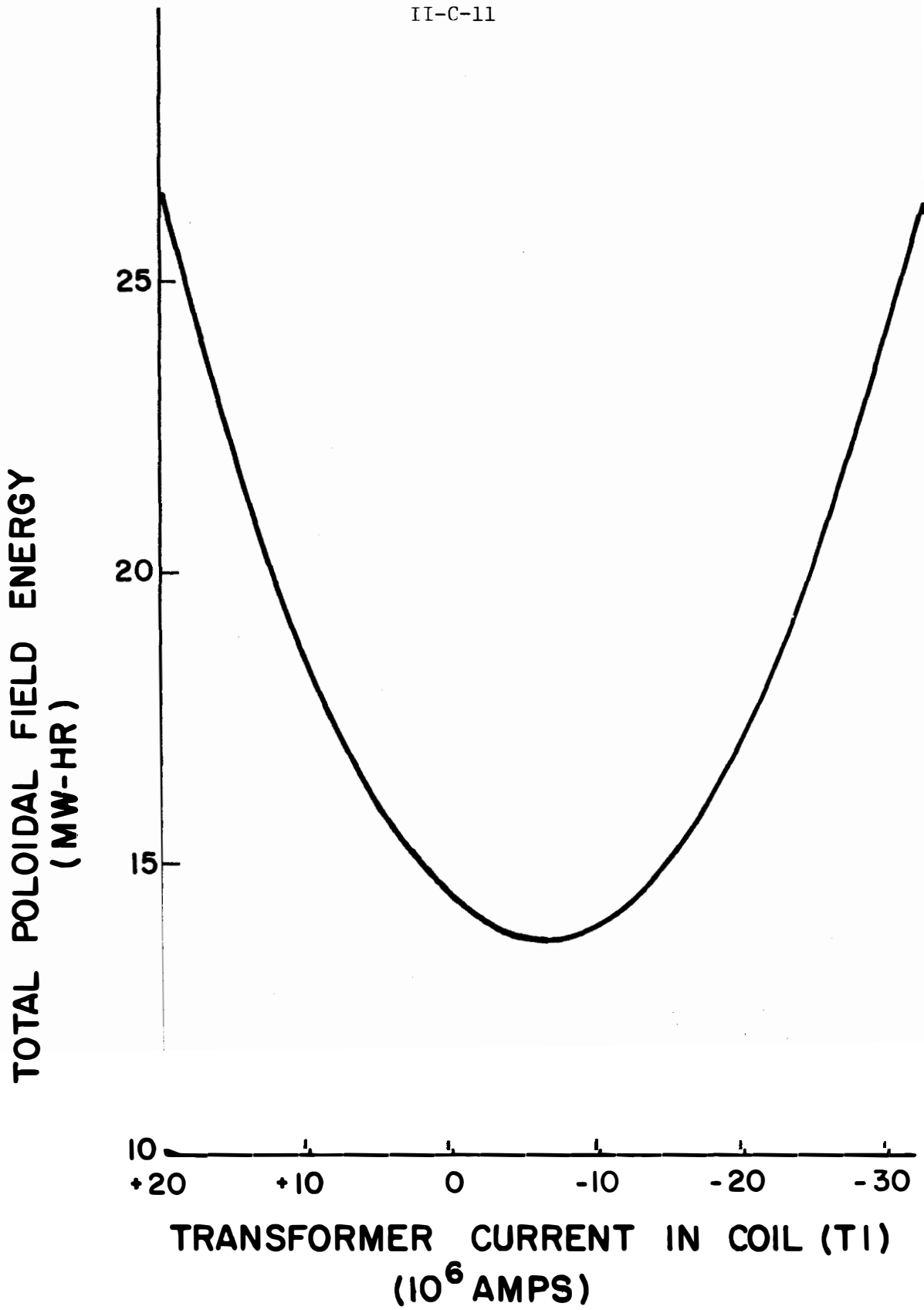


FIGURE II-C-6

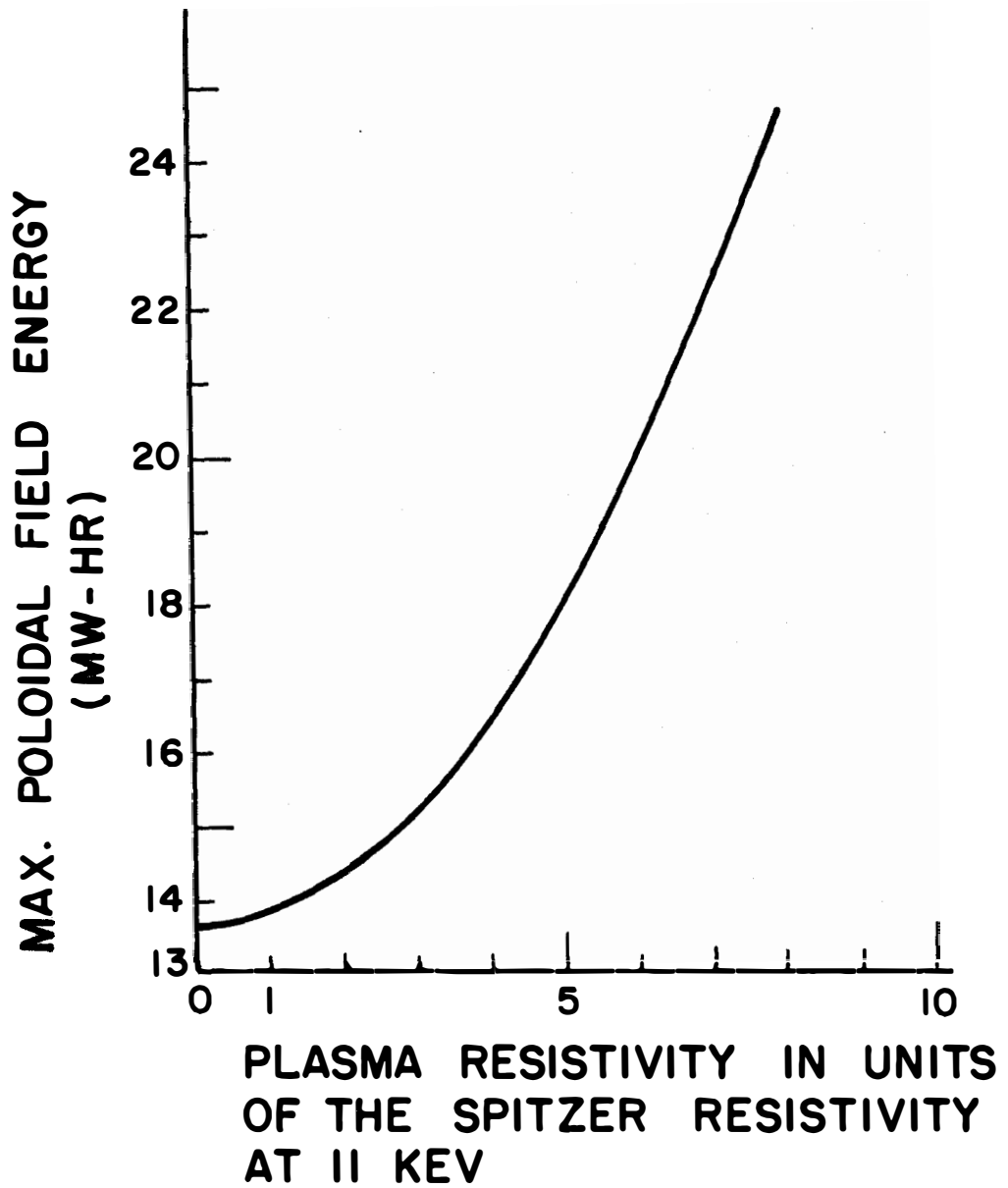


FIGURE II-C-7

$$P = \sum_{K=1}^N \sum_{L=1}^N M_{KL} I_K I_L + \sum_{K=1}^N I_K^2 R_K.$$

The peak power required from the line or a superconducting energy storage unit determines the major SCR bridge necessary for the system. The peak power during the startup and shutdown phases is almost independent of the absolute values of the transformer current, having values around 1000 MW. The coils contributing most to the power requirements are the divertor coils, which are charged and discharged during the startup and shutdown. On the other hand, the peak power of the reset phase is strongly dependent on both the range and the magnitude of the transformer currents since the divertor coils are idle at this time. The optimum current ranges previously defined also yield the lowest peak power values in this phase. For example, the power values

corresponding to the energy values of curve A (Figure II-C-5) in the reset phase was ~1500 MW as opposed to 750 MW for the optimum case. The ΔI_{burn} also affects the magnitude of the peak power in the reset phase. However, where $\eta < 7 \eta_{\text{sp}}$, the reset phase does not determine the peak required power. Figure II-C-8 follows the development of the plasma and transformer currents, the total poloidal energy and the power as a function of the time during the power cycle.

Having indicated the impact of anomalous resistivity on transformer design, and having discussed some of the uncertainties in just how anomalous the resistivity will be, we will use the neoclassical case of $\eta = 3.50\eta_{\text{sp}}$ for the design basis case in further discussions of the UWMAK-I reactor.

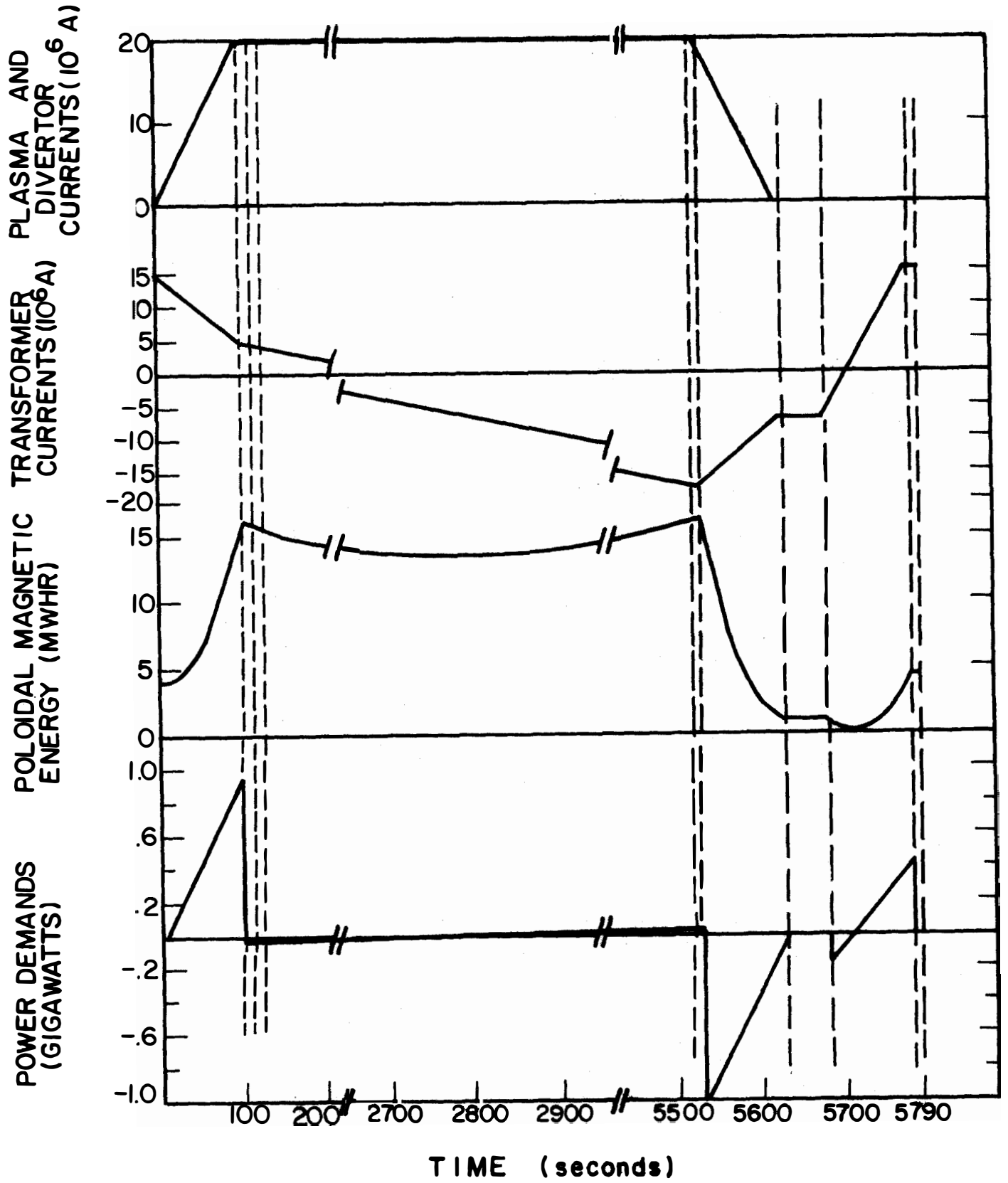


Figure II - C - 8

II-D. Neutral Beam Plasma Heating to Ignition*

1. Introduction

The prospect of heating toroidally confined plasmas by energetic neutral beam injection has stimulated much interest and optimism in the beam heating technique and predictions for present day experiments⁽¹⁻⁴⁾, lend support to this optimism. Results have recently been reported from the ATC,⁽⁵⁾ CLEO⁽⁶⁾ and ORMAK⁽⁷⁾, experiments where modest amounts of power have been injected via neutral beams. Although the Tokamak injection experimental program is still at an early stage, these recent results indicate heating rates consistent with expectations with no apparent adverse effects on plasma confinement.

The analysis is primarily for UWMAK-I, but the results are generally applicable to toroidal systems. We have indicated wherever possible, the implications of our results for other, in particular, smaller feasibility or reactor size plasmas.

The plasma model and method of solution are discussed in Section II-D-2. However, several general assumptions applicable to the model are the following: 1) the presence of background neutral gas and impurities in the plasma are not considered; 2) the possibility of a deleterious plasma response due to neutral injection⁽⁹⁾ is not included; 3) neoclassical ion transport and pseudoclassical electron transport^(15,16) are the only transport effects examined. Possible additional effects on transport, such as trapped particle instabilities⁽¹⁰⁾ are not studied. The remainder of the paper is structured as follows. In Section II-D-3, we discuss the results obtained from the study of a particular large CTR Tokamak system. In Section II-D-4, injection criteria are applied to a smaller system and the resulting beam energy and power requirements are discussed. The general conclusions of the analysis are summarized in Section II-D-5.

2. The Calculational Model for Plasma Simulation

To simulate the time evolution of the plasma parameters during heating, a two-fluid numerical model, accounting for electromagnetic field diffusion and energy flows within the plasma, is used⁽¹¹⁻¹³⁾. The electron-ion rethermalization, bremsstrahlung and synchrotron radiation, ohmic heating, thermonuclear alpha particle heating and heating by means of injected power. The governing equations for the system are written in cylindrical coordinates and depend only on the minor radius, r , and the time, t . Toroidal transport coefficients, accurate to first order in $\epsilon = 1/A$, the inverse aspect ratio, are used. The equations are as follows:

*The references for Section II-D are at the end of this section.

1) Particle Conservation:

$$\frac{\partial n}{\partial t} = -\frac{1}{r} (rnW_r) + \frac{P(r)}{E_0} \quad (33)$$

where W_r is the radial diffusion velocity, $P(r)$ is the injected power density and E_0 is the neutral beam particle energy.

2) Particle Diffusion

$$nW_r = -D_{\perp} \frac{\partial n}{\partial r} \quad (34)$$

3) Ion Energy Conservation:

$$\begin{aligned} \frac{\partial}{\partial t} \left(\frac{3}{2} nT_i \right) = & 4.77 \times 10^{-12} \left(\frac{T_e - T_i}{T_e^{3/2}} \right) n^2 Z_i^2 \frac{\ln \Lambda}{A_i} \\ & - \frac{1}{r} \frac{\partial}{\partial r} \left(r \left\{ \frac{3}{2} nW_r T_i + Q_i \right\} \right) \\ & + \frac{n}{4} \langle \sigma v \rangle_{DT} E_{\alpha} f_{\alpha i} + P(r) f_{bi} \end{aligned} \quad (35)$$

$$Q_i = -\kappa_i \frac{\partial T_i}{\partial r} \quad (36)$$

where Q_i is the ion heat flux and f_{bi} is the fraction of beam power absorbed by the ions.

4) Electron Energy Conservation:

$$\begin{aligned} \frac{\partial}{\partial t} \left(\frac{3}{2} nT_e \right) = & -4.77 \times 10^{-12} \frac{(T_e - T_i)}{T_e^{3/2}} \frac{n^2 Z_i^2 \ln \Lambda}{A_i} \\ & - \frac{1}{r} \frac{\partial}{\partial r} \left(r \left[\frac{3}{2} nW_r T_e + Q_e \right] \right) + \frac{n}{4} \langle \sigma v \rangle_{DT} E_{\alpha} f_{\alpha e} + 6.25 \times 10^{15} E_{\phi} J_{\phi} \\ & + P(r) f_{be} - P_{\text{Brem}} - P_{\text{sync}} \end{aligned} \quad (37)$$

$$Q_e = -\kappa_e \frac{\partial T_e}{\partial r} \quad (39)$$

$$P_{\text{Brem}} = 9.48 \times 10^{-17} Z_i^2 n^2 T_e^{1/2} \quad (40)$$

$$P_{\text{sync}} = 4.0 \times 10^{-12} B_\phi^{5/2} (1-R)^{1/2} n^{1/2} T_e^2 \quad (41)$$

Q_e is the electron heat flow, f_{be} is the fraction of beam energy absorbed by the electrons and R is the wall reflectivity to the synchrotron radiation. Equations (34), (36) and (39) signify that a diagonal simulation model is being used. We do not include cross flow terms, such as energy flow due to density gradients or particle flows due to temperature gradients, which are expected on general grounds(17). P_{Brem} and P_{sync} represent energy losses from bremsstrahlung(18) and synchrotron(19) radiation, respectively.

The first term on the right hand side of equations (35) and (38) accounts for electron-ion rethermalization, and $P(r)f_{bi}$ and $P(r)f_{be}$ are external sources of energy for the ions and electrons, respectively. Also $E_\alpha = 3.5$ MeV is the energy of the alpha particle produced in a D-T fusion reaction, $f_{\alpha i}$ and $f_{\alpha e}$ are the fractions of the alpha energy deposited in the ions and electrons, respectively(14). The form of the particle and energy source terms due to neutral beam injection will be developed shortly.

5) Electromagnetic Equations:

$$\frac{\partial B_\theta}{\partial t} = 10^5 \frac{\partial E_\phi}{\partial r} \quad (42)$$

$$E_\phi = \eta J_\phi \quad (43)$$

In equations (33) to (43), lengths are in cm, time is in milliseconds, density is in cm^{-3} temperature and energy are in eV, current density is in amps/cm^2 , electric fields are in Volts/cm, and magnetic fields are in gauss.

As has been noted, it is still uncertain which theory describes present day experiments and whether or not direct scaling of any existing theory to large plasmas is appropriate. In this analysis, the electron heat conduction coefficient is assumed pseudoclassical(15,16) and the ion heat conduction coefficient is taken as the banana regime of neoclassical theory(17). The particle diffusion coefficient, D_\perp , can be assumed zero for the large plasmas studied in this paper. This simplification is justified by estimating the particle confinement time as $\tau_p \approx \frac{a^2}{4D_\perp}$. Based on the initial plasma conditions and taking D to be pseudoclassical, typical particle confinement times are found to be greater than 50 seconds. The time scale for heating

the plasma is expected to be on the order of 10 seconds or less so that particle diffusion during the heating phase is negligible. The plasma density profile thus changes during heating only as a result of the addition of plasma particles by neutral injection. The transport coefficients used in the numerical simulation are given by,

$$\kappa_i = 0.68 \epsilon^{1/2} \rho_{i0}^2 n v_i \quad (44-a)$$

$$\kappa_e = 10 n v_e \rho_{e0}^2 \quad (44-b)$$

$$D_i \approx 0. \quad (44-c)$$

The forms of bremsstrahlung and synchrotron radiation loss terms and the electrical resistivity are those of Rose and Clark(18), Rosenbluth(19), and Spitzer(20), respectively. A reflection coefficient of 0.9 is assumed in the case of synchrotron radiation.

Equations (35) and (38) include terms representing the energy deposited in the plasma by alpha particles produced in deuterium-tritium fusion events. We assume that the flux surfaces in the plasma are circular and that an alpha particle deposits 3.5 MeV uniformly over the flux surface on which it is produced. In addition, the characteristic slowing down time for an alpha particle in an electron density of 3×10^{13} electrons/cm³ at a temperature of 5 KeV is less than half a second. Therefore, it is assumed that the alpha particle energy is instantaneously deposited in the plasma.

The equations for the model are non-linear coupled differential equations and require linearization of the transport coefficients. Following linearization, an implicit finite difference method(21) is used to obtain the time dependent radial profiles. Details of the numerical solution method are given by Dory and Widner(12).

The neutral beam heating phase of reactor startup is assumed to follow initial gas breakdown and the time during which the plasma current rises to its final operating value. During the beam heating phase, the plasma current remains fixed and the core flux is increased to make up for the resistive drop as the plasma temperature increases. Thus, the times to ignition given in the next section refer strictly to the beam heating phase and do not include the current rise time.

The analysis here begins with a fully ionized plasma characterized by the following relatively flat radial dependent profiles:

$$T_i(r, t=0) = T_{i0} (1 - r^2/a^2)^{1/3} + 10\text{eV}, \quad T_{i0} = 500 \text{ eV} \quad (45)$$

$$T_e(r,t=0) = T_{e0}(1 - r^2/a^2)^{1/3} \pm 10\text{eV}, T_{e0} = 500 \text{ eV} \quad (46)$$

$$n(r,t=0) = n_0(1 - .95 r^2/a^2)^{1/2}, n_0 = 3 \times 10^{13}/\text{cm}^3 \quad (47)$$

$$J_\phi(r,t=0) = J_0(1 - r^2/a^2)^{1/2}, J_0 = 40.2 \text{ amps}/\text{cm}^2 \quad (48)$$

$$E_\phi(r,t=0) = \eta J_\phi(r,t=0) \quad (49)$$

The initial temperature profiles are assumed relatively flat because the conceptual reactor, UWMak-I, is proposed to operate with an axisymmetric, poloidal field divertor. The action of the divertor should mean that a relatively rarefied zone, dominated by atomic processes, will surround the plasma outside the separatrix. The 10 eV temperature is inserted to indicate the presence of this blanket plasma. The density profile given by equation (47) is also relatively flat and the factor, .95, means the density on the edge will be roughly 20% of the center line density. We have varied the boundary temperature from 10 eV to 100 eV and varied both the shape of the density profiles and the density of the plasma at the edge. It is found that the plasma heat up rates are basically not affected. On the other hand, beam penetration is strongly dependent on the density profile. Actual beam power deposition profiles for different density profiles will be given shortly. Finally, the safety factor, $q(a)$, is set at 1.75 and the initial profiles are consistent with $q > 1$ at all plasma radii.

The energetic neutral beam injected into plasma is assumed to be composed of a deuterium-tritium neutral of atomic mass 2.5. A single equivalent atom beam of zero cross sectional area (pencil beam) is considered. In practice, the required total power would be injected by several neutral beams located symmetrically around the torus to minimize the disturbance of axisymmetry in the plasma. Rome, Callen and Clarke⁽²²⁾ have recently studied the injected energy density deposition rate profiles which result from finite beams. We find, using the computer code developed in their work, that the pencil beam approximation is accurate except in the region near the plasma center. For the UWMak-I system, the pencil beam and finite beam give essentially the same results for $r \geq .15a$. In addition, the time required to heat the plasma to ignition is not sensitive to the detailed injected energy profile near $r = 0$ since the toroidal plasma volumes in this region are small.

The neutral beam strength is defined, in equivalent amperes, by

$$I = P_T/E_0 \quad (50)$$

where P_T is the beam power in watts and E_0 is the beam particle energy in electron volts. The number of particles injected into the plasma per second, I/e , where e is the electron charge, is accounted for in equation (33).

The neutral beam particles are ionized in the plasma primarily by electron and ion impact and by charge exchange⁽²³⁾. The geometry for neutral beam injection tangent to the center of the cross section is shown in Figure II-D-1. For a neutral current, I_0 , entering the plasma, the attenuation of the beam as a function of distance along the injection chord is given by,

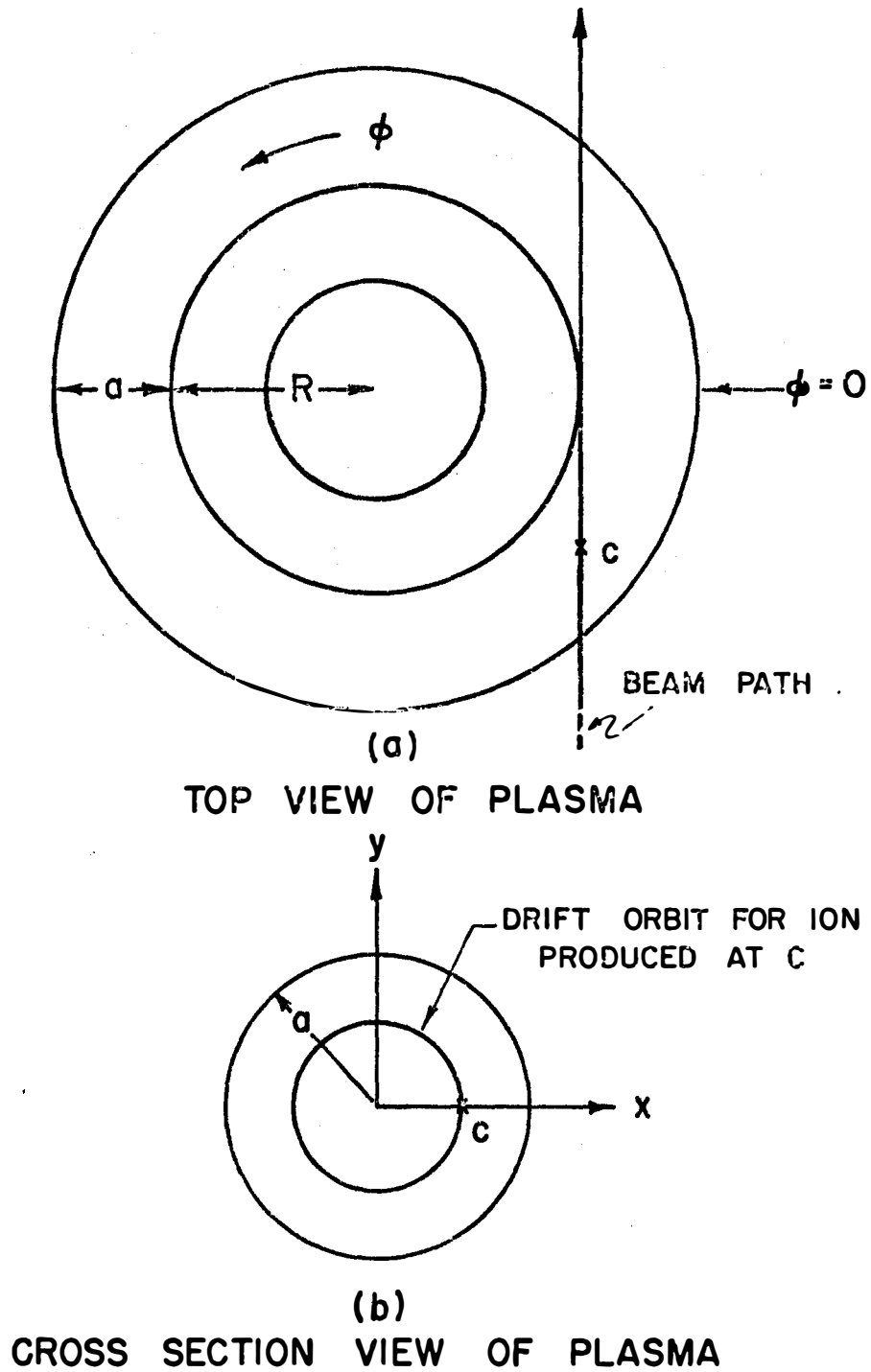


Figure II-D-1 (a) Geometry for neutral injection tangent to the geometric center of the plasma. (b) Plasma cross section view showing a typical fast ion orbit.

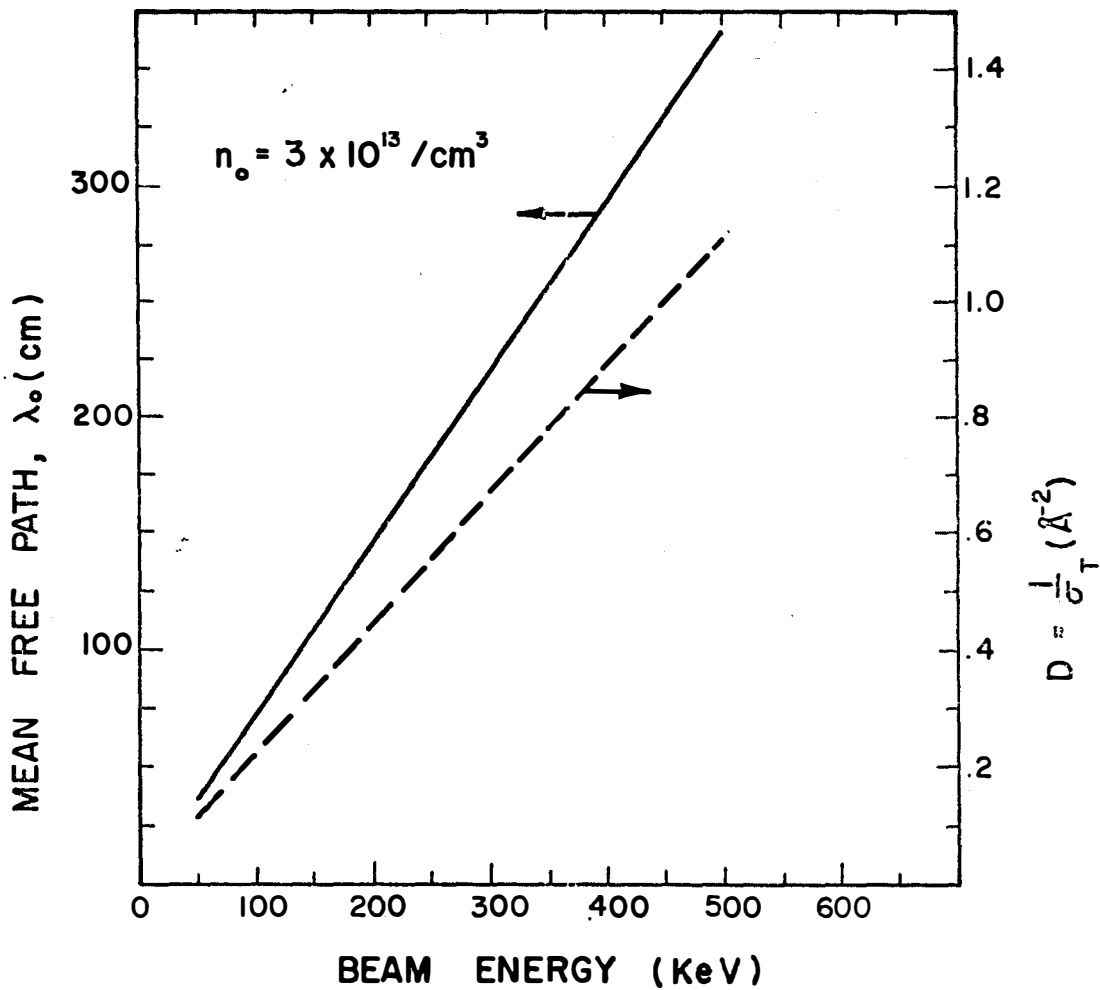


FIGURE II-D-2

Mean free path and reciprocal of the total attenuation cross section for injected neutrals, as a function of the neutral particle energy, using the fit given by Sweetman.⁽²⁴⁾ (λ_0 evaluated at a density of $3 \times 10^{13}/\text{cm}^3$.)

$$I(s) = I_0 e^{-\int_0^s n(s') \sigma_T ds'} \quad (51)$$

where

$$\sigma_T = \sigma_{cx} + \sigma_i + \frac{\langle \sigma v \rangle}{v_0} \quad (52)$$

σ_{cx} is the charge exchange cross section, σ_i is the ion impact cross section, $\frac{\langle \sigma v \rangle}{v_0}$ is the Maxwellian averaged electron impact cross section, v_0 is the neutral particle velocity and s is the distance along the chord. It is assumed that the cross sections are functions of the relative velocity of the colliding species only. For the beam energies examined in this paper ($E_0 > 100$ KeV), ion and electron impact ionization are dominant and charge exchange is small. Thus, neutral injection is not a source of warm neutrals as it can be in present injection experiments. Numerical values of the cross sections are given in references (23) and (24). We use the approximation to the data given by Sweetman⁽²⁵⁾ and shown in Figure II-D-2. In the worst case, equivalent to a 200 KeV hydrogen neutral, the error introduced by this fit to the attenuation cross section is 25%.

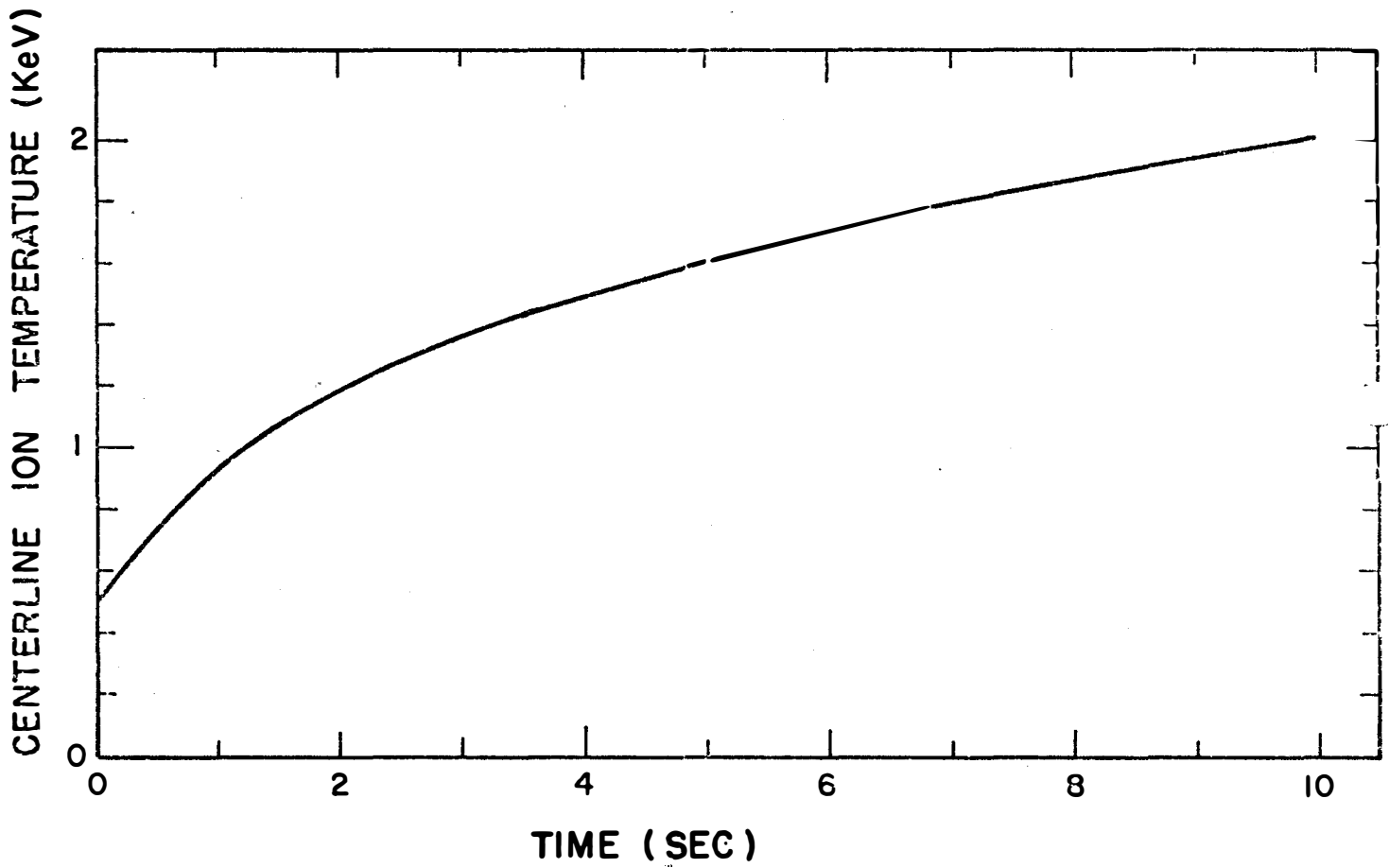
The drift orbits of the fast ions produced as the neutrals are ionized must be considered in determining the energy density deposition rate in the plasma. It has been shown that ions produced parallel to the magnetic field follow orbits which are approximately circular and centered at $x = x_s$, when projected onto a plane containing the plasma cross section^(1,22). The stagnation distance, x_s , is defined by

$$x_s \doteq qmv_\phi / eB_\phi \quad (53)$$

and for 500 KeV injected ions, the center of the orbit is $x_s \approx 7$ cm in a system the size of UWMAK-I. Since x_s is less than 7 cm for injection energies less than 500 KeV, this small shift in the orbit center is neglected. Thus, the fast ions resulting from injection are assumed to traverse circular orbits centered at $r=0$.

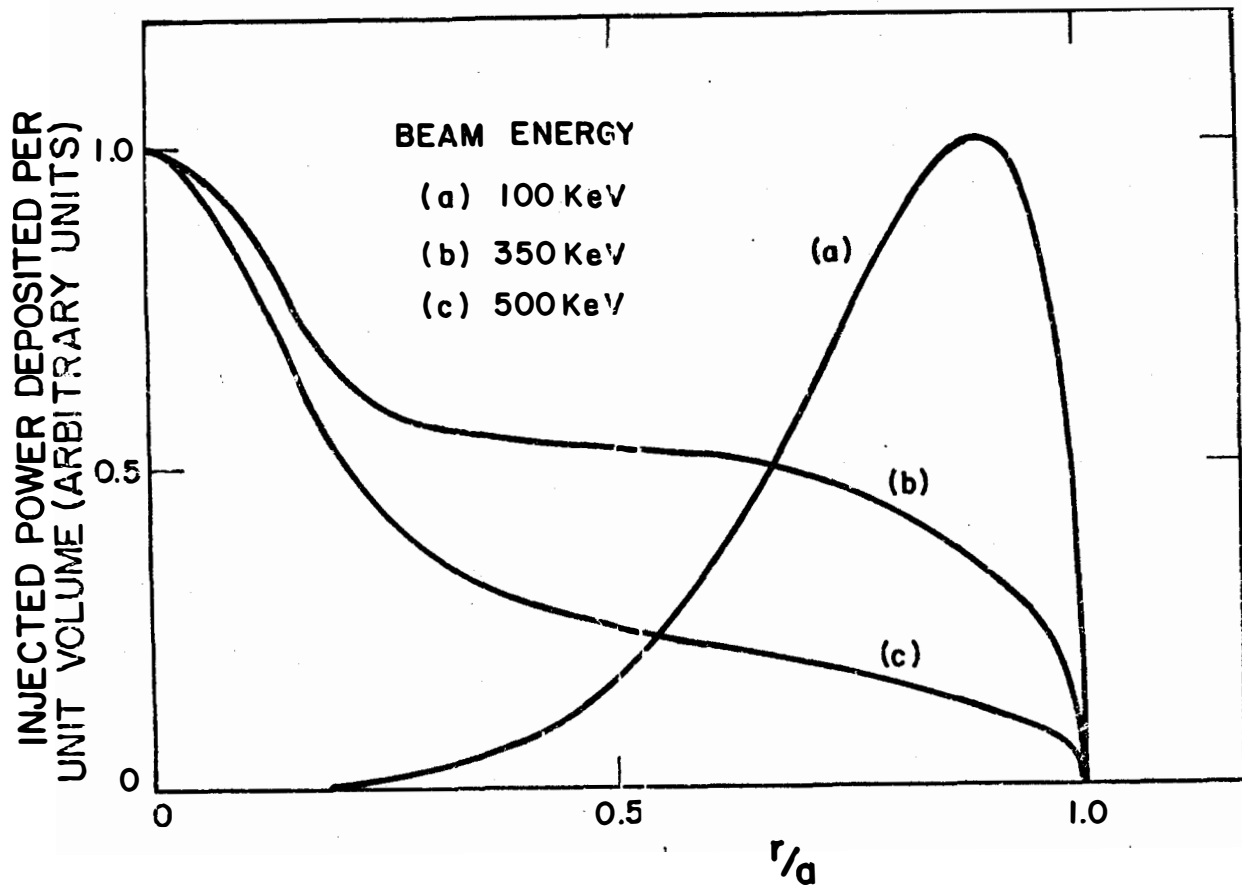
The fast ion slowing down time, as for the alpha particles is short compared with the particle confinement time so that it is assumed the ions deposit energy instantaneously over the flux surface on which they are produced. The radial shape of the energy density deposition rate for a particular beam energy is calculated numerically using the attenuation and orbit considerations just outlined and the assumed plasma density profile. In addition, the total beam power has a radial distribution in the plasma. Therefore, the total power deposited is defined as

$$P_T = 2\pi R_0 \int_0^a 2\pi r P_0 f(r) dr, \quad (54)$$



Peak ion temperatures as a function of time for the ohmically heated case. There is no neutral beam energy injected.

Figure II-D-3



Radial shape factors for beam energies of 100, 350, and 500 KeV. Shape factors are normalized to 1.0 at the radius of maximum deposition.

Figure II-D-4

where $P(r) = P_0 f(r)$ is the energy density deposition rate profile, P_0 is the power density at $r=0$, and $f(r)$ is the radial shape factor for a beam of energy E_0 . The shape factor $f(r)$ is calculated numerically and is included in equations (35) and (38) in this manner.

In a large plasma governed by the transport laws we have assumed, the time scale for rethermalization between plasma electrons and ions is small compared to the plasma heating time. Therefore, the heating times calculated are not sensitive to the exact fraction of the injection energy absorbed by each plasma specie as the fast ion slows down. We have assumed 70 percent of the injected energy is absorbed by the electrons in all cases considered in Sections II-D-3 and II-D-4.

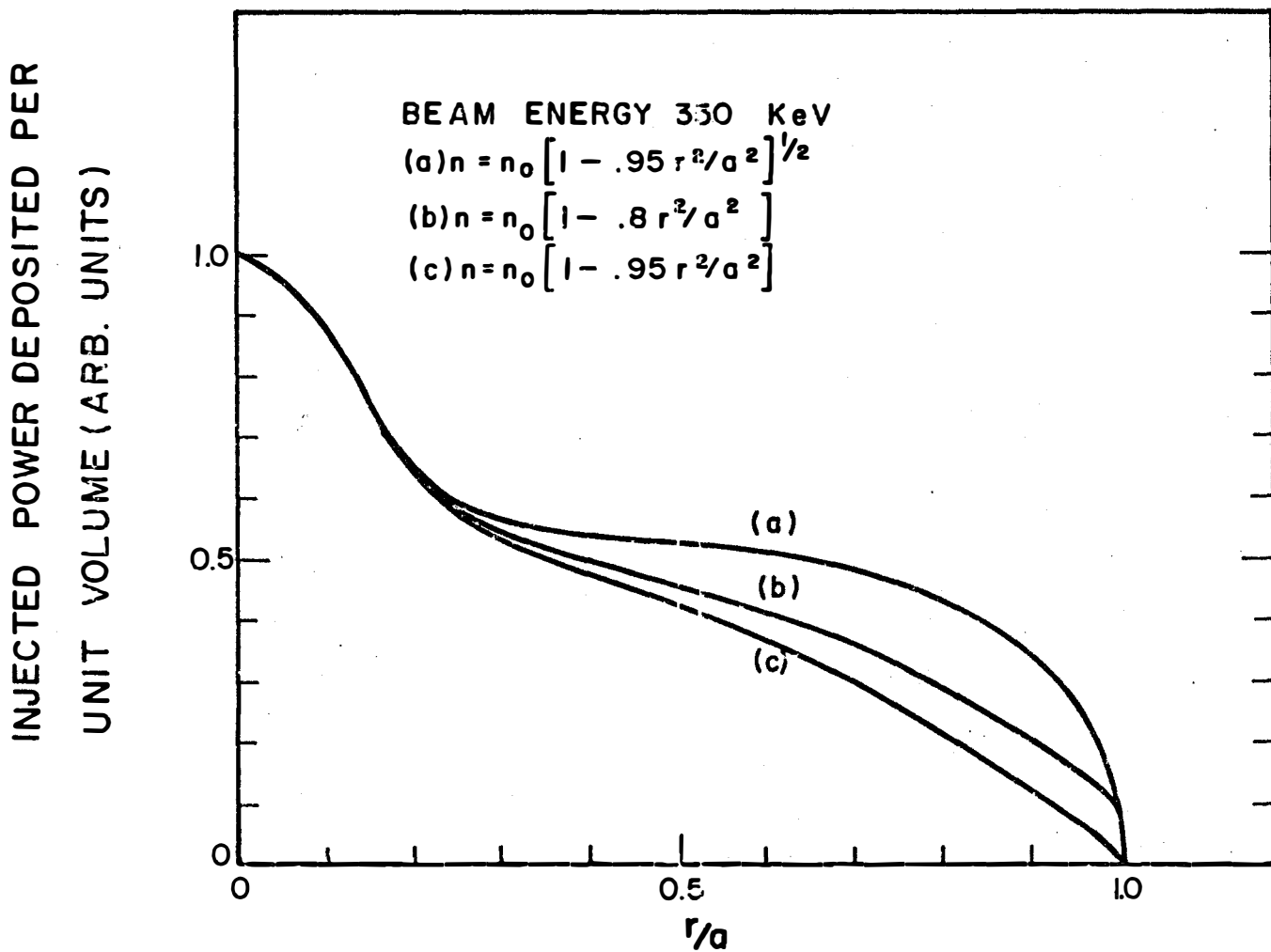
3. Plasma Heating by Neutral Beam Injection

The approach of the plasma toward thermal equilibrium, considering only ohmic heating and no beam heating, has been calculated for a five second time interval. The peak ion temperature as a function of time is given on Figure II-D-3. Using the Spitzer formula for electrical resistivity⁽²⁰⁾, heating alone is not sufficient to ignite the system. Since the temperature rise due to ohmic heating is a relatively slow process, there is no advantage in delaying injection heating until the ohmic heating phase has concluded. Therefore, injection heating will begin immediately after the plasma current has been fully established, i.e., $t=0$ with respect to the heating phase.

We now consider the neutral beam energy and power that are required to ignite such a reactor size plasma. Clearly, the beam must be energetic enough to adequately penetrate the plasma before ionization occurs. On the other hand, the beam energy is bounded from above by requiring that a large fraction of the injected neutral particles be trapped in the plasma. In large systems, such as UWMAK-I, this maximum energy requirement is really inconsequential since trapping of the injected neutrals is highly efficient.

Since the plasma is quite large in this system, we have chosen to ignite the plasma at low density, $n_0 = 3 \times 10^{13}/\text{cm}^3$, to improve beam penetration. We assume subsequent fueling after ignition can build the plasma density to a desired operating value. In addition to the penetration problem, the stored energy in the hot, dense operating plasma is very high, on the order of 1000 MJ. Therefore, it is advantageous to ignite the system at a lower stored energy⁽¹⁾. By heating the plasma to a temperature above the ignition temperature, the stored energy will increase further due to thermonuclear power, and fueling can then be accomplished by alternate means⁽²⁶⁾.

The radial shapes of the power density deposited in the plasma from 100, 350 and 500 KeV beams are shown on Figure II-D-4. The shape factors are independent of the total power in the beams and are normalized to 1.0 at the radius of maximum deposition. The fraction of the 100, 350, 500 KeV



Radial shape factors for a 350 KeV beam injected into a plasma with different density profiles.

Figure II-D-5

beams trapped in the plasma are $>.999$, $>.999$, and $>.995$, respectively. The effect of different density profiles for the 350 KeV beam is shown in Figure II-D-5. It is clear that the most concave density profile gives the most peaked power deposition profile. However, we have found that the plasma heating rate and the time to ignition are only slightly affected.

Since we consider plasma heating at a density below that desired during the burn, we are interested in both igniting the plasma and perhaps more importantly, in achieving a prescribed heat up rate to allow for subsequent fueling and density buildup. A rigorous monitor of plasma behavior relevant to ignition and heatup is the plasma stored energy, W , defined as

$$W(t) = \int_0^t (P_\alpha + P_{OH} + P_{INJ} - P_L) dt' \quad (55)$$

Here, P_α , P_{OH} , and P_{INJ} are the powers due to alpha particles, ohmic heating and injection, respectively, and P_L is the total power loss from the plasma volume. The rate of change of the stored energy is

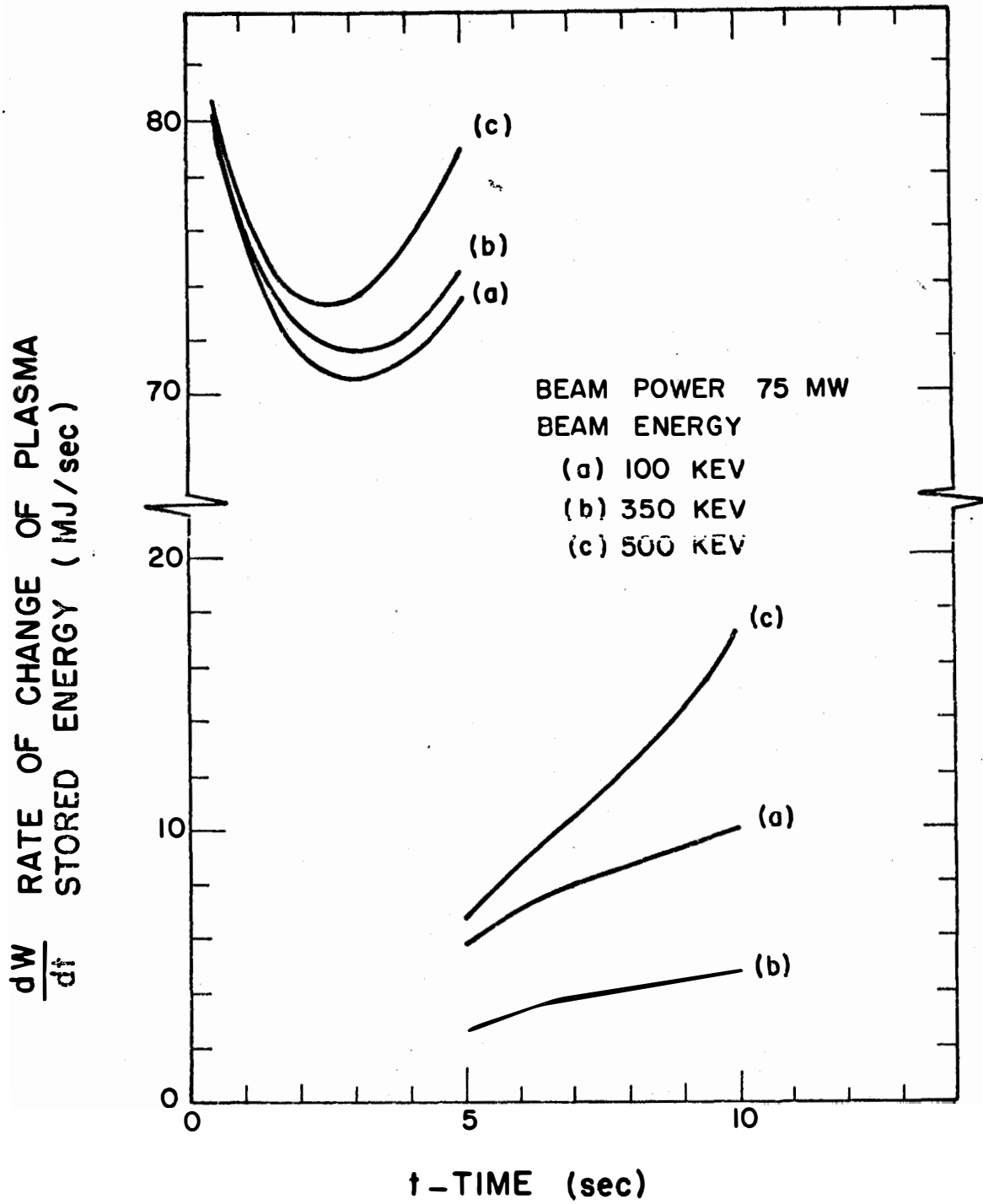
$$\frac{dW}{dt}(t) = P_\alpha + P_{OH} + P_{INJ} - P_L. \quad (56)$$

From equation (56), one sees of course that W will increase without injection if

$$P_\alpha + P_{OH} > P_L. \quad (57)$$

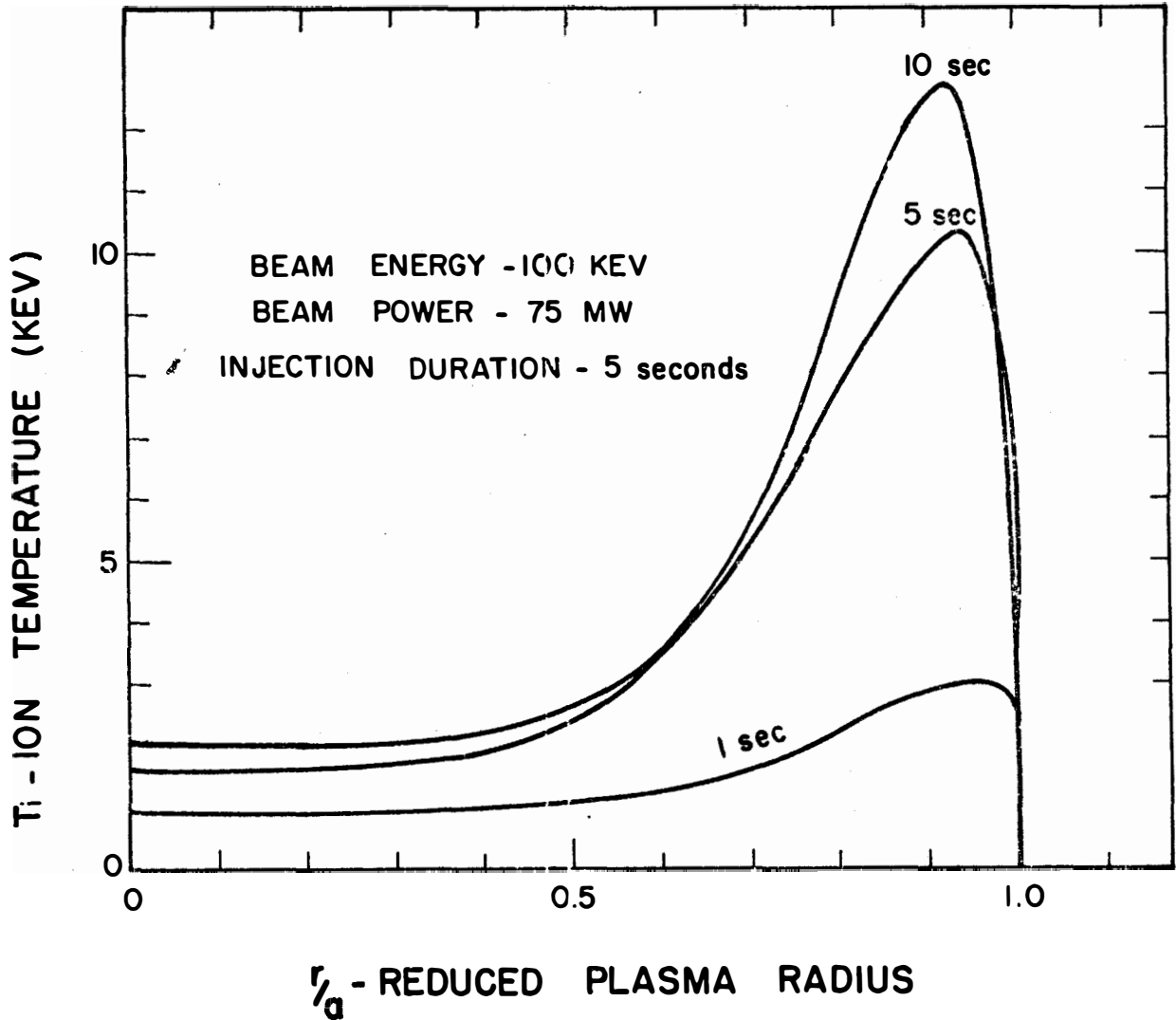
This condition, $P_\alpha + P_{OH} = P_L$, can occur at low temperature when the plasma approaches a thermal equilibrium maintained by ohmic heating. It also occurs at a higher temperature when the power deposition from alpha heating becomes dominant and the plasma ignites. As the plasma approaches the lower temperature equilibrium, the stored energy is increasing but dW/dt is decreasing and d^2W/dt^2 is negative. This equilibrium point is thermally stable, i.e., stable against excursions in plasma temperature. On the other hand, if beam heating is used until d^2W/dt^2 becomes positive, the plasma will have reached the higher temperature, thermally unstable, ignition point and the plasma will have ignited. (If plasma resistivity is anomalously large, ohmic heating alone could drive d^2W/dt^2 positive and the plasma will ignite without auxiliary heating.) Once d^2W/dt^2 is positive, the plasma will have a positive heatup rate even if beam heating is discounted. The reason is the second derivative,

$$\frac{d^2W}{dt^2} = \frac{d}{dT} (P_{OH} + P_\alpha - P_L) \frac{dT}{dt}, \quad (58)$$



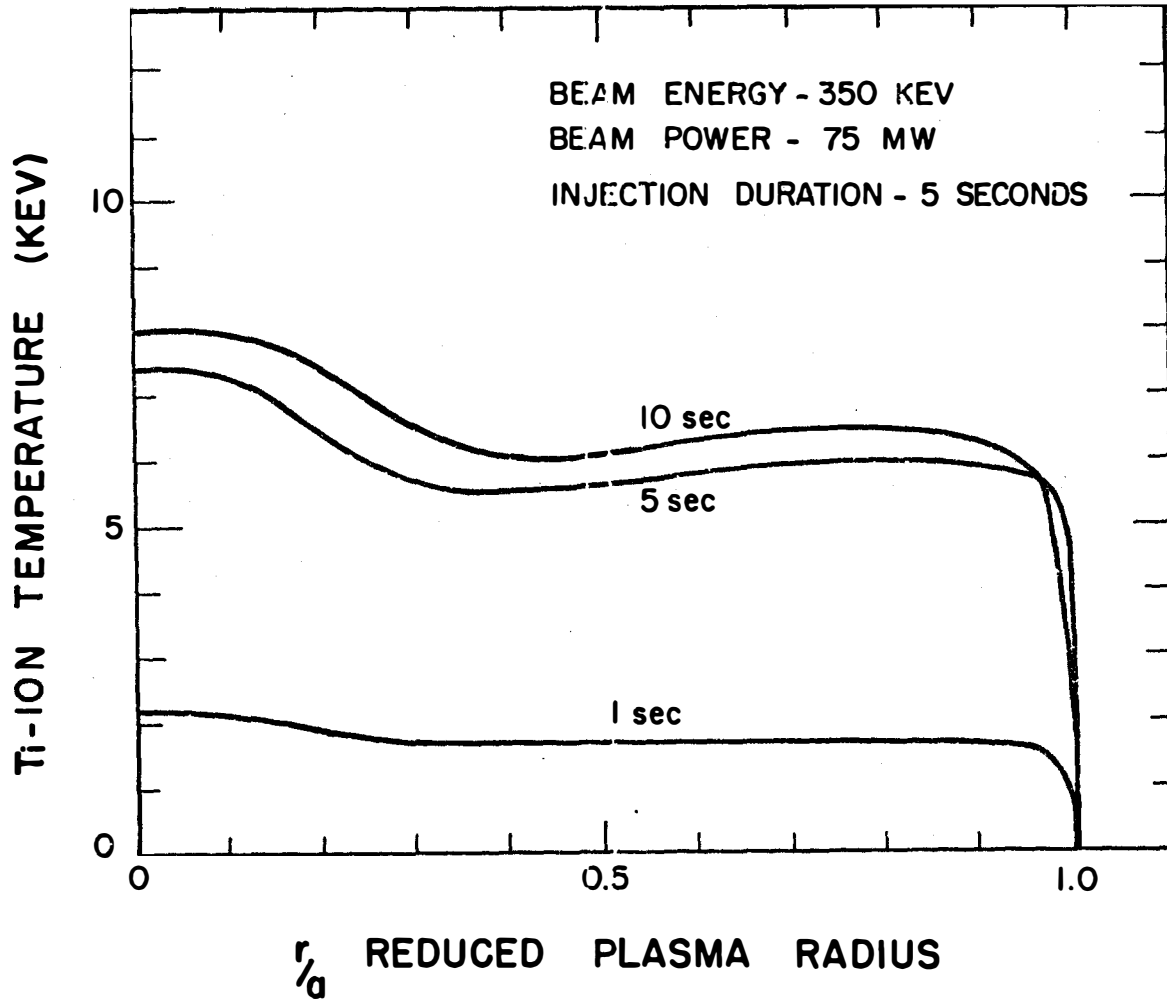
Heatup rate as a function of time for 75 MW of power injected at 100, 350, and 500 KeV for 5 seconds

Figure II-D-6



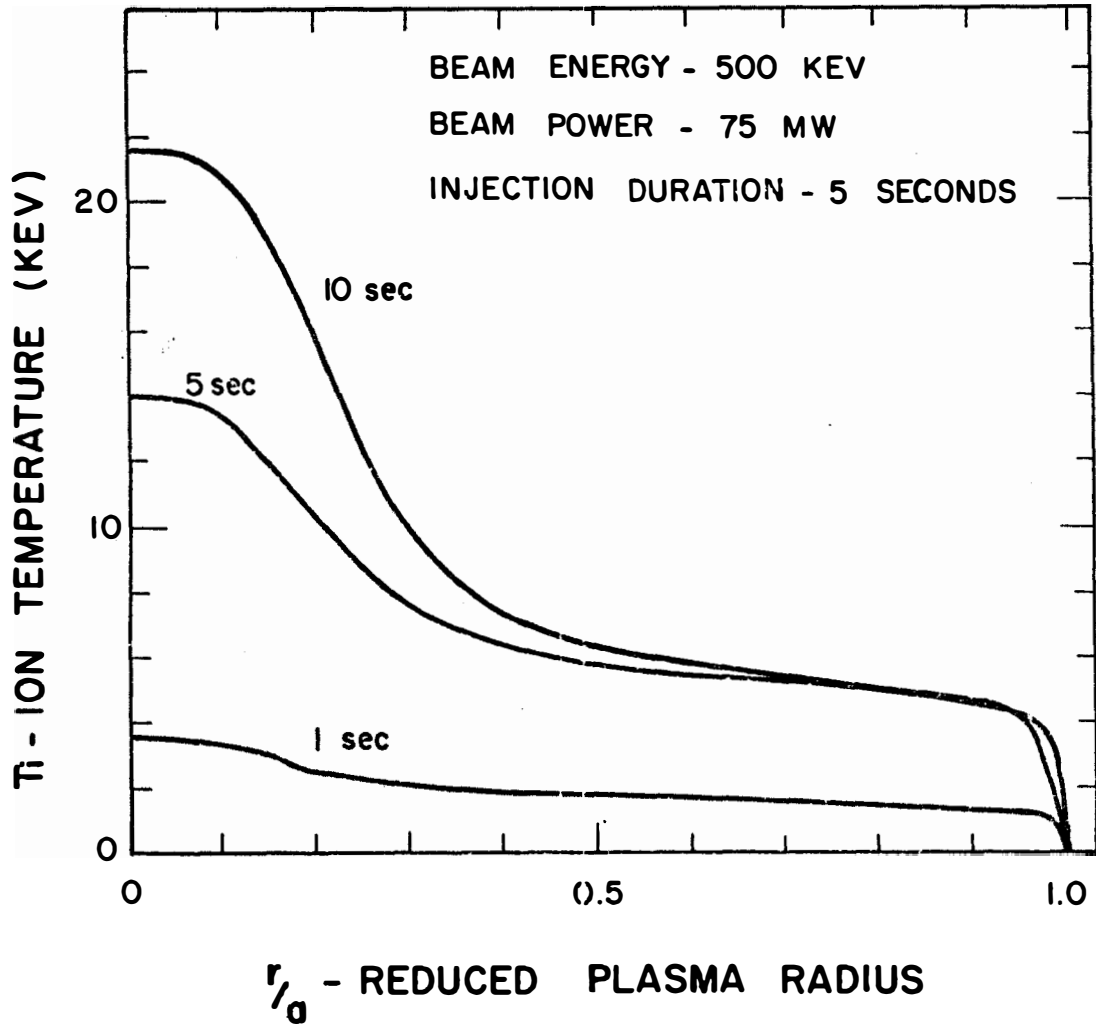
Radial ion temperature profiles after 1, 5, and 10 seconds resulting from injection of 75 MW of 100 KeV neutrals for 5 seconds.

Figure II-D-7



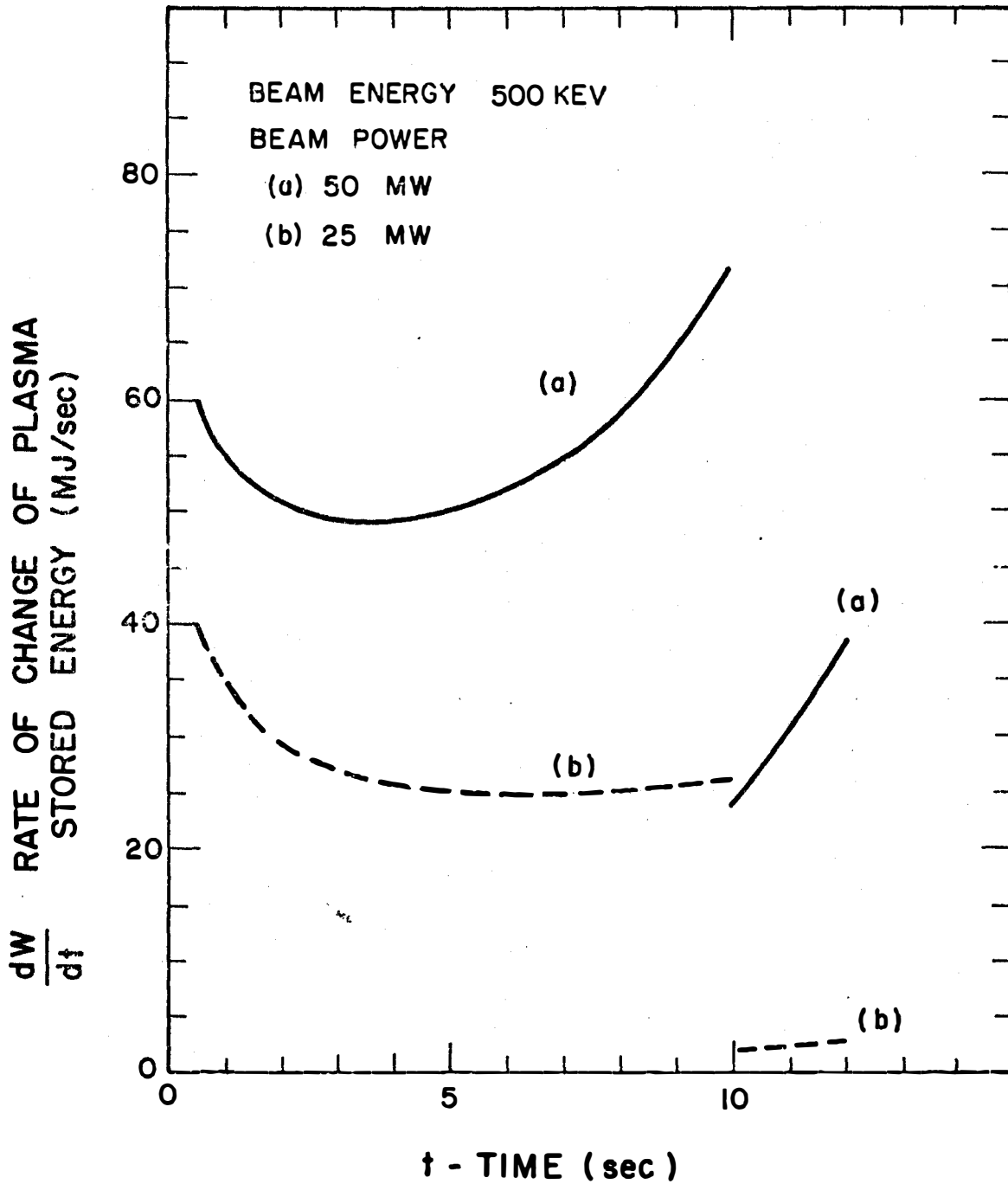
Radial ion temperature profiles after 1,5, and 10 seconds resulting from injection of 75 MW of 100 KeV neutrals for 5 seconds.

Figure II-D-8



Radial ion temperature profiles after 1, 5, and 10 seconds resulting from injection of 75 MW of 500 KeV neutrals for 5 seconds.

Figure II-D-9



Heating rate as a function of time for 25 and 50 MW of power at 500 KeV injected for 10 seconds

Figure II-D-10

can be positive only when P_α is dominant since $\frac{d}{dt}(P_{OH} - P_L)$ is negative and $\frac{dT}{dt}$ is positive. Therefore, assuming constant injection power, the ignition condition is

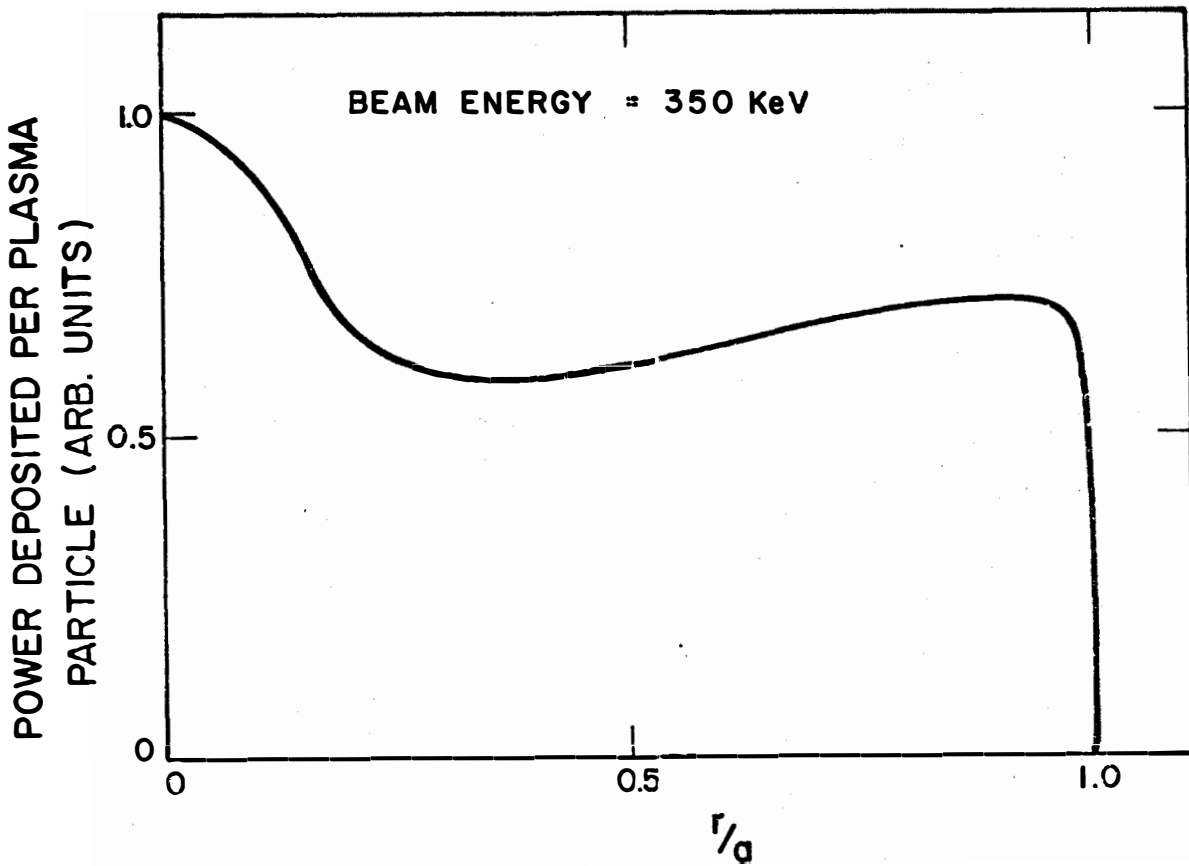
$$\frac{d^2W}{dt^2} > 0. \quad (59)$$

At the time of ignition, injection can be discounted and the plasma will heatup at an accelerating rate.

Figure II-D-6 illustrates these points by showing the heating rates resulting from 75 MW of injection for 5 seconds and for three different beam energies. In all cases, the plasma is ignited in less than 5 seconds. Ignition occurs where dW/dt is a minimum. When the beams are turned off at $t = 5$ sec, the 500 KeV case exhibits the fastest heatup rate, approximately 7.5 MJ/sec. However, the 100 KeV beam has been more efficient in heating the plasma than the 350 KeV beam. When the beams are turned off, the 100 KeV case gives a heating rate of 5.9 MJ/sec compared to 2.3 MJ/sec from the 350 KeV beams. The reasons for this difference can be understood by examining the ion temperature profiles in Figures II-D-7, D-8 and D-9. One notes first that injection of 500 KeV beams for 5 seconds produces high ion temperatures in the central zone of the plasma. Therefore, the production rate of alpha particles is also high in this zone and the result is an appreciable total alpha power production. In the 100 KeV case, the maximum ion temperatures are lower and occur near the plasma edge. However, the plasma volume associated with the high temperature zone is greater than for the 500 KeV beam case. As such, the total alpha power produced is again appreciable. The 350 KeV neutral beam is calculated to produce a relatively uniform ion temperature profile. However, the temperature level of approximately 6 KeV means the total alpha power produced is, in fact, less than in each of the previous two cases. The result is the low heatup rate of 2.3 MJ/sec once injection is terminated. We conclude that the plasma heatup rate resulting from injection at constant power for a specific length of time depends on the ion temperature profiles established in the plasma. This in turn is clearly a function of the beam energy.

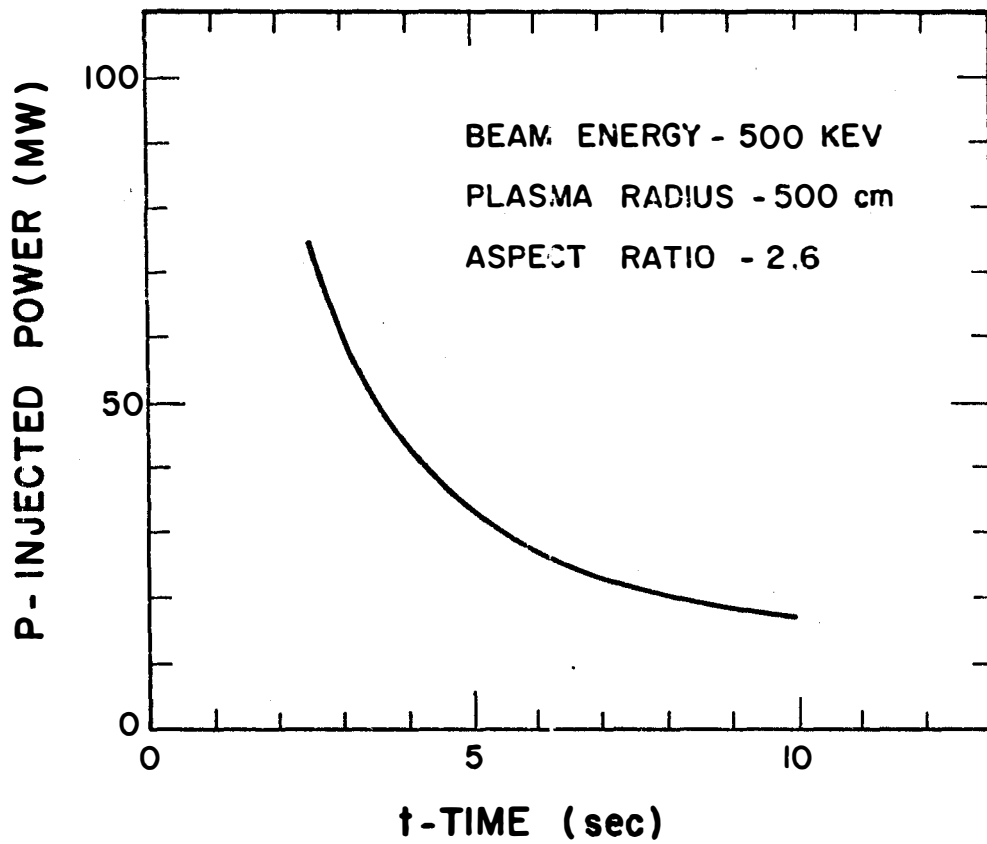
Turning to another point, Figure II-D-10 illustrates the effects of using different beam powers at a given beam energy. The calculations were for 10 seconds of neutral beam injection in both cases. For 25 MW of 500 KeV beams, the plasma barely ignites and d^2W/dt^2 is positive but small. The heatup rate is thus also small. On the other hand, 50 MW of power produces a heatup rate of approximately 24 MJ/sec. This can be compared to the 75 MW, 500 KeV, 5 second injection case shown in Figure II-D-6 where the heatup rate at the end of injection is 6.8 MJ/sec. A cross comparison of Figures II-D-6 and II-D-10 indicates, for various beam energies and different beam powers, the time required to ignite the plasma and the heatup rates which result from injection times in the 5 to 10 second range.

Some further comments should be made on the temperature profiles shown in Figures II-D-7,8,9. In the 100 KeV case shown on Figure II-D-7,



Radial profile of the power density deposited per plasma particle by a 350 KeV beam

Figure II-D-11



Power for ignition as a function of time to ignition
 (a=5m) using 500 KeV beams

Figure II-D-12

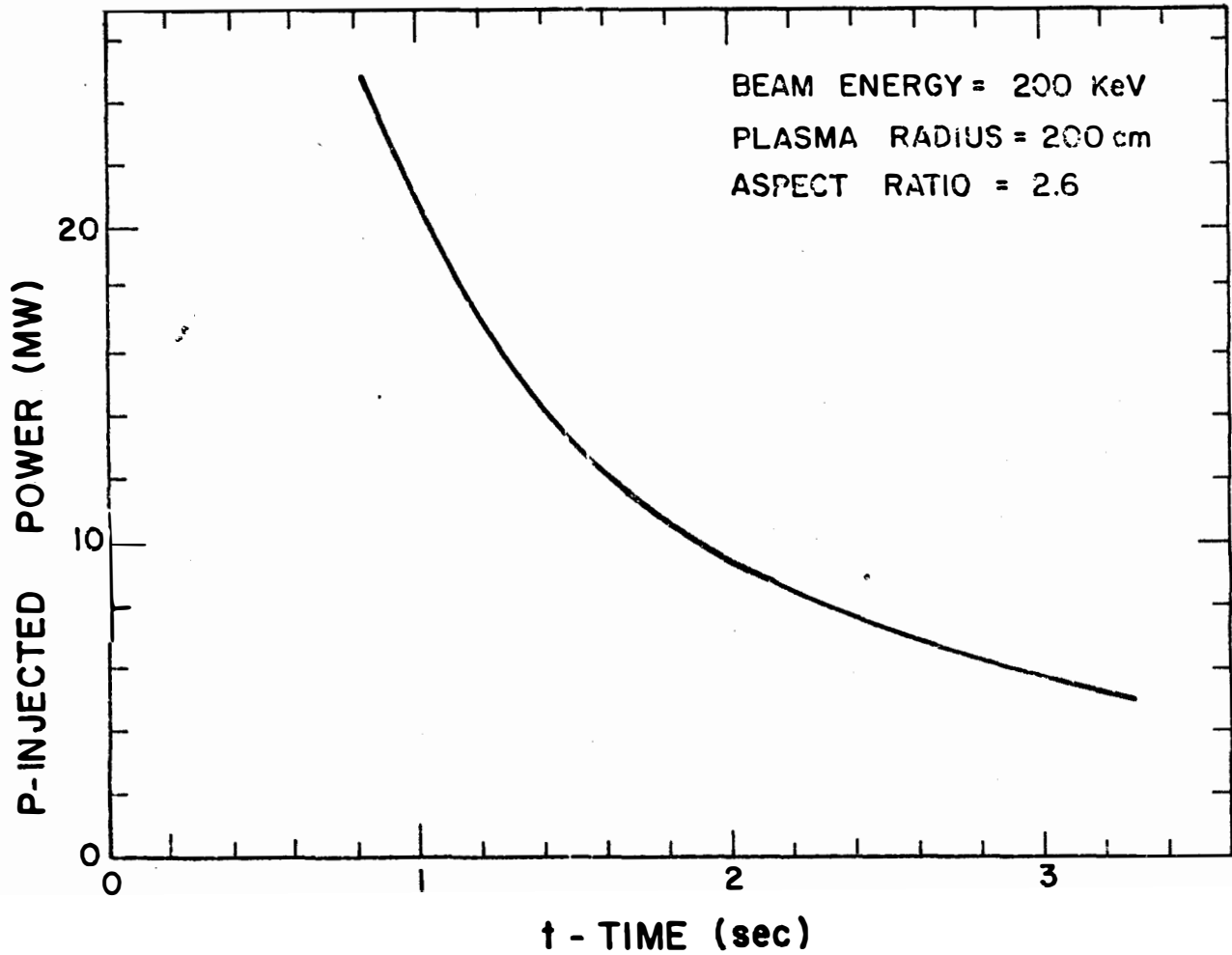
the beam energy is too low to penetrate the plasma appreciably. The injected power is, therefore, deposited in the outer plasma regions. Yet even with the steep temperature gradients that develop, energy transport from large to small plasma radii is too slow to cause appreciable temperature increase at the plasma center. The implication is that for large plasmas operating at low q values, and governed by the transport coefficients we have assumed, the plasma energy balance is local. That is, two adjacent volumes of plasma are only weakly coupled energetically. As such, the plasma temperature profile can be expected to follow the injected power profile.

The strongly inverted temperature profiles in the 100 KeV beam case are similar to profiles predicted to develop from skin currents and may have adverse effects on plasma confinement. The questions of plasma equilibrium and stability are not investigated here. Rather, we have determined the beam energy necessary to produce non-inverted temperature profiles. The injection profile for a 350 KeV beam does not have a local peak off axis, as is seen in Figure II-D-4, case (b). The temperature response to a 75 MW, 350 KeV neutral beam has been computed and the profiles are given in Figure II-D-8. As with the 100 KeV beam, though to a lesser extent, the temperature profiles are locally peaked off axis even though the injected energy density deposition rate is maximum on axis and is monotonically decreasing to $r=a$. This result is clarified by considering Figure II-D-11.

Figure II-D-11 shows the 350 KeV injection case, renormalized on a power deposited per plasma particle basis. Since the plasma density decreases monotonically with radius, the 350 KeV beam produces a heating rate (as opposed to an energy density deposition rate) which is a maximum on axis but is also locally peaked near the plasma boundary. Therefore, even a constant power density input can result in preferential heating off axis because the plasma density decreases with radius.

A 500 KeV beam does yield plasma temperature profiles in this reactor size plasma that are not inverted. Yet this energy is less than the approximately 1 MeV beams previously suggested to achieve adequate penetration in a somewhat smaller toroidal plasma⁽²³⁾. We find that a lower beam energy is acceptable for three reasons; 1) a low density startup is used, ($3 \times 10^{13} \text{cm}^{-3}$ vs $3 \times 10^{14} \text{cm}^{-3}$ in reference (23)), 2) the density profile is included in the calculation, and 3) the variation with radius of the plasma volume per radial increment along the tangential injection path shown in Figure II-D-1 is included. The temperature response to 75 MW of 500 KeV beam particles is shown in Figure II-D-9. Again, we discontinued injection heating in the calculations after 5 seconds.

The use of 75 MW of neutral beam power gives examples of fast plasma heating and thus rapid startups. Since the burn time for reactors may be long, (such as the 90 minute burn assumed for UWMAK-I), a slower startup is acceptable. A slower startup may be desirable since there is a trade-off between the time to ignition and the power required. Figure II-D-12 shows the power required for ignition as a function of the time to ignition, using 500 KeV beams. Even a long startup (for example, the



Power required to achieve ignition as a function of time to ignition in a 2m plasma ($A=2.6$) using a 200 KeV beam
Figure II-D-13

15 MW case) requires only about 10 seconds. Depending on the additional time required to increase the density and temperature to operating conditions after ignition, the time for ignition can be shortened by increasing the beam power.

4. Impact of Results on Other Machines

To determine how these results scale with system size, we have analyzed a system with a plasma radius of 2 meters, a major radius of 5.2 meters and otherwise identical to the conceptual design, UWMAK-I, in toroidal field strength, MHD safety factor, profile shapes, and so on. To obtain the same injected power deposition profile as in the 500 KeV case studied in section 3, one must keep a/λ_0 the same in both cases. a/λ_0 is the ratio of plasma radius to the mean free path of the injected neutrals at the peak plasma density (see Figure II-D-2). The required beam energy in the 2 meter system is approximately 200 KeV. Figure II-D-13 shows the power required to ignite this smaller system, as a function of the time to ignition, using a 200 KeV neutral beam. In both the case of UWMAK-I and the system with a 2 meter plasma radius, the beam energy required may be reduced in two ways. First, we have assumed for calculational convenience that the injected neutral has an atomic mass of 2.5. The total attenuation cross section for the neutral beam is a function of the relative velocity of the beam particles and the background plasma. For the same relative velocity, the beam energy required varies linearly with mass. Therefore, the minimum energy required is reduced by 20 percent if a pure deuterium neutral beam is used. Second, as pointed out in reference (22), the beam can be injected inside the geometric center of the plasma cross section, which results in a shorter chord length to the plasma center. Changing the injection angle requires consideration of the finite size of the beam to be certain the beam does not intersect the torus inner wall. Also, additional analysis of the orbits of ions produced at large pitch angles is required.

5. Summary of Beam Heating Analysis

The analysis reported in the preceding sections, based on pseudoclassical scaling for the electron conductivity and neoclassical scaling for the ion conductivity, indicates that large Tokamak plasmas can be ignited at low density ($\sim 3 \times 10^{13}$ particles/cm³) using moderate levels of neutral beam power and beam energies of several hundred KeV. For a reactor size plasma like UWMAK-I, a 500 KeV beam is adequate to provide the injected power deposition and heating rate profiles that ignite the plasma and yield non-inverted temperature profiles. Lower beam energies can also yield injected power deposition profiles that are peaked on axis. However, the heating rate in the plasma causes local maxima to occur in the temperature profiles in the outer zones of the plasma. This is found in the analysis of smaller systems as well. The maxima develop because the injected power deposited per plasma particle depends on the density profile. For a scaled down machine

with $a=200$ cm and the same aspect ratio, 200 KeV gives results similar to the 500 KeV beam in the larger system.

A low density startup is used because beam penetration is enhanced while plasma losses are reduced. Therefore, a large system can be ignited in reasonably short times. For example, in the conceptual UWMAK-I system studied here, power levels on the order of 50 MW give ignition times in the 2 to 10 second range. In smaller feasibility or reactor size plasmas, such as the $a=200$ cm system, approximately 10 MW of beam power is sufficient to ignite the system in about 2 seconds with 200 KeV beams.

The time to ignite reactor size plasmas using a given beam power are found to be about the same where beam energies are in the range from 100 KeV to 500 KeV ($A_i = 2.5$). However, the final heatup rate of the plasma is sensitive to beam energy when a given power is injected for a fixed length of time. In particular, we have found that lower energy, less penetrating, neutral beams can actually produce faster plasma heating rates in some cases,

Finally, we note that the time scale for heat conduction using pseudoclassical and/or neoclassical transport coefficients is long in a large plasma compared with the heating times of several seconds. As such, thermal diffusion does not effectively suppress the local maxima in the temperature profiles which are reported here. For the same reason, adjacent volumes of plasma are found to be very weakly coupled, from an energy viewpoint, so that approximately equal electron and ion temperatures are found throughout the beam heating phase. In summary, for UWMAK-I, we chose the 15 MW injection startup, which reaches injection in 11 seconds.

References

1. T. H. Stix, Plasma Physics 14, (1972) 367.
2. R. Dei-Cas, et al, "The Neutral Injection Heating into the Fontenay-Aux-Roses Tokamak," Paper E9, Third Intl. Symposium on Toroidal Plasma Confinement, Max-Planck-Institut fur Plasma Physik, Garching (1973).
3. L. D. Stewart, et al., "Neutral Beam Injection Heating of ORMAK," Paper E12, Third Intl. Symposium on Toroidal Plasma Confinement, Max-Planck-Institut fur Plasma Physik, Garching (1973).
4. D. Aldcroft et al, Nuclear Fusion 13, (1973) 393.
5. K. Bol et al, Proc. Sixth European Conf. on Controlled Fusion and Plasma Physics, Moscow, (1973) Vol. II (to be published).
6. J. Sheffield et al, Ibid.
7. C. F. Barnett et al, Ibid.
8. B. Badger et al, "Wisconsin Tokamak Reactor Design UWMAK-I," (University of Wisconsin Fusion Design Memo 68, Nucl. Eng. Dept., University of Wisconsin, Madison, November 1973) Vol. I.
9. J. D. Callen et al, "Theory of Neutral Beam Injection into a Tokamak," Paper E14, Third Intl. Symposium on Toroidal Plasma Confinement, Max-Planck-Institut fur Plasma Physik, Garching (1973).
10. B. B. Kadomtsev and O. P. Pogutse, Nuclear Fusion 11, (1971) 67.
11. The computer simulation model used herein was developed from the model discussed in references 12 and 13.
12. R. A. Dory and M. M. Widner, Bull. Am. Phys. Soc. 11, (1970) 1418, Also ORNL-TM-3498.
13. J. T. Hogan and R. A. Dory, Proc. Fifth European Conf. on Controlled Fusion, Grenoble (1972) Vol. I, p. 40.
14. D. J. Sigmar and G. Joyce, Nuclear Fusion 11, (1971) 447.
15. S. Yoshikawa, Phys. Fluids 13, (1970) 2300.
16. L. A. Artsimovich, Soviet Physics JETP Letters, 13, (1971) 70.

II-E-1. Neutral Injector Design

The heating calculations discussed in Section II-D indicate that to ignite the plasma in UWMAK-I using energetic neutral beams requires 30 amperes equivalent of neutral particles at an energy of 500 keV. This is a power input of 15 MW during the eleven second time interval required to bring the plasma to ignition. The injectors required to accomplish this task will be scaled from the Oak Ridge duopigatron⁽³³⁾ and duoplasmatron.⁽³⁴⁾ The duopigatron is capable of producing a total current of 8A at 101 KW for 0.2 second pulses. However, the energies are only 20 to 40 keV. Because of this low energy, some of the features of the duoplasmatron in reference⁽³⁴⁾ will be used since it operated at energies up to 600 keV. For UWMAK-I, there are 20 injectors situated around the reactor, each supplying 1.5 amperes of particles and therefore .75 MW of power per injector.

The ion sources consist of a plasma source, which produces a bright, large area plasma surface, and an extraction system which accelerates the ions that are the ion beam. To extract the ions from the plasma surface, a potential, negative with respect to the plasma, is applied a short distance from it. Since the plasma cannot support a potential gradient, a sheath forms and the associated sheath current constitutes the ion beam. The fact that the ions are accelerated preferentially in one direction leads to an electric field which tends to oppose the applied field. This plasma phenomenon, known as space charge, limits the current that can be extracted. A potential of $-\phi$ volts applied a distance of z centimeters from the plasma surface results in a space charge limited current density of⁽³⁵⁾

$$j = \frac{5.44 \times 10^{-8} \phi^{3/2}}{\sqrt{A} z^2} \quad \text{amperes/cm}^2 \quad (60)$$

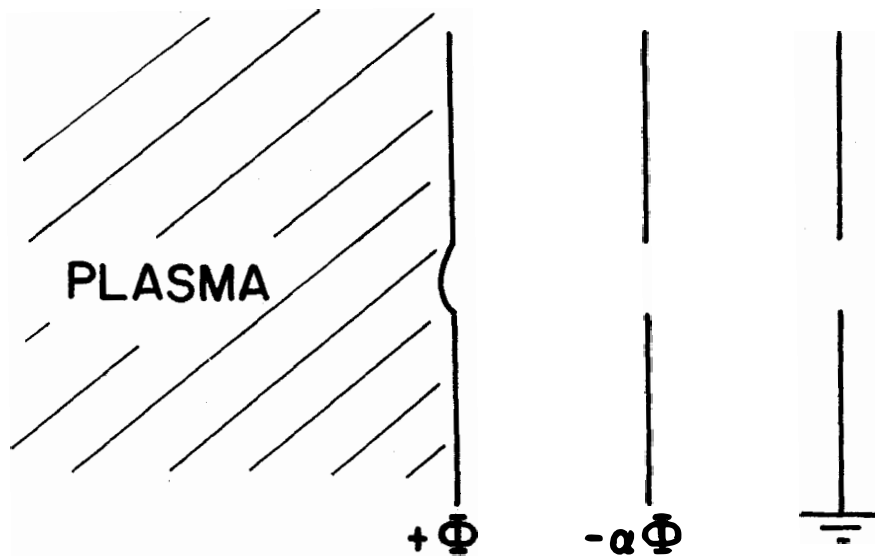
where A is the atomic mass of the gas specie being used, in atomic mass units. As discussed later, the divergence of the beam leaving the extraction system is proportional to r/z where r is the radius of the hole, or holes, in the electrodes (r will be referred to as the aperture size). From equation(60), one sees that producing large currents for fixed extraction voltages requires small spacings, z . However, decreasing z for fixed aperture size causes the beam divergence to increase.

One method to avoid large divergences and still extract large currents is to use a multi-aperture system.⁽³⁶⁾ In this setup, the electrodes are spaced as close together as possible to minimize z , but each electrode now has hundreds of small holes drilled through it. The holes in the successive electrodes are aligned to allow the beam to pass. Each set of aligned holes gives a small beam from a miniature extraction system having both z and r small. Thus the current density is high and the divergence low. By having several thousand of these holes in the electrode, the beam current can be made large.

The extraction system will be of the three electrode accel-decel type with each electrode being a copper disk with several thousand apertures (the transparency will be assumed to be 50%). One of the electrodes will be at the plasma surface, the accel or extraction electrode will be a distance, z , away, and an equal distance further away will be the grounded decel electrode. Figure II-E-1 is a schematic diagram of one hole in such an extraction system. The electrode at the plasma surface and the plasma source are both raised to $+\Phi$ volts, when a beam energy of $e\Phi$ is desired. The accel electrode is operated at an intermediate negative potential, $-\alpha\Phi$. The difference between this potential and the potential on the first electrode determines the extraction potential and thus the plasma shape. By operating the accel electrode at a negative potential, any electrons created downstream from the source are prevented from reaching the high positive potential of the source. Finally the decel electrode decelerates the beam energy for singly charged ions to the potential applied to the source.

Since a beam energy of 500 keV is required, a modification of the simple three electrode extraction system is needed to stand off the high voltages. It is possible to withstand the 500 kV by merely increasing z . However, the space charge limited current decreases as z .⁽³⁴⁾ Thus, to avoid this problem, the acceleration can be achieved in stages, as was done with the 600 keV duoplasmatron in reference 34. There, a 100mA beam was obtained in four 150 kV acceleration stages, the first of which had an extraction gap of 7.6 mm. This gave a proton space charge limited current density of 5.45 A/cm². The last three stages of acceleration are done over a distance of approximately 30 cm. Actual operation of the source did not approach the space charge current density limit, but was rather limited to only 0.0142 A/cm². In this design of the injectors for UWMAK-I, this later current density will be assumed since going to higher currents involves increasing the gas flow rate and hence the pressure. Increasing the pressure may result in breakdown in the extraction gap and termination of the beam. Until further study indicates just how conservative the 0.0142 A/cm² current density is, it will be used here since it has been shown experimentally to stand off 150 kV at 7.6 mm. In the present case the 500 kV required will be obtained in four 125 kV stages. The first stage has an extraction gap of 7.6 mm. The remaining three stages of acceleration are done over 30 cm. With the beam current density at 0.0142 A/cm², an extraction area of 106 cm² is required to attain a 1.5 A beam. Taking into account the 50% transparency of the electrodes yields an electrode area of 212 cm², corresponding to a diameter of 16.4 cm.

We now comment briefly about the various divergences of the neutral beam and begin with a few comments regarding the all important shape of the plasma surface. The plasma surface, being



EXTRACTION GEOMETRY

FIGURE II-E-1

an equipotential surface, is deformed by the applied potential so that the plasma boundary recedes from or advances toward the extraction electrode. This occurs until the current is space charge or power supply limited at all points along the surface. For any extraction system, there is an optimum plasma surface shape and a corresponding density. This optimum plasma boundary shape is concave toward the electrode, as in Figure II-E-1. The reason is that the ions leave the surface along the field lines, and since the plasma surface is equipotential, the field lines are normal to the surface. Thus a concave surface starts the ions initially toward the axis of the beam. (A convex surface would cause the ions to diverge as they leave the plasma.) Any deviations from the optimum plasma boundary shape and density lead to ion losses in the extraction system.

As noted above, for any extraction system, there is an optimum plasma boundary shape and a corresponding plasma density. Therefore if the plasma density at the extraction surface varies radially, the optimum plasma shape will not be attained for each aperture in a multi-aperture system. In this case, one must resort to a system in which the spacings and aperture sizes vary radially so that each hole has the optimum plasma shape opposite it. Such a system has been proposed by Oak Ridge^(33,37) and is called the Matched Aspect Ratio with Variable Density (MARVAD) system.

The divergence of the beam is the angle with which it spreads out as it travels. Ideally one would like to have a beam with no divergence, that is one in which all of the particles traverse parallel trajectories. The extraction electrode acts as a diverging lens because of the shape of the field lines at the electrode. Assuming the plasma surface to be flat and that the ions emerge from it with zero energy, an approximate formula for this divergence is⁽³⁶⁾

$$\alpha = r/4z \quad (61)$$

From this, one sees that beams with small aspect ratios, $(2r/z)$ ⁽³⁵⁾ have the smallest divergences. Oak Ridge's duopigatron has an aspect ratio of approximately one, which translates to a divergence of 7° . Experimentally it was observed that 60% of the beam was within a half-angle divergence of 1.2° . The reason is that the flat plasma boundary approximation is pessimistic. As stated above, by shaping the plasma surface properly, the beam can be made initially converging which leads to partial cancellation of the diverging effect. Taking 3 mm as the diameter of the aperture in the present design yields an aspect ratio of 0.79 and a calculated divergence of 5.7° . To calculate the divergence accurately involves the use of a computer program to calculate particle orbits in the extraction system.⁽³⁸⁾ Because of the similarity between the extraction system used here and that of the duopigatron, it is assumed that 60% of the beam is within a half-angle divergence of 1.2° . Having the injection port tapered at 1.2° would imply that 40% of the beam is

lost to the walls. This divergence can be improved via magnetic focusing as the beam emerges from the extraction system. However in such a case, only one ion species can be focused since the focal length depends on the charge to mass ratio. Therefore unless more than 60% of the beam can be made of one specie, it is to our advantage not to use magnetic focusing. Electrostatic focusing is independent of the charge to mass ratio of the ion specie. However it cannot be used since it drains the beam of electrons needed for space charge neutralization. The duopigatron produces approximately 50% of both D^+ and D_2^+ (or T^+ and T_2^+) so that no magnetic focusing will be used for positive beams.²

Another type of divergence encountered is that due to space charge. This effect can be calculated from the universal space-charge beam spreading curve.⁽³⁶⁾ Using this curve for our injector design and assuming no neutralization of any kind, leads to increase by a factor of 11 in the beam diameter over the 5 meter path to the plasma. This is based on a 1.5 A deuteron beam with an initial diameter of 16.4 cm. In actuality, the beam need only travel to the gas cell before it is neutralized. This eliminates further space-charge expansion from this point to the plasma. The gas cell should be placed as close to the exit of the extraction system as possible to reduce this effect. In practice it can be attached directly to the source and the neutral gas streaming from the source can serve as the charge exchange medium. Taking the total extraction distance as 30 cm, followed immediately by the gas cell, the space-charge expansion is found to be negligible.

To this point, only the ion source problems have been considered. The problem of ion beam neutralization must also be considered. The gas cell will be assumed to be in equilibrium, which means that any increase in cell thickness (product of density and length) does not yield a change in the fractions of the ion and atom species present. Figure II-E-2 shows the efficiency of converting different deuterium ion species to neutrals, as a function of energy.⁽³⁹⁾ It is obvious that the use of positive ion beams is not the way to proceed since most of the beam would not neutralize in the charge exchange cell. These unneutralized ions would be lost at high energy to the walls of the injector ports before reaching the plasma. One would like to use negative ion beams since it is much easier to strip an electron from a high energy negative ion and neutralize it, than to add an electron to a high energy positive ion. A leading method for obtaining negative ion beams is to pass a positive ion beam through a cesium gas cell. For 1.5 keV deuterons incident on an equilibrium cesium gas cell, 20% of the deuterons are converted into negative deuterium ions.⁽⁴⁰⁾ By using ten successive cesium gas cells, removing the D^- from the output of

each stage, a theoretical conversion efficiency of 74% can be attained. (41)

In summary, the 500 keV D^0 beam is produced by starting with a 1.5 keV D^+ beam produced in a scaled version of the duopigatron. (33) This beam is injected into a series of 10 equilibrium cesium cells which converts 74% of the incident D^+ beam into D^- ions. Losses suffered in this conversion process are at the relatively low energy of 1.5 keV and should present no problem. At this point, we have a 1.5 keV D^- beam which serves as the plasma surface for the 500 kV extraction system mentioned earlier. Extraction of the D^- beam proceeds in essentially the same manner as for positive ions except that now, the D^- source is operated at high negative potential and some means must be provided to eliminate electrons from the beam. The next step is to pass the 500 keV D^- beam through the gas neutralization cell. In this case, the neutralization cell must have a gas-feed mechanism other than the ion source because the cesium cell is now in between. Assuming a 70% neutralization efficiency (see Figure II-E-2 for the D^- ions at 500 keV), a 2.14 ampere D^- beam has to be extracted to produce 1.5 A at the plasma. At 0.0142 A/cm² current density, this implies a beam with a diameter of 19.5 cm. Since D^- is the only ion specie emerging from the extraction system, magnetic focusing can be used before the neutralization cell to reduce the beam divergence. Hence the neutral beams emerging from the neutralization cell should be essentially parallel.

Once the neutral beam leaves the last gas cell, it must transverse a hole through the blanket before it reaches the first wall and the plasma. This whole region is immersed in a strong magnetic field which might strip bound electrons from the neutral atoms. The velocity of the neutrals coupled with the magnetic field is equivalent to an electric field, $v \times B$, acting on the atom. If this equivalent electric field is strong enough, it can ionize the most excited atoms which are then lost from the beam. This effect, known as Lorentz ionization, was studied briefly in an earlier FDM, (42) where neutral beams of energies less than 200 keV were studied as they pass through the blanket region. By assuming a $1/n^3$ population distribution, the fraction of the beam lost via Lorentz ionization was determined. Neglecting the competing effects of spontaneous decay and inverted cascade, it was found that less than one per cent of the beam will be lost through Lorentz ionization. On the basis of this information, it can be assumed that 100% of those particles leaving the gas will reach the plasma.

At the present time one of the main technological problems preventing further development of high current ion sources is the cooling of the extraction electrodes. The calculations of the heating problem presented here follow closely the calculations

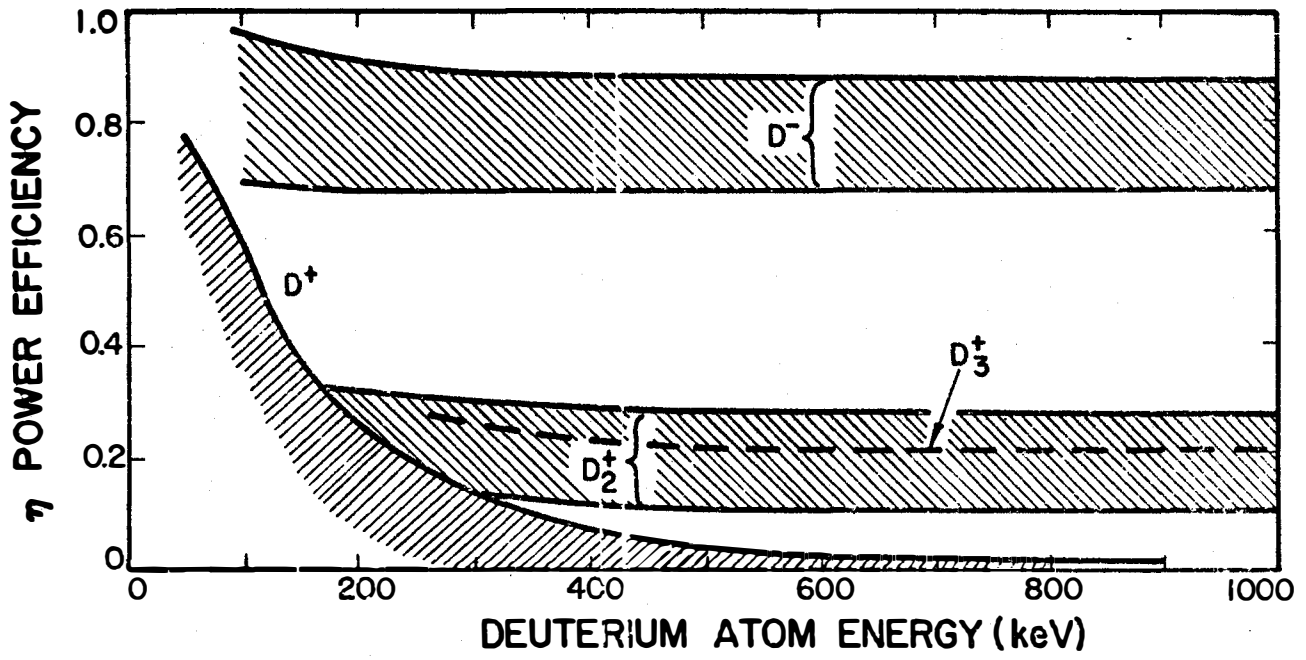


FIGURE II-E-2

of Reference 43. The problem is divided into two time periods, $\tau < t_{cr}$, and $\tau > t_{cr}$, where τ is the injection time and t_{cr} is a characteristic time for conduction of heat from the center of the electrodes to the edges where they are cooled. For times less than t_{cr} , conduction is not effective in removing this heat, and can therefore be neglected. The calculations are done for both copper and molybdenum as electrode materials. For an electrode radius, a , in centimeters, this characteristic time is found to be approximately $1.1a^2$ for molybdenum and $0.33a^2$ for copper. In our present case this yields

$$t_{cr} \sim 105 \text{ seconds for Mo}$$

$$t_{cr} \sim 32 \text{ seconds for Cu.}$$

Since the injectors will only be on for eleven seconds, conduction of heat can be neglected.

As the electrodes heat up during a pulse, they will expand and tend to buckle. To prevent this buckling the electrodes will initially be constructed slightly concave toward the plasma (in the same direction as the plasma surface curvature in figure II-E-1). The criterion used to determine the maximum allowable temperature rise at the center of the electrode is that ΔT which causes a further increase of 3.2° in the curvature of the electrodes. The temperature rises, ΔT_c , at the center of the electrode which give this 3.2° curvature of the electrodes are $140^\circ K$ for molybdenum and $60^\circ K$ for copper. The maximum permissible beam power density,

$$P_m = \frac{4.2 z_1 (1-P) \rho C_v \Delta T_c}{F \tau} \quad \text{watts/cm}^2 \quad (62)$$

where z_1 is the electrode thickness in centimeters, P is the electrode transparency, ρC_v is $0.98 \text{ cal/cm}^3 \text{ }^\circ K$ in copper and $1.13 \text{ cal/cm}^3 \text{ }^\circ K$ in molybdenum, and F is the fraction of the beam power which strikes the electrode (about 1%). With $\tau = 11$ seconds and $z_1 = 3 \text{ mm}$, equation 62 yields 337 watts/cm^2 for copper and 785 watts/cm^2 for molybdenum. The injector power density is 523 watts/cm^2 at exit indicating that the thermal limit has been exceeded for copper. These calculations indicate that the electrodes should be made from molybdenum rather than copper to prevent excessive bowing of the electrodes. They also show the electrodes should be at least 3 mm thick.

In summary, neutral beam heating of the plasma to ignition will be accomplished by 10 deuterium atom beams and 10 tritium atom

beams. In this section, we have considered only the basic design concepts for the deuterium beam, noting that the tritium beam is similar in nearly all respects. To produce the 1.5 amperes equivalent of deuterium atoms, a 2.14 ampere negative deuterium ion beam is required. Such a beam is produced by passing a 1.5 keV deuteron beam through a series of cesium gas cells and accelerating the D^- obtained in this manner. The 500 kV acceleration system will require five electrodes with 2125 aligned 3 mm holes on 19.5 cm diameter electrodes. The cesium gas cells and the first electrode will be at a potential of minus 500 kV. The holes in this first electrode will form the plasma surface from which the D^- beam can be extracted. The next electrode is at a potential of minus 375 kV and is spaced at 7.6 mm from the first electrode. It is operated such that the extracted current density is 0.0142 A/cm^2 . The last three acceleration stages take place over a distance of 30 cm. The last electrode is at ground potential. To prevent excessive heating and bowing of the electrodes they should be constructed of molybdenum and be at least 3 mm thick. Such sources represent a considerable improvement of existing technology especially as far as beam power and pulse length is concerned. That is, sources are now operating above the currents desired but at an energy an order of magnitude below that required and also at pulse lengths two orders of magnitude too low. Also the field of negative ion sources is still in its infancy and much work needs to be done to produce respectable beams. The 19.5 cm size of the electrodes is a considerable increase over existing sources. However, this could be decreased by operating near the space charge limited current density. Whether or not this is possible depends on the gas pressure in the extraction system. It may be possible, by using differential pumping between the electrodes in the extraction system to run at higher current densities and still avoid breakdown between the electrodes. Such an idea deserves future consideration. The large size of the electrodes presents problems regarding accurate alignment of the 2125 3 mm holes in the five electrodes. Also, cooling the electrodes presents a problem, especially if the injectors must operate steady state so they can be used for fueling as well as heating.

II-E-2 Fueling

Once the plasma has been ignited, one must fuel the reactor to make up for the losses of D and T due to fusion and diffusion. The use of neutral beams for fueling purposes is highly questionable. For one thing, at the plasma operating conditions (see Section II-F.) the peak plasma density is 1.2×10^{14} (D + T ions)/cm³. This is to be compared with the low density startup value of 3×10^{13} (D + T ions)/cm³. This higher density, coupled with the higher temperatures, means neutral beams with energies in excess of 1 MeV would be required to achieve penetration. Yet even if penetration is not required (for example, if there is turbulence and higher than expected diffusion coefficients and thermal conductivities) and one injects with 500 keV beams, as during startup, the power required at the operating point would be unacceptably large. In Section II-F., we conclude that for an acceptable plasma power balance, the particle leakage rate is 3.6×10^{22} (D + T ions) sec. To make up this loss rate using 500 keV neutral beams would require ~3000 MW of power, an unacceptably large value in a 5000 MW_{th} (~1500 MW_e) unit. Therefore, an alternative means of fueling the reactor after ignition must be developed.

The proposed method is that of pellet injection, in which small solid pellets of deuterium and tritium are accelerated into the plasma. This problem is one where, as plasma ablates from the pellet surface, it shields the pellet from the thermonuclear plasma and thus allows greater penetration. Reference (44-a) presents a study of this problem and some of its results are presented here.

The loss rate of deuterium and tritium from the plasma due to fusion and diffusion is 3.9×10^{22} (D + T)/second (see Section II-F.). This is therefore the rate at which pellets must supply D + T atoms to the plasma. The number of 2.5 atomic mass unit atoms in a pellet is

$$N = \frac{4}{3} \pi r^3 n_s^a, \quad (63)$$

where r is the pellet radius and n_s^a is the solid number density of atoms. Since hydrogen is a diatomic molecule, the solid number density of atoms is twice the solid number density of molecules, which for an equal mixture of deuterium and tritium is 2.69×10^{22} molecules/cm³. From this information, the required pellet injection rate, R_p , is found to be

$$R_p = \frac{173}{3r} \text{ pellets/second} \quad (64)$$

where r is measured in millimeters.

Another important parameter for pellet injection is the percentage of the total reactor charge contained in one pellet. For our reactor, this is

$$\frac{100N}{C} = .044 r^3 \quad (65)$$

where C is the total number of ions in the plasma, namely 5.12×10^{23} . Figure II-E-3 is a plot of R_p and $100N/C$ as functions of the pellet radius. From this graph, an upper limit for the pellet radius can be assumed to be 3 mm, corresponding to 1% of the total reactor charge. Making the pellets much larger will cause large density perturbations in the plasma, the effects of which are unknown. Six pellets per second of 3 mm radius would be required to fuel UWMAK-I. This indicates that smaller pellets and higher pellet injection rates are feasible. A lower limit for the pellet radius of about 0.5 mm seems reasonable (making the radius much smaller will result in inordinately large injection rates). Using 0.5 mm for the pellet radius means an injection rate of 1400 pellets per second. Each pellet now is a negligible fraction of the total reactor charge. In further calculations, we will assume a pellet radius intermediate to those discussed, namely 2 mm. This corresponds to an injection rate of 20 pellets/second and 0.35% of the total reactor charge per pellet.

Figure II-E-4 shows how far the pellets penetrate into the plasma, for various pellet velocities and radii (44-a). The penetration distance used here is the distance required to ablate one half of the atoms in the pellet. These penetration depths are based on a reactor with an average plasma density of 10^{15} cm^{-3} and a temperature of 10^8 K . Also the density profile was assumed to have the Gaussian shape,

$$n = n_{oe}^{- (0.017r)^2} \quad (66)$$

Until penetration distances are calculated for UWMAK-I, Figure II-E-4 will be used. Since the plasma radius of UWMAK-I is 5 meters, a penetration depth of several meters is required, which from Figure II-E-4 indicates velocities in excess of 10^7 cm/s . We will, however, calculate two cases: one for a velocity of $2 \times 10^7 \text{ cm/s}$ (corresponding to Figure II-E-4) and another with a velocity of $2 \times 10^5 \text{ cm/s}$, on the assumption that greater penetration can be attained under the lower density operating conditions of UWMAK-I.

To be able to electrostatically accelerate pellets containing 1.8×10^{21} atoms to the required velocities is a most difficult technological problem (44-b). By accelerating a particle of mass m and charge q through a potential of V volts the resulting energy is

$$\frac{1}{2} mv^2 = qV \quad (67)$$

II-E-12

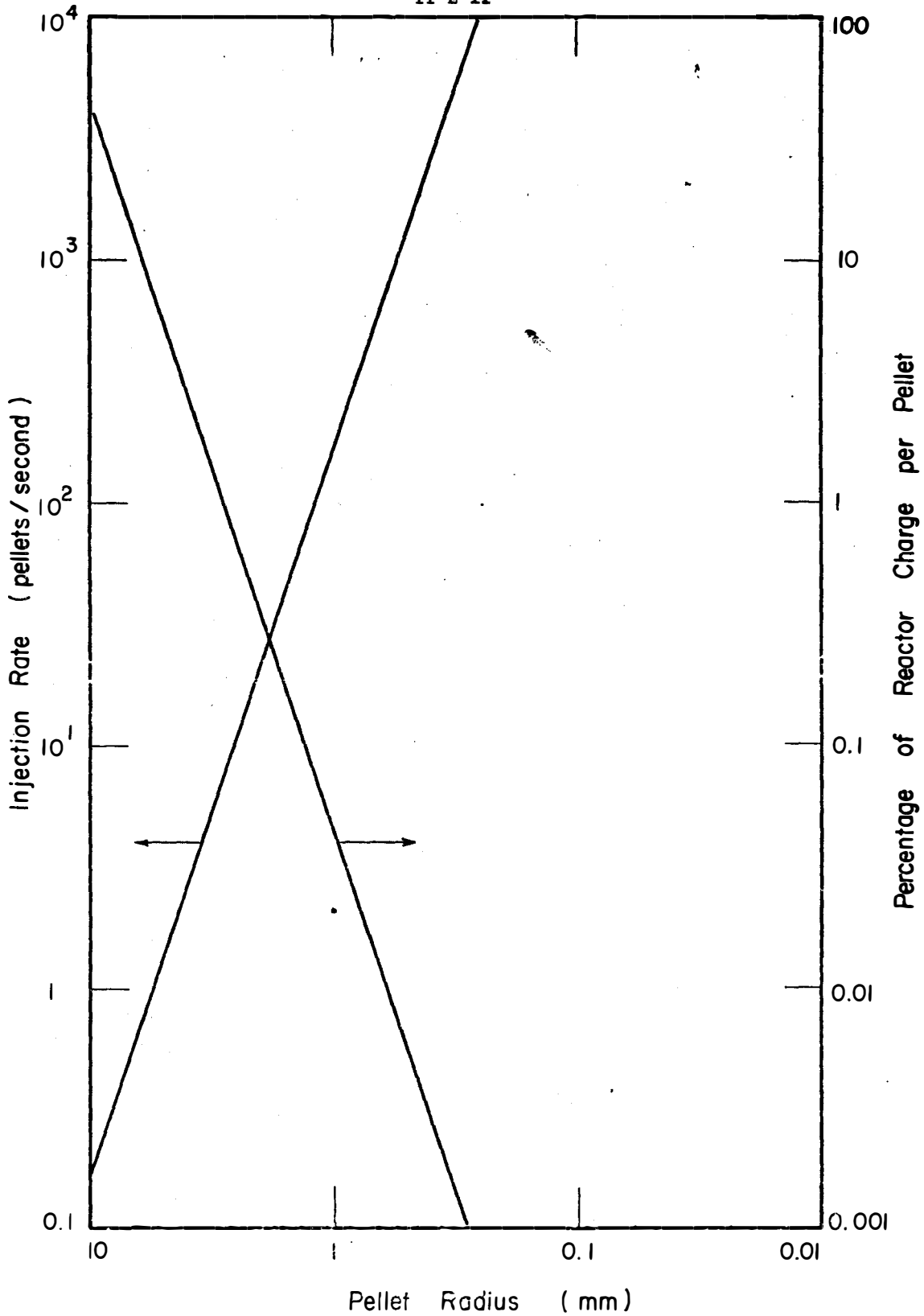


FIGURE II-E-3

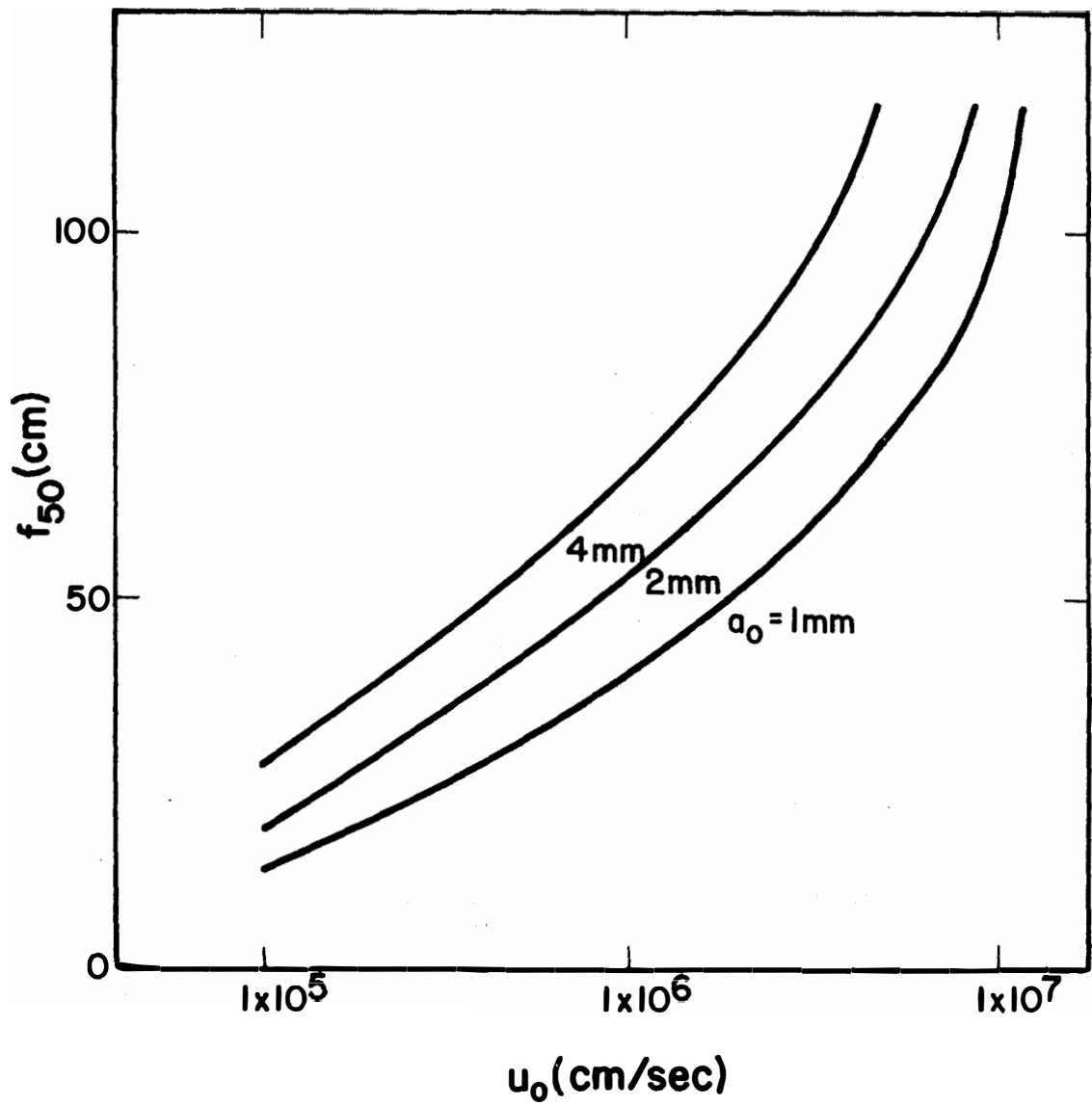


FIGURE II-E-4

(assuming non-relativistic particles). Placing as much charge on the pellet as possible results in the greatest energies. If the charge is placed uniformly over the pellet, an electric field is produced at the pellet's surface given by Gauss's law as

$$E = \frac{q}{4\pi\epsilon_0 r^2} \quad (68)$$

If negative charge is placed on the pellet, one is limited by field emission to electric field less than 10^9 V/m (44-b). For positive charges, one is limited by the binding forces holding the pellet together to fields less than 10^8 V/m. If one combines equations (67) and (68) and uses the relationship between the masses and density, ρ , of the pellet, one finds that the resulting velocity after acceleration is

$$v = \frac{6\epsilon_0 EV}{r\rho} \quad (69)$$

For 2 mm pellets, assuming $E = 10^9$ V/m, and a solid density of 1.8×10^2 kg/m³ yields a velocity of

$$v = 0.383 \sqrt{V} \text{ m/s.} \quad (70)$$

Therefore, a potential of 2.73×10^{11} volts is required to attain a velocity of 2×10^7 cm/s. The charge on the pellet is 4.45×10^{-7} Coulombs or the equivalent of 2.78×10^{12} electrons. This means the energy after acceleration is 7.6×10^{23} eV or 1.21×10^5 Joules. It is obvious that the construction of an accelerator to achieve these energies for millimeter size pellets would be very difficult indeed. The only advantage of such a system is that the current is very low, $8.9 \mu\text{A}$ in our case. This, combined with the potentials required, corresponds to a total accelerator power of 2.43 MW.

In the lower velocity case, the required potential is reduced to 2.73×10^7 volts. It appears in any event, that millions of volts will be required to accelerate the pellets to the velocities needed for penetration. The 10^{23} eV energies should be compared with current accelerator technology which is in the 10^{12} eV range. It appears that accelerators capable of fueling fusion reactors with penetrating pellets are a long way off unless even lower final velocities can be utilized. If velocities like 2×10^5 cm/s are all that is required, it may be possible to use some mechanical means of acceleration. In any event, it appears that fueling UWMAK-I with 2mm pellets or energetic neutral beams is quite difficult

C. D. Hendricks (44-b) has pointed out that as the pellet enters a plasma with $T_e > 2\text{KeV}$, the electrons striking the pellet imbed so deeply that reemission does not equal or exceed the incident electron flux and the pellet becomes negatively charged. This in turn leads to a reduction in the electron heat flux to the pellet and can therefore result in lower ablation rates and greater pellet penetration. If it is possible to inject 10-100 micron diameter pellets and achieve penetration, then the fueling picture changes dramatically. In this case, the technology of pellet injection is at hand. For example, using a nominal 20 micron radius pellet, the rate of pellet

injection into UWMAK-I is 20×10^6 pellets/sec. This is just about in the range of present day capabilities. Experiments to be performed by Hendricks on ATC in the next several months should indicate, first, if the penetration depths required can be achieved and, second, whether the pellets injection and the ablation process has a detrimental effect on plasma confinement.

II-F. Plasma Operating Conditions

1. Introduction

Once the plasma is ignited, by definition the alpha particles from fusion deposit more energy per unit volume than is lost via radiation, diffusion, and conduction. The plasma therefore is self-heating and the question becomes "What is the set of plasma conditions which characterize a favorable operating point?"

It has been previously established^(45,46) that there exist both thermally stable and unstable operating points for the plasma in a low- β toroidal system. It has also been pointed out that the enhancement of both radiation and diffusion losses are necessary to achieve the most desirable plasma operating points.^(45,18)

To study this problem further, and to establish operating parameters to characterize the plasma in UWMAK-I, we derive here a set of point plasma equations which describe particle and energy balances in the plasma. Also discussed are the implications of some of the assumptions made in deriving the equations and their solutions. In particular, we discuss the limitation on β and the radial profiles for the particle density and temperature. The question of plasma control is discussed in the next section.

In the remaining parts of this section, we discuss the transport equations of Rosenbluth, Hazeltine and Hinton^(17a) (RHH), the diffusion driven bootstrap current predicted by Galeev and Sagdeev⁽¹³⁾ and results of the recent MHD equilibria studies of Callen and Dory.^(17c) As part of this discussion, we settle on the β -limitation to be imposed on UWMAK-I. The impact of alternate assumptions are discussed in section II-I. Also discussed in the present section are solutions to the RHH equations which provide information to guide the choice of radial profiles, the plasma energy and particle balance equations and their solutions, and finally the operating conditions during the burn phase in UWMAK-I.

2. Transport Equations and the β Limit

The research in neoclassical transport theory has lead to the derivation of a new set of transport equations for low- β , large aspect ratio, toroidal systems.^(17a,b) Rosenbluth, Hazeltine, and Hinton^(17a) derived equations for a hydrogenic plasma consisting only of a single ion species and electrons. Connor^(17b) has just recently extended this work, using a model collision operator, to include an arbitrary number of ion species. The work reported here was completed prior to Connor's work and is thus based on the RHH equations. We will, however, indicate effects predicted in Connor's work, in particular regarding the diffusion and radial density profiles of high Z impurities.

The equations of RHH are for an axisymmetric Tokamak plasma operating in the banana regime of neoclassical diffusion ($\omega_{\text{bounce}} > \nu_{ei}$).

In Gaussian units, the equations are:

a. Particle conservation

$$\frac{\partial n_j}{\partial t} = -\frac{1}{r} \frac{\partial}{\partial r} (r\Gamma) + S_p^j(r,t) - L_p^j(r,t); j=(i,e) \quad (71)$$

$$\Gamma = \Gamma_i = \Gamma_e = n \left(\frac{r}{R}\right)^{1/2} \left(\frac{B_\phi}{B_\theta}\right)^2 (D_{\text{class}}^e) [-1.12(1 + \frac{T_i}{T_e}) \frac{1}{n} \frac{\partial n}{\partial r} + \frac{0.43}{T_e} \frac{\partial T_e}{\partial r} + \frac{.19}{T_e} \frac{\partial T_i}{\partial r}] - 2.44 \frac{c E_\phi n}{B_\theta} \left(\frac{r}{R}\right)^{1/2} \quad (72)$$

b. Electron energy conservation

$$\frac{3}{2} \frac{\partial (n_e T_e)}{\partial t} = -\frac{1}{r} \frac{\partial}{\partial r} [r(Q_e + \frac{5}{2} \Gamma T_e)] - \frac{\Gamma}{n} (T_i \frac{\partial n}{\partial r} - .17n \frac{\partial T_i}{\partial r}) + \frac{c E_\phi}{4\pi} \frac{1}{r} \frac{\partial (r B_\theta)}{\partial r} - \frac{3m_e}{m_i} n \langle v_e \rangle (T_e - T_i) + S_E^e(r,t) - L_E^e(r,t) \quad (73)$$

$$Q_e = \text{electron heat flux} = n T_e \left(\frac{r}{R}\right)^{1/2} D_{\text{class}}^e \left(\frac{B_\phi}{B_\theta}\right)^2 [-\frac{1.81}{T_e} \frac{\partial T_e}{\partial r} - \frac{.27}{T_e} \frac{\partial T_i}{\partial r} + 1.53(1 + \frac{T_i}{T_e}) \frac{1}{n} \frac{\partial n}{\partial r}] + 1.75 \frac{cn T_e E_\phi}{B_\theta} \left(\frac{r}{R}\right)^{1/2} \quad (74)$$

c. Ion energy conservation

$$\frac{3}{2} \frac{\partial (n_i T_i)}{\partial t} = -\frac{1}{r} \frac{\partial}{\partial r} [r(Q_i + \frac{5}{2} \Gamma T_i)] + \frac{\Gamma}{n} (T_i \frac{\partial n}{\partial r} - .17n \frac{\partial T_i}{\partial r}) + \frac{3m_e}{m_i} n \langle v_e \rangle (T_e - T_i) + S_E^i(r,t) \quad (75)$$

$$Q_i = \text{ion heat flux} = -.48 n D_{\text{class}}^e \left(\frac{m_i T_e}{m_e T_i}\right)^{1/2} \frac{\partial T_i}{\partial r} \left(\frac{B_\phi}{B_\theta}\right)^2 - 1.17 \Gamma T_i \quad (76)$$

d. Equation for plasma current

$$\frac{c}{4\pi r} \frac{\partial}{\partial r} (rB_{\theta}) = j_{\phi} \left(1 - 1.95 \left(\frac{r}{R} \right)^{1/2} \right) + c \left(\frac{r}{R} \right)^{1/2} \frac{1}{B} \left[-2.44 (T_i + T_e) \frac{\partial n}{\partial r} - .69n \frac{\partial T_e}{\partial r} + .42n \frac{\partial T_i}{\partial r} \right] \quad (77)$$

$$\frac{\partial B_{\theta}}{\partial t} = c \frac{\partial E_{\phi}}{\partial r}$$

The notation is:

Γ	= particle flux
n	= particle density
r	= Radial coordinate measured from center of the plasma
R	= major radius of torus
a	= plasma radius
S_p^j	= source of particles of species j
L_p^j	= loss of particles of species j
S_E^j	= source energy to species j
L_E^e	= energy losses from the electrons due to radiative processes
D_{class}^e	= $\langle v_e \rangle \rho_e^2$ = classical diffusion coefficient
B_{θ}	= poloidal magnetic field
B_{ϕ}	= toroidal electric field
ρ_e	= electron gyroradius in toroidal field
σ	= Spitzer conductivity

subscripts i, e label ions and electrons.

The assumptions that are important for the studies of this section are that $n_i = n_e$, the plasma is hydrogenic, no alpha particles are present, and that there are no radiation losses. We will add the effects of alpha

particles and radiation shortly. The quantities $\langle v_e \rangle$ and ρ_e are

$$\rho_e = \frac{(2m_e T_e)^{1/2}}{eB_\phi} \quad (80)$$

$$\langle v_e \rangle^{-1} = \frac{3m_e^{1/2} T_e^{3/2}}{4(2\pi)^{1/2} e^4 n \ln \Lambda} \quad (81)$$

Electron-ion rethermalization terms are included in eqns (73) and (75).

The possibility for steady-state operation of a Tokamak requires that the plasma current, $j(r)$, be maintained without an externally induced electric field, E_ϕ . Conditions under which this is possible can be obtained from equation (77) and lead to the restriction that peak β_θ , $\beta_\theta^0 \sim \sqrt{A}$. This is to be compared to the limit $\beta_\theta \leq A$, discussed by Shafranov. (2) The former condition is more restrictive in that it requires plasma operation at lower β_θ thus making less effective use of a given magnetic field. Nevertheless, the possibility of steady-state operation is there and to derive the condition, $\beta_\theta^0 \sim \sqrt{A}$, set $E_\phi = 0$ in equation (77) and solve for j_ϕ . The solution is

$$j_\phi(r) = -\frac{cT_e}{B_\theta} \left(\frac{r}{R}\right)^{1/2} \left[2.44 \left(1 + \frac{T_i}{T_e}\right) \frac{\partial n}{\partial r} + \frac{.69}{T_e} \frac{\partial T_e}{\partial r} - \frac{.42}{T_e} \frac{\partial T_i}{\partial r} \right]. \quad (82)$$

Suppose $\frac{\partial T_i}{\partial r} = 0$, $\frac{\partial T_e}{\partial r} = 0$ and $T_i = T_e$ so that

$$j_\phi(r) = -\frac{4.88cT}{B_\theta} \left(\frac{r}{R}\right)^{1/2} \frac{\partial n}{\partial r}. \quad (83)$$

This equation must be solved self-consistently with Ampere's law

$$\vec{j} = \frac{c}{4\pi} \nabla \times \vec{B} \quad (84)$$

which, for $A \gg 1$, can be written as

$$\frac{c}{4\pi r} \frac{\partial}{\partial r} (rB_\theta(r)) = j_\phi(r) \quad (85)$$

Following Galeev and Sagdeev⁽¹³⁾, assume the density profile is parabolic,

$$n(r) = n_0 (1 - r^2/a^2). \quad (86)$$

Then (83) and (85) can be solved for $B_\theta(r)$ to yield

$$B_\theta^2(r) = \frac{4.35(4\pi)n_0 T}{a^2 R^{1/2}} r^{5/2}. \quad (87)$$

Noting that the plasma pressure at $r = 0$ is $2n_0 T$, we can evaluate equation (87) at the plasma radius, $r = a$, and use

$$\beta_\theta^\circ = \frac{2 n_0 T}{B_\theta^2(a)/8\pi} \quad (88)$$

to find

$$\beta_\theta^\circ = .92\sqrt{A}. \quad (89)$$

As discussed shortly, the profiles we have assumed are a flat temperature profile ($\frac{\partial T}{\partial r} = 0$) and a density profile for which $n^2(r)$ is parabolic, i.e.,

$$n(r) = n_0 (1 - r^2/a^2)^{1/2}. \quad (90)$$

For this latter profile, the condition on β_θ° is

$$\beta_\theta^\circ = .62\sqrt{A}. \quad (91)$$

In either case, $\beta_\theta^\circ \sim \sqrt{A}$ is therefore the condition under which the plasma current can be maintained by density and temperature gradients alone and no external E_ϕ is required. The current that results in this limit is called the bootstrap current and its physical origin and effects have been discussed in the literature.^(12,13,47) There is some doubt regarding the order 1 coefficient of \sqrt{A} in condition (89) or (91) so we shall simply use in our study here the limit

$$\beta_\theta^\circ = \sqrt{A}. \quad (92)$$

Shafranov⁽²⁾ has derived the limit, $\bar{\beta}_\theta = A$, at which point the last closed, nested flux surface shrinks down to the plasma itself. Further increase of $\bar{\beta}_\theta$ causes a splitting of the magnetic surfaces inside the plasma boundary and results in a deleterious effect on

plasma confinement. The limit, $\bar{\beta}_\theta = A$, is larger than the bootstrap limit of \sqrt{A} and thus would lead to more effective use of a given magnetic field.

Recently, Callen and Dory^(17-c) have relaxed the traditional large aspect ratio assumption and examined MHD equilibria in low aspect ratio Tokamaks. They found, for $A = 3$, that in the best case, $\bar{\beta}_\theta$ was about 2 and toroidal beta, $\bar{\beta}_\phi$, was 0.1. It is emphasized that this was a best case and that other equilibria were found at lower $\bar{\beta}_\theta$.

In determining the β - limitations to impose on UWMAK-I, we considered all the points reviewed in the above discussion and, in addition noted the fact that most Tokamaks to date have achieved $\bar{\beta}_\theta$ on the order of one half. It was decided to choose a middle ground between the more optimistic limit, $\bar{\beta}_\theta = A$ ($A=2.6$ for UWMAK-I), and the most pessimistic limit, $\bar{\beta}_\theta = 0.5$. The limits chosen are thus $\bar{\beta}_\theta \sim 1$ and $\bar{\beta}_\phi \sim 0.05$. These values are half of those found in the best case by Callen and Dory but are twice as large as has yet been achieved experimentally. It can be noted parenthetically that the condition, $\bar{\beta}_\theta = \sqrt{A}$ (1.61 for UWMAK-I,) means $\bar{\beta}_\theta = 1.08$. Since this is so close to the $\bar{\beta}_\theta \sim 1$, the actual values of beta used are $\bar{\beta}_\theta = 1.08$ and $\bar{\beta}_\phi = 0.052$. Thus, if the bootstrap current materializes (and it has not yet been experimentally observed), UWMAK-I could operate steady state. However, it is the MHD equilibria studies which must be of primary concern and the operation of UWMAK-I is not predicated on the existence of the bootstrap current. As noted in section II-C, the excess core flux is sufficient to provide a burn time of 90 minutes. In section II-I of this chapter, the values just quoted are the values used.

3. Radial Profiles for n, T, j, and q.

If a Tokamak reactor operates without a divertor, the density should be relatively flat from the plasma center to the first wall.

The temperature, on the other hand, should be decreasing with increasing minor radius to a value, T_w , equal to the wall temperature. (48) If for no other reasons than radiation damage, this is an unacceptable arrangement (see Chapter VI). Therefore, UWMAK-I is designed to operate with a divertor, the double-null poloidal divertor described in Chapter III. A plasma with a poloidal divertor has a separatrix such that flux surfaces inside the separatrix form a closed, nested set and the separatrix becomes a natural plasma boundary. We expect therefore that the plasma density on the last closed flux surface becomes quite small so that the gas pressure between the separatrix and the vacuum wall is also very small. This region then acts to thermally insulate the plasma from the first wall and one expects a uniform temperature profile. The density profile, on the other hand, would not be flat and energy losses would result from particle diffusion, i.e., convective energy losses. Golovin et al (22) have also argued in this way for the temperature profile in a Stellarator by noting that the plasma density becomes zero at the last closed flux surface. For these reasons, we have assumed the temperature profile across the plasma during operation is uniform i.e., $\frac{\partial T}{\partial r} = 0$.

To have some indication of what density profile is reasonable during steady-state operation, we have solved the RHH equations analytically for the case, $\frac{\partial T}{\partial r} = 0$ and $T_i = T_e$. (48) The former assumption has just been discussed and the assumption of equal species temperatures during operation is quite good for the thermally unstable equilibrium point, as our energy balance studies will indicate (see also reference 18). Assuming first that $T_i = T_e$, the steady state form of the RHH equations become

$$\frac{1}{r} \frac{\partial}{\partial r} (r\Gamma) = S_p(r,t) - L_p(r,t) \quad (93)$$

and

$$\frac{1}{r} \frac{\partial}{\partial r} rQ_T = E_\phi j_\phi + S_E(r,t) - L_E(r,t) \quad (94)$$

where

$$\Gamma = c(r) \frac{n^2}{\sqrt{T}} \left[- \frac{2.24}{n} \frac{dn}{dr} + \frac{.62}{T} \frac{dT}{dr} \right] \quad (95)$$

$$Q_T = c(r) \frac{n^2}{\sqrt{T}} \left(- 29.9 \frac{dT}{dr} - \frac{5.52}{n} T \frac{dn}{dr} \right) \quad (96)$$

$$c(r) = \frac{8\sqrt{2\pi}}{3} \frac{e^2 \sqrt{m_e} \ln \Lambda}{B_\theta(r)^2} \left(\frac{r}{R} \right)^{1/2} \left(\frac{B_\phi}{B_\theta} \right)^2 \left(\frac{r}{R} \right)^{1/2} \frac{\rho e^2}{\tau e} \quad (97)$$

and $Q_T = Q_i + Q_e + 5\Gamma T$. Also, L_p is the particle loss rate from fusion and we will assume low fractional burnup so that $L_p = 0$ is a safe assumption.

S_p and S_E are sources of particles and energy, respectively, L_E is the loss rate of energy due to radiation, and E_ϕ and j_ϕ are the electric field and plasma current in the toroidal direction. For $\frac{dT}{dr} = 0$, the particle and energy balance equations become

$$-\frac{1}{r} \frac{d}{dr} (rc(r) \frac{dn^2}{dr}) = \frac{\sqrt{T}}{1.12} S_p(r,t) \quad (98)$$

$$-\frac{1}{r} \frac{d}{dr} (rc(r) \frac{dn^2}{dr}) = \frac{1}{2.76\sqrt{T}} (E_\phi j_\phi + S_E - L_E) \quad (99)$$

$E_\phi j_\phi$ is small compared to alpha heating and radiation and can be neglected. Clearly, a sufficient condition for a unique solution to equation (98) and (99) is the equivalence of the right hand sides, i.e.,

$$S_p(r) = \frac{1.12}{2.76 T} (S_E(r) - L_E(r)). \quad (100)$$

In a D-T fusion reactor plasma, S_E comes from α -particle heating and is proportional to n^2 . If $L_E(r,t)$ is primarily bremsstrahlung radiation, which it is, then it too is proportional to $n^2(r)$. Thus, condition (100) becomes

$$S_p(r) = f_0 n^2(r) \quad (101)$$

where f_0 is a constant. This means $S_p(r)$ should be peaked on axis and decrease as r tends to a . As we have seen in section II-D, tailored profiles peaked on axis can be produced with neutral beams by appropriate choice of injection direction and beam energy. In any case, for the purposes here, we assume condition (101) is matched closely enough that the density profile which results is indicative.

To solve equation (98) with condition (101), we need $c(r)$.

Assume a flat current profile such that $B_\theta(r) = 2\pi r j_0$. Then the equation for $x(r) \equiv n^2(r)$ is

$$\frac{d}{dr} (r^{-1/2} \frac{dx}{dr}) + b^2 r x(r) = 0 \quad (102)$$

where b^2 is a positive constant depending only on T . Make the change of variables, $Z = (\frac{r}{a})^{3/2}$, to find

$$\frac{d^2 x}{dZ^2} + \frac{4b^2}{9} a^{7/2} Z^{1/3} x = 0 \quad (103)$$

This is a special form of Bessel's equation⁽⁴⁹⁾ and the solution satisfying the boundary conditions,

$$\Gamma(r = 0) = 0 \quad (104)$$

$$n(r = a) = 0 \quad (105)$$

is

$$x(r) = n^2(r) = n_0^2 \left(\frac{r}{a}\right)^{3/4} J_{-3/7} \left(\alpha_0 \left(\frac{r}{a}\right)^{7/4}\right). \quad (106)$$

Here, $J_{-3/7}$ is the Bessel function of $-3/7$ order⁽⁴⁹⁾ and n_0 is the peak density, determined by the boundary condition at $r = 0$, which fixes T . α_0 is the first zero of $J_{-3/7}$. Figure II-F-1 is a plot of $n(r)/n_0$ versus $\rho \equiv r/a$. The analytic solution is fit well by the form

$$\frac{n(r)}{n_0} = (1 - \rho^3)^{1/2}. \quad (107)$$

For comparison, we include the parabolic profile, $(1 - \rho^2)$, and the square root of a parabola, $(1 - \rho^2)^{1/2}$. Since the solution, equation (106), was obtained assuming condition (101), and since this condition is not likely to be exactly satisfied, we have made the conservative choice that

$$n(r) = n_0 (1 - .99(\rho)^2)^{1/2}. \quad (108)$$

This is conservative in that it gives lower average densities for a given n_0 , than the analytic solution and yields a finite outward flux of particles. It also yields a density value one order of magnitude lower at $r = a$ than at the center. This is reasonable since we do not expect absolute zero for $n(r)$ at $r = a$. With $n(r)$ given by equation (108) and assuming a flat temperature profile ($\frac{dT}{dr} = 0$), we can proceed to reduce the RHH equations to a set of point kinetics equations, which in the steady-state limit, can be used to discuss the plasma operating conditions during the burn time.

Before proceeding with this, it is worthwhile making some comments about the current profile in the plasma and the radial dependence of the MHD safety factor, $q(r)$. The Kruskal-Shafranov limit requires

$$q(r) \equiv \left(\frac{r}{R}\right) \frac{B_\phi}{B_\theta} > 1. \quad (109)$$

Thus, the radial variation of $q(r)$ depends on $B_\theta(r)$ which in turn is coupled to $j(r)$. In the bootstrap limit, where $E_\phi = 0$, we previously found, using $\frac{dT}{dr} = 0$ and $n(r) = n_0 (1 - r^2/a^2)$, that

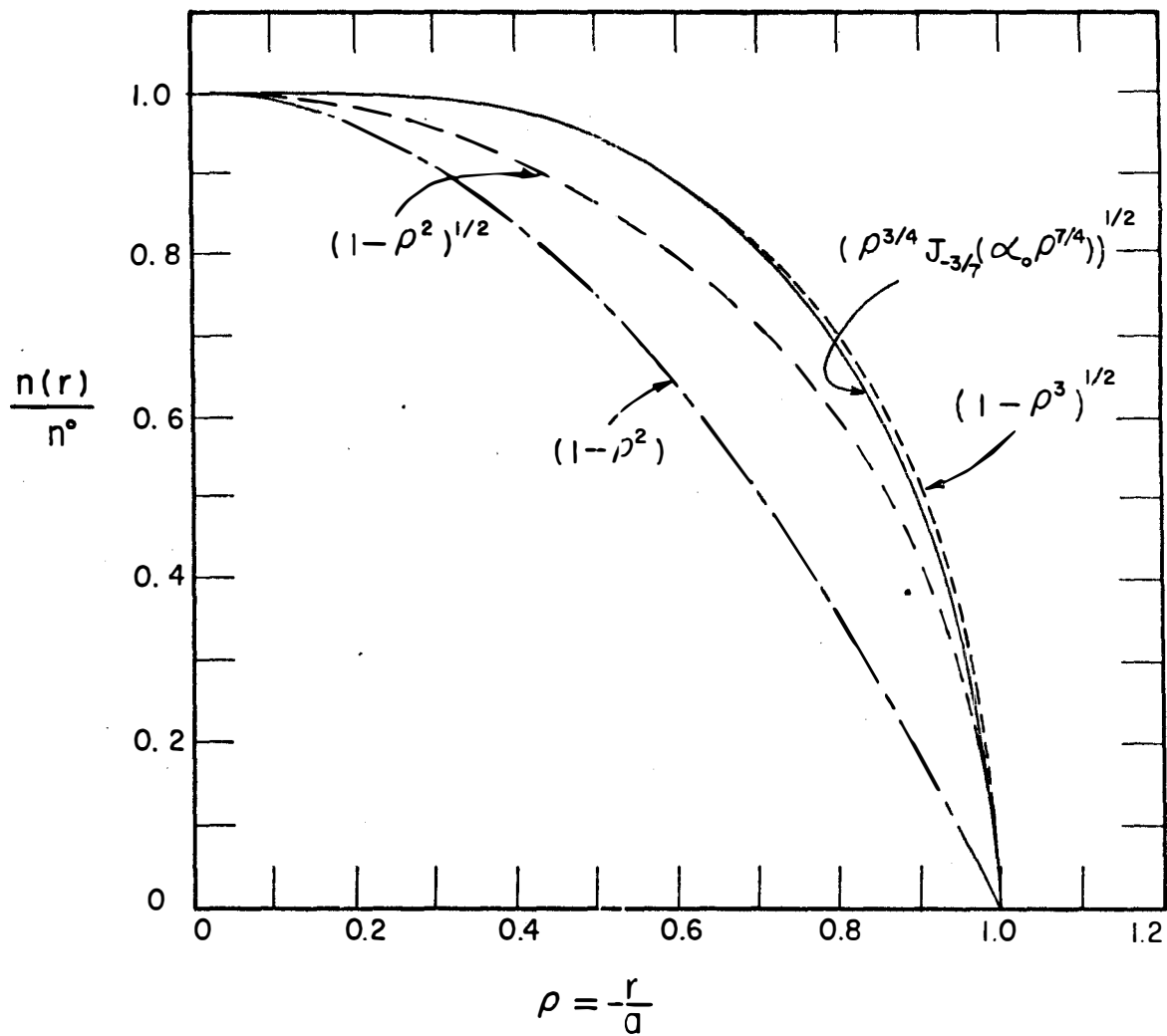


FIGURE II-F-1

$$B_{\theta}^2(r) = \frac{4.35(4\pi)n_o T_o}{a^2 R^{1/2}} r^{5/2} \quad (110)$$

Using equation (77) then gives

$$j(r) = \frac{9}{4} \frac{(4.35(4\pi)n_o T_o)^{1/2}}{a} \left(\frac{r}{R}\right)^{1/4} \quad (111)$$

and

$$q(r) = \left(\frac{r}{R}\right) \frac{B_{\theta} a R^{1/4}}{(4.35(4\pi)n_o T_o)^{1/2} r^{5/4}} \quad (112)$$

Thus, $q(r)$ is monotonically decreasing in r with the value at $r = a$ of

$$q(a) = \frac{1}{A^{3/4}} \sqrt{\frac{.92}{\beta_{\phi}^{\circ}}} \quad \left(\begin{array}{l} n(r) \\ \text{parabolic} \end{array} \right) \quad (113)$$

For the density profile given by equation (108), $q(r)$ is again monotonically decreasing in r and $q(a)$ is

$$q(a) = \frac{1}{A^{3/4}} \sqrt{\frac{.62}{\beta_{\phi}^{\circ}}} \quad \left(\begin{array}{l} n^2(r) \\ \text{parabolic} \end{array} \right) \quad (114)$$

Of course, if we simply use $\beta_{\theta}^{\circ} = \sqrt{A}$, then $q(a)$ is

$$q(a) = \frac{1}{A^{3/4}} \sqrt{\frac{1}{\beta_{\phi}^{\circ}}} \quad (\beta_{\theta}^{\circ} = \sqrt{A}) \quad (115)$$

An alternative view of this problem is to assume that the bootstrap limit is not valid and that the plasma current is driven by the externally induced E_{ϕ} . Then

$$j_{\phi}(r) = \sigma E_{\phi} \quad (116)$$

and if σ is taken as the Spitzer conductivity, ⁽⁵⁴⁾ it will vary as $T^{3/2}$. Thus, if $\frac{dT}{dr} = 0$, σ does not depend on r and if the induced electric field is constant in r , then so is j_{ϕ} . Thus $q(r)$ is also independent of r and can be conveniently chosen. More generally, if E_{ϕ} is flat in r but the temperature has the characteristic shape

$$T(r) = T_o (1 - r^2/a^2)^p, \quad (117)$$

then $q(0)$ is related to $q(a)$ by

$$q(0) = \frac{q(a)}{\left(\frac{3}{2}p + 1\right)} \quad (118)$$

Thus, assuming $p \geq 0$, we have $q(0) \leq q(a)$. This is contrasted to the bootstrap limit where $q(0) > q(a)$.

Based on these considerations, we have chosen an intermediate value of $q(a)$ as 1.75. If it turns out that equations (116) and (117) apply, one has $q(0) > 1$ for $p < 1/2$ and $q(0) = 1.75$ if $\frac{dT}{dr} = 0$. On the other hand, in the bootstrap limit, namely equation (92), we would have $q(a) = 1.75$ and $q(r) > q(a)$ for $r < a$. Thus, in either case, the Kruskal-Shafranov criterion is satisfied.

In summary, the chosen radial profile for the density is equation (108) and the temperature profile is assumed flat ($\frac{dT}{dr} = 0$). $q(a)$ is set at 1.75 and $q(0) > 1$ for both the case of bootstrap current and for operation at finite E_ϕ with $j_\phi = \sigma E_\phi$, a uniform E_ϕ , and $p \leq 1/2$ in equation (117).

4. Point Kinetics and Steady State Equations

With the density and temperature profiles chosen, one can proceed to reduce the RHH equations to a set of point dynamic equations (no spatial variable). There are several ways this can be done, such as integrating the equations over the plasma volume using an appropriate, space-dependent weighting function. However, it is not clear what weighting function is indeed "best" and we have therefore proceeded in the most straightforward manner (using the principle of Ockum's razor) and volume averaged the RHH equations. The reduction is carried out for $n_i(r,t) = n_i^0(t)(1 - .99(r/a)^2)^{1/2}$, uniform T_i and T_e , and uniform toroidal current profile.

$$j_\phi(r) = \left(\frac{I_\phi}{2a}\right), \quad (119)$$

where I_ϕ is the total plasma current. Since the system is axisymmetric, the ϕ variable (see Figure II-A-1) is ignorable and the θ variable has already been averaged over in producing the radial particle and energy fluxes. Thus, the average required here is over the radial variable, r , and for this purpose, it is convenient to define the operator

$$U_r \equiv \frac{2}{a} \int_0^a r dr \quad (120)$$

Consider the particle conservation equation for ions

$$\frac{\partial n_i(r,t)}{\partial t} = -\frac{1}{r} \frac{\partial}{\partial r} (r\Gamma_i) + S_p^{(i)}(r,t) - L_p^{(i)}(r,t) \quad (121)$$

Operating with U_r gives

$$\frac{2}{3} \frac{dn_i(t)}{dt} = -\frac{2D_{nc1}(t)n_i^{\circ}(t)}{a^2} + S_p^{(i)}(t) - L_p^{(i)}(t) \quad (122)$$

where

$$S_p^{(i)}(t) = U_r(S_p^{(i)}(r,t)) \quad (123)$$

$$L_p^{(i)}(t) = U_r(L_p^{(i)}(r,t)) \quad (124)$$

$$D_{nc1}(t) = 1.12 \left(1 + \frac{T_i(t)}{T_e(t)}\right) q(a)^2 A^{3/2} D_{c1}(t) \quad (125)$$

and

$$D_{c1}(t) = \frac{\rho e^2}{\tau_e} = \frac{2m_e T_e(t)}{eB_{\phi}^{\circ}} \cdot \frac{4\sqrt{2\pi} e^4 \ln \Lambda n_e^{\circ}(t)}{3\sqrt{m_e} T_e(t)^{3/2}} \quad (126)$$

Thus,

$$D_{nc1}(t) \propto \left(1 + \frac{T_i(t)}{T_e(t)}\right) \frac{n_e^{\circ}(t)}{T_e(t)^{1/2}} \quad (127)$$

When fusion events are taking place at the rate of $\frac{n_i^2 \langle \sigma v \rangle}{4}$ fusions per second, the loss rate, $U_r(L_p^{(i)}(r,t))$ is

$$L_p^{(i)}(t) = \frac{1}{2} \left(\frac{n_i^{\circ}(t)^2 \langle \sigma v \rangle}{2} \right) \quad (128)$$

It is convenient to define a time-dependent particle confinement time as

$$\tau_c(t) = \frac{a^2}{4D_{nc1}(t)} \quad (129)$$

so that the particle conservation equation (122) is

$$\frac{2}{3} \frac{dn_i^{\circ}}{dt} = S_p^{(i)}(t) - \frac{n_i^{\circ}(t)}{2\tau_c(t)} - \frac{1}{2} \frac{n_i^{\circ}(t)^2 \langle \sigma v \rangle}{2} \quad (130)$$

A similar analysis on the electron conservation equation yields

$$\frac{2}{3} \frac{dn_e^{\circ}(t)}{dt} = S_p^{(e)}(t) - \frac{n_e^{\circ}(t)}{2\tau_c(t)} \quad (131)$$

The analysis of RHH^(17-a) did not include alpha particles, which must be included for a CTR system. We have included alphas through the conservation equation

$$\frac{2}{3} \frac{dn_{\alpha}^{\circ}(t)}{dt} = \frac{1}{2} \frac{n_i^{\circ}(t)^2 \langle \sigma v \rangle}{4} - \frac{n_{\alpha}^{\circ}(t)}{2\tau_c(t)} \quad (132)$$

which assumes the alphas have the same radial profile and confinement time as the D+T ions and the electrons. Charge neutrality adds the condition

$$n_e^{\circ}(t) = n_i^{\circ}(t) + 2n_{\alpha}^{\circ}(t) \quad (133)$$

A more detailed treatment based on the recent work of Connor^(17-b) is in progress.

The reduction of the ion and the electron energy conservation equations, neglecting the $E_{\phi j \phi}$ term, yields

$$\begin{aligned} \frac{d}{dt} (n_e^{\circ} T_e) = & - \left(2.28 T_e(t) - 2\gamma_o T_i(t) \right) \frac{n_e^{\circ}(t)}{\tau_c(t) 4} \\ & - \frac{3}{2} \frac{m_e}{m_i} \frac{(T_e(t) - T_i(t))}{\tau_e^{\circ}(t)} n_e^{\circ}(t) \end{aligned} \quad (134)$$

$$\begin{aligned} \frac{d(n_i^{\circ} T_i)}{dt} = & - (2.66 T_i(t) + 2\gamma_o T_i(t)) \frac{n_e^{\circ}(t)}{4\tau_c(t)} \\ & + \frac{3}{2} \frac{m_e}{m_i} \frac{(T_e - T_i)}{\tau_e^{\circ}} n_e^{\circ}(t). \end{aligned} \quad (135)$$

The parameter γ_0 arises in averaging the term, $\frac{T_i \Gamma}{n_e} \frac{\partial n_e}{\partial r}$ in equations (73) and (75), and has the numerical value, $\gamma_0 = 5.39$. For the electron equation, one must add losses due to bremsstrahlung and synchrotron radiation and alpha heating must be added to both equations. The averaging procedure using U is straightforward for all but the synchrotron term. For that term, the analysis is more difficult. Yang⁽⁵⁰⁾ has recently extended the work of Rosenbluth⁽⁵¹⁾ to cover the temperature range above 10 KeV. He has evolved a fit, valid for T_e in the range 3 KeV to 100 KeV, to his numerical results as

$$W_c = \frac{2C_1}{a} [5 + .17(5-A)]^3 \Lambda^{1/2} B_\phi^3 T_e^{2.1} (1-R)^{1/2} \text{(watts/cm}^3\text{)} \quad (136)$$

where

$$\Lambda = \frac{\omega_p^2 a}{c \omega_b}$$

$$\omega_p^2 = \frac{4\pi e^2}{c} \left(\frac{2}{3} n_e^\circ(t) \right)$$

$$\omega_b = \frac{eB_\phi}{m_e c}$$

R = Wall Reflectivity.

With B_ϕ measured in Tesla and T_e in KeV, the constant C_1 is 10^{-4} . Therefore, including α -heating, bremsstrahlung, and synchrotron radiation, the energy conservation equations are

$$\begin{aligned} \frac{d(n_e^\circ T_e)}{dt} &= \frac{1}{2} \frac{(n_i^\circ)^2 \langle \sigma v \rangle}{4} E_\alpha U_{\alpha e} - (2.28 T_e - 2\gamma_0 T_i) \frac{n_e^\circ}{4\tau_c} \\ &- \frac{3}{2} \frac{m_e}{m_i} \frac{(T_e - T_i)}{\tau_e^\circ(t)} n_e^\circ - \frac{2C_1}{a} [5 + .17(5-A)]^3 \Lambda^{1/2} B_\phi^3 T_e^{2.1} (1-R)^{1/2} \\ &- \frac{C_2}{2} n_i^\circ n_e^\circ T_e^{1/2} \end{aligned} \quad (137)$$

$$\frac{d(n_i^\circ T_i)}{dt} = 1/2 \frac{(n_i)_{\langle \sigma v \rangle}^2}{4} E_\alpha U_{\alpha i} - (2.66 + 2\gamma_o) \frac{n_e^\circ T_i}{4\tau_e} + \frac{3}{2} \frac{m_e}{m_i} \frac{(T_e - T_i)}{\tau_e(t)} n_e^\circ. \quad (138)$$

E_α is the α -energy from fusion, $U_{\alpha i}$ is the fraction of α -energy deposited directly in the ions on slowing down, and $U_{\alpha e}$ is $(1 - U_{\alpha i})$. We have used $U_{\alpha i}$ and $U_{\alpha e}$ from the slowing down calculations of Conn. (52) Because of the nearly equal masses of alphas and ions, the alphas will thermalize to the ion temperature (52) and we have used $T_\alpha = T_i$. However, the mean α -energy is not $3T_i/2$, even though they thermalize to T_i before diffusing from the plasma, because the α -spectrum includes a slowing down tail. This has been accounted for in computing the α -pressure. (18)

In summary, equations (132), (133), (137) and (138) are a set of point plasma dynamic equations to be solved self-consistently with the conditions, $\beta_\theta = 1.08$ and $q(a) = 1.75$. Steady-state energy balance equations for analysis of the plasma operating conditions are obtained by setting the time derivatives to zero.

5. Energy Balance Studies and Plasma Operating Conditions

The point kinetic equations in the steady state limit have been used to study the equilibrium conditions (in an energy balance rather than an MHD sense) of a CTR Tokamak plasma. As has been previously discussed, (45,46,18) the plasma can exist in two equilibrium conditions, one which is thermally stable and the other unstable. The unstable point is always at a lower ion temperature than the stable point and the spread in T_i can be substantial (4 KeV to > 100 KeV). The simplest way to see this is, of course, to recognize that the ignition point, where power into the plasma from α - heating balances all losses, is an unstable equilibrium. Once ignited the plasma self-heats, as we have discussed in Section II-D, until it reaches another, stable equilibrium. A more detailed analysis based on linear stability theory readily establishes the basic points. In Section II-D, we found that ignition occurred in UWMK-I for T_i in the 6-7 KeV range. It was also noted in Section II-B that for a β - limited system using the D-T fuel cycle, the optimum ion operating temperature would be in the 10 to 15 KeV range. This requires adjusting the balance between α - heating and plasma losses to achieve an operating condition that is economically favorable. (18) Controlled operation at the ignition point found in Section II-D would be less economical.

To achieve operating temperatures in the 10-15 KeV range, it is necessary to enhance one or more of the plasma energy loss mechanisms so that a balance can be achieved only by increasing the alpha heating rate. If one examines $\langle \sigma v \rangle_{D-T}$ given in Figure II-B-1 and recalls that α -heating is proportional to the alpha production rate, $n_i^2 \langle \sigma v \rangle$, it is

clear that one can increase the alpha heating rate by increasing the plasma operating temperature above the 5-7 KeV range found for ignition. Of course, one could also increase n^2 but this is ineffective since the losses also increase as n^2 . Bremsstrahlung losses vary as n^2 , as do the particle and energy loss rates when classical scaling applies. Only synchrotron radiation varies differently (as \sqrt{n}) but this is small in the 10-20 KeV range. Therefore, factoring out the n^2 density dependence, the alpha heating varies with temperature as $\langle \sigma v \rangle$. Bremsstrahlung has a $T^{1/2}$ temperature dependence and if the transport coefficients scale classically (classical, neoclassical, pseudoclassical) the energy loss processes related to convection and conduction also vary as $T^{1/2}$. A schematic illustration of the temperature dependence of these various terms is shown in Figure II-F-2. Clearly, the low temperature thermal equilibrium is unstable. At higher temperatures ($T > 20$ KeV), synchrotron radiation becomes more important and it scales approximately as T^2 (see equation (136)). Thus, the higher temperature thermal equilibrium, though outside the optimal range of 10-15 KeV, is stable.

One can see from this illustration that the unstable equilibrium temperature can be raised to the optimum range by enhancing either the bremsstrahlung radiation losses, the losses due to convection and conduction, or both. In the process, temperatures at the stable equilibrium come down. This is also illustrated in Figure II-F-2. Of course, there is a limit to the amount one can enhance the losses and still find a solution to the equations. This is case (c) in Figure II-F-2, where the gain and loss curves are tangent at one point. For larger loss rates, no solution exists. We thus conclude that it is desirable, indeed it seems economically necessary, to enhance loss mechanisms in the plasma to achieve a more optimum plasma operating temperature.

Loss mechanisms that can be adjusted for this purpose are radiation, conduction and convection. The bremsstrahlung radiation losses can be enhanced substantially by the addition of a small amount (less than 1-3% of the ion density) of high Z impurities. Conduction and convection losses may be enhanced to increase the particle and heat fluxes by, perhaps, the selective excitation of specific instabilities. It is not clear exactly how this can be achieved but there are several instabilities, such as trapped particle instabilities, which may enhance these fluxes. In addition, non-axisymmetry will lead to superbanana effects and increased losses. In any event, it is assumed for our purposes here that both bremsstrahlung enhancement and confinement spoiling are possible.

To provide a measure of just how much radiation losses are enhanced, the bremsstrahlung loss rate, including impurities, is written as

$$W_x = N_H W_x(\text{normal}) \quad (139)$$

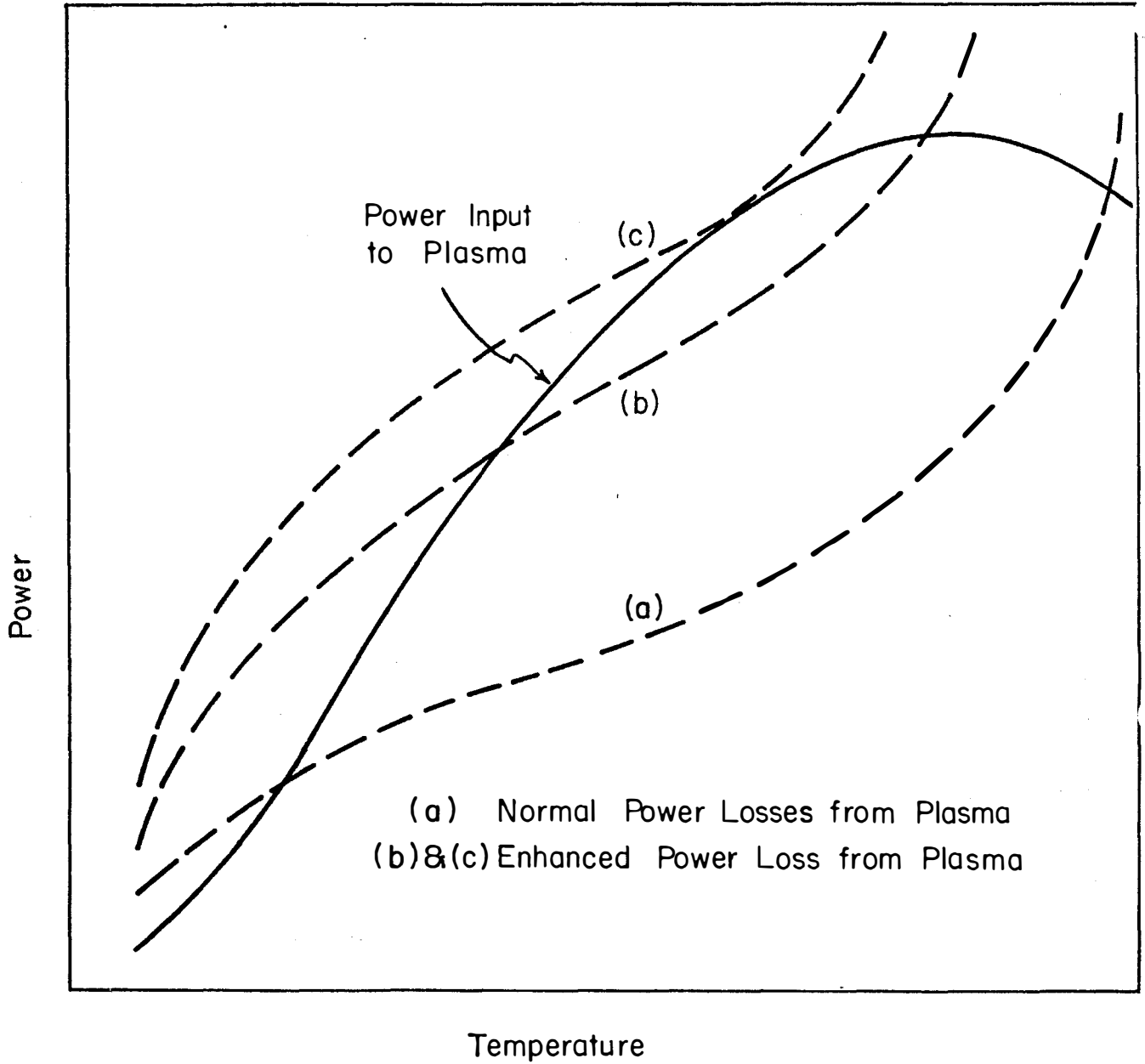


Figure II-F-2

Schematic of Power Gains and Loss in Plasma

where N_H is a bremsstrahlung enhancement factor and indicates how much W_x has been increased over the corresponding value in the absence of impurities ($W_x(\text{normal})$). Likewise, the neoclassical diffusion coefficient will be used as the scaling law from present-day experiments and we introduce a spoiling factor, S , via

$$D_{ncl}^S = S D_{ncl}. \quad (140)$$

Thus, $S > 1$ measures how much the diffusion has been enhanced, or equivalently, how much the confinement time has been reduced, relative to the value predicted by neoclassical theory, for the same conditions of plasma density, temperature, geometry, and magnetic field strength.

The plasma size has already been set in Section II-B by optimization considerations. With the limitations placed on $\bar{\beta}_\theta$ and $q(r)$, the question is "What plasma is optimum in the sense that it produces the specified power output with minimum toroidal field?" Since there are two parameters available for variation, S and N_H , we have solved the equilibrium equations for different N_H and S values to find the minimum B_ϕ^0 which yields 5000 MW_{th} , within the established plasma limits. The results are shown in Figure II-F-3 where we have plotted the maximum power obtained as a function of N_H , with B_ϕ^0 set at 38.2 KG. The maximum of the maxima is 5000 MW_{th} at a bremsstrahlung enhancement of 7.5. The corresponding confinement spoiling factor is 450 which means the particle confinement time is orders of magnitude shorter than the neoclassical formula would predict. Included in the figure is a plot of the ion temperature at each equilibrium. This shows that the maximum power versus N_H curve reflects the $\langle \sigma v \rangle / T^2$ curve, Figure II-B-2. As T_i passes beyond the 10-15 KeV range, the maximum possible power decreases sharply. Figure II-F-4 shows the effect of wall reflectivity on these results. Since synchrotron losses only become significant at reasonably large T_e ($> 15\text{-}20 \text{ KeV}$), the effect of different R values is only seen at large N_H values. (See equation (136)). For $T_i < 15 \text{ KeV}$, we find T_e is approximately equal to T_i .

To relate these results to those of other workers, we plot in Figure II-F-5 the average power versus the center line $n_i^0 \tau^0$ value. This is a closed curve, as noted by Mills, who has studied this problem thoroughly.⁽⁵³⁾ One can see again the effects of different wall reflectivities. The concave (upper) portions of these curves correspond to thermally unstable equilibria while the convex (lower) portions are thermally stable equilibria. In Figure II-F-6, the ion temperature is plotted versus $n_i^0 \tau^0$. Here, it is the upper portion that corresponds to thermally stable points and the lower portion that corresponds to unstable points. It is clear that while there is only one "best" thermally unstable equilibrium, namely that which gives maximum power, there can be two stable equilibria, at small and large $n\tau$ values, which will give the same power. While the main UWMAK-I analysis is carried out for the optimum, unstable

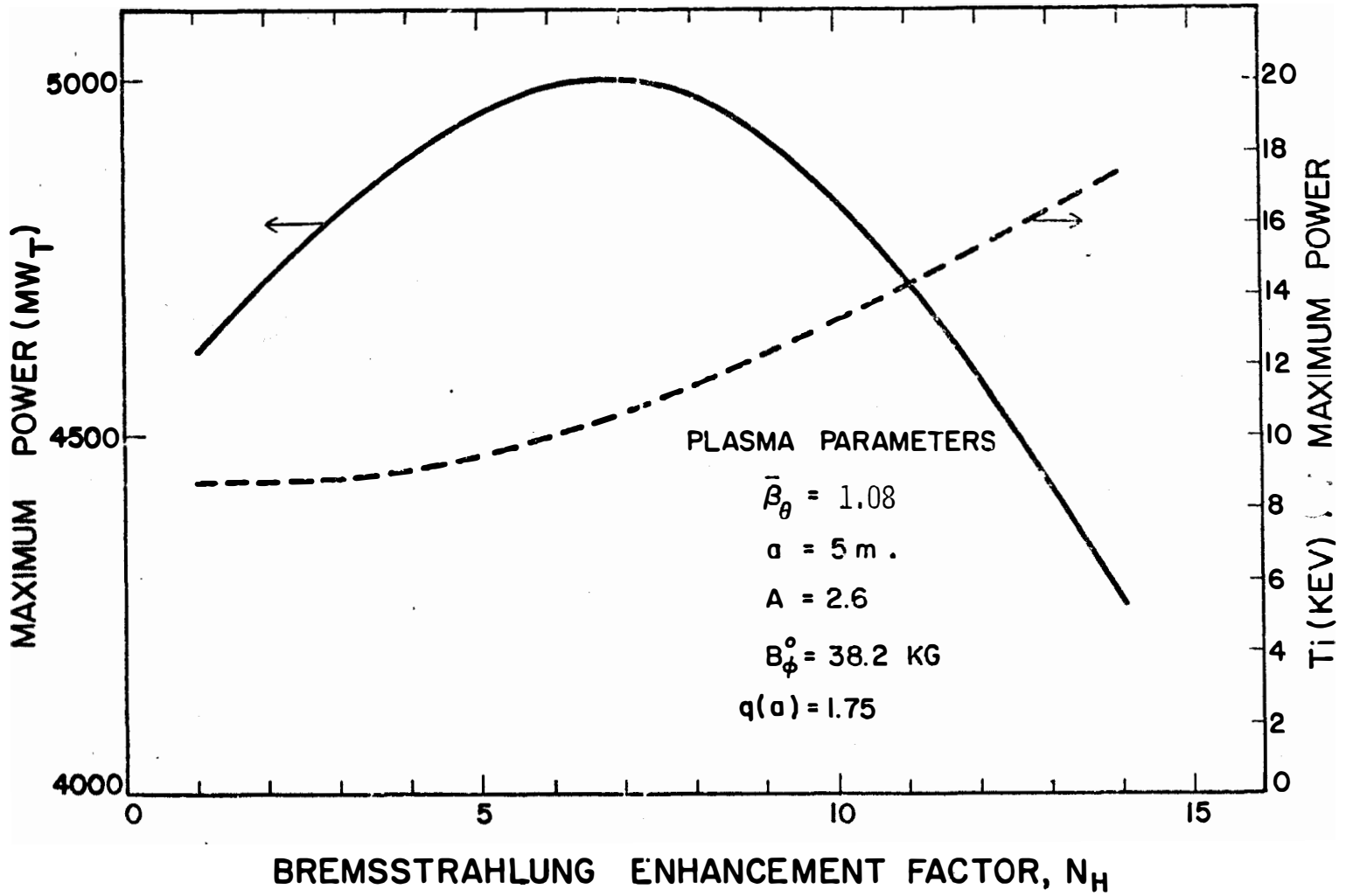


FIGURE II-F-3

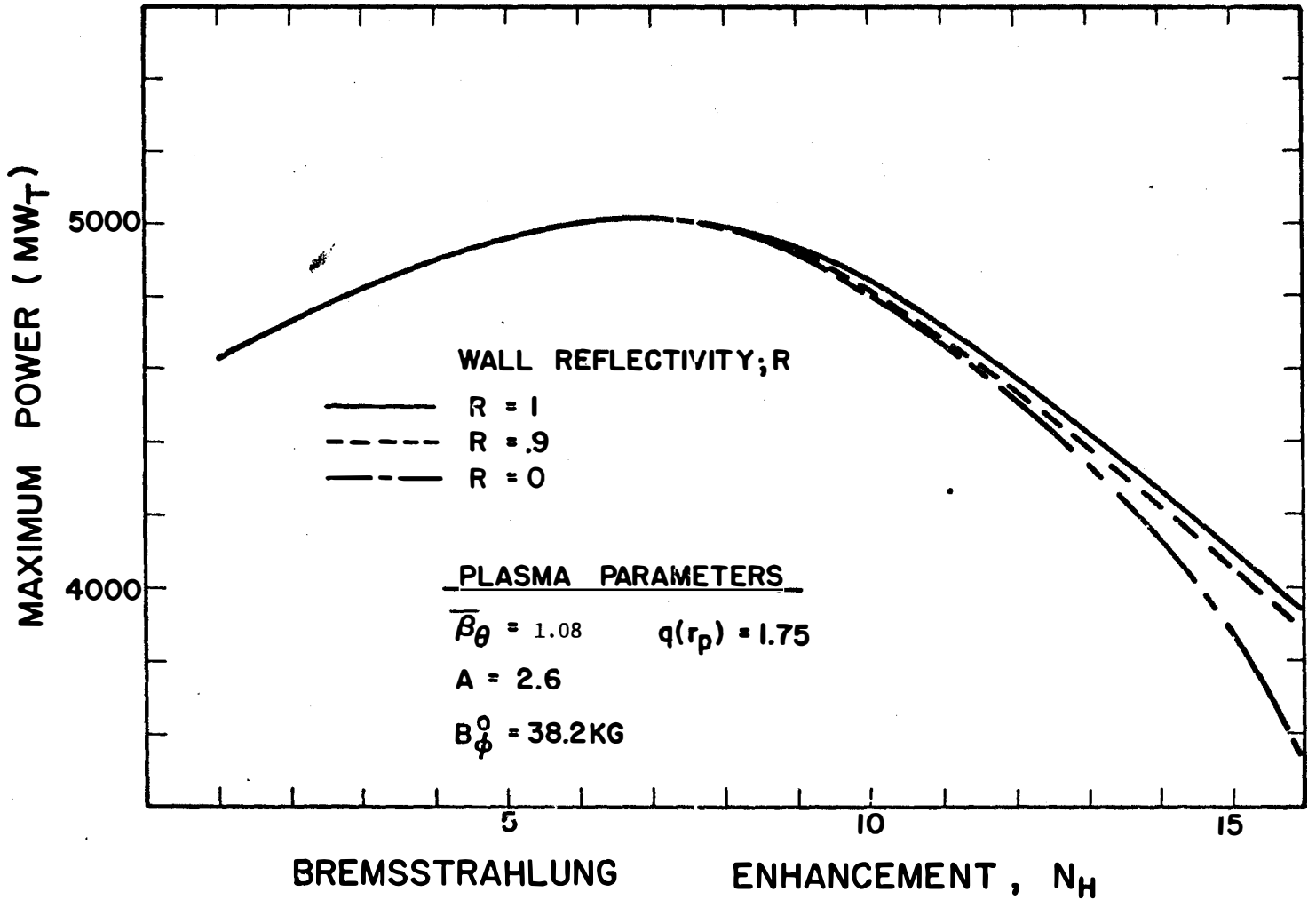


FIGURE II-F-4

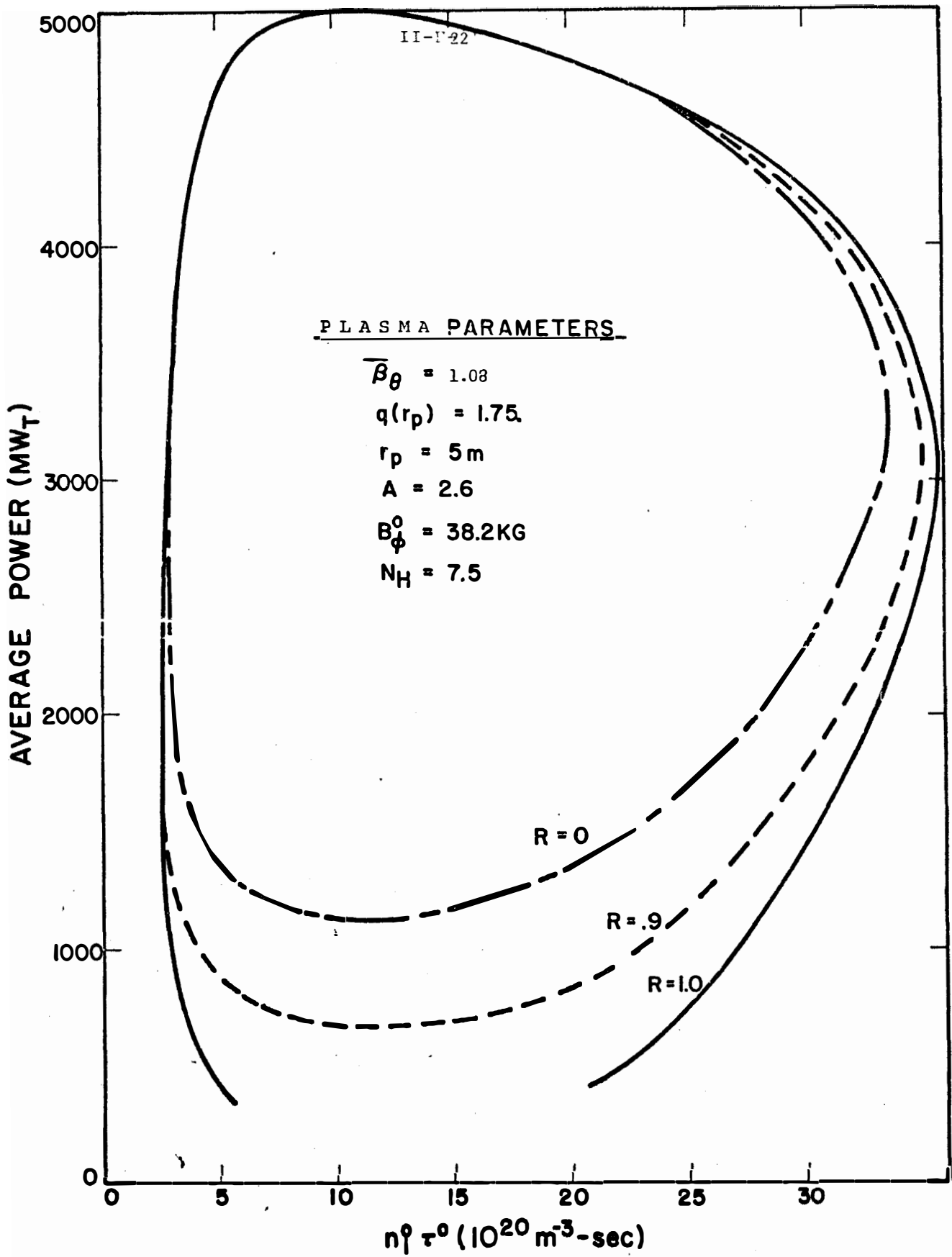


FIGURE II-F-5

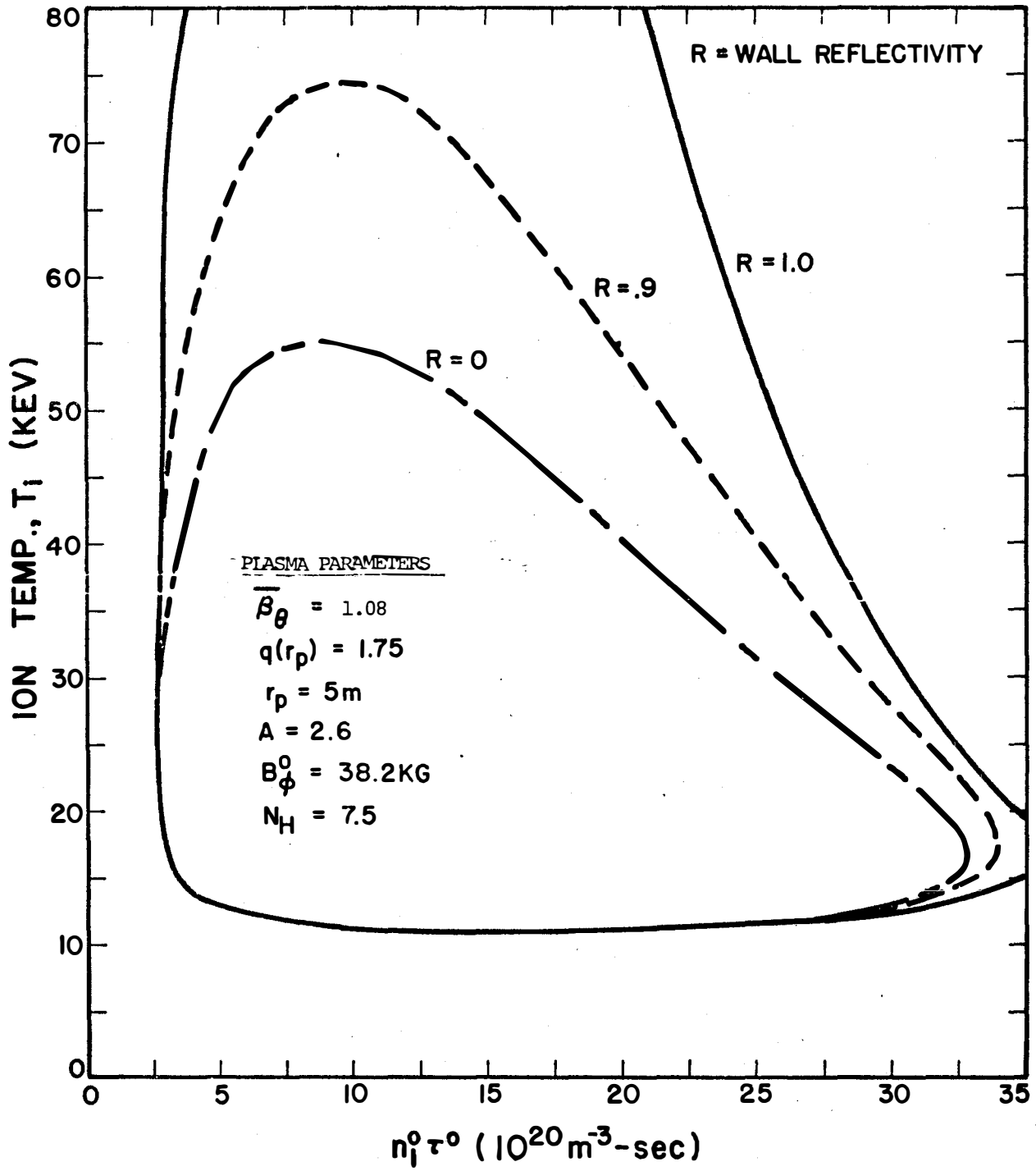


FIGURE II-F-6

equilibrium, we have also evolved parameters for a thermally stable point at the larger of the two possible $n\tau$ values. It is noted that, other things equal, one should choose the larger $n\tau$ point since it will correspond to a higher fractional burnup (less fuel handling with more burn per pass) and a low particle diffusion rate (less of a burden on both the divertor and the fueling systems).

Figures II-F-7 and II-F-8 illustrate the effect of different choices of N_H on these $n\tau$ -plots. Figure II-F-3 is basically obtained by plotting the maximum $\langle P \rangle$ for the various enhancements, versus N_H . There exists a maximum N_H beyond which no equilibrium solutions exists. This corresponds simply to pushing the loss curve in Figure II-F-2 completely above the gain curve.

We also see here that when $N_H = 1$ (no impurities), the maximum power is about $4600 \text{ MW}_{\text{th}}$. Thus, the process of enhancement of bremsstrahlung increases the maximum power output by $\sim 8\%$. Thus, should impurities produce unmanageable plasma problems, the plasma can be operated purely on (D+T) without severe deterioration in plasma power output. Of course, to achieve the same power without impurities requires a higher B_ϕ^0 and, since magnet costs scale as $(B_\phi^0)^2$ (see section II-B and chapter VII), magnet costs would go up by $\sim 4\%$.

Other parameters, such as density, fractional burnup, and confinement time, also form closed curves when plotted against $n\tau$. Figure II-F-9 is typical and shows n_i^0 versus $n_i^0 \tau^0$. Note that the curves of temperature and density versus $n\tau$ at different bremsstrahlung enhancement factors are closed and nested. The power versus $n\tau$ curves, while closed, are of course not nested.

The characteristic parameters describing the optimum plasma and its operation at $5000 \text{ MW}_{\text{th}}$ are given in Tables II-F-1 through II-F-3. This equilibrium is thermally unstable so that some form of control is required to operate at steady state. A thermally stable plasma can be evolved to yield the same power and its characteristic parameters are given in Tables II-F-4 through II-F-6. UWMAK-I has been chosen to operate at the thermally unstable point because magnet costs are $\sim 50\%$ higher at the stable point. The reason is $B_\phi^0 = 38.2 \text{ KG}$ at the unstable point but is 47.3 KG for the stable point. A 20% increase in field increases magnet costs by $\sim 50\%$ (see section II-B and chapter VII.) This would translate into $\sim \$100$ million dollars for the UWMAK-I design. In the next section, some comments are made about the control problem and operation at the unstable point, but at this stage it is clearly an unsolved problem. We argue simply that the savings in magnet costs are sufficient incentive for feedback control and operation at the thermally unstable equilibrium.

In summary, UWMAK-I operates at the thermally unstable equilibrium with characteristic parameters as given in Tables II-F-1 to II-F-3. β_θ has been limited to ~ 1 and $q(a) = 1.75$. The toroidal field on

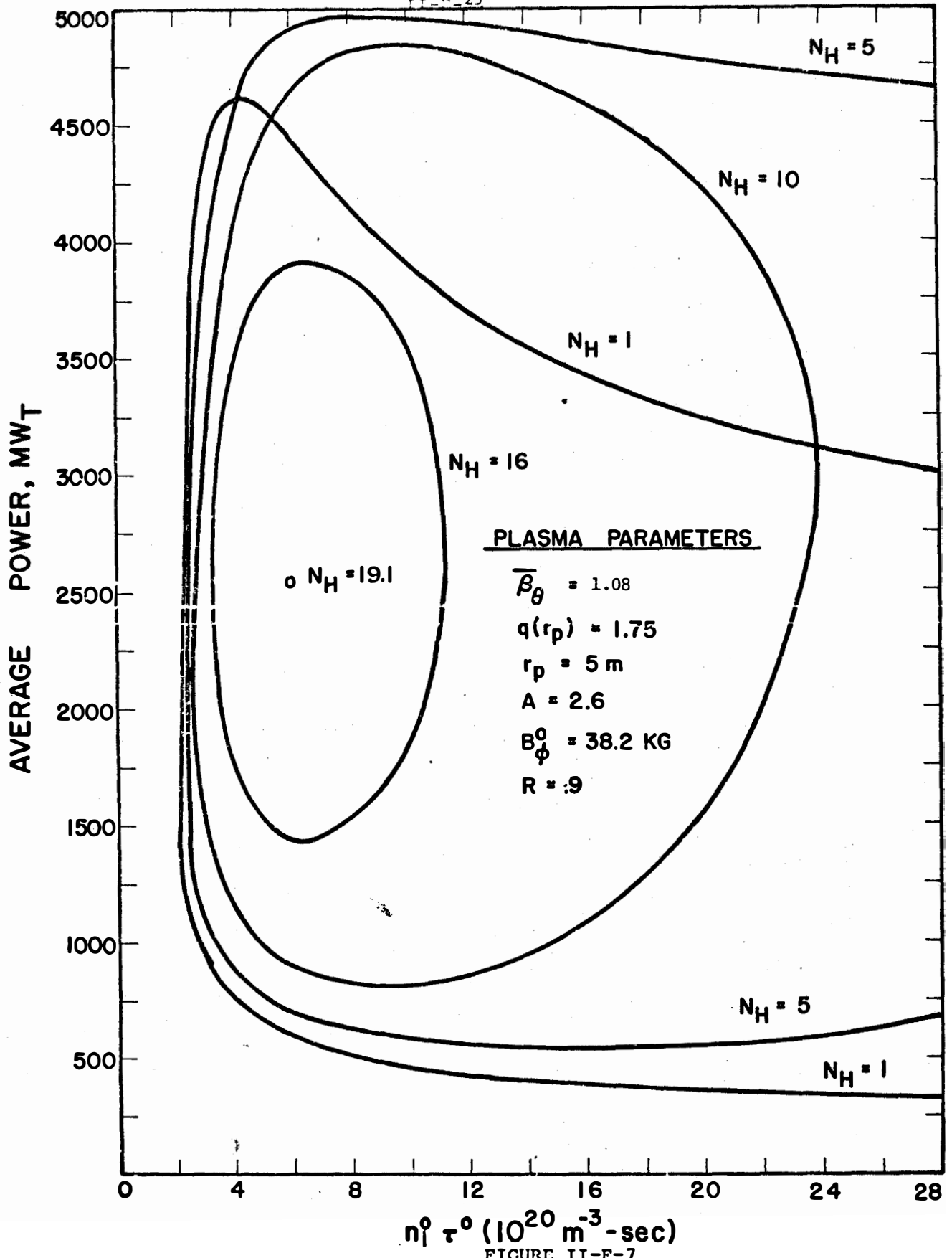


FIGURE II-F-7

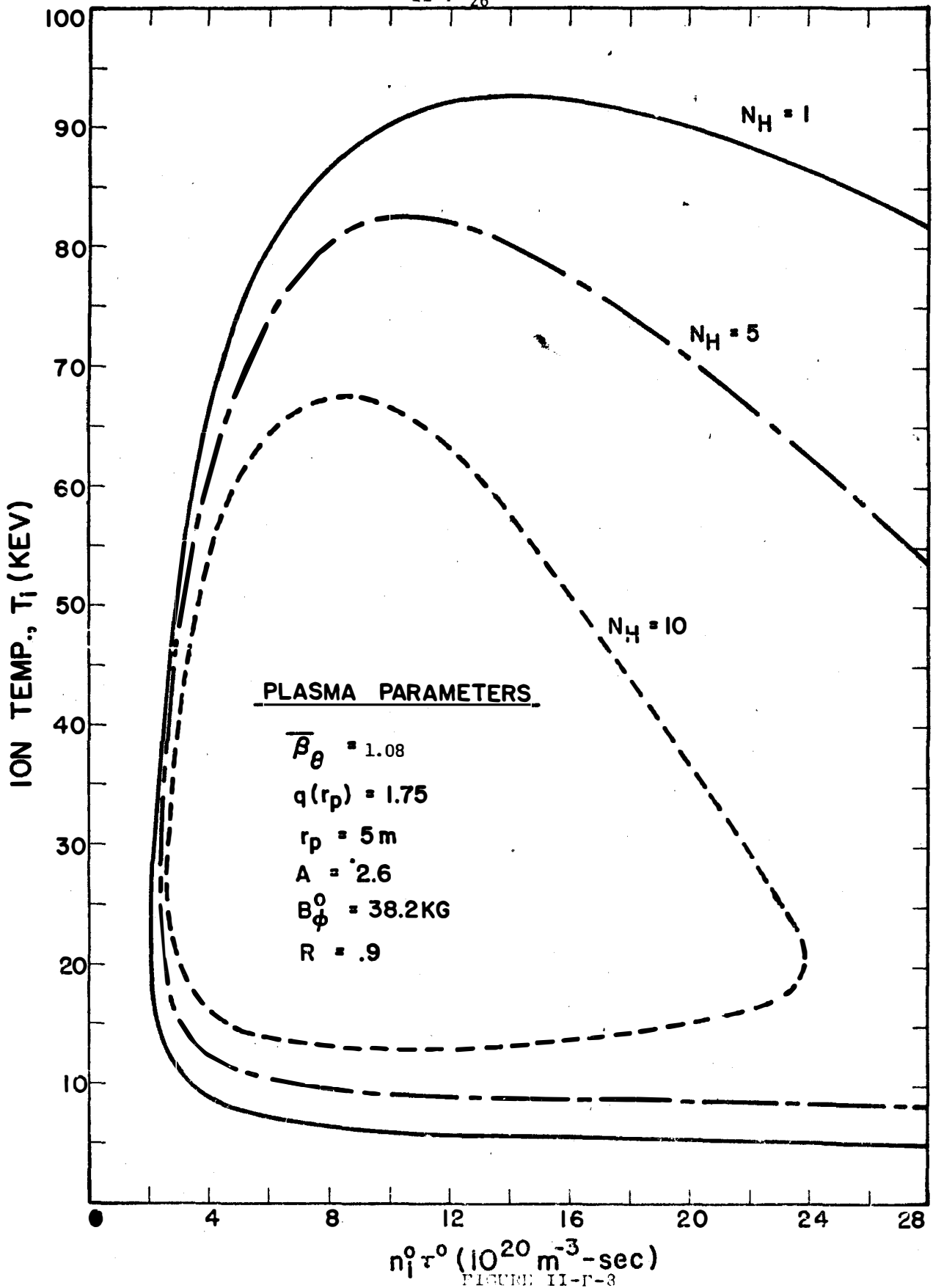


FIGURE II-F-3

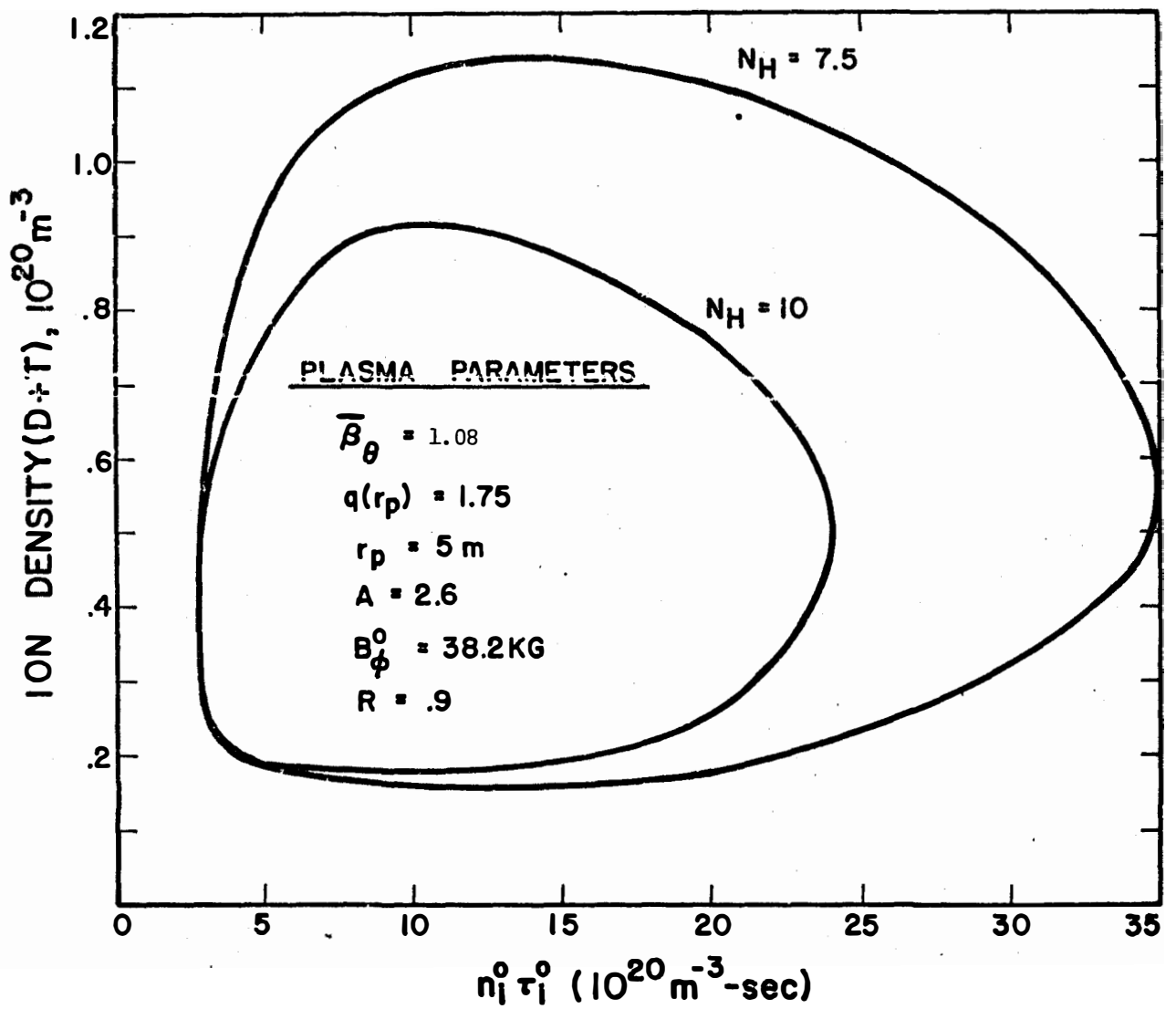


FIGURE II-F-9

axis is only 38.2 KG, a relatively low field, which means superconducting magnet design can use NbTi superconductor, a "present technology" decision (see chapter VII). The power output is 5000 MW_{th} (using 20 Mev per fusion, see chapter V) and the neutron wall loading is 1.25 MW/m² (see chapter VI). The minor and major radii have been set to minimize cost per unit power and bremsstrahlung enhancement and confinement spoiling have been used to achieve an optimum plasma that minimizes B_{ϕ}^0 for a given power output. The required bremsstrahlung enhancement can be achieved with argon (z=18) at a density which is .0095 of the (D+T)-ion density. The plasma is assumed to operate in this mode during the burn time or, if truly steady state, until wall initiated impurities build the impurity density to an intolerable level.

PLASMA PARAMETERS
(Unstable Equilibrium Point)

$$T_{\text{ions}} = 11.1 \text{ KeV}$$

$$\bar{\beta}_{\theta} = 1.08$$

$$T_{\text{el}} = 11.0 \text{ KeV}$$

$$\bar{\beta}_{\phi} = .052$$

$$\bar{n}_{\text{D+T}} = 0.8 \times 10^{14} / \text{cm}^3$$

$$q(a) = 1.75$$

$$\bar{n}_{\alpha} = .0295 \times 10^{14} / \text{cm}^3$$

$$a = 5 \text{ m}$$

$$\bar{\tau}_c = 14.2 \text{ sec}$$

$$R = 13 \text{ m}$$

Confinement Spoiling

$$r_w = 5.5 \text{ m}$$

Factor = 450

$$A = 2.6$$

Bremsstrahlung Enhancement

$$B_{\phi}^{\circ} = 38.2 \text{ KG}$$

Factor = 7.5

$$B_{\theta}(a) = 8.4 \text{ KG}$$

Impurity = Argon

$$\bar{n}_{\text{imp}} = .0073 \times 10^{14} / \text{cm}^3$$

Plasma Vol. = 6400 m³ (nominal)

Chamber Vol. = 7750 m³ (nom.)

$$\frac{\bar{n}_{\text{imp}}}{\bar{n}_{\text{(D+T)}}} = .0095$$

Wall Area = 2830 m² (nom.)

$$f_b = 7.2\%$$

$$I_{\phi} = 21 \times 10^6 \text{ Amps}$$

$$n\tau_c = 11.35 \times 10^{14} \text{ sec-cm}^{-3}$$

POWER PARAMETERS**(Unstable Equilibrium Point)****Total ENERGY PER FUSION = 20 MeV**

$$\langle P \rangle = 5000 \text{ MW}_{(\text{th})}$$

$$\langle P \rangle / \text{Vol} = .8 \text{ MW/m}^3$$

Neutron Wall Loading, $P_{nw} = 1.25 \text{ MW/m}^2$ **Brem. Wall Loading, $P_{xw} = .215 \text{ MW/m}^2$** **Synch. Wall Loading, $P_{cw} = .002 \text{ MW/m}^2$** **(Wall Reflectivity = .9)****Power to Divertor = 237 MW****Particle Wall Loading, $P_{pw} = .0092 \text{ MW/m}^2$** **Relative Cost Factor = 1.0**

TABLE II-F-2

FUELING PARAMETERS
(Unstable Equilibrium Point)

Tritium Consumption Rate = .672 Kgm/day

Deuterium Consumption Rate = .448 Kgm/day

Diffusion Rate (D+T+alpha) = 3.74×10^{22} /sec

Fueling Rate (D+T) = $\left\{ \begin{array}{l} 3.9 \times 10^{22} \text{ (D+T) / sec} \\ 8.4 \text{ Kgm (T) / day} \\ + 5.6 \text{ Kgm (D) / day} \end{array} \right.$

TABLE II-F-3

PLASMA PARAMETERS
 (Stable Equilibrium)

$$T_{\text{ions}} = 28 \text{ KeV}$$

$$\bar{\beta}_{\theta} = 1.08$$

$$T_{\text{el}} = 21 \text{ KeV}$$

$$\bar{\beta}_{\phi} = .052$$

$$\bar{n}_{\text{D+T}} = .367 \times 10^{14} / \text{cm}^3$$

$$q(a) = 1.75$$

$$\bar{n}_{\alpha} = .127 \times 10^{14} / \text{cm}^3$$

$$a = 5 \text{ m}$$

$$\bar{\tau}_c = 61 \text{ sec}$$

$$R = 13 \text{ m}$$

Confinement Spoiling

$$r_w = 5.5 \text{ m}$$

$$\text{Factor} = 308$$

$$A = 2.6$$

Bremsstrahlung Enhancement

$$B_{\phi}^{\circ} = 47.3 \text{ KG}$$

$$\text{Factor} = 10$$

$$B_{\theta}(a) = 10.4 \text{ KG}$$

Impurity - Argon

$$\text{Plasma Vol} = 6400 \text{ m}^3 (\text{nominal})$$

$$\bar{n}_{\text{im}} = .0133 \times 10^{14} / \text{cm}^3$$

$$\text{Chamber Vol} = 7750 \text{ m}^3 (\text{nom.})$$

$$\frac{\bar{n}_{\text{im}}}{\bar{n}_{\text{D+T}}} = .0365$$

$$\text{Wall Area} = 2830 \text{ m}^2 (\text{nom.})$$

$$f_b = 42 \%$$

$$I_{\phi} = 25.7 \times 10^6 \text{ Amps.}$$

$$n \tau_c = 22.3 \times 10^{14} \text{ sec-cm}^{-3}$$

TABLE II-F-4

POWER PARAMETERS**(Stable Equilibrium)****Total ENERGY / FUSION = 20 MeV**

$$\langle P \rangle = 5000 \text{ MW}_{(th)}$$

$$\langle P \rangle / \text{Vol.} = .8 \text{ MW} / \text{m}^3$$

Neutron Wall Loading, $P_{nw} = 1.25 \text{ MW} / \text{m}^2$ **Brem. Wall Loading, $P_{xw} = .282 \text{ MW} / \text{m}^2$** **Synch. Wall Loading, $P_{cw} = .0106 \text{ MW} / \text{m}^2$** **(Reflectivity = .9)****Power to Divertor = 45 MW****Particle Wall Loading, $P_{pw} = .0018 \text{ MW} / \text{m}^2$** **Relative Cost Factor = 1.55**

FUELING PARAMETERS
(Stable Equilibrium)

Tritium Consumption Rate = .672 Kgm / day

Deuterium Consumption Rate = .448 Kgm / day

Diffusion Rate (D+T+ alpha) = .86 x 10²² /sec

Fueling Rate (D+T) = $\left\{ \begin{array}{l} 1.04 \times 10^{22} \text{ (D+T) / sec} \\ 2.3 \text{ Kgm (T) / day} \\ 1.53 \text{ Kgm (D) / day} \end{array} \right.$

TABLE II-F-6

II-G. Control and Economics

It has been noted in the previous section that the reactor presented in this report has been designed to operate at an equilibrium for which the plasma is thermally unstable. This implies that a feedback or dynamic control system is required to maintain the plasma at the desired temperature. Parameters for an alternative reactor based on a thermally stable plasma equilibrium are given in Tables II-F-4 to II-F-6. The stable design requires ~20% higher toroidal field and plasma current. This translates into ~50% higher costs for the toroidal field coils, divertor coils and transformer coils. Consequently, there is a significant economic benefit in designing the reactor for the unstable equilibrium and incorporating a feedback system to maintain the plasma temperature. We present in this section some preliminary thoughts on how such a control system might operate.

A rough idea of the required response time and power changes required in a feedback control system can be obtained by linearizing the time-dependent point reactor energy balance and particle balance equations. One finds that the temperature variation, δT , has an exponential time dependence

$$\delta T(t) = \delta T(o) e^{\gamma t}$$

where $\gamma \sim .64 \text{ sec}^{-1}$. This implies that, unless counteracted, the temperature excursion doubles approximately every second. With a linear feedback system, γ can be made equal to $-.5 \text{ sec}^{-1}$ if the feedback system supplies $\sim 280 \text{ MW}$ per keV of temperature excursion. If one assumes the uncertainty in the temperature measurement is $\sim 5\%$, then a control capable of adding or removing 100-200 MW with a rise time of about 0.1 seconds is required for successful stabilization of the temperature. This sets the scale for the requirements of the feedback system. A more sophisticated analysis which included space-dependent and delayed response effects will be done, but it should not change the order of magnitude of the control requirements.

Monitoring the plasma temperature to the accuracy indicated (or perhaps better) is beyond the capability of present day plasma diagnostics, but fortunately a thermonuclear plasma emits copious quantities of X-rays and neutrons which perhaps can be used as a sufficiently accurate monitor of the plasma behavior.

A somewhat more difficult problem is the mechanism by which the plasma is heated or cooled to return it to the proper temperature. To heat the plasma, one could use neutral beam injectors, as we have proposed for the initial heating phase to ignition. These are easily controllable on the time scale required and the power requirements are a bit higher but about the same as required for ignition heating (less power is required during startup because of the lower initial density.) Electromagnetic (microwave, radio frequency, etc.) radiation is another possibility if good absorption can be attained.

Cooling the plasma if the temperature gets too high is not quite so straightforward. One could inject impurities to enhance the bremsstrahlung radiation, but a way is needed to remove them when the plasma returns to the desired temperature. If the particle transport is by turbulent diffusion, the impurities come out on a time scale the order of of the particle confinement time, which is too long. If the particle transport is by Coulomb collisional processes, the situation is even worse; the impurities do not come out at all. (17-b) Another possibility is to increase the particle loss rate. This would appear to be too sluggish because the time required for magnetic field diffusion through the conducting blanket is long. An interesting possibility is to excite collective oscillations in the plasma which lead to turbulence and increase the particle loss rate without grossly disrupting the plasma column. If the increase in power transported by the particles is greater than the power required to excite the oscillation, then a cooling effect is obtained. Low frequency oscillations could possibly be excited by modulation of neutral beams or microwave power. The reverse effect of using modulated microwave power to feedback stabilize plasma instabilities has been demonstrated in some small-scale laboratory experiments.

Another possible operating mode for feedback control of the plasma is a variation on the operation of a subcritical fission reactor in the presence of a source. In the fission case, the source provides the extra neutrons to keep the subcritical system from shutting down. In the plasma problem under discussion, one designs the steady state operating condition such that the plasma requires externally injected energy (for example, 100 MW of neutral beam power) to maintain a thermal balance. The external power is of a form which is easily modulated on a .1 sec time scale. The basic idea is shown in Figure II-G-1. P_0 denotes the injected power required to maintain an equilibrium at temperature, T_0 . Figure II-G-2 illustrates a control scheme assuming the injected power can be doubled to $2P_0$ or shut off. If the temperature rises above T_0 ($T_0 < T < T_1$), the injected power is turned off so that the losses now exceed the α -heating and the plasma cools. If the temperature drops below T_0 , the injected power is doubled to $2P_0$, the heating exceeds the losses and the plasma heats up. There is a finite range, $T_2 < T < T_1$, determined by P_0 , over which the system can be controlled.

These are only some of the possibilities for feedback control of the thermally unstable equilibrium. We are now beginning a more refined analysis to better assess the problem and the proposed solutions. It appears at this stage, however, that feedback control is not unmanageably difficult.

SUB-EQUILIBRIUM, STEADY STATE PLASMA OPERATION

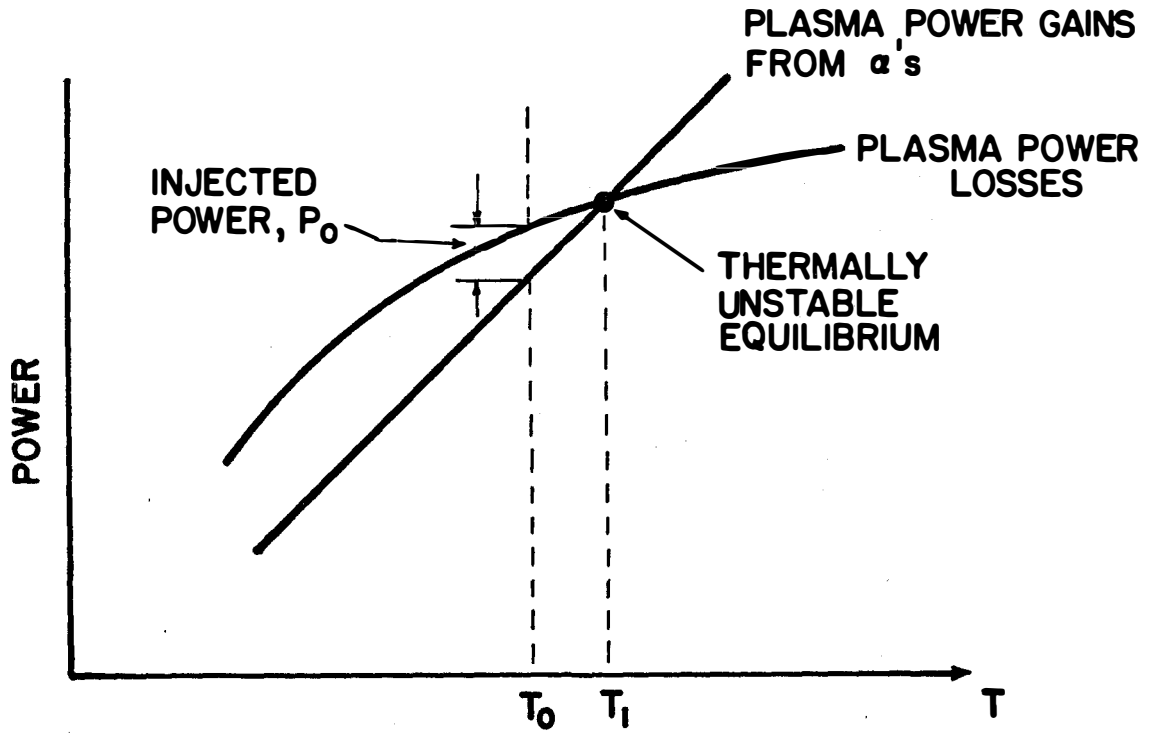


FIGURE II-G-1

CONTROL of SUB-EQUILIBRIUM PLASMA

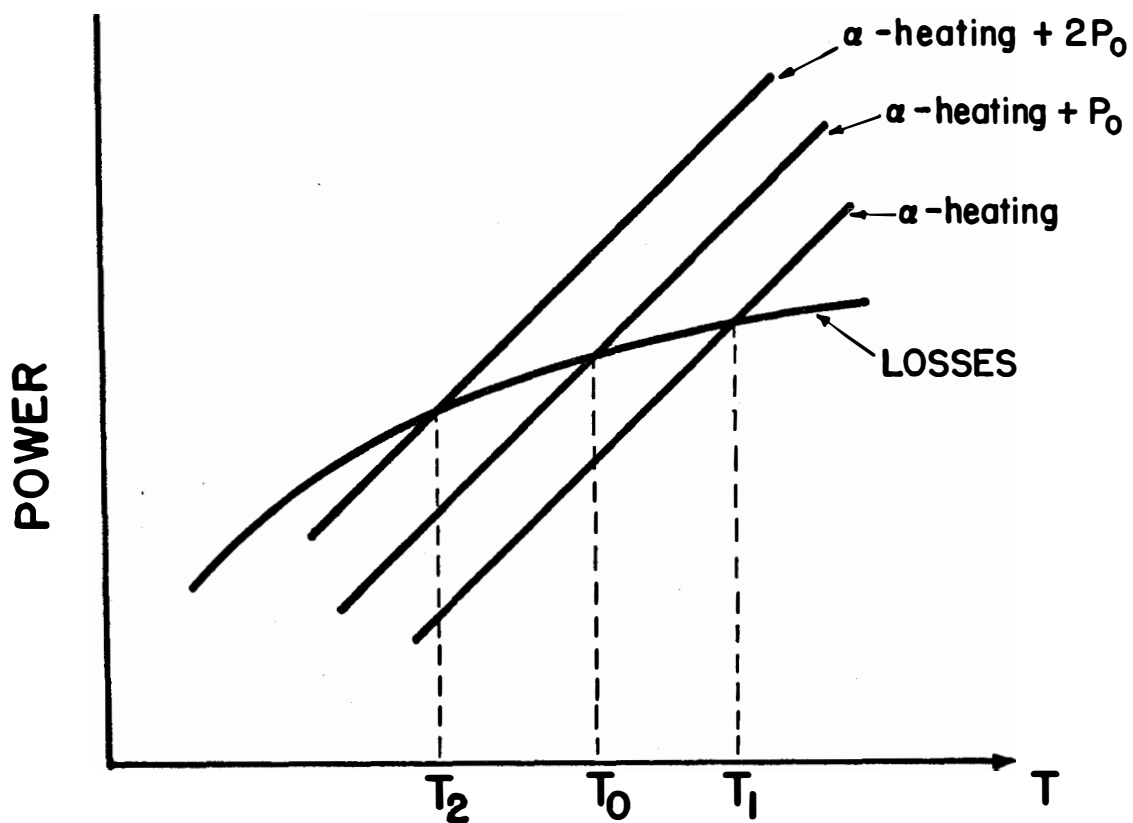


FIGURE II-G-2

II-H. Recycle and Shutdown

A Tokamak plasma must operate on a pulsed basis for one or both of two reasons, although pulse lengths may be long. First, the divertor will not be 100% effective in preventing ions from hitting the wall and impurities from entering the plasma. Consequently, the impurity level will eventually rise to an intolerably high level. The plasma discharge will therefore have to be periodically terminated, the chamber evacuated, reloaded with clean fuel and the plasma reignited. Second, if the diffusion driven current, which presently is an unobserved prediction of neoclassical theory, does not appear, the plasma current will have to be maintained by a slowly rising current on the primary side of the transformer (see Section II-C.) In this case, the burn must be terminated when the primary current reaches its design limit. A burn time of 90 minutes is easily achieved so that the Tokamak can be considered to be quasi-steady state during each burn. In this section, we consider the process that must occur between each burn period. We will assume a burn time of 90 minutes based on the design limit of the transformer primary.

The burn is terminated by cooling the plasma, at constant plasma current, to a temperature of ~500 eV in about 10 seconds. This can be accomplished by shutting off the refueling injectors and injecting impurities to further enhance the radiation level. At this time, the cryopumps are isolated from the vacuum chamber by valves, the current in the transformer primary is reversed, and the divertor currents are turned off. This drives the plasma current to zero and takes about 100 seconds. Confinement is lost and the particles go to the walls of the chamber. The plasma is neutralized and comes into thermal equilibrium with the walls at a pressure of $\sim 8 \times 10^{-3}$ torr. The chamber is then evacuated in 50 seconds, using the diffusion and backing pumps and the lithium trapping surfaces to 1×10^{-5} torr. This reduces the impurity level in the chamber. The transformer coils are then "recocked" in ~100 sec. After a 10 second pump out to clean up the plasma chamber, it is then reloaded with clean 50% D-T gas to a pressure of 2.3×10^{-3} torr. The transformer current is reversed again to create the plasma and drive the plasma current. The divertor coil currents rise with the plasma current. The neutral beam injectors are turned on to heat the plasma to ignition and the refueling injectors are turned on to raise the average plasma density to the design value of 0.8×10^{20} ions/m³. Simultaneously, the vacuum pumping reduces the pressure in the divertor zone to 2×10^{-5} torr. This level is reached at about 40 seconds after ignition. Half of the cryopumps are valved on when the pressure in the divertor zones drops below 2.5×10^{-4} torr.

The cycle, which is shown schematically in Figure II-H-1, requires about 390 seconds between the end of one burn and the beginning of the next burn. Since the burn time is 90 minutes, the duty factor is 93.3. However, when scheduled maintenance are taken into account, the plant factor is ~80%. During the 390 second interval in which no neutrons are being produced, the lithium flow rate in the blanket is reduced to minimize thermal stress cycling.

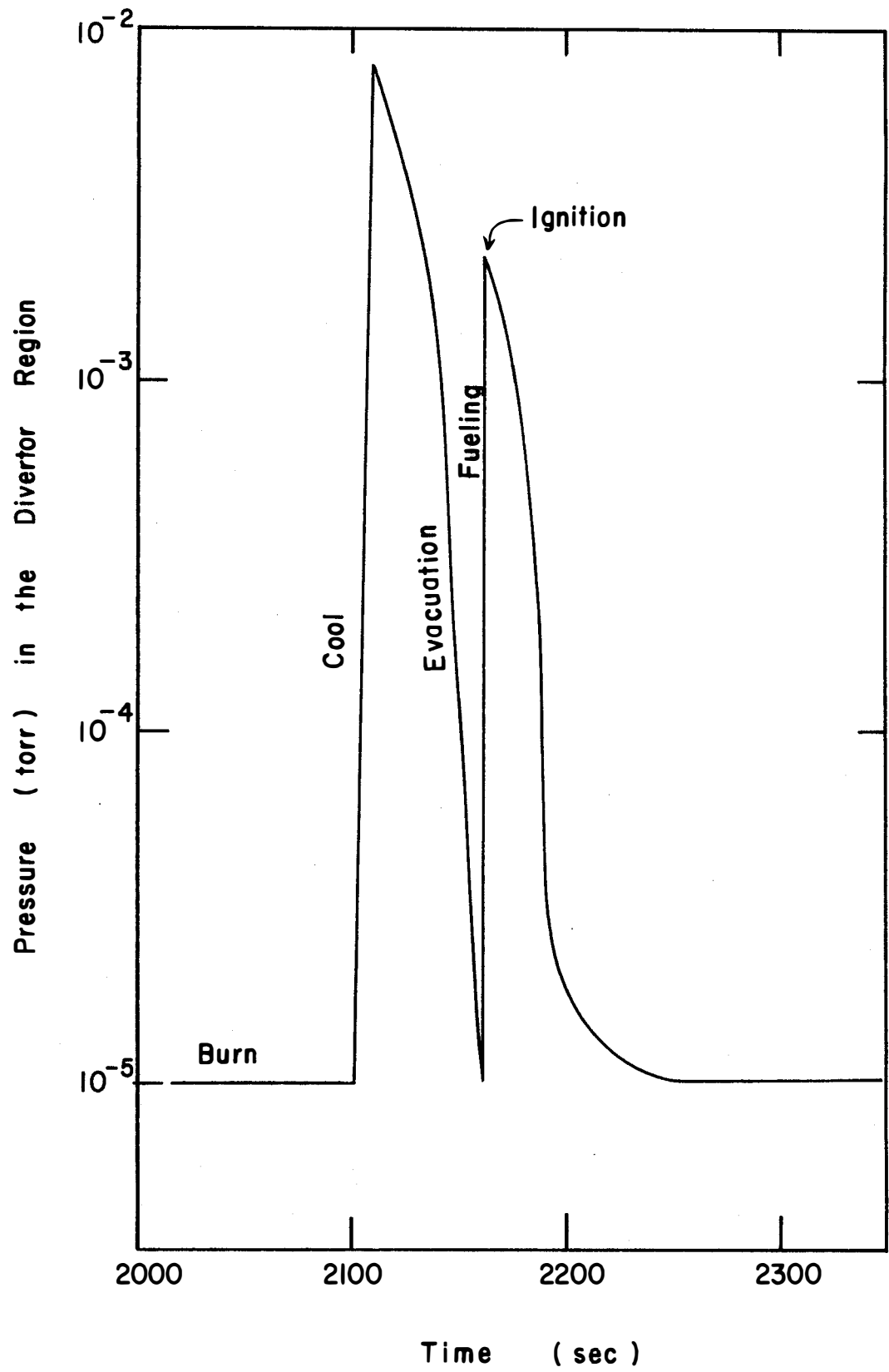


FIGURE II-H-1

II-I. Alternate Plasma Assumptions and Economic Implications

In each section of this chapter, assumptions have been made as the detailed analysis is carried through. The results obtained are often insensitive to some assumptions but quite sensitive to others. We attempt here to spell out the important assumptions in each of the preceding sections, discuss the reasons such assumptions were made, and consider the impact, particularly on reactor performance and economics, of plausible, alternative assumptions.

1. Optimization

The optimization studies in section II-B contain three basic assumptions: 1) the reactor has a β -limited plasma as its core; 2) a reasonable measure of nuclear island cost scaling is the scaling of magnet costs; and 3) the toroidal field magnet costs scale as the energy stored in the field, which in turn varies as the square of the maximum field strength. We have also used various limits on β_θ , such as A and \sqrt{A} , but found this had little effect on the basic conclusions. Survey studies on the variation of other parameters, such as the safety factor, q , and the neutron wall loading P_{nw} , and the effects of constraints, such as on core size, are the substance of section II-B and will not be given here.

2. Start-Up, Transformer Design, and Energy Storage.

A restricting consideration in the design of the transformer system is the rate of current rise in the superconducting transformer and vertical field coils. A 100 second rise time is satisfactory on this basis. The reason for a fast plasma current rise time, T_1 , comes from the desire to achieve the most stable plasma discharge. In a Tokamak reactor, one must balance this desire for a fast current rise with the limits imposed by both the superconducting windings and the energy stored in primary and divertor coil currents. Calculations show the energy storage requirements of the transformer and divertor field coils is the order of 15MW-hr. For example with a 10 second rise time, the average power requirement is 5250 MW_e. The voltage on the coils is limited to 10 kV and is held constant so the current rises linearly. This means one must buy 10500 MW_e, which is clearly too large an amount to consider buying "off the line." Thus, to maintain a 10 second or less rise time for the plasma current entails some form of energy storage. For even shorter startup times, a serious problem will be helium vaporization caused by eddy current losses in the magnets. Today, a user can purchase up to 200 MW_e directly from the line. The National Accelerator Laboratory in Batavia, Illinois purchases this much power from Commonwealth Edison of Chicago. If one assumes that in the future it will be possible to purchase 500 MW_e, then a total of 10.4 MW-hr can be obtained in 100 seconds and only 4.6 MW-hr will be needed from an energy storage unit. For $T_1 > 200$ sec, the energy can be bought directly from the line.

3. Neutral Beam Heating

The use of neutral beam heating to ignite UWMAK-I, discussed in section II-D, seems feasible if the scaling laws used for the diffusion coefficient and thermal conductivity prove applicable. In the analysis, it is assumed that the electron thermal conductivity scales pseudo-classically⁽²⁵⁾ while the ion conductivity scales neoclassically.⁽¹⁷⁾ Such scaling leads to reasonably accurate numerical simulation of present day experiments. However, if a different form of scaling prevails, the task of using neutral beams to ignite large plasmas will be more difficult. In particular, there is a large class of trapped particle instabilities which predict less favorable, indeed unfavorable, scaling of the electron conductivity with collision frequency. It is proposed that non-circular plasma cross sections, in particular plasmas elongated vertically to reduce the ∇B variation (such as elliptical and D-shapes), can reduce or remove adverse trapped particle effects. This has not yet been verified experimentally. To date, no machine has operated enough into the collisionless regime to verify the predicted trapped particle effects even in plasmas with circular cross sections. In addition, the numerical coefficients in many of the scaling formulas for trapped particle modes are, at best, known only to within an order of magnitude or so. Thus, while transport coefficients other than pseudoclassical or neoclassical can make igniting a large CTR Tokamak more difficult, it is not possible to say now just how much more difficult the task will be.

4. Plasma Operation, Thermal Stability and Limits on β and q .

The question of transport coefficients and scaling laws also has a significant bearing on the operating mode of a CTR-Tokamak. In particular, in section II-F, the thermal instability of a plasma at equilibria in the temperature range below 20 KeV was discussed. Indeed, parameters are presented in tables II-F-1 to II-F-6 for two thermal equilibria, one stable and the other unstable. We noted that operation at the thermally stable point would cost an additional 100 million dollars in magnet costs because 20% higher magnetic fields are requested to produce the same power.

The classification of the stable and unstable equilibria depends critically on the form and scaling of the transport coefficient. In particular, we used neoclassical transport coefficients and introduced an anomalous spoiling factor, S , to scale confinement time down. Nevertheless, with basically classical scaling, the energy confinement time, τ_E varies as $T^{1/2}$. We have not found it possible to obtain stable equilibria in the 10-15 KeV range with such scaling. On the other hand, transport coefficients for which $\tau_E \sim T^{-p}$ with $p > 0$ could yield a thermally stable equilibrium at the lower temperatures desired. Whether the proper scaling can be made to prevail in the desired operating regime is an open question.

Finally, the effects of different assumptions for the plasma beta and the safety factor, q , must be examined. In section II-F, it was assumed that $\beta_\theta \sim 1$ and $q(a) = 1.75$. We argued there that these assumptions were consistent with MHD equilibrium and stability theory which predicts β_θ values of the order of 5%. Further, most experimental data from high current Tokamaks have $\beta_\theta \sim 1/2$ so that $\beta_\theta \sim 1$ seemed a reasonable choice. Since β is effectively a measure of just how well one uses the magnetic field available, the costs are sensitive to any choice made. Further since power output varies as $\beta^2 B^4 / q^4$, one would like as large a β and as small a q as possible.

Figure II-I-1 shows the scaling of magnet costs (toroidal field, transformer and divertor field coils) as a function of the safety factor, $q(a)$, for different poloidal beta limits using UWMAK-I as the reference point. Note that along a constant β_θ line, the plasma current is fixed. This means the cost of the transformer and divertor windings are also fixed and only the toroidal field magnet costs vary. On the other hand, all magnet costs scale as one moves vertically along a line of constant q . The reason is that both B_ϕ and B_θ change such that the ratio remains constant.

From figure II-I-1, it is clear that the best case is the line of largest constant β_θ , taken here to be $\beta_\theta = A$. The right hand scale translates magnet costs to dollars per KW_e and all costs are for NbTi superconducting magnets. Along a constant β_θ line, q can only be increased by increasing the toroidal field, B_ϕ , which means increasing the maximum field at the toroidal field magnets. We have set 110 K Gauss as the upper limit for NbTi coils (allowing for pumping on the helium) and have indicated this limit by the hatched line in figure II-I-1. For β_θ and q combinations above this line, the superconductor must be changed, the technology will change, and the costs will show a different scaling. As such, the curves have not been extended beyond the NbTi technology limit. It suffices to conclude that there is strong incentive for achieving high β and low q in a Tokamak (and other β -limited devices, such as stellartors), as we have known, and the costs figures in Fig. II-I-1 give some quantitative indication of the economic penalties involved in various choices.

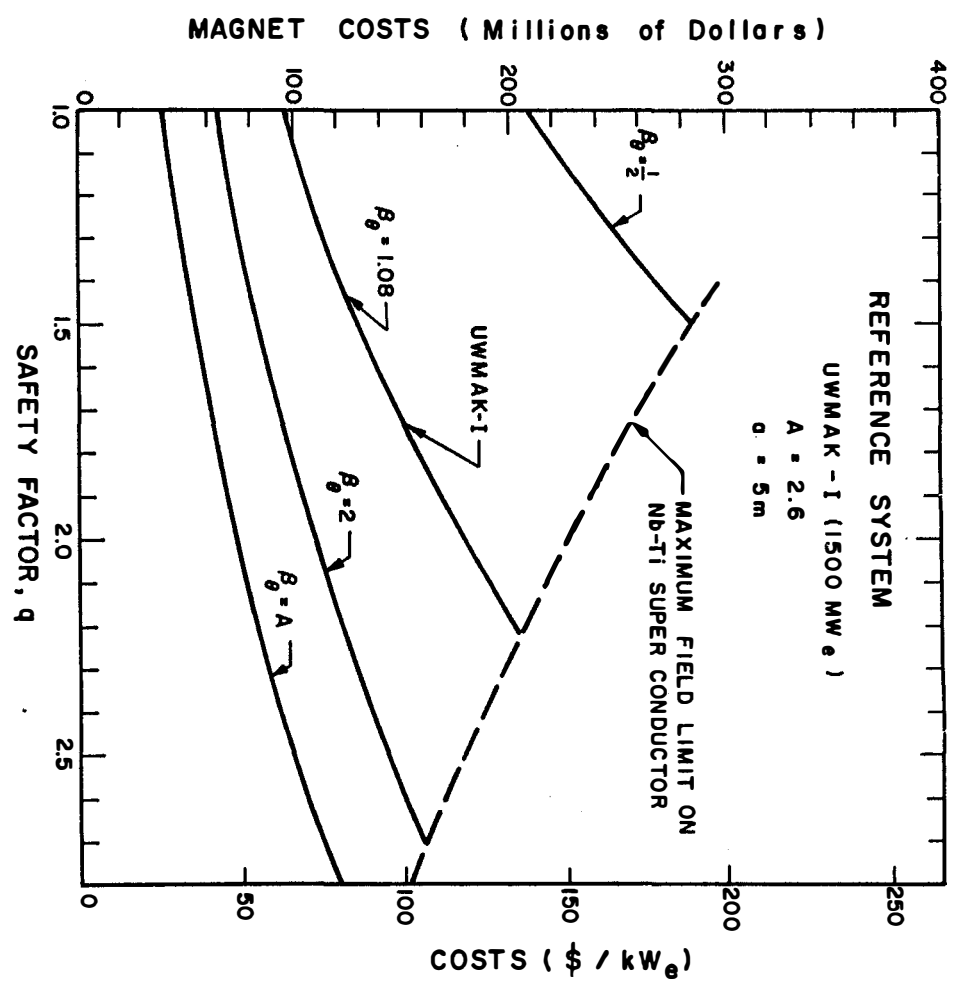


Figure II-I-1

As a final point, the possibility of a steady-state Tokamak operating at $\bar{\beta}_\theta = \sqrt{A}$ has been discussed in section II-F and while $\bar{\beta}_\theta \sim 1$ is a most reasonable choice from an MHD equilibria and stability viewpoint, the possibility of a steady-state Tokamak is most intriguing. Aside from the inherent advantages of steady-state operation, such as no thermal cycle on the first wall and no duty cycle factor, it would either relieve the need for an energy storage unit or substantially reduce the cost of such a system for Tokamaks. The reason is that relatively longer startup times would not be economically disadvantageous. The estimated cost breakdown for large magnet energy storage units are $\$1.67 \times 10^6$ per MW-hr for the storage units and $\$20$ to $\$40$ per KW_e for the bridges. Thus, at short startup times where large specific powers are involved, the cost of bridges is very large. However, for a 500 sec rise time, the peak power reduces to 200 MW_e , which could be bought off the line without the need for any energy storage. Such a unit may be built and be available for other purposes but it would no longer be required to energize the primary and divertor windings. Again, this option is available only if steady-state operation, or burn times much longer than an hour, are possible and only if a Tokamak plasma can be made to operate with long current rise times.

References for Chapter II

1. L. A. Artsimovich, Nucl. Fusion 12 (1972) 215.
2. V. S. Mukhaovатов and V. D. Shafranov, Nucl. Fusion 11 (1971) 67.
3. B. B. Kadomtsev and O. P. Pogutse, Nucl. Fusion 11(1971) 605.
4. V. D. Shafranov, Atomn. Energ. 5 (1956) 38.
5. V. D. Shafranov, Zh. tekhn. Fiz. 40 (1970) 741.
6. C. Mercier, Nucl. Fusion Suppl. 2 (1962) 801.
7. V. D. Shafranov, Zh. Eksp. Feor. Fiz 37 (1959) 1088.
8. J. M. Greene, J. L. Johnson, and K. E. Weimer, Phys. Fluids 14 (1971) 671.
9. H. P. Furth and S. Yoshikawa, Phys. Fluids 13 (1970) 2593.
10. R. C. Davis, O. B. Morgan, L. D. Stewart and W. L. Stirling, Rev. Sci. Instr. 43 (1972) 278.
11. A. A. Galeev and R. Z. Sagdeev, Zh. Eksp. Theo. Fiz. 53 (1967) 348.
12. R. J. Bickerton, J. W. Connor, and J. B. Taylor, Nature 229 (1972) 110.
13. A. A. Galeev and R. Z. Sagdeev, Zh. Eksp. Theo. Fiz. 53 (1967) 348, Sov. Phys. Dokl. 14 (1970) 1198, Sov. Phys. JETP 32 (1971) 572, JETP Letts 13 (1971) 113.
14. P. H. Rutherford, Phys. Fluids 13 (1970) 482.
15. A. A. Ware, Phys. Rev. Letts. 25 (1970) 15 and 25 (1970) 916.
16. L. M. Kovrizhnykh, Zh. Eksp. Theo. Fiz. 56 (1969) 877.
17. a. M. N. Rosenbluth, R. Hazeltine and F. L. Hinton, Phys. Fluids 15 (1972) 116.
17. b. J. W. Connor, Plasma Physics 15 (1973) 765.
18. R. W. Conn, D. G. Mc Alees, and G. A. Emmert, "Self-Consistent Energy Balance Studies for CTR Tokamaks," Texas Symposium on the Technology of Controlled Fusion Experiments and the Engineering Aspects of Fusion Reactors, Austin, Texas, November 20-22, 1972. (To be published by A. E. C.).

19. Univ. of Wisconsin Fusion Feasibility Study Group, "Preliminary Conceptual Design of a Tokamak Reactor," *ibid.*
20. M. S. Lubell et al. "The Economics of Large Superconducting Toroidal Magnets for Fusion Reactors," ORNL-TM-3927, August, 1972.
21. W. C. Young and R. W. Boom, "Materials and Cost Analysis of Constant-Tension Magnet Windings for Tokamak Reactors," Fourth International Magnet Conference, Brookhaven, September 1972 - Also private communications.
22. I. N. Golovin, Yu. N. Dnestrovsky, and D. D. Kostomarov, "Tokamak as a Possible Fusion Reactor - Comparison with Other CTR Devices," Proceedings of the Conference on Nuclear Fusion Reactors, Culham Laboratory, September 1969, pp. 194-221, British Nuclear Society, London, 1970; also G. A. Emmert "Transformer Schemes for Tokamak Reactors," Fusion Design Memo 35 - University of Wisconsin, January 1973.
23. G. A. Emmert, "Transformer Schemes for Tokamak Reactors," (FDM-35, N. E. Dept., University of Wisconsin, January 1973).

Note: References 24-32 were not used.

33. R. C. Davis, O. B. Morgan, L. D. Stewart, and W. L. Stirling, Rev. Sci. Instr. **43**, 278 (1972).
34. O. B. Morgan, G. G. Kelley, and R. C. Davis, Rev. Sci. Instr. **38**, 467 (1967).
35. G. G. Kelley, IEEE Trans. on Nucl. Sci. **14**, 29 (1967).
36. O. B. Morgan, Ph.D. Thesis, University of Wisconsin (1970).
37. W. L. Stirling, R. C. Davis, O. B. Morgan, and L. D. Stewart, in Proceedings of the Symposium on Ion Sources and Formation of Ion Beams, Brookhaven National Laboratory (1971), p. 167.
38. D. G. Bate, "A Computer Program for the Design of High Perveance Ion Sources," CML-R53 (1966).
39. A. C. Riviere and D. R. Sweetman, "Fast Neutral Injection for Plasma Heating and Reactor Start-up," Fourth Conf. on Plasma Physics and Controlled Nuclear Fusion Research, Madison, Wisconsin, June 17-23, 1971.
40. A. S. Schlachter, P.J. Bjorkholm, D. H. Loyd, L. W. Anderson, and W. Haeberli, Phys. Rev. **177**, 184 (1969).
41. J. E. Osher, "Formation of a $D^{\bar{0}}$ Beam for Efficient Production of $D^{\bar{0}}$ at High Energies," UCID-15893 (1971).

42. J. H. Kamperschroer, "Lorentz Ionization of 20-200 KeV Neutral Deuterium Beams," FDM-31, University of Wisconsin, N. E. Dept. (1972).
43. H. C. Cole D. P. Hammond, E. M. Jones, A. C. Riviere, and J. Sheffield, "Electrode Heat Dissipation Limits on Multi-Aperture Ion Source Performance," CLM-P313 (1972).
- 44a S. L. Gralnick "Solid Deuterium Evaporation in a Fusion Plasma," Ph.D. Thesis, Columbia University (1972).
- 44b C. D. Hendricks, (private communication).
45. R. G. Mills, "Time-Dependent Behavior of Fusion Reactors," Proc. Nucl. Fus. Reactors Conf. (Culham Lab 1969).
46. M. Ohta, H. Yanato, and S. Mori, "Thermal Instability and Control of Fusion Reactors," Plasma Physics and Controlled Fusion (IAEA, Vienna, 1971) p. 423.
47. D. J. Sigmar, Nuclear Fusion 13, 17 (1973).
48. R. W. Conn and G. A. Emmert, "Solutions to the Neoclassical Transport Equations," Bull. Am. Phys. Soc. (to be published, Nov. 1973).
49. W. Magnus, F. Oberhettinger and R. P. Soni, Formulas and Theorems for the Special Functions of Mathematical Physics (Springer-Verlag, N. Y., 1966).
50. T. F. Yang, "The Calculation and Parametric Study of the Synchrotron Radiation Loss for Tokamak Plasmas," FDM-49, Nuclear Engineering Dept., University of Wiscon, July, 1973.
51. M. N. Rosenbluth, Nuclear Fusion 10 340 (1970).
52. R. W. Conn, "Alpha Particle Heating in CTR Plasmas: Energetics and Time Dependences," FDM-10, Nuclear Engineering Dept., University of Wisconsin, March, 1972.
53. R. G. Mills, "The Lawson Criterion", MATT-844, Princeton Plasma Physic Laboratory, May, 1971.
54. L. Spitzer, Jr., Physics of Fully Ionized Gases (2nd. revised edition, Interscience Publishers, New York, 1967) Chap. 5.
55. R. D. Richtmyer, K. W. Morton, Difference Methods for Initial-Value Problems, (2nd. revised edition, Interscience Publishers, New York, 1967) p. 201.
56. ~~F. W. Grover~~, Inductance Calculations: Working Formulas and Tables (Von Nostrand Co., New York, 1946) Chapter 13.

III. Divertor

III-A. General Considerations

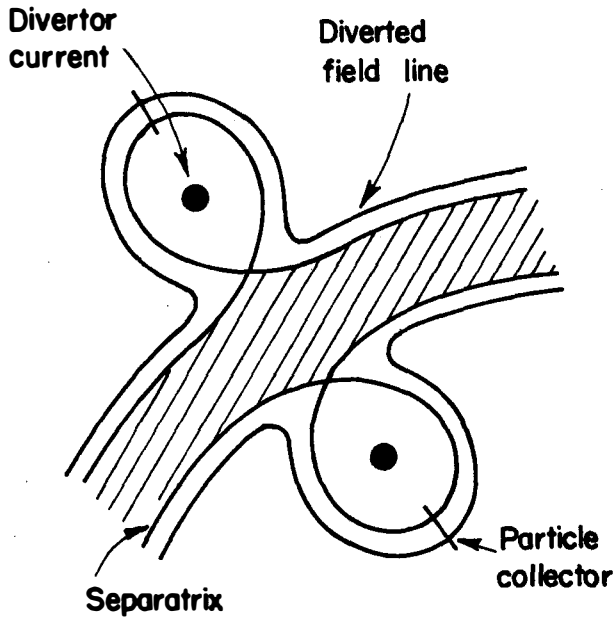
UWMAK-I utilizes an axisymmetric poloidal divertor to "divert" particles diffusing out of the plasma away from the first wall of the plasma chamber. The particles are guided along magnetic field lines to special particle collectors. By this method, one hopes to reduce first wall erosion due to energetic particle bombardment and also to protect the plasma from the high Z impurities which would be released. Another reason for incorporating a divertor zone is its effect on the average power density in the plasma. If the divertor zone has a low neutral pressure, then the boundary condition for the diffusion equations governing the density and temperature profile in the plasma is $dT/dr \approx 0$ at the plasma boundary, not $T \approx 0$. The reason is that the diverted field zone surrounding the plasma acts as a thermal insulator between the plasma and the first wall. Consequently, the plasma temperature profile is much flatter than it would otherwise be, resulting in a higher average power density. This is an important consideration since in a CTR power reactor one wants as flat a power density as possible.

Various types of magnetic field divertors have been devised for toroidal devices. All are based upon the idea of generating a null at some point or points in a component of the magnetic field. This generates a separatrix and field lines on the outside of this separatrix are carried away from the plasma surface as they pass the neutral point (null point). Magnetic flux surfaces on the inside remain closed within the plasma volume. The separatrix then becomes the boundary of the toroidally confined plasma. The separatrix is sometimes referred to as a magnetic limiter. (It should be noted that the boundary defined here is in terms of the magnetic field topology, not the density profile. It will be shown in Section III-C. that there will be plasma of lower density in the divertor zone; i.e. outside the separatrix.) The basic idea of the divertor is that as particles diffuse across the separatrix, they follow along the field lines and are carried away from the plasma to special particle collectors. The implied assumption is that particle mobility along the field is greater than cross-field diffusion. Some considerations in evaluating the validity of this assumption are discussed in Section III-C.

Three different types of divertors are shown in Figure III-A-1. The toroidal divertor has been used on stellarators at Princeton.⁽¹⁾ This type of divertor generates a null in the toroidal magnetic field. A disadvantage is its substantial perturbation on the symmetry of the toroidal field. In the Model C stellarator, the toroidal magnetic field perturbation is about 60% at the center of the plasma.

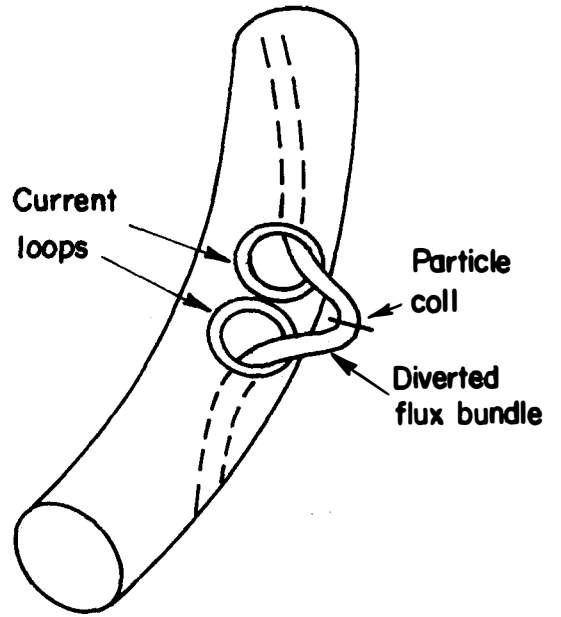
A variation on the toroidal divertor is the so-called bundle divertor recently proposed by a Culham group.⁽²⁾ Two opposing current loops

FIGURE I

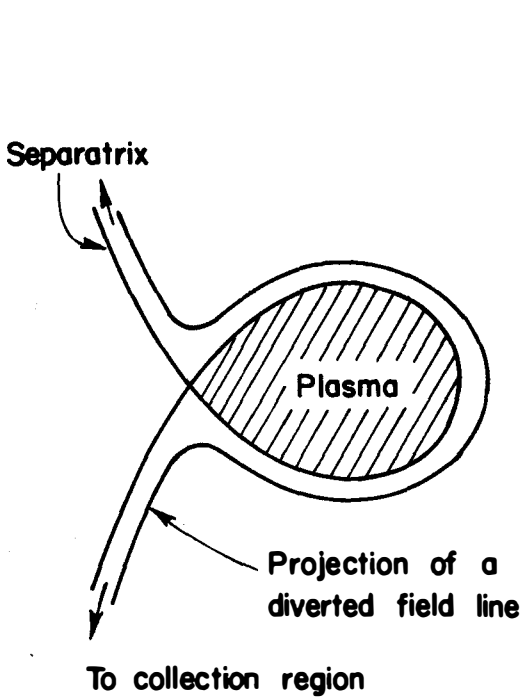


TOROIDAL DIVERTOR

(Top view of torus)

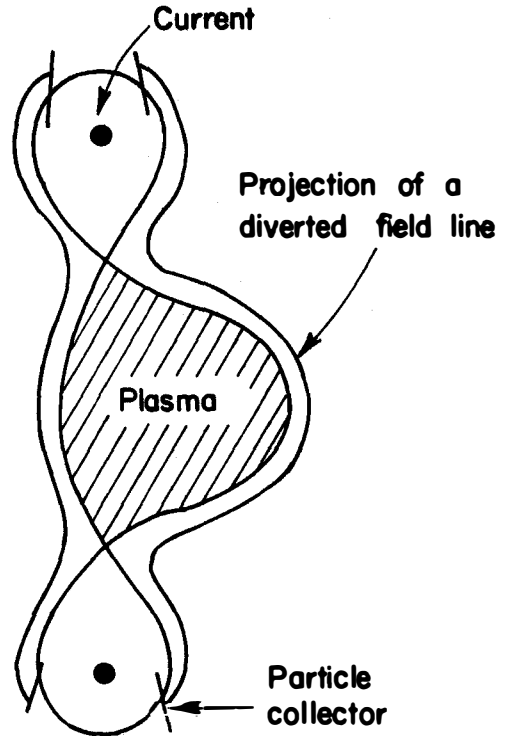


BUNDLE DIVERTOR



SINGLE NEUTRAL POINT

(Currents not shown)



DOUBLE NEUTRAL POINT

(Not all currents shown)

POLOIDAL DIVERTORS (CROSS-SECTION OF TORUS)

adjacent to each other divert a bundle of magnetic flux. The main advantage of this approach is that it produced only a minor perturbation ($\sim 1\%$) in the magnetic field at the center of the plasma. Its use in a fusion reactor is questionable, however, because the coils would have to be placed outside the blanket and shield regions. This raises the currents required immensely. Further, several bundle divertors distributed around the torus would be required in order to have 1) a sufficiently short path along the field between collectors, and 2) sufficient collection area to handle the heat load of 237 MW in UWMak-I from particles entering the collector.

The poloidal divertor diverts the poloidal magnetic field of the plasma using currents located outside the blanket and shield and perhaps even outside the main "D" magnets producing the toroidal field. This concept has been used in the FM-1 divertor. There is some freedom in the location of the neutral points and thus in the field lines that guide the particles away from the plasma. One can have a single neutral point on the midplane at the inside of the torus or two neutral points symmetrically above and below the midplane towards the inside of the torus (see Figure III-A-1). We have chosen the double neutral point configuration and named it the double-null divertor. This configuration requires less hardware in the central core of the torus, where things are already crowded, compared to the single null divertor. From an optimization viewpoint and the desire for a small aspect ratio, it would be most desirable to place the neutral points on the outside of the torus. However, this does not appear to be feasible because the vertical field required for radial equilibrium has the opposite direction to that required for a null point on the outside. The external poloidal field would then be even more grossly non-uniform in comparison with that producing a null point towards the inside of the torus.

Poloidal divertors preserve the axisymmetry of the Tokamak. As a consequence the banana orbits of particles are not affected and superbanana orbits, with their much larger radial excursions, are not produced. The toroidal and bundle divertors destroy the axisymmetry and lead to superbanana effects, especially near the separatrix. Even if the corresponding enhancement of diffusion is tolerable, a significant number of α particles born on superbanana orbits near the plasma edge may hit the first wall at high energy and produce erosion by blistering. This suggests that the poloidal divertor will better protect the first wall when the plasma is thermonuclear.

Recent results from ST Tokamak⁽⁵⁾ indicate that a substantial amount of wall-originated impurities are released into the plasma during the early stages of the discharge. In order to intercept these impurities with a divertor, it is necessary for the divertor to be operative during the initial stages of the current rise phase as well

as during the burn. With proper programming of the external currents, it is conceivable that the discharge could be initiated at a multipole null in the center of the vacuum chamber and a poloidal divertor configuration established with a small plasma at the center of the chamber. This plasma is then allowed to expand in a controlled manner during the current rise in such a way as to avoid skin currents, maintain reasonable q in the plasma, and maintain the poloidal divertor geometry. The external currents, in this chain of events, both establish a divertor and an expanding magnetic limiter. Some of these possibilities are being considered for PLT and PDX. (6)

References - Section III-A.

1. C. R. Burnett et al, Phys. Fluids 1, 438 (1958).
2. C. Colven, A. Gibson, P. E. Stott, Proceedings Fifth European Conference on Controlled Fusion and Plasma Physics (Grenoble France) 1, 6 (1972).
3. R. G. Mills, Lectures presented at the International School of Fusion Reactor Technology, Erice, Sicily, 1972; Published as "Course on Stationary and Quasi-Stationary Toroidal Reactors," (Comm. European Communities, Luxembourg, 1973) EUR 4999e, pp. 325-375.
4. A. Kitsunezaki, Proc. Third International Symposium on Toroidal Plasma Confinement (Garching, F.R.G. March 26-30, 1973) Paper G-2.
5. E. Hinno, L. C. Johnson, E. B. Meservey, and D. L. Dimock, Plasma Physics 14, 755 (1972).
6. Private communication, H. P. Furth, and D. Meade.

III-B. Magnetic Field Design

The magnetic field of the plasma current and the divertor is obtained as a superposition of the magnetic fields from circular filaments. The centers of the filaments all lie on the major axis and the filaments themselves are parallel to the equatorial plane of the plasma. The magnetic field of a filamentary current is known analytically in terms of elliptic integrals. The computer code⁽¹⁾ approximates the elliptic integrals using Hasting's approximation. The use of filamentary loops to represent fields from finite size currents is considered very accurate as long as one is several coil cross-sectional radii away from the coil of interest. The plasma current is represented as a filamentary loop placed between the magnetic axis, R_m , and the center, R_ψ , of the last ψ surface of the equivalent circular torus. This is based on the computer calculations by Callen and Dory⁽²⁾ for Tokamak equilibria with $\beta_\theta \geq 1$. Precisely where in the interval (R_ψ, R_m) the current is placed is arbitrary. The distance $\Delta = R_m - R_\psi$ is given by⁽³⁾

$$\Delta = \frac{a^2}{2R} \left[\bar{\beta}_\theta + \frac{1_i}{2} - \frac{1}{2} \right] \quad (1)$$

$$1_i = \frac{1}{\pi a^2 B_\theta^2(a)} \int_0^a B_\theta^2(r) 2\pi r dr$$

$$\bar{\beta}_\theta = \frac{2\mu_0}{\pi a^2 B_\theta^2(a)} \int_0^a 2\pi r p(r) dr$$

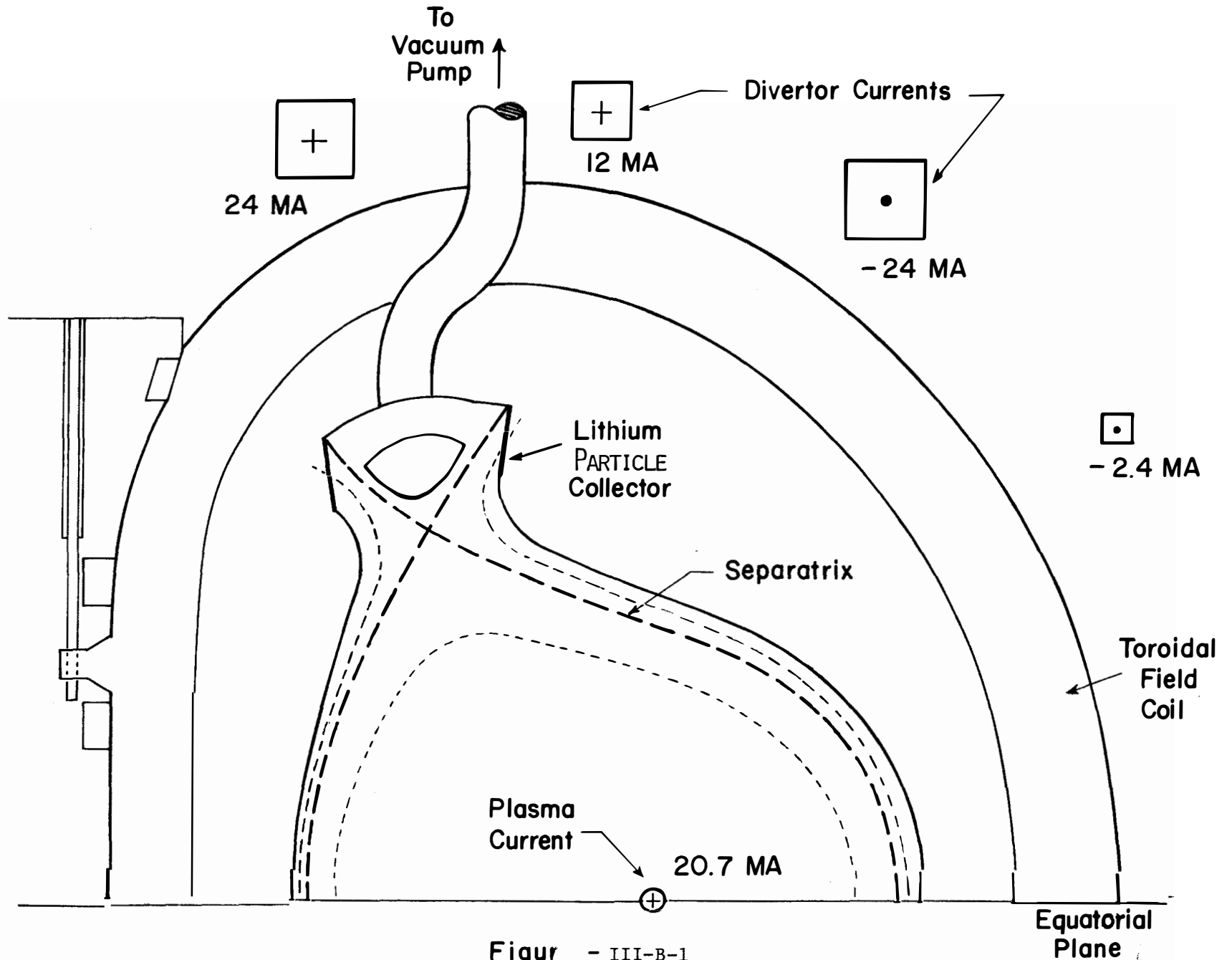
where R and a are the major and minor radii, respectively, of the equivalent circular torus. Equation (1) is valid only for $\bar{\beta}_\theta < 1$. There exist similar results⁽³⁾ for $\beta_\theta \sim A$ which differ from (1) by a factor which depends on the pressure profile, but is of order unity.

The position and magnitude of the external currents are varied to produce a magnetic flux configuration of "reasonable" shape subject to the following constraints:

- (1) The volume within the separatrix must be that determined by the plasma physics calculations. (Section II-F.)
- (2) The vertical field at the location of the plasma current filament is the correct value for radial equilibrium of the plasma column⁽³⁾;

$$B_z = \frac{\mu_0 I_\phi}{4\pi R} \left(\ln \left(\frac{8R}{a} \right) + \frac{1_i}{2} + \bar{\beta}_\theta - \frac{3}{2} \right). \quad (2)$$

UWMAK-1 DOUBLE NULL, POLOIDAL DIVERTOR



Figur - III-B-1

III-B-2

- (3) The decay index of the vertical field at the plasma current filament location is in the range required for vertical and radial stability of the plasma, namely⁽⁴⁾,

$$0 < -\frac{R}{B_{\perp}} \frac{\partial B_{\perp}}{\partial R} < .42 \quad (3)$$

One would like to satisfy the equation (3) over the entire cross section of the plasma. However, it does not seem to be possible to do this and also have a divertor.

It should be noted that equations (1), (2), and (3) are based on the assumptions of low β_{θ} , large aspect ratio, and round cross sections. These conditions are not satisfied by the plasma considered here, but nothing else is available in the present state of the theory. Furthermore, since the toroidal current, which is a distributed current, is simulated by a single filament, the resulting magnetic flux configuration is not consistent with the pressure balance equation,

$$\vec{j} \times \vec{B} = \nabla p \quad (4)$$

In principle, one can design the divertor magnetic field consistent with equation (4), but the calculation is considerably more complicated. It is felt that these more complicated calculations will not change the divertor currents enough to seriously modify the basic characteristics and feasibility of the divertor. The more important and much more difficult question of MHD stability of a Tokamak plasma with a poloidal divertor has not yet been investigated. There is also the additional question of the effectiveness of the divertor in preventing particles from hitting the first wall. This is discussed more fully in the next section.

The configuration (currents and separatrix) which results for UWMAK-I is shown in Figure III-B-1. It is interesting to note that the divertor coils are all outside the toroidal "D" magnets. This greatly facilitates the disassembly of the device for maintenance and should produce a more economically attractive design.

References - Section III-B.

1. The program was furnished to us by Mr. Ufa Christensen of the Princeton Plasma Physics Laboratory.
2. J. D. Callen and R. A. Dory, Phys. Fluids 15, 1523 (1972).
3. V. S. Mukhavatov and V. D. Shafranov, Nuclear Fusion 11, 605, (1972).
4. J. M. Greene, J. L. Johnson, and K. E. Weimer, Phys. Fluids 14, 671 (1971).

III-C. Particle Dynamics and Transport in the Divertor

In order to assess the ability of the divertor to reduce erosion of the first wall and the release of impurities into the plasma, it is necessary to determine the fraction, F , of particles entering the divertor zone which escape the particle collectors and hit the first wall. In this section, we comment on some of the phenomena that may be important in determining F . The phenomena that will be considered are 1) single particle dynamics in the divertor zone, 2) cross-field and parallel transport in the divertor zone due to collisional and collective processes, and 3) the effectiveness of the finite plasma density in the divertor zone in shielding the plasma core from entering neutral particles.

The magnetic field structure in the divertor zone is essentially the same as in the plasma. The poloidal field is responsible for carrying the particles to the collectors, but the gradient of the toroidal field provides magnetic mirrors and guiding-center drifts. We begin with some considerations from single particle dynamics. For simplicity let us consider the outer divertor zone, i.e., the region to the right of the plasma in Figure II-B-1. The spacing between the separatrix and the wall (50 cm.) is chosen such that a 3.5 Mev α -particle born at the edge of the plasma on a weakly trapped banana orbit will not contact the wall. This is to avoid blistering by energetic alpha particles. Since the slowing down time is much longer than the bounce time for banana orbits, particles born on trajectories which hit the wall in fact do so at the energy with which they were born. For the purpose of protecting the wall from energetic alphas, we require that no single particle orbits for 3.5 Mev α 's intersect the wall; this sets the minimum spacing between the plasma and the wall.

It has been pointed out that a negative plasma potential can reduce banana widths of ions near the plasma surface.⁽¹⁾ It is easily shown however, that this effect is not significant for 3.5 Mev alpha particles unless the plasma potential is $\sim 10^6$ volts negative with respect to the wall. It seems unrealistic to expect to maintain such a potential, especially since the edge of the plasma is connected by field lines to the divertor collector plates. The plasma diffusing across the separatrix and flowing to the collectors can adjust itself to neutralize any tendency to develop a significant plasma potential.

Let us now consider single particle dynamics of thermal ions and electrons in the divertor. We define the divertor mirror ratio as B_{\max}/B_{\min} where B_{\max} (B_{\min}) is the maximum (minimum) magnetic field experienced by a particle following a field line to a collector. This mirror ratio determines a loss-cone for particles in the divertor. If a particle, upon crossing the separatrix, has its velocity vector in the loss-cone, it will travel freely along the field line to the collector. If, however, it enters the divertor with its velocity vector

outside the loss-cone, it is mirror trapped and cannot get to the collector until its velocity vector is scattered, either collisionally or by collective processes, into the loss-cone. The divertor thus resembles a mirror machine but the objective is to avoid mirror confinement of the particles without causing excessive cross-field transport.

If the cross-field transport in the plasma is neoclassical, then an interesting difference between the single null and double null divertor appears. In the single null divertor, the divertor loss-cone is smaller than the plasma loss-cone (trapped-circulating transition) while in the double null divertor it is the other way around. This is shown in Figure II-C-1. Since neoclassical diffusion is primarily due to trapped-circulating transitions in the plasma, the particles entering the divertor should be primarily in the vicinity of the plasma loss-cone in velocity space. In the single null divertor, these particles are mirror-trapped in the divertor and hence must scatter before they can reach the collectors. In the double null divertor, particles near the plasma loss-cone are inside the divertor loss-cone and can free stream to the collectors. Consequently, the particle has a lower probability of escaping the divertor and getting to the wall.

If a significant number of particles are mirror trapped in the divertor, then the distribution function is anisotropic, as in a mirror machine, and high frequency microinstabilities will develop. The resulting turbulence will increase the rate of pitch angle scattering⁽³⁾; this is good because it helps to put particles into the loss-cone so that they can get to the particle collectors. Low frequency modes driven by the density gradient or magnetic field curvature (or trapped particle modes in the body of the plasma which produce fringing turbulent fields in the divertor zone) are undesirable because they can lead to enhanced cross-field transport without increasing the rate of pitch angle scattering.

One can get some insight into how the various processes affect the divertor by considering a one-dimensional model which treats these effects phenomenologically⁽²⁾. Let x represent a coordinate pointing from the plasma ($x=0$) to the wall. Let $n(x)$ be the density of particles at position x in the divertor. The density $n(x)$ is assumed to satisfy a one-dimensional diffusion equation:

$$\frac{d}{dx} \left[D \frac{dn}{dx} \right] = \frac{n(x)}{\tau_F} \quad (1)$$

For the diffusion coefficient D , we consider the two extremes of neoclassical and Bohm diffusion; the latter is taken to represent anomalous transport due to any of several possible causes (convective cells, instabilities, etc.). Thus we have

$$D = 2.24 q^2 A^2 \frac{\rho_e}{\tau_e} f_t = b n(x) \quad (2)$$

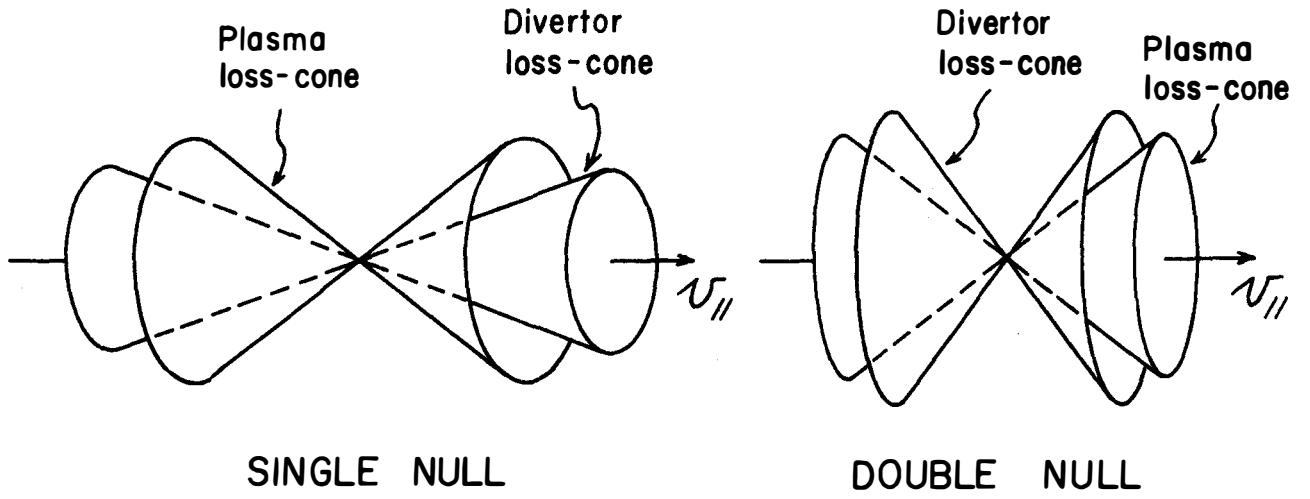


Figure III-C-1

or

$$D = \frac{1}{16} \frac{kT}{eB} \quad (3)$$

where f_t is the fraction of particles trapped in the divertor mirrors.

The term n/τ_F in (1) represents absorption by the collectors; we also consider two limiting cases for this. First, if pitch angle scattering is the primary effect limiting particle flow to the collectors, then

$$\tau_F = \left(\frac{2}{\pi} \theta_d \right)^2 \frac{a}{n(x)} = \frac{c}{n(x)}, \quad (4)$$

where $a/n(x)$ is the classical 90° scattering time of an ion in a plasma of density $n(x)$ and $\frac{\pi}{2} - \theta_d$ is the loss-cone angle for the divertor. The other extreme is to assume extremely rapid pitch angle scattering because of high frequency microinstabilities; then particle flow to the collectors is limited by the distance along the field line a particle has to travel to get to the collectors. In this case

$$\tau_F = \frac{L}{v_i} \quad (5)$$

where L is the distance along the field line to the collector and v_i is the thermal velocity of an ion

$$v_i = \sqrt{\frac{kT}{M}}$$

We assume, rather arbitrarily, that $L = 10 \pi R$, where R is the major radius of the plasma. We also assume, primarily for simplicity, that the temperature in the divertor is uniform.

The diffusion equation (1) with the two choices for D and for τ_F is thus to be solved with boundary conditions. For these we take

$$- D \left. \frac{dn}{dx} \right|_{x=0} = \Gamma_0$$

$$\lim_{x \rightarrow \infty} n(x) = 0$$

where Γ_0 is the flux entering the divertor from the plasma core and is assumed given. The second boundary condition assumes the wall is effectively at infinity. This latter boundary condition is imposed for simplicity. It is equivalent to assuming the wall is far enough away that its presence does not affect the density near the separatrix. The flux at the wall is then evaluated by $\Gamma_w = - D \left. \frac{dn}{dx} \right|_{\text{wall}}$.

The results for each of the four cases follow:
Case I: D neoclassical, τ_F pitch angle scattering

$$n(x) = n_o \exp \left[-\frac{x}{\sqrt{2bc}} \right] \quad (6)$$

$$\Gamma(x) = \Gamma_o \exp \left[-\sqrt{\frac{2}{bc}} x \right]$$

where $n_o = \left(\frac{2c}{b} \Gamma_o^2 \right)^{1/4}$.

For UWMAK-I, equation (6) gives negligible flux at the first wall ($x = 50$ cm); the e-folding distance for the decay of the flux is about 1/2 cm and $n_o \approx 8 \times 10^{13}/\text{cm}^3$. If we assume that whatever process spoils confinement in the plasma also increases the cross-field transport in the divertor by the same amount without affecting pitch angle scattering, then the flux at the wall is $\Gamma_W \approx .07 \Gamma_o$. In this case, the divertor is marginal in its effectiveness for collecting particles. If the process which increases cross-field transport also increases pitch angle scattering proportionally, then the effects cancel and we recover the "non-confinement spoiled" results.

Case II: D neoclassical, τ_F parallel flow

$$n(x) = \begin{cases} \left(n_o^{1/2} - \sqrt{\frac{v_i}{6bL}} x \right)^2 & 0 < x < \left(\frac{6bLn_o}{v_i} \right)^{1/2} \\ 0 & x > \left(\frac{6bLn_o}{v_i} \right)^{1/2} \end{cases} \quad (7)$$

$$\Gamma(x) = \begin{cases} \sqrt{\frac{2v_i b}{3L}} \left(n_o^{1/2} - \sqrt{\frac{v_i}{6bL}} x \right)^3 & 0 < x < \left(\frac{6bLn_o}{v_i} \right)^{1/2} \\ 0 & x > \left(\frac{6bLn_o}{v_i} \right)^{1/2} \end{cases}$$

where $n_o = \left(\frac{3L\Gamma_o^2}{2v_i b} \right)^{1/3}$

For UWMAK-I, $n \approx 3 \times 10^{13} \text{ cm}^{-3}$ and the flux at the wall is zero. This case corresponds to highly optimistic and unrealistic assumptions.

Case III: D Bohm, τ_F pitch angle scattering

$$n(x) = \frac{n_o}{(1 + \beta x)^2} \quad (8)$$

$$\Gamma(x) = \frac{\Gamma_o}{(1 + \beta x)^3}$$

where

$$\beta = \left[\frac{64}{3} \frac{\Gamma_o}{c} \left(\frac{eB}{kT} \right)^2 \right]^{1/3}$$

$$n_o = \left(\frac{24ceB\Gamma_o^2}{kT} \right)^{1/3}$$

For the conditions of UWMAK-I, $\beta = 4 \times 10^{-4} \text{ cm}^{-1}$, $\Gamma_{\text{wall}}/\Gamma_o \approx .94$; almost all particles escape the divertor and reach the first wall.

Case IV: D Bohm, τ_F parallel flow.

$$n(x) = n_o e^{-\alpha x} \quad (9)$$

$$\Gamma(x) = \Gamma_o e^{-\alpha x}$$

where

$$\alpha = \left(\frac{16v_i eB}{L kT} \right)^{1/2}$$

$$n_o = \Gamma_o \left(\frac{16eB L}{kT v_i} \right)^{1/2}$$

Again, for UWMAK-I, $\Gamma_{\text{wall}}/\Gamma_o \approx .25$, $n_o = 4 \times 10^{10} \text{ cm}^{-3}$. Under these assumptions, the divertor is better than in case III, but still not adequate.

A conclusion to be drawn from these calculations is that, even with the most optimistic assumptions about parallel flow to the collectors, it is essential to have the cross-field transport considerably lower than Bohm diffusion. Pseudoclassical diffusion is essentially a numerical factor times neoclassical diffusion and can thus be treated as a minor variation on Cases I and II. Pseudoclassical diffusion is acceptable

if the turbulence level enhances the rate of pitch angle scattering by about one order of magnitude.

The above considerations neglect charge exchange as a mechanism for energetic particles to get to the wall. The number of fast neutrals produced per unit area of plasma surface per second is

$$\dot{N} = n_n \langle \sigma_{ex} v \rangle \int_0^{\text{wall}} n(x) dx$$

where n_n is the neutral density and σ_{ex} is the charge exchange cross section. Half of these fast neutrals go into the plasma and become ionized or engage in subsequent charge exchange. The other half go directly to the wall. Neglecting second generation effects, the fast neutral flux on the wall is

$$\Gamma_{nw} = \frac{\dot{N}}{2} = \frac{1}{2} n_n \langle \sigma_{ex} v \rangle \int_0^{\text{wall}} n(x) dx \quad (10)$$

Let us apply this to Case I. We put (6) into (10) and assume the wall is at infinity for purposes of calculating charge exchange rate. The wall flux of hot neutrals is

$$\Gamma_{nw} = \frac{1}{2} n_n \langle \sigma_{ex} v \rangle n_o \sqrt{2bc}$$

To have $\Gamma_{nw} \leq .1 \Gamma_o$, we need

$$n_n \leq 5 \times 10^8 \text{ cm}^{-3}$$

for the UWMAK-I. If we consider Case II, then we need

$$n_n \leq 8 \times 10^9 \text{ cm}^{-3}.$$

Both of these requirements are beyond the capability of the vacuum pumping system; one must depend on the plasma to "burn out" the divertor zone to this low a neutral density. It should be noted that this consideration applies only to D and T ions. For α particles to escape the divertor by charge exchange there must be two successive charge exchanges; this is much more improbable.

A final aspect of the divertor is that neutral impurities from the wall can be ionized in the divertor zone by electron or ion impact ionization. This can occur by the divertor plasma itself or by particles from the body of the plasma whose banana orbits reach several centimeters across the separatrix. The impurity ions can then migrate to the collectors because their guiding-centers are attached to field lines in the divertor. Consequently, the divertor may shield the plasma from impinging neutral particles. The degree to which this is effective will depend on the density profile in the divertor.

References - Section III-C.

1. H. P. Furth and M. N. Rosenbluth, Third IAEA Conf. on Plasma Physics and Controlled Fusion (Novosibirsk, U.S.S.R., 1968) Vol. I, p. 821.
2. A somewhat similar calculation has been done by M. Yoshikawa, JAERI-M 4494 (1971).
3. D. E. Baldwin and J. D. Callen, Phys, Rev. Lett. 28, 1686 (1972).

III-D. Divertor Particle Collectors and Vacuum System

The vacuum requirements for a Tokamak controlled-fusion reactor are such that static vacuum systems can no longer be relied upon. The equipment is too large in volume and a large gas throughput requires high pumping speeds. This design is based on an optimization of the mercury diffusion pump with freon and liquid-nitrogen cooled traps, augmented by the extensive use of cryopumping at liquid helium temperatures to achieve pumping speeds in the multi-million liters per second range. The system is incorporated into the modular design of the Tokamak, with a complete vacuum system contained in each of the twelve sectors of the torus.

The vacuum system design is based on steady-state operation at a diffusion rate of 3.56×10^{22} D+T+He atoms/sec. This represents a throughput of 2.6×10^3 torr-l/sec of D+T atoms and 107 torr-l/sec of helium. In addition, outgassing from the vacuum wall must be considered. Estimates vary from 1.5 to 6×10^{-9} torr-l/sec per cm² of surface area. Initial bake-out of the vacuum wall before assembly could reduce this, but the most pessimistic estimate results in a gas throughput of 0.2 torr-l/sec from this source.

To maintain a sufficiently large mean free path in the divertor, at 10^{-5} torr, a pumping speed of 2.6×10^8 l/sec for helium at thermal energies is required. This is a factor of 25 beyond the range of present day technology, so trapping and burial of ions in a liquid lithium surface in the divertor region will be relied upon. A description of the essential components of the vacuum system and the lithium trapping surface, all located in or outside the divertor region, follows.

There are four divertor slots. Each set of two, the upper and the lower, is connected to a plenum outside the twelve D-magnets. The pumps are arranged in four rows, three pumps side-by-side, attached to each plenum. For each set of three, the outer two are cryopumps and the center is a mercury diffusion pump. The circular orifice to each pump is 75 cm in diameter. Since the cryopumps must be serviced periodically, only one set of 96 is operated at a time, while the other set is being degassed.

Mercury diffusion pumps are chosen to avoid the problem of hydrogenation of the pump oil, as would be the case if a fractionating oil diffusion pump were used. The pump is mounted outside the D-shaped magnet, the blanket, and the shield. An Edwards 24M4 pump is suitable, and its aperture is 75 cm and height 130 cm. Its pumping speed for hydrogen, un baffled, is 14,000 l/sec. When an allowance is made for the flow conductance of the liquid-nitrogen-cooled baffles and traps, the ductwork, and the plenum, the net pumping speed for helium is 8×10^5 l/sec at 10^{-4} torr.

Augmenting the diffusion pump with cryopumps is a reasonable way to increase pumping speed at low pressure for deuterium and tritium. Cryopumps of 2×10^5 ℓ /sec capacity are available, and they are relatively small. In this design, the aperture to each pump is 75 cm in diameter. These pumps rely on cryotrapping using liquid-helium cooled charcoal absorption, with a liquid-nitrogen cooled shield. Diffusion pumps are used to evacuate to 10^{-4} torr or less before cooling with liquid helium on the inner component of the pump. This can allow the system to cryopump helium in the 10^{-5} torr range. These pumps are closed off from the rest of the system by remotely-controlled valves so that while 96 of them are in use, the other set is degassed.

The cryopumps are in service only below 2.5×10^{-4} torr during the final evacuation after ignition and during the burn. All cryopumps are valved off during the cooling, evacuation, and re-fueling cycle between burn sequences.

The diffusion and cryogenic pumps, which operate in parallel, must be backed by pumps which can take a gas load of 2.6×10^3 torr- ℓ /sec. Roots blower pumps in combination with a mechanical forepump provide a mechanical system of high pumping speed in the range of 760 to 10^{-2} torr. Roots blower pumps are preferred to vapor booster pumps because the rotors are not lubricated. Oil must be provided only for the various gears and bearings required in the operation. The Heraeus VPR6000A pump in series with a Heraeus VPR1600 pump and backed by a 130 cfm forepump is attached to each set of three parallel pumps on the plenum. The VPR6000A-VPR1600 tandem arrangement pumps 1600 ℓ /sec at .3 torr, dropping off to 1400 ℓ /sec at 10^{-2} torr. For 96 of these pumps the throughput is 50,000 torr- ℓ /sec. The fore pressure is 10 torr, so the pumps are adequately backed by a 130 cfm forepump at each of the 96 pumping stations.

An efficient means of trapping hydrogen isotopes in lithium might be devised because of the large heat of formation of the hydride. However, trapping will continue only as long as the concentration near the surface remains low. Efficient trapping of 96% of the incident ions will continue to doses of 2×10^{19} particles/cm².⁽¹⁾ Theoretically, all the atoms striking the lithium surface will condense and be trapped until the pressure is reduced to the vapor pressure of the gas at the temperature of the surface.

The system proposed here is to trap deuterium and tritium ions in a liquid lithium surface placed in each divertor slot. Liquid lithium at an exit surface temperature of 325°C flows down a vertically oriented stainless steel sheet. It is collected in a trough at the bottom and is cycled through a tritium scrubber. If a sheet is at least one meter high, efficient trapping will be sustained. Experimental data⁽¹⁾ indicates that 96% of the incident deuterium and tritium ions will be trapped at 325°C.

There is no experimental evidence to support an estimate of the trapping of helium in liquid lithium. Since the residence time in the divertor of any part of the flowing lithium surface is less than 1 second, it can be assumed that 50% of the helium will diffuse toward the surface and escape if the diffusivity is greater than $1 \times 10^{-6} \text{ cm}^2/\text{sec}$. McCracken⁽¹⁾ predicted that the diffusion rate could be estimated from the self-diffusivity of the metal. That implies $D \sim 12 \times 10^{-4} \text{ cm}^2/\text{sec}$, a very high number. However, his prediction was based on an experiment in which 1 MeV alphas bombarded a thin sheet of Mg.⁽²⁾ The conclusions of this experiment were: (1) inert gas bubbles do not form in Mg; (2) helium diffuses via a mechanism involving vacancies; (3) as helium atoms are considerably larger and have very different electronic structures from Mg^{++} , the size differences rather than the charge differences between the inert gas and host atoms determine the diffusion and solution properties. All of this suggests that only experimental evidence can indicate how much trapping of helium can be expected in liquid lithium.

The thermal load of the plates due to impinging particles is 1 MW/m^2 . This energy will be deposited on the surface of the falling lithium film. We propose to circulate enough lithium to absorb this heat so that no additional cooling will be required.

For each plate, a half meter feed tube is used. The feed tube will open into a reservoir, which will feed the collector plate, as shown in Figure III-D-1. The lithium will flow as a falling film along the surface of the plate, accelerating on the way by gravitational force. A gutter will receive the lithium from the plate and, by gravitational force, feeds the lithium to a discharge tube. An electric current is applied to the discharge tube, in the direction of $-\underline{V} \times \underline{B}$, to pump the lithium out. The lithium enters at 200°C and exits at 325°C . The mass flow rate of lithium is 10 kg/sec for each plate corresponding to each magnet, or 480 kg/sec for the whole reactor. At the exit temperature of 325°C the vapor pressure of lithium is less than 10^{-5} torr; substantially no re-emission of particles occurs.

The falling lithium is in a strong magnetic environment. The magnetohydrodynamic effects have yet to be studied. If the film is fully developed, there will be no retarding force since $\underline{V} \times \underline{B}$ is perpendicular to the plate and is constant along the plate. However, the lithium element will tend to accelerate along the plate due to gravitational force. This causes a $\underline{V} \times \underline{B}$ difference along the plate. However, $\int_0^b \underline{V} \times \underline{B} \, dy$ is still constant (b is the thickness of the film) since the mass flowrate is constant. Therefore, for a first order approximation, the magnetic field has no effect on the bulk flow of lithium. The bulk velocity of the lithium at the end of the collector plates is approximately 4 m/sec . The film thickness is 1 mm . For such a film, the exit temperature of lithium will be very uniform (the thickness of the film \ll thickness of thermal boundary layer).

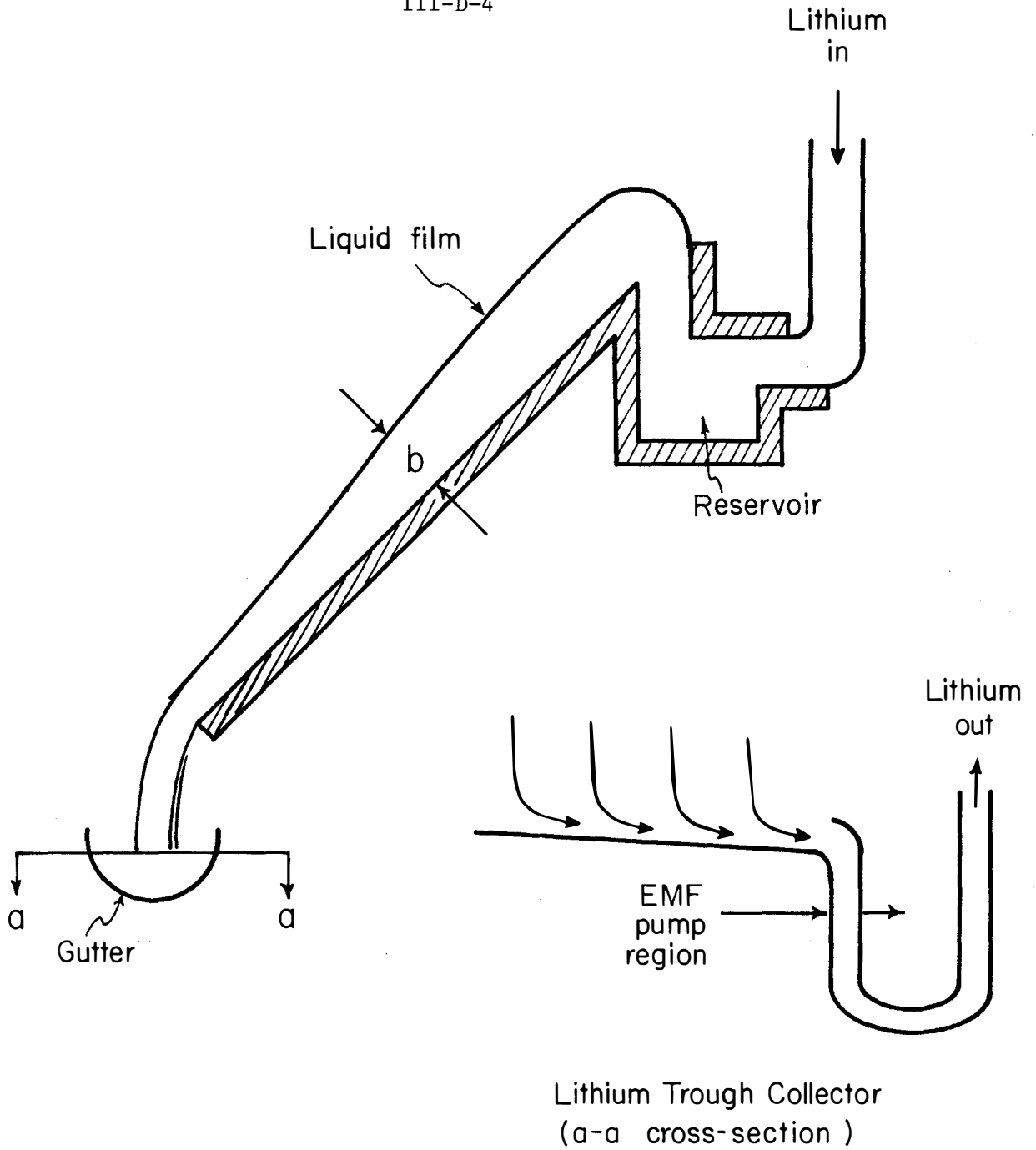


Figure III-D-1

Schematic of One Diverter Liquid Lithium Collector Plate.

If a half meter feed tube and discharge tube are used for each plate of each module, the entrance and exit pressure drops will be 20 psi each, which can easily be accommodated. The pumping power for the whole collector plate system is 13 kW.

Tritium recovery from the vacuum system is accomplished by compressing and storing the forepump exhaust gas in cylinders for subsequent handling. The holdup of tritium in pump oil is minimized through the use of mercury diffusion pumps and Roots blowers. Recovery of tritium from the oil in the large forepumps is an unsolved problem.

The volume of the torus, exclusive of divertor slots, is 7750 m^3 and the surface area is 2830 m^2 . The initial pump-down time from 760 torr to 10^{-2} torr is 65 minutes. Using diffusion and backing pumps alone, the additional pump-down time to 10^{-5} torr is 4 minutes. The total pumping speed for 96 diffusion pumps and the same number of cryopumps is 2×10^7 l/sec, and the flow conductance of the divertor slots and ductwork is the same. Thus, for a throughput of 2.6×10^3 torr-l/sec, the base pressure is 2.6×10^{-4} torr. With lithium trapping at 96% efficiency, the base pressure for steady state operation can be reduced to 10^{-5} torr.

The pump-down time for portions of the cycle of operation, which includes purging, fueling, ignition and evacuation and analysis of the duty cycle are considered in Section II-H on Recycle and Shutdown.

References - Section III-D.

1. McCracken, G., B.N.E.S. Nuclear Fusion Reactor Conf., Culham, 1969.
2. H. R. Glyde and K. I. Mayne, Phil. Mag. 12 (1965) 919.

IV. Blanket and Shield

IV-A. General Design Features

1. Requirements

The blanket of a fusion reactor can be looked at as simply an energy convertor which is coupled to the energy producer, the plasma. The primary requirements of the blanket are listed below (not necessarily in the order of importance.)

- . Breed tritium (neutronically in this case)
- . Convert the kinetic energy of the D-T reaction products into heat
- . Conduct that heat away to an electrical production system
- . Provide vacuum tight enclosure for the plasma; passages for fueling, heating, and diagnostic equipment; and coolant channels to conduct the heat away

The blanket must satisfy these requirements subject to economic and environmental constraints. Stated simply, the blanket should operate at as high a temperature as is feasible to maximize efficiency, and be constructed of materials which ensure safe operation at a minimum cost.

The breeding material must obviously have a high tritium production cross section and a low inelastic cross section for all other non-productive reactions. There is no ambiguity about its choice, it must be lithium in one form or another.

The requirement to convert kinetic energy to heat can be divided into two categories; absorption of photons and charged particles as they are emitted from the plasma, and moderation of the neutrons which contain ~ 80% of the D-T reaction energy. The solid wall which surrounds the vacuum chamber (referred to hereafter as the first wall) must accept the heat load directed on it by the plasma and conduct that heat to a coolant. The problem here is to obtain a material with reasonable thermal conductivity to avoid high temperature gradients. The first wall of UWMAK-I must also be able to maintain its structural integrity in the face of high radiation damage rates, high corrosion rates and high temperature.

The moderation of neutrons must be accomplished in a manner which is consistent with the breeding of tritium (see chapter V). It must also be noted that the traditional concept of a good moderator having low atomic weight is not sufficient when dealing with 14 MeV neutrons. Materials like Fe, which have high inelastic cross sections can be quite effective in slowing neutrons down to

a few MeV where the traditional concepts of moderation dominate.

The cooling of a CTR can be accomplished by using a material which has a low vapor pressure at high temperatures; which is compatible with the structural members of the blanket; which is consistent neutronically with concept of tritium breeding; and which can be circulated through the reactor with reasonable pumping power. The coolant must also be relatively inert to tritium so that it does not tie up large inventories of that isotope, i.e., tritium must be easily separable from the coolant.

Finally, the blanket must be constructed of a material which has good high temperature strength and which is neutronically consistent with the concept of tritium breeding. The structural material must also be compatible with the coolant and moderator and it must retain its mechanical integrity in an extremely severe radiation environment. The blanket structure must be easily fabricated meet strict construction requirements at low cost. As stated previously, the first wall must also absorb large heat loads and safely conduct this heat to coolants in the blanket.

There are several combinations of materials and design possibilities that successfully meet the above requirements and it is almost impossible at this stage to make a universally accepted decision for a given set of materials. The choices that we have made for the UWMAK-I design are listed in Table IV-A-1 and they are compared to decisions made by other designers. No comparison is made for the breeding material as it is Li (or Li containing salts) in every case. Finally, one will note that our choice of a Li coolant and moderator coupled with 316 stainless steel is similar to only one other design - the LASL system.

The order in which the materials were chosen for the reactor blanket was

1. Breeder
2. Coolant
3. Structural Material
4. Moderator, Reflector

The background of decisions 2-4 will be reviewed in sections 2-4 of this chapter.

The choice of shield materials is much simpler in that the temperature, radiation and stress levels are considerably lower than in the blanket. The main problem is to find materials with suitable cross sections for the various types of radiation emanating from the blanket and which have acceptable economic

properties. The materials should be good moderators and absorbers of neutrons as well as high attenuation of gamma radiation. The detailed reasoning behind our choice of B_4C , Pb and stainless steel for the UWMAK-I shield is given in Chapters V and VI.

2. Choice of Coolant

The possible choices of coolants that could have been used in UWMAK-I are given below:

Liquids -	H ₂ O, D ₂ O
	Organics
	Na, NaK
	Li
	Li Salts such as Flibe
	K
Gases -	He
	CO ₂

It is not the purpose of this section to justify in detail why one of these materials has been chosen over the others, especially when other factors such as structure, breeding and moderation must be considered. However, we will outline very qualitatively why we chose Li over the other materials and more details will be given in later sections.

Liquid lithium is an efficient heat transfer medium which can serve two other functions in the reactor simultaneously; breeding and moderating. Such multiple duty allows a much simpler design and maximum use of the CTR blanket space. Lithium is radiation damage resistant and has a low induced activity from neutron irradiation. This latter point would alleviate maintenance problems in the pumping and heat exchanger areas.

A potential disadvantage of Li is connected with the large pressure drop required to circulate Li. However, by clever design, this disadvantage can be minimized as has been done in UWMAK-I. Finally, Li is quite compatible with all of the refractory metals but it does have some problems with Fe and Ni based alloys. This latter point will turn out to be one of the most severe limitations on the UWMAK-I operating temperature.

Light water has been shown to be an economical and safe coolant (and moderator) in current fission reactors. However, once the decision had been made to breed tritium with Li, there were serious safety questions associated with keeping Li and H₂O in close proximity in the blanket. Another problem, perhaps

Table IV-A-1
 Comparison of Blanket Materials
 For Recent D-T Fusion Reactor Designs*

<u>Design</u>	<u>Type</u>	<u>Moderator</u>	<u>Coolant</u>	<u>Structure</u>
Wisconsin (UWMAK-I)	Tokamak	Li	Li	316 SS
PPPL (1)	Tokamak	Flibe	He	PE 16
ORNL (2)	Tokamak	Li & Graphite	Li	Nb-1Zr
Culham (3)	Tokamak	Li & Graphite	Li	Nb-5Zr
LASL (4)	θ Pinch	Be & Graphite	Li	Nb
LLL (5)	Mirror	Li & Graphite	Li	Nb
ORNL (6)	Laser	Li	Li	Nb
LASL (7)	Laser	Li	Li	Austenitic SS

*all the systems use Li or Li containing salts for breeding purposes.

equally serious, has to do with the difficulty of separating tritium from water. A significant amount of tritium will undoubtedly diffuse into the coolant from the breeding material. This would result in an extremely difficult recovery problem with hydrogenous coolants as an acceptable release of tritium to the environment. Finally, the use of liquid water as a coolant would require much lower operating temperatures than is anticipated with other coolants.

Deuterium oxide, (D₂O) was not considered for much the same reasons as light water with the additional concern that heavy water is more expensive.

Organic coolants were also not considered for the same reasons as given for water. Another consideration was that the degradation of the organic in the radiation field would require large amounts of crosslinked materials to be removed and replaced at considerable cost.

Sodium or sodium-potassium alloys are likely coolants that would allow high temperature operation, be compatible with Li, resistant to radiation damage and inert to tritium. These materials are even cheaper than Li and in some cases less corrosive to selected structural materials. However, such liquid metals have the same problems of pumping power losses in high magnetic fields as does Li and are subject to considerable induced activity which makes maintenance of coolant systems difficult. While such a choice (Na or NaK) would have been possible, the requirement to have lithium in the blanket for breeding means that separate pumping systems and heat exchangers would have been necessary.

Flibe was ruled out because of its low thermal conductivity and the availability problems associated with procuring large amounts of Be. Flibe does have some advantages with respect to tritium extraction and compatibility with steels, but it is more corrosive to some refractory elements. Flibe also has a relatively high melting point (~460°C) which might present some problems during shutdown and which would reduce the allowable coolant temperature rise when some structural materials are used (namely Fe or Ni based alloys).

Finally, potassium was not considered for somewhat the same reasons as sodium; the necessity for dual liquid metal systems. The possibility of using boiling potassium is attractive for relatively high temperature systems and should be investigated.

The use of helium is still being considered although it was not given the primary choice. It appears that helium pressures of ~50 atm would be required for cooling and these pressures

would require large numbers of small diameter tubes at stresses of 10,000-15,000 psi in the high radiation zone. It is possible that because of the radiation embrittlement problem there may be a substantial number of failures which would hamper the efficiency of the plant. Pumping power requirements for high pressure helium may also be substantial. Helium does have the advantage of

low induced activity. The use of a gaseous coolant would also minimize radioactive corrosion product transport problems. Tritium separation would presumably not be difficult and helium has very good compatibility with steels and molybdenum. However, trace amounts of oxygen may limit the useful temperatures of some Nb and V alloys to less than optimum temperatures if in leakage cannot be controlled. It was felt that helium is a reasonable back up coolant and it will be explored in Section IV-H.

Carbon dioxide was not considered because of its compatibility problem with CTR alloys. In addition, it would be more difficult to separate any tritium from this gas in the event of contamination.

In summary, lithium was chosen for the coolant in this design because of its high thermal conductivity, low melting point, the fact that it is an efficient moderator with no adverse neutronic reactions and because it is required for tritium breeding regardless of the coolant choice. Table IV-A-2 summarizes the properties of Li used for this study.

3. Choice of Structural Material

The main problem here is the choice of the structural material in the blanket. The shield materials are subject to much less stringent environments and allow a multitude of choices. We will again give only a qualitative argument of how we arrived at the decision for the CTR structural material.

It is evident that the choice of the structural material for the blanket is closely coupled to the choice of the coolant and the breeding material. In fact, the final choice of this structural material can only be made once the coolant-breeder combination has been designated! This subservience stems from the fact that the structural material plays no direct role in the production of energy (as does U or Pu in fission reactors) nor does it play a dominant role in the conversion of that energy into heat (such as graphite does in a HTGR). Therefore, the structural material must respond to the needs of the reactor, not dictate them.

It is not desirable to go into a detailed description here of how we arrived at 316 SS for the blanket structural material, this will become more evident later in the report (Chapters IV, V, VI, IX, and XII). We will use as our starting point a preliminary survey which narrowed the potential candidates down to four non-magnetic alloys:

316 Stainless Steel
 Nb-1Zr
 V-20Ti
 TZM (a Mo-Ti-Zr-C alloy)

Table IV-A-2
 Properties of Lithium Used for this Study⁽⁸⁾

<u>Property</u>	<u>Value</u>
Melting Point	180.6°C
Boiling Point	1342°C
Heat of Fusion	717 cal/ g-atom
Heat of Vaporization	37.7 Kcal/ g-atom
Volume Change on Melting	1.5% of Solid Volume
<u>Property</u>	<u>(Equation, t = °C, T = °K)</u>
Density d, g/cm ³	$d = 0.515 - 1.01 \times 10^{-4} (t-200)$ (200 - 1600°C)
Vapor Pressure P, Torr	$\log_{10} P = 10.2788 - 8283.1/T$ $- 0.7081 \log_{10} T$ (800 - 1400°C)
Viscosity μ , centipoise	$\log_{10} \mu = 1.4936 - 0.7368 \log_{10} T$ $+ 109.95/T$ (185 - 1000°C)
Thermal Conductivity λ , cal/(sec)(m)(°C)	$\lambda = 10.1 + 2.94 \times 10^{-3} t$ (250 - 950°C)
Electrical Resistivity ρ , $\mu\text{ohm-cm}$	$\rho = 18.33 + 3.339 \times 10^{-2} t$ $- 6.795 \times 10^{-6} t^2$ (200 - 1000°C)

The way in which these alloys are assessed depends to a large degree on the type of power plant to be built; e.g. a near term commercial plant or long term maximum efficiency plant. As stated previously, it was our objective to design a plant which could be built with a minimum extension of present technology, even though that may produce a conservative design.

Table IV-A-3 contains a qualitative comparison of the four alloys considered in terms of the properties we felt were most important to our design philosophy. Such a comparison is undoubtedly controversial and it should be only viewed as an attempt to give the reader an insight into how we arrived at our choice.

It is noted in Table IV-A-3 that the most important criterion for choosing the blanket structural material for a near term power plant is availability of a qualified metals industry. This point must not be taken lightly as has been evidenced in the recent problems for LMFBR's. The Public has taken, and rightly so, a keen interest in the safety and environmental impact of electrical power plants. In order to insure safety, strict design procedures and standards will have to be adhered to and constantly upgraded. The development of these design codes can only proceed after sufficient experience has been obtained with the alloys used in construction. This process takes many years before authorities will accept a proposed design code, the basis for all licensed construction.

A necessary prerequisite for even beginning this long arduous procedure is the ability of industry to consistently reproduce time and again a metal or alloy with similar properties. For example, such a situation existed in the middle 1960's for some austenitic stainless steels which were designated as prime candidates for LMFBR's. Before this alloy could be fully accepted, even though the steel industry had over 20 years of experience of making this particular alloy, rigid quality assurance programs had to be designed and implemented in the mills. After considerable effort it is expected that by the mid 1970's 316 SS will have an accepted set of design criteria for application in nuclear systems. The point of this brief example is to show that even for an industry that produces over a million metric tons of steel a year, even though it has a long history of casting, fabricating, and joining techniques, and even though there is a wealth of information on mechanical, chemical and physical properties of these alloys in a wide range of temperatures, stresses, and chemical environments, the development of design codes for these materials to operate, safely, in power plants required a major effort.

It should be evident even to the non-metallurgist that of the four alloys listed previously, only one stands out as having a reasonably qualified industry behind it. The molybdenum alloy, TZM, would perhaps be the second choice under this criterion from

Table IV-A-3
 Choice of CTR Blanket Material for Near Term
 Power Plant with Lithium Coolant^(a)

	<u>Property</u>	<u>First Choice</u>	<u>Second Choice</u>
	Qualified Metal Industry	316 SS	?
	Fabricability, Weldability	316 SS	Nb-1Zr
	Radiation Damage Embrittlement	?	?
	Swelling Resistance	V-20Ti	316 SS
	Sputtering and Blistering	Nb-1Zr	TZM
	Interstitial Embrittlement	316 SS	TZM
	Allowable Operating Temp.	TZM	Nb-1Zr
	Effect on Breeding Ratio ^(b)	V-20Ti	316 SS
	Induced Activity & Afterheat	V-20Ti	316 SS
	T ₂ Permeation	TZM	316 SS
	Fabricated Costs	316 SS	Nb-1Zr
important	Long Term Availability to U.S.	TZM	316 SS

increasing importance

(a) Only the following non-magnetic alloys were considered - 316 SS, TZM Nb-1Zr, V-20Ti.

(b) All the alloys allow breeding, the question here is the value of the doubling time.

the standpoint of experience of production and in service properties, but it is so far behind the 316 SS case that we did not include it as a second choice. The Nb-1Zr alloy would follow behind TZM in that it is commercially available and some information is available on its properties. Finally, V-20Ti is a rather specialized alloy that was once considered as a possible backup cladding material for LMFBR's. However, it was dropped because of corrosion problems in reactor grade sodium. This alloy can be purchased in limited quantities by special order but only a relatively small amount of information exists on its properties at the present time.

The next requirement which we felt to be important, in view of the requirements of CTR's, is that the blanket material be easily fabricated. The sheer size of fusion reactors means that many components must be easily welded in the field to provide vacuum tight seals for the plasma chamber. Another consideration here is the possibility that the first wall will have to be replaced several times during the reactor lifetime. This means that a new wall will have to be assembled remotely; therefore simple and reliable welding properties are required.

The first choice under these criteria is clearly 316 SS. The Nb-1Zr alloy would be a possible second choice provided extreme care is taken not to embrittle the weld with contaminants in the welding covergas. The vanadium alloy will be a third choice with the Mo alloy a poor fourth. This requirement of weldability (TZM is easily fabricated) is perhaps the major reason TZM is not considered as a primary CTR alloy.

Assuming that we could build a CTR structure to conform with existing design codes, we must then be concerned about its properties during irradiation. The most severe of these problems is irradiation-induced embrittlement which could cause the first wall of the reactor to fail in a brittle manner during the application position of a few tenths percent of strain (Section VI-B). At the present time, none of the four alloys have been shown to be superior to the others in this respect, mainly because of the lack of data. We do know that for 316 SS, perhaps the most thoroughly studied alloy in the world, with respect to radiation damage, severe embrittlement takes place long before the goal exposures for a 30 year plant life would be reached. We must be careful about judging 316 SS too harshly, for it is probably one of the most resistant alloys to embrittlement known at this time, especially in the exposure region envisioned for CTR's. The next property which must be considered for safe long term operation is swelling. This will be treated in Chapter VI, but V-20Ti seems to have a curious resistance to this phenomenon and therefore would be our first choice. Voids have been found in all of the other alloys, but so far only for 316 SS has a method been

found to retard this problem (cold working and coherent precipitate formation).

Another concern for the safe and economical operation of CTR's is the thinning of the first wall by neutrons and charged particles (Chapter VI). Very little information is available on this subject but it appears that Nb (or possibly its alloy Nb-1Zr) might be the first choice with respect to this problem. Molybdenum (or its alloy TZM) would be a close to second choice here on the basis of its sputtering coefficients alone.

There is another type of embrittlement which is independent of irradiation and that is interstitial embrittlement caused by impurities in the coolant or from the plasma. Body centered cubic materials (e.g. Nb, Mo, and V) are particularly subject to this problem and extreme care must be exercised to prevent it from occurring. The 316 SS alloys (fcc structure) are far less susceptible than the other alloys and therefore are the first choice. The TZM alloy is the second choice because its solubility for the interstitial elements (O, N, or C) is much lower than that of Nb or V.

Up to this point we have been discussing problems which could actually prevent the construction or operation of a safe CTR. We will now assess the materials from the standpoint of economic or environmental arguments.

It is obvious that we would like to run at a very high temperature to increase the efficiency of the plant. Therefore, one would like to have materials with acceptable mechanical strength at high temperatures. This criterion favors TZM, which could be used with Li up to ~1000-1100°C. The Nb-1Zr would closely follow, having a useful temperature of 900-1000°C. It is interesting to note that 316 SS is a dismal fourth in this rating scheme because it can be only used up to ~500°C because of preferential dissolution of Ni, Cr or C by the Li (see Section IV-C).

All of the four alloys considered here will allow a breeding ratio of greater than 1 so that one could not rule out any materials on that basis. However, the V-Ti alloy and 316 SS both allow quite high B.R.'s with Nb and Mo alloys being less favorable. No one alloy is clearly favored over the others in this respect.

The loss of tritium by permeation through the blanket walls not only represents a loss of potential fuel but represents a hazard as well. It is quite desirable to have the blanket material which is relatively impervious to T_2 diffusion. This criterion clearly favors TZM over the other alloys and 316 SS comes in second.

The fabricated costs of high quality blanket components become important because of the sheer size of CTR's. The stainless steels are by far the best alloys here, having fabricated costs 15 times less than Nb-1Zr, 20 times less than TZM and 30 times less than V-20Ti.

Finally, if we are to build a large number of plants (hundreds to perhaps thousands) then the availability of structural elements to the United States becomes quite important. This problem, coupled with the balance of payments, national security and long term stability will have to be faced in long term planning. Surprisingly, the TZM alloy is the best choice here because of the large Mo reserves in this country.⁽⁹⁾ Niobium and vanadium supplies are quite scarce and even some of the alloying elements of 316 SS such as Cr, Mn, or Ni are not abundant in this country.

In summary, the choice of the CTR blanket material is not an easy one, it depends on many complex factors and of the four alloys considered one could find ample reasons to choose one or complete disregard it. Nevertheless, we felt that 316 SS represented the best choice at the present time for a near term power plant. This decision could be reversed, when, and if, a qualified refractory metals industry can be established, and when irradiation data on these alloys is comparable to that available for 316 SS.

4. Choice of Moderator-Reflector

The real question that one needs to answer is how can this choice be made to maximize breeding, not whether one can find a material that will actually slow down the neutrons. The decision then boils down to a question of neutronics. In some systems such as the LASL design⁽⁴⁾, graphite has been chosen to help reflect the neutrons because of the small blanket size. In addition, Be is used as its (n,2n) reaction produces extra neutrons while the Be is a good moderator and reflector as well. In systems which use large amounts of lithium for cooling and breeding, it is questionable whether one needs an extra moderating material. If the breeding ratios are already high(see Section VIII-B), it is possible that one would rather breed "energy" than tritium.

It has been the conclusion of this study (see Chapter V) that there is no need for materials such as Be or graphite when one makes the choice of Li as a coolant. It is shown that, in fact, the use of graphite in the place of steel in UWMAK-I makes little difference in the breeding ratio and actually lowers the total power generated in the blanket. Therefore, the decision was made in the UWMAK-I design to use no auxiliary moderating material in addition to Li and to use 316 SS as the major reflector in the blanket.

5. System Description

This section will briefly describe the geometric arrangement of the blanket and shield in UWMAK-I in addition to the inventory of materials and coolant flow patterns in the reactor. Complete details on these are given in Sections IV-B thru F.

a.) Blanket

Figure IV-A-1 shows a cross sectional view of the UWMAK-I. The blanket and shield are the cross hatched regions. The blanket is 14 meters high and 11.5 meters wide. The blanket is made up of two regions, one near the center of the torus (region I) and the other at the outside of the torus (region II). Each region is made up of 87 sections. (see Figure IV-A-2) These sections are 1.5 meters by a dimension which varies from 1.25 to 2.4 meters (see Section IV-E). There are four complete Li flow circuits in the blanket. These will be described in more detail in Section IV-B.

A schematic view of a partial section is given in Figure IV-A-3. The lithium flows in special poloidal headers, then down toward the plasma through "U" shaped cells and back out through another set of poloidal headers. A more detailed description of this flow pattern is also given in Section IV-B.

Figure IV-A-4 shows a schematic of the composition and dimensions of the blanket. The first wall thickness is 2.5 mm (the first wall is shown as 4mm which is an effective smooth wall thickness) and it is followed by a 95% Li-5% 316 SS heat removal zone, a 15 cm 316 SS reflector, a 5 cm lithium channel for cooling and a 2 cm 316 SS wall.

There is a 1 cm thick vacuum gap between the blanket and shield to cut down thermal losses to the shield.

The flow rates and Li temperatures in and out of the blanket are shown in Figure IV-A-5. Note that the total lithium flow rate is 2.0×10^7 kg/hr which enters the blanket at 283°C and leaves at 483°C.

b.) Shield

Surrounding the blanket in Figure IV-A-1 is the magnet shield which tends to conform more with the "D" shaped magnets than with the blanket itself. This shield is 77 cm thick and is cooled by He. Figure IV-A-4 shows the schematic of the shield materials. It is noted that after an initial 1 cm of 316 SS, there is a 20 cm region of 90% Pb and 10% 316 SS. This is followed by an eight cm region of B₄C and a one cm helium cooled zone. The B₄C is used to moderate and absorb the neutrons. This sequence (He-Pb-B₄C) is repeated three times before the outer shell of the shield is reached.

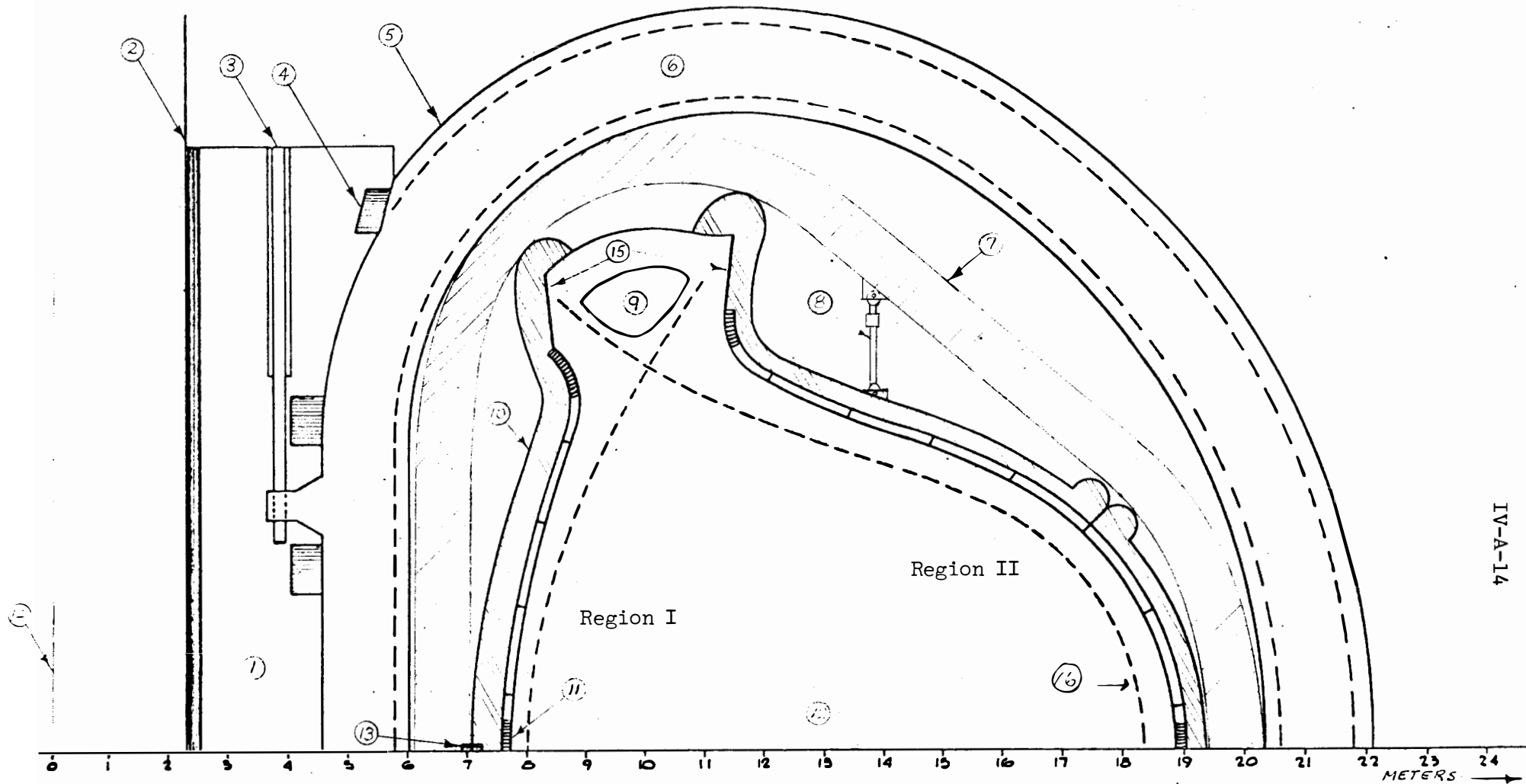


Fig. IV A-1 CROSS SECTION OF UWMAK-I

- | | | |
|------------------------------|-----------------------------------|------------------------|
| 1- Central core | 6- Toroidal magnet | 11- Heat removal cells |
| 2- Superinsulation | 7- Shield | 12- Plasma |
| 3- Magnet support shear pins | 8- Blanket support | 13- Blanket support |
| 4- Transformer coils | 9- Vacuum port shield | 14- Reactor centerline |
| 5- Toroidal magnet dewar | 10- Reflector and Poloidal header | 15- Collector plates |
| | | 16- Separatrix |

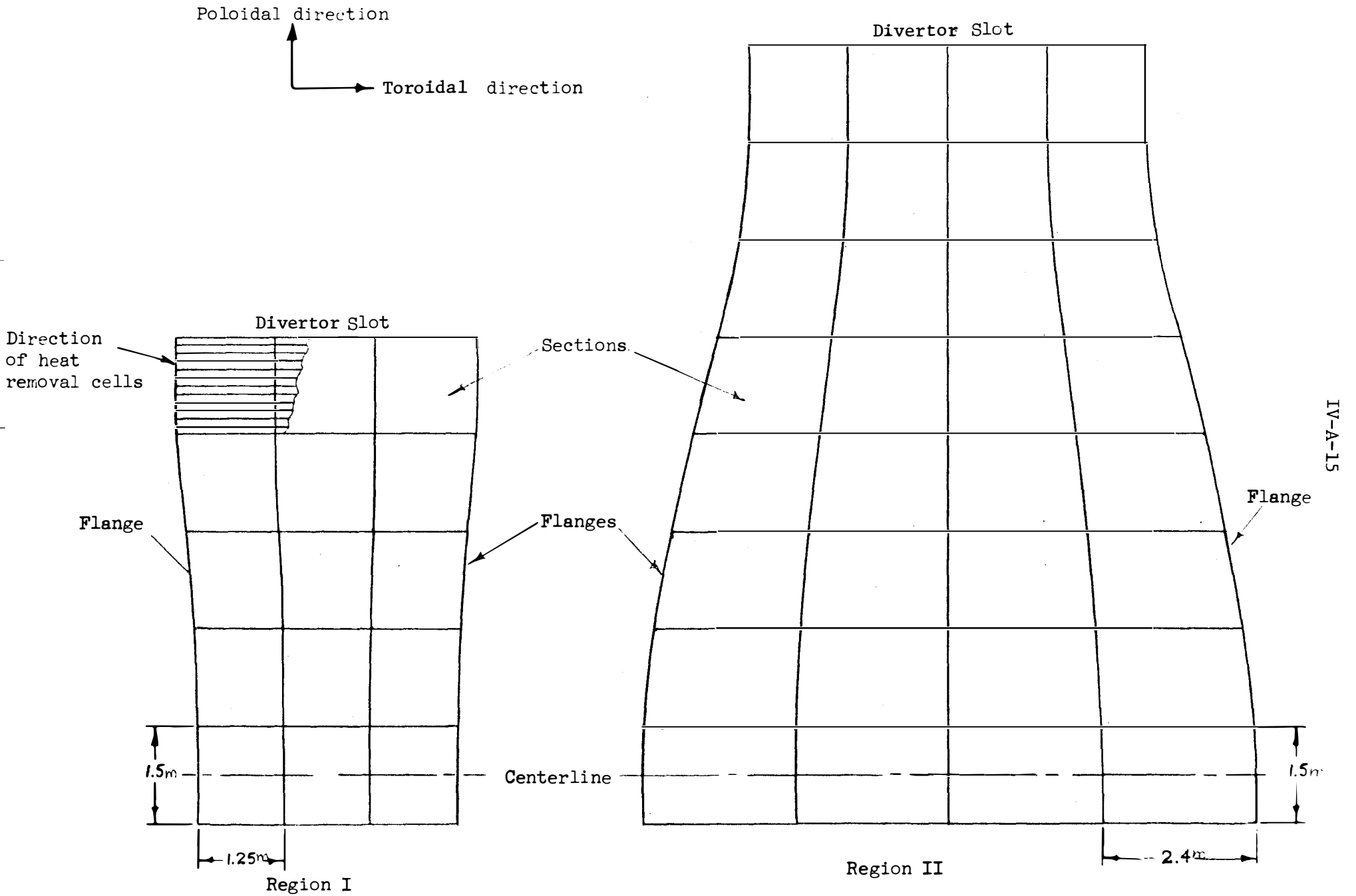


Fig. IV A-2 HEAT REMOVAL SECTIONS AS VIEWED FROM PLASMA CENTER

IV-A-16

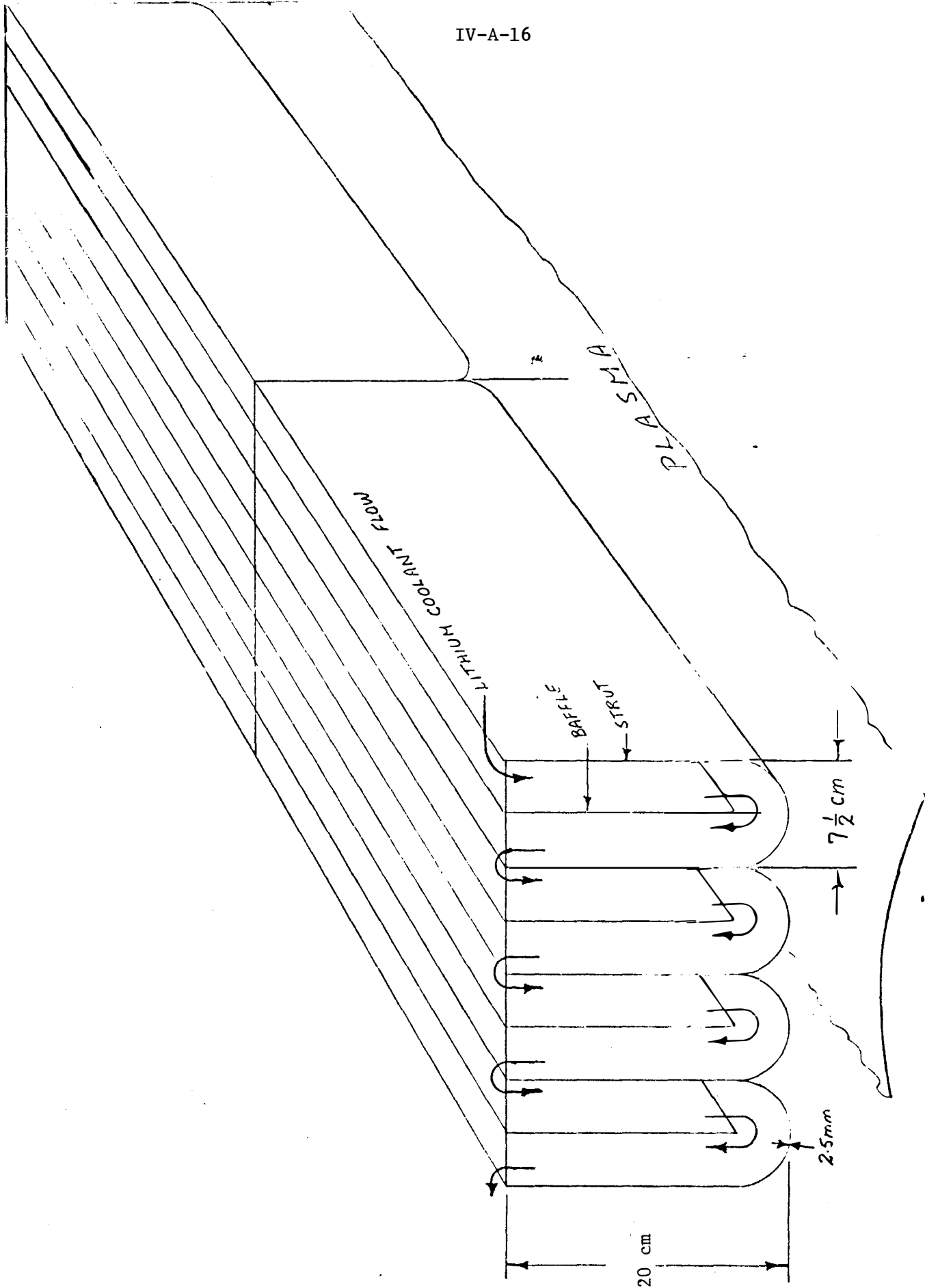


Fig. IV A-3 ISOMETRIC VIEW OF UWMK-1 HEAT
REMOVAL CELLS

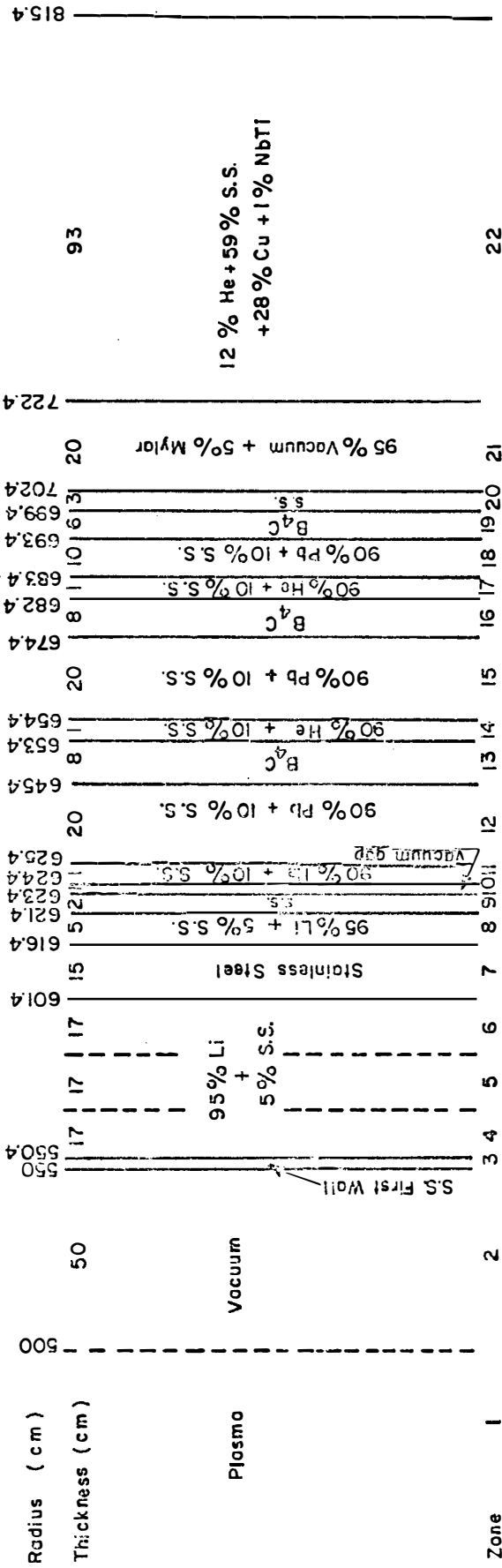
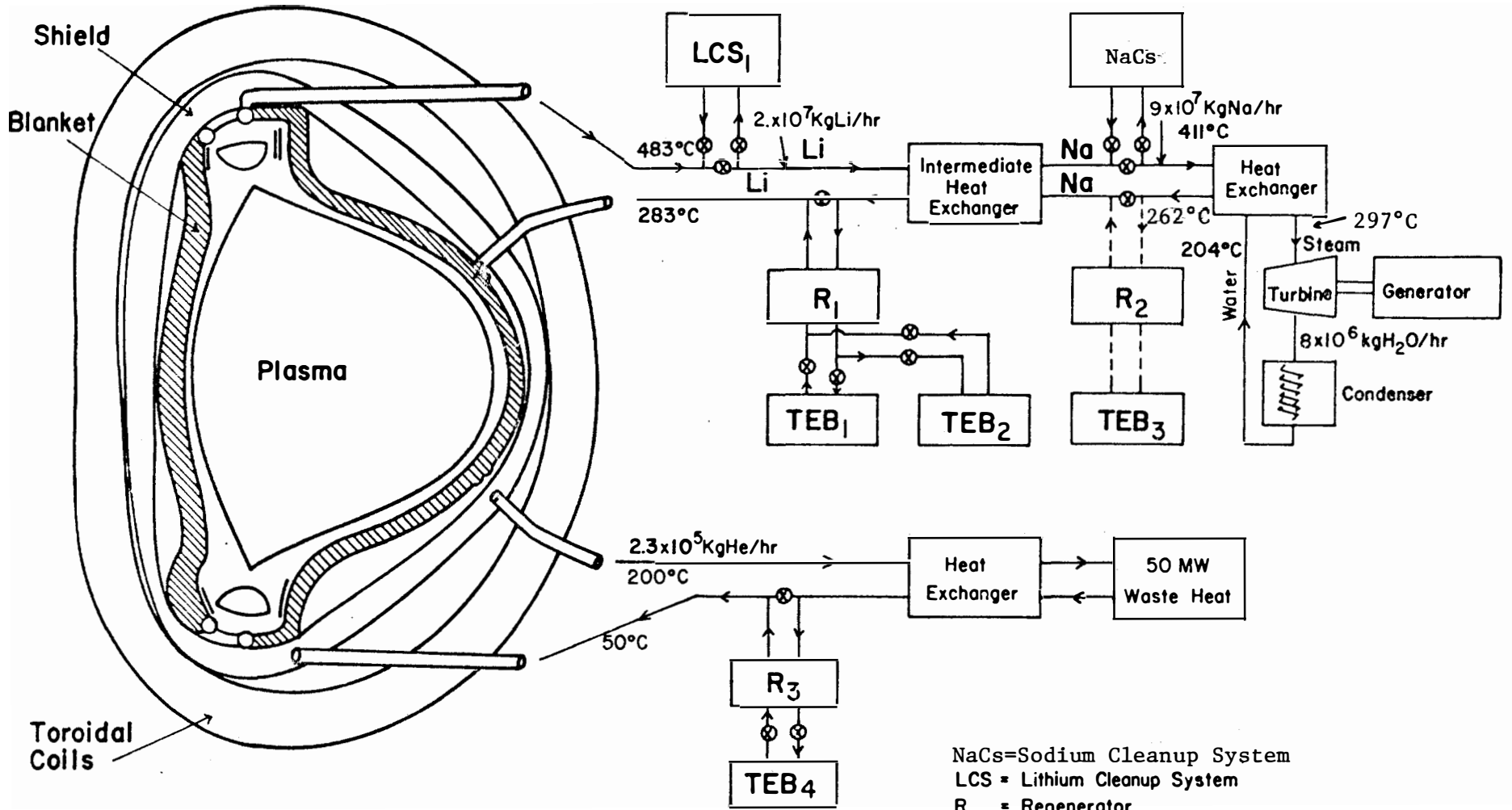


Figure IV-A-4 University of Wisconsin CTR Blanket, Shield and Magnet Structure for 5000MW_T System.



Coolant Loops for Wisconsin Toroidal Fusion Reactor - UWMAK-1

NaCs=Sodium Cleanup System
 LCS=Lithium Cleanup System
 R=Regenerator
 TEB=Tritium Extraction Bed
 Flow Rates are for Whole Reactor

Figure IV-A-5

Figure IV-A-5 also shows a flow diagram for the helium cooling indicating that the ΔT is 150°C and the flow rate to each zone is 2.3×10^5 kg/hr at $520,000$ kg/m² (50 atm).

Some specific details on the amount of material in each section, zone and region and the entire blanket are given in Tables IV-A-1 and IV-A-2 in the next section.

The heat transfer problems of the blanket are given in Section IV-B, and the corrosion effects are described in Section IV-C. The thermal and mechanical stresses are presented in Section IV-D while Section IV-E describes the procedure for changing the first wall. Finally, the support structure for the blanket and shield are given in Section IV-F.

6. Summary of Blanket and Shield Dimensions and Masses.

We have attempted to list in this section the numbers that are important to the UWMAK-I blanket and shield design. More specific information can be found on the origin of these numbers in later sections.

Table IV-A-4 lists the information on the dimensions and placement of various components in the blanket and shield. The numbers in this table refer to Figure VI-A-6. A slightly altered view of the divertor region was made to simplify the calculations of total blanket volume.

Table IV-A-5 lists the total mass of the various materials in the blanket and shield. The information is listed for each module, region, and ultimately summed up for the entire reactor. Some of the more important points of Table IV-A-5 are:

- . There is a total of 9,300 kg of 316SS in the first wall of each module. The total in the first wall of the reactor is 111,600 kg.
- . The total amount of 316SS in the disposable heat removal cells is ~491,000 kg in the entire reactor.
- . The fraction of the total 316SS in the reactor which is disposed of every two years is ~6%.
- . The total mass of Li in the reactor is 1.42×10^6 kg.
- . The total mass of B₄C is quite large; $\sim 1.62 \times 10^6$ kg.
- . The largest mass requirement for UWMAK-I is for Pb; over 16 million kg.
- . The weight of a single module (with Li drained out) is ~2,200,000 kg.

Close examination of Table IV-A-5 will emphasize the sheer bulk of this reactor.

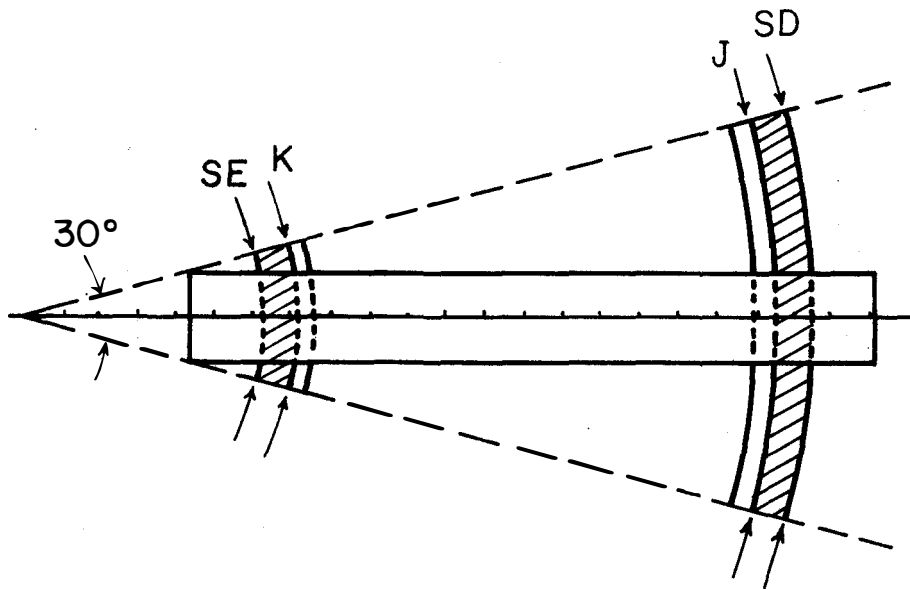
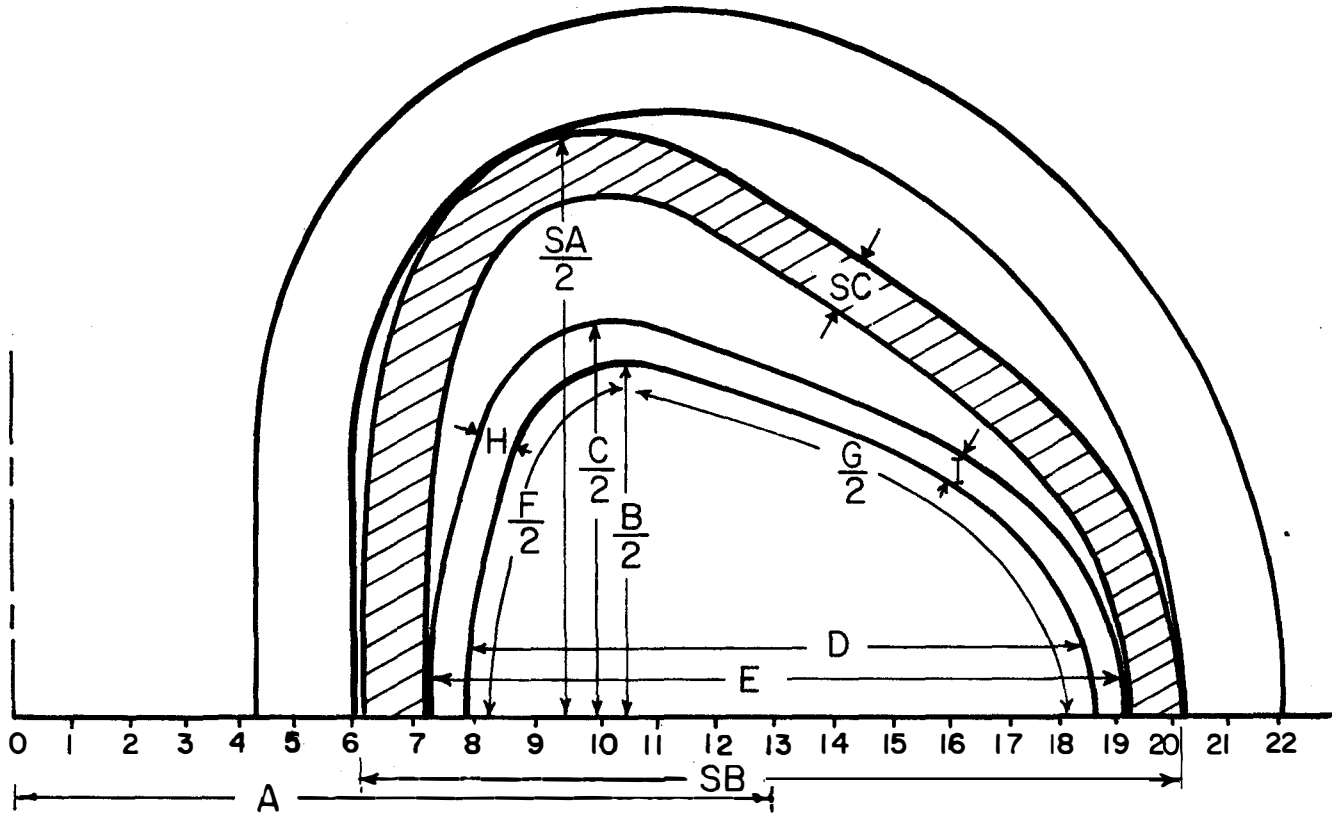
Table IV-A-4

Summary of Blanket and Shield Dimensions

<u>Blanket</u>		
<u>Component</u>	<u>Key*</u>	<u>Dimension, m</u>
Major Radius	A	13.00
Maximum Heights (outside)	B	13.60
Maximum Heights (inside)	C	12.14
Maximum Width (outside)	D	12.47
Maximum Width (inside)	E	10.80
Linear Length - Region I*	F	15.65
Linear Length - Region II*	G	24.93
Blanket Thickness - Region I	H	0.93
Blanket Thickness - Region II	I	0.73
Toroidal Length, Max.	J	10.07 (per module)
Toroidal Length, Min.	K	3.54 (per module)
<u>Shield</u>		
Maximum Heights (outside)	SA	20.8
Maximum Width (outside)	SB	14.05
Shield Thickness	SC	0.77
Toroidal Length, Max.	SD	10.48 (per module)
Toroidal Length, Min.	SE	3.13 (per module)

*See Figure IV-A-6

Figure IV-A-6 - Critical Dimensions for UWMAK-I
Blanket, Shield and Magnet Module.



TOP VIEW

Table IV-A-5
Summary of Blanket and Shield Materials

		<u>Blanket</u>	
<u>Material</u>	<u>Location</u>	<u>Weight (kg)</u>	
		Region I	Region II
316 SS	First Wall	2.06×10^3	7.24×10^3
	Rest of radial cells	6.98×10^3	2.46×10^4
	Headers	1.78×10^4	5.27×10^4
	Reflector	7.38×10^4	2.77×10^5
	Outer Wall	1.23×10^4	4.62×10^4
	Total/module	1.13×10^5	4.08×10^5
	Each module	5.21×10^5	
	Total reactor	6.25×10^6	
Lithium	First Wall to reflector per module	2.35×10^4	5.89×10^4
	Behind reflector/module	1.57×10^3	1.26×10^4
	Feed pipes to edge of CTR module	2.20×10^4	
	Total per module	1.19×10^5	
	Total per reactor	1.42×10^6	
		<u>Shield</u>	
		<u>Weight (kg)</u>	
		Per module	Per reactor
316 SS		1.69×10^5	2.03×10^6
B ₄ C		1.35×10^5	1.62×10^6
Pb		1.36×10^6	1.64×10^7
He		5.55×10^1	6.66×10^2
<u>Total Blanket and Shield</u>			
316 SS		6.90×10^5	8.28×10^6
Li		1.19×10^5	1.42×10^6
B ₄ C		1.35×10^5	1.62×10^6
Pb		1.36×10^6	1.64×10^7
He		5.55×10^1	6.66×10^2
Total		2.30×10^6	2.77×10^7

IV-B. Heat Transfer

1. General Discussion

Once the coolant has been chosen for a CTR blanket it is necessary to perform detailed calculations on the flow rates, temperatures and pressures required to maintain the proper temperatures in the system. This is not an easy job in a "normal" power plant and the situation is even further complicated by trying to pump electrically conducting fluids through high magnetic fields as we do in UWMAK-I.

Early workers (10,11) reported unacceptably large pressure drops for lithium cooled systems, but this difficulty has been greatly reduced by more efficient flow designs (12, 13, 14). The present design represents a further improvement, such that lithium cooling now appears to be very attractive for Tokamak systems.

We will precede the discussion of the UWMAK-I design by reviewing some general principles of magneto-hydrodynamics (MHD) and the flow of electrically conducting fluids in magnetic fields. Next we will develop the design procedure that was followed for the current reactor concept. A general system description of UWMAK-I will be followed by some details on the pressure drops incurred, pumping power required and temperature distribution in the blanket and shield. Finally, a summary of the important parameters is given.

Magnetohydrodynamic Effects

A detailed discussion of magnetohydrodynamic effects is available in Reference 15. A brief discussion and introduction to the working equations is given here. The most important effects of the magnetic field on the reactor coolant design are the suppression of turbulence and the increase in flow resistance. These effects are discussed separately below.

1. Turbulence Suppression

The flow regime in a tube or duct depends mainly on the following dimensionless groups:

$$\text{Reynolds number } Re = 4 R_H v \rho / \mu$$

$$\text{Transverse Hartmann Number } H_{\perp} = R_H B_{\perp} \sqrt{\sigma / \mu}$$

$$\text{Parallel Hartmann Number } H_{\parallel} = R_H B_{\parallel} \sqrt{\sigma / \mu}$$

where R_H = hydraulic radius (cross section area divided by wetted perimeter)

v = bulk velocity

ρ = density

μ = viscosity

B_{\perp} = component of the magnetic field perpendicular to the bulk velocity

B_{\parallel} = component of the magnetic field parallel to the bulk velocity

σ = electrical conductivity of the coolant.

The Reynolds number is the main criterion for the onset of turbulence in the absence of magnetic effects. The transition Reynolds number is around 2300 for fully developed flow in a smooth-walled tube.

When a magnetic field is applied to an electrically conducting fluid, the magnetic force [$\underline{v} \times \underline{B}$] resists the development of the turbulent eddies. This damping effect delays the laminar-turbulent transition to a higher Reynolds number, as shown in Figure IV-B-1.

In a toroidal fusion reactor, the Hartmann number will be on the order of 10^5 if lithium is used as the coolant. The transition Reynolds number for such a flow should be on the order of 10^8 according to the trend of the data in Figure IV-B-1. The actual Reynolds numbers in a lithium-cooled reactor will be considerably below this limit when allowable coolant pressures and pumping costs are taken into account. Therefore, it is realistic (as well as conservative) to assume laminar flow of the coolant throughout the reactor.

2. Magnetohydrodynamic Pressure Drop

It is well known that whenever an electrically conducting fluid flows across field lines, eddy currents will appear wherever curl [$\underline{v} \times \underline{B}$] is non-zero. This produces a retarding force which causes extra pressure drops in the fluid. These pressure drops will be classified here into two categories (15): the Hartmann and end-of-loop effects.

The Hartmann pressure gradient arises in fully-developed laminar flow with a uniform transverse magnetic field. For such a flow between parallel plates, in a uniform magnetic field normal to the plates, the pressure gradient is given by the following equation: (16)

$$-\frac{dP}{dx} = \frac{\mu v}{a^2} \left[\frac{H_{\perp}^2 \tanh H_{\perp}}{H_{\perp} - \tanh H_{\perp}} + \frac{H_{\perp}^2 C}{1+C} \right] \quad (\text{IV-B-1})$$

where C = wall conductance ratio, $\sigma_w t_w / a\sigma$

a = channel half-width

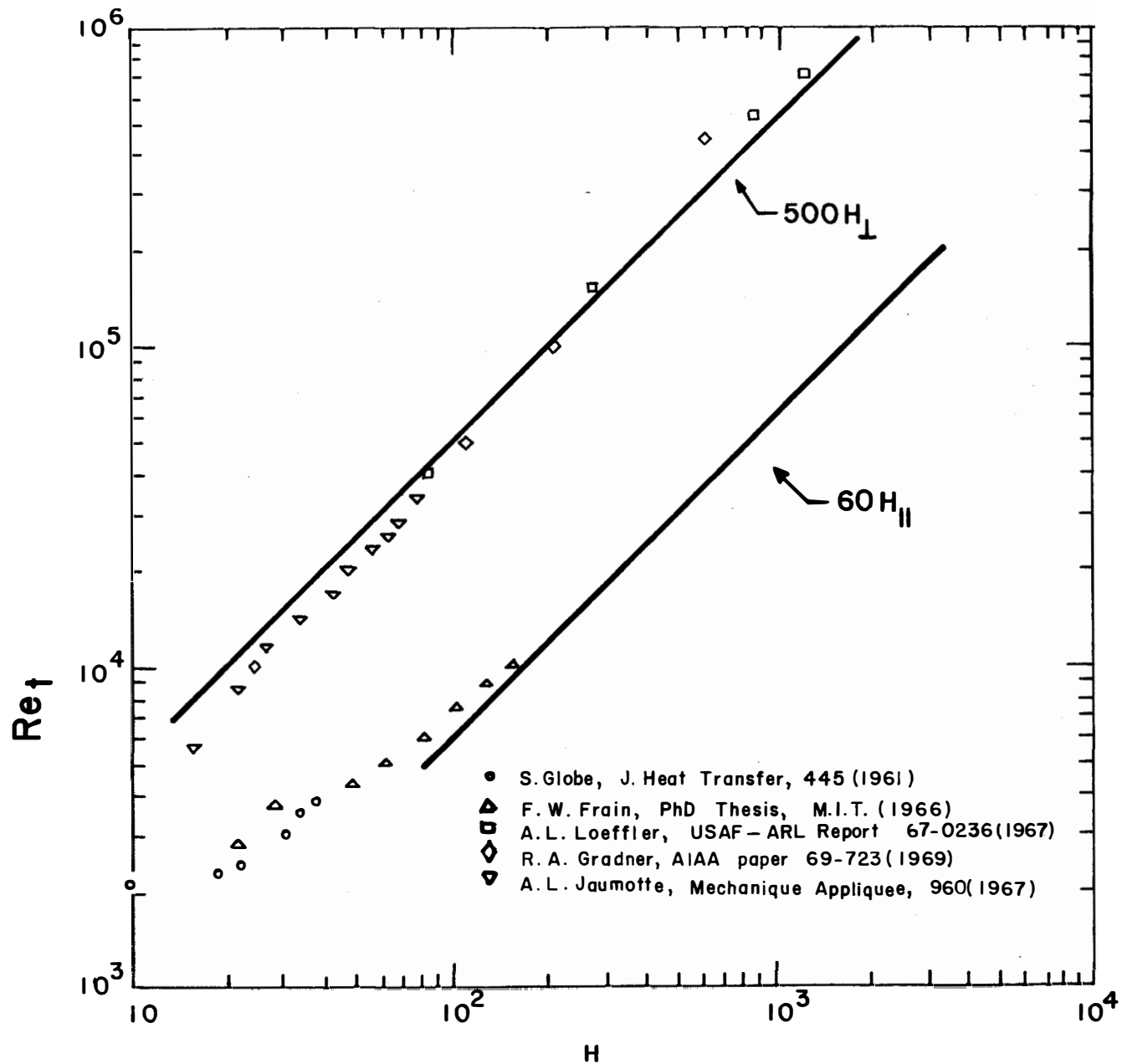


FIG. IV-B-1. TRANSITION REYNOLDS NUMBERS FOR FLOWS OF CONDUCTING FLUIDS IN CIRCULAR PIPES IN PARALLEL AND TRANSVERSE MAGNETIC FIELDS.

σ_w = electrical conductivity of the wall material

t_w = wall thickness

When the fluid is in a channel with a conducting wall and under large magnetic fields ($H \gg 1 + 1/C$), the last term of Equation IV-B-1 dominates, giving

$$-\frac{dP}{dx} = \frac{vB_{\perp}^2 \sigma_w t_w}{a(1 + C)} \quad (\text{IV-B-2})$$

If the wall is strong enough to withstand the pressure and the corrosion of the lithium, the value of C is usually on the order of 10^{-2} or larger; hence, Equation IV-B-2 is an excellent approximation in the present range of Hartmann numbers ($H \sim 10^5$).

Hoffman and Carlson (15) have given useful approximate formulas for the Hartmann pressure gradient in rectangular and circular ducts. In the region of interest here, namely $H \gg 1 + 1/C$, their results are closely represented by Equation IV-B-2 provided that we generalize the definition of "a" follows:

a = mean half width of flow cross section in the direction of B_{\perp}

This gives $a = \pi D/8$ for a circular channel, as used in Reference 12. The empirical coefficient 1.3 in Hoffman and Carlson's Equation (12) is thereby approximated by $(4/\pi) = 1.273$.

The end-of-the loop effects are caused by gradients of $[\underline{v} \times \underline{B}]$ in the flow direction. The resulting pressure drops are given approximately by the following generalization of Equation (16), Reference 15:

$$\Delta P = K_{PIE} \frac{\sigma_b}{v_{av}} \Delta(v_{\perp}^2 B_{\perp}^2) \quad \text{IV-B-3}$$

Here b = mean half-width of the local cross section in the direction normal to B_{\perp}

v_{av} = arithmetic mean of values for initial and final cross sections.

The coefficient K_{PIE} has been presented by Hoffman and Carlson (15) for flows in tubes and ducts with varying B_{\perp} ; the results are summarized in Figures IV-B-2 and 3. We will use the same plots here to estimate K_{PIE} for changes of velocity and channel width; in this estimation L_F is taken as the downstream length of the region of varying vB_{\perp} .

3. Design Strategy

The design given here is based on several simple rules obtained from Figure IV-B-4 and physical considerations:

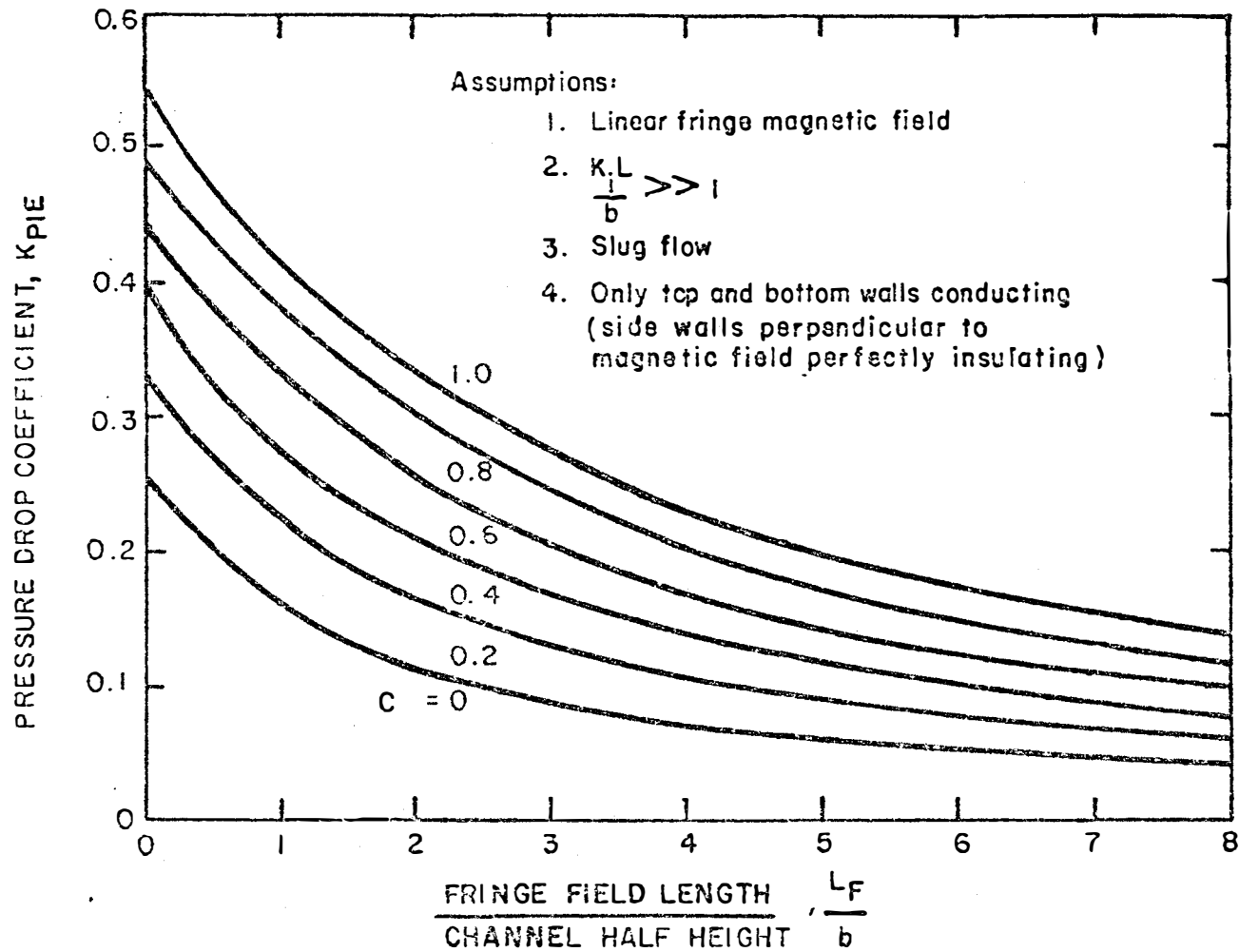


FIG. IV-B-2. PRESSURE DROPS DUE TO ENTRANCE AND EXIT EDDY CURRENT FOR LINEAR FRINGE MAGNETIC FIELDS SEPARATED BY A LONG REGION OF UNIFORM MAGNETIC FIELD.

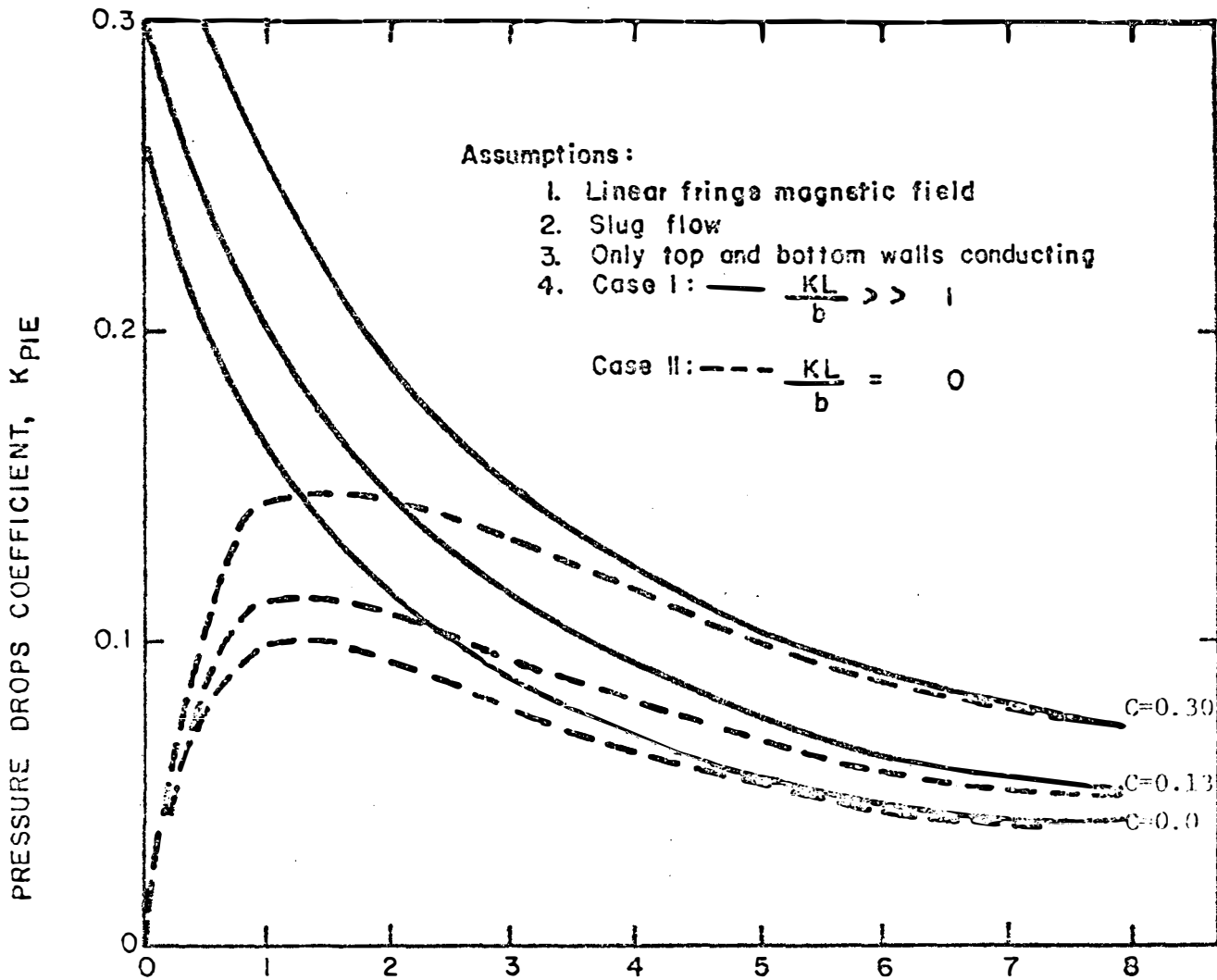


FIG. IV-B-3. PRESSURE DROP DUE TO ENTRANCE OR EXIT EDDY CURRENTS.

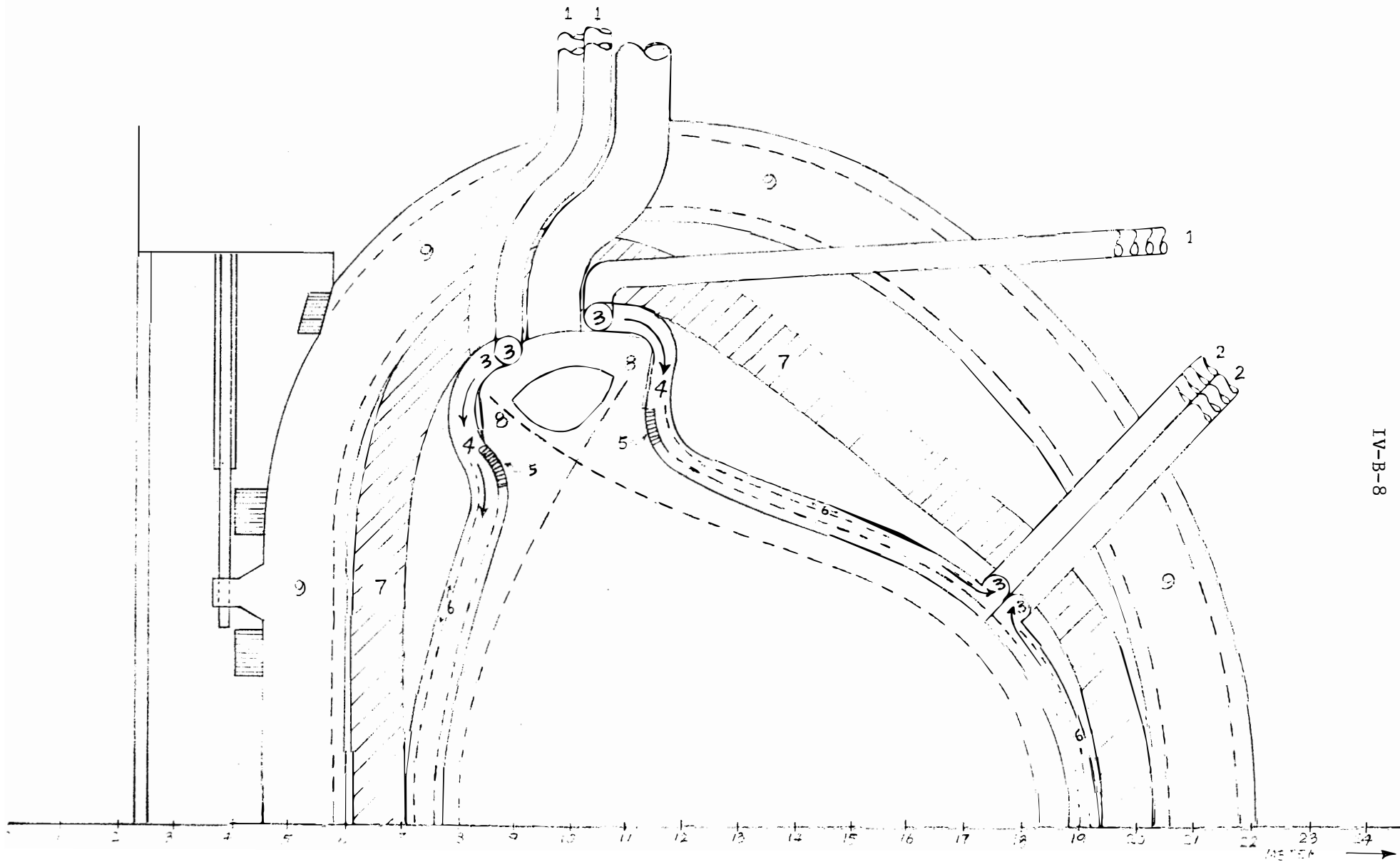
- a. Coolant must enter and leave the torus through the gaps between the D-shaped magnets.
- b. The main headers inside the magnets should follow the toroidal magnetic field lines to minimize pressure drops and utilize available space.
- c. Large cross sections should be provided for coolant distribution in the poloidal direction, to minimize the pressure drops in these long flow paths perpendicular to the toroidal field.
- d. The coolant for the inner zone of the blanket should be routed to the first wall in large radial ducts. The velocities should be small to minimize magnetohydrodynamic pressure drops, but large enough to avoid undesired heat exchange between adjacent radial streams.
- e. The stainless steel moderator-reflector in the outer zone of the blanket should have a separate coolant loop, to accommodate its different heat load and flow resistance.

4. System Description

A design consistent with these ideas is shown in Figures IV-B-4 and IV-B-5. The blanket structure is 316 stainless steel, and is designed with a maximum temperature of 500°C on the coolant walls to limit corrosion by the lithium. A corrosion allowance of 0.6 mil/year (0.00152 cm/year) is included in the initial wall thickness. The first 20 cm of the blanket is designed for 2 years life, while the rest of the reactor is designed for a 30 year life.

The reactor has 12 independent modules, one for each magnet. Each module has four blanket units: one between the upper and lower divertors (region I) and three for the rest of the wall (region II) (see Figure IV-B-1). The coolant is supplied and removed through bundles of four pipes, rather than single large pipes, in order to reduce magnetohydrodynamic losses as discussed below. Each pipe is connected to a toroidal header for the inner or outer zone of the blanket (Figure IV-B-4).

The coolant for the inner zone flows from the inner toroidal headers into poloidal headers, and then to the radial flow cells as shown in Figure IV-B-5. Each radial flow cell consists of four U-bends connected in series along the first wall. Series connection is used to decrease the residence time in each bend, and thus reduce undesired conduction of heat between adjacent radial streams. (12) To further reduce this exchange, the outlets of adjacent cells are juxtaposed; this requires provision of a different flow resistance in each cell to distribute the coolant properly. The U-bends are reinforced by poloidal tie-rods to maintain their alignment and contain the coolant pressure.

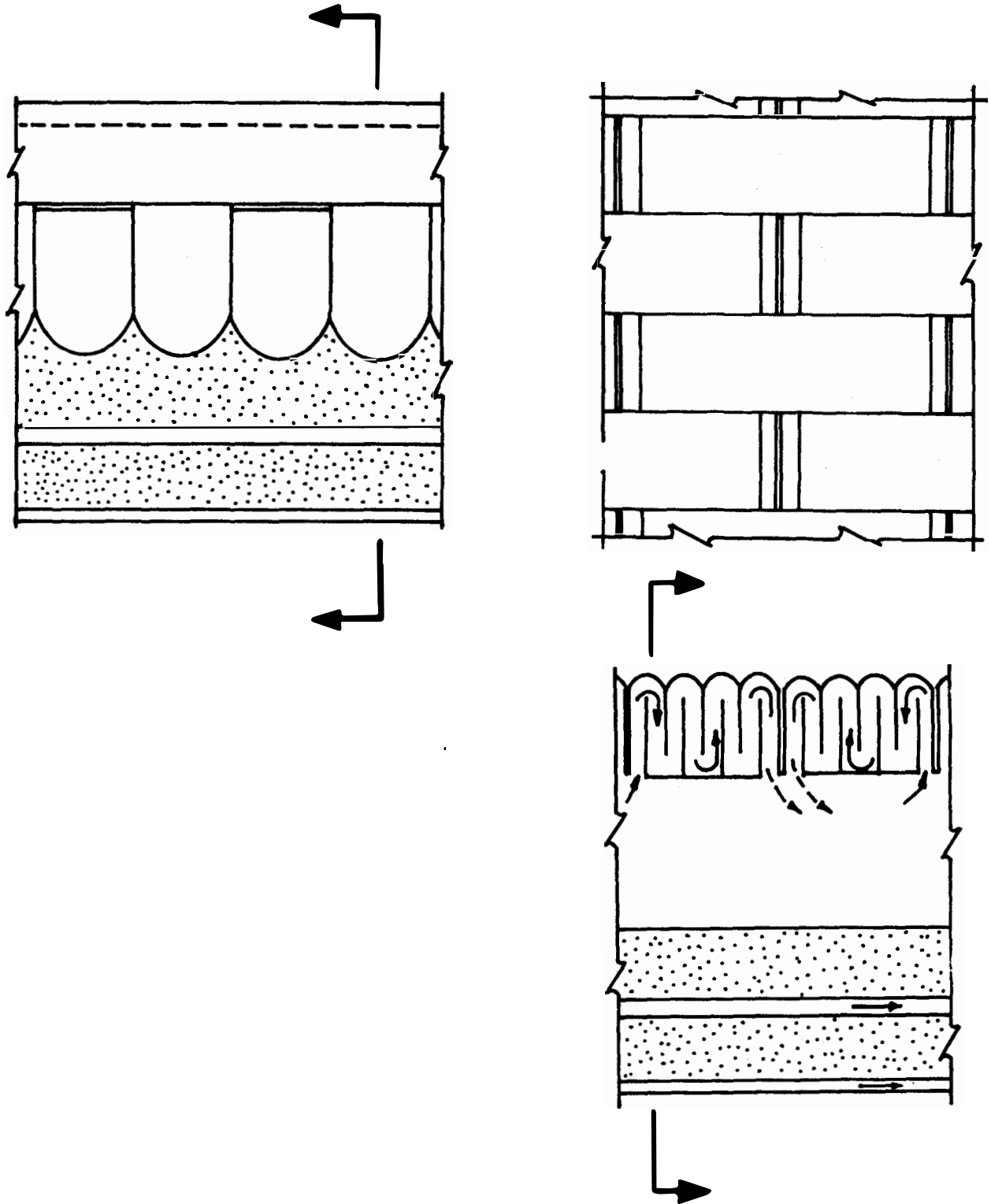


IV-B-8

FIGURE IV-B-4 SECTION VIEW OF A TOROIDAL MODULE

- | | | |
|---------------------|------------------------------------|----------------------------|
| 1. Feed Pipes | 4. Poloidal Headers and Connectors | 7. Shield |
| 2. Discharge Pipes | 5. Radial Flow Cells | 8. Divertor Slots |
| 3. Toroidal Headers | 6. S. S. Reflector | 9. Superconducting Magnets |

FIG. IV - B-5 SECTION VIEWS OF BLANKET



The alternating inward and outward radial flows in the U-bends produce corresponding alternations in the induced electric field $[v \times B]$. It is desirable to place the walls normal to this electric field to avoid short circuits between the adjoining radial streams. The arrangement in Figure IV-B-5 is consistent with this except for the small poloidal component of the magnetic field.

The stainless steel moderator-reflector in the outer zone of the blanket generates 25% of the 5000 MW thermal output. To avoid overheating, the steel is divided into two layers, each cooled by lithium on both sides. The maximum allowed temperature at the interface of the coolant and stainless steel is 500°C. The calculated maximum temperature in the steel is 670°C.

a. Pressure Drop

The Li coolant pressure drops are calculated from Equations IV-B-2 and IV-B-3. The results are summarized in Tables IV-B-1 and IV-B-2 for each region of the blanket. The calculations are based on local magnetic fluxes B , including the poloidal and toroidal components. The resulting pressures are shown in Figure IV-B-6 for the inner unit between the divertors. The pressures are much lower than in the design of Reference 12; this is mainly due to changes in the feed and discharge tubes and in the structure of the poloidal headers. The maximum coolant pressure on the first wall is 300 psia. The pumping power input to the Li is 22 MW, which amounts to 0.44% of the reactor's thermal output.

Equation IV-B-3 indicates that a bundle of feed or discharge pipes gives less entrance pressure drop than a single pipe of the same total cross section, since both b and K_{PIE} increase with the pipe diameter. The pressure gradient of Equation IV-B-3, however, increases with decreasing pipe size when a corrosion allowance is included in t_w . The pressure gradient is reduced in this design by using laminated feed and discharge pipes with an electrical insulating layer protected by a thin inner wall of stainless steel. An inner wall thickness t_w of 2 mm is used to withstand corrosion by the lithium; a heavier outer wall carries the hoop stress.

The poloidal headers constitute the main flow resistance in the coolant system. These channels are tapered to equalize the velocities in adjoining headers, and thus minimize electromagnetic interactions. Heat exchange between the adjoining header streams is a minor factor because of the substantial width of the channels and the insulating effect of the stainless steel header walls. Electrically insulated liners were considered for reducing the pressure drop, but they are not used in this region, in view of uncertainties about radiation damage.

Rectangular orifices are used to connect the poloidal headers to the radial flow cells. The pressure drop, according to Equation IV-B-3,

FIG. IV-B-6. COOLANT PRESSURE DISTRIBUTION

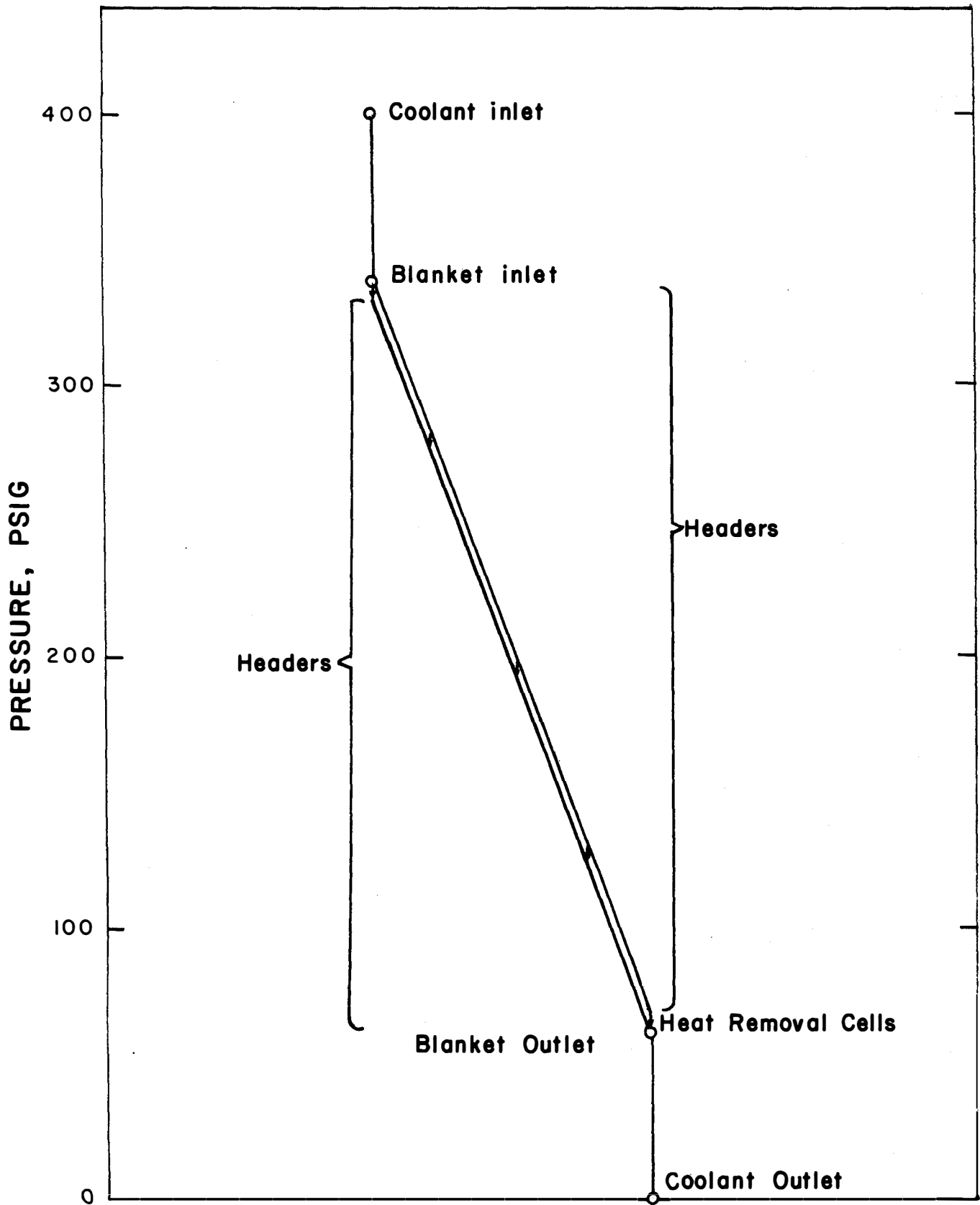


Table IV-B-1

Summary of Li Pressure Drop Calculations
(Inner zone of the blanket)

	<u>v,m/s</u>	<u>a,m</u>	<u>b,m</u>	<u>L_F/b</u>	<u>K_{PIE}</u>	<u>t_w,mm</u>	<u>L,m</u>	<u>B_z,Tesla</u>	<u>ΔP_E,$\frac{kg}{m^2}$</u>	<u>ΔP_H,$\frac{kg}{m^2}$</u>	<u>ΣΔP_E,$\frac{kg}{m^2}$</u>
<u>For unit nearest reactor axis</u>											
Feed pipe; Discharge pipe	.18	.196	.196	5.1	.05	2.0	1.83	5.9	31,400	11,600	43,000 (x 2)
Toroidal headers	.705	.196	-	-	-	4.0	3.4	.6	-	1,000	1,000 (x 2)
Poloidal headers	.083	.15	.25	2	.11	3.0	16.0	6.5	48,400(x2)	95,600	192,400
Radial cells	.038	0.5	-	-	-	3.0	1.6	6.5	-	1,500	<u>1,500</u> 281,700 (=401 psi)
<u>For units on top and bottom of the torus</u>											
Feed pipe	.235	.196	.196	10.2	.025	2.0	8.0	3.9	9,000	28,200	37,200
Toroidal headers	.939	.196	-	-	-	4.0	6.8	.5	-	3,200	3,200
Poloidal headers	.092	.15	.15	2.0	.11	2.0	8.0	4.2	6,700(x2)	17,100	30,500
Radial cells	.038	0.5	-	-	-	3.0	1.6	5.0	-	1,100	1,100
Toroidal headers	.939	.196	-	-	-	4.0	6.8	.3	-	1,200	1,200
Discharge pipe	.235	.196	.196	5.1	0.05	2.0	5.0	2.64	7,900	8,100	<u>16,000</u> 89,200 (=127 psi)
<u>For unit farthest away from reactor axis</u>											
Feed pipe; Discharge pipe	.235	.196	.196	5.1	0.5	2.0	5.0	2.6	7,700	7,900	15,600 (x 2)
Toroidal header	.939	.196	-	-	-	4.0	6.8	.3	-	1,100	1,100 (x 2)
Poloidal header	.092	.15	.15	2.0	.11	2.0	8.0	2.6	2,800(x2)	6,500	12,100
Radial cells	.038	0.5	-	-	-	3.0	1.6	2.6	-	500	<u>500</u> 46,000 (=65 psi)

IV-B-11

Table IV-B-2

Summary of Pressure Drop Calculations
(Outer zone of blanket)

	<u>v,m/s</u>	<u>a,m</u>	<u>b,m</u>	<u>L_F/b</u>	<u>K_{PIE}</u>	<u>t_w,mm</u>	<u>L,m</u>	<u>B₋,Tesla</u>	<u>ΔP_E,$\frac{kg}{m^2}$</u>	<u>ΔP_H,$\frac{kg}{m^2}$</u>	<u>ΣΔP$\frac{kg}{m^2}$</u>
<u>For unit nearest reactor axis</u>											
Feed pipe (discharge pipe)	.24	.196	.196	5.1	.05	2.0	1.83	5.9	41,800	15,400	57,200(x2)
Toroidal headers	.235	.196	-	-	-	4.0	3.4	.6	-	300	300(x2)
Coolant channels	.276	.60	.025	2	.11(x2)	4.0	16.0	7.0	18,700(x2)	122,900	<u>160,300</u> <u>275,300</u> (=391 psi)
<u>For units on top and bottom of the torus</u>											
Feed pipe	.313	.196	.196	10.2	.025	2.0	8.0	3.9	12,000	37,600	49,600(x2)
Toroidal headers	.313	.196	-	-	-	4.0	6.8	.5	-	1,100	1,100(x2)
Coolant channels	.184	.60	.025	2	.11	4.0	8.0	4.2	2,200(x2)	17,100	21,500
Discharge pipe	.313	.196	.196	5.1	.05	2.0	5.2	2.64	10,500	10,800	<u>21,300</u> <u>94,600</u> (=135 psi)
<u>For unit farthest away from reactor axis</u>											
Feed pipe (Discharge pipe)	.313	.196	.196	10.2	.025	2.0	8.6	2.6	10,500	10,800	21,300(x2)
Toroidal headers	.313	.196	-	-	-	4.0	6.8	.3	-	1,000	1,000(x2)
Coolant channels	.184	.60	.025	2	.11	4.0	8.0	2.6	800(x2)	6,600	<u>8,200</u> <u>52,800</u> (=75 psi)

IV-B-12

is nearly proportional to $vb = V/4a$, where V is the volumetric flow and a is the orifice width in the poloidal direction. This gives the surprising result that the pressure drop is independent of the orifice length b in the toroidal direction. The length b is taken here as half of the full poloidal header width, to aid in distributing the coolant along the radial flow cells.

The pressure gradient in the radial flow cells is due mainly to eddy currents, which flow through the fluid in the direction of $[\underline{v} \times \underline{B}]$ and return through the poloidal tie-rods. Radial flow is thus resisted by the toroidal magnetic field, but toroidal flow is not; this causes the flow to distribute readily over the toroidal length of each heat removal cell. For these cells, t_w/a of Equation IV-B-2 is taken as the ratio of the conducting cross sections of the tie-rods and fluid.

b. Temperature Distribution

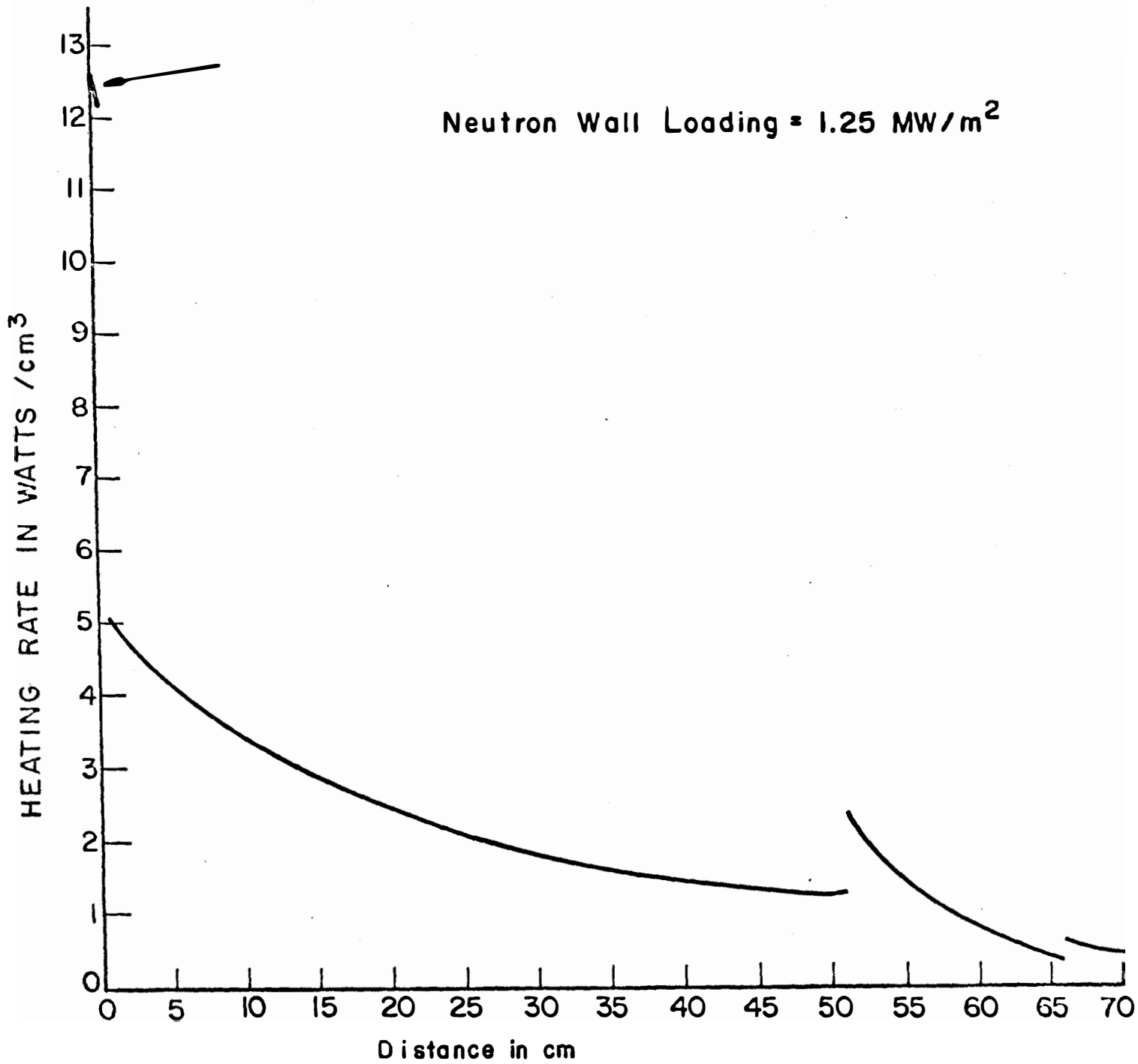
Steady state temperature profiles have been calculated for a radial flow cell on the assumption of negligible temperature changes in the headers and uniform fluid speed throughout the cell. The uniform-speed assumption is adequate in view of the high transverse Hartmann numbers and small Peclet numbers encountered in this design. The calculation was done as in Reference 12, by an implicit finite-difference method with a two-dimensional point mesh conforming to the streamlines. The surface and volumetric heat input rates were taken from neutronics calculations as shown in Figure IV-B-7. For simplicity, the heat generation for the header region was set to zero, and an equal heat input was added to the radial flow cells; thus the calculated temperature gradients in the radial flow cells are conservative (larger than actual) by about 20%.

The calculated coolant temperatures in a radial flow cell are summarized in Figure IV-B-8. The main conclusion to be drawn is that the coolant can be discharged at a temperature quite close to the structural material corrosion limit of 500°C. The temperature approach is closer than in Reference 12 because the coolant residence time is more nearly optimal.

c. Cooling of the Shield

The shield of the reactor contains a large amount of lead, which melts at 327°C. Therefore, the temperature in this zone was designed to be kept below 200°C for safety reasons. The heat load is small and easily removed by pressurized helium in coils imbedded in the shield.

A gap is required between the blanket and the shield for thermal insulation. This will allow the blanket to be a hot zone while the shield is relatively cool. Helium enters at 50°C and 53 kg/cm² (760 psi), and makes three passes in each heat transfer unit before it exits at 200°C. The pressure drop of the helium is only 5×10^{-4} kg/cm² ($<5 \times 10^{-3}$ psi), and the pumping requirement is only 7 kW.



(Zero corresponds to inner radius of first wall.)

FIGURE IV-B-7 SPATIAL DISTRIBUTION OF HEATING RATE IN THE BLANKET AND REFLECTOR REGIONS

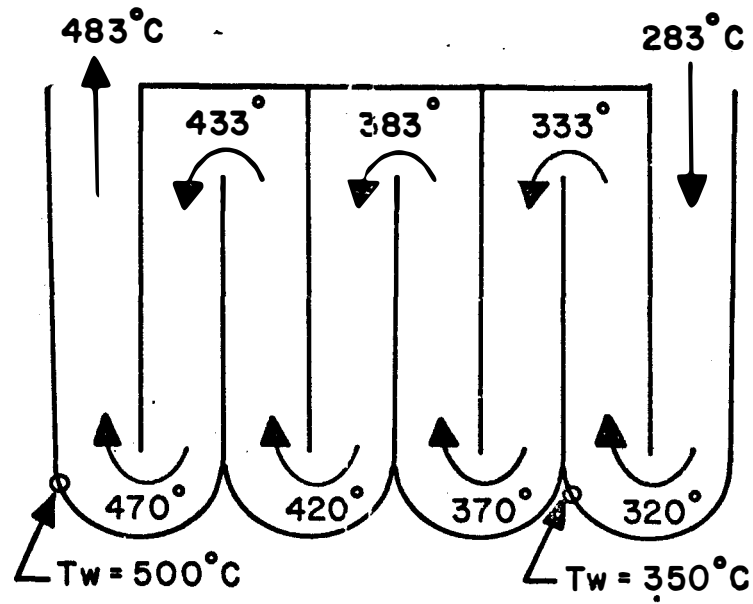


FIG. IV-B-8. BULK AND MAXIMUM COOLANT TEMPERATURES IN A RADIAL FLOW CELL

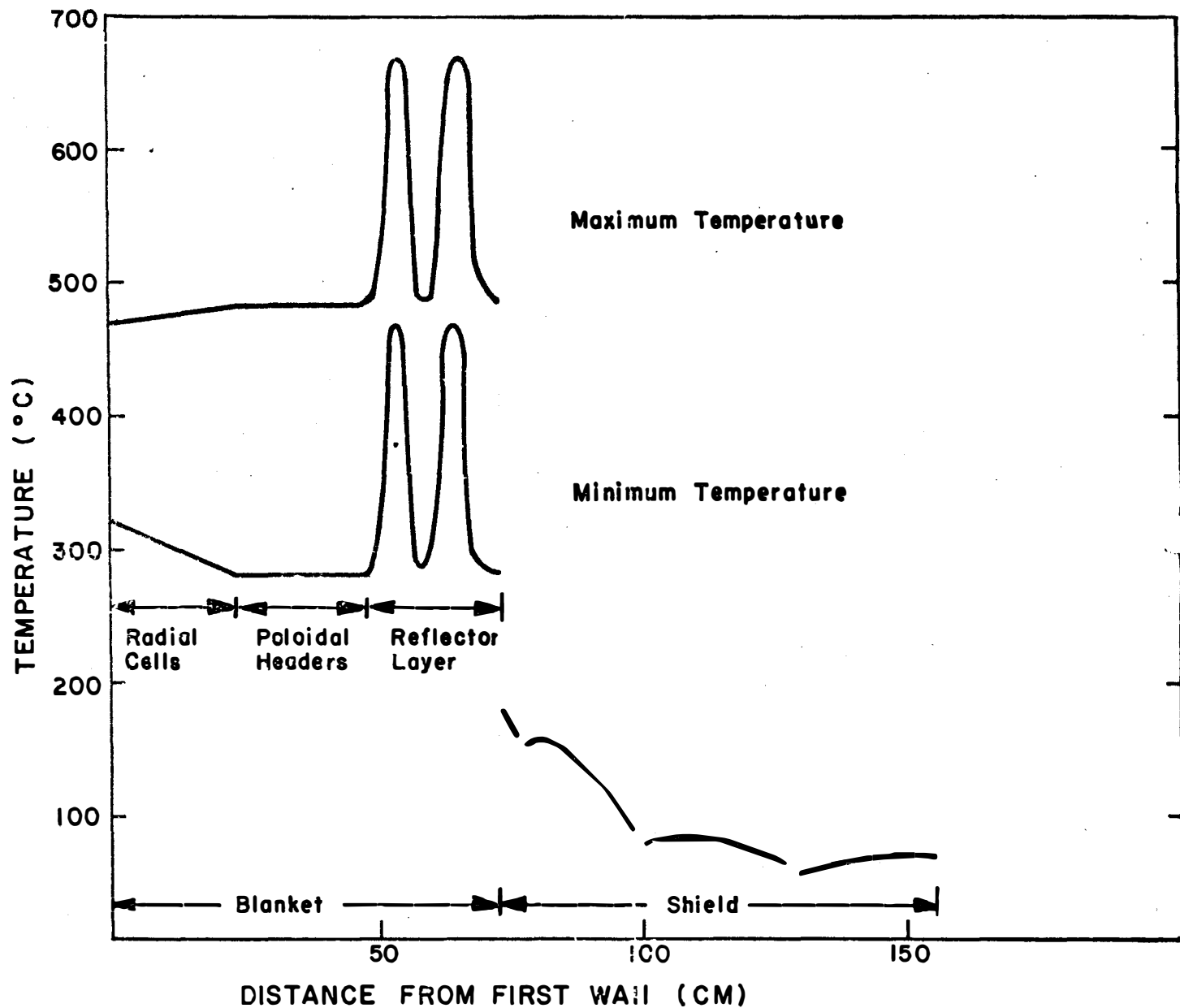
The temperature distribution from the first wall to the edge of the shield is shown in Figure IV-B-9.

Summary

An efficient design has been proposed for a lithium cooled reactor blanket. The major parameters of this design are listed on Table IV-B-3. The same type of design is also adaptable to higher wall loadings and magnetic fields. The following points are the unique features of this design:

1. Maximum utilization of the available space for the coolant flow to minimize the velocity.
2. Proper orientation of the coolant channels to avoid interaction of the eddy currents.
3. U-bend design to provide radial mixing of the blanket coolant.

The limiting factor of this design is probably the high internal pressure in the blanket. The high pressure requires a thick first wall which will cause stress problems (see Section IV-D). The heat transfer performance power requirements are very satisfactory.



DISTANCE FROM FIRST WALL (CM)
 FIG. IV-B-9. TEMPERATURE OF BLANKET AND SHIELD

Table IV-B-3

Summary of Important Parameters for Heat Transfer

Total Thermal Load	5000 MW _T
Major Radius	13 m
Minor Radius	5.5 m
Total Thermal Wall Loading	1.77 MW/m ²
B axis	3.86 Tesla
Structural Material	316 SS
Blanket Coolant	Lithium
Maximum Lithium Temperature	500° C
Lithium Temperature Rise	200° C
Lithium Flow Rate	5.6 x 10 ³
Maximum Lithium Pressure Drop	281,900 kg/m ² (401 psi)
Maximum First Wall Pressure	200,800 kg/m ² (300 psia)
Lithium Pumping Required	22 MW
Shield Coolant	He
He Pressure	5.2 x 10 ⁵ kg/m ² (50 atm)
He Temperature Rise	150° C
He Flow Rate	64.5 kg/sec
He Pumping Required	7 kW

IV-C. Corrosion and Corrosion Product Transport in Lithium-Cooled Stainless Steel Fusion Reactor Circuits

1.) General Discussion

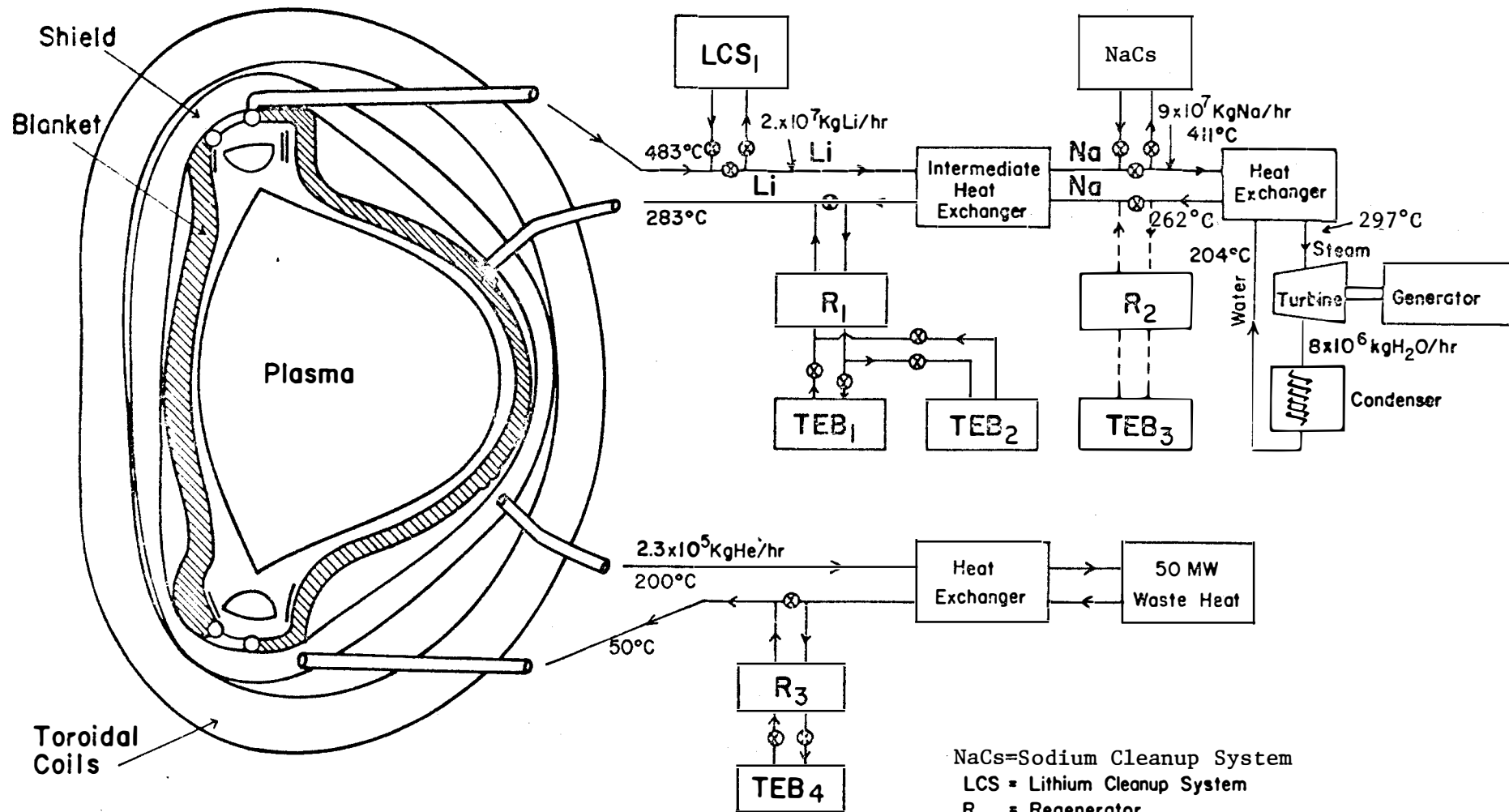
The University of Wisconsin Toroidal Fusion Reactor (UWMAK-I) comprises the following major systems where corrosion potential exists (refer to Figure IV-C-1):

- . the lithium-cooled primary circuit including the heat removal cells, headers, and the intermediate heat exchanger (lithium-to-lithium);
- . the secondary lithium circuit, including two heat exchangers and associated headers;
- . the steam system, including the lithium-to-steam heat exchanger, turbine, condenser, preheater and associated headers;
- . the tritium extraction system, consisting principally of a tritium getter (yttrium metal) and associated tanks and piping;
- . the lithium cleanup systems, which will consist principally of a hot trap (zirconium getter bed) and associated tanks and piping;
- . the helium system for cooling the shield(see Figure IV-C-1)
- . the lithium circuit employed in cooling and pumping the exhaust from the divertor.

The design material in the liquid metal circuits is 316 stainless steel (see Table IV-C-1 for metal composition). The lithium-to-sodium heat exchanger design material is 304L SS, on the evidence that tritium permeation rates are mildly lower for 304 than 316 SS.⁽²⁵⁾

Table IV-C-1
Stainless Steel Composition Specifications

<u>316 Stainless Steel</u> <u>Weight Percent</u>	<u>Element</u>	<u>304L Stainless Steel</u> <u>Weight Percent</u>
Balance	Fe	Balance
16/18	Cr	18/20
10/14	Ni	8/12
2.0/3.0	Mo	-
2.0 max.	Mn	2.0 max.
1.0 max.	Si	1.0 max.
0.080 max.	C	0.030 max.
0.045 max.	P	0.045 max.
0.030 max.	S	0.030 max.



Coolant Loops for
 Wisconsin Toroidal Fusion Reactor - UWMAK-1

FIGURE IV-C-1

Incoloy 800 has been selected for the Na-to-H₂O heat exchanger in a recent sodium-cooled nuclear system⁽²⁶⁾. For this study, however, a duplex tube consisting of Inconel in contact with the sodium and Croloy T22 on the steam side was utilized for the steam generator, as described in Volume 2 of this report.

The subjects addressed in this treatment will be: lithium-stainless steel compatibility; corrosion product transport; corrosion in auxiliary systems; and lithium purity requirements. The corrosion of stainless steel will be compared to corrosion behavior of other candidate Controlled Thermonuclear Reactor (CTR) materials. The principal alternate materials now being considered are molybdenum, niobium, vanadium and their alloys. Stainless steel behavior in lithium and in flibe (lithium beryllium fluoride) also will be compared.

2.) Lithium-Stainless Steel Compatibility

The size parameters and exposure conditions in the primary and secondary circuits and the steam system are summarized in Table IV-C-2.

a. Lithium Chemical Corrosion

Early corrosion results⁽²⁷⁾ indicated that iron, niobium, tantalum and molybdenum have good corrosion resistance to lithium up to 900°C; ferritic steels were resistant to lithium to ~800°C; austenitic steels had good resistance to ~500°C; nickel and its alloys had only limited resistance at 300-500°C. However, the studies often were conducted in lithium of questionable purity, precluding full confidence in the results.

There are essentially no long-term corrosion parameter studies for stainless steel in lithium. Projections of corrosion behavior, therefore, must be based on short-term data. Systematic studies of impurity effects also are largely lacking.⁽²⁸⁾

Gill, et al,⁽²⁹⁾ performed a series of corrosion tests in lithium over a temperature range from 510 to 612°C. The tests were conducted principally on 304 SS, but corrosion on other 300-series steels did not differ statistically from results on 304 SS. Corrosion rates from the study are summarized in Table C-3 as a function of temperature.

The data in Table IV-C-3 were determined for lithium flow rates in the range of 15 to 85 cm/sec, which are low compared to typical dynamic liquid metal systems. However, the magneto-hydrodynamic (MHD) effect⁽³⁰⁾ in lithium flowing in intense magnetic fields precludes high flow rates (see Section IV-B.) The maximum design flow rate in the UWMAK-I blanket

Table IV-C-2

U. W. Toroidal Fusion Reactor Parameters

Plant Rating	5000 MW _{th}
Major Radius	13 m
Minor Radius	5.5 m
Neutron Wall Loading	1.25 MW/m ²
<u>Primary Lithium Circuit^a</u>	
Area in Contact with Lithium	6 x 10 ⁴ m ²
Lithium Weight	1.7 x 10 ⁶ kg
Lithium Inlet Temperature	283°C
Lithium Outlet Temperature	483°C
Lithium Linear Flow Rate (Blanket)	4 cm/sec
Lithium Linear Flow Rate (Headers)	94 cm/sec
Lithium Mass Flow Rate	2 x 10 ⁷ kg/hr
Intermediate Heat Exchanger Area	1.9 x 10 ⁴ m ²
Neutron Flux, E = 0 - 14 Mev (Lithium-side of first wall)	4.7 x 10 ¹⁴ n/cm ² sec ^b
<u>Secondary Sodium Circuit^a</u>	
Area in Contact with Sodium	5.2 x 10 ⁴ m ²
Sodium Weight	7.4 x 10 ⁵ kg
Sodium Inlet Temperature	262°C
Sodium Outlet Temperature	411°C
Sodium Mass Flow Rate	9 x 10 ⁷ kg/hr
<u>Steam/Water Circuit^a</u>	
Heat Exchanger Area	3.2 x 10 ⁴ m ²
Maximum Steam Temperature	297°C
Maximum Steam Pressure	3.5 x 10 ⁵ kg/m ² (500 psi)
Steam Flow Rate	8.5 x 10 ⁶ kg/hr.

a. Preliminary design parameters; may be revised at a later date.

b. The primary current of 14 MeV neutrons is 5.7 x 10¹³ n/cm² sec.

is 4 cm/sec. It is also noted that at locations in the primary circuit where MHD effects are small, anticipated flow rates are up to 94 cm/sec.

Table IV-C-3
Corrosion Rates for Stainless Steel in Lithium⁽²⁹⁾

<u>Temperature</u> °C	<u>Corrosion Rate</u>	
	<u>mg/cm² mo.</u>	<u>micron/y</u>
300 (extrapolated)	0.01	0.15
400	0.11	1.6
500	1	15
550	3	45
600	6	90

The data of Gill, et al⁽²⁹⁾ suggest that corrosion rates are not strongly influenced by lithium flow rates in the range of their tests. Corrosion rates for a 1Cr18Ni9Ti steel in lithium at 700-900°C were higher under natural convection than in static lithium, but the effect was not large.⁽²⁸⁾ It will be assumed that the data in Table IV-C-3 account for flow rate effects on corrosion in the UWMAK-I, until fully pertinent data are available.

At the UWMAK-I inlet and outlet temperature extremes (~300 and 500°C) the corresponding thermal corrosion rates are 0.15 and 15 microns/y. These corrosion rates can be safely accommodated in the design thickness of the primary lithium system components. Maximum metal penetration from thermal corrosion will be 0.03 mm for the anticipated 2-year blanket life and 0.45 mm for a 30-year design life of other components. Potential contributions to the corrosion rate from radiation effects will be discussed in the following section. It would be desirable on thermal efficiency grounds to increase the lithium temperature. Estimates of the limiting temperature for stainless steel-lithium compatibility vary: Ref. 27 indicates 500°C; Ref. 29 suggests ~590°C. In another study, iron and austenitic stainless steels underwent severe solution corrosion, intergranular attack and mass transfer at 700 to 815°C. Type 316 SS was said to be suitable for only limited service at 590°C in a loop having a 100°C temperature gradient.⁽³¹⁾ While penetration rates in Table IV-C-3 at 600°C may be acceptable from a structural standpoint, they magnify an already serious corrosion transport problem, treated in a later section. Thus, if the corrosion rates indicated in Table IV-C-3 accurately represent corrosion product transport rates in the UWMAK-I, further increases in temperature appear undesirable.

The release of corrosion products from stainless steel does not generally occur in the stoichiometry shown in Table IV-C-1 for alloy constituents. Nickel was leached preferentially from 304 SS exposed to high-purity lithium at 500-600°C.⁽²⁹⁾ Deposits in the low-temperature loop region were high in nickel; Cr, Mn, Si and C also were detectable. In another study, nickel was removed preferentially from 316 SS in lithium at 590-769°C.⁽³²⁾ The attack was largely transgranular. Gamma iron

was found in cold-zone deposits. At 760-870°C, the attack was intergranular; when sigma phase was present, the cold-zone deposit was high in Cr, Ni and Fe. When sigma phase was absent, the cold-zone deposit was high in Ni and low in Cr. Carbon transport occurred when sigma phase was absent in low-nitrogen lithium. The carbon deposited in the cold zone as iron carbides. Tests in lithium above 540°C resulted in selective attack on nickel and carbon in austenitic stainless steels.⁽²⁷⁾

Selective leaching also occurs in refractory metal coolant systems. A Nb-1Zr alloy exposed to lithium at 1200°C (150°C ΔT) lost nitrogen, carbon and zirconium, which deposited in the cold region, principally as zirconium nitride.⁽³³⁾

A few studies are reported indicating effects of contaminants on stainless steel corrosion in lithium. High-purity lithium contaminated with 0.36 percent air reacted rapidly with 304 SS at 816°C, resulting in tube plugging after 72 hours.⁽³⁵⁾ Chromium was selectively removed from the stainless steel to depths of 10 mm under these conditions. In high-purity lithium, only mild intergranular attack occurred after 720 hours at 816°C. Chromium appeared to have an unusually high solubility in lithium in these studies, compared to data shown in Figure IV-C-2; selective leaching of nickel was not observed, in contrast to studies cited earlier.^(27,28,32) Furthermore, the corrosion rates in high-purity lithium appeared to be surprisingly low.

In Russian work cited earlier, corrosion rates were measured on a 1Cr18Ni9Ti steel in lithium at 700, 800 and 900°C.⁽²⁸⁾ Weight losses correspond to a metal penetration of ~30 microns in 1000 hours at 700°C in static, contaminated lithium (~1% O₂ and 1% N₂ by weight); penetrations in high-purity static lithium were 8-15 microns in 1000 hours. One weight percent nitrogen caused substantial increases in corrosion rate, while a similar oxygen concentration had little effect. Corrosion rates in static lithium were initially rapid, but decreased with time, apparently as the solution became saturated with corrosion products. Lithium flowing by natural convection caused corrosion rates higher than those in static lithium, due to mass transport effects. In the flowing system, specimens lost weight in the hot zone and corrosion products were transferred to the cold zone. The attack was largely intergranular. There was considerable evidence of selective nickel transport between materials with differing nickel contents.

Hoffman reported that nitrogen contamination in lithium resulted in accelerated corrosion of 316 SS at 870°C.⁽³⁶⁾ Devries reported that stainless steels, (including 316 SS) had good corrosion and stress corrosion resistance in air-contaminated lithium at 315 and 480°C, but the tests were short (up to seven days).⁽³⁷⁾

Oxygen has a significant effect on stainless steel corrosion in sodium, and there are indications that it may be desirable to operate Liquid Metal Fast Breeder (LMFBR) systems at <2 ppm oxygen.⁽³⁸⁾ The emerging evidence for lithium suggests nitrogen may be more significant than oxygen in stainless steel corrosion.

The corrosion of niobium and tantalum in static lithium was not affected by oxygen concentrations of 100-2000 ppm in the lithium, contrary to behavior in sodium.⁽³⁹⁾ On the other hand, oxygen dissolved in the refractory metals, above some threshold value (~400 ppm for Nb), caused rapid intergranular penetration by lithium. Zirconium alloy additions serve to getter the oxygen in the Nb and Ta and preclude the rapid penetration by lithium. Russian work indicates that oxygen dissolved in steel also enhances lithium penetration.^(28a)

Fusion reactors constructed from the refractory metals are projected to operate at substantially higher temperatures than the 500°C maximum UWMAK-I design temperature. Even at temperatures above 800°C, corrosion rates for the refractory metals generally are reported as "nil" or "slight". Selected exposures of refractory metals to lithium are summarized below:

<u>Material</u>	<u>Max. Temp</u> <u>°C</u>	<u>Thermal</u> <u>Gradient, °C</u>	<u>Velocity</u> <u>m/sec</u>	<u>Test Time</u> <u>hr</u>
Vanadium ⁽⁴⁰⁾	870	204	4.0	1194
Mo-0.5Ti ⁽⁴⁰⁾	815	93	4.0	694
Nb-1Zr ⁽³³⁾	1200	100-150	3.2	3000

Corrosion and mass transfer rates for V and Mo-0.5Ti were reported as nil after the above exposures. The weight loss from Nb-1Zr was up to 0.3 mg/cm² (0.07 mg/cm²mo), which is similar to the stainless steel mass transfer rate at ~375°C (Table III).

Corrosion data for stainless steels in a molten salt (LiF-BeF₂-ThF₄-UF₄) indicate a maximum corrosion rate of 50 microns/y at a hot leg temperature of 688°C and a cold leg temperature of 588°C.⁽³⁴⁾ Grain boundary attack and voids extend into the matrix, apparently due to selective chromium diffusion from the specimen. Weight losses occurred over exposures up to 32,000 hr.; the corrosion rates decreased with decreasing temperature over the range of 688 to 668°C. The corrosion rate was controlled by the solid state diffusion of chromium.

Another molten salt test series at 663°C indicated a corrosion rate of 28 micron/y for 304 SS. At 650°C, 316 SS corroded at maximum rates 20-25 micron/y. However, only a fraction of the system area corroded at the maximum rates.

b. Irradiation Effects on Corrosion

Irradiation of Type 316 stainless steel in lithium was reported to have no effect on corrosion at 540°C,⁽⁴¹⁾ but the neutron fluences ($3-7 \times 10^{16} \text{n/cm}^2$) were too low to draw definitive conclusions. Limited evidence suggests that radiation does not accelerate corrosion rates of stainless steel in sodium.⁽⁴²⁾ However, there is speculation that in high-flux sodium-cooled reactors, fast neutron sputtering would add substantially to corrosion rates,⁽⁴³⁾ involving damage to a rate-limiting ferrite layer. Similar layers also are reported to form on stainless steel exposed to lithium,^(29,32) and to flibe.⁽³⁴⁾ Whether such a layer would in fact develop on stainless steel at 500°C is not clear, but it would almost certainly be very thin (probably <1 micron).

Sputtering rates for stainless steel were calculated by Anno and Walowit to be 38 micron/y at a fast fission neutron flux of $10^{16} \text{n/cm}^2 \text{sec}$, applying a sputtering ratio for Cu (2×10^{-3}) in the absence of direct data for stainless steel.⁽⁴³⁾ At 600-700°C in sodium, the ferrite layer on stainless steel reaches a steady state thickness of ~10 microns⁽⁴⁴⁾. Assuming that the ferrite layer thickness controls the corrosion rate, the sputtering rate indicated above would have two effect on material transport: a) direct removal of material from the ferrite layer; b) thinning of the layer, resulting in increased corrosion of the steel substrate.

The calculated neutron current for the UWMAK-I is 5.7×10^{13} 14 MeV neutrons per sq. cm. per sec on the first wall. The total neutron flux on the inside surface of the first wall is $4.7 \times 10^{14} \text{n/cm}^2 \text{sec}$. (E, 0-14 MeV) and greater than 99 percent of the neutrons have energies above 0.1 MeV. Using an estimated sputtering ratio for iron of $9 \times 10^{-3} \text{atoms/n}$ ⁽⁴⁵⁾, the sputtering loss from the inside surface of the first wall is estimated to be 16 microns/y, based on the relationship:

$$\text{Metal Loss} = \frac{S \phi t A}{N_o \rho}$$

where, S is sputtering ratio (atoms/neutron); ϕt is neutron fluence; A is atomic weight; N_o is Avogadro's number; ρ is metal density. The area of the first wall surface is $\sim 4 \times 10^3 \text{m}^2$, slightly less than 10 percent of the total primary circuit area. Neutron attenuation probably will preclude major sputtering problems in other regions of the circuit. From the above calculation, sputtering would increase the corrosion product inventory in the primary circuit by ~10 percent (250 kg/y) by direct removal. However, the foregoing calculation is based on new sputtering ratios estimates for the data obtained under vacuum conditions. Sputtering into a condensed phase (e.g., liquid lithium) may produce substantially lower sputtering ratios. Therefore, sputtering calculations may have to be regarded with reservations until accurate sputtering ratios have been determined in liquid metal

systems. Recent weight measurements on stainless steel specimens exposed to the sodium coolant in EBR-II suggest that sputtering was negligible in terms of material transport.^(45a) The effect of sputtering appears to offer a potential accelerating effect on corrosion which would justify experimental study.

It also is possible that other radiation effects may accelerate corrosion processes in the lithium system. While direct parallels between aqueous and liquid metal systems are not justified, unusual effects of radiation on corrosion have occurred in aqueous systems⁽⁴⁶⁾ which were not anticipated from experiments in unirradiated systems. No unusual radiation effects have been recognized for stainless steel corrosion in sodium, but much less is known about the corrosion behavior of stainless steel or refractory metals in lithium.

c. Solubilities of Selected Elements in Lithium

While liquid-phase solubility is not necessarily rate-determining in liquid metal corrosion, it is an important consideration in evaluating corrosion and corrosion product transport mechanisms. Solubilities of stainless steel constituents⁽⁴⁷⁾ and refractory metals^(47,48) have been summarized. Solubility data from Ref. 47 are shown in Figure IV-C-2 indicating that the solubility of nickel in lithium is nearly two orders of magnitude higher than the solubilities of chromium and iron, and nearly three orders of magnitude higher than the refractory metals. The summary of solubility data in Ref. 48 indicates considerable variation in results from one observer to another, suggesting that solubilities in lithium must be applied with caution on present knowledge.

The temperature range for the data in Figure IV-C-2 is above the design temperature range for the UWMAK-I. If the solubility trends continue at lower temperatures, the solubilities will be approximately as shown in Table IV-C-4.

When saturated at 500°C, the UWMAK-I primary coolant (8×10^5 kg Li from Table IV-C-2) would contain ~280 kg of Ni. The significance of corrosion product transport to plant operation will be discussed later in this section.

Table IV-C-4
Solubilities of Selected Elements in Lithium^{a)}

<u>Element</u>	Solubility, ppm by wt. ^{b)}	
	500°C	300°C
Nickel	350	80
Iron, Chromium	8	2
Niobium, Molybdenum	3	1

a) Extrapolated from data in the temperature range ~940-650°C, Ref. 48.

b) In the UWMAK-I primary circuit, one ppm by weight is equal to ~1.5 kg.

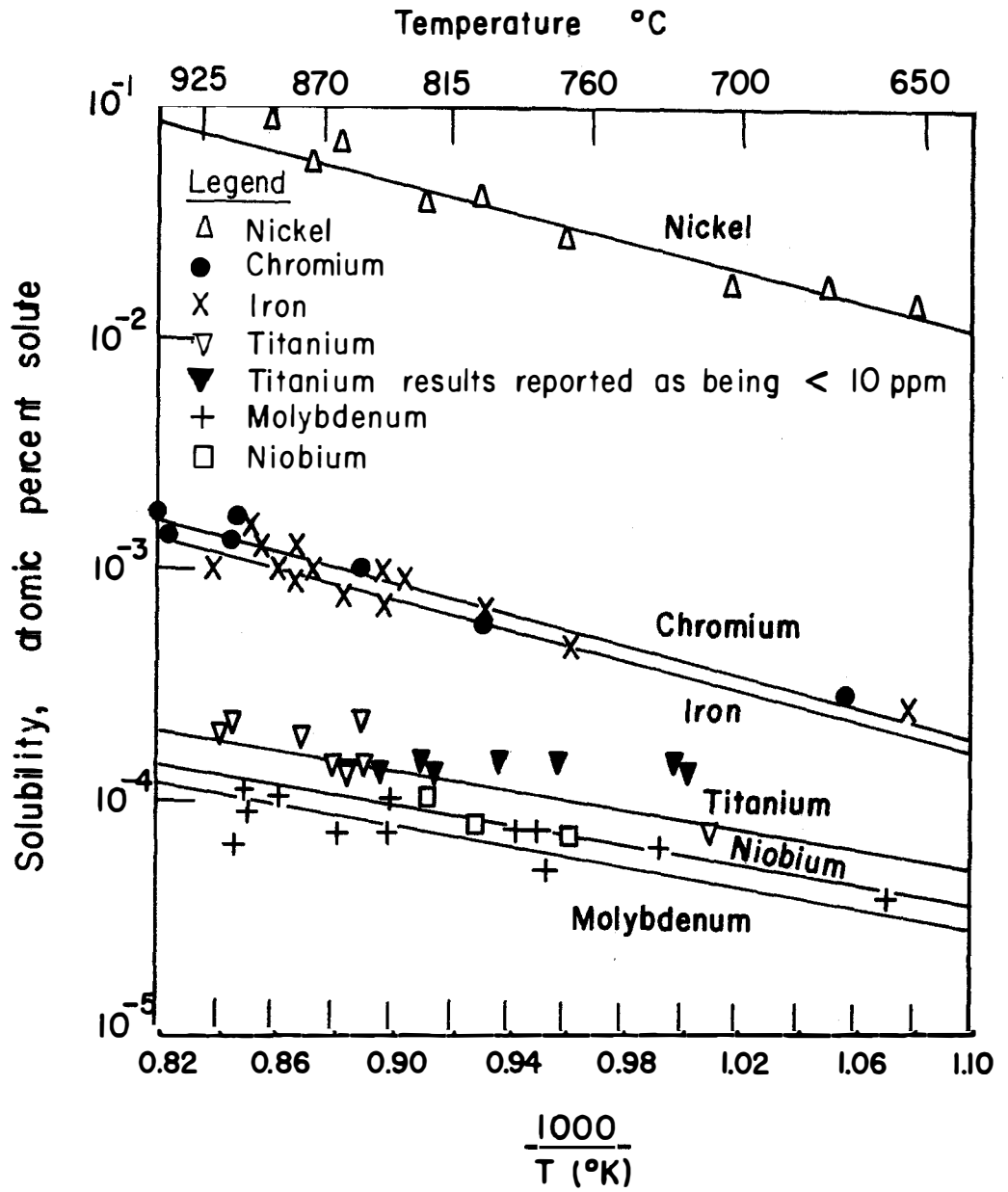


FIG. IV-C-2

SOLUBILITY OF SOME METALS IN LITHIUM (47)

Nitrogen contamination 25 to 150 ppm.

Solubilities of nitrogen and oxygen in lithium are summarized in Table IV-C-5.

Table IV-C-5
Solubilities of Nitrogen and Oxygen in Lithium

<u>Element</u>	<u>Temperature, °C</u>		
	<u>500°C^{a)}</u>	<u>400</u>	<u>250</u>
Nitrogen, ppm by weight	-	12,100	400
Oxygen, ppm by weight	1700	650	90

a) Extrapolated from data in the range 250-400°C cited in Ref. 48.

Consistent with the data in Table IV-C-5, oxygen concentrations in lithium can be reduced to <100 ppm by cold trapping; nitrogen is less susceptible to removal by cold trapping, due to its relatively high solubility in lithium, even near the lithium melting point (186°C).

d. Corrosion Mechanisms

Liquid metal corrosion mechanisms potentially include the following types of attack: (27,49)

- i. solution attack - relatively uniform dissolution of the metal by the liquid metal;
- ii. selective dissolution - leaching of one or more alloy constituents;
- iii. direct alloying - formation of surface films from reactions between the solid and the liquid metal;
- iv. intergranular penetration - often a variation of selective dissolution, where minor alloy constituents which concentrate in grain boundaries are selectively attacked. The attack often is accelerated by stress.
- v. erosion corrosion - mechanical attack by turbulent coolant, suspended particles, or in extreme cases, cavitation.
- vi. fretting corrosion - corrosion which results from vibration between two adjacent components in contact.
- vii. stress corrosion cracking - failure of a metal by the combined action of corrosion and mechanical stress.

The emerging data from stainless steel exposures in sodium, (43,44) lithium, (29,32) and flibe (34) indicate that mechanism ii is important in all three systems. Selective removal of nickel and/or chromium leaves an iron-rich layer (identified as ferrite in the liquid metal systems). Subsequent corrosion rates are considered by some observers to be controlled by solid state diffusion through the iron-rich layer. (29,32,34,43) However, other mechanistic interpretations have been presented for steel corrosion in sodium systems. (50)

Mechanism iv also is important in lithium metal (27,33,36) and molten salt (34) systems. Mechanism v probably will be relatively unimportant in CTR lithium primary circuits, due to low lithium linear velocities. Higher flow rates may occur in secondary circuits, where MHD effects are not restrictive, imposing a concomitant increase in the likelihood of erosion corrosion effects.

Evaluation of mechanism vi is highly empirical and difficult to predict without a detailed knowledge of component design and local exposure conditions. Mechanism vii also is difficult to predict on the basis of very few systematic stress corrosion studies. Russian work indicated that steel corrosion rates in lithium were accelerated by stress. (28a) A case of stress cracking was reported for 310 SS exposed to lithium. (51) Austenitic stainless steels resisted cracking in air-contaminated lithium at 315 and 480°C, but the exposures were short. (37) Di Stefano and Litman reported that no example of stress corrosion has occurred for refractory metals exposed to alkali metals. (49) However, the present approach to defining stress corrosion cracking behavior is largely empirical. Stress corrosion studies clearly will be a necessary factor in a CTR development program.

e. Summary of Thermochemical Relationships for Carbides, Nitrides and Oxides

The thermochemistry of selected carbides, nitrides and oxides appears in Appendix IV-C-1. Several generalizations from the literature and from Appendix IV-C-1 are summarized below.

- . Group IVB Metals (Ti, Zr, Hf) form oxides, nitrides, and carbides which are more stable than the corresponding lithium compounds^{a)} and are more stable than corresponding compounds from Groups VB, VIB and VIIB of the periodic table. (48)
- . Group VB metals (V, Nb, Ta) form oxides which are less stable than Li_2O , but their nitrides and carbides are more stable than the corresponding lithium compounds. (48)
- . Niobium, tantalum and vanadium lost oxygen to lithium; titanium and zirconium gettered oxygen from lithium at 816°C. (49)

a) Values in Appendix IV-C-1 show Li_2O to be slightly more stable than ZrO_2 , however, zirconium has functioned successfully as a getter in lithium systems.

- . Regarding the major stainless steel constituents, Fe and Ni compounds are less stable than the corresponding lithium compounds; Cr carbide is slightly more stable than Li carbide, but the lithium oxide and nitride are more stable than the chromium compounds.
- . Yttrium carbide and oxide appear to be slightly more stable than corresponding lithium compounds in the range of 500-650°C.

f. Mechanical Property Effects.

Lithium may degrade stainless steel mechanical properties by

- a) corrosion penetration, or
- b) addition to or removal of elements in the steel matrix.

Data in Table IV-C-3 suggest that corrosion penetration will be acceptable from a mechanical property standpoint for stainless steel exposed to lithium at 500°C. Carburization and decarburization and other material transport phenomena have occurred in stainless steel exposed to lithium, portending that under certain conditions changes in mechanical properties may occur. A detailed analysis of possible mechanical property changes is beyond the scope of this treatment, but data from stainless steel exposures to lithium and sodium will be discussed.

The ultimate tensile strength (UTS) of a 1Cr18Ni8Ti steel decreased by 14% and the ductility increased slightly on exposure to lithium at 700 and 800°C under natural convection.⁽²⁸⁾ The major changes occurred prior to 200 hours, but a small downward trend in UTS was present at test termination (1000 hours). Short-term (up to 500 hours) tests of the Cr-Ni-Ti steel in static lithium resulted in very little difference in UTS and elongation between specimens exposed to lithium and controls exposed to argon at 500°C.^(28a) In long-term exposures at 700°C, strength decreased with time, but there was little difference between behavior of specimens exposed to pure static lithium and those exposed to argon. Addition of 1 wt.% of oxygen to the lithium had only minor effects on strength. Carbide precipitation occurred in controls and specimens exposed to lithium, causing reductions in ductility.

Reductions in strength occurred for Cr-Ni-Ti steel specimens exposed to flowing lithium in a loop with a hot zone at 700°C and a cold zone at 400°C.^(28a)

Stress rupture experiments with 310 SS tubes exposed to lithium at 549 to 871°C showed no effect of exposure on tensile strength.⁽⁵¹⁾

Stress rupture properties of non-stabilized 304 and 316 stainless steels were degraded by sodium exposures for 10,000 hours at 705°C.⁽⁵²⁾ However, no changes in properties occurred in exposures at 620°C. Reduced strength at 705°C was due to loss of carbon and boron from the steels

and concurrent sigma phase formation. Stabilized alloys (321, 347, Incoloy-800) did not lose carbon, but did lose boron and nitrogen, though in smaller quantities than non-stabilized alloys.

The above data suggest that high-purity lithium at 300-500°C probably will not induce performance-limiting degradation of stainless steel mechanical properties, provided that the presence of zirconium hot traps and tritium getter materials do not cause excessive loss of carbon and other interstitial materials from the stainless steel. If carbon transport from 316 SS proves to be excessive, use of stabilized steels may be necessary. Carbon and nitrogen transfer from stainless steel to Nb-1Zr in potassium at 760°C were reduced or eliminated when 321 SS, containing titanium was substituted for non-stabilized 316 SS.⁽⁵³⁾ Stabilized alloys also have been effective in controlling carbon transport in liquid sodium systems.⁽⁵⁰⁾

g. Lithium Purity

Lithium purity is an important consideration in defining the corrosion of materials exposed to a lithium coolant. Impurities in lithium may be grouped into three classes:⁽⁵⁴⁾

1. foreign alkali or alkaline earth metals
2. transition and heavy metals
3. nonmetals, principally oxygen, carbon, hydrogen and nitrogen.

Systematic studies of oxygen and nitrogen effects on stainless steel corrosion in lithium were discussed in an earlier section, indicating that nitrogen at a concentration of 1 wt. percent had an adverse effect at 700°C; oxygen at a similar concentration has very little effect. Other evidence points to nitrogen as the more significant impurity, having an adverse effect on stainless steel corrosion. Systematic studies of metallic impurity effects on stainless steel corrosion in lithium are lacking.

Typical analyses of as-produced lithium are summarized in Table IV-C-6. Lithium does not appear to become contaminated by contact with anhydrous gases, (O₂, CO₂, N₂) at least to 160°C. At elevated temperatures, lithium reacts readily with nitrogen to form a nitride.⁽⁵⁴⁾

Effects of successive purification steps on a given batch of lithium are summarized in Table IV-C-7. The as-received impurity content in lithium from a commercial source is shown in the upper analysis. Comparing the as-received analysis in Table IV-C-7 with Table IV-C-6, nitrogen is substantially higher in Table IV-C-7; as-received metallic impurities are relatively low in Table IV-C-7; oxygen and carbon (not specified in Table IV-C-6) are 130 and 149 ppm respectively in the as-received lithium.

Table IV-C-6

Purity of Commercial Lithium⁽⁵⁴⁾

<u>Metal Grade</u>	<u>99.5%^{a)}</u>	<u>Reactor^{b)}</u>
Major Impurities		
Na	150	40
K	70	75
Total Alkali Metals	220	115
Alkaline Earths	300	10
Other Metals	150	70
Chlorine	70	50
Nitrogen	100	40
American Producers	Footc Mineral Lithium Corp. Maywood Chemical	
Price/lb. (1967)	\$9-\$11	\$12.00

Impurity values in ppm by weight

a) Typical analyses

b) Expressed impurity levels are maximum values.

Table IV-C-7

Influence of Purification Techniques on Lithium Purity (55)

IDENTITY	ppm	ppm	ppm																					
	N	O	C	Ag	Al	B	Be	Ca	Cb	Co	Cr	Cu	Fe	Mg	Mn	Mo	Na	Ni	Pb	Si	Sn	Ti	V	Zr
LITHIUM AS- RECEIVED	835	130	149	<5	<5	-	<5	135	<25	<5	<5	<5	<5	5	<5	<5	55	<5	<25	5	<25	<5	<25	<5
LITHIUM AS- RECEIVED AFTER FILTRATION	791	155	99	<5	<5	-	<5	55	<25	<5	<5	<5	5	<5	<5	5	<135	<5	<25	5	<25	<5	<25	<5
LITHIUM AFTER HOT TRAPPING 280 HOURS AT 1500°F	<10	-	25	<5	<5	<55	<5	5	<25	<5	<5	55	5	5	<25	<5	55	5	<25	5	<25	5	<25	<25

Filtering (single-pass) at 205°C through a 5 micron sintered Type 316 SS filter had little beneficial effect on impurity levels. However, heating in a titanium-lined zirconium-gettered hot trap at 815°C for 280 hours sharply reduced nitrogen, oxygen, carbon and calcium. The area of the zirconium getter was 6.5 cm² per 3.4g of lithium. The zirconium surface area which would be required to clean up 1.4 x 10⁶ kg Li is ~2.7 x 10⁹ cm². Assuming a foil thickness of 0.01 cm, the zirconium getter weight in the primary system (LCS, in Figure IV-C-1) would be ~10⁵ kg; while this may not be the optimum amount of zirconium for a large system, it probably is of the right order of magnitude. The amount of getter required for the secondary sodium system would be nearly an order of magnitude less than the primary system requirement. The relatively high getter cost opts for careful pre-purification of lithium and for system design and operation to minimize impurity in-leakage. The fabricated cost of zirconium foil in 1973 is ~\$45 per kg. On this basis, the cost of the getter for the primary system would be ~\$4.5 x 10⁶ in 1973 dollars. Based on published data,⁽⁵⁶⁾ the 0.01 cm foil thickness appears to be marginal; thicker foil may be necessary, depending on the required gettering capacity.

The example cited above (Ref. 55) indicated that zirconium gettered oxygen from lithium to undetectable concentrations, despite indications from thermodynamic data at 870°C that Li₂O is slightly more stable⁽⁵⁷⁾ (-105 kcal/g atom O for Zr; -106 kcal/g atom O for Li₂O). Data in Table A-IV-C-3 indicate that between 25 and 625°C the equilibria also slightly favor stability of Li₂O. It is possible that certain impurities in the system altered the thermodynamic relationships or that the thermodynamic data are in error. However, it seems more likely that the thermodynamics of the oxides does not accurately state the energetics of a system where oxygen is dissolving rapidly into the base metal, as it would be expected to do for the case of zirconium at the hot trap temperature (815°C).

Yttrium has been recommended as a hot trap material for lithium systems, because the thermodynamics slightly favor Y₂O₃ formation over Li₂O formation.⁽⁵⁷⁾ From the above discussion, it is not clear that yttrium has an advantage over the zirconium for the hot trap getter.

A desirable feature of the lithium cleanup system hot trap would be to minimize tritium accumulation in the getter; however, both yttrium and zirconium getters are strong hydride-formers. This problem can be minimized if the vapor pressure of tritium in the LCS is higher than in the tritium extraction bed. Because the tritium vapor pressure above ZrT₂ is higher than for YT₂ (Figure VIII-C-2) and for both tritides the vapor pressure increases with temperature, then the LCS should contain Zr at a relatively high temperature and the tritium extraction bed should contain yttrium at a lower temperature, as shown in Figure IV-C-1.

The entire lithium purification sequence would be operative as follows:

- a) Careful purification of the lithium charging into the fusion reactor, probably involving filtration and possibly hot trapping and special treatments to reduce specific metal impurities.
- b) Final purification with the lithium cleanup system containing zirconium and operating between a temperature yet to be determined between 550° and 816°C. In sodium, the minimum effective temperature for zirconium hot trap operation was ~550°C⁽⁵⁷⁾; however, the use of zirconium as a getter in a lithium system has only been demonstrated at 816°C⁽⁵⁵⁾
- c) When tritium generation begins, the valves to the TEB, containing yttrium at 283°C, will be opened. The LCS will remain in the system but at a temperature between 550-816°C. As soon as the #1 TEB is saturated with YT_2 , its valves are closed and #2 TEB is utilized. Immediately, the lithium is drained from #1 TEB and the tritium recovered by thermal regeneration of the yttrium. After several sequences of these operations, the oxygen and nitrogen levels in the lithium may be sufficiently low so that the LCS can be disconnected and used only as required to maintain acceptable impurity concentrations. Nitrogen appears to be the critical impurity from the standpoint of minimizing stainless steel corrosion, but a high nitrogen solubility in lithium is indicated. This makes cold trapping relatively ineffective for nitrogen removal and suggests that a cold trap probably would be unnecessary in the lithium systems.

The clean up of sodium for the intermediate heat exchanger system will follow accepted practices^(54,57). Initially, the sodium impurities will be filtered and cold-trapped at ~120°C to remove gross quantities of oxygen, nitrogen, carbon and hydrogen. Then, the hot-trap containing zirconium (NaCS) (Figure IV-C-1) will be activated at 550°C. This hot-trap will probably remain in operation during the power cycle in order to remove steam and air which will leak by diffusion or failures in the steam generator tubes.

3.) Corrosion in Auxiliary Systems

a. Lithium Cleanup System

Zirconium corrosion in high purity lithium was reported as nil after the following exposures: 1070 hours at 816 to 871°C; 400 hours at 1000°C.⁽⁴⁸⁾ In general, the corrosion behavior of zirconium in lithium getter applications appears to be satisfactory. Specific data are needed to indicate effects of impurities, e.g., carbon and nitrogen, on the long-term corrosion and embrittlement of thin foils in lithium.

b. Tritium Extraction System

Relatively little is known about yttrium corrosion in lithium at UWMAK-I temperatures. In the temperature range 1041-1150°C, yttrium was used as a getter in a lithium system.⁽⁵⁸⁾ After what appears to have been a 30-hour exposure, the lithium had dissolved 5 wt.% yttrium; the yttrium corrosion was substantial but not catastrophic. Yttrium forms an oxide slightly more stable than Li₂O at 500°C (Appendix, Table A-IV-C-1) and is used to getter oxygen from lithium.⁽⁵⁷⁾ This may suppress yttrium dissolution, but it may also inhibit tritium extraction and eventually will lead to oxygen saturation of the yttrium. The yttrium carbide also is more stable than lithium carbide and carbides of the major stainless steel components except chromium. Some carbon transport to yttrium therefore may occur. The effect of carbon, nitrogen and oxygen transfer on yttrium corrosion and kinetics of tritium absorption will need to be investigated.

c. Helium Circuit for Cooling the Shield

The helium coolant for the UWMAK-I shield will be contained in a stainless steel circuit. Preliminary design calculations indicate that the system temperature probably will not exceed 200°C. The principal impurities in helium are H₂O, CO, CO₂, H₂, N₂ and CH₄. The total impurity in the helium can be controlled to about one ppm by volume.⁽⁵⁹⁾ Corrosion of stainless steel in helium has not caused problems of metal penetration even at temperatures in the range of 600-980°C.⁽⁶⁰⁾ However, some oxide spallation has occurred at the higher temperatures. At 416°C, 316 SS has a weight loss of 5 mg/dm² (~0.06 micron) after 1000 hours. Based on the above evidence, it is safe to assume that corrosion will not be a problem in the shield cooling circuit.

On the contrary, DeVan has indicated concern regarding corrosion of niobium in high-purity helium.⁽⁴⁰⁾ Other work indicates that substantial corrosion and oxygen solution can occur in niobium at 1000-1200°C in helium having impurity concentrations of ~1 vpm.⁽⁵⁹⁾ The basic questions are

- a) whether the relatively large niobium surface area can getter the impurities initially in the niobium without reaching damaging concentrations of impurities,
- and b) whether in-leakage can be controlled to tolerable levels.

d. Heat Exchanger Corrosion

The sodium-steam interface is a critical area in the context of corrosion control. Stress corrosion cracking failures of steam generators have occurred in nuclear systems.⁽⁶¹⁾ The prospects of sodium-steam reactions and of tritium release to the steam system will require that a highly-reliable steam generator material is available when the first system is built. The design material for the steam generator in this study is a duplex tube consisting of a 1.02 mm wall of stainless steel and a 0.63 mm wall of ferritic steel, Croloy T22. The intermediate heat exchanger design utilized 304L stainless steel; tritium diffusion rates are lower for 304 than for 316 SS,⁽²⁵⁾ and 304 SS is reported to have better metallurgical stability than 316 SS.⁽²⁶⁾

Steam-side corrosion resistance of austenitic stainless steels and nickel-base alloys has proved satisfactory in sodium-steam generator applications, from the standpoint of metal penetration. With regard to stress corrosion cracking, the nickel-base alloys are somewhat better but not immune.⁽²⁶⁾ For the high-integrity needed in a lithium-cooled CTR, development of heat exchanger materials with improved stress corrosion resistance and concomitant compatibility with lithium is a major need.

Considerable evaluation preceded the selection of Incoloy-800 as the steam generator material for the Westinghouse LMFBR demonstration plant.⁽²⁶⁾ Because nickel-base alloys have relatively poor corrosion resistance in lithium⁽²⁷⁾ their use for lithium systems without a comprehensive evaluation program must be treated caustiously.

The trend in liquid metal systems for corrosion to occur at high-temperature locations and deposition to occur at low-temperature locations will have a strong bearing on heat exchanger corrosion performance in a lithium-cooled CTR. Experience with steam generators in sodium systems has confirmed minimal corrosion and substantial deposition.⁽²⁶⁾ However, some selective removal of alloy agents and interstitial impurities has occurred, even at cold-leg locations. Selection of a material which is amenable to chemical cleaning of fouled heat transfer surfaces probably would be a major consideration in a lithium-cooled stainless steel circuit.

4.) Corrosion Product Transport

Corrosion products generated at one location in a flowing circuit typically are transported and deposited at other locations. This process has caused some problems in water reactors.^(62,63) Potential corrosion product problems and associated solutions are being evaluated in LMFBR technology studies, including identification of the types and amounts of mobile corrosion products which are generated^(38,52,64-66); where they deposit; the consequences of the deposits and their associated radioactivity on plant performance; methods to control and remove the deposits which develop in liquid metal circuits.

Corrosion product deposits up to 0.25 mm thick developed in a stainless steel circuit exposed to sodium for 10,000 hours at 720°C (hot leg) and 550°C (cold leg).⁽⁶⁴⁾ The amount and composition of deposits varied with location in the circuit. Deposition varied as a function of temperature, coolant velocity, turbulence level, and operating time. Temperature differences as small as ~30°C promoted deposition. Maximum deposition occurred at the lowest temperature in

Note: The low lithium temperature (200-325°C) in the divertor system will result in minimal corrosion (see Table IV-C-3). Corrosion product transport from the divertor plate (approximately 250 m²) will be less than 1 kg/y.

the circuit. The deposition rates generally decreased with exposure time, tending to reach a steady state rate of 0.1 to 0.2 mg/cm²hr after a few thousand hours.

In fusion reactor systems relying on lithium or molten salts for heat transfer, corrosion product transport considerations may have a significant bearing on materials selection and plant design. The four essential factors considered here are: corrosion product generation, transport, deposition and removal.

Corrosion product generation in CTR's is amplified by the relatively large areas in contact with the primary coolant. The system parameters which apply to the Wisconsin Toroidal Fusion Reactor (UWMAK-I) appear in Table IV-C-2. The primary circuit area is $6 \times 10^4 \text{ m}^2$; by comparison, the area of the Fast Flux Test Facility (FFTF) primary circuit is $\sim 1 \times 10^3 \text{ m}^2$. (38)

Accurate assessment of corrosion phenomena in lithium-cooled CTR's is compromised by the relatively small amount of pertinent data. The UWMAK-I lithium inlet and outlet temperatures are ~ 300 and 500°C . Corresponding stainless steel corrosion rates are reported to be 0.01 and 1 mg/cm²mo based on the data of Gill, et al in exposures to flowing lithium (15-85 cm/sec). (29) The corrosion rates, extended to an annual basis, indicate that approximately 2500 kg/y of corrosion product would be released to the primary circuit. In addition to the thermal corrosion cited above, a potential substantial contribution from radiation sputtering on the inside surface of the first wall was identified in an earlier section, amounting to about ten percent of the thermal value ($\sim 250 \text{ kg/y}$). Further increases in corrosion rate also may occur if sputtering removes a rate controlling layer from the stainless steel surface. However, accurate measurement of sputtering ratios in liquid metal systems will be necessary before the effect on material transport can be clearly defined.

While the accuracy of the calculated rates of corrosion product release are in question, the magnitudes focus on the importance of considering corrosion product generation and transport in future experiments and eventually in plant design and materials selection if the order of magnitude is correct.

The corrosion of 316 SS in lithium at $500\text{--}600^\circ\text{C}$ does not release the individual constituents in the stoichiometry shown in Table IV-C-1. Nickel is reported to be the principal element transferred; chromium, manganese, silicon, and carbon were detectable in the stainless steel corrosion product deposits. (29,31) Selective leaching of nickel results in development of a ferrite phase on the corroding stainless steel surface. The corrosion rate reportedly is controlled by solid-phase diffusion through the ferrite layer in the temperature range of $510\text{--}610^\circ\text{C}$. (29,32) Corrosion data for other CTR candidate materials (alloys of Mo, Nb, and V) suggest that corrosion product transport rates from thermal corrosion may be orders of magnitude lower than those calculated

for stainless steel, even at higher operating temperatures projected for CTR's constructed from the refractory metals. The corrosion rates generally are reported as "nil" or "slight". Quantitative corrosion rate data for a Nb-1Zr alloy in flowing lithium at 1200°C⁽³³⁾ indicate that the corrosion product transport rate would be ~5 kg/y in a system having the area shown in Table IC-C-2. The 5 kg would include principally N, C and Zr. Very little Nb was found in the transferred deposits.

On the other hand, sputtering may contribute to sizable mass transport for the refractory metals, paralleling the earlier calculation for stainless steel. Assuming a niobium sputtering rate about a factor of two lower than the number used in the stainless steel calculation,⁽⁴⁵⁾ sputtering from the first wall would propel ~125 kg/y into the circulating lithium, but the reservations mentioned earlier regarding lack of sputtering data in liquid metal systems also apply to this calculation.

Corrosion rates cited earlier for stainless steel in flibe are on the order of 25 micron/y at 650-680°C.⁽³⁴⁾ The temperature range is near the operating temperature of a helium-cooled CTR having a molten salt blanket.⁽⁶⁷⁾ Since the flibe is not the heat transfer medium, corrosion product transport and deposition will be less severe than in lithium-cooled stainless steel plants. However, circulation of the flibe to the tritium extraction system almost certainly would result in radiation problems and possibly fouling and plugging, in view of the relatively high stainless steel corrosion rates.

5.) Problems Associated with Radioactive Crud

Mechanisms of corrosion product transport include dissimilar-metal mass transfer and temperature gradient mass transfer. Both types will occur in the UWMAK-I circuits. Dissimilar metal transfer can occur between stainless steel, zirconium getter beds, and the yttrium metal in the tritium extraction beds. Temperature gradient mass transfer will occur by dissolution of stainless steel in the high-temperature regions and deposition in the low-temperature regions.

Corrosion products will be carried to all parts of a lithium-cooled primary circuit in solution and also possibly as particulates, with maximum deposition occurring in the heat exchanger and tritium extraction systems. Potential problems due to corrosion product deposition in the primary CTR unit include: fouling of heat transfer surfaces; plugging of heat exchanger tubes, valves and instrument sensor lines; fouling of tritium extraction surfaces; development of high radiation levels in reactor maintenance areas. The radioactivity content of 2500 kg of stoichiometric stainless steel corrosion product is estimated to be 4×10^6 curies. Radiation levels in an FFTF heat transport system cell are estimated to be 1 to 15 Rad/hr,⁽³⁸⁾ based on a stainless steel corrosion product inventory which appears to be approximately three orders of magnitude below the estimated CTR inventory, portending that relatively high radiation

fields would develop (1000-10,000 Rad/hr) near out-of-reactor regions of a stainless steel CTR circuit. Based on half life considerations, stainless steel is the least desirable and vanadium appears to be the most desirable for rapid decay of activity in reactor maintenance areas.⁽⁶⁸⁾

Stainless steel is the only CTR candidate material with a well-developed industry, opting for its consideration as a construction material in first-generation plants. If this incentive persists as the time to build the first plant approaches, a major effort will be needed to determine corrosion and corrosion product transport rates under prototypical CTR conditions. Extraction of corrosion products from the primary system almost certainly would be required if the estimated transport rate is accurate.

Preliminary studies are underway to investigate corrosion product removal from LMFBR systems, either continuously⁽⁶⁹⁾ or by dissolution of deposits during plant shutdowns.⁽⁶⁶⁾ Possible methods for continuous corrosion product removal include hot trapping, cold trapping and high temperature ion exchange. However, the technology for successfully applying these methods remains to be developed. Proper selection of materials, e.g., minimizing cobalt in the primary loop, can assist in control of radiation buildup in maintenance areas. Studies of decontamination techniques for LMFBR systems are underway,⁽⁶⁶⁾ but are in early stages. Successful operation of lithium-cooled stainless steel CTRs almost certainly would require technology development for corrosion product control paralleling that now underway for LMFBR systems.

6.) Summary of Corrosion Product Transport Considerations

In summary, Table IV-C-8 compares corrosion product transport effects for two materials, 316 SS and Nb-1Zr. Literature values for thermal corrosion of stainless steel at 300-500°C indicate substantially higher rates than the rates for Nb-1Zr at 1200°C. Therefore, corrosion product transport for stainless steel appears to present substantial problems to CTR operation from corrosion product deposition and radioactivity transport. Corrosion product removal during plant operation, during shutdowns, or both almost certainly would be required.

A system designed at Princeton⁽⁶⁷⁾ consists of a molten salt blanket and a helium coolant. In this concept, transport of large amounts of corrosion product to the primary heat exchanger could be avoided, but substantial problems may occur from transport to the tritium extraction system. However, the distribution of radioactivity would be more localized and heat exchanger fouling would be avoided, suggesting that the concept also may be attractive for a lithium system where corrosion product transport presents problems.

Thermal corrosion of Nb-1Zr appears to be sufficiently low, even at 1200°C, to offer essentially no problem from deposition or radioactivity distribution. However, sputtering imposes additional considerations. In the case of stainless steel, sputtering adds an increment to an already-serious problem. In the case of Nb-1Zr, sputtering becomes the major source of circulating material, portending that it may impose the need for corrective measures in a system which otherwise might operate without cleanup.

TABLE IV-C-8

Comparison of Corrosion Product Transport in Lithium Primary Coolant

	<u>Source of Product</u>	
	<u>Thermal Corrosion</u>	<u>Sputtering</u> ^{a.}
316 Stainless Steel	2500 kg/y ^{b.}	250 kg/y
Nb-1Zr	5 kg/y ^{c.}	125 kg/y

- a. Based on sputtering from first wall, which is approximately 10 percent of the total primary system area; however, sputtering ratios were measured under vacuum conditions and therefore must be regarded with reservations until accurate measurements are made in liquid metal systems.
- b. Based on thermal corrosion rates in the range of 300-500°C.
- c. Based on thermal corrosion rates at 1200°C, for the same system area used for 316 stainless steel.

IV-D. Thermal and Mechanical Stresses in the Heat Removal Cells

One of the major difficulties in the design of a fusion reactor is the selection of a material for the front wall. From a stress standpoint, the difficulty arises from the fact that materials tend to become very brittle under constant neutron bombardment. (See Chapter VI) In the case of stainless steel, the main causes of embrittlement are the displacement of atoms from their equilibrium positions and the helium generated by (n,α) reactions. Experimental data available for stainless steel indicates that during the first 2-3 years of projected operation, strains of more than a few tenths of a percent should never be exceeded or the metal will fracture in a brittle manner.

The front wall will experience maximum embrittlement and it is, therefore, imperative to keep the stresses in it as low as possible. Figure IV-D-1 is an isometric view of the front wall. It consists of rectangular cells with the long dimension in the toroidal direction, terminating in a cylindrical skin which faces the plasma. The cells are 7.5 cm wide and 1 m long.

There are three main sources of stresses at the front wall facing the plasma. They are:

- (a) Thermal stresses induced by the difference in temperature across the front wall of the heat removal cells.
- (b) Pressure stresses induced by the coolant.
- (c) Mechanical stresses due to material weight, support structures and vacuum load.

1. Thermal Stresses

The thermal load on the front wall of UWMAK-I is divided into two parts: (1) the energy radiated to the wall by the hot plasma in the form of photons and charged particles, $W_s = 22.6$ watts/cm², (2) the nuclear heating due to moderation and nuclear reactions in the metal, $W_n = 13$ watts/cm³. The total energy which produces the temperature gradient in the front wall is

$$W = (W_s + W_n t) \text{ watts/cm}^2 \quad \text{IV-D-1}$$

where t is the material thickness.

The temperature gradient is then,

$$\Delta T = \frac{1}{k} (W_s + \frac{W_n}{2} t) t \quad \text{IV-D-2}$$

in which k is the thermal conductivity.

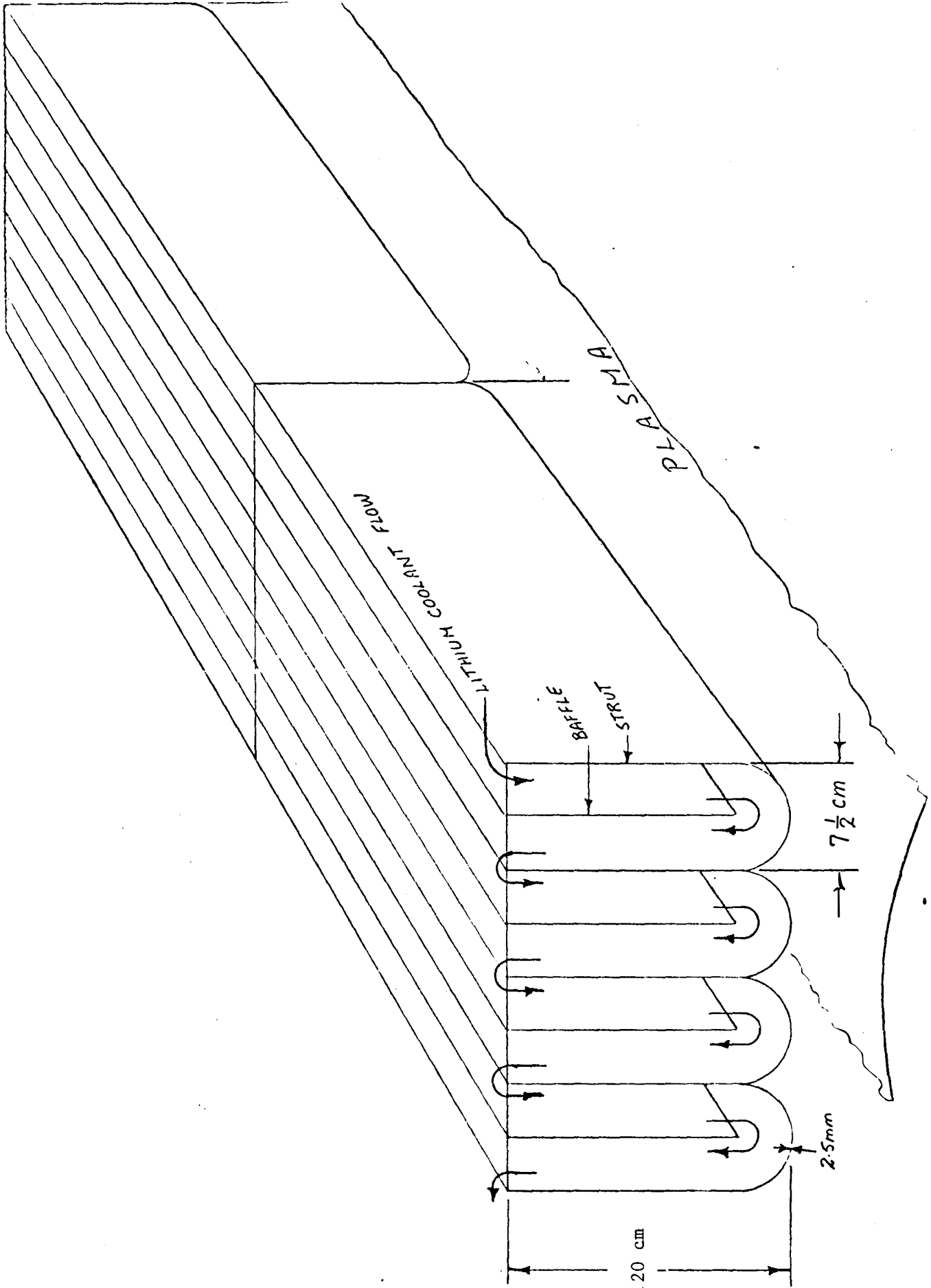


Fig. IV D-1 ISOMETRIC VIEW OF UMWAK-1 HEAT REMOVAL CELLS

The equation for thermal stress is then

$$\sigma_{th} = \pm \frac{\alpha}{2} \frac{E}{(1-\nu)} \Delta T$$

or

$$\sigma_{th} = \pm \frac{\alpha}{2} \frac{E}{k(1-\nu)} \left(W_s t + \frac{W_n}{2} t^2 \right) \quad \text{IV-D-3}$$

where α is the coefficient of expansion, E is the modulus of elasticity and ν , the Poisson's ratio at the average temperature of the wall, and the sign of the stress indicates compression (-) or tension (+).

The properties of 316 SS at 500°C used in equation IV-D-3 are the following:

$$\begin{aligned} \alpha &= 18 \times 10^{-6} \text{ } ^\circ\text{C}^{-1} \\ \nu &= 0.30 \\ E &= 23.2 \times 10^6 \text{ psi} \\ k &= .0478 \text{ cal sec}^{-1} \text{ cm}^{-1} \text{ } ^\circ\text{C}^{-1} \end{aligned}$$

The thermally induced stress is plotted in Figure IV-D-2 as a function of wall thickness. The overall effect puts the outer fiber (facing the plasma) of the cylindrical cell into compression and the inner fiber (on the lithium side) into tension.

2. Pressure Stresses

The hoop stress in a thin walled cylinder is expressed as

$$\sigma_h = \frac{pr}{t} \quad \text{IV-D-4}$$

where p is the pressure, r the average radius of the cylinder and t the material thickness.

Although the system pressure may be higher, the front wall will not experience any pressure greater than 285 psig (see Section VI-B). A pressure of 300 psi was used in computing the hoop stress which is intended to include the atmospheric pressure on the blanket surrounding the vacuum chamber.

The longitudinal stress is equal to one half of the hoop stress and is, therefore, neglected here.

The thermal and hoop stresses for 316 stainless steel at 500°C are tabulated in Table IV-D-1 and plotted in Figure IV-D-2 as functions of

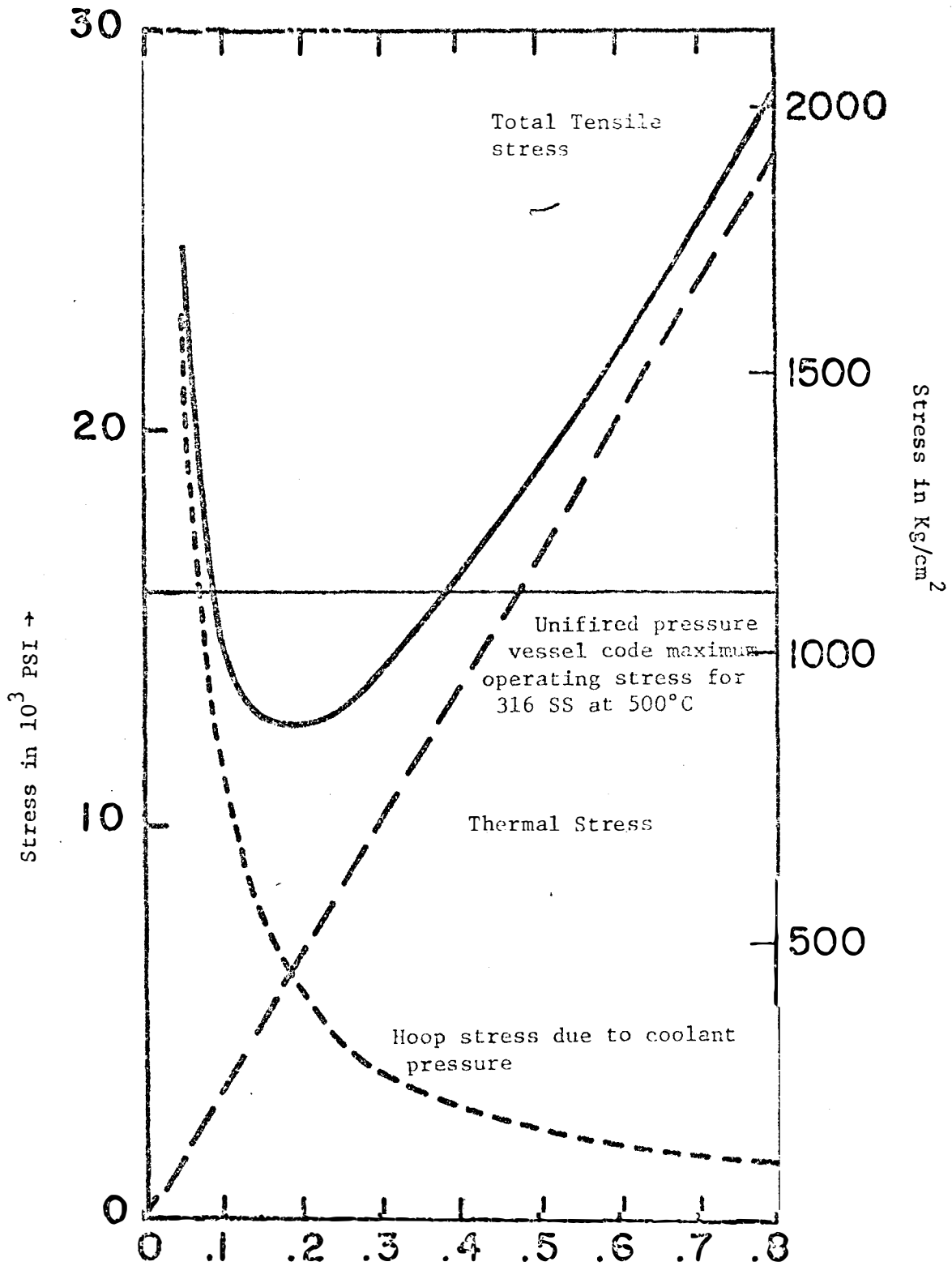


Figure IV-D-2 Stresses in a 316 SS Front Wall As A Function of Metal Thickness at 500°C and 300 PSIA Coolant Pressure

TABLE IV-D-1

Thermal and Pressure Induced Stresses
in
316 Stainless Steel at 500°C^(a)

<u>Wall Thickness</u> (cm)	<u>Thermal Stress</u> (psi)	<u>Pressure Hoop Stress</u> ^(b) (psi)	<u>Maximum Tensile</u> <u>Stress Total</u> (psi)
0.025	± 842	45,720	46,562
0.050	± 1,685	22,860	24,545
0.100	± 3,370	11,430	14,800
0.150	± 5,055	7,620	12,675
0.200	± 6,739	5,715	12,454
0.250	± 8,424	4,572	12,996
0.300	±10,109	3,810	13,919
0.350	±11,794	3,266	15,060
0.40	±13,479	2,858	16,337
0.50	±16,848	2,286	19,134
0.60	±20,218	1,905	22,123
0.70	±23,588	1,633	25,221
0.80	±26,957	1,429	28,386
0.90	±30,327	1,270	31,597
1.00	±33,697	1,143	34,840

a) Surface wall loading 22.6watts/cm² and nuclear heating rate of 13watts/cm³

b) 300psia coolant pressure

wall thickness. The sum of these stresses is given as the total stress which is tensile on the inside of the wall facing the lithium coolant. The difference is, of course, the stress on the outside of the wall facing the plasma. The fact that the maximum tensile stress is on the inside of the cell means that cracks, if initiated, will propagate toward the plasma zone. Allowing for sputtering (Chapter VI) and corrosion (Section IV-C), a front wall of 2.5 mm was selected. The total stress here is 12,400 psi. A value of 16,000 psi is given as the maximum allowable working stress for 316 SS at 500°C by the Unfired Pressure Vessel Code. Even at this stress, taking the reduced E for 316 SS at 500°C into account, the total elongation under equilibrium conditions is 0.07%.

For purposes of comparison, similar total stress curves for molybdenum, niobium and vanadium front walls are presented in Figure IV-D-3. The conditions are as follows:

- a. Molybdenum at 1000°C and Li at 300 psia.

$$\alpha = 6.7 \times 10^{-6} \text{ } ^\circ\text{C}^{-1}$$

$$E = 39.6 \times 10^6 \text{ psi}$$

$$\nu = 0.32$$

$$k = 0.275 \text{ cal cm}^{-1} \text{ sec}^{-1} \text{ } ^\circ\text{C}^{-1}$$

- b. Niobium at 1000°C and Li at 300 psig

$$\alpha = 8.52 \times 10^{-6} \text{ } ^\circ\text{C}^{-1}$$

$$E = 15.3 \times 10^6 \text{ psi}$$

$$\nu = 0.39$$

$$k = 0.151 \text{ cal sec}^{-1} \text{ cm}^{-1} \text{ } ^\circ\text{C}^{-1}$$

- c. Vanadium at 800°C and Li at 300 psig

$$\alpha = 10 \times 10^{-6} \text{ } ^\circ\text{C}^{-1}$$

$$E = 17.9 \times 10^6 \text{ psi}$$

$$\nu = 0.36$$

$$k = 0.098 \text{ cal sec}^{-1} \text{ cm}^{-1} \text{ } ^\circ\text{C}^{-1}$$

It is interesting that the total stress for a molybdenum wall is the same as for a niobium wall under identical conditions in spite of their different properties. However, the allowable working stress for molybdenum is higher.

It is immediately obvious that the refractory metals display a much lower total stress than stainless steel because of their lower coefficient of expansion, and higher thermal conductivity.

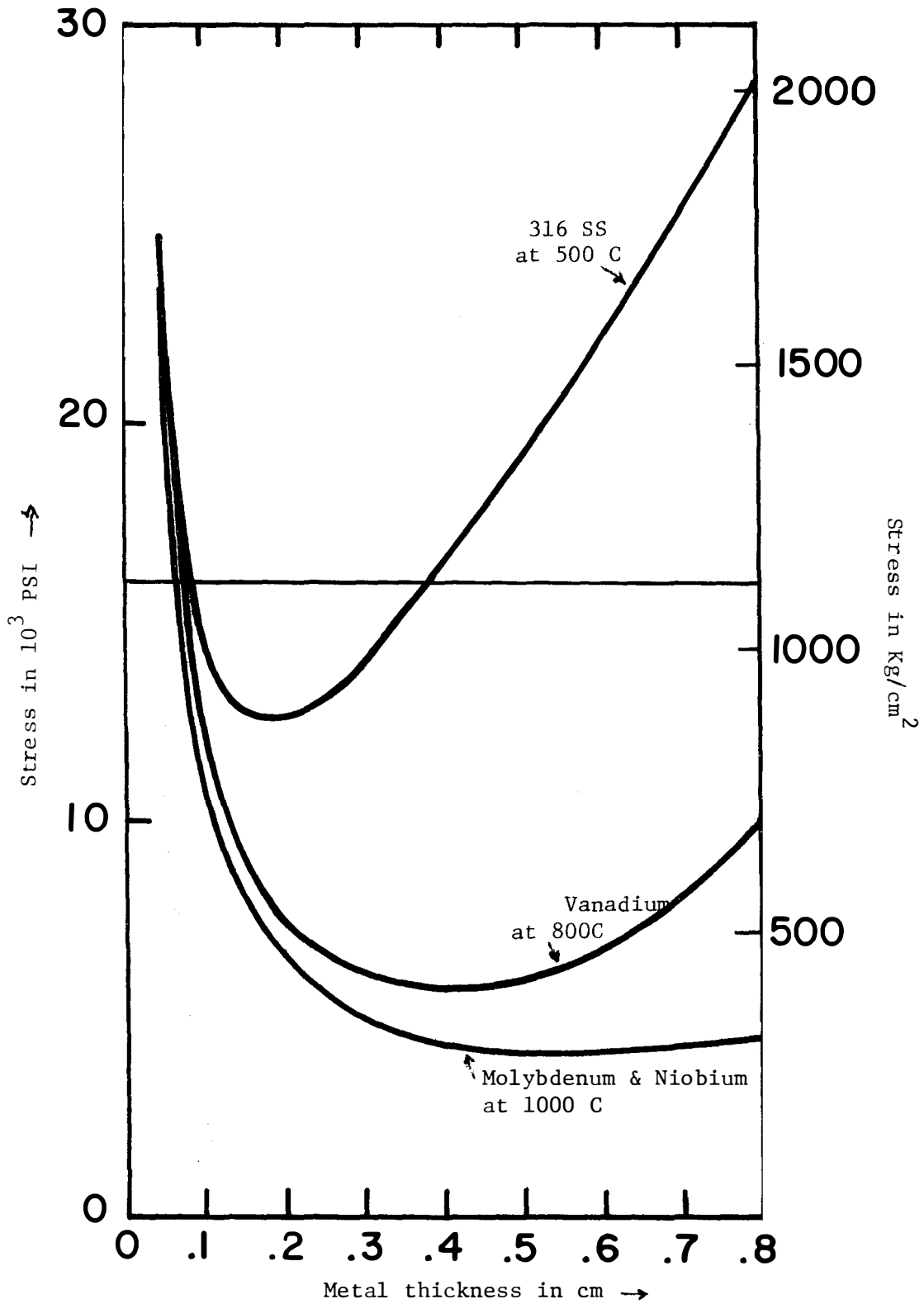


Figure. IV-D-3 Stresses in Front Wall as Function of Metal Thickness for 316 SS, Vanadium, Molybdenum and Niobium

However, radiation damage, activation, and afterheat are other considerations in selecting material for the front wall, and these subjects will be treated elsewhere in this report. As was stated previously, (Section IV-A), when other factors such as economics, availability, and ease of fabrication are considered, then stainless steel is certainly a favorable candidate for CTR blankets.

3. Mechanical Stresses

The structure of the front wall which is perpendicular to the plasma (referred to hereafter as a strut) will have to support the pressure load of one cell. Thus, the stress on a 2.5 mm thick strut will be ~9100 psi.

The front wall structure will be suspended from the poloidal headers which supply and remove the coolant from it. For the present, it will be assumed that this suspension is such as to prevent any mechanical support stresses of the headers from being transmitted to the front wall. This is not an unreasonable assumption, since the massive poloidal header structure will carry the vacuum load and the pressure load at a very low stress level and there is no rigid coupling between the headers and the heat removal cells. Finally, the total weight of the largest section of heat removal cells is ~320 kg which would add a negligible stress to the existing stress levels.

IV-E. First Wall Replacement

1. Reasons for Consideration

It has already been mentioned that the front wall of a fusion reactor is extremely vulnerable to radiation damage and this will be considered in more detail in Chapter VI. Because of a severe degradation in ductility we may be faced with the problem of having to replace the front wall every two or three years. The other option is to wait for a technological breakthrough that will allow a front wall to be designed for a period of twenty or more years. This is certainly within the realm of possibility, but may not be forthcoming for many years. In the meantime, we will take a conservative approach and assume that the wall must be designed so that it can be replaced several times during the lifetime of the plant.

The above reasoning especially applies to prototypes which are expected to be designed in 10-15 years and built in 15-20 years. If and when a better material for the front wall is discovered, one can merely replace the old wall with one made of the new material and extend the lifetime of the reactor. It may be that large resources of the refractory metals will be discovered and the technology for fabricating them will advance to a point where they could easily be used in front walls. By then, maybe some of the other problems of fusion reactors will be solved and we will be in a good position to make fusion power a reality. But none of this will be possible unless man proceeds now, using the materials and the technology available to him, with plans for prototype fusion reactors.

2. Proposed Removal Scheme

In order to understand the proposed method for removing and replacing the front wall, we must review how the whole reactor will be put together.

The toroidal reactor is divided into twelve identical modules each consisting of a superconducting toroidal magnet, blanket and shield wedges, vacuum pumps, coolant headers and all the other necessary plumbing and electrical connections for fueling and heating the plasma.

The blanket wedges will be held together at radial seams located in the gaps between adjacent magnets. These seams will have flanges holding adjacent wedges together, and the vacuum seal will be made with an annealed copper wire. It is anticipated that the whole reactor enclosure will be evacuated to a vacuum of approximately 10 microns (see Section XI-B). This means that the seal need not be mass-spectrometer tight. Nevertheless, an inflatable gasket will be used to provide a force on the copper wire in order to produce and maintain the seal. The insert in Figure IV-E-1 shows a typical seal which is attached to an expansion joint. These joints will be closed during reactor operation

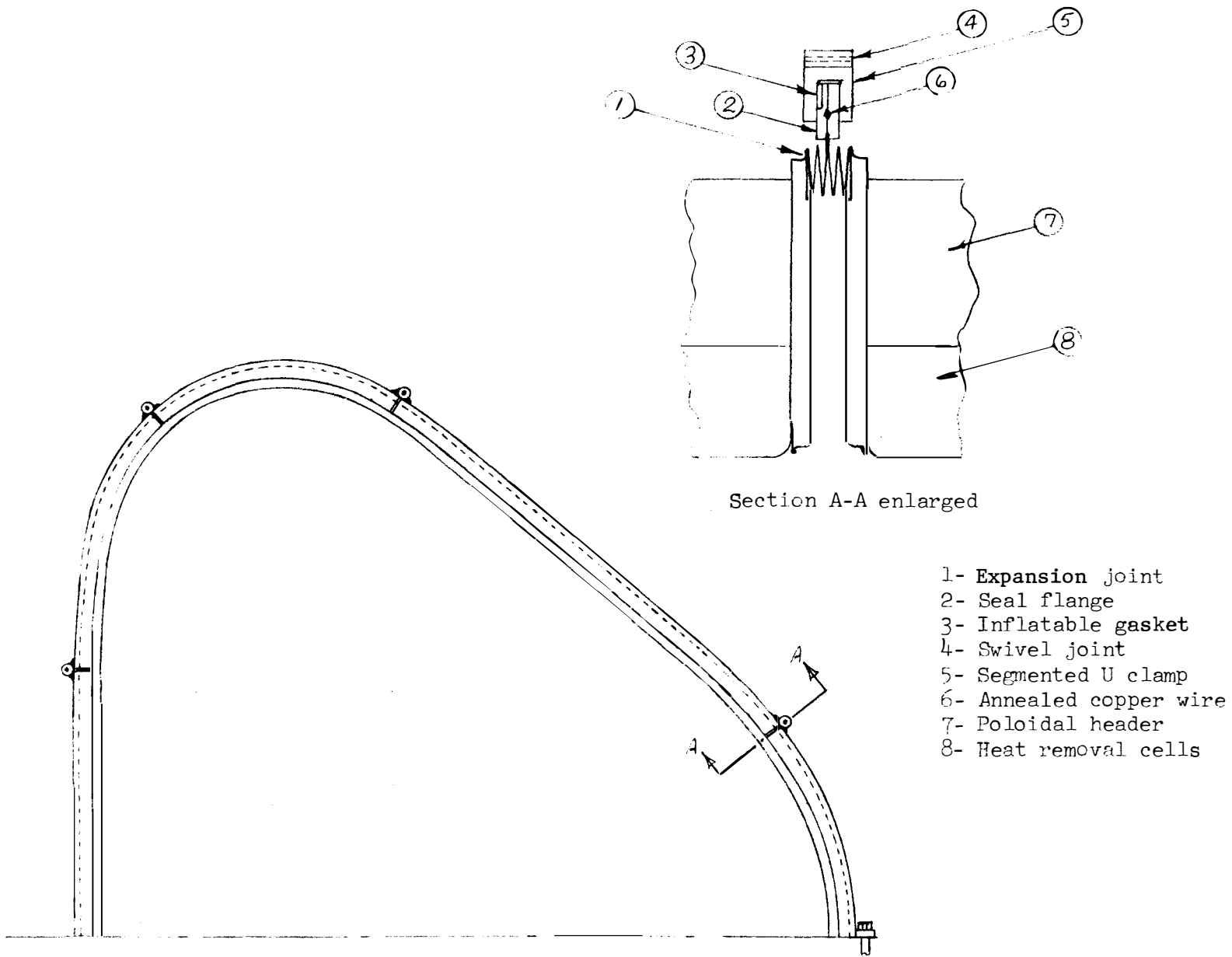


Fig. IV E-1 TYPICAL BLANKET SEAL BETWEEN MODULES

due to the large thermal expansion of the blanket and shield. At room temperature, there will be a gap between each blanket wedge of about 9 cm at the outer circumference and 3.25 at the inner circumference. The yoke which clamps the flanges together will be segmented and the pieces held together by swivels to facilitate its removal (Figure IV-E-1). Clamping the ends of the yokes will provide the force needed to hold the flanges together and to make the initial seal.

Figure IV-E-2 is a cross section of a single module showing the blanket and shield wedges inside the magnet. It should be noticed that the blanket is divided into two distinct regions, one located between the divertor slots and the inside core and the other, between the divertor slots and the outer periphery of the reactor. The first region mentioned (region I) will have a single coolant distribution system, in other words, it will have a single set of supply and return headers. The second region (region II) will be divided into three parts, and will be serviced by three different sets of supply and return headers. The two regions are, in turn, divided into sections 1.5 m. long in the poloidal direction.

If one were to stand inside of the vacuum chamber on the center line and look at the heat removal cells, he would see them as in Figure IV-E-3. These regions are divided into trapezoidal sections, differing in shape, depending on where they are located in the reactor blanket wedge. The section dimensions will range from 1.5 m x 1.25 m to 1.5 x 2.4 m.

Figure IV-E-4 is an isometric view of one section consisting of twenty cells, each 7.5 cm wide for a total width of 1.5 meters. Each section is two cells deep, the length in the toroidal direction of the cell depending on its location in the blanket as previously described. The weight of the largest section (without lithium) is ~320 kg (~700#).

The lockings studs attached to the top of the cells (shown only on one half of the section) will mate with slots in the bottom plate of the header structure. Figure IV-E-5 shows how that will be accomplished. Figure IV-E-5a and IV-E-5b are two views of a section of heat removal cells attached to the bottom plate of the headers. Figure IV-E-5c is a view from outside the blanket toward the plasma with the top header plate removed. It shows the feeder cavities which will distribute and collect the lithium coolant from and into the supply and return headers and the stud locking slots. Attachment of the front wall consists of inserting the studs into the appropriate holes and, with a single motion, locking the section in place onto the header. Each section is surrounded by a welding lip (Figure IV-5a and 5b). This protrudes slightly into the scalloped region and will be used to weld adjoining sections together.

Enough background information has now been supplied to provide a reasonable description of how the front wall will be replaced.

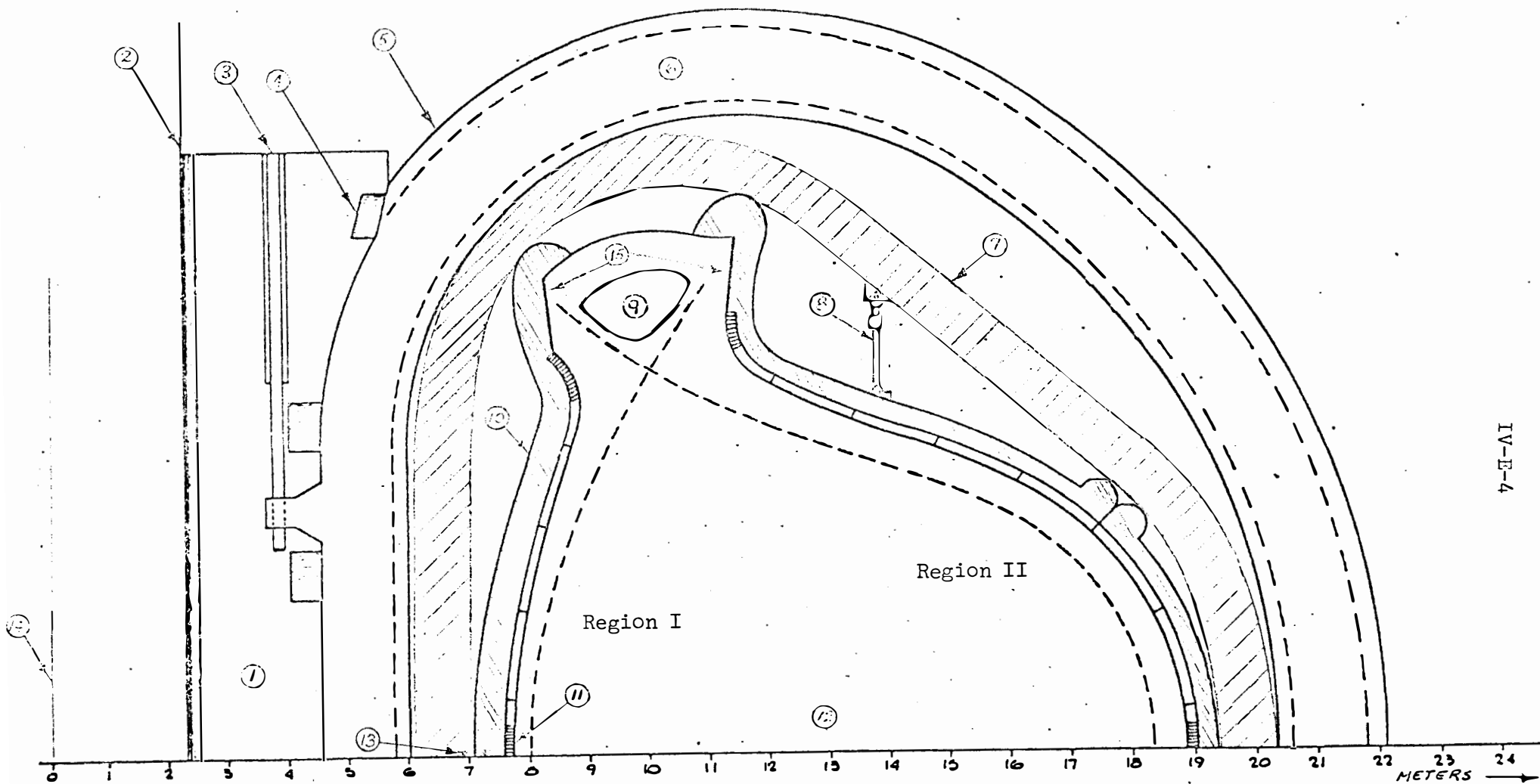


Fig. IV E-2 CROSSSECTION OF UMAK-1 HALF-SHELL

- | | | |
|------------------------------|-------------------------|---------------------------|
| 1- Central core | 6- Torroidal magnet | 11- Heat removal cells |
| 2- Superinsulation | 7- Shield | 12- Plasma |
| 3- Magnet support shear pins | 8- Rear blanket support | 13- Front blanket support |
| 4- Transformer coils | 9- Vacuum port shield | 14- Reactor centerline |
| 5- Torroidal magnet dewar | 10- Poloidal header | 15- Collector plates |

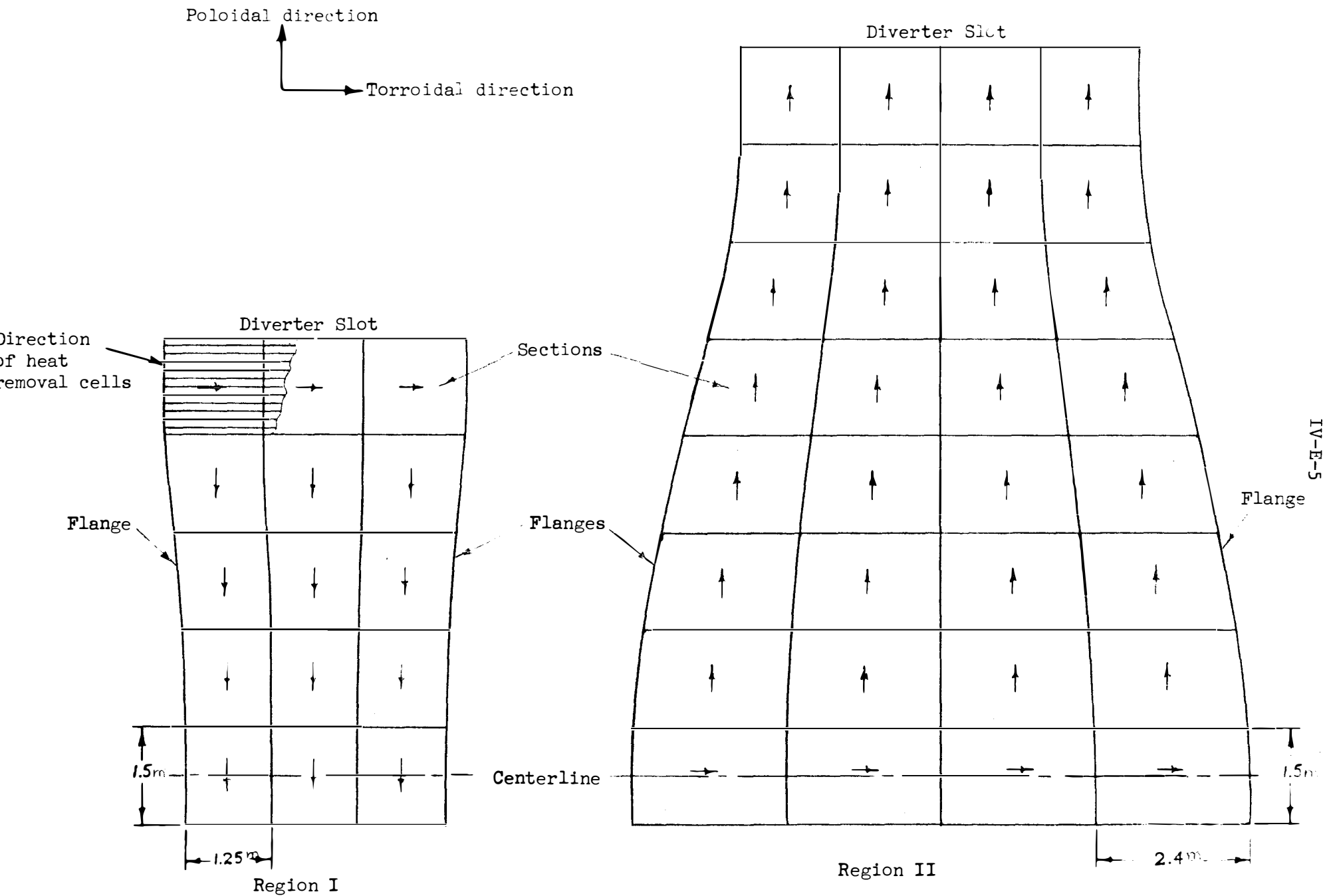


Fig. IV E-3 HEAT REMOVAL SECTIONS AS VIEWED FROM PLASMA CENTER

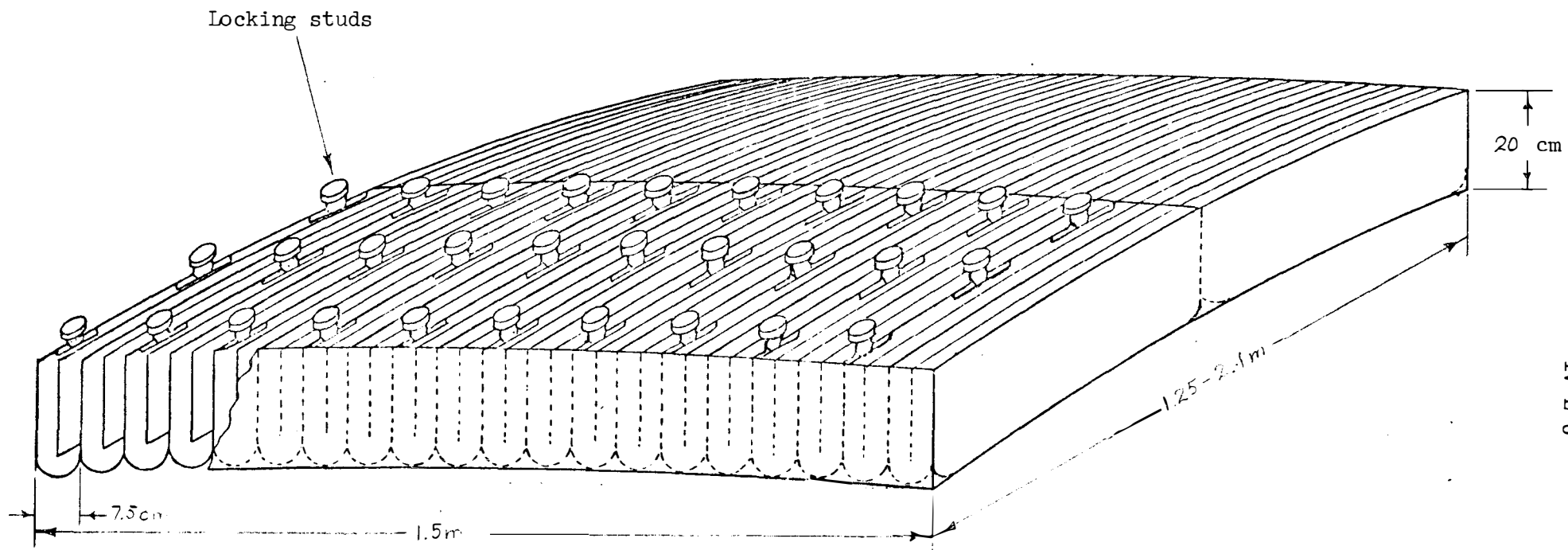


Fig. IV E-4 ISOMETRIC VIEW OF A COMPLETE SECTION OF HEAT REMOVAL CELLS
(Locking studs are shown on one half of the section only)

To begin with, the bare headers are assembled in, and supported from the unitized shield which is in turn supported by jacks on the ground. The sections of the front wall will then be inserted and attached to the headers. In the case of region I (Figure IV-E-3a) attachment will start at the center line and proceed toward the divertor slot, while in region II (Figure IV-E-3b), attachment will start at the divertor slots and continue down to the center line. In each case, it is obvious that the shapes involved dictate that one has to start with the smaller sections in order to be able to assemble them together. The locking direction of the last row of sections will have to be perpendicular to the others in order for this scheme to work. Arrows on Figure IV-E-3 show the proposed locking orientation of each section.

After the sections are in place, they can be welded. The sections adjoining the outside edge of the wedges will be welded to the wedge flanges themselves, while those adjoining the divertor slot will be welded directly to the header flanges. The important feature of this design is that all the welds are on the plasma side of the heat removal cells making the first wall the vacuum barrier between the plasma and lithium coolant.

Two important considerations have been made in designing the front wall. The first is that the mechanical operations necessary to assemble the front wall should be very simple. The second requirement is that all operations should be able to be performed from the inside of the reactor, eliminating the necessity of removing the headers from the shield in order to replace the heat removal cells.

The procedure which will be followed in replacing the front wall will now be described. It is assumed that the following conditions will exist: (see Figure IV-E-6)

- 1 - The reactor has been shut down for a period of time during which the coolant has been continually circulated to remove the afterheat generated by the radioactive decay of the structural material.
- 2 - The coolant has been pumped out and all the residual lithium has been evaporated (by vacuum pumping).
- 3 - The magnets have been turned off, although they can still be maintained in a cold condition.
- 4 - The plasma region and the reactor enclosure is back to atmospheric pressure.
- 5 - All coolant connections to the blanket headers are disconnected.
- 6 - All transfer lines and electrical connections to the magnets have been removed.

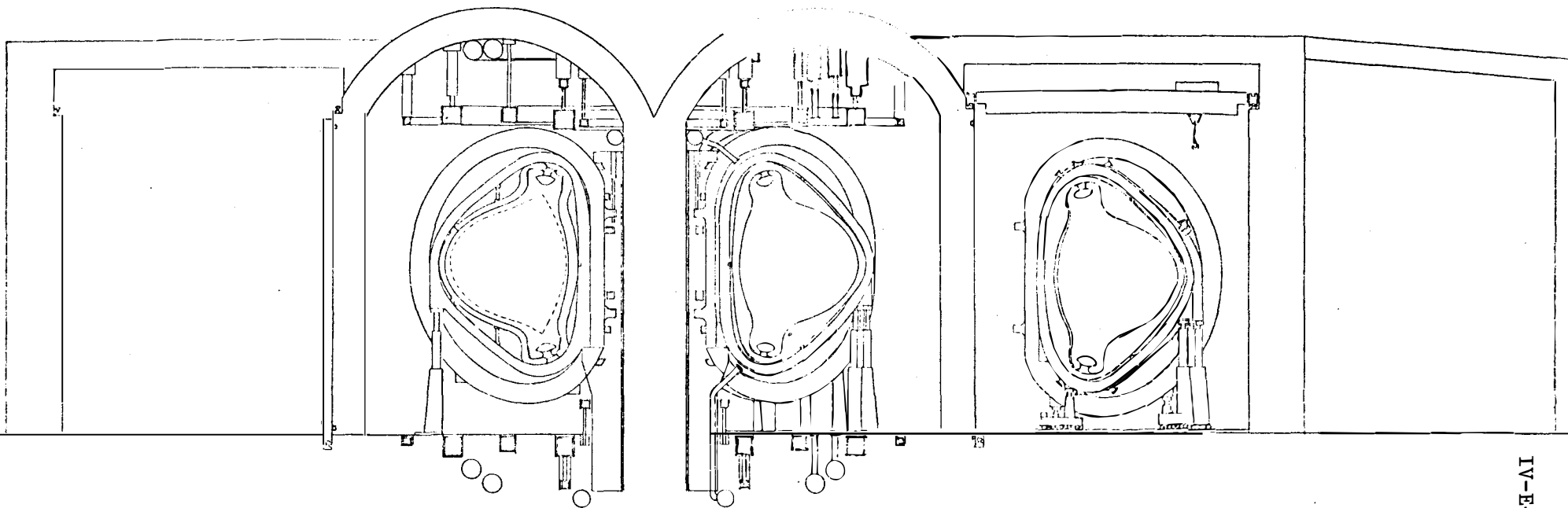


Fig. IV E-6 VIEW SHOWING A COMPLETE MODULE REMOVED FROM THE REACTOR ENCLOSURE
SUPPORTED ON MOTORISED CATERPILARS IN THE SERVICE TUNNEL ON THE
WAY TO THE SERVICE CELL

The following procedure will then be used:

- 1 - The bottom divertor magnets will be lowered into slots in the floor and covers placed over the slots to prevent damage during the removal of the reactor module. The upper divertor coils D3 & D4 (see Figure VII-B-1) are raised upwards.
- 2 - The carriage used for transporting a module will then be inserted under the magnet and the load of the magnet shifted from the central core to the carriage by means of jacks which mate with pads going through the magnet dewars (see Section VII-A for details)
- 3 - The support of the shield is also transferred to the carriage.
- 4 - The portion of the shield covering the blanket joints will be disassembled in sections, making the joint accessible (the joints are between toroidal magnets).
- 5 - The flange clamps will be unbolted and taken off. The blanket wedges are now free to come apart.
- 6 - The carriage supporting the whole module will then be moved radially out of the reactor to a tunnel behind the reactor and then circumferentially to a service area (Figure IV-E-6).
- 7 - A radiation and contamination shield is placed over the open ends of the torus.
- 8 - At the service area, men in shielded capsules can enter the blanket enclosure in order to grind off the welds and lift out the front wall sections. This can be either performed through a shielded tunnel over which the blanket wedge will be placed, or it could be performed by a mobile shielded machining facility. In either case, accessibility to the front of the wall, where all the needed operations can be performed, has been made fairly easy.
- 9 - Used blanket sections are discarded.
- 10 - New sections of heat removal cells are inserted and welded.
- 11 - The module is then taken back to the reactor where it is replaced in its original slot.
- 12 - The adjoining module can then be taken out for first wall replacement.

3. Impact on Reactor Efficiency

It is clear that replacing the front wall of a fusion reactor will decrease the plant availability. There are 87 sections of heat removal cells to be removed and replaced in each of 12 modules. This requires removal of 1044 sections for the entire reactor. In spite of the fact

that the operation has been simplified, it will still be quite time consuming. How long a reactor can be down for heat removal cell replacement and still be economical to operate is a problem that should be studied very carefully!

There is one redeeming feature which may be very important in this case. Several modules could be worked on simultaneously in several service areas to speed up the operation. This, of course, requires more equipment, facilities and manpower which may very well be justified by the down-time saved.

It would seem that crews working around the clock could replace the blanket sections of a module in a week (one section every 2 hours). This means a down-time of twelve weeks if there was only one service area or six weeks if there are crews working in each of the two service areas.

A down-time of six weeks every 2 years (~6%), during which time other maintenance can be performed, would be comparable to the down-time needed to refuel a fission reactor and comparable to routine maintenance of fossil fueled plants. Such a down-time factor does not seem excessive at this time.



IV-F. Support for Blanket and Shield Structures

1. Blanket

The method for attaching the front wall of the reactor to the massive coolant headers has already been discussed (Section IV-D-1). Immediately behind the headers, there is a 10 cm thick stainless steel layer which acts as a reflector. This layer is part of the blanket and the headers will be welded to it. The reflector in turn will have swivel joints welded to it, by means of which the whole blanket will be suspended on the shield. (Figure IV-E-2)

The total weight of a single blanket section, including the reflector and the lithium coolant, is 355 tons. Using twelve supports, the load on each support will be 59,000 pounds. The supports will be 1.25 in. diameter rods spring loaded with Belleville washers and capable of swinging radially, as shown in Figure IV-F-1. At operating temperature, the point of support, which is also the center of gravity of the blanket will move out radially 3.5 in. due to thermal expansion. The length of the support rod will have to increase 0.25 in. without appreciably increasing the tension on the rod. Belleville washers can be designed to provide a fairly uniform loading over a large range of stroke.

The blanket will also bear on the shield at the inner radius as shown in Figure IV-E-2. The total load of the blanket will then be distributed between the bearing point (which will not move with temperature because of the expansion joints provided between adjacent blanket wedges) and the upper support rods. The lower support rods will act as guides to keep the blanket centered and balanced. (See Figure IV-F-1)

2. Shield

The criteria for the designing of the shield is that it be strong enough to support itself and the blanket as well, and that it be reasonably easy to fabricate and assemble.

Figure IV-F-2a shows three adjacent toroidal magnets with their associated shield wedges. In IV-F-2b, the shield wedge is shown by itself and IV-F-2c is a cross section of it.

The shield will have zones in it which will be filled with B_4C and with lead, as well as cooling passages. It is reasonable to think of the shield in terms of layers with compartments provided for the B_4C and lead. In Figure IV-F-2b, we have divided the shield into 12 identical rings (recall that there will be 12 blanket support rods per wedge) and in IV-F-2c, each flattened ring has been divided further into three regions, the upper and lower yoke, and a central region.

It appears that a good way to build the shield is to use I beams. The beams can be prefabricated with tapered upper and lower flange, and

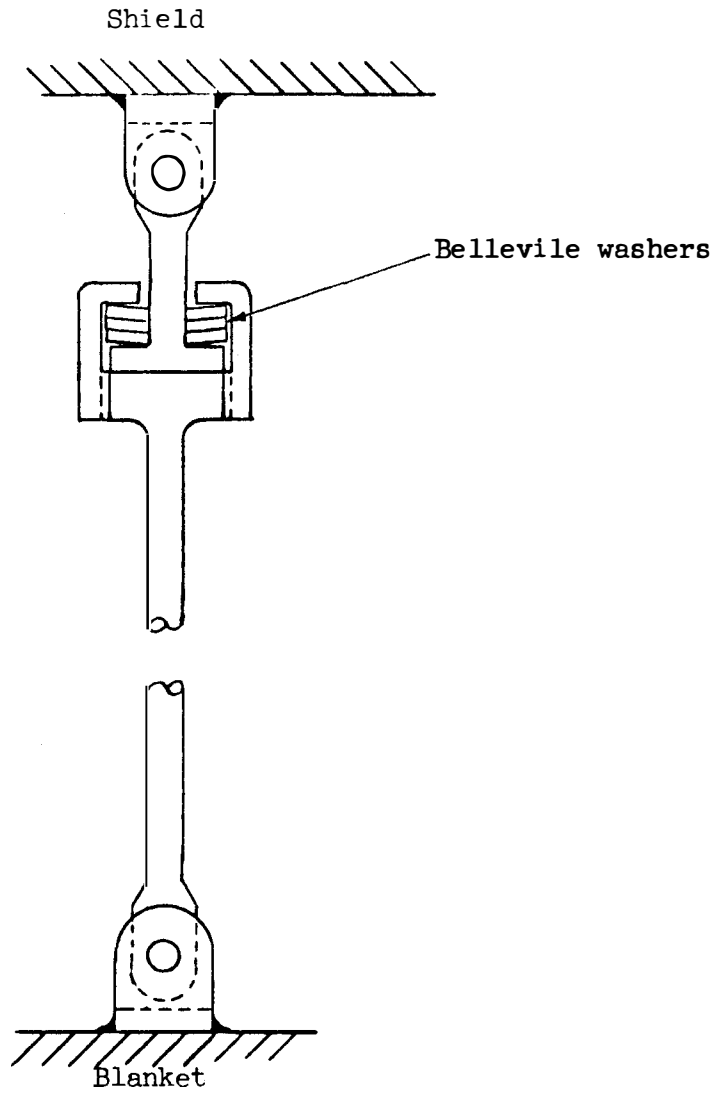


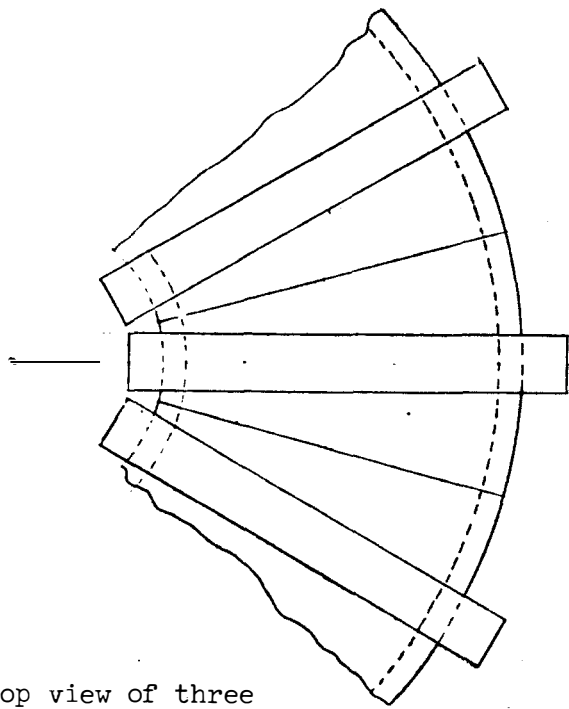
Fig. IV F-1 SPRING LOADED SWIVEL MOUNTED BLANKET SUPPORT ROD

forged to the proper curvature. Stacking the beams in layers will provide the compartments needed for placing blocks of B_4C or lead in the proper locations. This method of construction also distributes the structural metal in the most advantageous way. A preliminary calculation shows that a single beam with a 1 in. thick web and flanges, 34 in. deep will support itself and the concentrated load from the blanket support at a stress level of $<18,000$ psi. A composite beam with properly placed weldments can be made even stronger.

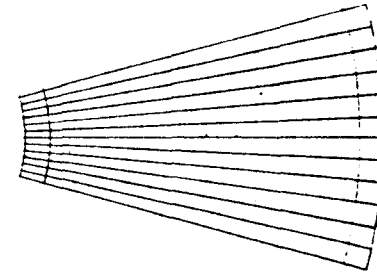
By making the shield in parts, as shown in Figure IV-F-2c, it will make the process of assembling the blanket within it fairly easy. There would have to be massive shear pins locking the parts together and enough bolts to provide moment restraint.

The weight of a single shield wedge is 2250 tons and with the blanket in place the total weight is 2605 tons. The load distribution is such as to have 935 tons on the inner shield support and 1670 tons on the outer shield support (see Figure IV-F-2c). The inner support will rest on a ledge which will be part of the inner core. There is about 15 cm of space available between magnets and these ledges will be located in these spaces. The outer shield support will have six 300 ton jacks. These jacks will be on a platform which will become part of the module removal carriage.

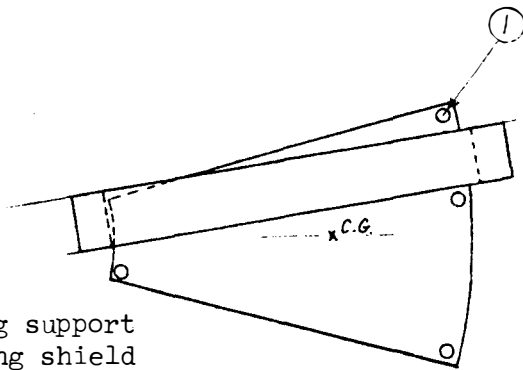
The problem of inserting the shield wedge into the toroidal magnet has also been solved. Figure IV-F-2d shows how that can be accomplished. The circles on the shield show the locations of supports as the shield is inserted. The center of gravity is such as to allow the shield to be supported in a stable way during insertion.



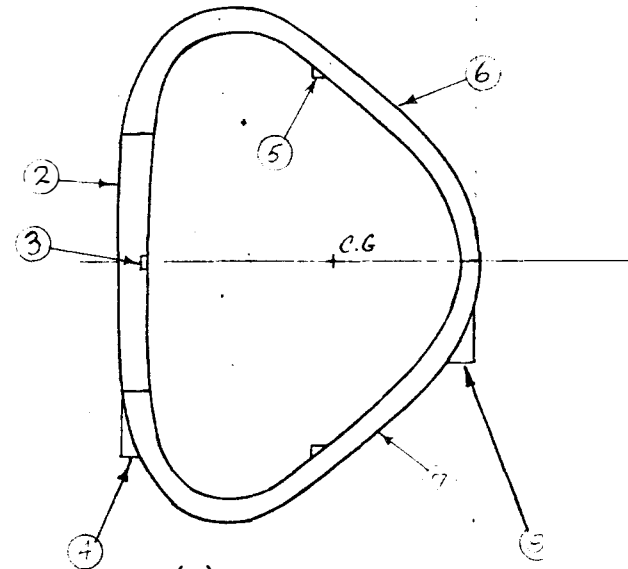
(a) Top view of three torroidal magnets



(b) Shield wedge



(d) View showing support points during shield insertion into magnet



(c) Single shield ring

Fig. IV F-2

- 1- Support points
- 2- Central shield region
- 3- Front blanket support point
- 4- Front shield support ledge

- 5- Rear blanket support point
- 6- Upper shield yoke
- 7- Lower shield yoke
- 8- Rear shield support ledge



GULF GENERAL ATOMIC

GULF-GA-A12789
UC-20

FUSION TECHNOLOGY

SUMMARY PROGRESS REPORT

FOR THE PERIOD OCTOBER 1, 1972 TO SEPTEMBER 30, 1973

by

G. R. Hopkins

Prepared under
Contract No. AT(04-3)167
Project Agreement No. 48
for the
San Francisco Operations Office
U. S. Atomic Energy Commission

Gulf General Atomic Project 0559

October 1, 1973

IV-G. Summary Progress Report for the Period Oct. 1, 1972 to Sept. 30, 1973

1. Introduction

The purpose of this study was to investigate the application of helium cooling to the University of Wisconsin Tokamak reactor conceptual design. This was done as an iteration on their basic design which employed flowing lithium as the blanket coolant and stainless steel as the first wall and blanket structural material.

The basic approach for the Gulf General Atomic study was to consider the lithium as static in the blanket and to provide cooling by means of flowing pressurized helium contained in small diameter stainless steel tubing inserted into the basic blanket assembly. Thus the blanket becomes a lithium to helium heat exchanger.

The effects on the blanket and first wall may be simply expressed then as the amount of additional material needed for the tubing and the amount of "void" space needed for the pressurized helium. These are dependent on the specific conditions chosen for helium pressure, system temperatures and temperature limits, material properties and design conditions, mechanical arrangement of the assembly, and energy deposition. Specific cases for these factors are considered and described below.

These results may then be interpreted in terms of their effect on the system parameters of blanket thickness, tritium breeding and pumping power for the helium. These provide a basis for comparison of parameters of the helium cooled and liquid lithium cooled systems.

2. Design Considerations

One of the major limitations of the stainless steel-lithium system is the maximum temperature of the stainless steel. This arises from (1) radiation damage considerations and (2) limitations on corrosion rates at the liquid lithium-stainless steel interface. This maximum temperature is not a well identified or fixed value, and thus two cases are considered in the calculations that follow, 500°C (Cases 1 and 2) and 650°C (Case 3). The lower value was chosen to match that of the University of Wisconsin flowing lithium design. The higher value was considered as a reasonable upper limit from corrosion rate considerations. A static lithium system, i.e., the helium cooled case, could tolerate a higher temperature (corrosion rate) since mass transfer would be limited by diffusion processes rather than fluid flow. Even natural convection of the liquid lithium in the blanket would be suppressed due to the high magnetic fields.

Three cases were chosen for calculation of the blanket parameters. These are Cases 1 and 3 as described above for the two temperature limits, and Case 2 which was devised to reduce the helium pumping power, compared to Case 1 by increasing the amount of coolant tubing in the blanket structure. (This was accomplished computationally by decreasing the amount of lithium cooled per tube and hence heat load per tube.) In essence, the parameters for Case 1 were chosen to match those of the flowing lithium design where appropriate and are shown in Table IV-G-1 for the material properties and limit

Table IV-G-1

STAINLESS STEEL, LITHIUM, AND HELIUM MATERIALS DESIGN PARAMETERS

Stainless Steel - 316

Thermal Conductivity		0.23 W/cm ⁰ C
Maximum Mechanical Stress		500 atm
Poisson's Ratio		0.31
Young's Modulus		1.43 x 10 ⁶
Linear Expansion Coefficient		1.8 x 10 ⁻⁵ /°C
Maximum Temperature - 316 SS	Case 1 & 2	773°K (500°C)
	Case 3	923°K (650°C)

Lithium

Thermal Conductivity		0.625 W/cm ⁰ C
Maximum Lithium Temperature	Case 1	848°K (575°C)
	Case 2	813°K (540°C)
	Case 3	963°K (690°C)

Helium

Specific Heat - Constant Pressure		5.2 Watt-Sec/gm ⁰ C
Specific Heat Ratio C_p/C_v		1.67
Stanton Number		3 x 10 ⁻³
Friction Factor		4.5 x 10 ⁻³

Table IV-G-2

REACTOR SYSTEM DESIGN PARAMETERS

Major Radius		13.0 meters
First Wall Minor Radius		5.5 meters
Reactor Power Output		5000 MW (th)
Unit Cell Module Length		3 meters
Neutron Energy Flux on First Wall		1.25 MW/m ²
Bremsstrahlung Energy Flux on First Wall		0.25 MW/m ²
Total Blanket Energy Generation		1.77 MW/m ²
First Wall Thickness		0.25 cm
Blanket-Lithium Thickness		70 cm
Internal Energy Generation in First Wall	SS	12.3 W/cm ³
Internal Energy Generation in First Wall Lithium (max)		4.91 W/cm ³
Internal Energy Generation in Blanket Lithium (max)		4.5 W/cm ³
Helium Inlet Temperature - first wall		573°K
	blanket	573°K
Helium Exit Temperature - blanket - Cases 1 & 2		748°K
	Case 3	873°K
Helium Temperature Rise	Cases 1 & 2	175°C
	Case 3	300°C
Helium Pressure Range		50 & 70 atm

Table IV-G-3a

RESULTS FOR STAINLESS STEEL-LITHIUM HELIUM COOLED MODULES

BASE CASE 1

	<u>Static Helium Pressure</u>	
	<u>50 atm</u>	<u>70 atm</u>
Blanket Helium "void" Volume (%)	1.2	1.2
Metal Volume (%)	0.5	0.7
Tube Diameter (ID, cm)	0.5	0.5
Tube Wall Thickness (cm)	0.026	0.04
Thermal Stress (max, atm)	47	66
Total Stress (atm)	547	566
Number of Tubes (around minor dimension circumference)	2,480	2,480
Pumping Power (% of thermal output)	12	6
Mean Outlet Temperature ($^{\circ}$ K)	742	742
Tritium Breeding Ratio	1.47	1.47

Table IV-G-3b

RESULTS FOR STAINLESS STEEL-LITHIUM HELIUM COOLED MODULES
WITH INCREASED METAL VOLUME

CASE 2

	<u>Static Helium Pressure</u>	
	<u>50 atm</u>	<u>70 atm</u>
Blanket Helium "void" Volume (%)	1.7	1.7
Metal Volume (%)	0.73	1.00
Tube Diameter (ID, cm)	0.78	0.78
Tube Wall Thickness (cm)	0.040	0.054
Thermal Stress (max, atm)	76	106
Total Stress (atm)	576	606
Number of Tubes (around minor dimension circumference)	4140	4140
Pumping Power (% of thermal output)	3.2	1.6
Mean Outlet Temperature ($^{\circ}$ K)	733	733
Tritium Breeding Ratio	1.47	1.06

Table IV-G-3c

RESULTS FOR STAINLESS STEEL-LITHIUM HELIUM COOLED MODULES

WITH HIGH TEMPERATURE LIMIT ON METAL

CASE 3

	<u>Static Helium Pressure</u>	
	<u>50 atm</u>	<u>70 atm</u>
Blanket Helium "void" Volume (%)	1.5	1.5
Metal Volume (%)	0.60	0.87
Tube Diameter (ID, cm)	0.6	0.6
Tube Wall Thickness (cm)	0.030	0.042
Thermal Stress (max, atm)	53	74
Total Stress (atm)	553	574
Number of Tubes (around minor dimension circumference)	3600	3600
Pumping Power (% of thermal output)	1.6	0.8
Mean Outlet Temperature ($^{\circ}$ K)	873	873
Tritium Breeding Ratio	1.47	1.46

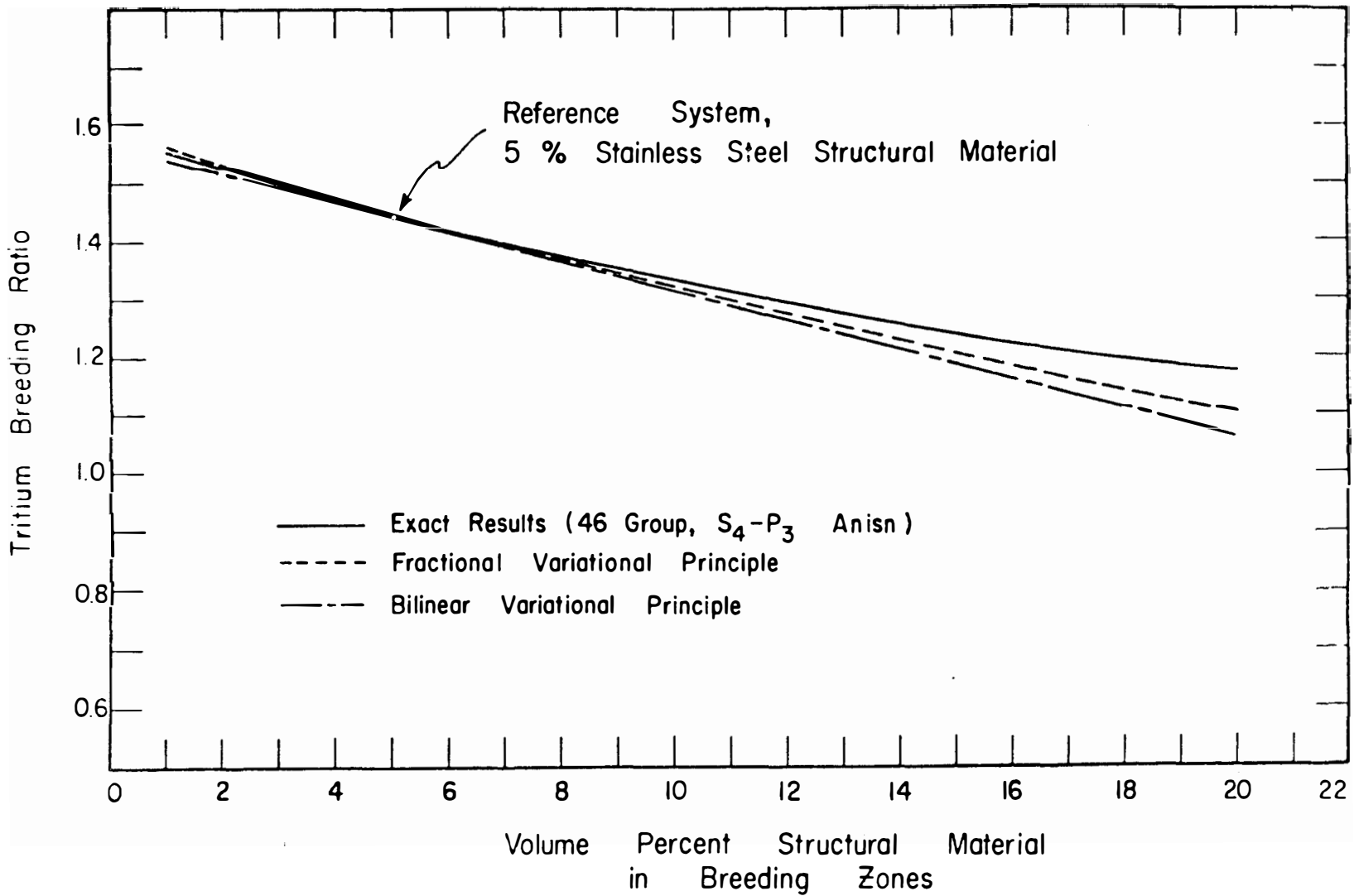


Fig. IV-G-1 --Tritium breeding ratio as a function of 316 SS content in the blanket
(from University of Wisconsin)

and Table IV-G-2 for the system parameters. The values in these tables represent the input numbers for the calculations. Note that two values of helium pressure, 50 to 70 atm, were used in each of the cases. In all cases, a design mechanical stress of 5000 atm was used for the stainless steel. The maximum recommended design stress at 500°C for stainless steel is approximately 1000 atm.

3. The Model

The approach taken was to consider the blanket as composed of modules, 3 meters long, and of arbitrary width. The lengthwise direction is oriented in a direction parallel to the main toroidal magnetic field and the helium flow is taken as this direction also. The coolant tube spacing, size, and wall thickness are calculated in the same manner as used previously for helium cooled niobium and molybdenum structural material systems.^(70,71,72) The width of such a module could range from less than a meter to a cylindrical shaped unit that covered the entire circumference in the minor dimension of the torus. The liquid lithium container and first wall were considered as composed of the same amounts of stainless steel as the University of Wisconsin 5000 MW (th) design. Thus the iteration for helium cooling consisted of inserting (1) a row of coolant tubes along the inside of the first wall and (2) throughout the lithium blanket region, in sufficient number and size to remove the heat generated in these regions.

4. Results and Discussion

The major results to be considered are (1) the amounts of coolant tubing material and helium "void" space that are required in the blanket-first wall regions, (2) the effect of the additional metal on tritium breeding, (3) the tubing dimensions and number of tubes, (4) the thermal stresses on the metals, and (5) the pumping power required to circulate the helium coolant. These and other values are given in Tables IV-G-3a, 3b, and 3c for the three design cases and the two values of static helium pressure chosen.

The tritium breeding ratio change was obtained from Fig. IV-G-1, a curve provided by the University of Wisconsin Group showing the tritium breeding as a function of stainless steel content in the blanket lithium. The amount of stainless steel needed for coolant tubing was added to the 5% value for structure and the breeding ratio then obtained from the curve. The 5% structural content is the value used for the flowing lithium design and has a breeding ratio of 1.49. Inspection of the curve shows a slope at ~5% stainless steel content of -0.03% SS; thus the change in breeding ratio for the additional stainless steel may be readily calculated and the values for the cases are shown in Tables IV-G-3a, 3b, and 3c. It is evident that the amount of stainless steel utilized for helium cooling does not change the breeding ratio by a large amount, that is, does not impose a severe limit on blanket design. This permits a further increase in stainless content for systems optimization of other parameters such as a reduction in design stress load on the coolant tubing, decrease in pumping power for the helium flow, and an increase in the helium coolant pressure.

The pumping power for circulating the pressurized helium is a significant parameter since it affects the overall thermodynamic efficiency of the systems. This shows a wide variation in the cases analyzed, ranging from 0.8% to 12% of thermal power output. The higher temperature and helium pressure cases provide the smallest values as expected. Note that even with the low temperature limits of Case 2, the pumping power can be reduced to 1.6%, a very low value.

The volume within the magnet structure of a fusion reactor is important from the magnet cost aspect. The additional volume within the 70 cm thick blanket required for incorporation of helium cooling in the cases analyzed ranges from 1.7% to 2.43%, the sums of metal and helium volumes from Tables IV-G-3a, 3b, and 3c. These result in an increase of blanket thickness of 1.2 cm and 1.7 cm respectively. If these are interpreted as increases in the inside minor diameter of the magnet structure (~7.5 meters), the volume increases within the magnet of 0.16% to 0.22% may be calculated, and the cost of the toroidal magnet system would increase accordingly.

The increases in cost of the blanket and magnet may be offset by several other fusion reactor system factors that result with pressurized helium cooling. Some of these are as follows:

1. The helium system provides an effective barrier between the steam generator and liquid lithium, thus secondary loops may be eliminated.
2. The employment of static lithium in the blanket and cleanup system only, compared to use as a primary coolant would reduce the inventory of lithium and hence tritium in lithium by a large amount. This would ease the tritium containment requirements.
3. The higher temperatures perhaps obtainable with helium cooling would increase plant efficiency and hence electrical power output.
4. The corrosion of the stainless steel would be decreased, possibly leading to a longer useful life in the reactor. The smaller amounts of corrosion products in the lithium and their more limited distribution should reduce radioactive material containment problems.

These and other system considerations need to be considered in more detail for a better assessment of the relative merits of helium vs. lithium cooling.

5. Conclusions

The primary purpose of this study was to investigate the helium coolant parameters for a stainless steel structure, static liquid lithium, pressurized helium cooled blanket assembly, for a fusion reactor with a first wall neutron energy flux of 1.25 MW/m^2 . The results show that the amounts of stainless steel and helium volume required in the blanket for the helium

coolant are small enough that the major system parameters of blanket volume and tritium breeding are changed by only small amounts. Further trade off studies to maximize helium outlet temperature, minimize pumping power, minimize stresses on the metal, or reduce the maximum metal or lithium temperatures, appear possible without major changes in the system parameters.

IV-H Insulator Requirements in the Blanket

The plasma current is initially driven by the inductive electric field produced by a changing core-flux. In order to allow this electric field to appear in the plasma, there must be at least one insulated gap in the blanket and shield. The average voltage across the gap during the rise of the plasma current is about 30-50 volts if the rise time of the plasma current is 100 seconds.

The peak voltage is much higher than this because a stronger electric field is required for adequate ohmic heating when the plasma is still cold. A simple estimate of the initial electric field required is obtained from the following analysis. We assume the plasma has been preionized and heated to an ion temperature of 5 eV at a density of $3 \times 10^{13} \text{ cm}^{-3}$. We assume the ion temperature is temporarily fixed because of good thermal conduction to the outside. The electrons are assumed to be heated by joule heating and cooled primarily by electron-ion rethermalization. The electron energy equation is then

$$\frac{d}{dt} \left(\frac{3}{2} nkT_e \right) = \sigma E^2 - \frac{3}{2} nk \frac{(T_e - T_i)}{\tau_{eq}} \quad \text{IV-G-1}$$

where $\sigma(T_e) = T_e^{3/2} / 65.3 \ln \Lambda$ mho/m is the Spitzer conductivity and

$$\tau_{eq} = \frac{2.52 \times 10^4 T_e^{3/2}}{n \ln \Lambda} \text{ sec,}$$

is the electron-ion rethermalization time. Here T_e is in $^{\circ}\text{K}$ and n is in particles/ m^3 . For the electrons to heat, we need $dT_e/dt > 0$, or

$$E^2 > \frac{\frac{3}{2} nk(T_e - T_i)}{\sigma(T_e) \tau_{eq}} \quad \text{IV-G-2}$$

The right hand side of (IV-G-2) peaks at $T_e = \frac{3}{2} T_i$, for which the corresponding electric field is

$$E_{m_{in}} = 180 \text{ volts/m.} \quad \text{IV-G-3}$$

If $E > E_{m_{in}}$, then the electrons will heat and the ion temperature will eventually rise.

This $E_{m_{in}}$ implies an initial voltage of 16 kV around the torus. Neglecting back emf from the plasma current, the insulated gap sees a peak voltage of 16 kV. If necessary, this can be reduced by a factor of 12 by insulating between every sector of the torus. The insulator subjected to this voltage will be at the back side of the blanket and before the shield in a region of high neutron flux and temperature (300-500 $^{\circ}\text{C}$). The insulator thickness need not be small (\sim a few centimeters), so the electric field in the insulator is \sim 500 volts/cm, which is quite modest.

References for Chapter IV

1. R. G. Mills, To be published.
2. A. P. Frass, ORNL-TM-3096, May 1973.
3. R. Hancox, International Conference, World Energy Problems: Nuclear Solutions, 1972; American Nuclear Society, Inc., Hinsdale, Illinois, p. 209.
4. S. C. Burnett, W. R. Ellis, T. A. Oliphant and F. L. Fibe, LA-5121-MS, December 1972.
5. R. W. Werner, G. A. Carlson, J. Hovingh, J. D. Lee, and M. A. Peterson, UCRL-74054, November 1972.
6. M. J. Lubin and A. P. Fraas, Scientific American, Vol. 224, No. 6, June 1971, p. 21.
7. L. A. Booth, LA-4858-MS, Vol. #1, 1972.
8. V. A. Maroni, E. J. Cairns and F. A. Cafasso, ANL-8001, March 1973.
9. Not used
10. W. G. Homeyer, "Thermal and Chemical Aspects of the Thermonuclear Blanket Problem, Research Laboratory of Electronics, M.I.T. TR435, 1965.
11. Hancox, R., and Booth, J.A., "The Use of Liquid Lithium as a Coolant in a Toroidal Fusion Reactor," UKAEA Culham Laboratory Report CLM-R 115 and 116, 1971.
12. D. K. Sze, and W. E. Stewart, "Lithium Cooling for a Low- β Tokamak Reactor," Texas Symposium on the Technology of Controlled Thermonuclear Fusion Experiments and the Engineering Aspects of Fusion Reactors, 1972.
13. J. T. D. Mitchell and R. Hancox, "A Lithium Cooled Toroidal Fusion Reactor," Energy '72, San Diego.
14. Fraas, A. P., "Conceptual Design of the Blanket and Shield Region of a Full Scale Toroidal Fusion Reactor," USAEC Report ORNL-TM-3096, 1972.
15. M. A. Hoffman and G. A. Carlson, "Calculation Techniques for Estimating the Pressure Losses for Conducting Fluid Flows in Magnetic Fields," USAEC Report UCRL-51010, 1971.
16. Sutton, G. W., and A. Sherman, Engineering Magnetohydrodynamics, McGraw Hill, N.Y., 1956.
17. - 24. Not used

25. R. W. Webb, Permeation of Hydrogen Through Metals, NAA-SR-10462, July 1965.
26. W. E. Ray, S. L. Schrock, S. A. Shiels and K. C. Thomas, "Selection of Steam Generator Tubing Material for the Westinghouse LMFBF Demonstration Plant," Nucl. Tech. 11, 222 (1971).
27. R. N. Lyon (Ed.), Liquid Metals Handbook, Report NAVEXOS-F-733 (Rev.), Superintendent of Documents, U. S. Government Printing Office, p. 158ff, June 1952.
28. M. S. Goikhman, A. M. Datisishin, I. G. Shtykalo, V. F. Shatinskii, and M. I. Chaevskii, "Corrosion Failure of 1Cr18Ni9Ti Steel in Liquid Lithium," Soviet Materials Science, 6 491 (1968).
- 28a. V. V. Popovich, M. S. Goikhman, E. I. Polyakov and M. I. Chaevskii, "The Effects of Lithium on the Mechanical Characteristics of Austenitic Stainless Steels," Soviet Materials Science, 5, 345 (1969).
29. W. N. Gill, R. P. Vanek, R. V. Jelinek and C. S. Grove, Jr., "Mass Transfer in Liquid-Lithium Systems," AICHE Journal 6, 139 (1960).
30. Dai-Kai Sze and W. E. Stewart, Thermal and Mechanical Design Considerations for Lithium-Cooled Tokamak Reactor Blankets, University of Wisconsin Fusion Design Memo No., 41, March 1973.
31. J. H. Strong, E. M. Simons, J. A. DeMastry and J. M. Genco, Compatibility of Liquid and Vapor Alkali Metals with Construction Materials DMIC Report 227, April 1966, p. 89.
32. H. W. Levenworth and D. P. Gregory, "Mass Transfer of Type 316 Stainless Steel by Liquid Lithium," Corrosion, 18, 43t (1962).
33. J. H. DeVan and C. E. Sessions, "Mass Transfer of Niobium-Base Alloys in Flowing Non-Iso-thermal Lithium," Nucl. Appl. 3, 102 (1967).
34. J. M. Kroger, Alloy Compatibility with LiF-BeF₂ Salts, ORNL-TM-4286, in press.
35. R. E. Seebold, L. S. Birks, and E. J. Brooks, "Selective Removal of Chromium from Type 304 Stainless Steel by Air-Contaminated Lithium," Corrosion, 16, 468t, (1960).

36. E. E. Hoffman, "Liquid Metal Corrosion," Symposium on Corrosion Fundamentals A. de A. Brasunas and E. E. Stausburg, Eds., Univ. of Tenn. Press, p. 65ff, 1956.
37. G. DeVries, "The Corrosion of Metals by Molten Lithium," Corrosion by Liquid Metals, J. E. Draley and J. R. Weeks, Eds. Plenum Press, p. 251ff, 1970.
38. T. J. Kabele, W. F. Brehm and D. R. Marr, "Activated Corrosion Product Radiation Levels in FFTF," Trans. Am. Nucl. Soc. 16, 108 (1973). See also HEDL-TME-72-71 (1972).
39. R. L. Klueh, Effect of Oxygen on the Corrosion of Nb and Ta by Liquid Lithium, ORNL-TM-4069, March 1973.
40. J. H. DeVan, "Compatibility" Fusion Reactor First Wall Materials, L. C. Ianniello, Ed. p. 25-29, April 1972.
41. W. E. Berry, Corrosion in Nuclear Applications Wiley, New York, p. 293.
42. W. E. Berry, loc. cit. p. 256.
43. J. N. Anno and J. A. Walowit, "Analysis of Corrosion of Stainless Steel in a Sodium and High Radiation Environment," Nucl. Tech. 10, 67, (1971).
44. W. E. Berry, loc. cit., p. 252-3.
45. R. G. Brown, "The Effects of Sputtering and Blistering on the UWCTR First Wall," UWFDM-60, May 1973.
- 45a. W. E. Ruther and S. Greenberg, "Investigation of Material Compatibility Relevant to EBR-II System," ANL-8042, in press.
46. A. B. Johnson, Jr., "Aqueous Corrosion and Hydriding of Airconium Alloys in Nuclear Reactor Environments," Proceedings of the Fourth International Congress on Metallic Corrosion, Sept. 7-14, 1969 Amsterdam, p. 168, National Association of Corrosion Engineers, 1972.
47. R. E. Cleary, S. S. Polecherman and J. E. Corliss, "Solubility Refractory Metals in Lithium and Potassium," TIM-850, November 1965. See also, W. E. Berry, Corrosion in Nuclear Applications Wiley & Sons, New York, 1971, p. 291.
48. E. J. Cairns, F. A. Cafasso and V. A. Maroni, "A Review of the Chemical, Physical and Thermal Properties of Lithium that are Related to Its Use in Fusion Reactors," The Chemistry of Fusion Technology, D. E. Gruen, Ed., Plenum Press, New York, 1972, p. 116, 129 ff.

49. J. R. DiStefano and A. P. Litman, "Effects of Impurities in Some Refractory Metal - Alkali Metal Systems," Corrosion, 20, 392t (1964).
50. J. R. Weeks and H. S. Isaacs, "A General Model for the Corrosion of Steels in High Velocity Sodium," Chemical Aspects of Corrosion and Mass Transfer in Liquid Sodium, S. A. Jansson, Ed., Metallurg. Soc. AIME. p. 207 (1972).
51. J. O. Cowles and A. D. Pasternak, Lithium Properties Related to Use as a Nuclear Reactor Coolant, UCRL-50647, April 1969.
52. G. D. Collins, Summary Report - Sodium Mass Transfer Program - Effects of Sodium Exposure on the Corrosion and Strength of Stainless Steels, GEAP-10394, August 1971.
53. J. W. Semmel, Jr., L. B. Engel, Jr., R. G. Frank and R. W. Harrison, "Carbon Mass Transfer in Multimetallc Systems Containing Potassium," Alkali Metal Coolants Proceedings of Symposium, Vienna, Nov. 28 - Dec. 2, 1966, International Atomic Energy Agency, Vienna, 1967 p. 181ff.
54. J. E. Mausteller, F. Tepper, S. J. Rodgers, Alkali Metal Handling and Systems Operating Techniques, AEC Monograph, Gordon and Breach, New York, 1967, p. 8-34.
55. R. W. Harrison, "The Effect of Welding Atmosphere Purity on the Lithium Corrosion Resistance of Refractory Alloys" Corrosion by Liquid Metals, J. E. Draley and J. R. Weeks, Plenum Press, New York, 1970, p. 223ff.
56. F. A. Kozlov and E. K. Kuznetsov, "The Use of Hot Traps for Removing Oxygen from Sodium," Liquid Metals, P. L. Kirillov, et al, Ed., NASA-TT-F-522, May 1969, p. 340.
57. J. E. Mausteller, et al, loc. cit., p. 61-64.
58. W. M. Phillips, "Some Alkali Metal Corrosion Effects in a Rankine Cycle Test Loop," Corrosion by Liquid Metals, J. E. Draley and J. R. Weeks, Eds., Plenum Press, 1970, p. 214.
59. L. A. Charlot and R. E. Westerman, High Temperature Corrosion of Candidate ATR Structural Materials, BNWL-100, September 1965.
60. W. E. Berry, loc. cit., p. 394.
61. S. H. Bush and R. L. Dillon, "Stress Corrosion in Nuclear Systems" paper for presentation at the International Conference on Stress Corrosion Cracking and Hydrogen Embrittlement of Iron Base Alloys, Firminy, France, June 1973.

62. G. J. Walke, R. W. Sinderman, C. E. Axtell, "The Effects of Failed Fuel on the Operation of a Commercial BWR Plant," Trans. Am. Nucl. Soc. 13, 165 (1970).
63. D. H. Charlesworth, "Water Reactor Plant Contamination and Decontamination Requirements - A Survey," Proceed. of Am. Power Conf. 33, 749 (1971).
64. W. E. Ray, R. L. Miller, S. L. Schrock, and G. A. Whitlow, "Structure of Sodium Corrosion Deposits and Their Effect on Heat Transfer Coefficients," Nucl. Tech. 16, 249 (1972).
65. K. T. Claxton and J. G. Collier, "Mass Transport of Stainless Steel Corrosion Products in Flowing Liquid Sodium," Chemical Aspects of Corrosion and Mass Transfer in Liquid Sodium, S. A. Jansson, Ed., The Metallurgical Society, New York, 1972, p. 101ff.
66. S. Weaver and E. Berkey, "Radioactive Decontamination Studies of LMFBR Coolant Systems:", Trans. Am. Nucl. Soc. 16, 109 (1973).
67. Course Outline, A Short Course in Fusion Power, Princeton University, Oct. 30-Nov. 3, 1972 - Available from Princeton University, Princeton, N. J.
68. R. W. Boom, G. L. Kulcinski, C. W. Maynard and W. F. Vogelsang, "Engineering Feasibility of a Fusion Reactor," University of Wisconsin Fusion Design Memo 43, May 1973.
69. W. F. Brehm, oral presentation of Ref. 14, American Nuclear Society Meeting, Chicago, June 1973.
70. G. R. Hopkins and G. Melese-d'Hospital, in Proceedings of the British Nuclear Energy Conference on Nuclear Fusion Reactors, Culham, United Kingdom, Dept. 17-19, 1969, page 522.
71. G. Melese-d'Hospital and G. R. Hopkins, in Proceedings of Energy '70, Intersociety Energy Conversion Engineering Conference, Las Vegas, Nevada, Sept. 22-25, 1970, page 1-65.
72. G. R. Hopkins and G. Melese-d'Hospital, Gulf General Atomic Co., San Diego, Calif., "Helium Cooling of Fusion Reactors," to be published in Nuclear Engineering and Design.



Chapter V. Neutronics and Photonics

V-A. Blanket and Shield Responses

It is important to note at the outset that a D-T reaction produces ~20 MeV (including a 14 MeV neutron) while a fission reaction produces ~200 MeV, including ~2.5 neutrons with an average energy of 2 MeV. Thus, for the same power, there are 3-4 times as many neutrons produced in a fusion as in a fission reactor. In addition, they carry seven times the energy per neutron. Thus the neutron flux in a fusion reactor is very high and the spectrum is very hard.

This gives rise to a variety of nuclear effects which are in many respects as diverse and intricate as those found in a fission reactor. However, the important behavior is quite different; for there is no eigenvalue problem for neutron multiplication. Further, no single problem dominates the subject like the neutron multiplication problem of fission reactors. Instead, a number of different, but more or less equally important, responses of the system to the neutron flux occur.

The energetic 14 MeV neutrons from the $D(T,n)\alpha$ reaction produce a highly anisotropic angular flux, at the first wall, which requires a high order transport approximation for its accurate determination. Much new data in an energy range not previously of great importance is also required.

These problems could in principle challenge the feasibility of fusion power and will in any case strongly affect the economics of the system. For these reasons, a treatment of much of the material usually referred to as fusion neutronics and photonics will be given here in considerable detail.

The responses of the blanket and shield of importance for reactor design are given next. This is followed by the main section of this chapter which presents the results in detail. The reasoning behind various design choices is explicitly discussed. Sections V-C and V-D discuss nuclear data requirements and calculational procedures. We have expended considerable effort to produce suitable energy deposition factors. Since these results are important in their own right, an appendix is devoted to the documentation of these results in addition to the discussion in the data section.

As mentioned earlier in Section IV-A, the blanket and shield must serve the diverse purposes of accepting and removing most of the energy produced, shielding the magnets from the radiation,

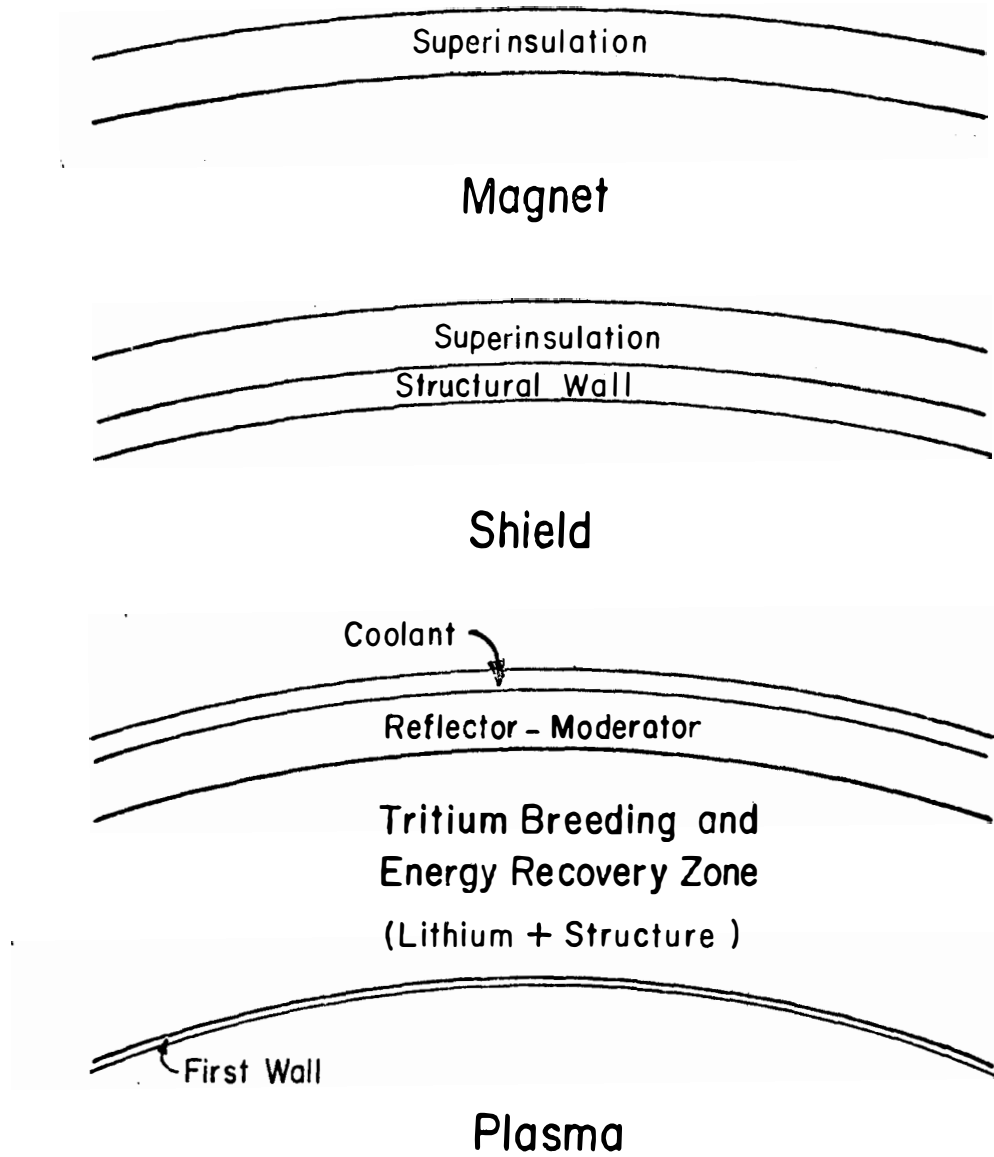
providing such structure as is necessary to form the confinement chamber and support itself, and in most D-T fueled cases, to breed additional tritium. A representative system proposed to perform these functions is shown schematically in Figure V-A-1. A first wall is shown which must withstand the most extreme environment in the system. It must be both a good heat and electric conduction medium and capable of operation at high temperatures and in the presence of intense radiation of all kinds. This narrows the choice to non-magnetic steels and the refractory metals and their alloys. Behind the first wall, a zone containing lithium in some form for tritium breeding extends for the order of 50 cm. The coolant may, in principle, either contain the lithium as a constituent or be a separate material. Further into the blanket and shield, the details could vary from that shown in the figure, but a reflector zone is often employed followed by further cooling and attenuation zones as required to protect the magnet and cryogenic systems. The responses of the system will be important in determining both the technical and economic feasibility of fusion power.

1. Tritium Production

The most obvious response is the tritium production. The only effective reactions for this purpose are the neutron reactions in Li^6 and Li^7 . The possibility of producing as much or more tritium than the D-T fusion reactions consume is based on capturing most fusion neutrons in Li^6 and losing very few fusion neutrons to parasitic capture, the production of tritium by inelastic scattering from Li^7 , and the multiplication of fusion neutrons by (n,2n) reactions in some materials. The response function required here is simply the sum of the tritium production cross sections of Li^6 and Li^7 weighted by their respective number densities. The actual response can be influenced directly by the lithium density through changes in the lithium bearing materials and the fractional content of structure and other constituents of the breeding zone and by intentionally changing the isotopic composition of the lithium. Indirectly, the response is influenced by wall, structure and other composition influences on the spectral and spatial flux dependence. The feasibility of fusion power is clearly dependent on the possibility of tritium production exceeding its consumption; however, inventory considerations detailed in Chapter VIII of this report indicate that the ratio of production to consumption (i.e. the breeding ratio) need only slightly exceed unity.

2. Radiation Damage Responses

A set of responses of great importance to reactor performance are those which relate to materials damage by the radiation (effects of charged particle fluxes are taken up elsewhere). While the ideal response functions would relate the radiation



SCHMATIC OF BLANKET AND SHIELD REGIONS

Figure V-A-1

fluxes to the specific material property effects, the phenomena involved are much too complex to allow such a direct approach. Instead, one can only determine transmutation, impurity production, and initial displacement rates in the material. Composition changes, due to hydrogen and helium production, can cause deleterious property changes which limit the time during which acceptable performance can be assured (see Chapter VI). The transmutation products may influence materials properties, but they may also be radioactive and thus create a new set of problems. For these reasons, cross sections for the various reactions form a set of response functions of great importance. A slightly different case is the displacement of atoms from their positions in the crystal lattice of the material. The damage due to displacements is complex since many displacements are offset by recombination of the vacant lattice sites with displaced atoms. The degree of recovery and the interaction of vacant sites and displaced atoms with one another and with other lattice imperfections depends on temperature and imperfection densities and is a major study area taken up elsewhere. However, even the initial displacement rate is a complex topic which depends on lattice properties as well as nuclear cross sections. Thus, a desirably response function, the displacement cross section, which would give the displacement rate when multiplied by the flux and integrated, must be based on a model of the displacement process and the various nuclear cross sections. This response function is important enough that it will be determined along with the more conventional responses.

3. Energy Deposition and Gamma Production

Most of the energy produced is carried by the neutrons. To determine the spatial distribution and the exact total amount of energy produced, neutron energy deposition cross sections known as kerma factors must be available. The energy deposition depends on the reaction Q values as well as the cross sections. Closely related to the kerma factors, the gamma production cross sections complete the energy balance for the reactions and provide the source for gamma transport calculations. Thus, while gamma production is not directly a response function of interest, it is related to energy deposition both through reaction energy conservation and through the eventual energy deposition by the gamma photons.

4. Energy Attenuation

A response which is somewhat different is the energy attenuation. This is not a reaction rate and is not even a volumetric effect. While it is related to all reactions taking place, its determination by subtracting incident energy absorbed from the incident energy would be an awkward procedure. The energy weighted current can be used to determine the attenuation achieved, but

the high energy total cross section is the data which most readily indicates the approximate attenuation rate. In any case, the energy leakage represents an important response of the blanket and shield since it measures the energy load to the magnets and thus to the cryogenic refrigerators.

5. Energy Production and Economics

The responses discussed to this point are required in the technical analysis of reactor performance. Energy production is included in 3 above, where the emphasis is on the determination of the energy deposited. However, from an economic point of view, a comparative study of alternative materials and their relative energy production may strongly influence design decisions. Thus, while energy production is not a separate response function, this discussion is introduced to emphasize that a different set of calculations may be important when optimizing the response than in simply analyzing a particular system.

The response functions mentioned here are very different from one another and are generally important in different zones of the blanket and shield. The only response which could challenge technical feasibility is tritium breeding. However, all data to date indicates that adequate breeding should occur with enough margin for error that it seems exceedingly unlikely that this will be a problem. The remaining responses, as well as the tritium production, strongly influence economic questions.

V-B. Results and Conclusions of Neutronics and Photonics Design Studies of the Blanket and Shield

1. Introduction

A detailed study of several alternative blanket and shield materials and configuration has been carried out in our program. The results of these studies were published in references 1 and 3. This section is devoted to a summary of the results. The section is organized into five parts. The next four parts deal with the main blanket and shield regions, i.e., first wall and structural materials, blanket, reflector, and shield. For each region, a series of designs is investigated using the calculational techniques described later. The leakage via divertor slots and fueling-heating ports is discussed in section 6 along with other Monte Carlo studies. Section 7 is concerned with a study of tritium breeding using variational calculations. Section 8 takes up the details of the present design and the last section draws conclusions from these studies.

2. First Wall and Structural Materials

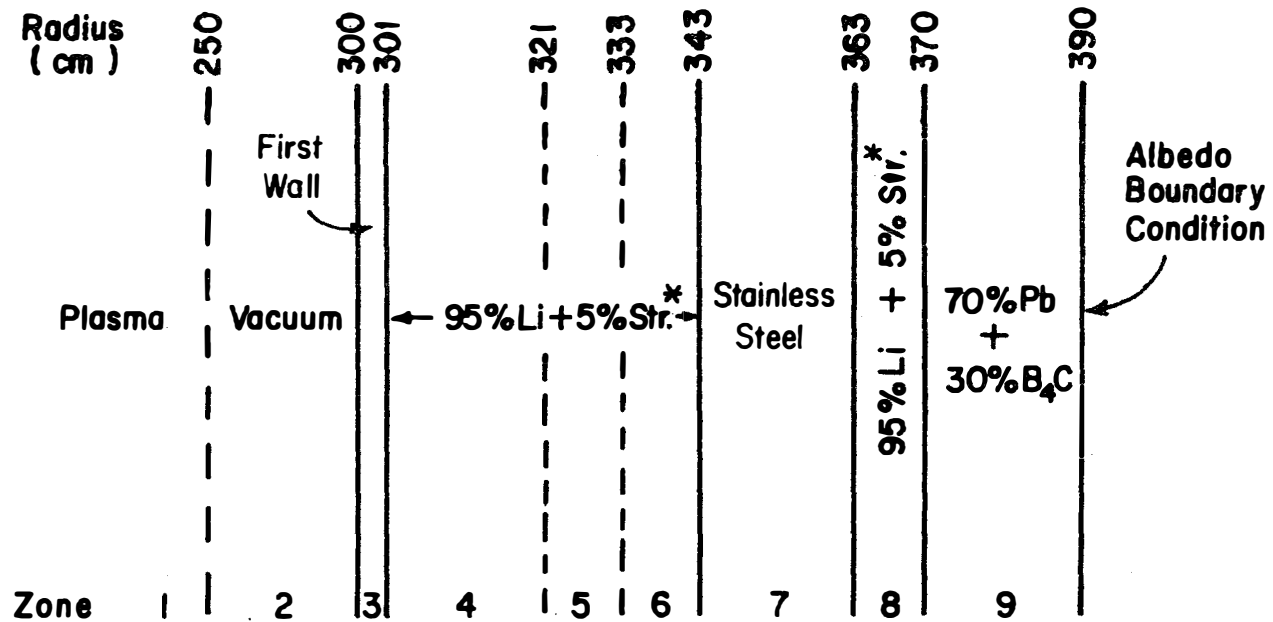
The most difficult question in the nuclear design of fusion reactors is the performance of the first wall for which several materials have been proposed. To compare the various responses for these materials, a series of neutronics and photonics calculations were carried out for the configuration of Figure V-B-1 with the first wall and structural materials chosen as vanadium, niobium, and stainless steel. Molybdenum was not included because of nuclear data deficiencies. All the designs in this section are given three digit identification numbers. Here, the identification numbers are 301 for niobium, 302 for vanadium, and 303 for stainless steel first walls and structure designs.

Figures V-B-2 and V-B-3 compare the spatially dependent helium and hydrogen production for Nb, V, and SS. These figures show that helium and hydrogen production are highest in stainless steel, lower in vanadium, and lowest in niobium. Figure V-B-4 compares the spatially dependent dpa (displacements per atom) in three structural materials. For $1\text{MW}/\text{m}^2$ neutron wall loading, each atom is displaced about 15 times each year in niobium and vanadium and about 20 times each year in stainless steel.

Table V-B-1 summarizes all the important results for the three structural materials. A comparison of the heating rates in the three designs is included in the table. These results show that the total heating rate in niobium is about 2.3 times that in vanadium and 1.2 times that in a stainless steel first wall. The relative magnitude of the neutron heating follows that of the neutron kerma factors as discussed in section C. The gamma production is largest in niobium because of the large inelastic scattering. The gamma energy deposition is also the highest in niobium as it has the largest atomic number and secondary gamma source among the three materials. The comparison of the total energy deposition in the system for the three designs shows that use of niobium increases the useful power by about 1.1 MeV per fusion reaction over a stainless steel and by 1.0 MeV over a vanadium system. This is a nontrivial gain since it represents an increase in the system power output by about 6 to 7%. Vanadium is also slightly better than stainless steel in this regard.

3. Blanket Region

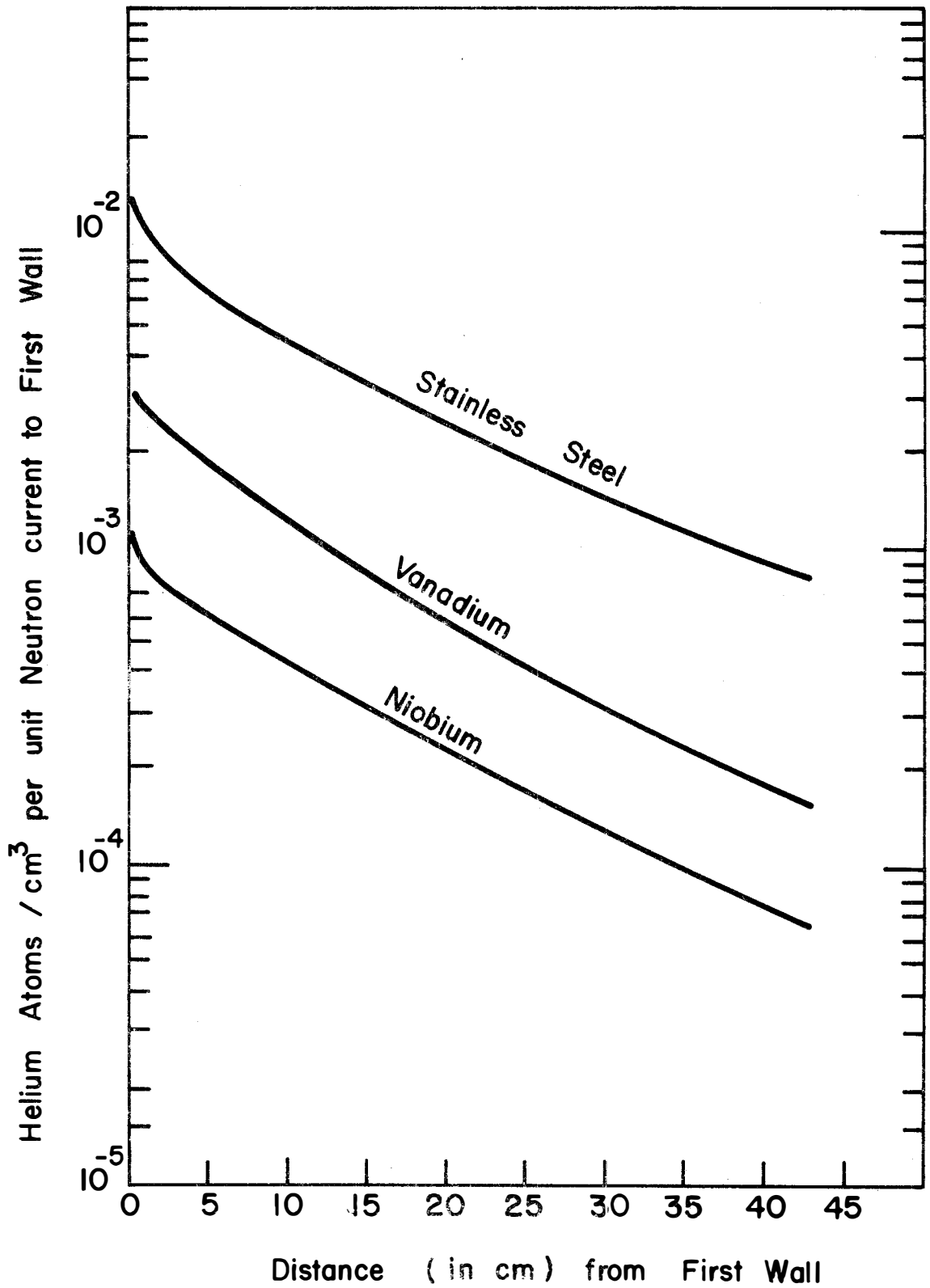
In D-T reactors, 17.6 MeV is released in a fusion reaction compared with 200 MeV per fission reaction. In addition, all the useful energy in a fusion reactor must pass through one critical section and hence the wall loading seems to be limited to values lower than desired from an economics point of view. Further, the



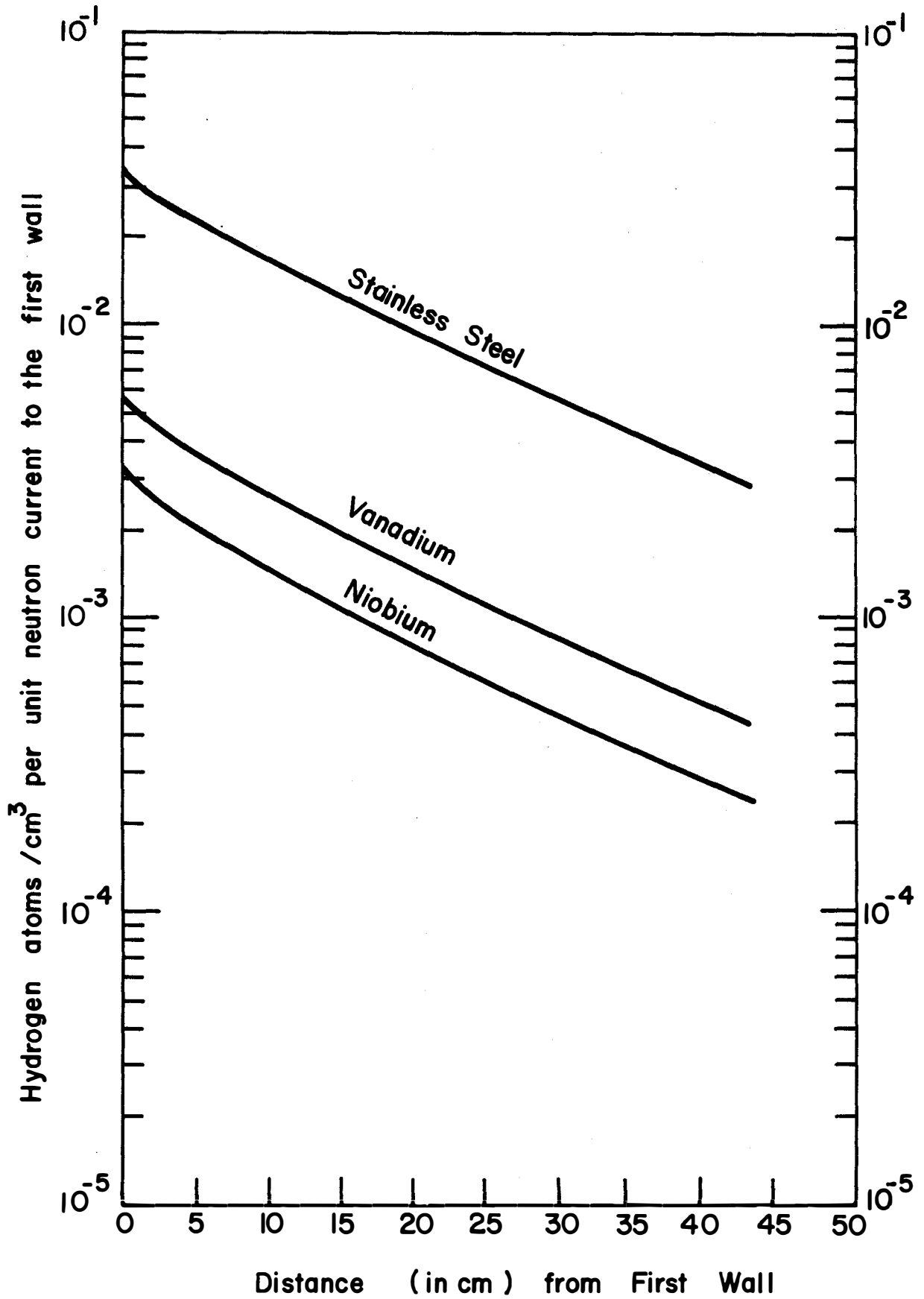
* Materials for first wall and structure are as follows:

Design 301: Niobium, Design 302: Vanadium, Design 303: Stainless Steel

Figure V-B-1 Reference Design for Comparison of the performance of several materials for first wall and structure



Comparison of Helium Production in Vanadium, Niobium & Stainless Steel



Comparison of Hydrogen Production in Vanadium, Niobium and Stainless Steel

FIGURE V-B-3

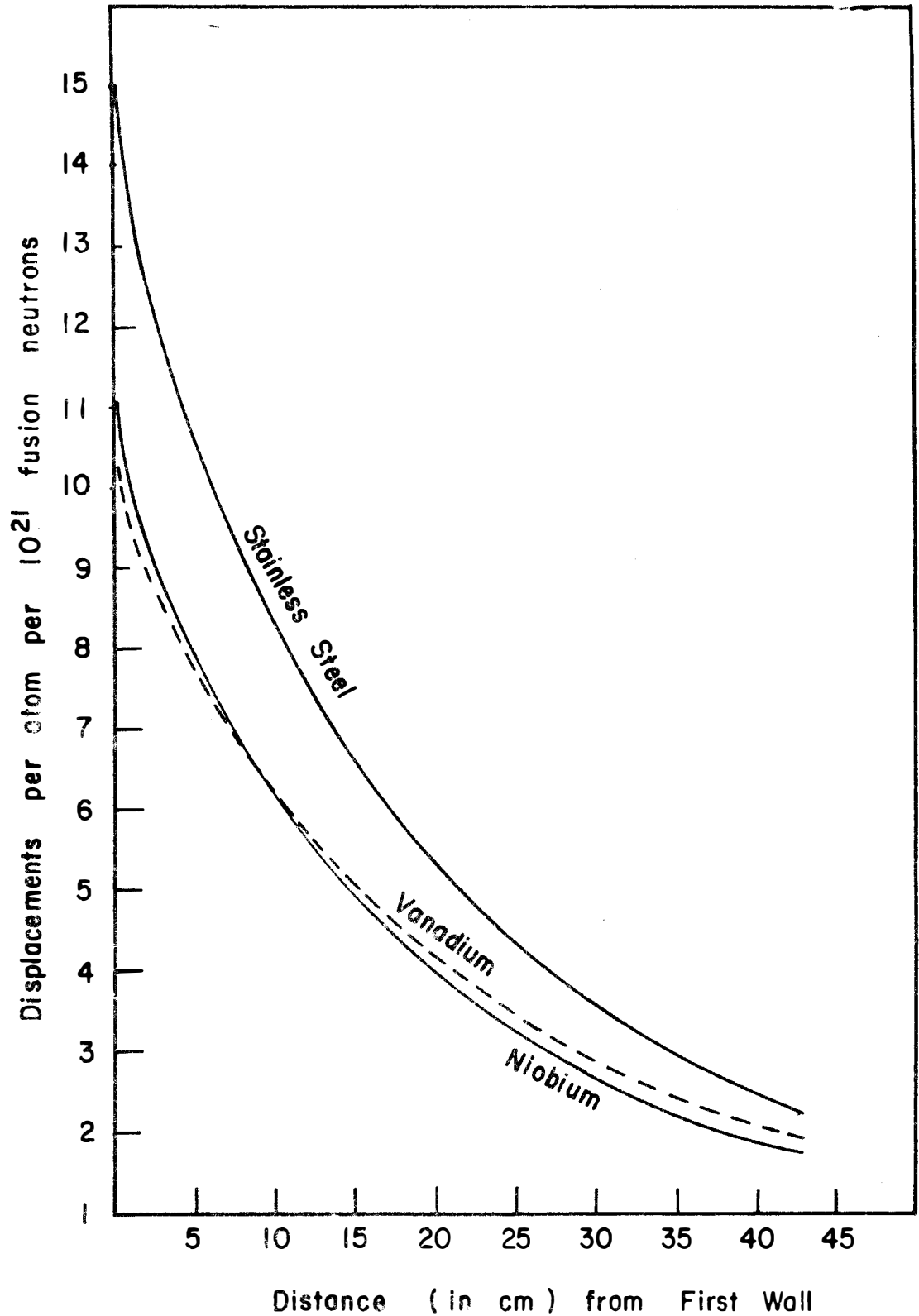


FIG. V-B-4 Comparison of Atomic Displacement for Vanadium, Niobium and Stainless Steel

Table V-B-1 Comparison of Radiation Damage Parameters, Tritium Production, and Nuclear Heating for Various Structural Materials (Designs 301, 302 & 303)

Design ID		301	302	303
First Wall & Structure		Niobium	Vanadium	Stainless Steel
Response	Zone			
(n, α) in structural material (reactions per one fusion neutron) $\times 10^4$	3	9.4470	28.9301	124.0960
	4	4.3312	12.3060	55.1620
	5	0.9119	2.2741	10.3739
	6	0.4181	1.0062	4.6977
	7	-----	-----	-----
	8	0.0084	0.0020	0.1019
	S ₂ *	15.1166	44.5364	194.4315
	displacements per atom per 10 ²¹ fusion neutron	3	10.6349	9.9863
(n,p) in structural material (reactions per one fusion neutron) $\times 10^3$	3	3.1985	5.4179	25.0850
	4	1.5423	2.7168	12.0252
	5	0.3440	0.6203	2.6478
	6	0.1601	0.2915	1.7909
	7	-----	-----	-----
	8	0.0032	0.0058	0.0361
	S ₂ *	5.2482	9.0522	41.5850
	(n,2n) in structural material	3	0.1099	0.0858
4		0.0478	0.0351	0.0199
5		0.0094	0.0061	0.0033
6		0.0042	0.0026	0.0033
7		-----	-----	-----
8		0.0001	0.0001	≈ 0.0
S ₂ *		0.1715	0.1296	0.0760
Li ⁶ (n, α) t		4	0.3671	0.4329
	5	0.2016	0.2362	0.2114
	6	0.1763	0.2035	0.1836
	T ₆	0.7734	0.9042	0.8161
Li ⁷ (n,n' α) t	4	0.3566	0.4009	0.3598
	5	0.0910	0.1033	0.0908
	6	0.0434	0.0496	0.0429
	T ₇	0.4918	0.5547	0.4944

(continued on next page)

Table V-B-1 (continued)
Comparison of Radiation Damage Parameters, Tritium
 Production, and Nuclear Heating for Various Structural
 Materials (Designs 301, 302 & 303)

Design ID		301	302	303
First Wall & Structure		Niobium	Vanadium	Stainless Steel
Response	Zone			
Tritium Breeding Ratio	T	1.2652	1.4589	1.3105
Neutron Heating in MeV per one fusion neutron	3	0.1275	0.2208	0.6016
	4	6.1366	6.9487	6.4003
	5	2.1180	2.4352	2.1895
	6	1.4315	1.6445	1.4734
	7	0.3330	0.2958	0.3204
	8	0.1615	0.1805	0.1608
	S _Z *	10.3081	11.7255	11.1458
Gamma Heating in MeV per one fusion neutron	3	1.5361	0.4881	0.7732
	4	1.7399	0.9494	1.2061
	5	0.6781	0.4135	0.4809
	6	0.4247	0.2766	0.3058
	7	2.1933	2.0718	1.8749
	8	0.0120	0.0093	0.0023
	S _Z *	6.5841	4.2087	4.6432
Total Heating in MeV per one neutron fusion	3	1.6635	0.7089	1.3748
	4	7.8765	7.8981	7.6064
	5	2.7961	2.8487	2.6704
	6	1.8562	1.9211	1.7792
	7	2.5263	2.3676	2.1953
	8	0.1735	0.1898	0.1631
	S _Z *	16.8921	15.9342	15.7890
Net Energy [†] Leakage from Zone 8				
neutrons-----		0.0672	0.0754	0.0649
gammas-----		0.0367	0.0404	0.0324

(continued on next page)

Table V-B-1 (continued)
Comparison of Radiation Damage Parameters, Tritium
 Production, and Nuclear Heating for Various Structural
 Materials (Designs 301, 302 & 303)

Design ID		301	302	303
First Wall & Structure		Niobium	Vanadium	Stainless Steel
Response	Zone			
Secondary	3	2.4370	0.7903	1.2514
Gamma	4	1.8610	1.1724	1.3190
Production	5	0.4686	0.3311	0.3555
in MeV per	6	0.2341	0.1758	0.1819
one fusion	7	1.6147	1.7700	1.5683
neutron	8	0.0078	0.0075	0.0020
	S*	6.6232	4.2471	4.6781

† in MeV per source neutron

* sum over Zones 3 through 8

(end Table V-B-1)

capital cost of fusion reactors is likely to be higher than that of fission reactors [6] and low fuel cost in fusion compared with fission reactors will only partly compensate for the low energy produced per fusion reaction. Hence, ways of increasing the energy multiplication per fusion neutron must be investigated. Fission-fusion symbiosis has been proposed [7] for the purpose of increasing energy multiplication but the complicated safety and maintenance aspects in such systems is a strong disadvantage. The subject of increasing energy multiplication in fusion reactors deserves a separate detailed study. However, two concepts for improving the effective energy produced per fusion neutron are investigated next. Before proceeding into this discussion it should be noted that higher effective energy production values (22 to 30 MeV per fusion neutron) have been quoted in literature. Much lower values are calculated here.

This low value has an important impact on the economics of fusion reactors. The reasons for the difference between our value and that obtained in previous work is discussed in great detail in reference 1. The approach we have used to calculate the energy production is based on an accurate theoretical model and an efficient computational algorithm^[4]. Furthermore, in the present work, we use consistent and energy preserving sets of kerma factors and gamma production cross sections. Two schemes for investigating the validity of energy release parameters were developed [1] and it was shown that our results are indeed correct. A comparison of the energy release parameters obtained in this work and those obtained in previous work is given in Appendix A.

Lithium Enrichment

Natural lithium consists of 7.42% Li^6 and 92.58% Li^7 . The dominant reaction in Li^7 is the (n, n^{\prime}) which is important at high energy and has a Q-value of -2.467 MeV. The most important reaction in Li^6 is the (n, α) which has a large $1/v$ cross section at low energy and a Q-value of +4.785 MeV. Both isotopes have other exothermic and endothermic reactions but these two dominate the total reaction rates. Therefore, the energy multiplication may be increased by enriching lithium (increasing the isotopic ratio of Li^6). To see the effect of enriching lithium on energy multiplication in the blanket, a series of neutronics calculations were carried out for the system shown in Figure V-B-1 with a vanadium first wall and structure. The isotopic ratio of Li^6 in lithium was increased from the natural abundance of 7.42% (design 401) to 15% in design 402, 30% in design 403 and 50% in design 404. The total energy produced in the system (first wall, lithium blanket and reflector region; see Figure V-B-1) is given as a function of Li enrichment in Table V-B-2. The results show that the gain in energy multiplication as the Li^6 isotopic ratio is increased is only 0.06% for 15% Li^6 , and 0.5% for 50% Li^6 .

Table V-B-2 Effect of enriching lithium in Li⁶ on Energy Multiplication
in the blanket

Design ID	401	402	403	404
% of Li ⁶ in Lithium	7.42 (natural)	15.0	30.0	50.0
Neutron Heating*				
in Li ⁶	4.9966	6.1338	7.6839	9.3943
Li ⁷	6.0376	5.4082	4.3270	2.9924
V	0.3953	0.3750	0.3590	0.3481
Fe	0.2340	0.2278	0.2208	0.2153
Ni	0.0801	0.0785	0.0765	0.0749
Cr	0.0538	0.0521	0.0502	0.0487
H _n = SUM	11.7974	12.2754	12.7174	13.0737
S _{Eγ} = Total Gamma Energy	4.2533	3.7893	3.3851	3.0627
H _n + S _{Eγ}	16.0507	16.0647	16.1025	16.1364
* in MeV per one fusion neutron				

Given the fact that isotopic enrichment is an expensive process, these results imply that the economics for lithium-enriched systems may be worse than for systems operating with natural lithium.

Beryllium Effects

Design 401 described earlier which is shown in Figure V-B-1 with vanadium as the first wall and structure was chosen for investigating the effect of adding beryllium to the blanket. The design was kept the same but an amount of beryllium equivalent to a 4 cm thick layer was homogenized with the first lithium region which is 20 cm of 95% natural lithium plus 5% vanadium and the new design was given the identification number 405. Design 406 is the same as design 405 except that the equivalent beryllium thickness was increased to 10 cm. Table V-B-3 summarizes the effect of adding 4 cm and 10 cm of Be on the important reactions, on heating, and on secondary gamma energy production. The results show that the tritium breeding ratio in natural lithium increases from 1.46 in design 401 (no beryllium) to 1.68 in design 405 (4.0 cm Be) to 1.91 in design 406 (10.0 cm Be). The total energy production increases by 9.3% and 18.45% when 4.0 cm and 10.0 cm of Be, respectively, are added. The energy leakage to the shield was not added in all cases because this energy is generally not recoverable with high efficiency for power production. However, it is generally 0.02 to .07 MeV and does not affect any of the above results appreciably.

It is seen from the above results that adding 4 cm of beryllium increases the power output by about 10% which is large enough to offset the high cost of beryllium. Unless the cost of 4 cm of Be is greater than 9% of the total plant cost, it is economical to use beryllium. The first wall, blanket, reflector, shield and magnet regions are of roughly 3.0 meters thickness. The average density of the materials in this region is about three times that of Be with an average cost that is uncertain at present but is somewhere between \$7/lb and \$15/lb [6]. The price of beryllium is high and uncertain too but has an estimated upper price of \$60/lb [8]. Therefore, the price of 4 cm Be is less than 3% of the total reactor cost. Since the net gain in power is greater than 9%, it is economical to use beryllium. 10 cm of Be costs roughly 8% or less of the total cost but the power increases by about 18% with the net result of a lower cost per unit power. These qualitative arguments show that the benefits from using beryllium warrants future studies for assessing the various problems associated with it, such as toxicity and high helium production. Each (n,2n) reaction in beryllium is followed by the emission of two alpha particles and table V-B-3 shows that for each fusion neutron, 0.69 alpha particles are produced in a beryllium layer 4.0 cm thick.

4. Reflector Region

As shown above, a lithium region of about 40 cm is adequate for

Table V-B-3 Effect of adding Beryllium on Energy Multiplication
in the blanket

Design	401	405	406
Thickness of Beryllium	0.0	4.0 cm.	10.0 cm.
<u>Reactions[†]</u>			
Li (n,α)	0.9042	1.2361	1.5803
Li (n,n')αt	0.5547	0.4410	0.3249
Li Tritium Breeding ratio	1.4589	1.6771	1.9052
Be (n,2n)	0.0	0.3301	0.6627
Be (n,t)	0.0	0.0055	0.0104
Be (n,α)	0.0	0.0303	0.0628
<u>Neutron Heating*</u>			
in Li ⁶	4.9966	6.4462	7.9520
Li ⁷	6.0376	4.7795	3.5067
V	0.3953	0.3756	0.3528
Fe	0.2340	0.1507	0.0774
Ni	0.0801	0.0519	0.0269
Cr	0.0538	0.0347	0.0179
Be	0.0	2.2193	4.3891
H_n = Total Neutron Heating*	11.7974	14.0579	16.3497
Gamma Energy* Production = $S_{E\gamma}$	4.2533	3.4891	2.6623
$H_n + S_{E\gamma}$	16.0507	17.5470	19.0120
% increase in energy	0.0	9.322	18.450
† reactions per one fusion neutron			
* in MeV per one fusion neutron			

satisfying the requirements of tritium regeneration even without the use of Be. Most of the neutrons are also slowed down converting their kinetic energy into heat in this lithium region. However, the average kinetic energy of the neutrons streaming out of the region is roughly 7 MeV and the net energy leakage is about 1.0 to 1.5 MeV per source neutron. Clearly, this large amount of energy cannot be allowed to pass directly into and be "wasted" in the shield which must be operated at relatively low temperatures. Therefore, an intermediate region between the lithium and shield regions is required to perform the following functions:

- 1 - moderates and reflects a large fraction of the neutrons back into the lithium region increasing the tritium production per unit volume and allowing a thinner lithium region.
- 2 - extracts nearly all the remaining kinetic energy from the neutrons thus increasing the recoverable energy and decreasing the energy leakage into shield, and
- 3 - if possible - increases the energy production.

Obviously, the thickness of the lithium region can be increased to perform the above functions. However, such a choice has disadvantages. The moderating power of lithium for fast neutrons is low and is roughly one-third that of graphite and one-fifth that of several heavy materials. Since it is important to minimize the thickness of the blanket and shield as discussed shortly, it is highly desirable to use materials with high moderating power. Further, due to the relatively low moderating power of lithium, increasing the lithium region lowers the tritium production per unit volume in the inner lithium regions with a net modest increase in the tritium breeding ratio. Both effects are undesirable because increasing the total tritium production beyond that required results in more tritium hazard and lower tritium concentration complicates the problem of tritium recovery. Increasing the lithium inventory increases the hazard of accidental potential energy release. We have also found that increasing the size of the lithium region to more than 40 cm does not produce enough added energy multiplication to be worthwhile.

For the above reasons, the thickness of the lithium region should be kept to a minimum that satisfies the tritium regeneration requirements and the lithium region should be followed by a better moderator, reflector, and energy multiplying material. Graphite has been widely used for neutron moderating applications and has also been proposed for use in fusion reactors. Iron, on the other hand, has considerably better neutron attenuation characteristics and the possibility of using it in the reflector region is explored here. In order not to perturb the magnetic field it is necessary that the materials employed be nonmagnetic. Hence, stainless steel which has more than 70% iron and is nonmagnetic should be used. Furthermore, the nickel and chromium contents of stainless steel are useful for covering the well known iron "windows" associated with the minima in its total cross section.

To bring up the salient points in comparing graphite and stainless steel in the intermediate reflector region, the configuration of Figure V-B-5 is considered. The system consists of a 1 cm first wall, 40 cm of 95% Li plus 5% structure, a 25 cm intermediate region, and a one-meter shield consisting of 50% Pb + 20% Fe + 30% B₄C. Calculations were carried out for three designs. The composition of the intermediate region is graphite in design 110, iron in design 112, and 50% Pb + 20% Fe + 30% B₄C in design 111. Iron was used in this series of calculations for the purposes of comparison but stainless steel does not change results significantly as is shown later.

Table V-B-4 is a summary of the results for the comparison between the three materials. Two important conclusions can be from this table.

- 1 - The total recoverable energy per fusion neutron in design 112 (iron reflector) is higher than that for design 110 (graphite reflector) by 1.5 MeV. In other words, replacing graphite by iron increases the recoverable energy by 9.5%.
- 2 - The total (neutron plus gamma) energy leakage from the iron is about an order of magnitude lower than that from the graphite reflector.

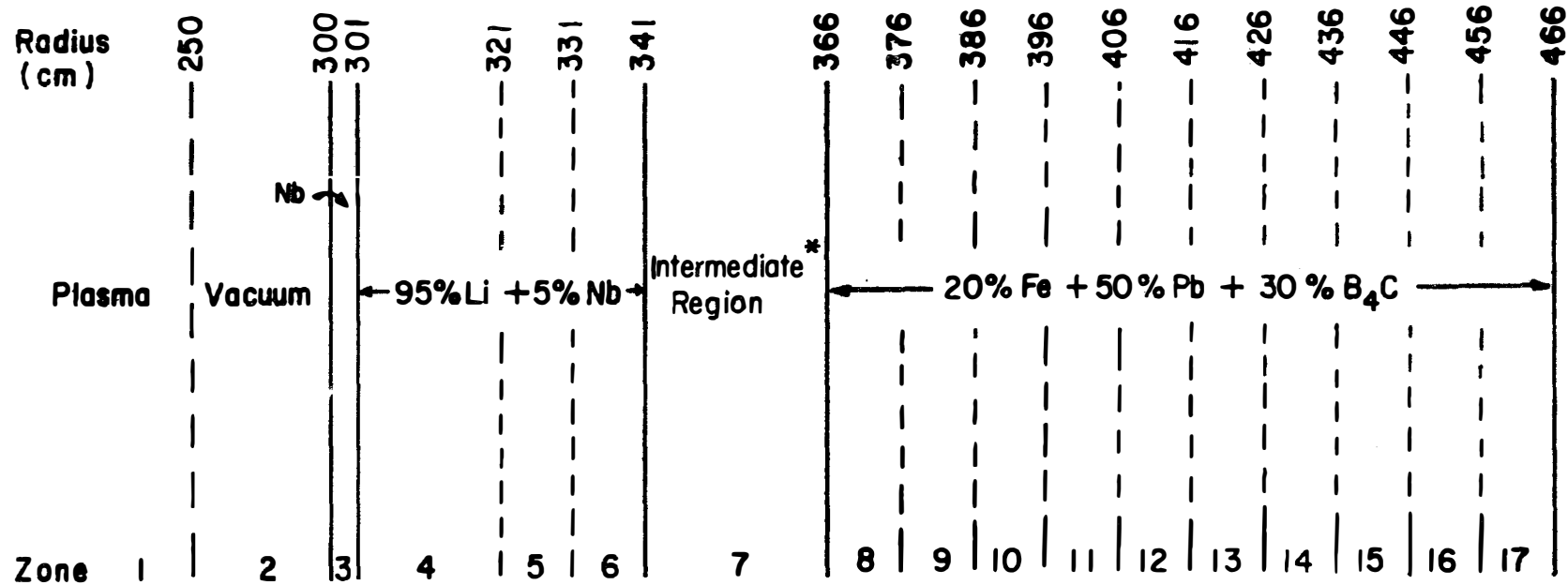
A mixture consisting of 50% Pb plus 20% Fe plus 30% B₄C is better than graphite in the reflector region from the energy attenuation and multiplication of recoverable energy points of view, but iron is better than either. The tritium breeding ratio drops to 1.06 when this mixture is used and this is unacceptable in one-dimensional calculations. In addition, the heat generation in the reflector region is so high that it would be difficult to employ lead in this region.

From the above results, iron is superior to graphite in the reflector region from both an energy multiplication, and a neutron and gamma attenuation point of view. In addition, graphite suffers from severe radiation damage [9] (mainly dimensional changes) when irradiated to fluences higher than 10^{22} n/cm² while stainless steel has better radiation resistance at such fluences. Hence, stainless steel is superior to graphite in the reflector region. The only question remaining to be answered is the effect of cost considerations. Since no quality control is required in fabricating the stainless steel for this region, its cost is roughly the same as that of graphite. In addition, the gain in energy multiplication would offset the increase in cost if stainless steel prices were higher. The stainless steel thickness required to perform the attenuation function of 25 cm of graphite is roughly 9 cm. If the cost of 9 cm of stainless steel were the same as 25 cm of graphite, there is still a benefit from using stainless steel since the shield and magnet volumes would be decreased by decreasing their inner radii.

5. Magnet Shield

a. Introduction

If the neutrons and gammas streaming out of the blanket region



* The material composition in the intermediate region was varied as follows:

Design 110: Graphite

Design 111: 20% Fe + 50% Pb + 30% B₄C

Design 112: Iron

Figure V-B-5. Reference Design for comparing the performance of various materials in the intermediate region

Table V-B-4 Comparison of Various Materials in the Reflector Region

Design	110	111	112
Reflector Material	Graphite	20% Fe + 50% Pb + 30% B ₄ C	Iron
Neutron Heating*	10.6659	10.6585	10.1790
Gamma Energy Production*	5.1714	5.6580	6.8217
Gamma Heating*	4.8306	5.6481	6.794
Total Heating	15.4965	16.3073	16.9731
Neutron Energy Leakage* from reflector	0.2794	0.0914	0.0616
Gamma Energy Leakage* from reflector	0.3399	0.0025	0.0257
Total Energy Leakage*	0.6193	0.0939	0.0873
Li ⁶ (n,α)t	0.7707	0.5808	0.7645
Li ⁷ (n,n'α)t	0.4877	0.4850	0.4836
Tritium Breeding Ratio	1.2584	1.0658	1.2481

* in MeV per one fusion (14.06 MeV) neutron

are allowed to pass directly into the superconducting magnet, the total plant power output will not be sufficient to supply the power requirements of the refrigeration system. Hence, the need for a magnet shield is obvious. No quantitative design for the magnet shield has been previously investigated. The following discussion is devoted to the nuclear design of the magnet shield.

The shield is required to perform three major functions:

1 - reduces the nuclear radiation heating of cryogenic coils to a permissible level to be defined shortly,
 2 - reduces the radiation level to the superinsulation at the inner surface facing the shield in order that it may function properly without deterioration; and 3-keeps the radiation to the magnet to that allowed by a tolerable increase in the resistivity of the copper stabilizer and radiation damage to the superconductor for a satisfactory lifetime.

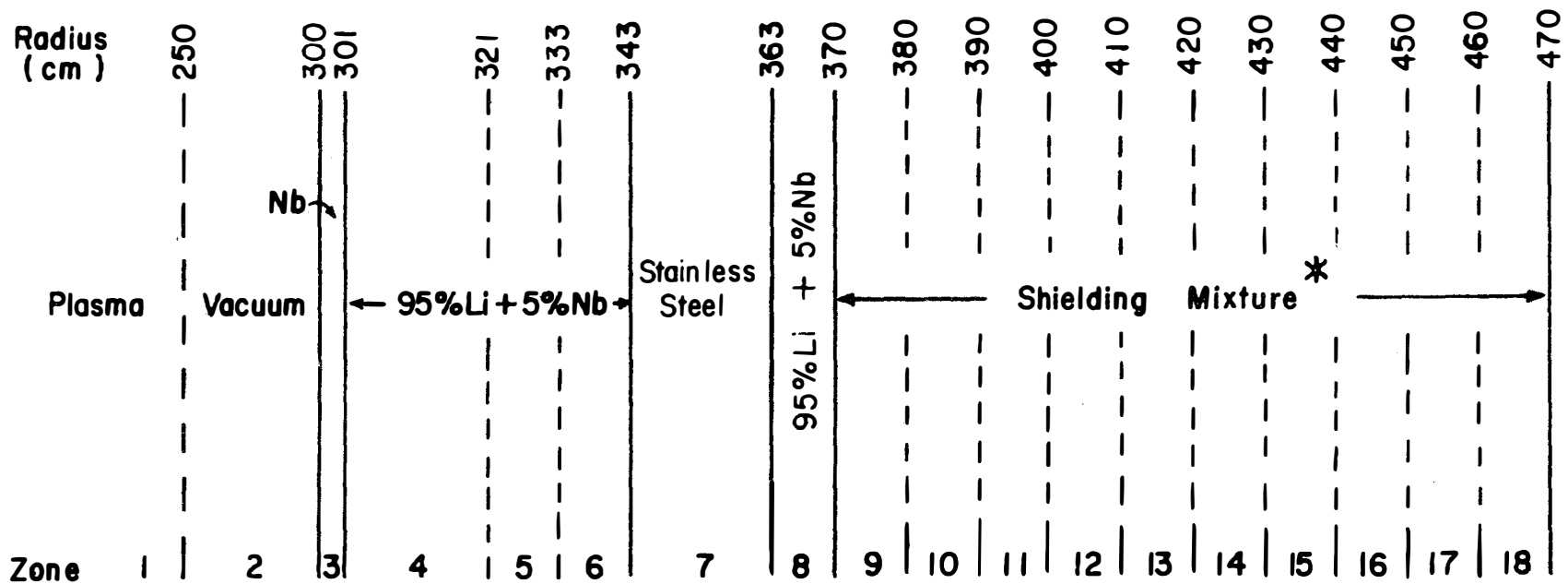
The energy attenuation required by the refrigeration system can be determined by a compromise between its operating and capital cost, the shield cost, and the increase in the magnet cost if the shield thickness is increased. On the other hand, an increase in the resistivity of the copper stabilizer, or radiation damage to the superconductor cannot be compromised beyond a tolerable level for the reactor lifetime. Therefore, a point of immediate interest is to see if the attenuation required by the refrigeration system is sufficient to satisfy the stringent requirements of radiation damage. However, before this can be done we have to investigate first the various possible shielding materials and configurations and find out the energy attenuation coefficients obtainable.

b. Shield Composition

A considerable fraction of the neutrons leaking from the blanket have kinetic energies above a few MeV. A basic requirement therefore of the shielding material is to have a large attenuation coefficient for high energy neutrons. Inevitably, this has to be a material of moderate or large mass number since inelastic scattering is the most efficient mechanism for reducing the energies of high energy neutrons. Further, light materials such as water, LiH, and lithium have small total cross sections at high energies compared with heavy materials. Stainless steel and lead have relatively large total cross sections above 3 MeV and the average secondary neutron energy per inelastic collision at 14 MeV is 2.2 and 2.5 MeV in lead and iron, respectively. Both materials are available, relatively inexpensive, and a great deal of knowledge about their characteristics exists. Below the inelastic threshold, these materials are no longer effective and a light material should be present.

Borated water is efficient and is almost cost free. However, the presence of water in the same system with a high-temperature liquid metal increases significantly the potential for accidental energy release. Graphite is an alternative choice. In addition, to minimize the gamma emission from radiative capture reactions, it is desirable to use B^{10} , which has a large (n,α) cross section for low energy neutrons and is associated only with soft gamma (.5 MeV) emission (compared with a strong line at 7.6 MeV in the capture gamma ray spectrum for iron). Boron carbide (B_4C) has been used in control rod applications in fission reactors [10] and seems to represent an excellent choice for neutron moderation and absorption at low energies. With the theoretical density, B_4C has a high content of B^{10} (0.0217 atoms/cm³). No significant radioactive decay products are formed in B_4C irradiation but helium production is significantly large. However, if B_4C is used in the shield with only 80% of the theoretical density, the swelling problem due to the excessive helium production can be tolerated. Boral (50% B_4C and 50% Al) is another good choice.

Based on the above discussion, a mixture of stainless steel and boron carbide, or of lead and B_4C , or a combination of the three materials are reasonable choices and further investigation is needed to find the optimum composition and shield depth for an overall low cost. For this purpose, a fixed composition and configuration of the blanket coupled to a shield for which the parameters are to be varied is shown in Figure V-B-6. Based on the results presented earlier in this section, the blanket consists of a 1 cm first wall, 42 cm of 95% Li plus 5% structure, 20 cm stainless steel, and 7 cm of 95% Li plus 5% structure. The first wall and blanket structure is niobium in the following calculations but the results in the shield are insensitive to this choice. The extra 7 cm of lithium at the outer face of the reflector region was introduced to meet the cooling requirements of the reflector. As a preliminary criteria, the attenuation required in the blanket and shield should be roughly 10^6 . From the previous results for design 112, this requirement can be satisfied by roughly 70 cm of stainless steel plus boron carbide following the blanket described above. As a starting point, Figure V-B-6 in which the blanket is followed by a one meter shield was considered as a reference design for investigating the various aspects of the shield design. Four cases for the composition of the shield were considered; 70% SS plus 30% B_4C (design 114), 70% Pb plus 30% B_4C (design 115), 35% SS plus 35% Pb plus 30% B_4C (design 116), and 100% SS (design 117) where percentages are by volume. Neutronics and photonics calculations were carried out for the four designs. It will be shown in a later section that the convergence of the discrete ordinates results for such system are achieved by S_8 and that S_4 overestimates the leakage by 10 to 15%. In order to reduce the cost for these calculations, S_4 was used. However the comparison is not significantly



* Shielding mixture varies in this series of designs as follows:

Design 114: 70% SS + 30% B₄C, Design 115: 70% Pb + 30% B₄C, Design 116: 35% SS + 35% Pb + 30% B₄C,

Design 117: 100% SS

Figure V-B-6. Reference Design for Shield Calculations

affected by the difference between S_4 & S_8 . P_3 scattering anisotropy and cylindrical geometry approximations were used in all these calculations. Before proceeding to discuss the results, a few words about "terminology" will be helpful.

The energy deposition in the magnets by neutrons and photons streaming out of the shield increases, in general, with the neutron and photon energies. Hence, it is appropriate in comparing the performance of the various shield compositions to compare the "energy" rather than the "number" attenuations. The net neutron energy leakage at the right boundary for a spatial zone is defined as the total energy of the neutrons streaming out (to the right) of the zone minus the total energy of the neutrons entering the zone at the right boundary. Mathematically, the neutron energy leakage, L_{nE} , at a zone boundary is then given by

$$L_{nE} = \int E_n J_{no}(E_n) dE_n \cdot (2\pi r_0)$$

and in multigroup representation,

$$L_{nE} = \sum_g E_{ng} J_{nog} \cdot 2\pi r_0 \quad (1)$$

where $J_{no}(E_n)$ is the neutron current density for neutrons of energy E_n at the outer (right) boundary for the zone. The current density here is the net current density (i.e. $J = J^+ - J^-$). The subscript g denotes an energy group and J_{nog} is the neutron current density in the group. E_{ng} is the midpoint energy for group g and $2\pi r_0$ is the surface area at the zone outer boundary per unit length in the unbounded direction. A similar term is defined for photons with the subscript γ replacing n . The total energy leakage, L_{TE} , is the sum of neutron and photon energy leakage, i.e.

$$L_{TE} = L_{nE} + L_{\gamma E} \quad (2)$$

The average kinetic energy for the neutron leakage at the outer boundary is defined as

$$\bar{E}_n = \frac{\sum_g E_{ng} J_{nog}}{\sum_g J_{nog}} \quad (3)$$

with a similar term for the gammas.

We will assume that L_{nE} , $L_{\gamma E}$, and L_{TE} vary exponentially with the spatial variable within the shield (it will be shown shortly that, to an excellent approximation, this is indeed so within a region of uniform composition), i.e.

$$L_{nE}(r) = L_{nE}(0) e^{-\mu_n r} \quad (4.a)$$

$$L_{\gamma E}(r) = L_{\gamma E}(0) e^{-\mu_\gamma r} \quad (4.b)$$

$$L_{TE}(r) = L_{TE}(0) e^{-\mu r} \quad (4.c)$$

Each μ is called the energy attenuation coefficient of the appropriate type as indicated by the subscript or by no subscript for the total. The energy attenuation coefficient, A_f , for a distance of width $r_2 - r_1$ is defined as

$$A_f = \frac{L_{TE}(r_2)}{L_{TE}(r_1)} \quad (5)$$

with a similar term for neutrons and photons. All the results are usually quoted here per fusion neutron (14 MeV) unless otherwise indicated. The above symbols and definitions will be employed in the tables and text to follow.

The energy leakage, L_{TE} , is plotted against the distance from the inner boundary of the shield for the four compositions in Figure V-B-7. Inspection of this figure reveals the following:

- 1 - L_{TE} varies exponentially with the spatial variable in the shield, to an excellent approximation, as assumed in equations 4.
- 2 - The total energy attenuation coefficient is equal to $.1445 \text{ cm}^{-1}$ for design 114, 0.1113 for design 115, $.1283$ for design 116, and $.0902$ for design 117.
- 3 - Comparison of L_{TE} for designs 114 and 117 shows that the presence of B_4C (or an alternative) is necessary. At the end of a one meter shield the total energy leakage in a 100% stainless steel shield is about two orders of magnitude higher than that in a shield consisting of 70% SS plus 30% B_4C . This is mainly due to the fact that B_4C is better than SS in attenuating neutrons below about 2 MeV, and in the absence of B_{10} , neutrons slowed down eventually gets absorbed in radiative capture reactions in stainless steel increasing the gamma energy production.
- 4 - Comparison of designs 114, 115 and 116 shows that stainless steel has considerably better neutron attenuation characteristics than lead if both are mixed with a fair amount of light material.

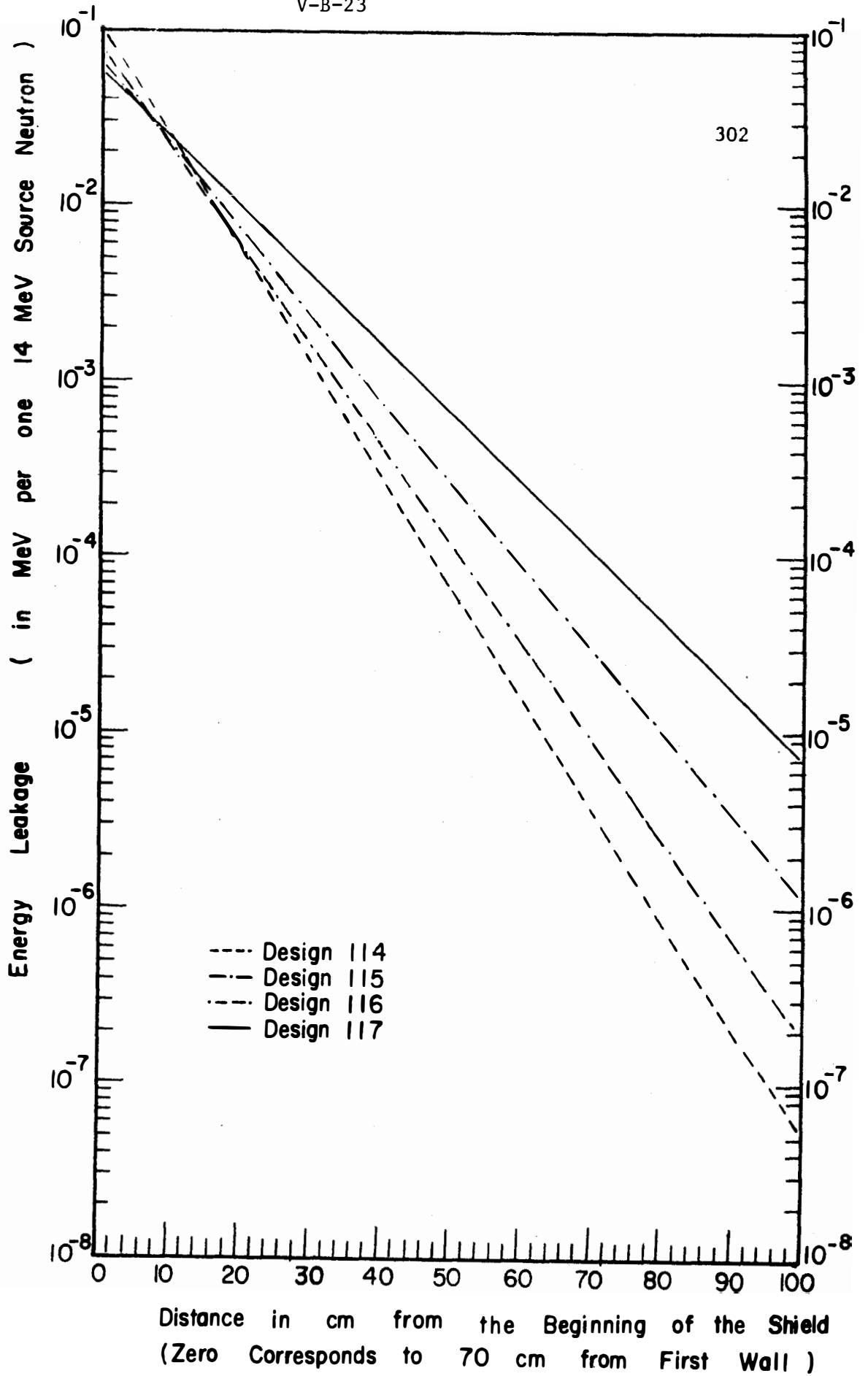


FIGURE V-B-7

c. Optimum Shield Thickness

Increasing the thickness of the shield increases its cost and the magnet cost but lowers the refrigeration power requirements. In the following, an attempt is made to find the optimum thickness that minimizes the cost for a given shield composition.

The total cost of the reactor as a function of the shield thickness is given by
 Total Cost = Magnet cost + shield cost + refrigeration cost +
 other fixed costs independent of the shield parameters.

Since the reactor is fairly uniform in the toroidal direction the cost can be stated per unit length in the toroidal direction. The above equation can be rewritten as

$$C_T = C_M + C_S + C_R + C_F \quad (6)$$

where the subscripts M, S, R, and F denotes magnet, shield, refrigeration, and fixed costs, respectively. All the C's are in dollars per unit length. An expression for each of these items as a function of the shield parameters is derived next.

The magnet cost is assumed to be proportional to the energy stored in the magnetic field (see Chapter VII). This is a function of the field strength, the major radius for the torus, (R), and the inner radius, (r_M), of the magnet. Since our concern is the dependence of the magnet costs on the shield thickness, all these parameters except r_M are assumed fixed. Further, it is assumed that the magnet cost, C_M , varies with r_M to the power m, i.e.

$$C_M = a'_M \left(\frac{r_M}{r_{ref}} \right)^m \quad (7)$$

where r_{ref} is the inner radius of the magnet in a reference design.

$$C_M = a_M r_M^m, \quad a_M = \frac{a'_M}{(r_{ref})^m} \quad (8)$$

$$r_M = r_b + t_s \quad (9)$$

where r_b is the outer radius for the blanket (inner radius for the shield)^b. t_s is the shield thickness and is the parameter to be optimized.

The shield cost is taken to be that of the material in the shield, i.e.

$$C_S = \pi(t_S^2 + 2r_b t_S) \cdot a_S \quad (10)$$

where a_S is the cost of the shielding material in dollars per unit volume.

The refrigeration cost is estimated to be \$6000 per watt of thermal load (see Chapter VII) and it varies with the capacity as

$$C_R = 6000 P^{0.6} \quad (11)$$

where P is the thermal load in watts and is given by

$$P = 2\pi r_w \cdot W_n \cdot e^{-\mu_b t_b} \cdot e^{-\mu_s t_s} \quad (12)$$

Here, r_w is the first wall radius, W_n is the neutron wall loading, μ_b and μ_s are the energy attenuation coefficients in the blanket and shield respectively, and t_b is the blanket thickness. Thus

$$C_R = a_R e^{-0.6\mu_s t_s} \quad (13)$$

where

$$a_R = 6000(2\pi r_w W_n e^{-\mu_b t_b})^{0.6} \quad (14)$$

Rewriting equation (6) in terms of the above parameters and minimizing C_T with respect to t_s , the optimum shield thickness, t_{so} , is found to be given by

$$t_{so} = \frac{1}{0.6\mu_s} \text{Log}_e \left[\frac{0.6 \mu_s a_R}{m a_M (r_b + t_{so})^{m-1} + 2\pi a_S (r_b + t_{so})} \right] \quad (15)$$

Tables V-B-5 and V-B-6 tabulate the values of the optimum shield thickness for different values of the parameters in equations (6) through (15). The energy attenuation coefficient, μ_s , for the shield is taken as 0.1447 cm^{-1} (which is obtained from the results of design 114 for 70% SS + 30% B₄C) and 0.1113 cm^{-1} (which is obtained from design 115 for 70% Pb + 30% B₄C) in tables V-B-5 and V-B-6, respectively. In all cases, the value of $\exp(-\mu_b t_b)$ was taken as .007 which was found to represent the energy attenuation in the blanket in all of the designs 114 through 117 without any significant variation. The values of a' and r_{ref} in equation 7 were taken from Lubell's work [11] as 70×10^6 and 5.6 meters, respectively. It was found that 50% change in this typical cost results in less than 5% change in the optimum shield thickness for the conditions of tables V-B-5 and V-B-6.

From equation (15) it is noted that the optimum shield thickness varies inversely with μ_s^m , a_M , r_b , and a_S and increases with the refrigeration coefficient, a_R . Except for μ_s , the dependence of t_{so} on these parameters is relatively weak due to the nature of the logarithmic function. For example, inspection of both tables V-B-5 and V-B-6 shows that changing the dependence of the magnet cost on r_M in equation 7 from $m = 1$ to $m = 2$, changes t_{so} by only 3 to 8% depending on the other parameters. Doubling the wall radius (compare cases 1 & 7, and 4 & 8 in table V-B-5; 1 & 5, and 4 & 7 in table V-B-6) changes the optimum thickness of the shield by roughly 2%. The results show a relatively strong dependence of t_{so} on the wall loading. It is worth noting that if one assumes that a specified fraction of the power output is to run the refrigerators, the attenuation required is fairly independent of the wall loading.

In table V-B-5 two prices for the stainless-B₄C mixture were used. The value a_S of 6.26 gm/cm^3 . The other value of a_S is 0.035 and corresponds to \$2.55/lb of the mixture. The price for the lead-B₄C mixture was taken as \$0.92/lb.

Case number 5 in table V-B-5 represents typical conditions for the reactor. The wall loading is 1 MW/m^2 , μ is taken from transport calculations and the price of the shield and magnet are realistic. This case shows that for these conditions and for the blanket shown in Figure V-B-6 the total cost is minimized for a shield consisting of 70% SS + 30% B₄C by a thickness of 66.97 cm. The total cost in this case is $\$19,220 \times 10^4$ /cm and for a major radius of 12 meters is 144.8 million dollars. The corresponding case with the lead-B₄C mixture is case number 1 in table V-B-6. The total price for a major radius of 12 meters is 128.42 million dollars. These prices do not include fixed costs (see equation V-B-6). From these two cases, it is concluded that using the lead-B₄C mixture saves 16 million dollars compared with the SS-B₄C mixture. Furthermore, these optimum thicknesses correspond to 4.17×10^{-6} MeV to the magnet per MeV in the first wall for SS-B₄C and 1.85×10^{-7} per MeV for the lead-B₄C. Hence the lead-B₄C mixture is cheaper to use and optimum thickness corresponds to better attenuation.

Table V-B-5 Values of Optimum Shield Thickness for several values of the Parameters in equations 6 through 15 for an energy attenuation coefficient of 0.1447 in the shield
(corresponding to 70% SS + 30% B₄C)

parameter	r_w (cm)	r_b (cm)	W_n watts/cm ²	m	a_S^* \$/cm ³	a_M \$/cm	a_R \$/cm	t_{so} (cm)
Case No.								
1	400	470	100	1	0.088	18.96	5.312(+5)	57.60
2	400	470	1000	1	0.088	18.96	2.115(+6)	73.19
3	400	470	50	1	0.088	18.96	3.504(+5)	52.90
4	400	470	100	2	0.088	0.03386	5.312(+5)	57.00
5	400	470	100	1	0.0352	18.96	5.312(+5)	66.97
6	200	270	100	1	0.0352	18.96	3.504(+5)	66.65
7	200	270	100	1	0.088	18.96	3.504(+5)	57.87
8	200	270	100	2	0.088	0.03386	3.504(+5)	57.69
9	200	270	50	1	0.088	18.96	9.204(+5)	68.65

* a of 0.088 corresponds to \$6.4/lb for a density of 6.26 gm/cm³ and 0.0352 corresponds to \$2.55/lb for a density of 6.26 gm/cm³

Table V-B-6 Values of Optimum Shield Thickness for several values of the Parameters in equations 6 - 15 for an energy attenuation coefficient of 0.1113 cm^{-1} in the shield
(corresponding to 70% Pb + 30% B_4C)

Parameter	r_w	r_b	W_n	m	a_S^*	a_M	a_R	t_{so}
Case No.	(cm)	(cm)	$\frac{\text{watt}}{\text{cm}^2}$		$\$/\text{cm}^3$	$\$/\text{cm}$	$\$/\text{cm}$	(cm)
1	400	470	100	1	0.0176	18.96	5.312(+5)	91.06
2	400	470	1000	1	0.0176	18.96	2.115(+6)	111.3
3	400	470	50	1	0.0176	18.96	3.504(+5)	84.96
4	400	470	100	2	0.0176	0.03386	5.312(+5)	87.98
5	200	270	100	1	0.0176	18.96	3.504(+5)	89.65
7	200	270	100	2	0.0176	0.03386	3.504(+5)	88.38

* a_S of 0.0176 corresponds to 0.92 $\$/\text{lb}$ for 70% Pb + 30% B_4C

6. Monte Carlo Calculations

Almost all of our neutrons calculations have been based on one dimensional geometries, such as the infinite cylinder. These 1-D calculations have been based on the multigroup Sn approximation to the transport equation. To date, no transport solutions have been carried out in toroidal geometry, the actual geometry of Tokamak reactors.

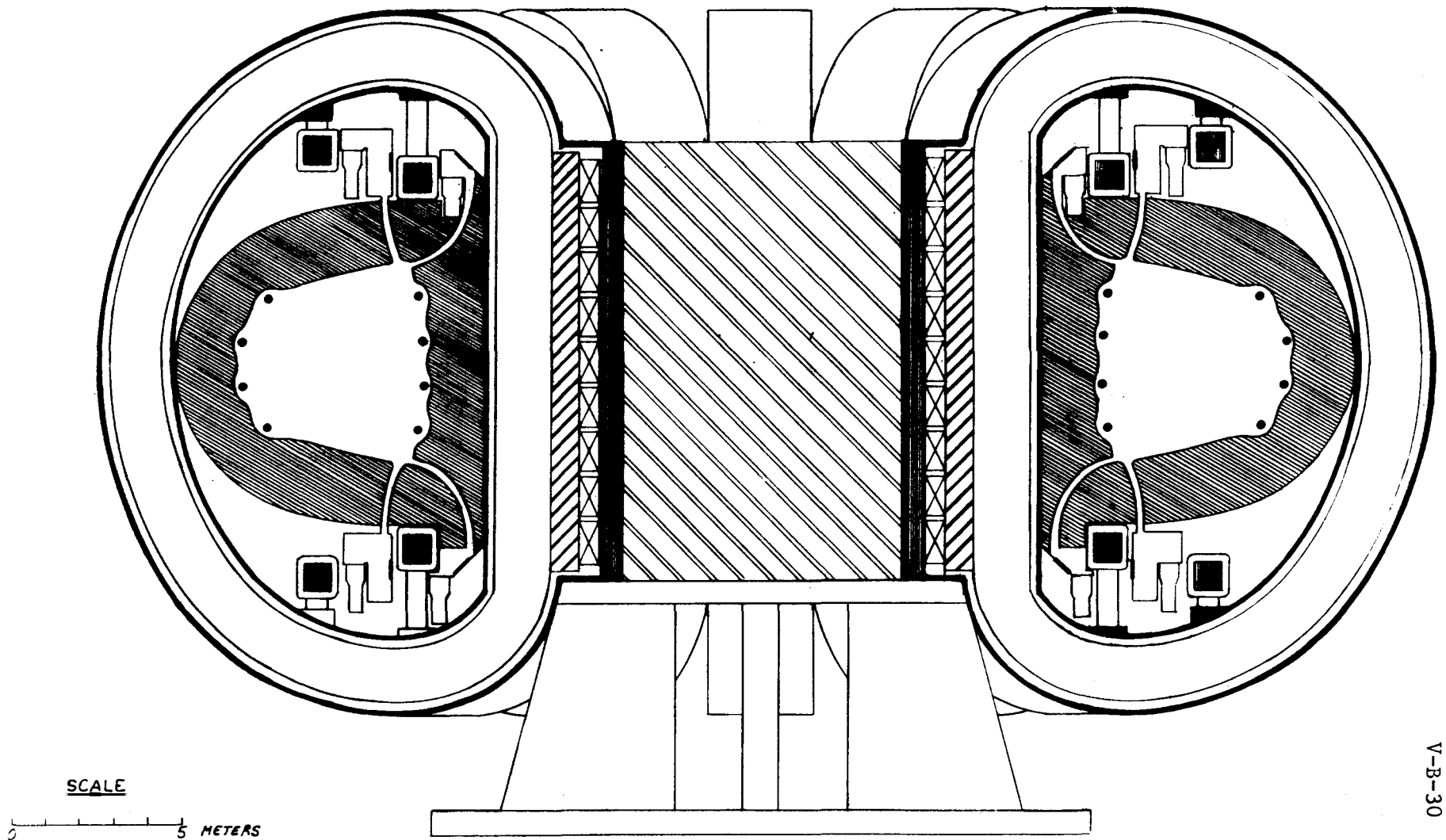
Monte Carlo methods are generally more adaptable to studies requiring realistic treatments of the geometry of a problem. In fact, it is possible to develop a toroidal geometry routine for Monte Carlo computer programs, although this has not been done to date. Even without this refinement, there are a number of geometry questions which can be investigated with the aid of Monte Carlo. The types of problems of interest here are those involving neutron leakage through divertor slots and fueling ports, and those related to homogenization to obtain a simple cylindrical representation for survey studies.

Our implementation of these calculations employed the MORSE computer program. ^(12-b) This is a multigroup program with a flexible geometry routine allowing rather arbitrary quadratic surfaces. The nuclear data employed is in the form of 46 energy group sets derived from ENDF data. It is the same data and group structure as is used in the Sn calculations. P₃ anisotropy is retained in the scattering treatment.

The initial calculations were based on the interim UW design presented at Austin, Texas in November, 1972 and shown schematically in Figure V-B-8. As the slots for the divertor do not directly face the center of the confinement region, it is of considerable concern that the correct spatial distribution of the neutron source be employed. The geometry used is shown in Figure V-B-9, which is an accurate representation of the main features of the confinement region, blanket, and shield. In order to see the influence of source geometry, three different source representations were chosen based on plasma density distributions. These are:

- 1 - the actual plasma shape with a uniform density distribution,
- 2 - a circular plasma shape with a uniform density distribution, and
- 3 - a circular plasma shape with a parabolic density distribution.

Leakage of neutrons and energy in the form of neutrons for cases 1, 2, and 3 above are given in Table V-B-7 and the tritium production in the various regions is given in Table V-B-8. The leakage in this 1,000 MWth plant amounts to 340 KW at the back of the slots in the worst case. Referring to the attenuation indicated for various shields in Figure V-B-7, additional shielding of 30 to 40 centimeters at most are required to shield the magnets. As is readily seen, in Figure V-B-8, there is more than adequate room behind the slots for such a special shield in this design. The tritium production differs very little for the different cases and compares favorably with the value 1.5 from the simple infinite cylinder results. There is a very significant difference in the leakage through the slots for the different



SCALE

5 METERS

FIGURE V-B-8

UNIV. OF WIS. CONCEPTUAL DESIGN FOR A
FUSION
POWER (KOMAK)

V-B-30

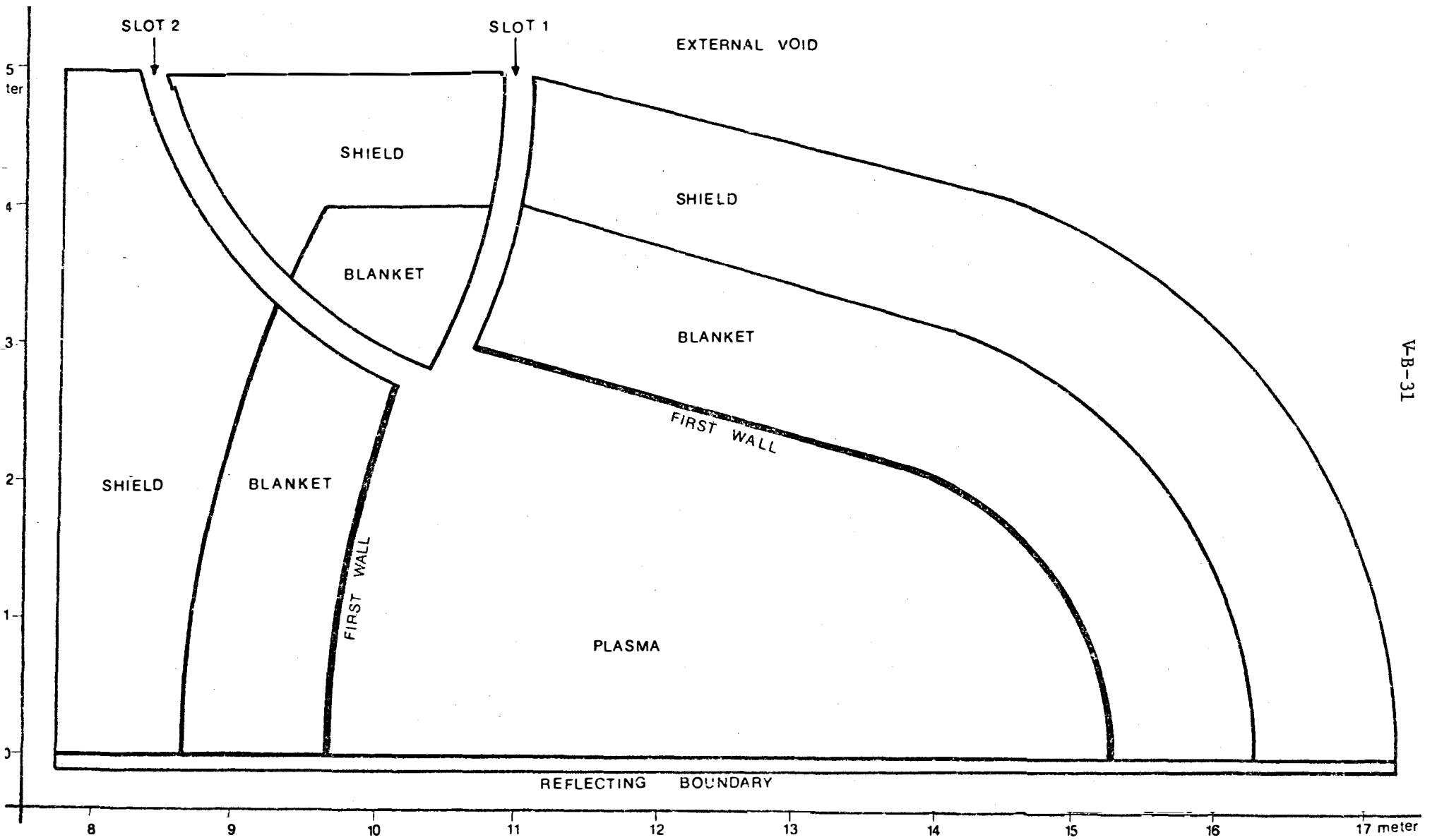


Figure V-B-9 - Blanket and Shield Configuration

Table V-B-7
Summary of Leakage Probabilities

Case Leakage	1	2	3
Leakage prob. from slots	0.256%	0.222%	0.231%
Energy leakage from slots (Mev/Mev)	0.34×10^{-3}	0.186×10^{-3}	0.145×10^{-3}
Leakage prob. from the system	0.204%	0.151%	0.172%

Table V-B-8
Tritium Production

Case	Case 1		Case 2		Case 3	
T Region	T ₇	T ₆	T ₇	T ₆	T ₇	T ₆
1	0.1731	0.2961	0.1374 ± .0041	0.3037 ± .0064	0.1357 ± .0043	0.2985 ± .0069
2	0.1372	0.2853	0.1322 ± .0043	0.2880 ± .0060	0.1391 ± .0042	0.2908 ± .0048
3	0.0278	0.0679	0.0298 ± .0018	0.0669 ± .0031	0.0321 ± .0028	0.0684 ± .0033
4	0.1274	0.2768	0.1288 ± .0041	0.2792 ± .0062	0.1268 ± .0045	0.2782 ± .0062
Total	0.4655	0.9261	0.4282 ± .007	0.9378 ± .011	0.4337 ± .007	0.9359 ± .011
T ₇ + T ₆	1.3916		1.3660 ± 0.02		1.3696 ± .02	

source distributions. Inspection of the table shows the expected actual source shape, as used in case 1 yields about twice the leakage from the slots compared to case 2. Case 1 is almost certain to overestimate the leakage since the source is not expected to extend, with uniform strength, to the boundary of this plasma. The overestimate may well be of the order of 30% as would be indicated by comparing cases 2 and 3.

The homogenization of a unit cell of the blanket coolant structure is required in the S_n infinite cylinder studies. The cell is shown in Figure V-B-10. The one space dimension treatment is obtained by replacing the actual first wall by a one space parameter simulation which preserves at least approximately the volume of the actual wall (.73 cm thick as compared with the real .5 cm wall thickness). The remainder of the wall is included by treating the coolant region as a mixture of 95% lithium and 5% structure. An intermediate stage in this simplification is shown in Figure V-B-11. Tables V-B-9 and V-B-10 show the comparison the the flux and tritium production in the two cells shown. Essentially all results are the same within the statistical uncertainty. These results also agree very well with the corresponding results for the completely homogenized discrete ordinates calculations. Thus, the homogenization employed in the S_n calculations is adequate.

V-B-35

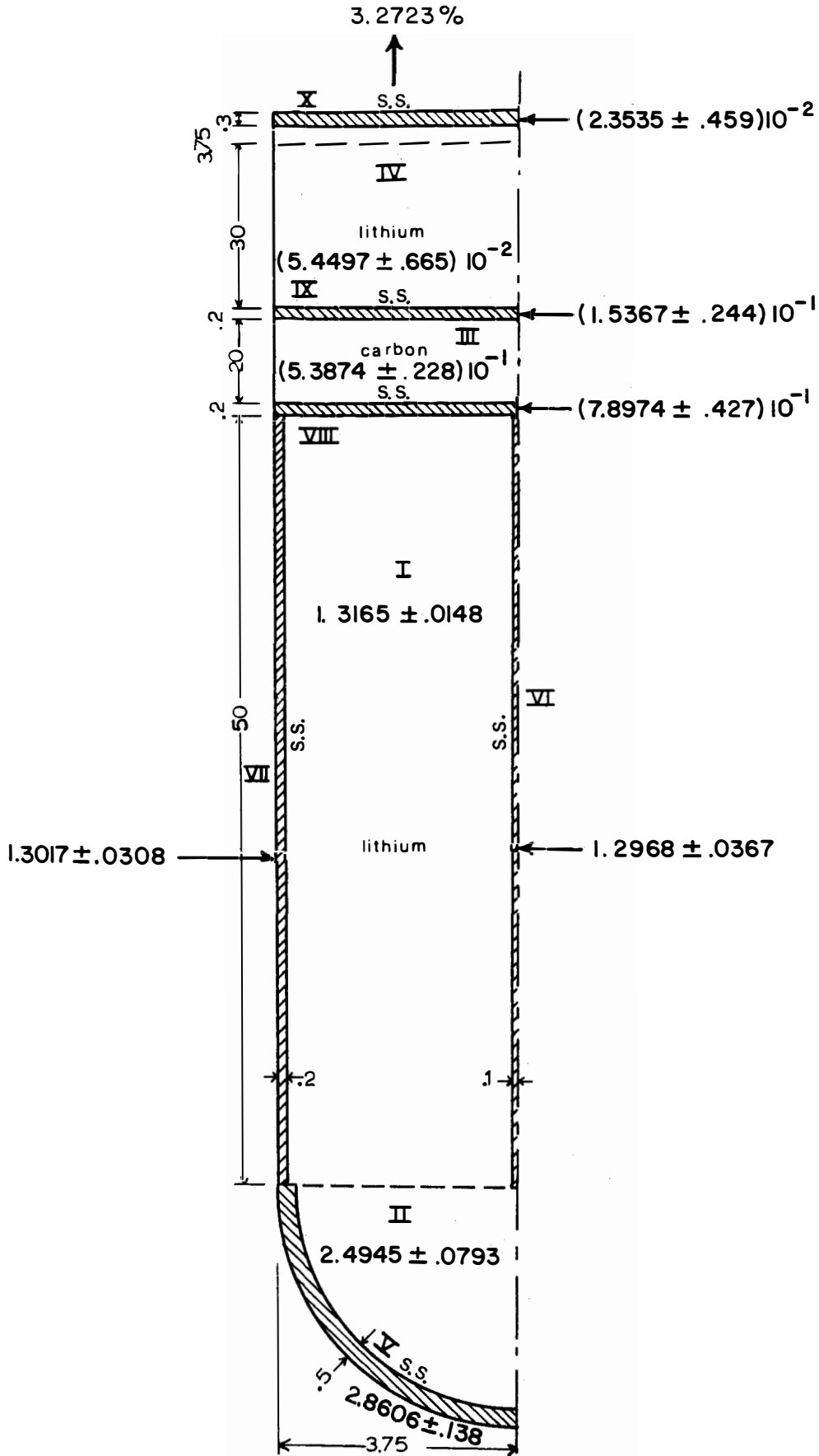
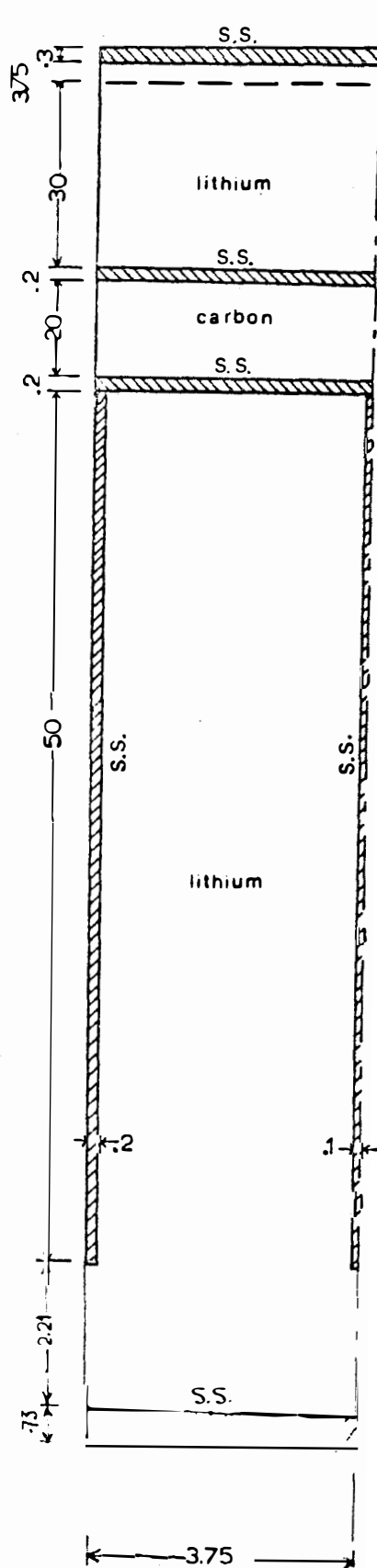


FIGURE V-B-10. Schematic of Unit Cell



all units are in cm

Figure V-B-11-Schematic of Unit Cell

Table V-B-9

Region	Case	1	2
I		$1.3165 \pm .0148$	$1.3268 \pm .0193$
II		$2.4945 \pm .0793$	$2.6137 \pm .0876$
III		$(5.3874 \pm .228)10^{-1}$	$(4.5662 \pm .23)10^{-1}$
IV		$(5.4497 \pm .665)10^{-2}$	$(6.1263 \pm .65)10^{-2}$
V		$2.8606 \pm .138$	$3.0198 \pm .131$
VI		$1.2968 \pm .0367$	$1.3245 \pm .0289$
VII		$1.3017 \pm .0308$	$1.3102 \pm .027$
VIII		$(7.8974 \pm .427)10^{-1}$	$(7.3825 \pm .378)10^{-1}$
IX		$(1.5367 \pm .244)10^{-1}$	$(1.2462 \pm .2068)10^{-1}$
X		$(2.3535 \pm .459)10^{-2}$	$(1.2471 \pm .346)10^{-2}$

Table V-B-10 - Tritium Production

Case	Curved First Wall		Straight First Wall	
Region ^T	T ₇	T ₆	T ₇	T ₆
I	.3944 ± .01536	.8693 ± .01129	.3585 ± .01278	.8719 ± .0112
II	.08615 ± .004552	.05014 ± .001693	.07896 ± .005536	.05425 ± .00233
IV	.003275 ± .001622	.1065 ± .008144	.006818 ± .022424	.1111 ± .009036
TOTAL	.048494 ± .0161	.1026 ± .014	0.44427 ± .0141	1.0372 ± .0145
T ₆ + T ₇	1.51094 ± .02		1.48147 ± .02	

7. Variational Sensitivity Study

It is expected that variational procedures will allow extensive survey and sensitivity studies at reasonable computing costs. As an example of this type of calculation in a case of considerable interest, Conn and Cheng [14] have carried out a study of the influence of varying amounts of structural material in the coolant region on the tritium breeding ratio.

The results, shown on Figure V-B-12, give the breeding ratio plotted against the volume percent of stainless steel. A set of discrete ordinates calculations using the ANISN computer program were carried out in this case to illustrate the accuracy of the less expensive variational results. Two variational curves are shown corresponding to bilinear and fractional (Roussopolous and Schwinger) functionals. Both are within a few percent of the exact result for small composition variations about the reference case (at 5 volume percent) but for very large increases in the structural content, the fractional form is more accurate and is still within 7% of the exact calculation.

The breeding ratio is seen to vary from 1.55 at 1% structure to 1.17 at 20% structural content. At the design content of 5% structure, the ratio is 1.44. These are S4-P3 46 group slab geometry calculations and differ slightly from the full cylindrical calculation.

8. Details of Present U.W. Design

From the neutronic and photonic studies discussed to this point, the following blanket and shield design has been chosen for UWMAK-I. The design is shown schematically in Figure V-B-13. Heat transfer, radiation damage to materials, superinsulation and magnet considerations were taken into account in this design.

The plasma and wall radii, a and r_w , were given from other studies of the plasma parameters (see Chapter II, Section F). In the previous section, it was shown that no undesirable neutronics effects would arise from choosing a first wall thickness somewhere between zero and 2 cm. Therefore, the first wall thickness was determined from considerations, including hoop and thermal stresses, and corrosion problems. The wall thickness chosen is 2.5 mm. For one-dimensional calculations, the effective wall thickness which approximately preserves the first wall volume, is taken as 4 mm. The main blanket region consists of 51 cm of 95% Li plus 5% stainless steel, by volume. It was shown earlier that adequate tritium breeding could be obtained with a thinner blanket (about 35 cm). However, in order to achieve adequate heat transfer and reduce the pressure of the coolant on the first wall, the blanket thickness was increased to 51 cm. This also reduces the pumping power losses. The reflector region (zone 7) is stainless steel. The merits of this choice over other alternatives, such as graphite, were discussed in the previous sections. Zone 8 consists of 5 cm of 95% Li plus 5% SS and provides for cooling the reflector and the blanket structural wall (zone 9).

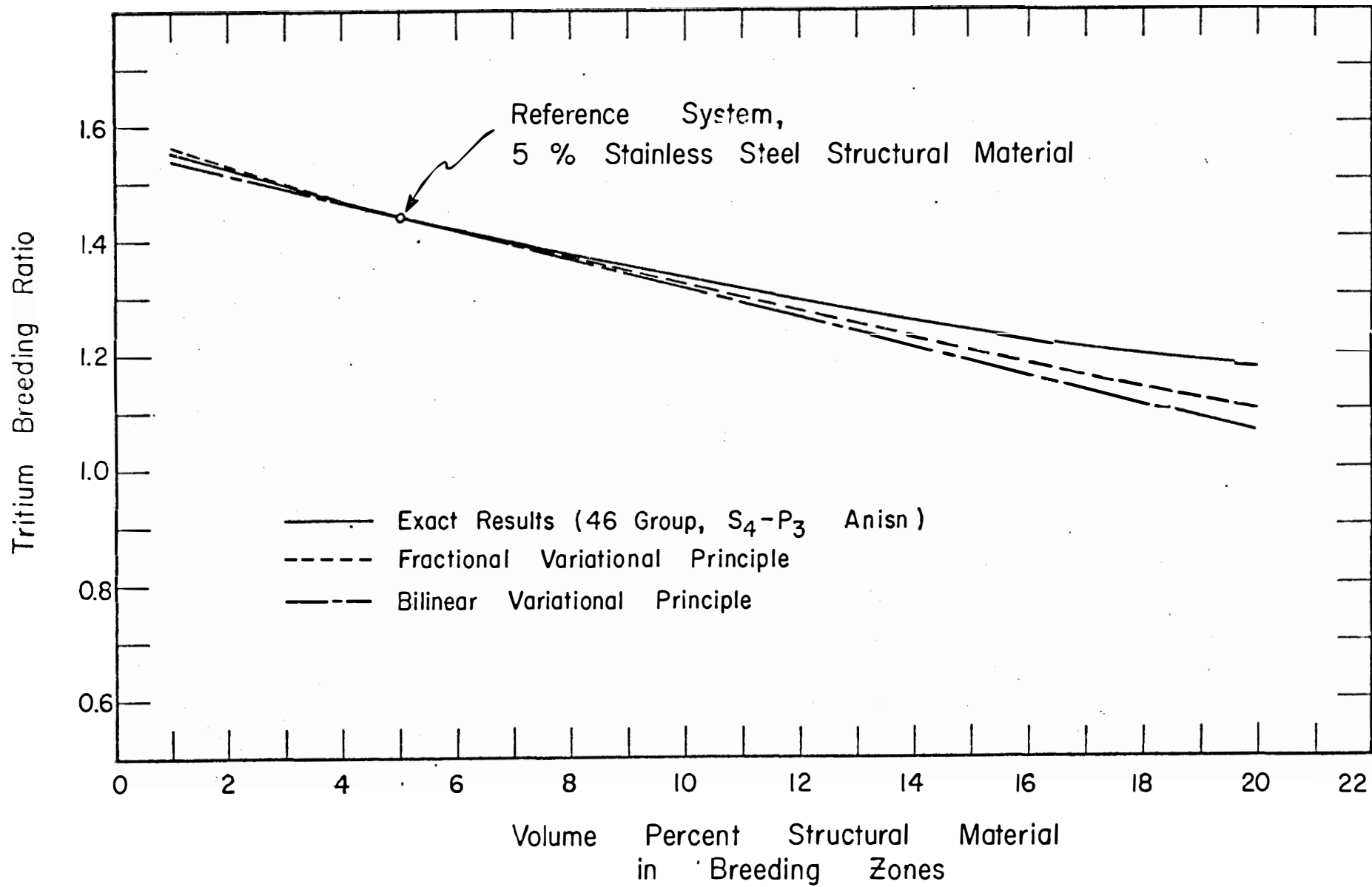
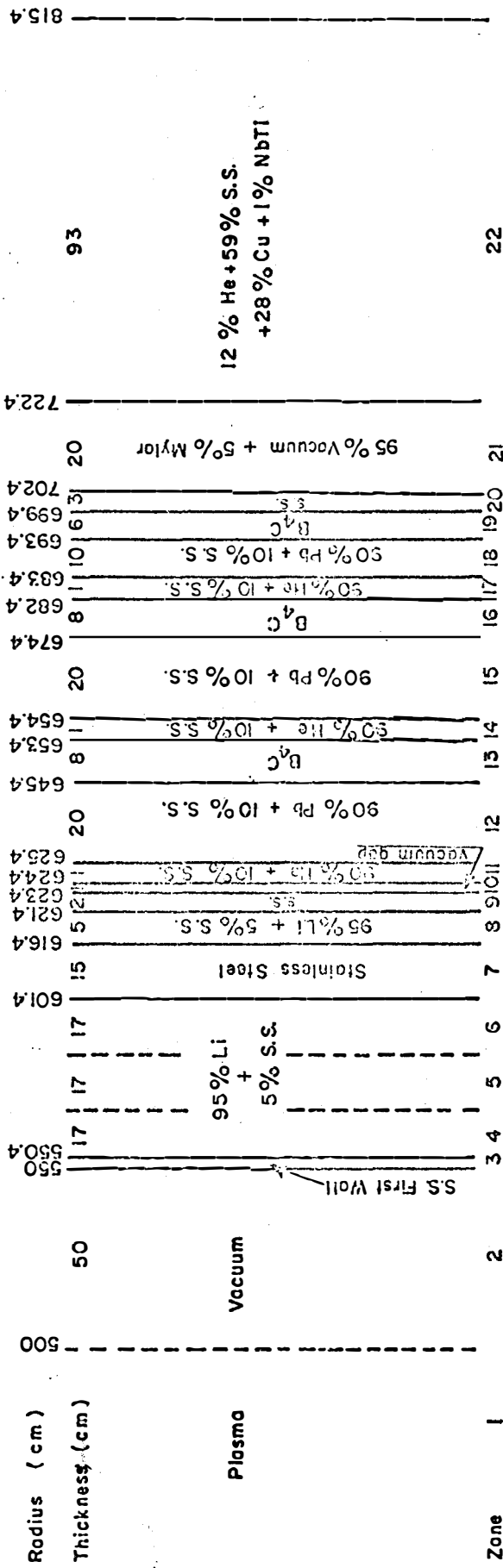


Figure V-B-12. Tritium Breeding Ratio as a Function of Percentage Structure in the Breeding Region.



University of Wisconsin CTR Blanket, Shield and Magnet Structure for 5000MW_T System.

Figure V-B-13

In order to provide maximum cooling efficiency, this 5 cm lithium zone is rearranged within the reflector region, as described in the heat transfer section (see section IV-B). The neutronics results in the main blanket and shield regions are not appreciably affected by redistributing the coolant inside the reflector zone.

Zone 10 is a 1 cm vacuum gap and it serves as a thermal barrier between the high temperature blanket region (about 500°C) and the low temperature shield (approximately 200°C). Zones 12 through 20 comprise the magnet shield. As shown in the previous section, for the materials investigated, an optimum shield, from a cost point of view, consists of a homogeneous mixture of 70% Pb plus 30% B₄C. The total energy attenuation is obtained using the heterogeneous arrangement of lead and B₄C shown in Figure V-B-13. However, 10% of the total volume is occupied by stainless steel for structural purposes. Zones 11, 14 and 17 are for helium cooling of the shield. Zone 20 serves as the dewar and for further attenuation of the nuclear radiation. Zone 21 is thermal insulation for the magnet and cryogenic systems. The vacuum in this zone is to prevent heat transfer by conduction and the nylon superinsulation reduces thermal radiation losses. (see Chapter VII for the details of the magnet design.) The magnet region was homogenized for neutronics and photonics calculations as shown in zone 22 of Figure V-B-13. All percentages in Figure V-B-13 are by volume and the nuclide densities used in the calculations are given in Table V-B-11. The nuclide densities used in the calculations accounted for thermal expansion at the operating temperatures.

We turn now to the important neutronics and photonics parameters for the present UW design. These results provide the basic input to other areas of the design; thus, the implication of most of these results are discussed in other chapters.

Neutron and gamma heating are given by material and zone in MeV per source neutron in Tables V-B-12. Several observations are in order. The gamma heating is only about 25% of the total nuclear heating in the blanket and shield. The neutron heating in lithium alone contributes about 70% of the total nuclear heating in the system. The nuclear heating in the shield (zones 11 through 20) is 1.26% of the total nuclear heating in the blanket and shield. In other words, for the 5000 MW(th) plant and with ~ 20 MeV per fusion reaction (as discussed next), only 51 MW of thermal power is dissipated in the shield. Extracting this amount of energy at high efficiency is therefore not crucial from a total plant economics point of view. It is however, necessary to remove this energy to ensure the physical integrity of the shield.

Tables V-B-12a,b show that the total nuclear heating is 16.56 MeV per source neutron. Hence, the net energy per fusion reaction is 20.06 MeV, which is lower than the values reported in earlier literature (as discussed earlier in this chapter). However, these results

Table V-B-12-a
 Neutron Heating by Material and Zone
 (in units of MeV per source neutron)

<u>Zone</u>	<u>Composition</u>	<u>Li⁶</u>	<u>Li⁷</u>	<u>Fe</u>	<u>Cr</u>	<u>Ni</u>	<u>B-10</u>	<u>B-11</u>	<u>Pb</u>	<u>C-12</u>	<u>Sum by Zone</u>
1	Plasma										0.0
2	Vacuum										0.0
3	S.S.			0.165	0.036	0.057					0.258
4	95% Li	1.848	3.836	0.182	0.040	0.065					5.970
5	+	1.473	1.713	0.070	0.010	0.026					3.298
6	5% S.S.	1.377	0.823	0.031	0.007	0.012					2.250
7	S.S.	-	-	0.146	0.034	0.050					0.230
8	95% Li + 5% S.S.	0.234	0.023	0.0007	0.0002	0.0002					0.258
9	S.S.	-	-	0.0047	0.0012	0.0014					7.30(-3)
10	Vacuum	-	-	-	-	-					.0
11	90% He + 10% S.S.			2.0(-4)	5.2(-5)	6.15(-5)					3.14(-4)
12	90% Pb + 10% S.S.			2.2(-3)	5.4(-4)	5.93(-2)			4.66(-3)		6.20(-2)
13	B ₄ C			-	-	-	1.29(-1)	6.2(-3)		1.88(-3)	1.37(-1)
14	He + 10% S.S.			9.9(-6)	2.42(-6)	3.0(-6)					1.53(-5)
15	90% Pb + 10% S.S.	-	-	1.0(-4)	2.6(-5)	2.86(-5)			2.3(-4)		3.85(-4)
16	B ₄ C	-	-	-	-	-	3.95(-4)	2.51(-5)		7.6(-6)	4.28(-4)
17	He + 10% S.S.	-	-	4.5(-7)	1.1(-7)	1.3(-7)					6.90(-7)
18	90% Pb + 10% S.S.	-	-	3.07(-6)	7.6(-7)	8.67(-7)			6.60(-6)		1.13(-5)
19	B ₄ C	-	-	-	-	-	3.95(-4)	2.51(-5)		7.60(-6)	4.28(-4)
20	S.S.			1.53(-6)	3.70(-7)	4.68(-7)					2.37(-6)
Sum by Material		4.932	6.395	0.604	0.135	0.213	0.135	0.006	0.005	0.002	12.43

V-B-43a

Table V-B-12-b

Neutron and Gamma Heating by Zone (in units of MeV per source neutron)

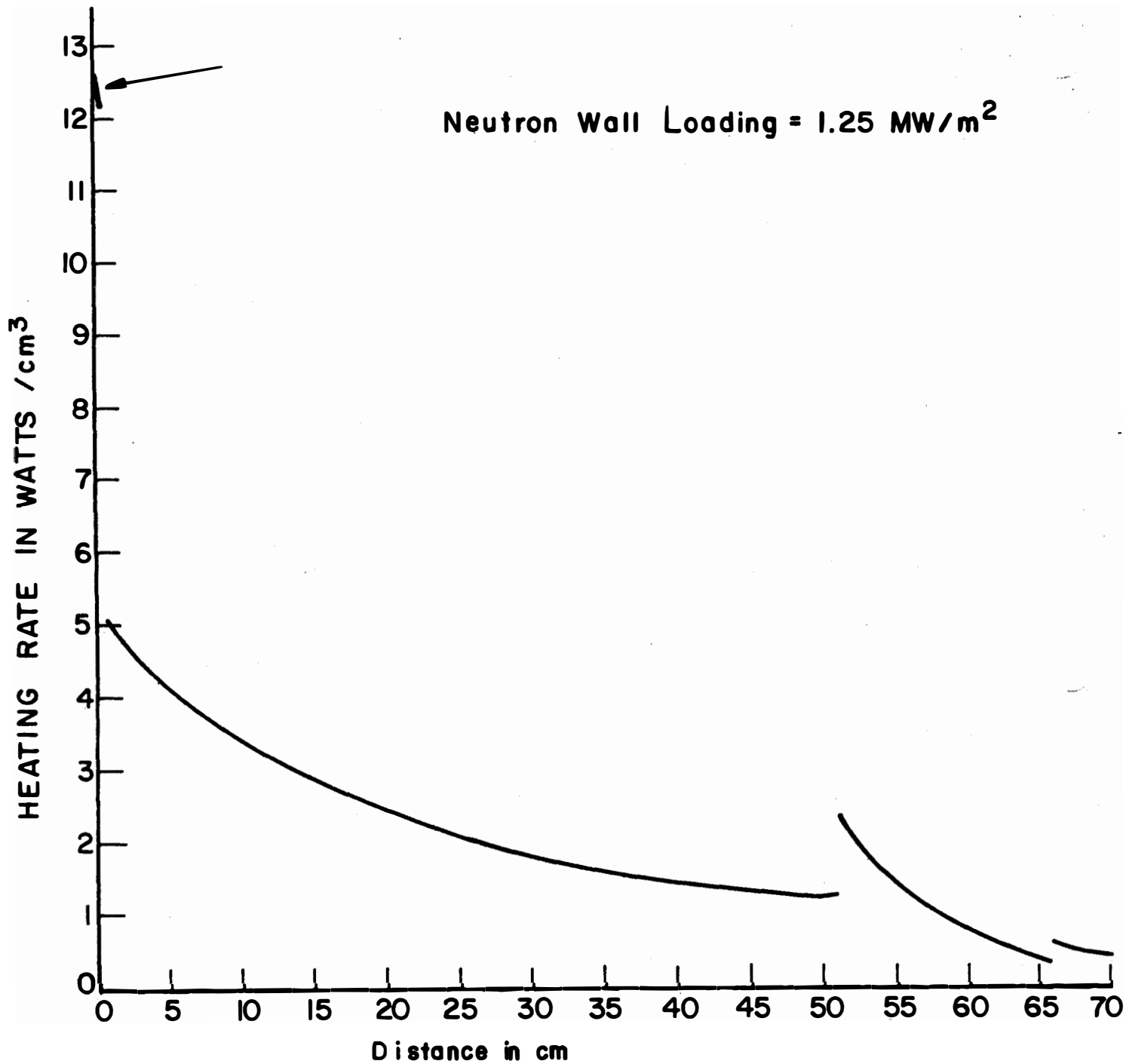
Zone	Composition	Neutron Heating		Gamma Heating		Total Heating	
1	Plasma	_____		_____		_____	
2	Vacuum	_____		_____		_____	
3	Stainless steel	0.258		0.300		0.558	
4	95% Li	5.9		1.027		6.997	
5	+	3.298		0.703		4.001	
6	5% Stainless steel	2.250		0.479		2.729	
7	Stainless steel	0.230		1.462		1.692	
8	95% Li + 5% SS	0.258		0.014		0.272	
9	Stainless steel	7.30		0.046		0.053	
10	Vacuum	_____		_____		_____	
11	90% He + 1% SS	3.14	(-4)	1.589	(-3)	1.89	(-3)
12	90% Pb + 10% SS	6.20	(-2)	9.64	(-2)	1.58	(-1)
13	B ₄ C	1.37	(-1)	4.86	(-4)	1.37	(-1)
14	90% He + 10% SS	1.53	(-5)	2.32	(-5)	3.85	(-5)
15	90% Pb + 10% SS	3.85	(-4)	2.62	(-3)	3.00	(-3)
16	B ₄ C	4.28	(-4)	2.09	(-5)	4.49	(-4)
17	90% He + 10% SS	6.90	(-7)	1.00	(-6)	1.69	(-6)
18	90% Pb + 10% SS	1.13	(-5)	8.60	(-5)	9.73	(-5)
19	B ₄ C	4.28	(-4)	4.41	(-6)	4.32	(-4)
20	SS	2.37	(-6)	1.58	(-5)	1.60	(-5)
	SUM	12.43		4.13		16.56	

are not explained on the basis of simply having different systems. They result rather because the kerma factors and gamma production data used are thorough and self-consistent.

Figure V-B-14 shows the spatial distribution of the total nuclear heating in the first 70 cm of the blanket. Figure V-B-15 gives this heating broken down into the two types, neutron and gamma heating. The neutron wall loading in our design is 1.245 MW/M² and is rounded off to 1.25 MW/M² throughout this report. From Figure V-B-14, it can be seen that the heating in the first wall is about 12.5 watts/cm³. The maximum volumetric heating rate in the blanket is less than one-half of this value

Table V-B-13 gives the tritium production per source neutron by zone from Li⁶ and Li⁷. The tritium breeding ratio is 1.49. The spatial distribution of tritium production in Li⁶, Li⁷, and the sum is shown in Figure V-B-16. The atomic displacement rates in stainless steel are shown versus distance in the blanket in Figure V-B-17. Helium and hydrogen production are given by zone in Tables V-B-14 and V-B-15.

The neutron and gamma flux spectra at several positions in the blanket and shield are given in Appendix B.



(Zero corresponds to inner radius of first wall.)

Fig.V-B-14 SPATIAL DISTRIBUTION OF HEATING RATE IN
THE BLANKET AND REFLECTOR REGIONS

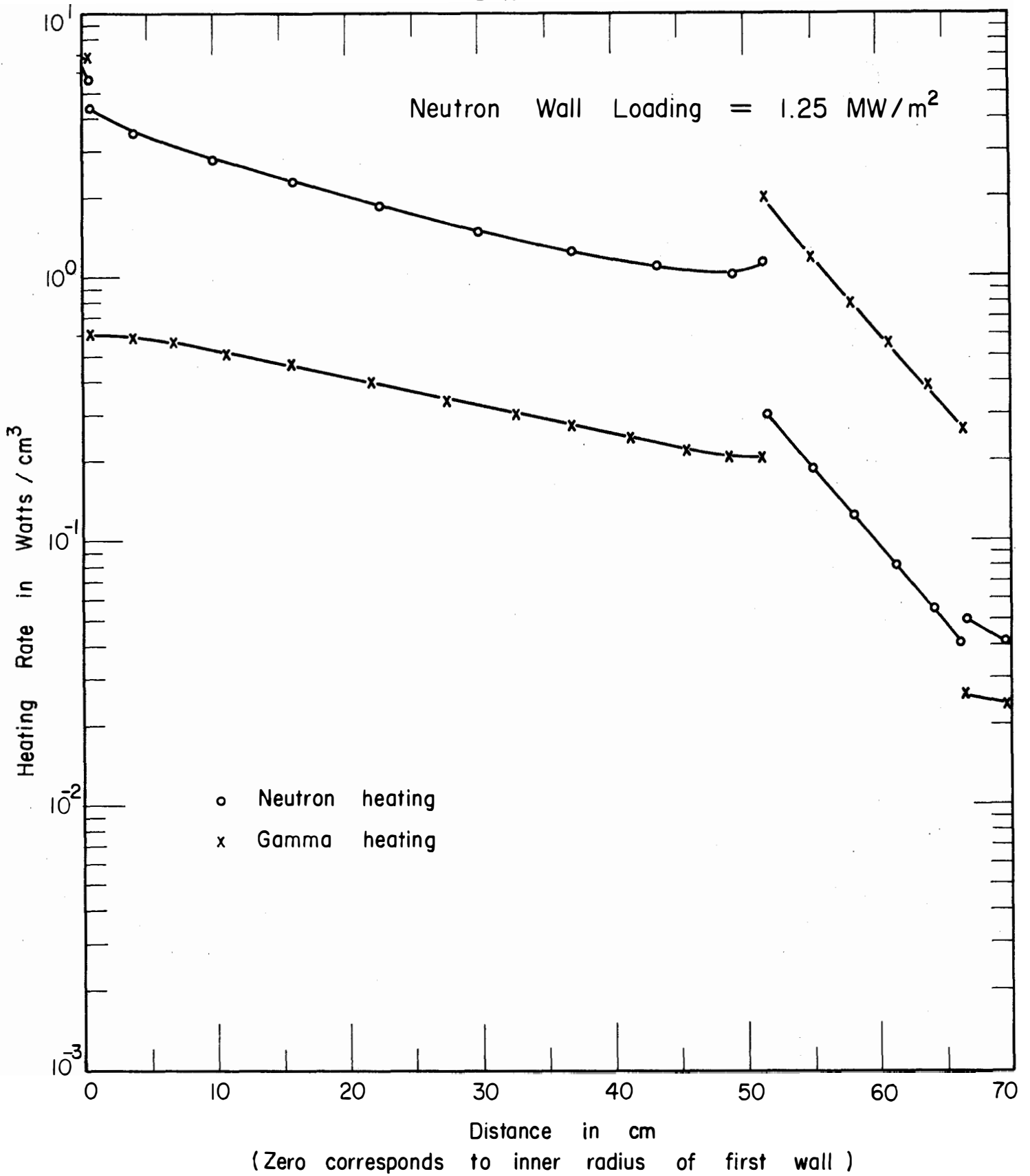


FIGURE V-B-15. Neutron and Gamma Heating Spatial Distribution in Blanket and Reflector Regions

Table V-B-13 Tritium Production Per Source Neutron

Zone	$L_i^6 (n,\alpha)t$ (T6)	$L_i^7 (n,n^1\alpha)t$ (T7)	$T=T_6 + T_7$
4	0.301126	0.370365	0.671491
5	0.267564	0.16039	0.427954
6	0.266870	0.072047	0.338917
8	0.047924	0.000908	0.048832
sum by zone	0.883481	0.603706	1.48719

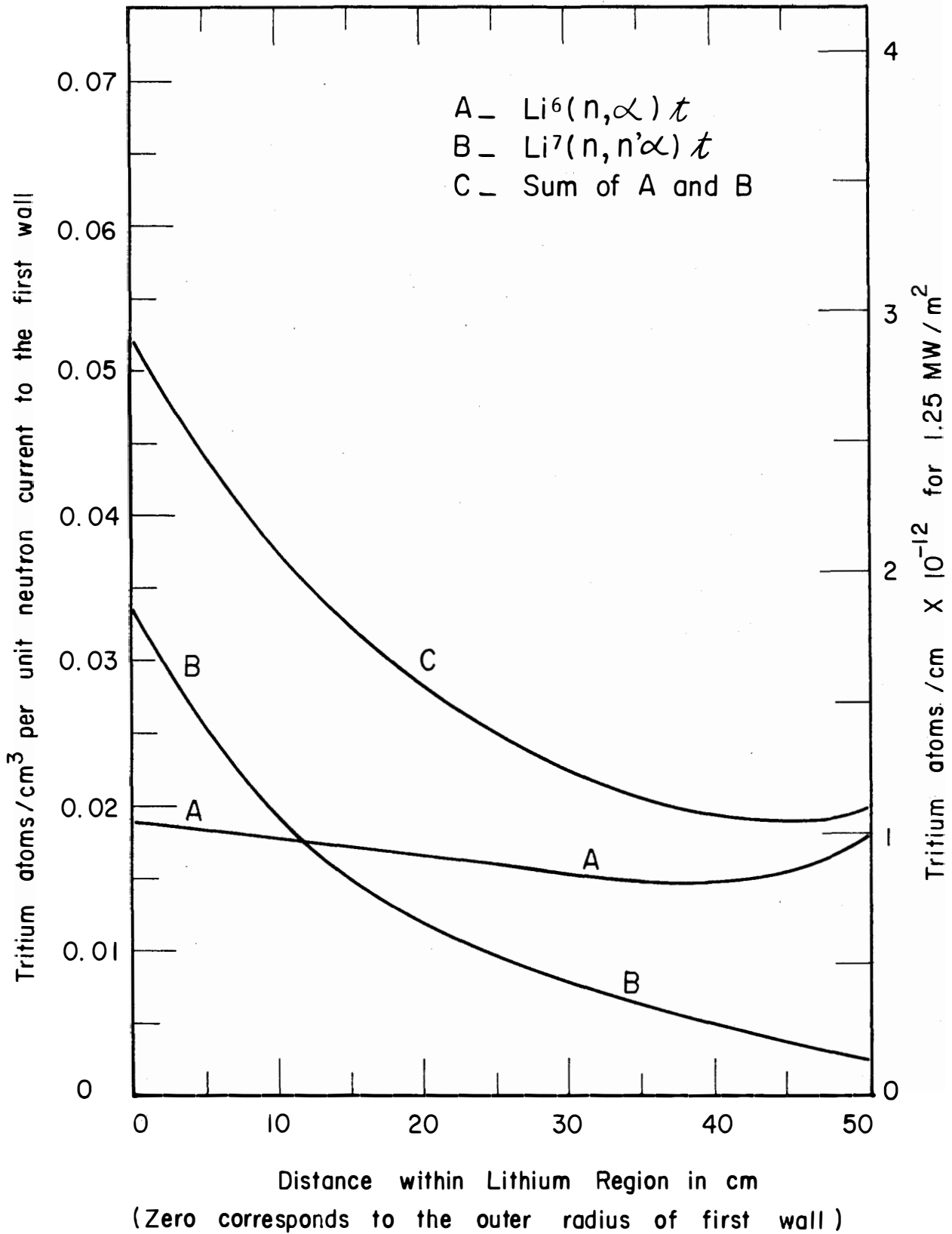


FIGURE V-B-16. Spatial Distribution of Tritium Production

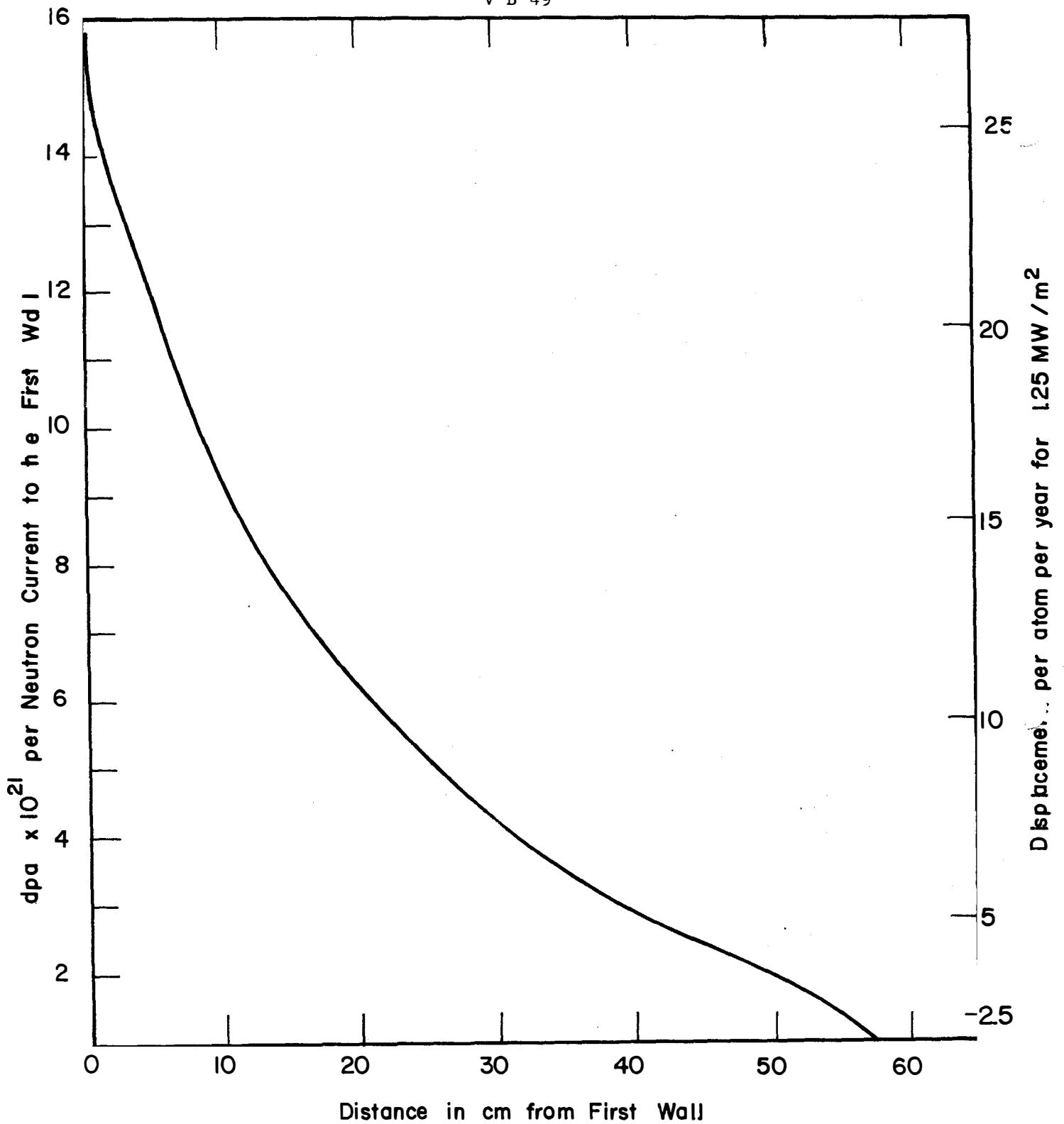


Fig. V-B-17
Spatial Distribution of Atomic Displacement
in Stainless Steel

Table V-B-14 Helium Production by Zone in Stainless Steel
(in helium atoms per source neutron)

Material Zone	Fe	Cr	Ni	SS
3	4.1360 (-3)	7.7360 (-4)	4.1388 (-4)	5.323 (-3)
4	4.2942 (-3)	8.4660 (-4)	4.3715 (-4)	5.578 (-3)
5	1.5023 (-3)	3.1697 (-4)	1.5793 (-4)	1.977 (-3)
6	6.0310 (-4)	1.3234 (-4)	6.4651 (-5)	8.001 (-4)
7	2.3742 (-3)	5.2023 (-4)	2.5309 (-4)	3.147 (-3)
8	8.0156 (-6)	1.7648 (-6)	8.5210 (-7)	1.063 (-6)
9	5.0829 (-5)	1.1196 (-5)	5.4134 (-6)	6.744 (-6)
11	2.0997 (-6)	4.6098 (-7)	2.2289 (-7)	2.783 (-6)
12	1.6759 (-5)	3.6433 (-6)	1.7693 (-6)	2.217 (-5)
15	7.0259 (-7)	1.5468 (-7)	7.5439 (-8)	9.327 (-7)
18	2.1822 (-8)	4.8669 (-9)	2.38068 (-9)	2.907 (-8)
20	1.38858 (-8)	3.1395 (-9)	1.53408 (-9)	1.856 (-8)
Sum over all Zones	1.29902 (-2)	2.6074 (-3)	1.33525 (-3)	

Table V-B-15 Hydrogen Production by Zone in Stainless Steel
(in hydrogen atoms per source neutron)

Material Zone	Fe	Cr	Ni	SS
3	6.6293 (-3)	1.4128 (-3)	3.2785 (-3)	1.132 (-2)
4	7.6714 (-3)	1.5448 (-3)	4.3038 (-3)	1.352 (-2)
5	3.0952 (-3)	5.7781 (-4)	2.0065 (-3)	5.680 (-3)
6	1.3452 (-3)	2.4111 (-4)	9.3332 (-4)	2.520 (-3)
7	5.1725 (-3)	9.4778 (-4)	3.6189 (-3)	9.739 (-3)
8	1.7789 (-5)	3.2151 (-6)	1.2745 (-5)	3.375 (-5)
9	1.1222 (-4)	2.0396 (-5)	8.1223 (-5)	2.138 (-4)
11	4.6166 (-6)	8.5338 (-7)	3.3887 (-6)	8.859 (-6)
12	3.6884 (-5)	8.3979 (-7)	2.8398 (-5)	6.612 (-5)
15	1.67891 (-6)	2.8179 (-7)	1.4402 (-6)	3.401 (-6)
18	5.5204 (-8)	8.8654 (-9)	4.9461 (-8)	1.135 (-7)
20	3.5849 (-8)	5.7179 (-9)	3.0998 (-8)	7.256 (-8)
Sum over all Zones	2.40913 (-2)	4.7565 (-3)	1.4272 (-2)	

9. Conclusions

The important question of tritium breeding has been given a high priority in all studies of fusion reactors. Our results do not differ significantly from those of other groups. From the results obtained; it seems very unlikely that any uncertainty in nuclear data or in required amounts of structural materials will cause fusion reactors to be unable to produce enough fuel for their needs and an excess for initial fueling of other fusion reactors in an expanding economy.

Assuming tritium production is potentially greater than the minimum for feasibility, the use of the extra neutrons that can be diverted to other purposes becomes important. Also important is the materials choices which are used to achieve the stated purpose. One can attempt to produce excess tritium for fueling special fusion reactors which consume but do not produce tritium (for safety or environmental reasons). In addition, at least one alternative is to produce exothermic nuclear reactions and thus increase, to the maximum extent possible, the energy production per fusion reaction. This spreads the resources usage over more materials, lowers plant capital costs per unit power, and helps alleviate the materials problems of the first wall by reducing the neutron wall loading for a given plant power. We have not explored this point exhaustively. However, this was the basis for choosing steel over graphite for the reflector region. The relative advantages of the different first wall materials in this respect, was also noted, as was the effect of enriching natural lithium in Li_6 . A related point regarding energy production, which is elaborated on in the data sections of this chapter, concerns the reduced energy per fusion reaction obtained in our work compared with that usually stated. Our results, which place this energy at about 20 MeV, are 2 MeV or more lower than one often sees in the literature. The difference arises from the inclusion of data for more reactions and a careful treatment of all available data.

The energy attenuation requirement of the shield is governed by economics according to our present understanding of the system. Nuclear heating in the magnets, rather than radiation damage, is the limiting factor. If one can then spend a fixed percentage of plant capacity on refrigeration, the shield attenuation and thickness may become rather insensitive to plant size. Optimization of the shield thickness, including magnet, shield, and refrigeration costs, showed the optimum to be insensitive to most parameters (for a fixed composition). The best materials choice turned out to be 70% lead plus 30% baron carbide mixture, when only the above criteria were included. Our actual design incorporates a good deal of stainless steel for structural reasons.

The optimum shield is thinner than is usually employed, as is

the blanket region. The blanket could easily have been thinner yet and still have produced adequate tritium production. The blanket sizes was therefore governed by heat transfer and coolant flow considerations. It should be noted that the tritium production remains unnecessarily high. A possible choice of poison, which could produce about as much energy as the displaced Li^0 , is boron preferably enriched in B^{10} .

Conclusions regarding materials problems are mainly taken up in other chapters. The main conclusion here is that uncertainties in the displacement and charged particle production data are generally larger than in other nuclear data and these preclude a very accurate determination of damage.

V-C. Nuclear Data Requirements

1. Introduction

One of the most important requirements for carrying out the neutronics design of fusion reactor blankets is the availability and accuracy of neutron and photon cross sections for all nuclides of interest for use in the blanket and shield over the energy range from 0 to 14 MeV. Our efforts in this area of nuclear data are summarized in this section.

The basic quantity of interest in neutronics and photonics takes the form of a response rate

$$R = \int_{\vec{P}} F_R(\vec{P}) \psi(\vec{P}) d\vec{P} \quad (16)$$

where F_R is the response function, ψ is the angular flux, and \vec{P} represents a point in the phase space (\vec{r}, \vec{v}) . Calculation of the neutron and gamma fluxes requires:

- 1 - neutron multigroup cross sections (including transfer matrices),
- 2 - gamma multigroup cross sections (including transfer matrices),
- 3 - gamma production cross sections, and
- 4 - a transport code.

The response functions of importance are 1-group cross sections for the important reactions; e.g. (n,t), (n,n't), (n, α), (n,n' α), (n,p) and (n,n'p), 2-displacement cross sections, and 3-neutron and gamma kerma factors. These items are discussed in the following sections.

2. Multigroup Neutron Cross Sections

Fine-group parameters and group-to-group scattering matrices were obtained as the DLC-2D^[12] data package from RSIC. The DLC-2D library was generated by the program SUPERTOG^[16] from nuclear data in ENDF/B version III. This data has been averaged over each specified energy group with the assumption that the flux (used as a weighting function) per unit lethargy is constant. Resolved and unresolved resonance contributions have been calculated where resonance data is available using the infinite dilution approximation. The thermal group constants were obtained using a Maxwellian weighting. Some of these assumptions and approximations are not accurate for CTR neutronics and will be discussed shortly.

The library is in the GAM-II one-hundred group structure shown in Table V-C-1. The machine storage increases as the square of the number of energy groups. Thus, the use of a fine energy group structure limits the use of necessary high order approximations for the scattering anisotropy and angular quadrature. Therefore, the 46 group structure in Table V-C-2 was constructed and the one-hundred group

Table V-C-1 Neutron 100 Energy Group Structure in ev

Group	Group Limits			E(Mid Point)		
	E(Top)		E(Low)			
1	1.4918	(+7)*	1.3499	(+7)	1.4208	(+7)
2	1.3499	(+7)	1.2214	(+7)	1.2856	(+7)
3	1.2214	(+7)	1.1052	(+7)	1.1633	(+7)
4	1.1052	(+7)	1.0000	(+7)	1.0526	(+7)
5	1.0000	(+7)	9.0484	(+6)	9.5242	(+6)
6	9.0484	(+6)	8.1873	(+6)	8.6178	(+6)
7	8.1873	(+6)	7.4082	(+6)	7.7977	(+6)
8	7.4082	(+6)	6.7032	(+6)	7.0557	(+6)
9	6.7032	(+6)	6.0653	(+6)	6.3843	(+6)
10	6.0653	(+6)	5.4881	(+6)	5.7767	(+6)
11	5.4881	(+6)	4.9659	(+6)	5.2270	(+6)
12	4.9659	(+6)	4.4933	(+6)	4.7296	(+6)
13	4.4933	(+6)	4.0657	(+6)	4.2795	(+6)
14	4.0657	(+6)	3.6788	(+6)	3.8722	(+6)
15	3.6788	(+6)	3.3287	(+6)	3.5038	(+6)
16	3.3287	(+6)	3.0119	(+6)	3.1703	(+6)
17	3.0119	(+6)	2.7253	(+6)	2.8686	(+6)
18	2.7253	(+6)	2.4660	(+6)	2.5956	(+6)
19	2.4660	(+6)	2.2313	(+6)	2.3486	(+6)
20	2.2313	(+6)	2.0910	(+6)	2.1251	(+6)
21	2.0910	(+6)	1.8268	(+6)	1.9229	(+6)
22	1.8268	(+6)	1.6350	(+6)	1.7399	(+6)
23	1.6350	(+6)	1.4957	(+6)	1.5743	(+6)
24	1.4957	(+6)	1.3534	(+6)	1.4245	(+6)
25	1.3534	(+6)	1.2246	(+6)	1.2890	(+6)
26	1.2246	(+6)	1.1080	(+6)	1.1663	(+6)
27	1.1080	(+6)	1.0026	(+6)	1.0553	(+6)
28	1.0026	(+6)	9.0718	(+5)	9.5488	(+5)
29	9.0718	(+5)	8.2085	(+5)	8.6401	(+5)
30	8.2085	(+5)	7.4274	(+5)	7.8179	(+5)
31	7.4274	(+5)	6.7206	(+5)	7.0740	(+5)
32	6.7206	(+5)	6.0810	(+5)	6.4008	(+5)
33	6.0810	(+5)	5.5023	(+5)	5.7917	(+5)
34	5.5023	(+5)	4.9787	(+5)	5.2405	(+5)
35	4.9787	(+5)	4.5049	(+5)	4.7418	(+5)
36	4.5049	(+5)	4.0762	(+5)	4.2906	(+5)
37	4.0762	(+5)	3.6883	(+5)	3.8827	(+5)
38	3.6883	(+5)	3.3373	(+5)	3.5128	(+5)
39	3.3373	(+5)	3.0197	(+5)	3.1785	(+5)
40	3.0197	(+5)	2.7324	(+5)	2.8761	(+5)
41	2.7324	(+5)	2.4724	(+5)	2.6024	(+5)
42	2.4724	(+5)	2.2371	(+5)	2.3547	(+5)
43	2.2371	(+5)	2.0242	(+5)	2.1306	(+5)
44	2.0242	(+5)	1.8316	(+5)	1.9279	(+5)
45	1.8316	(+5)	1.6573	(+5)	1.7444	(+5)

Table V-C-1 Continued

Group	Group Limits			E(Mid Point)		
	E(Top)		E(Low)			
46	1.6573	(+5)	1.4996	(+5)	1.5784	(+5)
47	1.4996	(+5)	1.3569	(+5)	1.4282	(+5)
48	1.3569	(+5)	1.2277	(+5)	1.2923	(+5)
49	1.2277	(+5)	1.1109	(+5)	1.1693	(+5)
50	1.1109	(+5)	8.6517	(+4)	9.8803	(+4)
51	8.6517	(+4)	6.7379	(+4)	7.6948	(+4)
52	6.7379	(+4)	5.2475	(+4)	5.9927	(+4)
53	5.2475	(+4)	4.0868	(+4)	4.6671	(+4)
54	4.0868	(+4)	3.1828	(+4)	3.6348	(+4)
55	3.1828	(+4)	2.4788	(+4)	2.8308	(+4)
56	2.4788	(+4)	1.9305	(+4)	2.2046	(+4)
57	1.9305	(+4)	1.5034	(+4)	1.7169	(+4)
58	1.5034	(+4)	1.1709	(+4)	1.3372	(+4)
59	1.1709	(+4)	9.1188	(+3)	1.0414	(+4)
60	9.1188	(+3)	7.1017	(+3)	8.1103	(+3)
61	7.1017	(+3)	5.5308	(+3)	6.3163	(+3)
62	5.5308	(+3)	4.3074	(+3)	4.9191	(+3)
63	4.3074	(+3)	3.3546	(+3)	3.8310	(+3)
64	3.3546	(+3)	2.6126	(+3)	2.9836	(+3)
65	2.6126	(+3)	2.0347	(+3)	2.3236	(+3)
66	2.0347	(+3)	1.5846	(+3)	1.8096	(+3)
67	1.5846	(+3)	1.2341	(+3)	1.4094	(+3)
68	1.2341	(+3)	9.6112	(+2)	1.0976	(+3)
69	9.6112	(+2)	7.4852	(+2)	8.5482	(+2)
70	7.4852	(+2)	5.8295	(+2)	6.6573	(+2)
71	5.8295	(+2)	4.5733	(+2)	5.1847	(+2)
72	4.5733	(+2)	3.5358	(+2)	4.0379	(+2)
73	3.5358	(+2)	2.7536	(+2)	3.1447	(+2)
74	2.7536	(+2)	2.1445	(+2)	2.4491	(+2)
75	2.1445	(+2)	1.6702	(+2)	1.9074	(+2)
76	1.6702	(+2)	1.3007	(+2)	1.4855	(+2)
77	1.3007	(+2)	1.0130	(+2)	1.1569	(+2)
78	1.0130	(+2)	7.8893	(+1)	9.0097	(+1)
79	7.8893	(+1)	6.1442	(+1)	7.0168	(+1)
80	6.1442	(+1)	4.7851	(+1)	5.4647	(+1)
81	4.7851	(+1)	3.7267	(+1)	4.2559	(+1)
82	3.7267	(+1)	2.9023	(+1)	3.3145	(+1)
83	2.9023	(+1)	2.2603	(+1)	2.5813	(+1)
84	2.2603	(+1)	1.7603	(+1)	2.0103	(+1)
85	1.7603	(+1)	1.3710	(+1)	1.5657	(+1)
86	1.3710	(+1)	1.0677	(+1)	1.2193	(+1)
87	1.0667	(+1)	8.3153	(+0)	9.4962	(+0)
88	8.3153	(+0)	6.4760	(+0)	7.3956	(+0)
89	6.4760	(+0)	5.0435	(+0)	5.7597	(+0)
90	5.0435	(+0)	3.9279	(+0)	4.4857	(+0)

Table V-C-1 Continued

Group	Group Limits			E(Mid Point)		
	E(Top)		E(Low)			
91	3.9279	(+0)	3.0590	(+0)	3.4934	(+0)
92	3.0590	(+0)	2.3824	(+0)	2.7207	(+0)
93	2.3824	(+0)	1.8554	(+0)	2.1189	(+0)
94	1.8554	(+0)	1.4450	(+0)	1.6502	(+0)
95	1.4450	(+0)	1.1254	(+0)	1.2852	(+0)
96	1.1254	(+0)	8.7643	(-1)	1.0009	(+0)
97	8.7643	(-1)	6.8256	(-1)	7.7949	(-1)
98	6.8256	(-1)	5.3158	(-1)	6.0707	(-1)
99	5.3158	(-1)	4.1399	(-1)	4.7279	(-1)
100	4.1399	(-1)	2.2000	(-1)	2.1800	(-1)

*(n) represents (10^{-n})

Table V-C-2 Neutron 46 Energy Group Structure in eV

Group	Group Limits		E(Mid-Point)
	E(Top)	E(Low)	
1	1.4918 (+7)	1.3499 (+7)	1.4208 (+7)
2	1.3499 (+7)	1.2214 (+7)	1.2856 (+7)
3	1.2214 (+7)	1.1052 (+7)	1.1633 (+7)
4	1.1052 (+7)	1.0000 (+7)	1.0526 (+7)
5	1.0000 (+7)	9.0484 (+6)	9.5242 (+6)
6	9.0484 (+6)	8.1873 (+6)	8.6178 (+6)
7	8.1873 (+6)	7.4082 (+6)	7.7977 (+6)
8	7.4082 (+6)	6.7032 (+6)	7.0557 (+6)
9	6.7032 (+6)	6.0653 (+6)	6.3843 (+6)
10	6.0653 (+6)	5.4881 (+6)	5.7767 (+6)
11	5.4881 (+6)	4.9659 (+6)	5.2270 (+6)
12	4.9659 (+6)	4.4933 (+6)	4.7296 (+6)
13	4.4933 (+6)	4.0657 (+6)	4.2795 (+6)
14	4.0657 (+6)	3.6788 (+6)	3.8722 (+6)
15	3.6788 (+6)	3.3287 (+6)	3.5038 (+6)
16	3.3287 (+6)	3.0119 (+6)	3.1703 (+6)
17	3.0119 (+6)	2.7253 (+6)	2.8686 (+6)
18	2.7253 (+6)	2.4660 (+6)	2.5956 (+6)
19	2.4660 (+6)	1.8268 (+6)	2.1464 (+6)
20	1.8268 (+6)	1.3534 (+6)	1.5901 (+6)
21	1.3534 (+6)	1.0026 (+6)	1.1780 (+6)
22	1.0026 (+6)	7.4274 (+5)	8.726 (+5)
23	7.4274 (+5)	5.5023 (+5)	6.4648 (+5)
24	5.5023 (+5)	4.0762 (+5)	4.7892 (+5)
25	4.0762 (+5)	3.0197 (+5)	3.5480 (+5)
26	3.0197 (+5)	2.2371 (+5)	2.6284 (+5)
27	2.2371 (+5)	1.6573 (+5)	1.9472 (+5)
28	1.6573 (+5)	1.2277 (+5)	1.4425 (+5)
29	1.2277 (+5)	6.7379 (+4)	9.508 (+4)
30	6.7379 (+4)	3.1828 (+4)	4.9604 (+4)

Table V-C-2 (cont.)

Group	Group Limits		E(Mid-Point)
	E(Top)	E(Low)	
31	3.1828 (+4)	1.5034 (+4)	2.3431 (+4)
32	1.5034 (+4)	7.1017 (+3)	1.1068 (+4)
33	7.1017 (+3)	3.3546 (+3)	5.2281 (+3)
34	3.3546 (+3)	1.5846 (+3)	2.4696 (+3)
35	1.5846 (+3)	7.4852 (+2)	1.1666 (+3)
36	7.4852 (+2)	3.5358 (+2)	5.5105 (+2)
37	3.5358 (+2)	1.6702 (+2)	2.6030 (+2)
38	1.6702 (+2)	7.8893 (+1)	1.2296 (+2)
39	7.8893 (+1)	3.7267 (+1)	5.8080 (+1)
40	3.7267 (+1)	1.7603 (+1)	2.7435 (+1)
41	1.7603 (+1)	8.3153 (+0)	1.2959 (+1)
42	8.3153 (+0)	3.9279 (+0)	6.1216 (+0)
43	3.9279 (+0)	1.8554 (+0)	2.8917 (+0)
44	1.8554 (+0)	8.7643 (-1)	1.3659 (+0)
45	8.7643 (-1)	4.1399 (-1)	6.4521 (-1)
46	4.1399 (-1)	2.2000 (-2)	2.1800 (-1)

data were properly collapsed using typical CTR blanket spectra. The 46 group data has the same fine group structure above 2 MeV as the one-hundred group set.

A general sensitivity study is currently underway to evaluate the adequacy of presently available transport cross sections. An outline of this study was given in ref.[14] The accuracy of present and needed nuclear data for calculation of nuclear heating in CTR blankets and shields is discussed later in this section.

3. Multigroup Gamma Cross Sections

The gamma cross sections as used in transport and heating calculations result from a simplified picture of the complex interaction processes of gamma photons with matter. The primary processes that are accounted for in the gamma transport and heating calculations undertaken in this study are the photoelectric effect, Compton scattering, and pair production. All other processes make very small contributions to the total cross section.

Gamma multigroup cross sections were generated for this work with the MUG code [5] for the 43 group structure shown in Table V-C-3 for all materials of interest in CTR applications. This group structure is based on the use of equal energy widths of 1.0 MeV for groups above 8 MeV and 0.25 MeV in the 1 to 8 MeV range. The gamma cross section variation with energy for the most important CTR materials was taken into account in choosing this group structure. The gamma interaction data are available with reasonable accuracy for all materials of interest.

4. Photon Production Cross Sections

In performing gamma-ray transport calculations, secondary gamma-ray spectra must be available in addition to gamma group to group cross sections. The basic quantity to be calculated from gamma production cross sections is the secondary photon production source represented by

$$S_{\gamma}(\vec{r}, E_{\gamma}) = \sum_j N_j(\vec{r}) \int \phi_n(\vec{r}, E_n) \sigma_p^j(E_n, E_{\gamma}) dE_n \quad (17)$$

$$\sigma_p^j(E_n, E_{\gamma}) = \sum_i \sigma_i^j(E_n) f_i^j(E_n, E_{\gamma}) \quad (18)$$

where

$$\sigma_p^j = \text{photon production cross section in element } j.$$

Table V-C-3 Gamma-Ray 43 Energy Group Structure in MeV

Group	Group Limits		Mid Point Energy
	E(Top)	E(Low)	
1	14.00	13.00	13.50
2	13.00	12.00	12.50
3	12.00	11.00	11.50
4	11.00	10.00	10.50
5	10.00	9.00	9.50
6	9.00	8.00	8.50
7	8.00	7.75	7.875
8	7.75	7.50	7.625
9	7.50	7.25	7.375
10	7.25	7.00	7.125
11	7.00	6.75	6.875
12	6.75	6.50	6.625
13	6.50	6.25	6.375
14	6.25	6.00	6.125
15	6.00	5.75	5.875
16	5.75	5.00	5.375
17	5.00	4.75	4.875
18	4.75	4.50	4.625
19	4.50	4.25	4.375
20	4.25	4.00	4.125
21	4.00	3.75	3.875
22	3.75	3.50	3.625
23	3.50	3.25	3.375
24	3.25	3.00	3.125
25	3.00	2.75	2.875
26	2.75	2.50	2.625
27	2.50	2.25	2.375
28	2.25	2.00	2.125
29	2.00	1.75	1.875
30	1.75	1.50	1.625
31	1.50	1.25	1.375
32	1.25	1.00	1.125
33	1.00	0.75	0.875
34	0.75	0.55	0.650
35	0.55	0.45	0.500
36	0.45	0.40	0.425
37	0.40	0.30	0.350
38	0.30	0.20	0.250
39	0.20	0.15	0.175
40	0.15	0.10	0.125
41	0.10	0.05	0.075
42	0.05	0.01	0.030
43	0.01	0.001	0.0055

$\sigma_i^j(E_n)$ = microscopic neutron cross section in element j for gamma production reaction i at neutron energy E_n .

$f_i^j(E_n, E_\gamma)$ = number of photons produced with energy E_γ per reaction i in element j induced by neutrons of energy E_n .

Thus, the gamma production cross section data are extremely important for determining gamma fluxes, heating, and leakage. Unfortunately, the data on gamma production suffers from large uncertainties at present. For example, Li⁶, Li⁷, C¹², niobium, molybdenum, boron, copper and several other materials are the strongest candidates for use in a CTR. However, there exists no information about gamma production for these materials in the widely used nuclear data libraries such as ENDF/B. In addition, the unevaluated gamma production data for these materials available in the literature suffers from very large uncertainties as shown in reference 1. The gamma production cross sections used for deriving the photonics results of this study are discussed below.

The gamma production cross sections for H-1, Be-9, N-14, O-16, Na-23, Al-27, K, Fe, and Pb were generated from ENDF.B [17] with LAPHFOR [16] which is a revision of the program LAPHANO [17]. The resonance cross sections required by LAPHANO and LAPHFOR were calculated for Na-23 and Fe with the MACK program. Vanadium gamma production cross sections were also generated with LAPHFOR from a recent ORNL evaluation [18]. Photon production cross sections for Li-6, Li-7, Nb, and C-12 were obtained from data in reference 28 which were generated with the POPOP4 program [19 & 20]. It is shown in references 1 and 3 that these gamma production cross sections for Li-6, Li-7, Nb and C-12 suffer from large uncertainties. For a blanket of 50 cm consisting of 95% natural lithium and 5% structure, the total energy of the gammas produced by the lithium is roughly 30% of the total energy of photons produced in the blanket. The total energy is only about one-third of the total gamma energy production produced in the 1 cm first wall, the 50 cm blanket, and the 20 cm stainless steel reflector region. Furthermore, the total gamma heating in such systems is about 30 to 40% of the total nuclear heating. Therefore, 20 to 30% error in the lithium gamma production data has the effect of changing the nuclear heating by only about 1 to 2%. This is fortunate since lithium is used in all the designs presented in this chapter. For systems employing niobium in the first wall, the error in the total nuclear heating due to a 20% error in the gamma production in a niobium first wall is roughly the same as the error in the niobium secondary photon production. In a system consisting of a 1 cm first wall, a 40 cm blanket of 95% Li plus 5% structure, followed by a 25 cm reflecting region of graphite, the total energy of the secondary photons produced by C-12 is only about 4% of that produced in the system. Hence, 20 to 30% uncertainty in the data

for C-12 gamma production has little effect on the total nuclear heating in the system.

5. Response Functions

The neutronics and photonics analysis of the system provide the basic input for other areas of the design such as heat transfer, tritium removal, radiation damage, magnet design, and decay heating and emergency cooling. The quantities required by such studies as described in V.B can generally be formulated into response rates (as shown in equation 16) such as spatial distribution of nuclear heating, charged particle production, and atomic displacement. In addition to the neutron and gamma fluxes, the required response functions can be divided into four types:

- a - partial cross sections for reactions of importance, e.g. (n,t) , $(n,n't)$, (n,α) , $(n,n'\alpha)$, (n,p) and $(n,n'p)$.
- b - neutron kerma factors,
- c - gamma kerma factors, and
- d - displacement cross sections.

A major effort has been devoted in our program to the development of theoretical and computational algorithms for calculation of kerma factors. The next section is devoted to this subject. Calculation of other response functions such as helium and hydrogen production is automated for multigroup representation by integrating the required processing with the computational capability developed for kerma factors. This is also discussed in the next section. The displacement cross sections for stainless steel and refractory metals were obtained from Doran's work [39]. The calculational methods currently available for calculating the displacement cross sections [40] need to be refined. This is scheduled for future studies.

6. Kerma Factors

Calculation of the heat generation rate and dose due to the interaction of nuclear radiation with matter is of prime importance in almost any nuclear system. These calculations are particularly easy in the case of fission systems since the fission reaction dominates and most of its energy is deposited locally. The remainder of the energy is a small correction and can be treated by relatively crude approximations. In fusion systems, on the other hand, the high energy neutrons undergo a variety of reactions which contribute significantly to the energy release. Thus an accurate determination of the energy generation rate requires careful evaluation of the energy release of the various reactions in the first wall, blanket, shield, and magnets.

For the purposes of calculation, the heating rate due to neutron reactions with nuclei of the target material is divided into two types; the first due to neutron reactions, and the second due to absorption of secondary gamma radiation produced by these

neutron reactions. As an example, consider the (n,p) reaction. The energy deposited of the first type is the kinetic energy of the recoil nucleus, the proton emitted and of any charged particle (e.g. β^-) which may be emitted from the activated residual nucleus. The energy deposition by the gamma-photons emitted is treated separately.

Heating by neutrons at any spatial point can be express as

$$H(r) = \int \phi(\vec{r}, E) \sum_{ji} N_j(\vec{r}) \sigma_{ij}(E) E_{ij}(E) dE (\text{MeV/cm}^3 \text{sec}). \quad (19)$$

where

$\phi(r, E)$ = neutron flux at spatial point r and energy E ,

$N_j(\vec{r})$ = number density of element j at point r , (atoms/cm^3)

$\sigma_{ij}(E)$ = microscopic cross section of element j for reaction i at neutron energy E (cm^2/atom)

$E_{ij}(E)$ = energy deposited per reaction i in element j (MeV).

The units have been chosen as those normally employed in nuclear calculations.

The terms k_{ij} and k_j defined as

$$k_{ij}(E) = \sigma_{ij}(E) E_{ij}(E) \quad (20)$$

$$k_j(E) = \sum_i k_{ij}(E) \quad (21)$$

are flux and density independent. Hence, the heating rates can be calculated from particle transport results for any system if the factors k_j are predetermined for all materials in the system.

k_{ij} is called the microscopic kerma factor for reaction i in element j . The term "kerma" is an acronym standing for the Kinetic Energy Relaxed in Materials. The phrase "fluence-to-kerma factors" was introduced by the International Commission on Radiological Units and Measurements [21]. The term "kerma" will be used throughout this report as defined by equation 20 and 21 shown above, with E_{ij} as defined next.

$E_{ij}(E)$ is the energy released in element j per reaction i induced by a neutron of energy E . The energy release considered here is the energy which can be assumed to be deposited locally, i.e., within a negligible distance from the site of the reaction. This implies that E_{ij} is the sum of kinetic energies of the recoil nuclei, charged particles emitted, and charged particles produced by radioactive decay of the residual nucleus and such other processes as internal conversion. The addition of the contribution from radioactive decay to energy deposition depends on the type of calculation performed, time dependent or steady state. This comment will be elaborated on later.

The gamma-ray kerma factors are defined in a similar manner and can be determined from

$$k_{\gamma}^j = \sigma_{pe}^j E + \sigma_{pp}^j (E - 1.02) + \sigma_{ca}^j E \quad (22)$$

where

$k_{\gamma}^j(E)$ = gamma kerma factor for element j (MeV . cm²/atom)

E = photon energy (MeV)

σ_{pe}^j = photoelectric microscopic cross section for element j
(cm²/atom)

σ_{ca}^j = Compton microscopic absorption cross section for element j
(cm²/atom)

σ_{pp}^j = pair production microscopic cross section for element j
(cm²/atom)

In pair production, 1.02 MeV (two electron masses) of the photon energy is not available for local heat deposition. The two .51 MeV photons produced by the pair are accounted for in the transfer cross sections of gamma energy multi-group cross section sets, hence the energy balance is maintained. Implicit in the use of Eq. 22 is the assumption that photoelectric, pair production, and Compton scattering are the only processes that contribute to energy deposition, thus all other possible processes are assumed negligible.

The evaluation of gamma kerma factors (Eq. 22) is straightforward and is usually performed by the codes which generate multigroup photon cross sections such as MUG [15] and GAMMA [22]. Therefore, gamma kerma factor calculations present no problem at present.

Calculation of neutron kerma factors, on the other hand, is complicated by the variety of reactions which a neutron can undergo, and the

emission of more than one particle in many of these reactions. However, the kinematics and theory are still simple and the limitation on the accuracy of a neutron kerma calculation is set by the availability and accuracy of the nuclear data.

Prior to the work reported here there were several efforts at calculating kerma factors. Some of these are reported in references 23 through 28. However, these efforts were directed mostly toward calculating kerma for elements which are major constituents in the human body. Furthermore, they involved several simplifying assumptions such as neglecting inelastic scattering entirely, anisotropy of elastic scattering, and several others. The work of Ritts et al. 27 included a larger number of reactions and was an improvement over all preceding work. They calculated kerma factors for 11 elemental constituents of the human body. This work was extended^[28] to calculate kerma for seven elements of interest in fusion reactor blankets. However, Ritts et al. in their work did not have a general format or algorithm for calculating kerma and the same effort had to be duplicated for each material or for a new evaluation of the basic data for the same material. In addition, it involved some approximations in calculation of the secondary neutron energy distribution and the excitation of residual nuclei in non-elastic reactions.

The Evaluated Nuclear Data File (ENDF)^[29] provides a unified format that is used to store and retrieve evaluated sets of neutron and photon cross sections. The ENDF formats are versatile and flexible enough that almost any type of neutron interaction mechanism can be accurately described. Further, the nuclear data in the ENDF/B library is continuously revised, re-evaluated, and updated. Thus, it provides the most suitable up-to-date nuclear data library.

A computer program was written to calculate neutron fluence-to-kerma factors from nuclear data in ENDF/B format based on the theoretical model described shortly. The name of the code is MACK (MACK: Mohamed Abdou Computes Kerma).

The basic purpose of the MACK program is to calculate neutron-induced kerma factors as a function of neutron energy. The calculation is carried out for a discrete energy mesh flexibly specified by input options for any desired energy range. In addition, several calculational routines were included in the program to generate energy group kerma factors and energy group cross sections (group constants, not transfer matrices) for any reaction type desired. These options provide a rapid and economical way of obtaining cross sections in multigroup form for calculation of reaction rates of interest; e.g., helium, hydrogen and tritium production. The MACK code also has a built-in resonance treatment and the resonance cross

sections can be computed, Doppler-broadened at an arbitrary temperature, from resonance parameters (ENDF/B) file 2). This provides the code with independence from other programs in processing ENDF/B data for resonance nuclides.

The theory involved in evaluating kerma factors, the algorithm for the MACK program, and the models for processing nuclear data in ENDF/B format are discussed in great detail in reference 4 but a brief summary is given next. This is followed by an analysis of the kerma factor results for CTR materials. A discussion of the generation of libraries of group kerma factors and partial cross sections with MACK from ENDF/B3 is given in Appendix A.

Theory for Kerma Factor Calculation

The theory required for calculation of neutron kerma factors is primarily that associated with the kinematics of collisions of both elastic and nonelastic types. Thus, in addition to cross sections for excited levels both discrete and in the continuum, the average direction cosine for each reaction, the energies of the excited levels, Q values, and internal conversion factors must also be known. Further, if the product nucleus is radioactive with a short enough half-life that its energy release should be included in a steady state calculation of the energy deposition, there must be data on its mode of decay and the energetics of the process. Thus, rather complete data is required on the nuclei and the reaction processes involved as compared to that normally used. There is an additional complication in that it is not readily possible to combine the different isotopes of an element and simply give elemental data. Of course, one must finally combine microscopic data to obtain macroscopic kerma factors.

The theory has been given elsewhere in considerable detail^[4] and will not be repeated here. It is reasonably straightforward in most cases. An exception arising in multiple particle reactions such as the (n,2n) reaction in which the intermediate nucleus can be left in more than one state of excitation. The averaging required over intermediate states to determine how much of the energy is deposited and how much goes to gamma production is more complicated.

Reaction Types

For kerma calculation, the nuclear reactions are conveniently classified into the seven types given in Table V-C-4. In this table MT is the ENDF/B reaction number and LR is a flag used in ENDF/B3 to allow inclusion of information about the (n,n') part of a combined inelastic reaction (other than γ -ray emission) by presenting these reactions with MT = 50-91 (inelastic scattering to levels and continuum) and using the appropriate MT number in the LR flag field.

Since ENDF data generally extends only to 15 MeV at present,

TABLE V-C-4

REACTION TYPES

For the Purpose of Kerma Calculation, The Nuclear Reactions are Classified Into the Following Types:

	<u>REACTION TYPE</u>	<u>MT</u>
(n,n)	Elastic	2
(n,n') γ	Inelastic	51-90
(n,n') γ	Inelastic Continuum	91
(n,mn') $a_{c_1}, a_{c_2} \dots$	(n,mn') Charged Particles m =1 or 2	22,23,24,28 and 51-91 with Flag LR
(n, $a_{c_1}, a_{c_2}, a_{c_3} \dots$)	(n, Charged Particles)	103-109 700-799
(n, γ)	Radiative Capture	102
(n,2n)		16

which is the energy range required for most applications, contributions to the kerma factors from (n,3n) reactions and from secondary nuclear reactions caused by charged particle products of the primary reaction are neglected.

Energy Deposition Due to Radioactive Decay

Particle emission from the decay of the activated residual nuclei must be considered in the calculation of neutron kerma factors as it is another mechanism for local energy deposition. Since radioactive decay is time dependent, the kerma factors for nuclear reactions followed by radioactive decay is time dependent.

However, the most important contribution to energy deposition from radioactive decay is generally from short-lived residual nuclei since the mean-life time for decay decreases rapidly as the disintegration energy increases. The contribution from activated residual nuclei with a mean life time greater than a few days is usually negligibly small. Thus, kerma factors in which radioactive decay is considered for half-lives less than an arbitrary cut-off (e.g. 10 days) only are suitable for steady state heating rate calculations. If the heating rate is to be calculated for a short period of operation of the nuclear system (e.g. start-up), then the contribution from radioactive decay should be calculated separately from the contribution to energy deposition by charged particle recoil from nuclear reactions. Clearly, the latter is always time-independent (energy release not heating rate).

The most frequent type of decay is by emission of β particles. β^+ decay may occur after (n,2n) reactions and β^- after (n, γ) and (n, charged particles) reactions. Since β particles are emitted with an energy spectrum, the average kinetic energy of β particles, \bar{E}_β must be calculated. Previous works [27 and 28] assumed the average kinetic energy of a β particle to be 30% of the end-point for all isotopes and end-point energies. This assumption severely underestimates \bar{E}_β .

Use of the Fermi theory of β decay allows a more careful treatment of this energy. This has been carried out in detail [1]. The average energy of β decay is not usually given in the table of isotopes [30] nor in other compilations radioisotopes. The β endpoint energy, relative intensities, fraction of electron capture, α -particle energies, half-lives and other required information are usually given in such compilations. This suggests generating a library for the average energy release from radioactive decay for all reactions and isotopes of importance. Such a library will not only be useful for adding the contribution of radioactive decay to kerma factors but also will provide necessary information for calculation of decay heat in nuclear devices. It is also suggested

that the average energy release from radioactive decay following a nuclear reaction be specified in ENDF/B file 1 section 453.

The MACK code provides several options for adding the energy release contribution of radioactive decay that follows a nuclear reaction to the energy release calculated from recoil of charged particles. These options are fully described in reference 4.

A final point worth mentioning concerns the contribution to energy release by gamma emission from radioactive decay. Since the gammas are frequently of high energy, they are transported through the medium away from the site of the neutron reaction and they do not contribute to the local energy deposition. The energy deposition by these gammas can be properly accounted for by adding them to the secondary gamma production source.

7. Comparison and Analysis of Neutron Kerma Factors For CTR Materials

The neutron fluence-to-kerma factors presented here are for materials of prime interest for use in CTR blankets, shields and magnets. The kerma factors are plotted for the energy range to 15 MeV at 100 points generated by taking every tenth point from the 1000-point energy mesh described in Appendix A. This reproduces clearly the gross behavior of the neutron kerma factors for all materials but does not exhibit all the fine details.

Before discussing the results it is useful to summarize the technique for calculating the total nuclear heating. In the preceding subsections, the nuclear heating was divided into two contributions. The first type is the energy deposition by charged particles and recoil nuclei from the neutron reactions and the second type is the heat generated by the secondary gammas. This classification is rather artificial and is made only to facilitate the calculations. In any nuclear system both types occur. The nuclear heating is a function of the nuclide densities, neutron and gamma flux spectra in addition to the neutron and gamma kerma factors. The ratio of gamma heating of H_Y to the neutron heating H_n varies considerably from material to material. Materials which attenuate neutrons mostly through inelastic scattering reactions have, generally, small neutron kerma factors and large photon production cross sections. Furthermore, these materials are in most cases of high atomic number and attenuate the photons effectively resulting in a high H_Y to H_n ratio. Therefore, in comparing the neutron kerma factors for various materials it is not true in many cases that the material with the smallest k_n has the lowest nuclear heating. However, this is generally true for materials of approximately the same atomic number.

Comparing the neutron kerma factors for several materials for the purpose of comparing "energy multiplication" also does not yield useful results in many cases since the energies of the secondary

neutrons and photons are not included in local energy deposition factors. Further since k_n combines the energy release per reaction with the neutron reaction cross sections a lower neutron kerma factor does not necessarily imply energy "gain" or "loss". For example, an endothermic (n,α) reaction usually yields a higher k_n , than the exothermic (n,γ) reaction.

The purpose of the above comments was to show that it is difficult in some instances to draw conclusions about "energy breeding", relative magnitude of total heating rate, etc. in various materials by comparing the neutron kerma factors alone. It is also sometimes difficult to get information about energy breeding from the reaction Q-values alone. The ratio of exothermic and endothermic reaction rates to the total reaction rate should also be examined. In addition, a material can have a net "energy gain" in one system and an "energy loss" in another system depending on the spectra and the energy ranges of importance for exothermic and endothermic reactions. In some cases, however, many conclusions can be reached by inspecting the neutron kerma factors alone as long as care is exercised. Of course, in all cases, the required information can be obtained from calculating the various response rates in the system of interest.

Since the neutron heating depends strongly on the spectrum it is helpful here to introduce two reference spectra. The first is the blanket first wall flux given in Appendix A and will be referred to as the FWS (fusion wall spectrum). The second is a constant flux in all groups of the GAM-II group structure given Table V-C-1. The GAM-II one hundred group structure employs 0.1 lethargy unit intervals from 15 MeV to 111 KeV and 0.25 lethargy unit intervals at lower energies. Therefore a uniform GAM-II group flux represents a C/E spectrum above 111 KeV and C_2/E spectrum below with $C_2 = .25 C_1$. The integrated flux below 111 KeV is approximately equal to that above i.e. 50% of the total. Hence, the uniform GAM-II spectrum emphasizes the low energy range while the FWS emphasizes the high energy range. These two spectra represent the opposite ends of the shield and blanket spectra. Two integral quantities for comparing neutron kerma factors based on these spectra are defined as follows:

η_s = heat generated per unit fluence per atom for uniform GAM-II group flux (qualitative shield spectrum)

η_w = heat generated per unit fluence per atom in the reference CTR first wall system

Table V-C-5 tabulates the values of η_s and η_w for CTR materials calculated from the kerma factor results of this work. Very useful information can be deduced from comparing η_s and η_w for the same material and comparing each of them for different materials.

From Figures V-C-1 to V-C-8 it is evident that the energy dependence of the neutron kerma factor, k_n , for a material does not resemble that of the total cross section for the material in the high energy region. In

Table V-C-5 Neutron Heating per Unit Fluence for Uniform Group Flux (C/E) and CTR Blanket First Wall Flux

Material	Heating per Unit Fluence in eV. barn/atom	
	Uniform (GAM-II) Group Flux (η_s)	Blanket First Wall Flux (η_w)
H-1	1.3232 (⁺ 6)	1.9220 (⁺ 6)
H-2	8.9317 (⁺ 5)	1.2875 (⁺ 6)
He	6.8592 (⁺ 5)	9.4207 (⁺ 5)
Li-6	1.1684 (⁺ 8)	4.9455 (⁺ 6)
Li-7	4.7525 (⁺ 5)	7.9208 (⁺ 5)
Be-9	4.8390 (⁺ 5)	8.8523 (⁺ 5)
B-10	2.7463 (⁺ 8)	7.2484 (⁺ 6)
B-11	2.8431 (⁺ 5)	5.0805 (⁺ 5)
C-12	3.1895 (⁺ 5)	7.4605 (⁺ 5)
O-16	2.9897 (⁺ 5)	7.3357 (⁺ 5)
Na-23	2.7397 (⁺ 5)	6.6978 (⁺ 5)
Al-27	2.8324 (⁺ 5)	8.1872 (⁺ 5)
V	2.6729 (⁺ 5)	2.8960 (⁺ 5)
Cr	1.7750 (⁺ 5)	5.7093 (⁺ 5)
Ni	5.7031 (⁺ 5)	1.3559 (⁺ 6)
Fe	1.9151 (⁺ 5)	6.2025 (⁺ 5)
Cu-63	3.1195 (⁺ 5)	6.6301 (⁺ 5)
Cu-65	3.1737 (⁺ 5)	3.5170 (⁺ 5)
Cu(natural)	3.1362 (⁺ 5)	5.6682 (⁺ 5)
Nb	9.0062 (⁺ 4)	2.2813 (⁺ 5)
Ta-181	4.3584 (⁺ 4)	7.6382 (⁺ 4)
W-182	4.5902 (⁺ 4)	8.5089 (⁺ 4)
W-183	4.4777 (⁺ 4)	8.5610 (⁺ 4)
W-184	4.3192 (⁺ 4)	8.4098 (⁺ 4)
W-186	6.7309 (⁺ 6)	1.5949 (⁺ 5)
Pb	4.4141 (⁺ 4)	7.2026 (⁺ 4)

Figure V.C.1 Neutron Kerma Factors for Lithium-6 and Lithium-7

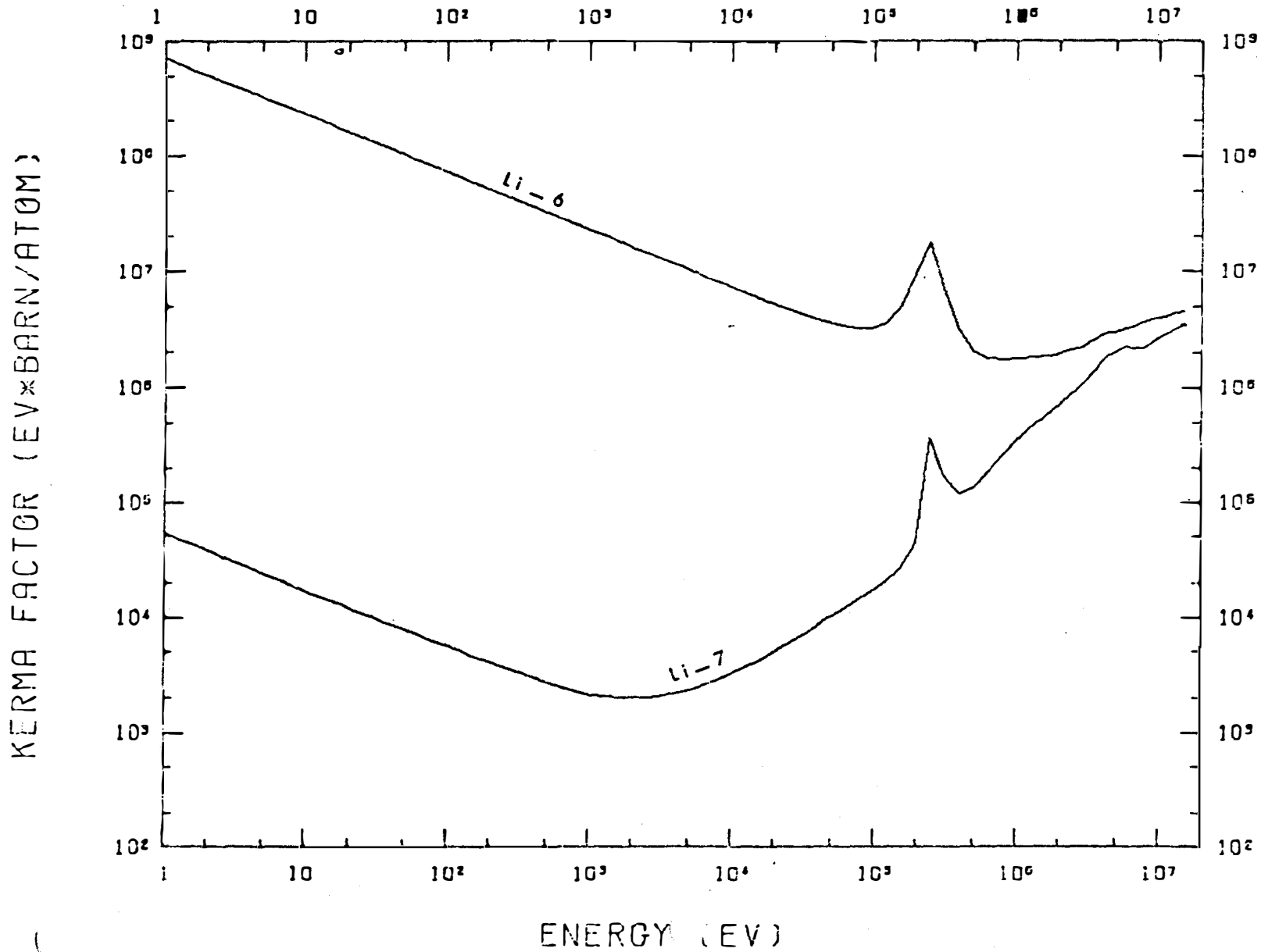
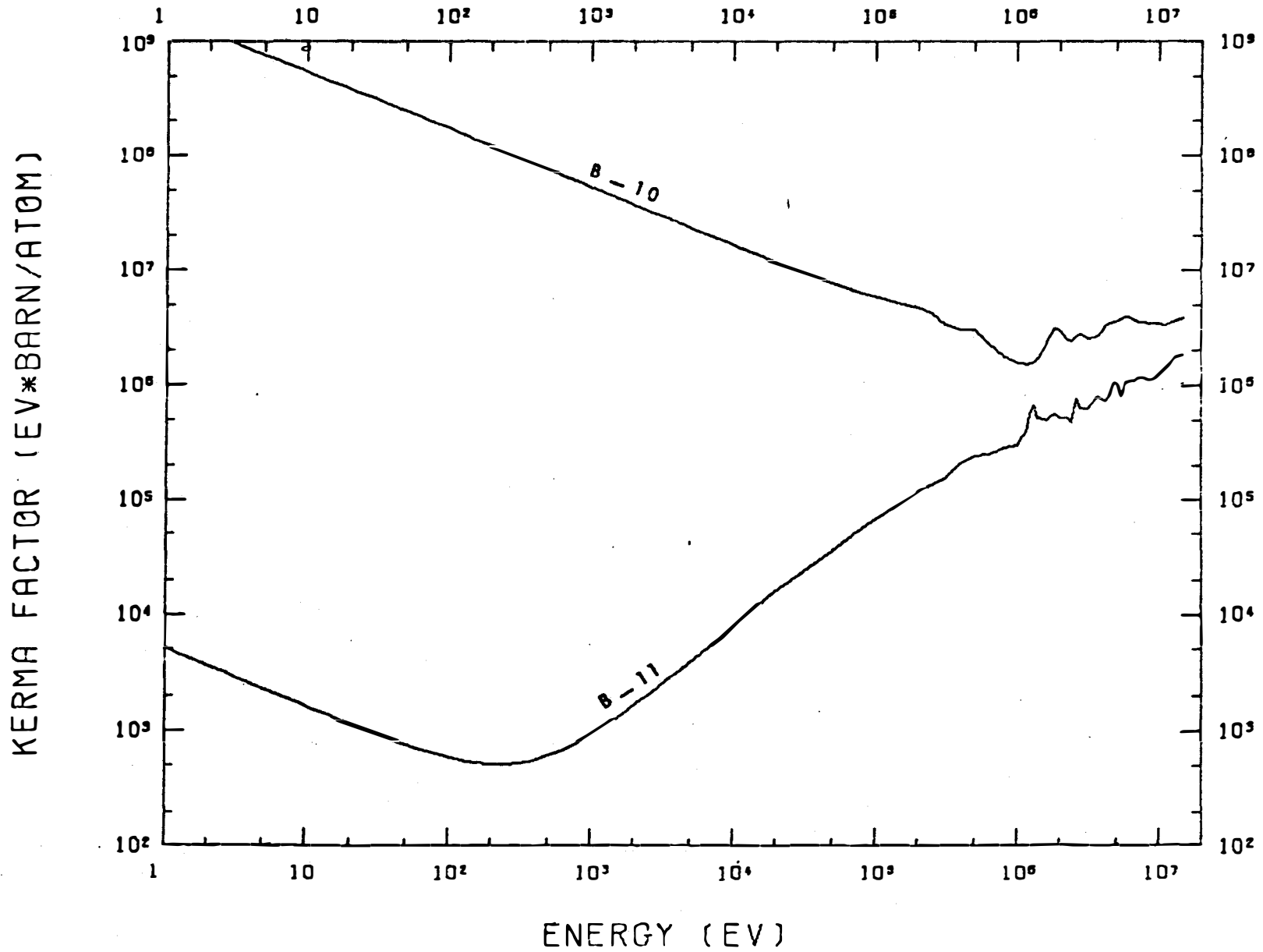


Figure V.C.2 Neutron Kerma Factors for Boron-10 and Boron-11



general, the total cross section decreases with energy in the MeV region while k_n increases because the energy release per reaction increases linearly or faster while the total cross section decreases slowly with energy. On the otherhand, in the resonance region, the energy dependence of k_n follows closely that of the total cross section. In the electron volt region, k_n decreases with energy for all but a few materials. In this energy range, k_n is dominated by $\frac{1}{\sqrt{E}}$ reactions such as (n,γ) in most materials or (n,α) in Li-6 and

B-10. The energy release per reaction is rather constant in these cases and k_n follows roughly the energy dependence of the cross sections.

The kerma factor plots are arranged in groups of two or three materials on the same graph for comparison purposes. Figure V-C-3 shows the kerma factor for the three basic elements in the human body. More than 95% of the dose in a Standard Man results from energy deposition in hydrogen, carbon and oxygen for incident neutron energies greater than 1 KeV. Below 10 eV the dose comes mostly from neutron interactions in nitrogen. Although k_n for carbon is higher than k_n for oxygen over most of the range the oxygen dose in Standard Man is higher because of elemental percentages. Kerma factors for hydrogen, carbon and oxygen have proved extremely useful in Section B in calculating the dose in the coil insulators.

Figure V-C-1 shows that k_n for Li-6 is higher than for Li-7 over the entire energy range from 0ⁿ to 15 MeV (This contradicts previous results by Ritts et al. [28]). Since both materials have the same atomic number the total nuclear heating in Li-6 is always higher than in Li-7 for equal nuclide number density for any spectrum. Table V-C-5 shows that η_s for Li-6 is about 800 times η_s for Li-7 but η_w is higher by only a factor of six. Therefore, in the first few mean free paths (for 14 MeV neutrons) of natural lithium (7.42% Li-6 and 92.58% Li-7) the nuclear heating in Li-7 is higher than in Li-6. In the rest of the blanket the reverse is true. Above 5 MeV, the energy deposition in Li-7 is mainly due to the $(n, n'\alpha)$ reaction and elastic scattering. The elastic scattering contribution dominates in Li-7 at lower energies down to about 0.1 MeV where the (n,γ) reaction comes into play. k_n for Li-7 at thermal energies is essentially that of radiative capture which is followed by the 0.85 second β^- decay of Li-8. In Li-6, more than 50% of the energy release comes from the $(n, n')d$ reaction for incident energies above 6 MeV with elastic, (n,α) and $(n,2n)\alpha$ reactions contributing the other 50%. The (n,α) reaction has an exothermic Q-value in Li-6 of 4.786 MeV and a large $\frac{1}{v}$ cross section at low energy. For incident energies less than 200 KeV, almost all the heat generated in Li-6 comes from this reaction. In an optically thick Li-6 region with a 14 MeV neutron source, the (n,α) reaction rate is more than 90% of the total nonelastic reaction rate. Hence, more than 4 MeV is converted from mass to kinetic energy and Li-6 is an excellent clean "energy breeder". Except for the radiative capture

reaction, all nonelastic reactions in Li-7 are endothermic and hence there is an "energy loss" in Li-7 through conversion of kinetic energy to mass. The situation is different in Li-7 for incident energies of about 1 KeV or lower. In this low energy range, the (n, γ) reaction dominates and there is a gain in energy of 11.3 MeV per reaction (2 MeV neutron binding energy and 9.3 MeV from the β^- decay of Li-8 to Be-8 which disintegrates into two alpha particles). The energy multiplication in natural lithium at low energies is governed, however, by the Li-6 (n, α) reaction which has a much larger cross section than the (n, γ) in Li-7.

Figure V-C-2 shows the neutron kerma factor, k_n , for the two isotopes of natural boron which is the basic neutron absorber in most shields. k_n is much higher for B-10 than for B-11 in the entire energy range from zero to 15 MeV. This is primarily because of the large energy release from the (n, α) reaction at lower energies. Both reactions are exothermic with a Q-value of 2.79 MeV for (n, α) and 0.23 MeV for (n,t) in addition to 0.95 MeV average decay energy per (n,t) reaction. Except for radiative capture, all nonelastic cross sections in B-11 are endothermic. η for B-10 is three orders of magnitude higher than η for B-11. Therefore, the heating rate in natural boron (19.6% B-10 and 80.2% B-11) is essentially that of B-10 for a typical shield spectrum. For high energy spectra such as the first wall spectrum, the neutron heating in B-10 is also more than 70 times the neutron heating in B-11. Although k_n for B-10 is higher than that of Li-6 at energies below 7 MeV Li-6 is a better energy multiplier. The B-10 (n, α) cross section is larger than the Li-6 (n, α) cross section but the (exothermic) Q-value for the latter is about 1.7 times the Q-value for the former.

Figures V-C-3 through V-C-8 show the neutron kerma factors for other materials of great importance for use in CTR. Vanadium and niobium are proposed for use as the first wall material. Iron, chromium and nickel are the basic constituents of stainless steel which may be used as the first wall material in the first generation of fusion reactors. In addition, stainless steel will very likely be employed for high energy neutron attenuation in the shield and as structural material for the magnet. Copper is used as the stabilizer for the superconducting magnet.

Figure V-C-8 compares the neutron kerma factors for the important elements in stainless steel, Fe, Cr, and Ni. It can be seen from this graph that k_n for nickel is roughly twice that of iron from 3 to 15 MeV. Hence, k_n for stainless steel can not be approximated by that of iron as is frequently assumed [31]. Stainless steel has usually 10 to 15% nickel. For a typical CTR blanket, approximating the neutron kerma factor for a stainless steel first wall by that of iron underestimates the neutron heating by more than 10%. For the C/E flux in the range 0 to 15 MeV the neutron heating per Ni atom is about three times the neutron heating per Fe atom and approximating the stainless steel kerma factor by iron underestimates the neutron heating in the shield and magnet by more than 20%.

Figure V.C.3 Neutron Kerma Factors for Hydrogen-1, Oxygen-16, and Carbon-12

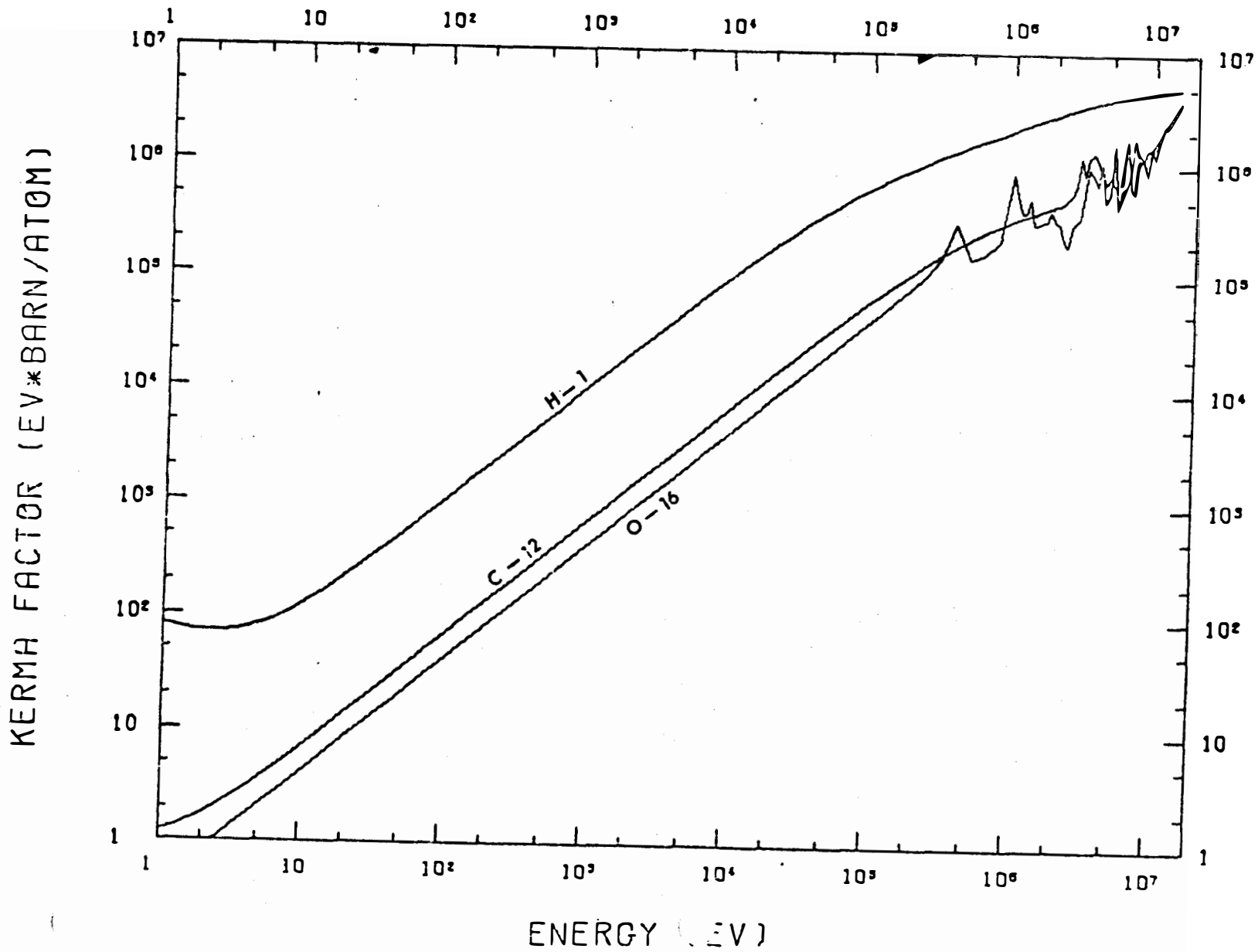


Figure V.C.4 Neutron Kerma Factors for Iron and Lead

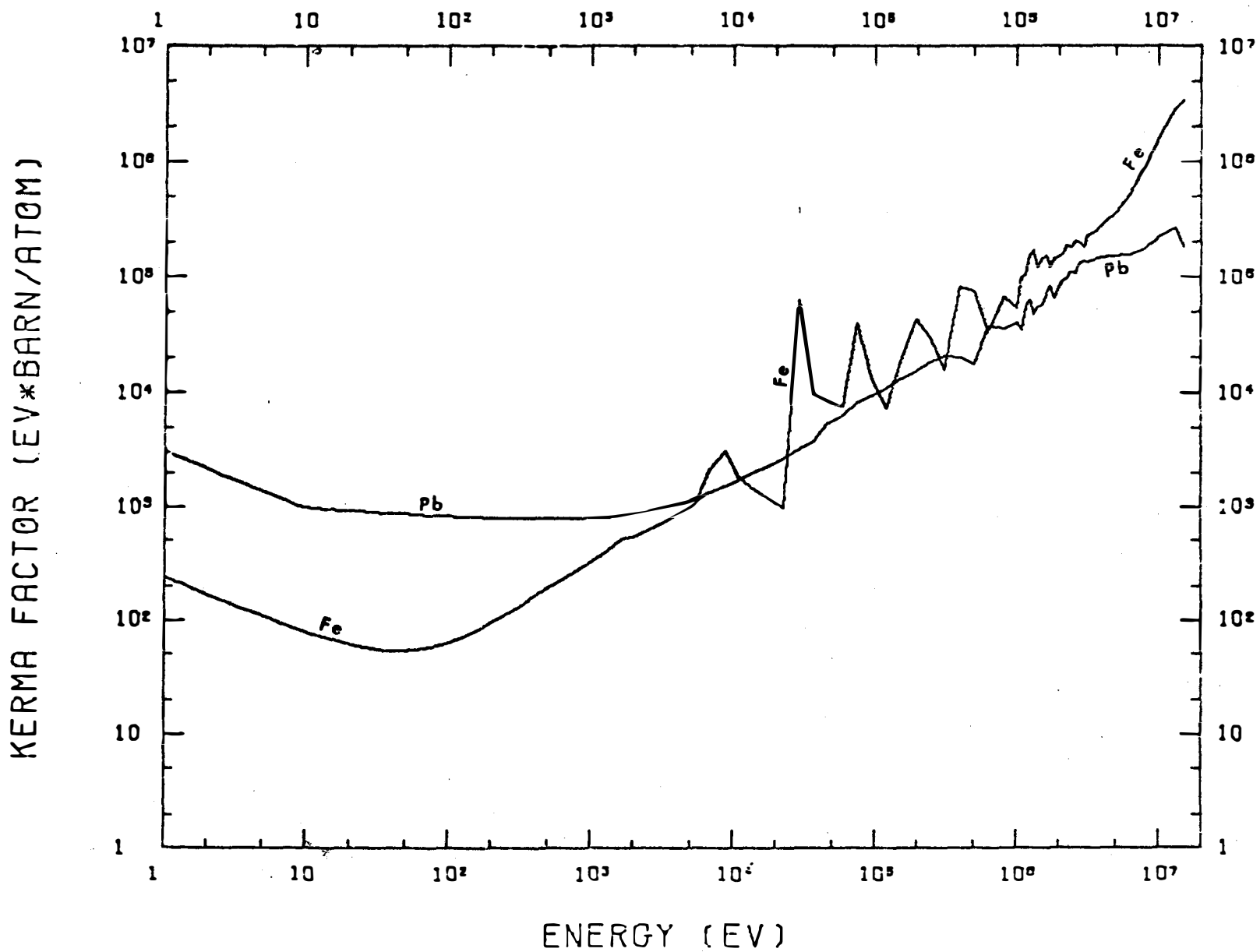


Figure V.C.5 Neutron Kerma Factors for Niobium and Iron

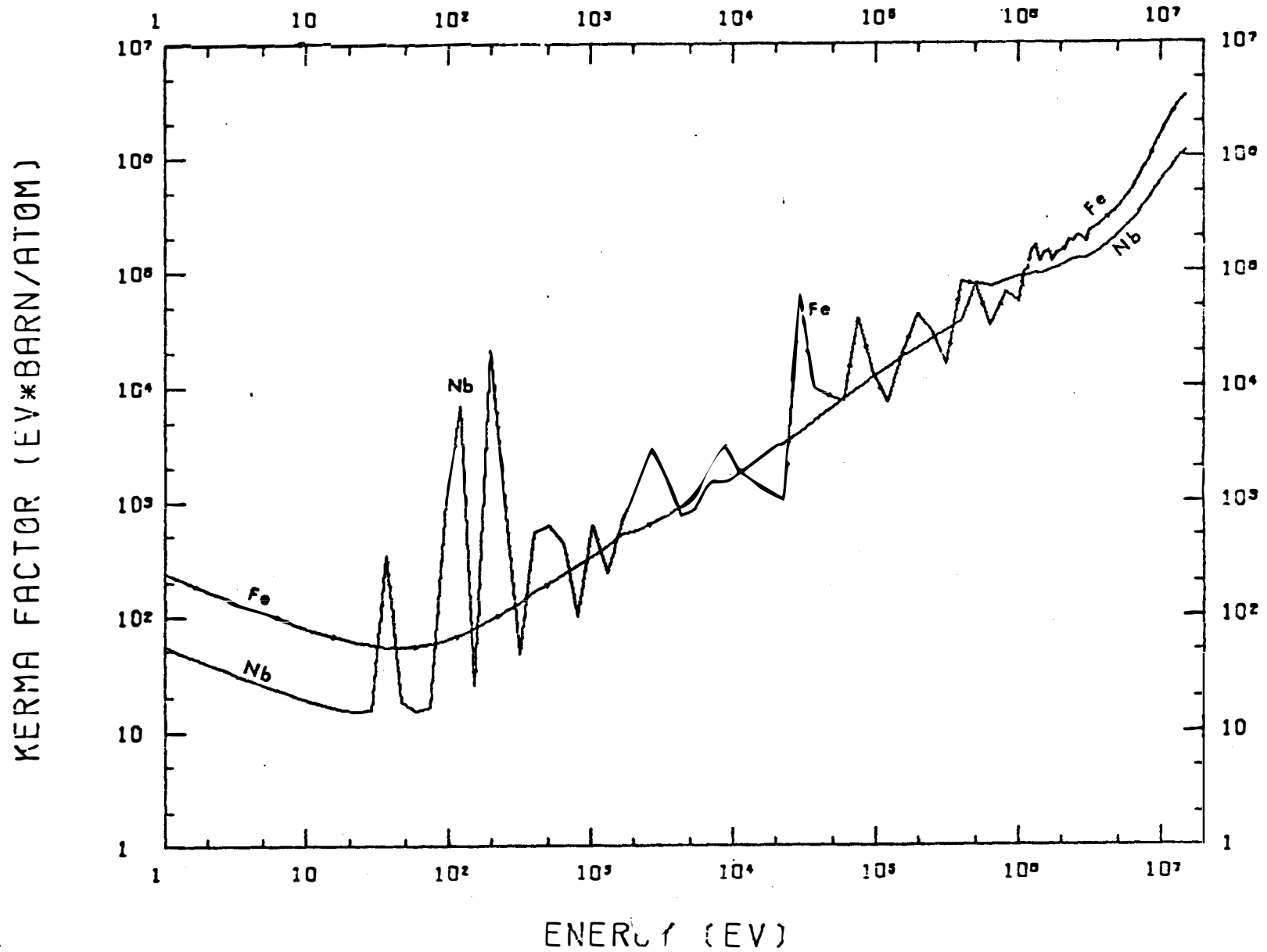


Figure V.C.6 Neutron Kerma Factors for Iron and Copper

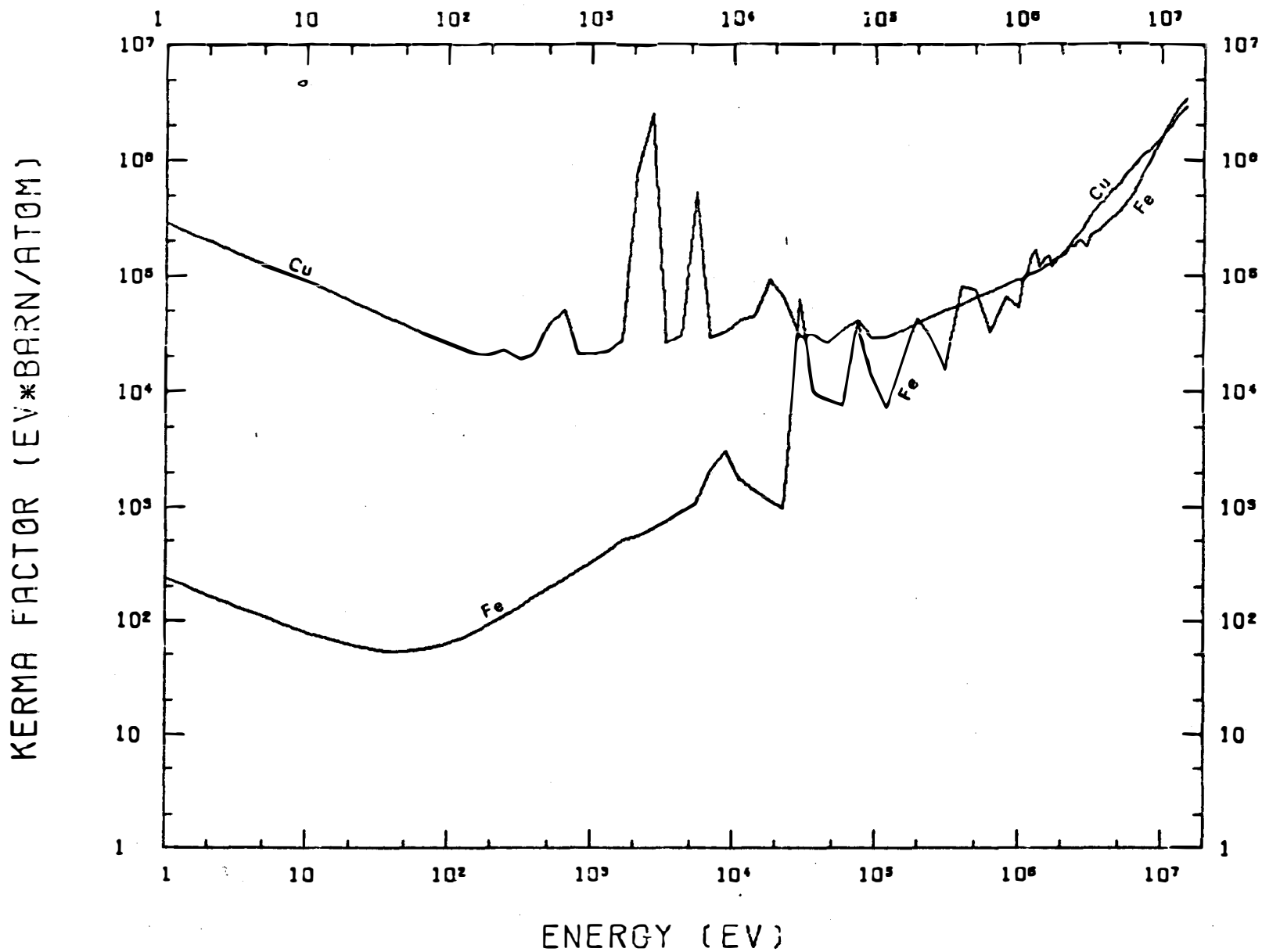


Figure V.C.7 Neutron Kerma Factors for Vanadium, Niobium, and Iron from 1 to 15 MeV

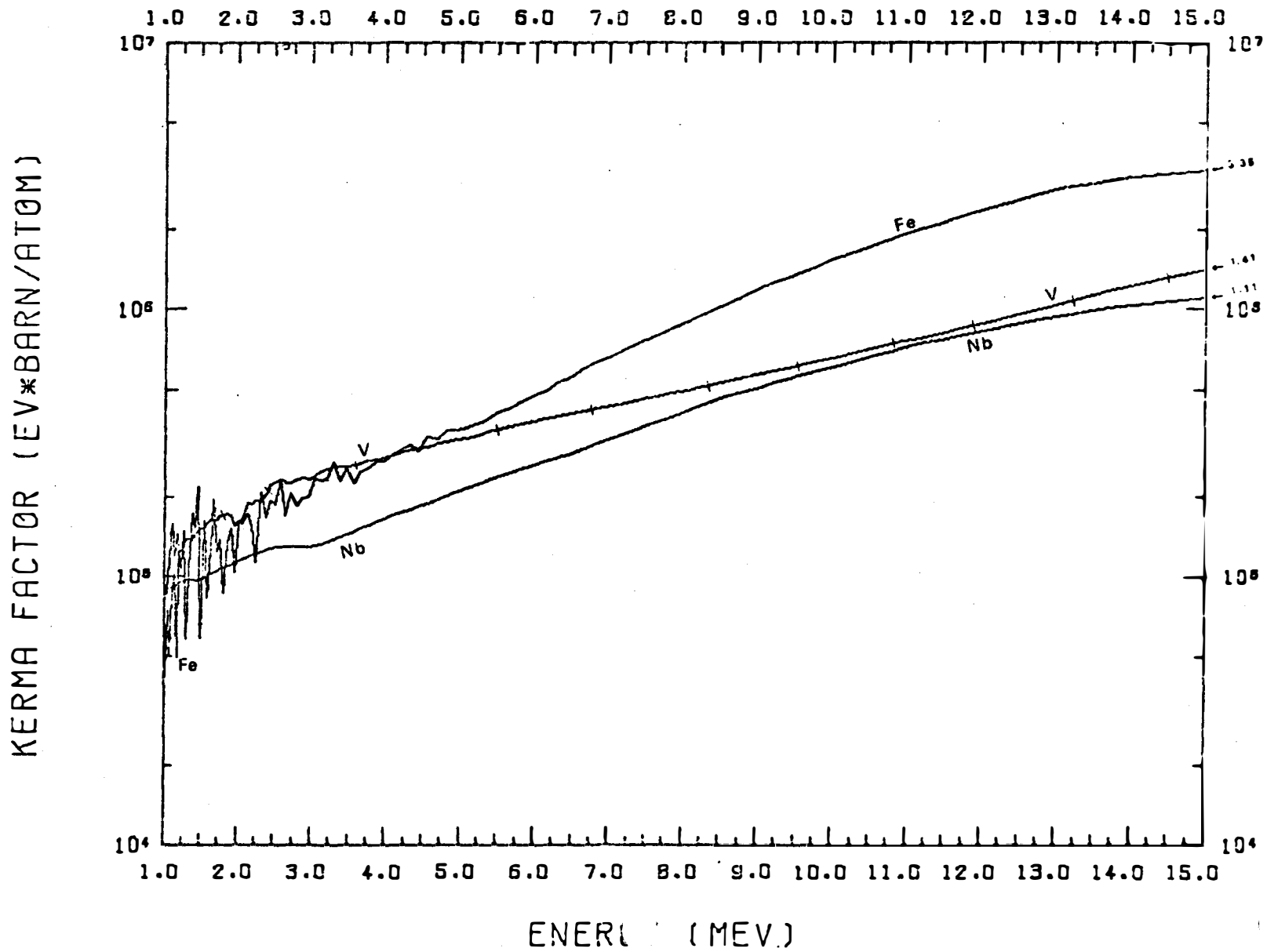
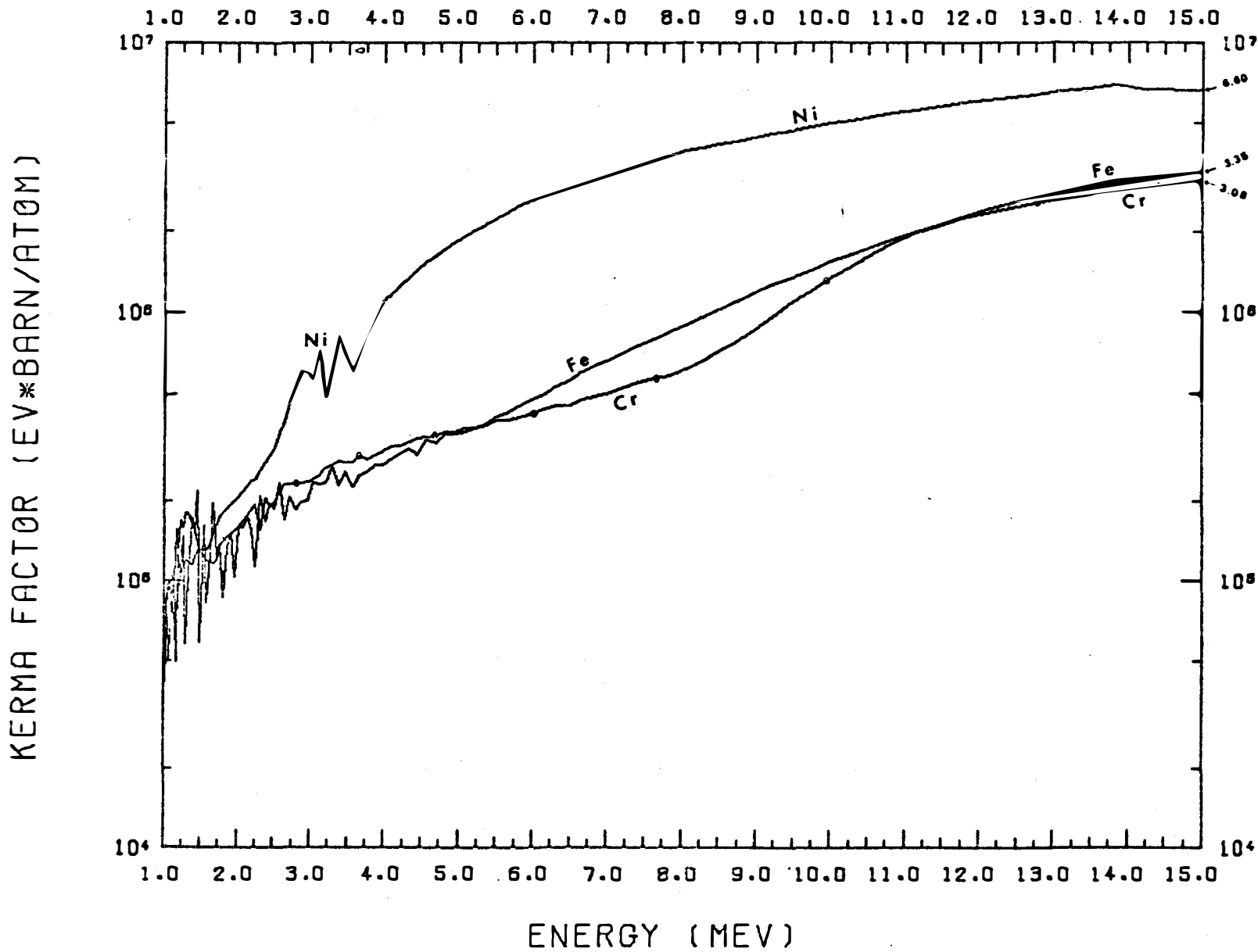


Figure V.C.8 Neutron Kerma Factors for Iron, Chromium, and nickel from 1 to 15 MeV



The neutron kerma factors for natural copper and iron are compared in Figure V-C-6. Below 10 MeV, copper has a higher kerma factor. η_s for copper is about 50% higher than η_s for iron and about 45% lower than for nickel. The copper gamma kerma factor is also (slightly) higher than for iron and nickel. Therefore, for a typical CTR shield spectrum at the magnet edge the total heating rate per unit volume in copper is roughly 25% higher than in stainless steel (the number of nuclei per unit volume is approximately the same for the two materials). The neutron kerma factor is compared for iron, niobium, and vanadium in Figure V-C-7 for the energy range 1 to 15 MeV which is the range of importance for energy deposition in the first wall. Above 5 MeV, k_n is highest for iron followed by vanadium and lowest for niobium. The main reason for that is the relative magnitude of the (n, α) and (n,p) cross sections for the three materials in this energy range. From Table V-C-5, η_w for iron is about 2.7 times that of niobium and 2.1 times that of vanadium. η_w for vanadium is 1.26 times η_w for niobium. The difference in the first wall neutron spectra for the three materials does not affect significantly the relative magnitude of η_w . However, the gamma heating in the first wall is considerably higher than the neutron heating (a factor of about 10 for niobium). The relative magnitude of the gamma production source and the gamma kerma factors are not in the same order as for the neutron heating. Gamma production and heating is highest in niobium and lowest in vanadium.

8. Conclusions

A large effort has been devoted in our program to collect and organize the nuclear data parameters required for CTR neutronics and photonics calculations. The data library is currently organized into four major parts: 1- neutron multigroup cross sections in GAM-II one-hundred and UW-46 group structures, 2-gamma multigroup cross sections in the UW-43 group structure, 3-photon production for the (100,43) and (46,43) neutron-gamma group structures, and 4- neutron and gamma kerma factors and partial cross sections.

In addition to the data libraries, we have operated several computer programs including ANISN, MORSE, LAPHANO, and MUG. Our efforts have also produced a program, MACK, which computes energy deposition parameters (kerma factors) and partial cross sections. A program, LINK [46], has also been developed for calculations of the gamma production source. A one-dimensional variational program, VARI-ED (14-b) has been developed to carry out sensitivity studies at low computational cost. Our studies [1-3] have shown that there is a lack of information about some important nuclear data parameters. In particular, a large effort should be devoted to measuring and calculating charged particle and gamma production cross sections. The data in the energy range 5 to 15 MeV seems to suffer from the largest uncertainties.

V-D Flux Calculations

1. Introduction

In neutronics and photonics analysis of fusion reactor blankets and shields the basic problem is calculation of "response" rates. A response rate generally takes the form

$$R = \int_{\vec{P}} \Sigma_R(\vec{P}) \psi(\vec{P}) d\vec{P} \quad (23)$$

where $\Sigma_R(\vec{P})$ is the response function, $\psi(\vec{P})$ is the angular flux, and \vec{P} represents a point in the phase space. The previous section was devoted to calculating the response functions of interest, namely, neutron and gamma kerma factors and group cross sections by reactions. An adequate calculational model for determination of ψ in the blanket and shield is investigated in this Section.

The angular flux, ψ , is obtained from a solution of the Boltzman transport equation:

$$L\psi = S \quad (24)$$

where L is the Boltzman operator and S is the external Source. [41] The calculations reported here used a 1-D discrete ordinates program, ANISN, [42] to solve equation (24).

In this stage of fusion reactor design, it is expected that steady-state fusion reactors will be either cylindrical or toroidal in geometry with some possible variations foreseen in practical designs of full-scale reactors. The cylinder is conceived to have a large height-to-diameter ratio with large plasma diameters anticipated. The toroidal geometry is expected to have an aspect (major-to-minor diameter) ratio of about 3 for Tokamak-type devices and roughly 200 or more for theta-pinch reactors with the major diameter so large that the curvature can be neglected at least to first order, in neutronics calculations. Full-scale reactors will employ feed pipes, divertors and several other necessary access regions. Therefore, very accurate neutronics and photonics analysis of full-scale reactor designs have to be carried out eventually in three-dimensional geometry. From the neutronics point of view, the access regions built into fusion blankets and shields will have the effects of 1 - having regions of low nuclide density from which neutrons and photons can stream out of the system affecting the neutron economy, energy deposition and multiplication, and requiring shields somewhere near the outer ends of the ducts; and 2 - increasing parasitic absorption of neutrons by neutron collisions

in the access region walls. However, survey studies have been carried out using one dimensional models for the transport calculations. Some of the multi-dimensional aspects of the neutron transport have been investigated using Monte Carlo calculations as discussed in a previous section.

In fusion reactors with magnetic confinement schemes, the blankets and shields have unique characteristics that are not frequently met in other areas of nuclear work. The fusion shell (blanket and shield) has a strong volumetric neutron source in vacuum on one side and a superconducting magnet cryogenically cooled to about 4°K on the other side. To reduce the heat load into the refrigeration system to a reasonable limit, the neutron and gamma fluxes must be attenuated by a factor of about 10^6 . In addition, the neutrons are born as roughly a delta function in energy and only at one end of the blanket and therefore the error in predicting the neutron flux in the first few mean free paths in the upper energy group propagates rapidly to lower energy groups and deeper regions of the blanket and shield. Therefore, CTR blanket and shields represent deep penetration problems which have the characteristic that low-order approximations will usually poorly predict results. In the following, an attempt is made to find the orders of approximation adequate for predicting acceptably accurate neutronics and photonics results without excessive costs. The effects studied here are the source form and geometry, anisotropy of scattering, angular quadrature, and spatial mesh spacing for both neutrons and photons for the discrete-ordinates method.

Before proceeding to a discussion of results, a few words about the nuclear data used in the calculations is in order. Most of the investigation carried out for assessing adequate approximations for flux determination was completed before ENDF/BIII data was available to us. Therefore, most of the results presented in this section were carried out using ENDF/BII data. The neutron heating rates were also calculated using the kerma factors given in reference 28 because the MACK program discussed in the previous sections was not developed at that time. While there is a change in the absolute magnitude of the parameters calculated here when ENDF/BIII data is used, e.g. $Nb(n,2n)$, cross sections, the relative magnitude of the results predicted by the various approximations do not change. Therefore, repeating these calculations would not change the conclusions derived here nor add anything new to our understanding of the problems investigated. Thus, we present the results calculated from ENDF/B2 as noted in each table. Results in tables given in this section without a note about the source of data are derived from ENDF/B3. All other calculations presented in this work were carried out using ENDF/B3 data with the partial group cross sections and neutron kerma factors generated with the MACK program. [4]

The calculations given here are based primarily on a standard fusion reactor blanket model adopted for benchmark and cross sections

at the International Working Sessions on Fusion Reactor Technology held at Oak Ridge in June 1971^[32]. This standard blanket is shown schematically in Figure V-D-1.

2. Neutron Source Distribution

The nearly monoenergetic neutron source is essentially isotropic because the ions are nearly isotropically distributed; and so little of the available momentum of the products is needed to balance the initial momentum, that the neutrons would be virtually isotropic regardless of the ion distribution. The source intensity is proportional to the square of the ion density and to the cross section which in the temperature range of interest for practical applications is essentially linear in the temperature. The equations governing the spatial distribution of these quantities are the energy and particle conservations and Maxwell's equations. This system of coupled equations can only be solved numerically^[33] or by rather drastic simplifying assumptions. It has been shown^[33] that plausible source spatial distributions take the form

$$S(r) = S_0 \left(1 - \left(\frac{r}{r_p} \right)^\alpha \right)^\beta \quad (25)$$

where α is two for slabs and cylinders and 5/2 for toroidal geometry and β is one for neo-classical and two for Bohm diffusion^[34]. The radius r at which the ion density and neutron source become zero is fixed by a system of magnet windings which divert any ions beyond this radius out of the central reactor region. From the point of view of the neutron source r_p is a parameter.

Table V-D-1 shows the influence of the neutron source distribution on helium and hydrogen production and atom displacement in the structural material, tritium production in Li, neutron heating, and leakage. The calculations were carried out for the energy range 8 to 14.1 MeV. This energy range was chosen to reduce the cost; however, it is the dominant energy range from a neutronics effects point of view. Table V-D-1 shows that the change in the reaction rates due to changing the source distribution is small and is generally within 1 to 2% for (parabolic)², parabolic, and uniform distributions. Hence, the results are relatively insensitive to the exact distribution and it suffices to use something resembling a parabola.

3. Neutron Source Geometry Effects and Cylinder-Slab Comparison

Table V-D-3 shows the most important neutronics and photonics results for the standard blanket of Figure V-D-1. The table shows that the slab representation overestimates all the neutronics results in the first wall by about 17%, and underestimates the results in the outer regions. The neutron leakage from the slab for neutrons above 8 MeV is 50% lower than the leakage from cylindrical blanket. Approxi-

Table V-D-1 Neutron Source Distribution Results for Cylindrical Geometry (S_{12} and P_3 approximations)

(Results normalized to unit neutron source)

Source Form	Zone	Volumetric (parabolic) ²	Volumetric parabolic	Volumetric uniform	Line isotropic
Niobium (n, α) $\times 10^4$	3	4.42	4.46	4.56	3.57
	5	3.01	3.04	3.09	2.77
	T ^a	15.01	15.07	15.20	14.40
Niobium (n,p) $\times 10^3$	3	1.46	1.47	1.50	1.18
	5	1.01	1.01	1.03	0.93
	T ^a	5.07	5.09	5.13	4.77
Niobium Displacement (DPA/n. sec) $\times 5 \times 10^{20}$	3	3.74	3.77	3.86	3.03
	5	2.62	2.64	2.69	2.40
Li ⁷ tritium production	4	0.062	0.062	0.064	0.054
	6	0.214	0.214	0.210	0.220
	7	0.085	0.084	0.082	0.093
	8	0.034	0.034	0.0327	0.039
	T ^b	0.395	0.395	0.394	0.404
Neutron Heating rate in watts $\times 10^{14}$	3	0.81	0.81	0.83	0.65
	4	15.78	15.90	16.27	13.77
	5	0.55	0.56	0.57	0.51
	6	52.40	52.47	52.60	53.05
	7	19.82	19.60	19.19	22.01
	T ^b	95.95	95.82	95.58	97.94
Right boundary Leakage $\times 10^4$	T ^c	37.8	35.97	34.4	43.3

a - sum over all zones (for neutrons above 8 MeV)

b - sum over breeding zones (for neutrons above 8 MeV)

c - sum for outgoing neutrons above 8 MeV

This table based on ENDF/B II data

Table V-D-2 Effect of Plasma and Wall Radii on Response Rates(uniform source, S_{12}, P_3)

(Results Normalized to a Unit Neutron Source)

Wall Radius r_w (meters)	Zone	2	2	2	8
Plasma Radius r_p (meters)		line	0.1	1.5	7.5
		source			
Niobium (n, α) $\times 10^4$	3	3.57	4.33	4.56	4.92
	5	2.77	2.95	3.09	3.24
	T ^a	14.1	14.8	15.2	15.6
Neutron Heating Rate in watts $\times 10^{14}$	3	0.65	0.79	0.83	0.89
	4	13.77	15.45	16.27	17.28
	5	0.51	0.54	0.57	0.59
	T ^b	97.94	96.10	95.94	94.90
Leakage $\times 10^4$	T ^c	43.3	38.3	34.4	28.2

a. sum over all zones (for neutrons above 8 MeV)

b. sum over breeding zones (for neutrons above 8 MeV)

c. sum for neutrons above 8 MeV (assuming no reflection)

This table based on ENDF/B II data

Table V-D-3 Slab - Cylinder Comparison (Reference Design of Figure V-D-1)

(S₈,P₃)

(Results normalized to a unit neutron source)

Geometry Source		Cylinder Volumetric Uniform	Slab Volumetric Uniform	Slab Shell Isotropic
Niobium (n,α) × 10 ⁴	3	4.61	7.77	5.27
	5	3.14	3.68	3.32
	T ^a	15.28	18.4	16.02
Niobium (n,p) × 10 ³	3	1.52	2.56	1.74
	5	1.05	1.23	1.11
	T ^a	5.16	6.17	5.41
Niobium Displacement (DPA/n. sec) × 5 × 10 ²⁰	3	3.90	6.53	4.45
	5	2.73	3.20	2.89
Li ⁷ tritium production	4	0.065	.089	.071
	6	0.214	.193	.214
	7	0.081	.057	.074
	8	0.0325	.020	.028
	T ^b	0.393	.361	.387
Neutron Heating Rate in watts × 10 ¹⁴	3	0.84	1.41	0.96
	4	16.54	22.84	18.07
	5	0.52	0.68	0.61
	6	52.39	47.03	52.30
	7	19.04	13.18	17.30
	T ^b	99.28	87.62	94.07
Leakage × 10 ⁴	T ^c	33.75	17.6	26.1

a - sum over all zones (for neutrons above 8 MeV)

b - sum over breeding zones (for neutrons above 8 MeV)

c - sum for outgoing neutrons above 8 MeV

ENDF/B II data used in obtaining these results

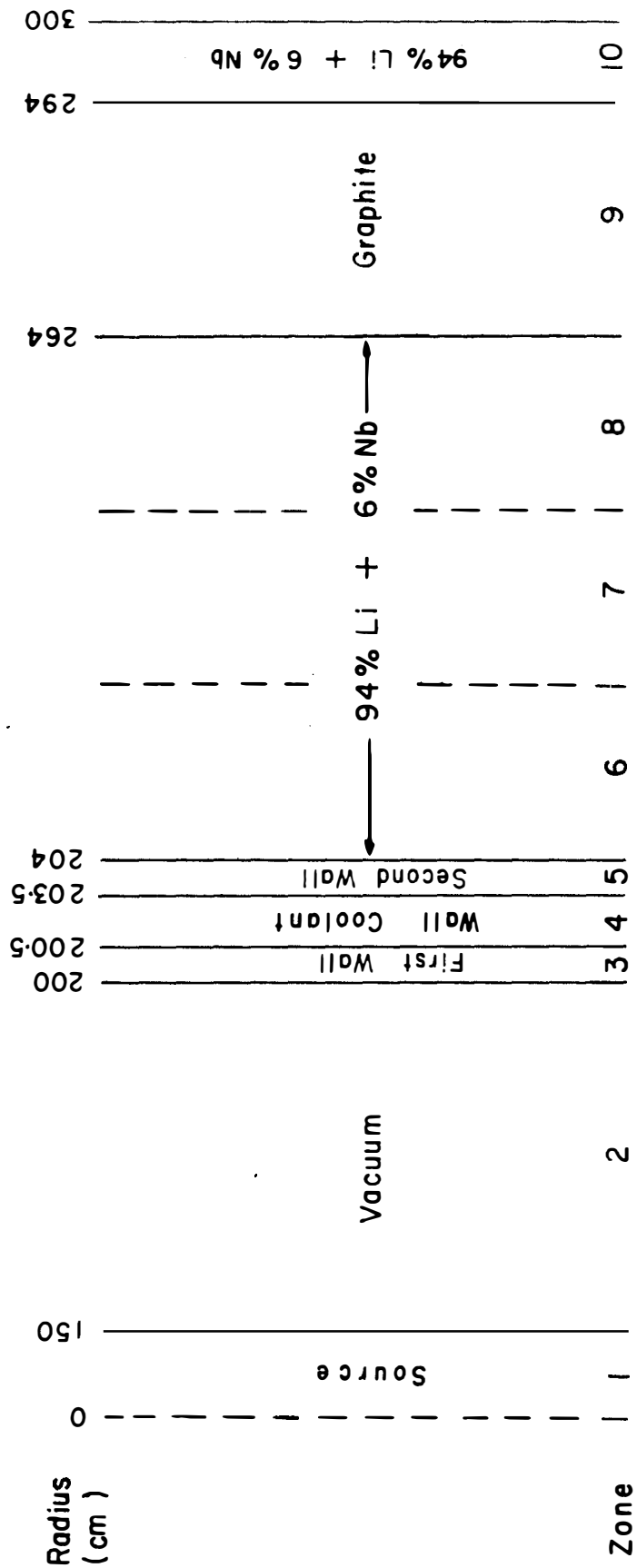


Figure V-D-1 Schematic of Standard Blanket for Benchmark Calculation

mating the neutron source in slab geometry by an isotropic shell improves the results but the difference from cylindrical geometry is still very large. Therefore, slab geometry is unacceptable.

The reason slab geometry gives poor results can be seen intuitively from the fact that the results are independent of the spatial distribution and the angular distribution incident on the first wall becomes infinite as the angle of incidence approaches a parallel to the wall. In a cylinder with the source not extending to the wall, there are no incident neutrons at right angles to the normal except in the vertical direction and the spatial distribution further increases the tendency to normal incidence.

The effect of the plasma and wall radii is shown in Table V-D-2. As expected from the above results, the smaller the ratio, the smaller the reaction rates in the first few zones and the larger the leakage.

4. Effects of Scattering Anisotropy

Since the neutrons have high energies, anisotropy of the scattering has important effects on neutron transport. As is well known, the differential scattering cross section is usually approximated by a truncated Legendre polynomial expansion in the scattering angle,

$$\sigma(\mu_0) = \sum_{l=0}^L \sigma_l P_l(\mu_0) \quad (26)$$

where μ_0 is the cosine of the scattering angle and L is chosen sufficiently large to adequately describe the anisotropy of the angular distribution. An adequate value of L for CTR blankets is discussed next.

Table V-D-4 shows the important neutronics results as a function of L for the standard blanket of Figure V-D-1. This series of calculations was carried out for the P_0 through the P_8 approximations for slab and cylindrical geometries. The results show that convergence is achieved by P_5 . However, Table V-D-4 shows that results obtained using P_3 are adequate to better than 1% accuracy. The results also show that increasing the order of anisotropy retained in the scattering increases the streaming tendency and lowers the heating and reactions in the inner blanket regions.

5. Order of S_n Angular Quadrature

The next problem posed is the order required of the angular quadrature for the S_n method. It has been established [35] that the inherent approximations in the S_n method are adjustable such that these approximations do not materially affect the desired solution. Practical limitations, however, prohibit using the finest energy, spatial, and angular mesh. Since the number, M , of angles in one-dimensional cylindrical geometry is equal to $n(n+4)/4$ where n is the order of the quadrature used and the computation (CPU) time increases linearly with

Table V-D-4 Neutron Scattering Anisotropy (order of P_n)
(cylindrical geometry, S_{16})
(Results normalized to a unit neutron source)

Scattering order	Zone	P_0	P_1	P_2	P_3	P_4	P_5
Niobium (n, α) $\times 10^4$	3	6.015	4.568	4.558	4.548	4.549	4.540
	4	1.709	1.340	1.325	1.329	1.328	1.328
	5	3.836	3.137	3.068	3.085	3.080	3.082
	6	4.402	4.288	4.185	4.199	4.199	4.199
	7	1.000	1.459	1.481	1.469	1.472	1.472
	8	0.235	0.507	0.554	0.546	0.546	0.547
	T*	17.198	15.304	15.178	15.183	15.181	15.175
Li ⁷ tritium production $\times 10^2$	4	8.321	6.403	6.335	6.352	6.349	6.350
	6	22.948	21.967	21.441	21.517	21.514	21.517
	7	5.65	8.207	8.271	8.215	8.227	8.228
	8	1.399	3.087	3.323	3.284	3.285	3.286
	10	0.007	0.039	0.051	0.051	0.051	0.051
T*	38.324	39.703	39.422	39.419	39.426	39.433	
Neutron Heating in watts $\times 10^4$	3	1.099	0.834	0.832	0.830	0.830	0.828
	4	20.962	16.302	16.122	16.168	16.159	16.163
	5	0.704	0.575	0.562	0.565	0.564	0.565
	6	55.723	53.831	52.540	52.723	52.717	52.724
	7	13.162	19.157	19.376	19.230	19.261	19.264
	8	3.177	6.929	7.514	7.418	7.420	7.424
	9	0.628	2.010	2.500	2.491	2.484	2.485
	10	0.015	0.081	0.109	0.096	0.110	0.110
	T*	95.47	99.717	99.554	99.520	99.546	99.563
		GRP					
System Leakage $\times 10^4$	1	1.336	5.302	9.084	9.806	9.791	9.788
	2	0.720	5.557	9.174	9.462	9.426	9.429
	3	0.498	4.225	6.097	6.109	6.094	6.097
	4	0.488	3.421	4.307	4.270	4.267	4.268
	5	0.397	2.183	2.522	2.512	2.510	2.511
	6	0.428	1.973	2.224	2.222	2.221	2.221
	T ^c	3.866	22.661	33.408	34.381	34.308	34.315

* sum over all zones for neutrons above 8 MeV

c sum over outgoing neutrons of energies above 8 MeV

This table is based on ENDF/B II data.

the number of angles, the cost of computation increases roughly as n^2 for high order S_n . Therefore, it is highly desirable to find the smallest order of quadrature that provides the desired accuracy.

Table V-D-5 shows the effect of the order of angular quadrature on the important neutronics results for the standard blanket of Figure V-D-1. The results are given for both slab and cylindrical geometry. A uniformly distributed volumetric source and the P_3 approximation were employed in both cases. The spatial mesh was chosen with a step size fine enough to essentially eliminate the effect of the spatial mesh on the accuracy of the results. The cylinder results in Table V-D-5 show that as the order of approximation is increased, the flux anisotropy is treated more adequately and it becomes more forward peaked resulting in decreased reactions in the first zones. In the following discussion it is assumed that the S_{16} results represent the "exact results" and the accuracy of the lower order S_n is quoted relative to the S_{16} results. The results of S_4 overpredict the neutronics results in the first zone by about 7 to 10%, overestimates the neutron heating in the last zone by more than 20%, and underestimates the neutron heating, Tritium and charged particle productions in zones 6,7, and 8. S_8 provided better than 5% accuracy almost everywhere in the blanket. A 5% accuracy was also found to be obtainable with S_6 provided that an adequate spatial mesh is used.

As is well known, the accuracy of the discrete ordinate solution does not necessarily improve by increasing the order of angular quadrature alone or decreasing spatial mesh size alone. Studies were carried out in the present work as to adequate mesh spacing for a given angular quadrature and conformed to a rule that an adequate mesh for any region resulted if the steps were $1/\Sigma_t N$ where N is the order of S_n used and Σ_t is the largest total cross section in any group for the n mixture in that region. Following this rule guarantees improvement of the accuracy of the solution as N is increased. It was also found that the calculations in groups corresponding to energies lower than a few KeV could be performed in lower approximations without degradation of the quality of the neutronics results. This is very convenient since Σ_t increases rapidly for most materials in this lower energy range and applying the above rule at such low energies would require a very fine spatial mesh.

6. Gamma Computational Model

A calculational model for photonics is investigated next. The effects of scattering anisotropy were studied in slab geometry for economy using S_{16} . Convergence is not greatly affected by geometry. The results of interest in photonics are energy deposition and leakage. The system employed for the calculations is that of Figure V-D-1. The boundary condition or albedo is reflecting in this series and a set of results in selected blanket regions for anisotropy through P_n with n from zero to seven is shown in Table V-D-6. These results are converged by P_3 . However in the problem studied here P_1 doesn't give bad results

Table V-D-5 Order of S_n Approximation

(Results normalized to a unit neutron source)

Geometry Order of S_n	Zone	Cylinder				Slab		
		S_4	S_8	S_{12}	S_{16}	S_4	S_8	S_{16}
Niobium (n, α) $\times 10^4$	3	4.819	4.609	4.567	4.548	6.148	7.771	8.178
	4	1.439	1.360	1.338	1.329	1.772	1.881	1.848
	5	3.320	3.141	3.096	3.085	3.931	3.682	3.547
	6	4.126	4.172	4.189	4.199	4.139	3.719	3.698
	7	1.351	1.454	1.466	1.469	0.970	0.992	0.991
	8	0.521	0.540	0.545	0.546	0.317	0.326	0.326
	T*	15.585	15.282	15.209	15.183	17.280	18.375	18.591
Niobium (n,p) $\times 10^3$	3	1.590	1.519	1.505	1.499	2.029	2.556	2.687
	4	0.478	0.452	0.444	0.441	0.589	0.625	0.614
	5	1.109	1.049	1.034	1.030	1.315	1.233	1.188
	6	1.412	1.426	1.432	1.435	1.421	1.280	1.272
	7	0.480	0.516	0.520	0.521	0.350	0.356	0.356
	8	0.190	0.198	0.199	0.120	0.118	0.121	0.121
	T*	5.263	5.163	5.139	5.130	5.823	6.172	6.239
Niobium Displace- ment (dPa/n.sec) $\times 5 \times 10^{20}$	3	4.081	3.899	3.862	3.845	5.204	6.528	6.855
	5	2.881	2.726	2.687	2.676	3.413	3.205	3.090
Li ⁷ tritium produc- tion $\times 10^2$	4	6.865	6.492	6.392	6.352	8.452	8.955	8.802
	6	21.206	21.389	21.468	21.517	21.435	19.352	19.235
	7	7.588	8.135	8.201	8.215	5.653	5.719	5.708
	8	3.124	3.248	3.277	3.284	1.983	2.026	2.022
	T*	38.837	39.314	39.389	39.419	37.551	36.079	35.795
Neutron Heating in watts $\times 10^{14}$	3	0.879	0.841	0.833	0.830	1.122	1.415	1.489
	4	17.492	16.535	16.273	16.168	21.536	22.840	22.444
	5	0.608	0.576	0.567	0.565	0.720	0.675	0.650
	6	51.879	52.391	52.598	52.723	52.219	47.029	46.755
	7	17.726	19.036	19.197	19.230	12.963	13.187	13.165
	8	7.069	7.336	7.403	7.418	4.397	4.507	4.500
	9	2.508	2.453	2.483	2.491	1.351	1.348	1.347
	10	0.115	0.108	0.109	0.096	0.059	0.057	0.057
	T*	98.277	99.275	99.464	99.520	94.40	96.80	95.30
	Leakage $\times 10^4$	T ^c	36.919	33.752	34.258	34.381	18.012	17.604

* sum over all zones (for neutrons above 8 MeV)

c sum over outgoing neutrons above 8 MeV

This table is based on ENDF/B II data

Table V-D-6 Gamma Scattering Anisotropy Convergence
 (21 energy groups, slab S₁₆, 1 photon/sec)

Order of P _n Zone	P ₀	P ₁	P ₂	P ₃	P ₄	P ₆	P ₇	P ₇ ^a
3 ^b	8.0597	7.9087	7.9432	7.9297	7.9342	7.9324	7.9316	7.9240
4	2.7702	2.7180	2.7297	2.7257	2.7271	2.7268	2.7267	2.7238
5	7.0977	6.9699	6.9960	6.9876	6.9902	6.9895	6.9894	6.9814
6	12.0342	11.874	11.8916	11.8923	11.8906	11.8917	11.8925	11.8686
7	6.0468	6.0767	6.0542	6.0656	6.0615	6.0626	6.0627	6.0245
8	3.0105	3.1059	3.0828	3.0894	3.0885	3.0886	3.0885	3.0184
9	2.5544	2.9073	2.8667	2.8695	2.8697	2.8695	2.8695	2.3770
10	0.2470	0.2868	0.2903	0.2884	0.2888	0.2886	0.2886	0.1398
1c	1.1515	1.5254	1.5742	1.5648	1.5670	1.5665	1.5664	1.2543

- a. All cases except this carried out with a reflecting boundary condition on the right, while here a void condition is used
 b. Heating rates in niobium (zones 3 - 8 and 10) and graphite (zone 9) are in watts $\times 10^{15}$
 c. Right boundary positive current $\times 10^3$

and one strongly suspects that a transport corrected P_0 would be satisfactory. However, the combination of an isotropic and distributed source cause very low order approximations to work well in this instance. Experience with other gamma flux problems indicated that a P_3 treatment would be prudent even though the above results would allow less. The last column in Table V-D-6 gives the P_7 results but with a void boundary condition. The only results that are affected in a major way are near the right boundary as would be expected. Table V-D-7 shows the same general results for a void at the right boundary in two lower order S_N calculations for both slab and cylindrical geometries. The S_6 slab results are within 1% of the S_{16} results and compare very favorably with the last column of the preceding table indicating that S_6 is adequate as is P_3 anisotropy. However, the cylindrical and slab result differ enough even here to require the cylindrical model; further, the S_4 - P_0 results are inadequate with respect to the leakage and other results near the right boundary.

7. Variational Procedures

Almost all of the response or performance criteria of the nuclear aspects of a reactor take the form of an integral of the neutron flux times a response function which is generally a property of the materials constituents of the system. A quantity of this type is called a linear functional and in survey and sensitivity studies they must be repeated many times. Often the repetitions are for systems which differ in only a small way from one another in geometry, composition or nuclear properties.

The calculation of the flux is basically an expensive undertaking. Thus, a procedure which allows a flux calculated for one problem to be used to determine the response of a somewhat different problem with little error will save substantial computing costs and may even result in studies previously considered prohibitively expensive. The use of a bilinear functional representing the response which is stationary with respect to small changes in the flux, achieves this goal. As a small change in the system, such as geometry, composition, or cross sections results in a small flux change, the functional is also correct to first order when treated as a perturbation theory. Thus, the same fluxes may be used in sensitivity studies.

The response function is denoted $s^*(\underline{x})$ where \underline{x} is the set of variables describing the phase space of the problem and the response is the scalar product of s^* with the flux $\phi(\underline{x})$. Thus,

$$G(\phi) = (s^*, \phi) = \int d\underline{x} \quad s^*(\underline{x}) \phi(\underline{x}) \quad (27)$$

Table V-D-7 Slab - Cylinder Comparison For Gamma Transport Calculation

Order of Approximation	S_6, P_3		S_4, P_0	
	Cylinder	Slab	Cylinder	Slab
3 ^a	7.25828	7.80623	7.36158	7.83919
4 (Nb)	2.53098	2.69892	2.57156	2.71759
4 (Li)	0.73625	0.78866	0.760072	0.80484
5	6.58181	6.95842	6.69689	7.03164
10	2.73871	2.36319	2.46407	2.12604
L ^b	1.57105	1.25367	1.03650	0.81425

a. Heating rates in watts $\times 10^{15}$

b. Right boundary leakage $\times 10^3$

References - Chapter V

1. M. A. Abdou, "Calculational Methods for Nuclear Heating and Neutronics and Photonics Design for CTR Blankets and Shields," A doctoral thesis, Nuclear Engineering Department, University of Wisconsin - July 1973.
2. M. A. Abdou and C. W. Maynard, "Calculational Methods for Nuclear Heating," University of Wisconsin Fusion Design Memo 66 - July 1973.
3. M. A. Abdou and C. W. Maynard, "Neutronics and Photonics Design for CTR Blankets and Shields," University of Wisconsin Fusion Design Memo 67 - July 1973.
4. M. A. Abdou, C. W. Maynard and R. Q. Wright, "MACK: A Computer Program to Calculate Neutron Energy Release Parameters (Fluence-to-Kerma Factors) and Multigroup Neutron Reaction Cross Sections from Nuclear Data in ENDF Format," ORNL-TM-3994; also issued as University of Wisconsin Fusion Design Memo 37 - January 1973.
5. M. A. Abdou, "Response, A Library of Kerma Factors and Multigroup Reaction Cross Sections," University of Wisconsin Fusion Design Memo 45 - July 1973.
6. A. P. Fraas, "Conceptual Design of the Blanket and Shield Region of a Full Scale Toroidal Fusion Reactor," to be published (1973).
7. L. N. Lontai, Study of a Thermonuclear Reactor Blanket with Fissile Nuclides, Technical Report No. 436, M.I.T. Laboratory of Electronics, Cambridge, Mass. (1965).
8. "An Assessment of Fusion Power," WASH-1239.
9. "Proceedings of the Conference on Continuum Aspects of Graphite Design," Gatlinburg, Tennessee, CONF-701105 (November 1970).
10. T. W. Evans, "The Effects of Irradiation on Boron Carbide," BNWL-679 (February 1968).
11. M. S. Lubell et al., "Economics of Large Superconducting Toroidal Magnets for Fusion Reactors," ORNL-TM-3927 (1972) and I.E.E.E. Conf. Record, I.E.E.E. Cat. No. 72 CHO 682-5 TABSC.
- 12a. R. Q. Wright and R. W. Roussin, "DLG 2/100G Neutron Transport Code Cross Section Data Generated by SUPERTOG from ENDF/B3," - July 1972. This library can be obtained through the Radiation Shielding Information Center (RSIC) at Oak Ridge National Laboratory.
- 12b. E. A. Straker et al., "The MORSE Code. . . , " ORNL-4585- September 1970.

13. R. Q. Wright, N. M. Greene, J. L. Lucius, and C. W. Craven, Jr., "SUPERTOG: A Program to Generate Fine Group Constants and P_n Scattering Matrices from ENDF/B," ORNL-TM-2679 - 1969.
- 14a. R. W. Conn and W. M. Stacey, "Variational Methods for Controlled Thermonuclear Reactor Blanket Studies," Nuclear Fusion 13, (1973) 185.
- 14b. E. Cheng and R. W. Conn, University of Wisconsin, Private Communication.
15. MUG; A Program for Generating Multigroup Photon Cross Sections," J. R. Knight and F. R. Mynatt, CTC-19 - January 1970.
16. W. E. Ford III, ORNL (private communication)
17. D. J. Dudziak, R. E. Seamon, and D. V. Susca "LAPHANO: A P_0 Multigroup Photon-Production Matrix and Source Code for ENDF," LA-4750-MS (ENDF-156) - January 1972.
18. S. K. Penny and L. W. Owen, "A Re-Evaluation of Vanadium Neutron and Gamma-Ray Production Cross Sections," ORNL-TM-4007 - November 1972.
19. W. E. Ford III, "POPOP4: A Code for Converting Gamma-Ray Spectra to Secondary Gamma-Ray Production Cross Sections," USAEC Report CTC-12 - May 1969.
20. W. E. Ford III, "POPOP4 Library of Neutron-Induced Secondary Gamma-Ray Yield and Cross Section Data," USAEC Report CTC-42.
21. a. Radiation Quantities and Units, compiled by Commission on Radiological Units and Measurements (ICRU), National Bureau of Standard Handbook 84 (ICRU report 10a), - November 1962.
b. D. K. Trubey, "Use of ICRU-Defined Quantities and Units in Shielding," ORNL-RSIC-16 - October 1968.
22. M. J. Stanley, "Kelin-Nishina Photon Cross Sections (Program GAMMA)," APEX-487, General Electric Company - May 1959.
23. Protection Against Neutron Radiation up to 30 Million Electron Volts, compiled by the Subcommittee on Heavy Particles (Neutrons Protons, and Heavier), National Bureau of Standards Handbook 63 - November 1957.
24. B. J. Henderson, Conversion of Neutron or Gamma Ray Flux to Absorbed Dose Rate, XDC 59-8-179, General Electric Company - August 1959.
25. J. A. Auxier and W. S. Snyder, The Calculation of Kerma as a Function of Neutron Energy, Oak Ridge National Laboratory, ORNL-4168 - 1967.

26. R. L. Bach and R. S. Caswell, "Energy Transfer to Matter by Neutrons," Radiation Res., 35, 1 - 1968.
27. J. J. Ritts, M. Solomito, and P. N. Stevens, "Calculation of Neutron Fluence-to-Kerma Factors for the Human Body," Nucl. Applic. and Tech., 7(1) 89-99 - July 1969.
28. J. J. Ritts, M. Solomito, and D. Steiner, "Kerma Factors and Secondary Gamma-Ray Sources for Some Elements of Interest in Thermonuclear Blanket Assemblies," ORNL-TM-2564 - June 1970.
29. M. K. Drake, Editor "Data Formats and Procedures for the ENDF Neutron Cross Section Library," BNL-50279 - October 1970.
30. C. M. Lederer, J. M. Hollander, and I. Perlman, "Table of Isotopes," 6th edition, John Wiley and Sons, New York - 1967.
31. W. Kohler et al., Proceedings Texas Symposium on Technology of Controlled Fusion Experiments and the Engineering Aspects of Fusion Reactors, Austin Texas - November 1972.
32. "Proceedings of the International Working Sessions on Fusion Reactor Technology," Oak Ridge National Laboratory, CONF-710624 - June 28 - July 2, 1971.
33. C. W. Maynard and M. A. Abdou, "Neutron and Gamma Physics Problems in Fusion Reactors," Conference on New Developments in Reactors Physics and Shielding, CONF-720901, Book 2 - September 1972.
34. M. N. Rosenbluth, R. D. Hazeltine and F. L. Hinton "Plasma Transport in Toroidal Confinement Systems," Phy. Fluids 15, 116 - 1972.
35. D. K. Trubey and Betty F. Maskewitz, "A Review of the Discrete Ordinates S_n Method for Radiation Transport Calculations," ORNL-RSIC-19 - 1968.
36. W. E. Alley and R. M. Lessler, "Semiempirical Neutron-Induced Reaction Cross Sections," UCRL-50484 Rev. 1 - August 1972.
37. J. T. Kriese, ORNL (private communication).
38. D. W. Muir, Los Alamos Scientific Laboratory, private communication - December 1972.
39. D. G. Doran, "Neutron Displacement Cross Sections for Stainless Steel and Tantalum Based on a Linhard Model," Nucl. Sci. Eng. 49, 130 - 1972.
40. J. D. Jenkins, "RICE: A Program to Calculate Primary Recoil Atom Spectra from ENDF/B Data," ORNL-TM-2706 - February 1970.

41. G. I. Bell and S. Glasstone, "Nucleus Reactor Theory," Van Nostrand R. Comp. - 1970.
42. W. W. Engle, Jr., "A Users Manual for ANISN" K-1693, Oak Ridge Gaseous Diffusion Plant, March 1967.
43. R. Q. Wright et al., "UKAEA to ENDF/B Translation . . .," ORNL-TM-2880; also ENDF-134.
44. J. Blatt and V. Weisskopf, "Theoretical Nuclear Physics," J. Wiley and Sons, Inc., New York - 1940.
45. B. Nicolaienko, "Energy-Dependent Boltzmann Equation in the Fast Domain," J. Math Physics, 11, 174 - 1970.
46. M. A. Abdou, University of Wisconsin - private communication.

VI. Radiation Damage

Most discussions of nuclear fission systems include the topic of radiation damage under the rather general heading of materials or neglect it all together. However, in the case of fusion reactors, one of the most, if not the most important problem to be faced after scientific feasibility has been demonstrated is that of radiation damage. The major limitation in the power level of UWMAK-I at the present time is the degradation of the mechanical and physical properties of the blanket first wall. If such a limitation were removed, the reactor would be cheaper to build and maintain, and the cost of electricity from CTR's would be considerably less. In view of such an important impact on fusion power, we have decided to devote a whole chapter to the topic of radiation damage.

A short introduction to the general features of radiation damage in metallic components is included here to familiarize the reader with the terms which will be used later in the chapter. The discussion will then turn to the specific problems that are expected to be found in the UWMAK-I blanket followed by a brief consideration of the problems in the UWMAK-I shield. Radiation effects in the toroidal magnets will then be explored and the chapter will end with a summary of the limitations that we believe are imposed on UWMAK-I operation by irradiation.

A. Potential Radiation Effects in D-T Fusion Reactors

It is not an exaggeration to state that the structural materials of a D-T fusion reactor, and in particular those in the first wall, will be subjected to the most intense radiation environment ever produced by man. Each 14 MeV neutron will cause tens of thousands of displaced atoms as it slows down to thermal energy. Most of the displaced atoms (> 99.99%) will rearrange themselves on the other lattice sites so it would appear that no long lasting damage would remain. However, if just a few hundredths of 1% of the atoms do not regain a suitable lattice position, the metal can be severely damaged. This damage can be measured in such mechanical properties as

- . reduction of ability to absorb small strains without fracturing,
- . a reduction in the rupture life at a given stress and temperature,
- . a reduction in fatigue life,
- . excessive creep
- . a shift in the temperature above which the metal will fail in a ductile fashion and below which it will fail in a brittle manner.

This displacement damage can also effect the dimensional stability of the reactor materials. The phenomena of void induced swelling has been known since 1966 and has already been the cause of considerable concern for fast breeder reactors. Such swelling effects are also anticipated in fusion reactors.

VI-B-1

Aside from simply displacing the lattice atoms in a solid, neutronic reactions also can have a deleterious effect on CTR materials. The generation of helium or hydrogen can cause severe embrittlement in metals and, if the amount of gas is large enough, one can even observe volume changes as a result of internal gas bubble expansion. The transmutation products, if different from the host material, can also have a deleterious effect on the mechanical behavior of a metal.

Finally, the charged particles associated with a D-T plasma (D,T and He) can inflict severe damage to the first wall. Atoms can be sputtered off of the surface and in some cases, whole layers may be removed by the blistering effect (see Section VI-C-5).

B. Damage Units

1. General Considerations

Before investigating each of these radiation effects in more detail, we must define the general unit of damage we will be using throughout this paper; dpa for displacements per atom.

Early workers in the nuclear field were content with calibrating the damage produced in their samples by quoting the total fluence of neutrons (of all energies) that impinged on the sample. It was quickly recognized that the higher energy neutrons produce more damage than lower energy neutrons and that one could reasonably neglect those neutrons below some threshold energy which at various times was taken as 0.1, 0.18, 1 or 2.9 MeV. This philosophy prevailed until the advent of fast neutron reactors and workers then began to pay more attention to the finer details of the neutron spectrum. It still was rather awkward to quote the entire flux spectrum of a particular position in a reactor but it was better than some of the earlier methods.

The situation was further aggravated by recent attempts to simulate extremely high neutron fluence damage (10-20 years exposure) in a few hours or days by irradiating samples with high fluxes of charged particles (heavy ions, light ions, or electrons). It was no longer meaningful to compare neutron fluences with 5 MeV Ni⁺ or 1 MeV electron fluences. Therefore, the scientific community decided to use, as the basic unit of damage, the fraction of atoms which are displaced from their lattice positions during the lifetime of the sample.

The details of how one calculates the dpa value are given elsewhere⁽¹⁻³⁾ but the general idea can be conveniently summarized in equation VI-B-1 on the following page.

$$\left(\frac{\text{number of atoms displaced}}{\text{total number of filled lattice sites}} \right) = \iint \left(\text{number of particles of energy } E \text{ hitting the solid} \right) \times$$

$$\left(\text{probability of particle of energy } E \text{ imparting } E' > E_d \text{ to a stationary lattice atom} \right) \times \left(\text{number of atoms displaced by the knocked on atom with energy } E' \right) dE dE'$$

VI-B-1

or

$$dpa = \int \int \phi(E) \sigma(E, E' > E_d) v(E') dE dE'$$

Equation VI-B-1 can be used regardless of the type of incident particle as long as we know

1. the cross section for interaction between the particles
2. the manner in which the displaced atoms cause further displacements

It will be the policy of this report to quote all of the irradiation damage in terms of the dpa unit so that we can estimate the damage state in 14 MeV irradiated metals from information already gathered in fission spectrum environments, by heavy ion, or by electron irradiation.

A note of caution should be given here as there are some drawbacks to the use of this unit of damage. First of all, it does not tell the investigator how the atoms of the solid were displaced, one by one as in the case of electron irradiation, or in cascades as in the case of neutron or heavy ion bombardment. Some metallurgical phenomena are quite sensitive to the size of the disrupted zone. Secondly, nothing can be inferred from the dpa unit about the corresponding gas generation rates. Processes such as void nucleation can be quite sensitive to the amount of neutronically produced gas in the metal. Third, unless one is very specific about the rate at which damage is produced, the exact variation of radiation damage with temperature cannot be easily assessed.

Even with the above qualifications, we will use the dpa unit in our discussions for one simple reason - There are no 14 MeV neutron irradiation data from which to draw conclusions about the stability of CTR materials! When and if such data becomes available, we will certainly reassess our conclusions stated throughout this chapter.

2. Displacement Cross Sections for Potential CTR Materials

The general scheme used for these calculations is described below for four materials, 316 stainless steel, Mo, Nb and V. (4,5) Neutron interactions treated explicitly were elastic scattering, inelastic scattering (n,n'), (n,2n) reactions and (n, γ) reactions. The (n, γ) reaction was included because it is the sole source of displaced atoms at neutron energies below several hundred eV. Other reactions such as (n, α) and (n,p) were neglected at this time in calculating displacement cross sections. Their contribution at 14 MeV is estimated to be less than 5% for Nb, Mo, and V and less than 15% for the stainless steel; at lower energies, their contribution drops off rapidly.

The four mechanisms listed above produce primary knock-on atoms (PKA's) which in turn lose their energy by electronic excitation or nuclear energy transfers to surrounding atoms. This latter form of energy transfer causes further displacements. The total displacement cross section at energy E is just

$$F(E) = F_{el}(E) + F_{inel}(E) + F_{(n,2n)}(E) + F_{(n,\gamma)}(E) \quad \text{VI-B-2}$$

where $F_{el}(E)$ is the displacement cross section due to elastic scattering, isotropic at low energies (< 0.1 MeV) and anisotropic at higher energies.

$F_{inel}(E)$ is the displacement cross section due to inelastic scattering - anisotropy was taken into account in the case of iron.

$F_{(n,2n)}(E)$ is the displacement cross section due to (n,2n) reactions.

$F_{(n,\gamma)}(E)$ is the displacement cross section due to the energetic recoils which result from (n, γ) reactions (mainly from low energy neutrons).

The general expression for F(E) is

$$F(E) = \sigma(E) \int_{E_d}^{T_{max}} p(E,T) v(T) dT \quad \text{VI-B-3}$$

where $\sigma(E)$ is the appropriate interaction cross section.

$p(E,T)$ is the probability that a neutron of energy E transfers T to the PKA.

$\nu(T)$ is the number of displacements produced by a PKA with energy T . and E_d is the energy required to displace an atom.

The problem then is to determine $p(E,T)$ and hence, the number and energy spectrum of the PKA's, and to choose a model to calculate the average number of atoms displaced by each PKA of energy T . The evaluation of $\nu(T)$ is essentially independent of the type of scattering that produced the PKA and we will consider this problem first.

The results for this study are based on the Lindhard⁽⁶⁾ theory of slowing down of energetic atoms in solids. Lindhard has derived from Thomas-Fermi theory, a function of $L(\epsilon)$ which is the kinetic energy (in dimensionless form) that is transferred to the atoms of a cascade initiated by a PKA having initial dimensionless energy ϵ . That is, the fraction of PKA energy available to cause displacements is $L(\epsilon)/\epsilon$; the remainder is lost in electron excitation. It has recently been suggested that this fraction be reduced by 20% to account for deviation from hard sphere interactions.⁽⁶⁾ In the present work, the number of displacements per PKA was taken to be

$$\nu(T) = \frac{\beta L(\epsilon)}{\epsilon} \frac{T}{2E_d} \quad \text{VI-B-4}$$

where $\beta = 0.8$

For a material of atomic number Z and atomic weight A^* , Lindhard et al.⁽⁷⁾ give

$$L(\epsilon) = \epsilon [1 + K_L g(\epsilon)]^{-1} \quad \text{where } \epsilon = A_L T,$$

$$A_L = (0.01151) (Z)^{-7/3} \text{ eV}^{-1}, \text{ and } K_L = 0.1337 (Z)^{2/3} A^{-1/2}.$$

The convenient numerical approximation to $g(\epsilon)$ given by Robinson⁽⁸⁾ was used here, viz.,

$$g(\epsilon) = \epsilon + 0.40244 \epsilon^{3/4} + 3.4008 \epsilon^{1/6}.$$

It should be noted that $\nu(T)$ is inversely proportional to E_d . It should then follow that the displacement cross section calculated from Equation IV-B-3 is inversely proportional to E_d except that E_d appears as the lower limit of the integral. Actually this limit can be taken as zero except for a narrow range of neutron energies so low that PKA energies are near E_d . Therefore, spectral-averaged displacement cross sections vary inversely with E_d with the exception of possible specialized neutron spectra concentrated in the few hundred to few thousand eV range.

* Weighted averages were used for stainless steel--the assumed composition was 18% Cr and 10% Ni by weight. The results are insensitive to small changes of composition.

There is considerable uncertainty as to what one should use for the displacement energy because the threshold energy required to displace an atom in the easiest direction may be a small fraction of that required to displace an atom in the most difficult direction. Because of this uncertainty, we have chosen to report the product of the displacement cross section and E_d in units of barn-eV. (See Table VI-B-2)

The absolute displacement cross sections used for this work can be obtained by dividing the values in Table VI-B-2 by E_d . It has been recently decided^(6,9) that the standard value of E_d for steel should be 40 eV. This is somewhat higher than the threshold displacement energy of 24 eV⁽¹⁰⁾ and qualitatively, it represents a value averaged over all the directions of displacement in the crystal structure. Equation VI-B-4 then becomes for stainless steel

$$\nu(T) \approx 10 \frac{L(\epsilon)T}{\epsilon} \text{ (keV)} \quad \text{VI-B-5}$$

The threshold displacement values of 36 eV for Nb⁽¹¹⁾ and 37 eV for Mo⁽¹⁰⁾ have been raised to values commensurate with 40 eV for iron and were used to calculate displacement functions for these two metals by

$$\text{Nb} \quad \nu(T) = 6.6 \frac{L(\epsilon)}{\epsilon} T \text{ (keV)} \quad \text{VI-B-6}$$

$$\text{Mo} \quad \nu(T) = 6.5 \frac{L(\epsilon)}{\epsilon} T \text{ (keV)} \quad \text{VI-B-7}$$

In the absence of experimental data for V, we have assumed the same displacement function as used for stainless steel. (equation VI-B-5)

The principal source of scattering cross section data was the Evaluated Nuclear Data File, Version III (ENDF/B III)⁽¹²⁾, for V(MAT 1017), Nb(MAT 1164), Mo(MAT 1111), Cr(MAT 1121), and Ni(MAT 1123). In the regions of resonance elastic scattering, BNL-325 was also used for Mo, Cr, and Ni, and a mean value was used between 800 and 8000 eV for Nb. ENDF/B data (MAT 1124), obtained in pointwise form from the Oak Ridge Radiation Shielding Information Center, were used for iron. These data were subsequently modified slightly--primarily by raising a prominent trough at ~24 keV--for inclusion in ENDF/B III under a new number MAT 1180. The difference between the two evaluations are believed to be insignificant for present purposes.

The n, γ cross sections are proportional to $1/\sqrt{E}$ over most of the energy range of interest. With the exception of iron, BNL-325 data were used in the resonance regions. Because of incomplete knowledge of the gamma emission process, the estimates of the n, γ contributions to the displacement cross sections are more uncertain than for the other processes. For neutron energies above several keV, the n, γ contribution is negligible in comparison with other contributions. On the other hand, for neutron energies below that required to displace an atom in an elastic encounter--ranging from ~300 to ~900 eV for metals considered here--the n, γ reaction is the principal source of displacement events.

The energy of the recoil atoms from (n, γ) reactions was taken as

$$T = \frac{[E_{\gamma}(\text{MeV})]^2}{1.862 \times 10^{-3} (A+1)} \quad \text{VI-B-8}$$

where the mean recoil energies were derived from a recent compilation of gamma ray spectra by Orphan et al.⁽¹³⁾ It was further assumed that the recoil energy was independent of the incident neutron energy for neutron energies sufficiently low for the n, γ contribution to be significant.

Both isotropic and anisotropic scattering were considered for the case of elastic collisions. For neutron energies below perhaps 0.1 MeV, elastic scattering is sufficiently isotropic that $p(E,T)$ is just $(T_{\text{max}})^{-1}$ where $T_{\text{max}} = \gamma E =$ and $\gamma = 4.036 A / (1.009 + A)^2$. At higher energies, available data in the ENDF file on angular distributions permit the calculation of $p(E,T)$ from the expression $(2\pi/\sigma(E))(d\sigma(E,\mu)/d\Omega)$, where $\mu = \cos\phi$, $\phi =$ angle of scattering in the center of mass (CM) system, and Ω is the unit of solid angle. The recoil energy T and μ are related through the expression

$$T = \frac{\gamma E}{2} (1 - \mu). \quad \text{VI-B-9}$$

For energies not greatly exceeding the inelastic scattering (n,n') threshold, the n,n' contribution to the displacement cross section can be obtained as a sum of contributions from resolved energy levels Q_i (taken positive here). At higher neutron energies, inelastic scattering is described by an evaporation model characterized by an effective temperature $\theta(E)$. In this model, the energy E_m of the scattered neutron in the CM system is distributed as⁽⁵⁾

$$F(E, E_m) = \frac{E_m}{I(E, \theta)} \exp(-E_m / \theta) \quad \text{IV-B-10}$$

where $I(E, \theta) = \theta^2 \{1 - (1 + E_m^{\text{max}}/\theta) \exp(-E_m^{\text{max}}/\theta)\}$

and $E_m^{\text{max}} = n_1 (n_1 E - Q_1)$.

The value of Q_1 is the lowest resolved energy level and $n_1 = \frac{A}{1.009+A}$. The upper (+) and lower (-) limits of the recoil energy are n_{now}^{\pm} .

$$T^{\pm} = n_1 n_2 E + \frac{n_2}{n_1} E_m \pm 2n_2 (E E_m)^{1/2} \quad \text{V-B-11}$$

where $n_2 = \frac{1.009}{1.009+A}$.

Finally, the (n,2n) contribution was based on a sequential emission model.^(14,15) A second neutron can be emitted only if the residual excitation of the nucleus after emission of the first neutron exceeds the binding energy U of a neutron in the mass A nuclide. The recoil energy after the emission of the first neutron was taken to be the average value $\bar{T}_1 = n_1 n_2 E + \frac{n_2}{n_1} E_m$; the total recoil energy after emission of a second neutron is then*

$$T = \left(\frac{A}{A-1} \right) \left(\frac{n_2}{n_1} \right) E'_m + \left(\frac{A-1}{A} \right) \bar{T}_1^{-2} \left(\frac{n_2}{n_1} \right)^{1/2} (\bar{T}_1 E'_m)^{1/2} \mu \quad \text{VI-B-12}$$

The forms of F(E) used for the four cases of interest are summarized in Table IV-B-1 and the cross sections are graphically compared in Figure IV-B-1 and listed in Table IV-B-2 in units of barn-ev. It is interesting to note that the normalized displacement cross sections are quite similar and, in fact when the displacement energy is taken into account, all the displacement cross sections in the 10-14 MeV region are within 20% of each other. The absolute displacement cross sections used for this study are listed in Table VI-B-3 using effective displacement energies of 40, 40, 60 and 62 eV for 316 SS, V, Nb and Mo respectively.

3. Typical Dpa Values for Fission Reactors

The displacement cross sections derived in the previous section can be used to calculate the displacement rate in present test reactors. Since most of the high fluence, high temperature data of interest to reactor designers has come from the fast reactor, EBR-II, we will confine our remarks to that system. Table VI-B-4 summarizes the spectral averaged displacement cross sections for three positions in EBR-II with a metallic fuel⁽¹⁷⁾. The displacement cross section is given for the total neutron flux and for that flux of neutrons >0.1 MeV. Since most irradiation data is given in terms of the latter spectrum, the last column of Table VI-B-4 will be most useful. It is found that the displacement damage equivalent to 10^{23}n/cm^2 ($E > 0.1 \text{ MeV}$) ranges from 42 to 52 dpa depending on where the samples were irradiated, i.e., core center or row 3 in EBR-II. For the purposes of this report we will assume that the displacement equivalent for EBR-II materials data is 47 dpa per 10^{23}n/cm^2 ($E > 0.1 \text{ MeV}$). We also realize that this number may vary by 10 to 20% when compared to other fast reactor spectra.

*Odette⁽¹⁶⁾ has recently used a Monte Carlo procedure to determine the PKA spectrum from (n,2n) reactions. His results lead to (n,n') + (n,2n) contributions to the displacement cross sections that are 3 to 15% higher than those used here.

TABLE IV-B-1

Summary of Various Displacement Cross Section Used for This Study

Method of
Recoil Production

Form of F(E) - Displacement Cross Section per atom per unit of fluence

Elastic Scattering
(isotropic & anisotropic)

$$\sigma^{el}(E) \int_{-1}^{1-r} p(E, \mu) v [T(E, \mu)] d\mu \quad r \equiv 2 E_d / T_{max}$$

Inelastic Scattering

Resolved Energy Region

$$\sum_i \sigma_i^{in}(E) \int_{-1}^1 p_i(E, \mu) v [T(E, \mu)] d\mu$$

Continuum

$$\frac{\sigma^{in}(E)}{2} \int_0^{E_m^{max}(E)} \int_{-1}^1 f(E, E_m) v [T(E, E_m, \mu)] d\mu dE_m$$

(n, 2n) reaction (a, b)

$$\sigma^{n, 2n}(E) \int_0^{E-U} \frac{E_m}{I(E)} \exp[-E_m/\theta(E)] \int_0^{E-U-E_m} \frac{E'_m}{I(E, E_m)} \exp[-E'_m/\theta(E)] \int_{-1}^1 \frac{v}{2} [T(E, E_m, E'_m, \mu)] d\mu dE'_m dE_m$$

(n, γ) reaction

$$\sigma^{(n, \gamma)}(E) \frac{[E_\gamma (\text{MeV})]^2}{3.724 \times 10^{-3} (A+1) E_d}$$

a) $I(E) = I(E, \theta)$ of Eq. 5 with $E_m^{max} = E-U$

b) $I(E, E_m) = I(E, \theta)$ of Eq. 5 with $E_m^{max} = E-U-E_m$

Table VI-B-2

Displacement Functions for Potential CTR Materials *
barn - eV

<u>Lower Energy</u> <u>MeV</u>	<u>316 SS</u>	<u>Mo</u>	<u>Nb</u>	<u>V</u>
13.50	89,000	108,000	103,000	91,400
12.21	83,100	103,000	96,800	86,900
11.05	79,700	96,000	91,100	84,000
10.00	78,200	90,100	86,100	82,300
9.048	76,500	84,000	82,300	80,500
8.187	76,100	79,000	78,300	79,000
7.408	75,900	77,300	74,300	77,600
6.703	73,900	71,300	69,900	76,100
6.065	70,500	68,300	65,200	74,500
5.488	68,100	64,600	60,600	72,800
4.966	66,400	59,500	56,100	70,200
4.493	64,900	56,500	51,800	67,800
4.066	62,400	54,700	47,800	65,200
3.679	59,700	52,000	44,200	60,300
3.329	56,400	48,100	41,000	59,000
3.012	55,000	46,800	38,200	55,700
2.725	51,800	45,700	36,600	54,500
2.466	51,000	43,900	36,600	50,100
2.231	46,700	41,700	35,900	44,900
2.019	42,000	39,500	34,200	40,200
1.827	39,900	37,400	32,700	41,500
1.653	33,000	35,300	31,400	39,700
1.496	31,600	33,100	30,000	38,800
1.353	30,300	30,700	28,900	37,200
1.225	29,100	28,600	28,500	34,800
1.108	26,000	27,300	27,900	33,200
1.003	20,700	26,200	27,100	30,600
0.9072	18,300	24,200	26,400	27,100
0.8208	17,400	23,300	25,600	26,700
0.7427	20,400	22,700	25,000	19,300
0.674	19,600	22,200	23,800	19,900
0.6081	15,300	21,300	22,500	19,900
0.5502	12,500	20,100	21,100	17,000
0.4979	13,900	18,800	19,700	13,700
0.4505	14,700	17,700	14,000	14,700
0.4076	16,600	16,800	11,900	16,200
0.3688	16,900	16,300	11,100	14,600
0.3337	9,740	15,300	10,400	14,800
0.3020	8,960	14,300	9,640	15,900
0.2752	7,980	13,300	8,970	15,700
0.2472	7,900	12,400	8,300	12,200
0.2237	7,720	11,600	7,700	13,400
0.2024	7,200	10,900	7,100	7,960
0.1832	9,580	10,200	6,570	12,300
0.1657	6,980	9,450	6,090	12,900

* including $\beta = 0.8$

Table VI-B-2 continued

<u>Lower Energy</u> <u>MeV</u>	<u>316 SS</u>	<u>Mo</u>	<u>Nb</u>	<u>V</u>
0.1500	6,460	8,690	5,650	12,800
0.1357	8,890	7,940	5,230	7,900
0.1228	6,430	7,220	4,860	9,610
0.1111	3,590	6,520	4,510	12,700
0.08652	5,120	5,540	3,970	4,290
0.06738	5,880	4,360	3,190	7,040
0.05247	2,980	3,420	2,540	8,980
0.04087	2,840	2,700	2,030	3,022
0.03183	2,680	2,140	1,640	2,650
0.02479	7,600	942	1,310	3,620
0.01930	714	1,700	1,030	8,900
0.01503	1,200	1,350	836	11,300
0.01171	1,160	1,070	667	10,200
eV				
9119	756	838	546	2,710
7102	1,260	653	473	9,440
5531	810	513	383	5,860
4307	617	403	306	838
3355	452	318	245	676
2613	288	249	198	239
2035	203	231	160	141
1585	117	191	131	102
1234	127	160	109	60.8
961.1	230	136	91.1	34.9
748.5	78.4	120	77.6	19.1
582.9	63.2	134	73.3	10.3
457.3	48.1	107	79.4	10.2
353.6	5.03	118	79.4	12.3
275.4	5.07	91.0	79.4	14.9
214.5	5.70	51.2	79.4	6.58
167.0	6.35	66.0	79.4	10.9
130.1	7.17	144	79.4	25.4
101.3	8.10	126	79.4	21.3
78.89	9.10	94.0	79.4	10.1
61.44	10.2	190	79.4	11.1
47.65	11.54	584	79.4	12.9
37.27	13.1	945	79.4	14.4
29.02	14.8	184	79.4	16.8
22.60	16.8	26.2	79.4	19.4
17.60	19.1	12.4	46.5	21.5
13.71	21.6	19.1	2.50	24.2
10.68	24.6	39.3	2.83	27.4
8.315	27.6	20.8	3.22	31.2
6.476	31.2	12.3	3.64	35.2
5.043	35.3	11.8	4.13	39.9
3.928	40.0	12.5	4.67	45.2
3.059	45.4	13.9	5.29	50.8

VI-B-11

Table VI-B-2 continued

<u>Lower Energy</u> <u>MeV</u>	<u>316 SS</u>	<u>Mo</u>	<u>Nb</u>	<u>V</u>
2.382	51.3	14.7	5.99	58.0
1.855	58.2	16.6	6.81	65.7
1.445	66.8	18.8	7.69	74.5
1.125	76.3	21.3	8.73	84.4
0.8764	84.4	24.2	9.91	95.6
0.6826	95.0	27.4	11.2	108
0.5316	108	31.0	12.7	123
0.4140	122	35.2	14.4	158
0.220	212	61.0	24.9	273

Table VI-B-3

Displacement Cross Sections for Potential CTR Materials

Lower Energy MeV	barns			
	316 SS (Ed) _{eff} =40eV	Mo (Ed) _{eff} =62eV	Nb (Ed) _{eff} =60eV	V (Ed) _{eff} =40eV
13.50	2,220	1,740	1,710	2,280
12.21	2,080	1,660	1,610	2,170
11.05	1,990	1,550	1,520	2,100
10.00	1,950	1,450	1,440	2,060
9.048	1,910	1,350	1,370	2,010
8.187	1,900	1,270	1,310	1,980
7.408	1,900	1,250	1,240	1,940
6.703	1,850	1,150	1,170	1,910
6.065	1,760	1,100	1,090	1,860
5.488	1,700	1,040	1,010	1,820
4.966	1,660	960	935	1,760
4.493	1,620	912	863	1,700
4.066	1,560	883	797	1,630
3.679	1,490	839	737	1,510
3.329	1,410	776	683	1,470
3.012	1,380	755	637	1,390
2.725	1,300	738	610	1,360
2.466	1,270	707	610	1,250
2.231	1,170	673	598	1,120
2.019	1,050	637	570	1,010
1.827	997	603	545	1,040
1.653	824	570	523	994
1.496	790	534	500	970
1.353	758	495	481	930
1.225	727	461	475	871
1.225	649	441	465	830
1.003	516	422	452	765
0.9072	459	391	440	678
0.8208	435	376	427	667
0.7427	511	366	416	483
0.674	489	358	396	496
0.6081	382	344	375	497
0.5502	313	324	351	424
0.4979	349	302	328	343
0.4505	366	285	233	367
0.4076	415	271	198	405
0.3688	423	263	185	364
0.3337	244	247	173	370
0.3020	224	230	160	396
0.2752	199	215	150	392
0.2472	197	200	138	306
0.2237	193	187	128	335

VI-B-13

Table VI-B-3 (Con't)

Lower Energy MeV	316 SS (Ed) _{eff} =40eV	Mo (Ed) _{eff} =62eV	Nb (Ed) _{eff} =60eV	V (Ed) _{eff} =40eV
0.2024	180	176	118	199
0.1832	240	165	109	308
0.1657	174	152	102	322
0.1500	161	140	94	321
0.1357	222	128	87.2	198
0.1228	161	116	81.0	241
0.1111	89.8	105	75.2	317
0.08652	128	89.3	66.2	107
0.06738	147	70.3	53.2	176
0.05247	74.5	55.2	42.3	224
0.04087	71.0	43.6	33.8	75.6
0.03183	67.1	34.5	27.3	66.2
0.02479	190	15.2	21.8	90.4
0.01930	17.9	27.4	17.2	222
0.01503	29.9	21.8	13.9	282
0.01171	29.0	17.3	11.1	255

eV

9119	18.9	13.5	9.10	67.8
7102	31.6	10.5	7.88	236
5531	20.2	8.28	6.38	147
4307	15.4	6.50	5.10	21.0
3355	11.3	5.12	4.08	16.9
2613	7.21	4.01	3.30	5.97
2035	5.08	3.73	2.67	3.53
1585	2.92	3.07	2.18	2.54
1234	3.18	2.57	1.82	1.52
961.1	5.76	2.20	1.52	0.872
748.5	1.96	1.94	1.29	0.477
582.9	1.58	2.15	1.22	0.257
457.3	1.20	1.73	1.32	0.254
353.6	0.126	1.91	1.32	0.308
275.4	0.127	1.47	1.32	0.372
214.5	0.143	0.825	1.32	0.164
167.0	0.159	1.06	1.32	0.272
130.1	0.179	2.32	1.32	0.635
101.3	0.203	2.03	1.32	0.533
78.89	0.228	1.51	1.32	0.253
61.44	0.256	3.06	1.32	0.278
47.65	0.289	9.41	1.32	0.324
37.27	0.328	15.2	1.32	0.360
29.02	0.371	2.96	1.32	0.420
22.60	0.421	0.423	1.32	0.484
17.60	0.477	0.200	0.780	0.537

Table VI-B-3 (Con't)

Lower Energy MeV	316 SS (Ed) _{eff} =40eV	Mo (Ed) _{eff} =62eV	Nb (Ed) _{eff} =60eV	V (Ed) _{eff} =40eV
13.71	0.541	0.308	0.0417	0.604
10.68	0.616	0.634	0.0472	0.685
8.315	0.689	0.336	0.0537	0.776
6.476	0.779	0.200	0.0607	0.880
5.043	0.884	0.190	0.0688	0.996
3.928	0.999	0.202	0.0778	1.13
3.059	1.13	0.224	0.0882	1.27
2.382	1.28	0.237	0.0998	1.45
1.855	1.46	0.268	0.114	1.64
1.445	1.67	0.304	0.128	1.86
1.125	1.91	0.344	0.146	2.11
0.8764	2.11	0.390	0.165	2.39
0.6826	2.37	0.442	0.187	2.71
0.5316	2.70	0.501	0.212	3.07
0.4140	3.06	0.568	0.240	3.94
0.0220	5.31	0.984	0.415	6.83

Figure VI-B-1 - Displacement Functions For Potential CTR Materials

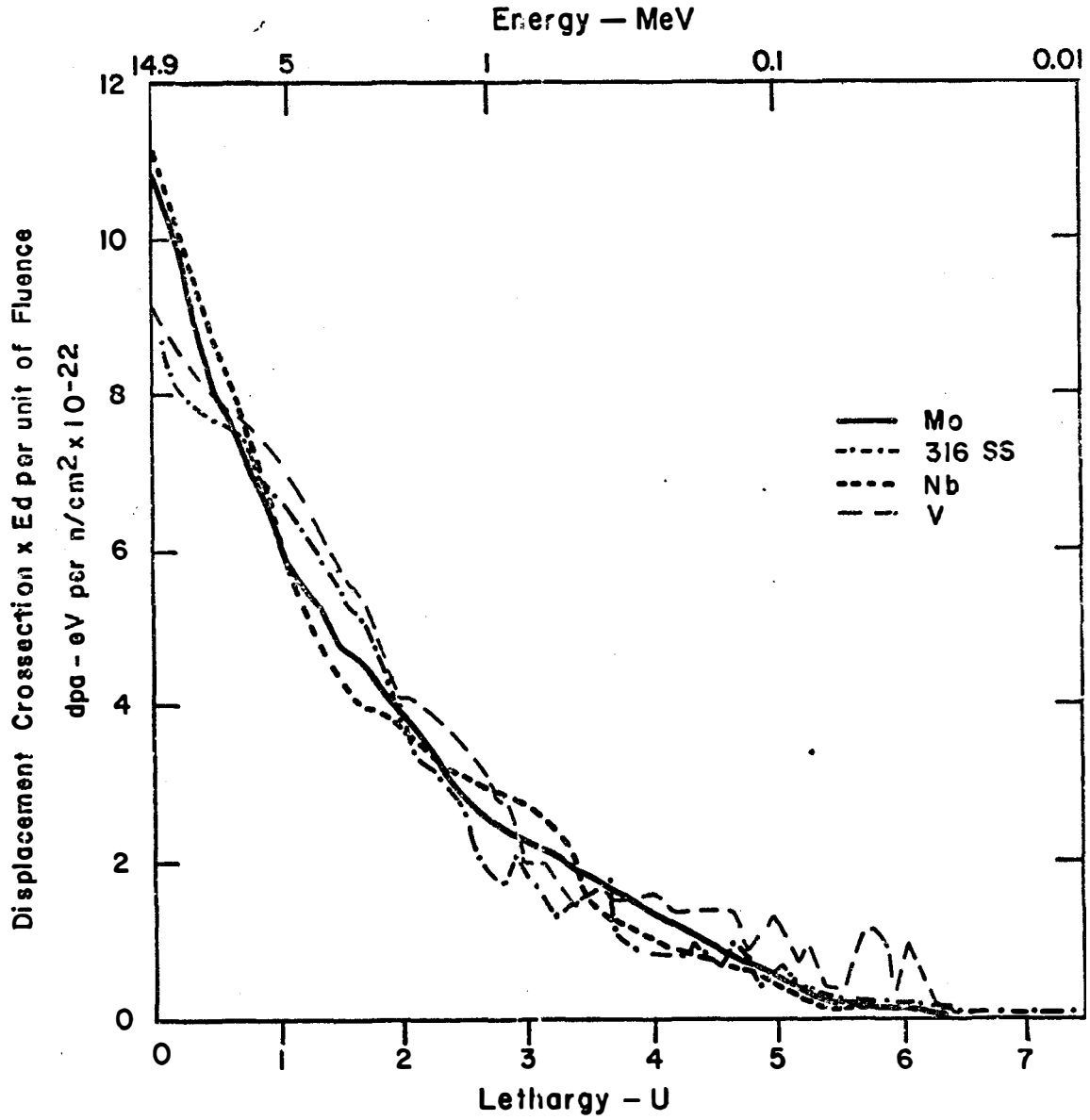


Table VI-B-4

Spectral Averaged Displacement Cross
Section for Neutrons in 18/10 Stainless Steel (17)

<u>Spectrum</u>	<u>Displacement Cross Section-barns</u>			
	<u>Mean Neutron Energy (MeV) ^(a)</u>	<u>Fraction of Flux >0.1 MeV</u>	<u>Total Neutrons (E>0)</u>	<u>Neutrons of E>0.1 MeV</u>
EBR-II Core	0.85	0.87	450	520
EBR-II Row 3	0.42	0.64	270	420
EBR-II Blanket	0.20	0.43	160	370

(a) defined as $\bar{E} = \frac{\int_0^{\alpha} E\phi(E)dE}{\int_0^{\alpha} \phi(E)dE}$

VI. C. Potential Radiation Effects in D-T Fueled Fusion Reactors

1. Void Induced Swelling

a. Development of General Swelling Equation

Irradiation of metals by energetic neutrons produces equal number of vacancies and interstitials. If these defects are mobile at the irradiation temperature, there are three possibilities for their eventual disposition;

- a) The vacancy and interstitial can recombine, thus annihilating each other.
- b) The defects could be attracted to traps such as dislocations, precipitates, grain boundaries, etc.
- or c) They could coagulate into clusters of like defects, i.e., vacancy or interstitial loops, or vacancy clusters called voids.

The first possibility removes the defects completely from the solid and the second possibility in itself rarely results in any volume change. However, if either of the defects are more strongly attracted to a given trap, then an excess of the opposite type of defect will be left in the lattice. When the concentration of these excess defects reaches a critical value, the defects will precipitate into "second phase" particles. Interstitial clusters do not cause significant swelling of the metal but vacancy clusters can induce rather large volume changes. Swelling values of 40-50% have already been observed in alloys like 316 SS when irradiated to damage levels equivalent to ~7 years in a reactor like UWMAR-I(18). Before we examine some of the data, it is worth while to examine the general damage-temperature dependence of swelling.

Several models for void growth have been proposed in the past four years (19-27). The situation with respect to void nucleation is unclear at this time and we will not include that in the present discussion. The reader is referred to several recent conference proceedings and literature articles for this information(28-37). We have chosen to use the void growth (and hence swelling) model proposed by Bullough and co-workers (20,22,23,25-27) for this work. There are some minor differences between the various models currently proposed in the literature but we feel that, at this time, the rate theory model by Bullough et.al., is sufficient to describe the general features of void swelling in 316 SS.

The concentration of interstitials and vacancies in an irradiated solid can be determined by the following equations;

$$K - D_i C_i k_i^2 - \alpha C_i C_v = 0$$

$$K' - D_v C_v k_v^2 - \alpha C_i C_v = 0$$

VI-C-2

where K is the displacement rate in dpa sec^{-1} $K' = K + K_e$
 K_e is the rate of thermal vacancy emission from all sinks in the material,
 C_i, C_v are the concentrations of interstitials and vacancies respectively,
 D_i, D_v are the diffusivities of interstitials and vacancies respectively,
 α is a recombination coefficient,
 and k_i^{-1}, k_v^{-1} are the mean free paths of an interstitial and vacancy in the presence of various sinks.

The first term in the above equations represents the production rate of defects while the second term represents the loss to all sinks (voids, dislocations, grain boundaries, etc.). The final term represents the loss of defects to mutual recombination.

The parameters k_i and k_v can be deduced by carefully calculating the effective sink strengths in the continuum and have the explicit form

$$k_i^2 = Z_i \rho_d + 4\pi r_s C_s + Y_i 4\pi r_p C_p \quad \text{VI-C-3}$$

$$k_v^2 = Z_v \rho_d + 4\pi r_s C_s + Y_v 4\pi r_p C_p \quad \text{VI-C-4}$$

where C_s is the concentration of neutral sinks (e.g. voids)
 r_s is the radius of neutral sinks,
 Z_i, Z_v are the preferences of dislocations for interstitials and vacancies. (It is assumed that dislocations have a 1% preference for interstitials, i.e., $Z_i = 1.01, Z_v = 1.00$)
 ρ_d is the total dislocation density $\rho_d^L + \rho_d^n$

where ρ_d^L = radiation produced loop density

ρ_d^n = dislocation density present prior to irradiation.

C_p is the concentration of coherent precipitates,

Y_i, Y_v are the preferences of coherent precipitates for interstitials and vacancies respectively.

$$Y_i = k_i^2 / k_v^2, Y_v = 1$$

Equations VI-C-1 and VI-C-2 can be solved to give

$$C_i = \frac{D_i k_i^2}{2\alpha} \left[-(1+\mu) + \{(1+\mu)^2 + \eta\}^{1/2} \right] \quad \text{VI-C-5}$$

$$C_i = \frac{D_i k_i^2}{2\alpha} \left[-(1-\mu) + \{(1-\mu)^2 + \eta\}^{1/2} \right] \quad \text{VI-C-6}$$

where

$$\eta = \frac{4\alpha K}{D_i D_v k_i^2 k_v^2}$$

$$\mu = \frac{k_i \eta}{4K}$$

The rate of swelling is just the net flux of vacancies into the voids; i.e.

$$\frac{d(\Delta V/V)}{dt} = 4\pi r_s^2 C_s \frac{dr_s}{dt} \quad \text{VI-C-7}$$

$$= 4\pi C_s r_s \{D_v C_v - D_i C_i - D_v C_v^e\} \quad \text{VI-C-8}$$

Substituting C_i , C_v from equations VI-C-5, 6 into equations VI-C-7 and 8 one can find the dose dependence of swelling if ρ_d and r_s do not depend on time. The general swelling expression is then,

$$\frac{\Delta V}{V} = K(t-t)_o S_o F(\eta) \quad \text{VI-C-9}$$

where Kt_o is an arbitrary incubation dose required to nucleate the voids and ranges from 1 to 10 dpa for austenitic stainless steels and other terms are defined below

$$S_o = \frac{(Z_i - Z_v) \rho_d 4\pi r_s C_s}{(\rho_d + 4\pi r_s C_s)(\rho_d + 4\pi r_s C_s + 4\pi r_p C_p)}$$

$$F(\eta) = \frac{2}{\eta} [- (1+\mu) + (1+\mu^2) + \eta^{1/2} - \xi\eta]$$

$$\text{and } \xi(T) = \frac{D_v (Z_v \rho_d + 4\pi r_s C_s) \{Z_i \rho_d + 4\pi (r_s C_s + r_p C_p)\}}{2K(Z_i - Z_v) \rho_d \{Z_v \rho_d + 4(r_s C_s + r_p C_p)\}} [4\pi r_p C_p C_v^e + Z_v \rho_d^L (C_v^e - \bar{C}_{vL})]$$

$$\text{and } \bar{C}_{vL} = C_v^e \exp \left[- \frac{(\gamma_F + F_{el}) b^2}{kT} \right]$$

γ_F is stacking fault energy

$F_{el} b^2$ is the change in elastic energy of the loop per vacancy emitted.

It should be noted that the material properties are mainly concentrated in the term S_0 while $F(\eta)$ represents the main temperature dependence [although there is also a weak rate (K) dependence in F.] At a given temperature equation VI-C-9 predicts a linear dependence of swelling on dose (Kt).

b. Observations on the General Swelling Formula

It is worthwhile to examine equation VI-C-9 developed by Bullough et. al. (20,22,23,25-27) in some detail as it has a bearing on the choice of swelling resistant materials and reveals some of the major fluence and temperature dependence of swelling in metals.

i. Dependence on Material Properties

First of all, it should be noted from the numerator of S_0 that both neutral sinks ($4\pi r_s C_s$) and biased sinks [$(Z_i - Z_v) \rho_d$] are required for swelling to occur. The denominator of S_0 reveals the importance of sinks to provide recombination sites for the point defects. It is obvious that in order to alleviate swelling we would like ρ_d or $4\pi r_p C_p$ to be much larger than $4\pi r_s C_s$. In most solids $\rho_d > 4\pi r_s C_s$ and therefore S_0 becomes

$$S_0 \rightarrow \frac{(Z_i - Z_v) 4\pi r_s C_s}{(\rho_d + 4\pi r_p C_p)}$$

Hence large numbers of coherent precipitates or dislocations will tend to reduce S_0 , and in turn the swelling. An alloy which has been developed to incorporate the first mechanism is PE-16, a nimonic alloy containing $Ni_3(Ti,Al)$ precipitates which are $\sim 100 \text{ \AA}$ in diameter. Another mechanism for reducing S_0 is to increase ρ_d by prior cold working of the metal. This technique is the basis for choosing 20% cold worked 316 SS over the well annealed (solution treated) 316 SS in UWMMAK-I.

ii) Dependence on Temperature

One can easily deduce from the definition of $F(\eta)$ that at low temperatures $\eta \gg 1$ because $\eta \propto (D_i D_v)^{-1}$ and hence

$$F(\eta) \cong \frac{2}{(\eta)^{1/2}}$$

At intermediate temperature, $\eta \sim 1$,

$$F(\eta) \approx 1$$

and at higher temperatures

$$F(\eta) \rightarrow 0$$

The general form of the temperature dependence of swelling is given in Figure VI-C-1. At low temperatures swelling is low because the low mobility of vacancies increases the recombination rate. Materials which have high vacancy migration energies should have small swelling at low temperatures.

As the temperature is increased and $\eta \rightarrow 1$, recombination becomes more difficult because the vacancies are so mobile and they can easily find a neutral sink (e.g. a void) before they encounter an interstitial. This corresponds to the peak swelling regime and in practice occurs at roughly 40% of the melting point. However, we can see from the definition of η that this peak temperature is quite sensitive to the displacement rate K and increasing K will necessarily shift the peak swelling to higher temperature (see example in Figure VI-C-1). This has the important consequence of shifting the "effective" temperature of simulation experiments to lower temperatures. A similar situation exists in pulsed CTR's such as the LASL theta pinch or a laser fusion reactor where the instantaneous displacement rates may be 10^{-4} dpa sec^{-1} to 10^{-1} dpa sec^{-1} respectively. Current fission reactor displacement rates are $\sim 10^{-6}$ dpa sec^{-1} (4) so that one must be careful to adjust the irradiation temperatures of various damage rate experiments so as to have the proper defect kinetics.

The final drop in swelling at high temperatures occurs when the thermal emission of vacancies from dislocations and voids eventually dominates the production of vacancies by displacement events.

c. Experimental Data on Swelling in 316 SS

The current information on swelling in 316 SS generally falls into three categories;

- . Data from fast neutron test reactors
- . High energy charged particle simulation studies
- . High voltage electron microscopy simulation studies

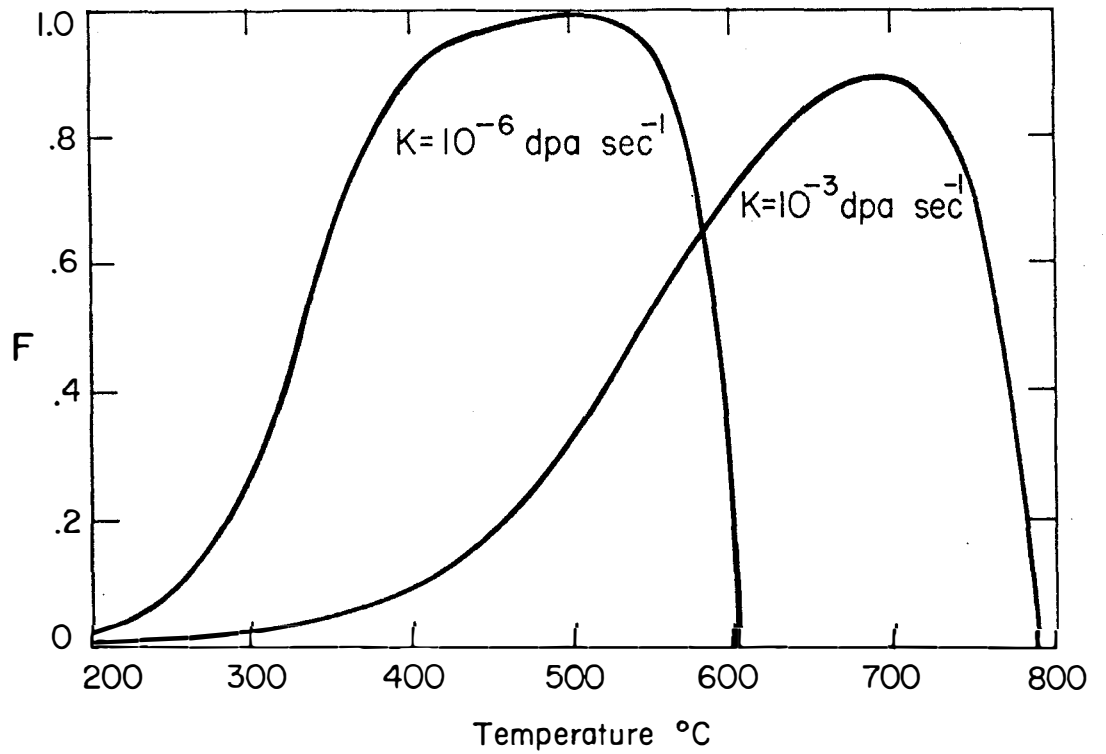


Figure VI-C-1 Effect of Displacement Rate on the Temperature Dependence of Void Swelling in Metals-Brailsford and Bullough (25)

We will use, wherever possible, the data generated by fast neutron irradiation fully realizing that the high helium generation rates typical of fusion reactor spectra may significantly alter the swelling behavior. It will also be necessary to use data from simulation studies to extrapolate the present neutron data to the much higher damage levels expected in fusion reactors because of the longer component life.

i) Neutron Irradiation Data

A large fraction of the high fluence swelling information on both solution treated (ST) and 20% cold worked 316 SS has been generated at the Hanford Engineering Development Laboratory (HEDL) in Richland, Washington and at the A.E.R.E. Laboratory at Harwell in the United Kingdom. For the sake of consistency, we will use data from the above laboratories⁽³⁸⁾ in this work and will not attempt a complete survey of all data on 316 SS at this time.

The maximum exposure, temperature and swelling data for both ST and cold worked 316 SS is listed in Table VI-C-1 and plotted in Figure VI-C-2. It is noted that very little data exists for temperatures below 400°C because that temperature is very close to the inlet coolant value for both the U.S. and U.K. fast test reactors.

It is interesting to note that the ST 316 SS swells more than the cold worked material in accordance with equation VI-C-9. There also appears to be some discrepancy between swelling data on cold worked U.S. steel and cold worked U.K. steel. The discrepancy is illustrated in Figure VI-C-3. Essentially no swelling has been observed in the U.S. cold worked samples out to $\sim 4 \times 10^{22}$ n/cm² (E>0.1 MeV) which is roughly equivalent to 19 dpa. On the other hand, U.K. data shows from swelling at the same damage level depending on the irradiation temperature. Another important point from Figures VI-C-2 and 3 is that there is not enough data to comfortably extrapolate the behavior of the steel at dpa values of several hundred dpa.

In order to predict the degree of swelling in 316 SS at high fluences, reactor designers have established empirical equations based on the best neutron irradiation data and they have used heavy ion simulation studies to guide the high fluence predictions. The general feeling now is that the cold work is certainly increasing the incubation period for void nucleation. However, even after this incubation period has passed, the fluence dependency of void swelling in cold worked 316 SS will certainly not exceed that for solution treated material. An example of how this philosophy has been utilized is shown in Figure VI-C-4, where data for both ST and cold worked samples are plotted as a function of dpa for 4 temperature ranges⁽³⁸⁾. After empirically fitting curves to the solution treated data, it has been assumed that the increased incubation period ends with the highest fluence data point reported for CW 316 SS.

We were unable to obtain the proper release of the data in Table VI-C-1 in time for publication of this report. When such data is released by the USAEC we will send the information to the reader.

We were unable to obtain the proper release of the data in Figure VI-C-2 in time for publication of this report. When such data is released by the USAEC we will send the information to the reader.

We were unable to obtain the proper release of the data in Figure VI-C-3 in time for publication of this report. When such data is released by the USAEC we will send the information to the reader.

We were unable to obtain the proper release of the data in Figure VI-C-4 in time for publication of this report. When such data is released by the USAEC we will send the information to the reader.

It is then assumed that the cold worked material will swell at the same rate as the solution treated alloy. This obviously represents the worst case and the swelling in the cold worked material could be substantially lower than predicted.

ii) Void Swelling in 316 SS During Simulation Studies

Recent work at General Electric with 5 MeV nickel ions has shown fair agreement with neutron irradiation studies at low fluences <20 dpa⁽¹⁸⁾. It has also been found that the swelling continues with increasing fluences and in fact approaches 100% at ~200 dpa. These latter results were obtained with ST 316 SS (10 appm injected helium) bombarded at 625°C in order to simulate neutron irradiation at 500°C. Figure VI-C-5 shows how the G. E. data agrees with some of the recent G. E. neutron irradiation of ST 316 SS⁽¹⁸⁾.

Studies have also been conducted at Atomic International with 1 MeV protons⁽³⁹⁾. Figure VI-C-5⁽⁴¹⁾ shows that there is reasonable agreement between the slope of the swelling curve for both protons and neutrons, but the proton studies appear to significantly over-estimate the swelling at any given dpa value.

We have also included some recent High Voltage Electron Microscopy work by Laidler on 316 SS⁽⁴⁰⁾. Again it can be seen that the slope of the swelling curves are similar but that the absolute values at a given dpa are considerably different.

The important point of Figure VI-C-5 is that ion simulation studies conducted in this country indicate that there is no saturation level in swelling in ST 316 SS, at least up to ~50-100%. The only evidence against this conclusion comes from the charged particle irradiation work at Harwell⁽⁴²⁾. Nelson et. al. show that swelling in 316 SS begins to saturate at ~50 dpa at 10-20% (Figure VI-C-6). Since this data was obtained by bombarding with carbon ions, which have recently been shown to significantly suppress swelling in austenitic steel⁽⁴³⁾, the saturation of swelling is somewhat questionable.

For the purposes of UWMAK-I design, we will not rely on saturation of swelling but rather assume that it will continue up to 100% or greater consistent with recent observations at General Electric⁽¹⁸⁾. This assumption means that if the U.K. data⁽⁴²⁾ is correct, then we will over-estimate the swelling (above the 20% value) in the UWMAK-I blanket.

d. Design Equations for Swelling in 316 SS

We will use the following equations to describe the swelling in ST and 20% cold worked 316 SS⁽⁴⁴⁾. One alteration has been made to the HEDL equation; the neutron fluence terms were expressed as dpa levels based on 47 dpa per 10^{23} n/cm² (E>0.1 MeV)

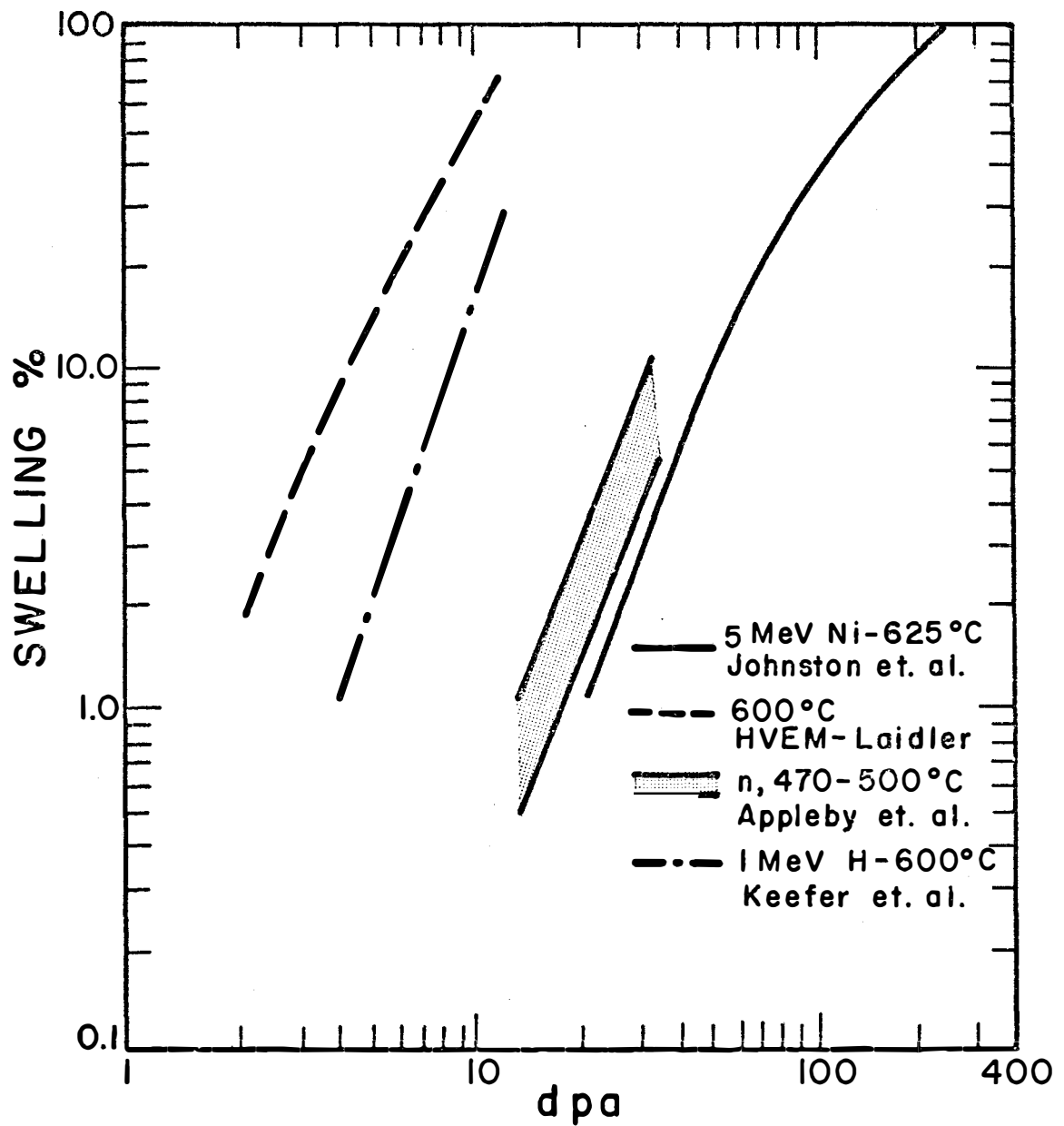


Figure VI-C-5

Comparison of actual neutron induced swelling in ST 316 SS to that determined by H⁺, Ni⁺, and HVEM simulation studies. Note that the ion bombardment studies were conducted at a high enough temperature to overcome the temperature shift.

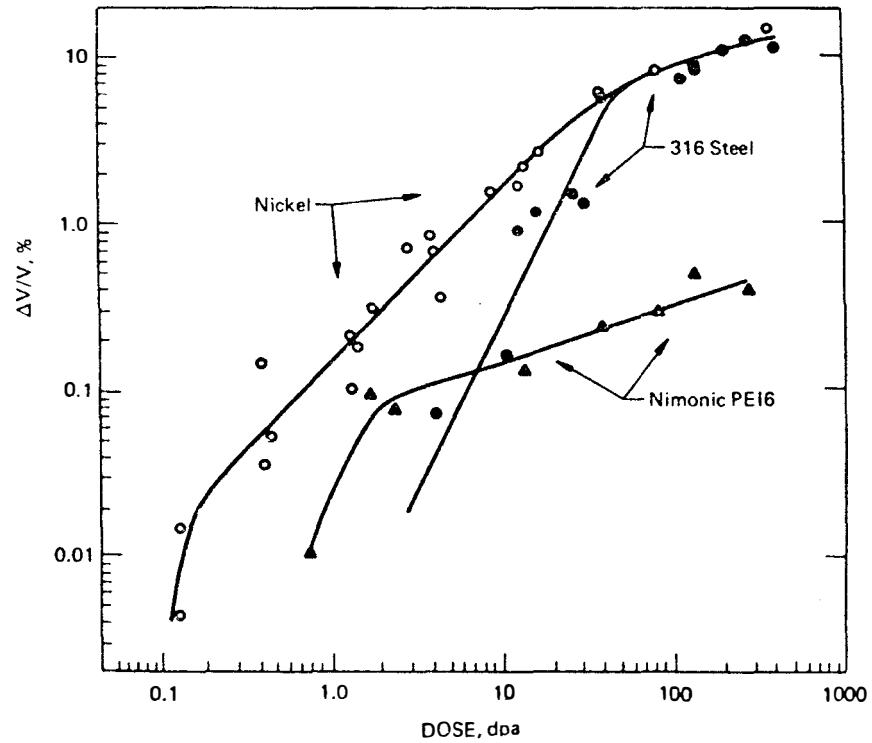


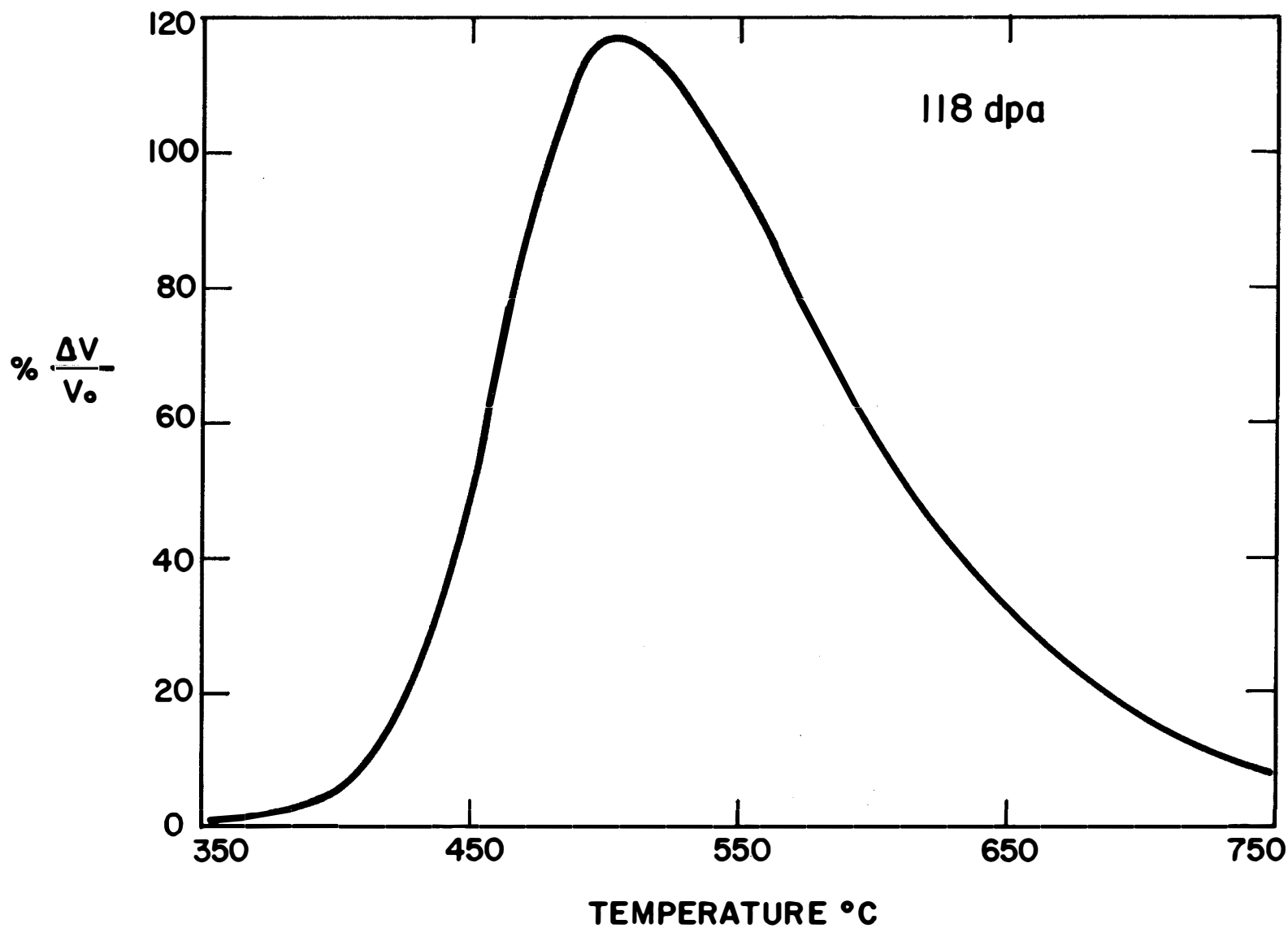
Figure VI-C-6 Swelling behavior of Ni, 316 SS and PE-16 during 525°C bombardment with 20 MeV carbon atoms. All materials contain 10 ppm He. (42)

We were unable to obtain the proper release of the data in Equation VI-C-10 in time for publication of this report. When such data is released by the USAEC we will send the information to the reader.

The temperature dependence of swelling at a damage level of 118 dpa (~6 years in UWMak-I) is shown in Figures VI-C-7 and 8. Several features of these figures are worth noting. First of all, it is seen that for any temperature, the solution treated stainless steel swells much more than does the cold worked steel. Secondly, the maximum of the swelling curves occurs at ~575°C for the cold worked steel with little swelling expected below 350°C and above 750°C. The maximum for ST curves calculated for the cold worked material show that less than a factor of two exists between the most pessimistic and optimistic swelling values at any given temperature.

Figure VI-C-7

**PREDICTED SWELLING FOR SOLUTION TREATED
316 STAINLESS STEEL AT 2.5×10^{23} n/cm² (E > 0.1 MeV)**
Reference 44



We were unable to obtain the proper release of the data in Figure VI-C-8 in time for publication of this report. When such data is released by the USAEC we will send the information to the reader.

VI-C-2. Bubble Induced Swelling

a. General Considerations

The generation rate of gas atoms by the (n, α) and (n,p) reactions in fusion reactor materials will be much higher than in fission reactor materials. These gas atoms may act as nuclei for voids (see Section VI-C-1) or they may alter the mechanical properties of the metal. If the gas concentration and the irradiation temperature are high enough, and the solubility low enough, the gas atoms could precipitate into bubbles which will in turn, cause dimensional instabilities. We will examine two cases here, the possibility of gas induced swelling in the 316 SS of the UWMAK blanket and the potential gas swelling in the B₄C of the shield.

Let us assume for the time being that the mobility of the helium atoms is high enough such that once a gas atom is produced, it can migrate to a nucleation site and form a bubble. In the presence of the large flux of vacancies produced by irradiation, the bubble will grow with an equilibrium gas pressure P of

$$P = \frac{2\gamma}{r} \quad \text{VI-C-11}$$

where

γ is the surface energy
r is the radius of the bubble.

If we assume that the bubble radius is small ($< 1000 \text{ \AA}$) then we must use a Van der Waals equation to describe the volume, V, occupied by a bubble which contains m' atoms. Neglecting the attractive terms we find

$$P(V - m'b) = m'kT \quad \text{VI-C-12}$$

where

b is Van der Waals constant
k is Boltzmann's constant
T is the temperature °K

The volume change induced by a density of bubbles, ρ , which have radius r and contain m' atoms is

$$\left(\frac{\Delta V}{V_0}\right)\% = 100 N \left[\frac{rkT}{2\gamma} + b \right] \quad \text{VI-C-13}$$

where

$N = \rho m'$ number of atoms cm^{-3}
 ρ = bubbles cm^{-3}
 m' = atoms per bubble of radius, r

$$m' = \frac{8\pi \gamma r^3}{3(kTr + 2\gamma b)}$$

Hence, given the amount of gas produced per cm^3 at some temperature T in a solid with surface energy γ , we can calculate the volume change provided we specify either the bubble density or the bubble size. Equation VI-C-13 will be used in subsequent analyses.

b. Gas Induced Swelling in Boron Carbide

The effectiveness of boron carbide to absorb neutrons in the shield region stems from the large $\text{B}^{10}(\text{n},\alpha)\text{Li}^7$ reaction cross section. Both of the reaction products occupy more volume than the original boron atom. Boron has an atomic radius of 0.8 Å while the atomic radius of helium is 1.31 Å and the atomic radius of lithium is 1.55 Å. Hence, every boron-10 "fission" creates two atoms which occupy more than ten times the volume occupied by the original boron atom. This situation is analogous to the swelling caused by solid fission products in uranium. At low temperatures where the reaction products do not migrate in the matrix, swelling would be expected to be a linear function of fluence.

The data for boron carbide swelling is normally measured as a function of boron-10 depletions per cm^3 rather than as a function of fluence. To a first approximation this allows measurements made in one flux spectrum to be applied directly to any other flux spectrum.

Gray and Lynam⁽⁴⁵⁾ have measured the swelling of natural boron carbide in thermal reactors at temperatures below 300°C. Their data which is approximated by a solid line in Figure VI-C-9 indicates that swelling is indeed a linear function of boron-10 fissions below 100×10^{20} depletions cm^{-3} . In this range, Gray and Lynam suggest that swelling occurs at a rate of ~0.05% per 10^{20} reactions cm^{-3} . The increase in swelling rate above 100×10^{20} depletions cm^{-3} appears to be due to intergranular cracking. It also appears that the magnitude of swelling is very sensitive to the porosity of the B_4C prior to irradiation. The material used in Figure VI-C-9 varied from 90 to ~100% theoretical density and the solid curve in this figure is believed to apply to the less dense material.

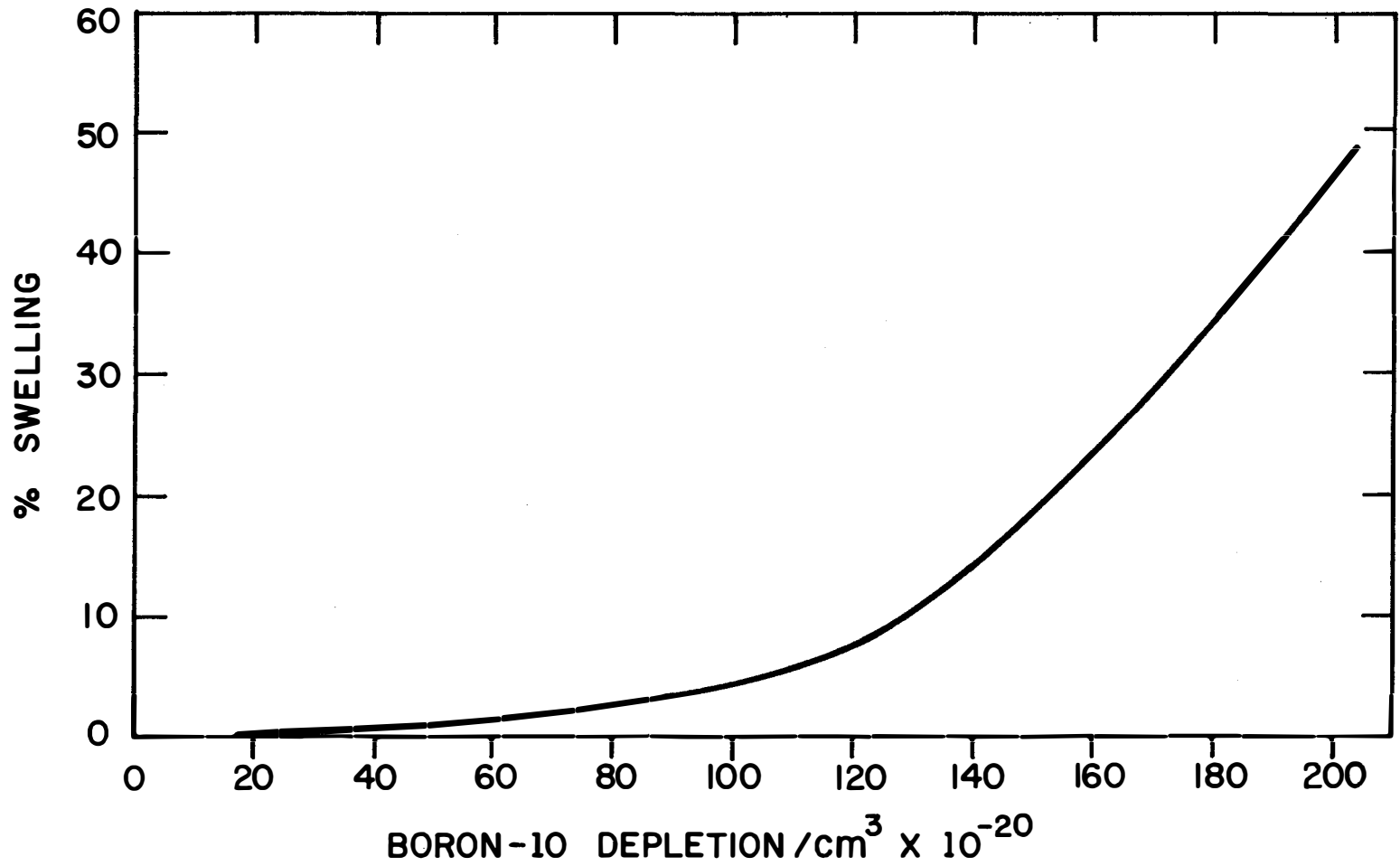
As the irradiation temperature is increased above 300°C, the insoluble helium atoms begin to migrate. There are two major effects of this migration—gas is released from the boron carbide and gas bubbles form within the material. Gas release will reduce the amount of swelling observed, but the formation of gas bubbles will increase the amount of swelling.

The temperature dependence of gas release is shown in Figure VI-C-10. Depending on whether the spectrum is typical of a thermal or fast flux, one can see that less than 10% of the helium is released below the 400-500°C range.

The formation of gas bubbles could cause large amounts of swelling. The equations describing this effect are given in Section VI-C-2a. Homan⁽⁴⁶⁾ has utilized a modified Greenwood-Speight model to calculate the swelling induced by helium if the bubbles were allowed to move and coalesce. The results are shown in Figure VI-C-11a. Due to faster diffusion rates at higher temperatures, the bubble size increases sharply.

Figure VI-C-9

REACTION PRODUCT SWELLING IN B_4C



As shown in Figure VI-C-11b, these calculations have been modified to include gas release. For these calculations, it has been assumed that ten percent of the gas is never released. Below 800°C, only a small number of the gas atoms escape. Between 800 and 1000°C, there is some gas release and after that the amount of swelling increases steadily with temperature.

The swelling of boron carbide can then be divided into three temperature regions. Below 500°C helium migration is minimal and the swelling is primarily due to the increased volume of the reaction products. In this low temperature region, an increase in the lattice parameter can also be measured. Gas bubbles begin to form between 500 and 1000°C. The lattice parameter is decreased as the helium begins to leave the matrix to form bubbles and to migrate out of the boron carbide. After large burn-ups, the internal stresses due to reaction product buildup may lead to internal cracking. Above 1000°C, diffusion will relieve the internal stresses that led to cracking. In this high temperature region, the swelling is entirely due to the large gas bubbles.

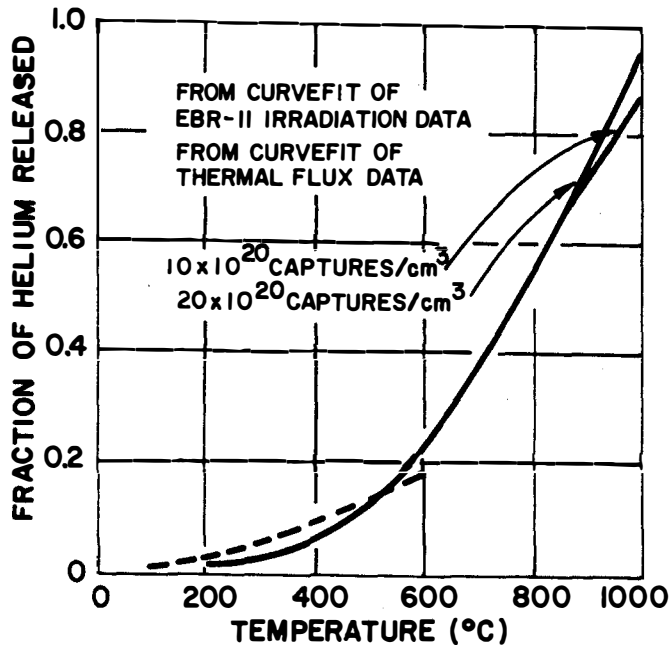


Figure VI-C-10 Helium release from irradiated B₄C (92% TD).

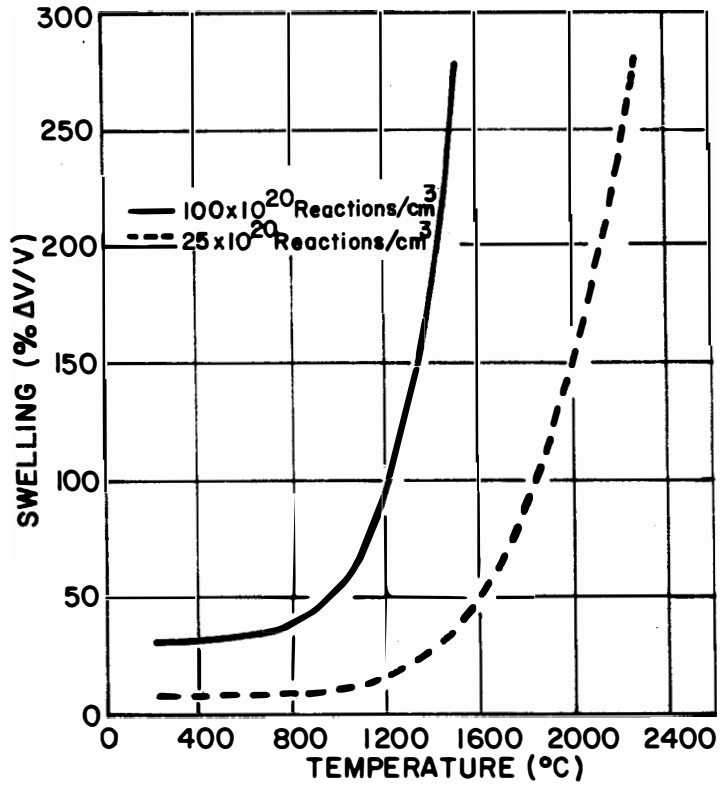


Figure VI-C-11a Calculated swelling in boron carbide due to helium bubbles (assuming no gas release).

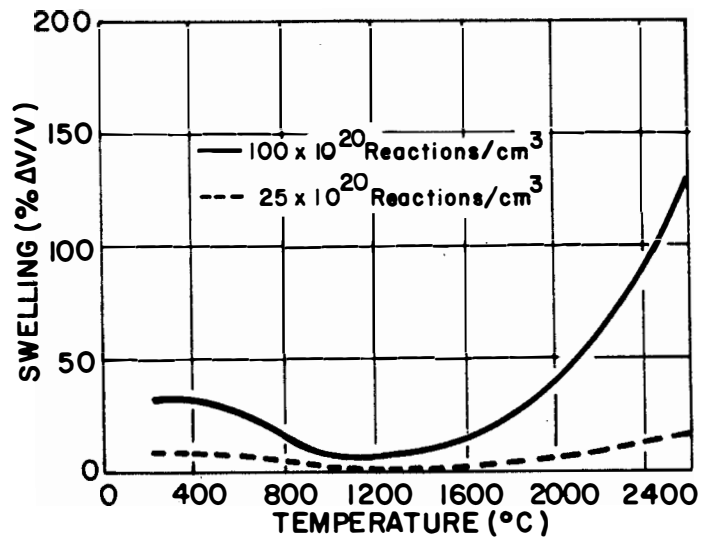


Figure VI-C-11b Calculated swelling in boron carbide due to helium bubbles (after gas release).

VI-C-3. Effect of Irradiation on the Mechanical Properties of Steel

The effect of neutron irradiation on the mechanical properties of 316 SS has been the object of much study in the past few years. (47-63) This interest stems from the projected use of 316 SS for core components in future LMFBR's. The general conclusions of the recent work are:

- The yield strength (0.2% offset) and ultimate strength are significantly increased with irradiation, the former more than the latter.
- The ductility of 316 SS is severely reduced by irradiation with the uniform ductility suffering the greatest degradation.
- Large reductions in stress rupture life have been observed at 600°C with lesser effects at 550 and 650°C.

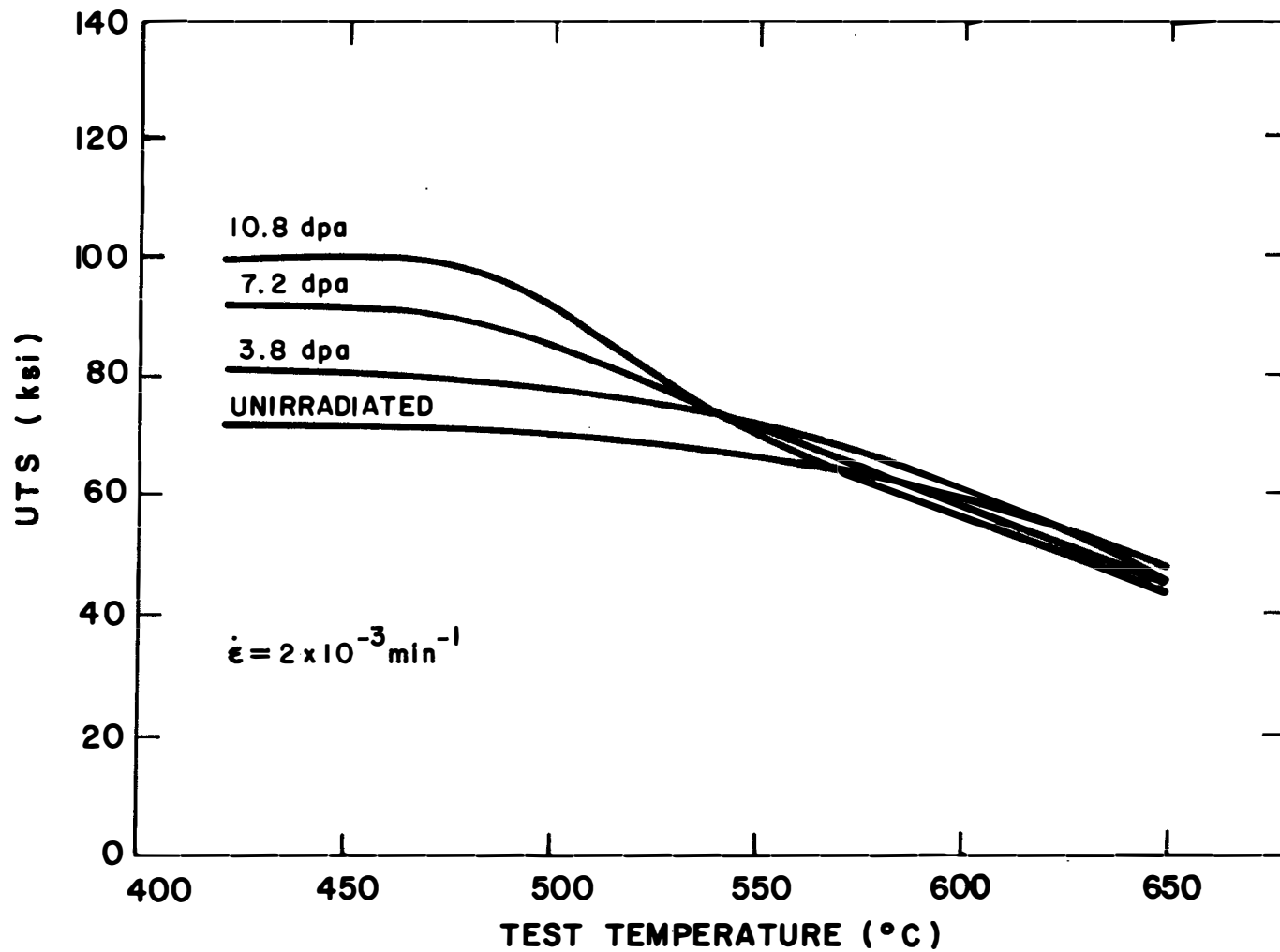
No attempt will be made here to assess all of the data in the literature, rather, we will quote what appears to be the most pertinent information for UWMK-I and then resort to empirical design equations to predict the expected behavior. We will use 20% CW 316 SS data where available but will use ST 316 SS data if none exists for the cold worked alloy.

i) Tensile Properties

The major effect of irradiation on the ultimate yield strength (UYS) and tensile yield strength at 0.2% offset (TYS) is due to the generation of microstructural defects. These defects (voids, dislocation loops, and precipitates) increase the force required to move a dislocation through the matrix. Information on the effect of irradiation on the UYS and TYS of ST 316 SS is shown in Figures VI-C-12 and 13 and Figures VI-C-14 and 15 display the results for 20% CW 316 SS. (64-70) The general behavior for the solution treated material in the temperature range 426-538°C is described by the equations in Table VI-C-3.

As stated previously, the general trend for solution treated material is to increase the yield strength faster than the ultimate strength. (Compare Figure VI-C-12 to VI-C-13.) However, this effect is more prevalent at low temperatures and as the radiation temperature increases a large fraction of the damage is annealed out resulting in only small changes in the mechanical properties.

The effect of temperature and irradiation on the tensile properties of 20% CW 316 SS is shown in Figures VI-C-14 & 15. It is noticed that the difference between the UYS and TYS is reduced by cold-working and that the irradiation has little effect on this properties compared to the effect on the solution treated alloy. This can be understood by



VI-C-24

Figure VI-C-12 Parametric dpa Plots for Ultimate Strength of Type 316 Stainless Steel Annealed and Irradiated (EBR-II) Versus Temperature. Irradiation within $\pm 50^\circ\text{C}$ of Test Temperature. (64-67)

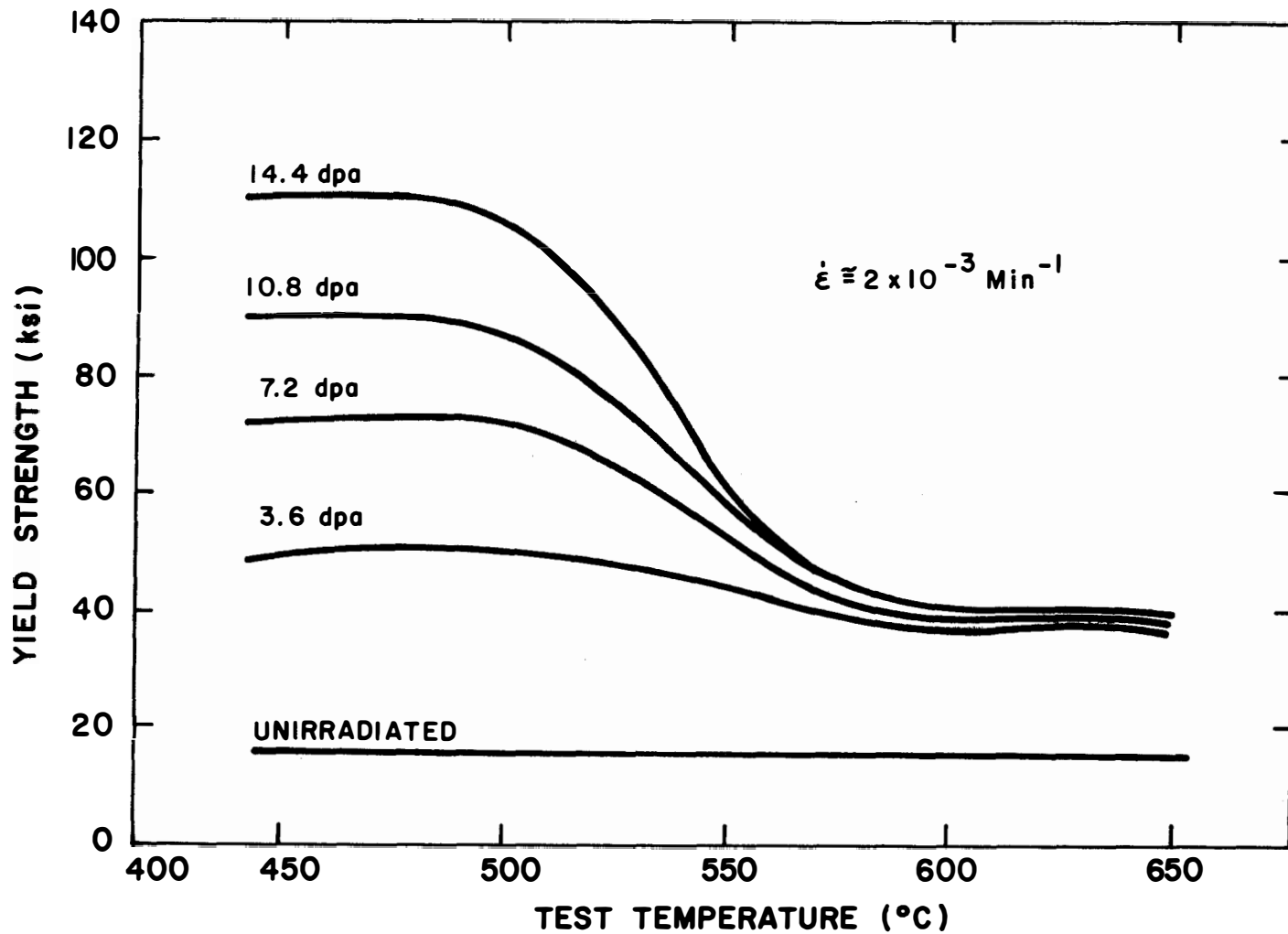


Figure VI-C-13 Parametric dpa Plots for Yield Strength of ST Type 316 Stainless Steel Irradiated (EBR-II) vs Temperature. Irradiation within $\sim 50^\circ\text{C}$ of Test Temperature (64-67)

We were unable to obtain the proper release of the data in Table VI-C-3 in time for publication of this report. When such data is released by the USAEC, we will send the information to the reader.

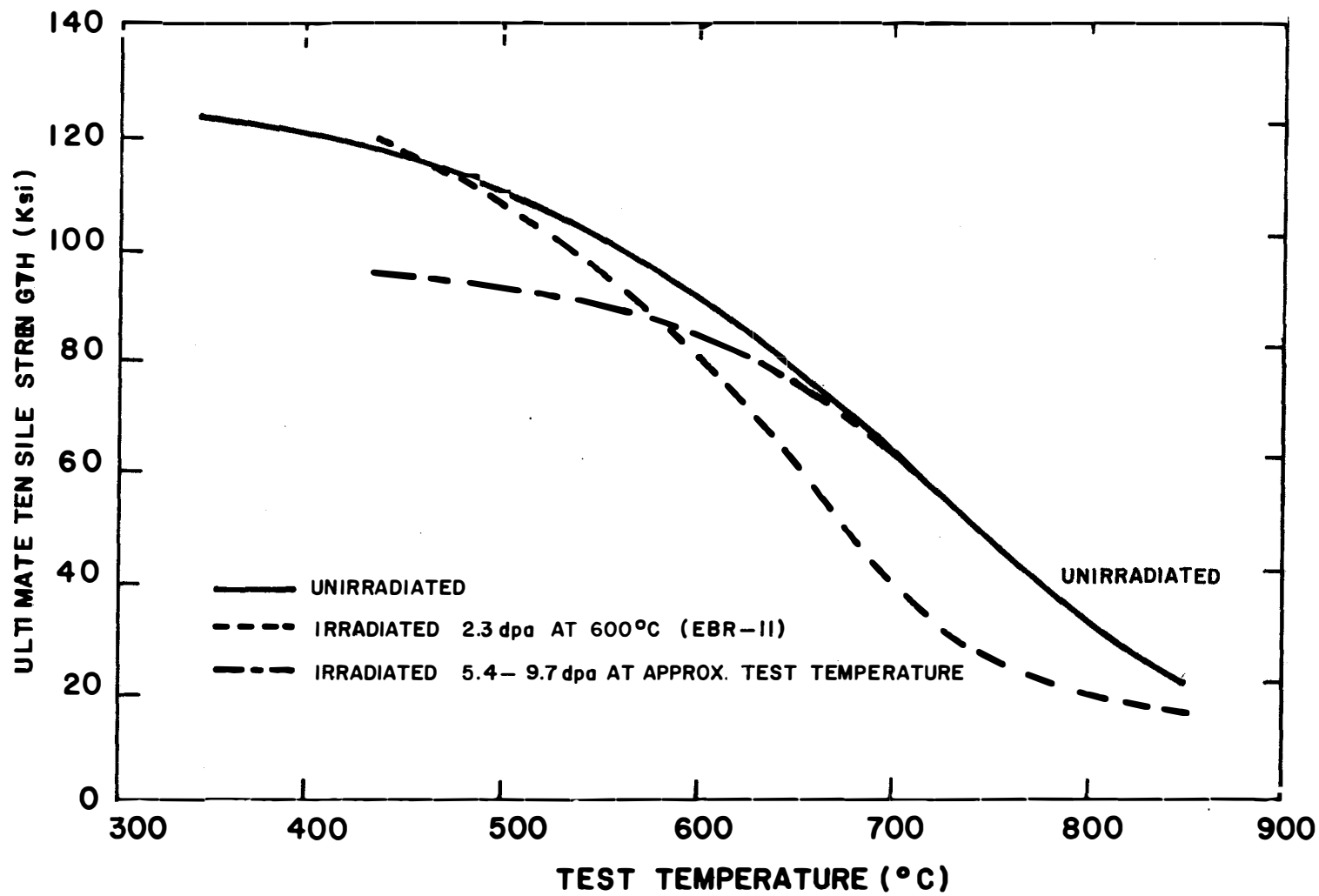


Figure VI-C-14 Ultimate Strength Versus Test Temperature for Unirradiated and Irradiated 20% CW Type 316 Stainless Steel (64, 68-70)

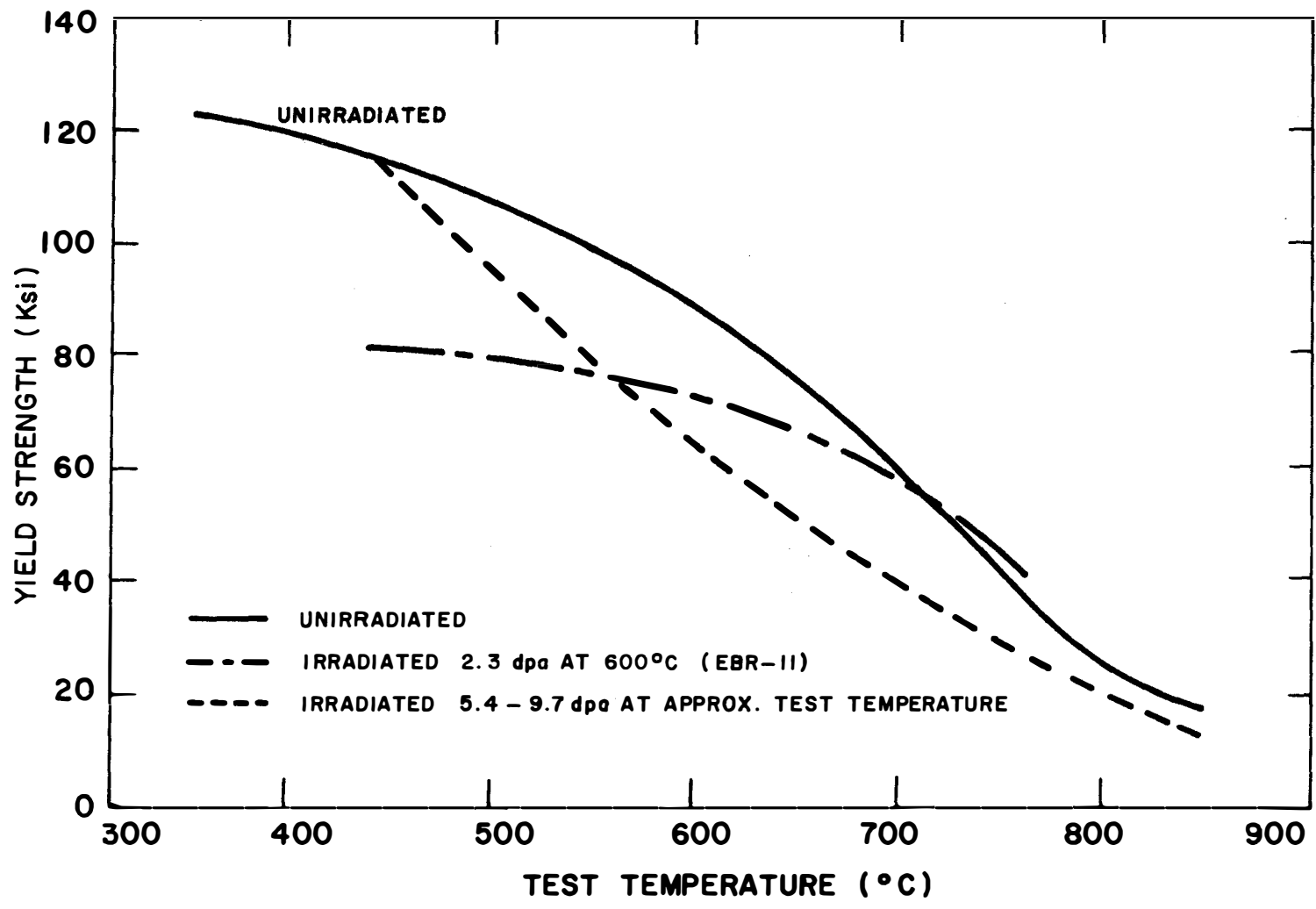


Figure VI-C-15 Yield Strength Versus Test Temperature for Unirradiated and Irradiated 20% CW Type 316 Stainless Steel (64, 68-70)

remembering that radiation induced dislocations are the cause of strengthening in well annealed metals while the cold worked 316 SS already contains an extremely high density of barriers to dislocation motion. Since irradiation enhances diffusion, it may actually induce some recovery, which in turn, causes a reduction in the UYS and TYS.

ii) Ductility

The three primary measures of ductility commonly used in tensile tests are;

- . Uniform elongation
- . Total elongation at failure
- . Reduction of area at failure

These terms are defined in reference (71). We will use the uniform elongations (ϵ_u) as a primary measure of ductility since this factor is easily applied in engineering analysis.

Uniform elongation is defined as the plastic deformation which occurs prior to the onset of plastic instability and is coincident with the strain at maximum load for time independent plastic flow. Another way to define uniform elongation is from the stress-strain relationship, (54)

$$\bar{\sigma} = K(\bar{\epsilon})^\eta \quad (\text{VI-C-14})$$

where

$\bar{\sigma}$ is the true stress

$\bar{\epsilon}$ is the true strain

η is the strain hardening exponent

K is a constant

From the above relationship, plastic instability (or the end of uniform strain in the concept of necking) occurs when $\bar{\epsilon} = \eta$. Irradiation at temperatures below 550°C decreases η because once the yield strength has been exceeded and deformation initiated, the deformation is restricted (or confined) to narrow bands or channels in the metal. (72) The passage of the first few dislocations weakens the barriers within the bands and occurs with little strain hardening. The reduction in η also means that ϵ_u is reduced.

Experimental information on the effect of irradiation of ϵ_u is given in Figures VI-C-16 thru VI-C-18. (64-70) It is noted that for ST 316 SS irradiated at 430-480°C, ϵ_u is quite dramatically reduced by irradiation and at ~13 dpa falls below 1%. Projections of this

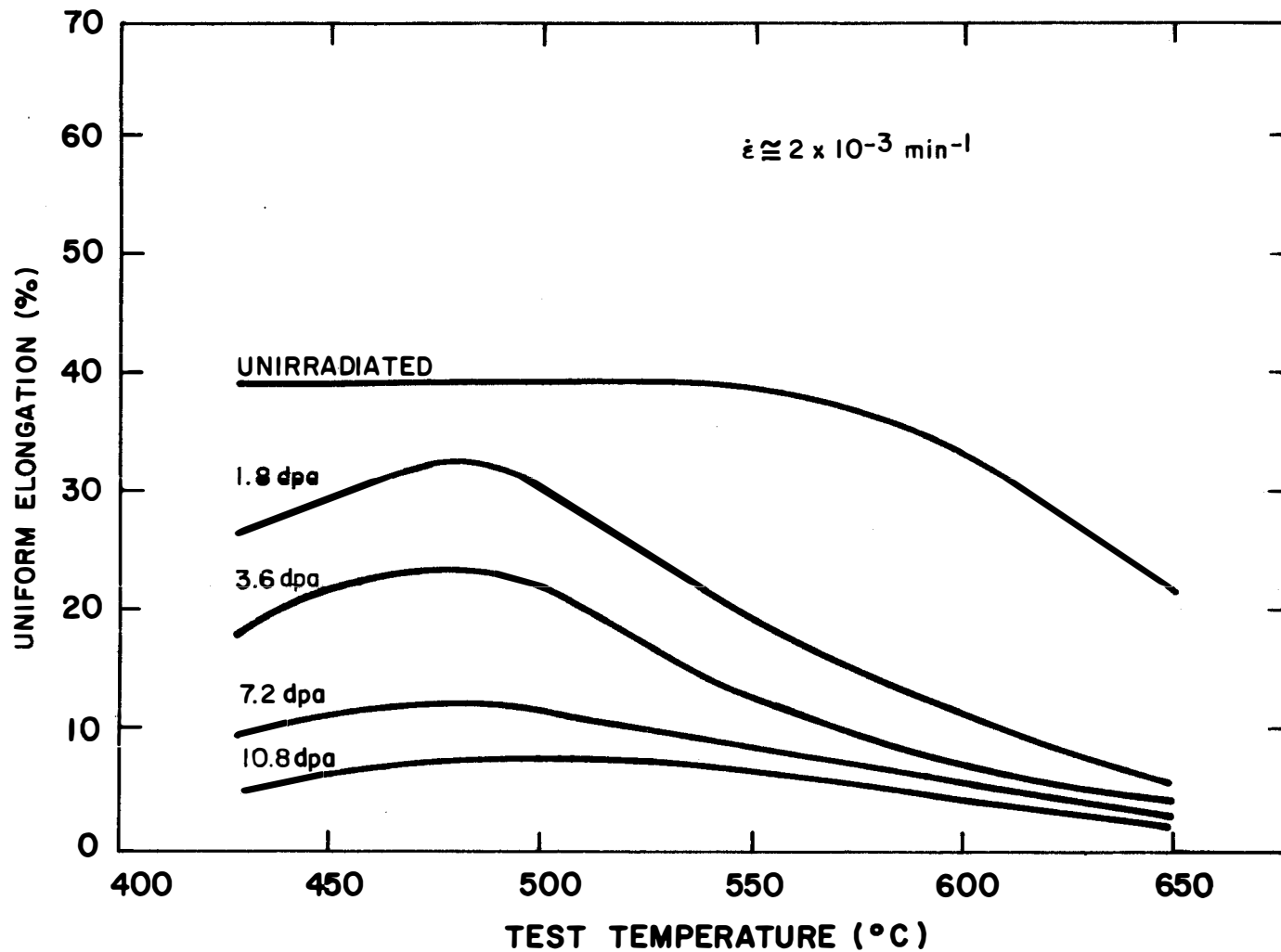


Figure VI-C-16 Parametric dpa Plots of Uniform Elongation Versus Test Temperature for ST Type 316 Stainless Steel Irradiated (EBR-II). Irradiated within $\pm 50^\circ\text{C}$ of test temperature (64-70)

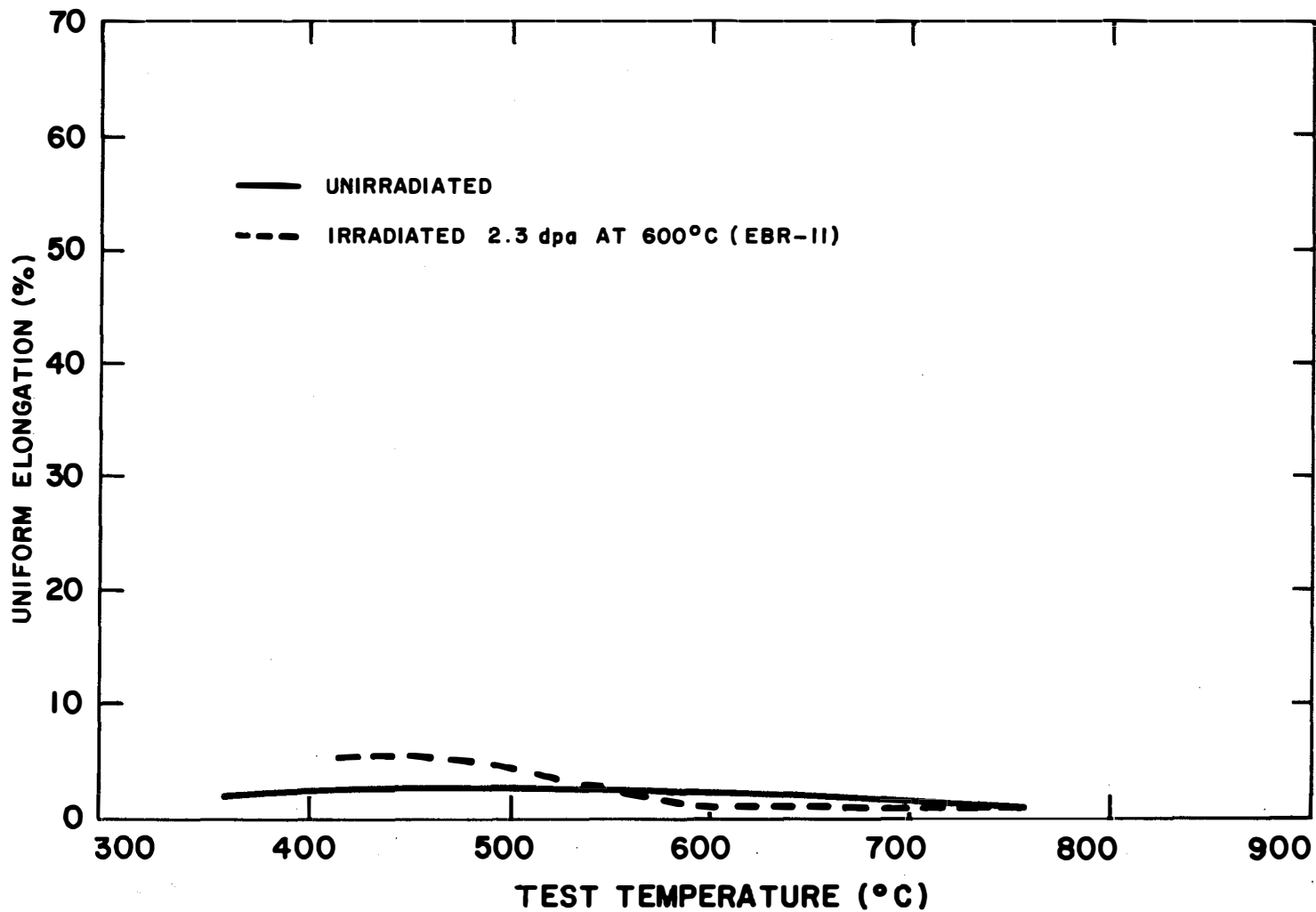
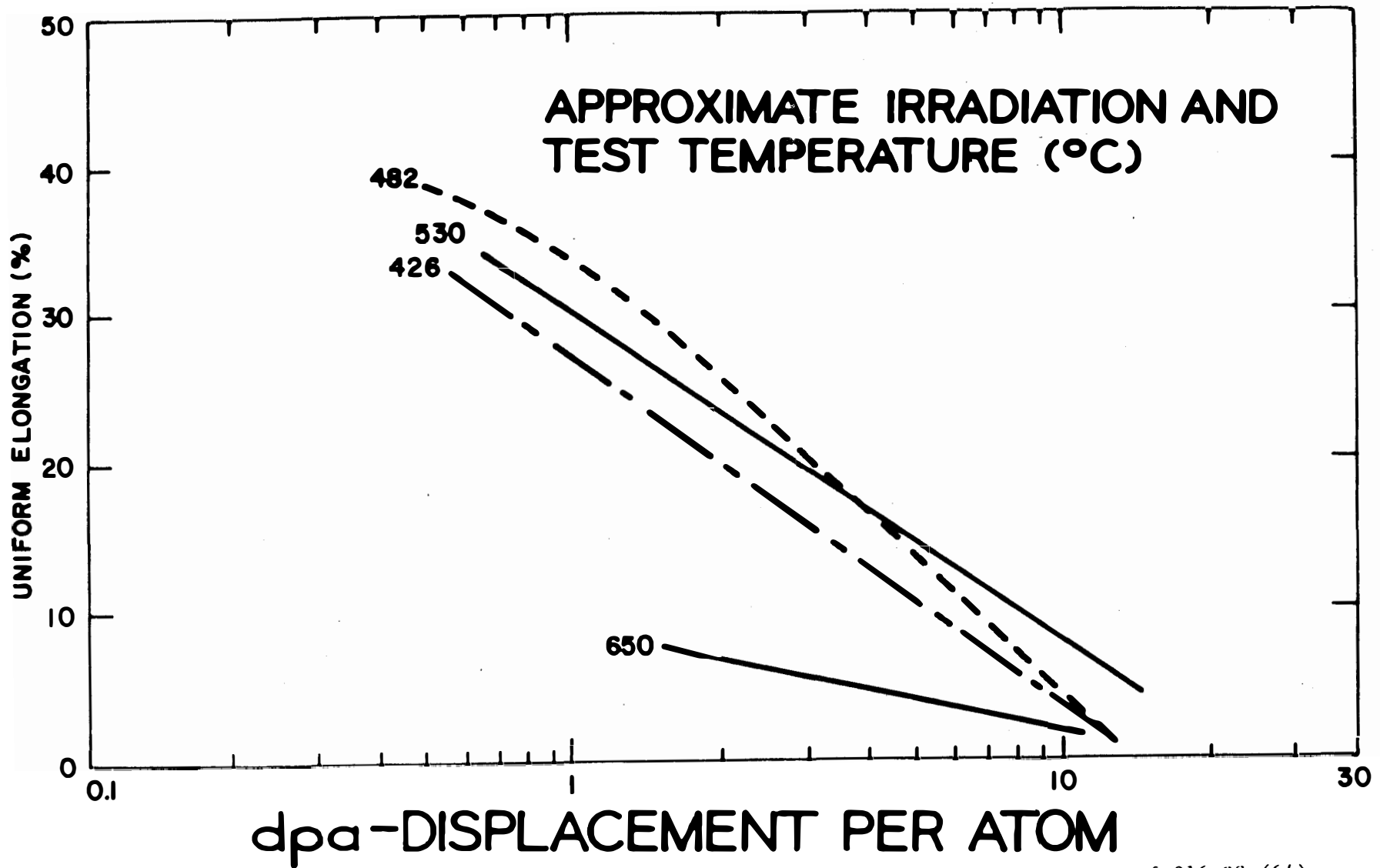


Figure VI-C-17 Uniform Elongation Versus Test Temperature for Unirradiated and Irradiated 20% CW Type 316 Stainless Steel. Irradiation within $\pm 50^{\circ}\text{C}$ of Test Temperature (64,70)



VI-C-32

Figure VI-C-18 Design Curves for the Effect of Irradiation on Uniform Elongation of 316 SS (64)

curve would predict that by 15 dpa, ϵ_u would be at 0.5% which is the design limit for UWMAK-I.

There is very little data available on irradiated 20% CW 316 SS at the present time (Figure VI-C-18) so that we will assume that the data for ST 316 SS applies to cold worked steel. However, it does appear that the cold worked alloy is less ductile after irradiation than the ST 316 SS.

Before leaving this topic, it is worthwhile to review the mechanisms that control the ductility. We will follow the approach of Holmes et. al. (51,53,55,62) and the reader is referred to their work for more detail.

Figure IV-C-19 outlines the three general deformation processes which operate the 320-760°C range for various strain rates. These include;

- . Strain independent athermal plastic flow
- . Diffusion controlled deformation
- . Irradiation creep

At the very high strain rates, diffusion controlled deformation and irradiation creep are too slow to contribute to plastic flow. Ductility in the athermal region is nearly independent of second phase precipitation and is almost temperature and strain rate independent. Failure during athermal flow is characterized by ductile transgranular fracture. Fracture in the diffusion control range is usually intergranular and is often affected by second phase precipitation. Finally, when the strain rates are less than $10^{-6}h^{-1}$, irradiation creep is predominate. This process is characterized by a low stress component and is weakly temperature dependent.

As was stated previously, ϵ_u in domain I is controlled by plastic instability due to the generation of microdefects. In principle, ϵ_u (72) should decrease continuously with irradiation but results on 304 SS indicate that ϵ_u saturates in the neighborhood of 0.5% regardless of the defect concentration (Figure VI-C-20). The increase in ϵ_u with increasing temperature in domain I is attributed to the decreasing defect concentration.

The mechanism in domain II is not as simple as for domain I. It now appears that two mechanisms are important; helium embrittlement and matrix hardening. Helium embrittlement results from the generation of helium gas within the matrix by (n,α) reactions and the collection of the helium gas bubbles at grain boundaries. These bubbles can grow under the action of applied stress by diffusional properties until the grain boundaries fail. Ultimately, the bubbles may lead to failure by assisting crack nucleation and second phase particles within the boundaries.

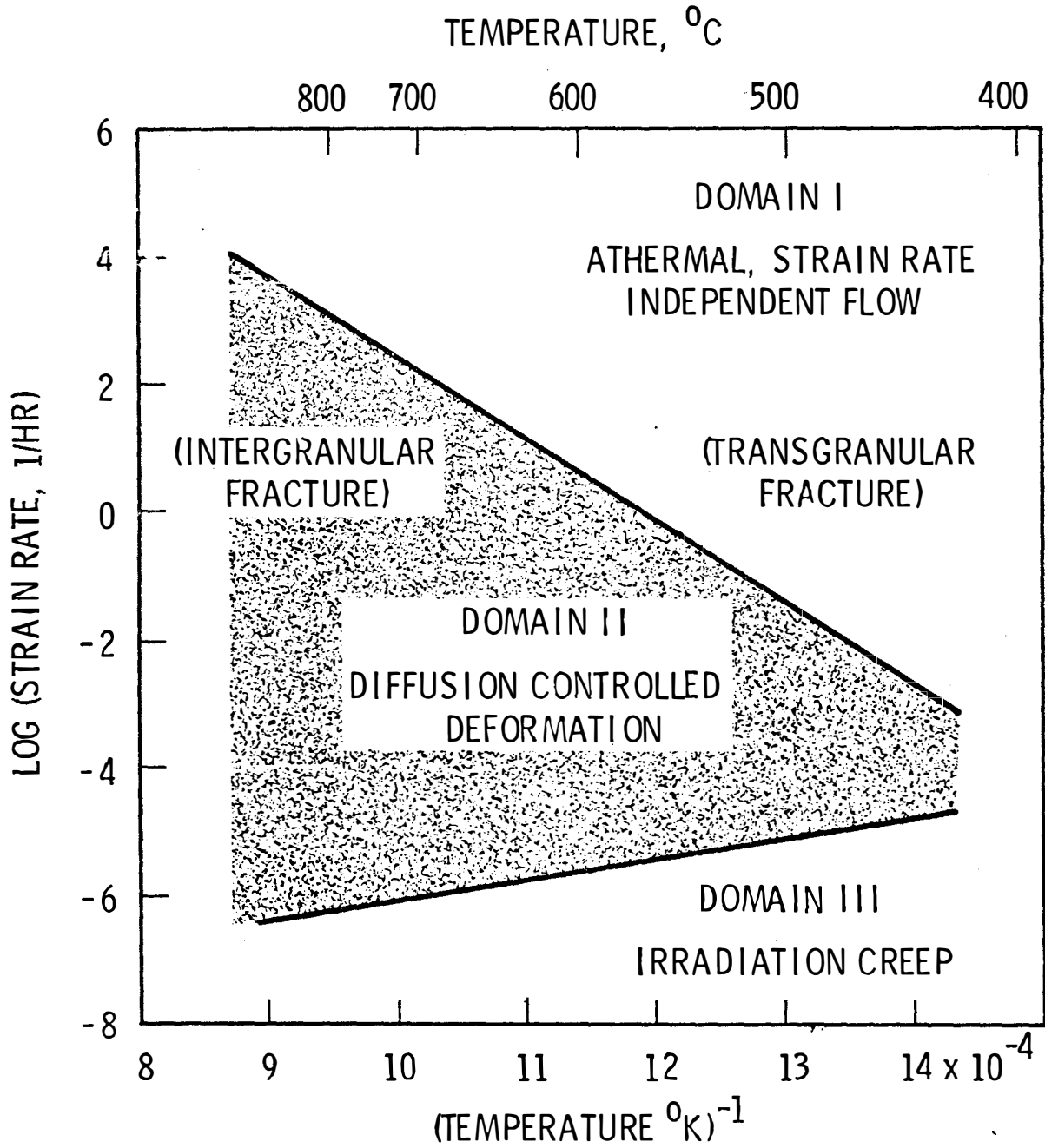


Figure VI-C-19 Deformation Mechanisms in Annealed AISI Type 316 Stainless Steel During Fast Reactor Irradiation (53)

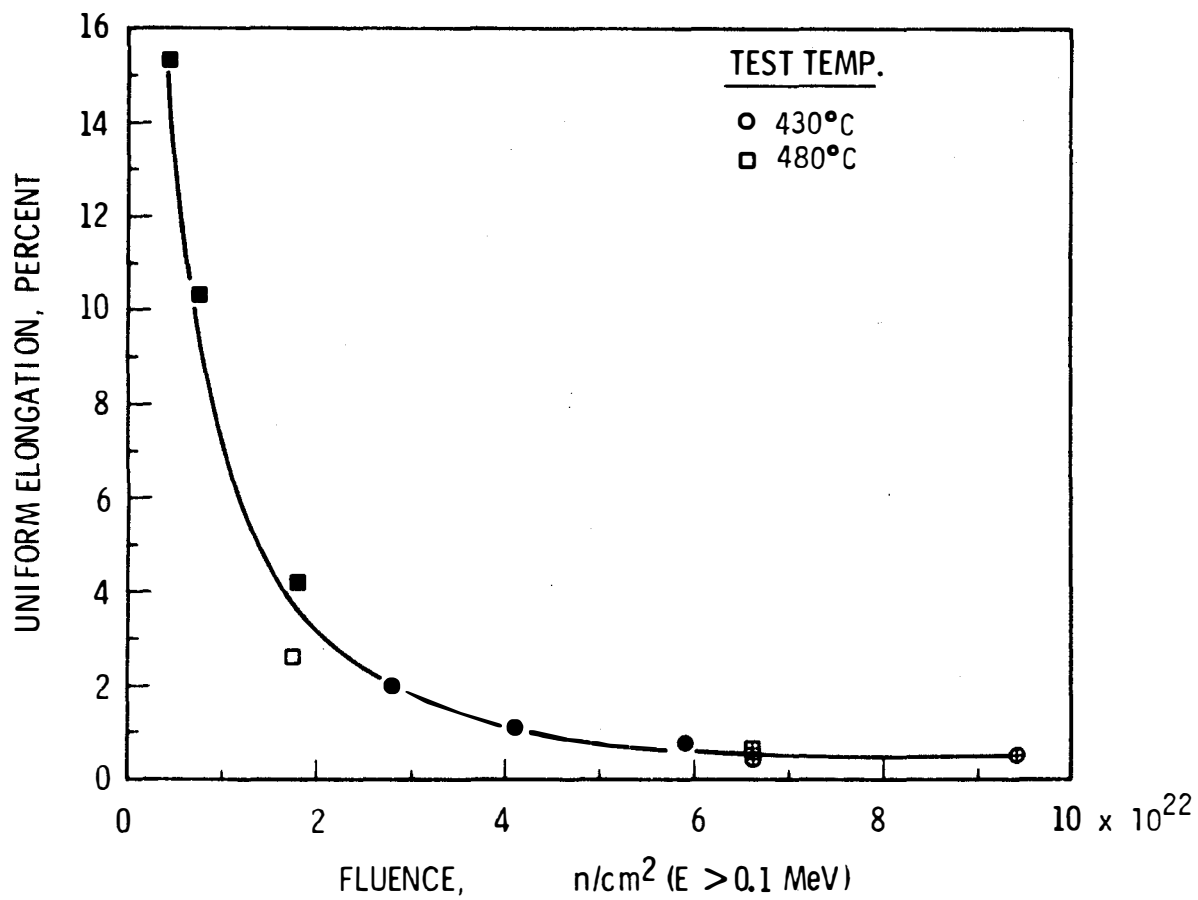


Figure VI-C-20 The Effect of Fluence on the 430 and 480°C Yield Strength and Uniform Elongation of EBR-II Type 304 Stainless Steel Thimbles (72)

Matrix hardening can lead to premature failure in domain II by forcing most of the deformation to be absorbed by the grain boundaries. Such an effect results in excessive grain boundary shearing which leads to high stresses and subsequent failures initiated at grain boundary triple points.

It is extremely important to note that when helium is present at boundaries and irradiation hardening is significant, the helium embrittlement and matrix hardening may combine to produce ductility losses more severe than the two processes acting alone! Under such conditions, strain is concentrated at the grain boundaries which, because of helium embrittlement, are less able to withstand shear than before irradiation. These result in grain boundary failure at much smaller strains than simple matrix hardening alone.

The temperature and fluence dependence of the two ductility degradation processes are shown in Figure VI-C-21. (55) In general, pure helium embrittlement in 316 SS is limited to temperatures above 600-700°C except for very low fluences. When the temperature is too low for significant diffusion (less than 550°C) but high enough for void formation, the ductility in this region is mainly guided by matrix hardening. In between 550 and 700°C matrix hardening and helium embrittlement can combine to cause a reduction in ϵ_u previously described.

The temperature behavior of ductility for materials at a given damage level (e.g. 14.1 dpa) can be understood in the schematic in Figure VI-C-22. Below 480°C, low ductility is simply a consequence of premature plastic instability. As the radiation temperature is increased, the defect concentration in the matrix decreases, causing an increase in work hardenability which results in increased uniform elongation. Near approximately 540°C, diffusion processes become significantly effective such that helium embrittlement contributes to ductility loss. As the radiation temperature increases above 540°C, matrix strength drops very rapidly but diffusion increases the efficiency of the helium embrittlement process resulting in a net decrease in ductility. Above 650°C, the effect of matrix strength rapidly decreases producing a temporary but small increase in ductility. Above 700°C, helium embrittlement is the principle contributor of ductility loss.

The above analysis applied to a fission reactor spectrum, and we must note that fusion reactor radiation will produce about 20 times more helium per displacement than in fission reactors. (4) This high helium concentration will have the effect of lowering the temperature for the helium dominated regions.

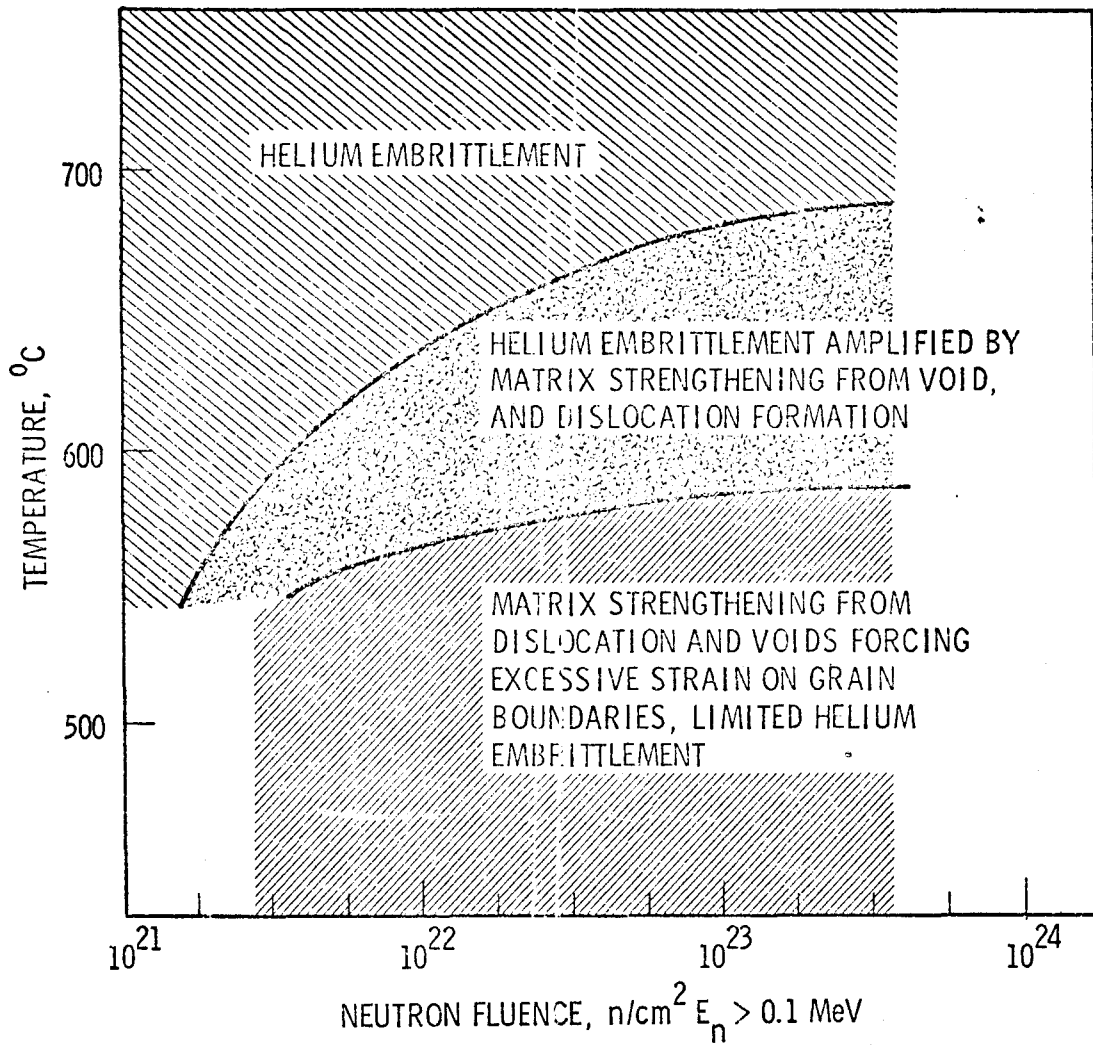


Figure VI-C-21 Schematic Representation of Range of Operation of Various Ductility Degradation Processes in Domain II of Figure VI-C-20 (53)

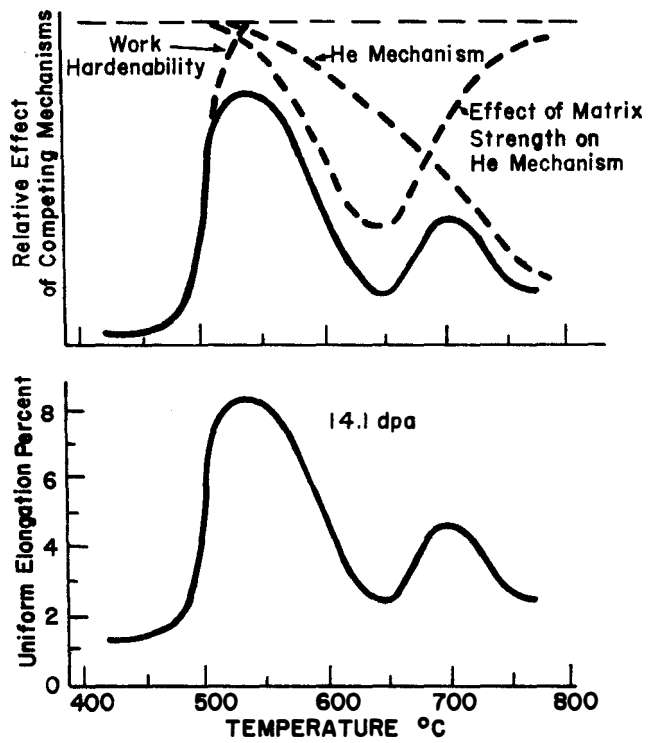


Figure VI-C-22 Effect of temperature on the uniform elongation of irradiated Type 316 SS (55)

VI-C-4 Transmutation Effects in 316 SS

The transmutation reactions in metals can not only produce radioactive species (Section IX-B), afterheat (Section IX-C), swelling (Section VI-C-2), and degradation of mechanical properties (Section VI-C-3), but they can significantly alter the chemical compositions of a metal. The classic example of this is the transmutation of Nb into Zr in a fusion reactor spectrum.⁽⁷³⁾ The purpose of this section is to investigate the potential transmutation effects that might be expected in 316 SS when irradiated with fusion spectrum neutrons.⁽⁷⁴⁾ Previous work has also been done on V-20Ti and Nb - 1Zr alloys.

The composition of 316 SS used for this work is given in Table VI-C-5. We have calculated the transmutation reactions for all elements in Table VI-C-5 except those indicated. The only serious omission is Mo, an element for which there is no complete isotopic data in ENDF-III files.

The neutronic reactions considered are listed in Table VI-C-6 and those not considered are listed in Table VI-C-7. It is important to study these lists as future work will probably be aimed at reducing the number of isotopes not considered. The neutron fluxes as a function of position were obtained from calculations outlined in Chapter V. However, for purposes of this report we will confine our attention to the first wall only.

The transmutation rates are reported in a rather unique unit called an amy for atomic parts per million per Megawatt year/m² or appm. This normalized unit can be converted to atomic (MW/m²)-year parts per million by multiplying by the neutron wall loading in MW/m² and the number of years of irradiation.

Table VI-C-8 lists the original composition and the net amys of an element lost or produced. The major changes are the loss of Fe and Ni and the production of Mn, V, and Ti. The exact magnitude and the consequence of such changes will be explored in Section VI-D-3.

Finally, it is of interest to calculate the origin of the helium and hydrogen gas from the various alloying elements. The results of such a calculation are listed in Table VI-C-9. It is noted that almost 65% of the helium comes from iron, ~15% from chromium and only 9.4% from the Ni. We have not included the Ni⁵⁹ (n, α) reaction in this work but preliminary calculations reveal that in the extremely hard spectrum of the first wall, such an omission is not serious. Finally it should be noted that ~10% of the helium generated in 316 SS comes from the interstitial elements (Si, C, N, O, and B).

Table VI-C-5

Typical Chemical Analyses of Commercial 316 Stainless Steel
Parts Per Million by Weight

<u>Element</u>	<u>316 Stainless Steel</u>
Al	500
As	300*
B	10
Co	500*
Cr	18%
Cu	1,000
Fe	Bal
Mn	2%
Mo	2%
Nb	500*
Ni	14%
P	200
S	100*
Si	.7%
Ta	200*
Ti	100
V	2,000
C	600
H	?
N	100
O	<200

*Not Considered for this Work

Table VI-C- 6

Transmutation Reactions Considered for
Transmutation Reactions in 316 SS

<u>Isotopic Abundance-%</u>	<u>Reaction</u>	<u>Important Isotope for 30 year Life</u>
100	Al ²⁷ (n,2n)	Mg ²⁶
"	Al ²⁷ (n,p)	Al ²⁷
"	Al ²⁷ (n,α)	Na ²⁴
18.7	B ¹⁰ (n,α)	Li ⁷
Total	Cr(n,p)	15% V, 85% Cr
"	Cr(n,2n)	0.2% Ti, 99.8% V
"	Cr(n,α)	98% Ti, 2% V
Total	Cu(n,2n)	Ni
"	Cu(n,p)	90% Ni, 10% Cu
"	Cu(n,α)	Ni
Total	Fe(n,p)	25% Mn, 75% Fe
"	Fe(n,2n)	98% Mn, 2% Fe
"	Fe(n,α)	90% Cr, 10% V
100	Mn ⁵⁵ (n,p)	Mn
"	Mn ⁵⁵ (n,2n)	Cr
"	Mn ⁵⁵ (n,α)	Cr
100	Nb ⁹³ (n,2n)	33% Zr, 67% Nb
"	Nb ⁹³ (n,p)	Zr ⁹³
"	Nb(n,α)	Zr ⁹⁰
"	Nb(n,α)	Zr ⁹⁰
Total	Ni(n,p)	82% Fe, 18% Ni
"	Ni(n,α)	68% Mn, 28% Fe 4% Co
100	P ³¹ (n,p)	P
"	P ³¹ (n,α)	Si
Total	Si(n,p)	Si
"	Si(n,α)	97% Mg, 3% Si
99.987	Ta ¹⁸¹ (n,p)	Ta ¹⁸¹
"	Ta ¹⁸¹ (n,α)	Hf ¹⁷⁸
99.76	V ⁵¹ (n,α)	Cr ⁵²
"	V ⁵¹ (n,p)	V ⁵¹
"	V ⁵¹ (n,α)	Ti ⁴⁸

Table VI-C-6
(cont.)

<u>Isotopic Abundance-%</u>	<u>Reaction</u>	<u>Important Isotope for 30 Year Life</u>
98.892	$C^{12}(n,\alpha)$	Be^9
"	$C^{12}(n,n)$	$3 He^4$
99.635	$N^{14}(n,p)$	C^{13}
"	$N^{14}(n,p)$	C^{14}
"	$N^{14}(n,\alpha)$	B^{11}
99.759	$O^{16}(n,p)$	O^{16}
"	$O^{16}(n,\alpha)$	C^{13}
Total	$Ti(n,2n)$	8% Sc, 92% Ti
"	$Ti(n,p)$	Ti
"	$Ti(n,\alpha)$	21% Ca, 74% Sc, 5% Ti

Table VI-C-7

Transmutations Reactions Not Considered for
UWMAK-I Transmutation Reactions in 316 SS

<u>Isotopic Abundance-%</u>	<u>Reaction</u>	<u>Important Isotope for 30 Year LiFe</u>
100	Al ²⁷ (n,γ)	Si
100	As ⁷⁵ [(n,γ), (n,p), (n,α)]	Se, Ge, As
18.7	B ¹⁰ [(n,p), (n,T)]	Be, He
81.3	B ¹¹ [(n,p), (n,α), (n,γ)]	B, He, C
100	Co ⁵⁹ [(n,γ), (n,p), (n,α)]	Ni, Fe
4.31	Cr ⁵⁰ (n,γ)	V ⁵¹
2.38	Cr ⁵⁴ (n,γ)	Mn ⁵⁵
Total	Cu(n,γ)	Zn
5.84	Fe ⁵⁴ (n,γ)	Mn ⁵⁰
100	Mn ⁵⁵ (n,γ)	Fe ⁵⁶
Total	Mo[(n,γ), (n,p), (n,α), (n,2n)]	Tc, Ru, Zr, Y
100	Nb ⁹³ [(n,np), (n,T)]	Zr
1.16	Ni ⁶⁴ (n,γ)	Cu ⁶⁵
100	P ³¹ (n,γ)	S
Total	Si(n,2n)	Al, Si
Total	S[(n,γ), (n,p), (n,α)]	Si, Cl
99.987	Ta ¹⁸¹ (n,γ)	W ¹⁸²
0.013	Ta ¹⁸⁰ [(n,p), (n,2n), (n,α)]	Hf
0.24	V ⁵⁰ [(n,p), (n,2n), (n,α)]	Ti
98.892	C ¹² (n,p)	C ¹²
98.892	C ¹² (n,2n)	B ¹¹
0.108	C ¹³ [(n,p), (n,α)]	C, Be
0.365	N ¹⁵ [(n,γ), (n,p), (n,α)]	O, N, C
99.759	O ¹⁶ (n,2n)	N ¹⁵
0.037	O ¹⁷ [(n,p), (n,γ)]	O, C
0.204	O ¹⁸ [(n,γ), (n,p), (n,α)]	F, O, N

Table VI-C-8

Summary of Major Metallic Transmutation
Rates in 316 Stainless Steel*

<u>Element</u>	<u>Original Concentration appm</u>	<u>Net Change-amys appm/MW-year/m²</u>
Fe	626,000	-1,224
Cr	180,000	+ 24
Ni	140,000	- 177
Mn	20,000	+1,160
Si	15,000	- 12
Cu	1,000	- 5.6
Al	1,000	- 0.6
B	52	- 0.1
Co	500	+ 0.3
Nb	300	- 0.5
P	360	- 0.1
Ti	115	+ 45.1
V	2,200	+176.7
C	2,800	- 3.4
O	400	- 0.4
N	400	- 0.5
Be	N	+ 1.6
Mg	N	+ 12.3
Na	N	+ 0.5
Zr	N	+ 0.5

N = Negligible

* UWMAR-I Spectrum, First Wall

Table VI-C-9

Summary of Gas Production in 316 Stainless Steel First Wall-UWMAK-I

<u>From</u>	<u>Original Concentration appm</u>	<u>amys-</u> <u>appm/MW-year/m²</u>		<u>Atomic % of Total</u>	
		<u>He</u>	<u>H</u>	<u>He</u>	<u>H</u>
Fe	626,000	154	230	64.7	45.2
Cr	180,000	35	63.9	14.7	12.6
Ni	140,000	22.5	184	9.4	36.2
Mn	20,000	2.6	8	1.1	1.6
Si	15,000	12.6	17.6	5.3	3.5
N	400	0.2	0.3	0.1	N
O	400	0.4	0.1	0.2	N
C	2,800	9.3	N	3.9	N
B	52	0.3	N	0.1	N
Al	1,000	0.5	0.3	0.2	N
V	2,200	0.2	0.3	0.1	N
Cu	1,000	0.1	3.8	N	0.7
P	360	<u>0.2</u>	<u>0.2</u>	<u>0.1</u>	<u>N</u>
		238.2	508.5	~100	~100

N = Negligible

The source of hydrogen in 316 SS is somewhat different than for helium in that nickel generates a disproportionate amount. More than one third of the hydrogen comes from Ni which only constitutes 1/7 of the atomic fraction. It is also noted that ~5% of the hydrogen comes from the interstitial elements and practically all of that comes from silicon.

Finally it should be noted that the calculations here cannot be directly compared to those in Chapter V because a different 316 SS composition was used there (72% Fe, 17% Cr, 11% Ni) and no provision was made to include the gases from impurity atoms.

VI-C-5 Surface Effects

The first wall of a thermonuclear reactor will be exposed to high fluxes of charged particles, neutrons, neutral atoms, and gamma rays throughout its life. Primary and secondary interaction processes will occur which can result in a degradation of mechanical properties and an effective erosion of the first wall. Primary reactions may be defined as those interactions between the incident ion and the target where a momentum transfer occurs, a change in the internal energy state of one or both particles occurs, or when a nuclear reaction takes place. As a result of these reactions, secondary processes such as lattice atom displacement, or ionization and x-ray emission may occur. Such processes can cause a variety of phenomena: physical and chemical sputtering, blistering, secondary electron emission, x-ray emission, backscattering of particles and photons, release of absorbed gases, radiation damage, photodecomposition of surface compounds, particle entrapment and re-emission of trapped particles.⁽⁷⁵⁾

Although several of the above processes have been investigated, very little experimental data is available for the extreme environment and the various types of metals that might be found in a fusion reactor. Sputtering and blistering appear to be the most significant of these processes in fluencing the first wall lifetime and as such, will be the only phenomena considered here. Sputtering and blistering have two deleterious effects on the CTR system. The first is an effective erosion or thinning of the first wall. The atoms removed by these processes can also return to the plasma and in some systems cause energy losses that could bring the plasma below the minimum temperature needed to sustain the fusion reaction. The effects of sputtering and blistering on fusion reactors, particularly the UWMAK-I, will be discussed in Section VI-D-4 and only a brief review of the theory and experimental results pertaining to these phenomena will be given here.

a) Sputtering

i) General Considerations

Bombarding a metallic target by high energy ions, neutrons, or neutral atoms will displace atoms in the target from their lattice sites. Not all of these displaced atoms remain in the target. They may be sputtered off the front surface of the target and ejected from the back surface. The phenomena whereby atoms are ejected from the lattice only by momentum transfers in the collision process is termed physical sputtering. Several theoretical studies on sputtering have been developed⁽⁷⁶⁻⁷⁹⁾ and good reviews of the theory are presented elsewhere.^(78,80)

Physical sputtering may be understood by analyzing the individual collisions of the incident ion and its primary knock-on atoms (PKA's) in the lattice. The displaced atoms in the lattice all slow down by undergoing further collisions. As this occurs, they may diffuse and escape. Also, collisions beneath the surface may result in focusing events which transfer momentum along close-packed rows of atoms. If

these close-packed rows terminate on the surface, enough energy might be imparted to the atom at the surface so that it is ejected from the surface.

The collisions in the lattice may be treated as falling into one of three groups, depending on the incident particle energy and the distance of closest approach.(76,78) The potential describing the interaction between the projectile and target atom is assumed to be a screened Coulomb potential.

$$V(r) = \frac{Z_1 Z_2 e^2}{r} \exp \left[-\frac{r}{a} \right] \quad \text{VI-C-15}$$

where Z_1 and Z_2 are the atomic numbers of the projectile and target atom, respectively.

e is the charge on an electron
 r is the distance between the two nuclei
 a is the electron cloud radius defined by

$$a = \frac{a_0}{(Z_1^{2/3} + Z_2^{2/3})^{1/2}} \cdot$$

a_0 is the Bohr radius.

For incident ions having a high enough energy to penetrate the electron clouds around the nucleus, the interaction will be through the Coulomb repulsion of the nuclear charges. This interaction can be described as Rutherford scattering when the ions possess an energy greater than E_B where

$$E_B = 4E_R^2 Z_1 Z_2 (Z_1^{2/3} + Z_2^{2/3})^{1/2} \frac{M_1}{M_2} \frac{1}{E_d} \quad \text{VI-C-16}$$

where E_R is the Rydberg energy (13.61 eV),

E_d is the displacement energy for the lattice atom,

M_1 and M_2 are the atomic weights of the projectile and

target atoms, respectively.

Typical values of E_B for various projectiles of interest in CTR applications are listed in Table VI-C-10.

For energies less than E_B , electron screening becomes important. The lower limit for the use of a weakly screened Coulomb interactions is given by

$$E_A = 2E_R Z_1 Z_2 (Z_1^{2/3} + Z_2^{2/3})^{1/2} \frac{M_1 + M_2}{M_2} \quad \text{VI-C-17}$$

Table VI-C-10

Values of the limiting energies E_A between the hard-sphere collision region and the weakly-screened Coulomb collision region and E_B between the latter and the Rutherford collision region. The projectiles and wall materials shown are some of those of interest for Fusion reactors. All energies are in keV.

Projectile	Vanadium ^{a)}		Niobium ^{a)}		Molybdenum ^{a)}		Iron	
	E_A	E_B	E_A	E_B	E_A	E_B	E_A	E_B
H+	1.9	2.8	4.1	7.0	4.2	7.2	2.7	3.0
D+	2.0	5.7	4.1	14.0	4.3	14.5	2.8	6.1
He+	4.2	48.3	8.6	117.2	8.9	120.8	6.1	51.5

a) Reference 75

Weakly screened interactions may be assumed to occur for particle energies between E_A and E_B .

The final type of collisions that will be considered are for energies much smaller than E_A where there is very little electron cloud penetration. In this region, the collisions are of the hard sphere type. There is also a lower threshold below which no sputtering will occur. This value varies from 12 to about 30 eV.⁽⁷⁵⁾ Attempts have been made to measure a threshold energy for sputtering experimentally, but sputtering yields are so low at these energies that a definite threshold is hard to pinpoint.⁽⁷⁸⁾ The value of the sputtering threshold will depend both on the incident ion and the target material. Extrapolation of higher energy sputtering data to zero sputtering yield has given values as low as 4 eV for Ar^+ on a silver target.⁽⁷⁸⁾

It should be mentioned that the energy boundaries just described are approximate. To obtain a better prediction of the energy transfers an interaction potential should be used that describes collisions for all distances of closest approach, spanning the gap from simple Coulomb to hard sphere type collisions. Unfortunately, no one potential describing the entire range of interactions has been discovered.

In order to predict the rate at which sputtering will erode a surface, a factor called the sputtering ratio is often computed. The sputtering ratio is simply the number of atoms sputtered off the wall per incident particle striking the wall. Several theories have been proposed^(76,77,81) to predict this value and a good summary of these can be found in references [78,80]. A brief outline of the model proposed by Pease⁽⁷⁶⁾ is presented below.

In calculating the sputtering yields, the displacement cross sections for each of the energy regions mentioned above must be known. These relations are listed below.

$$E > E_B \quad \sigma_d = \frac{4 \pi a_o^2 M_1 Z_1^2 Z_2^2 E_R^2}{M_2 E_d} \frac{1}{E} \left(1 - \frac{E_d}{E_{\max}} \right) \quad \text{VI-C-18}$$

$$E_A < E < E_B \quad \sigma_d = \pi a^2 \quad \text{VI-C-19}$$

$$E < E_A \quad \sigma_d = \pi R^2 \left(1 - \frac{E_d}{E_{\max}} \right) \quad \text{or} \quad \text{VI-C-20}$$

$$\sigma_d = \pi \left[b \ln \left(\frac{M_2}{M_1 + M_2} \cdot \frac{E}{A} \right) \right]^2 \left(1 - \frac{E_d}{E_{\max}} \right) \quad \text{VI-C-21}$$

where R is the distance of closest approach in hard sphere scattering. The minimum value of R can be found by noting that at the distance of closest approach, the relative energy of the projectile-tangent system must equal the potential energy. Using a Born-Mayer potential, $V(r) = A \exp(-r/b)$, a value of R can be calculated and inserted in equation VI-C-20 to yield the expression VI-C-21. A and b are constants determined by compressibility experiments. E_{\max} is the maximum possible energy transfer to the PKA given by

$$E_{\max} = 4 \frac{M_1 M_2}{(M_1 + M_2)^2} E$$

Pease⁽⁷⁶⁾ has considered the form of the sputtering ratios to be as follows,

$$S = (\sigma_d \bar{E} n^{2/3}) \frac{1}{4E_d} \left(1 + \frac{\log(\bar{E}/E_s)}{\log 2} \right)^{1/2} \quad \text{VI-C-22}$$

where \bar{E} is the average PKA energy, n is the atom density, and E_s is the energy below which an atom cannot escape from the surface and $2E_d < \bar{E} \ll \bar{E}_{\max}$

Figure VI-C-23 shows the results of applying the above analysis to the bombardment of silver by several ions of various energies. The variation of S with energy is quite evident. For $E < E_A$, the sputtering ratio increases sharply above some threshold energy and then levels off. The reason for the rapid rise in S is that the average energy transferred to the PKA increases in direct proportion to the initial particle energy in hard sphere scattering. From equation VI-C-22, an increase in \bar{E} raises S . A higher initial energy, \bar{E} also results in an increase in the displacement cross section, σ_d (see equation VI-C-21). Note that the threshold energy for sputtering predicted by Pease Model⁽⁷⁶⁾ is an order of magnitude higher than Kaminsky's values.⁽⁷⁵⁾ In the region around E_A , sputtering yields are maximum and decrease slightly over the range from E_A to E_B . In the Rutherford scattering region ($E > E_B$), S decreases with increasing particle energy. Equation VI-C-22 shows that S depends strongly on the displacement cross section σ_d and the average energy transferred to a PKA. Equation VI-C-18 shows that σ_d is proportional to $1/E$ above E_B . Also, the average energy transferred to a PKA in Rutherford scattering is very small and increases only slightly with large increases in incident particle energy. For these reasons, the sputtering ratio will tend to drop above E_B .

Pease⁽⁷⁶⁾ explains that his model is most accurate at the higher energies, $E > E_B$, where the only large uncertainty affecting S is the displacement energy. Application of this model below E_B is uncertain since the cross sections are not well known, and the energy spectrum of the PKA's changes more rapidly with ion energy. Experimental results have also shown that when $E > E_B$ the charge (neutral, single or doubly charged)⁽⁸²⁾ of the bombarding particle does not affect the sputtering yield.⁽⁸²⁾ Table VI-C-11 shows some calculations of sputtering ratios for various ions and metals of interest in CTR's. Calculations were made using⁽⁷⁷⁾ the above model and another relation derived by Goldman and Simon.

ii) Self Sputtering

The values of the sputtering ratios in Table VI-C-11 are for the light ions that leak out of plasma and strike the first wall. Much more serious erosion will occur if the projectile atom is heavier. Atoms sputtered off the vacuum wall in a CTR may enter the plasma where they gain energy through collisions with the plasma ions. If these atoms return to the wall, self sputtering can result. Summers et.al.⁽⁷⁹⁾ have measured sputtering ratios for Nb^+ ions with energies of 10 to 80 KeV on a niobium target at 50 to 100°C. The results are illustrated in Figure VI-C-24. Sputtering coefficients are greater than one atom per Nb^+ ion over this energy range. This is due mainly to the high average energy transfer from a niobium ion colliding with a niobium atom. Most of the self-sputtering collisions that occur in a CTR will be in the hard sphere region ($E < E_A$). In the hard sphere region, the average energy transfer is one-half^A of the maximum possible energy transfer (E_{max}). From the relation for E_{max} it is easily seen that maximum and average PKA energies are highest^{max} when $M_1 = M_2$ i.e. self-sputtering. Summers et al.⁽⁷⁹⁾ have calculated that the flux of 20 KeV Nb^+ ions needed to produce a given level of erosion is only 1/200 the flux of deuterium, tritium and helium ions necessary to

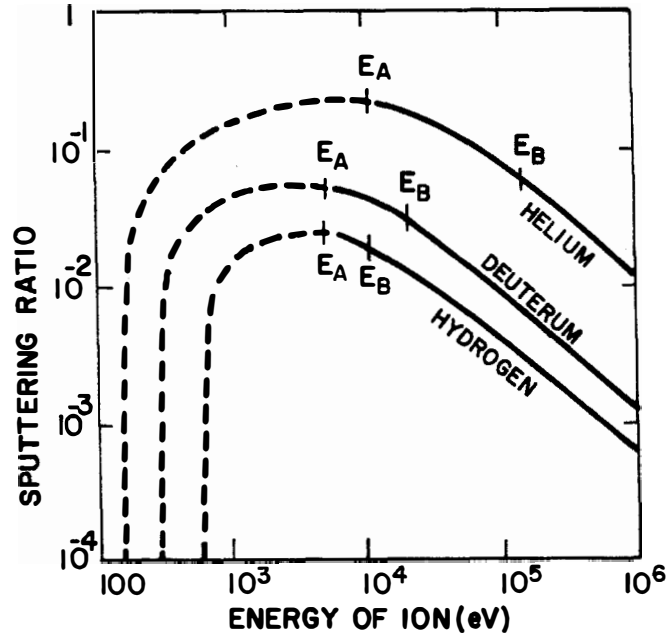


Figure VI-C-23 Calculated sputtering ratio of various ions on silver, as a function of energy. The energy limits for weak screening and hard sphere collision are E_B and E_A , respectively. The dashed portion of the curves indicate regions of decreased reliability. (76)

TABLE VI-C-11

Sputtering yields S (atoms/ion) for wall materials and projectiles of interest in fusion reactors. The values calculated according to the theories of Pease (P) and of Goldman and Simon (G) are compared with the experimental values (Exp).

Wall	H^+						D^+					
	Projectile energy E (keV)						Projectile energy E (keV)					
	10	20	50	100	200	500	10	20	50	100	200	500
V P	0.0097	0.0061	0.0031	0.0018	0.0010	0.0005	0.0240	0.0150	0.0072	0.0041	0.0023	0.0011
G	0.0030	0.0018	0.0008	0.0005	0.0003	0.0001	0.0069	0.0040	0.0019	0.0011	0.0006	0.0027
Nb P	0.0081	0.0056	0.0031	0.0018	0.0011	0.0005	0.022	0.014	0.0073	0.0043	0.0024	0.0011
G	0.0027	0.0016	0.0008	0.0005	0.0003	0.0001	0.0065	0.0038	0.0018	0.0010	0.0006	0.0003
Exp							0.0059 ^c	0.0040 ^d				
								0.0042 ^e				
Mo P	0.0086	0.0060	0.0033	0.0020	0.0012	0.00055	0.0240	0.0150	0.0079	0.0046	0.0026	0.0012
G	0.0029	0.0018	0.0009	0.0005	0.0003	0.0001	0.0070	0.0042	0.0020	0.0011	0.0006	0.0003
Cu P	0.0160	0.0100	0.0053	0.0031	0.0018	0.0008	0.041	0.025	0.012	0.0070	0.0039	0.0018
G	0.0036	0.0021	0.0010	0.0006	0.0003	0.0002	0.0085	0.0049	0.0023	0.0013	0.0007	0.0003
Exp	0.022 ^a				0.0013 ^b	0.0010 ^b				0.0028 ^f	0.0020 ^f	0.0011 ^f

Wall	He^+					
	Projectile energy E (keV)					
	10	20	100	500	1000	3500
V P	0.2300	0.1350	0.036	0.0092	0.0050	0.0017
G	0.0630	0.0360	0.0093	0.0023	0.0012	0.0004
Nb P	0.2250	0.1370	0.0390	0.0100	0.0055	0.0018
G	0.0610	0.0350	0.0093	0.0023	0.0013	0.0004
Exp		0.051 ^e				
Mo P	0.2410	0.1470	0.0042	0.011	0.0060	0.0020
G	0.0660	0.0380	0.010	0.0026	0.0014	0.0005
Cu P	0.3910	0.2300	0.0620	0.0160	0.0085	0.0028
G	0.078	0.0440	0.0110	0.0028	0.0015	0.0005

^aRef. 37. Value measured for 8-keV H^+ on Au.

^bRef. 18. Value measured for monocrystalline Cu(111) target, theories not applicable.

^cRef. 7. Value measured for 12.2-keV D^+ .

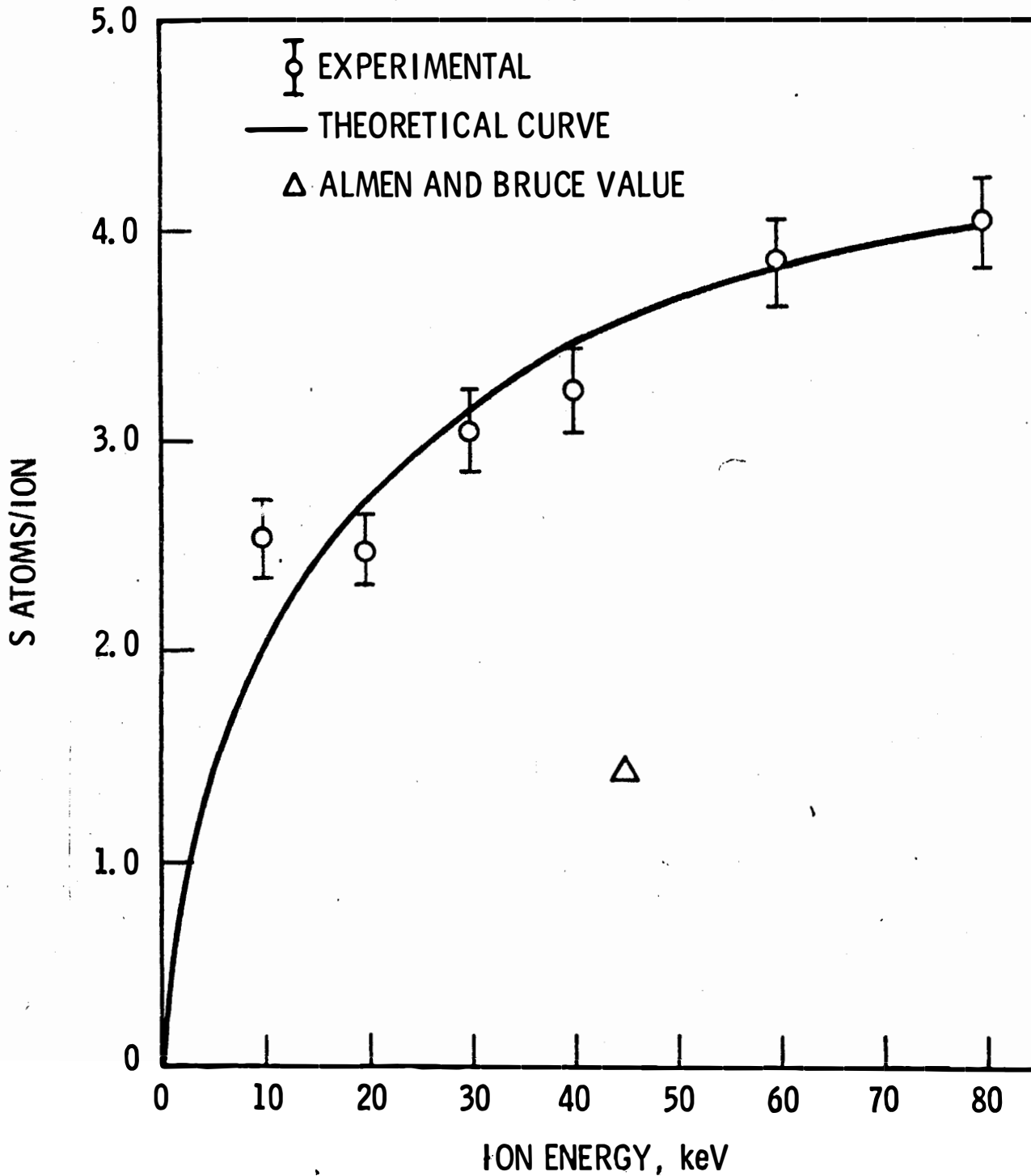
^dRef. 7. Value measured for 18.8-keV D^+ .

^eRef. 8. The Nb target temperature was 1100°C.

^fRef. 16. Values measured for monocrystalline Cu(100) target, theories p. 236. not applicable.

M. Kaminsky, "Surface Phenomena Leading to Plasma Contamination and Vacuum Wall Erosion in Fusion Reactors and Devices," Proceedings of the International Working Sessions on Fusion Reactor Technology, Oak Ridge, Tenn., CONF-710624, p. 86, (June 28-July 2, 1971).

Figure VI-C-24

SELF-SPUTTERING COEFFICIENTS OF NIOBIUM
IN THE ENERGY RANGE 10-80 keV

A. J. Summers, N. J. Freeman, and N. R. Daly, "Sputtering Coefficients of Niobium," Proceedings of the Nuclear Fusion Reactors Conference, BNES, Culham, p. 347 (September 1969).

cause the same damage.

iii) Neutron Sputtering

The first wall of a CTR will be subjected to high neutron fluxes as well as ion and neutral atom bombardment. Added to the incident 14 MeV neutron flux is an even higher flux of lower energy neutrons that come from (n,2n) reactions in the blanket and from backscattering. The energies of the back streaming neutrons range from about 0.1 to 6 MeV. As can be seen by the following example, neutron sputtering may be a problem in CTR systems. ^(75,82)

Consider the irradiation of a niobium target by separate beams of 14 MeV neutrons and 14 MeV deuterons. The cross section for elastic scattering of a 14 MeV neutron is on the order of 2 barns. A 14 MeV deuteron has a displacement cross section of 4800 barns. The average energy of the neutron produced PKA is approximately 146 KeV. The D⁺ produces a PKA with average energy of 0.364 KeV. Kaminsky calculated the average number of displacements produced by each of these ions to be: 2800 displaced atoms per PKA caused by the neutron. Thus, although the cross section is 3 orders of magnitude less for neutron reactions, the number of displacements per PKA is almost 3 orders of magnitude higher for neutrons. Kaminsky computed sputtering yields for these two particles and found slightly higher values for the 14 MeV neutrons.

Garber et.al., ⁽⁸³⁾ have presented results of extensive irradiations for 25 elements by a fission reactor flux of 2×10^{12} n/cm²sec (E > 1 MeV). They discovered that there is a periodic dependence of the sputtering yield on the atomic number of the target. Their results are given in Figure VI-C-25. Both polycrystalline and monocrystalline targets were used. It was also found that sputtering from single crystals was consistently higher by a factor of 1.5 to 2.5. From their work, it is possible to estimate the sputtering for any other target.

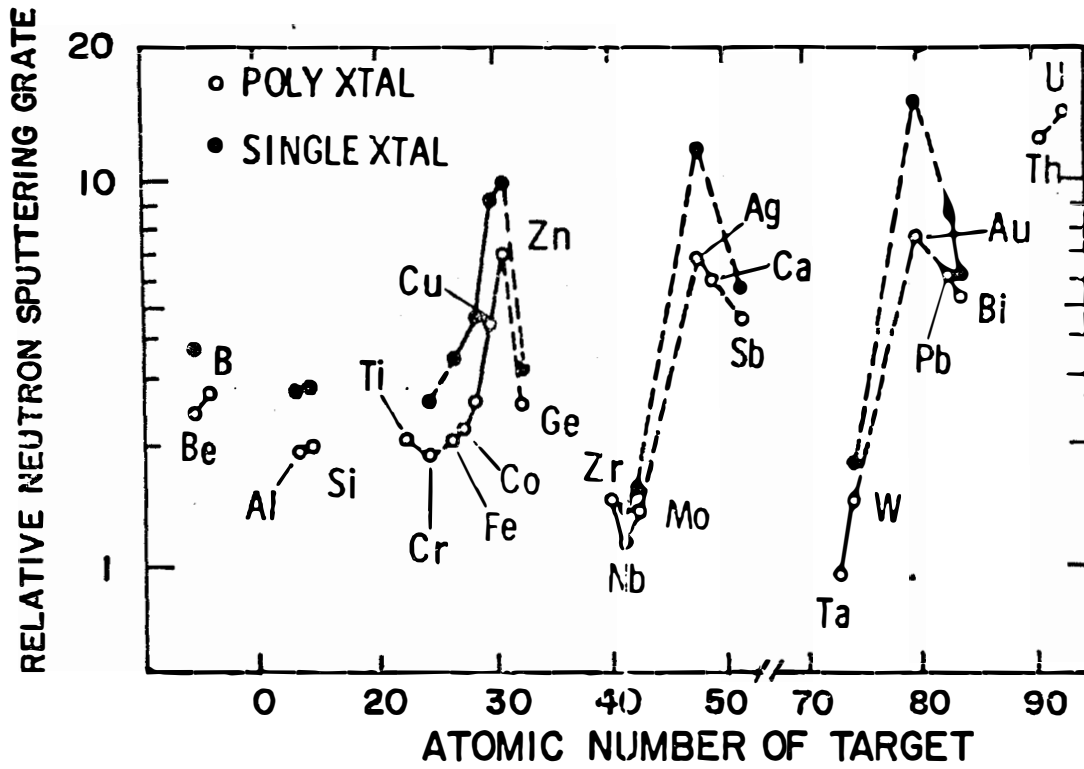
iiii) Design Equations for 316 SS

The erosion rate due to physical sputtering by many types of species may be calculated by

$$d(t) = \sum_{\mu} S_{\mu} \phi_{\mu} \frac{t A_w}{N_o \rho}$$

Figure VI-C-25

PERIODIC VARIATION OF
NEUTRON SPUTTERING RATE — GARBER et al.



where S_{μ} is the sputtering yield in atoms per particle for a

particular bombarding particle μ

ϕ_{μ} is the flux of the bombarding particle μ .

A_w is the atomic weight of the material

t is the irradiation time

N_0 is Avogadro's number

ρ is the density of the wall material

All of the factors in equation VI-C-23 are known with some certainty except S_{μ} . We will be faced with estimating this value for 316 SS without the benefit of any experimental data. Therefore, the sputtering ratio for iron will be estimated and it will be assumed that such a number also holds for the alloy-316 SS.

From Table VI-C-11, equation VI-C-22, and personal communication,⁽⁸⁴⁾ we will assume a value of S for 23 keV deuterium and tritium ions on Fe to be ~0.02 and 0.03 atoms/ion respectively.

Such a value is consistent with the calculations of Pease⁽⁷⁶⁾ for V and Cu which are close to Fe in mass and atomic number. The potential error in these numbers can be quite large (i.e. ± 0.01) so that considerable latitude should be given the results of these calculations.

The sputtering yield for helium ions will be estimated from data at lower energies and by comparison to similar elements at higher energies. For example, the value of S for 400 eV helium on Fe and Cu is 0.11 and 0.21 respectively.⁽⁷⁸⁾ McCracken and Erents have calculated the value of S for 10 keV helium on Cu to be 0.28 (close to value of 0.39 predicted from equation VI-C-22). If the ratio S_{Fe}/S_{Cu} is the same at 23 keV as it is at 0.4 keV, and if $S_{Fe, 10 \text{ keV}} \cong S_{Fe, 23 \text{ keV}}$ then $S_{Fe, 23 \text{ keV}} = 0.28 \times \frac{0.11}{0.21}$ or 0.15 atoms/ions. We

will extend this argument to the helium atoms which are in the process⁽⁸⁵⁾ of slowing down from 3.5 MeV to the plasma equilibrium of 11 keV. Mills has calculated that the average energy at the first wall will be ~100 keV from Table VI-C-11 and our previous Fe/Cu ratio we will estimate $S_{100 \text{ keV}} \cong 0.03$ atoms/ion.

The estimates of S for neutron sputtering can be broken up into two terms; one for 14 MeV neutrons and the other for back scattered neutrons. Recent experiments by Kaminsky⁽⁸⁴⁾ with 14 MeV neutrons suggest that $S=0.2$ for cold worked Nb at room temperature. Such a large S is found because of an unusual spike phenomena which causes large chunks of metal to be ejected. No explanation for such a large value has been made nor is it understood why it is almost two orders of magnitude from previous estimates. However, we will use this very pessimistic number which will if anything, tend to over estimate the wall

erosion rate.

The sputtering value for lower energy neutrons (i.e. 0.1 to 6 MeV) on Nb has been suggested to be 5×10^{-3} atoms/ion. (80) If one uses Garber's (83) values of the relative neutron sputtering rates, then a value of 9×10^{-3} atoms/neutron is predicted for iron. It must be remembered that neutron sputtering takes place on both sides of a wall, and proper care must be taken to include the value of two.

It must also be noted that the above estimates appear to be high in view of other early studies on neutron sputtering. Garber et.al. (83) suggest that S_{α} , for 14 MeV neutrons on Au is around 3×10^{-3} atoms/neutron. However, Figure VI-C-25 predicts that S for Au is 4.5 times higher than Fe for neutron sputtering. This means that optimistically the value of S for 14 MeV neutrons on Fe would be 6.67×10^{-4} atoms/neutron which is more than an order of magnitude lower than that for fission neutrons and more than two orders of magnitude below Kaminsky's recent value for 14 MeV neutrons. Nevertheless, we will continue our conservative approach and assume the worst possible wall erosion rates.

Finally, we must consider self atom sputtering. In calculating the self-sputtering rate, the following assumptions will be made. First, sputtering is assumed to occur uniformly over all first wall surfaces facing the plasma in the reactor. Also, all of the sputtered ions or atoms returning to the wall are distributed uniformly over the vacuum wall area. All wall atoms that make it back to the first wall have an energy of 23 KeV. Finally, because we assume a 90% efficient divertor, only 10% of the wall atoms sputtered are assumed to return to interact with the wall. The flux of wall atoms (mainly iron) returning to the wall, ϕ_{Fe} , is approximated by

$$\phi_{Fe} \approx 0.1 (S_D \phi_D + S_T \phi_T + S_{\alpha}^L \phi_{\alpha}^L + S_{\alpha}^H \phi_{\alpha}^H + S_n^{14} \phi_n^{14} + S_n^B \phi_n^B) \quad \text{VI-C-24}$$

Where S_D , S_T , S_{α}^L , S_{α}^H , S_n^{14} , and S_n^B are the sputtering yields in atoms/particle for deuterons, tritium ions, low energy alpha particles, high energy alpha particles, 14 MeV neutrons and back scattered neutrons respectively, and ϕ_D , ϕ_T , ϕ_{α}^L , ϕ_{α}^H , ϕ_n^{14} and ϕ_n^B are fluxes of deuterons, tritium ions, low energy and high energy alpha particles, 14 MeV neutrons and back scattered neutrons, respectively incident on the first wall.

Substituting the values in equation VI-C-24,

$$\phi_{Fe} \approx 0.1 [0.02 \phi_D + 0.03 \phi_T + 0.15 \phi_{\alpha}^L + 0.03 \phi_{\alpha}^H + 0.0091 \phi_n^L + 0.2 \phi_n^H.]$$

A self-sputtering coefficient for iron must now be chosen. Based on data presented by Kaminsky, (78) 45 KeV Fe⁺ ions incident on iron have a sputtering yield of 3 atoms/ion. Although no data is presented for the change in the self-sputtering coefficient with energy for iron, data is available for copper. (78) Based on this data, a self-sputtering coefficient of 2.5 is chosen for iron at KeV.

A summary of S and the wall erosion constants based on equation VI-C-23 is given in Table VI-C-12. The values in this table constitute the terms in the design equation for 316 SS.

Table VI-C-12

Summary of Potential Wall Erosion Rates Due to Sputtering

<u>Species</u>	<u>Energy keV</u>	<u>S atom/particle</u>	<u>mm/year per unit flux</u>
D	23	0.02	7.2×10^{-17}
T	23	0.03	1.09×10^{-16}
He	23	0.15	5.45×10^{-16}
He	~100	0.03	1.09×10^{-16}
Metal Ions (Fe,Cr,Ni,etc)	23	2.5	9.1×10^{-15}
n(14.1 MeV)	14.1	0.2	1.45×10^{-15} *
n(back scattered)	0.1 <E <14.1	0.009	6.53×10^{-17} *

* includes both sides of first wall

b) Blistering

Irradiation of metal surfaces with energetic charged particles can not only cause atoms to be sputtered from the first wall, but it can cause severe surface roughening and blistering (84). Qualitatively, the energetic ions (only hydrogen and helium isotopes will be considered here) displace atoms as they penetrate the solid. When they lose most of their energy, they slow down and become trapped because of their low diffusivity. Since the solubility of some of the gases in metals (e.g. helium) is extremely small, most of the gas precipitates into small bubbles. These small bubbles are formed near the end of the range for the gas atom and this region also corresponds with that for maximum vacancy production. The bubbles can capture these vacancies, grow and eventually coalesce with other bubbles to form lenticular bubbles below the surface of the metal. If enough atoms are injected at an elevated temperature, the pressure in these bubbles will be high enough to deform the metal surface causing it to protrude above the original surface. Eventually, this "blister" can rupture causing a large flake of the wall material to be spalled off.

Blister formation has been found with helium ions in Nb (87-95), Mo (93, 96-97), W (98), Pd (99), Cu (100), V alloys (90, 93, 95), and stainless steel (99, 101, 102). There have also been some instances where blisters have been formed by deuteron irradiation of Nb (95, 103), Mo (47), Be (97), and stainless steel (97). No attempt will be made here to review the literature and the reader is referred to articles listed above for a more extensive bibliography.

At the present time the size, density, and shape, and critical fluence for the formation of blisters is known to be a function of at least nine parameters:

1. Energy of ions (i.e. their range) (89, 91)
2. Diffusivity of injected ions (90)
3. Solubility of gas atoms in matrix (90)
4. Yield strength of the metal (96)
5. Temperature of the metal during bombardment (88-91, 93, 103)
6. The dose rate of bombarding ions (95)
7. Total dose (87, 89-91)
8. The orientation of the crystal structure to the ion beam (88-92)
9. The metallurgical state of the sample prior to irradiation, i.e., cold worked vs annealed (87, 90)

The occurrence of this phenomenon is so recent that no comprehensive theory has been developed to adequately predict the extent of wall erosion due to blistering. In the absence of such a theory, we will only be able to estimate the erosion rates based on simple concepts.

There have been three recent studies which have dealt with blistering in austenitic stainless steel.

Bauer and Thomas (102) have studied the temperature dependence of helium re-emission from 316 SS after 300 keV bombardment. The samples were implanted at a flux of $6.25 \times 10^{13} \text{cm}^{-2} \text{sec}^{-1}$. It was found that fractured helium blisters could be observed on the steel surface coincident with the sudden and dramatic release of helium. The critical fluence for blister formation was $\sim 1.4 \times 10^{18} \text{cm}^{-2}$ at -170°C , $1 \times 10^{18} \text{cm}^{-2}$ at 300°C , $7 \times 10^{17} \text{cm}^{-2}$ at 500°C and $\sim 4 \times 10^{17}$ at 700°C .

Irradiation beyond the critical fluence causes further blisters to form and burst and eventually several layers of surface are exfoliated. Figure VI-C-26 shows an example of 316 SS irradiated to $4 \times 10^{18} \text{cm}^{-2}$ at 500°C which has gone through 4 sequences of blister formation growth, rupture and exfoliation. A summary of Bauer and Thomas' results (102) is shown in Table VI-C-13.

Table VI-C-13

Summary of 300 keV Helium Implantation in 316 SS (102)

<u>Implantation Temperature Region °C</u>	<u>Surface Deformation</u>	<u>Critical Dose for Blister Rupture, cm^{-2}</u>	<u>Dominant Helium Release Mechanism</u>
$\leq -50^\circ\text{C}$	Mostly Blisters	14×10^{17}	Blister Cracking
-50°C to 500°C	Flaking	$7-14 \times 10^{17}$	Exfoliation
$>600^\circ\text{C}$	Blisters	$4-7 \times 10^{17}$	Blister Cracking Some bubble migration to surface.

Verbeek and Eckstein (97) injected H^+ , D^+ and He^+ into 4301 stainless steel at 15 and 150 keV. Blisters were formed in steel at both ion energies and it was found that the critical fluence for the occurrence of blisters at 300°K was $1.2-4 \times 10^{17} \text{cm}^{-2}$ for 15 keV helium bombardment. Blisters are even formed by 15 keV D^+ ions at 27 and 347°C . The critical fluence for blister formation was $\sim 5 \times 10^{18} \text{cm}^{-2}$ and the blisters appeared to be closely associated with grain boundaries and precipitates. It was concluded that hydrogen isotope blisters do not significantly contribute to wall erosion even though they may cause localized pitting.

Das and Kaminsky (101) have investigated the blister formation in 304 SS between room temperature and 550°C . Five hundred keV helium ions were used. It was concluded that the maximum temperature for blister exfoliation occurs at $\sim 500^\circ\text{C}$ and that the effective value of S (hereafter referred to as S') at that temperature is 0.48. This value dropped to 0.22 at room temperature. Both of these values are consistent with previous work which yield $S' \approx 0.1$ for V at RT and 600°C , and $S' = 0.2$ for Nb at RT (91,92,95). More recent work by Kaminsky (84) has yielded S' values of 3 for 100 keV ions on 304 SS. It appears that the lower energies are more effective in removing the surface layers in steel.

┌ 300 μ ─



300°C



500°C

Figure VI-C-26 Surface of 316 SS after 300 KeV helium ion injection. Fluence = 4×10^{18} cm⁻². Note several layers have been exfoliated at 500° (102).

VI-C-62

A crude method to estimate the maximum wall erosion rate is to assume that when the critical fluence is reached, an entire layer of the metal equal in thickness to the range of the incoming particle will be exfoliated. (Note: This is a rather conservative approach as experience shows that not all the surface comes off at one time). Figure VI-C-27 shows the projected ranges, R, of helium, deuterium and tritium in stainless steel. Given this range-energy relationship the effective wall erosion rate can be calculated by

$$S' = \frac{R}{(\phi t)_c} \times \frac{N_o \rho}{A_w} \approx \frac{R}{(\phi t)_c} (8.7 \times 10^{22}) \quad \text{VI-C-25}$$

where $(\phi t)_c$ is the critical fluence for exfoliation.

For 300 keV helium, $R \approx 0.98$ microns, $(\phi t)_c \sim 10^{18} \text{ cm}^{-2}$ and the value of $S' \approx 8$. Such a number is an order of magnitude above Das and Kaminsky's 500 keV value but less than a factor of 3 larger than the 100 keV data. This high value of S' indicates the large degree of conservatism built into this simple model. Some of the helium may get to the surface without forming major blisters while other helium certainly "leaks" out from the subsurface when a blister bursts.

The calculations of wall erosion in UWMAK-I will include a value of $S' \approx 3$ for 100 keV helium consistent with the Das and Kaminsky value for 100 keV particles. We will assume that 23 keV helium blistering occurs with $S' \approx 1$ due to the shorter ranges (Eq. VI-C-25). However, the latter assumption may underestimate the wall erosion rates and future data should be closely examined.

It is very difficult at this time to assess wall erosion due to D^+ and T^+ bombardment. Verbeek and Eckstein (97) have shown that the threshold fluence is a factor of 10 higher for the hydrogen isotopes compared to helium and that the blister formation is very inhomogeneous. We will take a very conservative approach at this time for hydrogen blistering and assume that the effective wall erosion rate is $\sim 1/100$ that of equivalent energy helium, yielding a value of $S' \approx 0.01$.

The design information for blistering in UWMAK-I is given in Table VI-C-14. It is noted that the wall erosion rates are much higher per unit of fluence for 23 keV helium than for the hydrogen isotopes. However, the increased D^+ and T^+ fluxes to the first wall will tend to equalize the wall erosion rates. The predominant wall erosion rate per unit of flux is the ~ 100 keV helium ions and efforts must be made to limit the ions of that energy from striking the wall.

RANGE OF CTR PLASMA IONS IN 316 SS

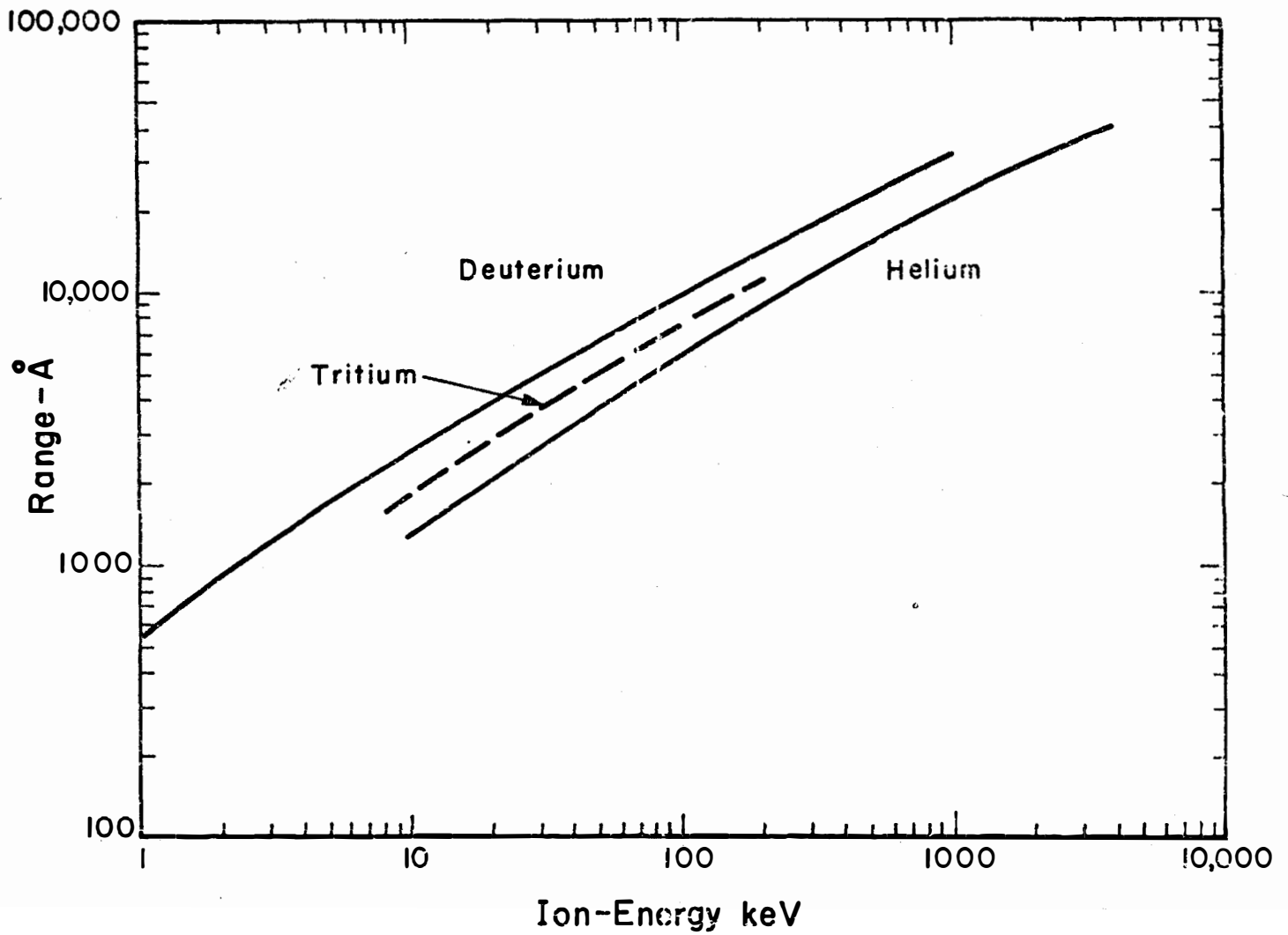


Figure VI-C-27

Table VI-C-14

Summary of Potential Wall Erosion Rates Due to Blistering

<u>Ion</u>	<u>Energy-keV</u>	<u>S'Atom/ion</u>	<u>mm/year</u> <u>Per Unit of Flux</u>
D ⁺	23	0.01	2.5 x 10 ⁻¹⁷
T ⁺	23	0.01	2.5 x 10 ⁻¹⁷
He	23	1	2.6 x 10 ⁻¹⁵
He	100	3	1.1 x 10 ⁻¹⁴

VI-D Specific Effects in UWMAK-I Blanket

1) Swelling

a) Void Swelling in 316SS

The design equations for solution treated (ST) and 20% cold worked 316SS given in Section VI-C-1-b have been used to calculate the swelling profiles to be expected in the UWMAK-I heat removal cells. The general schematic used for the calculations is shown in Figure VI-D-1. We have calculated the swelling at 9 points along the first wall at temperatures ranging from 300-500°C and exposures equivalent to 2, 10 and 30 years. The dpa values used for this work are plotted in Figure VI-D-2. The swelling has also been calculated for the steel 10, 20, and 30cm from the first wall at temperatures of 325°, 375°, 425°, 475°, and 500°C. The results are listed in Table VI-D-1 and displayed in Figure VI-D-3,4.

The first point to note in Table VI-D-1 is that if the heat removal cells are changed every two years the maximum swelling values in the first wall might vary from 0.25 to 7.9% depending on whether 20% cold worked or solution treated 316SS is used, respectively. It is felt that we could stand swelling values up to as much as 10% at the end of life without compromising the integrity of the first wall. Therefore either ST or 20% CW 316SS could be used for the UWMAK-I first wall for 2 year operation.

The second point to note is that swelling values at 10, 20, and 30 cm from the first wall are all negligible for CW 316 SS over the 2 year wall lifetime.

The third point of interest is the swelling gradients that will exist in the front wall and support struts for the heat removal cells. (e.g. Figure VI-D-4) The swelling is most pronounced at the highest temperature end of the cells and will fall quite rapidly as one proceeds towards the lithium inlet side of the section. Bending moments and stress gradients will obviously result from this arrangement but the magnitude of these stresses have not been calculated yet. Figures VI-D-5,6 show how much of a heat removal cell will be above 1, 5, 10, 20, 50 and 100% swelling for 10 and 30 year operation. The information in Figures VI-D-5,6 is summarized in Table VI-D-2 and it can be seen that swelling in ST 316SS is totally unacceptable for 10 and 30 year exposure. It is predicted that 6% of the structure will experience >100% swelling and almost 1/3 of the cell will swell more than 10%. The use of 20% cold worked steel will significantly reduce the swelling. After 10 years exposure only 10% of the structure will swell more than 10%. However after 30 years, almost 1/3 of the CW 316SS heat removal cell will swell more than 10% and 1% of the structure will expand more than 50%.

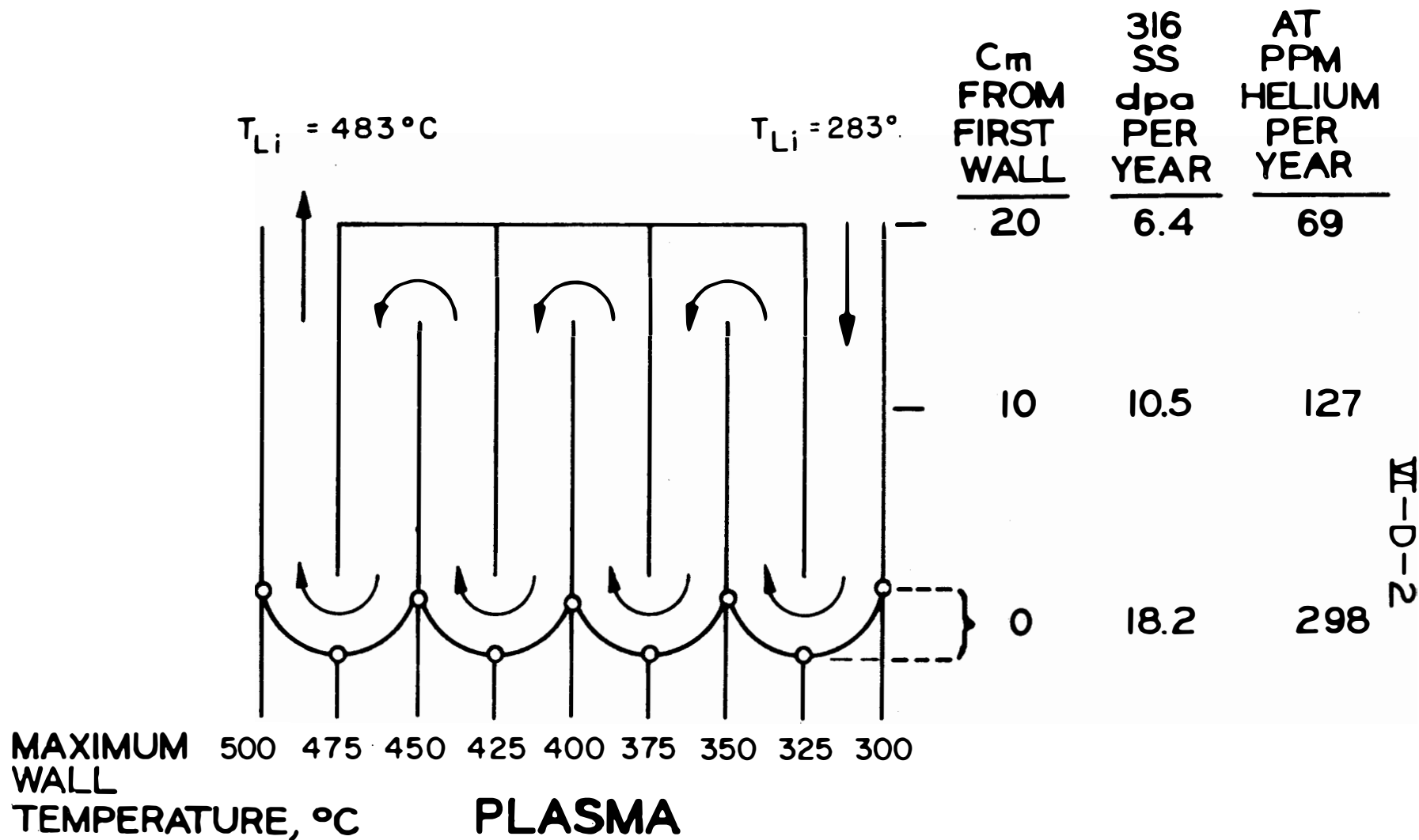


FIGURE VI-D-1 SPATIAL DISTRIBUTION OF TEMPERATURE AND DAMAGE IN UWMAK-I

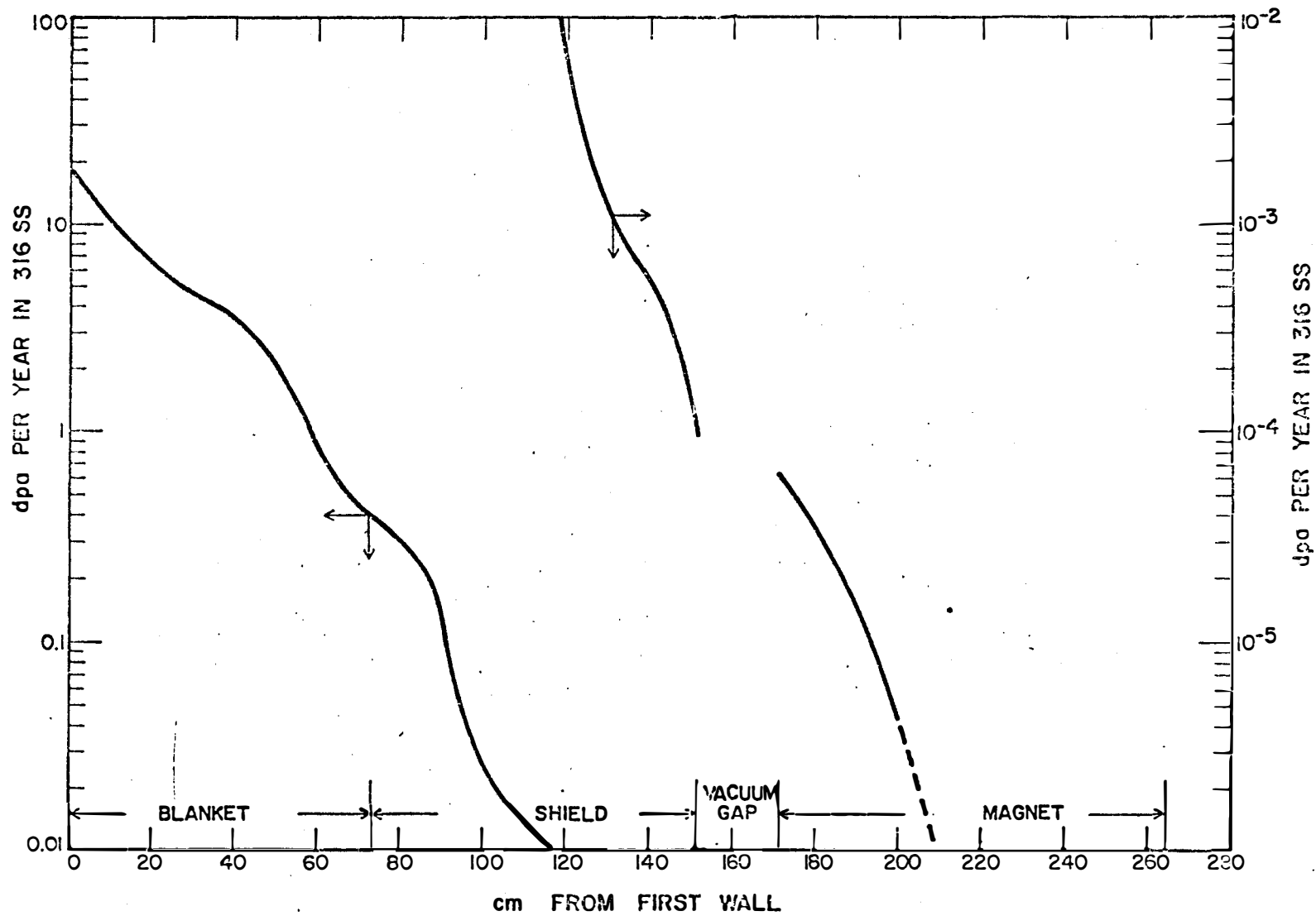
Table VI-D-1
Summary of Anticipated Swelling Behaviour of 316 Stainless Steel in UWMAK-I

Distance from First Wall-cm	Temperature oC	Damage Level dpa/year	%ΔV/V _o					
			2 years		10 Years		30 Years	
			Solution Treated	20% Cold Worked (a)	Solution Treated	20% Cold Worked	Solution Treated	20% Cold Worked
0	300	18.2	0.42	<0.1	1.5	<0.1	3.0	<0.1
0	325	18.2	0.51	<0.10	1.7	<0.1	4.0	0.1
0	350	18.2	0.59	<0.1	2.1	0.2	5.0	0.65
0	375	18.2	0.75	<0.1	3.2	0.8	8.6	2.5
0	400	18.2	1.2	0.14	7.6	2.4	26	7.5
0	425	18.2	2.2	0.19	28	6.2	>100*	21
0	450	18.2	4.8	0.24	>100*	10	>100*	34
0	475	18.2	7.1	0.24	>100*	17.5	>100*	57
0	500	18.2	7.9	0.25	>100*	25	>100*	80
10	325	10.5	0.38	<0.1	1.1	<0.1	2.6	<0.1
10	375	10.5	0.61	<0.1	2.0	<0.1	5.3	1.4
10	425	10.5	0.99	<0.1	12	2.5	65	8.5
10	475	10.5	2.3	<0.1	69	8	>100*	30
10	500	10.5	2.4	<0.1	87	13	>100*	48
20	325	6.9	0.26	<0.1	0.82	<0.1	1.8	<0.1
20	375	6.9	0.4	<0.1	1.3	0.25	3.8	0.9
20	425	6.9	0.55	<0.1	6.0	1.4	34	7.3
20	475	6.9	0.51	<0.1	28	4.5	>100*	20
20	500	6.9	1.0	<0.1	35	6.7	>100*	29
30	325	4.6	0.19	<0.1	0.6	<0.1	1.3	<0.1
30	375	4.6	0.22	<0.1	0.9	0.13	2.4	0.6
30	425	4.6	0.31	<0.1	3.3	0.58	16	4.2
30	475	4.6	0.38	<0.1	16	1.6	>100*	13
30	500	4.6	0.36	<0.1	14	3.6	>100*	18
40	500	3.2	0.15	<0.1	6.2	0.38	80	11
50	500	2.2	<0.1	<0.1	2.5	<0.1	30	5.8
60	500	0.87	<0.1	<0.1	0.36	<0.1	3.8	<0.1

*Values not considered as reliable
(a) Nominal equation VI-C-10

FIG. VI -D-2

CALCULATED DISPLACEMENT RATE FOR 316 SS IN UWMAK-I (WALL LOADING 1.25 MW/m²)



VI-D-2A

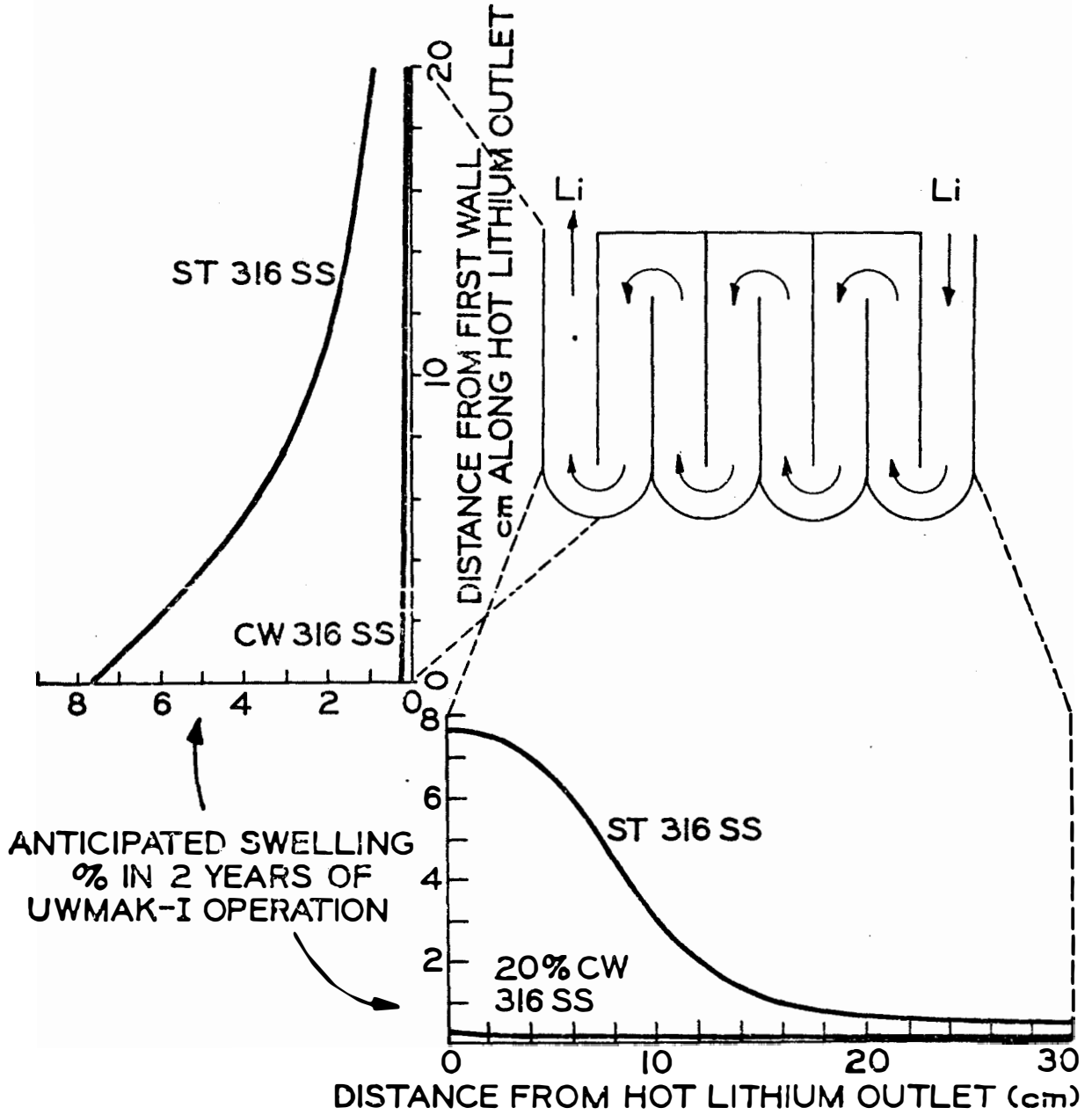


FIGURE VI-D-3
 ANTICIPATED SWELLING IN UWMak-I HEAT REMOVAL CELLS
 AFTER 2 YEARS OF OPERATION

VI-D-6

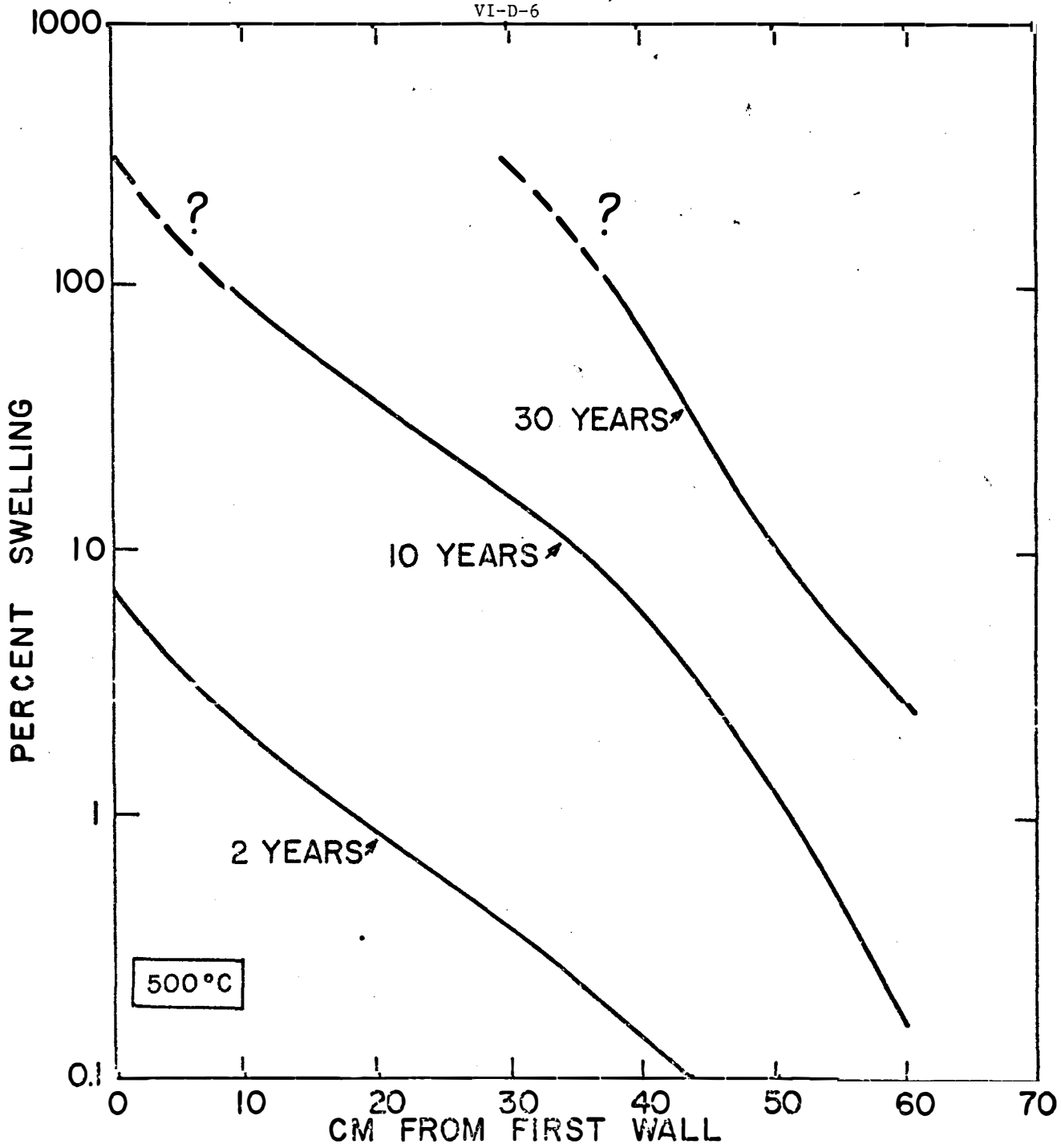


Figure VI-D-4a

ANTICIPATED MAXIMUM SWELLING FOR
20% CW 316 SS IN UWMAK-1 BLANKET

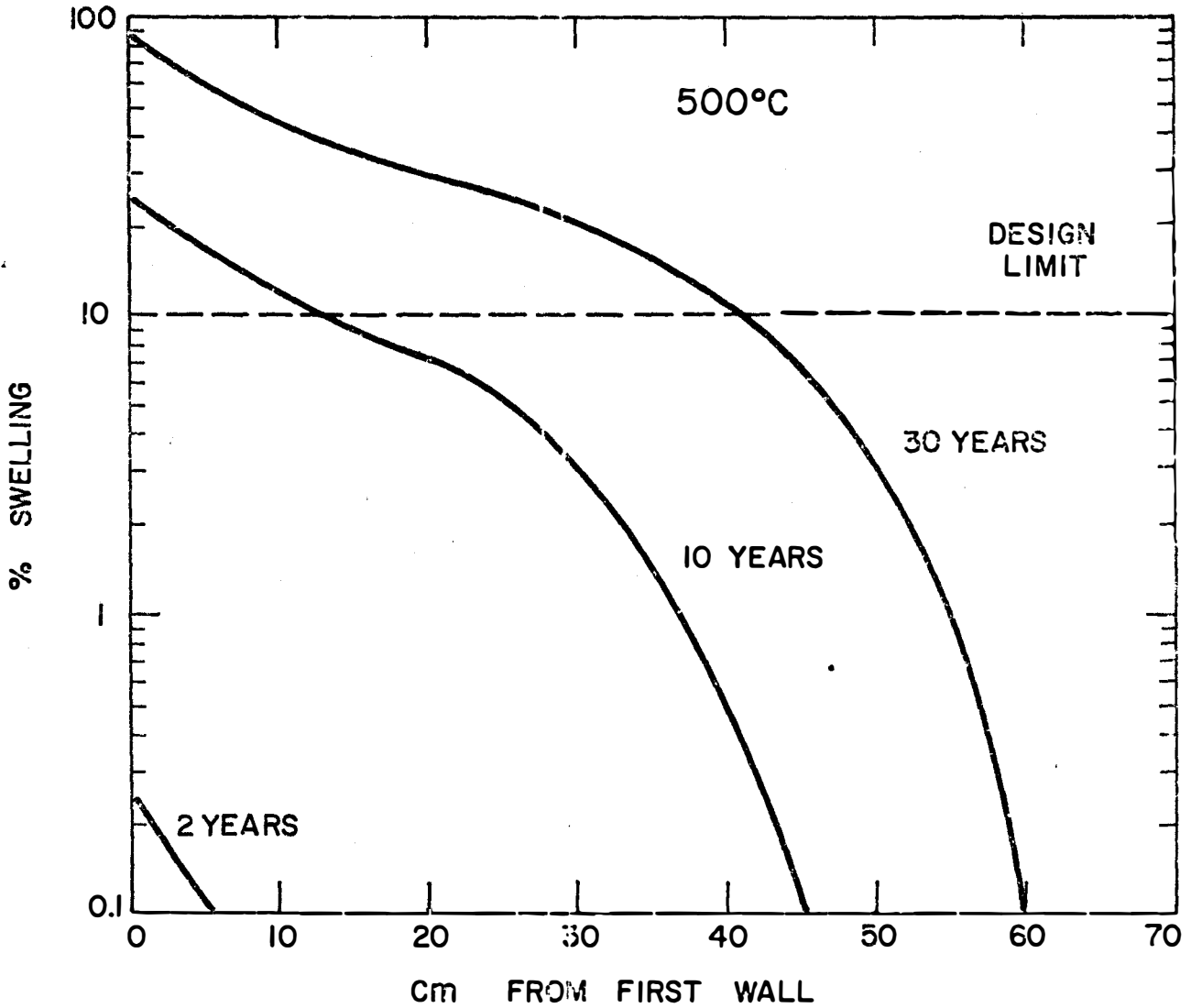
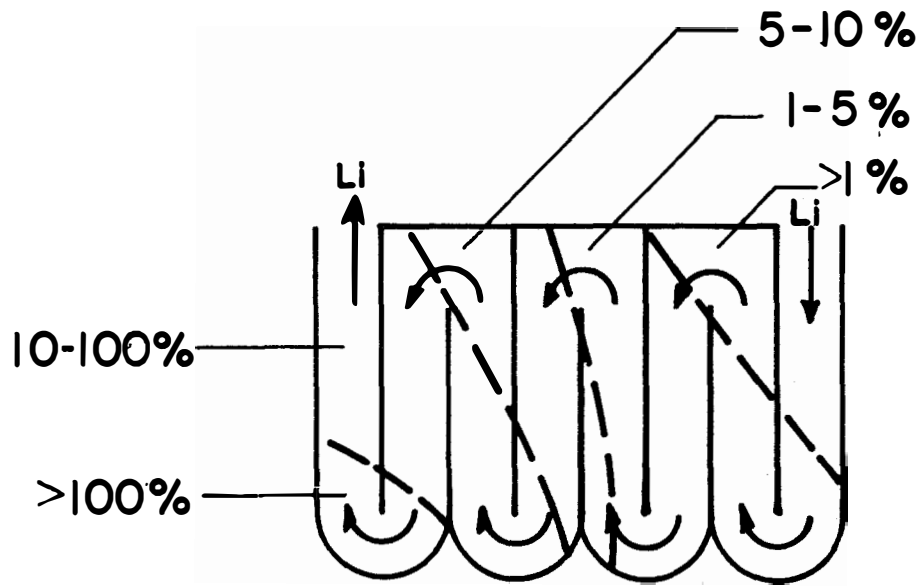
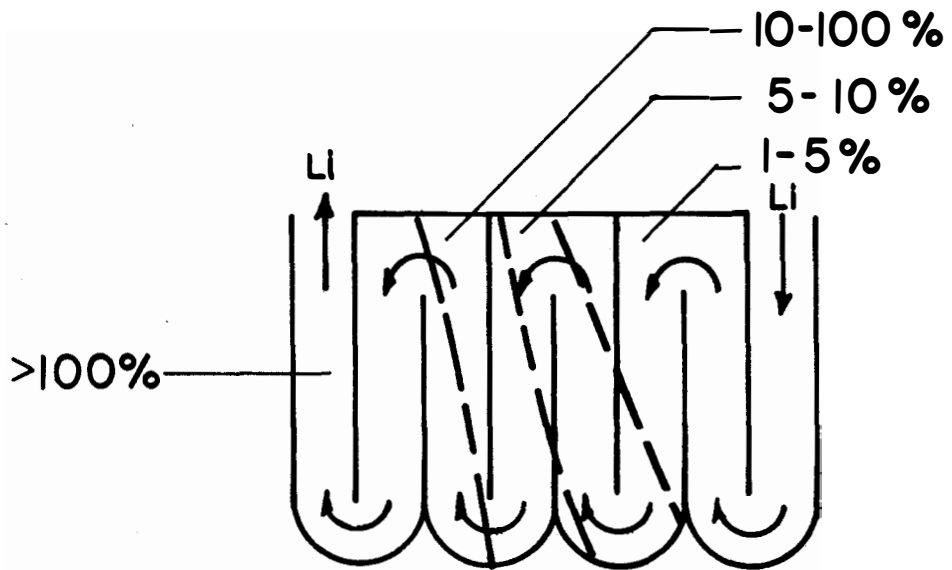


FIGURE VI-D-4b



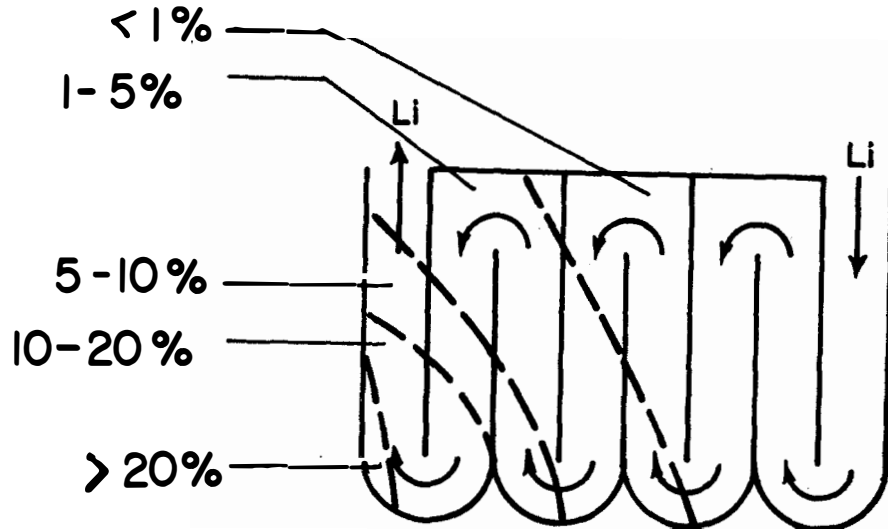
a) 10 Years



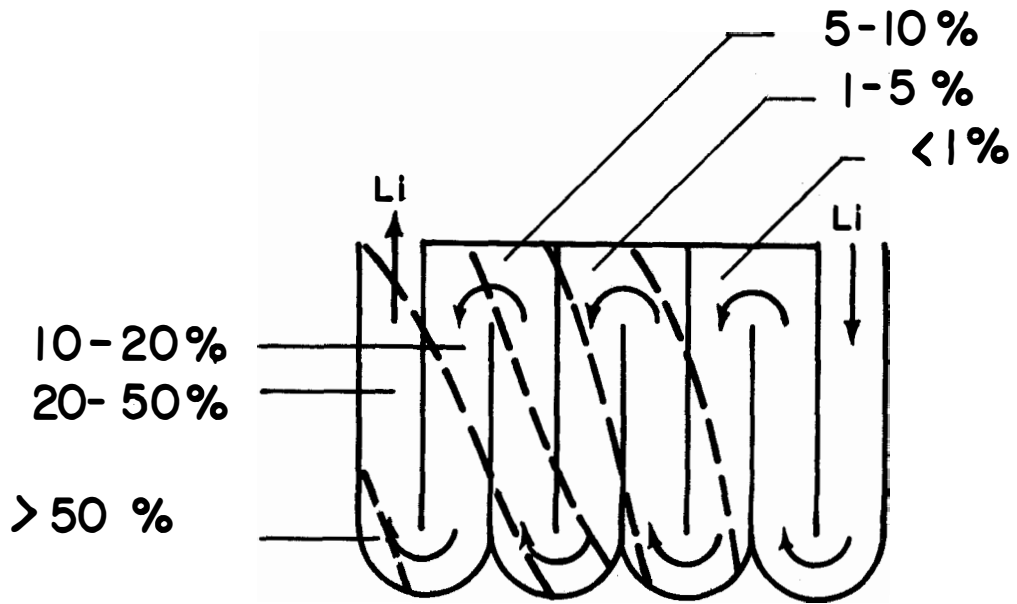
b) 30 Years

**ANTICIPATED SPATIAL DISTRIBUTION OF SWELLING
IN UWMak-1 HEAT REMOVAL CELL ST 316 SS**

Figure VI-D-5



a) 10 Years



b) 30 Years

**ANTICIPATED SPATIAL DISTRIBUTION OF SWELLING
IN UWMak-1 HEAT REMOVAL CELL 20% CW 316 SS**

Table VI-D-2

Anticipated Spatial Distribution of
316SS Swelling in UWMAK-I

	<u>Percent of Heat Removal Cell in Swelling Range</u>					
	<u><1%</u>	<u>1-5%</u>	<u>5-10%</u>	<u>10-50%</u>	<u>50-100%</u>	<u>>100%</u>
ST 316SS						
2 years	69	24	7	-	-	-
10 years	14	4	15	13	11	6
30 years	-	40	16	8	7	29
20% CW 316SS						
2 years	100	-	-	-	-	-
10 years	57	26	7	10	-	-
30 years	44	16	12	28	1	-

The question of how long one could operate UWMAK-I and still not exceed the arbitrary 10% swelling limit can now be answered. This time is only slightly longer than 2 years for ST 316SS and ~5 years if 20% CW 316SS were used. These short times make the concept of a changeable first vital even without other limitations such as ductility, decreases, surface effects, or corrosion. Once a reasonable procedure has been worked out, the question of changing the heat cells every 2, 5, or 10 years is only a question of economics. It is quite apparent that unless some saturation of the swelling takes place, there is no way of making the 316SS first wall last for a 30 year plant lifetime.

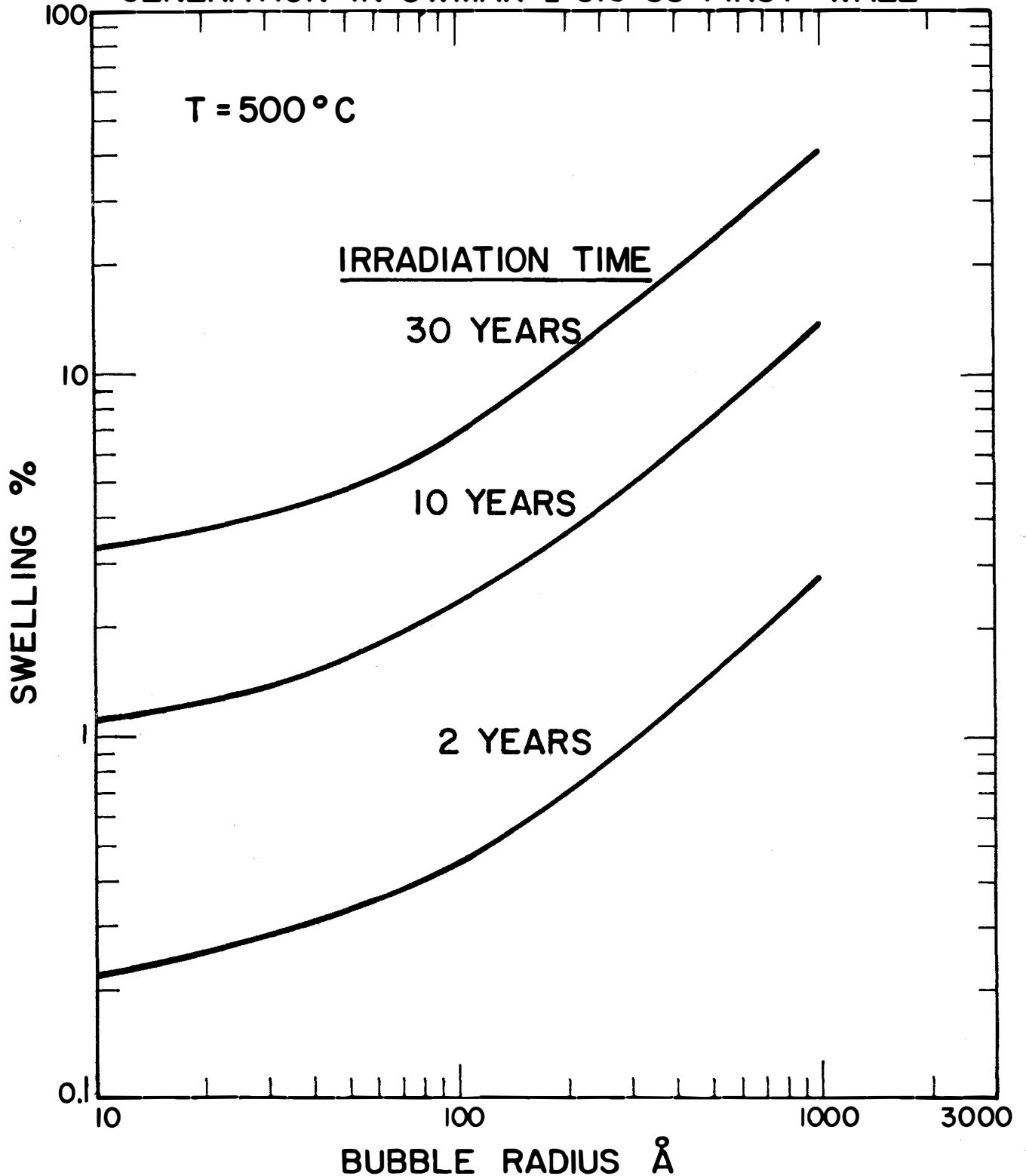
The swelling for the stainless steel which is more than 30 cm from the first wall should also be investigated. It is seen that in the region between 30 and 40 cm from the first wall, (Figure VI-D-4b) the swelling in the Li outlet header will exceed 10% after 30 years of operation even if CW 316SS is used. However, it is questionable whether the desired level of cold work can be retained over a 30 year (260,000 hr) time period at 450-500°C and the swelling may be more characteristic of the solution treated material. If that were true, then swelling values in excess of 100% may take place in the header region over the 30 year anticipated life of a reactor. (See Figure VI-10-4a) Changing the headers every 5-10 years may be a difficult job. It is also noticed from Table VI-D-1 that 316SS farther than 40 cm from the first wall (the reflector region) should be able to operate for the entire reactor lifetime without replacement.

b) Gas Bubble Swelling in 316 SS

Table VI-D-3 lists the gas atoms produced per cm^3 per year of irradiation as a function of distance from the first wall. We will assume that the hydrogen is soluble in 316 SS such that there will be no bubbles produced by that element. Furthermore, it is noted that at the operating temperatures of UWMAK-I, $T_{\text{max}} = 500^\circ\text{C}$, the Brownian diffusion of He is so slow that very few if any bubbles should form, even up to temperatures of $\sim 600^\circ\text{C}$. However, it is possible that in the presence of stress or temperature gradients, there may be limited bubble formation. We will calculate the swelling as if all the helium atoms were to collect into bubbles of various sizes (or densities) which should represent the worst possible case.

The maximum swelling in the first wall due to complete helium atom agglomeration is shown in Figure VI-D-7 for irradiation times of 2, 10 and 30 years. The results are listed in tabular form in Table VI-D-3. It is noticed that if the helium atoms collect into small bubbles ($r = 10\text{\AA}$) swelling would not exceed 3.3% even after 30 years of irradiation. The number density implied by the 10\AA radius bubbles varies from $6.5 \times 10^{16}\text{cm}^{-3}$ after 2 years to $9.8 \times 10^{17}\text{cm}^{-3}$ after 30 years of irradiation. The average spacing between the bubbles in the

FIG. VI - D - 7

MAXIMUM POSSIBLE SWELLING DUE TO HELIUM
GENERATION IN UWMAK-I 316 SS FIRST WALL

latter case is only $\sim 100 \text{ \AA}$ or ~ 17 lattice spacings. Such a diffusion distance is not too unreasonable. On the other hand, the average bubble spacing after 30 years if the bubbles are 1000 \AA in radius is $\sim 4400 \text{ \AA}$. This spacing increases to $10,600 \text{ \AA}$ for after 2 years of irradiation. It is expected that this latter spacing is too large for helium collection and hence it is extremely unlikely that such large bubbles will be formed at $T \leq 500^\circ\text{C}$.

It is concluded that helium gas bubble induced swelling of $< 0.3\%$ might be expected after 2 years of irradiation and this might rise to $\sim 3-7\%$ if the first wall was irradiated for 30 years. Such swelling values are of concern, but thought to be tolerable. The biggest uncertainty in this brief analysis is the synergistic effect of void and bubble induced swelling.

Table VI-D-3

Maximum Helium Gas Bubble Induced Swelling in the UWMAK-I First Wall After 2, 10 and 30 Years of Irradiation at 500°C *

<u>Irradiation Time-yr</u>	<u>Helium Gas Atoms/cm³</u>	<u>Percent Swelling for Given Bubble Radius**</u>		
		<u>10A</u>	<u>100A</u>	<u>1000A</u>
2	5.05×10^{19}	0.22	0.45	2.8
10	2.53×10^{20}	1.1	2.3	14
30	7.6×10^{20}	3.3	6.8	42

*Assuming all gas atoms collect into bubbles, an extremely unlikely circumstance at $< 500^\circ\text{C}$

**Assume $\gamma = 1000 \text{ ergs/cm}^2$, $b = 4 \times 10^{-23} \text{ cm}^3 \text{ atom}^{-1}$

VI-D-2 Mechanical Property Changes in 316 SS

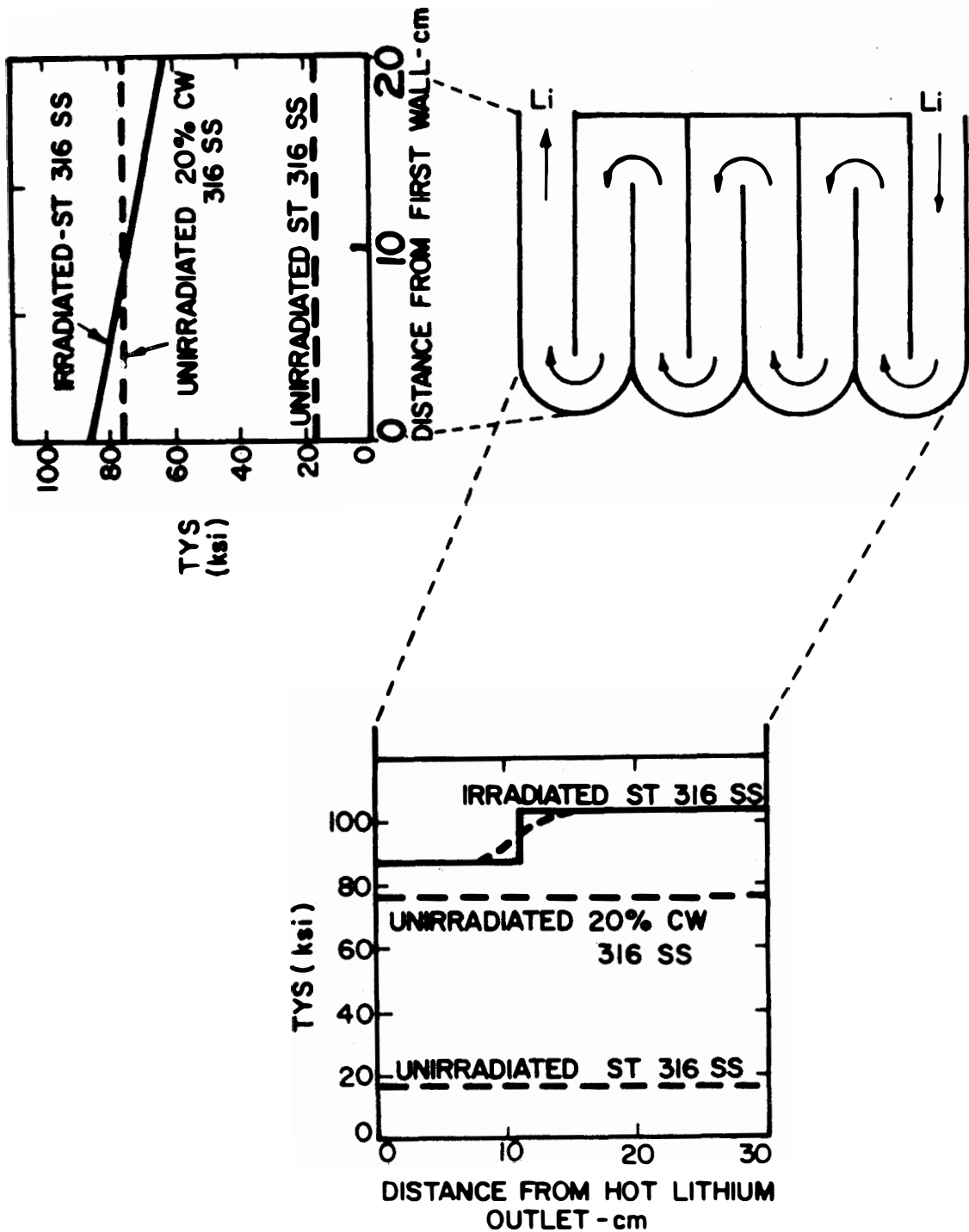
It is now possible to utilize the information in Section VI-C-3 to calculate the increase in TYS and decrease in uniform elongation due to irradiation in UWMAK-I. We have calculated the time and spatial variations in the heat removal cell in much the same way as was done in Section VI-D-1.

a. Changes in Yield Strength

The results for the change in TYS are shown in Figure VI-D-8. First of all, since we have no reliable design equation for the effect of

FIG. VI-D-8

ANTICIPATED CHANGE IN YIELD STRENGTH IN 316 SS AFTER 2 YEARS OF OPERATION



irradiation on cold worked 316 SS we will only quote the effect of irradiation on the TYS of ST 316 SS. Secondly, because of the lack of data for ST 316 SS below 422°C, we have assumed that the yield strength is only a function of displacement damage below that temperature. Hence, we have used the design equation given in Table VI-C-3 at 426°C to apply at all temperatures below 426°C & above 300°C. The equation for 482°C has been used to apply to all the temperatures between 426 and 500°C. A crude attempt has been made to match the data at 426°C.

It is noted that the TYS of a solution treated 316 SS first wall is increased by a factor of 5-6 after two years of irradiation. The steel is also hardened throughout the 20 cm depth of the heat removal cell as is shown in Figure VI-D-8; the components 20 cm from the first wall are still almost 4 times stronger at the yield point than the unirradiated material.

The unirradiated TYS of cold worked 316 SS is also given in Figure VI-D-8. Note that it is almost 4 times stronger than the ST 316 SS before irradiation and from Figure VI-C-5 we see that irradiation should have a relatively smaller effect on the TYS of cold worked steel.

The extent of the hardening can be seen in Figure VI-D-9 where the TYS of ST 316 SS is plotted vs distance from the first wall after 2, 10 and 30 years of irradiation for an isotherm of 482°C. (See also Table VI-D-4) There are three important points of this figure. First, the hardening effect of irradiation will extend throughout the entire blanket after 2 years of irradiation. Second, the design equation for 316 SS is probably not applicable above 110 ksi and it is quite possible that we might get a saturation in the yield strength somewhere 100-120 ksi. Saturation would only be important for a 30 year wall life. Finally, the irradiation induced hardening will probably extend back into the shield. However, since there is no data on 316 SS at high exposures and 200°C, it is difficult to estimate the absolute magnitude of TYS increase in threshold.

It is concluded from this investigation that the entire heat removal cell region will be hardened during its two year lifetime and that the TYS of the metal components in the header and reflector region will be increased by a factor of 3-4 over a 30 year exposure.

FIG. VI - D - 9
 ANTICIPATED YIELD STRENGTH OF ST 316 SS
 IN UWMAK-I BLANKET AND SHIELD

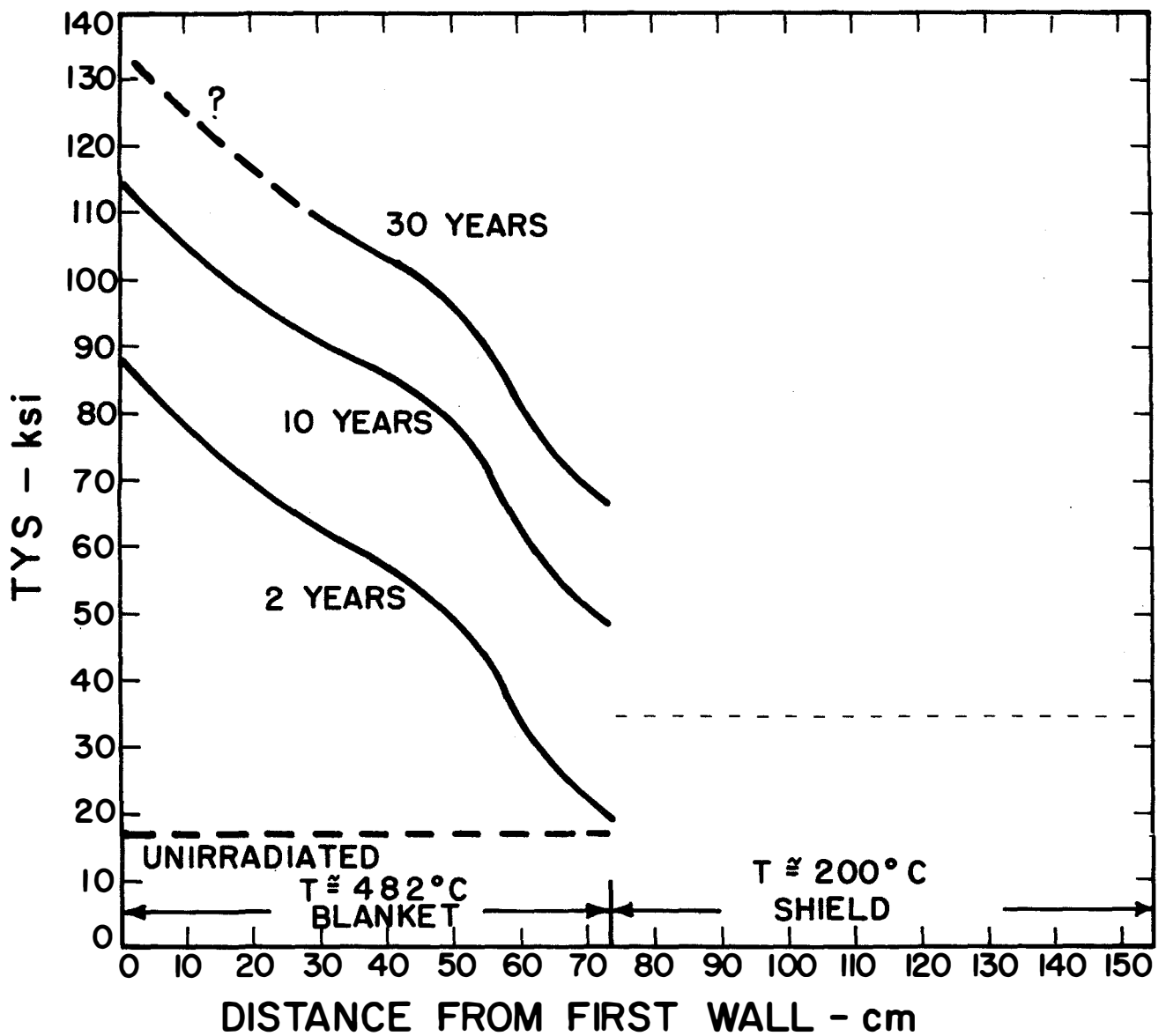


Table VI-D-4

Anticipated Change in Tensile Yield Strength For
ST 316 SS at 482°C

<u>Distance From First Wall - Cm</u>	<u>dpa per Year</u>	<u>TYS^{a)}</u>		
		<u>2 Years</u>	<u>10 Years</u>	<u>30 Years</u>
0	18.2	87	115 ^{b)}	134 ^{b)}
10	10.5	77	105	125 ^{b)}
20	6.9	70	98	117 ^{b)}
30	4.6	63	91	110
40	3.2	56	85	104
50	2.2	50	80	97
60	0.87	33	62	81
70	0.45	22	50	69
80	0.30	17	43	62
90	0.15	17	30	50
100	0.028	17	17	21
110	0.014	17	17	17

a) See equation in Table VI-C-3

b) Above limit of formula

b. Loss of Ductility in UWMAK-I Heat Removal Cells

It is clear from Section VI-C-3 that embrittlement will be a severe problem for CTR's constructed with stainless steel, or any other material for that matter. We have calculated the expected ductility (% uniform elongation) remaining in the UWMAK-I blanket material after several irradiation times. The results are listed in Table VI-D-5 and displayed in Figure VI-D-10. It should be noted that we are again forced to using design data for ST 316 SS instead of that applicable to the cold worked alloy. We have also assumed that the design data for 426°C (Figure VI-C-10) applies to all irradiation temperatures from 300-426°C. The damage incurred between 426 and 500°C will be described by the 482°C data. Since the design limitation occurs when the uniform elongation of any part of the heat removal cell drops below 0.5%, it is not too critical to describe the behavior at all of the temperatures.

It can be seen from Table VI-D-5, that after one year of UWMAK-I perhaps only the first wall has reached the 0.5% elongation limit. However, within the next year the first 20 cm will have reached that limit. In fact, within 3 years of irradiation 30 cm of the blanket will have uniform elongation values of <0.5%.

A rather disturbing feature of Figure VI-D-10 is the fact that even the 316 SS in the header region will fall below the ductility limit after 10 years of irradiation. Within 30 years, the projected lifetime of the plant, we will find that the entire blanket structure will be below or close to the design limit.

Table VI-D-5
Anticipated Ductility Changes in UWMAK-I
Structure Material (316 SS)

Distance From First Wall - cm	Temp- ature °C	Damage Level dpa/year	Uniform Elongation Remaining %			
			1 yr.	2 yrs.	10 yrs.	30 yrs.
0	300-426	18.2	<0.5	<0.5	<0.5	<0.5
0	426-500	18.2	<0.5	<0.5	<0.5	<0.5
10	300-426	10.5	4	<0.5	<0.5	<0.5
10	426-500	10.5	5	<0.5	<0.5	<0.5
20	300-426	6.9	7	~0.5	<0.5	<0.5
20	426-500	6.9	9	~0.5	<0.5	<0.5
30	300-426	4.6	11	4	<0.5	<0.5
30	426-500	4.6	15	8	<0.5	<0.5
40	300-426	3.2	15	8	<0.5	<0.5
50	300-426	2.2	20	12	<0.5	<0.5
60	300-426	0.87	27	19	5	<0.5
70	300-426	0.45	35	27	12	~0.5

ANTICIPATED UNIFORM ELONGATION REMAINING
IN 316 SS AFTER IRRADIATION IN UWMAK-1

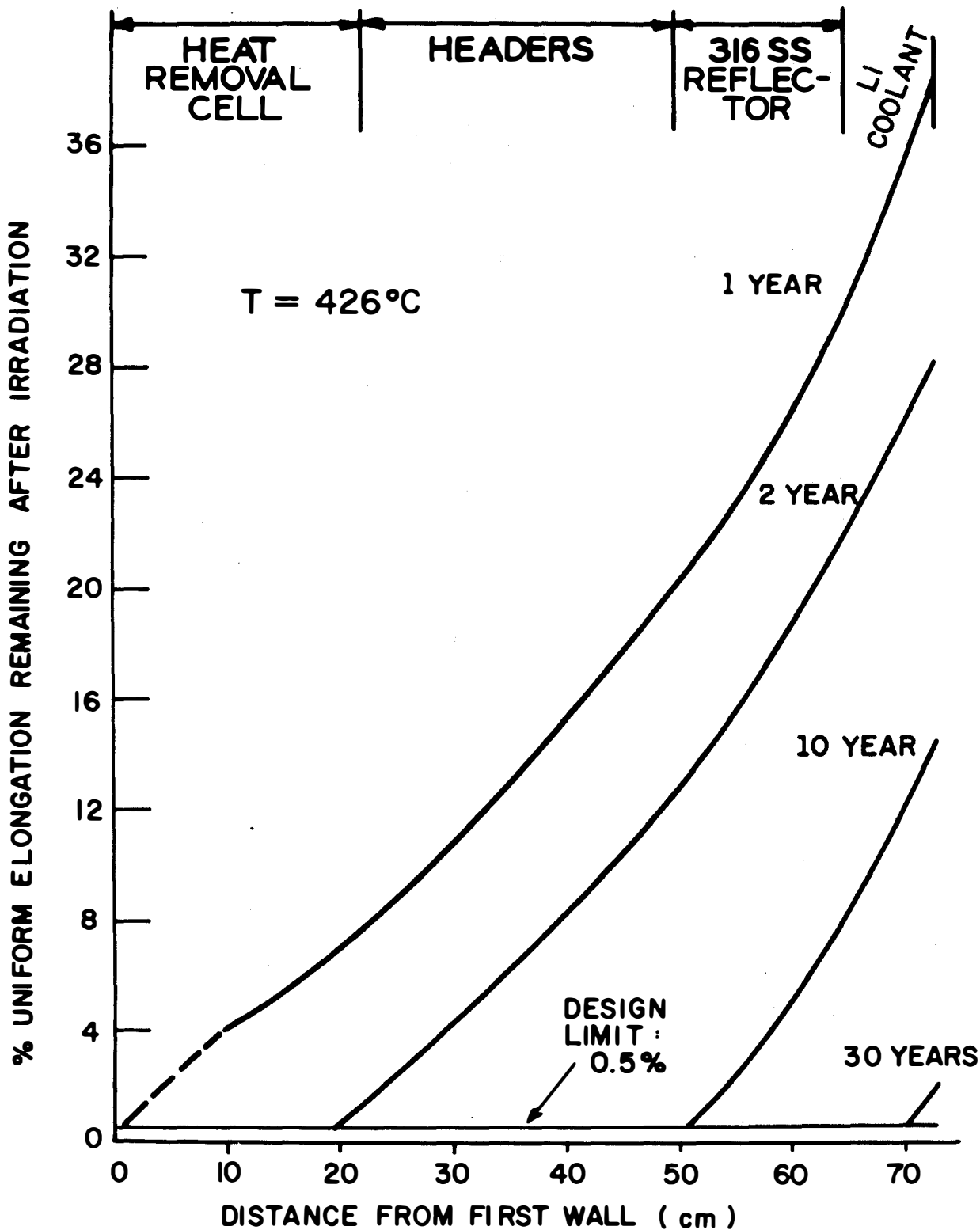


Figure VI-D-10

The conclusion of this work is that after one to two years of irradiation, we will have to remove the heat removal cells (first 20 cm of the blanket) and replace them with new units. Strictly speaking, we should change the units every year, but we feel that we might be able to stretch the life time to 2 years because of the uncertainties of the data.

It is quite apparent that if one is to retain any reasonable ability to absorb the stress and strains imposed on the blanket by start up, shut down, swelling and coolant pressures, one must begin to think now in terms of replaceable first walls! Once this concept can be mastered, the frequency of change (1 or 2 years) becomes a matter of economics.

There is one last point which should be emphasized and that is the problem of replacing the headers and reflectors in the blanket. The data in Figure VI-D-10 would indicate that the header region should be replaced every 10 years and the reflectors after 15-20 years. Such a possibility will greatly increase the amount of stainless steel which must be disposed of because there is ~10 times more steel in the reflector region than in the heat cells and the headers contain about twice the amount of steel as do the heat cells (See Table IV-A-2).

VI-D-3 Transmutation Effects in 316 SS for UWMAK-I First Wall

The absolute magnitude of the chemical change in the 316 SS first wall as a function of time is given in Table VI-D-6 and the more important changes are summarized in Table VI-D-7. The reduction in Ni content even after 30 years exposure, (<1%) is not considered too significant as it is within the allowable alloy variations for 316 SS; 10-14 weight percent. On the other hand a 320% increase in Mn content after a 30 year exposure is clearly outside the specifications for a 300 series stainless steel. The resulting alloy might tend to be more like a 200 series steel with high Mn content. Manganese is an austenite stabilizer which should keep the 316 from reverting to a ferrite structure. However, if one did want to keep the first wall in the reactor for 30 years, some work should be directed toward investigating these alloy compositions. Finally, the increase in Ti and V is clearly above specifications. The Ti would probably make the steel more like a 321 type alloy and it is not clear at this time what an increased V concentration weight would do. It is possible that the vanadium might act similar to the Nb in a 347 SS.

Since the design philosophy is to replace the first wall every two years it can be seen that very little, if any, problems will be incurred from transmutation reactions. The last question to answer is what transmutations might occur in the header region which may have to last for the plant lifetime. No detailed calculations were completed at the time of this report, but since the neutron flux in that region

is lower by over an order of magnitude, it appears that there should be no significant alloy changes.

Table VI-D-6

Summary of Transmutation Effects in 316 Stainless Steel of UWMAK-I* First Wall

<u>Element</u>	<u>Original Concentration appm</u>	<u>Change - appm</u>		
		<u>2 years</u>	<u>10 years</u>	<u>30 years</u>
Fe	626,000	- 3600	-15,300	-45,900
Cr	180,000	+ 60	+ 300	+ 900
Ni	140,000	- 440	- 2,200	- 6,600
Mn	20,000	+ 2900	+14,500	+43,500
Si	15,000	- 30	- 150	- 450
Cu	1,000	- 14	- 70	- 210
Al	1,000	- 1.5	- 7.5	- 23
B	52	- 0.3	- 1.3	- 3.8
Co	500	+ 0.8	+ 3.8	+ 11
Nb	300	- 1.3	- 6.3	- 19
P	360	- 0.3	- 1.3	- 3.8
Ti	115	+ 110	+ 560	+ 1,700
V	2,200	+ 440	+ 2,200	+ 6,600
C	2,800	- 8.5	- 43	- 130
O	400	- 1	- 5	- 15
N	400	- 1.3	- 6.3	- 19
Be	N	+ N	+ 20	+ 60
Mg	N	+ 30	+ 150	+ 460
Na	N	+ 1.3	+ 6.3	+ 19
Zr	N	+ 1.3	+ 6.3	+ 19

*1.25 MW/m² wall loading N = negligible

Table VI-D-7

Summary of Most Important Alloy Changes

In UWMAK-I 316 SS First Wall

<u>Element</u>	<u>Original Composition wt%</u>	<u>Final Composition %</u>		
		<u>2 Years</u>	<u>10 Years</u>	<u>30 Years</u>
Fe	62.6	62.3	61.1	58.0
Ni	14	14	13.8	13.3
Mn	2	2.3	3.5	6.4
Ti	0.01	0.02	0.07	0.18
V	0.2	0.26	0.44	0.88

The conclusion of this study is that neutron induced transmutations (excluding gas production) do not present a problem in 316 SS if the first 20 cm of the blanket is replaced every two years. If the wall must last 30 years, the mechanical property effects of Mn, Ti and V in amounts greater than 316 SS specifications should be investigated. It would also be of interest to determine how these elements will effect the void nucleation and growth process.

VI-D-4 Surface Effects - UWMAK-I First Wall

The thinning rate of the 316 SS UWMAK-I first wall was calculated by using the removal constants generated in Section VI-C-5, Tables V-C-12, 13. The particle fluxes and energies impinging on the UWMAK-I first wall are listed in Table VI-D-8 for operation at both thermally stable and unstable plasma conditions. A 90% efficient divertor is assumed. A summary of the individual as well as the total erosion rates is given in Table VI-D-9 and 10 and the results are displayed as a function of time in Figure V-D-11. Note that we have arbitrarily assumed that the high neutron sputtering coefficients apply for neutrons of energy >10 MeV. This was done to account for those neutrons which are only slightly degraded in energy by back scattering.

There are several points worth noting. First of all, the use of a 90% divertor with the plasma at the thermally unstable point results in a wall erosion rate of ~0.22 mm/year or 0.44 mm in 2 years of 6.6 mm in 30 years of operation. The major contributions to this effect stem from neutron and self ion sputtering with blistering contributing <10%.

The shift from a thermally unstable to thermally stable plasma has relatively little effect on the total wall erosion rate because the neutron sputtering is the controlling factor (~75%) in erosion of the 316 SS first wall.

It is evident that even if we decide not to replace the wall every two years, a major limitation on wall loading would result from surface effects. We have seen from Section IV-D that the difference between the maximum and minimum wall thickness for 316 SS is 3.3 mm. Allowing 0.6 mm for corrosion in 30 years (see Section IV-C) leaves a wall thickness of 3 mm which can be used to accomodate sputtering and blistering effects. This wall thickness would place a 30 year wall loading limitation of ~0.5 MW/m² for operation at both the thermally stable and unstable point. If the wall is replaced every two years then we find a maximum wall loading limitation of ~ 9 MW/m².

The use of a high sputtering coefficient for 14 MeV neutrons may overestimate the wall erosion rate. If we assume that the 14 MeV neutrons are only as effective as the backscattered neutrons in sputtering, then the wall loading limitations can be increased by a factor of two to three. Such an increase means that the first wall of the heat removal cells could operate for the full 30 year plant lifetime at current UWMAK-I operating conditions. Finally, it should be noted that the blistering produced by the low energy helium atoms may be more important than that produced by

the higher energy helium. This would be especially true when operating the plasma at the thermally unstable point because of the higher burn up and the longer confinement time at the thermally stable point.

In summary, surface erosion problems do not seem to be severe for the first wall of UWMAK-I. This is especially true for a two year replacement time and in fact the UWMAK-I does not need a divertor to protect the wall from the plasma as long as the wall loading is less than $\sim 9 \text{ MW/m}^2$ for 2 years.

Table VI-D-8

Summary of Particle Fluxes to the First Wall of UWMAK-I

<u>Ion</u>	<u>Mean Energy</u>	<u>Particle Flux at Thermally Unstable Operating Point</u>	<u>Mean Energy</u>	<u>Particle Flux at Thermally Stable Operating Point</u>
D+	23 keV	6.4×10^{13}	28 keV	6.8×10^{12}
T+	23 keV	6.4×10^{13}	28 keV	6.8×10^{12}
He+	23 keV	4.7×10^{12}	28 keV	4.7×10^{12}
He+	100 keV	1.7×10^{11}	100 keV	6.9×10^{10}
n	>10 MeV	9.4×10^{13}	>10 MeV	9.4×10^{13}
n	0.1 to 10 MeV	3.4×10^{14}	0.1 to 10 MeV	3.4×10^{14}
Fe+	23 keV	2.5×10^{12}	28 keV	7.8×10^{11}

Table VI-D-9

Summary of First Wall Erosion Rates in UWMAK-I for
Plasma Operation at the Thermally Unstable Point

<u>Ion</u>	<u>Mean Energy-keV</u>	<u>S</u>	<u>Flux</u> <u>$\frac{-2}{\text{cm}^2 \text{sec}^{-1}}$</u>	<u>Erosion Rates</u> <u>mm/year</u>	<u>% Total</u> ^{a)}
<u>Sputtering</u>					
D+	23	0.02	6.4×10^{13}	0.0047	2
T+	23	0.03	6.4×10^{13}	0.0070	3
He	23	0.15	4.7×10^{12}	0.0026	1
He	~100	0.03	1.7×10^{11}	0.00002	-
n	>10,000	0.2	9.4×10^{13}	0.14 ^{b)}	64
n	0.1-10,000	0.009	3.4×10^{14}	0.022 ^{b)}	10
Metal	23	2.5	2.6×10^{12}	<u>0.023</u>	10
Total Sputtering				~0.20	
<u>Blistering</u>					
He	23	1	4.7×10^{12}	0.017	8
He	~100	3	1.7×10^{11}	0.0019	1
D+	23	0.01	6.4×10^{13}	0.0023	1
T+	23	0.01	6.4×10^{13}	<u>0.0023</u>	1
Total Blistering				~0.024	

Total Wall Erosion Rate ~0.22 mm/year

a) will not total 100% due to round off

b) include both sides of wall

Table VI-D-10

Summary of First Wall Erosion Rates in UWMAK-I for Plasma
Operation at the Thermally Stable Point

<u>Ion</u>	<u>Mean Energy-keV</u>	<u>S</u>	<u>Flux</u> <u>$\text{cm}^{-2} \text{sec}^{-1}$</u>	<u>Erosion Rate</u> <u>mm/year</u>	<u>% Total</u> ^(a)
		<u>Sputtering</u>			
D+	42	~0.015	6.8×10^{12}	0.0004	<1
T+	42	~0.025	6.8×10^{12}	0.0006	<1
He	42	~0.12	4.7×10^{12}	0.0021	1
He	~100	0.03	6.9×10^{10}	Negligible	-
n	>10,100	0.2	9.4×10^{13} (b)	0.14	67
n	0.1-10,000	0.009	3.4×10^{14} (b)	0.022	10
Metal	42	3.8	2.3×10^{12}	<u>0.021</u>	10
			Total Sputtering~0.19		
		<u>Blistering</u>			
He	42	1.4	4.7×10^{12}	0.024	11
He	~100	3	6.9×10^{10}	0.0008	1
D+	42	0.014	6.8×10^{12}	0.00034	<1
T+	42	0.014	6.8×10^{12}	<u>0.0034</u>	<1
			Total Blistering~0.029		

Total Wall Erosion Rate ~0.22 mm/year

(a) Will not total 100% due to round off.

(b) Including both sides of wall.

WALL EROSION OF UWMAK-I 316 SS FIRST WALL

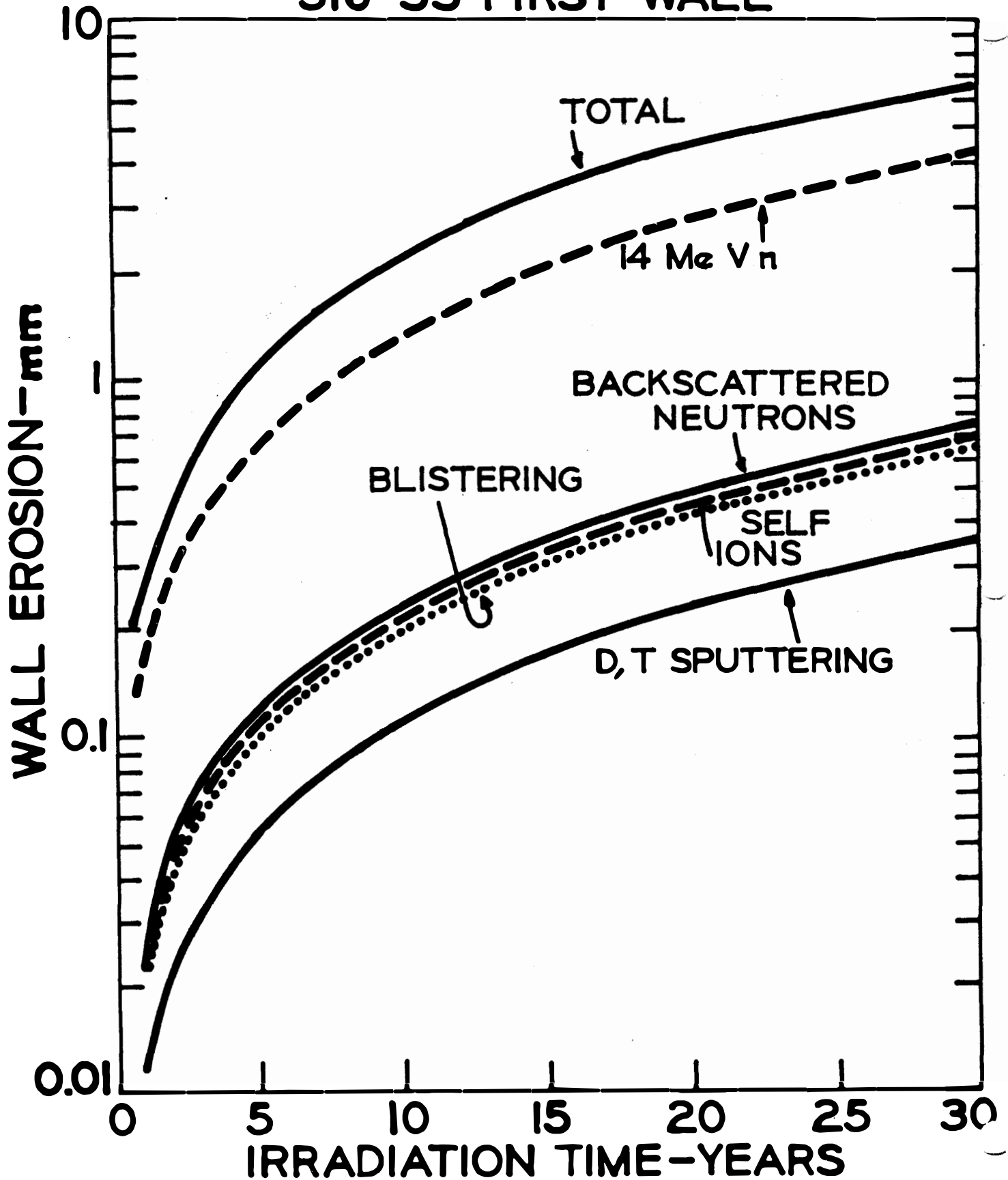


Figure VI-D-11

VI-E-1

VI-E-1 Specific Swelling Effects in B₄C for UWMAK-I Shield

The variations in boron-10 burn-up throughout the shield is shown in Table VI-E-1. It is noted that the burn-up of boron-10 atoms ranges from $5 \times 10^{17} \text{ cm}^{-3}$ to $9.5 \times 10^{20} \text{ cm}^{-3}$ for a 30 year exposure. Since the initial number of boron-10 atoms cm^{-3} (assuming natural boron) is $\sim 200 \times 10^{20} \text{ cm}^{-3}$, this amounts to burn-ups ranging from $2.5 \times 10^{-3}\%$ to 4.8%. Of course, the percentage burnups could be lowered by using enriched boron but there appears to be no need for such a measure.

The amount of swelling induced by such burn-ups can be measured in two ways. First of all, since the shield is operated at temperatures of less than 300°C we could use the data of Gray and Lynam⁽⁴⁵⁾ shown in Figure VI-C-9. Such a comparison would yield maximum swelling values of $\sim 0.5\%$ after 30 years exposure. The more conservative approach, but perhaps not too realistic, would be to assume that all of the helium gas will collect into bubbles. Using Homans⁽⁴⁶⁾ data, again for $T < 300^\circ\text{C}$, we would predict swelling values of $\sim 2\%$.

Regardless of how the B₄C swelling is calculated, it appears that it will be easy to accommodate values of 0.5-2%. However, care should be exercised if, by shield redesign, the B₄C were to be moved toward the plasma. Swelling values of $\sim 10\text{-}20\%$ should not be exceeded because of the extra thickness of the blanket required.

Table VI-E-1
Boron-10 Burn-Up in UWMAK-I Shield Material

<u>Distance From Plasma Axis-cm</u> (a)	Boron-10 Depletions $\text{cm}^{-3} \times 10^{20}$		
	<u>2 Years</u>	<u>10 Years</u>	<u>30 Years</u>
645.4	0.63	3.2	9.5
653.4	0.039	0.19	0.58
674.4	0.0098	0.049	0.15
682.4	0.0017	0.0087	0.026
693.4	0.00067	0.00067	0.01
699.4	0.00033	0.0017	0.005

a) See Figure IV-A-4

VI-F. Radiation Damage to Magnet Components

The magnet components affected by radiation can be divided into two categories:

1. conductor materials which are metallic
- and 2. insulator and spacer materials which are organic polymers.

The mechanism through which these two material types are damaged are quite different and must be treated separately.

1. The Magnet Conductor

The conductor is composed of superconducting NbTi filaments embedded in a copper matrix. The degradation of properties resulting from neutron irradiation will be dealt with independently and modifications to the conductor design, necessitated by this degradation, will be explored.

a. Superconducting Materials

The quality of a superconductor is judged by three properties simultaneously: its critical temperature, T_c , its critical current density, J_c , and its critical field, H_c . Both T_c and H_c are mainly properties of the materials electronic distribution and are generally insensitive to lattice effects. However, in some materials, Nb₃Sn for example, ordering plays an important role in T_c and therefore disordering effect due to displacements, and more important, replacements need to be considered.

The critical current density, J_c is strongly dependent on the defect structure. In order for a superconductor to carry current, the flux lines must be pinned by defects to stop their motion under the Lorentz force. However, not all defects are equally effective as pinning sites and therefore the better the defects are at pinning, the higher attainable J_c .

As a prelude to an indepth discussion of irradiation effects to superconductors, it is helpful to investigate where research has already been completed in terms of irradiation temperature in °K and damage level in displacements per atom. (Figure IV-F-1)^(104,120) Since the damage mechanisms operating at 300°K are quite different from those at 4.2°K, over 50% of the data points are not applicable to the fusion reactor case even though useful information may be obtained from them. Although several points at 4.2°K exist, those investigations include only one study of neutrons on NbTi and none of neutrons on Nb₃Sn. It would seem that more data is needed in the low temperature region in order to acquire the ability to predict the performance of a superconducting magnet system in a fusion reactor.

i.) NbTi Alloys

Attention has already been given to the fact that the current carrying capacity of a superconductor is due not only to the defect density but to the degree of difference between the defect and the matrix. Physical heterogeneities can be introduced into materials by mechanical deformation, second

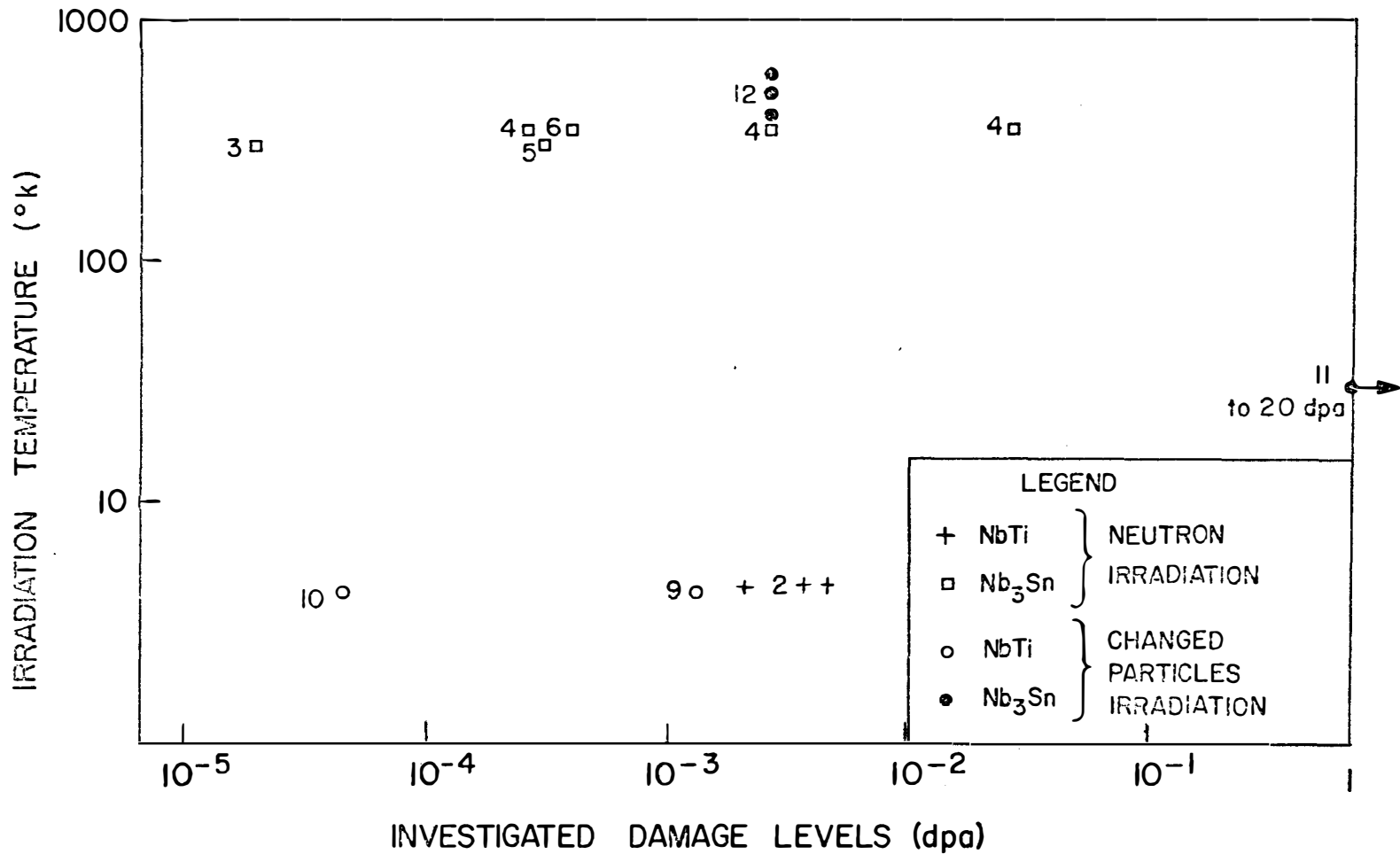


Figure VI-F-1 Mapping of investigations to date of the effects of energetic particles on NbTi and Nb₃Sn
References are listed at the end of Chapter

phase precipitation, impurities, or lattice imperfections. For the ductile alloy NbTi, second phase precipitates and mechanical deformation are the important mechanisms. Flux pinning precipitates can only be obtained in the high Ti content alloys and are formed by heat treatment. The role that precipitates play in increasing J_c can be seen in Figure VI-F-2 where J_c versus H curves are shown for various annealing procedures.⁽¹²¹⁾ Annealing at 450°C introduces α -Ti particles thereby increasing J_c .⁽¹⁰⁷⁾ On the other hand, annealing at 200°C and 650°C in the single phase regions, reduces the defect density and thus decreases J_c .

The fabrication process of lower Ti content alloys depends on a combination of deformation and heat treatment to achieve high critical current densities. It has been found⁽¹²²⁾ that maximum flux pinning is obtained for Nb "rich" alloys when the dislocations form a cellular structure referred to as tangles which are more much effective as pinning sites than are single dislocations. Once the cell structure is formed at a dislocation density of 10^9 (15-20% cold work), then additional deformation makes little change on the magnetization or the critical current. An analysis of the radiation damage studies to NbTi can be made taking into account these characteristics.

Several irradiation studies have been made on NbTi⁽¹¹²⁻¹¹⁴⁾ but the most significant study of low temperature irradiation effects has been made recently by Soell, Wipf and Vogl.⁽¹⁰⁵⁾ Figure VI-F-3 shows the effect of neutron irradiation on niobium rich alloys, but the value of their results is best seen in the explanations of the observed changes. In general, they found decreases in J_c with neutron dosage. The critical temperatures of these samples were not measured but the work of Coffey et al⁽¹¹⁴⁾ indicates that slight changes of less than -0.3°K can be expected. It is concluded, therefore, that the measured reduction in J_c can not be linked to a reduction in T_c . The source of this deterioration has been attributed to the reduction of the pinning strength of the dislocation tangles. Initially dislocation-free matrix is surrounded by dislocation cell walls which form pseudo-potential wells to flux-pinning. After irradiation, point defects have been introduced in the matrix decreasing the degree of difference between the walls and the matrix, and, in an explanatory way, decreased the depth of the potential well. This model, of course, assumes that the point defects do not increase the wall pinning effectiveness. Reasons for this assumption are the belief that the high defect density of the walls would suppress the effect of the point effects, and furthermore, that it is possible for the dislocations to act as sinks for the irradiation induced point defects.

At the present time, none of the highly Ti rich alloys have been irradiated. It is the belief of the author that these alloys will exhibit a much higher radiation resistance than those alloys dependent on cold-working for flux pinning. On the other hand, the damage to these alloys will probably only be recoverably by a high temperature anneal of 450°C similar to the initial heat treatment.

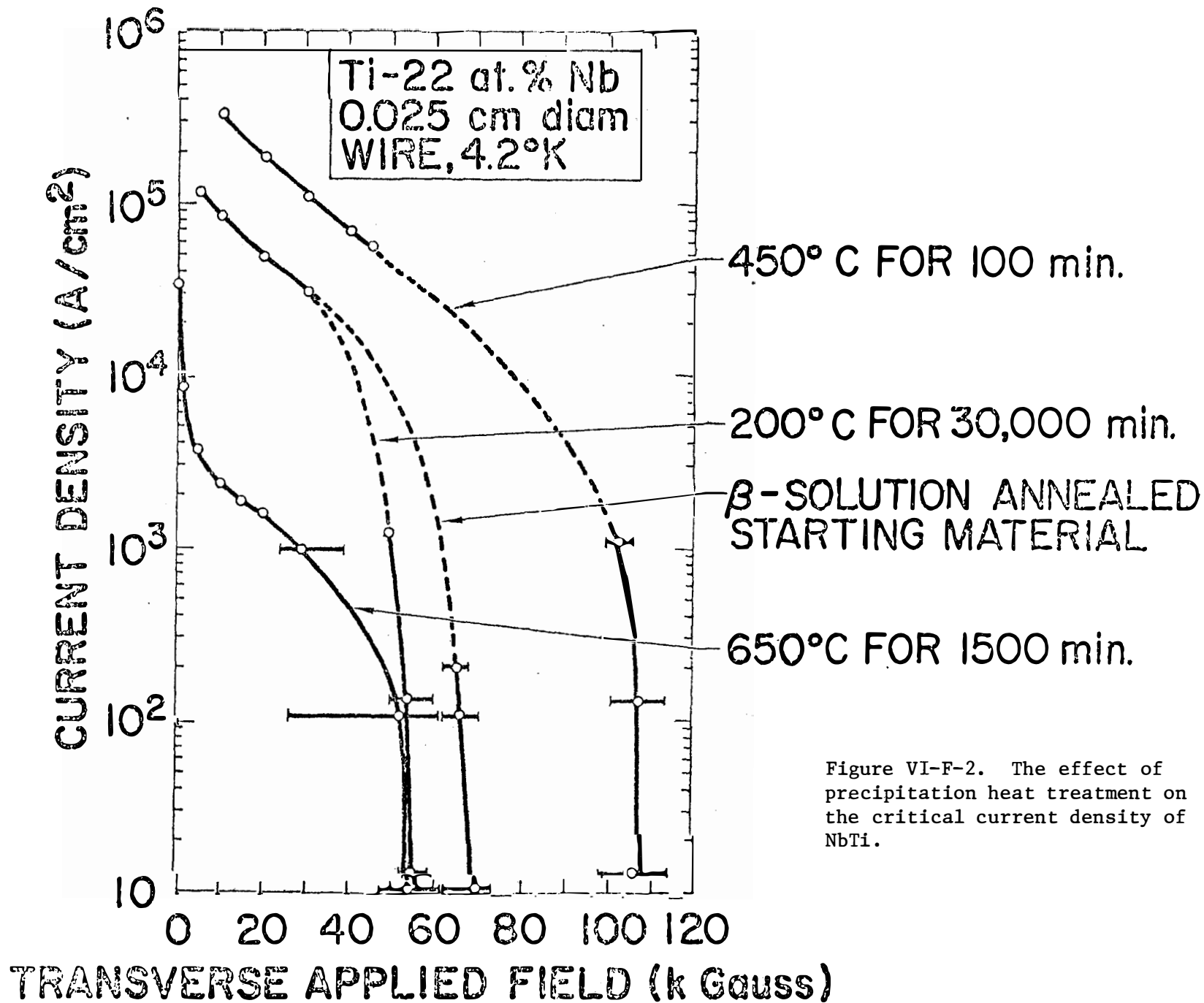
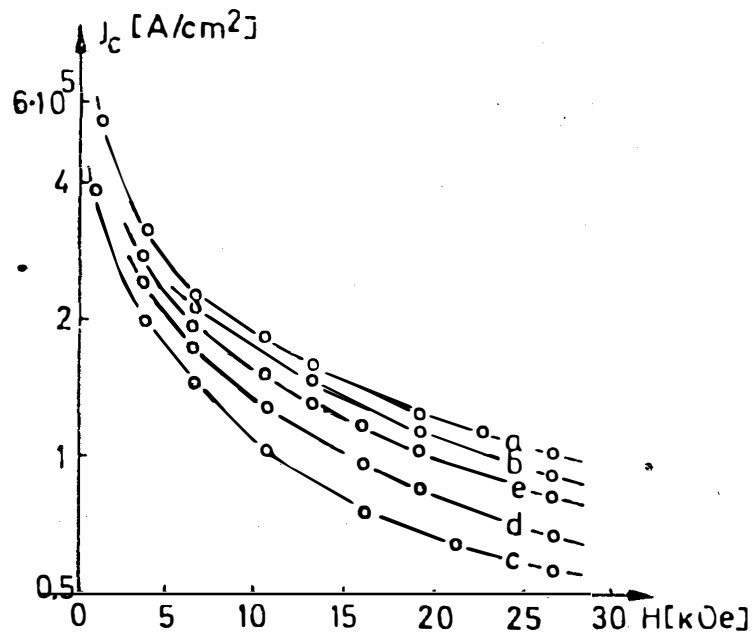
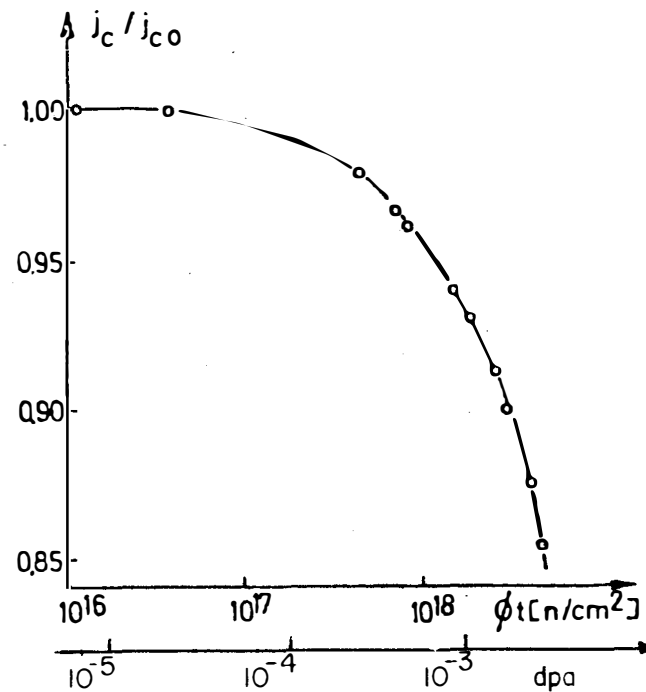


Figure VI-F-2. The effect of precipitation heat treatment on the critical current density of NbTi.



Critical current density j_c versus applied transverse magnetic field H for Nb-50wt%Ti at 5.3K. Curve a unirradiated, b irradiated with 3.2×10^{18} neutrons/cm² ($E > 0.1$ MeV), c irradiated with 7.5×10^{18} n/cm², d annealed at 100 K, e annealed at 270 K (after Soell).



Relative Change of the critical current density j_c of a Nb-50wt% Ti sample at zero field ($H=0$) as a function of the neutron dose $\phi \cdot t$. j_{c0} is the current density before the irradiation (after Soell).

Figure VI-F-3. The effect of fast neutron irradiation at cryogenic temperature on the critical current of Nb-50 w/o Ti. The conversion to dpa was made using a typical thermal reactor spectrum.

ii.) Intermetallic Beta-Tungsten Compounds (Nb₃Sn and others)

Coffey et al⁽¹¹⁴⁾ have completed the only cryogenic irradiation of Nb₃Sn. The J_c versus H curves derived from their experiments again indicates the difference between initially high J_c material and initially low J_c samples of Nb₃Sn. The critical current density increases in the low J_c case due to a small percentage of large displacement spikes whereas a decrease in T_c of 1.2°K (-8%) was measured for initially high J_c Nb₃Sn samples and the strong T_c dependence on H_c accounts for the net decrease of J_c at high fields.

This same effect has been seen in irradiations performed by Cullen, Novak, (106,109,116,117) and Bett (106). Basically, the effect can be separated into two counter-effects:

1. increase J_c by introducing defects,
- and 2. decrease T_c by introducing disorder thereby lowering J_c.

The damage level at which the decrease of J_c overtakes the increase depends on the initial current carrying capacity of the superconductor. In order to put Figure VI-F-4 into perspective, note that the ordinate represents J_c irr/J_c^o and J_c^o is not the same for each sample ranging from 1.36 x 10⁶ to 1.2 x 10⁷ amps/cm², lowest to highest respectively. The data of Bett Figure VI-F-5 illustrates clearly the magnitude of the decrease in T_c. (107)

When a fusion magnet engineer talks of annealing procedures, he is considering a relatively low temperature, rarely exceeding room temperature. In previous studies it has been established that point defects anneal at temperatures between 40°K and 300°K⁽¹²⁹⁾. In that range of temperature recovery of 85 to 100% of the current carrying capacity can occur depending on the material and the extent of radiation damage. (105) (Figure VI-F-6) This is particularly true for the metallic alloys. However, when decreases of T_c are significant as in Nb₃Sn, then much higher temperatures must be reached to regain the ordered structure. For Nb₃Sn, even temperatures of 450°C for periods of days yield little recuperation of T_c. (107)

b. Stabilizing Material

The primary property for which the stabilizing material is chosen is its low resistivity. The major candidates for this component are OFHC copper and ultra-pure aluminum. This design has opted for the use of copper on the basis of existing technology and mechanical strength properties. As has been noted previously, neutron irradiation at liquid helium temperatures creates point defects. These defects, as well as transmutation impurities, can dramatically increase the resistivity of both Cu and Al. An important parameter to be determined is the rate of increase of the resistance with respect to the damage level. This rate

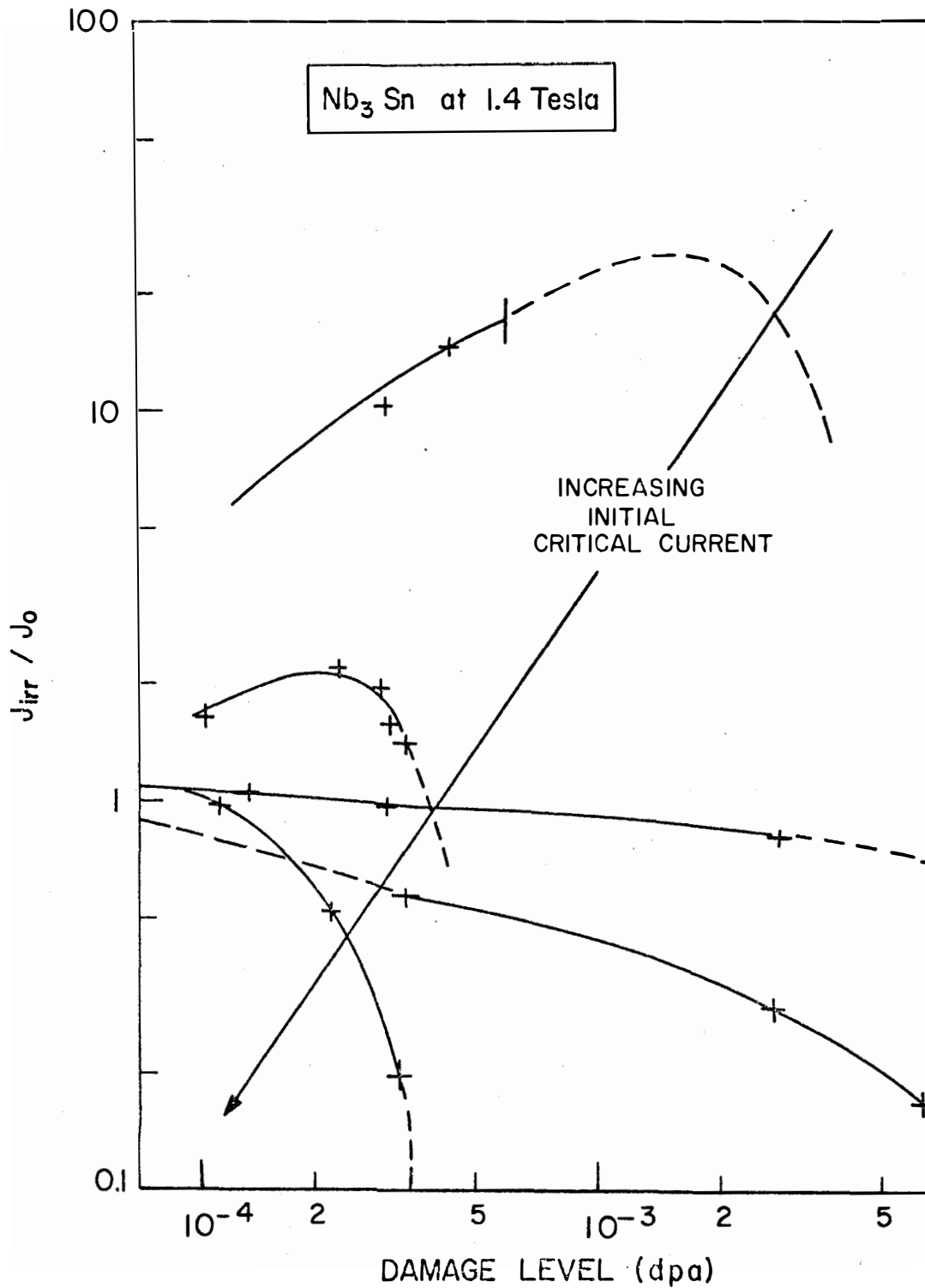


Figure VI-F-4. The effect of fast neutron irradiation on the critical current of Nb₃Sn. These irradiations were made at temperatures above 300°K. Conversion to dpa was made using a typical thermal reactor spectrum.

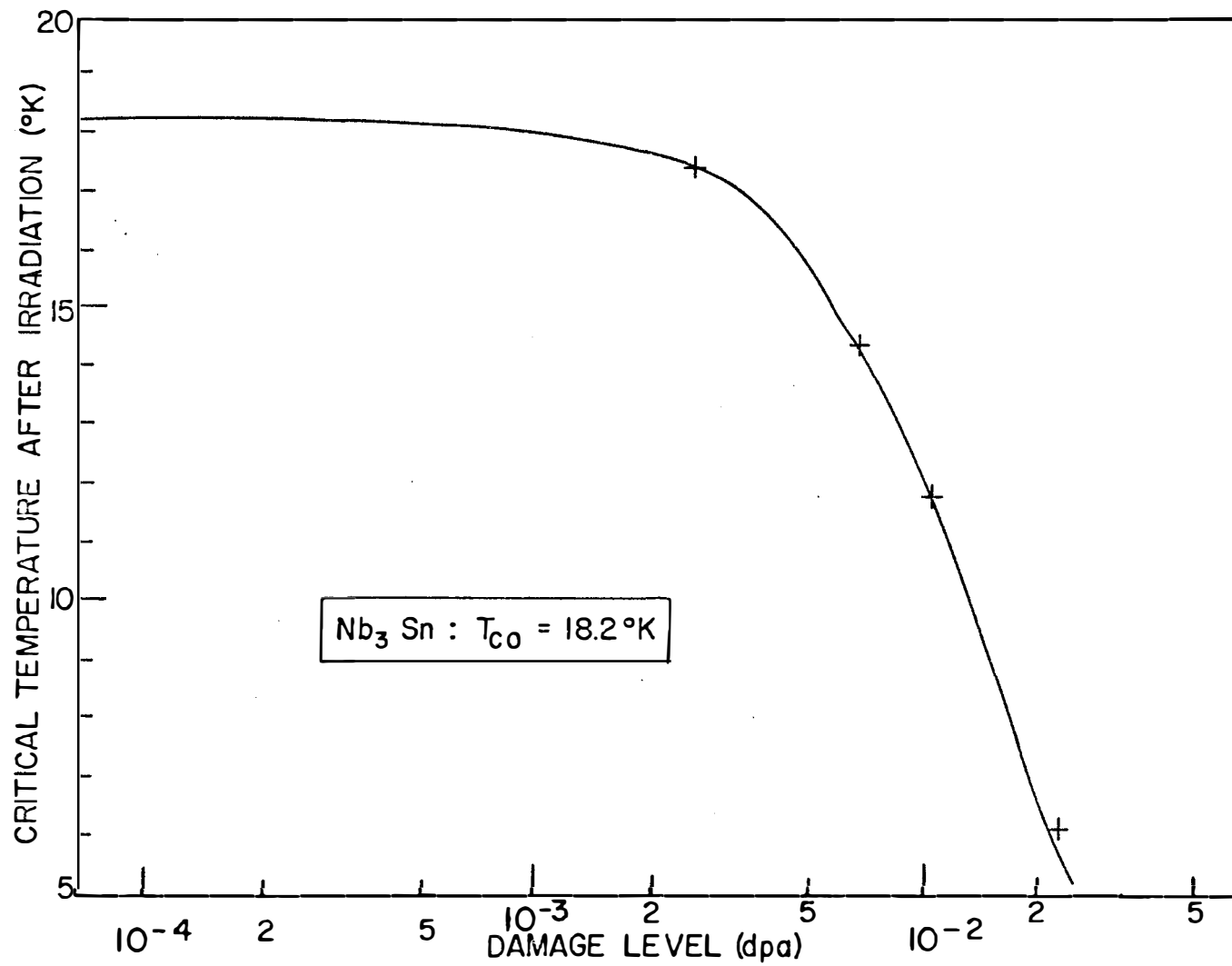
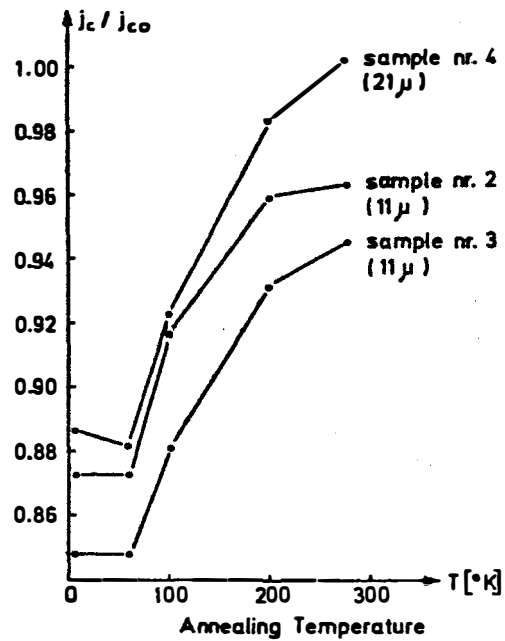


Figure VI-F-5 The degradation of the critical temperature of Nb₃Sn by neutron irradiation.



Recovery of the critical current (normalized to the value before irradiation) of the samples 2, 3, 4.

Figure VI-F-6 Annealing recovery of irradiation NbTi.

of resistance increase has been studied by several authors⁽¹²³⁻¹³¹⁾ most recent work by Horak and Blewitt⁽¹²⁴⁾ indicates that this rate decreases with dpa value and saturates due to the interaction between the defects through their own stress fields. The rate of resistivity change is given in equation VI-F-1

$$\frac{d\rho_r}{dt} = A [1 - B\rho_r]^2 \quad (\text{VI-F-1})$$

where ρ_r = radiation induced resistivity component and

A, B = constants.

The saturation resistivity $\rho_{r\infty}$ and the associated saturation defect concentration $C_{d\infty}$ for Cu are $33 \times 10^{-8} \Omega\text{cm}$ and 1.2×10^{-3} defects/atom. These values are $80 \times 10^{-8} \Omega\text{cm}$ and 1.2×10^{-3} defects/atom respectively for Al. The radiation induced resistivity can be obtained by integrating and making the appropriate substitutions for A and B in terms of the damage level in dpa, $\rho_{r\infty}$ and $C_{d\infty}$.

$$\rho_r = \rho_{r\infty} \left[\frac{\text{dpa}}{\text{dpa} + C_{d\infty}} \right] \quad \text{VI-F-2}$$

Equation VI-F-2 is plotted in Figure VI-F-7 versus dpa. The intrinsic resistivity of OFHC copper and 99.9999% pure aluminum are shown as reference points. Note the more rapid increase in resistivity of the aluminum at low dpa values as opposed to the copper.

It is easy to see that a factor of 30 increase in the copper stabilizer resistivity would be intolerable in a magnet system. Fortunately most of the conductivity can be restored by room temperature annealing. This effect of defects produced at 4.2°K has been extensively studied and 80% recovery of the Cu and 100% recovery of the Al by room temperature is annealing well established. The complete recovery of copper occurs only at temperatures greater than 500°K.

c. Modifications to Conductor Design

The present design has adopted the conservative total stability criterion first suggested by Stekly⁽¹³²⁾. This criterion states that the cooling capacity of the conductor to the helium must be greater than the amount of heat generated by the total current flowing in the stabilizer. This criterion presupposes that the current is forced to leave the superconductor for one reason or another. Stated mathematically,

$$I^2 \frac{\rho_T \cdot \ell}{wh} \leq qw \cdot \ell \quad \text{VI-F-3}$$

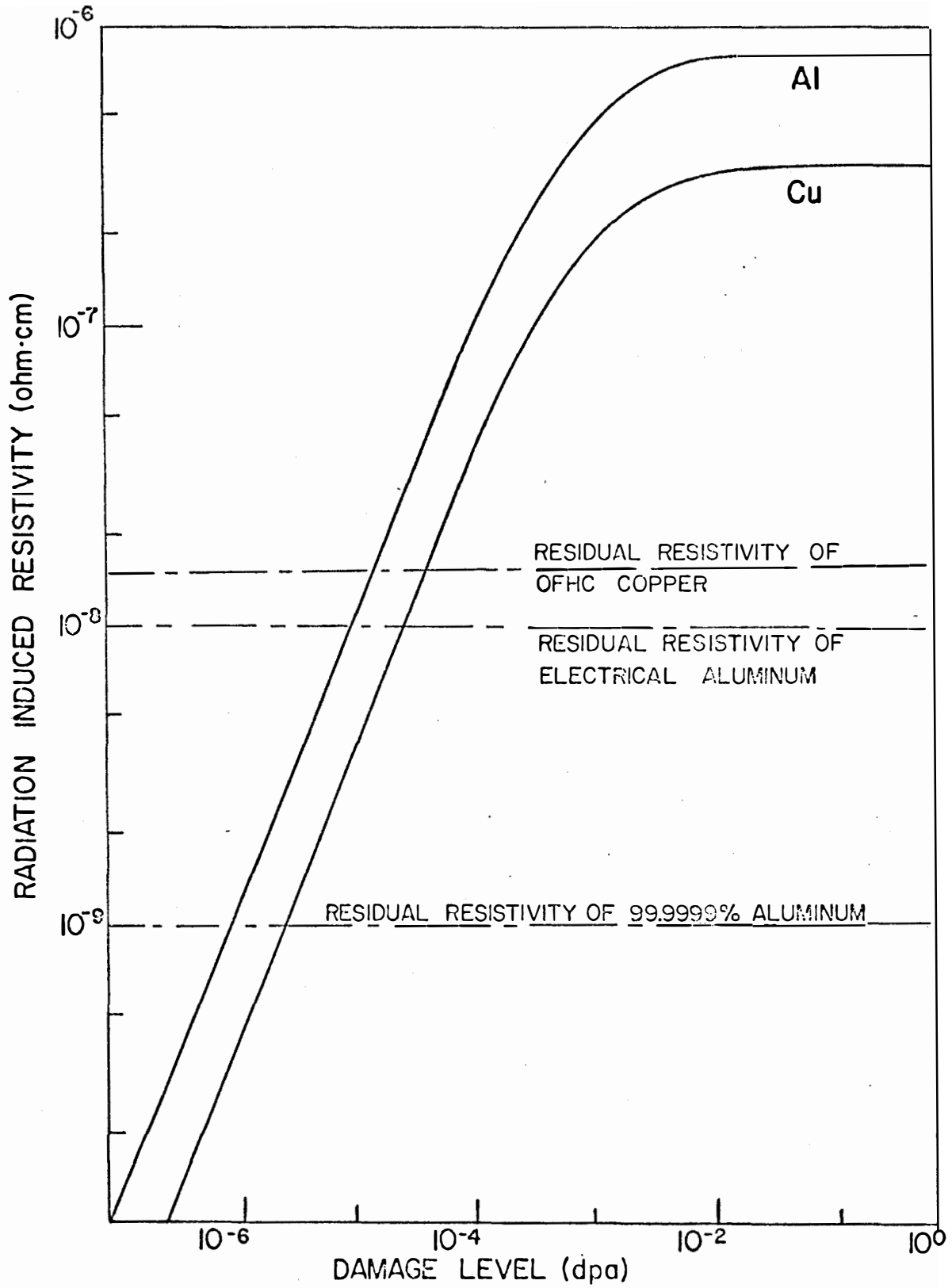


Figure VI-F-7 Radiation induced resistivity of copper and aluminum.

where I = conductor current in amps

ρ_T = total resistivity in Ωcm

q = heat flux in watts/cm^2

w = cooling surface width in cm

h = conductor thickness in cm

l = total conductor length

The total resistivity is comprised of the intrinsic ρ_o , the magnetoresistivity ρ_m and the radiation induced resistivity ρ_r which is a function of time. The magnet is designed such that the current is the same at all times, then;

$$I^2 = \frac{qw^2h}{\rho_o + \rho_m} = \frac{q(w+\Delta)^2h}{\rho_o + \rho_m + \rho_r} \quad \text{VI-F-4}$$

where the radiation-induced resistivity has been accommodated by the additional conductor width Δ .

Solving for $\frac{\Delta}{W}$ yields

$$\frac{\Delta}{W} = \sqrt{1 + \frac{\rho_r}{\rho_o + \rho_m}} - 1 \quad \text{VI-F-5}$$

Both ρ_r and ρ_m are functions of distance into the magnet and an expression for the conductor width as a function of position in the magnet can be obtained using the following relations for ρ_r and ρ_m .

$$\rho_r = \rho_{r\infty} \left[\frac{\text{dpa}(o) \exp\left(-\frac{x}{\lambda}\right)}{\text{dpa}(o) \exp\left(-\frac{x}{\lambda}\right) + C_{d\infty}} \right] \quad \text{VI-F-6}$$

$$\rho_m = .455 B_{\text{max}} \left(1 - \frac{x}{t}\right) \quad \text{VI-F-7}$$

This formulation permits the radiation damage to be accounted for within the conductor design. This additional width is plotted as a function of the depth into the magnet in Figure VI-F-8. Notice that this modification drops from 20% to less than 3% within the first 30 cm based on the dpa after 1 year of operation and a maximum field of 8.7 T. The length of the time between room temperature anneals has to be determined by the economic balance of the additional cost of copper versus the 60 days

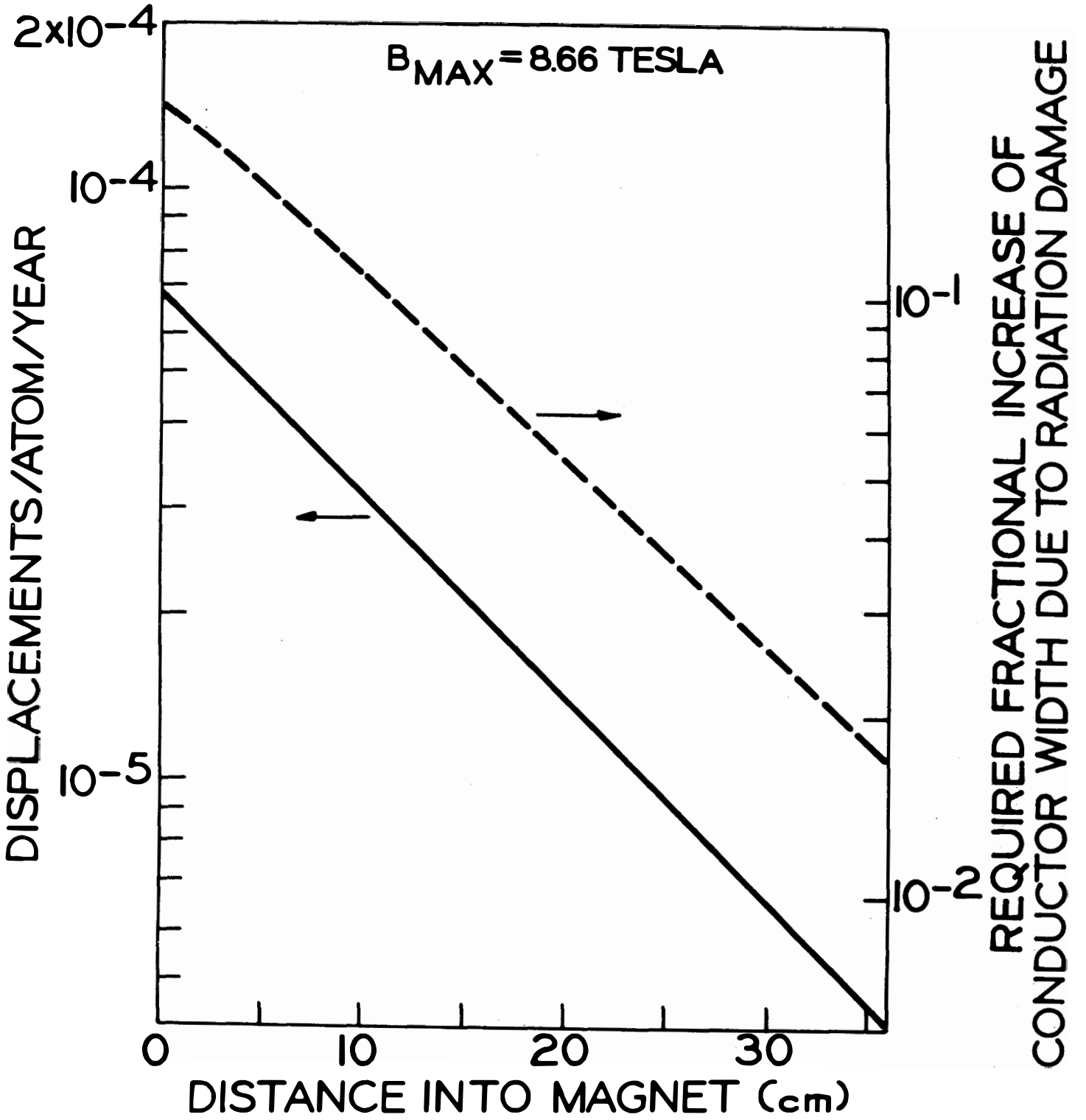


FIGURE VI-F-8

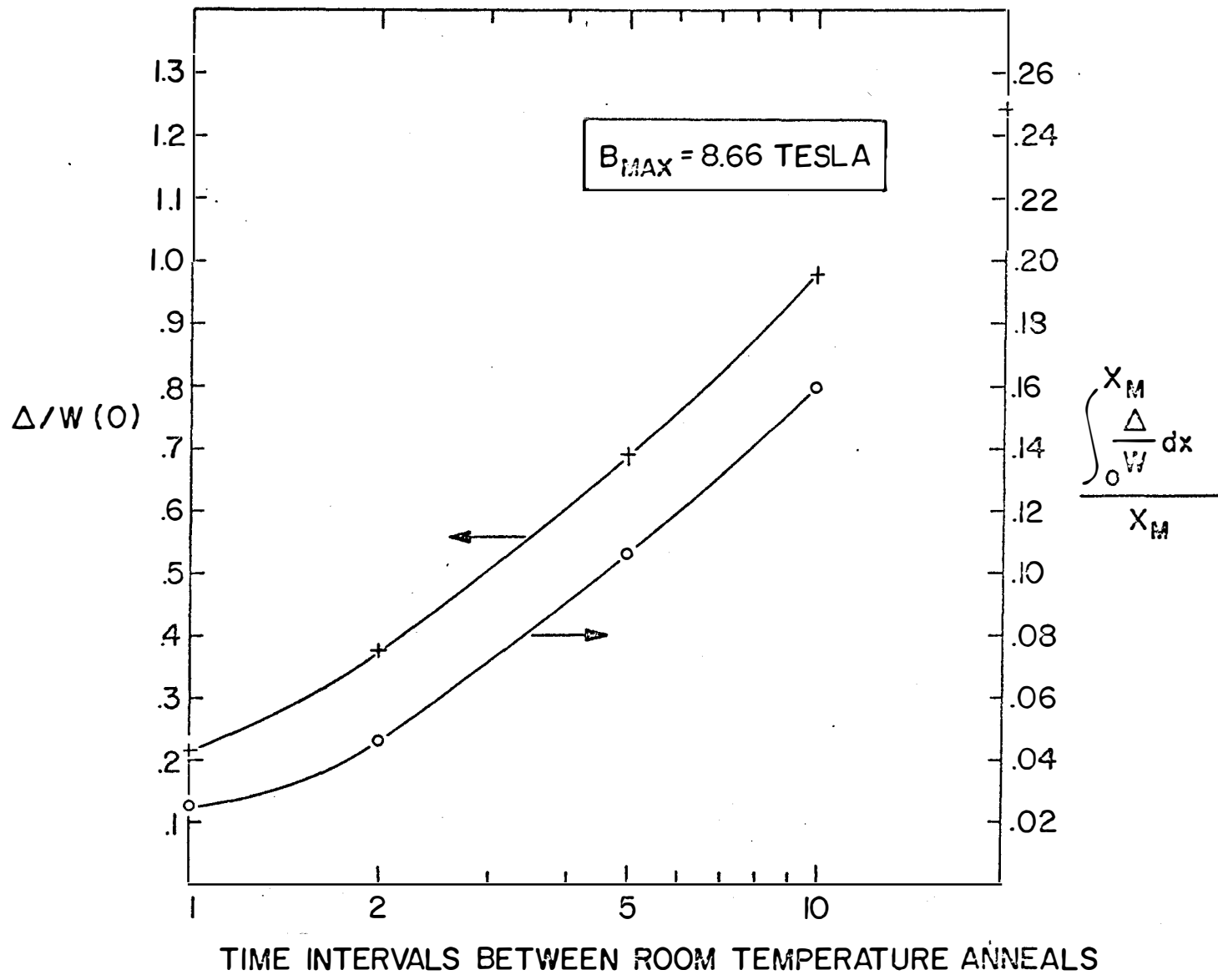


Figure VI-F-9

reactor down time necessary for the annealing procedure. From Figure VI-F-9 it can be seen that annealing at 10 year intervals or once in the reactor lifetime requires a factor of 2 increase in conductor width for the first turn and a 20% copper cost increase overall.

d.) Heat Deposition from Irradiation

An important parameter in the design of a cryogenic system is the heat load placed on the refrigerator. The heat flux into the magnet has many sources, one of which is the heat deposited by the energetic neutrons and gamma. Table VI-F-1 divides the neutronic contribution according to component per cm^3 of magnet material and gives the total gamma heating for the first turn of the magnet.

Table VI-F-1: Nuclear Heating

Material	Neutron contribution $10^9 \text{eV/cm}^3/\text{sec}$	Gamma contribution $10^9 \text{eV/cm}^3/\text{sec}$
Fe	2.57	-
Cr	.63	-
Ni	.78	-
Cu	<u>8.41</u>	<u>-</u>
TOTAL	12.39	69.0

The maximum nuclear heating is then $1.3 \times 10^{-8} \text{W/cm}^3$ which is insignificant compared to the possible joule heating already designed for in the magnet and can be ignored in the conductor design criterion. The total heat generation per cm of magnet length along the axis is $5.44 \times 10^{-4} \text{W/cm}$. Taking an efficiency of .002 and magnet length of 125 cm, the nuclear heating load is 34W/magnet or 408 Watts for the total system.

2. Polymeric Materials

a.) General Considerations

The reaction of polymeric materials to ionizing radiation must also be analyzed in the context of their use in a CTR superconducting magnet. The complexity of the problem is enormous. Each polymer, with its unique bonding and structure, has to be treated separately. Even though several basic damage mechanisms can be postulated, the predominance of any mechanism can not be predicted with any certainty. The usual approach is then to simply irradiate a variety of polymers and measure their properties as a function of dosage. Needless to say, this leads to a multitude of irradiations at a variety of conditions and it is a herculean task to analyze the results.

Fortunately the present design utilizes only 3 different polymers:

- 1) Super insulation, a composite of polyethylene terephthalate (trade names of Mylar, Dacron, or Terylene) and aluminum, used to reduce thermal radiation losses,
- 2) an interlayer electrical insulation consisting of a glass fiber reinforced, mineral filled, aromatically cured epoxy (also serves as the bond between the stainless steel reinforcing and the conductor itself), and
- 3) an insulating spacer between the discs made of micarta.

Radiation damage to organic materials is due to the ionization and excitation of electrons which disrupts the covalent bonding of these solids. These large electronic perturbations result in permanent chemical changes. The major chemical changes resulting in a change in physical properties are:

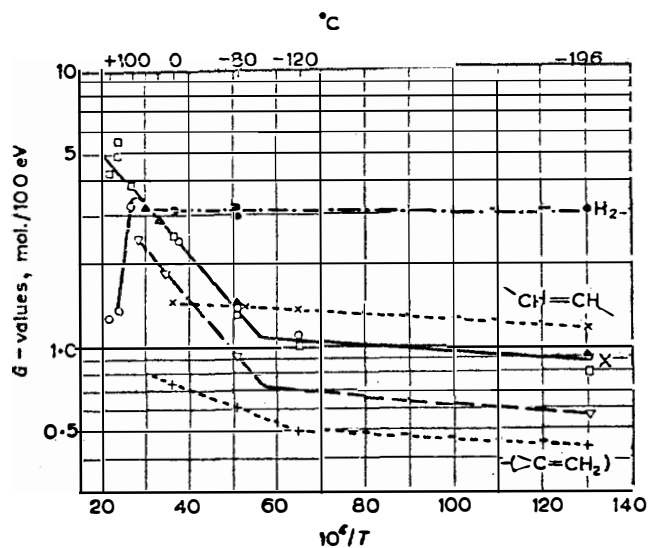
- a) The formation of new bonds between neighboring chains called crosslinking,
- b) the fracture of a polymer chain,
- c) the reaction of oxygen with free radicals referred to as oxidative degradation, and
- d) the evolution of gas from irradiated polymers changing the composition of the material.

It can be said that there definitely is a temperature dependence for these chemical changes. In general, the mechanisms listed above have a strong dependence on mobility of the free radicals. At low temperatures the mobility is decreased and so should the damage. Figure VI-F-10 shows this influence in terms of G-values for polyethylene.¹³³ There has been very little experimental data at liquid He temperature but indications are that low temperature damage is significantly less than that resulting from room temperature irradiation.^{140,143,144} However, it appears that temperature annealing of the low temperature samples causes a deterioration comparable to the damage resulting from room temperature irradiation.

Several review articles have been published that give a comprehensive survey of irradiation effects to polymers.¹³³⁻¹⁴¹ Figure VI-F-11 which shows the deterioration of mylar as a function of dosage, typifies the behavior of most polymers to irradiation. The most sensitive property to radiation is usually elongation however this is not always the case. Two dose levels characterize the sensitivity of polymers to radiation: a damage threshold and a 25% damage level. These two doses are given in table VI-F-2 for several polymers which may be utilized in a fusion reactor magnet.

b) Limitations in UWMAK-I

Neutronic calculations on the present system have yielded the energy deposited in Mylar which reaches a total dosage of .56 Mrads after twenty years. The dose for Micarta is approximately 0.8 Mrads over the same twenty year period. From Table VI-F-2 it is obvious that the most susceptible material to radiation damage, micarta, will suffer less than a 10% decrease in mechanical properties. Mylar and epoxy will not be noticeably affected since the dosage is far below the



Effect of temperature on crosslinking, unsaturation and hydrogen evolution.

G values are given for hydrogen evolution (●), formation of *trans*-unsaturation (x), and loss of initial unsaturation (+); they were all measured on the same samples (20 megarads).

G values for cross-links X were deduced from elasticity (▲ after correcting for end-effects; 25 and 40 megarads), from swelling (○) and solubility (□) by comparison with the dose required to give the same effect at room temperature and normalized to $G(X) = 2.5$ at 0°C (20 megarads).

$G(X)$ values deduced from elasticity measurements for γ -irradiation in air are shown (▽) for comparison, after correcting for $G(\text{Fe}) = 15.5$.

Figure VI-F-10 The influence of temperature on the radiation damage mechanisms in organic polymers.

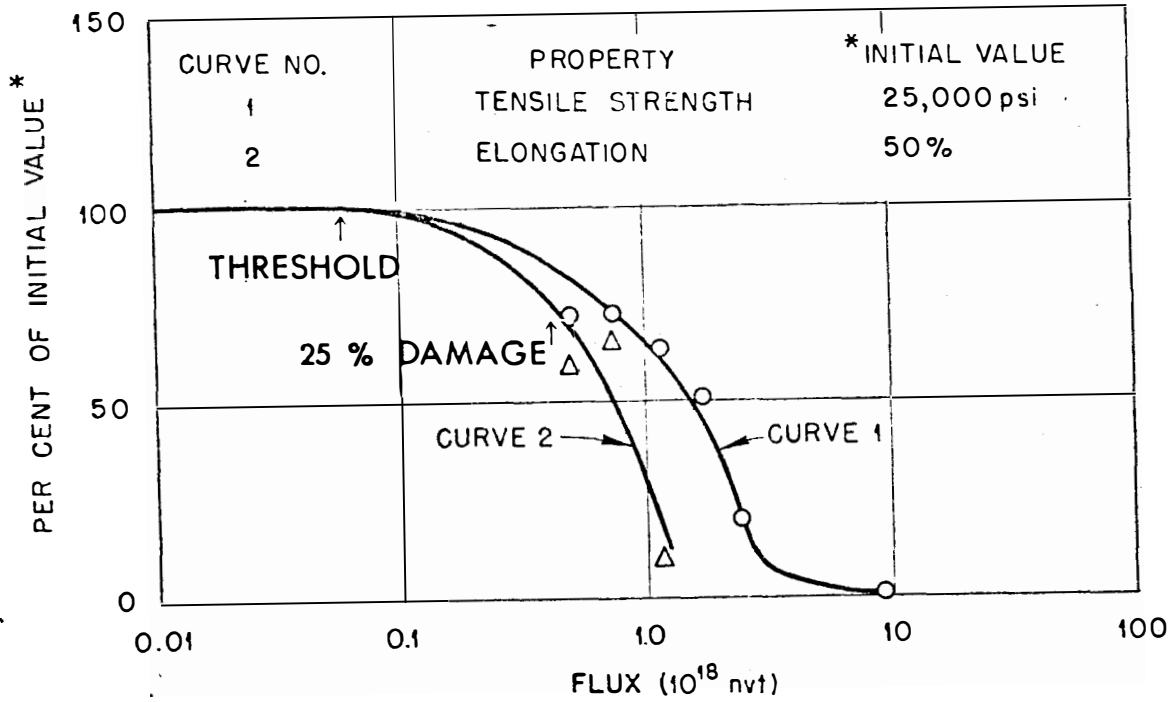


Figure VI-F-11. Physical Properties of Irradiated Mylar film. The conversion to Megarads is approximately 2×10^{15} nvt/Megarad. Both the irradiation and measurements were performed at room temperature.

Table VI-F-2: Resistance of Selected Polymers to Radiation at Room Temperature in Air

Polymer	Threshold Dose 10^6 rads	25% Damage Dose 10^6 rads
Teflon	.017	.037
Micarta	.34	8.2
Formvar	16	82
Polyethylene	19	93
Mylar	30	120
Epoxy	200	3200
Epoxy with glass fiber reinforcing	8000	50,000

3. Conclusion

Radiation damage to the magnet components is limited by the resistivity increase of the copper. This increase can be accommodated by increasing the conductor width simultaneously increasing the cooling area and the decreasing the resistance of the conductor. It seems economically reasonable to allow 10 years between room temperature anneals at a rate of 10^{-4} dpa/year. The critical current of NbTi at the accumulated 10^{-3} dpa would exhibit approximately a 2% decrease requiring only slight adjustment in design.

Neutronics calculations indicate that the mylar is exposed to 2.8×10^4 rads/year. According to the data presently available, all polymeric materials used in the magnet will operate reliably at this dose rate.

VI-G Summary of Limitations on UWMAK-I Power Levels Due to Radiation Damage

It is clear from the discussion in this chapter that the major barrier to increasing the wall loading in UWMAK-I is the loss of ductility due to displacement damage. A convenient way to state this limitation is in terms of MW-years/m². Table VI-G-1 summarizes the values that have been calculated in this chapter.

The loss of ductility limits the integral wall loading to ~2 MW-yr/m². That is, we expect the walls would have to be replaced after 1-2 years at a 1.25 MW/m² wall loading. If we had wanted the wall to last for the full 30 year lifetime, we would have to operate at ~0.06 MW/m². Clearly, from the discussion in Chapter 2, such an operating point is uneconomical.

It now appears that the integral wall loading limitation on the first wall is due to void swelling in 20% CW 316 SS is ~6.2 MW-yr/m². Such a limitation implies that the first wall could survive a 0.2 MW/m² neutron loading for 30 years. This low value again appears to be uneconomical.

It is possible to get some appreciation for the benefits of using the cold worked steel over the solution treated alloy by comparing the integral wall loading limitations for both metallurgical treatments. If one wants to limit the void swelling to less than 10%, then the ST 316 SS should be subjected to no more than 3.3 MW-year/m². This means that if embrittlement did not limit the wall lifetime to 1-2 years, swelling in ST 316 SS would limit it to 2-3 years. The use of cold-worked 316 SS raises the possible lifetime due to the swelling effect alone to ~5 years.

The third major limitation is due to erosion of the first wall. We have arbitrarily chosen 1 mm (40% of the original thickness) as a maximum allowable erosion. On this basis, it was discovered that, if the most pessimistic sputtering and blistering rates were assumed, then the integral wall loading limitation was ~6 MW-year/m². (The exact value depends on the time because of the loss of material due to corrosion). It appears that if no other limitations were placed on the first wall then a 30 year operation at 0.2 MW/m² would be marginally economical. However, if the high 14 MeV neutron sputtering rates of Kaminsky(84) are not substantiated in future experiments, then the integral wall loading limitation may be as much as 12 MW-year/m².

One might also place a limit on the transmutation effects in 316 SS in UWMAK-I. It is not easy to establish a very exact criteria but one might state that once the Mn content reaches 10%, the properties of the alloy may be no longer acceptable. This criteria would result in an integral limit of ~68 MW-year/m².

There appears to be no particular problem with B_4C swelling in the UWMAK-I shield configuration. In fact, it is expected that one could place a 1000 MW-year/m² wall loading limitation on UWMAK-I if the only concern was to limit the B_4C swelling to 20%.

It is interesting to note that the major limitation in the toroidal magnet is due to the increase in resistivity of the copper stabilizer. The integral wall loading limit resulting from this phenomena is ~25 MW-year/m². However, this can be extended by a factor of ~2 simply by warming the magnets up to room temperature. Another way to extend this limit is to include slightly more Cu in the magnet to increase the total current carrying area and lower the total resistance.

The integral limit from the standpoint of the superconductor, NbTi, depends on how much of a drop in T_c or J_c that we are willing to accept. If we arbitrarily assume that a drop in T_c of 2°K is the limit, then an integral value of ~160 MW-year/m². The limit on J_c (a 10% drop) is a bit more stringent at ~130 MW-year/m². Both of these limits would place a ~5 MW/m² wall loading value for a 30 year lifetime.

Finally, one should investigate the potential problems associated with a degradation of the mylar superinsulation. A reasonable limit might be the exposure at which its elongation at failure is reduced to 10% of its original value. From Figure VI-F-11, this occurs at ~1000 x 10⁶ Rads and at the radiation level of 0.028 x 10⁶ Rad/year, an integral wall loading limit of >10,000 MW-year/m² is suggested.

Table VI-G-1

Summary of Wall Loading Limitations Due to Radiation
Damage in UWMAK-I Blanket and Shield Geometry

<u>Phenomena</u>	<u>Design Limit</u>	<u>Integral Neutron Wall Loading Limit-MW-yrs./m²</u>
Embrittlement	>0.5% Uniform Elongation	2
Swelling - ST 316 SS	$\{\frac{\Delta V}{V} < 10\%\}$	3.3
- CW 316 SS		6.
Wall Erosion	(<1.0 mm)*	
High S for 14 MeV n		6
Low S for 14 MeV n		12
Transmutation	(Mn <10%)	68
B ₄ C	(<20% Swelling)	1000
Mylar	(elongation >10% unirradiated)	10,000
Cu Stabilizer	(<10% resistance increase)	25
NbTi	($\Delta T_c < -2^\circ K$)	160
	($\Delta J_c / J_c < -10\%$)	130

*Corrected for corrosion loss

References

- 1) G. L. Kulcinski, J. J. Laidler and D. G. Doran, Radiation Effects, 7, 195, 1971 and D. G. Doran, G. L. Kulcinski, ibid 9, 283, 1971.
- 2) D. K. Brice, Radiation Effects, 11, 51, 1971.
- 3) I. Manning and G. P. Mueller, to be published, Radiation Effects.
- 4) G. L. Kulcinski, D. G. Doran and M. A. Abdou, UW-FDM-15, 1973.
- 5) D. G. Doran, Nuclear Science and Engineering, 49, 130, 1972.
- 6) IAEA Specialists Meeting on Radiation Damage Units for Ferritic and Stainless Steels, Oct. 31-Nov. 1, 1972, Seattle Washington.
- 7) J. Lindhard, V. Nielsen, M. Scharff and P. V. Thomsen, Mat. Fys., Medd. Dan. Vid. Selsk., 33, No. 10 (1963)
- 8) M. T. Robinson, "Proceedings of Nuclear Fusion Reactors Conference, British Nuclear Society, Culham Laboratory, September 1969, p. 364.
- 9) M. J. Norgett, M. T. Robinson, and I. M. Torrens, "Proposed Standard for Calculating Displacement Dose Rates," Oak Ridge National Lab., CONF-721037-1 (1972).
- 10) P. G. Lucasson and R. M. Walker, "Production and Recovery of Electron Induced Radiation Damage in a Number of Metals," Phys. Rev., 127, 485, 1962.
- 11) G. Youngblood, S. Myhra, J. W. Deford, "Threshold Displacement Energy Measurements on Ta and Nb," C00-1494-7, 1968.
- 12) H. C. Honeck, "ENDF/B - Specifications for an Evaluated Nuclear Data File for Reactor Applications," BNL-50066 (May 1966).
- 13) V. J. Orphan, N. C. Rasmussen and T. L. Harper, Gulf Atomic Report GA-10248, DASA-2500, July 31, 1970.
- 14) G. R. Odette, "Energy Distribution of Neutrons from (n,2n) Reactions," Trans. ANS 15, 414 (1972).
- 15) M. Segev, ANL-7710, January 1971.
- 16) G. R. Odette, private communication.
- 17) D. G. Doran, to be published.
- 18) W. G. Johnston, J. H. Rosolowski, A. M. Turkalo, and T. Lauritzen, J. Nucl. Material 47, 155, 1973.

- 19) S. D. Harkness and Che-Yu Lie, "Radiation Damage in Reactor Materials", Vol. II, IAEA, Vienna, 1969. P. 189.
- 20) R. Bullough and R. C. Perrin, *ibid* P. 233.
- 21) S. D. Harkness and Che-Yu Lie, "Radiation Induced Voids in Metals", Ed. by J. W. Corbett and L. C. Ianniello, Proceedings of Int. Conference, Albany, N.Y., June 1971, AEC Symposium Series 26, P. 798.
- 22) R. Bullough and R. C. Perrin, *ibid* P. 769.
- 23) R. Bullough, B. L. Eyre, and R. C. Perrin, *J. Nucl. Appl. and Tech.* 9, 346, 1970.
- 24) H. Wiedersich, *Rad. Effects* 12, 111, 1972.
- 25) A. D. Brailsford and R. Bullough, *J. Nucl. Mat.*, 44, 121, 1972.
- 26) A. D. Brailsford and R. Bullough, AERE Report T. P. 486, 1972, also to appear in *Phil. Mag.*
- 27) R. Bullough and R. S. Nelson, AERE-R-7353, 1973.
- 28) Proc. of ASTM Conf. on Irradiation Effects on Structural Alloys for Nuclear Reactor Applications, Niagara Falls, N.Y., June 1970, ASTM-STP-484, 1971.
- 29) Proceedings of British Nuclear Energy Society European Conference, Voids Formed by Irradiation of Reactor Materials, Ed. by S. F. Pugh, M. H. Loretto, and D. I. R. Norris. Reading, England, March 24, 1971.
- 30) Proceedings of Int. Conf. on Radiation Induced Voids in Metals, ed. by J. W. Corbett and L. C. Ianniello, Albany, N.Y., June 9, 1971, CONF-710601, 1972.
- 31) Proceedings of ASTM Conf. on Effects of Radiation on Substructure and Mechanical Properties of Metals and Alloys, Los Angeles, Calif., June 1972, ASTM-STP-529, to be published.
- 32) Proceedings of the 1973 Int. Conf. on Defects and Defect Clusters in B.C.C. Metals and Their Alloys, ed. by R. J. Arsenault, National Bureau of Standards, Gaithersburg, Maryland, Aug. 14-16, 1973.
- 33) D. I. R. Norris, *Radiation Effects*, 14, 1, and 15, 1, 1972.
- 34) J. L. Katz and H. Wiedersich, *J. Chem. Phys.*, 55, 1414, 1971.
- 35) K. C. Russell, *Acta Met.* 19, 753, 1971.
- 36) J. L. Katz and H. Wiedersich, *J. Nucl. Mat.* 46, 41, 1973.
- 37) H. Wiedersich and J. L. Katz, P. 530 in Reference 32.

- 38) We are indebted to Dr. J. Straalsund of HEDL for the summary of this information which will be published shortly.
- 39) D. W. Keefer, A. G. Pard and D. Kramer in Reference 5.
- 40) J. J. Laidler, Paper presented at the International Conference on Physical Metallurgy of Reactor Fuel Elements, Berkeley Nuclear Laboratories 2-7 Sept., 1973, to be published.
- 41) G. L. Kulcinski, To be published in the Int. Conf. on Application of Ion Beams to Solids, Albuquerque, N. Mexico., Oct. 1973.
- 42) R. S. Nelson, J. A. Hudson, and D. J. Mazey, P. 430 in Reference 30 and P. 191 in Reference 29.
- 43) J. O. Steigler, J. M. Leitnaker, and E. E. Bloom, Int. Conf. on Physical Metallurgy of Reactor Fuel Elements, Berkeley Nuclear Laboratories, Sept. 2, 1973, To be published.
- 44) J. J. Laidler, HEDL personal communication.
- 45) R. G. Gray and L. R. Lynam, WAPP-261, 1963.
- 46) F. J. Homan, Nucl. Tech., 16, 216, 1972.
- 47) W. R. Martin et. al., Trans ANS, 9, 50, 1966.
- 48) F. A. Comprelli et. al., Trans ANS, 11, 145, 1968.
- 49) A. S. Fraser, I. R. Birss and C. Cawthorne, Nature, 211, 291, 1966.
- 50) M. Weisz et. al., P. 352 in "Irradiation Effects in Structural Alloys for Thermal and Fast Reactors", ASTM-STP-457, 1969.
- 51) A. L. Ward and J. J. Holmes , Nucl. Appl. Tech., 9, 771, 1970.
- 52) E. E. Bloom and J. O. Stiegler in Reference 31, To be published.
- 53) J. J. Holmes , A. J. Lovell and R. L. Fish in Reference 31, To be published.
- 54) E. E. Bloom and J. R. Weir Jr., To be published.
- 55) R. L. Fish and J. J. Holmes , J. Nucl. Materials, 46, 113, 1973.
- 56) "Irradiation Embrittlement and Creep in Fuel Clodding and Core Components" Proceedings of Conf., Brit. Nucl. Energy Soc., Nov. 9-10, 1972.

- 57) E. E. Bloom, *ibid.* P. 93.
- 58) D. Kramer, K. R. Garr, A. G. Pard, and C. G. Rhodes, *ibid.*, P. 109.
- 59) K. Q. Bagley, J. W. Barnaby, and A. S. Fraser, *ibid.*, P. 143.
- 60) J. D. Bleu, W. Van Witzenberg, M. I. deVries, and A. Glas, *ibid.*, P. 155.
- 61) D. Fahr, E. E. Bloom, and J. O. Stiegler, *ibid.*, P. 167.
- 62) R. L. Fish, A. J. Lovell, H. R. Brager and J. J. Holmes, *ibid.*, P. 187.
- 63) P. J. Ring, H. J. Busboom, and C. M. Spalaris, *ibid.*, P. 197.
- 64) P. Soo and J. McAndrew, WARD-3045T2C-3, Nov. 1972.
- 65) J. R. Hawthorne, NRL Memorandum Report 2088 (AD-703617), Feb. 1970, P. 7.
- 66) J. R. Hawthorne, WHAN-FR-40-1, Jan. 1971, P. 641.
- 67) T. T. Claudson, R.W. Barker and R.L. Fish, Nucl. Appl. & Tech., Vol. 9, July 1970, also Ref. 55.
- 68) J. O. Stiegler and E. E. Bloom, ORNL-TM-3550, Dec. 1971, P. 90.
- 69) M.M. Paxton and F.R. Schober, HEDL-71-61,-115,-134 and -176, 1971.
- 70) A. L. Ward, J.E. Irvin, L.D. Blackburn, G.M. Slaughter, G.M Goodwin and M. C. Cole, HEDL-TME-P1-118, Aug. 1971.
- 71) 1970 Annual Book of ASTM Standards, Part 31, Section F-8, July 1970, ASTM, P. 194-213, 1970.
- 72) R. L. Fish, J. L. Straalsund, C. W. Hunter, and J. J. Holmes , To be published in Reference 31.
- 73) D. Steiner, ORNL-TM-3094, 1970.
- 74) G. L. Kulcinski, R. G. Lott, T. Yang, UWFDM-42, March, 1973.
- 75) M. Kaminsky, Proc. of Int. Working Session on Fusion Reactor Technology, CONF-710624, P. 86, (June 28-July 2, 1971).
- 76) R. S. Pease, Rendiconti S.I.F., Corso 13:158, Sept. 1959.
- 77) D. T. Goldman and A. Simon, Phys. Rev., 111, P. 383, 1958.
- 78) M. Kaminsky, Atomic and Ionic Phenomena on Metal Surfaces, Academic Press, New York, 1965.

- 79) A. J. Summers, N. J. Freeman, and N. R. Daly, Proc. of Nucl. Fusion Conf., BNES, Culharn, P. 347, 1969.
- 80) G. Carter and J. Colligon, Ion Bombardment of Solids, American Elsevier Publishing Co., New York, 1968.
- 81) F. Keywell, Phys. Rev., 97, 1611, 1955.
- 82) M. Kaminsky, IEEE Trans, MS18, 1971.
- 83) R. I. Garber, Atomnaya Energiya, 28, 400, 1970.
- 84) M. Kaminsky, Personal Communication.
- 85) R. G. Mills, To be published.
- 86) M. Kaminsky, "Surface Effects in Thermonuclear Devices and Reactors" presented at the 7th Symposium on Fusion Technology, Grenoble, France (Oct 24-27, 1972).
- 87) S. K. Das and M. Kaminsky, J. Appl. Phys., 44, 25 (1973).
- 88) M. Kaminsky and S. K. Das, Appl. Phys. Lett. 21, 443 (1972).
- 89) S. K. Das and M. Kaminsky, J. Appl. Phys., 44, 2520 (1973).
- 90) S. K. Das and M. Kaminsky, in Defects and Defect Clusters in B.C.C. Metals and their Alloys, Nuclear Metallurgy Vol. 18, edited by R. J. Arsenault, National Bureau of Standards, Gaithersburg, Maryland, p. 240 (1973).
- 91) M. Kaminsky and S. K. Das, Rad. Effects, 18, 245 (1973).
- 92) M. Kaminsky and S. K. Das, Appl. Phys. Lett., 23, 293 (1973).
- 93) W. Bauer and G. J. Thomas, *ibid*, p. 255.
- 94) W. Bauer and D. Morse, J. Nucl. Mat. 44, 337 (1972).
- 95) S. K. Das and M. Kaminsky, To be published in Conf. Proc. of "Applications of Ion Beams to Metals", Albuquerque N. Mex., Oct. 2-4, 1974.
- 96) S. K. Erents and G. M. McCracken, CLM-P323, Sept. 1972.
- 97) H. Verbeek and W. Eckstein, To be published in Conf. Proc. of "Applications of Ion Beams to Metals", Albuquerque, N. Mex, Oct. 2-4, 1974.
- 98) E. V. Kornelsen, To be published.

- 99) G. J. Thomas and W. Bauer, Rad. Effects, 17, 221, 1973.
- 100) R. S. Nelson, Phil. Mag. 9, 343, 1964.
- 101) S. K. Das and M. Kaminsky. To be published in Conference Proceedings of 5th Symp. on Engineering Problems of Fusion Research, Princeton, Nov. 6-9, 1973.
- 102) W. Bauer and G. J. Thomas, J. Nucl. Materials, 47, 241, 1973.
- 103) J. M. Donhowe, D. L. Klarstrom, M. L. Sundquist and W. J. Weber, Nucl. Tech., 18, 63 (1973).
- 104) R. Benaroya, T. H. Blewitt, J. M. Brooks and C. Laverick, "Effect of Fast Neutron Irradiation at Low Temperature on NbZr Coil Performance", IEEE Trans. on Nucl. Sci., NS14, No. 3, 383 (1967)
- 105) M. Soell, S. L. Wipf, and G. Vogl, "Change in Critical Current of Superconducting NbTi by Neutron Irradiation:", Applied Superconductivity Conf., Annapolis, 1972
- 106) G. W. Cullen and R. L. Novak, "Effect of Neutron Induced Defects on the Current Carrying Behavior of Nb₃Sn:", J. Appl. Phys., 37, 3348 (1966).
- 107) R. Bett, AERE Harwell (private communication) (1972).
- 108) P. S. Swartz, H. R. Hart, R. L. Fleischer, "Effect of Fast-Neutron Irradiation on Magnetic Properties and Critical Temperature of Some Type II superconductors:", Appl. Phys. Letters, 4, 71 (1964).
- 109) J. P. McEvoy, R. F. Decell and R. L. Novak, "Effect of Neutron Irradiation on Critical Currents in Hard Superconductors", Appl. Phys. Letters, 4, 43 (1964).
- 110) E. I. Keller, H. T. Coffey, A. Patterson and S. H. Autler, "Radiation-Induced Peak Effect in Superconducting NbZr" App. Phys. Letters 9, 270, (1966).
- 111) R. Babcock and H. Riemersma, "Operation of a Superconducting Solenoid in a 440 Mev Proton Flux", Appl. Phys. Letters, 1, 43, (1962).
- 112) W. V. Hassenzahl, J. D. Rogers, H. L. Laquer, W. C. Armstrong, "Radiation Damage in NbTi Superconducting Wires", Third Intern. Conf. on Magnet Technology, Hamburg 1970.
- 113) D. G. Schweitzer, D. Parkin, M. Garber, A. Goland, "Low Temperature Electron Irradiation of Multifilament Superconductors", Applied Superconductivity Conf. Annapolis 1972.

- 114) H. T. Coffey, E. L. Keller, A. Patterson, and S. H. Autler, "Effect of Low-Temperature Deuteron Irradiation on Some Type II Superconductors", Phys. Rev., 155, 355 (1967).
- 115) H. J. Bode and K. Wohlleben, "Enhancement of J_c in Nb_3Sn Diffusion Layers Produced by Irradiation with Protons", Phys. Letters, 24A, 25 (1967).
- 116) G. W. Cullen and R. L. Novak, "Effect of Fast Neutron Induced Defects on the Current Carrying Behavior of Superconducting Nb_3Sn ", Appl. Phys. Letters, 4, 147 (1964).
- 117) G. W. Cullen, R. L. Novak and J. P. McEvoy, "Effect of Neutron Induced Defects on the current Carrying Behavior of Nb_3Sn " RCA Rev., 25, 479 (1964).
- 118) A. Echarri and M. Spadoni, "Superconducting Nb_3Sn : A Review", Cryogenics, August 1971, 274.
- 119) C. P. Bean, R. L. Fleischer, P. S. Swartz, H. R. Hart, "Effect of Thermal Neutron Irradiation on the Superconducting Properties of Nb_3Al and V_3Si Doped with Fissionable Impurities", J. Appl. Phys., 37, 2218 (1966).
- 120) G. W. Cullen, "The Effect of Radiation on the Properties of Superconducting Materials", Proceedings 1968 Brookhaven Summer Study on Superconducting Devices and Accelerators, BNL50155 (C-55), 438.
- 121) J. B. Vetrano and R. W. Boom, "A High Critical Current Superconducting Ti-Nb Alloy", Atomics International Report (1964).
- 122) A. V. Narlikar and D. Dew-Hughes, "Effect of Dislocation Configuration on the Superconducting Properties of Nb and V", Phys. Stat. Sol., 6, 383 (1964).
- 123) R. R. Coltman, C. E. Klabunde, D. L. McDonald and J. K. Redman, "Reactor Damage in Pure Metals", J. App. Phy., 33, 3509 (1962).
- 124) J. A. Horak and T. H. Blewitt, "Fast Neutron Irradiation Induced Resistivity in Metals", Phys. Stat. Sol., 9, 721 (1972).
- 125) R. R. Coltman, C. E. Klabunde and J. K. Redman, "Survey of Thermal Neutron Damage in Pure Metals", Phys. Rev., 156, 715 (1967).
- 126) T. G. Nilan and A. V. Grant, "Stored Energy Release Below 80°K in Deuteron Irradiated Copper", Phys. Rev., 137, A1233 (1965).
- 127) B. Lengeler, W. Schilling, H. Wenzl, "Deviation from Matthiesens' Rule and Longitudinal Magnetoresistance in Cold-Worked and Neutron Irradiated Copper", J. Low Temp. Phys., 2, 237 (1970).
- 128) J. A. Corbett, "Electron Radiation Damage in Semiconductors and Metals", Solid State Physics, Advances in Research and Applications, Vol. 7 (1966).
- 129) W. Schilling, G. Burger, K. Isebeck, and H. Wenzl, "Annealing States in the Electrical Resistivity of Irradiated FCC Metals," Vacancies and Interstitials in Metals, edited by A. Seeger, D. Schumacher, W. Schilling and J. Diehl (Wiley, New York, 1970).

- 130) G. Burger, H. Meissner and W. Schilling, "Analysis of Radiation Annealing Observed During Low Temperature Irradiation with Neutrons and Heavy Charged Particles," Phys. Stat. Sol., 4, 281, (1964).
- 131) H. Wenzl, "Physical Properties of Point Defects in Cubic Metals," Vacancies and Interstitials in Metals, edited by A. Seeger, D. Schumacher, W. Schilling and J. Diehl (Wiley, New York) 1970.
- 132) Z. J. J. Stekly, R. Thome, and B. Strauss, "Principles of Stability in Cooled Superconducting Magnets," Proc. of 1968 Summer Study on Superconducting Devices and Accelerators, Brookhaven, ENL501-55 (C-55), 748.
- 133) A. Charlesby, Atomic Radiation and Polymers, (Pergamon Press, New York), 1960.
- 134) J. F. Kircher and R. E. Bowman, Effects of Radiation on Materials and Components, (Reinhold Publishing Co., New York), 1964.
- 135) C. L. Hanks and D. J. Hamman, Radiation Effects Design Handbook, Section 3: Electrical Insulation Materials and Capacitors, NASA-CR-1787 (1971).
- 136) R. Harrington and R. Giberson, "Chemical and Physical Changes in Gamma-Irradiated Plastics", Modern Plastics, 36, 199 (1958).
- 137) O. Sisman and C. D. Bopp, "A Summary of the Effect of Irradiation on Some Plastics and Elastomers", ASTM Spec. Pub. 208, 119 (1956).
- 138) C. D. Bopp and O. Sisman, "Radiation Stability of Plastics and Elastomers," ORNL 1373 (1953).
- 139) O. Sisman and C. D. Bopp, "Physical Properties of Irradiated Plastics," ORNL 928 (1951).
- 140) R. Mowers, "Properties of Non Metallic Materials at Cryogenic Temperatures," Proceedings of the 1968 Summer Study on Superconducting Sevices and Accelerators, BNL 50155 (C-55), Volume 1, p. 311.
- 141) R. P. Reed, R. E. Schramm, and A. F. Clark, "Mechanical, Thermal, and Electrical Properties of Selected Polymers", Cryogenics, 13, 67 (1973).
- 142) H. Brechna, "Effect of Nuclear Radiation on Organic Materials; Specifically Magnet Insulation in High Energy Accelerators," SLAC Rep. No. 40, AEC Contract AT(04-3)-515 (1965).
- 143) M. Van de Voorde, "Results of Physical Tests on Polymer Materials at Cryogenic Temperatures" IEEE Trans. Nuc. Sci., NS-20 (3), 693 (1973).
- 145) W. Weleff, "Effect of Nuclear Radiation and Liquid Hydrogen on Mechanical Properties of Three Phenotic Materials", Adv. Cryo. Eng., 11, 486.

VII. Magnets

A. Toroidal Field Magnet

In this section we describe the design of the main toroidal magnets. Our design philosophy is based on the recognition that complete cryogenic stability is the only viable design at this time.

The alternative of using unstable magnets needs considerable developmental effort in both cost and experience before any reliability can be predicted. A goal to use unstable high current density magnets seems unwarranted since for tokamaks there is easily enough space available to produce the required fields at 1000 A/cm^2 , a typical cryogenically stabilized value. Unstable magnets only achieve reduction in the amount of copper or aluminum, which is in itself a minor consideration, at the risk of being highly unreliable.

The main design is a "D" shaped toroid producing 3.83T at $R=13\text{m}$, the plasma center. The general reasoning behind the specification and choices listed is given with the detailed reasoning presented in the remaining sections.

1. Specifications and Description of the Magnet Design

a. Specifications

- (1) On-axis field at a radius of 13m = 3.83 tesla
- (2) Field at inside turn at a radius of 20.55m = 2.42 tesla. (point A in Figure VII-A-1)
- (3) Field at inside turn at a radius of 5.75m = 8.66 tesla. (point B in Figure VII-A-1)
- (4) Maximum field in the self-supported portion of the magnet = 6.3 tesla (point C in Figure VII-A-1)
- (5) Design stress in 316 stainless steel at 4.2K = $4.14 \times 10^8 \text{ N/m}^2$ (60,000 psi)
- (6) Design strain in copper stabilizer ≤ 0.002 .

b. Descriptions of components

- (1) Number of magnets = 12
- (2) Number of discs per magnet = 34
- (3) Number of conductor turns per disc = 60 (30 each side)
- (4) Conductor current = 10,212 amperes
- (5) Disc cross section is 5 x 93 cm with 30 helical grooves forged, rolled or machined into each surface. (see Figure VII-A-2)
- (6) The conductor is NbTi superconductor in a copper stabilizer. The conductor cross-section is 2.99 cm wide x 2.00 cm thick on the inside turn and tapers linearly in both width and thickness to 2.53 cm wide x 1.60 cm thick on the 7th turn. For the remaining 23 turns, the width is tapered linearly

to 1.10 cm on the outside turn while the depth remains constant at 1.60 cm, see Figure VII-A-2.

- (7) There is 0.10 cm of reinforced epoxy insulation between the conductor and the stainless steel disc.
- (8) There are 0.635 cm thick micarta spacers between each disc which cover 50% of the area, see Figure VII-A-2.
- (9) Approximately 1670 aluminum alloy bolts one inch in diameter are used per magnet to fasten the 34 discs into a solid unit capable of resisting the necessary out of plane bending moments and torques without slipping at the interfaces between micarta and stainless steel, see Figure VII-A-3.
- (10) Reinforced epoxy struts of approximately $8,500 \text{ cm}^2$ cross section on each side of each magnet are required to provide lateral support between the magnet and dewar in the event of failure of the power supply in a magnet. Warm structural reinforcement of similar cross section is needed between adjacent dewars for the same purpose.

c. Materials required for 12 magnets

- | | |
|--|-------------------------|
| (1) NbTi superconductor alloy | 230,000 lb. |
| (2) Copper stabilizer | 10.75×10^6 lb. |
| (3) Stainless steel in discs | 9.89×10^6 lb. |
| (4) Stainless steel in dewars | 2.05×10^6 lb. |
| (5) Alloy steel in circumferential bracing | 1×10^6 lb. |
| (6) Reinforced epoxy conductor insulation in discs | 580,000 lb. |
| (7) Micarta spacers between discs | 324,000 lb. |
| (8) Reinforced epoxy circumferential bracing in dewars | 26,800 lb. |
| (9) Aluminum alloy bolts to assemble discs | 120,000 lb. |
| (10) Liquid helium inside dewars | 100,000 liters |
| (11) Liquid helium in storage | 200,000 liters |
| (12) Cryogenic superinsulation | $516,000 \text{ m}^2$ |
| (13) Refrigeration - Five 3 KW, 4.2K refrigerator liquifiers | |
| (14) Power Supplies | |

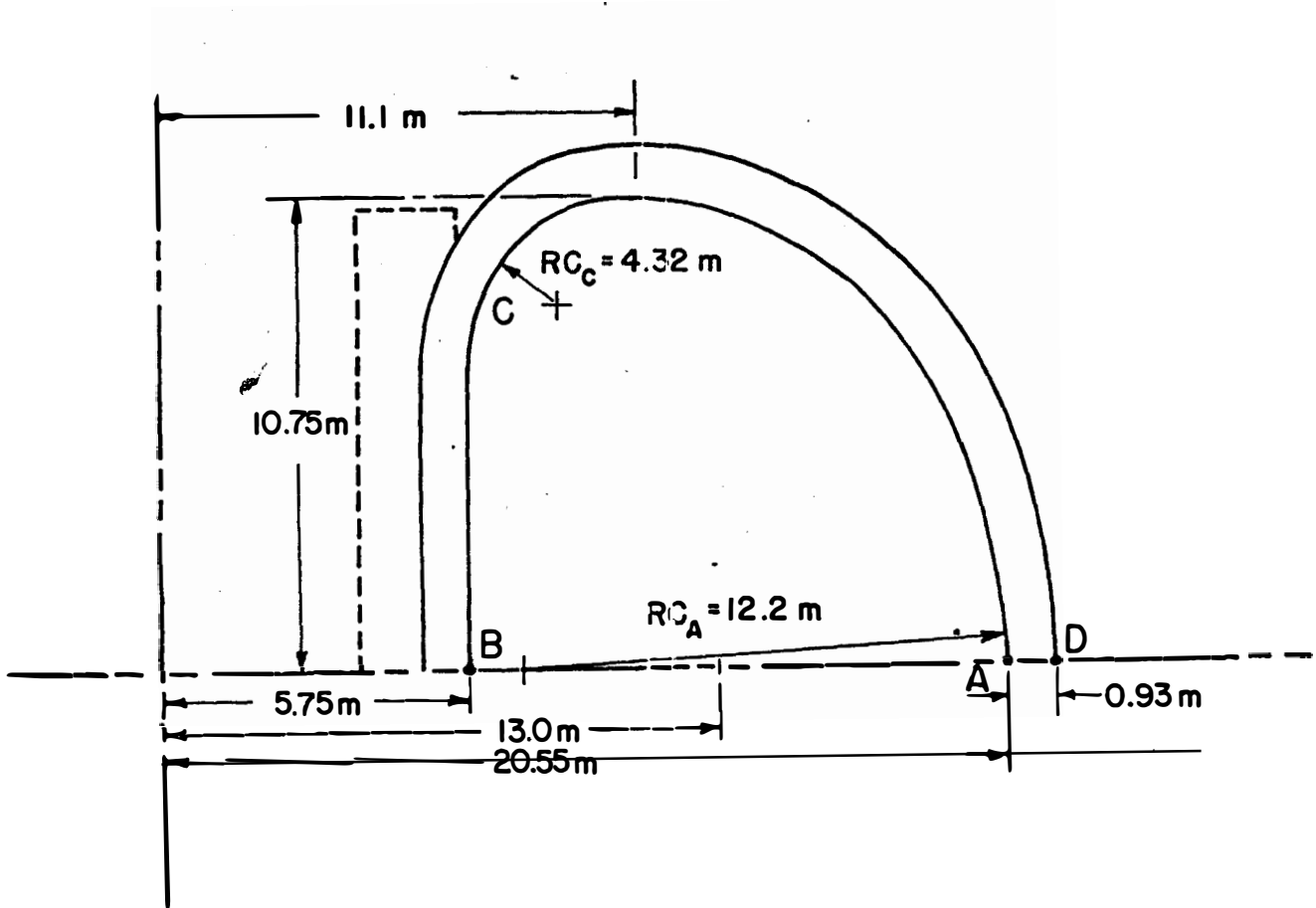
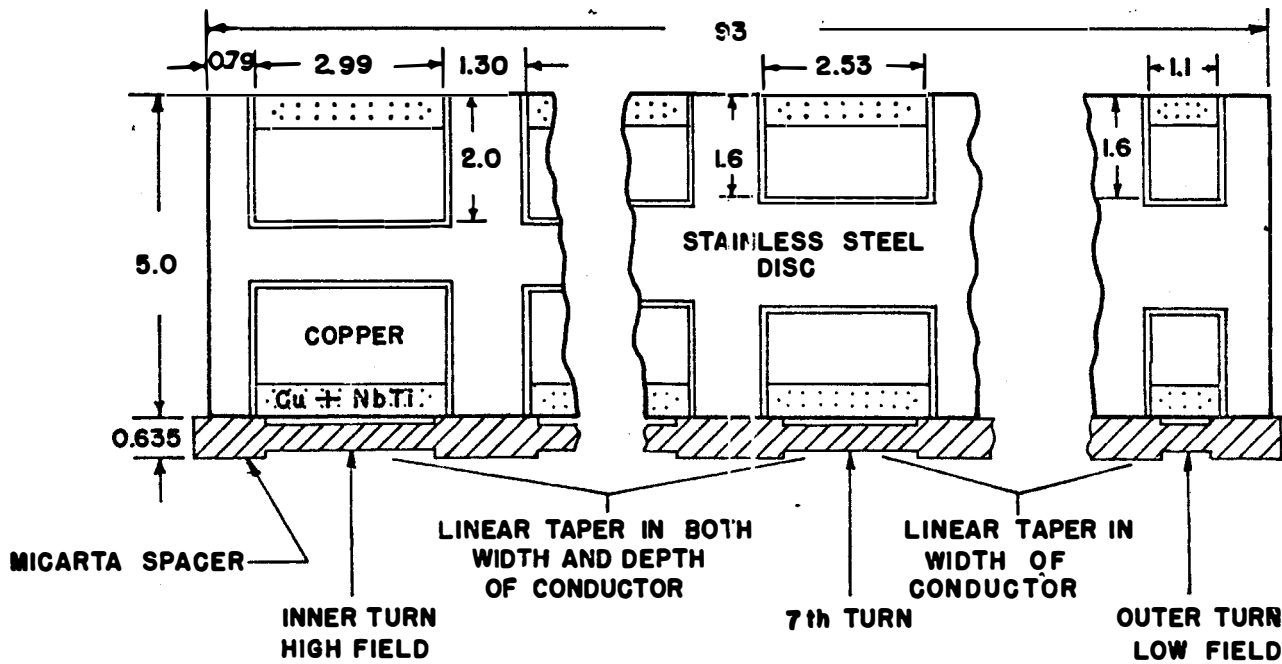


FIGURE VII-A-1 Stainless Steel Structural Disc for "D" Shaped Toroidal Field Magnet



ALL DIMENSIONS IN cm.

FIGURE VII-A-2 Cross Section of Conductor and Structural Disc for "D" Shaped Toroidal Field Magnet

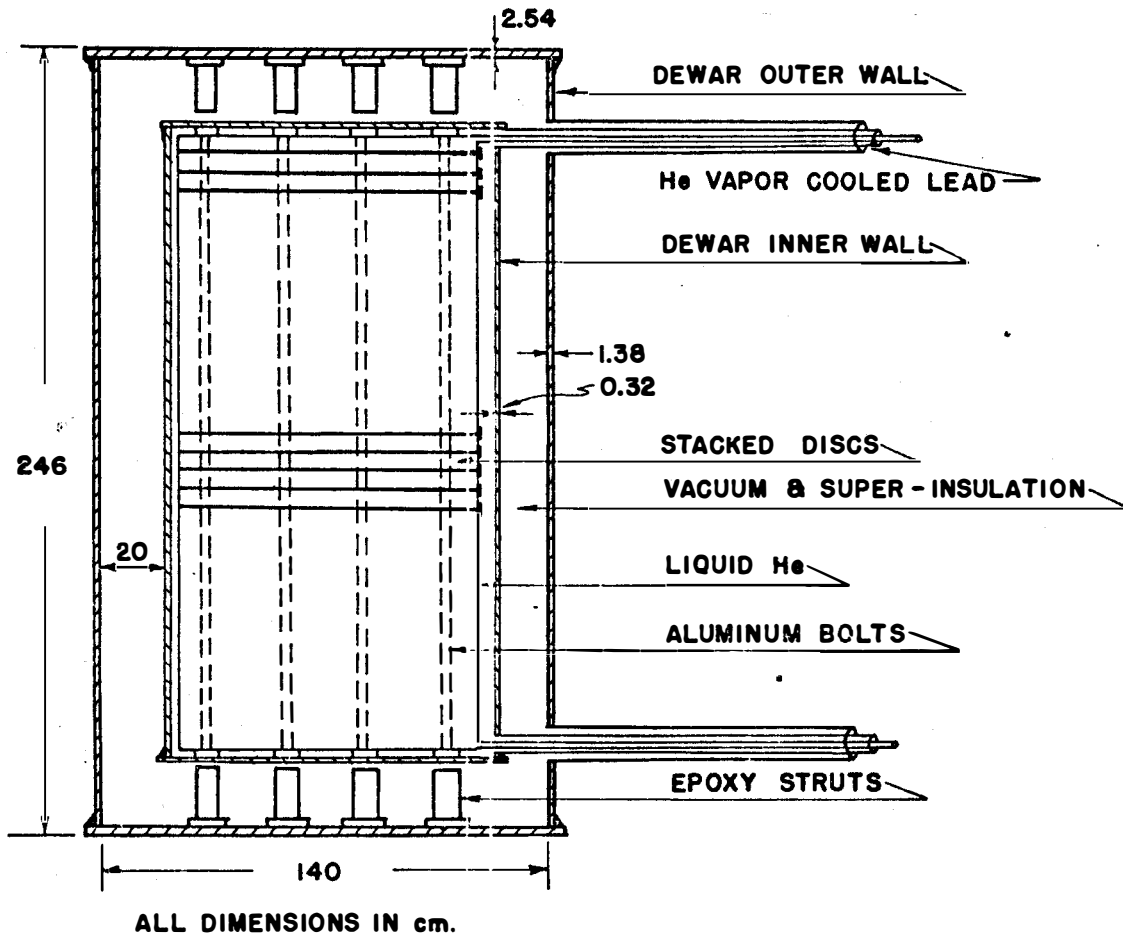


FIGURE VII-A-3 Typical Toroidal Field Magnet Cross Section

2. Construction Techniques

a. Conductor

The conductor will consist of an OFHC copper backing strip soldered to a thin surface strip which contains NbTi filaments. The conductor will taper from 2.99 cm wide x 2 cm deep at the high field inner turn to 1.1 cm wide by 1.6 cm deep at the low field outer turn. The surface strip will be 0.5 cm thick with width and NbTi content varied smoothly and in discrete steps from high to low field. Such soldered assembly is similar to the NAL bubble chamber conductor.¹ The Cu - NbTi conductor will be made in the standard well known fashion by filling drilled holes in a copper ingot with NbTi rods, extruding the combination to a smaller diameter which bonds the NbTi to the copper, wire drawing from about 20 cm to 1.2 cm (typically), twisting 1 turn per 30 cm, flattening to 2.0 x 0.5 cm (typically) and heat treating at the appropriate temperature for NbTi. Additional explicit fabrication details are given in the Mac Inturff¹⁷ report of Atomics International production techniques.

The transport current for the above conductor is 10,212A for one sided cooling in liquid helium. The magnetic field ranges from 8.7 to 0 tesla. There will be more than 120 NbTi filaments

b. Discs

Each of the 34 discs in each magnet is a "D" shaped washer 5 cm thick, 93 cm wide and weighs 11,018 kg. (24,240 lb). While this weight is within the capability of forging presses in operation at this time, the outer diameter of 23.36 m (76.6 ft.) is not. To be forged today would require that it be done in 3 or 4 pieces and welded. With the large number of discs to be manufactured it would seem reasonable to forge the grooves into the surface and only machine the connections and grooves at the weld joints.

A winding jig is needed to support a disc and a continuous conductor 3810 m (12,500 ft.) long which weighs 12,880 kg (28,300 lb.) after being formed as described in section 2a and then spiral wrapped with a partially cured reinforced epoxy. One half of the conductor is passed through the hole in the disc which is located at the inner turn at point A (see Figs. VII-A-1 and VII-A-6) and coiled with a large radius beneath the winding jig while the other half is wound into the groove in the top surface. During winding, a liquid epoxy is added to completely fill the grooves. After the epoxy is cured by heat on the one surface, the assembly is inverted and the winding and curing repeated on the second side.

To expose the conductor metal surface for liquid helium cooling the reinforced epoxy wrapping placed around the conductor before winding must be machined off the outer surface as a final clean-up operation.

c. Assembly of discs

The completed discs are very weak in out of plane bending so the transfer from the winding jig to the assembly jig must be done with care. In assembling the completed discs, they are lowered over 1670 aluminum bolts which have been inserted through the outer disc. The bolt pattern is such that the center to center spacing is approximately 12 inches typically. Adjustments in the pattern are made to minimize the strain changes in the micarta spacers from the prestress values to the full field values. The higher coefficient of expansion of the aluminum as compared to the stainless steel guarantees that the stack remains tight during cooldown. The amount of compression in the stack due to prestressing the aluminum bolts determines the shear resistance of the stack and this in turn determines the ability of the assembled magnet to resist the loads encountered while being assembled into the dewar and raised into a vertical position. This shear resistance is also important in resisting out of plane bending moments caused by the failure of one or more magnets of the twelve in the entire assembly.

d. Structural assembly

Figure VII-A-3 shows a typical cross section of a magnet inside the dewar. The inner dewar wall is assembled with micarta spacers to a tight fit around the magnet. A 20 cm vacuum space containing multiple layer aluminized mylar (superinsulation) provides the thermal insulation. The outer dewar wall is spaced out from the inner wall by a series of reinforced epoxy struts which provide lateral support to the magnet. This is needed primarily in case of failure of the current in an adjacent magnet which would distort the field and produce large lateral, out of plane forces.

The assembled magnet in its dewar is hung by lugs to the cold central core of the toroid structure. (See Section VII-A-5 and Figure IV-A-1).

3. General Restraints and Design Factors

a. Introduction

Ideally one would like to design a superconducting magnet by starting with the field requirements to determine an appropriate superconductor, proceed to the design of a fully stabilized

conductor to carry the superconductor filaments and finally design a structure to support the conductor. When the structure is examined, however, one realizes that the economics of the entire reactor depends primarily upon the cost of the structure of the toroidal field magnets. For this reason, the stress analysis will be discussed first with the interactions of structure, stabilizer and superconductor properties being considered where appropriate.

b. Stress analysis and design procedure for magnet windings and reinforcement

Many magnet shapes are possible but only two were seriously considered: a circular cross section with external reinforcement rings to resist bending and a "D" shaped magnet which provides a constant tension winding region without external rings. Lubell² has designed a toroidal system based on the circular cross section and has presented relations for extrapolation in size and field within the operating field region of NbTi as the superconductor. File³ has suggested the use of constant tension design and has outlined some of the design considerations. The virial theorem⁴ states that the minimum mass of structural material required to contain a magnetic field varies directly with the product of density of the structural material times the energy contained in the magnetic field and inversely with the design stress in the structure. To attain a minimum mass of structure, one would have to stress every portion of the containment vessel to the maximum permissible values in biaxial stress. The constant tension design makes best use of a uniaxial stressed member and for this reason and to accommodate the many diverse requirements of the plasma, the divertor, and the blanket and shield, an early decision was made to use a constant tension, "D" shaped, toroidal field magnet. A conductor in a magnetic field, supported only by tension, carries a tensile force $T = BIR$ where B is the perpendicular field, I the current in the magnet windings, and R the local radius of curvature. File⁽³⁾ has described a "D" shape which has its maximum radius of curvature at the maximum distance from the toroidal axis and becomes tangent to the vertical support at point A. Figure VII-A-4 shows the outline of this shape as curve a. If the winding thickness is small, the tensile stress through the winding is constant and both tensile stress and total tensile load can be maintained constant by matching the local radius of curvature to the local magnetic field. If the winding thickness is greater than the minimum necessary to assure constant tensile stress, then only the constant tensile load can be attained. A second consequence of a thicker winding is the need to consider the distribution

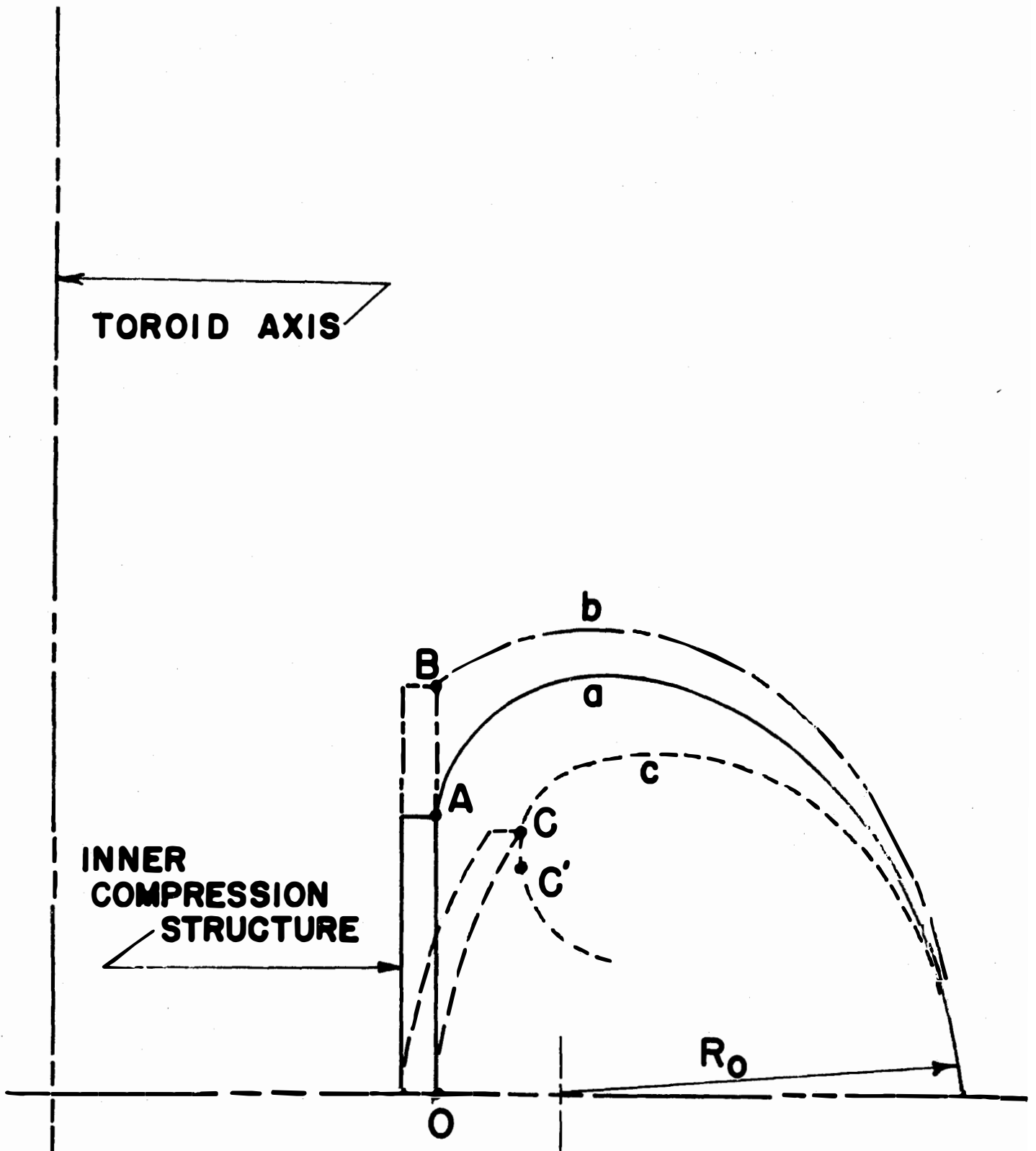


FIGURE VII-A-4

of magnetic loading within the winding itself. The maximum tensile hoop stress in a thick walled cylinder⁵ due to internal pressure p is

$$\max \sigma_h = p \frac{a_2^2 + a_1^2}{a_2^2 - a_1^2} . \quad (1)$$

As a first approximation, p can often be replaced by a magnetic pressure, $(K/2)(\bar{B}_m \times \bar{I})$, where K is constant. The

parameters, a_1 and a_2 are the internal and external radii respectively. One obtains a somewhat different value using this expression for internal pressure than if the actual distribution of current and forces throughout the thickness is used. In both cases, the field is assumed to vary linearly through the thickness from B_m to zero at the outer surface.

For the distributed force case, the maximum stress is given by

$$\max \sigma_h = \frac{q_i [2a_2^4 + (1+\nu)(5a_2^4 - 12a_2^3 a_1 + 6a_2^2 a_1^2) + (1-\nu)(3a_1^4 - 4a_2 a_1^3)]}{12(a_2 - a_1)(a_2^2 - a_1^2)} \quad (2)$$

where $q_i = K \frac{\bar{B}_m \times \bar{I}}{a_2^2 - a_1^2}$ and ν is Poisson's ratio.

For example, if $\nu = 0.3$ and if a representative value of $a_2/a_1 = 1.2$ is used, the ratio of correct maximum stress (eq. 2) to approximate maximum stress (eq. 1) is 1.09. To properly consider the distribution of current and magnetic field throughout the winding, as well as to account for the thick-walled nature of the windings being designed, the following steps were carried out for three basic conductor designs. Each of these conductor designs was based¹ on magnet coils constructed by stacking individual pancakes.

The first design (see Figure VII-A-5(A)) used interleaved stainless steel bands with¹ edge and face cooled copper bands such as the NAL conductor. The second (see Figure VII-A-5(B)) considered interleaved copper and stainless steel with edge cooling only, and the third and ultimately chosen design consisted of edge cooled "D" shaped forged stainless steel pancakes with spiral grooves of varying width and depth on each face. The copper conductor will be inserted into these spiral grooves and bonded with fiberglass-reinforced-epoxy as insulation, see Figure VII-A-5(C).

The design procedure is carried out in stages, described below as (1) through (4).

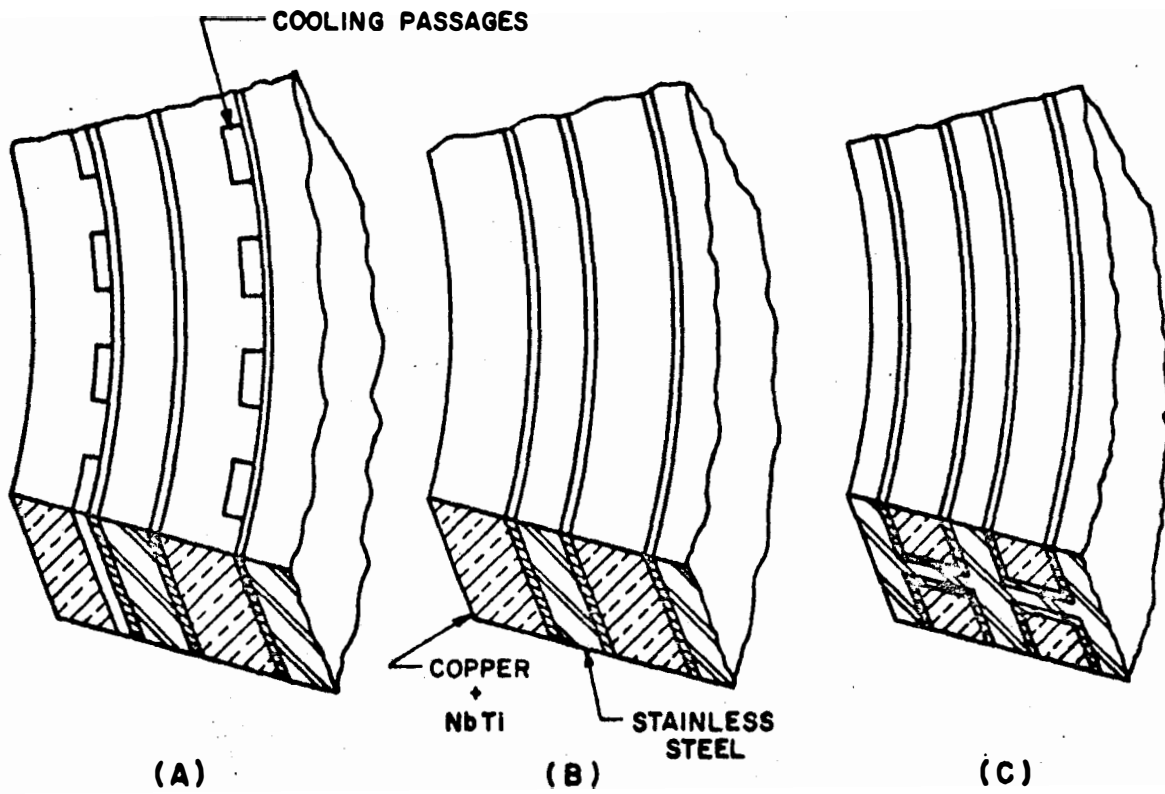


FIGURE VII-A-5 Pancake Designs

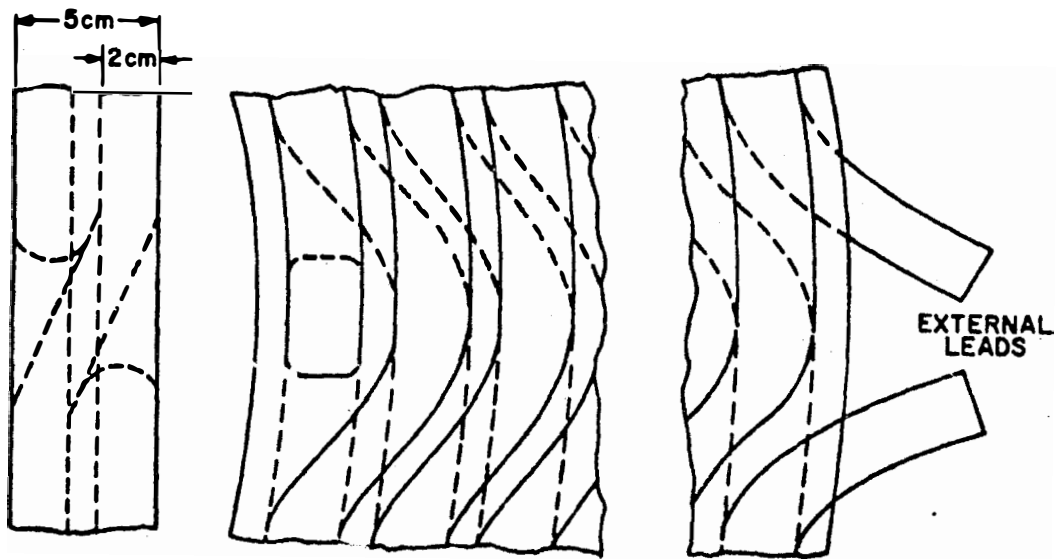


FIGURE VII-A-6 Details of Winding Conductor into Stainless Steel Pancake

(1) A simple finite element approach was used to analyze the equilibrium and compatability of each layer of copper, insulation and stainless steel in a cylindrical geometry. The six equations developed for each layer included the following:

- (a) Equilibrium of a layer of copper under three different pressures; 1) the internal and external radial pressures from the stainless steel layers pressing through the insulation, 2) the magnetic body forces on the conductor, and 3) the resulting hoop or circumferential stresses in the copper.
- (b) A similar equilibrium equation for a layer of stainless steel.
- (c) The relationship between radial displacement of a copper layer to the radial and circumferential stresses in the copper.
- (d) A similar relationship for a steel layer.
- (e) A compatability expression relating the radial displacements of adjacent steel and copper layers to the thickness changes from the center of a copper layer, through the cooling lugs used in the face cooled design, through the insulation and to the center of the next outer steel layer.
- (f) A similar expression from the center of a steel layer to the center of the next outer copper layer.

The equations were solved numerically and the output gives the hoop stresses in each layer of copper and steel, the radial stress in each layer of insulation, and the radial displacement of each layer.

This analysis was carried out for a variety of pancakes in which the following variables were considered:

- (a) Ratio of total conductor thickness to inside radius.
- (b) Volume fraction of copper, stainless steel and insulation.
- (c) Linear tapers in copper thickness.
- (d) Linear tapers in stainless steel thickness.
- (e) Varying sizes of cooling passages for the face cooled conductors.
- (f) The addition of an outer reinforcing band of stainless steel.

With so many variables, it is not feasible to show all of the inter-related effects but a few significant facts are worth noting. All of the following comments assume a constant field on the inside of the cylinder and a constant product of current flow and number of turns in a pancake.

- (a) The maximum copper stress varies linearly with the ratio a_1/t , where a_1 is the inside radius and t is the coil thickness, over the range of a_1/t from one upward.
- (b) If a given amount of stainless steel is to be used, the maximum stress in the copper is reduced if most of the steel is used near the inside where the fields are the largest.
- (c) The maximum copper stresses are increased by the radial softness created by deeper cooling lugs in the face cooled design, by thicker insulation, or, as noted in (b) above, by placing the steel more to the outside.

(2) From the output of section (1) just described, design curves were fitted to relate the maximum copper stress, maximum insulation pressure, total circumferential load and volume in the several designs. We then use a numerical analysis to compute the precise shape and size of the toroidal field magnets. Also computed are the quantities of materials required to produce "D" shaped magnets with the appropriate clear space inside to accommodate the divertor and associated pumping equipment.

The numerical analysis begins at the outside of the magnet with a given design stress in the copper, a given radius of curvature of the inside surface of the magnet, R_0 , a given thickness for a single pancake, the required copper dimensions to assure proper cooling and a given distribution of stainless steel in the pancake. With this information and the design curves, a total pancake width is determined as well as the total circumferential load. With the circumferential load and the total width now held constant, new radii of curvature are calculated to match the changing magnetic fields. The radii of curvature are of course used step by step to determine the magnet shape, which in turn permits the correct fields to be calculated. For a given set of magnet dimensions, field strength, and allowable stress in the copper, there is only one initial radius of curvature, R_0 , which will cause the magnet shape to be tangent to the inner reinforcing ring as indicated by curve (a) of Figure VII-A-4 (the tangent point is at point A.) By removing this restriction, one has the option of raising the height of the magnet, curve (b), or lowering the height, curve (c).

Curve (a) is the true "D" shape and the only one for which the tension is constant for all portions of the conductor including the straight, vertical inner portion. For curve (b), the tension is constant only over the portion from the outside up to point B and is somewhat larger than that for curve (a) due to the larger radii involved. Since the vertical portion is not tangent at B, the tensile force in the vertical portion provides only one component of the "constant tension." The remaining load must be provided by the

central core extending from 0 to B. For curve (c), the small starting radius and smaller tensile load will not permit the shape to reach the required inner dimension. There will be constant tension from the outside up to point C but from C to 0, the extra magnetic loading cannot be carried entirely by tension in the winding frame and is instead partially transmitted to the central core as described in part (3) of this section.

In addition to the discrete points calculated for the magnet shape, the computer printout also provided stresses in the copper and insulation.

To summarize, it is possible to economically accommodate various plasma shapes and various blankets, shields and divertors by exercising the options described to modify the basic constant tension "D" shaped magnet.

(3) The unbalanced radially inward magnetic loading on each pancake is resisted by a thick-walled structure provided at the center of the windings. This central force is equal to $\frac{B_m I}{2} \times h$, where h is $2 \times \overline{OA}$ in Figure VII-A-4 for curve (a). This structure is a cylinder which is under a uniform radial compression and is designed to be elastically stable under this load, as well as the loading from the transformer coils (see Figure IV-E-2 in Section IV-E).

For curve (b), (the higher magnet) the central core is also a cylinder, but in addition to the radially compressive magnetic load, it has at each end a radially outward load required to carry the horizontal component of the constant tension in the windings at point B.

For curve (c), (the lower magnet), the structure is a thick-walled shell of half height OC under a normal compressive magnetic loading on its outer surface.

(4) An initial decision to design the copper conductors such as not to exceed the yield stress at 4.2K, approximately $8.27 \times 10^7 \text{N/m}^2$ (12,000 psi), severely restricted the load carrying capability of the stainless steel reinforcement. Since the stainless steel has twice the modulus of elasticity as does the copper and will suffer very similar maximum strains, the maximum stress in the stainless steel is restricted to twice $8.27 \times 10^7 \text{N/m}^2$. A reasonable design stress at 4.2K would be closer to $41.7 \times 10^7 \text{N/m}^2$ (60,000 psi).

It should be understood that the maximum hoop stress of $41.7 \times 10^7 \text{N/m}^2$ is reached at only two points in each pancake. A typical stress distribution across a radial cross section of the magnet shows the largest stress at the inner surface with three quarters of this value on the outer surface. In the design of nuclear power plant components ⁽²⁶⁾ the average circumferential stress or what is called primary stress is taken as 67% of the yield strength at the operating temperature. In our design the primary stress is approximately 7/8 of $41.7 \times 10^7 \text{N/m}^2$ or $36.5 \times 10^7 \text{N/m}^2$. At 4.2K, 316 SS has a yield strength of $62.6 \times 10^7 \text{N/m}^2$, an ultimate strength of $137 \times 10^7 \text{N/m}^2$ and an elongation of 55% in 2 inches. Thus our ratio of primary design stress to yield strength is 0.58 which is substantially less than that permitted in the ASME Boiler and Pressure Vessel Code.

To make better use of the stainless steel, it was proposed to pre-stress the conductor during winding. Only for conductor design (c), Figure VII-A-5, is it possible to assure retention of the pre-stress which would be accomplished as follows. After construction of the "D" shaped stainless steel pancakes with forged, cast or machined grooves

for the conductor, the pancakes would be mounted in a hydraulically actuated jig which would hold it flat while providing an internal loading proportional to the magnetic loading during operation.

While in this condition, the conductors, which had previously been wrapped with a fiberglass insulation saturated with a partially cured epoxy, would be inserted in the channels with sufficient liquid epoxy to assure a solid, void-free, bond. After heat curing the epoxy, the entire pancake would be turned over and the second half of the conductor placed in the same manner and cured. After machining off the outer layer of insulation to expose the edge surface of the conductor to the coolant, the pancake would be placed in a stacking jig with previously manufactured pancakes and micarta spacers and clamped to keep it flat under the prestress loading. Table I shows the stress level proposed due to prestress, cool down and magnetic loading.

While this is a definite improvement in the stress level in the stainless steel, it still produces stress levels lower than are permissible and consequently increases the cost. After a study of permissible strain levels in an OFHC copper conductor at 4.2K where the principal concern is to assure that the thermal and electrical resistivities will not rise beyond acceptable levels incorporated in the sizing of the conductors, a strain level of 0.002 was deemed acceptable. (7) Since copper starts yielding at a strain level of approximately 0.0007, it was necessary to modify the existing design procedure to accommodate the yielding of the conductor. This was accomplished by fitting a curve of the form (8)

$$\epsilon = \frac{\sigma}{E} + K \left(\frac{\sigma}{\sigma_y} \right)^n \quad (3)$$

to a plot of stress versus strain for the conductor material. The values finally used were $\sigma_y = 6.89 \times 10^7 \text{ N/m}^2$, $E = 10.34 \times 10^{10} \text{ N/m}^2$, $K = 0.000091$ and $n = 6.32$. To utilize this expression for the stress-strain relationship most effectively in conjunction with the programs already developed for the elastic case, the following steps were taken.

- (a) An elastic solution was run as before and the elastic stresses obtained for the copper in each layer.
- (b) For every layer in which the stresses in the copper exceeded the yield stress, the strains were computed for the stresses.
- (c) Using equation (3) and the strains from step (b), a stress was found for each layer. With both a stress and strain assigned to each layer a secant modulus can be computed by $E_s = \sigma/\epsilon$ and substituted into the original program in place of the elastic modulus E.
- (d) Steps (a) through (c) were repeated until two successive runs showed that the stresses in each layer had converged. The stresses were then printed for each layer as previously indicated.

TABLE I
Maximum Stresses

<u>Loading</u>	<u>Copper</u>		<u>S. S.</u>	
	$N/m^2 \times 10^{-6}$	psi	$N/m^2 \times 10^{-6}$	psi
Prestress	-82.7	-12,000	41.4	6,000
Cool Down	24.8	3,600	-12.4	-1,800
Magnetic	140.6	20,400	281.3	40,800
Total	82.7	12,000	310.3	45,000

One can now proportion the amount of reinforcement to obtain the desired stress level in the stainless steel reinforcement. It should be made clear at this point that after the first application and release of full magnetic loading, the copper will be effectively prestressed and assembly prestress is not necessary or even desirable. Table II gives the stress levels, at various periods of operation, for the conductor design using 3.83 tesla as the B_{ϕ} field at the plasma center. This completes the description of the design procedure.

The following list summarizes the reasons why the solid forged pancake design was chosen.

- (a) Prestressing or designing for yielding of the copper conductor is possible only with the design using the solid stainless steel pancake or disc.
- (b) No interpancake electrical connections are necessary on the inside with the solid pancake design and the external electrical connections are extremely short and easily made (see Figure VII-A-6).
- (c) Internal heating due to relative motion of conductors and reinforcement should be minimized in the solid pancake design.
- (d) Bolting through the pancakes to assemble them into a magnet is possible only with the solid pancake design.
- (e) Compressive stresses in the insulation are lowest in the solid pancake design. Possible insulation stresses were found to be as high as 8,000 psi in design (b) and 24,000 psi in design (a).
- (f) While the best cooling is possible with design (a), it must be noted that this advantage is somewhat reduced when the magnets are used in a vertical position and the coolant channels become horizontal.
- (g) Coolant channels between pancakes are more stable in size and shape for the solid pancake design due to the bonding of conductors.
- (h) Although winding techniques are well documented for designs (a) and (b) and the forging and/or machining costs are unknown for the solid pancake design, the immense size of this construction makes accurate cost analyses of all of the designs very difficult.

TABLE II
Maximum Stresses

<u>Magnet Condition</u>	<u>Copper</u>		<u>S. S.</u>	
	$\text{N/m}^2 \times 10^{-6}$	psi	$\text{N/m}^2 \times 10^{-6}$	psi
After Assembly	0	0	0	0
After Cool Down	20.7	3,000	-20.7	-3,000
After Magnetic Loading	103.4	15,000	413.7	60,000
Cold After Removing Magnetic Loading	-68.9	-10,000	68.9	10,000
After Warm up to Room Temperature	-75.8	-11,000	75.8	11,000

In concluding this description of the design of the reinforcement for the conductor, it should be made clear that although only the use of stainless steel has been discussed, aluminum alloys have also been considered. For example aluminum 2219 is as strong as stainless steel at low temperature and costs much less. The lower modulus of the aluminum implies about three times the strain so that the conductors would have to be able to suffer this strain without degradation. Relaxation of the stress-strain limitations discussed earlier has been justified by recent experience at Wisconsin, in which it was shown experimentally that 500 resistance ratio aluminum does not change in resistivity significantly after several cycles of plastic deformation. The samples were fabricated by the extrusion of aluminum on a stainless steel wire to get a cross section about half aluminum and half steel. Microscopic examination after stress cycling at 4.2K showed that the aluminum seemed to develop an elongation pattern along easy glide planes. Two possible reasons for the small resistivity and hardness changes are: (1) the aluminum does not develop additional dislocation tangles since the steel reinforcement remains elastic and forces the aluminum to return to its original location along the glide planes, and (2) 500 ratio aluminum has a substantial number of dislocations and has started to exhibit saturation resistivity values. This latter reason is probably one of the strongest reasons not to use very high purity aluminum in composite conductors. Another reason, of course, is the cost. Aluminum that is purer than resistivity ratio 1000 would be zone refined at 5 to ²⁰ \$/lb, while less pure aluminum might cost only 0.5 to 1.0 \$/lb.¹⁰

In future design studies consideration will be given to using NbTi superconductor in 500 resistance ratio aluminum stabilizer and supported in an aluminum alloy disc.

c. Conductor thermal, mechanical and electrical design

With design strains in the conductor of 0.002 it is obvious that NbTi is the best available superconductor that can be considered. For higher fields one would like to use Nb_3Sn but it is a brittle material in the presently available forms and cannot be designed for a strain of 0.002 if one considers the additional strains encountered during assembly. NbTi can operate as a superconductor over a range of temperatures; two possible operating temperatures 4.2 and 1.8K will be discussed here. The first design and the one chosen for this magnet is one in which the stainless steel discs and the embedded conductors are submerged in a bath of liquid helium at 4.2K. The second design proposes to use superfluid helium at 1.8K.

(1) 4.2K design

The NbTi superconductor in copper is sized to carry the total

design current at 5.2K. The copper will be cooled so that no superconductor filament temperature can ever exceed 5.2K for either of two cases: (1) all the current is in the copper or (2) one half the current is carried by the superconductor while partially resistive. As Purcell¹ points out, this second case corresponds to maximum power generated in the filaments and determines the number of filaments required to ensure smooth current sharing with temperatures kept below a chosen limit. We select here a 0.4 W/cm^2 surface heat transfer to 4.2K liquid helium with a copper surface temperature of 4.7K. The copper at the filament location will not exceed 4.95K (for either case), and the NbTi filaments will not exceed 5.2K. Under these conditions a current density $j = 1.5 \times 10^4 \text{ A/cm}^2$ can be used at 8.66 tesla. In figure VII-A-7 we have estimated critical currents for NbTi at five different temperatures. The curves are composite idealized design curves using an alloy^{10,11} in each field region which has the highest current density at 4.2K. The higher temperature¹² curves result from extrapolations, using Hampshire's measurements, of j vs B and T for the Nb-44 w/o Ti system. The amount of superconductor required is minimized by using only the cross-section required according to the 5.2K curve in Figure VII-A-7. This fit is made to the maximum fields per turn, assumed to decrease linearly to zero away from the maximum field at the central median plane of a toroid.

Edge cooling only on one edge will be used for the composite copper superconductor so that the conductor can be firmly epoxied into the grooves in the stainless steel discs, (see Figure VII-A-2). This procedure dictates that the conductor grooves should be fairly shallow since the copper which is far from the cooling surface will not be adequately cooled and would therefore be of less value. For the first example, we chose a stainless steel disc which is 5 cm in thickness and grooved for conductors on both sides. Superconductor filaments will be positioned in the copper matrix within 0.5 cm from the cooled surface and that location will be held less than 4.95 K as mentioned above. The two thermal conditions which are satisfied are (1) the total stability criteria which is set at 0.4 watts/cm^2 when all the current is in the copper and (2) the temperature profile within the copper shall be such that the superconductor filament location is always colder than 4.95K. In establishing these limits, we use:

$$\rho = 10^{-8} (1 + 0.455 B) \Omega\text{cm} \quad (3)$$

$$k = 0.6 \left(\frac{T}{1 + 0.455 B} \right) \frac{\text{W}}{\text{cmK}}, \quad (4)$$

where ρ is the resistivity, k is the thermal conductivity for copper, T is the temperature in degrees K and B is the magnetic field in tesla.

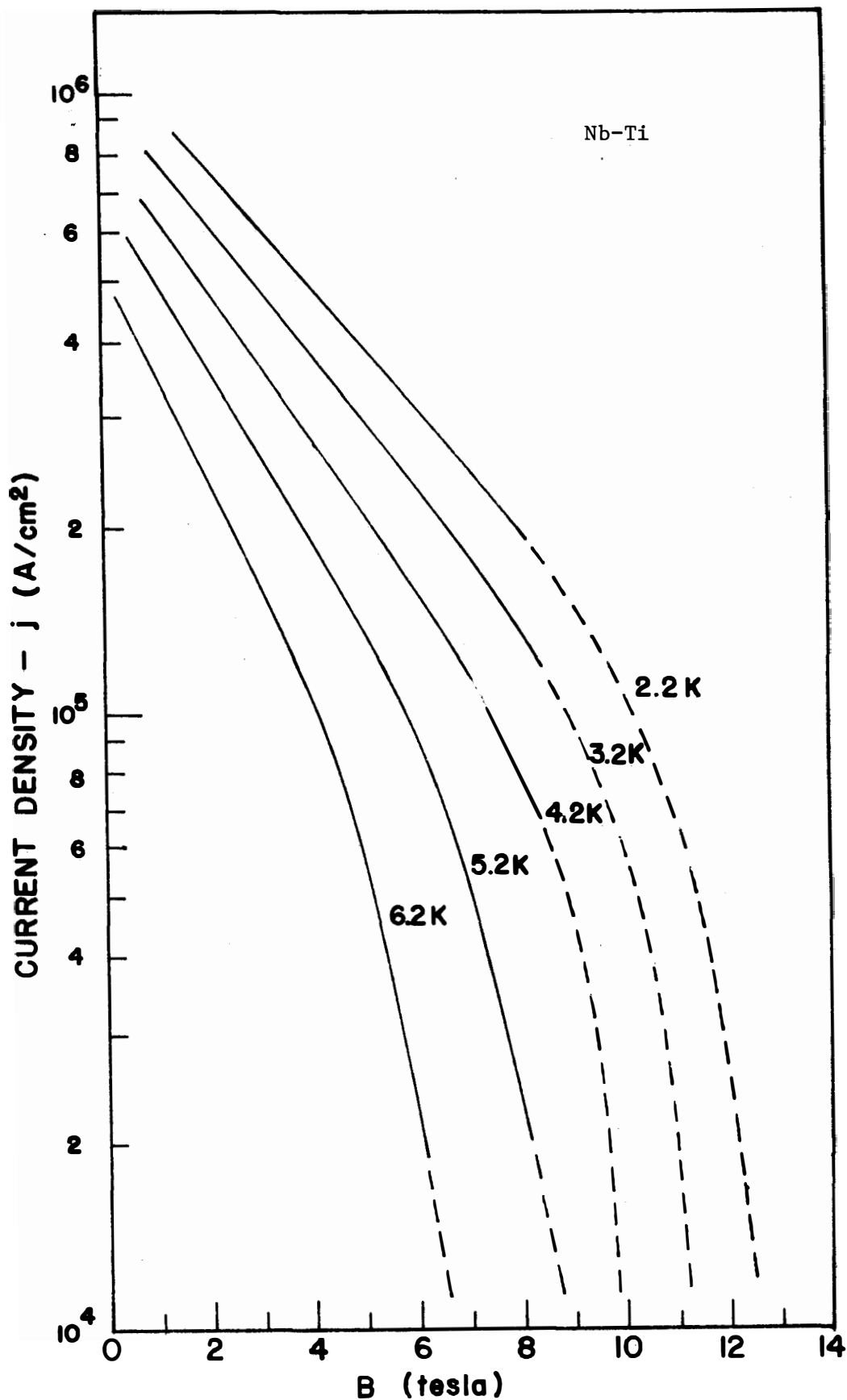


FIGURE VII-A-7 Superconductor Current Density Design Curves

Equation (3) applies to high conductivity copper which has been stress cycled several times. Eq. (4) is obtained by assuming that k is equal to 2.5 W/cm/K at 4.2K in zero field and that for small temperature excursions $k \propto T/\rho$. With these equations we find the usual results

$$\frac{w}{I} = \sqrt{\frac{\rho}{qh_c}} \quad \text{cm/A} \quad (5)$$

and

$$T^2(x) = T_0^2 + 1.67 \times 10^8 j^2 \rho^2 (2h_c x - x^2) \quad (6)$$

where

w = edge cooled width, cm

I = current, A

q = 0.4 W/cm², surface heat transfer

h_c = copper depth, cm

x = distance from copper surface, cm

$T(x)$ = temperature at x , K

T_0 = copper surface temperature, K

j = current density, A/cm².

If $h_c = 2$ cm then w/I is determined from Eq. 5 where B is below 7.8 tesla and by Eq. 6 for B between 7.8 and 8.66 tesla. A simple form for w/I which satisfies both Eq. 5 and 6 for constant $h_c = 2$ cm and $T - T_0 \leq 0.25$ K at $x = 0.5$ cm is

$$w/I = 1.3 \times 10^{-4} (1 + 0.125B) \quad \text{cm/A} \quad (7)$$

If w is to be constant, then we get, at $w = 2.55$ cm, that

$$h_c/I = 4.0 \times 10^{-5} (1 + 0.466B) \quad \text{cm/A.} \quad (8)$$

Equation (8) has been chosen for detailed design work since it applies to shallow conductors which are better cooled and use less copper.

Using either Eq. (7) or (8) the copper will be minimized by the indicated linear taper.

Radiation damage to the copper stabilizer in the conductor is discussed in detail in section VI-F of this report. Using this data and assuming that room temperature annealing would take place at least once a year, the conductor cross sections were increased on the inner seven turns over those required by Eq. (7) and (8). The increases in area varied from 18% on the inner turn to 4% on the seventh turn. The dimensions on Fig. VII-A-2 include the needed extra stabilizer to accommodate the radiation damage.

(2) 1.8 K design

Our recent studies have shown some benefits for designing the magnets for even lower temperature operation. The first benefit is the extension of NbTi use up to 11 tesla, which thus postpones plans for Nb₃Sn use until large magnet construction experience has been obtained.¹⁵ The second benefit is the use of superfluid helium,¹⁴ which forms excellent heat pipes without coolant pumping. Cooling has also been contemplated with supercritical helium, although experience to date indicates that pumping and pressurizing requirements are discouraging.¹⁵ The third benefit comes from a possible reduced volume of helium required for a superfluid system of small internal cooling tubes that are cast or formed inside a composite conductor. The volume of superfluid helium depends on the cross section of the heat pipes (~0.5 watts/cm² conduction) and the number of manifolds used in the system. In the design of a much larger magnet for an energy storage system,¹⁶ an aluminum conductor cooled with internal tubes containing superfluid helium was discussed. There for a 314,000 A conductor the cooling was sufficient to handle a normal hot spot while the pool cooling proposed in this report only has to stabilize a 10,000 A conductor. Obviously more study needs to be made of the various cooling schemes. Before leaving this topic it should be noted that lower temperatures have one drawback; the nuclear heat load, if accepted at 1.8K, would require three times the refrigerator capacity as required for the same load at 4.2K.

d. Design for component failures.

(1) Failure of a superconductor strand

After the final annealing of the drawn tapered conductor, the NbTi superconductor strands should be capable of at least 2% strain before failure. There are only two locations where assembly will yield the copper in the conductor; at midlength where the conductor passes from one surface of the disc to the other, point A on Fig. VII-A-1, and at the ends where the leads leave the disc, point D on Fig. VII-A-1. Both of these points have low fields. Where the conductor passes through the disc, the superconductor is sized for

a field of 8.66 tesla and actually is in a maximum field of 2.42 tesla. The leads come out at a point of essentially zero field. Even though the copper yields at these two locations during assembly the strains will not reach 2% and there is an excess of superconductor. If Nb_3Sn were used as a superconductor the maximum strain would be limited to 0.2%.

(2) Failure of the epoxy bond between conductor and disc.

On the inside surface of the outer discs in a magnet the bulges in the magnetic field lines between magnets will produce toroidal forces (at right angles to the surface of the disc) tending to move the conductors out of the grooves. The distance between the micarta spacers is such that the individual conductors are self supporting as continuous beams without large deflections so that no electrical short circuits should develop. However, the failure of the bonding will permit small motions of the conductor as the field changes. This motion will cause frictional heating which could cause trouble unless the heat is transferred rapidly by helium in the crack. Obviously it is important to pay strict attention to quality control during the bonding of the conductor and also to provide a clamping action with the micarta spacers. The clamping action would stop the spread of a crack and in steady state operation an existing crack which does not spread should cause no trouble.

(3) Failure of one magnet

In section 1-b-(10) and in Figure VII-A-3 reference is made to the reinforced epoxy struts inside the dewar at the sides of the magnet. It is conceivable that due to some unforeseen circumstance an entire magnet could fail. A large distortion in the field lines would be present if a steady state condition existed with 11 of the 12 magnets operating at the rated current of 10,212 amperes. A force in excess of 80×10^6 kg would act laterally on the magnets on either side of the inoperative magnet, tending to push them away from it.

A much smaller but similarly directed force would be present if mechanical, electrical and magnetic symmetry were not present in an operative system. The "D" shaped magnet is self supporting under radial loads but the attachment to the central core provides a minimal support against loads in the toroidal direction.

Cold supports between adjacent magnets, each in dewars connected to the magnet dewars, would be a feasible solution if only a few were needed. The lateral bending resistance of the magnet cross section is adequate but the resistance to shear stress is limited by the interface between the micarta spacers and the discs such that the magnet requires supports every 20 or 30 cm. Thus cold supports from magnet to magnet through dewars are not practical.

Warm lateral supports between dewars are necessary for stability where the loading is indeterminate but small. It is also necessary for the failure condition described above. To transfer the warm support through the dewar walls to the magnet requires a structural insulator and unfortunately this could provide a large heat load on the refrigerators. A sound solution to both of these problems is outlined in steps (a) to (c) as follows:

- (a) Warm support columns between adjacent dewars will be provided every three or four meters with length adjustments to provide for balancing the lateral loads on individual magnets.
- (b) Reinforced epoxy struts (see Fig. VII-A-3) will be spaced at approximately 30 cm intervals between the dewar and magnet with a one cm space between the inner end of the strut and the magnet. One strut out of every 10, however, will make solid contact with the magnet. The dewar wall at the location of this one longer strut will be designed to deform elastically by one cm before the strut will fail.
- (c) A control system capable of detecting a failure in the individual magnets will be used to release a fluid or gas in a cylinder-piston element in each warm support column. These elements will be capable of forcing all epoxy struts to full contact and provide the full supporting forces necessary in event of a failure in one magnet.

This design minimizes the heat loss, provides stability and guards against a failure in a magnet without any large dynamic conditions developing in a lateral direction.

e. Comparison between toroidal field magnets for stable and unstable plasma designs.

The toroidal field magnet necessary for a design using a stable plasma requires a central field of 4.73 tesla instead of 3.83 tesla for the unstable plasma. A direct comparison of costs is contained in section VII-E so only significant differences will be discussed here.

- (a) The higher field will require more NbTi superconductor at lower operating temperatures.
- (b) The number and width of the 5 cm discs in each magnet will increase from 34 to 42 discs and from 93 to 109 cm.
- (c) There will still be 30 conductor turns per side on each disc but the inner conductors are somewhat larger due to the higher resistivity of the copper at the higher fields. The same current 10,212 A will be carried by the conductor.

4. Magnetic Field Calculation

a. Computer code MAFCO-W (MAFCO-Wisconsin Version)

A general magnetic field code MAFCO-W which is a modified and extended version of MAFCO¹⁸ has been developed. The major difference between this code and MAFCO is that it can calculate accurately, and with high efficiency, the magnetic field inside a conductor of rectangular cross-section carrying uniformly distributed current. The original MAFCO handles only the case of separated filament windings so that a finite conductor has to be approximated by a large numbers of filaments. The calculation could therefore be very expensive and can also lead to difficulties inside a conductor.

MAFCO-W approximates a conductor of general configuration by arc and straight segments. The field is calculated by integrating the Biot-Savart law over the volume of the arc or straight segments. Three dimensional integrations are involved. The expressions for the field components have been reduced to a single integration analytically. The final integration is carried out numerically by employing the Gaussian Quadrature technique. Therefore MAFCO-W is able to calculate the field both outside and inside a conductor with much greater accuracy and efficiency, especially when a large cross section conductor is involved.

The mathematical expressions for calculating the field components from an arc segment are given, in cylindrical coordinates, as follows;

$$B_{R_p} = \frac{j}{10} \int d\theta \cos\theta \{R + R_p \cos\theta \log(\rho - R_p \cos\theta + R)\} + C,$$

$$B_{\phi_p} = -\frac{j}{20 R_p} \{(\rho - R_p \cos\theta)R + [R_p^2 \sin^2\theta + (Z_p - Z)^2] \cdot \log [(\rho - R_p \cos\theta)R]\} + C,$$

$$\text{and } B_{Z_p} = \frac{j}{10} \int d\theta (Z - Z_p) \left\{ \log(\rho - R_p \cos\theta + R) + \frac{R \cos\theta}{2|Z_p - Z|} \log \frac{R - |Z_p - Z|}{R + |Z_p - Z|} \right.$$

$$\left. - \frac{R |\sin\theta|}{|Z_p - Z|} \tan^{-1} \left[\frac{(\rho - R \cos\theta) |Z_p - Z|}{R_p |\sin\theta| R} \right] \right\} + C.$$

Here

$$R = [R_p^2 - 2R_p\rho \cos(\phi_p - \phi) + \rho^2 + (Z_p - Z)^2]^{1/2}$$

and (R_p, ϕ_p, Z_p) is the field point.

The coordinates of the arc segment and field point are shown in Figure VII-A-8. If the field points are on the Z axis, the expressions reduce to

$$B_{R_p} = \frac{j}{10} (Z - Z_p) \log(\rho + \sqrt{\rho^2 + (Z_p - Z)^2}) + C,$$

$$B_{\phi_p} = \frac{j}{10 R_p} \cos\theta [\rho^2 + (Z_p - Z)^2]^{1/2} + C,$$

and $B_{Z_p} = \frac{j}{10} (Z - Z_p) \log [R + [R^2 + (Z_p - Z)^2]^{1/2}] + C.$

The integration limits are from Z_1 to Z_2 , ρ_1 to ρ_2 and θ_1 to θ_2 . Here B is in gauss, R and Z are in cm and j is in amperes. If the arc segment is very thin i.e. $Z_p = Z_1 = Z_2 = Z_0$, then B_p, B_{ϕ_p}, B_{Z_p} become

$$B_{R_p} = \frac{j(Z_p - Z_0)}{5} \int_{\sigma_1}^{\sigma_2} \frac{R_p \cos^2\theta (\rho - R_p \cos\theta) d\theta}{[R_p^2 \sin^2\theta + (Z_p - Z_0)^2] R} + \frac{2j}{5} \frac{(Z_p - Z_0)}{k\sqrt{\rho R_p}} [-(1 - \frac{k^2}{2})E(k, w) + kK(k, w)].$$

$$B_{\phi_p} = \frac{j}{10} \frac{Z_p - Z_0}{R_p} \log(\rho - R_p \cos\theta + R).$$

and

$$B_{Z_p} = \frac{j}{5} \{k\sqrt{\frac{\rho}{R_p}} E(k, w) + \int_{\theta_1}^{\theta_2} \log(\rho - R_p \cos\theta + R) d\theta\}$$

where $E(k, w)$ are the elliptic integrals of the first and second kind, respectively, with $k = 4\rho R_p / [(R_p + \rho)^2 + (Z_p - Z_0)^2]^{1/2}$ and $w = (\sigma_2 - \sigma_1)/2$.

The expressions for the field components from a straight segment in cartesian coordinates, as shown by Figure VII-A-9, are given as follows:

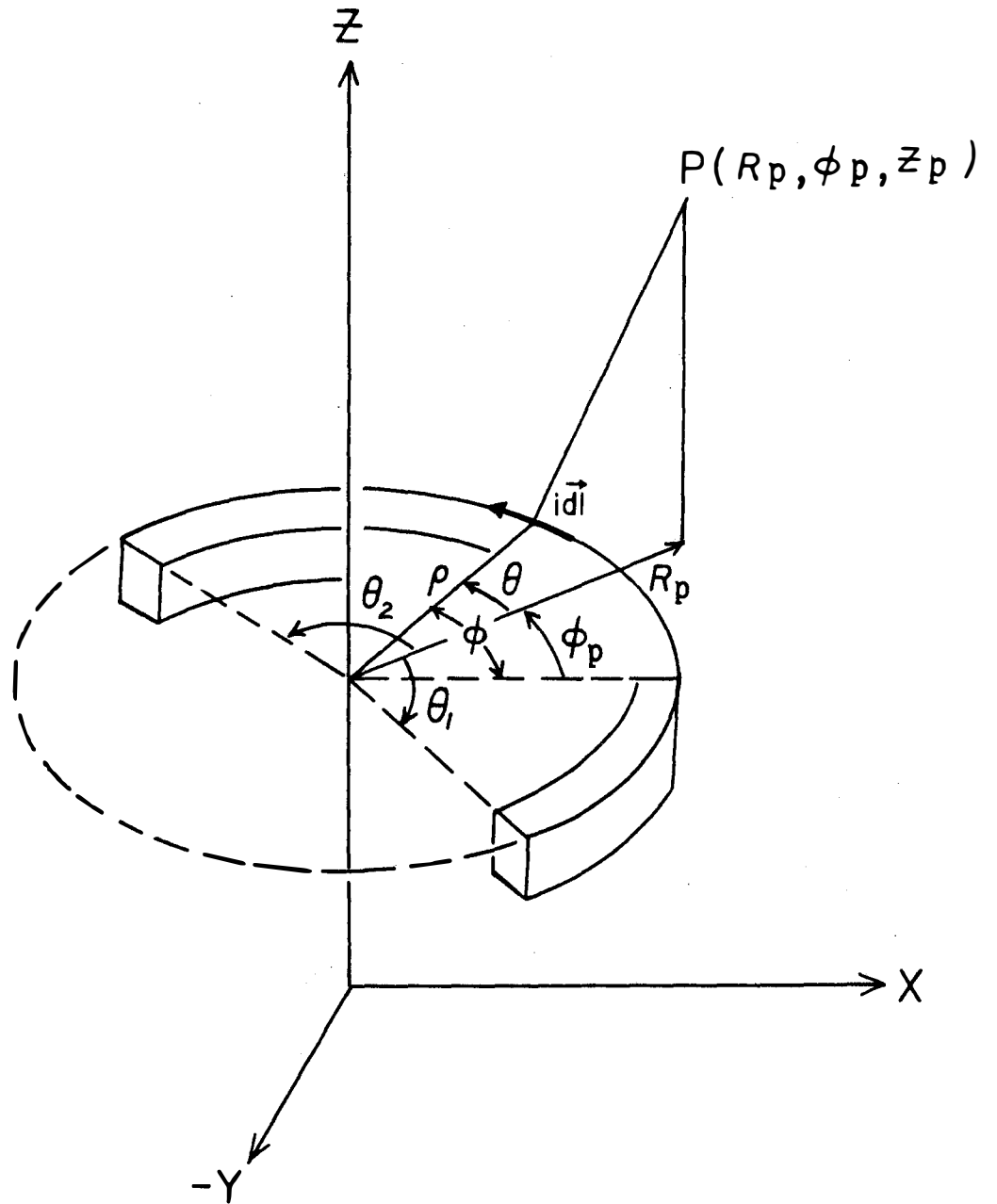


FIGURE VII-A-8 Arc Segment Coordinates

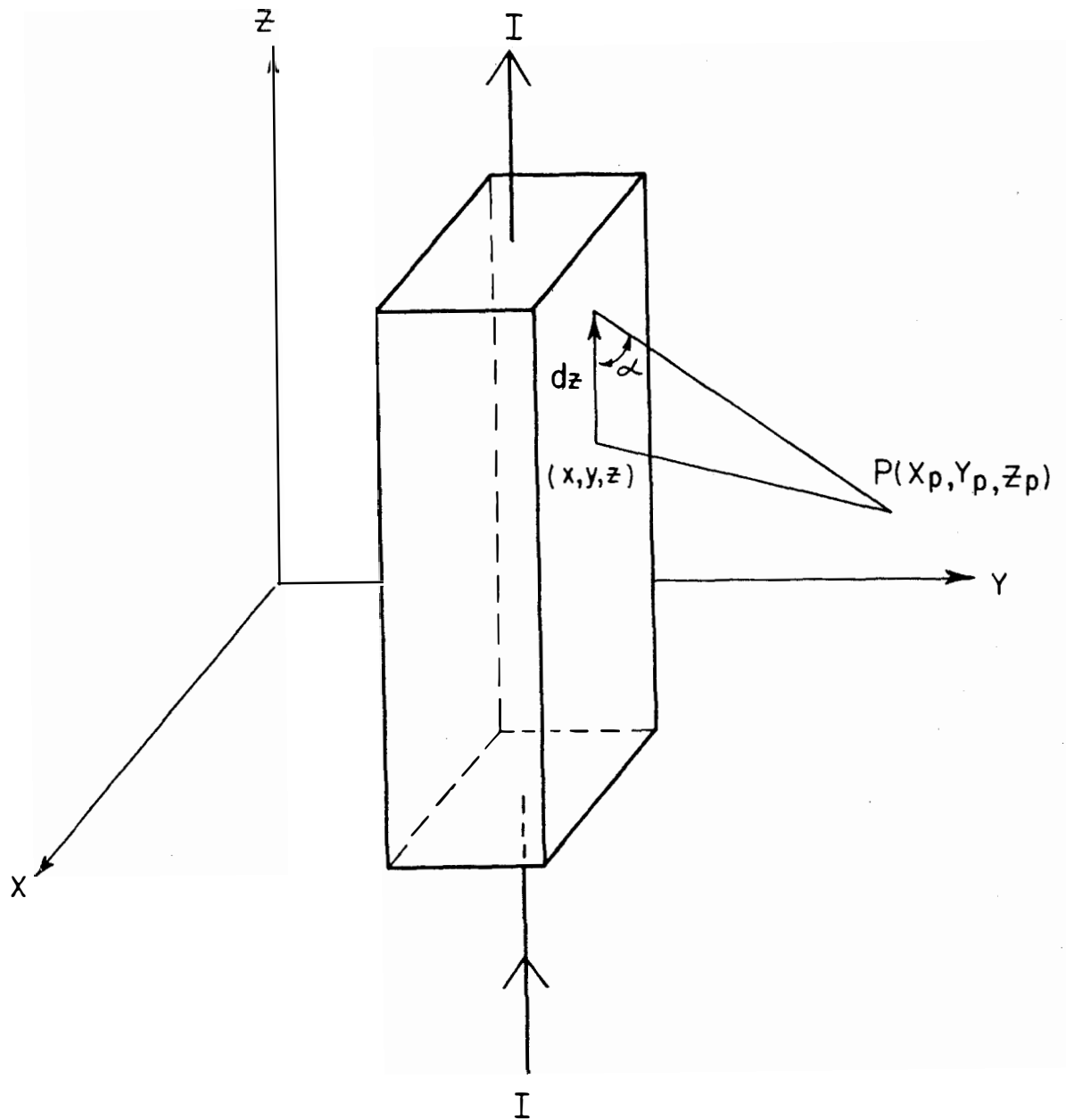


FIGURE VII-A-9 Straight Segment Field Components

$$B_{x_p} = -\frac{j}{20} \int dx \frac{(Z_p - Z)}{|Z_p - Z|} \log \frac{R - |Z_p - Z|}{R + |Z_p - Z|} + C,$$

$$B_{y_p} = \frac{j}{10} \int dy \frac{(Z_p - Z)}{|Z_p - Z|} \log \frac{R - |Z_p - Z|}{R + |Z_p - Z|} + C,$$

and $B_{z_p} = 0$, where $R = [(X_p - X)^2 + (Y_p - Y)^2 + (Z_p - Z)^2]^{1/2}$.

The integration limits are from Z_1 to Z_2 , X_1 to X_2 and Y_1 to Y_2 .

The positions and orientations of the arc segment and straight segment in the space of other reference frames are specified by the origin and the Euler Angles of the coordinates system of Figures VII-A-8 and 9. The method of transformation between the two systems has been discussed in detail in MAFCO.¹⁸ The general configuration of a solid conductor designated at any point in space can thus be approximated by a combination of arc and straight segments.

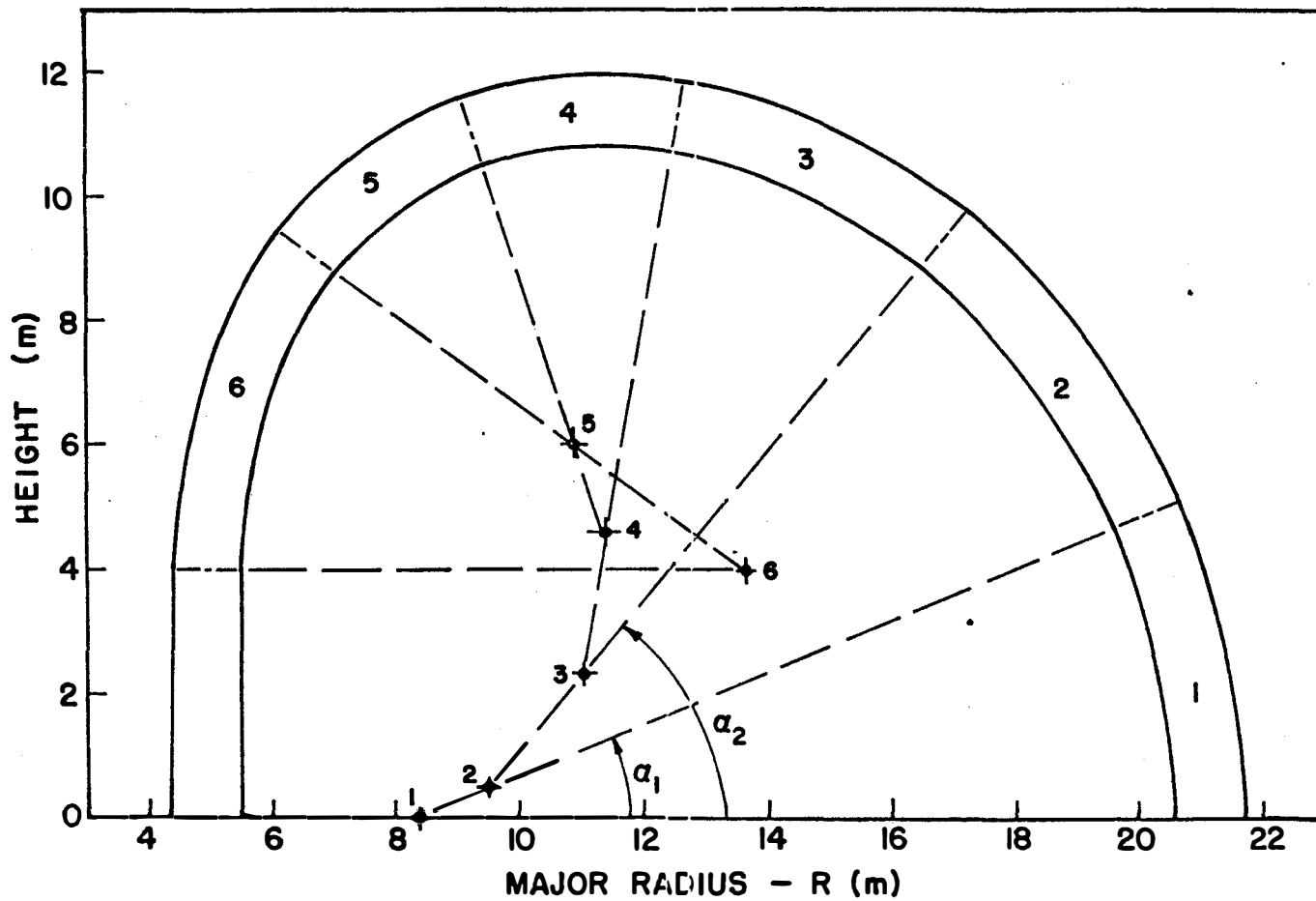


FIGURE VII-A-10 Geometry of Toroidal Magnetic Field Coil

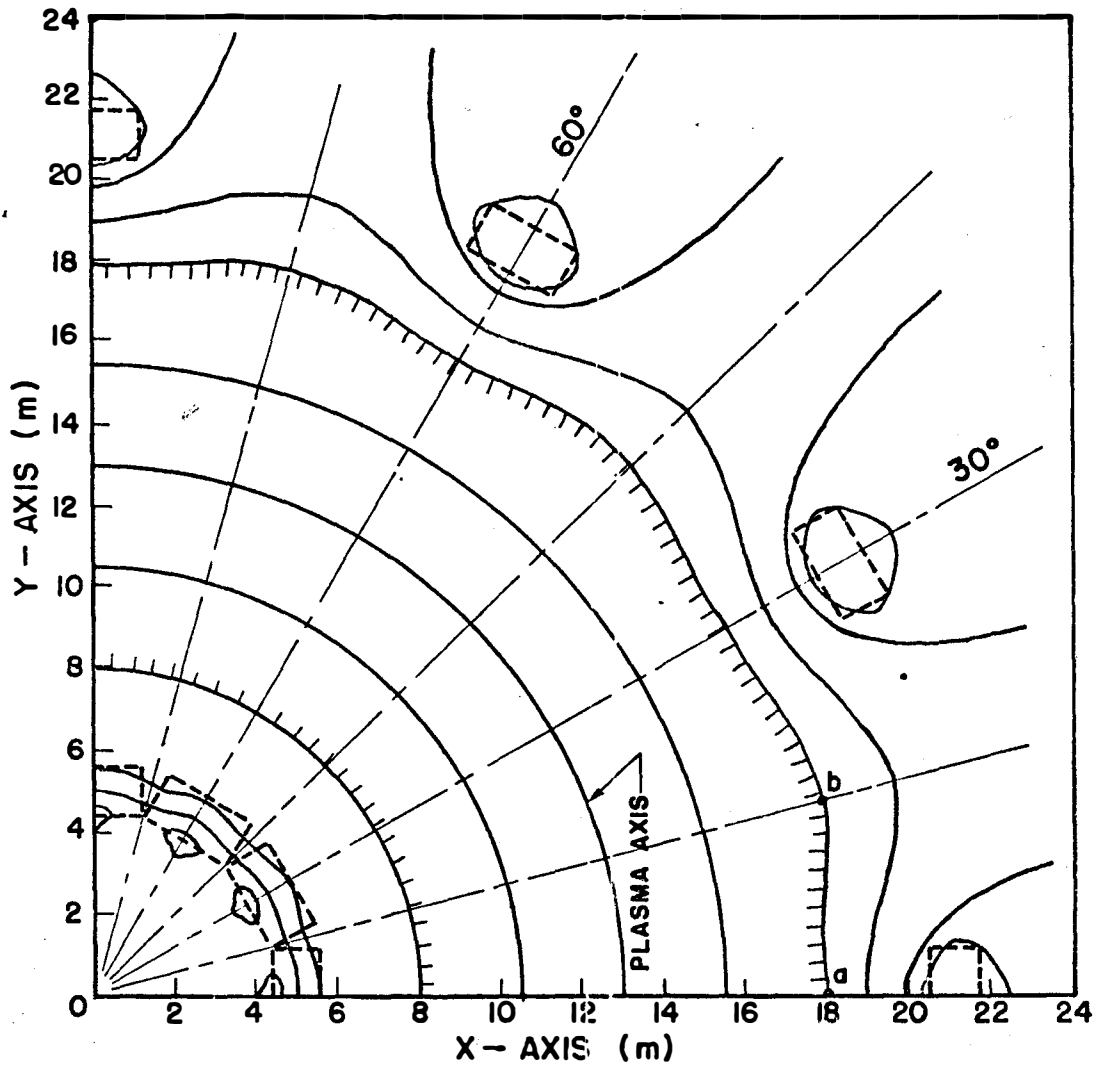


FIGURE VII-A-11 Field Pattern on Midplane of Torus

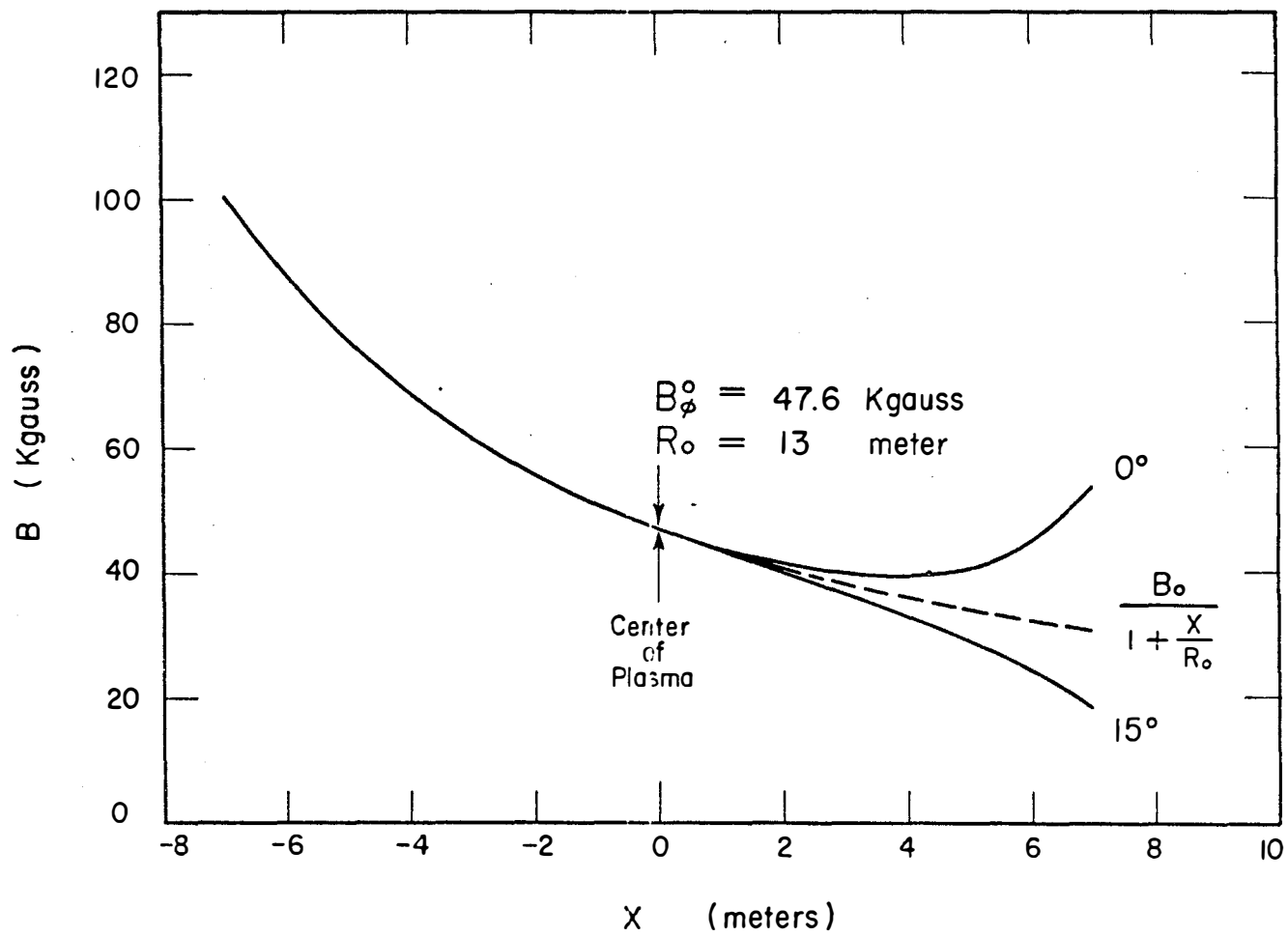


FIGURE VII-A-12
Field Magnitude Along Minor Radius at Midplane

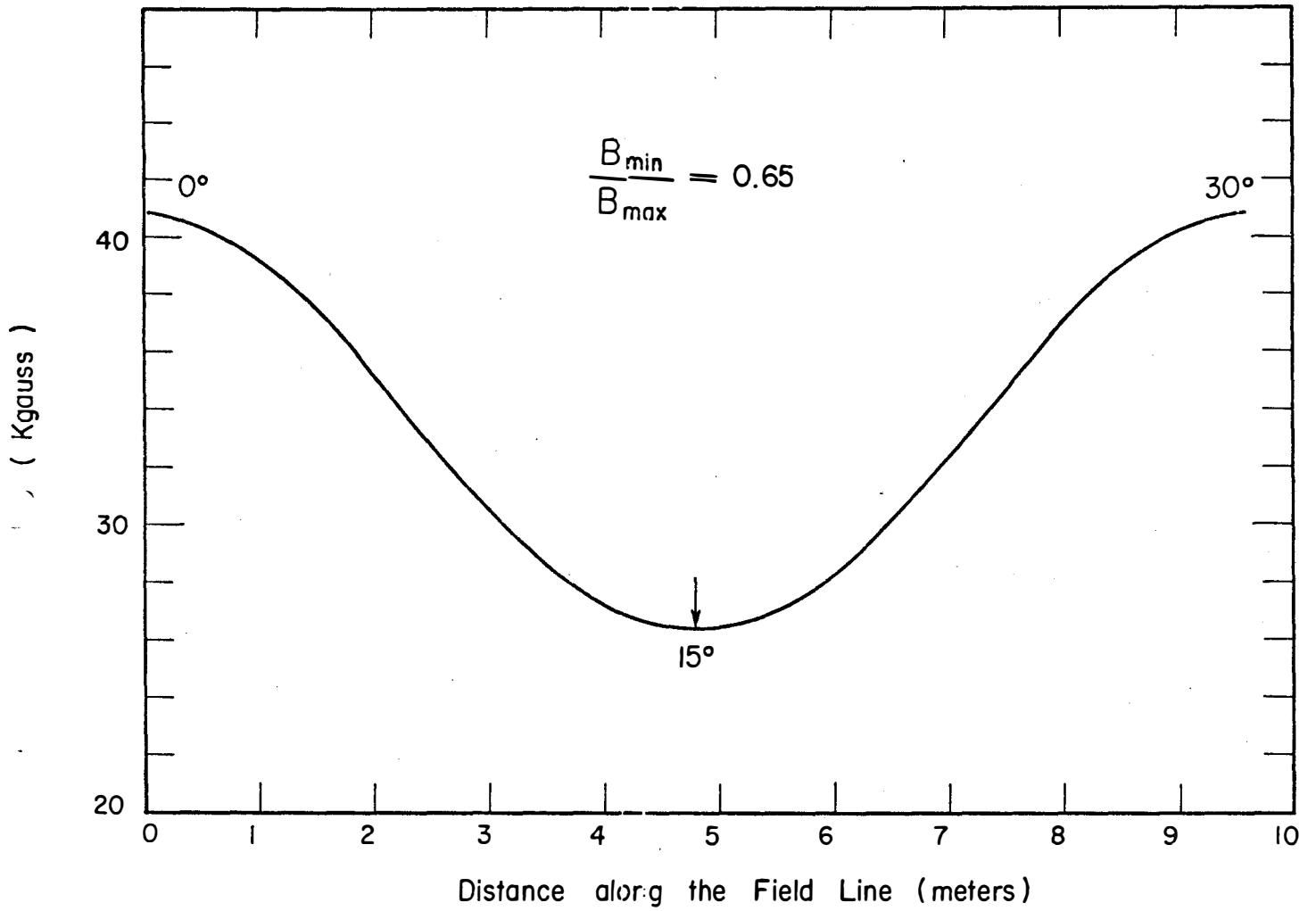


FIGURE VII-A-13
 Field Variation Along Outer Edge of Plasma at Midplane

b. The magnetic field structure for UWMAK-I

UWMAK-I has 12 constant tension D-shaped magnetic field coils spaced at equal angular intervals of 30° . The upper half of each coil is shown in Figure VII-A-10. For the magnetic field calculations, each half of the coil is approximated by 6 arc segments and one straight segment. This is the minimum number of segments which gives a smooth connection between the segments. The centers and radii of curvature of the arcs are also shown in the figure. α_1 and α_2 indicate the integration limits for the second segment.

The calculated field pattern of the first quadrant along the torus on the midplane is presented in Figure VII-A-11. The field pattern in the other three quadrants is the same. The cross sections of the magnetic field coils are shown by the dashed rectangle. The plasma occupies the space within the shaded field lines. Figure VII-A-12 shows the magnitude of the field along the minor radius at 0° and 15° on the midplane. Likewise, Figure VII-A-13 shows the magnitude of field along the outer edge of the plasma. The figures indicate maximum field errors on the outer edge of the order of 20%.

The fluctuation of the field on the magnetic axis and along the inner edge of the plasma is about 50 gauss, which is very small. The variation of the field along the vertical line at $R=13m$ is about 1.5 k gauss within the plasma boundary, increasing as one moves towards the edge of the plasma.

5. Magnet Support and Handling System

The toroidal magnets exert a tremendous force directed radially inward due to the magnetic field interaction and will, thus, require a massive cylindrical structure in the center of the reactor in order to balance this force. It soon becomes apparent that this cylindrical structure, hereon referred to as the central core, can also serve as the main support column for the toroidal magnets themselves. There are four main advantages to this scheme:

- a. The magnets touch the central core only at the straight section of the D shape, and are free to contract on cool-down without the encumbrance of ground supports.
- b. Since there is no superinsulation in existence which can withstand the compressive force between the toroidal magnets and the central core, this scheme provides the possibility of making the central core a part of the dewar, thus obviating the necessity of insulation at that point.
- c. The space under the magnets is crowded with divertor coils, shield supports, vacuum pumps and other necessary equipment. It is, therefore, advantageous to minimize any additional hardware.

- d. It is almost certain that the removal of a magnet from the reactor after it had been in operation will have to be done remotely. The self-locating feature of the supports in this scheme and the ease with which they interlock with the central core lends itself very nicely to remote operation.

The toroidal magnets are made up of D shaped discs with the windings embedded on both sides of the disc. In the unstable design there are 34 discs, 5 cm thick, with 0.635 cm of insulation between them. This makes the total width of the magnet 191 cm. The weight of the magnet is 900 M tons.

The discs will have notches machined in them at approximately 2.5 m from the start of the straight section at both ends. The notches will be 25 cm high and 3 cm deep. When the discs are all assembled, the notches will line up horizontally and, thus, will provide the slot for the shear beam.

Shear beams will be inserted into the slots at both ends of the straight section and welded to each disc. The shear load will be shared by both upper and lower beams at a shear stress $<175 \text{ kg/cm}^2$, see Fig. IV-A-1.

When the magnets are energized, the magnetic radial compressive force between the magnets and the central core will greatly exceed the radial tensile force component on the upper shear beam and shear pins due to the weight of the magnets. In the free hanging state before energizing, however, the radial tensile force on the upper shear beam and shear pins will equal 615 M tons. In order to keep the tensile stress on the welds $<1000 \text{ kg/cm}^2$ the width of the welds attaching the shear beam to the magnet discs should be not less than 1.5 cm. Ten shear pins, 6.25 cm in diameter, will be used for each magnet. The shear stress on the pins will also be $<1000 \text{ kg/cm}^2$.

The main function of the bottom shear beam is to provide more stability in the magnet support as well as aid in aligning and locating of the magnet during assembly. It does not appear necessary to use shear pins on the bottom beam.

The magnet dewars are supported independently from the magnets. They are supported at the inner radius on lugs welded to them and carried on the flat ledges of the central core which also support the shield. At the outer radius, similar lugs welded to the dewars are supported on the permanent rear jack assemblies which carry the shield.

Prior to the assembly of a magnet onto the central core and in subsequent handling operations as alternate means of support must be provided. At these times the magnet will be supported on jacks built into motorized caterpillars which will be used for transporting a complete module.

Two flat ledges will be provided on the bottom of each magnet running its full width (perpendicular to the stacked discs). The jack heads will not go through the dewar, but instead, will mate with pads attached to the dewar by means of bellows. These pads then support the magnet on the flat ledges and also support the dewar independently. After the magnet is hung on the central core, the pads are retracted and the jacks removed all together.

In Figure IV-E-6 we show a complete module being removed from the reactor. The transformer and diverter coils have been retracted, the lithium headers, the lateral magnet supports and the vacuum pumps have been disconnected and removed. Steel plates are placed over the concrete floor to cover the diverter coil slots and to provide a smooth surface for the caterpillars to ride on. Motorized caterpillars with built-in jacks are inserted under the module. The caterpillars may have to be designed to come apart into several pieces in order to fit between the rear shield support jacks. They would have to be re-assembled again under the magnet.

The front caterpillar will have six jacks, two for the magnet and four for the shield. The magnet jacks will each support 203 M tons and the shield jacks, 274 M tons.

The rear caterpillar will attach to the existing rear shield support assembly and will have two jacks for the magnet and six for the shield. Here, the magnet jacks will each support 240 M tons and the shield jacks, 211 M tons. The total load on the front caterpillar is 1,502 M tons and on the rear, 1,745 M tons.

There are several ways of moving heavy loads on even floors when the capacity of overhead cranes has been exceeded. Among them are compressed air cushions, walking hydraulic rams, compressed oil films and ball or roller carpets. In the present case, the aim is to provide self-propelled means for moving a complete module weighing over 3,000 M tons over a rather uneven concrete floor, with the capability of turning it on the spot and moving in any desired direction.

At CERN,¹⁹ motorized caterpillars have been used to move loads up to 80 M tons over concrete floors. By extrapolating this value to a larger unit, keeping contact stresses the same, and using several units under each carriage it would seem possible to use such caterpillars for transporting the reactor modules.

The rolling resistance over hot rolled high carbon steel plates

as measured at CERN was 1.4 - 1.8%. A motor of 2.8 HP was needed to move 80 tons. Based on this value we would need a total of 120 HP to motorize the two carriages. Not all the units would have to be motorized. A possible solution would be to have six caterpillar units under each carriage with only two of them motorized by 30 HP motors.

The caterpillars are mounted on shafts and can be rotated 90°, thus providing the capability of turning on the spot or proceeding in any direction. This flexibility would be indispensable for remote maneuvering.

B. Transformer and Divertor Coil Design

The requirements placed on these coils have been defined in an earlier section from the plasma point of view. The purpose of this section is to describe the steps used to design superconducting magnets such that the field and current requirements are met.

In the design of the toroidal magnets, the stresses created are of such a magnitude as to relegate a secondary position to the conductor design. In the divertor and transformer coils, this is not always the case due to the much lower stresses and to the short rise times of the magnetic field. This set of circumstances requires certain deviations from the design adopted for the toroidal magnet system. It will also be advantageous to adopt different designs for different stress requirements.

For high current coils in large magnetic fields resulting in high stresses, stainless steel reinforcement within the windings is necessary. Where reinforcement is not required, the conductor itself will be designed to carry the forces. The choice of either copper or aluminum for the stabilizing material in a particular coil will depend on the stress level experienced. Thus aluminum is used at low stress levels, OFHC copper for medium stress levels and with extra reinforcement at high levels. These regions will be defined more precisely later in this section.

This design adopts the total stability criterion in which resistivity and surface heat transfer are important properties. The resistivity of OFHC copper as a function of the magnetic field is given by $\rho = 10^{-10} (1 + .455 B)$ ohm·m with B in tesla. The magneto-resistivity of aluminum saturates at a low field. For these calculations a resistivity of 1×10^{-10} ohm·m is taken at all fields for 1000 ratio aluminum. A yield strength of 4000 psi ($2.76 \times 10^7 \text{N/m}^2$) was taken for Al and 12,000 psi ($8.27 \times 10^7 \text{N/m}^2$) for OFHC copper.

In order to design a totally stable magnet, the nucleate boiling heat flux must be used. Nucleate boiling heat transfer varies with the orientation of the cooling surface and ranges from 0.8 to 0.6 to 0.2 watts/cm² for 0°, 90° and 180° orientations respectively for open surfaces.⁽²²⁾ The coolant channels in this design are not all open and therefore a conservative average value of 0.3 w/cm² (3000 w/m²) was taken.

The design utilized in the toroidal magnets of stainless steel grooved discs cannot be adopted for the divertor and transformer coils due to the short rise times of the magnetic field. The continuous steel disc would act like a secondary in a transformer which dissipates large quantities of heat. In view of this difficulty, a layer-wound pancake design was chosen. An edge-cooled conductor wound together with stainless steel strip separated by mylar tape is described in Reference 1. In all cases the cooling surface will be formed by grooves in the conductor edge as shown in Figure VII-B-2b. With this enhancement, edge cooling is sufficient to provide cryogenic stability.

The following condition should be satisfied

$$\left(\frac{I}{N}\right)^2 \frac{\bar{\rho}}{wx} = \bar{q} fx \quad (1)$$

where x is the conductor thickness,
 w is the conductor width,
 f is the fraction of x cooled,
 I is the total coil current,
 N is the number of turns per coil,
 $\bar{\rho}$ is the average magnetic resistivity, and
 \bar{q} is the average heat transfer.

From equation (1)

$$\frac{1}{w} = \frac{w}{w^2} = \left(\frac{I}{Nxw}\right)^2 \frac{\bar{\rho}}{\bar{q}f} = j^2 \frac{\bar{\rho}}{\bar{q}f} \quad (2)$$

where j is the overall current density in the conductor then

$$w \leq \frac{\bar{q}f}{j^2 \bar{\rho}} \quad (3)$$

The value of f is >1 for grooves
 <1 for micarta coverage.

In order to avoid difficulty in winding many turns, w should be as large as possible. From equation 3 w can be larger if \bar{q} and/or f are larger or if j and/or $\bar{\rho}$ are smaller.

The total tensile force can be calculated as follows

$$T = \bar{B}IR = \sigma_{ss} Ntw + \sigma_{cu} N x w \quad (4)$$

where

\bar{B} is the average axial field,
 σ_{ss} is the average design stress in the stainless steel,
 σ_{cu} is the average design stress in the copper.

Assume $\sigma_{cu} = \frac{1}{2} \sigma_{ss} = 12000 \text{ psi } (1.103 \times 10^8 \text{ N/m}^2)$

then $T = \sigma_{ss} (A_{ss} + \frac{1}{2} A_{cu})$

where $A_{ss} = Nwt$
 $A_{cu} = Nwx$

In the case of aluminum

$$T = \sigma_{ss} A_{ss} + \sigma_{cu} A_{al}$$

where

$$\sigma_{al} = 4000 \text{ psi}$$

Table III is a display of the parameters for both the divertor and the transformer coils for the case of 331 volt. secs required to sustain the plasma current during the burn ($\eta = 3.5 \eta_{sp}$). Notice that all the coils except D4 require stainless steel in^{sp} order to carry the stress. This is not the case when bootstrap currents are presumed to exist. For that type of operation, practically all the transformer coils could be of aluminum construction.

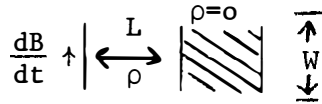
Each pancake will be separated from the other layers by a 0.635 cm micarta spacer. Clamped overlap joints will be made where necessary. Each stack will then be bolted together by pairs of 2" dia. bolts of aluminum stressed to 30,000 psi at 300 K. The spacing of these bolts along the length of the windings is given by

$$L = \frac{607}{w (3.69 - 4.11 h)}$$

for the copper construction (all units are inches). The differential shrinkage between the micarta spacers the pancakes and the aluminum bolts has been accomodated by the room temperature compression of the stack by the bolts, and the bolt stress of 30,000 psi is reduced to 1000 psi at 4.2K. (Figure VII-B-2a)

One special characteristic of these magnets is the short rise times required to attain full field. The plasma dynamics requires a 100 second rise to full field. The range of dB/dt is 0.42 to .7 kgauss/sec based on the average magnetic field from all sources. The minimization of a.c. losses requires that special attention be given to 1) the superconducting filament diameter, and 2) the coupling between filaments. The assumption is made that the conductor is designed in such a way that these losses are small compared to the possible I^2R losses accounted for by the total stability criterion. This is a reasonable assumption since several methods have already been devised to accomplish this goal. Filament sizes of 10 μ are readily available at the present time. Magnetic coupling of the filaments can be reduced by 1) filament twisting,⁽²³⁾ 2) transposition of the filaments⁽²⁴⁾ and 3) three component composites in which the third component is a high resistance alloy such as cupro-nickel reducing further filament coupling.⁽²⁴⁾ A detailed design of this conductor is beyond the scope of this paper but there is no doubt that all these methods will have to be used in combination to attain the low loss condition. Such conductors have been suggested and fabricated by Pooley et.al.⁽²⁵⁾

The primary source of energy loss in these magnets will be eddy currents generated during the start up exhaust and reset phases of the power cycle. We have not treated this problem exactly but have set up a model to obtain approximate values. Consider the case of a conductor of resistivity of ρ in front of a perfectly conducting slab in a constantly changing field.



The solution for J in this case is

$$J = \frac{8 \overset{\circ}{B} L}{\rho \pi^2} \sum_n \cos \left((2n+1) \frac{\pi x}{2L} \right) \frac{1}{(2n+1)^2} [1 - e^{-b(2n+1)^2 t}] \quad (5)$$

where

$$b = \frac{\rho \pi^2}{4 \mu_0 L^2}$$

For $\rho = 10^{-10}$ ohm·m and $L \approx 1$ cm, $b \approx 2 \text{ sec}^{-1}$ and the steady state is reached after a few seconds ($e^{-b(2n+1)^2 t} \approx 0$). In this case the energy dissipated per unit time per unit area of conductor is

$$\frac{P}{A} = \int_0^L J^2 \rho dx \quad \boxed{\approx \frac{32 \overset{\circ}{B}^2 L^3}{\pi^4 \rho}} \quad (6)$$

In our case the area is the face width of the conductor times the circumference of the coil.

$$P = \frac{32 \overset{\circ}{B}^2 L^3 (2 \pi R w)}{\pi^4 \rho}$$

$$\boxed{P = \frac{64}{\pi^3} \overset{\circ}{B}^2 L^3 R w} \quad (7)$$

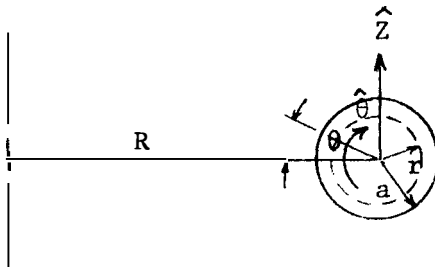
Additional approximations must be made however before the formula can be applied to a coil—namely $\overset{\circ}{B}$ is not uniform throughout the coil and arises from both external and internal currents. Consider now a circular cross section coil of radius a and constant current density.

$$\vec{B}_{int} = \frac{\mu_0 \overset{\circ}{I}}{2 \pi a^2} r \hat{\theta}$$

where \vec{B}_{int} is the field due to the current in the wire under consideration,

$$\text{and } \vec{B}_{ext} = \overset{\circ}{B}_{ext} \hat{z}$$

where \vec{B}_{ext} is the field due to the other wires in the coil.



$$\begin{aligned} \vec{B}^2 &= \left(\vec{B}_{\text{ext}} + \vec{B}_{\text{int}} \right)^2 \\ &= \vec{B}_{\text{ext}}^2 + 2 \vec{B}_{\text{ext}} \cdot \vec{B}_{\text{int}} + \vec{B}_{\text{int}}^2 \end{aligned} \quad (8)$$

The value of \vec{B}^2 to be used in expression (7) will be the \vec{B}^2 averaged over the cross sectional area.

$$\overline{\vec{B}^2} = \underbrace{\vec{B}_{\text{ext}}^2 + \frac{1}{A} \int_0^a \vec{B}_{\text{int}}^2 2\pi r dr}_{\text{I}} + \underbrace{\frac{1}{A} \int_0^a \int_0^{2\pi} \vec{B}_{\text{int}} \cdot \vec{B}_{\text{ext}} r d\theta dr}_{\text{II}}$$

However

$$\vec{B}_{\text{int}} \cdot \vec{B}_{\text{ext}} = |\vec{B}_{\text{int}}| |\vec{B}_{\text{ext}}| \cos \theta$$

and therefore the integral II = 0 since $\int_0^{2\pi} \cos \theta d\sigma = 0$

The first integral yields

$$\frac{1}{2} \frac{\mu_0^2 \vec{I}^2}{2(2\pi a^2)^2} = \frac{1}{2} |\vec{B}_{\text{ext}}(a)|^2$$

then

$$\overline{\vec{B}^2} = \vec{B}_{\text{ext}}^2 + \frac{1}{2} \vec{B}_{\text{int}}^2 \quad (9)$$

The final simplification concerns the conductor geometry. We consider a square conductor of side L. Then

$$P_{\text{av}} = \frac{64}{\pi^3 \rho} L^4 R \left[\vec{B}_{\text{ext}}^2 + \frac{1}{2} \vec{B}_{\text{int}}^2 \right] N \quad (10)$$

where N is the number of conductors in a given coil. This formula has been applied to the UWMAK-I coils for $\eta = 3.5 \eta_{\text{sp}}$ where the following numerical values were used:

$$\begin{aligned} L &= 1 \text{ cm} = 0.01 \text{ m} \\ \rho &= 10^{-10} (1 + 0.455 \bar{B}_{\text{av}}) \text{ ohm}\cdot\text{m}. \end{aligned}$$

Table IV gives the total net energy loss for the coils subdivided into the two major phases: startup and reset. The exhaust phase values are identical to the startup phase values and have therefore been omitted. Notice that the percent liquid helium boil off is very low and can be tolerated. The maximum power dissipation occurs for conductors at the surface of the coil where \vec{B}_{int} reaches a maximum. The resulting maximum heat flux was 2 orders of magnitude less than the heat flux possible from joule heating for which sufficient cooling capacity has already been provided. The conclusion can be then drawn that the eddy current power dissipation can be sustained by the conductor without going normal.

Table III

Parameters of Divertor and Transformer Coils

Coil	D1	D2	D3	D4	T1	T2	T3	T4	T5
R(m)	8	13	18	22	3.89	4.3	4.95	6.13	8.04
Z(m)	13	13.5	12	8	3.0	5.97	8.9	12.7	17.3
Total Coil Current (10^6 A)	24.5	12.3	-24.5	-2.5	-17.5	-15.2	-11.8	-11.0	-8.3
Maximum T (10^8 N)	2.72	----	4.57	0.0041	1.52	1.32	0.89	1.02	0.32
Maximum -T (10^8 N)	0.0027	2.23	----	0.028	0.029	0.036	0.10	1.64	0.025
Maximum B (tesla)	6.46	5.18	5.15	4.28	6.87	6.17	6.15	7.59	6.51
Layers	45	41	58	8	34	31	26	28	16
Turn per Layer	55	30	43	32	52	50	46	40	52
Thickness (m)	1.43	1.29	1.85	0.208	1.07	0.995	0.817	0.875	0.49
Height (m)	1.43	1.29	1.85	0.254	1.07	0.995	0.817	0.875	0.49
Over all Current density (10^6 A/m ²)	12	7.39	7.16	47.3	15.3	15.4	17.7	14.4	34.6

Table IV

Eddy Current Losses in the Poloidal Field Coils

	Start-Up Eddy Current Losses (10^5 joules)	Reset Eddy Current Losses (10^5 joules)	% helium Liquid loss
D1	0.86	~0	<1%
D2	0.34	~0	<1%
D3	1.32	~0	<1%
D4	0.59	~0	1%
T1	0.19	1.22	1%
T2	0.13	0.89	<1%
T3	0.05	0.32	<1%
T4	0.10	0.18	<1%
T5	0.49	2.70	5%

Table y
Inductance Matrix¹ (micro-henries)

Coil # ↓	1	2	3	4	5	6	7	8	9	10	11	12	13	14	15	16	17	18	19
1	22.49	3.223	3.223	6.632	6.632	10.66	10.66	15.11	15.11	2.038	2.038	2.038	2.038	2.039	2.039	2.039	2.039	2.039	2.039
2		25.08	.3589	11.50	.7643	7.564	1.320	5.521	2.093	.8454	.3168	1.779	.2537	4.117	.2305	12.59	.2272	8.280	.2419
3			25.08	.7643	11.50	1.320	7.564	2.093	5.521	.3168	.8454	.2537	1.779	.2305	4.117	.2272	12.59	.2419	8.280
4				51.24	1.699	23.37	3.043	15.09	4.985	1.058	.5300	1.798	.4654	3.172	.4527	6.215	.4766	9.278	.5364
5					51.24	3.043	23.37	4.985	15.09	.5300	1.058	.4654	1.798	.4527	3.172	.4766	6.215	.5364	9.278
6						68.80	5.623	34.57	9.483	1.186	.7439	1.742	.7062	2.630	.7290	4.305	.8129	6.492	.9599
7							68.80	9.483	34.57	.7439	1.186	.7062	1.742	.7290	2.630	.8129	4.305	.9599	6.492
8								149.3	16.52	1.269	.9710	1.658	.9922	2.232	1.083	3.224	1.274	4.555	1.568
9									149.3	.9710	1.269	.9922	1.658	1.083	2.232	1.274	3.224	1.568	4.555
10										10.70	9.348	3.037	.4727	1.312	.3065	.6620	.2192	.4093	.1774
11											10.70	.4727	3.037	.3065	1.312	.2192	.6620	.1774	.4093
12												12.74	.2859	3.930	.2107	1.545	.1695	.8016	.1511
13													12.74	.2107	3.930	.1695	1.545	.1511	.8016
14														16.74	.1705	4.142	.1501	1.749	.1447
15															16.74	.1501	4.142	.1447	1.749
16																21.84	.1447	5.403	.1511
17																	21.84	.1511	5.403
18																		37.21	.1702
19																			37.21

VII-B-8

1. Matrix is symmetric ($M_{ij} = M_{ji}$)
2. The diagonal has the self inductances (L_{ii})

SKS

It is now beneficial to investigate the conditions created by changes in the rise time. The eddy current losses are inversely proportional to the rise time. Consider first a risetime of 10 sec rather than 100 seconds. Helium usage due to eddy current losses would increase by a factor of 10, which would require a liquid transfer rate of approximately 1500 liters/sec.

The maximum possible plasma resistivity increase which this design can handle is $8\eta_{sp}$. This would increase the eddy current losses only by a factor of 5^{sp} causing a 20% liquid loss in the worst case.

It can not be overly stressed that these results may contain large errors resulting from the assumptions made. Nevertheless they certainly have an order of magnitude validity from which general conclusions can be drawn.

The cost estimates are based at \$1.95/lb of copper composite conductor including superconductor, \$2.00/lb for structural stainless steel, \$2.50/lb for composite aluminum conductor including superconductor and \$1.00/lb for assembly.

The total energy of the divertor-transformer system is calculated by first computing the inductance matrix M_{ij} , where each term is given as a function of complete elliptic integrals. This symmetric matrix is given in Table V. The maximum poloidal field energy stored,

$$E = 1/2 \sum_{K=1}^N \sum_{L=1}^N M_{KL} I_K I_L ,$$

in the unstable case is 16.0 MWhr.

The total cost of the divertor-transformer system is $\$67 \times 10^6$ excluding dewar and mechanical supports. Over 83% of this cost is attributed to the divertor coils. The total stored energy is 16.0 MWhr and the total volume of liquid helium stored in the coils themselves is 1.5×10^5 liquid liters (1.8×10^4 kg) allowing 1 cm on each vertical edge for coolant flow and gas escape.

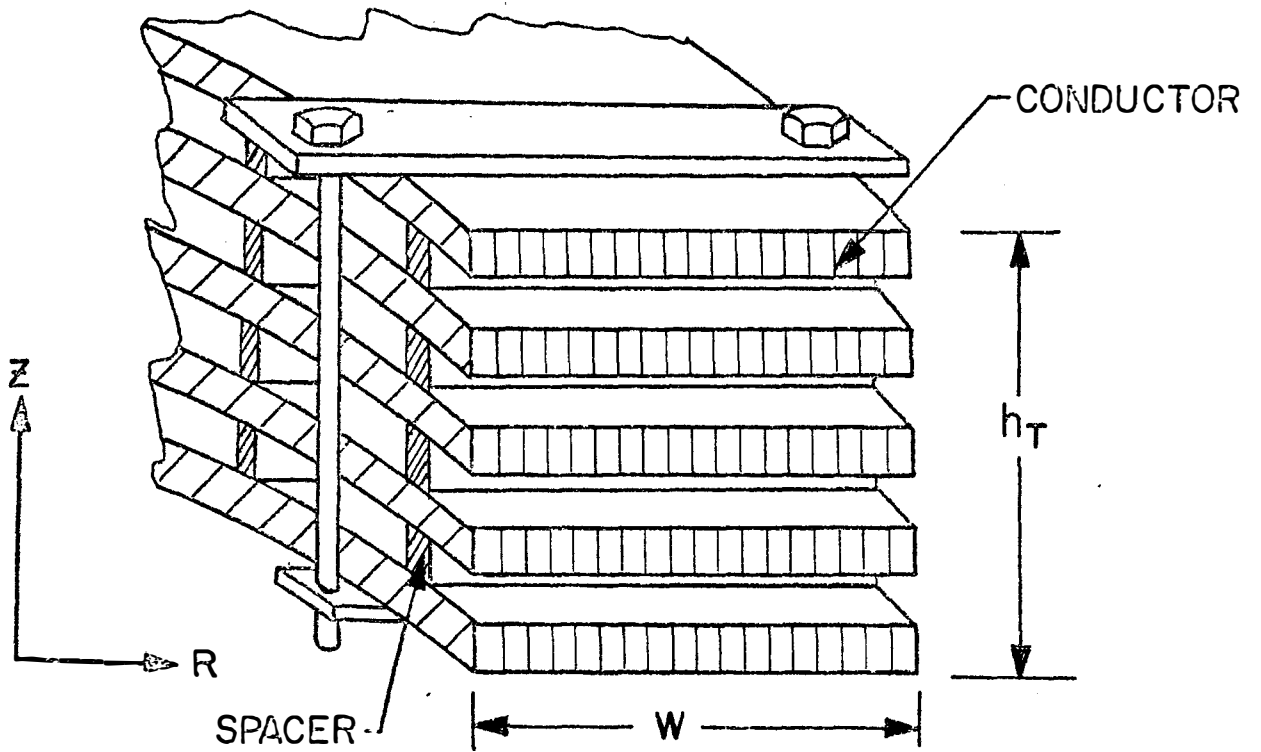


FIGURE VII-B-2a

Final Assembly of Low Stress Design

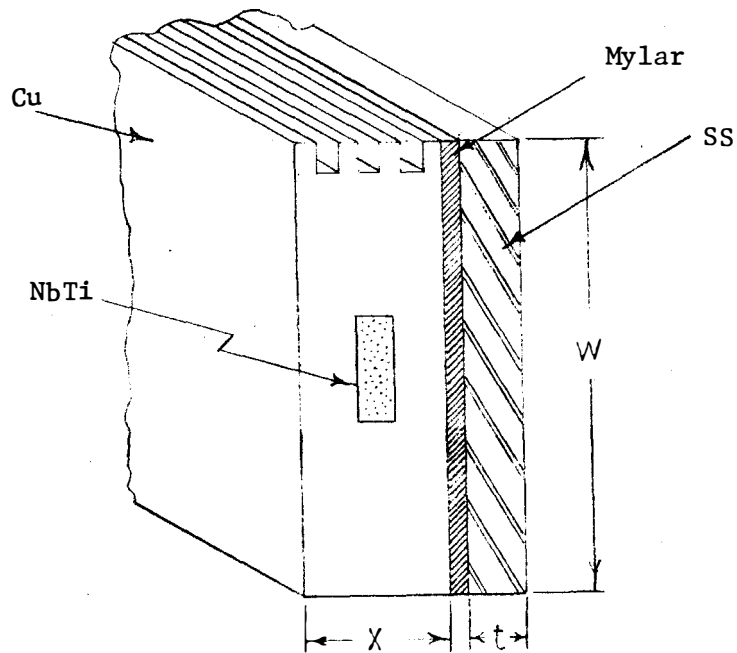


FIGURE VII-B-2b

C. Refrigeration Systems

1. Description

The estimated total refrigeration needed for UWMAK-I is 15 kw. It is felt that five 3 kw 4.2 K refrigerator liquifiers will be used, all feeding into a 200,000 litre liquid storage dewar located above the central core (see Figure I-2, Section I-1).

The inner vessel of the toroidal magnet dewars will consist of 3mm stainless steel sheets which surround the outer insulating spacers of the magnet structure and enclose it completely. Liquid helium will fill the inner vessel completely submerging the magnets.

The outer vessel will also be fabricated of stainless steel, the vertical sides being 2.5 cm thick and the inner and outer perimeter walls, 1.4 cm thick. Epoxy reinforced glass struts will be attached to the inside of the outer vessel, with 10% of them making contact with the magnet while the remaining 90% coming within 1.0 cm of the magnet. The 20 cm vacuum gap between the walls of the inner and outer vessels will be filled with superinsulation. Holes will be cut out in the superinsulation at the locations of the struts which contact the magnets and at the remaining struts, it will be compacted in the 1.0 cm gap. Structural beams will be attached from the outside of the outer vessel to distribute the loading from the struts to a network of bridges connecting adjacent magnets together. This is needed to contain the lateral forces on the magnets in the event of magnet misalignment or failure.

The main liquid helium distribution transfer line will be located inside the central core, with branches feeding the toroidal magnet dewars at the top. Vent lines will also be located at the top of the dewars where they can be used in conjunction with the vapor cooled electrical leads. Relief valves and rupture discs will also be provided. The boil off is then returned to the refrigerator liquifiers where it is recycled back to the central storage dewar.

Similar dewar construction will be used for the divertor and transformer coils. The retractable coils will need flexible transfer lines which will be connected to the central liquid helium distributor system. The transformer coils which are embedded in the central core will be maintained cold by the same system used to cool the core itself. Superinsulation is used to separate the cold portion of the central core used to support the toroidal magnets from the rest of the central column which supports the roof beams.

2. Losses

The following steady state losses can be expected during operation of the toroidal field magnet.

a. Radiation loss

There are 5160 m^2 of surface area on the 12 magnets and an additional 612 m^2 of surface area on the inside of the central core upon which the magnets are supported, see Fig.I-2. Using a radiation loss of $7.5 \text{ } \mu\text{W}/\text{cm}^2$ one obtains a total loss of 433 watts.

b. Conductive loss in the epoxy struts between inner and outer dewar walls. In section 1-b-(10) it was stated that $8,500 \text{ cm}^2$ of reinforced epoxy struts 20 cm long would be required on each side of each magnet to provide lateral support. 10% of these contact the dewar wall. A conductive loss of $1700 \text{ mW}/\text{cm}$ is appropriate for reinforced epoxy for a temperature range from 300 to 4.2K. The total loss is thus $1700 \times 10^{-3} \times 8,500 \times 0.1 \times 12 \times 2/20 = 1734$ watts.

c. Resistive losses in conductor joints

There are 34 joints carrying 10,000 amperes in each of the 12 magnets which will be made by lapping conductors from adjacent discs for 20 cm and clamping. The surfaces containing the superconductor will be facing one another as the conductors lay in the magnets so a path length in the copper would not exceed 0.5 cm. The joints are in a magnetic field of essentially zero so a resistivity of $\rho = 2(10^{-8}) \text{ ohm-cm}$ is realistic. The conductors are 1.1 cm wide where they are lapped. The resistance to current flow through the metal is then $R = \frac{\rho L}{A} = 2 \times 10^{-8} \times 0.5/20/1.1 = 4.55(10^{-10})$ ohm. A properly prepared surface should not give a contact resistance over 10^{-8} ohm so the total power loss is $1.0455 \times 10^{-8} \times 30 \times 12 \times 10,000 = 376$ watts.

d. Lead losses

Properly designed vapor cooled leads carrying 10,000 amperes should not require more than 100 watts/pair or a total of 1200 watts.

e. Nuclear heating load.

In section VI-D-1 the total nuclear heating load is given as 408 watts.

The sum of these five losses is 4151 watts. In Section VII-B-1 the construction of the divertor and transformer coils is described. Since the construction techniques are similar to those used in the toroidal field magnets the cooling requirements will be based upon the volume of liquid helium contained in the magnets. The volume of liquid helium in the toroidal field magnets is given as 100,000 liters and the total volume in all the divertor and transformer coils is 150,000. The losses then in the divertor and transformer coils are estimated at 6000 watts.

In ref. 20 a figure of 1 W/m is stated to be reasonable for transfer lines up to 1/2 inch in diameter. The total length of the distribution system to the toroidal field magnets and the divertor and transformer magnets is 786 m. The total loss is then 786 w. The 200,000 liter storage tank for the liquid helium reserve is a sphere of 3.6 m radius. With a surface area of 163 m^2 and a loss rate of 7.5 mw/cm^2 . The total loss is only 13 watts.

The total system loss rate is 11 Kw.

It is proposed to use five 3.0 KW refrigerators with four of them in operation and the fifth in reserve. The 200,000 liter store of liquid helium could supply the cooling heads of the system for 20 hours in the event of a complete failure of all refrigerators or for 80 hours if two of the five refrigerators were not operating.

In the event of a magnet failure which activated the emergency clamping action of the lateral struts, the heat loss by conduction would rise by 15,600 watts. The system would normally be deactivated as soon as the failed magnet could be returned to operation or until the reactor could be shut down. In the event that the deactivation of the clamping action is not accomplished immediately, the stored helium will be used up at the rate of 25,000 liters/hr. in order to keep the magnets cold.

3. Costs

For large refrigeration systems supplying liquid helium at 4.2K a cost figure of \$583,000/KW is assumed, see Ref. 21. This price includes all of the piping and installation so the total price should be $583,000 \times 15 = \$8.75 \times 10^6$. In addition to the refrigeration system a vacuum system is needed to evacuate the dewars.

D. Power Supplies

1. Toroidal field magnets.

The inductance L of the 12 magnet in series is approximately 5600 henries. If one assumes a reasonable charge time of say 24 hr. the required voltage from a power supply is 700 volts. For low voltage silicon rectifiers, a price of \$100 kW seems reasonable. The total cost is about \$700,000.

2. Divertor and transformer magnets.

In Table III are listed the values of stored energy in each of the magnets. Keeping in mind the fact that there are two of each magnet listed, the total energy stored in the divertor magnets is 674.8×10^8 joules or 18.74 MW hr. The total stored energy in the transformer magnets is 13.16×10^8 joules or 0.366 MW hr. If the effect of mutual inductance is considered, the total stored energy is reduced to approximately 15 MW hr. with the majority of it in the divertor magnets. With a linear rise in the divertor field in a 10 second time period, a peak power of 10.8×10^9 W is required which cannot be supplied from a commercial power grid. The cost of rectifiers to handle this power would also be excessive.

At the present time, 200 MW is about the maximum that can be purchased directly from a power company. If we assume that 500 MW can be purchased in the future, and purchase power as needed up to this maximum for the duration of the start up time, we will have to have the remaining energy available in a storage unit. The use of superconducting magnetic energy storage is a reasonable solution to this problem but the rapid discharge of the storage inductor will make the design of such an inductor differ in some details from those already designed at Wisconsin.⁽¹⁶⁾ Without carrying out a detailed design, one can only estimate the inductor costs. Based on costs of \$20/KW for convertors between the power line and the inductors and $\$1.67 \times 10^6$ /MWhr for a superconducting magnetic energy storage unit and assuming that only 25% of the energy so stored can be efficiently transferred into another set of inductors, the following capital costs seem approximate.

<u>Charge Time</u>	<u>Size of Storage Inductor</u>	<u>Total Cost</u>
10 sec.	55 MWh	$\$100 \times 10^6$
50 sec.	34 MWh	$\$67 \times 10^6$
100 sec.	15 MWh	$\$36 \times 10^6$
200 sec.	0 MWh	$\$11 \times 10^6$

E. Cost Estimate

1. Toroidal field magnets

The following tabulation describes the costs of building a magnet for the containment of the unstable plasma. A 4.2K liquid helium cooling bath is assumed.

<u>Material</u>	<u>Weight</u> <u>10⁶ lb.</u>	<u>Cost</u> <u>\$1 lb.</u>	<u>Total</u> <u>\$10⁶</u>
NbTi	0.23	15.00	3.5
Copper	0.70	1.00	0.7
Fabrication of above	(0.93)	1.50	1.4
Copper	9.74	1.50	14.6
Stabilizer (Total Conductor)	(10.67)	(1.89)	(20.2)
S.S. Discs	9.89	2.00	19.8
Epoxy Insulation	0.58	2.00	1.2
Winding & Assembly (Total Discs)	(21.14)	1.00	21.1
	(21.14)	(2.95)	(62.3)
Aluminum Bolts	0.12	1.00	0.1
Epoxy Struts	0.03	2.00	(62.3)
Cryogenic Insulation	5160: m ² x20 cm	180.00/m ²	0.9
S.S. Dewar Walls	2.05	1.50	3.1
Magnet Assembly (Total Magnets)	(23.34)	0.50	11.7
	(23.34)	(3.35)	(78.2)
Circumferential Bracing	1.00	2.00	2.0
Installation	(24.34)	.10	2.4
Total Installed Magnets	(24.34)	(3.39)	(82.6)

2. Divertor and transformer magnets

<u>Material</u>	<u>Weight</u> <u>10⁶ lb.</u>	<u>Cost</u> <u>\$1 lb.</u>	<u>Total</u> <u>\$10⁶</u>
D-1 Conductor	0.41	1.95	0.80
S.S.	1.16	2.00	2.32
Assembly	(1.57)	1.00	1.57
Total for D-1	(1.57)	(2.99)	(4.69)
D-2 Conductor	0.32	1.95	0.62
S.S.	1.68	2.00	3.36
Assembly	(2.00)	1.00	2.00
Total for D-2	(2.00)	(2.99)	(5.98)
D-3 Conductor	0.89	1.95	1.74
S.S.	4.78	2.00	9.56
Assembly	(5.67)	1.00	5.67
Total for D-3	(5.67)	(2.99)	(16.97)

<u>Material</u>	<u>Weight</u> <u>10⁶lb.</u>	<u>Cost</u> <u>\$1 lb.</u>	<u>Total</u> <u>\$10⁶</u>
D-4 Cu. Conductor	0.11	1.95	0.21
Assembly	(0.11)	1.00	0.11
Total for D-4	(0.11)	(2.95)	(0.32)
T-1 Conductor	0.15	1.95	0.29
S.S.	0.30	2.00	0.60
Assembly	(0.45)	1.00	0.45
Total for T-1	(0.45)	(2.98)	(1.34)
T-2 Conductor	0.14	1.95	0.27
S.S.	0.28	2.00	0.56
Assembly	(0.42)	1.00	0.42
Total for T-2	(0.42)	(2.98)	(1.25)
T-3 Conductor	0.12	1.95	0.23
S.S.	0.21	2.00	0.42
Assembly	(0.33)	1.00	0.33
Total for T-3	(0.33)	(2.97)	(0.98)
T-4 Conductor	0.15	1.95	0.29
S.S.	0.32	2.00	0.64
Assembly	(0.47)	1.00	0.47
Total for T-4	(0.47)	(2.98)	(1.40)
T-5 Conductor	0.14	1.95	0.27
S.S.	0.08	2.00	0.16
Assembly	(0.22)	1.00	0.22
Total for T-5	(0.22)	(2.95)	(0.65)

Total for 18 magnets (two each) \$67.16

Steel Support Structure 2.0 2.00 4.0

S. S. Dewars 3.0 2.00 6.0

Total for divertor and transformer magnets \$77.16

3. Refrigeration System

In Section C-3, the cost of a completely installed refrigeration system was quoted at \$583,000/KW. The requirement was given as five 3 KW units. In addition, the liquid helium inventory must be supplied at \$3/liquid liter.

<u>Material</u>	<u>Cost</u>
Five 3 KW units at \$583,000/KW	\$8.75 x 10 ⁶
Liquid Helium	
Toroidal Field Magnet 100,000 liters	
Divertor and Transformer Magnets 150,000 liters	
Storage 200,000 liters	
450,000 liters @ \$3	\$1.35 x 10 ⁶
Total Refrigeration	\$10.1 x 10 ⁶

4. Power supplies

a. For toroidal field magnets

700 V x 10,000 A = 7,000 kW @ \$100/kW. \$0.7 x 10⁶

b. For divertor and transformer magnets

A superconducting energy storage inductor
with associated switching and rectifying
equipment to deliver 16 MW hr in 100 seconds. \$36 x 10⁶

Total power supply \$36.7 x 10⁶

5. The total cost of the magnets, refrigeration and power supplies is
\$206.6 x 10⁶.

References

1. J. Purcell, H. Desportes and D. Jones, "Superconducting Magnet for the 15 Foot NAL Bubble Chamber," ANL-HEP-7215 (1970).
2. M. S. Lubell, H. M. Long, J. N. Luton, Jr. and W. C. T. Stoddart, "The Economics of Large Superconducting Toroidal Magnets for Fusion Reactors," ORNL-TM-3927 (1972) and I.E.E.E. Conf. Record, I.E.E.E. Cat. No. No. 72 CHO 682-5 TABSC.
3. J. File, R. G. Mills and G. V. Sheffield, "Large Superconducting Magnet Designs for Fusion Reactors," Princeton Report PPL-MATT-848-(1971) and Proc. 4th Sym. on Engr. Problems of Fusion Research, NRL, Washington, D. C. (1971).
4. E. N. Parker, "Reaction of Laboratory Magnetic Fields Against Their Current Coils, "Phys. Rev. 109, 1440 (1958).
5. R. J. Roark, "Formulas for Stress and Strain," 4th ed., McGraw Hill (1965) p. 308.
6. R. W. Boom and W. C. Young, "Design Notes for Fusion Reactor Magnets," Trans. Am. Nuclear Soc., Vol. 15, No. 1, 32 (1972).
7. J. R. Purcell, Private communication.
8. E. F. Byars, and R. D. Snyder, "Engineering Mechanics of Deformable Bodies," 2nd ed., International Textbooks Co. (1969) pg. 54.
9. R. W. Boom, P. Brown, J. C. Laurence and F. J. Worzala, "Nb₃Sn-Aluminum Composite Conductors," Bull. Amer. Phys. Soc., 17, No. 12 1972, p. 1195.
10. C. N. Whetstone, Alcoa Res. Lab., Pittsburgh, Private information.
11. R. L. Stoecker, Magnetic Corp. of Am., N. J., private information.
12. R. Hampshire, J. Sutton and M. T. Taylor, Conf. on Low Temp. and Electric Power, London, 1969, (International Inst. of Refrigeration) p. 69.
13. D. B. Montgomery, Solenoid Magnet Design (Wiley-Interscience, N. Y., 1969) Chap. 6, p. 180.
14. C. Linnet, V. Purdy, Y. W. Chang and T. H. K. Frederking, "Unsaturated Helium Cooling Limits," Report DAAK02-68-C-0064, UCLA, Oct. 1970.
15. J. W. Dean, "Refrigeration Systems for DC and Pulsed Superconducting Magnets in High Energy Physics," Proc. of Fourth International Conference on Magnet Technology, 1972.

16. R. W. Boom, G. E. McIntosh, H. A. Peterson and W. C. Young, "Superconducting Energy Storage," presented at Cryogenic Engineering Conference, August 1973, Atlanta, Georgia.
17. A. D. McInturff and G. G. Chase, "Effect of Metallurgical History on Critical Current Density in NbTi Alloys," JAP, Vol. 44, No. 5, May 1973.
18. W. A. Perkins, and J. C. Brown, MAFCO-A Magnetic Field Code for Handling General Current Elements in Three Dimensions, UCRL - 77411-Rev. II.
19. A. Achermann, "Caterpillars for Loads of up to 80 Tons," Cern 60-25, 1960.
20. R. H. Kropschot, B. W. Birmingham and D. B. Nann, eds., "Technology of Liquid Helium," NBS Mono. III, 1968, pg 214.
21. G. P. Coombs, CTi, Waltham Mass., private information.
22. D. N. Lyon, "Boiling Heat Transfer and Peak Nucleate Boiling Fluxes in Saturated Liquid Helium Between 2.1°K and Critical Temperatures," Adv. in Cryo. Eng., 11, 371 (1967).
23. G. H. Morgan, "Theoretical Behavior of Twisted Multicore Superconducting Wire in a Time-Varying Uniform Magnetic Field," J. Appl. Phy. 41, (9), 3673 (1970).
24. Martin N. Wilson, "Filamentary Composite Superconductors for Pulsed Magnets," Proc. 1972 Applied Superconductivity Conf. Annapolis, Maryland, p. 385.
25. R. A. Popley, D. J. Sambrook, C. R. Walters and M. N. Wilson, "A New Superconducting Composite with Low Hysteresis Loss," Proc. 1972 Appl. Superconductivity Conf., Maryland p. 516.
26. ASME Boiler and Pressure Vessel Code, Section III, Rules for Construction of Nuclear Power Plant Components, 1971.

VIII. Tritium

A. Release Rates

1. Factors Affecting Release Rates

Some tritium release is inevitable during operation of a fusion plant fueled by deuterium and tritium. The principal escape routes are outlined below:

- . permeation through the shield into the reactor hall;
- . permeation into the helium system;
- . permeation through headers and piping into the reactor hall and heat exchanger cells;
- . leaks through valves and joints (if any);
- . permeation through the heat exchanger and into the steam system.

The shield thickness is 81 cm from the outer edge of the blanket (see Figure IV-A-4). The shield consists of alternating layers of steel, lead and boron carbide. An analytical assessment of tritium permeation through the shield is difficult because of the complicated material and temperature distributions and because there are numerous penetrations through the shield, (piping, fueling ports, etc.) which provide alternate escape routes for the tritium. A void space at the outer edge of the blanket offers one method of tritium containment if required. Similarly, lithium headers, valves, etc. may be enclosed in a secondary container to prevent tritium and lithium escape in the event a pipe leaks develops. During normal plant operation the tritium which accumulates in the void space may be removed by pumping to a central location where it is fixed in a disposable solid or liquid. Tritium accumulating in the helium system would be removed by gettering if required.

The tritium escape route which appears most difficult to control is permeation through the heat exchangers, into the steam system. Tritium recovery from the steam would be expensive. It is likely, therefore, that release of the tritiated water to the atmosphere would have to be controlled to rates compatible with radiation release standards (see later discussion). Controlled disposal of the steam generator water would be necessary at the end of plant operation. The permeation rate from the primary-to-secondary-to steam systems depends on the tritium inventory in the lithium, which determines the driving pressure for permeation. Other important permeation parameters are the surface areas, wall thicknesses, temperature and construction materials of the primary and secondary heat exchangers.

The tritium inventory in the primary system is a system parameter which may be set by the designer to a certain extent. The leakage rate of tritium from the system will be small compared to the production rate. Therefore, the inventory is primarily set by the efficiency of

the tritium removal system. The point is not that one system can remove more tritium than another one - in the asymptotic case any system must remove as much tritium as is produced - but that one system can remove tritium efficiently at a lower concentration in lithium. To minimize tritium losses, the tritium concentration in the blanket will need to be on the order of a few parts per million. Thus, any extraction system which operates in this range is likely to be large and expensive. Aside from the lower leakage rate associated with a smaller inventory, there is another reason for keeping it small. One purpose of the blanket is to breed new fuel for the reactor. If significant tritium cannot be removed until the concentration and consequently the inventory became large, then fuel must be supplied from elsewhere to keep the reactor operating until the tritium concentration in the lithium rises sufficiently for the extraction process to produce enough fuel to fuel the reactor. In fact, once the tritium concentration becomes high enough to extract enough tritium for the reactor, the extraction system will begin to produce extra tritium for use in other devices. A third reason for keeping the inventory low is to minimize the radioactivity of the system. If some abnormal condition could be envisioned whereby the tritium in the blanket could escape, the radioactivity of the tritium could present a hazard. Thus, on one hand it is desirable to keep the tritium inventory low to minimize the startup requirements of the tritium and to minimize tritium radiological problems. On the other hand, efficient operation of the extraction system favors a high tritium concentration.

The surface area of the heat exchangers affects the release rate, since the tubes in the heat exchanger serve as the barriers between the lithium and steam systems. To isolate the lithium in the blanket from the steam system, an intermediate Li-to-Na heat exchanger will be used to transfer the heat produced to an intermediate loop. The sodium in the intermediate loop in turn will be used to produce steam in the steam generator. The area of these heat exchangers depends on the heat transfer properties of Li and steam as well as the detailed design.

The temperature is an important factor, not only because it influences the heat exchanger design but because the tritium diffusion rate and equilibrium pressure over the lithium are temperature dependent.

Finally, the release rate of tritium depends on the materials used for the heat exchangers. The tritium diffusion rate varies with the tube wall thickness; the thickness in turn is affected by mechanical and thermal properties. In addition, diffusion rates differ for various metals and alloys. This is illustrated in Figure VIII-A-1 taken from Webb⁽¹⁾, which shows the temperature dependence for hydrogen diffusion.

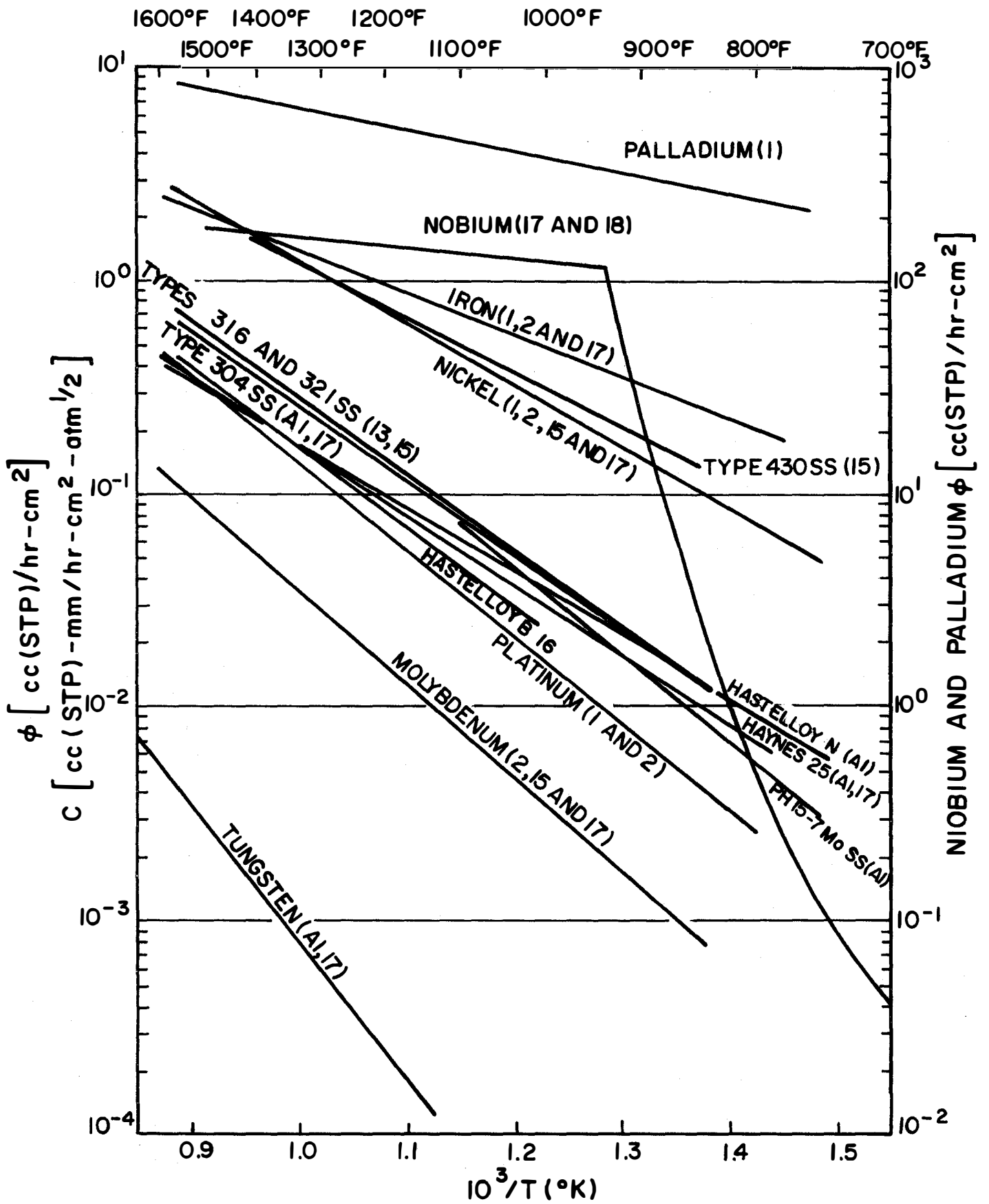


FIGURE VIII-A-1

2. Basis for Selecting Tritium Release Rates

Having established the parameters which affect tritium release rate, the designer must consider the mechanisms and paths for tritium release in order to obtain an allowable release rate. One approach has been to use a nominal release rate of 4 curies/day, since this corresponds to an amount released by a typical fission plant. This, however, is a very stringent requirement. Tritium released from a fusion plant is only a portion of the total plant radioactivity inventory. To do the problem correctly would require a complete evaluation of the mode of release, i.e., whether as a gas from a high stack or as tritiated water which could be discharged into condenser cooling water. A site would have to be chosen and the particular environmental conditions of that site considered. Such a study is beyond the scope of this treatment. However, some simple calculations will help put the problem into perspective. Suppose, for example, that all the tritium which gets into the steam system is lost during blowdown, mixes with the condenser cooling water and is discharged. Assuming the plant is 40% efficient (this value is too high, but using it tends to overestimate the concentration of tritium) then 3000 Mw must be dissipated by the cooling system. The mass flow of water through the condenser is

$$\dot{m}c \Delta t = P$$

$$\dot{m} = \frac{3 \times 10^6 \text{ kw} \times 3412 \frac{\text{BTU}}{\text{hr}}/\text{kw}}{1 \frac{\text{BTU}}{\text{lb}^\circ\text{F}} \times 20^\circ\text{F}}$$

\dot{m} = mass flow rate
 c = specific heat
 Δt = temperature rise across condensor
 P = power dissipated

where the temperature rise across the condensor is taken to be 20°F (11°C)

$$\dot{m} = 5.1 \times 10^8 \text{ lbs/hr} = 5.6 \times 10^9 \text{ l/day}$$

The permissible limit of tritium in water given in 10 CFR 20 Appendix B, Table II, column 2 is 3×10^{-3} uci/ml = 3×10^{-6} ci/l.

Taking 1.0% of the limit, in line with current practice, an allowable concentration would be 3×10^{-8} ci/l corresponding to a release rate of 3×10^{-8} ci/l \times 5.6×10^9 l/day = 168 ci/day.

While this calculation is only applicable to a once-through cooling system with the reactor operating as described earlier, it does give some idea of the order of magnitude of a tolerable tritium release rate and is considerably larger than the 4 ci/day value which has been used in the past.

Another approach is to look at what tritium release rates have been licensed for present operating facilities, e.g., fuel processing plants. Our best information indicates (2) that reprocessing plants will be licensed to release 100 ci/day. Again, this value is larger than the 4 ci/day assumed in the past, but somewhat smaller than that calculated above. However, allowable release rates will likely be lowered by the time a fusion reactor is operated so that a minimum tritium release rate must be considered.

3. Tritium Release Rate

Based on the preceding discussion, 100 ci/day of tritium release through the steam generator will be assumed. The actual plant release rate will be somewhat greater due to diffusion through other parts of the system, but by designing to this release rate, the result should approach that of a detailed calculation involving gaseous and liquid releases and taking site factors into consideration. The design philosophy will be to use the above release rate to calculate an allowable tritium inventory and then design the tritium removal system to maintain the inventory.

B. Breeding Ratio and Inventory

1. Summary of Heat Exchanger Design

In order to establish the tritium inventory, it is necessary to know the details of the intermediate heat exchanger and the steam generator, in particular the materials used, the thickness of the tubes and the total surface area of each. To do this it is in turn necessary to design the complete steam cycle. The detailed steam cycle design will occur in the next phase of the design. However, sufficient information is available to establish methods and the approximate inventory close enough to ascertain the characteristics of the system. The lithium conditions from the blanket are: T_{out} 483°C (901°F), T_{in} 283°C (541°F), mass flow rate 4.7×10^7 lbs/hr (2.1×10^7 kg/hr). The design of the intermediate heat exchangers and steam generators⁽³⁾ are discussed in Chapter X. The intermediate heat exchanger is designed with a log mean temperature difference of 39°C (70°F). The sodium temperatures are then 262°C (502°F) in, and 412°C (722°F) out with a flow rate of 9.3×10^7 kg/hr (2.04×10^8 lbs/hr) divided into twelve loops. The heat transfer surface area and consequently the area across which tritium can diffuse from the primary to intermediate loops is 1.86×10^4 m² (2.0×10^5 ft²).

The steam generators have been designed with a pinch point ΔT of 22.8°C (41°F). The steam conditions are 305°C (580°F) at a pressure of 39.8 atmospheres (565 psia) with feed water at 217°C (400°F) and a flow rate of 7.1×10^5 kg/hr (1.57×10^6 lbs/hr) per steam generator at full power. The resulting area for tritium diffusion into the steam from the sodium is 2.66×10^3 m² (2.86×10^4 ft²) per generator for a total of 3.15×10^4 m² (3.43×10^5 ft²). The tube walls in the intermediate heat exchanger are 1.067 mm of SS and the walls in the steam generator are 1 mm Inconel plus 0.63 mm of Croloy.

2. Inventory in the Primary System

The calculation of the inventory of the primary system is approached by first calculating the partial pressure of tritium in the secondary system. The equation used for determining the pressure is essentially that given in Reference 1.

$$V = \frac{CA}{\sqrt{3}X} (P_1^{1/2} - P_2^{1/2}) e^{-Q/RT} \cdot 10^{-5}$$

V = volume flow rate of tritium permeating in $\frac{\text{CC(STP)}}{\text{sec}}$
 X = thickness of metal (mm)
 P₁ = upstream pressure (mm Hg)
 P₂ = downstream pressure (mm Hg)
 Q = activation energy of diffusion (cal/mole)
 R = gas constant (cal/mole °K)
 T = absolute temperature
 A = area of diffusion surface in cm²
 C = permeation constant (CC(STP) - mm/hr/cm²/atm^{1/2})

and the $\sqrt{3}$ factor is inserted to correct for the fact that tritium is diffusing rather than normal hydrogen. The question of whether to use a P^{1/2} or P dependence has been discussed by Fraas.(4) In view of the fact that recent work reported by Strehlow (5) on SS shows a P^{1/2} dependence, there seems to be no convincing reason not to use this expression.

In the application of the previous equation to the present case the question arises as to what temperature to use. In the actual situation the temperature will vary along the length of the heat exchanger, affecting the magnitude of the exponential term. Also, as the coolant changes temperature the tritium partial pressure may also be changing. Furthermore, there is a temperature gradient across the tube wall which is not taken into account in the previous equation. In view of these uncertainties the gross average temperature of the coolants on both sides of the exchanger was used.

The pertinent data for the above equation taken from Reference (1) and the earlier part of this report are:

$$V = 100 \text{ curie/day} = 10^{-2} \text{ g/day} = 4.32 \times 10^{-4} \frac{\text{CC(STP)}}{\text{sec}}$$

$$A = 3.5 \times 10^5 \text{ ft}^2 = 3.19 \times 10^8 \text{ cm}^2$$

$$P_2 = 0$$

$$Q = 16,100 \text{ cal/mole}$$

$$T = 296^\circ\text{C} = 569^\circ\text{K}$$

$$R = 1.98 \text{ cal/mole } ^\circ\text{K}$$

$$C = 850 \frac{\text{CC(STP)-mm}}{\text{hr cm}^2 \text{ atm}^{1/2}}$$

$$X = 0.065 \text{ in.} = 1.65 \text{ mm}$$

$$P_1^{1/2} = \frac{\sqrt{3} X V \times 10^5}{C A e^{-Q/RT}} = 7.28 \times 10^{-4} (\text{mm Hg})^{1/2}$$

$$P_1 = 5.30 \times 10^{-7} \text{ mm Hg}$$

The same flow rate has to pass across the intermediate heat exchanger. The parameters in the flow equation are:

$$V = 4.32 \times 10^{-4} \text{ CC(STP)/sec}$$

$$A = 2 \times 10^5 \text{ ft}^2 = 1.86 \times 10^8 \text{ cm}^2$$

$$Q = 16,100 \text{ cal/mole}$$

$$T = 361^\circ\text{C} = 634^\circ\text{K}$$

$$R = 1.98 \text{ cal/mole}$$

$$C = 850 \text{ CC(STP)mm/hr cm}^2 \text{ atm}^{1/2}$$

$$X = 0.042 \text{ in.} \approx 1.067 \text{ mm}$$

$$P_2 = 5.30 \times 10^{-7} \text{ mm Hg}$$

$$P_1^{1/2} = \frac{\sqrt{3} V X}{C \times 10^{-5} A e^{-Q/RT}} + P_2^{1/2}$$

$$= 1.89 \times 10^{-4} + 7.28 \times 10^{-4}$$

$$= 9.17 \times 10^{-4}$$

$$P_1 = 8.41 \times 10^{-7} \text{ mm Hg}$$

The concentration of tritium in the lithium may be calculated using Sievert's law

$$\sqrt{P} = K N$$

N = mole fraction of T_2

P = pressure in mm Hg

K = Sievert's constant

K for tritium in lithium is given by (Ref.6)

$$\text{Log}_{10} K = 4.591 - 2809/T$$

The average temperature in the blanket is $383^\circ\text{C} = 656^\circ\text{K}$ yielding

$$K = 2.03$$

$$\text{and } N = \frac{\sqrt{P}}{K} = \frac{9.17 \times 10^{-4}}{2.03}$$

$$N = 4.52 \times 10^{-5} \text{ mole fraction of tritium.}$$

The tritium inventory is then

$$I_{B \text{ sat}} = N m_{Li} A_t / A_{Li}; m_{Li} \sim 6.3 \times 10^5 \text{ kg}$$

$$I_{B \text{ sat}} = 4.52 \times 10^{-4} \times 6.3 \times 10^5 \times 3/7 \text{ kg} = 122.2 \text{ kg}$$

This inventory of 122 kg of tritium is rather large. It represents an inventory of $\sim 1.2 \times 10^9$ curies of radioactivity. Beyond this, however, is the effect on the operation of the plant, which burns only 0.689 kg/day. Using the formulae in Reference (7), the mean residence time of a tritium atom in the blanket is:

$$\lambda = I/TN \text{ assuming a high breeding ratio, } T, \text{ of } 1.3$$

$$\lambda = \frac{122.2}{1.3 \times .689} = 136.4 \text{ day}$$

and the amount of tritium needed to start up the reactor above that needed for steady state operation is

$$\begin{aligned} \Delta I &= I_o - I_{\text{ex min}} = N \lambda [1 - (T - 1) \ln(T/T-1)] \\ &= .689 \times 136.2 [1 - .3 \ln \frac{1.3}{.3}] = 52.6 \text{ kg.} \end{aligned}$$

Assuming minimum operating inventory $I_{\text{ex min}} = 10 \text{ kg}$, the doubling time would be

$$t_d = \frac{I_{\text{ex min}} + I_{B \text{ sat}}}{N (T - 1)} = \frac{132.2}{.689 \times .3} = 639 \text{ days}$$

If the breeding ratio were even higher, say 1.5, ΔI would still have the rather large value of 42.2 kg.

The consequences of this rather large inventory are 1) The removal of tritium would be easier than that of a system with an approximately 10 kg inventory; 2) the amount of radioactivity in the system is large; 3) a large quantity of tritium must be supplied before initial operation to sustain the plant until the blanket inventory builds up to the point where the extraction system removes enough to keep the plant going; and 4) the doubling time is still quite adequate, being less than two years.

In considering the four items above, it would seem that the negative points 2) and 3) outweigh point 1), while as will be seen, adequate doubling times are readily attainable in almost any situation. Consequently, the rather interesting point emerges that with the particular parameters used above, the tritium release rate which may be tolerable from radiological considerations is too large when other plant factors such as plant inventories are considered. It therefore is necessary to reduce the inventory by a factor of ten or more to bring the inventory down to a more reasonable value. Since the release rates are proportional to the square root of the tritium pressure, and the mole fraction (and consequently the inventory), is also proportional to the square root of the tritium pressure, a reduction of the inventory by a factor of ten also results in a reduction of the release rate by the same factor. Summarizing the results we have:

release rate	10 ci/day
tritium pressure in intermediate loop	5.30×10^{-9} mm Hg
tritium pressure in primary loop	8.41×10^{-9} mm Hg
mole fraction of tritium in primary loop	4.52×10^{-5}
tritium inventory in primary loop	12.2 kg

3. Inventory, Breeding Ratio and Doubling Time

With the inventory calculated in section VIII-B-2, it is possible using the formulas in Reference (7) to find the mean residence time of tritium atoms in the blanket, the excess initial inventory above that required for steady state operation and the doubling time of the system as a function of the breeding ratio T . The mean residence time is given by

$$\lambda = \frac{I_{B \text{ sat}}}{T N} \text{ where } I_{B \text{ sat}} \text{ is the equilibrium blanket inventory}$$

in kg, and N is the rate tritium is burned, which for a 5000 Mw_{th} plant with an energy recovery of 20 Mev/fusion is 0.689 kg/day. λ is plotted in Figure VIII-B-1 for an inventory of 12.2 kg as a function of the breeding ratio T . Since λ is inversely proportional to T it varies less than 30% over breeding ratios of interest.

The excess initial inventory ΔI is given by:

$$\Delta I = \frac{I_{B \text{ sat}}}{T} [1 - (T-1)\ln(T/T-1)]$$

ΔI is plotted as a function of T in Figure VIII-B-2

Over the range of breeding ratios of 1.01 to 1.3, ΔI varies from ~12 kg to ~5 kg. This appears to be an acceptable range. A conservative estimate of the tritium required to operate the plant in the equilibrium situation is ~10 kg. Thus, the excess initial inventory for start-up is of the same order of magnitude and would likely not present unreasonable demand. For subsequent plants it would present no problem since it is likely that sufficient tritium would be available from the operation of earlier reactors.

The time for the minimum in the external inventory is shown in Figure VIII-B-3. Again it is seen that the times for any reasonable breeding ratio are quite acceptable.

The doubling time is defined as the time to produce enough additional tritium to supply the total amount needed to start a second plant. Doubling time as a function of breeding ratio is shown in Figure VIII-B-4. A minimum external inventory of 10 kg, needed to operate the plant, is assumed. It is apparent from this graph that breeding ratio and doubling time present no problem other than perhaps that of reducing the breeding ratio to lower the amount of tritium produced. If the blanket breeding ratio is as high as 1.5 as indicated in section V-B-1, a doubling time of ~70 days is obtained which is likely much too short and would require the removal of some 10 kg of tritium per month from the plant site. A doubling time of ~2 years minimum is more reasonable and would require a breeding ratio of only ~1.05 for this plant. Two years is chosen as a reasonable doubling time on the basis that it is unlikely that, at least for the first plants, fusion reactors will go on line at a rate faster than one every two years. At the same time, a doubling time of two years is short enough that a fusion power generation system could grow faster than the requirements for power and thus become the major source of production.

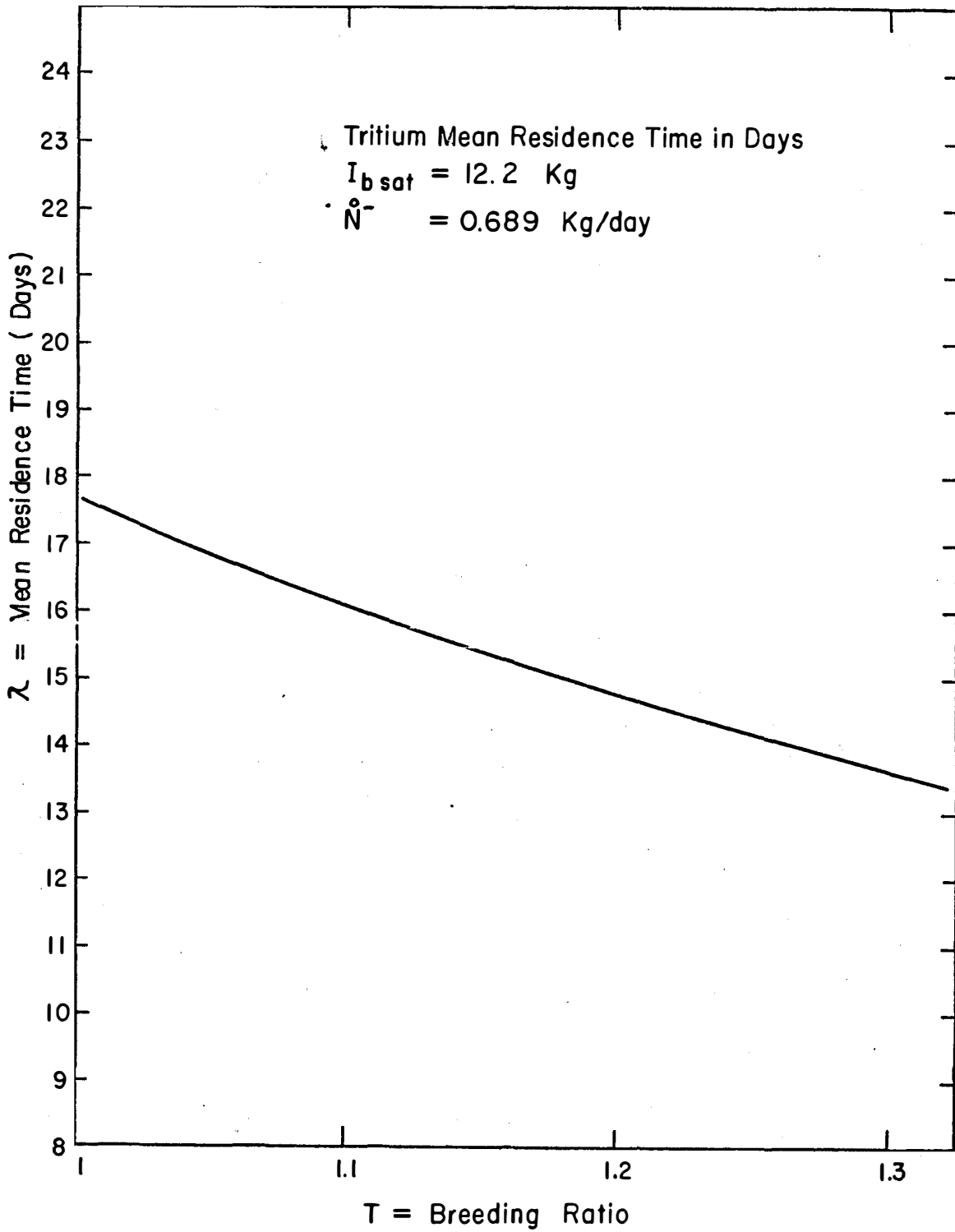


FIGURE VIII-B-1

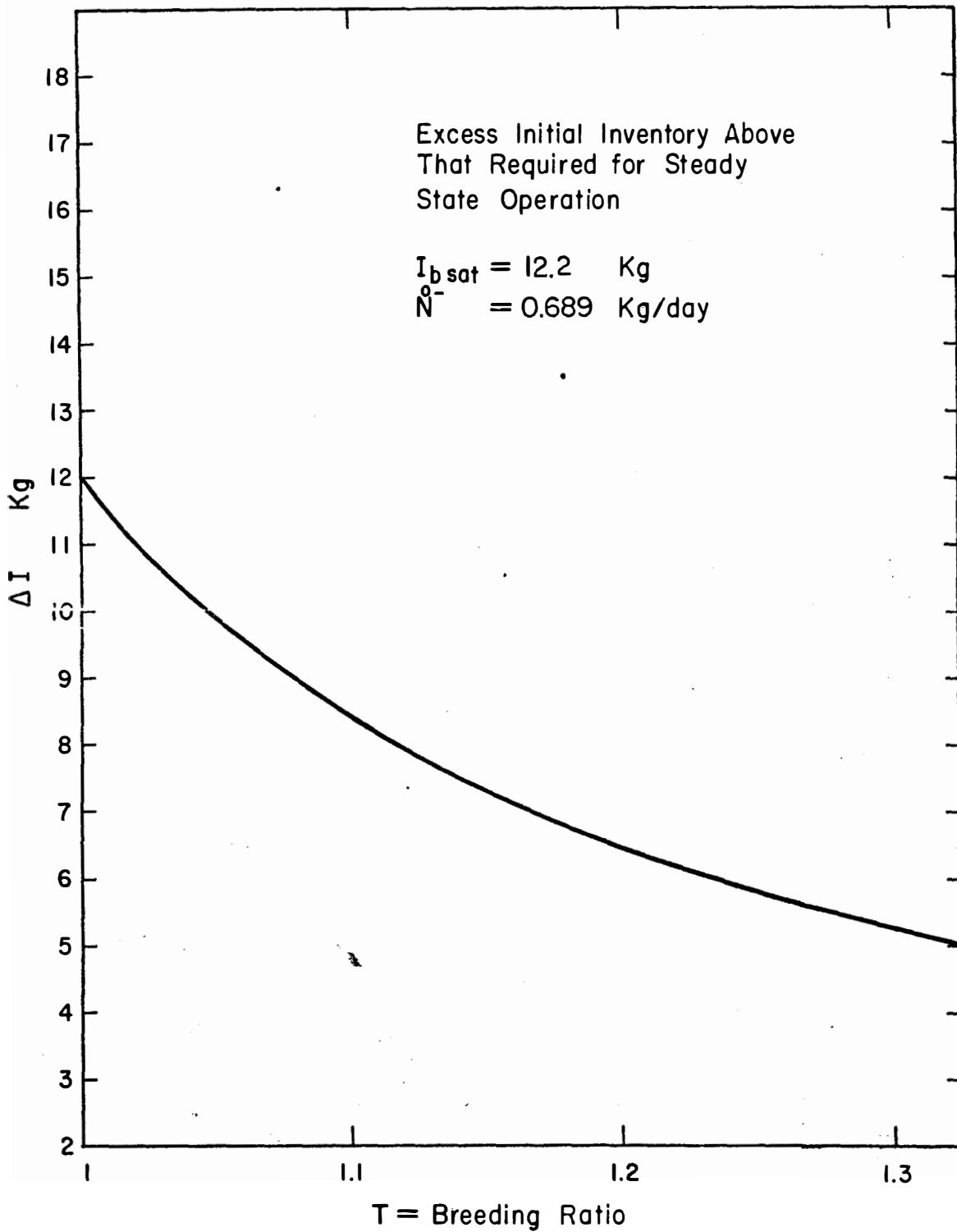


FIGURE VIII-B-2

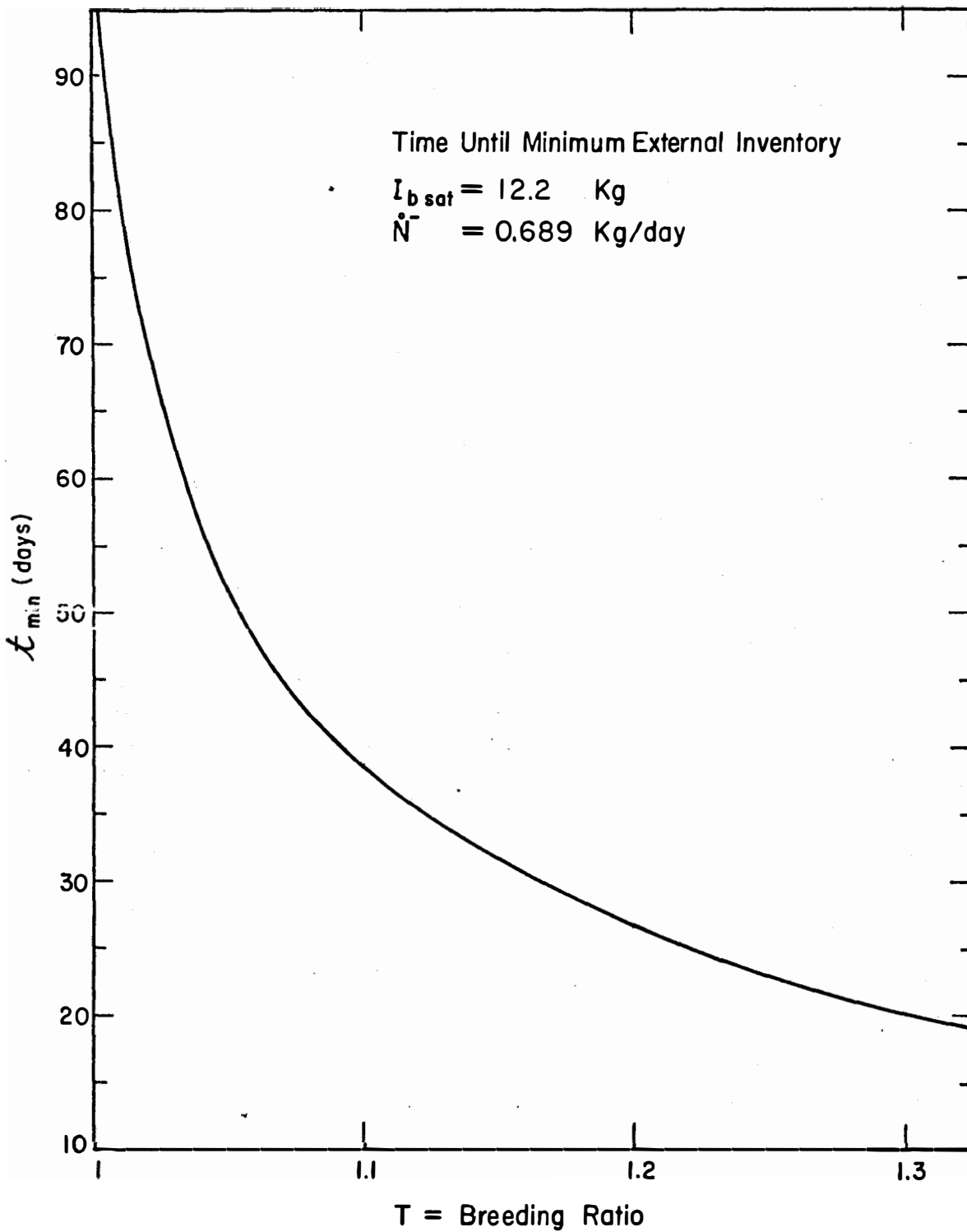


FIGURE VIII-B-3

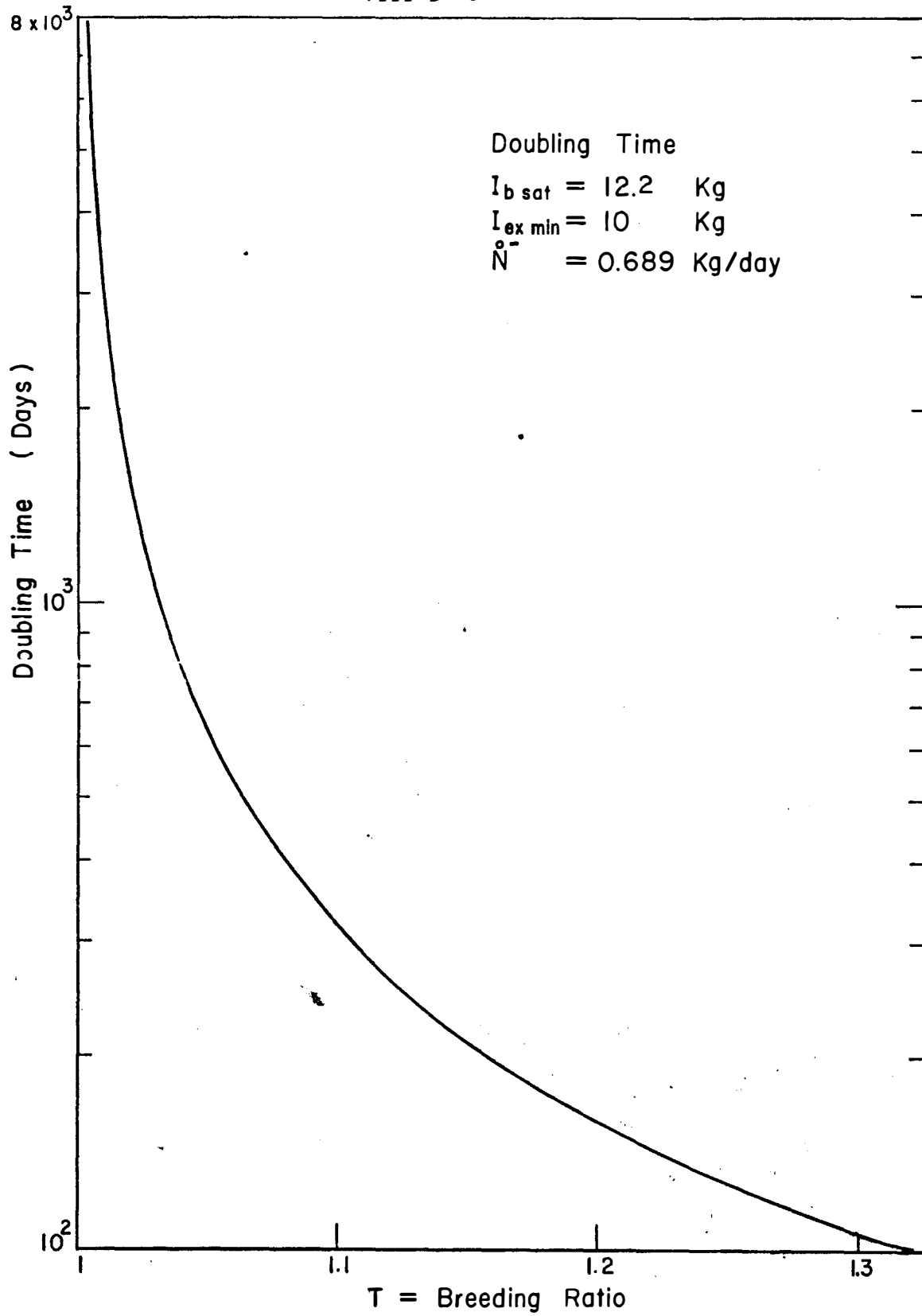


FIGURE VIII-B-4

VIII. Tritium

C. Tritium Extraction

In Section VIII-B the process of breeding tritium in the lithium blanket was described. The success of the fusion concept depends on development of a routine, economical method to extract tritium from the blanket at a rate sufficient to fuel the plant and to maintain a relatively low tritium inventory in the blanket. The UWMAK-I reactor would burn approximately 0.69 kg/d (2.9×10^6 cc, STP) of tritium, so the average daily extraction from the blanket must at least equal that amount.

The basic problems of tritium extraction from a CTR lithium blanket are:

- a) the tritium is necessarily dilute in the lithium blanket in order to minimize tritium losses to the environment by diffusion through the materials of construction (see Section VIII-A);
- b) the tritium forms a relatively stable tritide with lithium, LiT, tending to rule out certain straight forward tritium extraction methods, such as distillation or gas sparging.

1. Comparison of Hydride (Tritide) Stabilities

Lithium combines with hydrogen to form LiH, which has a relatively high standard free energy of formation (-16.8 k cal/mole at 298°K)⁽⁸⁾ and a high melting point (680°C).

The equilibrium hydrogen pressure over several metal-hydride systems are shown in Figure VIII-C-1 as a function of temperature. Lithium hydride is substantially more stable than the hydrides of other metals from Group I of the periodic table. At 300°C the extrapolated equilibrium hydrogen pressure over Li-LiH is $\sim 2 \times 10^{-5}$ torr (Fig. VIII-C-1), which is a factor of 10^4 greater than the tritium pressure desired (Section VIII-B-2).

Figure VIII-C-2 shows extrapolated values for partial molal free energy and decomposition pressure at 300°C for selected hydrides. Hydride stability increases as the decomposition pressure decreases. Figs. VIII-C-1 and -2 indicate that several metals form hydrides which are more stable than LiH. Both figures indicate that yttrium forms the most stable hydride. However, several other metals form hydrides more stable than LiH, including Zr, Sc, Sr, Ca and the lanthanides.^(8,9)

The above metals dissolve hydrogen exothermically, and their hydrogen solubilities increase with decreasing temperature.

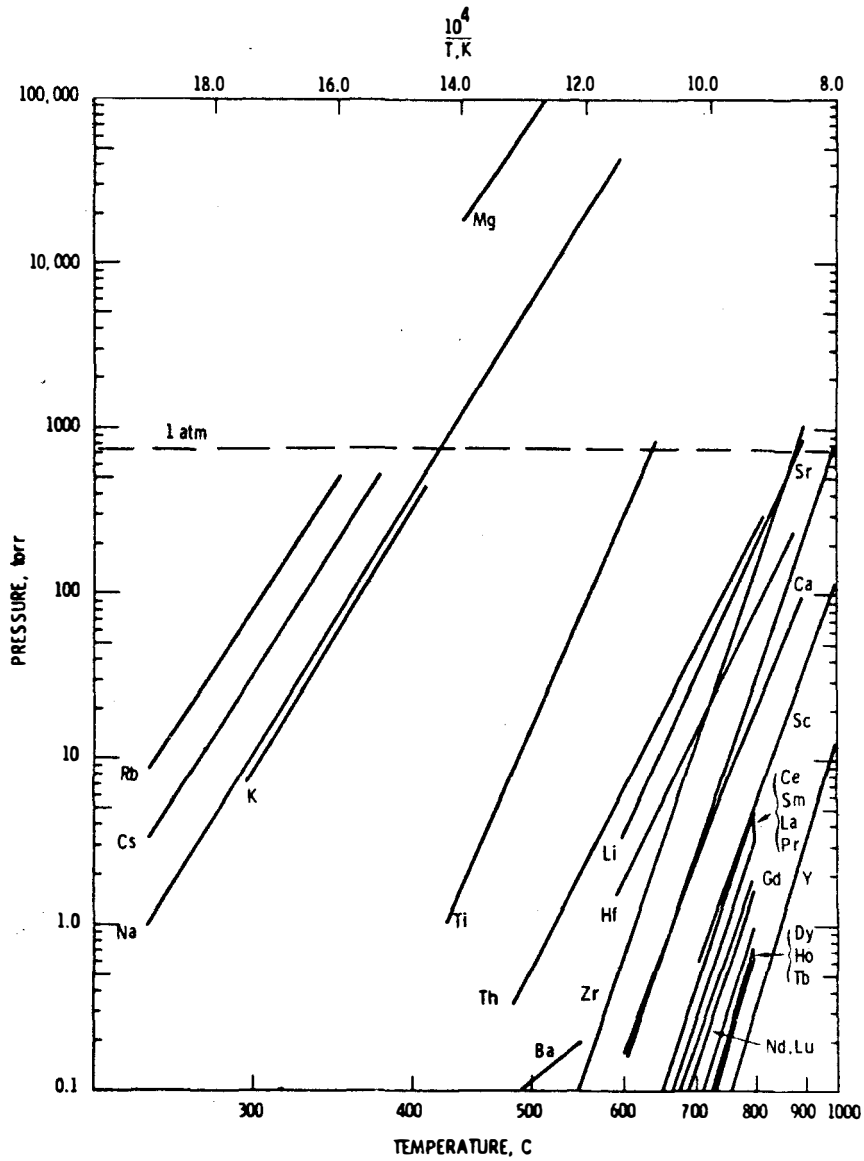


FIGURE VIII-C-1 Plateau pressures of the monohydrides and dihydrides of various metals. (8)

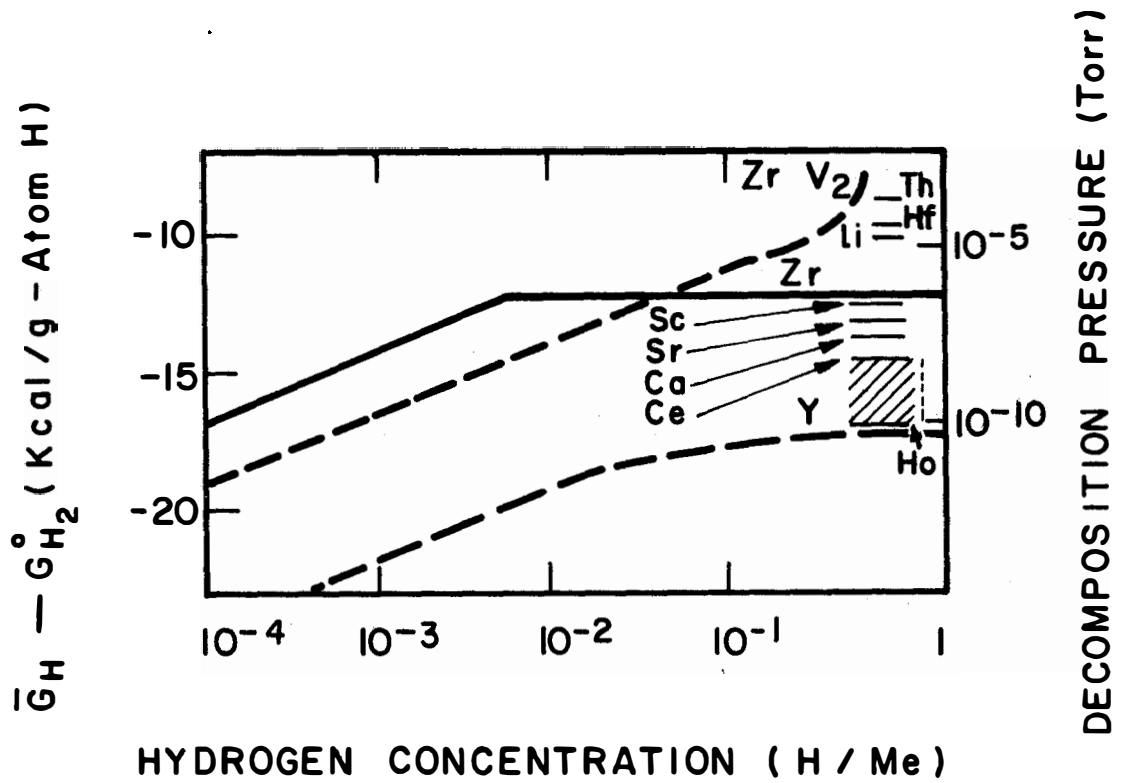


FIG. VIII - C-2 Partial molal free ENERGY OF hydrogen in systems Me - H 300 °C. (ref.9)

Data regarding tritium and tritide behavior are sparse. It is necessary, therefore, to infer tritium technology from existing data for hydrogen. The following section addresses the question of property comparisons for the three hydrogen isotopes, ordinary hydrogen (H), deuterium (D), tritium (T) and their compounds.

2. Isotope Effects on Hydrogen Reactions and Hydride Properties

In general, the reaction kinetics and thermodynamics are similar for the three hydrogen isotopes. (10) The differences in physical properties (e.g., density and lattice parameters) for hydrides, deuterides, and tritides are small, but detectable. Heats of formation for the metal deuterides and tritides often are slightly less than corresponding values for the hydrides. Dissociation pressures for the deuterides and tritides usually exceed the corresponding values for the hydrides, indicating that the hydrides have the highest stability (10,11), although VD_2 has been found to be more stable than VH_2 (24).

Sievert's Law constants for solutions of deuterium and tritium in lithium have been derived from data for dilute solutions of hydrogen in lithium. (6)

Classical diffusion theory predicts that diffusion rates will vary inversely with the square root of the mass of diffusing species, which in the case of hydrogen occurs in the atomic form. (12) Thus, the theoretical relationship between hydrogen and tritium diffusivities is:

$$D_T = \frac{D_H}{\sqrt{3}}$$

Experimental values for D_H/D_T are 1.97 for stainless steel and 1.69 for palladium, which are relatively close to the theoretical value of 1.73. (12)

The above examples indicate that while comparative studies of the hydrogen isotopes are not extensive, they provide a basis for preliminary estimates of tritium and tritide behavior from existing data for hydrogen and deuterium.

3. Discussion of Alternative Tritium Extraction Methods

Watson (13, 14) reviewed several extraction schemes for removing tritium from a niobium-contained lithium blanket. The alternative methods considered were:

1. distillation
2. gas sparging
3. cold trapping of lithium tritide
4. diffusion through metal surfaces to a collection system
5. absorption in a metal bed: yttrium was the preferred extraction metal.

Watson ruled out methods 1 and 2 due to unfavorable equilibria stemming largely from the relatively high stability of LiH. Cold trapping of LiH will be difficult due to the relatively high tritium solubility in lithium, even near its melting point (186°C). Solid sorbents were considered to be more effective in potassium than in lithium, because the lower potassium melting point allows operation at lower temperatures, where tritium solubilities are higher in prospective absorption materials. However, absorption kinetics tend to decrease with decreasing temperature. Therefore, a favorable balance must be sought between the kinetics and thermodynamics of tritium absorption.

Watson regarded diffusion through metal windows as the most promising tritium recovery method for a niobium system operating at ~1000°C.

Maroni and Velekis (15) proposed an extraction method based on tritium removal from liquid lithium in a molten salt, e.g., LiF-LiCl. Tritium reportedly is about eight times more soluble in the salt than in the liquid lithium at ~600°C. Use of a cascade system was said to offer potential for extraction to very low tritium concentrations, though obviously at increasing cost as the number of cascade cycles increases. Questions regarding lithium-salt mutual solubilities, extraction efficiencies of tritium from lithium and methods of tritium recovery from the salt need further evaluation to assess the applicability of the method to fusion technology.

4. Tritium Extraction in the UWMAK-I System

In the UWMAK-I stainless steel system, the temperature is limited to ~500°C by corrosion and radiation damage considerations. At this temperature, the area required to transfer tritium by diffusion through a stainless steel window ($\sim 7 \times 10^8 \text{ m}^2$) is too large for that method to be considered. Even palladium with its higher permeation rate (16) would require a window area of $\sim 1.9 \times 10^7 \text{ m}^2$. Furthermore, palladium is not compatible with lithium (13).

Ruling out gas sparging, distillation, diffusion and cold trapping on grounds assessed by Watson (13, 14) the preferred extraction method in the stainless steel system is a metal extraction bed. Watson proposed yttrium for the tritium extraction material. The following discussion will consider the advantages and disadvantages of yttrium and alternative tritium extraction materials.

a) Assessment of Yttrium as a Tritium Extraction Bed Material

The phase diagram for the yttrium-hydrogen system at atmospheric pressure is shown in Fig. VIII-C-3. The three pertinent phases are an yttrium-hydrogen solid solution; YH_{2-x} ; and YH_{3-x} . The solid solution

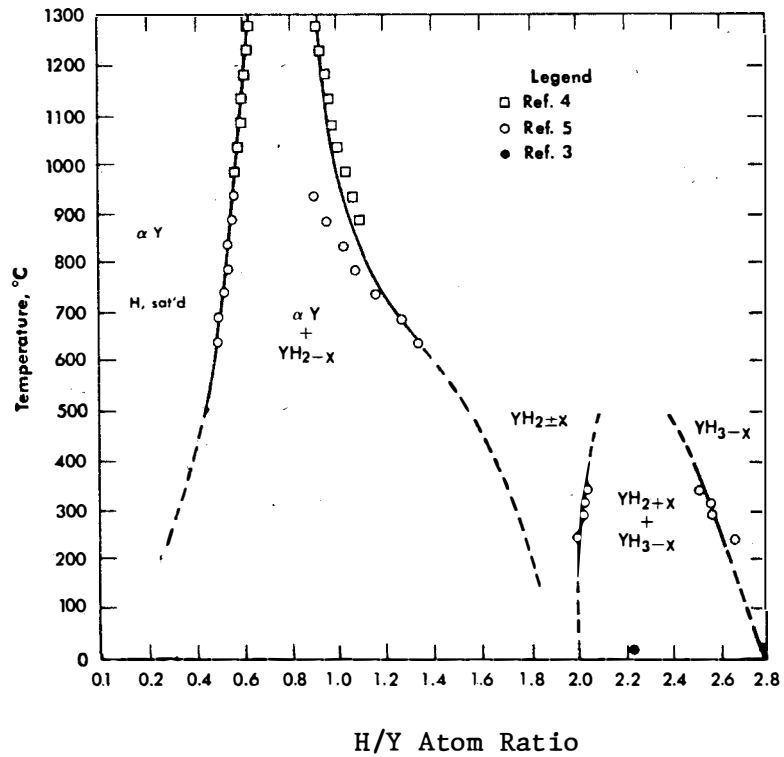


FIGURE VIII-C-3 Partial phase diagram of the yttrium-hydrogen system. (17)

and YH_{2-x} phases have relatively good mechanical stability. Embrittlement of the metal may occur by hydride precipitation along crystallographic planes. (17) Thermal shock can cause cracking of solid hydride phases. However, the extraction system very likely can be designed and operated to essentially eliminate problems from these sources.

The YH_{3-x} phase is stable in the vicinity of 300°C and below in one atmosphere of hydrogen; it reportedly reverts to powder (17), and therefore is an undesirable species in the tritium extraction cycle. It is not clear where the phase boundary for YH_{3-x} will be at the relatively low tritium pressures in the extraction system, but it will be necessary to adjust temperatures or regeneration frequency to avoid its formation. Because it occurs only at relatively high H/Y ratios, formation of YH_3 is unlikely; but at low temperatures, surface hydrides sometimes form, in preference to hydrogen diffusion into the metal substrate.

Previous reference to Fig. VIII-C-1 and -2 indicated that yttrium is an optimum tritium absorber on thermodynamic grounds. The hydrogen solubility increases with decreasing temperature, favoring relatively low extraction temperatures from a solubility standpoint. However, the kinetics of extraction are an equally important consideration, which are presently undefined for the Y-T₂-Li system.

There is broad experience indicating that even very thin oxide surface films inhibit hydrogen absorption in metals, despite large thermodynamic driving forces.

Yttrium is used to getter impurities, including oxygen, from lithium. (18) Yttrium oxide is reported to be slightly more stable than Li_2O . (19) This means that yttrium surfaces will form surface films in contact with lithium. Thus, while the thermodynamics for extraction of tritium in yttrium are favorable, several kinetic aspects of the absorption need evaluation, including:

- the rate of tritium absorption from lithium as a function of temperature
- the influence of temperature, impurity species and impurity concentrations on deactivation of the yttrium surface
- methods for restoring the activity of the yttrium surface if tritium extraction rates fall below acceptable levels.

Techniques for restoring rapid absorption kinetics to metal surfaces include mechanical cleaning of the surfaces or dissolution of surface films into the metal substrate. Both methods are effective for activating zirconium surfaces; yttrium has been activated by high-temperature anneals, (20) but grit blasting was ineffective for activating yttrium surfaces in one study. (21) However, cleaning the yttrium surface with a file resulted in rapid hydrogen absorption. (22)

b) Effect of Radioactivity on Yttrium Hydride

The tritium extraction system lies outside the direct radiation field (Fig. IV-C-1). However, radioactive species will be transported to the extraction system in the primary circuit. The metal in the extraction bed will be subjected to beta and gamma radiation, but not to neutrons. Radiation effects data reported in the literature for yttrium hydrides are for neutron exposures, but intense beta/gamma fields also would have accompanied the neutron fluxes.

Data from YH_2 irradiations indicate that the compound was stable in exposures of 7.5×10^{20} and 1.2×10^{21} n/cm^2 (neutron energy not reported). (17) Severe powdering of YH_2 took place at 2.1×10^{21} n/cm^2 . However, the corresponding gamma flux would likely have been $\sim 10^{11}$ to 10^{12} Rad. Radiation from circulating or deposited corrosion product will almost certainly not irradiate the metal extraction bed to that level over the length of a tritium extraction cycle. Yttrium tritide films stored at $\sim 22^\circ\text{C}$ were found to peel from their substrate after 4-5 years due to the accumulation of ^3He (25). Consequently, the yttrium will need to be replaced periodically because of helium embrittlement.

c) Yttrium Hydride Ignition Characteristics

Exposure of tritided yttrium to air is highly unlikely. However, if a massive break in the extraction system piping were to occur, air contact with tritided yttrium is conceivable. Massive yttrium hydride (YH_{2-x}) reportedly is stable in air to 750°C . (23)

5. Tritium Extraction Systems

Thus far, the discussion has been a general review of tritium extraction techniques. Now, tritium extraction systems will be proposed for the UWMAK-I design in which a secondary sodium system is utilized to cool the primary lithium system. A ferritic alloy, Croloy T22, is utilized for the Na-steam generator. Tritium extraction systems will be required for the following locations:

- the primary lithium system, which includes the lithium blanket (Figure IV-C-1);
- the secondary sodium system (Figure IV-C-1);
- the divertor lithium coolant (Section III-D)
- the helium circuit for cooling the shield (Figure IV-A-4);
- the divertor pumping system (Section III-D).

a) Primary Lithium System

From the foregoing discussion, an yttrium metal extraction bed is the proposed method of tritium removal from the lithium blanket. The average rate of tritium production is 1.05 kg/day at the maximum breeding ratio of 1.5. The corresponding rate of tritium concentration buildup in the lithium is 1.2 wt ppm/day.

The operating conditions will be based only on thermodynamic consideration, since kinetics and phase relationships are not known for the $\text{Y} - \text{T}_2 - \text{Li}$ system. The extraction temperature for the yttrium bed is chosen to be 283°C , which is the Li exit temperature from the intermediate heat exchanger. The tritium

pressure was calculated by extrapolating from the following expression for the Y - YH₂ equilibrium (17)

$$\log P_{H_2} \text{ (torr)} = 10.52 - \frac{11,869}{T}$$

where P is the tritium pressure and T is the absolute temperature.

At 283°C, the tritium pressure for the system Y-YT₂ is 1.48 x 10⁻¹¹ torr, which will also be the equilibrium pressure of tritium dissolved in the liquid lithium, as long as the yttrium is not saturated with YT₂. Based on the Sievert's Law relationship, page VIII-B-3, the mole fraction, N, of tritium in lithium can be calculated as follows:

$$P_{T_2}^{1/2} = K_s N$$

$$[1.48 \times 10^{-11} \text{ torr}]^{1/2} = [0.346 \text{ torr}^{1/2}/\text{atom fraction}]N$$

$$N = 1.11 \times 10^{-5} \text{ mole fraction } \sim 5 \text{ ppm (wt)}$$

It can be seen that this concentration is entirely satisfactory because it is only approximately one-third of the maximum proposed concentration determined by tritium diffusion considerations, page VIII-B-5.

The lithium inventory, composed of the amount in the reactor, plus an estimated amount in the intermediate heat exchanger, the pipes and extraction beds is approximately 1.73 x 10⁶ kg. The tritium inventory in the lithium will be

$$I_{B \text{ sat}} = N(m_{Li}) \frac{A_T}{A_{Li}} = 8.7 \text{ kg, where symbols are}$$

defined on page VIII-B-4.

While this constant level of tritium in the lithium appears to be satisfactory, it is necessary to know the concentration of T in Li as it comes from the blanket to be sure that LiT does not deposit in the heat exchanger since the lithium passes through the yttrium extractor bed after the heat exchanger. The concentrations, C, of T in Li upon exit from the blanket will be:

$$C = N + \Delta C,$$

where $\Delta C = \frac{\text{tritium generation}}{\text{lithium flow rate}}$

$$= \frac{1.05 \text{ kg/day}}{2.1 \times 10^7 \text{ kg/hr} \times 24 \text{ hr/day}} \frac{A_{Li}}{A_T}$$

$$\Delta C = 4.86 \times 10^{-9} \text{ mole fraction}$$

$$\text{and } N = 1.11 \times 10^{-5} \text{ mole fraction}$$

Therefore C \approx N.

The solubility of LiH in liquid Li is given by the relationship (6):

$$\log_{10} \frac{N_s}{1 + N_s} = 2.835 - 3381/T,$$

where N_s = mole fraction at saturation, and $T = 556^\circ\text{K}$; $N_s = 5.68 \times 10^{-4}$ mole fraction at 283°C . Because the tritium concentration, C , is only approximately 1/50 of the saturation concentration, there should be no danger of LiT precipitating in the heat exchanger.

The amount of yttrium required to absorb the tritium generated in one day (1.05 kg/day) and form the compound, $\text{YT}_{1.8}$, is calculated as follows:

$$\text{wt Y} = \frac{A_Y}{A_T} \frac{(1.05 \text{ kg T/day})}{1.8} = 17.3 \text{ kg/day}$$

An efficiency of 20% is typical (18) for such absorption beds so that the total bed should contain ~90 kg Y to absorb one day's generation of T. At a suggested cost of \$150/pound of yttrium fabricated as a foil 0.01 cm thick, the total cost for one bed would be $\$2.97 \times 10^4$. Because one bed would be regenerated while a second bed is on-steam, the total cost for yttrium would be ~\$60,000.

Furthermore, the flow of lithium through the bed, F_{Li} , can be estimated by the relationship

$$\Delta C = T_G / F_{\text{Li}}$$

where ΔC = the change in conc. of the T in the primary Li stream

F_{Li} = lithium flow rate

T_G = tritium generation rate.

If we permit ΔC to exceed 1% of the equilibrium tritium concentration and set the tritium absorption rate equal to the tritium generation rate (as was done in the calculations for the bed), then,

$$F_{\text{Li}} = \frac{A_{\text{Li}}}{A_T} [1.05 \text{ kg/day} \times \text{day}/24 \text{ hr}] / [1.11 \times 10^{-5} \text{ at fraction} \times 0.01]$$

$$F_{\text{Li}} \approx 9.2 \times 10^5 \text{ kg/hr.}$$

The total flow rate of lithium in the blanket is 2.1×10^7 kg/hr; therefore, only approximately 1/23 of the lithium flow need go

through a by-pass to the yttrium bed. Alternatively, if 1/10 of the Li flow were directed through the yttrium bed, an extraction efficiency of only 45% per transit would be required.

Extraction of the tritium from the yttrium would occur by thermal regeneration based upon the following sequence. The yttrium bed would be isolated from the lithium circuit and the bulk of the lithium drained from the bed. The temperature of the bed would be increased to 400°C and the remaining lithium distilled by vacuum distillation. At 400°C, good separation between the lithium and the tritium should be possible because the vapor pressure of Li is 9.3×10^{-5} torr while the tritium pressure over YT_{1.8} is only 7.7×10^{-8} torr. After the lithium has been removed, the temperature of the bed is increased to 500°C where the tritium pressure is 1.46×10^{-5} torr so that the tritium gas can be pumped by mechanical techniques into suitable storage containers. It may be necessary, however, to heat the yttrium to 700° for several hours in order to dissolve any surface oxide and reactivate the surface.

The use of the yttrium extraction bed appears to be very satisfactory based on thermodynamic consideration with the flow rate through the beds and the construction of the beds reasonable. Before the system could be operated, the proposed equilibria at the temperatures of interest need to be verified and the effects of impurities, oxygen, nitrogen and corrosion products upon the efficiency of the yttrium beds need to be determined.

b) Secondary Sodium System

The tritium concentration in the secondary sodium system will be a function of the tritium diffusion into the system from the primary lithium through the intermediate heat exchanger minus a function of the amount of tritium diffusion out of the sodium through the sodium-steam heat exchanger. At equilibrium, the value of tritium diffusing through the intermediate heat exchanger will be equal to the volume diffusing through the sodium-steam generator; consequently, the volume diffusion equations through each heat exchanger (page VIII-B-2) can be set equal to each other. When the terms are rearranged, the tritium pressure in the intermediate system, P_I , is given by the expression,

$$P_I^{1/2} = \frac{A_I \lambda_I}{X_I} P^{1/2} / \left[\frac{A_s \lambda_s}{X_s} + \frac{A_I \lambda_I}{X_I} \right]$$

where P_P = Pressure in primary system

$$P_P = 5.12 \times 10^{-10} \text{ torr @ } 383^\circ\text{C}$$

R = Gas Coolant

$$A_I = \text{Area of intermediate heat exchanger } (1.86 \times 10^8 \text{ cm}^2)$$

$$A_S = \text{Area of steam heat exchanger } (3.19 \times 10^8 \text{ cm}^2)$$

$$X_I = \text{Thickness of intermediate heat exchanger } (1.066 \text{ mm})$$

$$X_S = \text{Thickness of steam heat exchanger } (1.65 \text{ mm})$$

$$\lambda_I = \text{Permeability of intermediate heat exchanger } [\text{cc(STP)} \cdot \text{mm}/\text{cm}^2 \cdot \text{h} \cdot \text{atm}^{1/2}]$$

$$\lambda_S = \text{Permeability of steam heat exchanger } [\text{cc(STP)} \cdot \text{mm}/\text{cm}^2 \cdot \text{h} \cdot \text{atm}^{1/2}]$$

The numerical values given above correspond to the values given for the intermediate heat exchanger and the steam generator proposed in the volume 2 of this report⁽³⁾. In order to solve the above equation, the permeability, λ_S , of the steam generator tubing, Croloy T22, was determined from two reported experimental observations^(26,27). A least-squares fit of these data yielded the following relationship for hydrogen permeability

$$\log \lambda_S = 2.73 - 2.81 \times 10^3/T, \text{ which was}$$

evaluated at 296°C , the average temperature across the steam generator tubing. The hydrogen permeability of the 304 Stainless Steel tubing, λ_I , used in the lithium-sodium heat exchanger was determined from the relationship,

$$\log \lambda_I = 2.928 - 3.49 \times 10^3/T,$$

which was evaluated at 360°C , the average temperature of the tubes in this heat exchanger. The values of λ_S and λ_I were divided by $\sqrt{3}$ in order to compensate for the slower diffusion of tritium as compared with hydrogen.

Based upon the given parameters, the tritium pressure in the sodium system, P_I , is,

$$P_I = 3.82 \times 10^{-11} \text{ torr, or } 5.02 \times 10^{-4}$$

If it is assumed that all the tritium which enters the steam cycle is lost to the environment, then the volume of tritium which diffuses through the steam generator tubing depends only upon P_I in the following manner:

$$\text{Vol}(T_2) = 1.68 \times 10^7 \frac{\text{cc(STP)}}{\text{day} \cdot \text{atm}^{1/2}} [5.02 \times 10^{-4} \text{ atm}] = 3.77 \text{ cc/day} = 10.1 \text{ Ci/day}$$

These calculations show that without an additional tritium extraction system in the intermediate sodium system or any barrier coating on the two steel heat exchangers, the amount of tritium released to the steam cycle is a modest 10 Ci/day.

The amount of tritium dissolved in the sodium at the pressure P_I can be estimated based upon the measured values of the Sievert's constant⁽²⁸⁾, which is reported to increase from 4.70 to 5.03 ppm(wt) $\text{H}_2/\text{torr}^{1/2}$ from 375 to 500°C . The total quantity of sodium in the intermediate

heat exchanger, the steam generator and the connective piping is estimated to be approximately 7.62×10^5 kg. The tritium inventory in the sodium is, calculated to be:

$$N_{T_2} = \frac{3gT}{gH} \times 7.62 \times 10^5 \text{ kg(Na)} \left[\frac{4.7 \text{ ppm(wt)H}_2}{\text{torr}^{1/2}} \right] [3.82 \times 10^{-11} \text{ torr}]^{1/2}$$

$$N_{T_2} = 0.067 \text{ g}$$

The tritium inventory in the sodium appears to be very small, and very dilute. Extraction of additional tritium from the sodium by either cold trapping or a yttrium absorption bed is not practical, based upon the following reasons. The saturation concentration of tritium in the Na at 261°C , the coldest section of the Na system is 100 times greater than the actual concentration. Also, cooling the Na to 100°C presents no advantage because the saturation concentration is nearly 3 times the actual concentration; consequently, cold trapping the residual NaT is not possible. Also, the tritium pressure above the Na at 261°C (5.8×10^{-11} torr) is nearly the same as that of the Y-YT₂ equilibrium pressure (2.1×10^{-12} torr). Yttrium absorption beds are placed in the sodium system only as a precautionary measure, therefore, and would be activated only if the tritium leakage from the primary system becomes excessive. The yttrium required for these beds should be approximately one-half as much as for the primary system, 45 kg per bed, at a total of \$30,000 for the two beds.

c) The Divertor Lithium Coolant

Relatively large amounts of deuterium and tritium will accumulate in the lithium which cascades over the divertor plates, Section III-D. The rate of tritium diffusing from the plasma is 1.8×10^{22} T atoms/sec, which accumulates in the lithium at a rate of 7.12 kg/day based on the assumption of 96% efficiencies for both the divertor and trapping in the lithium. An equal amount of deuterium will also accumulate in the lithium. It would be desirable to recover the tritium and deuterium dissolved in the lithium as rapidly as possible for both efficient plant operation and to reduce the total tritium inventory.

The concentration of the hydrogen isotopes in the lithium, ΔC , upon exit from the divertor is equal to,

$$\Delta C = \frac{\text{rate of (D+T) accumulated}}{\text{rate of Li flow}}$$

$$= \frac{3.6 \times 10^{22} \text{ atoms/sec}}{480 \text{ kg/sec}} \times \frac{\text{at. wt. Li}}{6.02 \times 10^{23}}$$

$$\Delta C = 8.72 \times 10^{-7} \text{ mole fraction (D+T).}$$

The solubility of hydrogen isotopes in Li at 200°C is 4.9×10^{-5} mole fraction (as determined from Reference 6). If the hydrogen isotopes are not removed from the lithium, then after ~60 cycles through the divertor, the lithium would be saturated and Li(D+T) would begin to precipitate at 200°C in the cold-end of the heat exchanger. In order to avoid this possibility, a cold trap operating below 200°C but above the Li melting point (181°C) would have to be installed ahead of the heat exchanger. This cold trap would have to operate within a limited range of $\pm 9^\circ\text{C}$, which may be very difficult to achieve in a large system; therefore, the cold trapping technique was discarded as being impractical.

An yttrium absorption bed similar to the one utilized for the lithium blanket is proposed for operation in the lithium divertor system. This absorption bed is placed at the cold end of the heat exchanger to operate at 200°C. However, the diffusion of tritium in the yttrium may be too slow at this low temperature. Additional experiments are needed to clarify this point. In accordance with the previous calculations, the pressure of (D+T) at the Y-YH₂ plateau is 2.67×10^{-15} torr which is also the pressure of (D+T) in the lithium. Ignoring slight isotope effects, one can calculate the mole fraction, N, of hydrogen isotopes in the Li based upon the Sievert's constant for tritium as follows,

$$P^{1/2} = K_s N$$

$$[2.67 \times 10^{-15} \text{ torr}]^{1/2} = [0.0449 \text{ torr}^{1/2} / \text{mole fraction}] N$$

$N = 1.15 \times 10^{-6}$ mole fraction (D+T) in Li, or approximately 0.24 ppm(wt) tritium.

The total concentration of (D+T) upon exit from the divertor is as follows.

$$C = N + \Delta C$$

$$= [1.15 \times 10^{-6} \text{ mole fraction}] + [0.87 \times 10^{-6} \text{ mole fraction}]$$

$$C = 2.02 \times 10^{-6} \text{ mole fraction.}$$

Because the solubility of LiH in Li is 4.9×10^{-5} mole fraction at 200°C, the value of C is 1/25 of the saturation value so that precipitation should be avoided even though the temperature may fluctuate slightly or the equilibria may shift because of isotopic effects.

The amount of yttrium required to absorb all the accumulated Y(D+T)_{1.8} is calculated to be

$$\text{wt Y} = \frac{\text{at. wt. Y}}{1.8} [\text{moles(D+T)/day}]$$

$$\text{wt} = 2.81 \times 10^2 \text{ kg.}$$

With an assumed efficiency of 20%, the total yttrium required is 1400 kg at an estimated cost of $\$4.6 \times 10^5$. It would probably be advisable to divide the yttrium into four beds with each bed on stream only six hours so that the (D+T) could be returned rapidly for fueling. In such a case, the total tritium on the beds would be only one-half a day's accumulation, ~3.5 kg.

The fraction of the total flow which must pass through the yttrium bed on each cycle is larger for the divertor current than for the blanket system because the accumulation of D+T is much greater than in the divertor. If the residual concentration of D+T is permitted to rise to approximately 5×10^{-6} mole fraction (1/10 of the saturation limit), then the Li flow rate through the bed is a reasonable 22% of the flow rate in the main circuit.

Although the heat removal system for cooling the lithium in the divertor has not been designed, the use of an intermediate sodium system which transfers heat to a steam generator appears reasonable, similar to the system used to remove heat from the lithium blanket. The total lithium flow rate through the divertor system, 480 kg/sec, is approximately the same flow rate as through one module of the lithium blanket; therefore, the divertor cooling system was sized to correspond to one module of the lithium blanket and the same materials were assumed to be present. Based on these assumptions, several characteristics of the tritium in the divertor system can be assessed.

The total lithium inventory in the divertor system is estimated to be 3.4×10^4 kg. The tritium inventory in the lithium will be, therefore,

$$I_B = [0.24 \text{ ppm(wt)T}][3.4 \times 10^4 \text{ kg}] = 8.2 \text{ g.}$$

The tritium inventory in the sodium will be approximately 1/12 of the inventory in the blanket system, of 0.006 g., consequently, the tritium inventory in the Li and Na of the divertor system is small.

The tritium leakage into the steam generator can be calculated, also, in a similar manner as was utilized for the main blanket system. For the divertor system, the average temperatures are low, 263°C, for the Li-to-Na intermediate heat exchanger and 226°C for the steam generator. Consequently, because of the low temperatures, the tritium leakage into the steam is only 2×10^{-4} Ci/day. This steam is used in turn to heat the feed water in the first boiler of the power plant.

In summary, tritium management in the divertor system is shown not to be a problem, if the yttrium extraction beds function as proposed.

d) Helium Circuit

The shield which contains B_{10} as a neutron absorber will accumulate tritium by neutron reactions with boron at the rate of approximately

1.1×10^{-3} g/day. Some of this tritium will diffuse into the helium which is used to cool the shield. The temperatures in the shield are low, 200°C at Zone 13 and less than 100°C for Zones 16 and 19. Consequently, the diffusion rate of tritium into the helium will be very small initially. For instance in Zone 13 at 150°C , nearly six years are required for the permeability of tritium to attain an equilibrium value through a one cm thick stainless steel barrier between the B_4C and the helium coolant. After an initial time lag of several years, therefore, the diffusion of tritium will be in equilibrium with the generation rate so that a maximum of 10^{-3} g/day or 10 Ci/day will be introduced into the helium coolant. Because this is a closed helium system, this tritium is not lost. Eventually it may be necessary to design a tritium extraction system to remove the tritium from this helium system.

e) Divertor Vacuum Pumps

It is estimated that approximately four percent of the deuterium and tritium and all of the helium will by-pass the divertor lithium collector system and be swept into the pumping system. These hydrogen isotopes in the vacuum system will accumulate at the rate of 0.3 kg/day of tritium and 0.2 kg/day of deuterium. These hydrogen isotopes and the helium will be collected on cryogenically-cooled charcoal traps. Users of these traps have reported⁽²⁹⁾ that the helium can be purified to a residual limit of 10^{-11} mole fraction tritium. On this basis, the approximately 200 moles of helium generated per day would contain less than 1.2×10^{-4} Ci/day of tritium and would be discharged.

Table VIII-C-1 summarizes the characteristics of the five tritium extraction systems.

Table VIII-C-1

Summary of Tritium Extraction System Characteristics^(a)

<u>Coolant System</u>	<u>Temp. Range °C</u>	<u>Extraction Method</u>	<u>Tritium Accumulation Per Day (kg)</u>	<u>Tritium Leakage Ci/day</u>	<u>Total Na or Li (kg)</u>	<u>Tritium Concentration in Li or Na ppm (wt.)</u>	<u>Tritium Inventory (kg)</u>
Primary Lithium	283-483	Yttrium Metal Bed	1.05(b)	10.1	1.73×10^6	5	in Li 8.7 in beds 1.0
Secondary Sodium	261-411	Yttrium Metal Bed	~0		7.6×10^5	8.7×10^{-5}	in Na 6.7×10^{-5} in beds ~0
Divertor Lithium Sodium	200-325 190-265	Yttrium Metal Bed	7.4 T + 5.0 D	2×10^{-4}	3.4×10^4 6×10^4	0.24 3×10^{-4}	in Li 8×10^{-3} in beds 3.5 in Na 6×10^{-6}
Divertor vacuum	25	Charcoal-cooled with liq. He	0.3 T + 0.2 D	1×10^{-4}		Not applicable	0.3
Helium	50-200	Metal getter	1.1×10^{-6}	low		Not applicable	low
			Total	10.1		Total	13.5

(a) Based upon thermodynamic calculations; no kinetic considerations

(b) At maximum breeding ratio of 1.49

REFERENCES

1. R. W. Webb, Permeation of Hydrogen Through Metals, NAA-SR-10462, July 1965.
2. Barnwell Nuclear Fuel Plant-Safety Analysis Report, USAEC Docket 50332-1.
3. D. Schluderberg, Babcock and Wilcox, Private Communication.
4. A. P. Fraas, "Comparison of Two Tritium Removal Systems Designed to Minimize Contamination of Steam Systems in Full-Scale Thermonuclear Power Plants," ORNL-TM-2932, May 1970.
5. H. C. Savage and R. A. Strehlow. "Hydrogen Permeation Through Metals", Molten Salt Reactor Program Semi-annual Progress Report for the period ending August 31, 1972, March, 1973, p. 39-42.
6. V. A. Maroni, E. J. Cairns, and F. A. Cafasso, "A Review of the Chemical, Physical and Thermal Properties of Lithium that are Related to the Use in Fusion Reactors", ANL-8001, March 1973.
7. W. F. Vogelsang, "Breeding Ratio, Inventory, and Doubling Time in a D-T Fusion Reactor," Nuclear Technology 15, 470, 1972.
8. J. B. Vetrano, "Hydrides as Neutron Moderator and Reflector Materials", Nuc. Eng. and Design, 14, 390, 1970.
9. W. Spalthoff and H. Wilhelm, "The Use of Hydrogen Getters for Prevention of Hydrogen Embrittlement in Zirconium-Alloy Fuel Cans" Applications-Related Phenomena in Zirconium and Its Alloys, STP-458, p. 338ff, 1968.
10. W. M. Mueller, J. P. Blackledge, and G. G. Libowitz, Metal Hydrides, Academic Press, New York, 1968, p. 7-8.
11. E. J. Cairns, F. A. Cafasso and V. A. Maroni, "A Review of the Chemical, Physical and Thermal Properties of Lithium that are Related to its Use in Fusion Reactors", The Chemistry of Fusion, D. M. Gruen, Ed., Plenum Press, New York, 1972, p. 91ff.

12. C. R. Cupp and P. Flubacher, "An Autoradiographic Technique for the Study of Tritium in Metals and its Application to Diffusion in Zirconium at 149 to 240°C", J. Nucl. Mat., 6, 213, 1962.
13. J. S. Watson, An Evaluation of Methods for Recovering Tritium from the Blanket or Cooling Systems of Fusion Reactors, ORNL-TM-3794, July, 1972.
14. J. S. Watson and R. C. Forrester, III, "Tritium Handling in Fusion Reactors", presented at the 75th National AICHE Meeting, Detroit, MI, June, 1973.
15. V. A. Maroni and E. Veleckis, "Chemical Processing of Lithium for Fusion Reactors", presented at the 75th National AICHE Meeting, Detroit, MI, June, 1973.
16. R. W. Webb, Permeation of Hydrogen Through Metals, NAA-SR-10462, July, 1965.
17. W. M. Mueller, et al., loc. cit., pp. 441-484; p. 743.
18. J. W. Mausteller, F. Lepper and S. J. Rodgers, Alkali Metal Handling and System Operating Techniques, Gordon and Breach, New York, 1967, pp. 61-63.
19. W. M. Phillips, "Some Alkali Metal Corrosion Effects in a Rankine Test Loop", Corrosion by Liquid Metals, J. E. Draley and J. R. Weeks, Eds., Plenum Press, 1970, p. 206.
20. L. N. Yannopoulos, R. K. Edwards and P. G. Wahlbeck, "The Thermodynamics of the Yttrium-Hydrogen System", J. Phys. Chem. 69, 2510-15, 1965.
21. W. M. Mueller, et al., loc. cit., p. 677.
22. C. E. Lundin and J. P. Blackledge, "Pressure-Temperature Composition Relationships of the Yttrium-Hydrogen System", J. Electrochem. Soc., 109, 838, 1962.
23. W. M. Mueller, et al., loc. cit., p. 125.
24. R. H. Wiswall and J. J. Reilly, Inorganic Chem., 11, 1691 (1972)
25. L. C. Beavis and C. J. Miglionico, "Structural Behavior of Metal Tritide Films", J. Less-Common Metals, 27, 201, 1972.
26. H. C. Savage and R. A. Strehlow, "Hydrogen Permeation Through Clean and Oxide Coated Metals at Low Pressures", Trans. Am. Nucl. Soc., 17, 152 (1973).
27. E. L. Compere, B. Fleischer, W. R. Huntley, R. E. MacPherson, H. C. Savage and A. Taboada, SNAP-8 Corrosion Program Summary Report, ORNL-3898 (Dec. 1965).

28. D. R. Vissers, J. T. Holmes, L. G. Bartholme and P. A. Nelson, "A Hydrogen-Activity Meter for Liquid Sodium and Its Application to Hydrogen Solubility Measurements," Nuclear Technology, 21, 235 (1974).
29. T. B. Rhinehammer and P. H. Lamberger, Tritium Control Technology, WASH-1269, p. 227 (Jan. 1974).

IX. Safety

A. Magnet Failure

Safety considerations involve two general problems. First low temperature helium can warm up with a large increase in pressure or volume. Every effort must be made to anticipate pressure rises by using blow out panels so that helium can be safely dumped from all parts of the equipment. An evacuated room with helium recovery equipment will be included.

The second magnet safety problem involves the disposition of electromagnetic stored energy if one or more magnets ceases to be superconducting. For example, if one out of 12 sections loses current the mutual coupling with the other 11 sections should be sufficient to transfer the magnetic flux almost instantaneously. The mechanical loads which arise when one magnet loses power must be carried by passive braces between magnet sections. In order to reduce heat loss, the bumpers should be almost, but not quite, in contact with the low temperature magnet frames as is discussed in the magnet design section. This force which would tend to contract the perimeter of the toroid is about the same magnitude as the central force on each "D" section.

If high voltages arise, they could cause arcs which could melt out sections of the magnet assembly. This is a difficult problem that has been met by extensive use of shunts and solid state diodes so that high voltages are restricted. For smaller scale disturbances, shunts and diodes could switch current out from a hot disc until it cools down. Once cooled, the disc can resume carrying its fraction of the load.

Another aspect of the magnet safety problem involves personnel interaction. Electrical hazards are largely removed by interlocking all power sources with doors and other access entries. External surfaces should be grounded and connected to the ground side of the magnet system. High voltage terminals should be electrically shielded and kept evacuated to avoid arcs. Helium gas pressure relief systems should discharge harmlessly into a helium recovery container. Extensive failure modes must be studied; for example, if an unusual coincidence of short circuits to the stainless steel frame could cause a reversal of forces on conductors what is the likely consequence and the best protection scheme? Finally, an energy removal scheme for rapid shut-down of the magnet system must be designed. We expect to use something like the NAL bubble chamber water-cooled dump resistor which removes energy at the simple L/R rate.

B. Radioactivity.

It has been fashionable in the past to advertise fusion reactors as the ultimate, "clean" source of energy for society. Such a statement is certainly true with respect to chemical pollutants but it should be obvious that any power source which emits neutrons must generate large amounts of radioisotopes. The generation of these isotopes is not a serious problem if they

- 1) can be contained
- 2) have short half lives
- 3) are not particularly harmful to man

We will explore in this section the generation of radioisotopes in 316SS and how they might decay away. We will also investigate how much radioactivity might be contained in solution with the coolant. Finally, we will make similar observations on two alternate CTR materials Nb-1Zr and V-20Ti.

1. Radioactivity build-up in a SS blanket (a) Method of calculation

The radioactivity of the blanket has been calculated for the configuration described in Section V-F. For the purposes of the calculation the blanket was divided into 11 regions: (see Figure IX-B-1) one region for the first wall, five regions of 95% Li plus 5% SS, two regions in the 15 cm SS wall, one region of lithium plus SS, and two small SS regions. The fluxes used were the 46 group fluxes from Section V suitably normalized to 5000 Mw_{th} . Whenever possible ENDF III cross sections as averaged by the MACK code ⁽¹⁾ were used. For those isotopes or reactions not on ENDF tapes the cross sections were estimated from BNL 325 and the Nuclear Data Tables ⁽²⁾. This was especially necessary for the many isotopes in SS. For the niobium calculation described subsequently, the cross sections were taken from the suggestions of Steiner ⁽³⁾. In addition to the principal isotopes in SS, i.e. those of iron, nickel and chromium, isotopes of silicon and manganese were considered. Other possible minor constituents such as Mo, P, S, C were not considered either because of their small contribution or because of the lack of data. In calculating the concentration of the radioactive products, neutron absorption by the radioactive products was not considered in general, i.e. no double capture events were considered. This was done because of the relatively low flux in this design but more importantly because of the complexity of the isotope chains in SS and the lack of cross section data for these radioactive nuclei.

The radioactivity results are expressed in total curies regardless of the breakdown between various isotopes. Table IX-B-1 shows the isotopes and reactions considered in the calculations for 316 SS.

(b) Time Dependence of Radioisotope Generation

The radioactivity of the blanket as a function of time of operation is shown in Figure IX-B-2. The most obvious point is that the radioactivity increases quite rapidly after start up reaching 10^9 curies within two hours at full power and reaching 4×10^9 curies after two years. If the blanket were to run at full power for 40 years the activity in the 316 SS would approach 6×10^9 curies. The specific activity after 10 years of operation is one megacurie per megawatt (thermal).

(c) Time Dependence of Radioisotope Decay

The manner in which the radioactivity dies away after the plant is shut down is of considerable interest. Figure IX-B-3 shows the radioactivity as a function of time after shutdown in terms of megacuries per megawatt of operating power for a two and a ten year operating time. The predominant feature is the relatively slow decay with time. For example, after a 10 year operating time, at least two years are required before the activity from the first wall alone decays to 500 megacuries. The first wall initially contributes about 30% of the activity and maintains this fraction as the activity decays away. The activity of a wall operated for 2 years is 80% of a wall operated for 10 years, so that in replacing the wall every two years (Section IV-E) almost as much radioactivity is encountered as would be the case for a ten year first wall time.

It is noted that after shutdown the two curves are initially parallel, corresponding to the decay of the shorter lived isotopes. After about two hours, the curves start to diverge slowly with the activity from the two year operation dropping off faster as would be expected. Even after twenty years, the two-year wall still has more than 1/5 the activity of the 10 year wall.

Considering the first wall after ten years of operation, it is of some interest to consider the sources of the radioactivity. Figure IX-B-4 shows the fraction of the total radioactivity from the more abundant isotopes. At shutdown ($t=0$), the major contributor is Fe-55 which remains the major isotope

Table IX-B-1Reactions Considered in Stainless Steel

Si ²⁸	(n,p), (n,α)
Si ²⁹	(n,p), (n,α)
Si ³⁰	(n,α), (n,p), (n,γ)
Cr ⁵⁰	(n,np), (n,2n), (n,γ), (n,p)
Cr ⁵²	(n,p), (n,2n), (n,γ)
Cr ⁵³	(n,np), (n,p), (n,γ)
Mn ⁵⁵	(n,α), (n,p), (n,2n), (n,nα), (n,γ)
Fe ⁵⁴	(n,α), (n,p), (n,2n), (n,np), (n,γ)
Fe ⁵⁶	(n,α), (n,np), (n,p), (n,2n), (n,γ)
Fe ⁵⁷	(n,p), (n,np), (n,γ)
Fe ⁵⁸	(n,α), (n,p), (n,γ)
Ni ⁵⁸	(n,nα), (n,α), (n,np), (n,p), (n,2n)
Ni ⁶⁰	(n,α), (n,p), (n,np)
Ni ⁶¹	(n,α), (n,np), (n,p)
Ni ⁶²	(n,α), (n,np), (n,p)
Ni ⁶⁴	(n,np), (n,p), (n,γ)

FIG. IX-B-2
Radioactivity at Shutdown
as a Function of Operating Time
for UWMAK-I
316 Stainless Steel Blanket

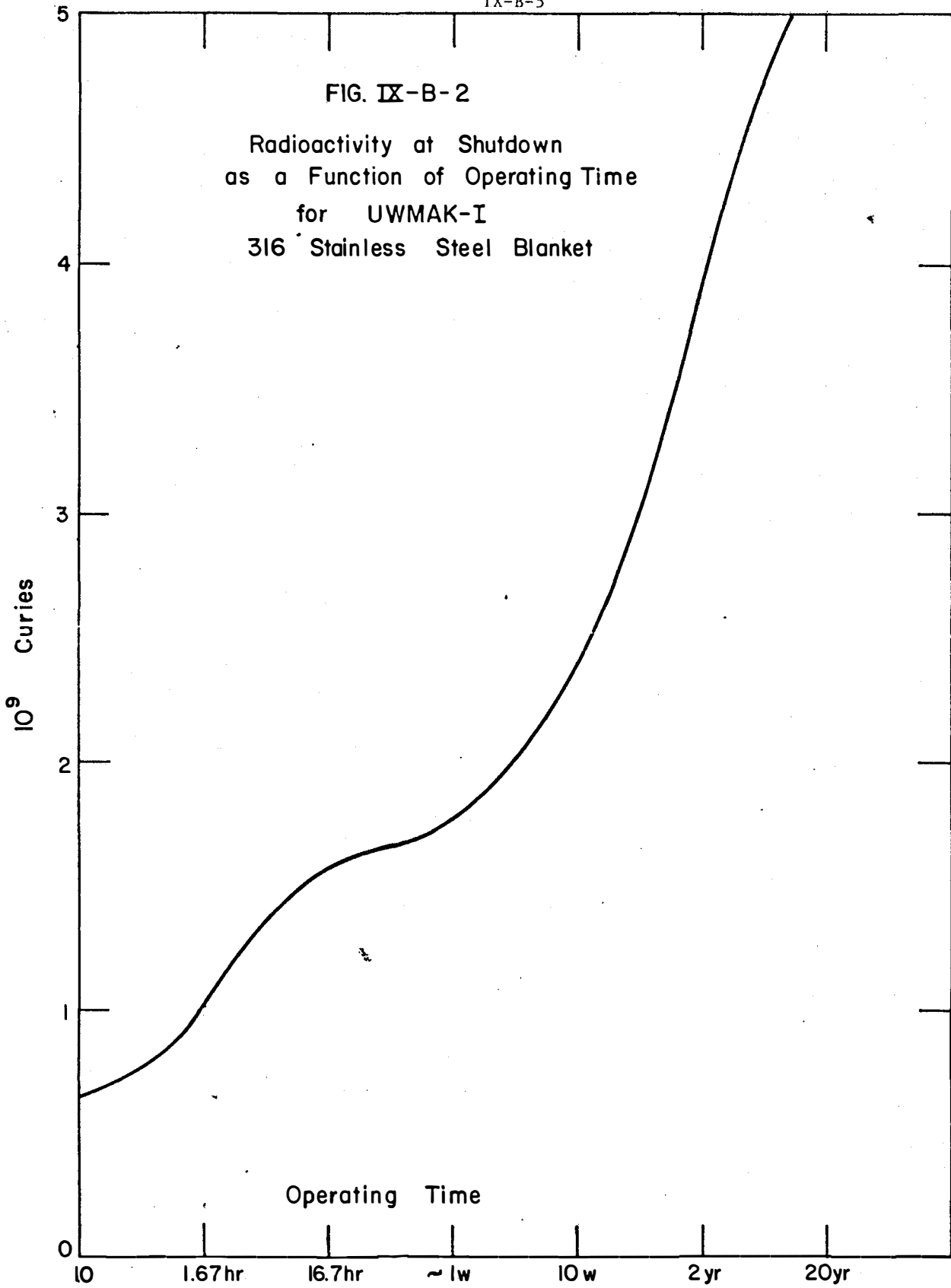


FIG. IX-B-3

UWMAK-I

316 Stainless Steel Blanket Radioactivity
after 2 and 10 Years Operating Time

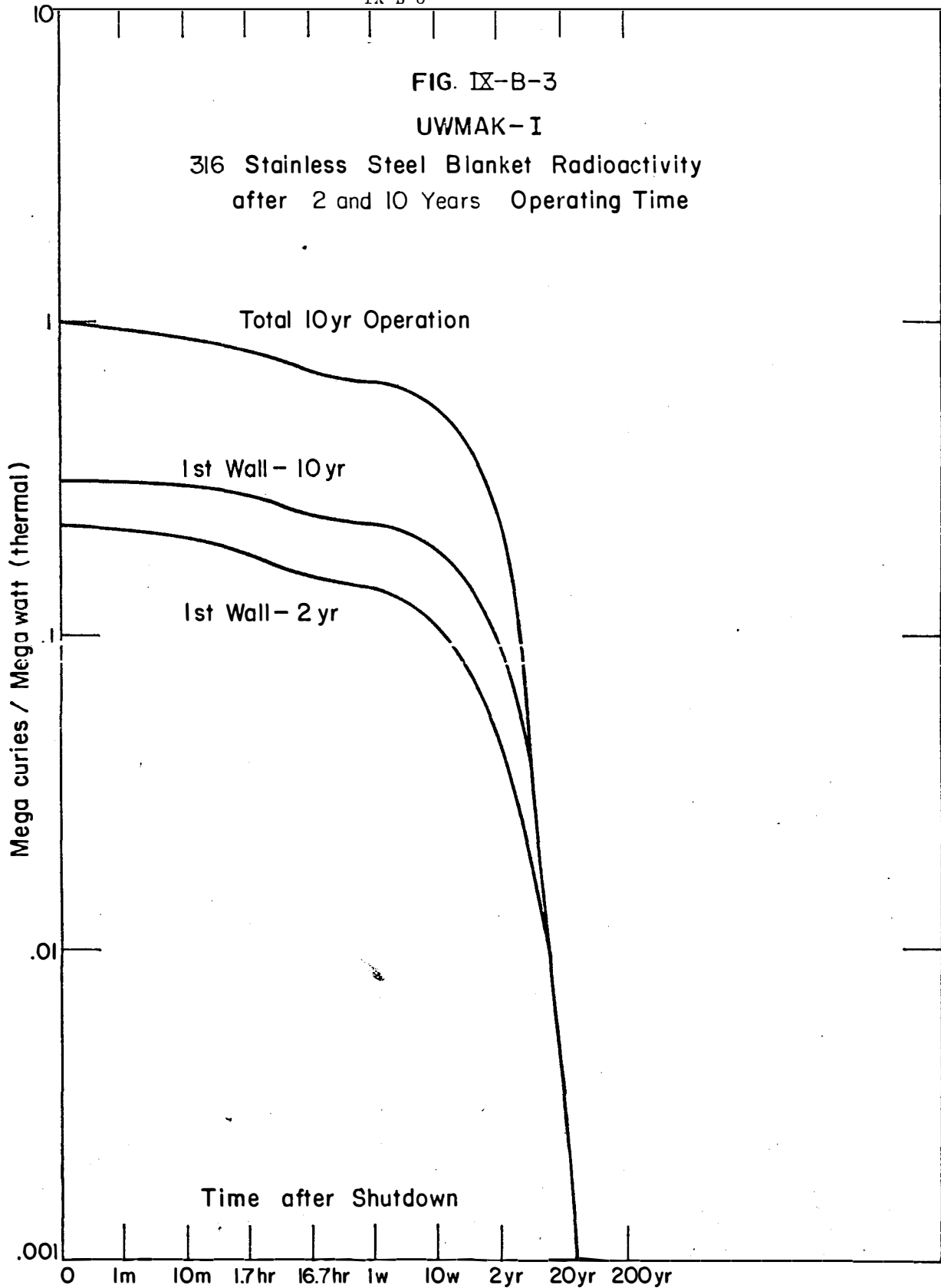
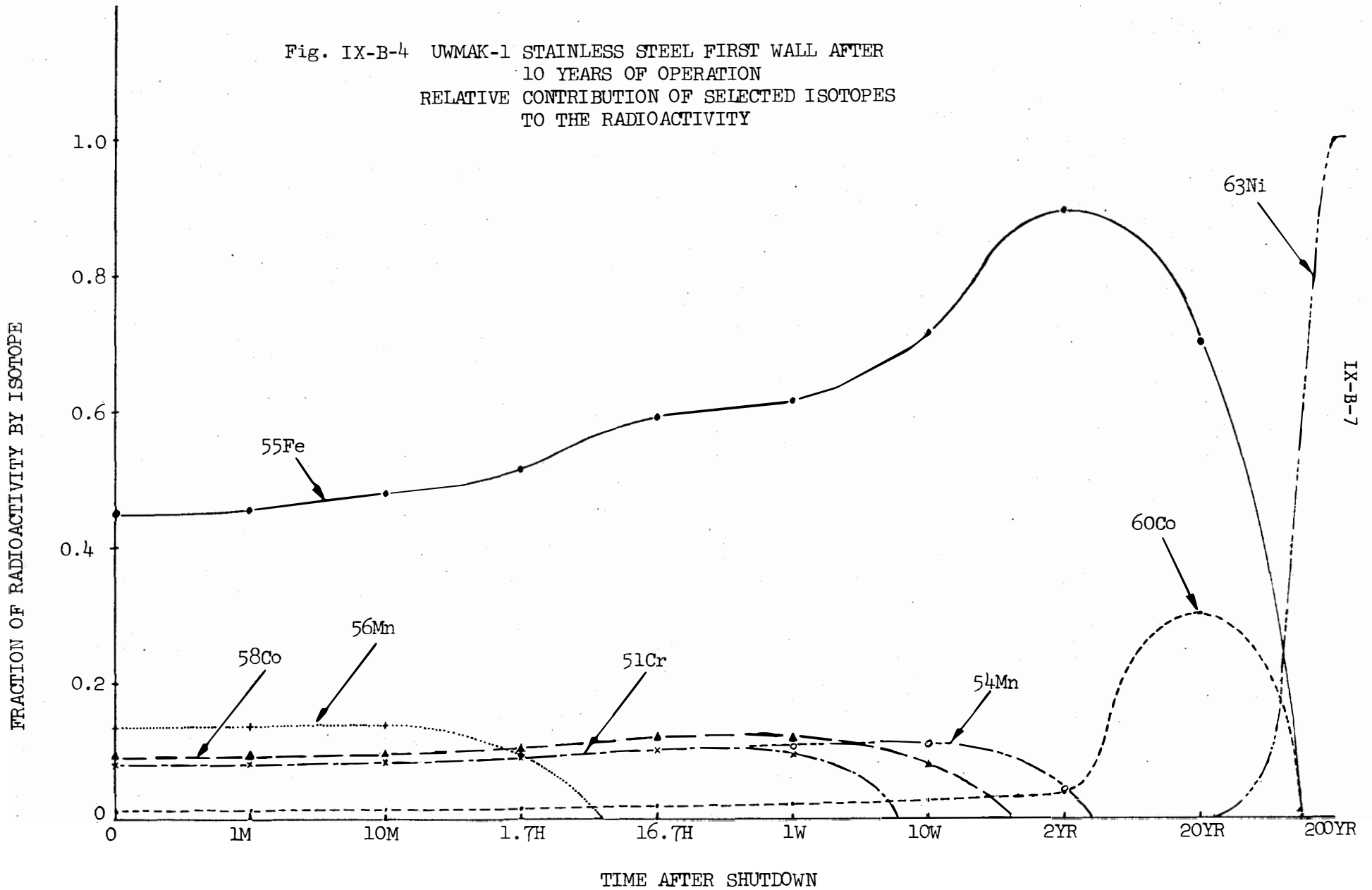


Fig. IX-B-4 UWMK-1 STAINLESS STEEL FIRST WALL AFTER
 10 YEARS OF OPERATION
 RELATIVE CONTRIBUTION OF SELECTED ISOTOPES
 TO THE RADIOACTIVITY



IX-B-7

for the first 40 years or so. As time progresses, the longer lived isotopes become relatively more important. For example, Co^{60} is initially a negligible fraction of the total activity but at 20 years after shutdown it contributes about 30% of the disintegrations. The dominant long lived activity is Ni^{63} with a half life of 97 $\frac{1}{2}$ years. Two hundred years after shutdown the activity from Ni^{63} in the 316 SS first wall is 348 curies corresponding to a density of only 0.031 millicuries/cm³ of blanket material.

(d) Nature of Activity

Following Steiner⁽³⁾ the "Biological Hazard Potential" (BHP) has been calculated at the time of shutdown for the first wall. This quantity which is the activity in curies/kwth divided by maximum permissible concentration (MPC) for general public exposure in curies/km³ of air as taken from 10CFR20 Appendix B, Table II, Column 2. The BHP is equivalent to the volume of air required to dilute the activity per thermal kilowatt to MPC. It provides a very convenient way of making relative comparisons between systems. Table IX-B-2 presents along with the specific activity of the various isotopes, the "Biological-Hazards Potential" for the first wall. To put these values in perspective, the values from an "Advanced Fission Reactor" as taken from reference 3 are also shown in Table IV-B-2. The values confirm that a fusion system may require the same degree of radiation protection as in a fission system in the short time after an as yet undefined catastrophic accident.

It is interesting to note that over 80% of the activity in 316SS comes from five isotopes; Fe-55, Mn-56, Co-58, Cr-51 and Mn-54. The activity of these isotopes is ~4 times that of the I and Pu in fission fuel used to generate the same power but that is not always the first measure of radioactivity hazard. The BHP of these isotopes is 0.01 to 1% of the BHP associated with I and Pu isotopes in the fission fuel. This fraction gets even smaller when one examines the situation 10-100 years after the generation of the radioisotopes. Therefore, it is concluded that the radioactivity in UWMMAK-I represents from 1/100 to 1/10,000 the radioactivity hazard associated with equivalent sized fission plants.

Table IX-B-2

First Wall Radioactive Inventory

at Shutdown after 10 Years of Operation

Isotope	Specific Activity (dps/cm ³)	Activity at t=0 Ci/kw _{th}	"Biological Hazard Potential" km ³ of air/kw _{th}
Mg-27	2.5 x 10(8)	1.5 x 10(-2)	5.1 x 10(-4)
Al-28	5.4 x 10(10)	3.3	0.11
Al-28	8.3 x 10(8)	5.1 x 10(-2)	1.7 x 10(-3)
Al-30	9.8 x 10(8)	6.0 x 10(-2)	2 x 10(-3)
Si-31	5.9 x 10(6)	3.6 x 10(-4)	1.2 x 10(-5)
V-49	1.1 x 10(10)	0.67	6.7
V-52	1.8 x 10(11)	11.	0.37
V-53	7.3 x 10(9)	0.44	1.5 x 10(-2)
Cr-49	9.0 x 10(8)	5.5 x 10(-2)	1.8 x 10(-3)
Cr-51	4.2 x 10(11)	26	0.32
Cr-55	2.3 x 10(10)	1.4	4.7 x 10(-2)
Mn-54	4.0 x 10(11)	24.	24
Mn-56	6.9 x 10(11)	42	2.1
Mn-57	6.6 x 10(9)	0.40	1.3 x 10(-2)
Mn-58	6.9 x 10(8)	4.2 x 10(-2)	1.4 x 10(-3)
Fe-53	3.3 x 10(9)	0.20	6.7 x 10(-3)
Fe-55	2.3 x 10(12)	140	4.6
Fe-59	8.2 x 10(8)	5.0 x 10(-2)	2.5 x 10(-2)
Co-57	1.7 x 10(11)	10.	1.7
Co-58m	2.0 x 10(11)	12	4 x 10(-3)
Co-58	4.7 x 10(11)	29	14.5
Co-60m	7.2 x 10(10)	4.4	0.15
Co-60	7.7 x 10(10)	4.7	15.6
Co-61	1.3 x 10(9)	8.0 x 10(-2)	2.7 x 10(-3)
Co-62	1.0 x 10(9)	6.0 x (-2)	2 x 10(-3)
Co-63	6.7 x 10(7)	4.0 x 10(-3)	1.3 x 10(-4)
Co-64	5.5 x 10(7)	3.4 x 10(-3)	1.1 x 10(-4)
Ni-57	1.8 x 10(10)	1.1	11
Ni-63	4.8 x 10(6)	2.9 x 10(-4)	1.5 x 10(-4)
Ni-65	8.9 x 10(7)	5.4 x 10(-3)	4.4 x 10(-2)
Total	<u>~5 X 10(12)</u>	<u>~310</u>	<u>~80</u>

Advanced Fission Reactor (ref. 7)

I-131	31.6	330
I-131 (milk pathway)	31.6	230,000
Pu-239	0.06	1000
Total plutonium Isotopes	18.2	8,300

IX.

B.

2) Radioactivity of Alternate Blanket Structure.

The radioactivity of the blanket was recalculated for two possible alternate choices of blanket structure; Nb-1% Zr and V-20% Ti. In both cases a one to one volume substitution was made for the SS in the first wall and for the 50 cm region immediately adjacent to the first wall (see Fig. IX-B-1). The remaining regions of what was defined as blanket, i.e. about 20 cm of 316SS and lithium was left unaltered. The neutron spectrum used was that of the stainless steel blanket. Past experience has shown that this is unlikely to affect the results more than a few percent. Table IX-B-3 shows the reactions considered in both alloys.

Figure IX-B-5 compares the radioactivity at shutdown as a function of operating time for the niobium and vanadium systems with that of the stainless steel system discussed earlier. Qualitatively, there are similarities in the results for all three materials i.e. a rapid initial rise followed by a much slower increase. The activities are of the same order of magnitude however there are some striking quantitative differences. The activity of the Nb-1Zr systems is significantly larger than that of either the V-20Ti and the 316SS system operated for similar times. This ratio is as high as a factor of four for operating times of a week or so. On the other hand, the activity of the V-20Ti system while initially slightly larger than that of the SS system remains relatively constant after the first week or so, and for twenty years of operation is less than one half that of 316SS. These features stem from the activities of long lived isotopes. In the V-20Ti system, for example, there are no long lived isotopes and the only long lived isotopes are those produced in the large SS region which is exposed to a relatively low neutron flux.

The radioactivity after shutdown for the alternate materials is shown in Fig. IX-B-6. The radioactivity of the 316SS blanket is also shown for comparison.

Table IX-B-3Isotopes and Reactions Considered in Nb-Zr Alloy

Zr ⁹⁰	(n,p), (n,2n), (n,γ)
Zr ⁹¹	(n,p), (n,γ)
Zr ⁹²	(n,α)
Zr ⁹⁴	(n,α), (n,p), (n,γ)
Nb ⁹³	(n,2n), (n,p), (n,α), (n,n), (n,γ)
Nb ⁹⁴	(n,γ)

Isotopes and Reactions Considered in V-20Ti Alloy

V ⁵⁰	(n,α), (n,α) (n,2n), (n,p)
V ⁵¹	(n,α), (n,p), (n,γ), (n,2n)
Ti ⁴⁶	(n,p), (n,2n)
Ti ⁴⁷	(n,p), (n,np)
Ti ⁴⁸	(n,p), (n,), (n,np)
Ti ⁴⁹	(n,p), (n,np)
Ti ⁵⁰	(n,p), (n,γ)

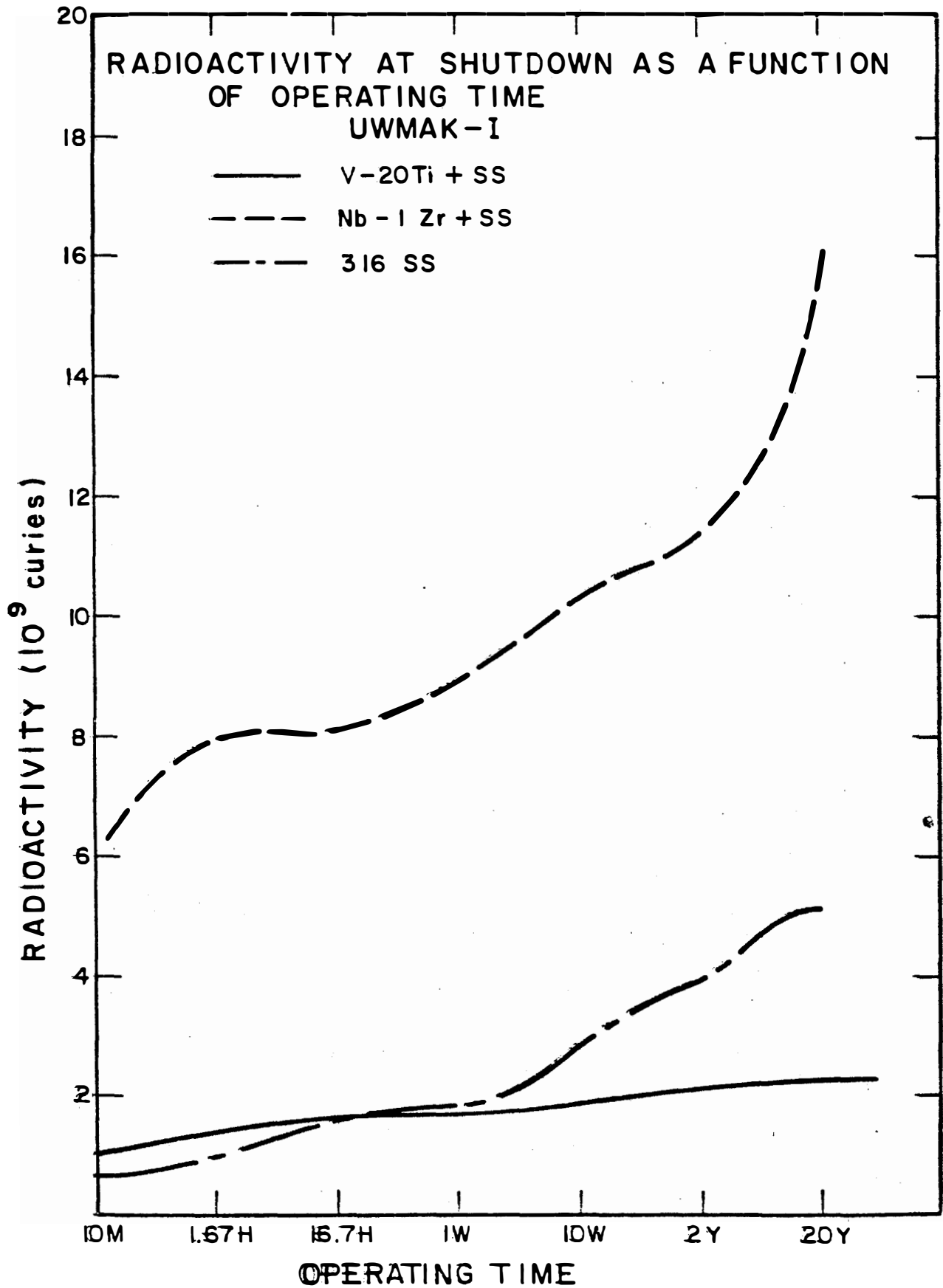


FIGURE IX-B-5

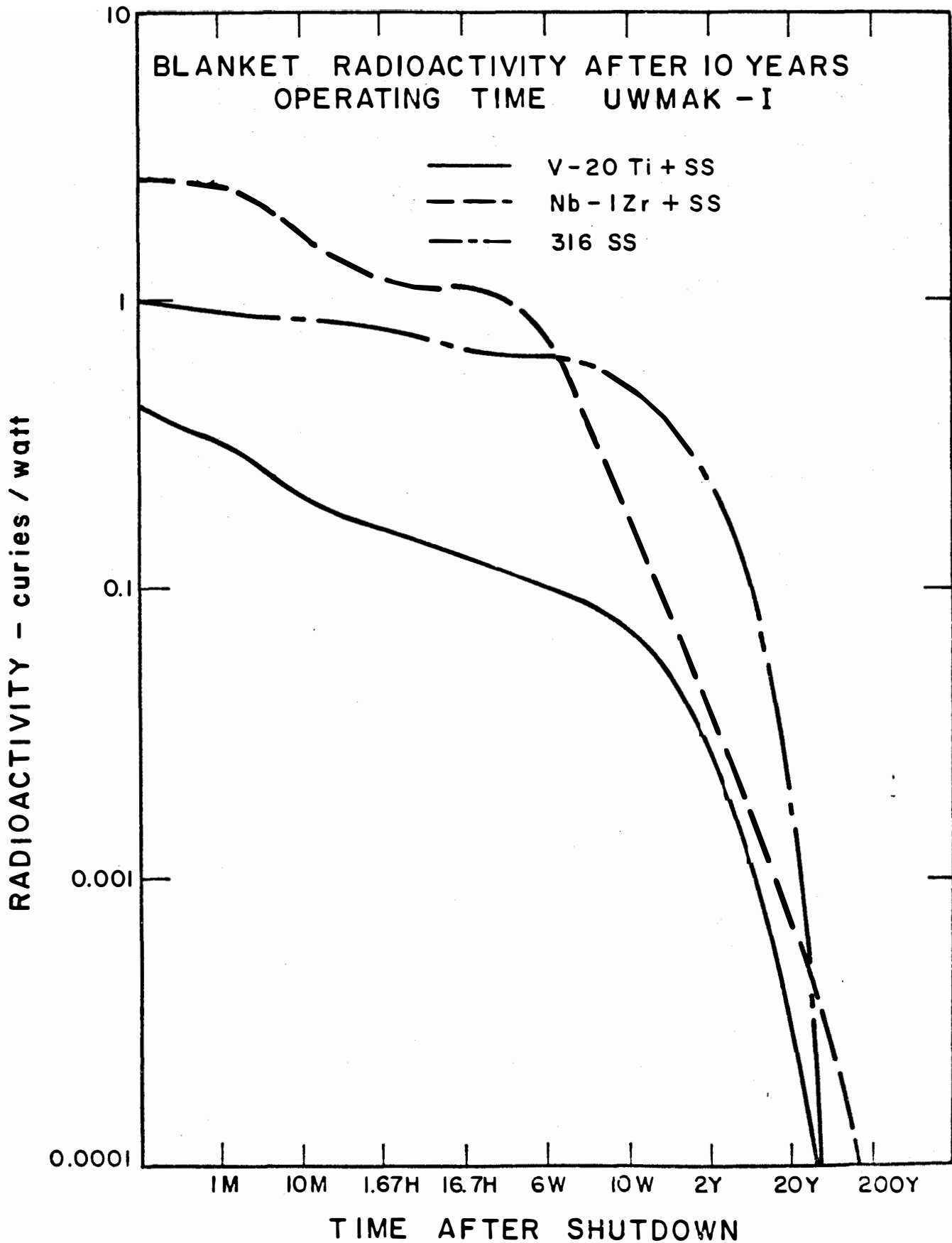


FIGURE IX-B-6

It is seen that the activity from the Nb-Zr system is initially a factor of 2.5 higher than the 316SS system. However the niobium decays rapidly enough that after 1-2 weeks the activity is below that of SS, dropping by a factor of 10 in about 10 weeks. At long times (~20 years) only the activity of Nb⁹⁴ ($t_{1/2} \approx 24,000$ Yrs.) remains and the activity is greater than that of SS.

The V-20 Ti system has an initial activity less than half that of the 316SS system. The relatively short lived isotopes in the activated vanadium dies away quickly and by 10 weeks the activity is approaching that of the stainless system. This is as expected because as the vanadium parts of the system decay, the major portion of the activity comes from the SS near the back of the blanket. Examination of a decay curve for a first wall bears this out. The activity of the first wall is about 13% of the total activity at shutdown. Since there is no stainless in the first wall, the decay is rather rapid, down by a factor of 10 in about one week and a factor of 100 in less than two years.

A tabulation has been made for the relative "Biological Hazard Potential" of the alternate first wall materials. The information for the Nb-1Zr first wall is listed in Table IX-B-4. Comparing this table with Table IX-B-2 for stainless there are some striking differences. The BHP of Nb-1Zr seems to be much greater than that of 316SS. The outstanding example is Nb^{92m} with a BHP of 1500 which is compared to a maximum BHP of any isotope in stainless steel of 24. However, the Nb-1Zr BHP may be too high. In 10CFR20, if a specific nuclide has not been evaluated, it is assigned an MPC value corresponding to 0.1ci/km³ in air. Nb^{92m} falls in this case. It is possible that an upward revision of the MPC would be made should that isotope be evaluated. This in turn, would lower the BHP. Even with a change of this sort, which is not likely to change the MPC by more than a factor of 10, it is apparent that the BHP of Nb-1Zr wall would still be significantly greater than that of stainless steel.

The BHP for the vanadium system is shown in Table IX-B-5. The situation in this alloy is probably the most favorable for any CTR wall material. The total BHP is a good order of magnitude less than for 316SS and in addition the half lives of the isotopes are generally shorter.

Table IX-B-4**"Biological Hazard Potential"**

of Nb-1Zr First Wall at Shutdown for 10 yr. Operation

Isotope	Specific Activity dps/cm ³	Activity at T=0 ci/kw _{th}	"Biological Hazard Potential" km ³ of air/kw _{th}
Nb-92	1.31 x 10(9)	0.079	0.79
Nb-92m	2.53 x 10(12)	1.54 x 10(2)	1.54 x 10(3)
Nb-93m	5.01 x 10(10)	3.05	0.76
Nb-94m	3.04 x 10(12)	185	6.2
Nb-95m	3.13 x 10(11)	50	500
Nb-95	6.79 x 10(11)	41	13.82
Zr-89	1.66 x 10(10)	1.01	10.1
Zr-93	9.87 x 10(7)	6 x 10(-3)	1.5 x 10(-3)
Zr-95	3.73 x 10(8)	2.27 x 10(-2)	2.3 x 10(-2)
Y-90	5.63 x 10(10)	3.42	1.15
Y-91	1.89 x 10(8)	1.15 x 10(-2)	1.15 x 10(2)
Sr-89	6.20 x 10(11)	37.7	126
Sr-91	3.874 x 10(7)	2.36 x 10(-3)	2.0 x 10(-3)

Table IX-B-5

Biological Hazard Potential of
V-20Ti First Wall, 10 Year Operating Time

Isotope	Specific Activity dps/cm ³	Activity at t=0 ci/kw _{th}	"Biological Hazard Potential" km ³ of air/kw _{th}
Ca-45	4.23 x 10(10)	2.48	2.58
Sc-46	3.06 x 10(10)	1.87	2.34
Sc-47	2.59 x 10(10)	1.58	0.079
Sc-48	1.99 x 10(11)	12.1	2.46
Sc-49	6.36 x 10(9)	0.39	0.013
Sc-50	9.33 x 10(9)	0.57	0.019
Ti-45	1.90 x 10(9)	0.12	1.16
Ti-51	2.60 x 10(11)	15.9	0.053
V-52	3.39 x 10(11)	20.7	0.09

C. Afterheat

A direct consequence of the generation of large amounts of radioisotopes is that they will generate heat as they decay away. If this heat is not properly disposed of, it can damage reactor components and/or make maintenance on the first wall a difficult task. We will briefly describe in this section the manner in which the afterheat was calculated and then will show how the afterheat builds up, decays away, and where it comes from (spatially) in the 316SS blanket. The significance of this afterheat in terms of temperature rise in the event of a loss of coolant accident (LOCA) will be explored. Finally, some observations will be made about the afterheat in the UWMAK-I shield and blankets and this section will end with a few comments on afterheat in Nb-1Zr and V-20Ti blankets.

1. Afterheat from a SS blanket

(a) Afterheat from a SS Blanket

The afterheat in the blanket was calculated using the information on radioactivity as calculated in section IX-B-1. The energies of the decay beta particles and photons are taken from reference 4. The energy of the beta particles is taken to be deposited at the site of the emission of the particle and the average energy of the particle is calculated as described in Chapter V. For simplification, the gammas were also assumed to deposit all of their energy in the immediate vicinity of the origin of the radiation. An examination of the mean free path of a typical decay gamma shows that this is not a good assumption and the energy of the gammas will likely not be deposited near the point of emission. However it probably is conservative in the sense that the largest source of gamma rays is the first wall and if the gammas which originate there do not deposit their energy in the first wall, then the decay heat there will be less than is calculated.

(b) Time Dependence of Afterheat Generation

Many of the features exhibited by the induced radioactivity of the blanket show up in the afterheat also. However the different decay energies of the various isotopes introduces significant changes in the shapes and relative magnitudes of the results. For example, Figure IX-C-1 shows the build-up of afterheat at shutdown as a function of operating time prior to shutdown. Here, as with the radioactivity, a rather rapid buildup of afterheat occurs initially. It is seen that after

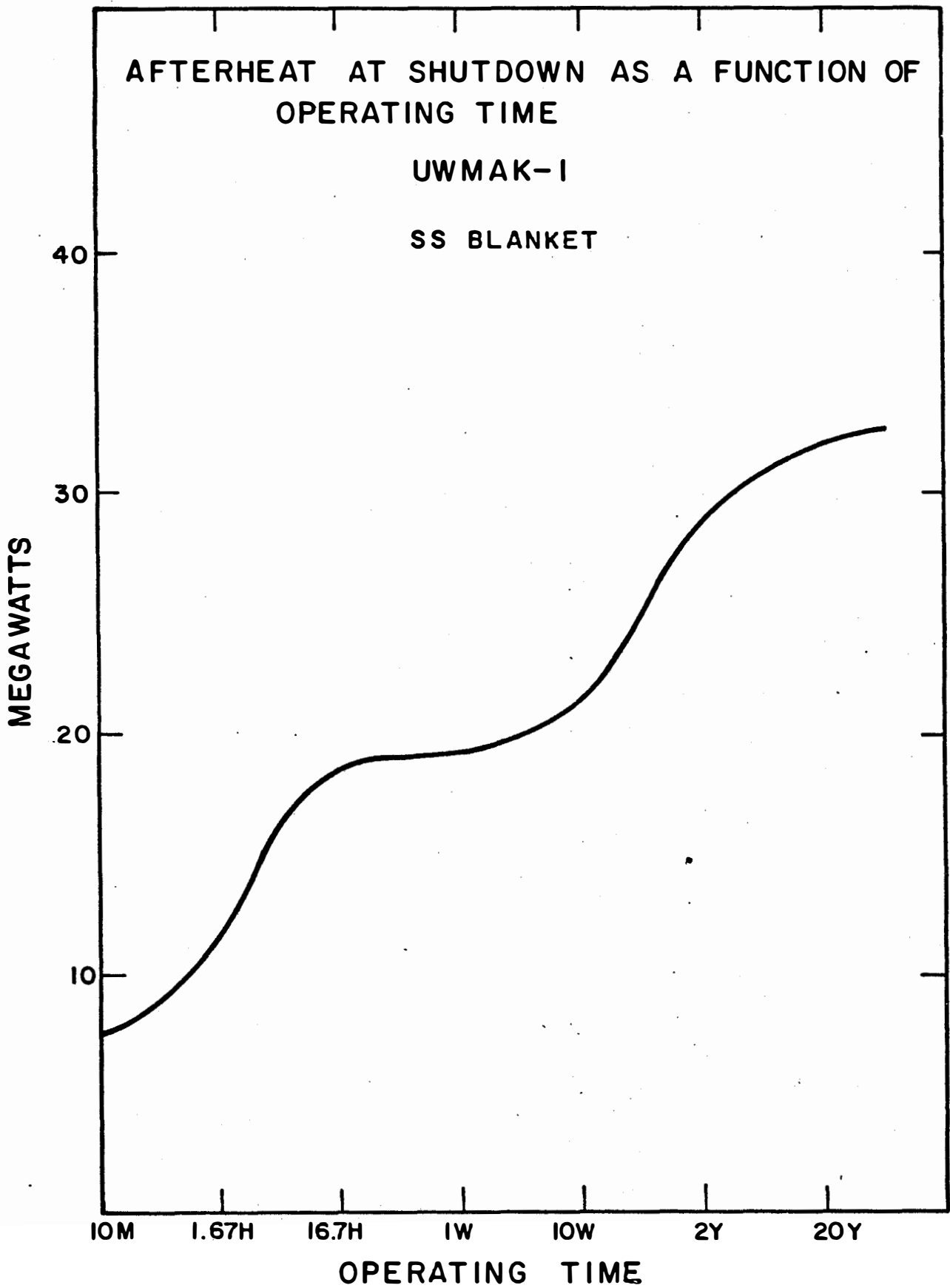


FIGURE IX-C-1

only 17 hours of operation the afterheat is 50% of the forty-year value. This behavior is again due to the saturation of the short lived isotopes which, in this case, have the more energetic decay products.

(c) Time Dependence of the Afterheat Following Shutdown

The time behavior of the decay heat after shutdown is shown in Figure IX-C-2 for 10 year operation. Again the behavior is qualitatively similar to that of the radioactivity. It is seen however that the afterheat decays somewhat more rapidly than the radioactivity. The decay is still relatively slow starting from 0.62% of the operating power, i.e. 31.6 Mwth and requires almost two years to be reduced by a factor of ten. The radioactivity (in curies) would take about three years to decay by the same factor. The afterheat from the first wall is also shown in Figure IX-C-2. Approximately 17%, or 8.5 megawatts out of 31.6 megawatts, comes from the first wall. The time behavior is quite similar to that of the total afterheat being 35% of the total after two years. Also shown on the same figure is the afterheat of the first wall for two years of operation. The initial afterheat has dropped slightly to 6.5 megawatts and falls off to a relatively lower value after the saturated activity dies away due to the lesser activation of the long lived components.

(d) Spatial Dependence of the Afterheat

The spatial dependence of the afterheat is shown in Figures IX-C-3,4, and 5. Figure IX-C-3 shows the afterheat in the various calculational regions immediately after shutdown for two and ten year operating times. It should be noted that the 20 cm region (heat removal cells) immediately behind the first wall produces more afterheat than the first wall. It is this region that will have to be removed every two years because of radiation damage problems. However, because of the larger volume of this region, the power density in the metal is reduced by over a factor of twenty.

The afterheat drop off steadily through the lithium regions until the large 15 cm steel region is reached. Because of the large quantity of steel in this region, it contributes about 10% of the total afterheat. The remaining regions contribute a negligible amount. Figures IX-C-4 and IX-C-5 show the spatial distribution for 2 years and 20 years after shutdown again for 2 and 10 year operating times. Qualitatively they are similar to the distribution at shutdown demonstrating, however, the

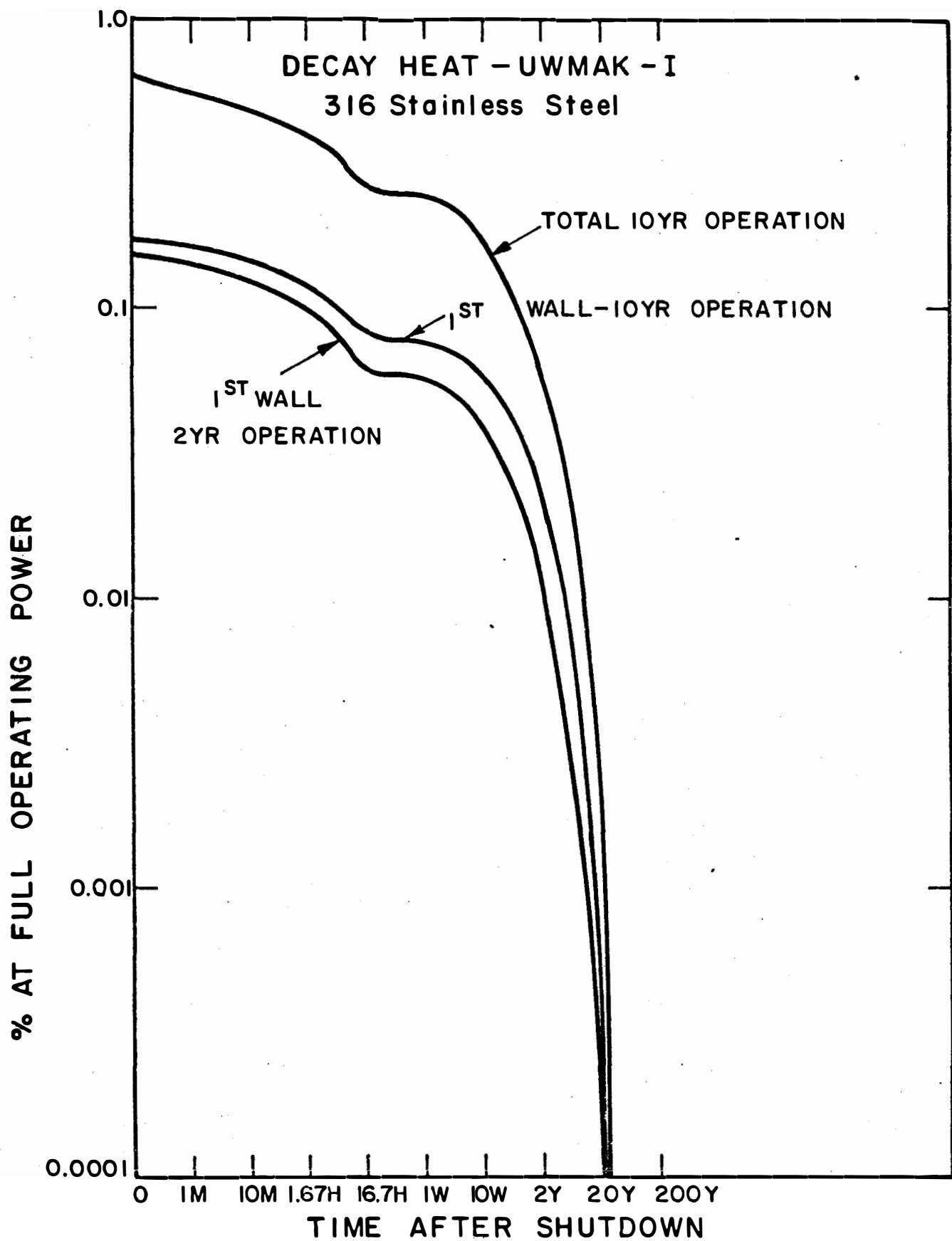


FIGURE IX-C-2

UWMAK-I

316 SS BLANKET

SPATIAL DISTRIBUTION OF AFTERHEAT AT SHUTDOWN

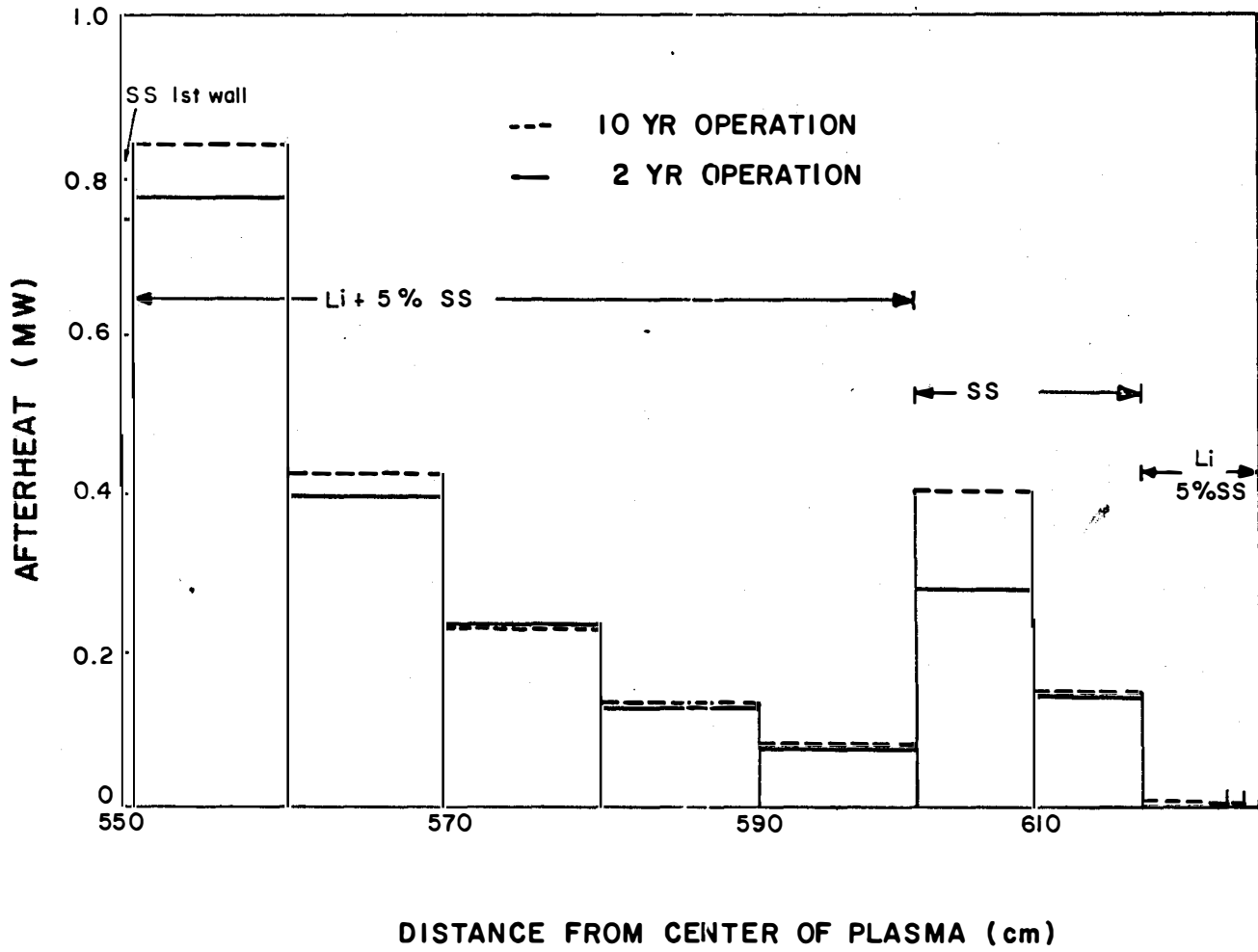


FIG. IX-C-3

UWMAK-I 316 SS BLANKET
SPATIAL DISTRIBUTION OF AFTERHEAT AT 2 YRS AFTER SHUTDOWN

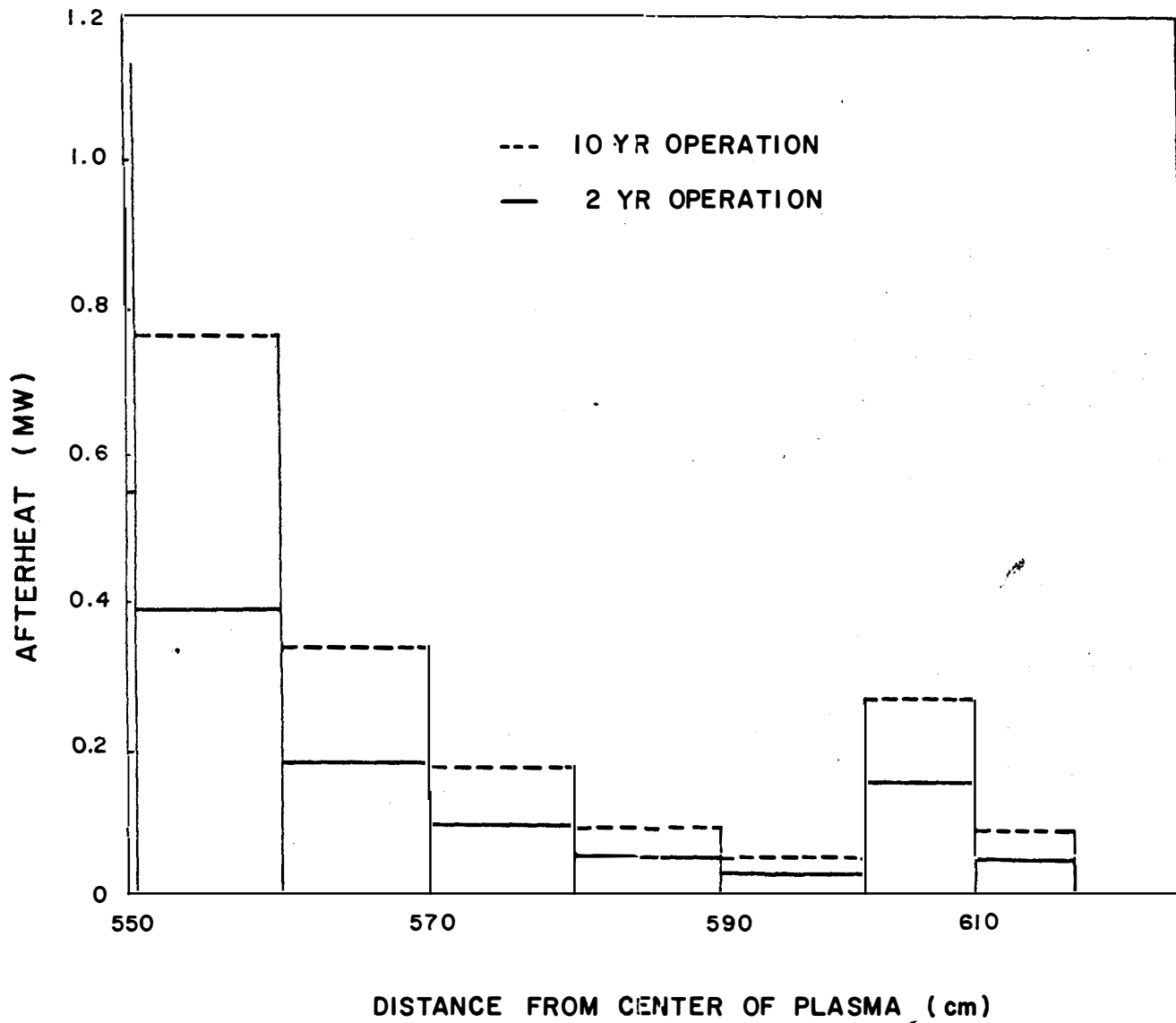


FIG. IX - C - 4

UWMAK - I 316 SS BLANKET

SPATIAL DISTRIBUTION OF AFTERHEAT AT 20 YRS AFTER SHUTDOWN

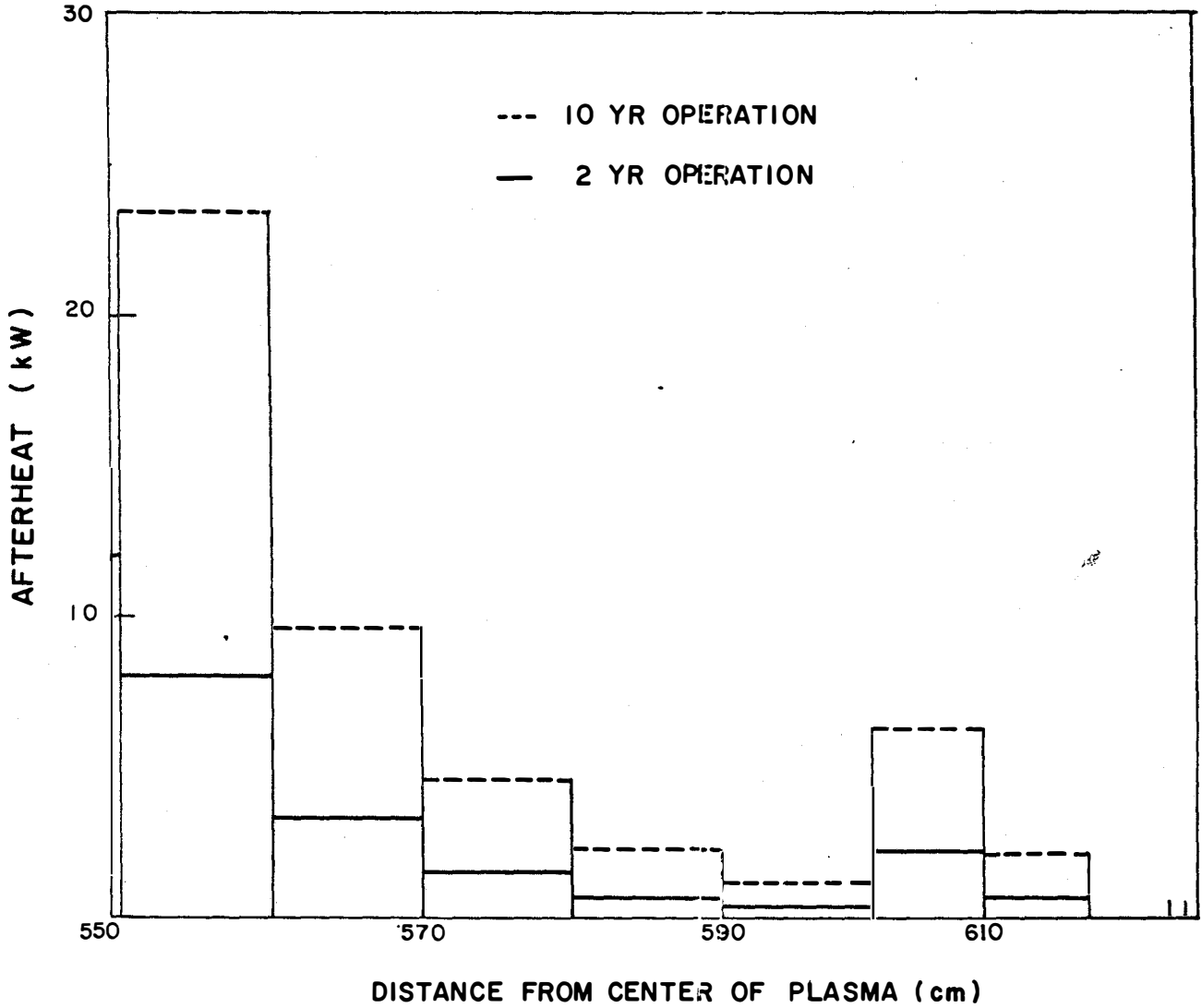


FIG. IX-C-5

relatively lower value of afterheat at long times after shutdown for two year operation and the extremely low total afterheat after 20 years of decay.

2. Afterheat in the Shield and Magnet Region

The afterheat was calculated for the shield and magnet regions using the same techniques as used in the blanket. The 75 cm of shield was broken up into 20 regions with each of the 10 materially different regions. (see Figure IX-B-1). Calculations were made in only the first 30 cm of the 125 cm magnet to further simplify the task. This is adequate as the calculations show the afterheat in the magnet is quite low. The data for 10 year operation and for up to 2 yrs decay times are shown in Tables IX-C-1 and IX-C-2. Figure IX-C-6 shows the spatial distribution of the afterheat at shutdown for the complete blanket and shield after 10 years of operation. The maximum after heat in any shield region is over two orders of magnitude down from that of the first wall while the afterheat in the magnet is down by another two orders of magnitude from the shield. The largest afterheat in the magnet is less than 200 watts in any region. The time dependence of the afterheat following shutdown is shown in Figures IX-C-7 for the shield and in IX-C-8 for the magnet. Because of the differences in the spectrum the decay of the afterheat in the shield and magnet regions is somewhat faster than in the blanket. The initial decay is still however relatively slow with a factor of 10 reduction not taking place until a decay time of 5-10 weeks has elapsed. The absolute values are relatively small being about 125 kw for the entire shield at shutdown and 250 watts for the magnet.

3. Temperature Rise Following Loss of Coolant Flow

To obtain a preliminary appreciation of the magnitude of the loss of flow problem the temperature rise in each region has been calculated assuming adiabatic conditions. The results are shown in Figure IX-C-9. It is seen that even in the region of highest afterheat power density, i.e. the first wall, the temperature rise is only $0.1^{\circ}\text{C}/\text{sec}$. In the major portion of the blanket the rise is less than $0.01^{\circ}\text{C}/\text{sec}$ while in the shield and magnet the rise is orders of magnitude lower being the order of 10^{-7} $^{\circ}\text{C}/\text{sec}$ in the most activated region of the magnet. These results indicate that it is not likely that removal of afterheat in the case of the loss of flow accident will be an extremely severe problem. Further calculations using a more realistic model are under-way.

4. Afterheat from Alternate Blanket Structures

The afterheat for the Nb-1Zr+SS and V-20Ti+SS blanket systems was calculated using the radioactivity of IX-C-1. Figure IX-C-10 shows the after heat builds up with operating time for all three systems (Nb, V, and 316SS). The behavior is qualitatively similar to that for the radioactivity in the sense of a rapid initial build up followed by a slower rise. Because of the short-lived isotopes in the V-20Ti system, it has a high activity at $t=0$. However, by the end of the first two hours of operation the afterheat from the V-20Ti and 316SS systems are comparable. Niobium-1Zr on the other hand starts out low and builds up more slowly than 316SS. By about 10-20 weeks

Table IX-C-1
 Afterheat of Shield (Megawatts)
 (10 yr. operation)

	Rad* in	Rad* out	thickness	Time after Shutdown			
				t=0	t=10 min.	t=1 week	t=2 yrs
1	624.4	625.4	1	.7216 x10(-2)	.6484x10(-2)	.2648x10(-2)	.3316x10(-3)
2	625.4	630.4	5	.4385 x10(-1)	.4062x10(-1)	.1175x10(-1)	.1311x10(-2)
3	630.4	635.4	5	.2972 x10(-1)	.2768x10(-1)	.7495x10(-2)	.7756x10(-3)
4	635.4	640.4	5	.1972 x10(-1)	.1848x10(-1)	.4653x10(-2)	.4536x10(-3)
5	640.4	645.4	5	.1220 x10(-1)	.1146x10(-1)	.2665x10(-2)	.2639x10(-3)
6	645.4	648.4	4	.2794 x10(-2)	.995 x10(-1)	-----	-----
7	648.4	653.4	4	.1623 x10(-2)	.5778x10(-17)	-----	-----
8	653.4	654.4	1	.2966 x10(-3)	.2648x10(-17)	.1085x10(-3)	.1467x10(-4)
9	654.4	658.4	5	.1966 x10(-2)	.1848x10(-3)	.4595x10(-3)	.5594x10(-4)
10	659.4	664.4	5	.1419 x10(-2)	.1325x10(-2)	.293 x10(-3)	.3356x10(-4)
11	664.4	669.4	5	.9916 x10(-3)	.9315x10(-2)	.1878x10(-3)	.2011x10(-4)
12	669.4	674.4	5	.6528 x10(-3)	.6151x10(-3)	.1164x10(-3)	.1206x10(-4)
13	674.4	678.4	4	.1114 x10(-3)	.3964x10(-3)	-----	-----
14	678.4	682.4	4	.6161 x10(-4)	.2300x10(-18)	-----	-----
15	682.4	683.4	1	.1290 x10(-4)	.116 x10(-18)	.4753x10(-5)	.6084x10(-6)
16	683.4	688.4	5	.879 x10(-4)	.817 x10(-4)	.2006x10(-4)	.2357x10(-5)
17	688.4	693.4	5	.547 x10(-4)	.510 x10(-4)	.117 x10(-4)	.136 x10(-5)
18	693.4	699.4	6	.171 x10(-4)	.610 x10(-19)	-----	-----
19	699.4	700.4	1.5	.299 x10(-4)	.271 x10(-4)	.130 x10(-4)	.155 x10(-4)
20	700.9	702.4	1.5	.317 x10(-4)	.294 x10(-4)	.169 x10(-4)	.185 x10(-4)
Total-Megawatts				.123	.1099	.3044x10(-1)	.328 x10(-2)

*All dimensions are in centimeters

IX-C-7

Table IX-C-2
 Afterheat of Magnet
 (10 yr. Operation)

	Rad in	Rad out	thickness	Time after shutdown			
				t=0	t=10 min.	t=1 week	t=2 yrs.
1	722.4	732.4	10.	.1626x10(-3)	.1267x10(-3)	.2793x10(-4)	.4272x10(-5)
2	732.4	742.4	10.	.6487x10(-4)	.4896x10(-4)	.7001x10(-5)	.1014x10(-5)
3	742.4	752.4	10.	.2372x10(-4)	.1771x10(-4)	.1984x10(-5)	.2784x10(-6)
Total <u>Megawatts</u>				.2512x10(-3)	.1934x10(-3)	.3692x10(-4)	.5564x10(-5)

*All dimensions are in centimeters

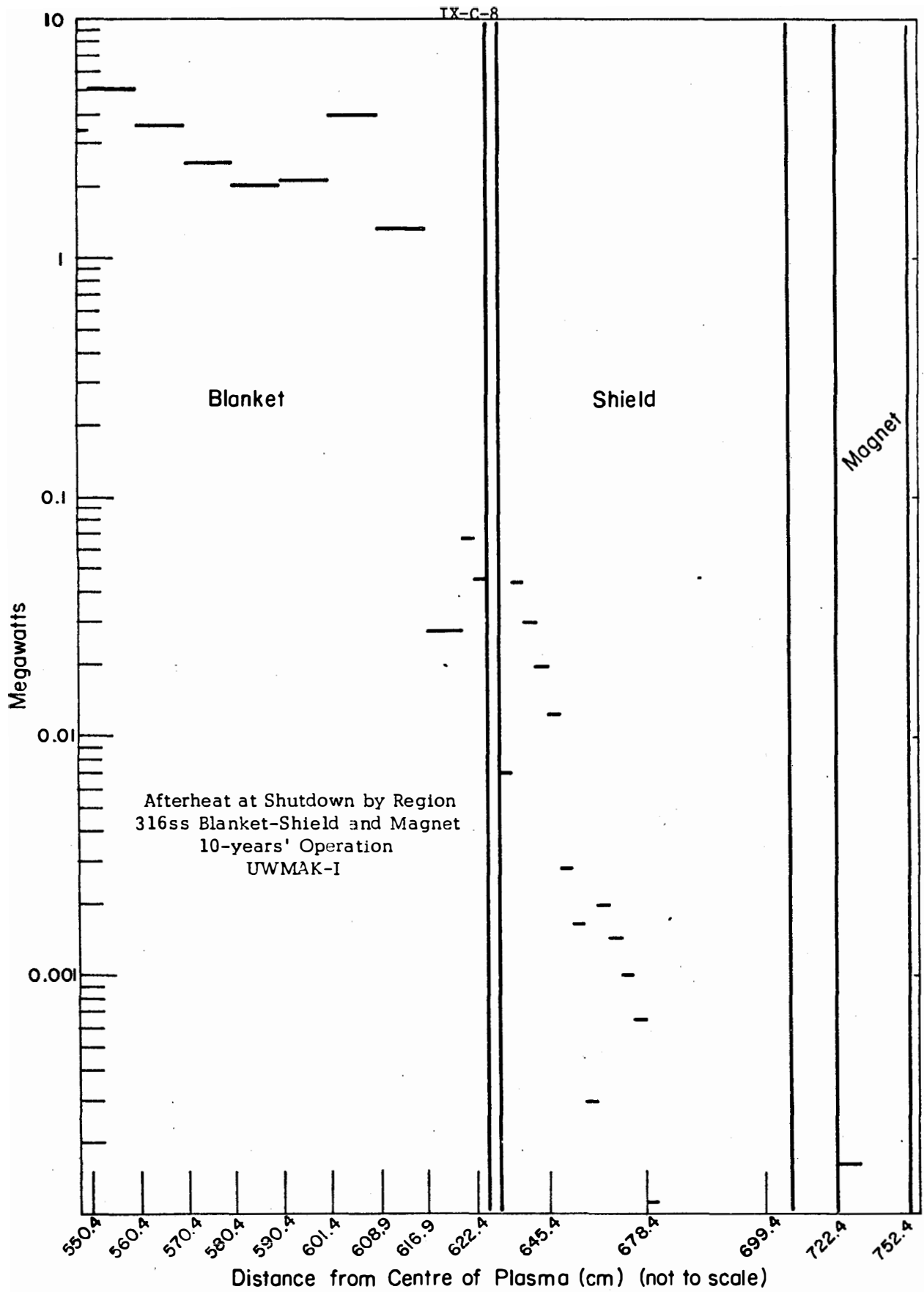


FIGURE IX-C-6

IX-C-9
AFTERHEAT (10 YR. OPERATION)

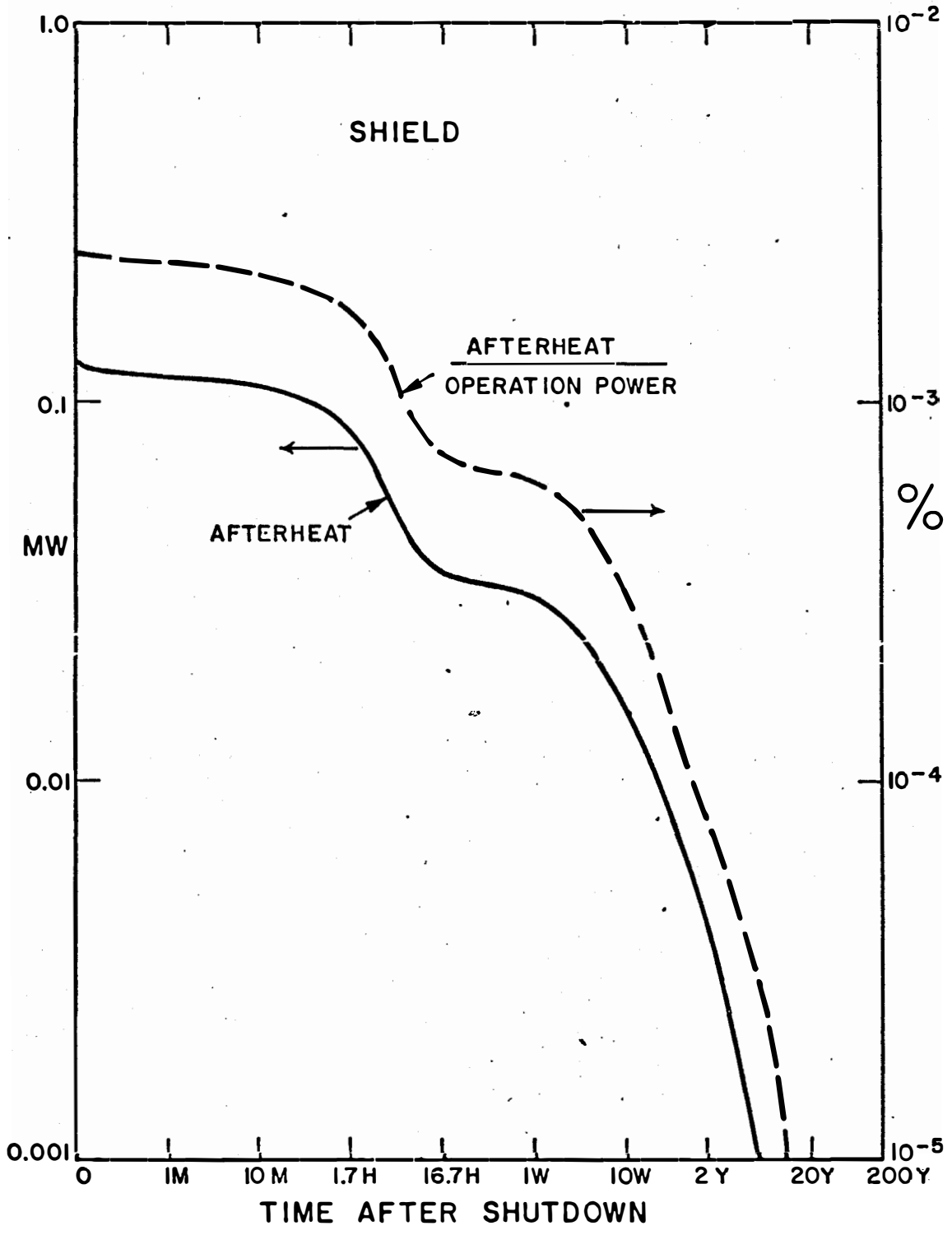


FIGURE IX-C-7

AFTERHEAT (10YR OPERATION)

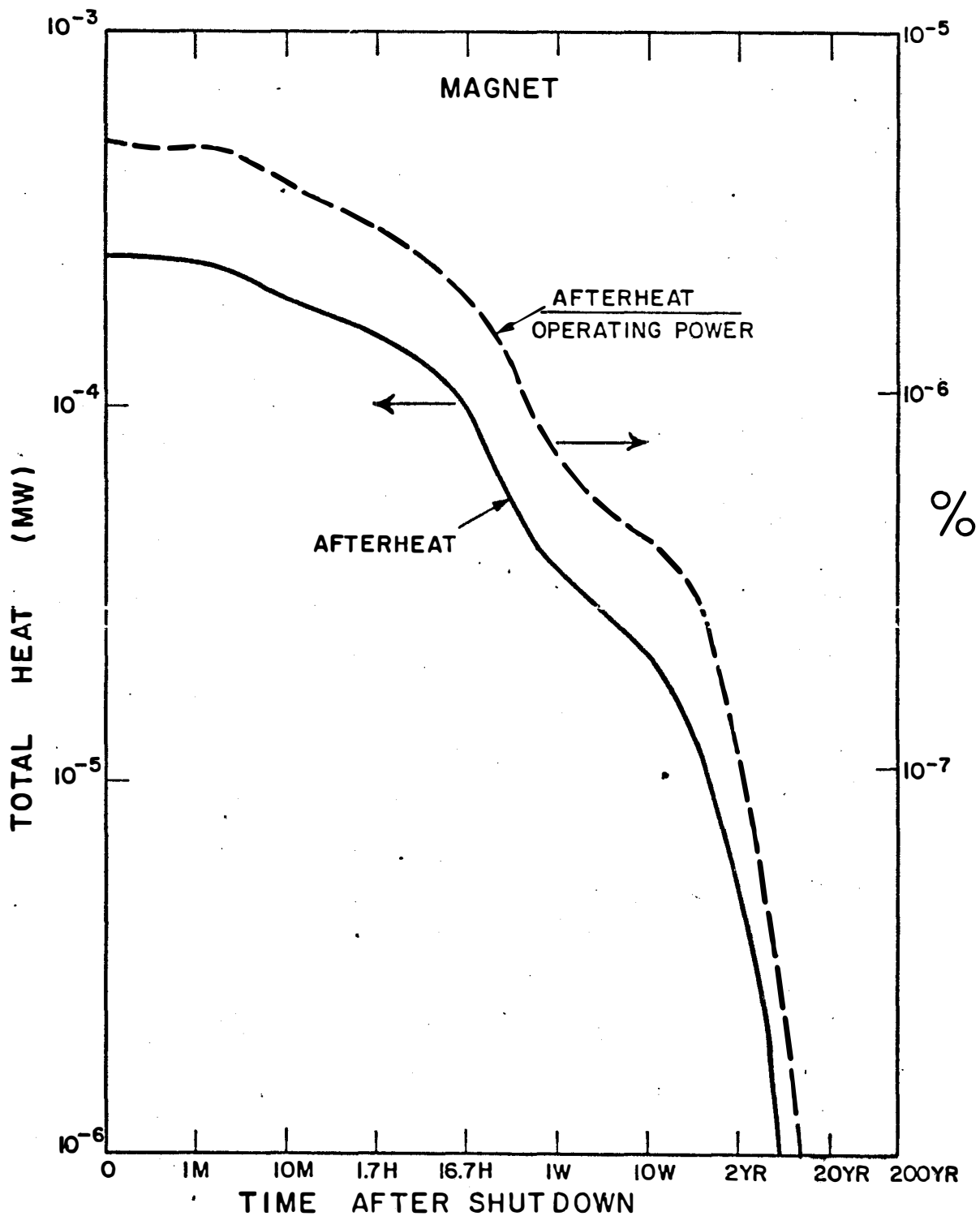
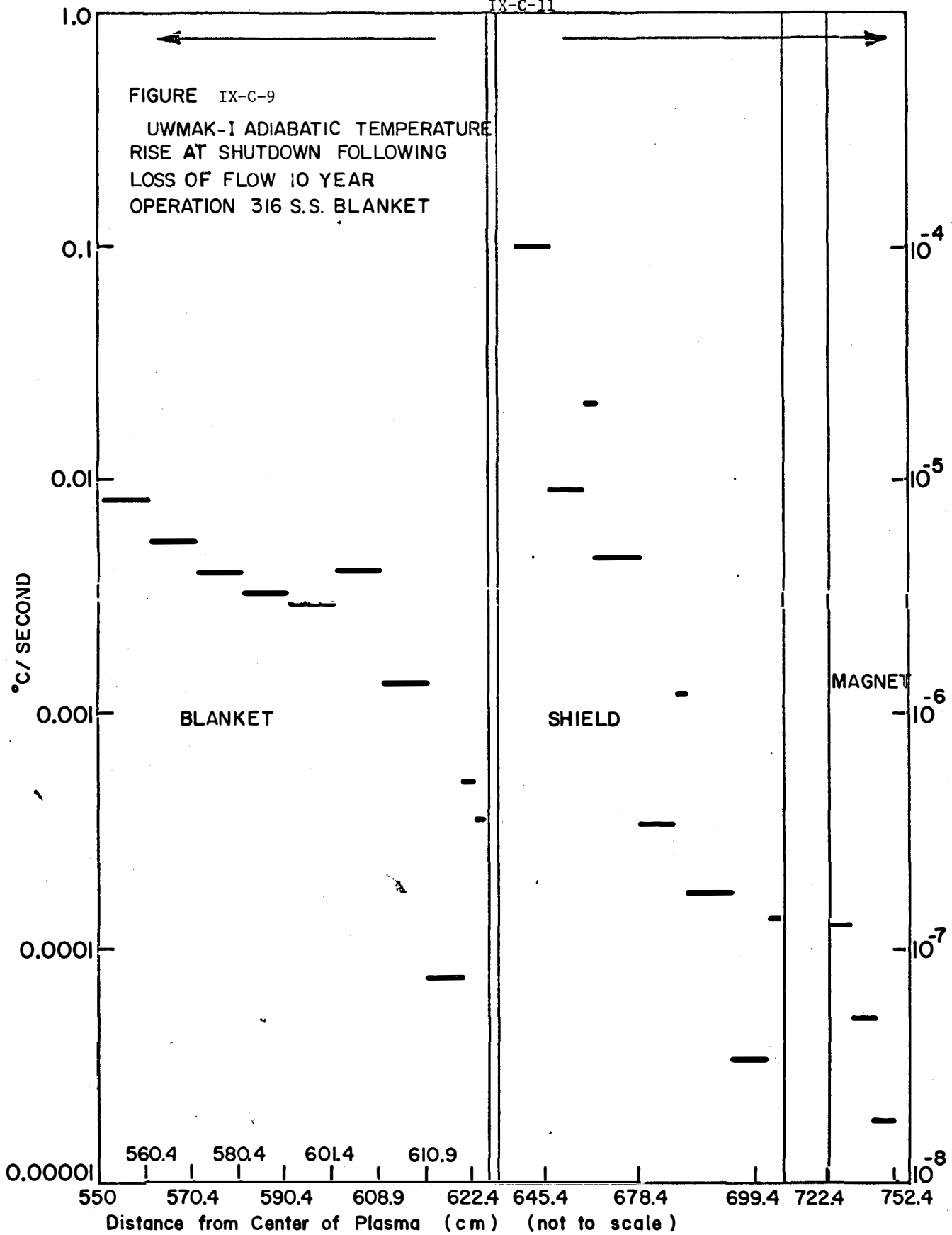
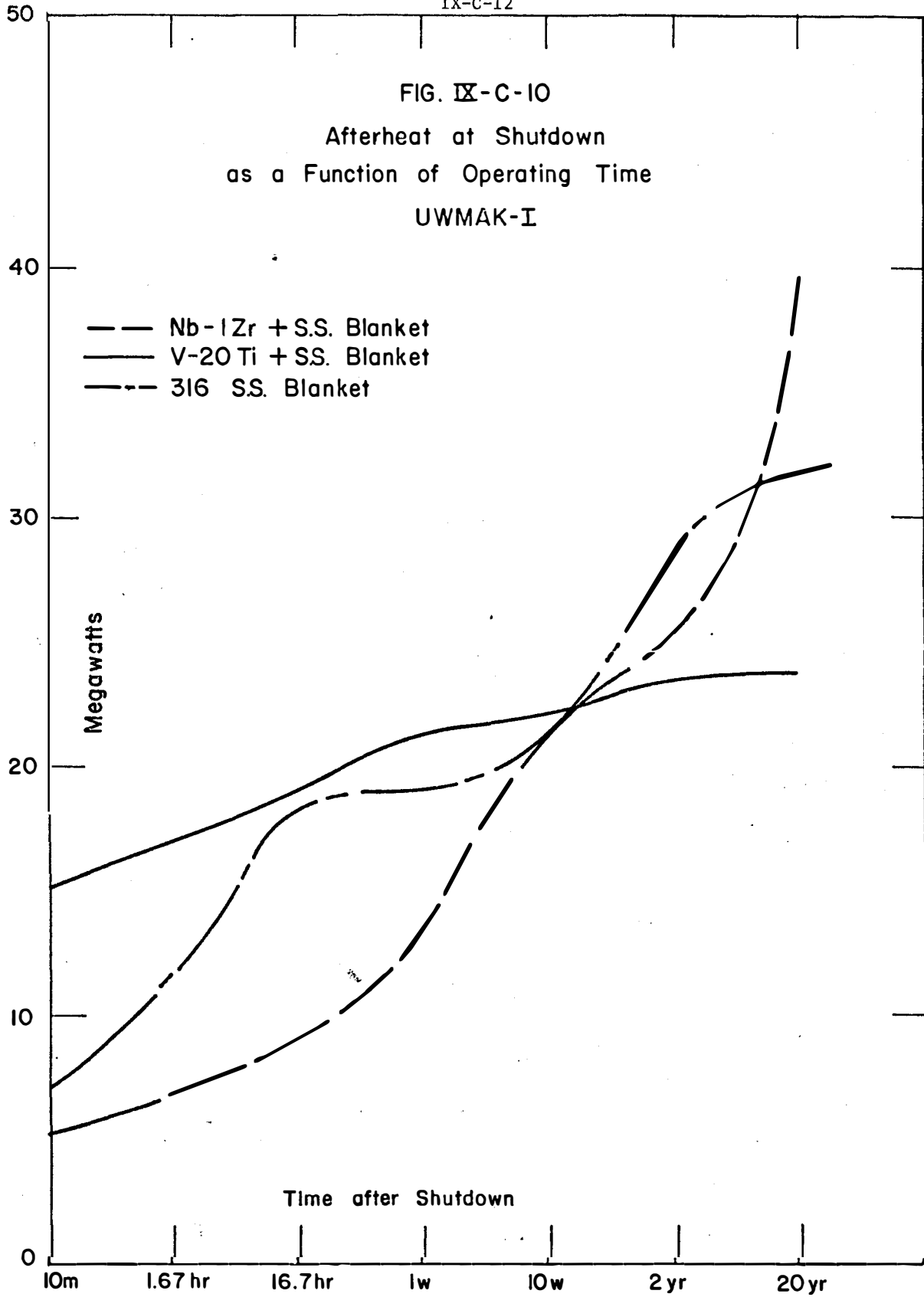


FIGURE IX-C-8

FIGURE IX-C-9
UWMAK-I ADIABATIC TEMPERATURE
RISE AT SHUTDOWN FOLLOWING
LOSS OF FLOW 10 YEAR
OPERATION 316 S.S. BLANKET





all three systems would yield approximately the same afterheat. For larger operating times however, the behavior is again different. The V-20Ti system begins to saturate and increases very little after a year or so. The isotopes in the 316SS system are longer lived and it begins to show saturation after about 5 years. The Nb-1Zr system shows no sign of saturation by twenty years.

The time dependence of the after heat following shutdown is shown in Figure IX-C-11 for the case of 10 year operation. The information on stainless steel from Figure IX-C-2 is reproduced for comparison. For this particular choice of operating time, the 316SS and Nb-1Zr systems have the same initial decay heat. The initial decay is rather slow for both systems with the 316SS decaying somewhat faster. After about five weeks however the short lived isotopes of 316SS have decayed leaving a relatively slow decay due to Fe^{55} ($t_{1/2} = 2.44$ years). In this time range the niobium isotopes have shorter half lives and the after heat of the Nb-1Zr system drops below that of the 316SS system. At long times the long lived activity from Nb^{94} dominates and Nb-1Zr is left with relatively high residual afterheat. (25kw at 200 years.) The result is that whereas the 316SS system requires almost two years for the afterheat to be reduced by a factor of ten the Nb-1Zr system is down by this factor in about 6 months.

The initial afterheat of the V-20Ti system is significantly lower than either 316SS or Nb-1Zr. The initial decay is relatively rapid, amounting to a factor of ten in one to two weeks. After about two years the afterheat from the vanadium and titanium isotopes has become negligible compared to that of the stainless in the system and from that time on the afterheat is due to the stainless regions in the back of the blanket. This is shown in Figure IX-C-12 in which the after heat following shutdown is plotted for the first wall. Again a 10 year operating time is chosen. Not only is the afterheat of the V-20Ti first wall lower at shutdown but the decay is much more rapid being down over a factor of 10 in a week. Examination of the data for long time shows that the residual afterheat is many orders of magnitude lower than either of the other two systems.

The spatial distribution of the afterheat for the V-20Ti system is shown in Figure IX-C-13,14, and 15. These illustrate again the large contributions from the 316SS regions, the saturation of the V-20Ti activity and the rapid decay of the vanadium contribution to the afterheat.

The conclusion which can be drawn from these data is that from an afterheat standpoint, the V-20Ti system is clearly superior. The choice between Nb-1Zr and 316SS is not so clear cut. For 10 year operation Nb-1Zr has a slight advantage at least at shutdown and for the intermediate time range. The long term storage of Nb-1Zr presents more of a problem than either of the other isotopes and the BHP is significantly worse. The final ranking on the basis of activity and afterheat would likely rank V-20Ti as the first choice and 316SS second on the basis of its lower BHP.

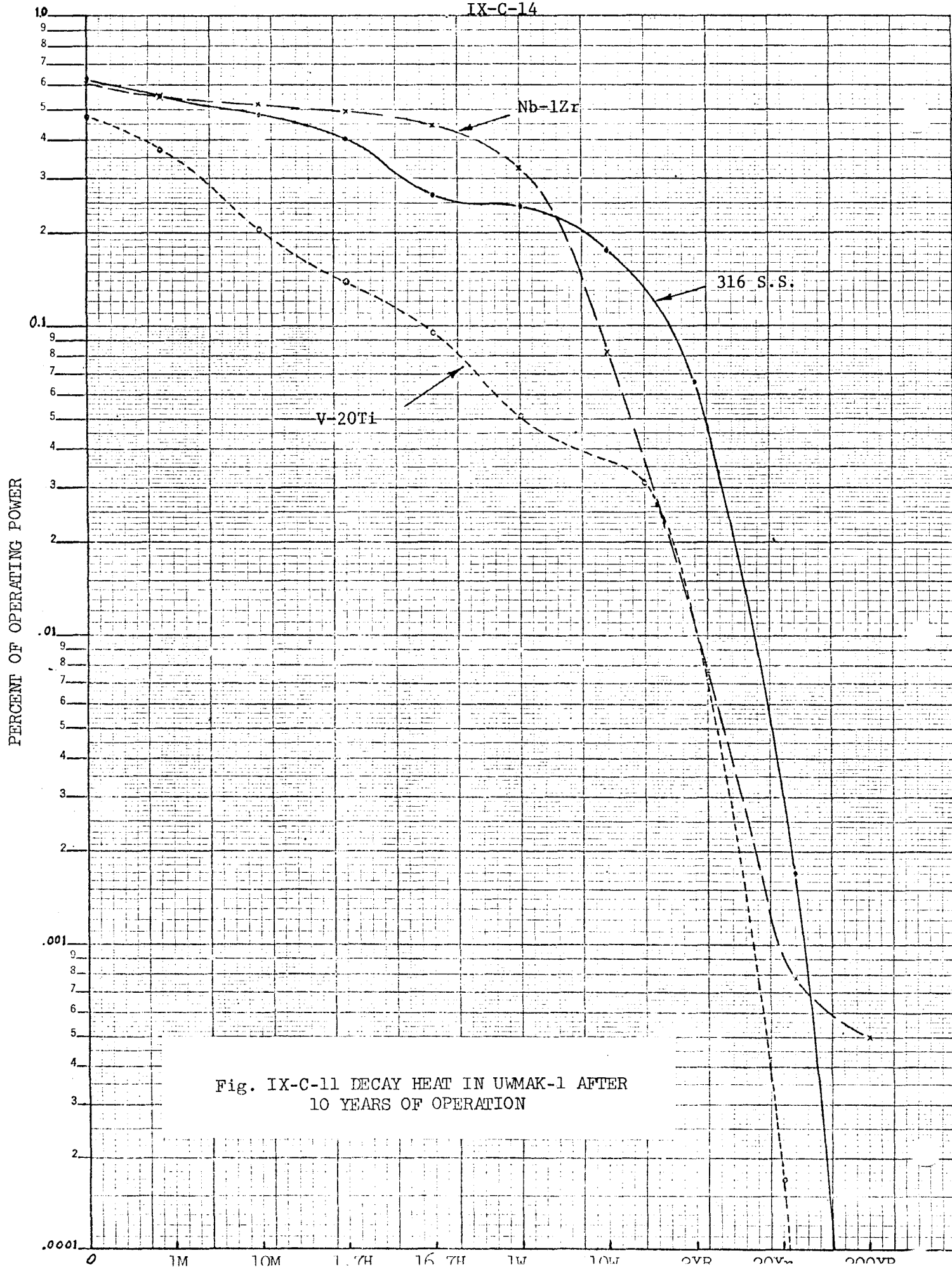
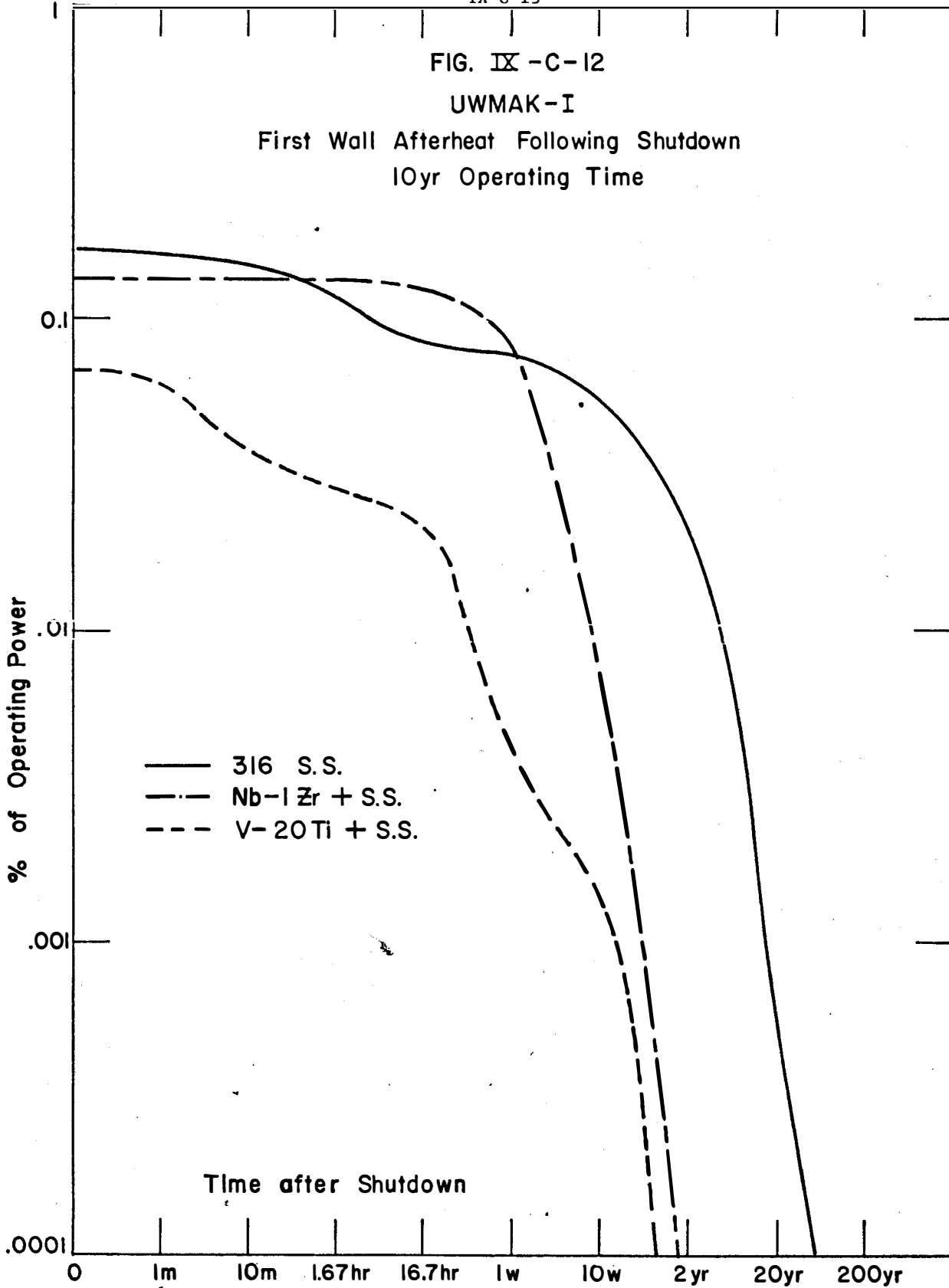


Fig. IX-C-11 DECAY HEAT IN UWMAK-1 AFTER 10 YEARS OF OPERATION

FIG. IX -C-12

UWMAK-I

First Wall Afterheat Following Shutdown
10yr Operating Time



UWMAK - I

SPATIAL DISTRIBUTION OF AFTERHEAT AT SHUTDOWN

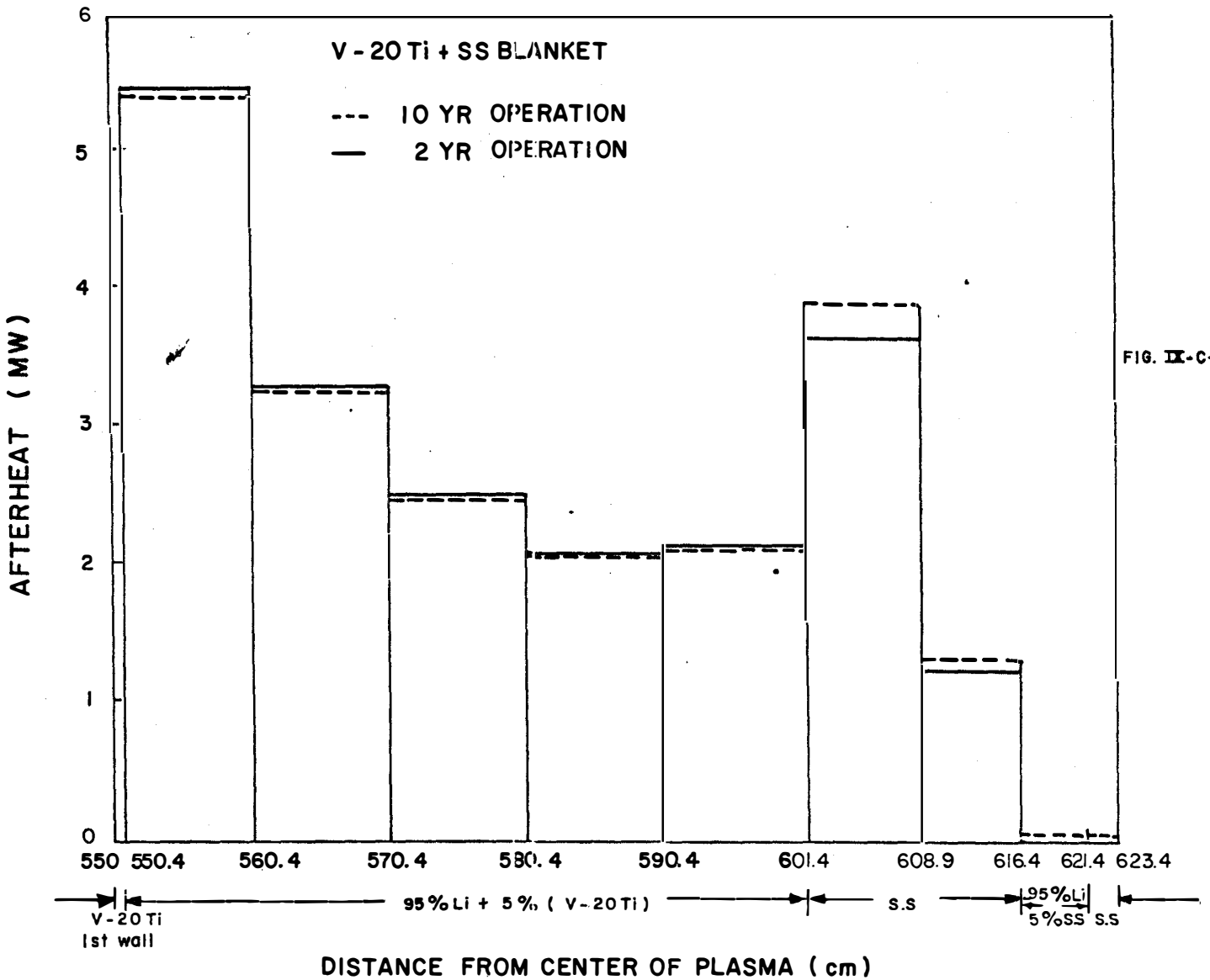


FIG. IX-C-13

UWMAK-I
SPATIAL DISTRIBUTION OF AFTERHEAT AT 2 YRS AFTER SHUTDOWN

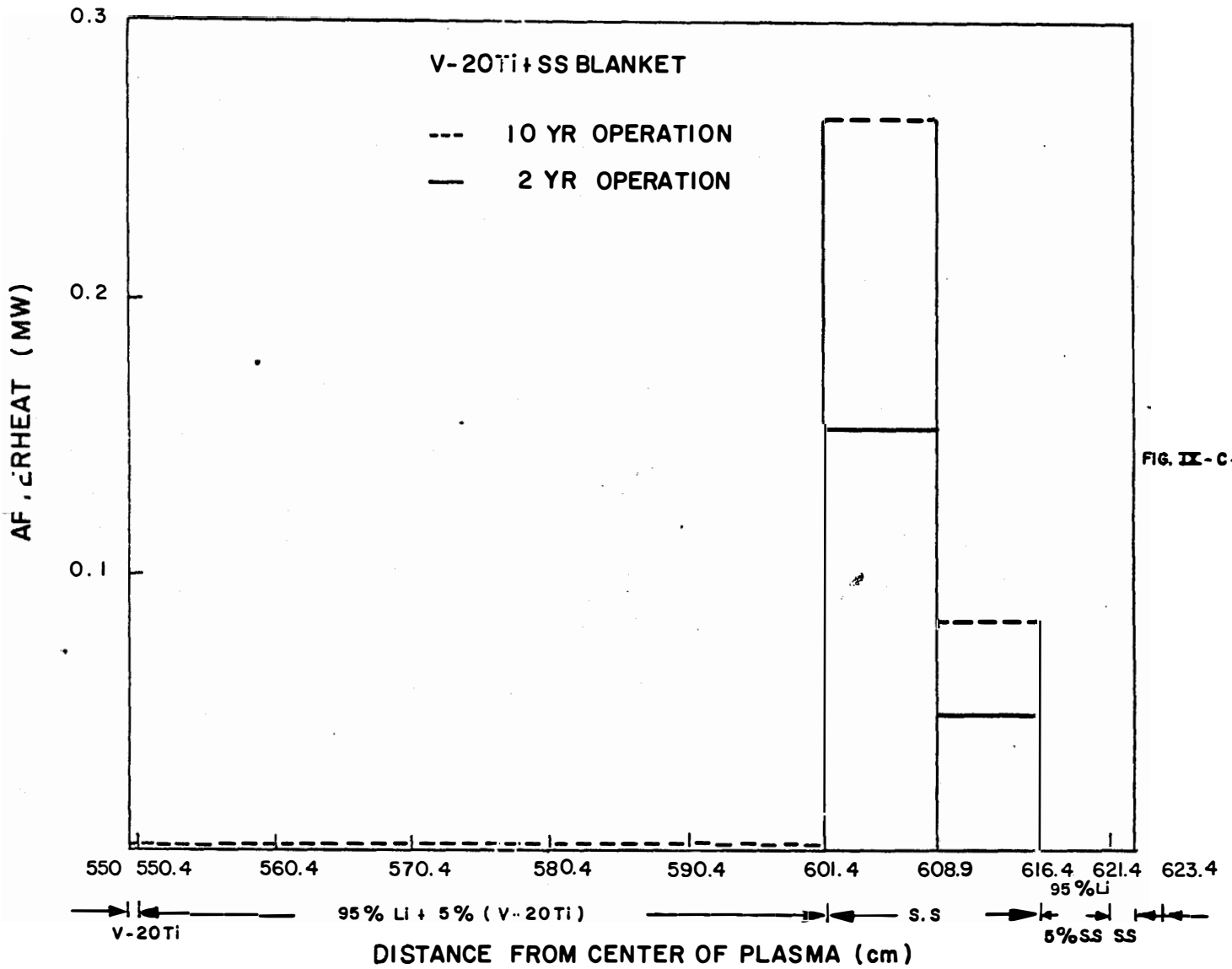
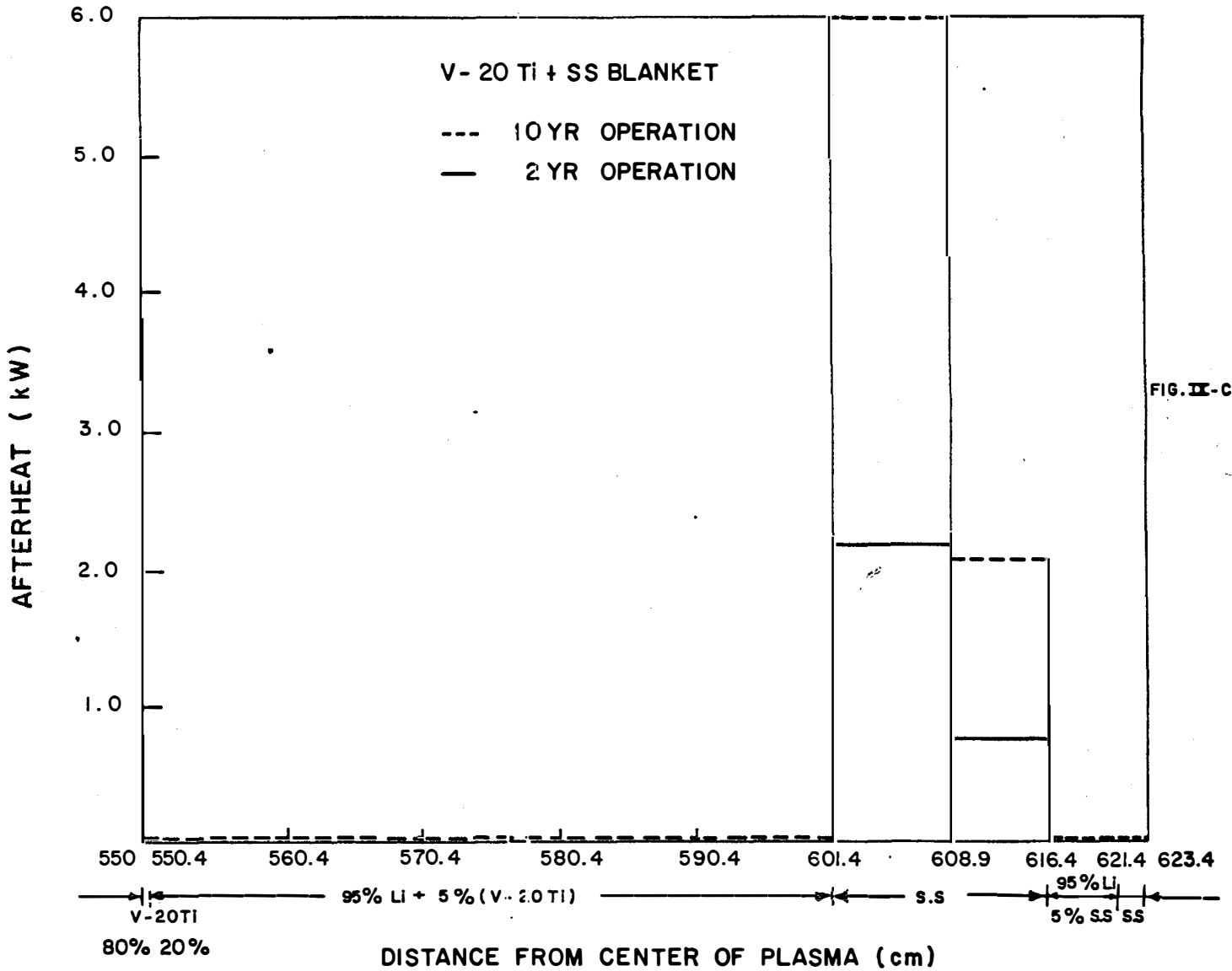


FIG. IX-C-14

UWMAK - I

SPATIAL DISTRIBUTION OF AFTERHEAT AT 20 YRS AFTER SHUTDOWN



IX-D. Lithium Fires

Lithium reacts exothermically with oxygen, nitrogen and water. It therefore is necessary to consider

- a.) the conditions under which lithium will ignite
- b.) the types of fusion reactor accidents which conceivably could lead to ignition;
- c.) measures to preclude accidental occurrences which could reach catastrophic proportions.

Methods of detecting and controlling sodium fires have been developed. (5) The presence of radioactive tritium in the primary circuit (Section VIII-B) provides an added incentive to eliminate fire hazards in a CTR cooled by metallic lithium. Furthermore, the primary circuit lithium will contain radioactivity from circulating corrosion product, (Section IX-B) which would complicate fire control measures.

Two classes of accidental reactions may occur in a lithium-cooled reactor having a steam cycle (Fig. IV-B-1):

- a.) a break in the primary lithium or secondary sodium systems, exposing lithium to inert cover gas.
- b.) a break in the sodium-to-steam heat exchanger, exposing sodium to water.

1. Conditions to Ignite Lithium in Air

Without specifying how the inert cover gas around the loops has been dispersed, let us now assume that we have a pipe break which releases Li into air. Some data indicate that lithium will ignite in air near its melting point (183°C) and burn with an intense white flame⁽⁶⁾. Other data indicate that small quantities of lithium are stable up to ~316°C⁽⁷⁾. When standing in an open container in air at 316°C, lithium will ignite and burn under some conditions. Prior to ignition, a black, hard brittle material forms on the surface, and appears to initiate ignition. If the black nodule is removed before ignition occurs, the lithium does not ignite. In another experiment, lithium ignited readily when suddenly exposed to air at 260°C⁽⁸⁾.

Some observers indicate that high humidity promotes ignition; (8,9) in contrast, Devries (7) indicated that molten lithium ignited more readily on dry days than when conditions were humid.

Molten lithium may react with metallic oxides on its container, causing ignition. (7)

Solid lithium may ignite if rubbed vigorously in air while heated near its melting point. At room temperature, lithium can be sawed, filed, cut, and hammered without igniting.

It is worth noting that lithium is the only alkali metal which reacts markedly with nitrogen so that simply removing oxygen from the vicinity is not sufficient to prevent reactions.

The above discussion indicates that there is controversy regarding the conditions which cause molten lithium to ignite. However, in the safety literature, (10) the lithium fire hazard is regarded as "dangerous when exposed to heat or flame or allowed to react chemically with moisture, acids or oxidizers." While lithium reportedly reacts less vigorously than the other alkali metals, (8) in a conservative treatment it must be regarded as prone to ignition in air at temperatures near and above the melting point.

Once ignited in air, lithium burns quietly in an open vessel, emitting dense, white, irritating fumes. (7)

2. Conditions to Ignite Sodium in Water

Experience indicates that leaks in a sodium-water heat exchanger do not generally result in explosions, (11, 12) but that they do lead to wastage of metal in the vicinity of the leaks, which eventually could result in massive intermixing of liquid metal and water.

As in the case of air, lithium is reported to react less vigorously with water than the other alkali metals. (6) However, molten or burning lithium can react explosively with water or moist materials, including concrete. (6, 9)

Where impingement of the molten lithium onto a concrete floor is possible, steel coverings are recommended. (8)

3. Measures to Prevent Lithium Fires

Given that ignition of lithium can occur in air or water in the temperature range of the UWMK-I primary and secondary coolants, the chemical and radiological hazards of a lithium fire dictate extreme measures to prevent occurrence of fires. The essential measures may be generalized as follows:

- 1) Design Considerations--Consideration of the fire hazard in plant layout, choice of maximum stress levels, pipe wall thickness, etc; double containment of piping in critical areas is a potential insurance measure.
- 2) Material Selection--Choice of materials with maximum resistance to stress corrosion cracking and mechanical failure; while Type 304 SS is the lithium-to-steam heat exchanger design material, the final material selection for an actual plant will be the culmination of a sizable development and testing program.
- 3) Evacuated Containment--The fire hazard can be minimized by evacuation of air from all areas where lithium could be released; the primary coolant is particularly critical because of its radioactive content. There is evidence (13) that maintaining dry conditions will essentially eliminate rapid reaction of lithium in air. However, maintaining dry conditions may be as difficult as maintaining a vacuum. It is not clear how good the vacuum must be to preclude the air-lithium reactions.

4. Measures to Control Lithium Fires

Lithium will exist at several locations in the CTR plant:

- in pre-exposure storage;
- in primary and secondary circuits;
- in tritium extraction and cleanup circuits;
- in interim storage;
- in post exposure storage.

Each area must be designed for fire control, including elimination of construction materials which will react with lithium; avoidance of water sprinkler systems; provisions to bring to bear large volumes of extinguishing materials (graphite, lithium chloride, and zirconium silicates for lithium); construction of sheet metal enclosures, drip pans and gratings; provisions for protective clothing and personnel access, where radiation and tritium levels will allow; provisions to seal off areas where tritium release is excessive; provisions for remote fire fighting where radiation levels will not allow personnel access.

Some of the above subjects are dealt with in detail elsewhere. (6, 8)
However, development of procedures to handle lithium fires remotely and to control large releases of tritium will present a major challenge.

References

1. M. A. Abdou, C. W. Maynard, and R. Q. Wright, MACK: A program to calculate Neutron Energy Release Parameters (Fluences-To-Kerma and Multigroup Neutron Reaction Cross Sections From Nuclear Data in ENDF Format), University of Wisconsin Fusion Design Memo No. 37.
2. e. g. Nuclear Data, Academic Press New York N. Y.
3. D. Steiner and A. P. Fraas, Preliminary Observations on the Radiological Implications of Fusion Power, Nuclear Safety, 13:353 (1972).
4. C. M. Lederer, J. M. Hollander, and I. Perlman, Table of Isotopes, 6th Ed., Wiley, New York, N. Y. (1967).
5. D. W. Cissel, et al., Guidelines for Sodium Fire Prevention, Detection, and Control, ANL-7691, June, 1970.
6. J. H. Miedel, Explosive and Toxic Hazardous Materials, H. N. Gruber, Ed., Glencoe Press, Beverly Hills, CA, p. 160.
7. G. DeVries, "The Corrosion of Metals by Molten Lithium," Corrosion by Liquid Metals, J. E. Draley and J. R. Weeks, Eds., Plenum Press, 1970, p. 252-253.
8. J. W. Mausteller, F. Lepper, and S. J. Rodgers, Alkali Metal Handling and Systems Operating Techniques, Gordon and Breach, New York, 1967, p. 207-214.
9. J. O. Cowles and A. D. Pasternak, Lithium Properties Related to Use as a Nuclear Reactor, UCRL-5047, April, 1969.
10. N. I. Sax, Dangerous Properties of Industrial Materials, Reinhold, New York, 1963, 2nd Ed., p. 940.
11. R. A. Davies, J. A. Bray, and J. M. Lyons, "Corrosion of steels in the Vicinity of a Sodium-Water Reaction," Alkali Metal Coolants, Proceedings of a Symposium, Vienna, Nov. 28-Dec. 2, 1966, IAEA, Vienna, 1967, p. 263.
12. H. O. Muenchow and W. L. Chase, "An Investigation of Tube Wastage Caused by Small Leaks of Water in Sodium-Heated Steam Generators," Alkali Metal Coolants, Proceedings of a Symposium Vienna, Nov. 28-Dec. 2, 1966, IAEA, Vienna, 1967, p. 263.
13. Mausteller, et al., loc. cit., p. 12,13.

X. Steam Cycle

The conversion of the thermal output of the UWMAK-I reactor to useful power has to be investigated in any review of potential reactor designs. This area has been briefly mentioned in earlier sections (e.g. Chapter VIII) and some of those comments will be repeated here. A more extensive discussion of the power systems will be presented in Volume 2 of this report.

The basic problem is to extract electrical power from a flowing liquid metal system which has lithium entering at 283°C (541°F) and leaving at 483°C (901°F) with a mass flow rate of 2.1×10^7 kg/hr (4.7×10^7 lbs/hr). The most likely way to accomplish this will be to transfer heat to a steam system and use a conventional steam turbine-electric generator. Consideration of such factors as the effect of leaking tubes in a liquid metal steam generator or release of tritium either in normal or abnormal situations dictates the use of a secondary liquid metal loop isolating the lithium in the reactor from the steam system. Because of the lower solubility of tritium in sodium as compared to lithium as well as the acceptable and well known heat transfer properties of sodium, sodium was chosen as the fluid in the intermediate loop. The intermediate heat exchanger was designed with a log mean temperature difference of 39°C (70°F) by Babcock and Wilcox⁽¹⁾ and the sodium temperatures are 262°C (502°F) in and 412°C (772°F) out with a flow rate of 9.3×10^7 kg/hr (2.04×10^8 lbs/hr) divided into twelve loops.

Using the above parameters a once through steam generator was designed by Babcock & Wilcox⁽¹⁾. Because of the high ΔT in the sodium the design is restricted by pinch point considerations to relatively low steam temperatures and pressures. As designed the steam generator would operate with feed water at 217°C (400°F) producing steam at 305°C (580°F) at a pressure of 39.8 atmospheres (565 psia) with a steam flow of 7.1×10^5 kg/hr (1.57×10^6 lbs/hr) per steam generator. The pinch point ΔT under these conditions would be 22.8°C (41°F).

Using the above steam condition the remainder of the steam cycle was designed by Sargent and Lundy⁽²⁾. To improve the efficiency of the cycle, reheat is performed with main steam. Feed water heating is used with the 237 MW of power from the divertor system being used as the source for the first stage of feedwater heating. The resulting efficiency of the steam is above 35.7%. The overall plant efficiency is ~27% when the circulating power is extracted. By contemporary standards of fossil plants or even light water fission reactor plants this is a rather low value for the efficiency. The basic reasons for this low efficiency are two fold. First, the outlet temperature of the primary system is rather low as compared for example, to an LMFBR. Secondly, and perhaps more important, the temperature rise through the lithium is too great. This has the consequence of reducing even further the average temperature at which heat is transferred, thus lowering the efficiency. A small improvement in efficiency could be made by redesigning the intermediate heat exchange to yield higher temperatures in the intermediate loop.

Such a change, however, would result in a marginal improvement in efficiency and would at the same time have increased costs and would lead to a higher tritium leak rate into the steam system. The other two possibilities for increasing the efficiency involve raising the lithium output temperature and/or reducing the temperature rise in the lithium. Recent data on the corrosion of stainless steel in flowing lithium⁽³⁾ indicate that it may well be possible to increase the lithium temperature to ~600°C (1080°F). On the other hand, a reduction in the lithium temperature rise would be of perhaps greater value. At present, the mass flow rate of lithium, and thus the temperature rise, is governed by consideration of the amount of power required to pump liquid lithium through the magnetic field and by material stress limits in the first wall structure. It is an open question as to whether any significant improvements in this area are possible.

References

1. D. C. Schluderberg, Private Communication. The design of the intermediate heat exchangers and steam generators will be treated more fully in Volume 2 of this report.
2. Eugene Norman, Private Communication. The design of the steam system will be treated more fully in Volume 2 of this report.
3. D. Sze, To be published.

Conclusions

The major conclusions which have been reached from this conceptual design study are given in this section by subject area. As is customary, the subject areas begin with the plasma and work outward, ending with conclusions regarding reactor safety. Recommendations based upon these conclusions are given in the next chapter.

A. Plasma

1. Small aspect ratios, less than 3 if possible, are desirable for economic Tokamak reactor designs. In addition, there is no strong economic incentive to increase the major radius of the torus beyond approximately 15 meters.

2. There is a serious competition between short start up times and the desire to minimize stored energy requirements and costs. Short plasma current rise times are desirable for stability of the discharge but mean that large stored energy systems would be necessary. For example, in UWMAK-I, it is found that a 100second current rise time requires an energy storage system of 3.2 MWhr. If this rise time can be extended to 200 seconds, the energy required can be bought directly from existing power utilities.

3. Neutral beams are a promising means of igniting large Tokamak reactors. The use of a low density startup ($n_0 \sim 3 \times 10^{13}/\text{cm}^3$) allows beam penetration and reduces plasma energy losses during this phase. For the UWMAK-I plasma ($a = 5\text{m}$), a 500 KeV neutral beam penetrates the plasma and produces beam power deposition profiles peaked on axis. Such penetration is not possible in such large systems, even at densities like $10^{13}/\text{cc}$, with beams under 100 KeV. However, if inverted temperature profiles are tolerable, the reactor can be ignited using beams of ~100 KeV with beam powers in the 10-100 MW range.

4. The assumption of either neoclassical or pseudoclassical scaling for the electron thermal conductivity leads to the conclusion that ignition times of less than 10 seconds can be achieved in large systems at moderate beam power levels (15-75 MW). These conclusions will be modified if less favorable scaling laws govern plasma transport for $T_e > 2-3 \text{ KeV}$.

5. The beam requirements for plasma heating are ~300-500 KeV, ~1-2 amperes equivalent per beam injector, and operation for 1-10 seconds. Such beams will heat the plasma and not generate inverted temperature profiles.

6. If neutral beams are required only for plasma heating, beam system efficiencies can be low (e.g., 10%) since burn times are expected to be long compared to the time to ignite reactor plasmas.

7. Fueling by large pellets (~2mm diameter D-T pellets) appears formidable if the accelerating velocities required for penetration are to be achieved. On the other hand, if micron size pellets will work, the technology is at hand. For UWMAK-I, $\sim 20 \times 10^6$ pellets sec of radius 40 μm are required.

8. Plasma operation requires confinement times that are several hundred Bohm times but are ~2-3 orders of magnitude shorter than neoclassical confinement times. These requirements are for plasma operation at quasi-steady state during a burn time. The most economical temperature range for the plasma operation in a β -limited plasma is 10-15 KeV.

9. If the scaling on τ_E and τ_C is basically "classical" (i.e. τ_E and $\tau_C \sim T^{1/2}$) then an energy equilibrium in the 10-15 KeV range is thermally unstable. Thermally stable operating conditions are possible at higher temperatures ($T_i > 25$ KeV) but require larger toroidal magnetic fields to produce the same power. For UWMAK-I, thermally stable and unstable equilibria have been calculated. Operation at the stable point would require magnets that are ~\$100 x 10⁶ more expensive than for operation at the unstable point (still within NbTi superconductor technology.)

10. From an economic viewpoint, one would like plasma operation at as high a β and as low a q as possible. For fixed q , all magnet costs increase as β_θ decreases. At fixed β_θ , only the toroidal magnet coil costs increase as q increases.

11. Extended burn times, up to one hour or longer, are feasible for a Tokamak reactor if divertors solve the impurity problem.

12. Steady state operation of a Tokamak is highly desirable because it can

- (1) minimize thermal cycling on the first wall
- (2) allow steady power output
- (3) allow for longer plasma current rise times following an outage. This latter factor alleviates or eliminates the need for energy storage related to startup requirements.

13. If plasma operation in the 10-15 KeV range is thermally unstable one will require a feedback control system. A feasible strategy is to operate the plasma in a sub-equilibrium state and maintain steady-state with an energy source, such as provided by neutral beams.

B. Divertor

1. Poloidal field divertors which preserve axisymmetry appear feasible.

2. The design of the divertor will determine the shape of the plasma cross section. To be consistent with the desire for a small aspect ratio and to keep the ratio, B_ϕ^{\max}/B_ϕ^0 , around 2, the plasma shape should be elongated vertically. The double neutral point divertor design on UWMAK-I appears feasible and produces a D-shaped plasma cross section. This is also consistent with the shape of the magnetic field coils.

3. A divertor will be required to protect the first wall from erosion and damage and to protect the plasma from wall initiated impurities. In UWMAK-I, the D & T particle fluxes to the wall, assuming a 90% efficient divertor, are $6.4 \times 10^{13} \text{ cm}^{-2} \text{ sec}^{-1}$.

4. Collection of escaping ions by wetted lithium collector surfaces appears reasonable. It simplifies magnetic field design since the particles are collected relatively near the null points.

5. The neutral points in the double null divertor on UWMAK-I can be achieved using divertor coils outside the main toroidal field coils, thus reducing the problems of disassembly.

C. Magnets

1. If the ratio of the maximum field at the magnets to the field on axis can be kept to about 2, magnets for Tokamak reactors can be superconducting using NbTi.

2. The magnets designed for UWMAK-I have complete cryogenic stability using copper as the stabilizer.

3. The required fields in Tokamaks can be produced at current densities of $\sim 1000 \text{ A/cm}^2$, a typical cryogenically stabilized value. Thus, there is no need for unstable magnets. Unstable magnets achieve only a reduction in the amount of stabilizer material, itself a minor consideration, at the risk of being highly unreliable.

4. Large bore, high field magnets required for CTR Tokamaks will require large conductors fabricated into a relatively rigid structure. Winding such magnets from wire or tape is not possible.

5. A large conductor design has been developed for UWMAK-I which is feasible for large CTR Tokamak magnets. In addition, the schematic for construction of the magnets has been developed. Each magnet consists of 34 discs which have helical grooves forged, rolled, or machined into each surface. There are 60 conductor turns per disc and the conductor is NbTi superconductor in copper stabilizer. The conductor is inserted into the spiral grooves and bonded with fiberglass reinforced epoxy as insulation.

6. The magnets will be a primary cost of CTR Tokamaks and the magnet costs depend primarily on the cost of the structure. It is therefore essential that detailed stress analysis guide any realistic magnet design.

7. The costs of the transformer and divertor coils are not small compared to the costs of the toroidal field coils. For example, the transformer and divertor coils cost approximately $\$77 \times 10^6$ for UWMAK-I, while the toroidal field coils cost $\$82 \times 10^6$.

8. The cost of refrigeration units is quite modest, on the order of 5% of the total magnet costs.

9. The toroidal field magnet designs are the same as those which would be required for energy storage requirements. Thus, design advances made on the large bore magnets for Tokamaks will contribute to the design solution of large magnetic energy storage systems.

10. As noted earlier, for short plasma current rise times, energy storage requirements are large and expensive. A magnetic energy storage system to supply 16 MW-hr in 10 seconds will cost approximately $\$100 \times 10^6$.

D. Neutronic and Photonics

1. The tritium breeding ratio is large enough in Li cooled blanket of SS, Nb, V, Mo that most conceivable variations in nuclear data are unlikely to change the conclusion that fusion reactors can produce enough fuel for their own needs, in addition to the excess required for an expanding industry. This is to be coupled with the fact that short doubling times (on the order of months) are possible, even at small breeding ratios.

2. Changes in the percentage of structural material from 5% to 20% in the tritium breeding zones lowers the breeding ratio but does not prevent breeding in reactors constructed of V, Mo, or SS. A Nb system, however, is more sensitive to the amount of structural material and for the UWMAK-I design, the blankets with more than 15% Nb in the lithium zones the breeding ratio is less than one. The range 0-15% can probably be extended by improved blanket design in that case.

3. Detailed energy production and deposition calculations using the MACK program developed at Wisconsin shows that the total energy produced per 14 MeV neutron is lower than previously assumed. For the UWMAK-I design, one finds a total energy production of 20 MeV per fusion reaction.

4. Enrichment of natural Li in ${}^6\text{Li}$ does not significantly effect energy multiplication and, given that it is an expensive process, such enrichment does not produce an economic gain. For UWMAK-I, enrichment to 50% ${}^6\text{Li}$ increases the energy multiplication by less than 1% over the natural lithium case.

5. The energy produced can be improved by addition of Be in the blanket and appears economical. For example, 4 cm and 10 cm of Be increases the total energy production by 9% and 19%, respectively. The additional costs appear to be less than half the decrease in cost per unit power.

6. A stainless steel reflector (or other iron containing material) is better than graphite. Thus, no graphite is used in the blanket of UWMAK-I. A SS reflector improves energy multiplication and energy attenuation. It also allows for a thinner reflector zone which allows the blanket and shield to be thinner and brings the magnets closer to the plasma, thus saving on magnet costs.

7. Shield optimization produces a thinner blanket and shield region than heretofore proposed.

8. Intercomparisons of Nb, V and SS show that, for tritium breeding, V is best followed by SS and Nb but for energy multiplication, Nb produces about 4% more energy than stainless steel or vanadium.

E. Blanket and Shield

1. 20% cold worked 316 stainless steel appears to be a reasonable choice for a CTR structural material to construct the first generation of Tokamak reactors. This conclusion is based on presently known thermal, mechanical, chemical and radiation damage information.

2. Lithium can be used as a reactor coolant in a Tokamak reactor. Proper design of flow paths can reduce the pumping power requirements to ~1.5% of the gross plant output.

3. The blanket and shield design for UWMAK-I will reduce the energy leakage to the magnet to 10^{-6} of that incident on the first wall.

4. The maximum temperature in the 316 SS will have to be limited to 500°C because of high corrosion rates in flowing lithium. This requirement limits the outlet Li temperature to 483°C and indicates a 283°C inlet temperature.

5. High pressure helium will be an effective and safe coolant for the UWMAK-I shield.

6. The first wall of a Tokamak reactor subjected to a 300 psia Li coolant pressure, an 22.6 watts/cm² surface wall loading and 13 watts/cm³ nuclear heating rate will have a thickness limited to not less than 0.9 mm and not more than 3.9 mm.

7. The first wall and structural components within the first 20 cm of the blanket will have to be replaced every 2 years because of radiation damage considerations. A replacement mechanism has been proposed and it appears that it will take 6 weeks every 2 years to replace the entire reactor heat removal cells.

8. Mechanisms for absorbing thermal expansion, maintaining vacuum during start up and shutdown and supporting the high module weights have been proposed.

F. Radiation Damage

1. The most severe limitation on the lifetime of the reactor wall is to restrict the uniform elongation to values above 0.5% during the components lifetime. Such a requirement at the temperatures in UWMAK-I limits the exposure to roughly 2 years at the maximum displacement rate of 18.2 dpa/year.

2. The use of 20% cold worked stainless steel will retard radiation induced swelling to <1% over the proposed 2 year wall lifetime. However, if a 10% swelling design limitation is placed on the first wall, it would have to be replaced every 5 years because of swelling alone. This design limit requires that a first wall made of ST 316 SS be replaced every 3 years.

3. The recycling of the first wall means that almost 246,000 kg of steel will have to be disposed of per year.

4. Swelling of some steel components which are farther than 30cm from the first wall will exceed 20% over a 30 year lifetime. It is possible that some of those components will have to be replaced, further increasing the radioactive waste disposal problem.

5. The production of helium at the rate of 298 appm yr^{-1} and its subsequent collection into bubbles will cause less than 1% swelling in 2 years and less than 7% in 30 years. However, the effects of such high helium concentrations on the void swelling phenomena are unknown.

6. Transmutation effects on the properties of 316SS appear to be minor provided the walls are changed every 2 years. A thirty year exposure would have the major effects of increasing the Mn content to >6%, increasing the Ti to ~0.2% and the V to ~0.9% while reducing the Fe content from 62% to 58%, and Ni from 14% to 13%.

7. Helium produced swelling in the B_4C of the shield is <2% over the lifetime of the reactor.

8. The major contribution to the wall erosion rates is the sputtering caused by the 14 MeV neutrons. This effect accounts for 65% of the total wall erosion rate which is 0.22 mm/year. Other major mechanisms and their fractional importance are (D,T) sputtering (5%), self ion sputtering (10%) and back scattered neutron sputtering (10%).

9. Blistering of 316 SS in UWMAK-I appears to be a serious but not prohibiting problem. Pessimistic wall erosion rates are ~0.024 mm/year or ~11% of the total.

10. Radiation damage of the superconducting material (NbTi) does not appear to be serious over the lifetime of the plant. There will probably be less than a 1°K drop in T_c and <2% change in J_c of the superconductor.

11. Radiation in the form of neutrons and gamma rays does not appear to be a problem for the Mylar super-insulation in the magnets.

12. The most severe problem for the superconducting magnets is the increase in resistivity for the Cu stabilizer. However, by increasing the Cu/Superconductor ratio and periodic annealing to room temperature, this problem can be solved.

G. Tritium

1. The breeding ratio of UWMAK-I is 1.49.
2. The release rate of tritium to the external environment is ~10 Ci/day based on a tritium inventory of ~13 kg in the primary lithium and 10 kg of externally stored lithium.
3. The use of yttrium to extract tritium from the primary lithium circuit appears reasonable enough to warrant further investigation.

H. Safety

1. At the present time there appears to be no serious personnel problems associated with the failure of superconducting magnets.
2. The 316 SS in the UWMAK-I blanket will become quite radioactive during operation, reaching 25% of its 2 year value in less than 2 hours.
3. The decay of the radioactivity in the 316 SS blanket is dominated by Fe-55 with a half life of ~30 years. It will take approximately 20 years to reduce the total radioactivity from ~310 curies/MW_{th} to <1 curie/MW_{th}.
4. On the basis of total number of curies generated in 2 years of operation, 316 SS produces about the same amount as Nb-1Zr but twice as much as V-20Ti. However, after ~2 months of decay, the activities of 316 SS and Nb-1Zr are equal and both are more than 8 times higher than V-20Ti.
5. From the standpoint of biological hazard potential, UWMAK-I has a Biological Hazard Potential index which is ~100-1000 times lower than a fission reactor at times close to shutdown.
6. The total amount of afterheat generated in the 316 SS blanket is ~28 Mw_{th} after 2 years of operation and ~33 megawatts after 30 years. Almost 50% of this afterheat is generated within the heat removal cells. This afterheat drops by a factor of 30 in ~20 years.
7. The maximum rate of temperature increase was calculated to be 0.1°C sec⁻¹ but it appears to be more like 0.01°C sec⁻¹ when convection and conduction forms of heat loss are considered. It is concluded that afterheat represents no serious problem even in the event of a loss of flow accident in UWMAK-I.
8. The total afterheat in UWMAK-I after shutdown and 10 years of operation is not particularly sensitive to blanket material. The value at shutdown varies from 0.55% to 0.1% of the operating power for the three metals studies here (316 SS, V-20Ti, Nb-1Zr). However, the afterheat in V-20Ti decays faster than the steel and Nb alloy and is at half the shutdown level after a month of decay.

9. A rupture in the lithium containment structure plus a resulting fire appears to be the most serious conventional safety problem for UWMAK-I. The conditions for fire are not well specified but it is concluded that reasonable safety measures can be instituted to reduce the hazard potential of such an accident should it occur.

XV. Recommendations

The major recommendations which have come from this conceptual design of a Tokamak fusion reactor are listed here by subject area. These recommendations relate to problem areas for reactors of the UWMAK-I type and therefore may not include areas of research that are important for the technical feasibility of other reactor concepts (e.g. mirrors, theta pinches, and laser systems). This chapter also will not include recommendations relevant to the non-nuclear aspects of the plant (e.g. steam cycle, economics, environmental impact, and unique building requirements) as these will be included in a subsequent report, Volume II of UWFD-68. This point should be kept in mind as the reader examines the following list.

A. Plasma

- 1) It is important to expand our knowledge of burn stability. This should include the effects of various transport mechanisms on burn stability. Much could be learned about this topic from the first prototype, D-T burner.
- 2) Research is required on transport processes in multispecies plasmas containing helium and higher Z impurities.
- 3) The various aspects of using energetic neutral beams to control the thermal burn should be investigated further.
- 4) A more detailed analysis is required of the effects of inverted temperature profiles that will be produced by only partially penetrating neutral beams. If such profiles do not extensively disrupt the discharge, neutral beams with energies ~ 100 KeV could be adequate for plasma heating.
- 5) Research on negative ion beams is necessary since high energy, quasi-steady-state, neutral beams are required either for penetration during heatup or for plasma control during the burn phase.
- 6) Fueling studies, in particular, the effects of pellet injection on plasma operation, are required. Analysis is also needed to better understand the physical processes involved as a pellet traverses a hot plasma.
- 7) Further research is needed on the stability of the plasma during the current rise phase with various values of I_p and, in particular, on the possibility of controlled or staged startups to mitigate against the need for large energy storage systems.

B. Divertor

- 1) Since divertors may be necessary, an experimental program aimed at understanding the basic aspects of divertor operation is required. Related directly to this is the need for further theoretical research on the transport processes taking place in the scrape-off region and on the influence of the neutral point in the poloidal magnetic field on the stability of the discharge.

The primary goal is to test and understand the efficiency of divertors in preventing particles from reaching the wall and the effect of the divertor on the confined plasma.

2) Further investigation is required to determine the energy spectrum of plasma particles reaching the walls in a system with a divertor.

3) Research is required to fully establish the viability of using liquid lithium as collecting surfaces to trap energetic particles (hydrogen isotopes and helium) which diffuse into the divertor and for vacuum pumping of cold neutral particles.

4) Further research is required into plasma-wall interactions, the effects of neutral gas in the diverted field zone, the impact of neutron sputtering, which may eject chunks of first wall material into the vacuum chamber, and on the blistering and sputtering caused by particles incident at grazing angles.

C. Magnets

1) Commercially available, large cross section, cryogenically stable conductors should be developed with provision for internal and/or external cooling.

2) Research programs should be initiated to develop ductile, less expensive, composite conductors from materials more generally available (preferably not based on Nb).

3) Research on the mechanical, electrical and thermal properties of stabilizer materials such as copper and aluminum at cryogenic temperatures should be conducted. These investigations should also include the effects of irradiation on the electrical resistivity of these metals under large stresses and with periodic warm-up.

4) Research is required to determine the mechanical and thermal properties, at cryogenic temperatures of structural materials such as aluminum, stainless steel, reinforced plastics, etc. which are required in the construction of large superconducting magnets.

5) The development of commercially available, inexpensive, load bearing insulation capable of spanning the temperature range from 1.8 to 300°K is required. The design of commercially stable conductors should also be studied.

6) The development of commercially available superfluid helium refrigerators in large sizes is needed, as is the development of large, commercially available, helium I refrigeration.

7) The heat transfer problems associated with superfluid helium is long hollow cryogenically stable conductors must be understood and solved.

8) Research is required on the minimization of A. C. losses in the cryogenically stable conductors of the divertor, transformer and toroidal field magnets.

9) An effective means of providing support for divertor, transformer and toroidal field magnets under earthquake loading should be investigated.

10) Development of control circuitry, power supplies and/or stored energy transfer equipment for pulsing the divertor and transformer magnets is required.

11) Control circuitry for providing lateral support of the toroidal field magnets under partial field failure must be developed to prevent severe bending moments which could cause vacuum leaks or pipe fractures within the nuclear island.

D. Neutronics and Photonics

1) Toroidal geometry transport equations and computer programs should be developed to adequately assess the leakage problems associated with fueling, heating and vacuum pumping ports in commercial reactors.

2) Charged particle (p, d, T & He) cross sections are inadequately known for most isotopes. Many of these cross sections and the energy distributions of the resultant particles should be measured and evaluated as a function of energy (1-15 MeV) as soon as possible.

3) Further information on secondary gamma and secondary neutron distributions are needed.

4) A careful program of integral experiments is required to test the validity of existing data and calculational techniques. This capability must be developed before the design of the initial power reactor is completed.

E. Blanket and Shield

1) The problem of periodic access to the first wall and its subsequent removal should be continuously examined. If we are not able to solve the radiation damage problems imposed on CTR materials, the development of the first wall replacement will have a large impact on CTR economics. Even if the radiation damage problems are solved, periodic access to the blanket will be required to repair routine failures of the thousands of welds and joints in a typical CTR which are to be expected from statistical considerations.

2) Experimental programs are required to verify the lithium pumping power requirements in high magnetic fields. Such facilities should be constructed and operated well before the design for the initial power plants is begun.

3) The corrosion rates of 316 SS in lithium should be studied as a function of flow rate, temperature, and coolant purity. The development of corrosion inhibitors for this particular system would greatly improve the economics of a stainless steel CTR.

4) The design and operation of very large hot cell facilities must be examined. It now appears that all currently envisioned fuel cycles will involve neutrons and hence large amounts of induced radioactivity in the CTR structures. This means that even routine maintenance (let alone first wall removal) will have to be accomplished by remote means.

5) Methods of making joints in lithium lines which are both leak tight and easy to disconnect remotely must be found.

6) An investigation of equipment capable of transporting over 3,000 metric tons (the weight of one UWMAK-I module) for distances of 100-500 meters should be initiated.

7) The availability of some prime material components for UWMAK-I must be closely examined. In particular, Ni, Cr, Mn and Nb (for magnets) reserves must be assessed relative to projected needs.

F. Radiation Damage

1) It is extremely important to assess the combined effect of high displacement damage (>30 dpa) and high helium contents (>600 appm) on the ductility of 316 SS at 300-650°C. Alloy development programs may have to be initiated to find more ductile but still readily available CTR structural materials if one wishes to construct economic CTR's.

2) Verification of the beneficial effect of cold working 316 SS before irradiation is necessary when examining its swelling behavior. In particular, it is necessary to see if swelling in CW 316 SS proceeds at a rate equal to or less than ST 316 SS beyond the incubation period required to produce voids in the cold worked material.

3) The synergistic effects of high helium concentrations on swelling in 316 SS (or other potential CTR materials for that matter) must be studied.

4) Blanket designs should be pursued that minimize the stresses and strains imposed by start up and shutdown. This will be necessary because of the extremely brittle nature of the CTR structure after a few months of operation.

5) The effect of high Mn (up to 6%), high Ti (up to 0.2%), and high V (up to 0.9%) content on the properties of 316 SS should be studied. The investigations should extend to swelling, embrittlement and corrosion behavior as well as mechanical properties.

6) Experimental programs should be conducted to evaluate the anomalously high sputtering coefficient of 14 MeV neutrons recently discovered. The potential of sputtering some of the highly radioactive first wall into liquid coolants as well as into the vacuum chamber should be closely examined.

7) Much more precise information on the fluxes and energy spectrum of the particles leaking from the plasma is required. Particular attention should be given to the helium ion energies and the effect of helium energy on blistering of 316 SS at temperatures of 300-650°C.

8) Blistering studies should be extended to the 10^{20} to 10^{21} cm^{-2} range to estimate the true wall erosion rate. Presently, linear extrapolations from low fluence data ($\sim 10^{18}$ - 10^{19}) are assumed to be valid without any proof.

9) Gas production cross sections for the isotopes of Mo are required to make a more meaningful comparison to other CTR materials.

10) The effect of neutron irradiation on the critical current of density of NbTi should be studied. The irradiations and testing should be carried out at 4.2°K and the effect of subsequent annealing at room temperature should be studied.

G. Tritium

1) Thermodynamic data is required for the following systems in the temperature range of 200-700°C.

- a) Li - T₂ - 316 SS
- b) Na - T₂ - 316 SS
- c) Li - T₂ - Y
- d) Na - T₂ - Y
- e) Li - T₂ - Zr

2) The effect of dissolved oxygen or nitrogen on the reactions in 1) is required.

3) The diffusion rates and solubility of tritium in 316 SS, Zr and Y is required in the range 200-700°C. It would also be helpful to know the effect of oxide coatings on the above information.

4) Experimental information on the fabrication and operation of yttrium hot traps is needed. Information such as the fabrication of yttrium of appropriate thickness, the effect of repeated extractions and charging cycles, and the effect of 316 SS corrosion products on the operation of the tritium extraction cells is required.

5) More quantitative information is needed on alternate tritium extraction schemes such as fused salt solvent extraction, electro-diffusion through ceramic membranes, etc.

6) An experimental program to test the reliability and performance of oxide or tungsten barrier coatings on stainless steel heat exchangers is needed. The compatibility of such coatings with liquid metals in a system with a large thermal gradients should be studied.

7) Experimental information on tritium leakage rates from large liquid metal valves, pumps and seals is required to assess the potential leakage rates. Such studies should also address the problem of how to extract the tritium from vacuum pump oil, etc.

8) There is a need to assess the modes of tritium release from Li during rupture of Li piping and/or Li fires (i.e. do such events lead to the formation of HT or HTO).

9) More detailed analysis is needed regarding the tritium inventory in vacuum pumps, recovery systems, structural metals, pellet fabrication devices and reserve fuel storage. Such an inventory is absolutely essential before realistic safety assessments can be made.

H. Safety

1) Methods must be developed to collect, store and ship several metric tonnes per year of radioactive corrosion products from the stainless steel.

2) More detailed calculations are required on the radioactivity levels at various maintenance points outside the reactor due to the deposition of 316 SS corrosion products.

3) Long term solutions to the concentration and storage of spent reactor components must be addressed. In particular, methods of handling ~250 metric tonnes of 316 SS heat removal cells per year must be developed. On site storage does not look attractive and central burial facilities should be investigated.

4) A detailed and complete analysis of the loss of coolant accident (both with the plasma on or off) should be made to insure that major damage will not occur in the CTR blanket.

5) Research must be continued into finding minimum activity materials which can operate at high temperatures, are economical, are compatible with CTR coolants, and are readily available to the United States.

6) A more complete analysis of the various ways in which tritium could be released in an operating CTR must be made. These release mechanisms should be clearly outlined and, if possible, the probabilities for their occurrence should be established.

Appendix A

Kerma Factor Results

Our efforts in the neutronics area resulted in a theoretical and computational algorithm for calculation of fluence-to-kerma factors.^(1,2) The computer program, MACK, which was written based on this algorithm to calculate kerma factors from nuclear data in ENDF format is described in reference 2. Since the neutron kerma factors have a wide range of application in other fields in addition to CTR, MACK was written as a general purpose program. It allows great flexibility in generating kerma factors. The energy mesh, group structure, weighting spectra, decay energies, and several other parameters are arbitrarily defined by input values as appropriate for the use to which the data will be applied.

In order to carry out the neutronics and photonics analysis given earlier in Chapter V, the neutron and gamma kerma factors and neutron cross sections by reaction were generated for materials of interest in a CTR. A list of these materials is given in Table A.1. The energy mesh, group structure, and weighting spectra used in generating this data is given next. The validity of the kerma factors calculated in this work is discussed in detail in reference 1. For the sake of completeness, a comparison of the neutron kerma factors obtained from present and previous work is included in this appendix.

A.1. Generation of Pointwise and Group Parameters

Pointwise and group libraries of kerma factors and partial cross sections were generated for CTR materials. A list of these materials is given in Table A.1 with the corresponding ENDF/B MAT numbers which are also used as the identification numbers in the libraries. The most recent ENDF/B III evaluations were used except for materials with MAT numbers 3023, 3111, and 3000. Fluorine was generated from the UK library data. MAT 3023 refers to vanadium data calculated from a recent ORNL evaluation⁽³⁾ which included $(n,n'\alpha)$ and $(n,n'p)$ reactions. The present ENDF/B evaluation for molybdenum (MAT 1111) does not provide any information about the $(n, \text{charged particles})$ reactions. Since the energy deposition by these reactions at high energy can be as large as 50% of the total neutron heating, it is necessary to include these reactions in kerma calculations. The molybdenum (n,p) cross sections in the UK library and the (n,α) cross sections given in reference 4 were used as zero-order approximations and added to the evaluation and the complete data set for molybdenum was given the identification number 3111.

Reactions considered in kerma factor calculations for each material are listed in Table A.2. Several evaluations of the present ENDF/B do not provide information about some of the important nuclear data such as the

(n,n' α) and (n,n'p) reactions. In all but a few evaluations, the individual level excitation cross sections are not provided for the (n, α) and (n,p) reactions. The total cross sections for these reactions are often given with an "effective" Q-value. The effect of such lack of information on the validity of the results has been investigated.

As explained in the main text, charged particle emission from the radioactive decay of residual nuclei should be included in calculating neutron kerma factors. The radioactive decay contribution is included with an arbitrary cut-off half-life of 50 days. The radioactive decay data such as half-lives, decay schemes, β endpoint kinetic energies, etc. given in the latest table of isotopes⁽⁵⁾ were used. The average β -particle kinetic energy was determined from the tables given in the MACK report.⁽²⁾ The calculated decay energies are tabulated in reference 1 for the appropriate reactions in each material.

The energy mesh used for generating the pointwise kerma factors is described next followed by a description of the group structure and weighting spectra used for calculating group parameters. Generation of gamma kerma factors is also discussed.

a. Pointwise Neutron Kerma Factors

The pointwise library was generated at 1000 energy points equally spaced in lethargy in three energy ranges. The first energy range extends from thermal energy to 1 eV with lethargy interval, ΔU , of 0.206; the second covers the 1 eV to 1 MeV energy range with ΔU of 0.204, and the third range employs a lethargy interval of 0.00677 from 1 to 15 MeV. The energy mesh emphasizes the 1 to 15 MeV energy range because of its importance in blanket and shield calculations. Since the neutron cross sections, and hence the kerma factors, show strong variation with energy in many nuclides in the 1 eV to 1 MeV range the energy mesh in this range was chosen such that there are at least five energy points within the boundaries of each group of the GAM-II energy group structure defined shortly. The ten energy points in the thermal range were found adequate to accurately describe a Maxwellian or any other appropriate weighting spectrum in this range.

The pointwise library was saved for future use such as 1-generating neutron energy release parameters and partial cross sections at any desired group structure; and 2-inclusion of pointwise kerma factors in nuclear data libraries such as the UK and ENDF/B evaluations.

b. Energy Group Neutron Kerma Factors and Partial Cross Sections

The multigroup neutron kerma factors and cross sections by reaction were generated from the pointwise data discussed above for the GAM-II one hundred group structure shown in Table V.C.1. The group average f_g , of an energy dependent parameter, $f(E)$, is obtained from

$$f_g = \frac{\int_{E_1}^{E_2} W(E) f(E) dE}{\int_{E_1}^{E_2} W(E) dE}$$

where E_1 and E_2 are the group energy limits and $W(E)$ is a weighting function. A discussion of the weighting spectra appropriate for fusion systems follows.

Weighting Spectrum

In choosing a weighting spectrum, $W(E)$, appropriate for fusion systems, it is desirable to use a single weighting function which is adequate for all materials at all spatial points. In the following, an attempt is made to develop a weighting scheme that introduces a minimal error in fusion system neutronics calculations.

In typical CTR systems, nearly monoenergetic neutrons impinge on the first wall; the blanket and shield are source free. As known from slowing down theory⁽⁶⁾, in the absence of absorption and inelastic scattering, the flux assumes a $1/E$ behavior below an asymptotic energy, E_{as} , which is roughly equal to $\alpha^3 E_s$ where E_s is the source energy and the parameter α is equal to $(A - 1/A + 1)^2$. For niobium and lithium, the parameter α is equal to .9579 and .5596 and for a 14 MeV source energy the asymptotic energy is equal to 12.4 and 2.5 MeV, respectively. The behavior of the flux changes significantly in the presence of non-elastic reactions. The presence of absorption has the effect of depressing the flux. Although the effect of inelastic scattering can not be treated analytically in most cases, its effect in qualitative terms is to change the $1/E$ energy dependence of $\phi(E)$ to E^{-n} with n roughly a constant within the energy limits of an energy group for a fine group structure.

Figure A.1 shows the flux, $\phi(E)$, versus energy at several spatial points in a typical blanket of a D-T fusion system. The blanket consists of a 1 cm niobium first wall, 42 cm region of 95% Li plus 5% Nb, a 20 cm stainless steel and a 7 cm Li region. The first wall inner radius (cylindrical geometry) is three meters and the blanket is followed by a one meter mixture of 70% stainless steel plus 30% B_4C . The neutron group fluxes were obtained from a 100 group transport calculation. $\phi(E)$ was obtained at the midpoint energy of each group by dividing the group flux by the energy width for the group. This method of calculating $\phi(E)$ does not provide accurate information about the exact variation of the flux within the groups but it suffices for our purposes here to assume a linear variation of the logarithm of the flux with the logarithm of energy within each group.

The first curve in Figure A.1a which covers the energy range above 1 KeV shows $\phi(E)$ versus E in the middle of the first wall. Since the mean free path for a 14 MeV neutron in niobium is about 4.5 cm (typical for other proposed first wall materials) a large portion of the source neutrons pass through the 1 cm thick first wall without collision. Hence, the flux in the first wall is high at 14 MeV and decreases very rapidly (faster than $E^{-1.5}$) as the energy decreases down to about 12 MeV. At lower energies, $\phi(E)$ varies with E as E^{-n} with n approximately 2.3 from 5 to 3 MeV, 1.8 from 3 to 1.5 MeV and 0.4 at lower energies. The second curve corresponds to the flux at a point 25 cm from the first wall, i.e. close to the middle of the lithium region. The qualitative behavior of this curve is the same as that of the first wall. The transition energy below which the flux assumes the E^{-n} behavior is, however, considerably lower and is approximately 6 MeV. Above the transition energy, the flux increases with E as E^5 which is more slowly than in the first wall and the absolute magnitude of $\phi(E)$ varies also with E as E^{-n} with an n of about 1.8 from 5 to 1.5 MeV and 0.5 at lower energies. The third plot in Figure A.1 is for $\phi(E)$ 50 cm from the first wall which is about two mean free paths (for a 14 MeV neutron) deep in the stainless steel region. The transition energy is about 6 MeV and the flux varies qualitatively with energy as in the lithium region but faster below the transition energy and slower above.

Figure A.1.b shows $\phi(E)$ versus E for E less than 1 KeV for the three blanket positions of Figure A.1.a. The general behavior of $\phi(E)$ at such low energies varies considerably with the position in the blanket and shield. The strong absorption of lithium-6 affects the spectrum markedly at such low energies in the lithium and neighboring regions. At these low energies, the fraction of neutrons scattered into this energy by inelastic scattering in structural material (5% by volume in the example considered here) and lithium decreases rapidly and most of the neutrons slowed down to this low energy range came from elastic scattering. In addition, because of the $1/v$ behavior of the (n,α) reaction in Li-6 the absorption increases so rapidly that the $1/E$ general behavior of $\phi(E)$ is no longer maintained. In the lithium region, flux shown in Figure A.1.b, $\phi(E)$ decreases as the energy decreases roughly as $E^{1/2}$ from about 100 down to 30 eV then linearly at lower energies. Since almost all neutrons in the first wall, at these energies come from the lithium region $\phi(E)$ in the first wall behaves roughly as that in the lithium. The third curve in Figure A.1b is for $\phi(E)$ 50 cm from the first wall which is several mean free paths for neutrons of intermediate energies. Because most of the neutrons below 1 KeV at such a point come from slowing down in iron rather than transport from the lithium region the $1/E$ behavior is maintained down to about 10 eV. Below about 2 eV, the flux in the iron region drops as the energy decreases because of absorption in iron and the decrease in the albedo at the lithium-iron interface. The behavior of $\phi(E)$ with E in the shield region below about 1 KeV is roughly the same as

in the lithium region because of the strong $1/v$ absorption in B-10 (the shield in the reference system discussed here employs 30% by volume B₄C).

In the energy range zero to 0.4 eV no information about the energy dependence can be obtained from the above calculations because the GAM-II group structure employed in these calculations has only one energy group covering this range. Predictions of the flux spectrum at such low energies is complicated by the presence of upscattering in addition to downscattering and strong absorption such as in Li-6 and B-10.

Upscattering is generally important only below a characteristic energy, E_m , of about 0.2 eV. In large systems with no sources from fast neutrons above E_m and no absorption the thermal flux is Maxwellian. In the presence of weak absorption, the neutron flux below E_m is conveniently fitted to a Maxwellian distribution with an empirical neutron temperature, T_n , which is related to the system thermodynamic temperature, T , by the relation⁽⁶⁾

$$T_n = T \left(1 + C \frac{\sigma_{a0}}{\xi \sigma_{s0}} \right)$$

where C is a constant of approximately 1.6, ξ is the average logarithmic energy decrement per collision, and $\sigma_{a0}(E)$ and $\sigma_{s0}(E)$ are the absorption and scattering cross sections at $E = kT$. The ratio $\sigma_{a0}/\xi\sigma_{s0}$ must be less than about 0.2 for the concept of the neutron temperature to be meaningful, otherwise the energy spectrum of thermal neutrons departs too much from Maxwellian. For natural lithium, the ratio $\sigma_a/\xi\sigma_s$ is about 260 at 20°C. Therefore, in natural or enriched lithium the energy spectrum of thermal neutrons is far from Maxwellian and will vary roughly linearly with energy as a result of the strong absorption of thermal neutrons in Li-6. The same conclusion is true for any system with a large concentration of B-10 or any other strong absorber. In any event, the energy range from zero to a few hundred electron volts is relatively unimportant in the blankets and shields of a D-T fusion reactor as will be seen later in this appendix.

In summary, the energy dependence of the CTR neutron flux can be divided into four energy ranges, thermal, epithermal up to about 1 KeV, slowing down or moderating region from about 1 KeV to a transition energy (approximately 12 MeV in the first wall and roughly 6 MeV in the rest of the blanket), and above the transition energy to 15 MeV. At thermal energies, the spectrum is not well known at present and $\phi(E)$ is likely to increase linearly with energy. From thermal to about 1 KeV, the energy spectrum of the neutrons varies with spatial position and $\phi(E)$ increases with energy in the first wall, the lithium, and high boron concentration regions and assumes $1/E$ behavior in other regions. From about 1 KeV to the transition energy, the flux decreases with energy

with a piecewise constant power of roughly 0.4 to 0.7 up to 1.5 MeV and 1.7 to 3 at higher energies. Above the transition energy, the flux increases (with a few exceptions) with energy as E^n with n between 3 and 30. Although the neutron energy spectra may be different for other blankets of different composition and configuration, the energy dependence is generally within these bounds.

Since the region above the transition energy is of great importance in calculating the various blanket parameters, a more detailed spectrum needs to be considered in this energy range. Because of ion motion the D-T neutron source has a Gaussian-like distribution of energy centered around 14.06 MeV. Therefore, the spectrum decreases with energy above 14.06 MeV. Again, this effect does not appear in the spectrum of Figure A.1 because the GAM-II group structure has only one energy group in the energy range 13.5 to 15.0 MeV.

A weighting spectrum that accounts for the energy distribution of the D-T neutrons was developed at LASL⁽⁷⁾. This spectrum is shown in Figure A.2 and has the form:

$$W(E) = \frac{A}{E} + B \int dT f(T) \exp \left\{ -\frac{5}{4} \frac{(E - E_0)^2}{E_0 KT} \right\}$$

where $f(T)$ is the fraction of the D-T neutrons which are generated when the plasma temperature is between T and $T + dT$. The broadening of the D-T neutron spectrum is taken into account in the exponential term. The average energy, E_0 , of a D-T neutron is 14.06 and the parameters A and B were chosen so as to put 25% of the flux into the 14 MeV peak⁽⁷⁾. Although the 14 MeV spectrum broadening was derived for Scyllac-type reactors (pulsed) it is fairly typical of all other reactor types.

The sensitivity of the energy group constants to variations in the weighting spectrum determines, to a large extent, the degree of elaboration required in spectrum weighting. Hence, it is necessary here to investigate the sensitivity of neutron group kerma factors and partial cross sections to changes in the weighting spectrum. Since the blanket and shield spectrum varies with energy to a power that varies in several energy ranges, the difference between the group constants obtained from flat and a $1/E$ weighting functions will be compared to the Maxwellian weighted constants. The effect of the D-T neutron energy distribution on high energy group constants will also be discussed.

Li-6, Li-7 and vanadium are chosen here for investigating the sensitivity of the group constants to variations in weighting spectra. Li-6 and Li-7 are chosen because the neutron spectrum in the blanket is affected most by these two materials. Furthermore, about 80% of the neutron heating is generated in the lithium region. Although the first wall is the most critical section from a heat removal point of view,

most of the energy deposition in the wall is generated by the secondary photons since the wall material is usually of a high atomic number. The sensitivity of group kerma factors to the weighting spectrum will be examined for vanadium because it has the highest neutron to gamma energy deposition ratio and also because the thermal group is unusually important in this material.

Table A.3 through A.5 show the kerma factor by group for flat, 1/E and LASL weighting spectra for Li-7, V, and Li-6, respectively. The results are presented for the groups that

- a. have the largest contributions to heat generation,
 - b. have fine cross section structure for these materials,
- and
- c. show the largest change in group constants for these weighting spectra.

As seen from Tables A.3 to A.5, changing the weighting spectrum, $W(E)$, from constant to 1/E changes the group kerma factors by less than 0.2% for groups of energies above 1 MeV. In this energy range, the kerma factors generally increase with energy and hence the 1/E weighting results in lower group average than the flat-weighted. In the KeV energy range, the difference between the group constants obtained from constant and 1/E weighting is higher than in the MeV range because the GAM-II group structure employs a wider lethargy range per group in this range. However, this difference is also small and about 0.5%.

The LASL weighting spectrum, W_L , is 1/E below 12.5 MeV and therefore, it reproduces the same 1/E group averaged constants in all but the first two groups. The 14 MeV peak in W_L increases with E up to 14.06 MeV then decreases. Since 14.06 is lower than the midpoint energy for the first group, the W_L -group averaged kerma factors for this group are smaller than those produced by 1/E weighting. The 14 MeV peak in W_L covers about two thirds of the energy width of the second group and is rapidly increasing with energy in this range. The largest difference between the W_L and 1/E weighted group kerma factors occur in this group and is about 1.4% for Li-7 and 5% for vanadium.

In contrast to all other energy groups, the thermal group in all three materials shows a large change of about 43% in group constants when the weighting spectrum is changed from constant to 1/E. This effect is due to the 1/v behavior of the kerma factors at thermal energies for the three materials. This in turn is due to the 1/v behavior of the Li^7 and $\text{V}(n,\gamma)$ and $\text{Li}^6(n,\alpha)$ cross sections. Questions relating to thermal group weighting are examined below.

In general, the kerma factors at thermal energies are much smaller than at higher energies. In the thermal energy range, elastic scattering and radiative capture are the only two mechanisms for energy deposition in most materials. The recoil energy from elastic scattering is very small because of the low incident energy. Although the binding energy for an additional neutron is relatively large in all materials, the

nuclide recoil energy from an (n, γ) reaction is small because of momentum conservation. Therefore, energy deposition by thermal neutron interactions is small in most materials. The three materials investigated in this section are among the exceptions. The thermal kerma factors is large for Li-7 because of β^- decay following radiative capture and are large for Li-6 because its (n, α) reaction is exothermic and has a large $1/v$ cross section at low energy. In these three materials, the energy release per reaction is constant at thermal energies (the energy dependence is extremely small). Therefore, the pointwise kerma factors vary inversely with \sqrt{E} . Thus, the change in the thermal group kerma factor due to changing $W(E)$ from constant to $1/E$ can be easily shown to be

$$C_1 = \frac{\bar{k}_a - \bar{k}_b}{\bar{k}_b} = \frac{E_2 - E_1}{\sqrt{E_1 E_2} \ln \frac{E_2}{E_1}}$$

where the subscripts a and b denote $1/E$ and flat-weighted quantities, respectively and E_1 and E_2 are the lower and upper energy limits of the group. With E_1 equal to .022 and E_2 equal to .414, C_1 is 43%. The change in the thermal group factor when the weighting function is changed from $W(E) = E$ to $W(E) = 1/E$ can also be obtained for $1/v$ kerma factors as

$$C_2 = \frac{\bar{k}_a - \bar{k}_c}{\bar{k}_c} = -1 + \frac{2}{3} \frac{\sqrt{E_1 E_2} (E_1 + \sqrt{E_1 E_2} + E_2) \ln E_2/E_1}{E_2^2 - E_1^2}$$

where the subscripts a and c denote $1/E$ and E -weighted quantities, respectively. C_2 is equal to 72% for E_1 equal to .022 and E_2 equal to .414 eV.

For $1/v$ pointwise kerma factors, the average over a Maxwellian distribution is simply

$$\bar{k}_m = \frac{\sqrt{\pi}}{2} \left(\frac{T_{no}}{T_n} \right)^{1/2} k_o$$

where T_n is the absolute temperature of the neutrons, T_{no} is the neutron temperature at reference energy E_o in the energy range where $1/v$ behavior prevails, and $k(R_o)$ is the pointwise kerma factor at E_o . The thermal group in the GAM-II group structure extends from .414 down to an arbitrary cut-off of .022 or lower. In the energyrange of 0.2 to 0.414 the upscattering can usually be ignored and the spectrum closely resembles

that at higher energies. The effect of using a Maxwellian weighting on the thermal group kerma factor is shown in Table A.6 for Li-6 at several neutron temperatures. From the results in this table, the following observations can be made. The flat weighting severely underpredicts the group average for a Maxwellian-like flux. The $1/E$ weighting is also unacceptable if the energy spectrum of thermal neutrons is Maxwellian with neutron temperature of about 300°K . It is also apparent from Table A.6 that changing the weighting spectrum from $1/E$ to Maxwellian in the energy range .2 to .414 eV has little effect on the group average. The group kerma factor averaged over a Maxwellian distribution decreases with the neutron temperature $T_n^{-1/2}$ and at about 700°K it is roughly equal to that obtained from $1/E$ weighting. For kerma factors and cross sections that exhibit $1/\sqrt{E}$ behavior, the average over $1/E$ weighting from E_1 to E_2 is equal to the average over a Maxwellian weighting from zero to E_2 if E_1 satisfies the equation

$$\sqrt{T} (\sqrt{E_2} - \sqrt{E_1}) = .433 \sqrt{E_1 E_2} \ln E_2/E_1$$

where T is the Maxwellian neutron temperature in energy units with the assumption that very little error is made in extending the upper limit of integration over the Maxwellian from E_2 to infinity. The above discussion about the thermal group averaging should not overemphasize the importance of this group. For the fusion blanket given earlier in this appendix the thermal group is of very little importance in calculating the neutron heating. However, for a nuclear system with a $1/E$ flux distribution and thermal neutrons following a Maxwellian distribution for 700°K representing only 1% of the integrated flux from thermal to 15 MeV, the neutron heating by thermal neutrons represents more than 20% of the total neutron heating in Li-6 and B-10. The effect of the weighting spectrum on the total neutron heating rate in Li-6, Li-7 and V is shown in Tables A.3 through A.5. In these tables, η_s is the neutron heating rate per unit fluence for uniform (GAM-II) group flux and η_w is the neutron heating rate per unit fluence for the first wall flux of the CTR blanket discussed earlier in this appendix. From these tables, it can be seen that η_w changes only about .1% when the weighting spectrum is changed from uniform to $1/E$. η_s changes by .06% for Li-7, 3.7% for vanadium and 7.4% for Li-6. The large change in η_s for vanadium and Li-6 essentially is because of the change in the kerma factor for the thermal group. In the uniform GAM-II group flux, the thermal group has 1% of the total population of neutrons. In a lithium blanket, however, the thermal neutron flux is only 10^{-10} of the total flux in a large portion of the lithium region with a maximum of roughly 10^{-5} at the lithium-iron interface in the reference design of Figure A.1. Therefore, the thermal group contribution to neutron heating is negligible in fusion blankets. The same conclusion is valid for magnet shields with high boron concentration.

From the above results, it is concluded that the group kerma factors and partial cross sections are relatively insensitive to weighting spectra which lie between $W(E) = \text{constant}$ and $W(E) = 1/E$ for groups above thermal.

This result is for GAM-II one-hundred group structure and is different for other group structures. A measure of the adequacy of the group structure is the sensitivity of the group constants to the weighting spectrum. In this context, it can be concluded that the GAM-II group structure is adequate for fusion systems in the energy range from 1 eV to about 12 MeV. Although Li-6, Li-7 and V were considered above, similar observations have been noted on other materials and it is believed that the results apply, in general, for all other materials investigated in this work.

From the study presented above, it is concluded that an appropriate weighting spectrum, $W(E)$, for D-T fusion systems is as follows. Above 1 KeV, the use of LASL weighting function is justified because it does reproduce the gross behavior of fusion spectra on one hand and the average group constants are relatively insensitive to detailed variations in the weighting spectrum on the other hand. This result applies only to fine group structures such as GAM-II one hundred group structure. Below 1 KeV, $W(E) = E$ is reasonable because 1 - the most important blanket and shield regions have neutron energy spectra that increase roughly linearly with energy, 2 - the group constants are relatively insensitive to more detailed variations in the weighting spectrum for fine group structures, and 3 - the energy range below 1 KeV is of little importance for neutron heating and reaction rates of interest in the regions where the neutron spectrum departs too much from $\phi(E) = cE$. The thermal group has a negligible effect on the neutronics results for the fusion systems considered in this work and it suffices to use $W(E) = E$ for thermal neutrons.

c. Gamma Kerma Factors

Gamma multigroup cross sections were generated with the MUG code for the 43 group structure shown in Table V.C.3. This group structure was constructed using an equal energy width of .75 MeV for groups above 8 MeV and .25 MeV in the 1 to 8 MeV range. The gamma cross section variation with energy for the most important CTR materials was taken into account in constructing this group structure.

The gamma kerma factors were generated on the same group structure with $1/E$ weighting.

A. 2. Comparison with Previous Work

Theoretical and computational models for calculation of fluence-to-kerma factors were developed earlier in this section. In the previous two subsections, the data libraries generated with these models were described and samples of the kerma factor results were presented earlier in Chapter V.

The question of the validity of these results is relatively complicated. In the thesis of Abdou⁽¹⁾, it is shown that these results are

indeed reliable as to the adequacy of the theoretical model and correctness of the computations. In the following, the comparison with previous work shows the importance of our study in providing reliable methods and data for accurate calculation of nuclear heating in CTR systems.

Most earlier kerma factor calculations were directed toward calculating kerma factors for elements which are major constituents in the human body. Several simplifying assumptions were usually employed.

The most notable of these are the neglect of the total contribution of some important reactions, ignoring the anisotropy of elastic scattering, failing to include the resonance contribution to appropriate reaction cross sections in several cases, and inadequate treatment of the partitioning of the energy deposition and secondary neutron and photon emission. In addition, none of the previous works has a general format or computational algorithm for calculating neutron fluence-to-kerma factors and the same effort had to be duplicated for each material or for a revision of the basic nuclear data for the same material.

The present work has the following merits over the previous work:

- 1 - development of a complete theoretical model for calculating the neutron kerma factors for all significant reactions based on accurate solution of the kinematics equations of nuclear reactions without incorporating any significant simplifying assumption,
- 2 - based on this theoretical model an efficient computational algorithm was developed for calculating neutron kerma factors directly from nuclear data in the widely used format ENDF/B. The computer program MACK which incorporates this algorithm processes all reactions significant to energy deposition and recognizes all of the multiplicity of data formats currently allowed by ENDF/B. Given also the fact that most of the other widely recognized data libraries such as the United Kingdom (UK) library can be converted to ENDF/B format by existing codes⁽⁸⁾ the neutron kerma factors can be processed with MACK using the most widely used, and in a sense the best, nuclear data currently available.
- 3 - an efficient treatment of the resonance region was built into the MACK program to calculate the contribution to cross sections from the resolved and unresolved resonance parameters including the Doppler effect,
- 4 - these theoretical and computational models are independent of the actual values of nuclear parameters, and as nuclear data is updated or new information becomes available the only requirement for calculating a new set of kerma factors is a few minutes of machine time,
- 5 - the contribution to energy deposition from radioactive decay of the residual nucleus of a nuclear reaction is calculated accurately. The Fermi theory (see references 1 and 2) of β^- decay is used to calculate the average kinetic energy of a β^- or β^+ particle for a given endpoint energy, E_0 , of the β -spectrum, and atomic number, Z , of the residual nucleus.
- 6 - the accuracy of the kerma factors calculated with the theoretical and computational algorithms of the present work is set only by the accuracy of the basic nuclear data used.

The most recent ENDF/B3 data and in some cases the UK data were used for calculating the neutron kerma factors presented here. The evaluation of these libraries are far from perfect as will be noted but due to the extensive efforts spent on preparing and revising these evaluations and their wide usage they represent the most recent and presumably the best data available at present. Thus it is fair to say that the neutron kerma factors presented in this work are calculated to the best of our present knowledge of nuclear data. The evaluations for materials of interest for CTR were investigated with particular care and revised to ensure that the kerma factors are adequately determined.

The most recent and extensive among the previous works is that of Ritts et al reported in references 9 and 10. They made an attempt to include a large number of significant reactions for several materials. However, their work has the following drawbacks which greatly affected the accuracy of their kerma factor results.

a - They assumed^(9,10) the evaporation model to be valid in all cases for describing the secondary neutron energy distribution from inelastic scattering to continuum and (n,2n) reactions. This assumption is known to be invalid in several cases; e.g. in the Be⁹ (n,2n) reactions. (The present work allows for a general format for describing the secondary neutron energy spectra.)

b - They also assumed⁽⁹⁾ that the nuclear temperature for this evaporation model can be calculated from the Fermi gas model the nuclear temperature θ as $\theta(E) = \sqrt{10E/A}$ where E and θ are in MeV. This relation is very approximate, particularly for magic or near magic and light nuclei.

c - The Ritts et al treatment of the inelastic scattering to the continuum yields particularly poor results for the following reasons. They always incorporated the evaporation model for representing the secondary neutron energy spectra which, if adequate, is valid only for true inelastic scattering to continuum, i.e. when the residual nucleus is left in the continuum energy range. However, the nuclear data they used combines all modes of inelastic scattering (level and continuum) for incident energies above certain energy (in rather arbitrary fashion in most cases) and the combined cross sections are identified as the cross sections for inelastic scattering to the continuum regardless of the state of the residual nucleus. Consequently, the secondary neutron energy distribution in such cases includes the discrete spectrum from level scattering and the use of an evaporation model for this secondary neutron spectrum yields poor results for the average energy of the secondary neutron. Furthermore, the solution of Ritts et al of the kinematics equation for inelastic scattering to the continuum relies on using the quantity Q_{\min} which is the Q-value for the minimum excitation energy for the continuum range in the residual nucleus. Since the data they used had a different definition of inelastic scattering to the continuum, Q_{\min} was given as zero in most of their nuclear data. Given the fact that Q_{\min} is typically a few MeV it is clear that the neutron kerma factors calculated in Ritts et al

were not correct in such cases. (The present work has intentionally avoided incorporating any Q-value in the calculations for inelastic scattering to the continuum for this reason. Rather, an accurate calculation of the known secondary neutron energy spectra was employed.)

d - In several cases, the anisotropy of the elastic scattering was entirely ignored in their work. This resulted in very poor kerma factors, particularly in the high energy range, as will be shown shortly. (Here, the anisotropy of both elastic and inelastic scattering are treated as accurately as the data permits.)

e - Some evaluations of nuclear data used by Ritts et al (O5R and ENDF/B1 & 2) provided the resonance parameters for the resonance region and the smooth cross sections given in this range were the background cross sections only. Due to the lack of a resonance treatment in Ritts technique, the contribution of the resonance cross sections was ignored in such cases. This affected their kerma factor results for elastic scattering and radiative capture in the resonance region. (The MACK program developed in the present work has a "built-in" capability for calculating the contribution from both the resolved and unresolved regions including the effect of Doppler broadening.)

f - No attempt was made in their work to calculate the excitation energy of the residual nucleus from the (n,2n) reaction and the gamma energy emission from this reaction was ignored, i.e. it was implicitly assumed to be deposited locally. This can be clearly seen from equation 17 in reference 9 and equation 12 in reference 10.

From the above discussion it is clear that large differences between the neutron kerma factor results obtained in the present work and those calculated by Ritts can be expected even if the nuclear data used in both works were the same because of the assumptions in the calculational and processing models. In addition, due to the frequent changes in basic nuclear data from one evaluation to another the nuclear data used by Ritts (O5R and ENDF/B1 & 2 libraries) several years ago is different in many instances from the most recent nuclear data used in the present work (ENDF/B3).

Tables A.8 through A.13 compare the neutron kerma factors obtained in the present work with those from Ritts et al for Li^6 , Li^7 , C^{12} , Nb and Fe. The neutron kerma factors in these tables of Ritts et al were obtained from the Radiation Shielding Information Center at ORNL. The comparison in Tables A.8 through A.13 shows that the difference between their results and ours is generally large, particularly in the 10 to 15 MeV energy range. The neutron kerma factors by reaction in their calculations are not available which makes it difficult to isolate the differences due to the calculational model from the differences arising from using different basic nuclear data. However, the sensitivity study of neutron kerma factors to variations in input nuclear parameters as discussed in

reference 1 shows that, in general, "reasonable" or "realistic" changes in nuclear parameters do not produce changes in neutron kerma factors as large as the difference between the results compared here. By "reasonable" or "realistic" changes in nuclear data, we mean changes that are within the "spread" of values reported in literature for a particular nuclear parameter. The sensitivity study shows, on the other hand, that a combination of assumptions such as ignoring the contribution of some important reactions, neglecting the resonance contribution, not including the anisotropy of elastic scattering, and inadequate treatment of the secondary neutron energy spectra do indeed produce large changes in neutron kerma factors similar to the differences between the results of this work and those of Ritts. While some of the differences can be shown to be due to differences in the basic nuclear data used in the two studies, differences exceeding 20% can generally be attributed to the different calculational model and processing techniques used. In the following, some of the large differences in Tables A.8 through A.13 are discussed.

Table A.10 shows that the neutron kerma factor for sodium obtained by Ritts et al is about 70% smaller than that obtained in this work in the energy range 10 to 15 MeV. This is one of a few examples for which the reason for the difference is obvious. In calculating the sodium kerma factors, they included only elastic and inelastic scattering and radiative capture. The present work included, in addition to these reactions, the (n,p), (n, α) and (n,2n) reactions. It is shown in reference 1 that the contribution of (n,p), (n, α) and (n,2n) reactions to the neutron kerma factor of sodium is more than 75% of the total from 10 to 15 MeV. Subtracting the contribution of these reactions from the k_n obtained with MACK shows that the Ritts result overestimates the kerma factor for the reactions which were included.

It is noted that their results are generally higher than ours in the energy range 10 to 15 MeV where the largest difference between the two works occur if the reactions included are the same in both cases. Further, it was noted that the difference is very large for materials in which energy deposition by elastic scattering represents a significant fraction of the total energy deposition. For example, the elastic scattering contribution to k_n at 15 MeV is about 16% in Li^6 and 29% in Li^7 . Ritts et al estimate k_n at 15 MeV about 13% higher for Li^6 and 51% higher for Li^7 than the current work. However, it is observed that if the center-of-mass anisotropy of the elastic scattering is ignored for Li^7 in the 10 to 15 MeV energy range (see reference 1) the result is only slightly higher than their result. Therefore, it is strongly suspected that they may have ignored the anisotropy of the elastic scattering.

Table A.11 shows the comparison between the kerma factor obtained here and that calculated by Ritts et al for niobium. The agreement between the two works is "unusually" good at high energy. That "compensation of error" has played an important role in this agreement can be seen by noting that the nuclear data used in the two works is different in this high energy range. In addition, the difference is large in the energy range 10 eV to a few KeV which is the resonance region for niobium. For practical reasons, we selected only a few

energy points at which to show the comparison in Tables A.8 through A.13. Table A.14 shows a detailed comparison between the niobium kerma factors of the two works at a finer energy mesh in the neighborhood of 1 KeV. These results were obtained directly from the two works without any interpolation. The basic nuclear data for niobium used in the present and in Ritts work is the same in the resonance energy region. These results show clearly that Ritts et al have ignored the resonance contribution entirely with the result that their neutron kerma factors are less than 5% of the actual values. At 1 KeV, their k_n is only about 0.4% of our value. Since the contribution to the neutron kerma factor at 1 KeV comes from elastic scattering and radiative capture; and since elastic scattering is isotropic in this energy range, the results obtained in the present work can easily be checked by hand calculations as shown at the end of Table A.14.

In reference 1, a method was developed for investigating the consistency of the neutron kerma factor results by comparing the neutron heating rate obtained from these kerma factors with that obtained from an energy balance over a finite volume of space for which the neutron flux and surface current are known. The method was then used to verify the results of the present work. When similar calculations are carried out with the neutron kerma factors obtained by Ritts et al, it is found that the energy balance is destroyed.

TABLE A.1

A list of materials of interest for use in CTR for which the following libraries were generated:

1. Pointwise neutron kerma factors and partial cross sections,
2. 100 neutron energy group kerma factors and partial cross sections; and
3. 43 gamma energy group kerma factors.

Material	ENDF B MAT	Material	ENDF/B MAT
He	1088	Cu-63	1085
Li-6	1115	Cu-65	1086
Li-7	1116	Cr	1121
N-14	1133	Ni	1123
O-16	1134	Fe	1180
H-1	1148	W-182	1060
Be-9	1154	W-183	1061
B-10	1155	W-184	1062
B-11	1160	W-186	1063
C-12	1165	Mo	1111
Al-27	1135	Mo	3111
Na-23	1156	Ta-181	1126
V	1017	Ta-182	1127
V	3023	Pb	1136
K	1150	Nb	1164

Table A.2
REACTION TYPES

For the Purpose of Kerma Calculation, The Nuclear Reactions
are Classified Into the Following Types

	<u>REACTION TYPE</u>	<u>MC</u>
1- (n,n)	Elastic	2
2- (n,n') γ	Inelastic Level	51-90
3- (n,n') γ	Inelastic Continuum	91
4- (n,m') $a_{c_1}, a_{c_2} \dots$	(n,m') Charged Particles m = 1 or 2	22,23,24,28 and 51-91 with Flag LR
5- (n, $a_{c_1}, a_{c_2}, a_{c_3} \dots$)	(n, Charged Particles)	103-109 700-799
6- (n, γ)	Radiative Capture	102
7- (n,2n)		15

TABLE A.3 Sensitivity of Lithium-7 Group Kerma Factor* to Weighting Spectrum (for GAM-II 100 Group Structure)

Group	Midpoint Energy (eV)	W(E) = constant A	W(E) = $\frac{1}{E}$ B	LASL W(E)	% change $\frac{B-A}{A} \times 100$
1	1.350 (+7)	3.3350 (+6)	3.3330 (+6)	3.3129 (+6)	- 0.06010
2	1.221 (+7)	3.1206 (+6)	3.1192 (+6)	3.1613 (+6)	- 0.04480
3	1.105 (+7)	2.9534 (+6)	2.9519 (+6)	a	- 0.05080
4	1.000 (+7)	2.7811 (+6)	2.7795 (+6)	a	- 0.05750
5	9.048 (+6)	2.5689 (+6)	2.5672 (+6)	a	- 0.06620
6	8.187 (+6)	2.3699 (+6)	2.3684 (+6)	a	- 0.06330
7	7.408 (+6)	2.2096 (+6)	2.2085 (+6)	a	- 0.04980
8	6.703 (+6)	2.1480 (+6)	2.1479 (+6)	a	- 0.00467
12	4.493 (+6)	1.9452 (+6)	1.9443 (+6)	a	- 0.04630
20	2.019 (+6)	7.6184 (+5)	7.6116 (+5)	a	- 0.08900
35	4.505 (+5)	1.3049 (+5)	1.3042 (+5)	a	- 0.05360
40	2.732 (+5)	2.7099 (+5)	2.7261 (+5)	a	+ 0.60000
61	5.531 (+3)	2.5279 (+3)	2.5220 (+3)	a	- 0.23300
81	3.727 (+1)	8.4222 (+3)	8.4430 (+3)	a	+ 0.24700
93	1.855 (+0)	3.6935 (+4)	3.7034 (+4)	a	+ 0.26800
99	4.140 (-1)	7.8485 (+4)	7.8690 (+4)	a	+ 0.26120
100	2.180 (-1)	1.3664 (+5)	1.9468 (+5)	a	+42.50000
		4.7472 (+5)	4.7503 (+5)	4.7525 (+5)	+ 0.06530
	ns				
	n _w	7.9548 (+5)	7.9498 (+5)	7.9208 (+5)	- 0.06290

* in units of electron volt . barn/atom
a = same as (B)

TABLE A.4 Sensitivity of Vanadium Group Kerma Factor* to Weighting Spectrum (for GAM-II 100 Group Structure)

Group	Midpoint Energy (eV)	W(E) = constant A	W(E) = $\frac{1}{E}$ B	LASL W(E)	% change $\frac{B-A}{A} \times 100$
1	1.350 (+7)	1.2692 (+6)	1.2671 (+6)	1.2459 (+6)	- 0.1654
2	1.221 (+7)	1.0264 (+6)	1.0246 (+6)	1.0758 (+6)	- 0.1755
3	1.105 (+7)	8.4191 (+5)	8.4065 (+5)	8.4065 (+5)	- 0.1496
4	1.000 (+7)	7.1644 (+5)	7.1550 (+5)	7.1550 (+5)	- 0.1312
5	9.048 (+6)	6.1716 (+5)	6.1646 (+5)	6.1646 (+5)	- 0.1134
6	8.187 (+6)	5.4255 (+5)	5.4201 (+5)	5.4201 (+5)	- 0.0995
7	7.408 (+6)	4.8465 (+5)	4.8423 (+5)	4.8423 (+5)	- 0.0867
8	6.703 (+6)	4.3868 (+5)	4.3834 (+5)	4.3834 (+5)	- 0.0775
12	4.493 (+6)	3.1761 (+5)	3.1741 (+5)	3.1741 (+5)	- 0.0630
20	2.019 (+6)	1.7928 (+5)	1.7908 (+5)	1.7908 (+5)	- 0.1115
35	4.505 (+5)	5.5182 (+4)	5.5458 (+4)	5.5458 (+4)	+ 0.5000
40	2.732 (+5)	5.4378 (+4)	5.4193 (+4)	5.4193 (+4)	- 0.3402
61	5.531 (+3)	1.1487 (+5)	1.1258 (+5)	1.1258 (+5)	- 1.9935
81	3.727 (+1)	1.3368 (+5)	1.3401 (+5)	1.3401 (+5)	+ 0.2470
93	1.855 (+0)	5.9293 (+5)	5.9449 (+5)	5.9449 (+5)	+ 0.2631
99	4.140 (-1)	1.2555 (+6)	1.2588 (+6)	1.2588 (+6)	+ 0.2630
100	2.180 (-1)	2.1956 (+6)	3.1375 (+6)	3.1375 (+6)	+ 42.8994
	η_s	2.5747 (+5)	2.6699 (+5)	2.6729 (+5)	+ 3.6975
	η_w	2.9305 (+5)	2.9258 (+5)	2.8960 (+5)	- 0.1604

* in units of electron volt . barn/atom

TABLE A.5 Sensitivity of Lithium-6 Energy Group Kerma Factor to Weighting Spectrum (for GAM-II Group Structure)

Energy Group	Midpoint Energy (eV)	W(E) = constant A	LASL W(E) B	%change $\frac{B-A}{A} \times 100$
1	1.350 (+7)	4.4111 (+6)	4.4003 (+6)	- 0.24480
2	1.221 (+7)	4.2642 (+6)	4.2925 (+6)	+ 0.66360
3	1.105 (+7)	4.1545 (+6)	4.1537 (+6)	- 0.01920
4	1.000 (+7)	4.0258 (+6)	4.0246 (+6)	- 0.02980
5	9.048 (+6)	3.8981 (+6)	3.8972 (+6)	- 0.02308
6	8.187 (+6)	3.7756 (+6)	3.7743 (+6)	- 0.03443
7	7.408 (+6)	3.6184 (+6)	3.6171 (+6)	- 0.35920
8	6.703 (+6)	3.4670 (+6)	3.4658 (+6)	- 0.03460
12	4.493 (+6)	2.9809 (+6)	2.9802 (+6)	- 0.02348
20	2.019 (+6)	2.0076 (+6)	2.0068 (+6)	- 0.03985
35	4.505 (+5)	2.1352 (+6)	2.1378 (+6)	+ 0.12170
40	2.732 (+5)	1.0099 (+7)	1.0137 (+7)	+ 0.37630
61	5.531 (+3)	9.0078 (+6)	9.0310 (+6)	+ 0.25750
81	3.727 (+1)	1.0982 (+8)	1.1011 (+8)	+ 0.26400
93	1.855 (+0)	4.9245 (+8)	4.9375 (+8)	+ 0.26400
99	4.140 (-1)	1.0429 (+9)	1.0457 (+9)	+ 0.26850
100	2.180 (-1)	1.8239 (+9)	2.6063 (+9)	+ 42.90000
	η_s	1.0878 (+8)	1.1684 (+8)	+ 7.40900
	η_w	4.9424 (+6)	4.9455 (+6)	+ 0.06272

TABLE A.6 Lithium-6 Thermal Group Kerma Factor for Various
Weighting Spectra

Energy Range	W (E)	k (thermal group kerma factor)
.022 < E < .414	constant	1.8239 (+9)
.022 < E < .414	1/E	2.6063 (+9)
.001 ≤ E ≤ .200	Maxwellian (300 ⁰ K)	3.9140 (+9)
.200 ≤ E ≤ .414	1/E	
0 ≤ E ≤ .414	Maxwellian (300 ⁰ K)	3.9609 (+9)
0 ≤ E ≤ .414	Maxwellian (600 ⁰ K)	2.8008 (+9)
0 ≤ E ≤ .414	Maxwellian (1000 ⁰ K)	2.1695 (+9)

TABLE A.7 Comparison of Neutron Kerma Factors Obtained from
Present Work and from Ritts et al. Data for Lithium-6*

ENERGY (eV)	MACK (A)	RITTS (B)	% difference $\frac{B-A}{A} \times 100$
15.00 (+6)	7.1779 (-6)	8.1176 (-6)	+ 13.09
13.74 (+6)	6.9865 (-6)	7.5881 (-6)	+ 8.61
12.58 (+6)	6.7908 (-6)	7.1611 (-6)	+ 5.45
11.52 (+6)	6.6443 (-6)	6.8483 (-6)	+ 3.07
10.06 (+6)	6.3442 (-6)	6.3711 (-6)	+ 0.42
9.08 (+6)	6.1675 (-6)	6.1610 (-6)	- 0.10
8.10 (+6)	5.8950 (-6)	5.9246 (-6)	+ 0.50
7.19 (+6)	5.5890 (-6)	5.8186 (-6)	+ 4.10
6.05 (+6)	5.1959 (-6)	5.6248 (-6)	+ 8.25
5.16 (+6)	4.9160 (-6)	5.0907 (-6)	+ 3.55
4.08 (+6)	4.5948 (-6)	4.5653 (-6)	- 0.64
3.18 (+6)	3.8316 (-6)	3.8070 (-6)	- 0.64
2.01 (+6)	3.1263 (-6)	3.0693 (-6)	- 1.82
1.55 (+6)	2.9606 (-6)	2.9596 (-6)	- 0.03
1.07 (+6)	2.8308 (-6)	3.1239 (-6)	+ 10.35
7.88 (+5)	2.7697 (-6)	3.2987 (-6)	+ 19.09
2.57 (+5)	2.5420 (-5)	2.2755 (-5)	- 10.48
1.17 (+5)	5.5352 (-6)	6.6766 (-6)	+ 20.62
5.73 (+4)	5.3700 (-6)	7.0333 (-6)	+ 30.97
1.37 (+4)	.98464(-5)	1.1797 (-5)	+ 19.79
1.02 (+3)	3.5715 (-5)	3.6355 (-5)	+ 1.79
5.46 (+1)	1.5488 (-4)	1.5570 (-4)	+ 0.53
9.16 (+0)	3.7861 (-4)	3.8432 (-4)	+ 1.50
1.00 (+0)	1.1465 (-3)	1.1492 (-3)	+ 0.23

* in units of erg . barn/atom

TABLE A.8 Comparison of Neutron Kerma Factors* Obtained from Present Work and from Ritts et al. Data for Lithium-7

ENERGY (eV)	MACK (A)	RITTS (B)	% difference $\frac{B-A}{A} \times 100$
15.00 (+6)	5.5610 (-6)	8.4077 (-6)	+ 51.19
13.74 (+6)	5.2127 (-6)	8.1303 (-6)	+ 55.97
12.58 (+6)	4.9426 (-6)	7.7682 (-6)	+ 57.17
11.52 (+6)	4.7118 (-6)	7.4047 (-6)	+ 57.15
10.06 (+6)	4.3100 (-6)	6.6240 (-6)	+ 53.69
9.08 (+6)	3.9599 (-6)	5.9849 (-6)	+ 51.14
8.10 (+6)	3.6304 (-6)	5.3451 (-6)	+ 47.23
7.19 (+6)	3.4451 (-6)	4.7421 (-6)	+ 37.64
6.05 (+6)	3.5092 (-6)	4.0888 (-6)	+ 16.51
5.16 (+6)	3.2791 (-6)	3.6657 (-6)	+ 11.79
4.08 (+6)	2.8070 (-6)	2.8084 (-6)	+ .05
3.18 (+6)	1.9212 (-6)	1.9025 (-6)	- .97
2.01 (+6)	1.1483 (-6)	1.1252 (-6)	- 2.01
1.55 (+6)	8.7685 (-7)	8.6984 (-7)	- .79
1.07 (+6)	6.0570 (-7)	5.9150 (-7)	- 2.34
7.88 (+5)	4.1466 (-7)	4.0516 (-7)	- 2.29
2.57 (+5)	9.2739 (-7)	9.3050 (-7)	+ .33
1.17 (+5)	3.1988 (-8)	2.7903 (-8)	- 12.77
5.73 (+4)	1.8157 (-8)	1.5379 (-8)	- 15.29
1.37 (+4)	6.1561 (-9)	4.7871 (-9)	- 22.24
1.02 (+3)	3.3403 (-9)	3.7655(-10)	- 88.72
5.46 (+1)	1.1955 (-8)	1.9531 (-8)	+ 63.37
9.16 (+0)	2.8068 (-8)	4.5971 (-8)	+ 63.78
1.00 (+0)	8.6508 (-8)	1.4156 (-7)	+ 63.63

* in units of erg . barn/atom

TABLE A.9 Comparison of Neutron Kerma Factors* Obtained from Present Work and from Ritts et al. Data for Carbon

ENERGY (eV)	MACK (A)	RITTS (B)	% difference $\frac{B-A}{A} \times 100$
15.00 (+6)	6.1465 (-6)	6.5561 (-6)	+ 6.66
13.74 (+6)	5.0155 (-6)	5.0326 (-6)	+ 0.34
12.58 (+6)	4.3233 (-6)	3.9690 (-6)	- 8.19
11.52 (+6)	3.6849 (-6)	3.0202 (-6)	- 18.04
10.06 (+6)	1.9683 (-6)	1.7594 (-6)	- 10.61
9.08 (+6)	2.1572 (-6)	1.6399 (-6)	- 23.98
8.10 (+6)	2.3454 (-6)	2.1192 (-6)	- 9.64
7.19 (+6)	.9734 (-6)	1.0411 (-6)	+ 6.95
6.05 (+6)	1.2718 (-6)	1.2718 (-6)	0.00
5.16 (+6)	1.1282 (-6)	1.1038 (-6)	- 2.16
4.08 (+6)	1.6244 (-6)	1.6637 (-6)	+ 2.42
3.18 (+6)	1.3670 (-6)	1.2754 (-6)	- 6.70
2.01 (+6)	7.5542 (-7)	7.6059 (-7)	+ 0.68
1.55 (+6)	6.6223 (-7)	6.6836 (-7)	+ 0.92
1.07 (+6)	5.6210 (-7)	5.7267 (-7)	+ 1.88
7.88 (+5)	4.8137 (-7)	4.9239 (-7)	+ 2.28
2.57 (+5)	2.2506 (-7)	2.2980 (-7)	+ 2.10
1.17 (+5)	1.1477 (-7)	1.1659 (-7)	+ 1.58
5.73 (+4)	5.9139 (-8)	5.9989 (-8)	+ 1.44
1.37 (+4)	1.4709 (-8)	1.4919 (-8)	+ 1.42
1.02 (+3)	1.1085 (-9)	1.1289 (-9)	+ 1.84
5.46 (+1)	5.9389(-11)	6.0507(-11)	+ 1.88
9.16 (+0)	1.0222(-11)	1.0098(-11)	- 1.21
1.00 (+0)	1.9662(-12)	1.1039(-12)	- 43.85

* in units of erg . barn/atom

TABLE A.10 Comparison of Neutron Kerma Factors* Obtained from
Present Work and from Ritts et al. Data for Sodium

ENERGY (eV)	MACK (A)	RITTS (B)	% difference $\frac{B-A}{A} \times 100$
15.00 (+6)	4.8781 (-6)	1.3787 (-6)	- 72.00
13.74 (+6)	4.9535 (-6)	1.3001 (-6)	- 74.00
12.58 (+6)	4.9771 (-6)	1.1905 (-6)	- 76.00
11.52 (+6)	4.5227 (-6)	1.1133 (-6)	- 75.00
10.06 (+6)	3.8837 (-6)	9.9110 (-7)	- 74.00
9.08 (+6)	2.4656 (-6)	8.6723 (-7)	- 65.00
8.10 (+6)	2.0279 (-6)	8.2005 (-7)	- 59.00
7.19 (+6)	1.3328 (-6)	7.6774 (-7)	- 42.00
6.05 (+6)	1.0607 (-6)	7.7151 (-7)	- 27.00
5.16 (+6)	8.3001 (-7)	7.7395 (-7)	- 6.75
4.08 (+6)	7.2651 (-7)	6.6941 (-7)	- 7.86
3.18 (+6)	6.1180 (-7)	5.6253 (-7)	- 8.05
2.01 (+6)	4.7496 (-7)	5.4073 (-7)	+ 13.84
1.55 (+6)	3.1112 (-7)	3.7786 (-7)	+ 21.45
1.07 (+6)	4.529 (-7)	4.9608 (-7)	+ 9.53
7.88 (+5)	4.3213 (-7)	5.0191 (-7)	+ 16.15
2.57 (+5)	1.1632 (-7)	1.0345 (-7)	- 11.06
1.17 (+5)	5.3342 (-8)	4.9424 (-8)	- 7.34
5.73 (+4)	3.3171 (-8)	4.4720 (-8)	+ 34.81
1.37 (+4)	8.1779 (-9)	9.2012 (-9)	+ 12.50
1.02 (+3)	8.5143 (-9)	4.2942 (-9)	- 49.56
5.46 (+1)	10.5491 (-9)	7.5355 (-9)	- 28.56
9.16 (+0)	2.5090 (-8)	1.8581 (-8)	- 25.90
1.00 (+0)	7.5943 (-8)	5.6718 (-8)	- 25.31

* in units of erg . barn/atom

TABLE A.11 Comparison of Neutron Kerma Factors* Obtained from
Present Work and from Ritts et al. Data for Niobium

ENERGY (eV)	MACK (A)	RITTS (B)	% difference $\frac{B-A}{A} \times 100$
15.00 (+6)	1.7772 (-6)	1.7531 (-6)	- 1.35
13.74 (+6)	1.6317 (-6)	1.6219 (-6)	- .60
12.58 (+6)	1.4356 (-6)	1.4315 (-6)	- .30
11.52 (+6)	1.2498 (-6)	1.2469 (-6)	- .24
10.06 (+6)	9.8998 (-7)	9.8203 (-7)	- .80
9.08 (+6)	8.3228 (-7)	8.2467 (-7)	- .91
8.10 (+6)	6.7931 (-7)	6.6569 (-7)	- 2.00
7.19 (+6)	5.4666 (-7)	5.3838 (-7)	- 1.51
6.05 (+6)	4.2712 (-7)	4.6278 (-7)	+ 8.34
5.16 (+6)	3.5191 (-7)	3.7405 (-7)	+ 6.29
4.08 (+6)	2.7143 (-7)	2.8913 (-7)	+ 6.52
3.18 (+6)	2.1575 (-7)	2.3167 (-7)	+ 7.37
2.01 (+6)	1.8243 (-7)	1.9505 (-7)	+ 6.91
1.55 (+6)	1.5944 (-7)	1.6412 (-7)	+ 2.93
1.07 (+6)	1.4511 (-7)	1.4413 (-7)	- 0.67
7.88 (+5)	1.3251 (-7)	1.3125 (-7)	- .95
2.57 (+5)	4.3537 (-8)	6.0453 (-8)	+ 38.86
1.17 (+5)	2.3153 (-8)	3.0315 (-8)	+ 30.93
5.73 (+4)	1.2249 (-8)	1.5008 (-8)	+ 22.52
1.37 (+4)	3.3501 (-9)	3.0714 (-9)	- 8.32
1.02 (+3)	10.0080(-10)	2.8076(-12)	- 99.72
5.46 (+1)	2.4066(-11)	1.1725(-11)	- 51.27
9.16 (+0)	3.1067(-11)	2.8655(-11)	- 7.76
1.00 (+0)	8.8335(-11)	8.6642(-11)	- 1.91

* in units of erg . barn/atom

TABLE A.12 Comparison of Neutron Kerma Factors* Obtained from Present Work and from Ritts et al. Data for Iron

ENERGY (eV)	MACK (A)	RITTS (B)	% difference $\frac{B-A}{A} \times 100$
15.00 (+6)	5.3687 (-6)	4.3778 (-6)	- 18.45
13.74 (+6)	4.9265 (-6)	3.7608 (-6)	- 23.66
12.58 (+6)	4.2257 (-6)	2.8277 (-6)	- 33.08
11.52 (+6)	3.4529 (-6)	2.1430 (-6)	- 37.94
10.06 (+6)	2.5111 (-6)	1.3942 (-6)	- 44.47
9.08 (+6)	1.9716 (-6)	1.1217 (-6)	- 43.11
8.10 (+6)	14.5796 (-7)	8.7463 (-7)	- 39.99
7.19 (+6)	11.2692 (-7)	6.8986 (-7)	- 38.78
6.05 (+6)	7.8779 (-7)	6.1223 (-7)	- 22.28
5.16 (+6)	6.0528 (-7)	4.3938 (-7)	- 27.41
4.08 (+6)	4.5956 (-7)	4.8268 (-7)	+ 5.03
3.18 (+6)	3.6801 (-7)	2.0940 (-7)	- 43.09
2.01 (+6)	2.5213 (-7)	1.7642 (-7)	- 30.02
1.55 (+6)	2.0984 (-7)	1.7399 (-7)	- 17.08
1.07 (+6)	10.6412 (-8)	9.3105 (-8)	- 12.50
7.88 (+5)	2.7814 (-7)	1.2859 (-7)	- 53.77
2.57 (+5)	3.6043 (-8)	3.3166 (-8)	- 7.98
1.17 (+5)	1.2461 (-8)	2.2335 (-8)	+ 79.24
5.73 (+4)	1.4445 (-8)	1.3377 (-8)	- 7.39
1.37 (+4)	2.3094 (-9)	3.3023 (-9)	+ 42.99
1.02 (+3)	5.3061(-10)	5.2481(-10)	- 1.09
5.46 (+1)	8.6046(-11)	8.9645(-11)	+ 4.18
9.16 (+0)	1.3083(-10)	1.1687(-10)	- 10.68
1.00 (+0)	3.7890(-10)	3.4598(-10)	- 8.68

* in units of erg . barn/atom

TABLE A.13 Comparison of Neutron Kerma Factors^{*} Obtained from
Present Work and from Ritts et al. Data for Beryllium

ENERGY (eV)	MACK (A)	RITTS (B)	% difference $\frac{B-A}{A} \times 100$
15.00 (+6)	6.2053 (-6)	1.1918 (-5)	+ 92.06
13.74 (+6)	.54154 (-5)	1.1609 (-5)	+114.30
12.58 (+6)	.48806 (-5)	1.0955 (-5)	+124.40
11.52 (+6)	.4334 (-5)	1.0369 (-5)	+139.30
10.06 (+6)	3.8381 (-6)	9.2613 (-6)	+141.30
9.08 (+6)	3.5878 (-6)	8.5437 (-6)	+138.10
8.10 (+6)	3.3678 (-6)	7.8777 (-6)	+133.90
7.19 (+6)	3.1346 (-6)	6.9825 (-6)	+122.70
6.05 (+6)	2.9031 (-6)	5.9107 (-6)	+103.50
5.16 (+6)	2.6148 (-6)	5.0177 (-6)	+ 91.89
4.08 (+6)	2.3722 (-6)	3.8639 (-6)	+ 62.88
3.18 (+6)	2.3402 (-6)	3.2239 (-6)	+ 37.76
2.01 (+6)	1.1102 (-6)	1.0273 (-6)	- 7.46
1.55 (+6)	8.1354 (-7)	7.6024 (-7)	- 6.55
1.07 (+6)	8.2838 (-7)	8.6286 (-7)	+ 4.16
7.88 (+5)	7.4371 (-7)	7.5710 (-7)	+ 1.80
2.57 (+5)	3.1838 (-7)	3.2117 (-7)	+ .87
1.17 (+5)	1.7944 (-7)	1.7622 (-7)	- 1.79
5.73 (+4)	9.5500 (-8)	9.2990 (-8)	- 2.62
1.37 (+4)	2.3833 (-8)	2.3022 (-8)	- 3.40
1.02 (+3)	1.7825 (-9)	1.7159 (-9)	- 3.73
5.46 (+1)	9.6003 (-11)	9.2855 (-11)	- 3.27
9.16 (+0)	1.7957 (-11)	1.7778 (-11)	- .99
1.00 (+0)	7.8243 (-12)	9.0808 (-12)	+ 16.05

* in units of erg . barn/atom

**Table A.14 Detailed Comparison of Niobium Kerma Factors obtained
in the Present Work with that by Ritts et al**

Present Work		Ritts et al Work	
E (eV)	k_n (E) eV·barn/atom	E (eV)	k_n (E) eV·barn/atom
8.8772 (+2)	98.87	8.7800 (+2)	2.84
9.0912 (+2)	22.49(+1)	9.1490 (+2)	1.85
9.5348 (+2)	59.47(+1)	9.5169 (+2)	1.81
9.7646 (+2)	16.01(+1)	9.8847 (+2)	1.78
1.0000 (+3)	425.20(+1)		
1.0241 (+3)	62.47(+1)	1.0252 (+3)	1.75
1.0488 (+3)	18.71(+1)	1.0620 (+3)	1.72
1.0741 (+3)	17.33(+1)	1.0988 (+3)	1.70
1.100 (+3)	37.69(+1)	1.1356 (+3)	0.71

Note:

At 1 KeV, the following parameters are given as can be calculated from ENDF/B (the values are the same in version II and version III)

Elastic scattering:

at 300°K $\sigma_{\text{resonance}} = 36.489$ barn, $\sigma_{\text{background}} = 0.0$

$\cos \theta_{\text{c.m.}} = 0.0$

$E_r = 21.250$ eV $k_{\text{elastic}} = 775.4$ eV·barn/atom

Radiative capture

at 300°K, $\sigma_{\text{resonance}} = 11.082$ barn, $\sigma_{\text{background}} = .1013$ barn

$Q = 7.2139$ MeV, $E_r = 310.86$ eV, $k = 3476.6$ eV·barn/atom

References for Appendix A

1. M. A. Abdou, "Calculational Methods for Nuclear Heating and Neutronics and Photonics Design for CTR Blankets and Shields," A doctoral thesis, Nuclear Engineering Department, University of Wisconsin - July 1973.
2. M. A. Abdou, C. W. Maynard and R. Q. Wright, "Mack: A Computer Program to Calculate Neutron Energy Release Parameters (Fluence-to-Kerma Factors) and Multigroup Neutron Reaction Cross Sections from Nuclear Data in ENDF Format," ORNL-TM-3994; also issued as University of Wisconsin Fusion Design Memo 37 - January 1973.
3. S. K. Penny and L. W. Owen, "A Re-Evaluation of Vanadium Neutron and Gamma-Ray Production Cross Sections," ORNL-TM-4007 - November 1972.
4. W. E. Alley and R. M. Lessler, "Semiempirical Neutron-Induced Reaction Cross Sections," UCRL-50484 Rev. 1 - August 1972.
5. C. M. Lederer, J. M. Hollander, and I. Perlman, "Table of Isotopes," 6th edition, John Wiley and Sons, New York - 1967.
6. G. I. Bell and S. Glasstone, "Nucleus Reactor Theory," Van Nostrand R. Comp. - 1970.
7. D. W. Muir, Los Alamos Scientific Laboratory, private communication - December 1972.
8. R. Q. Wright et al., "UKAEA to ENDF/B Translation . . .," ORNL-TM-2880; also ENDF-134.
9. J. J. Ritts, M. Solomito, and P. N. Stevens, "Calculations of Neutron Fluence-to-Kerma Factors for the Human Body," Nucl. Applic. and Tech., 7(1) 89-99 - July 1969.
10. J. J. Ritts, M. Solomito, and D. Steiner, "Kerma Factors and Secondary Gamma-Ray Sources for Some Elements of Interest in Thermonuclear Blanket Assemblies," ORNL-TM-2564 - June 1970.

Appendix B

Neutron flux spectra are given in the following table for three positions in UWMAK-I blanket and shield. The first position is at 1 mm depth from the inner surface of the first wall (first wall thickness in neutronics calculations is 4 mm). The second position is 25 cm from the first wall, i.e. about the mid point of the lithium region (mid point of zone 5 in Figure V-B-13). The third position is in the outer region of the shield and lies inside zone 18 (90% Pb plus 10% SS) of Figure V-B-13 at about 140 cm from the first wall.

The fluxes are given for 46 neutron energy groups. The energy group boundaries are also given so that differential fluxes ($\phi(E)$) can be easily derived if desired.

Neutron Flux Spectrum at Three Positions in
UWMAK-I Blanket and Shield
(neutron wall loading = 1.25 MW/m²)

Group No.	Upper Energy (eV)	Flux in First Wall (1 mm from inner surface)		Flux in the middle of the primary lithium region (25 cm from first wall)	Flux in outer region of the shield (140 cm from the first wall)
1	1.4918 (+7)	1.02213	+14	9.83993 +12	6.62715 +7
2	1.3499 (+7)	5.71820	+12	5.70295 +12	5.49278 +7
3	1.2214 (+7)	3.80135	+12	2.98739 +12	4.00829 +7
4	1.1052 (+7)	5.48941	+12	2.56123 +12	3.16662 +7
5	1.0000 (+7)	4.69964	+12	2.17718 +12	2.57225 +7
6	9.0484 (+6)	3.82653	+12	1.82353 +12	2.18966 +7
7	8.1873 (+6)	3.11143	+12	1.61462 +12	1.73834 +7
8	7.4082 (+6)	2.69767	+12	1.43955 +12	1.80589 +7
9	6.7032 (+6)	2.42107	+12	1.27724 +12	1.50987 +7
10	6.0653 (+6)	2.32419	+12	1.20624 +12	1.52173 +7
11	5.4881 (+6)	2.22100	+12	1.14026 +12	1.42409 +7
12	4.9659 (+6)	2.21289	+12	1.11277 +12	1.56637 +7
13	4.4933 (+6)	2.26542	+12	1.13842 +12	2.01804 +7
14	4.0657 (+6)	2.42901	+12	1.20611 +12	2.42804 +7
15	3.6788 (+6)	2.63525	+12	1.30976 +12	3.01858 +7
16	3.3287 (+6)	2.90263	+12	1.45668 +12	4.36128 +7
17	3.0119 (+6)	3.29001	+12	1.63389 +12	5.59405 +7
18	2.7253 (+6)	3.81248	+12	1.80854 +12	7.38495 +7
19	2.4660 (+6)	1.32089	+13	6.25939 +12	4.90319 +8
20	1.8268 (+6)	1.57116	+13	7.39396 +12	8.30737 +8
21	1.3534 (+6)	1.68548	+13	8.15028 +12	1.37398 +9
22	1.0026 (+6)	1.81145	+13	9.36440 +12	2.27956 +9
23	7.4274 (+5)	2.12012	+13	1.19366 +13	3.22083 +9
24	5.5023 (+5)	2.04969	+13	1.26897 +13	2.52429 +9
25	4.0762 (+5)	1.60409	+13	9.31201 +12	3.99929 +9
26	3.0197 (+5)	5.70661	+12	2.97706 +12	4.10519 +9
27	2.2371 (+5)	1.92206	+13	1.33260 +13	4.21262 +9
28	1.6573 (+5)	2.56284	+13	1.96858 +13	4.40452 +9
29	1.2277 (+5)	4.10730	+13	3.48089 +13	8.58064 +9
30	6.7379 (+4)	3.14386	+13	2.87672 +13	8.66369 +9
31	3.1828 (+4)	2.34361	+13	2.14113 +13	6.52663 +9
32	1.5034 (+4)	1.77938	+13	1.61259 +13	4.65802 +9
33	7.1017 (+3)	1.40619	+13	1.25051 +13	2.89565 +9
34	3.3546 (+3)	9.08034	+12	8.40879 +12	1.33097 +10
35	1.5846 (+3)	4.84094	+12	4.66020 +12	4.47701 +9
36	7.4852 (+2)	2.37074	+12	2.25055 +12	1.35254 +8
37	3.5358 (+2)	9.61259	+11	8.97951 +11	3.49475 +7
38	1.6702 (+2)	3.11505	+11	2.87076 +11	7.90038 +6
39	7.8893 (+1)	7.87407	+10	7.16153 +10	1.60853 +6
40	3.7267 (+1)	1.53249	+10	1.36041 +10	3.03628 +5
41	1.7603 (+1)	2.29795	+9	1.90567 +9	5.42471 +4
42	8.3153 (+0)	2.68982	+8	1.87862 +8	9.28483 +3
43	3.9279 (+0)	2.52431	+7	1.25240 +7	1.53939 +3
44	1.8554 (+0)	2.00425	+6	6.11660 +5	2.47391 +2
45	8.7643 (-1)	1.62317	+5	5.03177 +4	3.83356 +1
46	4.1399 (-1)	1.58639	+4	1.01745 +4	5.03167 +0

C. Standard free energies of formation of some oxides, carbides, nitrides and sulfides.^a

Compound	ΔF_f° kcal/g-atom 0		Compound	ΔF_f° kcal/g-atom 0	
	800°K	1500°K		800°K	1500°C
	<u>Oxides</u>			<u>Carbides Continued</u>	
Li ₂ O	-177	-92	Mo ₂ C	-13.1	-14.4
Cr ₂ O ₃	-72	-59	TiC	-42.0	-39.9
FeO	-50	-38	ZrC	-46.1	-44.7
NiO	-41	-27	HfC	-53.2	-51.5
Ta ₂ O ₅	-80.7	-66.9	ThC ₂	-23.0	-21.8
NbO	-80.7	-66.7			
WO ₂	-52.8	-38.6		<u>Nitrides</u>	
ReO ₂	-35	-22	Li ₃ N	-20.1	+3.8
Mo ₂	-52.8	-38.5	CrN	-13.2	+0.1
TiO	-106.9	-92.9	Fe ₄ N	+6.7	+16
ZrO ₂	-112.5	-97.0	Ta ₂ N	-48.5	-36.1
HfO ₂	-115.1	-100.3	Nb ₂ N	-43.3	-29.2
ThO ₂	-128	-112	W ₂ N	-0.2	+14.5
			Mo ₂ N	+0.2	+14.9
	<u>Carbides</u>		TiN	-62.5	-47.0
Li ₂ C ₂	-12.2	-10.4	ZrN	-69.2	-53.6
Cr ₄ C	-17.6	-18.6	HfN	-70.1	-54.8
Fe ₃ C	+1.8	-0.6	Th ₃ N ₄	-59.7	-44.0
Ni ₃ C	+5.2	+4.5			
TaC	-33.9	-34.0		<u>Sulfides</u>	
Nb ₂ C	-44.1	-42.3	WS ₂	-23.5	-10.2
W ₂ C	-14.5	-21.6	ReS ₂	-31.0	-5.1
			Mo ₂ S ₃	-28.0	-15.5

^aData summarized by J. O. Cowles and A. D. Pasternak, UCRL-50647, April 1969.

Appendix C

A. Enthalpies and free energies of lithium reactions^a

Reaction	ΔH°_{298} kcal	ΔF°_{298} kcal
$2 \text{ Li(c)} + 1/2 \text{ O}_2 \rightarrow \text{Li}_2\text{O(c)}$	-142.750	-133.950
$2 \text{ Li(c)} + \text{O}_2(\text{g}) \rightarrow \text{Li}_2\text{O}_2(\text{c})$	-151.9	-138.1
$\text{Li(c)} + 1/2 \text{ H}_2(\text{g}) + 1/2 \text{ O}_2(\text{g}) \rightarrow \text{LiOH(c)}$	-116.589	-105.676
$\text{Li(c)} + 3/2 \text{ H}_2(\text{g}) + \text{O}_2(\text{g}) \rightarrow \text{LiOH} \cdot \text{H}_2\text{O(c)}$	-188.926	-163.437
$\text{Li(c)} + \text{H}_2\text{O}(\ell) \rightarrow \text{LiOH(c)} + 1/2 \text{ H}_2(\text{g})$	-48.7	-48.99
$\text{Li(c)} + \text{H}_2\text{O}(\ell) \rightarrow \text{LiOH (in H}_2\text{O)} + 1/2 \text{ H}_2(\text{g})$	-53.142	
$\text{Li(c)} + 1/2 \text{ F}_2(\text{g}) \rightarrow \text{LiF(c)}$	-146.300	-139.650
$\text{Li(c)} + 1/2 \text{ Cl}_2(\text{g}) \rightarrow \text{LiCl(c)}$	-97.700	-92.500
$\text{Li(c)} + 1/2 \text{ I}_2(\text{g}) \rightarrow \text{LiI(c)}$	-64.790	(-62.200)
$3 \text{ Li(c)} + 1/2 \text{ N}_2(\text{g}) \rightarrow \text{Li}_3\text{N(c)}$	-47.500	-37.300
$\text{Li(c)} + 1/2 \text{ H}_2(\text{g}) \rightarrow \text{LiH(c)}$	-21.61	-16.72
$2 \text{ Li(c)} + 3/2 \text{ CO}_2(\text{g}) \rightarrow \text{Li}_2\text{CO}_3(\text{c}) + 1/2 \text{ C(c)}$	-148.6	-128.4
$2 \text{ Li(c)} + 3 \text{ CO(g)} \rightarrow \text{Li}_2\text{CO}_3(\text{c}) + 2 \text{ C(c)}$	-210.45	-171.38
$\text{Li(c)} + \text{NH}_3(\text{g}) \rightarrow \text{LiNH}_2(\text{c}) + 1/2 \text{ H}_2(\text{g})$	-32.46	
$2 \text{ Li(c)} + 2 \text{ C(c)} \rightarrow \text{Li}_2\text{C}_2(\text{c})$	-14.2	

B. Free energies of formation of oxides in kilocalories per gram mole of oxygen^{b,c}

Temperature °C	ΔF for Li_2O	ΔF for $1/2 \text{ ZrO}_2$	ΔF for $1/3 \text{ Y}_2\text{O}_3$
520	-117	-113	-120
722	-110	-108	-116
927	-103	-104	-111
1128	- 96	- 99	-106

a. Data summarized by J. O. Cowles and A. D. Pasternak, UCRL-50647, April, 1969.

b. Data summarized by W. M. Phillips, Corrosion by Liquid Metals, Ed. Draley and Weeks, Plenum Press, New York, 1970, p. 223 ff.

c. Data from J. P. Coughlin, "Contributions to the Data on Theoretical Metallurgy," Vol. XII, Inorganic Oxides, Bureau of Mines Bulletin 542, U. S. Printing Office, 1954.

Volume II

UWMAK-I

A WISCONSIN TOROIDAL FUSION REACTOR DESIGN

by

The University of Wisconsin Fusion Feasibility Study Group

B. Badger	J. W. Lue
H. Avci	H. Pearlman ^(b)
R. W. Boom	D. Schluderberg ^(e)
E. Cameron	T. Sung
R. W. Conn	I. Sviatoslavsky
D. Graber	D. Sze
A. B. Johnson ^(a)	W. F. Vogelsang ^(d)
G. L. Kulcinski	L. J. Wittenberg ^(d)
P. G. Lorenzini ^(b)	T. F. Yang ^(a)
C. W. Maynard	J. R. Young ^(a)
E. Normand ^(c)	W. Young

May 1975

Fusion Technology Program
Nuclear Engineering Department

University of Wisconsin

Madison, Wisconsin 53706

UWFEM - 68 Vol. II

- (a) Battelle Northwest Laboratories
- (b) Atomics International Division, Rockwell International
- (c) Sargent and Lundy Corporation
- (d) Monsanto Research Corporation
- (e) Babcock and Wilcox

Preface

The purpose of this report is to present a comprehensive view of the

- . Power cycle
- . Site and structure design
- . Environmental impact
- . Resource Requirements
- and . Economic considerations

of the hypothetical fusion power plant UWMAK-I which was described in Volume I of UWFD-68. We have also included some new ideas which occurred to us after Volume I was written. Even though every attempt was made to correct any discrepancies between the two volumes that may have resulted as a result of these ideas, some may still persist and we apologize for those errors.

It is quite possible that some of the numbers or ideas expressed here may have to be changed in the first few months after this issue. Therefore, we have tried to make each chapter as self-consistent as possible so that pages can be removed and inserted without disrupting an orderly numbering sequence of tables, figures, references, etc. in other chapters. The reader will note that each copy of this report is numbered and periodically replacement pages will be sent to the owner to update this report.

The preparation of this report represented no small task and we must commend several people for their skill, patience and dedication in the assembly of this document. Mrs. Connie Linehan did a remarkable job of typing the report and coordinating the secretarial activities. She was ably assisted by Mrs. Suzan Steindorf and Mrs. Debby Kamperschroer.

We enthusiastically acknowledge the financial support received from the Wisconsin Electric Utilities Research Foundation and the US Energy Research and Development Administration Division of Controlled Thermonuclear Research. Without their help and encouragement we would not have been able to pursue this very important study.

G. L. Kulcinski

R. W. Conn

Summary

The details of the balance of plant studies (power cycle, plant layout, environmental impact, resource requirements and economics) for the D-T Tokamak fusion power plant UWMAK-I are given in this volume. A previous document, University of Wisconsin Fusion Design Memo-68, Volume I, contains the details of the nuclear island part of this plant. Volume I includes the plasma physics, divertor design, magnet design, blanket and shield characteristics, neutronic and photonic calculations, radiation damage and tritium extraction considerations.

The reactor is a lithium cooled stainless steel structure which produces 5000 MW_t for a 90 minute burn time and requires approximately 6 1/2 minutes to recharge the transformer coils. The fusion energy is deposited in a primary lithium coolant ($T_{\max} = 489^{\circ}\text{C}$) and then transferred to the steam generator (pressure = 2000 psia, $T = 404^{\circ}\text{C}$) via a secondary sodium loop ($T_{\max} = 456^{\circ}\text{C}$). The design of intermediate Li-Na heat exchangers, Croloy-2 1/4 steam generators is given along with a complete turbine generator cycle design. The gross electrical output of the plant is maintained at a constant level of 1681 MWe by diverting ~7% of the secondary sodium into storage tanks during the 90 minute burn. This sodium is then used during the recharge cycle to generate steam while the lithium flow in the primary circuit removes the decay heat from the blanket. It has been determined that ~208 MWe of the plant output is required to maintain the plant components which means that 1473 MWe are available for sale. This is overall efficiency of 32%.

The design of a building which provides a vacuum of 1 torr around the reactor is described along with the plant layout for lithium loops, sodium loops, steam generating equipment, tritium extraction facilities, turbine-generator units, cooling towers, etc. Other special building considerations such as superconducting stored energy facility, harmonic filter building, switch yards, gas storage and cooling towers are also outlined.

The potential problems of siting a reactor like UWMAK-I have been considered. Such problems as plant size, stray magnetic fields, radioactive isotopes or the potential for large "conventional" accidents have been given preliminary consideration and the conclusion is drawn that the release of tritium is still the most serious problem to be faced. Various scenarios show that the equilibrium release rates of tritium to the environment should be within current regulatory limits but that such limits may be exceeded following a release of 1% of the tritium at ground level under the worst climatic conditions. No accident which would actually result in such a release has been envisioned. The use of 100 m high stacks can considerably reduce the magnitude of this problem.

It was shown that the materials resource demands of a UWMAK-I type reactor may be quite severe, especially for Cr. Approximately 144 metric tonnes of metal are required per electrical megawatt. Roughly 60% of this demand is for Fe, 10% for Pb, 8% for Na, 7% for Cr, 6% for Ni, 5% for Cu and 1% each for Mn, Li and B.

The cost of the UWMAK-I power plant was estimated following standard procedures for economic evaluation of nuclear power plants. It was found that the capital cost of the present plant would be \$971 per MWe and that the operating costs were ~ 21mills per kW-hr.

It was concluded that since the UWMAK-I reactor represents a first attempt at a detailed and self consistent reactor, the operating conditions, power output and economic costs were within reason. Several areas of further work were clearly outlined including such items as a superconducting stored energy facility design, methods for reducing tritium leakage, need for evacuated buildings, shielding requirements for personnel, need for reduced reliance on Cr containing alloys, and research into finding blanket materials which will have longer reactor lifetimes.

TABLE OF CONTENTS

	<u>Page</u>
Preface	
Summary	
Overview	1
I. Power Cycle	
A. Introduction and General Philosophy of Coolant System	I-1
B. Blanket Cooling System	I-1
1. Primary Lithium Loop	I-1
2. Secondary Sodium Loop	I-9
3. Steam System	I-11
a. Sodium to Water Steam Generator Design	I-11
b. Turbine-Generator System	I-19
i) Turbine	I-19
ii) Condenser	I-19
iii) Generator	I-19
iv) Condensate and Feedwater Systems	I-21
C. Divertor Cooling System	I-23
D. Shield Cooling System	I-23
E. Cooling Tower Requirements for UWMAK-I	I-23
F. Auxiliary Electrical Requirements for UWMAK-I	I-27
G. Electrical Equipment	I-27
H. Conclusions	I-27
I. Recommendations	I-31
II. Overall Layout	
A. Overview of Layout	II-1
B. Reactor Building	II-1
1. Primary Containment	II-7
2. Secondary Containment	II-7
3. Lithium Floor	II-8
4. Sodium Floor	II-8
5. HVAC Equipment Floor	II-9
C. Hot Cells	II-9
D. Auxiliary Building	II-10
E. Turbine Building	II-10
F. Service Building	II-10
G. Additional Buildings	II-10
1. Diesel-Generator Building	II-10
2. Helium Gas Storage Building	II-11
3. Energy Storage Building	II-11
H. Electrical Areas	II-11
I. Cooling Towers	II-11
J. Recommendations	II-11

	<u>Page</u>
III. Environmental Impact	
A. Introduction and General Environment Considerations	III-1
1. Siting Considerations	III-1
2. Magnetic Fields	III-2
3. Resources	III-3
4. Thermal Effects	III-5
B. Plant Effluents During Normal Operations	III-8
C. Plant Accidents	III-13
1. Safety Analysis and Design Philosophy	III-13
2. Safety Analysis of UWMAK-I	III-15
3. Specific Accident Considerations for the UWMAK-I	III-20
a. Lithium Fires	III-20
b. Loss of Cooling Accidents	III-20
c. Magnet Failures	III-21
d. Helium Release Accidents	III-23
e. Summary	III-23
D. Long Term Storage of Radioactive Waste and Transportation Problems	III-23
1. Radioactive Waste Storage	III-23
2. Transportation of Fuels and Radioactive Materials	III-32
IV. Materials Resource Considerations	
A-1. Introduction	IV-1
A-2. Materials Requirements for UWMAK-I	IV-1
a. Nuclear Island Requirements	IV-1
b. Materials Requirements for Balance of Plant	IV-4
B. Lithium Reserves and Resources	IV-11
1. Types of Lithium Deposits	IV-11
a. Pegmatite Deposits	IV-11
b. Brine Deposits	IV 11
C. Chromium Reserves and Resources	IV-15
1. Geologic Occurrence	IV-15
2. Reserve and Resource Data	IV-15
3. Other Sources	IV-15
D. Nickel Resources	IV-22
1. Occurrence of Nickel	IV-22
2. Reserves and Resources of Nickel	IV-23
3. Comments on U.S. and World Resources	IV-23
4. Selected References	IV-24
E. Copper Resources	IV-28
1. Geological Occurrence	IV-28
2. Stratabound Deposits in Sedimentary Rocks	IV-28
3. Volcanogenic Deposits	IV-29
4. Replacement Deposits	IV-29
5. Seafloor Nodules	IV-29
6. Reserves and Resources	IV-29
7. World Resources	IV-31
F. Titanium	IV-36
1. Types of Titanium deposits	IV-36
2. Sources of Data and Limitations	IV-36
3. Availability of Titanium at 3X and 10X Present Price Levels	IV-37

4.	World Identified Resources	IV-37
5.	Environmental Considerations	IV-38
G.	Aluminum Reserves	IV-41
1.	Introduction	IV-41
2.	Other Sources of Aluminum	IV-41
3.	Other Problems	IV-41
H.	Vanadium	IV-46
1.	Introduction	IV-46
2.	Sources of Data, Limitations and Definitions	IV-46
3.	Types of Vanadium Deposits	IV-46
4.	Resources of Vanadium	IV-46
5.	World Reserves and Resources	IV-48
6.	References	IV-48
I.	Molybdenum	IV-52
1.	Geology	IV-52
2.	Reserves and Resources	IV-53
3.	References	IV-53
J.	Niobium Reserves and Resources	IV-56
1.	Introduction	IV-56
2.	Geologic Occurrence	IV-56
3.	Reserves and Resources	IV-57
4.	Selected References	IV-58
K.	Summary Report on the Availability of Metals for the U.W. Tokamak Reactor	IV-60
1.	Introduction	IV-60
2.	316 SS	IV-60
3.	Lead	IV-62
4.	Copper	IV-63
5.	Lithium	IV-63
6.	Niobium	IV-63
7.	Titanium	IV-63
8.	Boron	IV-64
9.	Aluminum	IV-64
10.	Summary	IV-64
V.	Economics	V-1
A.	Introduction	V-1
B.	The UWMAK-I Operating Cycle	V-1
C.	Fusion Reactor Plant Factor	V-5
1.	The Biennial Wall Replacements	V-5
2.	Unscheduled Outage Time	V-6
3.	The Length of the Burn Period	V-6
4.	The Length of the Rejuvenation Period	V-8
5.	The General Plant Factor Correlation	V-10
6.	Summary	V-13
D.	Capital Costs	V-35
E.	The Electricity Production Cost	V-35
1.	The Operations and Maintenance Costs	V-35
a.	Salaries	V-35
b.	Miscellaneous Supplies and Equipment	V-36
c.	Outside Support Services	V-39
d.	Miscellaneous Costs	V-39
e.	General and Administrative Costs	V-39
f.	Replacement of Inner Walls	V-39
g.	Coolant Makeup	V-41

	<u>Page</u>
h. Working Capital Requirements	V-41
i. Total Operations and Maintenance Costs	V-41
2. The Fuel Costs	V-41
3. The Annual Return on Capital	V-42
4. The Total Electricity Cost	V-42
VI. Conclusions	VI-1
A. Power Cycle	VI-1
B. Plant Layout	VI-1
C. Environmental Impact	VI-2
D. Materials Resources	VI-3
E. Economics	VI-3
Appendix A Basis for Capital Cost Estimates for UWMAK-I	A-1
Appendix B Cost Data for 15 MWh Energy Storage Unit	B-1

OVERVIEWI. Introduction

The recent advances in magnetic confinement of hot plasmas have generated considerable optimism regarding the prospects of generating electrical power from the controlled fusion process. Much of this optimism is based on the success of the Tokamak confinement concept. Given these steps forward, it is proper and timely to begin serious studies of the technological aspects of power generation from the fusion process. In 1972, a group of scientists and engineers at the University of Wisconsin with cooperation from various industrial organizations initiated a design study of a large electrical power generating station based on the Tokamak concept and fueled with deuterium and tritium. The goal has been to develop a self consistent study from the standpoint of plasma physics, neutronics, materials, magnets, power cycle, environment, resources, and cost. The design details of the "nuclear island" portion of a 5000 MW_{th} D-T Tokamak conceptual power reactor called UWMAK-I (University of Wisconsin Tokamak) have been given in Volume I of the UWFDM-68. The purpose of Volume II is to present the "balance of plant" considerations for UWMAK-I. After a brief summary of the overall plant design, successive sections in this overview will be devoted to;

power cycle,
overall containment structure,
environmental impact,
resource requirements,
and economic considerations.

Finally, a few general and important conclusions will be presented for the design of this reactor.

II. Review of UWMAK-I Reactor Operating Characteristics

The UWMAK-I is based on the Tokamak confinement concept and has been designed with the philosophy that decisions should be made, whenever possible, on present-day technology. This means invoking as little extrapolation of present-day capabilities as is possible. The goal has been to perform a scoping study in sufficient detail to uncover potential technological problems that may be important as the CTR effort increases and the goal of fusion power comes closer.

The basic operating characteristics of the UWMAK-I reactor are given in Table 1, and for a more detailed discussion, the reader is referred to Volume I of this report. The reactor operated on a D-T (Li) cycle with an instantaneous power output of 5000 MW_{th} and a time averaged electrical output of ~1473 MW_e. The cross section of the nuclear island is given in Figures 1 and 2 where the double-null axisymmetric poloidal divertor is plainly evident. The operating cycle is given in Table 2 and the important point to note is that the reactor runs for 90 minutes followed by a 6 1/2 minute recycle period in which no power is being generated from D-T reactions. Such a down period is peculiar to Tokamak type reactors and must be properly treated to avoid large fluctuations in the power output of the reactor (see Section III).

UWMAK - I OPERATING CHARACTERISTICS	
POWER	5000 MW _† 1500 MW _e
FUEL CYCLE	(D-T), Li
DIMENSIONS	R = 13m, a = 5m
DIVERTOR	POLOIDAL, DOUBLE - NULL
BLANKET COOLANT	LITHIUM (489°C MAX)
BLANKET STRUCTURAL MATERIAL	316 SS
SHIELD MATERIALS	316 SS Pb B ₄ C
SHIELD COOLANT	HELIUM
NEUTRON WALL LOADING	1.25 MW/m ²
MAGNETIC FIELD	B _† ^o = 3.82 T B _† ^{max} = 8.66 T
MAGNETS (SUPERCONDUCTING)	NbTi + Cu CRYOGENICALLY STABILIZED
POWER CYCLE	Li - Na - STEAM

Table 1

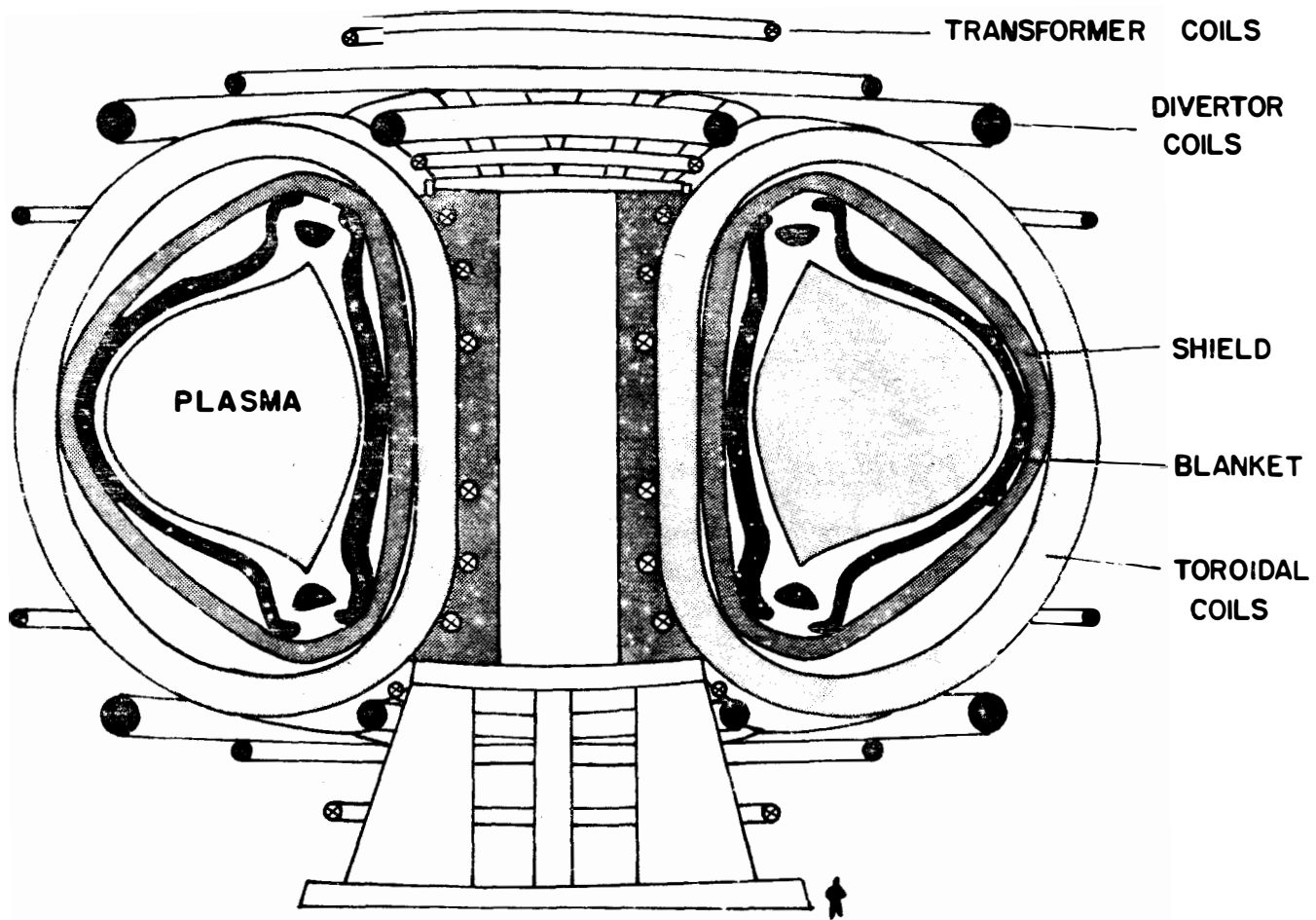


Figure 1 - Cross Section View of UWMAK-I Fusion Reactor

CROSS SECTION OF UWMAK-I

Figure 2

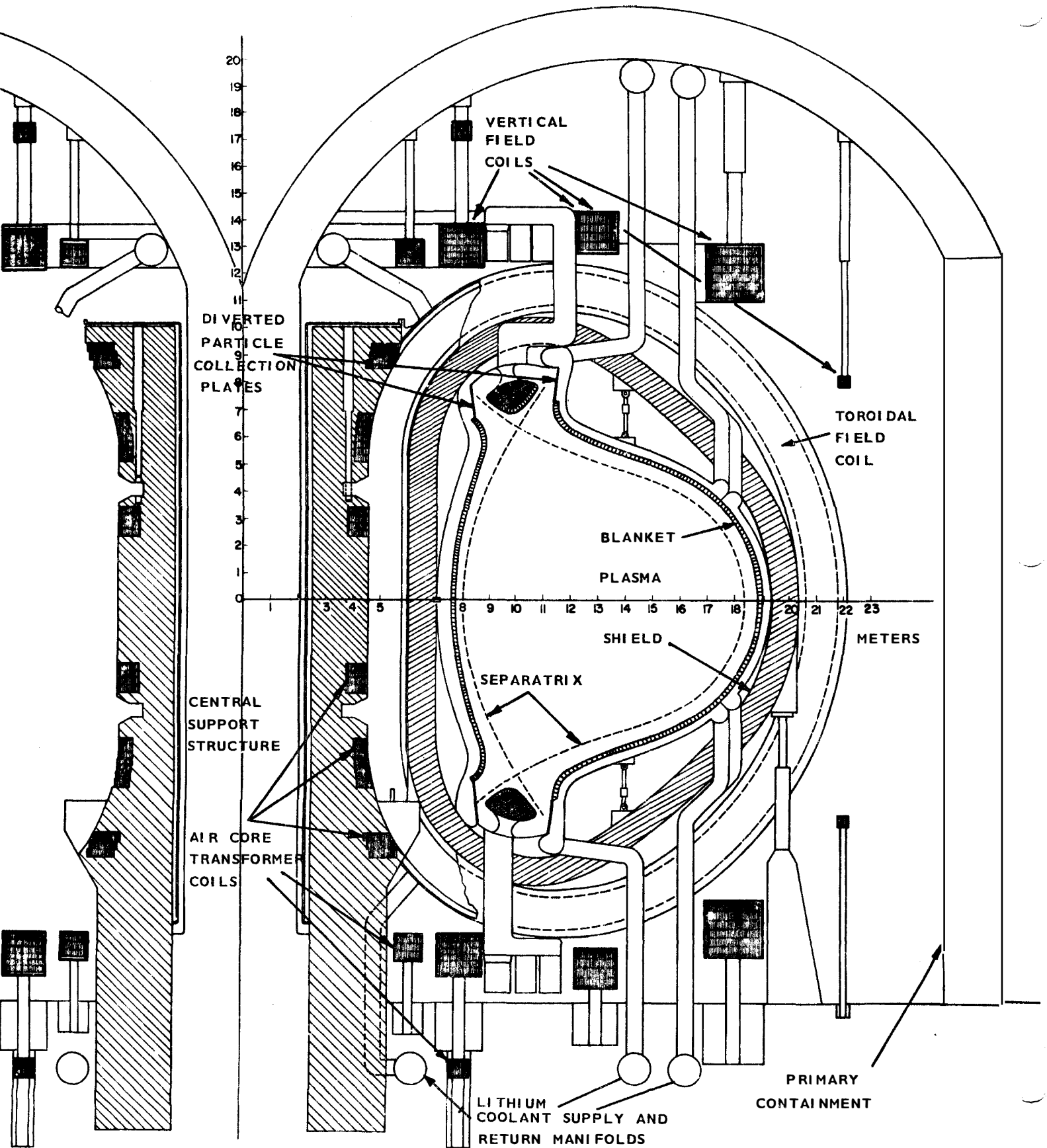


TABLE 2

START UP, BURN, AND SHUT DOWN
SEQUENCE FOR UWMAK - I

<u>TIME - SEC.</u>	<u>EVENT</u>
0 - 100	GAS BREAKDOWN, CURRENT RISE PHASE OHMIC HEATING
100 - 111	HEATING BY NEUTRAL BEAM INJECTION TO IGNITION
111 - 120	INCREASE TO FULL POWER FROM IGNITION
120 - 5520	THERMONUCLEAR BURN, PELLET FUELING
5520--5530	PLASMA COOL DOWN BY IMPURITY INJECTION
5530 - 5630	SHUTDOWN PLASMA CURRENT AND REVERSE TRANSFORMER AND DIVERTOR COILS
5630 - 5680	EXHAUST CHAMBER
5680 - 5780	COMPLETE CURRENT REVERSAL IN TRANSFORMER
5780 - 5790	PURGE RESIDUAL GAS - REFILL WITH FRESH (D+T) FUEL

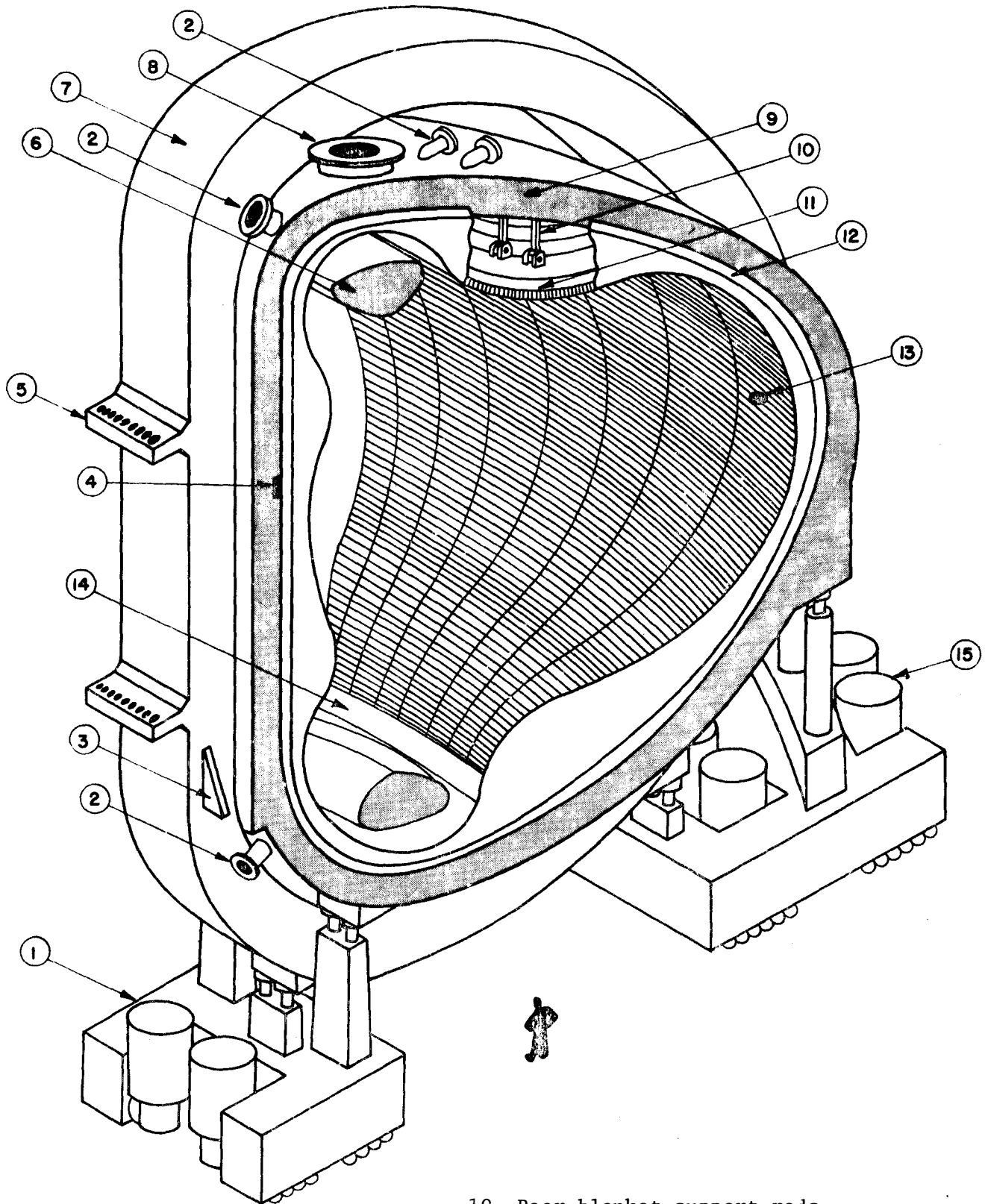
NEUTRONIC CHARACTERISTICS OF UWMAK-I BLANKET AND SHIELD	
TOTAL ENERGY PER NEUTRON	20.08 Mev
BREEDING RATIO	1.49
DOUBLING TIME	2-3 MONTHS
ENERGY AMPLIFICATION	17.8 %
ENERGY LEAKAGE TO MAGNETS PER Mev TO FIRST WALL	4.17×10^{-6} Mev
HEAT TO FIRST WALL	1.77 MW/m ²

Table 3

The structural material is 316 stainless steel and it is cooled by flowing Li at a maximum temperature of 489°C. The 14 MeV neutron wall loading is 1.25 MW/m² which produces damage at a sufficiently high rate so as to require the first 20 cm of blanket to be changed every two years. The breeding ratio is 1.49 implying a doubling time of 2-3 months. The final neutron protection is accomplished by a 78 cm shield which consists of alternate layers of 316 SS, Pb, and B₄C which are cooled with helium. The neutronic characteristics of the blanket and shield are given in Table 3.

There are 12 toroidal field magnets composed of superconducting NbTi filaments, cryogenically stabilized with copper. These coils are reinforced with 316 stainless steel. One such coil, along with the blanket and shield (i.e. one module) is shown in Figure 3. Each of these modules weighs 3500 tons and must be removed at least every 2 years to replace the first wall. Three spare units are ready at all times to replace damaged modules such that the repair can actually be done in hot cells while the reactor is running.

Finally, the reader is referred to Volume I of this report for more details on the plasma physics, divertor design and operation, blanket and shield design, neutronics and photonics, radiation damage, magnet design, tritium production and handling, and preliminary safety considerations.



- 1- Front motorised caterpillar
- 2- Lithium inlet or outlet
- 3- Front magnet dewar support
- 4- Front blanket support bar
- 5- Magnet support shear beam
- 6- Vacuum port shield
- 7- Toroidal magnet in its dewar
- 8- Vacuum connection
- 9- Shield

- 10- Rear blanket support rods
- 11- Heat removal cells
- 12- Blanket seal flange
- 13- Neutral beam injection port
- 14- Particle collection plate
- 15- Rear motorised caterpillar

FIGURE 12

III Power Cycle

An overall systems diagram of the UWMAK-I reactor is given in figure 4, while figure 5 is a simplified schematic of the power cycle. The distribution of power is given in table 4 and the coolant temperature and flow rates in Table 5. The instantaneous power generated during the burn is 5000 MW_{th} of which 4700 MW_{th} is deposited in the blanket, 250 MW_{th} is deposited in the divertor region and 50 MW_{th} in the shield. The temperature of the helium coolant in the shield is so low (200°C) that it is not efficient to attempt to recover that heat. Therefore the entire 50 MW_{th} is dumped directly to cooling towers.

The heat collected in the blanket modules is transferred to a sodium loop in an intermediate heat exchanger (IHX) and finally from the sodium to the steam. There are 12 individual loops, one for each module of the reactor. There are three main reasons for having a sodium secondary loop:

- 1.) To isolate the radioactive corrosion products in the primary Li circuit from the steam cycle in the event of a tube failure in the steam generator.
- 2.) To reduce the tritium leakage from the lithium loop into the steam cycle by lowering the partial pressure of tritium in the steam generator.
- 3.) To provide a mechanism by which the steam fed to the turbine can be kept at constant conditions despite the fact that the power is generated only 93.3% of a given operating cycle.

The necessity for the first two reasons was covered previously in Volume I, but it is worthwhile to expand on the third reason at this time. It is not desirable, from a utilities standpoint, to generate ~1600 MW_e for 90 minutes and then generate no electricity for 6.5 minutes. Such a variation is also undesirable for the turbine as well. Therefore some method of storing energy during the burn cycle must be developed and that energy recovered during the down cycle. We have chosen to accomplish this with the concept of "thermal flywheels". This concept means that a small amount of the secondary sodium (~7%) is bled off the sodium loop during the burn cycle and stored in an insulated tank. (See figure 6a.) At the end of the burn cycle, the stored Na is fed into the secondary loop, passed through the steam generator and the cooler Na stored in another tank. (Figure 6b) This sodium is slowly fed back into the secondary stream during the burn cycle. The important feature is that the steam conditions from the steam generator are constant with time.

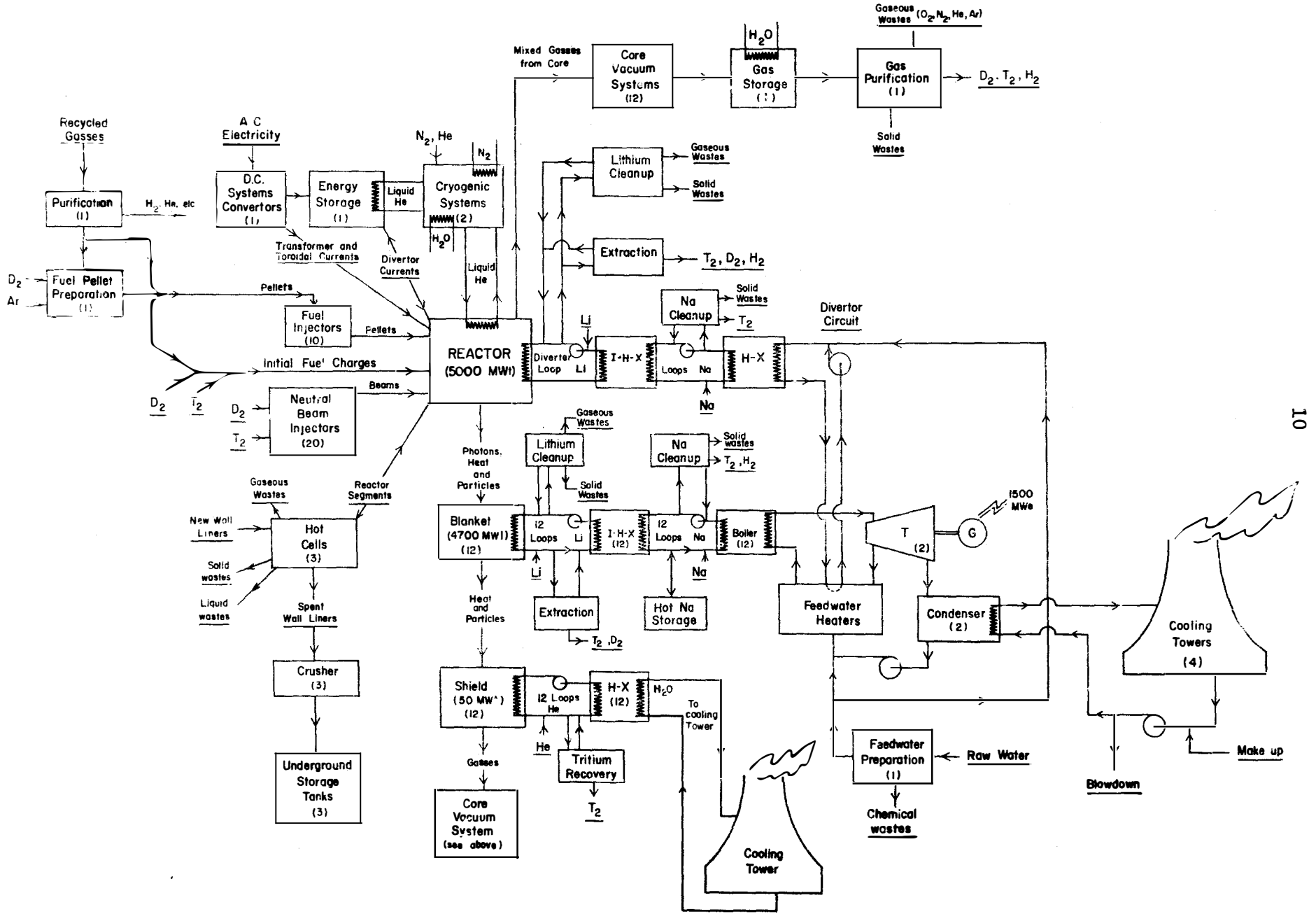
The use of the thermal flywheel is unique to the Tokamak system and requires that reactor power ratings be quoted in at least two different ways: 1) instantaneous thermal power generated and 2) time averaged electrical power output.

Both the primary system and divertor collection system are given in instantaneous and time averaged thermal outputs in table 4. The time average thermal input from the primary lithium to the steam is 4383 MW_{th} and the divertor adds another 233 MW_{th} to the feed water heaters.

The steam generator for UWMAK-I utilizes a proprietary combination of the latest steam generator technology from Babcock and Wilcox to:

Figure 4

UWMAK-I SYSTEMS DIAGRAM



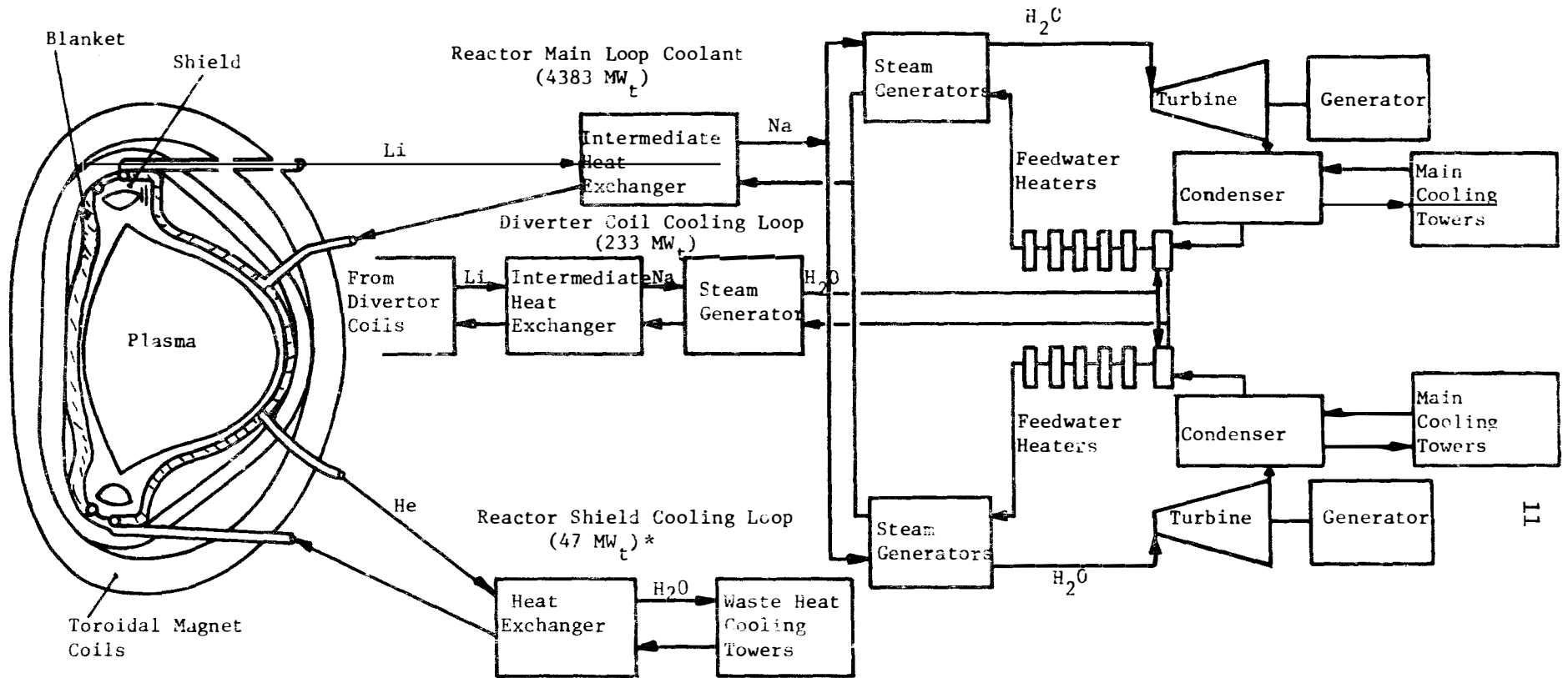


FIGURE 5

Schematic Plant Design
Wisconsin Toroidal Fusion Reactor - UWMAK-1

* Time averaged values

Table 4

Distribution of Power from the 5000 MW_t UWMAK-I

		<u>Number of</u> <u>Loops</u>	<u>MW_{th}</u> <u>per Loop*</u>	<u>Total</u> <u>MW_{th}*</u>	<u>Time Average</u> <u>MW_{th}</u>
Blanket	Li Primary Loop	12	392	4700	
	Na Secondary Loop	12	392	4700	
	Steam Loop	12	392	4700	4383
Divertor	Li Primary	1	250	250	
	Na Secondary Loop	1	250	250	
	Feedwater Loop	1	250	250	233
Shield	He Coolant	12	4.2	50	
	Coolant Water	12	4.2	50	

* Instantaneous values during burn cycle. Time averaged values (to account for down time) are 93.3% of that value

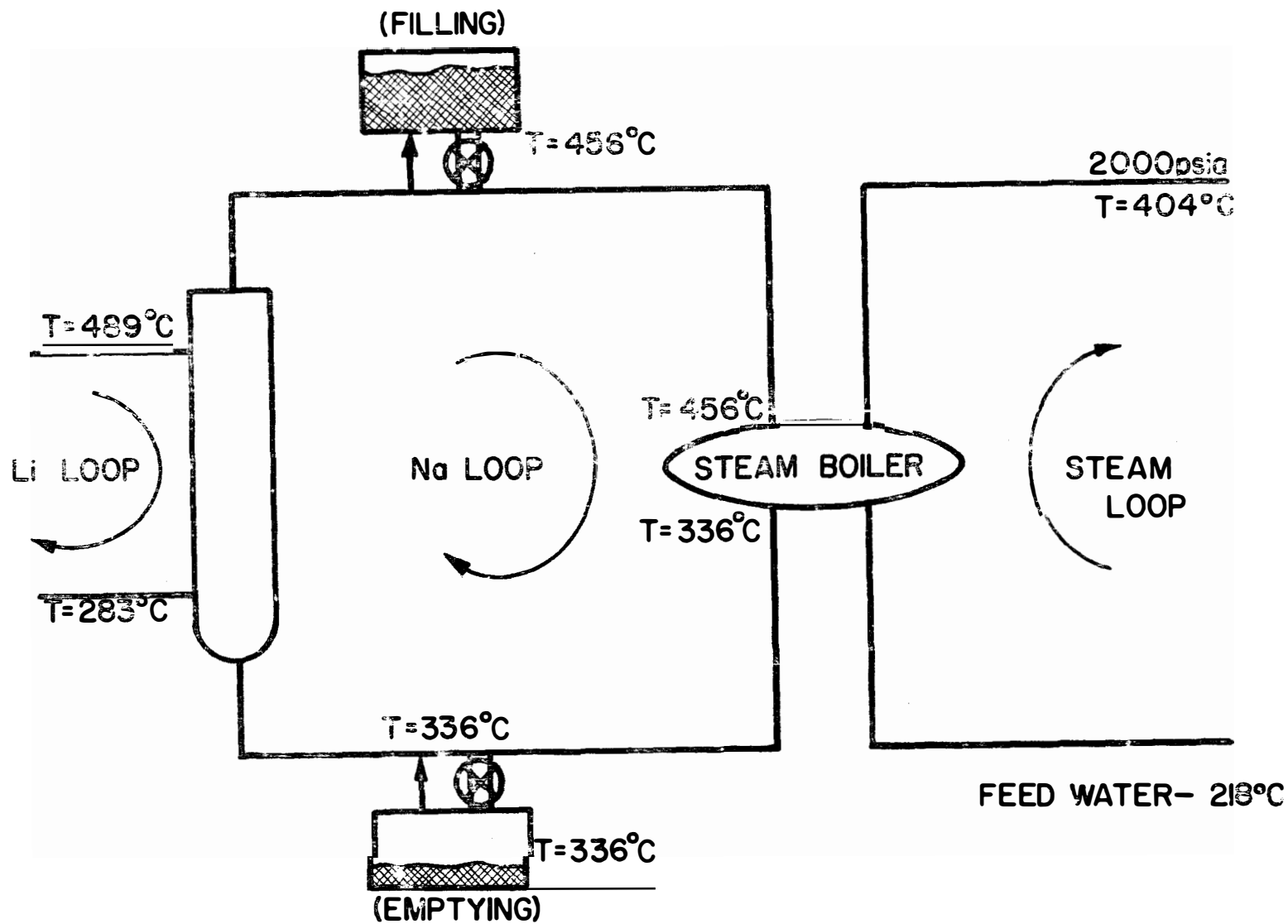


FIGURE 6a.— SCHEMATIC OF SODIUM THERMAL "FLYWHEEL" OPERATURATION DURING D-T BURNING.

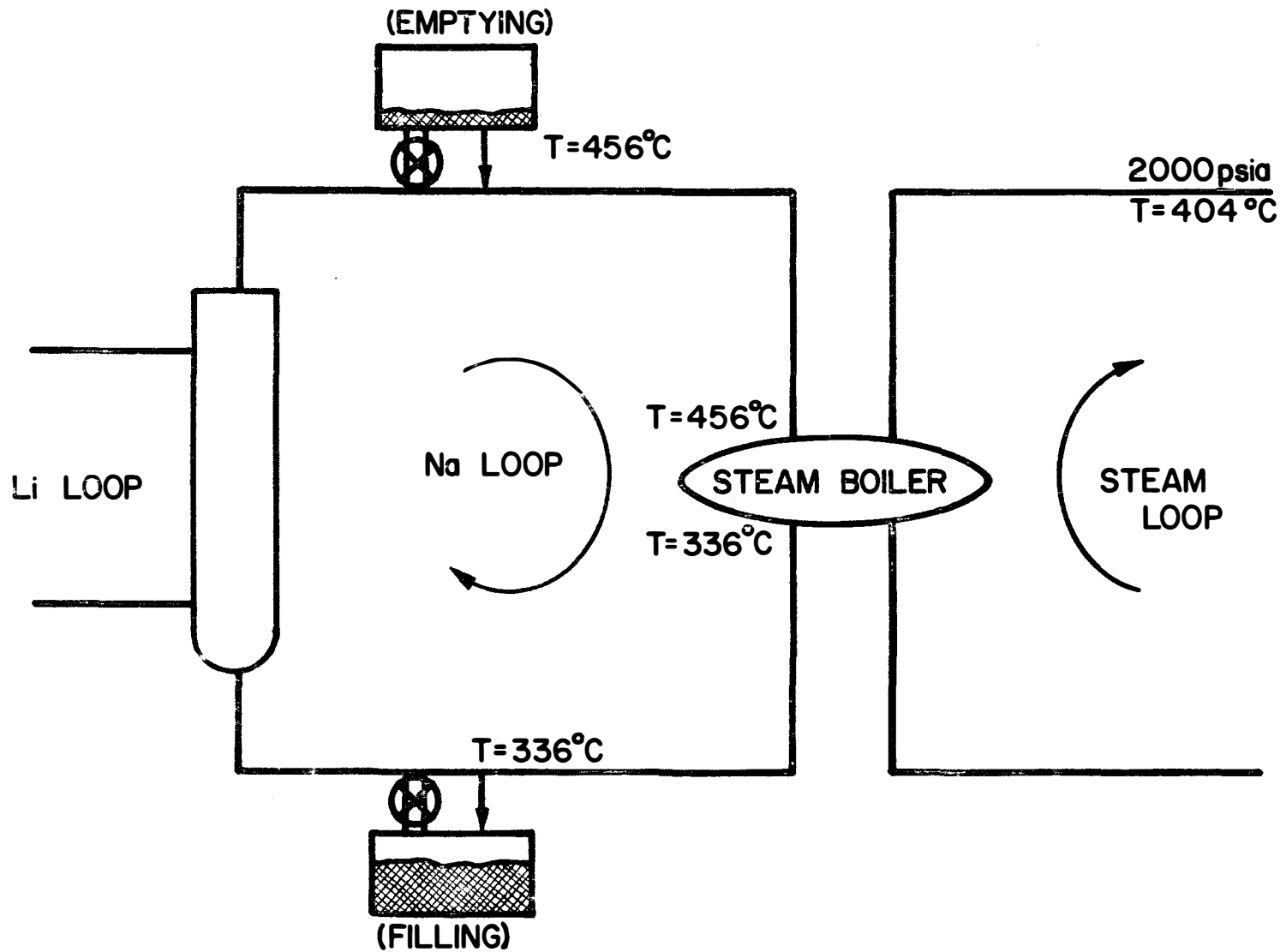


FIGURE 6b.- SCHEMATIC OF POWER GENERATION SCHEME BETWEEN BURN CYCLES. HOT Na FROM STORAGE TANK IS USED TO GENERATE STEAM, THEN Na IS STORED IN DUMP TANK.

Table 5

Summary of Coolant Parameters for UWMAK-I

<u>ITEM</u>	<u>Temperature °C</u>	<u>Flow Rate^(a) kg/sec x 10⁶</u>	<u>Pressure kg/cm² x 10⁴</u>
Li reactor outlet	489	2.7	2.8
Li reactor inlet	359	2.7	47
Na inlet IHX	336	9.8	4.9
Na outlet IHX	456	9.8	2.5
Na to storage tank	456	0.7	2.9
Na to steam generator	456	9.0	1.8
Na from steam generator	336	9.0	1.4
H ₂ O to steam generator	218	0.63	148
H ₂ O from steam generator	404	0.63	140

a) Per module, X12 for total reactor

- 1.) Minimize the tritium diffusion into the steam.
- 2.) Avoid the characteristic problems of liquid metal to water heat exchangers.
- 3.) Provide safety and high reliability.
- 4.) Facilitate inservice inspection and maintenance.

One key feature of this design is that both the Na and steam are in individual tubes separated by a 0.025mm helium gap. A trace amount of oxygen is included in the helium to scavenge any tritium leaking from the sodium tubes. The result of this total design is to reduce the tritium leakage rate to 10 curies per day, a factor of $\sim 10^7$ reduction from the inventory in the primary lithium.

The output from the 12 steam generators is fed into two identicle 1800 RPM tandem compound generating units for the UWMAK-I reactor. The steam conditions delivered to each of the two high pressure turbines are

Steam flow	3,787,100 kg/hr.
Temperature	399°C
Pressure	1900psi (1.3×10^6 kg/cm ²)

The details of the turbine generator cycle design are given in Figure 7.

6. The continuous output from each of the two generator units is

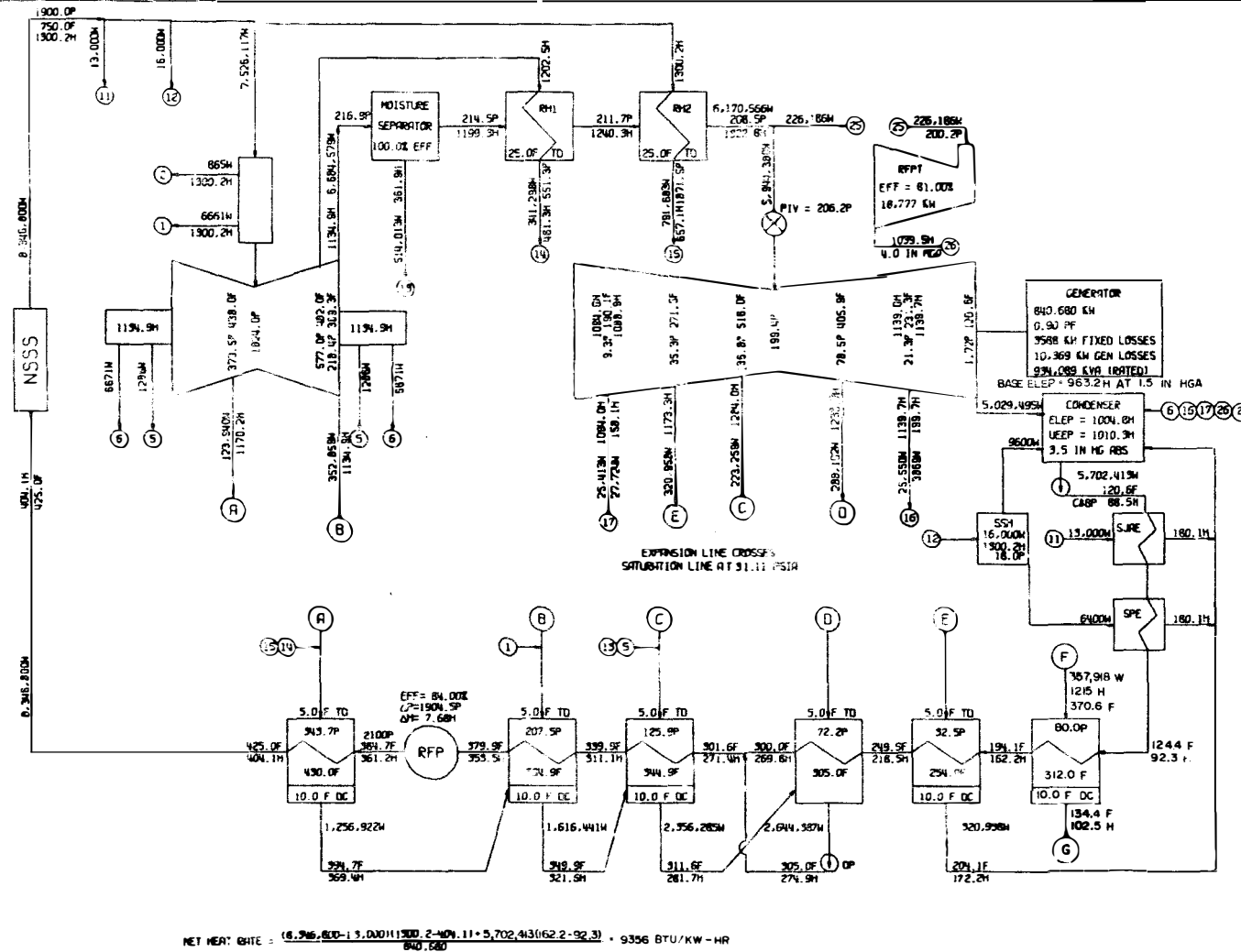
Gross generation	840,680 kW _(e)
required Auxillary power in plant	104,000 kW _(e)
net electrical power sent out	736,680 kW _(e)
<hr/>	
Total net electrical power	1,473,360 kW _(e)

The total overall efficiency for UWMAK-I is then over the entire burn cycle.

$$\frac{1,473,360 \text{ kWe}}{5,000,000 \text{ QW}_t \times 0.933} = 32\%$$

WISCONSIN TOKAMAK FUSION REACTOR CYCLE
 JOB NO. 4820-00 MAD 74-643
 G-HEATER CYCLE 2HR STAGES MS AND 2RH
 1900 PSIA 750.0F TC4F-38LS6 1300 RPM
 SEPTEMBER 20, 1974

FIGURE 7
 TURBINE GENERATOR CYCLE DESIGN



(F) - FROM DIVERTOR STEAM GENERATOR
 (G) - TO DIVERTOR STEAM GENERATOR

EQUIPMENT LIST:
 C&BP - CONDENSATE & BOOSTER PUMP
 DP - DRAIN PUMP
 NSSS - NUCLEAR STEAM SUPPLY SYSTEM
 RFP - REACTOR FEED PUMP
 RFP-T - REACTOR FEED PUMP TURBINE
 RH1 - FIRST REHEATER
 RH2 - SECOND REHEATER
 SJAE - STEAM JET AIR EJECTOR
 SPE - STEAM PACKING EXHAUSTER
 SSH - STEAM SEAL HEATER

LEGEND:
 H = ENTHALPY, BTU/LB
 F = TEMPERATURE, °F
 W = FLOW, LBS/HR
 P = PRESSURE, PSIA

MECHANICAL ANALYTICAL DIVISION

SARGENT & LUNDY

IV. Overall Plant Layout

The UWMAK-I nuclear power plant will resemble light water nuclear fission plants in its overall appearance. There will be a large reactor building as well as turbine, auxiliary, and service buildings, and cooling towers for the heat sink. Unique to this fusion plant will be the large hot cells required to replace the inner wall of the torus-magnet modules and the energy storage building to house the inductive coils for supplying power to the transformer and divertor coils during the ignition and burning. While the large electrical switch yard is also conventional, the inverter and harmonic filter areas are provided due to special requirements associated with the magnetic energy storage system. The other major building, housing the diesel-generators and diesel oil tanks, contains the emergency power supply for the equipment that is felt to be essential for maintaining the safety of the plant. A smaller helium storage building for the helium gas cylinders is also required.

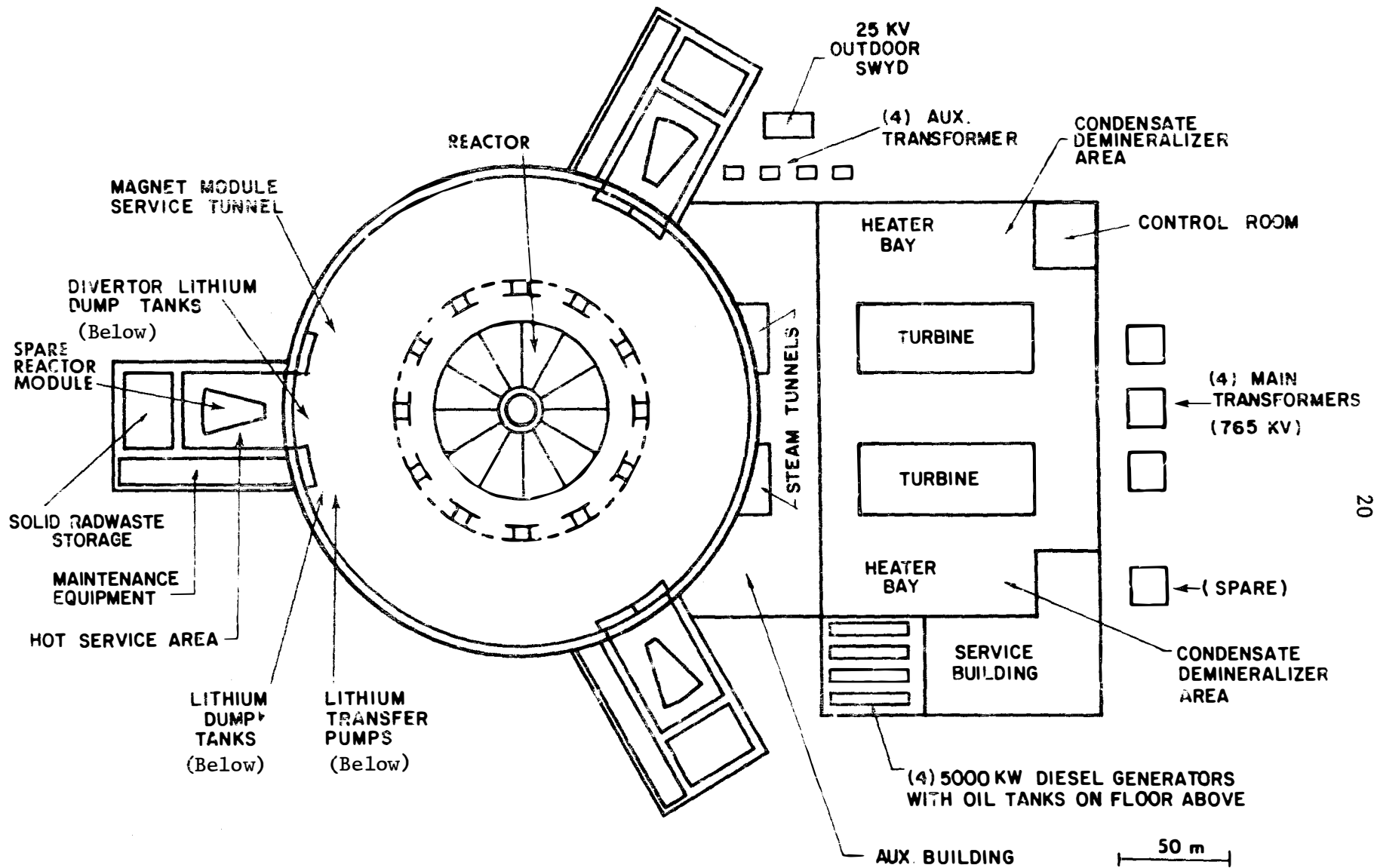
The location of these buildings and structures that comprise the complete plant are shown on the property plot Figure 8. The source of make up water, (lake or river) is not shown, but is assumed to be in the direction of the main cooling towers. A more detailed description of the plant is found in the general arrangement drawings, Figures 9 thru 11.

The reactor building will be a large cylindrical building approximately 120 meters in diameter and 102 meters high. It comprises four floors: the main floor containing the primary containment structure and access tunnel; the lithium and sodium floors containing the processing equipment for these respective coolant loops; and the fourth floor for heating, ventilation, air conditioning and miscellaneous equipment. The specific location of the major balance-of-plant equipment is shown on the general arrangement drawing, Figure 11.

One unique feature of this reactor design is the fact that the enclosure immediately around the nuclear island will be evacuated to 1 torr vacuum. This is desirable from three standpoints:

1. To collect tritium leaking from the nuclear island and prevent it from reaching the outside environment.
2. To eliminate the possibility of a liquid metal Li fire in the event of a pipe breakage.
3. To reduce the in-leakage of air from the outside of the reactor into the vacuum vessel.

The walls of the primary containment will be lined with 1.27 cm thick, non-magnetic steel to help protect against tritium leakage in the event of an accident. Finally, the concrete walls of the primary containment are 2.44 meters thick primarily to attenuate the neutron flux, leaking from the reactor, to acceptable levels.



20

FIGURE 9 - Top View of UWMAK-I Reactor Building

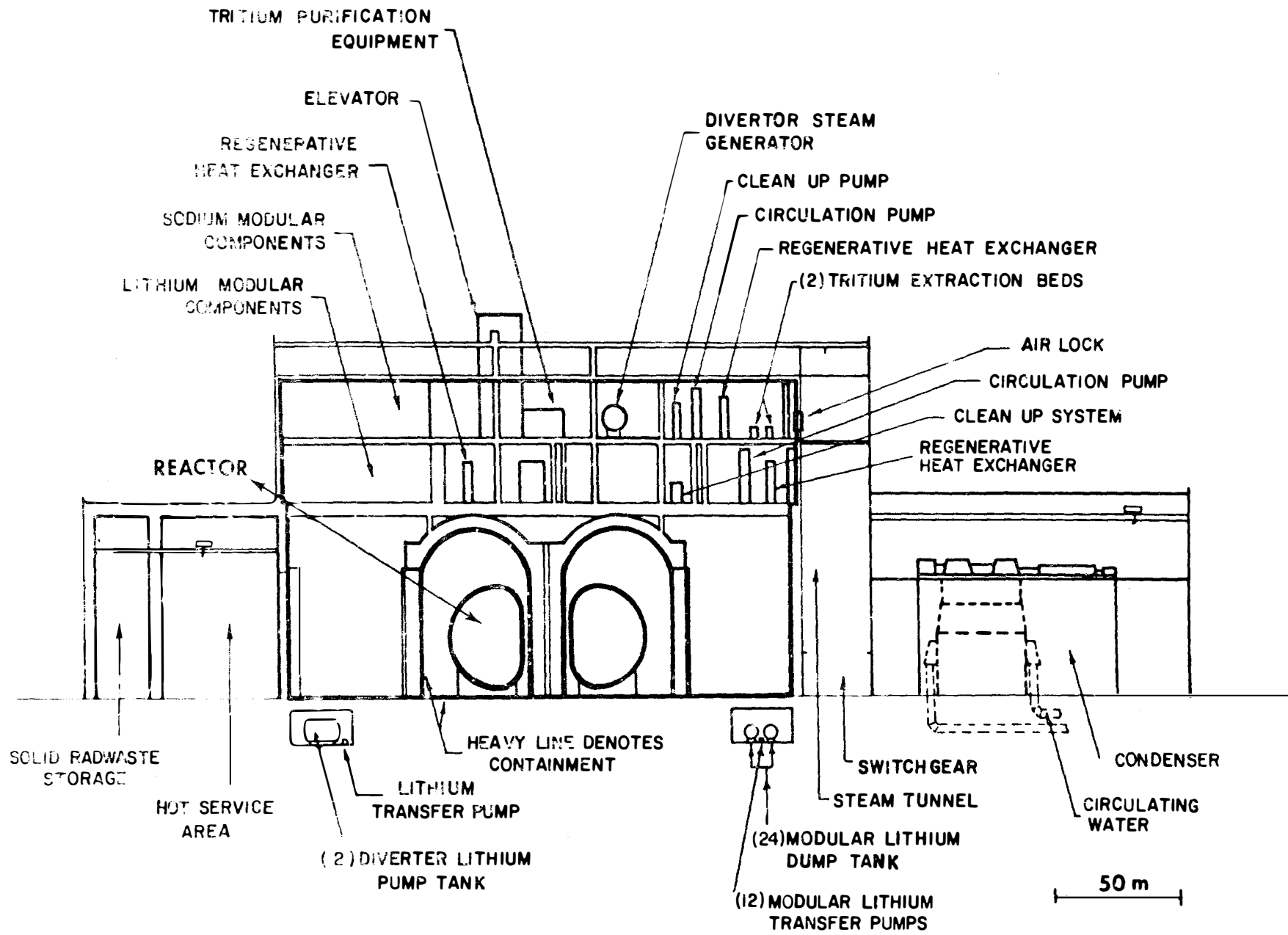


Figure 10- Cross Section of UWMAK-I Reactor Building

V. Environmental Impact

The first thing to make clear is that the numbers and ideas in this chapter only apply to the UWMAK-I facility and cannot be blindly generalized to other reactor types (i.e. mirrors, pulsed systems, etc.) or even other tokamak designs. It is also worth noting that a distinction is made in this report between the environmental impact resulting from radiological effects and the environmental impact resulting from other effects such as waste heat rejection and siting.

The siting of a facility like UWMAK-I (~102 m tall and ~300 m long) may be undesirable from aesthetic effects but no serious non-nuclear impact could be determined. Noise, land requirements, and magnetic field effects seem to be manageable. The waste heat rejection from a plant which has ~30% efficiency (excluding auxiliary power requirements) is comparable to LWR's (33%) and lower than HTGR's (38%) and LMFBR's (40%). The waste heat from UWMAK-I is put into the atmosphere via mechanically forced draft cooling towers and about the only serious problems associated with this scheme might be local fogging by the evaporation of ~20,000 gpm of water.

The tritium inventory (Table 6) and potential radioactive effluents during normal plant operation have also been analyzed (Figure 12). The conclusion is that the tritium is still the major isotope which could be released despite the inventory of some 13.5 kg (excluding storage) of tritium (1.35×10^8 curies), only 10.1 curies per day is released via the Li-Na-steam route. Such a release rate into 12,000 gpm blow down water from the condenser cooling water discharge would result in a discharge of 15×10^{-5} $\mu\text{Ci}/\text{m}^3$. This amount of tritium is only 6% of the current regulatory limit and would result in a dose of 6×10^{-4} rem/week to a person obtaining his entire daily intake of water from this source. This could be reduced even further if we used the blow down water to make concrete which could be stored until the tritium decayed to a reasonable value. (The half life of tritium is 12.4 years.)

The very difficult problem of plant accidents was considered for UWMAK-I and some preliminary calculations were made. There were 7 potential hazards identified in UWMAK-I.

1. Energy stored in the superconducting magnets (350 GJ)
2. Kinetic energy of the plasma (3 GJ)
3. Stored energy in the liquid helium (8+ GJ)
4. The stored energy in Li and Na and the potential for fires
5. Tritium inventory (at least 13.5 kg)
6. Structural materials with induced activity (5×10^9 curies)
7. Corrosion products in the lithium coolant ($\sim 5 \times 10^7$ curies)

Each of the potential hazards were considered and the results summarized below.

The failure of a toroidal field magnet could cause considerable harm to the magnet and structural members if not properly stabilized and structurally braced. Fortunately in UWMAK-I, the failure of a single TF coil can be accommodated by the other coils in the set and suitable energy dumping arrangements made.

The deposition of 3 GJ of plasma thermal energy uniformly on the 3000 m² of surface area would amount to 1 MJ/m² or 300 watt-hr-m². Assuming a 1 second deposition time, this is equivalent to ~ 1 MW/m², a level that the first walls are designed to withstand under normal conditions. However, if the plasma energy were deposited

Table 6

Summary of Tritium Extraction System Characteristics^(a)

Coolant System	Temp. Range °C	Extraction Method	Tritium Accumulation Per Day (kg)	Tritium Leakage Ci/day	Total Na or Li (kg)	Tritium Concentration in Li or Na ppm (wt.)	Tritium Inventory (kg)
Primary Lithium	283-489	Yttrium Metal Bed	1.05(b)	10.1	1.73×10^6	5	in Li 8.7 in beds 1.0
Secondary Sodium	261-411	Yttrium Metal Bed	~0		7.6×10^5	8.7×10^{-5}	in Na 6.7×10^{-5} in beds ~0
Divertor Lithium Sodium	200-325 190-265	Yttrium Metal Bed	7.4 T + 5.0 D	2×10^{-4}	3.4×10^4 6×10^4	0.24 3×10^{-4}	in Li 8×10^{-3} in beds 3.5 in Na 6×10^{-6} ²⁴
Divertor vacuum	25	Charcoal-cooled with liq. He	0.3 T + 0.2 D	1×10^{-4}		Not applicable	0.3
Helium	50-200	Metal getter	1.1×10^{-6}	low		Not applicable	low
			Total	10.1		Total	13.5

(a) Based upon thermodynamic calculations; no kinetic considerations

(b) At maximum breeding ratio of 1.49

locally in times shorter than 1 second, the first wall may be punctured and lithium released into the vacuum chamber. This would involve a costly shut-down but no serious danger to those outside the plant.

The liquid helium represents a potentially large source of stored energy if it could be vaporized at one time. However, pressure release valves and normal safety precautions should minimize this hazard.

The potential damage due to a liquid metal lithium fire can be reduced by surrounding the liquid metal systems with double wall piping, inert gas or by evacuating the reactor environment. The last two concepts were used in UWMAK-I because of the increased costs involved in double walled tubes.

The accidental release of tritium from UWMAK-I remains the major credible accident. The release of 1% (100 g) of the total inventory at ground level under the worst meteorological conditions would result in a radiation exposure level of 7 times the maximum allowable dose if the exclusion radius were 600 meters. Such a release would result in an exposure equal to the maximum allowable dose if the exclusion radius were 2100 meters. On the other hand, if release were made through a 100 meter stack, then the exposure level would be 1/10 of the present guidelines.

Before one can assess the potential hazard involved in the radioactive structural material it is necessary to have an extensive inventory of specific radioactive isotope (Table 7) and a good idea for their potential release into the atmosphere. Even though a large number of curies are present in the structural metals, this does not mean that it will all be released to the environment. Preliminary assessment of this problem reveals that the possibility of release of such isotopes in metallic structures is very low and the hazard far less than that for the release of tritium which is more volatile.

Finally, the release of radioisotopes from the corrosion products in the coolant is plausible during a lithium fire, but it is difficult to anticipate all of the Li burning and many of the corrosion product oxides and nitrides would plate out on the reactor containment walls. Again, the hazard is expected to be far less than the tritium release problem.

Loss of cooling accidents and afterheat problems were examined and because of the low specific heat generation were shown to be manageable.

The shipment and storage of long term radioactive wastes was also analyzed. Figure 13 summarizes the decay of such waste from UWMAK-I after a 1.4 year operating cycle and compares it to a LMFBR fission reactor. One can see that on the crude basis of curie per thermal watt, UWMAK-I is a factor of 7 better than the LMFBR at shutdown but loses that advantage after a few weeks of decay. After that the activity of ^{316}SS is comparable to or exceeds that of the LMFBR up to a few hundred years. However, considering the biological hazard potential (BHP), which is the source amount divided by the MPC in curies/cm³ of dilutant, one finds the situation somewhat improved (Figure 14). Now fusion reactors are a factor of 1000 better than fission systems at shutdown and remain so out to a year or two.

Table 7

First Wall Radioactive Inventory at
Shutdown After 10 Years of Operation of UWMAK-I

<u>Isotope</u>	<u>Specific Activity</u> <u>dps/cm³</u>	<u>Activity</u> <u>ci/kw_{th}</u>	<u>MPC</u> <u>μci/cm³</u>	<u>"Biological Hazard</u> <u>Potential"</u> <u>km³ of air/kw_{th}</u>	<u>t_{1/2}</u>
<u>316 SS</u>					
V-49	1.1 x 10(6)	0.67	1 x 10(-10)	6.7	331 days
Mn-54	4.0 x 10(10)	24	1 x 10(-9)	24	313 days
Mn-56	6.9 x 10(11)	42	2 x 10(-8)	2.1	2.58 hours
Fe-55	2.3 x 10(12)	140	3 x 10(-8)	4.6	2.7 years
Co-58	4.7 x 10(11)	29	2 x 10(-9)	14.5	71.4 years
Co-60	7.7 x 10(10)	4.7	3 x 10(-10)	15.6	5.26 years
Ni-57	1.8 x 10(10)	<u>1.1</u>	1 x 10(-10)	<u>11</u>	36.1 hours
<u>Total</u> ^(a)		~310		~80	

(a) Including those isotopes not listed here

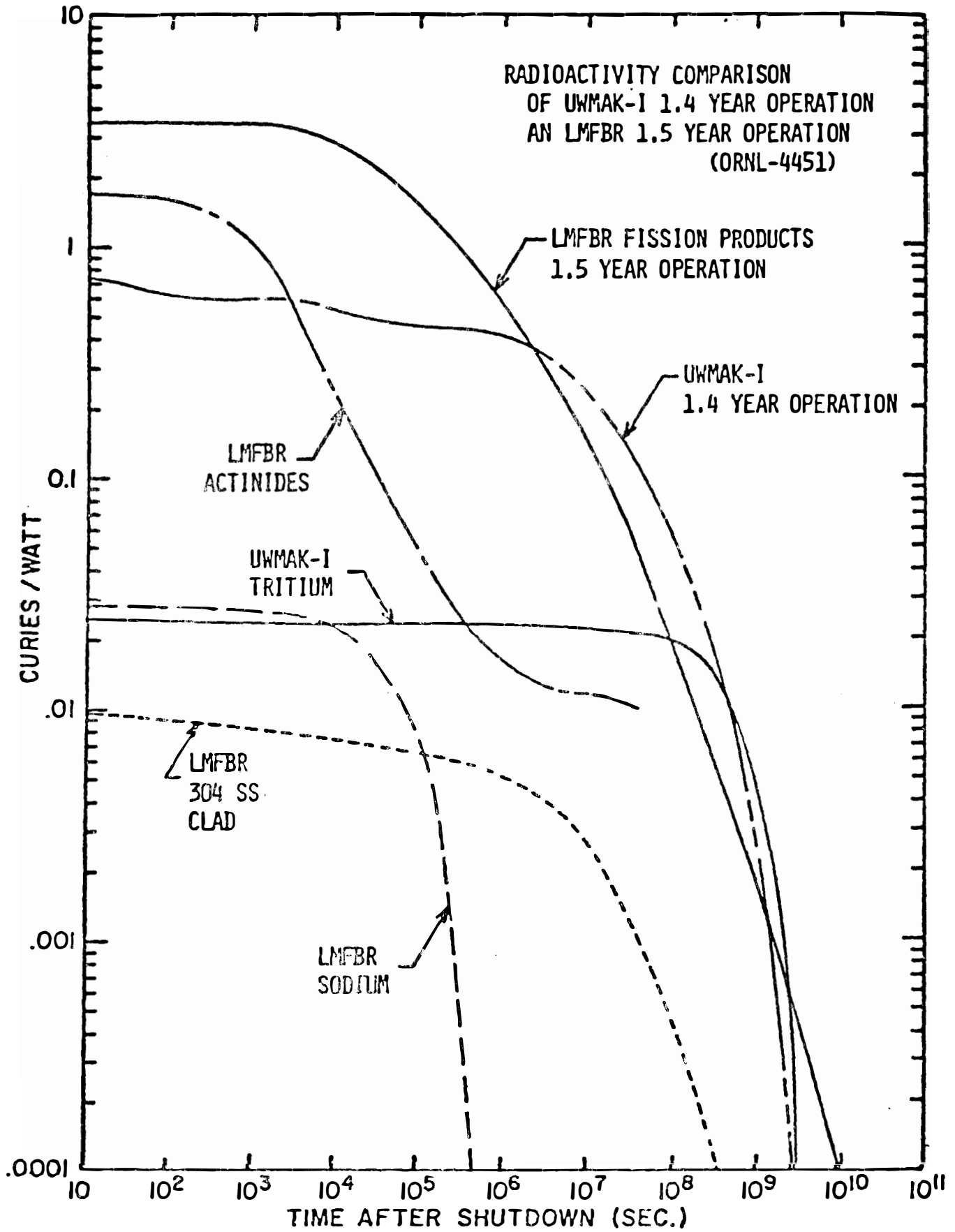
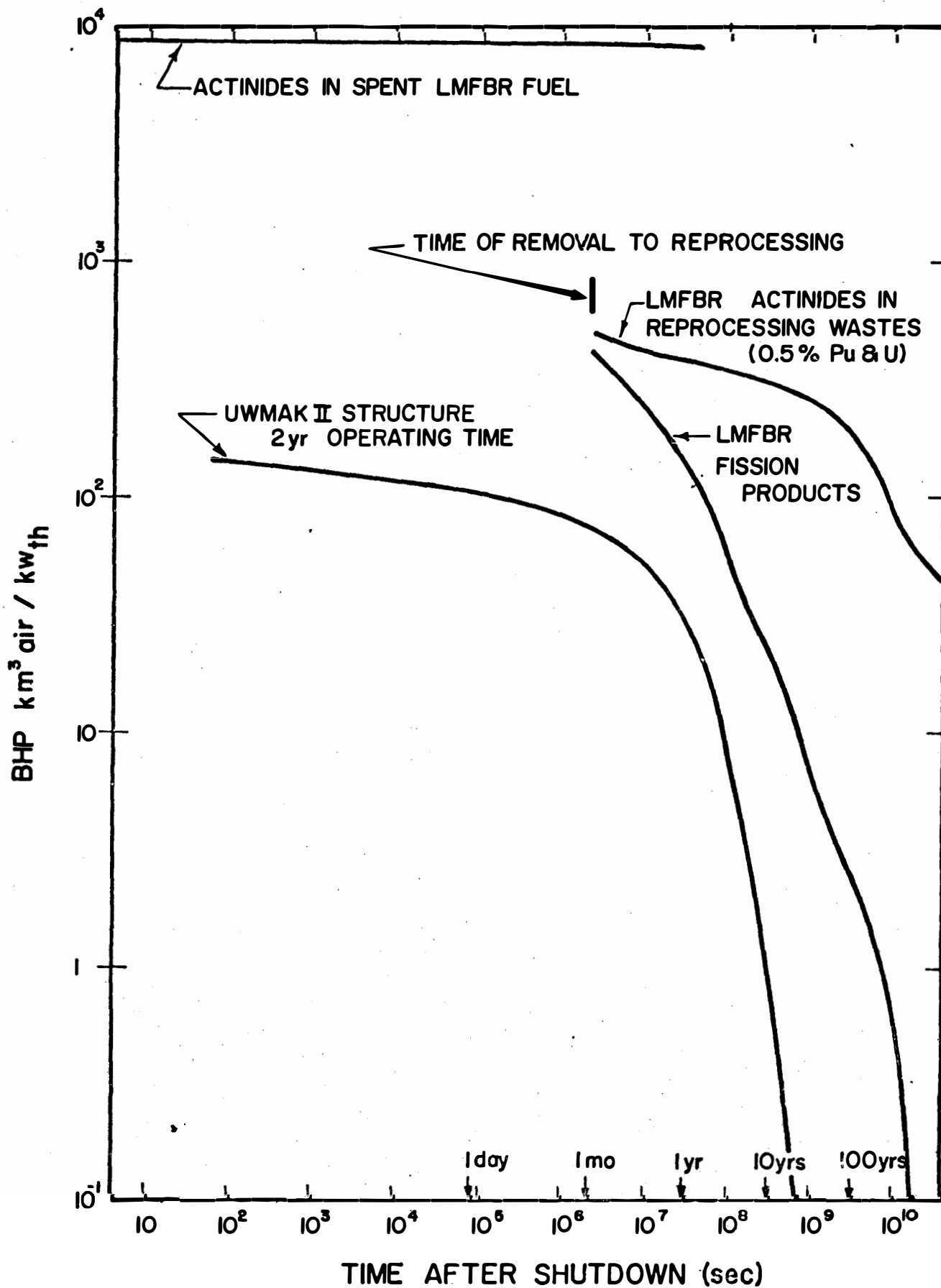


Figure 13

BHP vs TIME AFTER SHUTDOWN FOR AN LMFBR WITH
1.5yrs OPERATING TIME (ORNL-4451) and
U WMAK II



The volume of radioactive material generated in UWMAK-I was analyzed and is summarized in Table 8. The surprising thing to note is that the volume of radioactive material generated per year is actually greater in UWMAK-I than in similar sized fission plants. This stems from the necessity to change the first wall due to neutron damage. Approximately 250,000 kg/year is generated and, at theoretical density, represents some 1100 ft³ of high level waste per year. In addition to this amount an average of 488,000 kg is generated per year by having to change out the rest of the blanket and reflector region. When this amount of corrosion and sputtering products is added to the above numbers, we find that a minimum of ~3300 ft³ of highly radioactive material is generated per year. This is about half of the low level wastes and more than 10 times the high level waste from a fission plant.

It is difficult to translate the numbers in Table 8 into the number of truck or rail shipments required per year because the low afterheat density in fusion reactor materials would dictate a much different cask design than for fuel elements. However, if we use the current numbers of 500 kg of irradiated fuel per cask for truck and 3,200 kg of irradiated fission fuel for a single rail shipment, we find that ~1470 truck shipments or ~230 rail shipments would be required per year. Again, one might expect to get more irradiated structural material per cask than for fuel so that these numbers may be high for fusion systems like UWMAK-I. Finally, there is no urgency to ship or reprocess the CTR materials as there is for fuel. This may allow the option of storing all the used components until the end of the plant lifetime, or allow on site burial. Such possibilities need further investigation.

Table 8

Solid Wastes from UWMAK-I (1500 MWe) and a 1500 MWe LWR

UWMAK-I (with 316 SS First Wall)

First Wall	245,000 kg/yr
Reflector Region	488,000
Corrosion Products	2,500
Sputtering	250
Total Volume (7.8 gm/cm ³) - 94 m ³	~736,000

Low Level Solid from Power Plant

Cubic Feet/yr	3,000-6,000
Kilograms/yr	90,000-150,000
Number 55 gal. Drums/yr	400-800
Burial Ground Area Used Square Feet/yr	2,700-5,400

Produced at Reprocessing Plant SiteHigh Level Solid

Cubic Feet/yr	135
Kilograms/yr	7,250
Number 6" x 10' Containers/yr	90
Repository Space Required, Square Feet/yr	18,000

Cladding Hulls

Cubic Feet/yr	90
Kilograms/yr	11,400
Number 30 gal. Drums/yr	22

Area/yr

Depends on whether storage is
required at a commercial burial
ground or Federal Repository

Low-Level Solids

Cubic Feet/yr	900-6,000
Kilograms/yr	45,000-100,000
Number 55 gal. Drums/yr	120-800
Burial Ground Square Feet/yr	1,500-7,250

VI Materials Resources Considerations

The construction of large scale Tokamak fusion power plants will place severe demands on critical elements. This stems from two basic features of tokamak fusion power plants.

1. Low power density (i.e. 1 MW/m^3 vs $\sim 100 \text{ MW/m}^3$ for fission reactors)
2. Use of relatively scarce materials in some designs (i.e. Nb, Cr, Mn, Sn, Be, etc.)

Therefore it is important at this stage of reactor design to estimate the materials required for each reactor concept to make sure that such systems do not strain the materials reserves of a particular country or even the world.

We have attempted to estimate the materials requirements for the UWMAK-I "nuclear island" (Table 9) and, as much as possible, for the balance of plant (Table 10). The numbers quoted here are probably underestimates and do not take into account losses during fabrication and/or processing. However, the values should be within 50% of the ultimate amount and therefore represent minimum requirements.

The requirements are given by element and by alloy in Tables 9 & 10 and we have calculated the materials requirements in metric tonnes per MWe. The total materials requirements are summarized in Table 1.

There are a few points worth noting for UWMAK-I. The total amount of metal (including B & C but excluding concrete) is ~ 144 tonnes/MWe in UWMAK-I. Roughly 60% of this need is for iron, 10% for Pb, 8% for Na, 7% for Cr, 6% for Ni, 5% for Cu, and 1% each for Mn, Li and B. Approximately 60% of the metal mass is required for the balance of plant with 80% of this amount going into iron.

A breakdown of the fractional requirements for some of the critical elements such as Cr, Ni, Mn and Nb is given in Table 12. The requirements are broken up into those of the nuclear island, those parts of UWMAK-I peculiar to fusion power plants and those requirements from the balance of plant. Let us examine the requirements for Cr & Ni first. It can be seen that $\sim 60\%$ of the demand for these two metals is associated with the nuclear island, $\sim 12-16\%$ with the auxiliary components peculiar to the tokamak UWMAK-I and only 24-27% in the balance of plant. Secondly only about 10% of the total Cr & Ni requirement is associated with the initial blanket structure, 3% with the initial shield while almost 1/4 of the total requirement comes from the initial magnet structure. The replacement of the first 20 cm fourteen times during the lifetime of the plant only accounts for $\sim 8\%$ of the total requirement of a UWMAK-I type reactor while replacing the rest of the blanket and reflector region every 10 years accounts for another $\sim 17\%$. Finally it should be noticed that even if we made the entire blanket out of another material (Al, V, Nb, Mo) the total requirement

TABLE 9

Materials Requirements - UWMAK-I Nuclear Island
Metric Tonnes

Element	Blanket - 316 SS			Shield Structure & Absorbers	Magnets			Vacuum Pumps (c)	Misc.	Total	Tonnes MWe (1475 MWe)	
	Initial Structure (a)	1st wall replacement 14 times (b)	Reflector & Header replac. Twice		Toroidal Field Coils	T. F. Bracing (c)	Vertical Field Coils Incl. Dewar					Vertical Field Coil Support (c)
Al	79	69	146	26	123		118			562	0.38	
B				1580						1580	1.07	
C				446						446	0.30	
Cr	1406	1236	2636	457	1221	91	2126	181	9	9363	6.35	
Nb					86		15			101	0.07	
Cu	79	69	146	26	6163		1198			7681	5.21	
He				1	13		19			25	0.04	
Fe	4844	4253	9081	1573	4206	299	7322	599	29	(storage) 32211	21.84	
Pb				20500						20500	13.90	
Li	1159									(in pipes) 1700	1.15	
Mn	156	137	293	51	136	9	236	18	1	1037	0.70	
Hg									3	3	0.002	
Mo	156	137	293	51	136	236				1009	0.68	
Ni	1094	962	2051	355	950	54	1652	109	5	7233	4.90	
Ti					44		8			52	0.04	
Total Weight-	8973	6868	14647	25066	13078	453	12931	907	47	566	83534	56.63
Component Wt												
316SS	7814	6868	14647	2539	6895		11609				51122	
Li	1159									541	1700	
B ₄ C				2026							2026	
Pb				20500							20500	
He				1	13		19			25	58	
Cu Stabilizer					6040		1080				7120	
Nb-Ti					130		23				153	
Hg									3		3	
304SS						453		907	44		1404	

(a) 12 regular modules plus 3 spare units
 (b) first 20 cm only, 491 MT each time
 (c) 304 SS

TABLE 19
Summary of Elemental Requirements for UWMAK-I

<u>Element</u>	<u>Metric Tonnes</u>			<u>Tonnes</u>
	<u>Nuclear Island</u>	<u>Balance of Plant</u>	<u>Total</u>	<u>MWe</u> (1475 MWe)
Al	562	445	1,007	0.68
B	1,580	---	1,580	1.07
C	446	---	446	0.30
Cr	9,363	6,199	15,562	10.55
Nb	101	39	140	0.09
Cu	7,681	3,259	10,940	7.42
He	58	80	138	0.09
Fe	32,211	95,924	128,135	86.87
Pb	20,500	----	20,500	13.90
Li	1,700	----	1,700	1.15
Mn	1,037	608	1,645	1.13
Hg	----	3	3	0.002
Mo	1,009	22	1,031	0.70
Ni	7,233	4,484	11,727	7.95
Na	----	17,826	17,826	12.13
Ti	52	20	72	0.05
Y	----	5	5	0.003
Zr	----	100	100	0.07
	83,534	128,982	212,516	144.2

Table 12
Source of the Need for Critical Elements in the UWMAK-I
Reactor Facility*
% of Total Requirements

Element	Nuclear Island					Components Peculiar to UWMAK-I			Balance of Plant
	Initial Structure	1st wall Repl.	Balance of Blanket Repl.	Shield	Magnets	Energy Storage Unit	Thermal Fly-Wheel Tanks	Liner + Rev. Door	
Cr	9	8	17	3	23	3	10	3	24
Nb	-	-	-	-	72	28	-	-	-
Mn	9	8	18	3	24	2	10	3	27
Ni	10	8	17	3	24	2	8	2	27

*As compared to a Liquid metal cooled fission reactor

TABLE 13. W. TOKAMAK REACTOR

Data Relating to Metal Availability (All Quantities in 10⁶ m.t.)

Metal	Req. For 10 ⁵ MWe	U.S. Reserves		U.S. 1974 Production ^{3/}	U.S. 1974 Consumption ^{3/}	World - Ex - U.S.A. Reserves		1974 Prod.
		1X ^{1/}	3X ^{2/}			1X ^{1/}	3X ^{2/}	
304 & 316SS ^{4/}	56.89							
Fe	86.87	2000	>10,000	91.49	ca 91.0	246,000.0		413.0
Fe Ore (1973)				88.0	102.0			725.0
Cr	10.55	---	1.53	0.0	0.48	370.0	890.0	~2.0
Ni	7.95	0.2	~16.0	0.015	0.20	~24.0	?906.0	.67
Mo	0.70	5.4	>2.08	0.06	0.027	~4.0	~13.0	.021
Mn	1.13	0.0	>10.0	0.0	ca 0.81			~9.0
Pb	13.90	59.0		0.68	0.82	160.0	>500.0	2.81
Cu	7.42	>90.0	>100.0	1.70	1.79	>300.0	>500.0	5.75
Li	1.15	0.50	3.9	0.003	0.003	1.3 ^{7/}	0.2	.002
B	1.07	10.1	Large	~0.18	0.15	10.1		>0.15
Nb	0.09	.0054	.069	0.0	0.001	7.00	17.2	~.006 ^{6/}
Ti	0.05	>34.0	~ 29.0	ca 0.29 ^{8/}	0.200 ^{8/}	147.0		~.028 ^{6/}
Al	0.68	~2.0	>1000.0	0.40 ^{5/}	4.86	2000.0		13.4

37

^{1/} Reserves at present prices

^{2/} Reserves at 3X present prices.

^{3/} Primary metal only.

^{4/} 316 SS taken as Cr - 18%; Ni - 14%; Mo - 2%; Mn - 2%; Si - 1.0%; Cu-1.0%; Fe-62%; 304SS as Cr-20%;

^{5/} Primary metal from domestic bauxite. Ni-12%; Mn-2% and Fe-66%.

^{6/} Free World only. Ti metals only.

^{7/} Of this amount 1.1 x 10⁶ tons is Li estimated in brines of the Salar de Atacama; the validity of this estimate is in question.

^{8/} Titanium content of titanium minerals produced and consumed.

for Cr or Ni in a Li cooled UWMAK-I reactor would be reduced by only ~33%.

The requirements for Nb in UWMAK-I stem from two sources, the magnets associated with the nuclear island, (72%) and the magnets associated with the energy storage system (28%). The absolute amounts required at 0.14 tonnes/MWe are modest but the 212 tonnes of Nb-Ti alloy required for one UWMAK-I type plant represents an amount 38 times the present (1973) production of that alloy.

The reserves and resources of various elements (Li, Cr, Ni, Cu, Ti, Al, V, Mo, and Nb) have been investigated as a function of the present price, 3 times the present price, and 10 times the present price. A summary of the results is given in table 13, along with the amount of elemental metal which would be required to provide 10^6 MWe from UWMAK-I type reactors.

From the table we can categorize the needs of a UWMAK-I type reactor as follows;*

- 1.) Those elements for which there are ample US reserves at present prices and production capacity to absorb a move toward fusion power with UWMAK-I type reactors. (Fe, Mo, Cu, Ti, Al)
- 2.) Those elements for which the US has ample reserves at present or 3X present prices but where significant increase in mine and mill production would be required. (Ni, Mn, Pb, Li, Nb, B)
- 3.) Those elements for which the US has neither the reserves, resources or production capability. (Cr).

We will not address the first category here (the reader is referred to the detailed report) and would only comment that the demand for Ni, Mn, Pb, Li, Nb of UWMAK-I type reactors would produce serious strains on the production capabilities of the US mining and industrial community. Such large demands at 3 times present prices will also have the effect of increasing the capital and (to some degree) the operating costs of a reactor like UWMAK-I.

Finally, we have identified that the large demand for Cr in UWMAK-I (~16,000 tonnes) as the most critical resource problem to be faced. The US has essentially no Cr at current world prices and could satisfy only 10% of the needs of a 10^6 MWe economy at 3 times the present price. There are considerable reserves of Cr in the world but the US would have to rely on foreign sources for its supply just as it is now somewhat reliant on foreign oil sources. Such a situation must be examined very closely.

* Here we assume that the material required for 10^6 MWe would be produced over a 20 year time period so the required amounts must be divided by 20 to compare to current production rates.

VII Economics

The primary measures of the practicality of a power plant design are the reliability and cost of the electricity produced. Reliability is primarily a function of the plant design and the dependability of the fuel supply but will not be discussed in detail here because the design and operating details of UWMAK-I are not known well enough. We can only assume that the plant will be designed, built and operated such that it has adequate reliability. The reliability of the fuel supply is essentially 100 percent since it depends on purchase of relatively small amounts of readily-available deuterium and proper design and operation of the tritium recovery systems within the plant.

The cost of electricity produced in a power plant is determined primarily by the operating costs, the fueling costs, the capital costs, the amount of electricity generated, and the financial conditions for the utility operating the plant. Each of these primary factors is addressed in the bulk of the report. Before we can summarize those results we must briefly review a few of the definitions used in this study.

The plant factor for a power plant is defined as the ratio between the actual power generation and the power generation that would occur if the plant operated 100 percent of the time at the design power level. The plant factor is always less than 100 percent because of (1) outage time for maintenance (and refueling, in some cases) and (2) operation at less than the design level during startup periods and periods of time when there is not a need for all the electricity which could be generated.

The plant factor for the UWMAK-I is determined primarily by four factors:

1. The time required for wall replacement outages,
2. The amount of unscheduled outage time due to miscellaneous equipment failures and transmission system abnormal conditions,
3. The average length of the plasma burn, and
4. The length of the reactor rejuvenation time between plasma burns.

The inner wall is designed to last two years before replacement is necessary to prevent failure. During each two year period, the inner wall in each of the 12 reactor segments will be replaced.

The optimum schedule for replacing the wall segments is determined by making an economic balance of

1. the costs for keeping spare wall segments in inventory,
2. the costs for replacement of the segments, and
3. loss of income from sale of electricity during the outage period.

The cost of keeping spare segments in inventory is quite large and is directly proportional to the number replaced per outage. This cost decreases as the interval between outages decreases. Both the costs due to replacement of the segments and the loss of income from sale of electricity increases as the interval between outages decreases because the amount of outage time increases. (More time is required to prepare for the replacement and to prepare the reactor for operation after the replacements are completed.)

An economic balance for UWMAK-I shows that the optimum wall replacement interval is between 4 and 6 months. This interval would result in an outage during the spring and fall of each year when most utilities have minimum demand for electricity. Therefore, a 6 month replacement time was chosen for UWMAK-I.

During the wall replacement outages, all routine outage maintenance would be done. This includes such items as periodic inspection and maintenance of the turbine-generators, inspection and maintenance of large motors and pumps, etc. Also major equipment modifications would be done.

The unscheduled outage time was estimated to be 4 weeks per year due to minor equipment failures, loss of transmission systems, etc. This would also cover the replacement of a blanket module due to a statistical failure of one of the first walls.

We have already described the burn time as 90 minutes and the down time as 6 1/2 minutes. The sensitivity of the plant factor to these two parameters is shown in Figures 15 to 17. Note that with the above decisions, we find that the plant factor for UWMAK-I is 78-80%. Such a number is comparable to current plant factors for fossil and fission power plants and if no major unexpected outages occur, should be acceptable to electric utilities.

The capital costs for UWMAK-I were estimated by use of standard preliminary capital cost estimating procedures. The primary guide for estimation of the capital cost was the document NUS-531 "Guide for Economic Evaluation of Nuclear Reactor Plant Design." That document presents the general philosophy, procedures, and record tables for estimating all costs for a power plant.

A conservative approach was used in estimating the capital costs. Past experience has demonstrated that advocates of new facilities frequently underestimate the capital costs because of optimism in design and failure to include sufficient contingency for unforeseen difficulties. In this analysis, the construction costs were deliberately overestimated whenever uncertainties existed. An example, current maximum equipment sizes were used whenever there was any doubt that larger equipment could be produced. This eliminated the economies-of-scale that might be realized by use of larger equipment or increases in quantities manufactured.

No attempt was made to develop detailed designs for the numerous small support systems. It became apparent early in the effort that order-of-magnitude costs for such items would be adequate. Large errors in these costs would have no significant effect on the total capital costs because they cause a small fraction of the total costs.

Most of the costs were estimated by use of standard costs per unit of material. After development of a general design for a facility, the quantities of material needed for construction of that facility were estimated and then multiplied by the standard cost per unit of material to obtain the installed cost.

A summary of the estimated capital costs is given in Table 14. Much more detail is provided in the body of this report. The considerations have predicted that a UWMAK-I type reactor may cost in the neighborhood of \$1000/kW_e. This number is not too unreasonable when compared to fast breeder costs of \$600-800/kW_e. We feel the most important point about the present costs is that fusion is within a factor of 50% of fission facilities and in the future more detailed studies may provide closer correlations especially if large additional costs result from the disposal of high level wastes and the prevention of diversion of weapons grade material.

It is also of interest to note that 74% of the costs are direct costs and 26% are indirect. The indirect costs are dominated (60%) by the 8% interest costs for the assumed 5 year construction time. Taxes and insurance (part of the "Other Costs") amounts to 21% of the indirect costs while items such as engineering services, construction facilities, equipment and services amount to another 19% of the indirect costs.

Another way to look at the numbers in Table 14 is to distribute the indirect costs to the direct costs and determine how much is involved in the

Nuclear Island
Power Generating Equipment
Balance of Plant (structure, etc.)

On this basis, we find 51% of UWMAK-I costs are associated with the nuclear island, 28% with the electrical generating facilities, and ~20% for the balance of plant. This says that approximately 1/2 of the costs of UWMAK-I are associated with the "conventional" part of the plant while the other half is associated with the fusion reactor itself.

A breakdown of nuclear island costs is given in Table 15. Roughly 1/3 of the nuclear island costs and 17% of the total plant costs are involved in the reactor magnets while the corresponding numbers for the blanket and shield are 28% and 14% respectively. The heat transfer system, which includes the Li and Na, piping, pumps, intermediate heat exchangers, miscellaneous dump tanks and heating equipment, amounts to ~40% of the nuclear island costs and 20% of the overall plant costs. The importance of such comparisons shows that only ~30% of the total UWMAK-I costs are involved with really new technologies (magnets, injectors, vacuum systems, T₂ extraction, blanket and shield construction, etc.). Therefore, a major effort to reduce those costs must also be coupled with a reduction of the balance of plant and "conventional" technology costs.

Finally, we have calculated the electricity production costs which include

1. The operation and maintenance costs
2. The fuel cost
3. The annual return on capital .

The operation and maintenance costs are described in detail in the body of the report but the conclusion is that they will run ~12 million dollars a year, over 60% of which results from changing the first wall every two years.

TABLE V-3Cost Data

(Prices are Present Day and Based on a 40 Hour Work Week)

<u>Account Number</u>	<u>Account Title</u>	<u>Total</u>
<u>DIRECT COSTS:</u>		
Nondepreciating Assets:		
20	Land and Land Rights	\$1,200,000
Depreciating Assets:		
26	Special Materials	28,290,000
Physical Plant		
21	Structures and Site Facilities	139,807,000
22	Reactor Plant Equipment	573,636,000
23	Turbine Plant Equipment	170,580,000
24	Electric Plant Equipment	142,859,000
25	Miscellaneous Plant Equipment	9,410,000
	SUB-TOTAL Physical Plant	1,036,292,000
<u>INDIRECT COSTS (All Depreciating Assets):</u>		
91	Construction Facilities, Equipment and Services	24,300,000
92	Engineering Services	48,500,000
93	Other Costs	75,600,000
94	Interest During Construction	218,618,000
	SUB-TOTAL	367,018,000
	SUB-TOTAL (Total Depreciating Assets)	1,413,600,000
	TOTAL PLANT CAPITAL INVESTMENT:	1,432,800,000
	COST PER KILOWATT GENERATED	971

Table 15

Summary of UWMAK-I Nuclear Island Costs

<u>Nuclear Island Component</u>	<u>% of Nuclear Island</u>	<u>% of UWMAK-I</u>
Reactor Magnets	33	17
Blanket and Shield	28	14
Heat Transfer System	39	20

Table 16

UWMAK-I Electricity Costs

<u>Cost Item</u>	<u>Annual Cost</u>	<u>Unit Cost</u> (mills/kwh)
Operations and Maintenance	\$12,000,000	1.1
Fuel	127,000	0.01
Return on Capital	<u>214,920,000</u>	<u>20.1</u>
Total	227,047,000	21.2

The fuel costs are truly negligible amounting to annual costs for D_2 of \$123,000 per year and \$4,000 per year for the lithium.

Finally, annual return on capital was assumed to be 15% per year which is typical of private utilities.

A summary of the electricity costs is given in Table 16. It is obvious that both fuel and O & M costs are rather insignificant compared to the total costs of ~21 mills per kW-hr. It is also important to note that even if the frequency of first wall replacement doubled, from once every 2 years to once every year, the total operating costs would only increase by about 3% due to direct material costs and ~8% because of increased downtime. This indicates the relative insensitivity to the two year lifetime decision.

VII. Conclusions

The detailed design of a tokamak fusion reactor has uncovered many new problems and shown that some previously troublesome areas may be subject to engineering solutions. Particularly encouraging is that the costs of fusion power may be within reasonable limits of projected energy costs and future ingenuity should help to improve this picture. However, it is hard to see how fusion power from Tokamaks will ever be much cheaper than that from fission reactors because of the low energy density of the energy extracting units.

The demand on U.S. reserves and resources of critical elements is severe (as it is for other energy sources) and of particular concern is the requirement for large amounts of chromium. Self sufficiency in this element appears to be very difficult even if the present price were to be raised by a factor of three or more.

A first look at the environmental impact of a D-T fusion reactor like UWMAK-I reveals that it will have many of the same problems as are currently facing fission reactors. These areas of concern include the generation of large amounts of radioactive waste and the potential for release of volatile radioactive tritium both during routine operation and in the event of an accident. The source and consequences of a major accident seem to be much smaller for a fusion reactor like UWMAK-I than for a fission reactor, but it must be recognized that such a possibility exists.

The design of the "balance of plant" and power cycles has revealed only a few new problems but they must be thoroughly analyzed to see how much they tend to increase the cost of fusion power. The "thermal flywheel" concept (or something similar) will present a challenge to power engineers that they have not had to face previously. The design of large, partially evacuated buildings for the nuclear island will also test the skills of architect engineers as well as the design and construction of heat exchangers which limit the release of tritium to the environment.

We feel that the present design effort is only a beginning and that many more reactor concepts need to be investigated before definitive broad statements can be made. It is only by the continuous "shifting and winnowing" of new ideas that we hope to eventually be able to provide large amounts of electricity by fusion power.

I. Power Cycle

I-A Introduction and General Philosophy of Coolant System

The main purpose of a reactor like UWMAK-I is to produce electric power as safely and cheaply as possible. Such a goal sounds simple in principle, but in fact is quite complex in practice. Not only does such a goal involve the choice of coolants which are compatible with structural materials and tritium containment schemes, but it involves a complex balance of flow rates, temperatures, pressure drops and pumping power.

The basic power cycle for UWMAK-I is shown in Figure I-1. It utilizes a lithium primary coolant which transfers its heat in an intermediate heat exchanger to a sodium secondary fluid. The sodium in turn transfers its heat to a double walled steam generator.

The main purpose for the sodium intermediate loop is to reduce the amount of tritium and corrosion product leakage from the lithium primary loop to the steam cycle both during normal operation and in the event of a leak in the steam generator (see Chapter 8 in Volume I of this report for more details). The main constraint on the Li loop is that the maximum Li-SS contact temperature not exceed 500°C due to corrosion considerations (see Section IV-C in Volume I).

It was decided to have twelve reactor loops in UWMAK-I, one each for the twelve reactor modules. This was done in order to reduce the potential for tritium leakage in the event of a catastrophic accident in any one of the primary coolant streams and to reduce the amount of coolant channels that must be opened and rewelded during module change out. The distribution of the 5000 MW_t output from the plant is shown in Table I-1.

Before going into more detail on the specific coolant loops, there are two further points which need to be made. First, while the instantaneous reactor output is 5000 MW_t during the plasma burn, there is a 6.7% down time in which no power is being produced (see Chapter II of main report). Therefore, the time averaged output is 5000 MW_t x 0.933 or 4663 MW_{th} (4383 MW_{th} of which is in the blanket coolant circuit). The second point is to note that a "thermal flywheel" concept be used in conjunction with the secondary sodium system. This concept involves the diversion of a small amount (~7%) of the hot sodium into a well insulated storage tank. This Na is accumulated during the 5400 second burn time and then fed back into the Na loop during the 390 sec down time between burns. This maintains a constant power output to the electrical network which is a fundamental requirement for a practical power plant.

I-B Blanket Cooling System

I-B-1 Primary Lithium Loop

It was stated previously that there are 12 primary reactor coolant loops; each one of which feeds into an intermediate heat exchanger which in turn is connected to its own sodium loop. The twelve sodium loops then circulate the sodium through twelve steam generators where the steam is generated to feed into a common set of steam headers, and eventually into the turbine cycle.

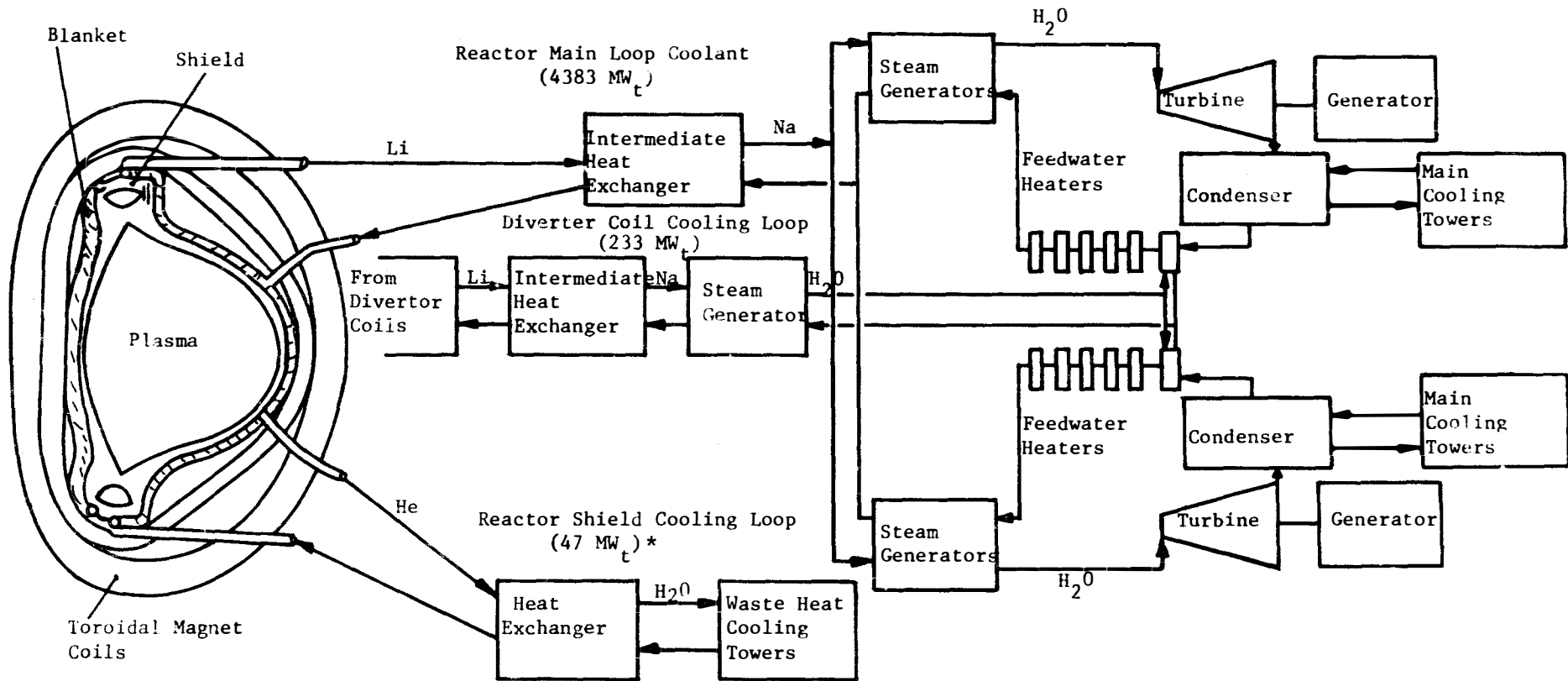


FIGURE I-1

Schematic Plant Design
 Wisconsin Toroidal Fusion Reactor - UWMAK-1

* Time averaged values

Table I-1

Distribution of Power from the 5000 MW_t UWMAK-I

		<u>Number of</u> <u>Loops</u>	<u>MW_{th}</u> <u>per Loop*</u>	<u>Total</u> <u>MW_{th}*</u>	<u>Time Average</u> <u>MW_{th}</u>
Blanket	Li Primary Loop	12	392	4700	-
	Na Secondary Loop	12	392	4700	-
	Steam Loop	12	392	4700	4383
Divertor	Li Primary Loop	1	250	250	-
	Na Secondary Loop	1	250	250	-
	Feedwater Loop	1	250	250	233
Shield	He Coolant	12	4.2	50	-
	Coolant Water	12	4.2	50	-

* Instantaneous values during burn cycle. Time averaged values (to account for down time) are 93.3% of that value

A schematic of a typical lithium coolant system is shown in Figure I-2 and Table I-2 lists the pertinent temperatures, pressures and flow rates for that system. There are six major subsystems in this loop and they are listed below.

- . Li cleanup
- . Intermediate heat exchanger
- . Li make-up loop
- . Tritium extraction beds
- . Major lithium circulation pump
- . Li dump tank and storage

The lithium comes from the reactor at a temperature of 489°C and a pressure of ~40 psi (2.8×10^4 kg/m²). It then passes the cleanup system where 1% of the main flow (2.7×10^4 kg/hr) is diverted for purification.

The primary purpose of the cleanup system is to remove corrosion products and oxygen that may have leaked into the system. This requires that a small amount of the lithium be heated from the reactor outlet temperature (489°C) to 645°C in order to reduce the solubility of these elements. (Figure I-3) After the lithium has been purified, it is passed into a regenerative heat exchanger and fed back into the main lithium stream. The regenerative heat exchanger raises 2.7×10^4 kg of lithium/hr from 489°C to 645°C on the entry side and lowers it from 662 to 519°C on the return side. It utilizes 91 - 2.54 cm OD by 0.089 cm thick wall tubes, 7.93 meters long on a 3.34 cm triangular pitch. Therefore, under equilibrium conditions, only ~30°C of thermal energy per unit of mass need be added to the Li for cleanup purposes.

The entire assembly of tubes, tube sheet, baffles and shrouds is attached to an upper shield plug to facilitate remote replacement if necessary. (Figure I-3) The tube side and shell side pressure losses are less than 0.1 and 0.3 psi, (70 to 211 kg/m²), respectively (excluding entrance and exit losses of connected piping).

The next step is to pass the lithium through the intermediate heat exchanger which is shown in Figure I-4. Figure I-4 also lists the pertinent data on flow rates, temperatures and pressures. This particular IHX design is one which is currently being considered for LMFBR's and represents state of the art technology. It has been modified to accommodate a lower Li flow rate (2.7×10^6 kg/hr) per unit in the primary system as compared to the higher sodium flow rate in the secondary system (9.1×10^6 kg/hr). The general configuration shown in Figure I-4 contains 4982-304 stainless steel tubes which are 2.06cm in diameter and 0.089cm thick. Tube length between tube sheets is 9.53 meters and the tubes are on a 2.69 cm triangular pitch. The lithium inlet temperature is 489°C and the outlet is 359°C.

This design is typical of those developed for LMFBR applications where the primary side fluid is highly radioactive. It is designed to permit tube bundle replacement through a shielded plug. Lithium with entrained and/or deposited quantities of activated corrosion products would be on the shell side of this design.

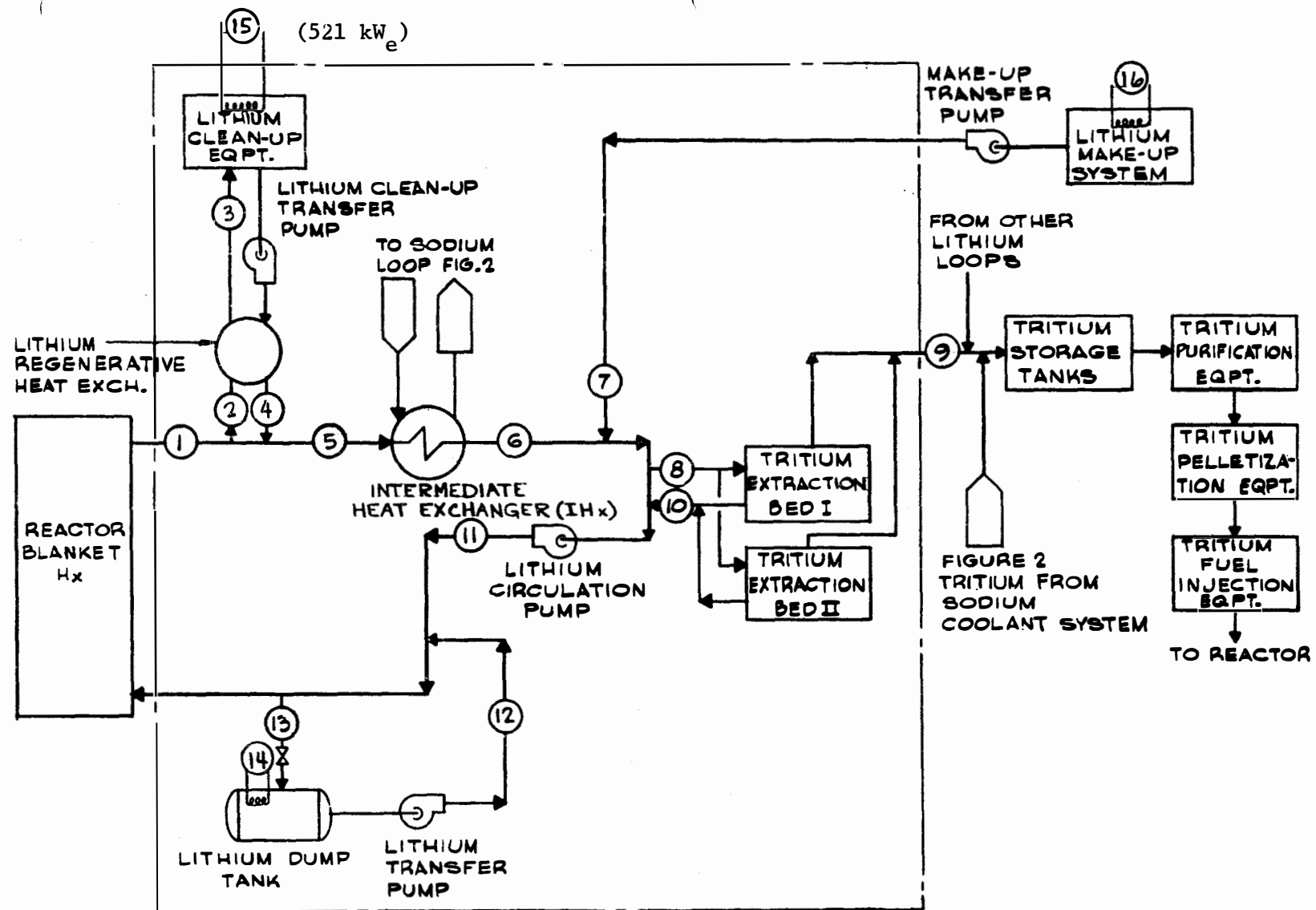


Figure I-2. Lithium Coolant System - UWMAK-I

TABLE I-2

DATA SUMMARY FOR FIGURES I-2 and I-3

SYSTEM LOCATION DESCRIPTION	Position	Temperature		Flow		Pressure	
		°F	°C	LB/HR	KG/HR	Psi	kg/m ² x 10 ⁴

NORMAL OPERATION

Lithium System: (Fig. I-2)							
Outlet From Reactor	1	912	489	6.0x10 ⁶	2.7x10 ⁶	40	2.8
To Li Reg. Heat Exchanger	2	912	489	6.0x10 ⁴	2.7x10 ⁴	40	2.8
To Li Clean-Up Equip.	3	1193	645	6.0x10 ⁴	2.7x10 ⁴	35	2.5
From Li Reg. Heat Exchanger	4	966	519	6.0x10 ⁴	2.7x10 ⁴	40	2.8
To IHX	5	912	489	6.0x10 ⁶	2.7x10 ⁶	35	2.5
From IHX	6	678	359	6.0x10 ⁶	2.7x10 ⁶	30	2.1
To Tritium Extraction Bed	8	678	359	6.0x10 ⁵	2.7x10 ⁵	20	1.4
From Tritium Extraction Bed	10	678	359	6.0x10 ⁵	2.7x10 ⁵	20	1.4
Inlet to Reactor	11	678	359	6.0x10 ⁶	2.7x10 ⁶	670	47
Sodium System: (Fig. I-5)							
From IHX	1	853	456	2.1x10 ⁷	9.8x10 ⁶	35	2.5
To Na Hot Storage	2	853	456	1.44x10 ⁶	7.1x10 ⁵	30	2.1
To Na Reg. Heat Exchanger	4	853	456	2.0x10 ⁵	9.1x10 ⁴	28	2.0
To Na Clean-Up Equip.	5	1119	604	2.0x10 ⁵	9.1x10 ⁴	23	1.
From Na Reg. Heat Exchanger	6	907	486	2.0x10 ⁷	9.1x10 ⁶	28	2.0
To Steam Generator (Na Side)	8	853	456	1.9x10 ⁷	8.6x10 ⁶	25	1.8
From Steam Generator (Na Side)	11	637	336	1.9x10 ⁶	8.6x10 ⁵	20	1.4
a) To Steam Generator (H ₂ O Side)	10	425	218	1.39x10 ⁶	6.3x10 ⁵	2100	148
b) From Steam Generator (H ₂ O Side)	9	760	404	1.39x10 ⁶	6.3x10 ⁵	2000	140
To Tritium Extraction Bed	12	637	336	2.0x10 ⁶	9.1x10 ⁵	20	1.4
From Tritium Extraction Bed	13	637	336	2.0x10 ⁶	9.1x10 ⁵	20	1.4
From Na Circ. Pump	15	637	336	2.0x10 ⁷	9.1x10 ⁶	70	4.9
From Sodium Dump Tank	17	637	336	1.44x10 ⁶	7.1x10 ⁵	40	2.8
To IHX	---	637	336	2.1x10 ⁷	9.8x10 ⁶	--	---

RECHARGING OPERATION

Sodium System: (Fig. I-5)							
From IHX				~0			
From Na Hot Storage Tank	3	853	456	2.0x10 ⁷	9.1x10 ⁶		
To Na Reg. Heat Exchanger	4	853	456	2.0x10 ⁵	9.1x10 ⁴	28	2.0
To Na Clean-Up Equipment	5	1119	604	2.0x10 ⁵	9.1x10 ⁴	23	1.6
From Na Reg. Heat Exchanger	6	879	471	2.0x10 ⁵	9.1x10 ⁴	28	2.0
a) To Steam Generator (Na Side)	8	853	456	1.9x10 ⁷	8.6x10 ⁶	25	1.8
b) From Steam Generator (Na Side)	11	637	336	1.9x10 ⁷	8.6x10 ⁶	20	1.4
To Steam Generator (H ₂ O Side)	10	425	218	1.4x10 ⁶	6.3x10 ⁵	2100	148
From Steam Generator (H ₂ O Side)	9	760	404	1.4x10 ⁶	6.3x10 ⁵	2000	140
To tritium Extraction Bed	12	637	336	2.0x10 ⁶	9.1x10 ⁵	20	1.4
From Tritium Extraction Bed	13	637	336	2.0x10 ⁶	9.1x10 ⁵	20	1.4
From Na Circ. Pump	15	637	336	2.0x10 ⁷	9.1x10 ⁶	70	4.9
To Na Dump Tank	16	637	336	2.0x10 ⁷	9.1x10 ⁶	--	---

a) Feedwater b) Steam

	Li	Na
T_1 °C	662	649
T_2	519	486
T_3	645	604
T_4	489	456
FLOW kg/hr	27,000	91,000

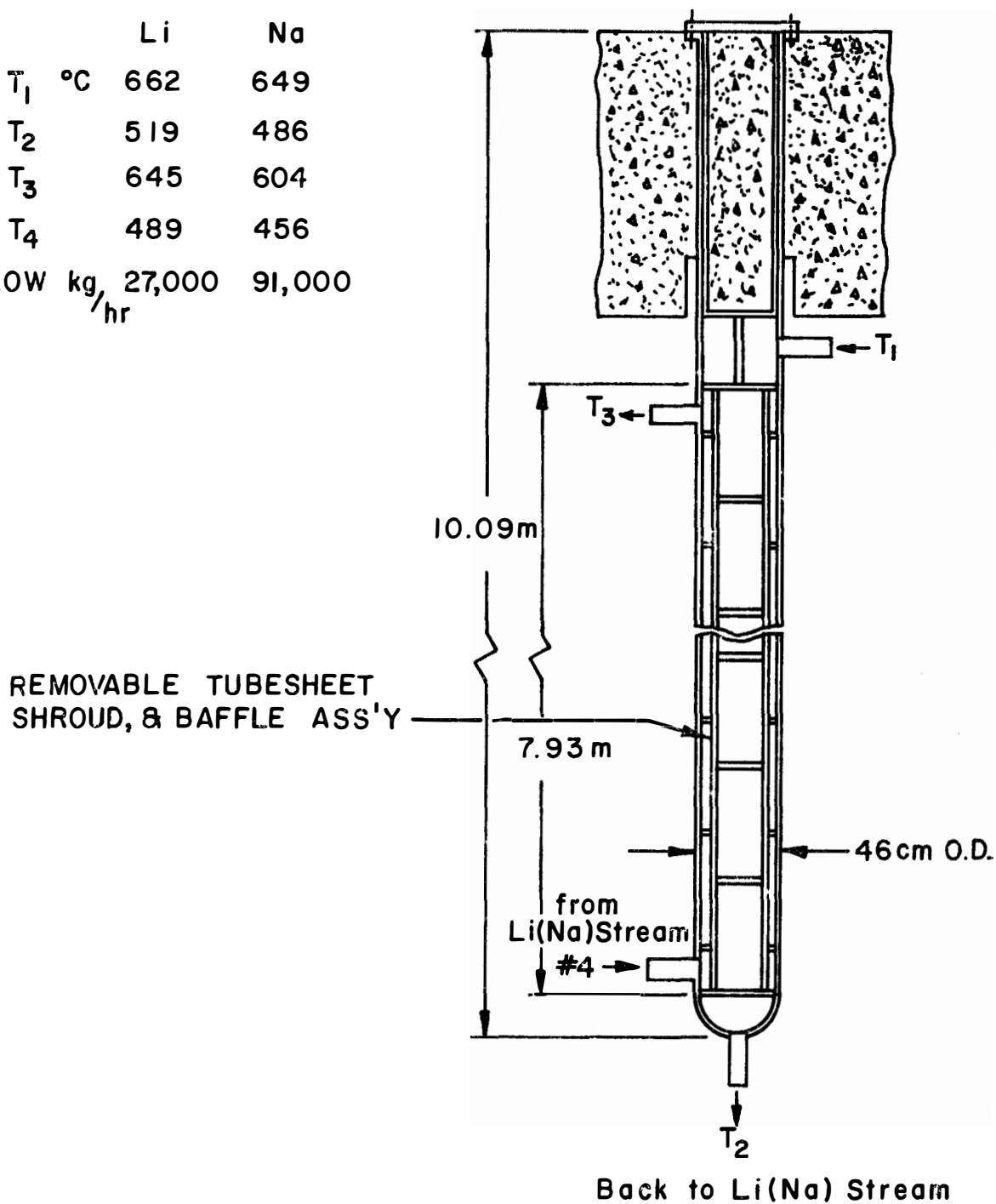


Figure I-3 LITHIUM AND SODIUM HOT TRAP HEAT EXCHANGER ARRANGEMENT.

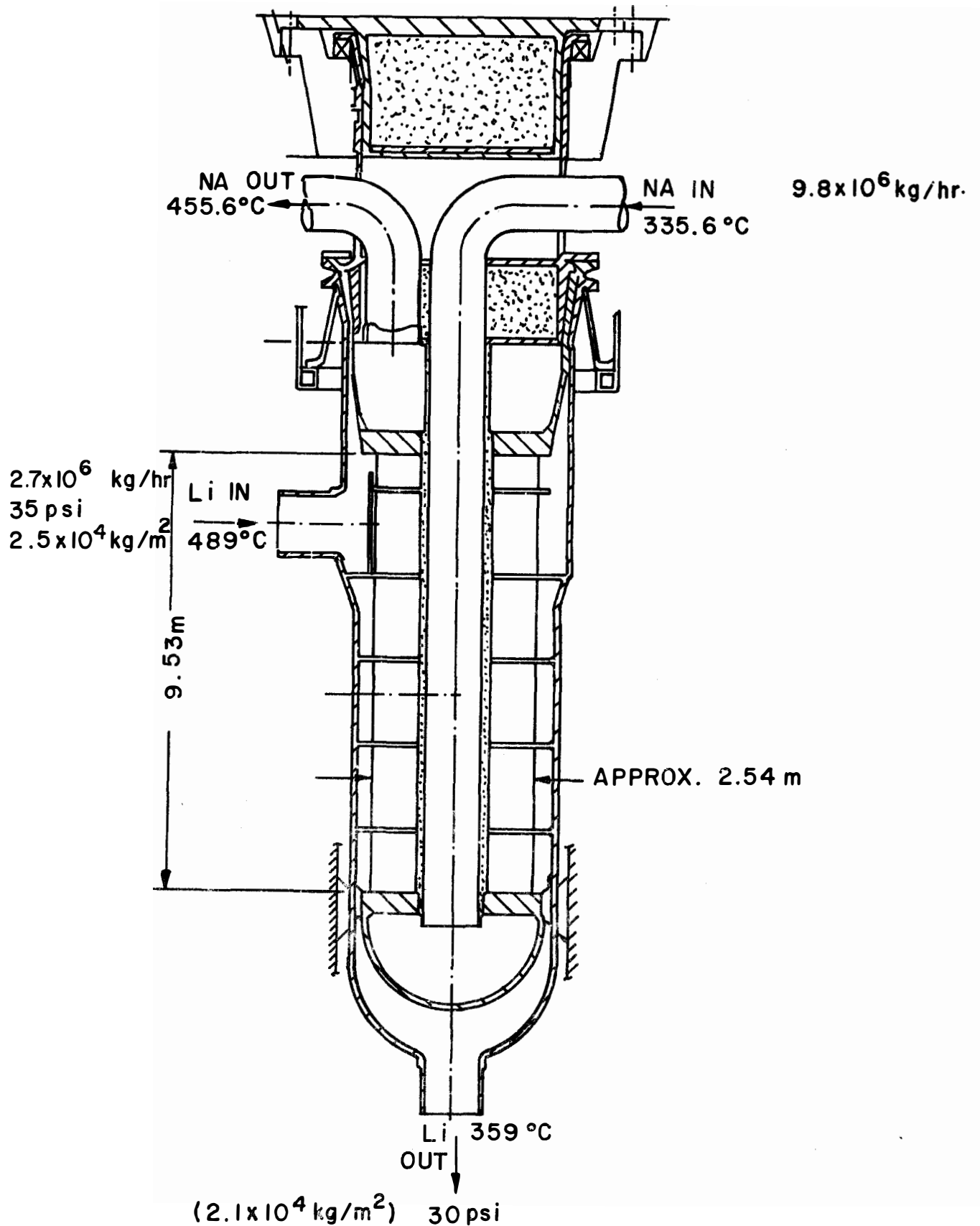


Figure: I-4 GENERAL ARRANGEMENT OF INTERMEDIATE HEAT EXCHANGER

The lithium makeup system represents a minor part of the overall power cycle and will not be treated in detail here. Basically, it would be used to supplement Li lost through leaks or it could be used to inject Li-6 to replace that burned up to produce tritium.

The operations of the tritium extraction beds have been described previously (see Chapter VIII in Volume I). The only point to note here is that approximately 10% of the main Li flow is passed through the extraction beds (via regenerative heat exchangers) and there is essentially no temperature change involved with this operation.

The main liquid Li pump is assumed to handle 2.7×10^6 kg of Li per hour per loop (22,500 gpm) and it increases the Li pressure from 30 to ~670 psi (2.1×10^4 to 47×10^4 kg/m²). It is assumed that liquid metal pump technology from the LMFBR will be applicable in this area.

Finally, provisions have been made to hold all of the lithium from the primary coolant loop in the event that the reactor module needs to be withdrawn for repair. The capacity of the tank is roughly 142,000 kg (~37,400 gallons) It should also be noted that since Li melts at ~190°C, special heaters will have to be installed in all makeup and storage tanks to keep the Li from freezing.

I-B-2 Secondary Sodium Loop

The main features of the sodium coolant for a reactor module are shown in Figure I-5 and the specific data on flow rates, temperatures and pressures are given in Table I-2. The sodium system is essentially the same as the lithium system except for the inclusion of the thermal "fly wheel." One key property of sodium is the fact that it has a heat capacity which is ~2.7 times smaller than that of Li. This means that roughly 2-3 times more Na is required to transfer the same amount of heat. Actually more than that is required to comply with the thermal fly wheel concept.

The sodium comes from the IHX at a temperature of ~456°C and a pressure of ~35 psi (2.5×10^4 kg/m²). Approximately 7% of the Na is bled off into the hot sodium storage tank where it is held until needed during the recharge cycle. Heaters need to be installed in this system to offset thermal leakage from the storage tanks and to keep the Na from freezing since its melting point is ~100°C. The tank must hold ~1,000,000kg of Na, or 250,000 gallons. This requires a cylindrical tank 41 feet (12.6m) in diameter and 35 feet (10.7m) tall. (Table I-3)

The sodium cleanup system has the main function of removing oxygen and corrosion products from the secondary loop. Approximately 1% of the Na (9.1×10^4 kg/hr) is passed through a regenerative heat exchanger, heated from 456 to 604°C, purified, and then passed back through the regenerative heat exchanger on its way back to the main coolant stream. The temperature drop on the return leg of the regenerative heat exchanger is from 649 to 486°C. The tube bundle design is the same as for the lithium regenerative heat exchanger except that the tube and shell side pressure losses are 0.3 and 3 psi (211 to 2110 kg/m²) respectively. Approximately 581 kW of electrical energy per loop is required to perform this operation.

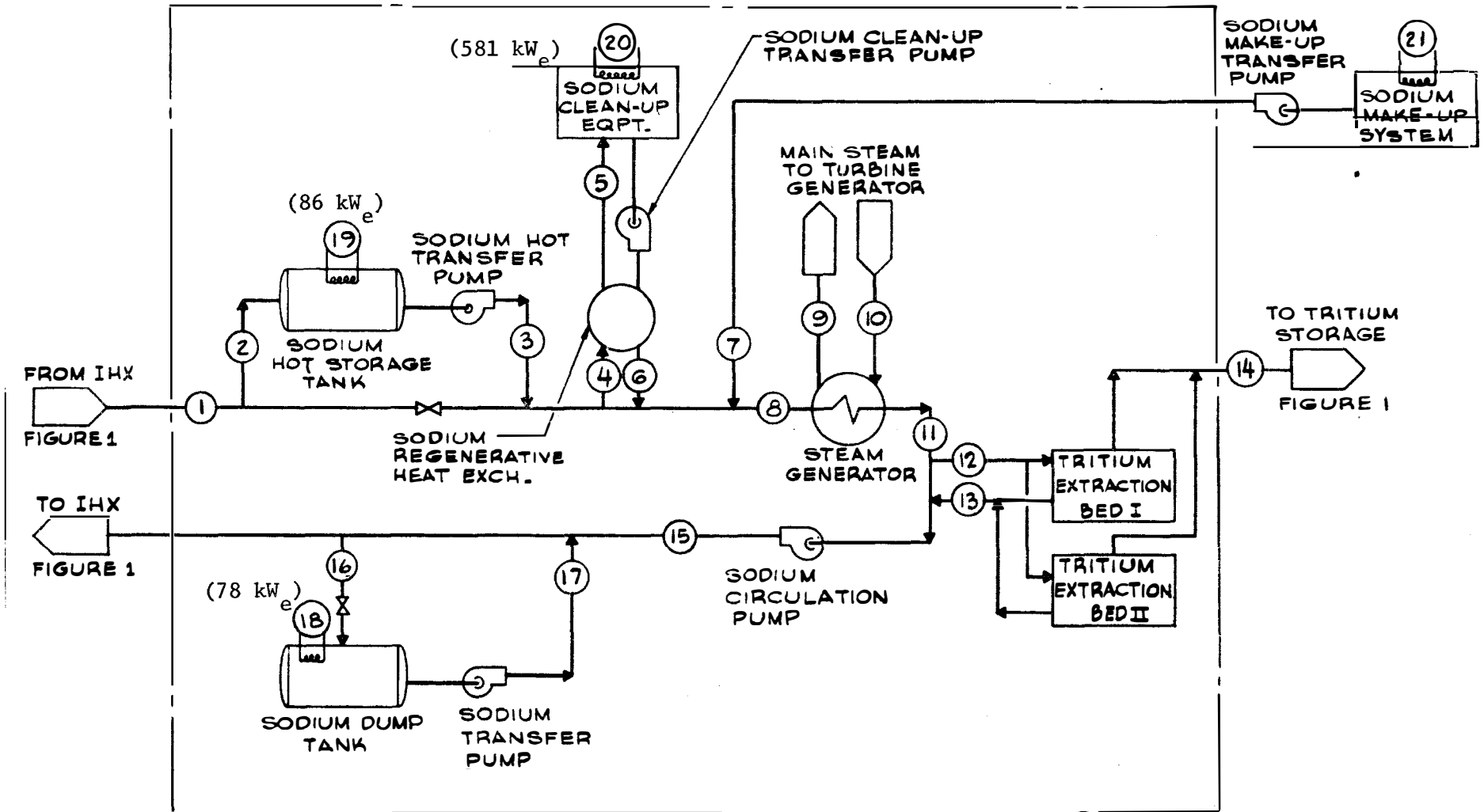


Figure I-5. Sodium Coolant System - UWMAK-I.

After passing the sodium make up system, the sodium is passed through the steam generator which will be described in more detail later. It enters the steam generator at 456°C and leaves at ~336°C.

Tritium extraction beds are also included on the secondary loops, but it is not expected that large amounts of tritium will have to be handled. (See Chapter VIII in Volume I.) The output from the tritium extraction beds will be fed into the main tritium handling stream.

The sodium circulation pumps will have to be capable of handling flow rates of 53,000 gpm (9.8×10^6 kg/hr) of Na at 336°C and increasing the pressure from 20 to 70 psi (1.4 to 4.9×10^4 kg/m²).

Finally, provisions have been made to hold all of the Na in a given secondary loop in the event that either the IHX or steam generator has to be repaired. These tanks must hold ~1,210,000 kg or ~320,000 gallons of Na. This corresponds to a cylindrical tank ~45 ft. (13.8m) in diameter and ~35 ft. (10.7m) tall. (Table I-3)

I-B-3 Steam System

I-B-3-a Sodium to Water Steam Generator Design

The steam generator for UWMAK-I utilizes a proprietary combination of the latest steam generator technology from Babcock and Wilcox* to:

- 1) Minimize tritium diffusion into the steam
 - 2) Avoid the characteristic problems of liquid metal to water heat exchangers
 - 3) Provide safety and high reliability
- and 4) Facilitate in-service inspection and maintenance.

It is expected that these characteristics would also make this generator suitable for application in LMFBR or MSR facilities.

Some engineering drawings of the steam generator are given in Figures I-6a-d and Table I-4 lists some of the important parameters. The design utilizes once thru steam generator modules with vertical 0.635cm OD. 0.089 cm thick Inconel-600 tubes which fit into semicircular grooves on the sides of horizontal rectangular (cross section) sodium platens (see Figs. I-6-a and I-6-b) made of Croloy 2 1/4 steel. The small dimensions of this geometry were chosen so that the thermal conductivity of Croloy 2 1/4 was adequate to satisfactorily transfer heat from sodium to the steam generator tubes across a 25.4 micron helium filled gap. Heat path temperature distribution is shown in Fig. I-6-c for average nucleate boiling section conditions. Figure I-6-d shows the overall steam generator arrangement. A trace amount of oxygen is maintained in the helium to getter tritium diffusing through the Croloy 2 1/4 walls. The exchanger equipment is contained within a 1.27 cm thick carbon steel vessel with a 195 inch OD (5.95 meters) diameter and an overall length of 478 inches (14.6 meters). It is expected that the unit would be mounted horizontally.

* D. Schluderberg, to be published.

TABLE I-3

SODIUM HOT STORAGE AND DUMP TANKS

ITEM DESCRIPTION	PARAMETER
Na Hot Storage Tank: (24 required)	
Size (Per module)	
Diameter m	9
Height m .	10
Weight kg	335,000
Weight (When Full) kg	<u>968,000</u>
Na Dump Tank: (12 required)	
Size (Per module)	
Diameter m	13.8
Height m	10.7
Weight kg	382,000
Weight (When Full) kg	<u>1,732,000</u>

FIG. I-6-a

DOUBLE WALLED LIQUID METAL TO WATER
OTSG DIAGRAM SHOWING BASIC
HEAT EXCHANGE ARRANGEMENT

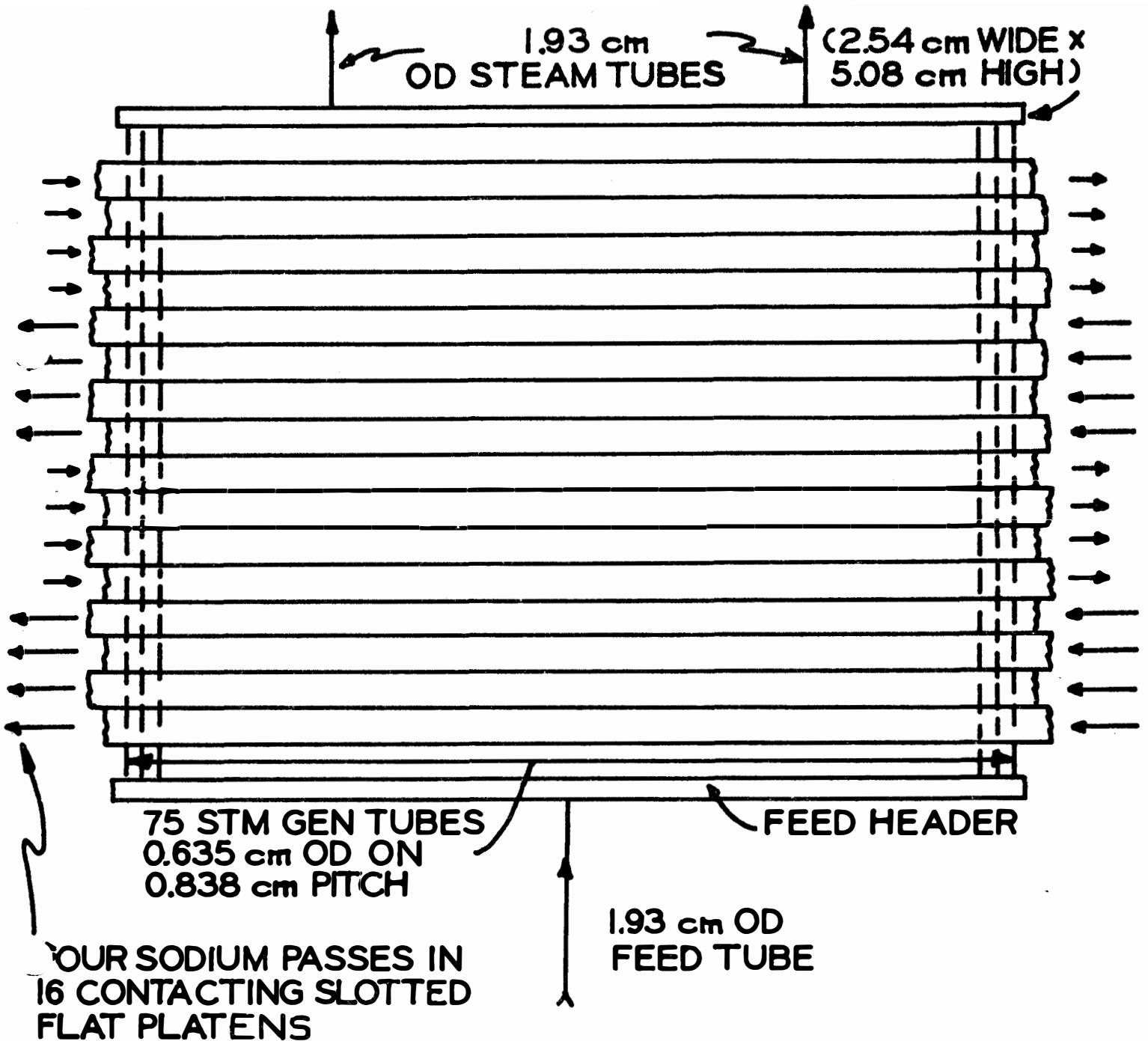


FIG. I-6- b
HORIZONTAL SECTION THRU
SODIUM PLATENS AND
STEAM GEN TUBES

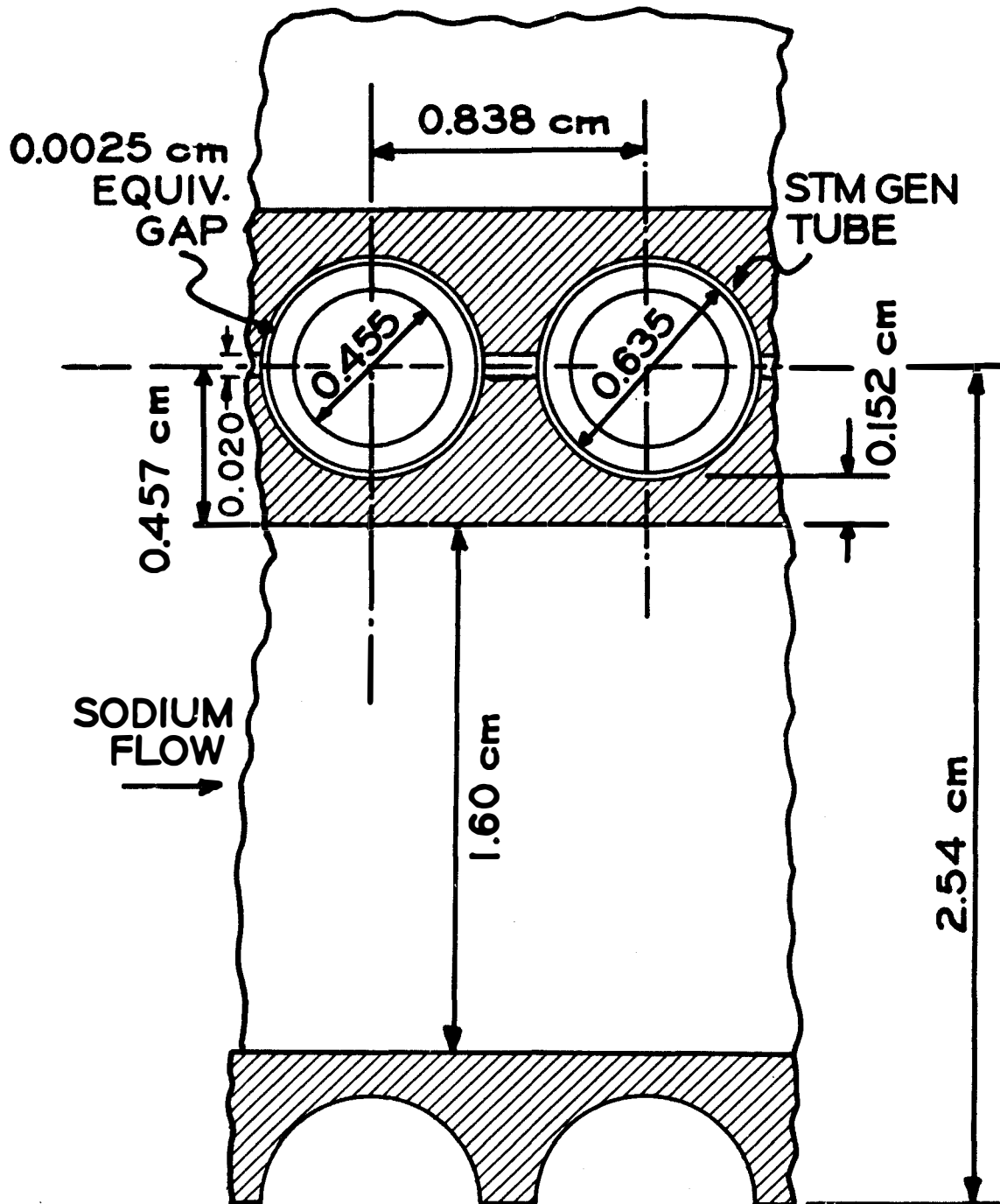
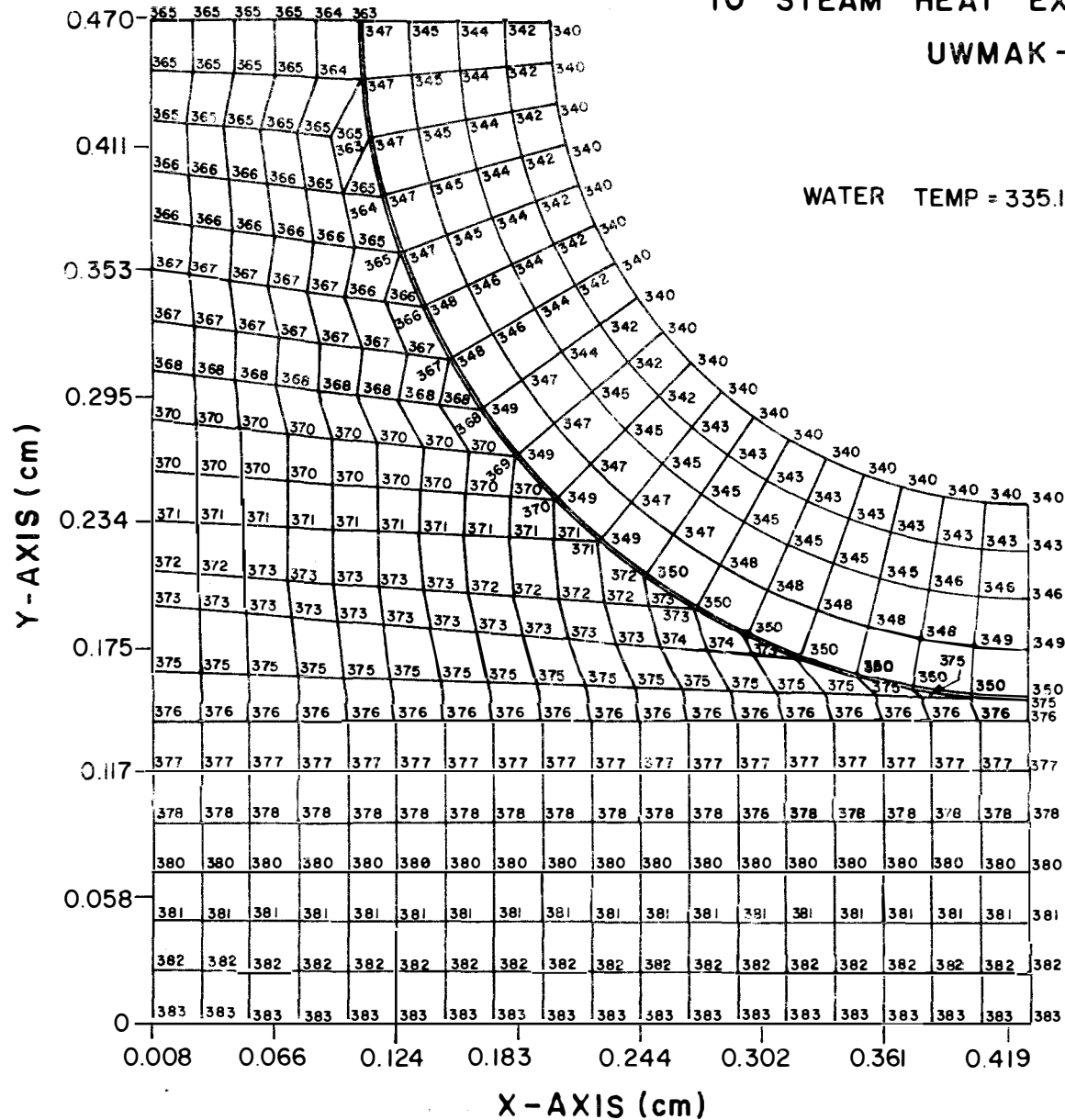


Figure I-6-d

TEMPERATURE PROFILES FOR SODIUM
TO STEAM HEAT EXCHANGER FOR

UWMAK-I

WATER TEMP = 335.1°C



NA. HT. TRANS COEFF. ON X AXIS
IS 5.7 watt/cm²°C

NUCLEATE BOILING COEFF. ON
TUBE I.D. IS 15.51 watt/cm²°C

AVE HEAT FLUX THRU NA FILM IS
25.12 watts/cm²

STM/WATER TEMP = 335.1°C

NA TEMP. = 393.8°C

A total of twelve (12) steam generators are required to handle the time averaged 4383 MW_t heat load. This particular system has used Na as the secondary heat fluid because :

- 1) The above design was tailored to Na corrosion characteristics.
- 2) To use Li would increase the cost of the heat transfer fluid as well as adversely effect the world reserves of Li if such a practice became wide spread.

However, if lithium had been used, the size of the secondary loop could have been reduced.

The sodium flow rates (Table I-4) have been adjusted to give a favorable balance of log mean temperature difference between the steam generator and intermediate heat exchanger and thus produce the highest practical steam pressure.

Table I-4
Principal Design Parameters of UWMAK-I Steam
Generators as Described in Figure I-5

Total Intermediate Flow Rate (12 units) kg/hr	1.028 x 10 ⁸
Sodium Flow Rate for each Boiler kg/hr	8.567 x 10 ⁶
Na Temperature Drop in Boiler °C	120
Na Inlet/outlet Temperature, °C	456/336
Heat load, each Boiler, kW	365,302
Steam Flow, each Boiler, kg/hr	630,000
Total Steam Flow kg/hr	7,543,000
Steam Pressure at Boiler Outlet Header psia	2,000
kg/cm ²	1.41 x 10 ²
Steam Temperature at Boiler Outlet Header, °C	404
Feedwater temperature at 100% Power, °C	218
Steam Generator Tube Heating Surface per Boiler, m ²	3088
Dry Weight of Steam Generator, kg/unit	149,300
Na Inventory at Operating Temperature, kg/unit	21,780
H ₂ O Inventory at Full Power, kg/unit	2970
Total Weight/unit, kg	171,150
Sodium Inlet and Outlet pipe, OD/ID, cm	107/102
Steam Outlet Pipe Size, OD cm	30.5
Feed Water Pipe Size, cm	20.3 Sch 40
Sodium Inlet Pipe Location, cm above Vessel ⌀	93.7
Sodium Outlet Pipe Location, cm below Vessel ⌀	101.9
Steam Pipe Location, cm above Vessel ⌀	200.3
Feed Pipe Location, cm below Vessel ⌀	208.3
Na Pressure Drop Through Unit - psi	11
Na Pressure Drop Through kg/m ²	7.73 x 10 ³

I-B-3-b Turbine-Generator System

i) Turbine

Engineers at Sargent and Lundy Corporation have taken the steam conditions from the previous section and designed two identical 1800 RPM tandem compound generating units for the UWMAK-I reactor. Each unit utilizes one double flow high pressure turbine (Figure I-7) followed by one moisture removal stage, two reheat stages and a four (4) flow (96.5cm last stage buckets) low pressure turbine with two (2) moisture removal stages. The steam conditions delivered to each of the two HP turbines are:

a.) steam flow	3,787,100 kg/ hr
b.) temperature	399°C
c.) pressure	1900 psi (1.3×10^6 kg/m ²)

Once the steam has expanded through the HP turbine the excess moisture in the steam is removed via the moisture removal equipment and the steam is then reheated first by extraction steam from the HP turbine and then with a quantity of throttle steam. This intermediate process improves cycle efficiency and also increases the quality of the steam delivered to the LP turbines.

ii) Condenser

After steam is expanded through the low pressure turbine, it is exhausted to the condenser. In the condenser, the latent heat of the steam is transferred to the circulating water. The design parameters used for the condenser are:

a.) operating backpressure	1.72 psi (1.19×10^3 kg/m ²)
b.) cooling water flow rate	4.135×10^5 GPM (9.4×10^7 kg/hr)
c.) cooling water temperature rise	13.3°C
d.) heat rejection rate	4.96×10^9 BTU/hr (1.45×10^9 watts)

The circulating water will then transfer the heat to the atmosphere via mechanical draft cooling to be described later.

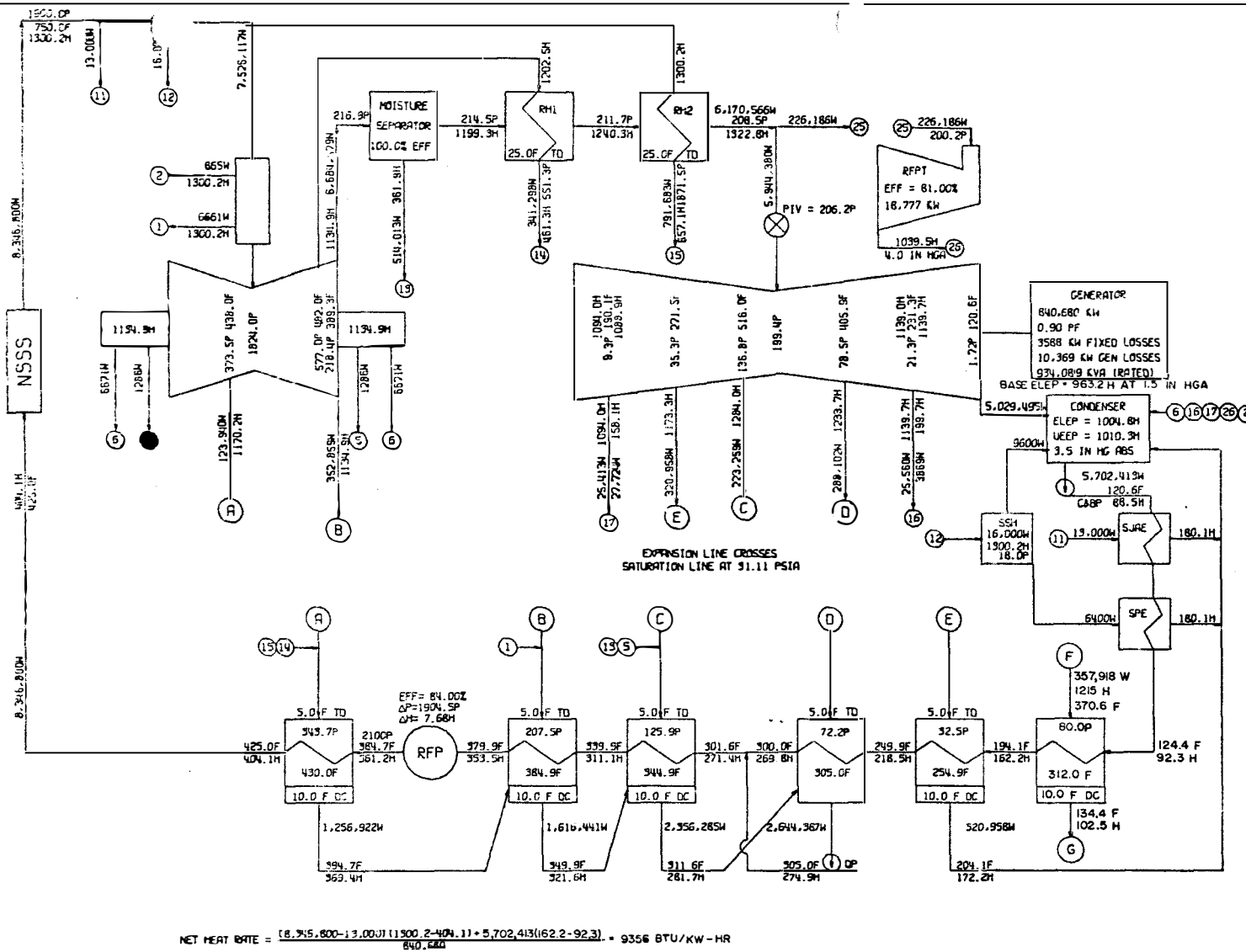
iii) Generator

Preliminary design calculations show each of the two generators will operate at the following conditions:

a.) gross generation	840,680 kW(e)
b.) auxiliary power	103,951 kW(e)
c.) net sent out	736,729 kW(e)
d.) rated KVA	934,089

WISCONSIN TOKAMAK FUSION REACTOR CYCLE
 JOB NO. 4820-00 MAD 74-643
 6-HEATER CYCLE 2MR STAGES MS AND 2RM
 1900 PSIA 750.0F TC4F-38LSB 1800 RPM
 SEPTEMBER 20, 1974

FIGURE I-7
 TURBINE GENERATOR CYCLE DESIGN



- (F) - FROM DIVERTOR STEAM GENERATOR
- (G) - TO DIVERTOR STEAM GENERATOR

- EQUIPMENT LIST:
- C&BP - CONDENSATE & BOOSTER PUMP
 - DP - DRAIN PUMP
 - NSSS - NUCLEAR STEAM SUPPLY SYSTEM
 - RFP - REACTOR FEED PUMP
 - RFPT - REACTOR FEED PUMP TURBINE
 - RH1 - FIRST REHEATER
 - RH2 - SECOND REHEATER
 - SJAE - STEAM JET AIR EJECTOR
 - SPE - STEAM PACKING EXHAUSTOR
 - SSH - STEAM SEAL HEATER

- LEGEND:
- H = ENTHALPY, BTU/LB
 - F = TEMPERATURE, °F
 - W = FLOW, LBS/HR
 - P = PRESSURE, PSIA

MECHANICAL ANALYTICAL DIVISION

SARGENT & LUNDY

iv) Condensate and Feedwater Systems

A diagrammatic representation of the condensate and feedwater system is given in Figure I-8. The next two sub-sections discuss briefly the operation of these systems relative to each of the twin turbine generator sets.

Condensate

Four 1/3 capacity condensate pumps (one supplied as a backup for emergencies) take the water from the main condenser hot well and pump the condensate through the steam jet air ejectors, steam packing exhausters and the condensate demineralizer to the condensate booster pumps. The purpose of the steam jet air ejectors is to draw air and other non-condensable gases from the condenser shell.

The steam packing exhausters are used during normal operation to draw seal steam from the turbine gland seals. The gland seals are provided to prevent steam from escaping the HP turbine and to prevent air from entering the LP sections.

Before the condensate is passed to the feedwater heaters, it will be processed by circulating it through the condensate demineralizers. This is done to prevent impurities from building up in the feedwater system and, more importantly, in the steam generators where high purity is essential for the once-through steam generator design used. The effectiveness of the once-through steam generator coupled with full flow demineralization has been effectively demonstrated to provide minimal tube leakage problems (See Nuclear News, Feb. 1975, p. 30).

Feedwater System

The turbine cycle has been designed to deliver 425°F (218°C) feedwater at 2100 psia ($1.45 \times 10^6 \text{ kg/m}^2$) to the main steam generators. This is accomplished in two steps. First, the four 1/3 capacity condensate booster pumps (one supplied as a spare) pass the condensate through two 1/2 capacity strings of low pressure feedwater heaters supplying a portion of the required amount of water to the two 1/2 capacity turbine-driven reactor feed pumps. (A spare motor-driven reactor feed pump is provided for startup and emergency situations.) The reactor feed pumps then increase the pressure of the condensate through one stage of high pressure heating and on to the main steam generators.

During normal operation, each of the feedwater heaters (refer to the heat balance diagram, Figure I-7), excluding the Heater F in both strings, is fed with extraction steam from the high and low pressure turbines. The steam is condensed on the tubes through which the feedwater is passing, thereby adding heat to the feedwater and raising its temperature. To improve efficiency of the cycle, all of the heaters, excluding Heater D, are provided with drain cooling sections. This allows additional heat from the condensed extraction steam to be utilized in heating up the feedwater.

Rather than dumping the heater drains to the condenser as is done for Heater E, the drains from Heaters A through D (which cascade back to Heater D) are collected in a heater drain storage located beneath Heater D and are pumped forward back into the feedwater line to further improve cycle efficiency by raising the temperature of the feedwater stream.

The steam supply for the first feedwater, Heater F, is taken from the steam generator which utilizes the 233 MW_t produced in the divertor lithium cooling system. This becomes an independent loop since the drains must return to the divertor steam generator. Each turbine generator unit will utilize one-half of the steam supply from the divertor cooling system's steam generator in Heater F.

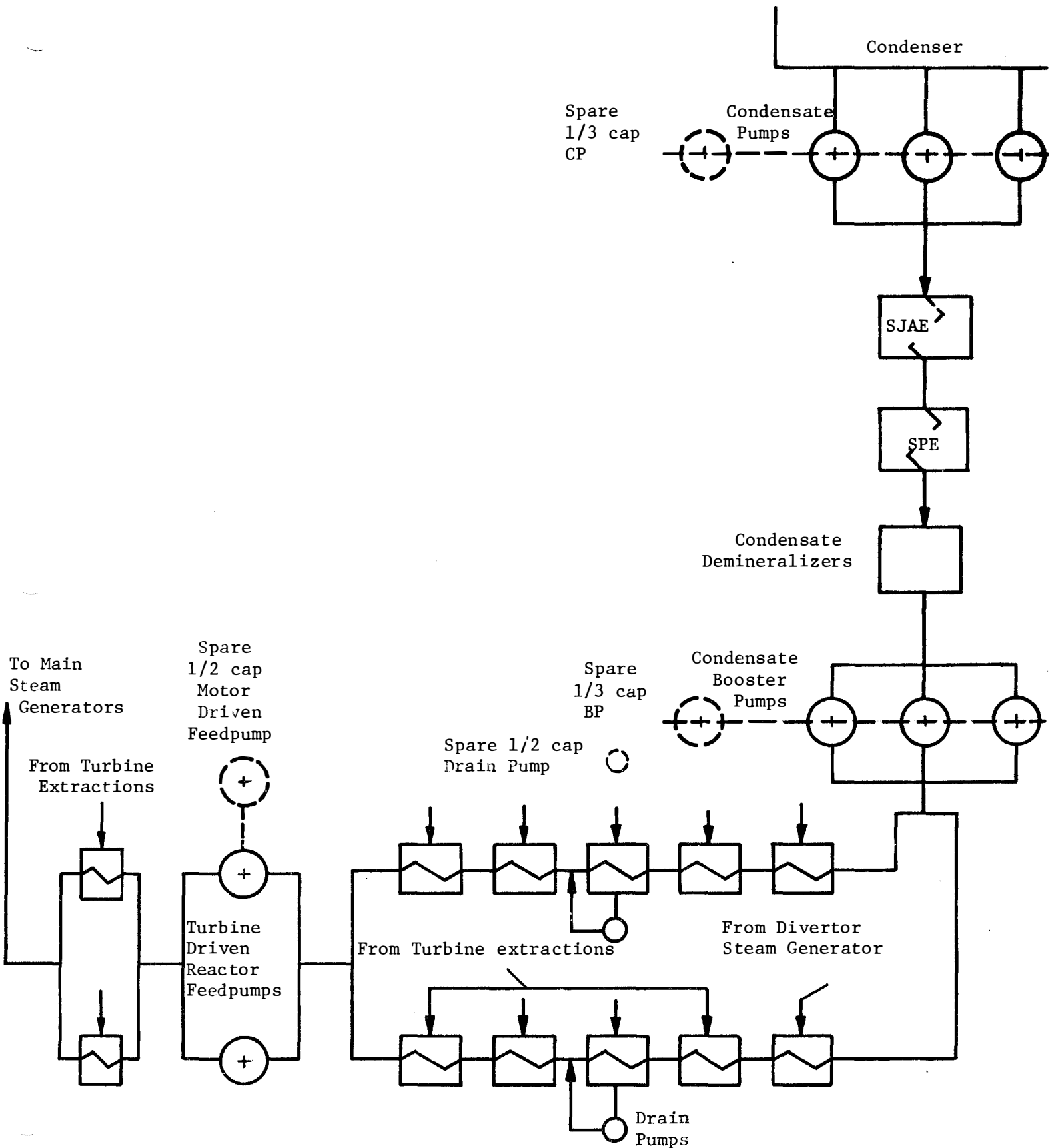


FIGURE I-8
Condensate and Feedwater System

C. Divertor Cooling System

The 250 MW_t of energy which is deposited during the burn in the divertor system appears at rather low outlet temperature (325°C) because of Li vapor pressure considerations (see Chapter III of Volume I). Hence, it is only suitable for feedwater heating. The energy is transferred from Li to Na via the same type of heat exchanger described in I-B-1 although at much different temperatures and flow rates. An additional feature of the divertor lithium stream is its high tritium content. However, since the temperature is much lower than in the primary blanket circuit (325°C vs 489°C) the rate of tritium loss due to diffusion is actually less than in the other 12 major loops.

The total flow rate of lithium from the divertor is 14,400 gallons/min (3.3×10^4 kg/hr). The pressure in the divertor liquid lithium loop is 20 psi (1.38×10^4 kg/m²) and the same type of liquid lithium and sodium cleanup, make up, storage and T₂ extraction equipment is used as described earlier (see Figures I-2 thru I-5).

Steam is generated from the same type of steam generator as described in Figure I-6. The steam generation rate is 3.2×10^5 kg/hr at 188°C and one half is condensed and exits as water at 57°C to be fed back into the divertor steam generator. The use of this energy contributes 1-2 percentage points to the overall plant efficiency.

D. Shield Cooling System

Approximately 1% of the heat generated in UWMAK-I ends up either as gamma rays or neutrons in the reactor shield. This heat (~50 MW_t instantaneous) is removed by circulating helium through the shield at 735 psi (5.07×10^5 kg/m²). The flow rate of the helium is 2.3×10^5 kg/hr and it is raised from 50°C to 200°C. The upper temperature limit is determined by the desire to keep below the melting point of lead (327°C).

The low grade heat cannot be efficiently used in the steam cycle so it is dumped directly to the atmosphere in a wet mechanical draft.

E. Cooling Tower Requirements

The heat rejected from the main condenser of each turbine-generator unit (3055 MW_{th}) is released to the atmosphere by circulation of cooling water through mechanical draft cooling towers. Each cooling tower is provided with 21 cooling cells in two structures 10 and 11 cells each (see Figure I-9). The location of these main coolant towers on the site is depicted in Fig. II-1. The design basis for these cooling cells was established using Madison, Wisconsin weather data. Table I-5 summarizes the conditions used for this study.

Normal operation of the cooling towers will require 26,200 GPM (6×10^4 kg/hr) due to losses such as drift. The calculated blowdown rate (an additional 12,000 gpm) is based on an assumed total dissolved solids level of 1000 ppm.

Cooling of the water will be performed by drawing air up through the towers while circulating water, pumped from the main condenser, cascades down through the cell along a series of splash bars. The cells will be positioned at 45° to the prevailing wind direction in order to minimize the interference between cell plumes which are discharged upward from each cell. There will

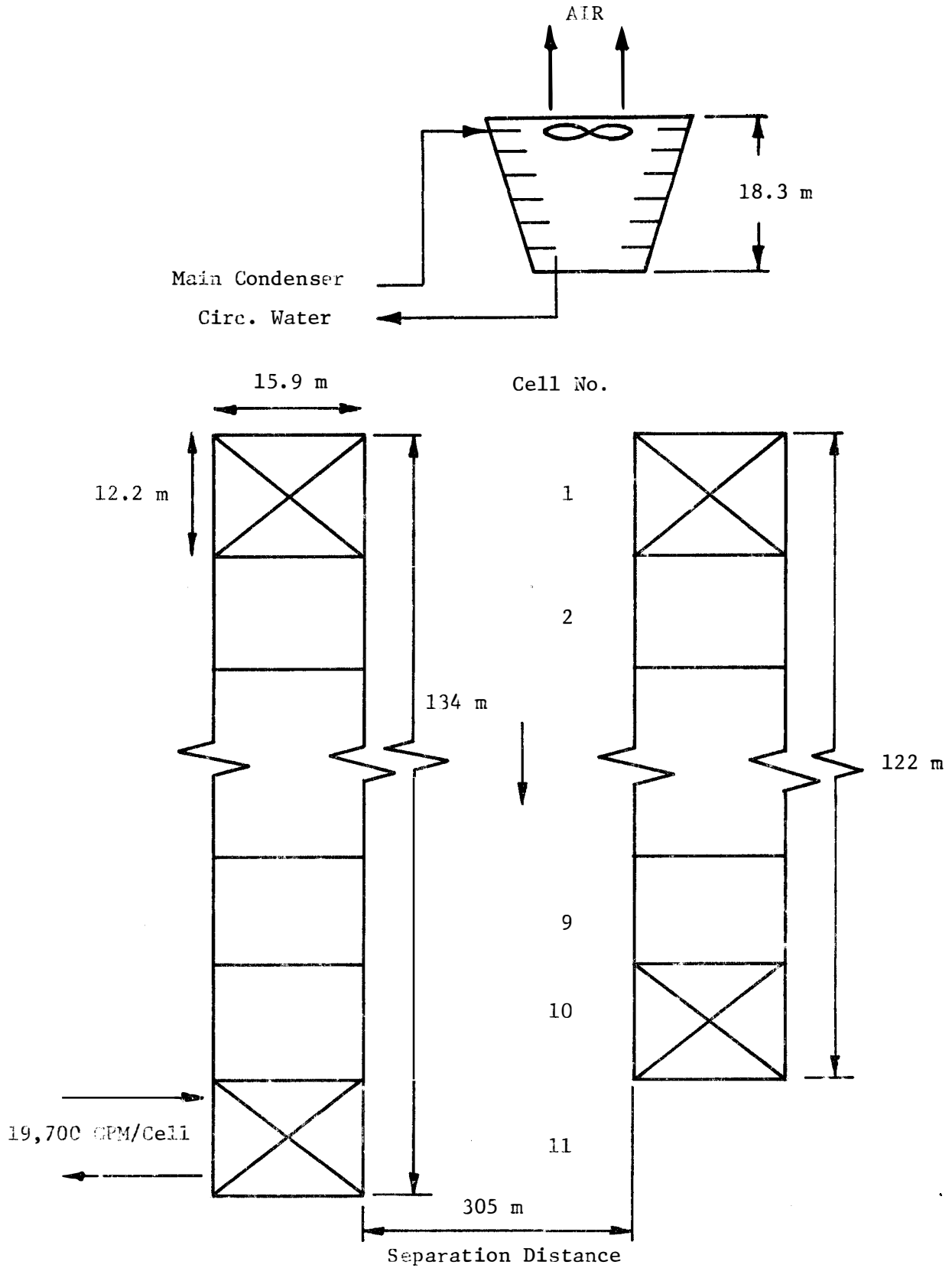


FIGURE I-9
Main Cooling Towers

Table I-5

Cooling Tower Data

	<u>Main Towers</u>	<u>Shield Waste Heat</u>
Flow Rate	4.5×10^5 kg/hr	2.9×10^5 kg/hr
Design Cooling Range	13°C	7.5°C
Design Approach	7°C	8.9°C
Wet Bulb Temperatures	23°C	23°C
Size Per Cell (LxWxH) meters	12.2 x 15.9 x 18.3	12.9 x 12.2 x 18.4
Number of Cells per Unit	26	1
Fan Rating-Kw	150	150

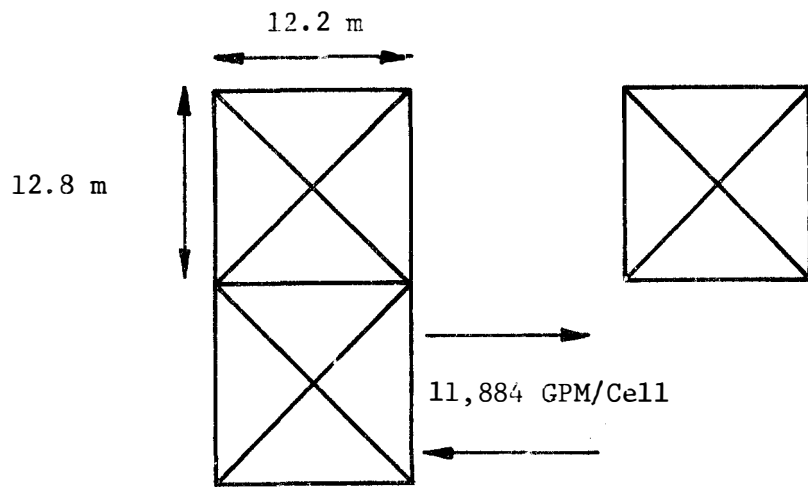
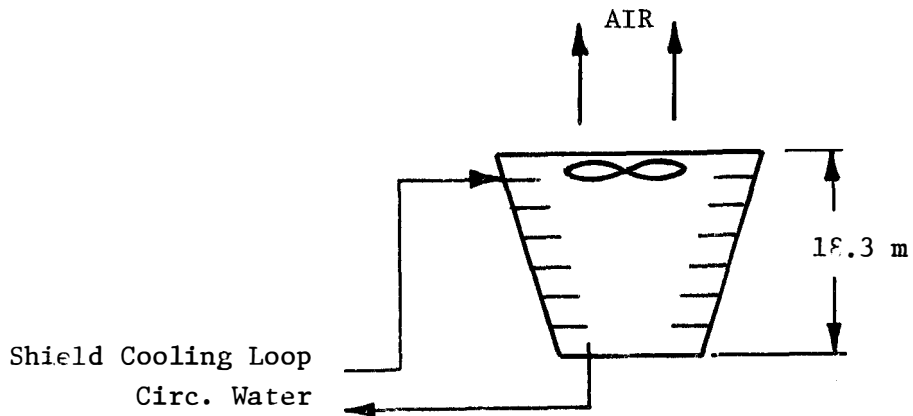


FIGURE I-10
Waste Heat Cooling Towers

be 4 main cooling tower arrangements, although 3 are needed at any one time. This tower will be designed for seismic category I construction.

The 47 MW_t (ave.) of waste heat from the shield will be dumped directly to the atmosphere by a separate set of cooling towers. Since this cooling loop is also essential for safe plant shutdown in the event of an accident, a redundant system has been employed which includes three 50% capacity cooling loops, each designed for seismic category I construction. A diagram of the tower is shown in Figure I-10 and pertinent data is also listed in Table I-5.

The normal operation of this cooling tower will require a water make up of 447 GPM (1×10^5 kg/hr) due to losses such as drift, evaporation and blowdown. The calculated blowdown rate is also based on an assumed total dissolved solids level of 1000 ppm.

In addition, as these towers are essential for safe shutdown of the reactor, a 30 day supply of water must be on reserve for emergency use at all times. The 30 day supply which amounts to 5.18×10^5 gallons (2×10^6 kg) can be stored in a reservoir beneath the tower basins.

I-F Auxiliary Electrical Requirements for UWMAK-I

A portion of the gross electrical output from UWMAK-I (1681 MWe) must be used for the operation of auxiliary plant equipment such as pumps, ventilation systems, cryogenerators, etc. We summarize in this section, to the best of our ability, the major identifiable components that require large amounts of power during (and after) plant operation.

The power requirements for UWMAK-I can be divided into 10 major sectors which are listed in Table I-6. A summary of this data is given in Table I-7.

The largest amount of power in UWMAK-I is consumed by the liquid metal pumps (110 MWe). Other requirements, in descending order, are water system (37 MWe), miscellaneous such as heating, lighting, A/C, etc., (19 MWe), fans (14 MWe), heaters (13 MWe), divertor and transformer power supply (6 MWe), cryogenerator (4 MWe), vacuum pumps (3 MWe), others such as injectors, fueling device and tritium purification systems (2.4 MWe) and finally the shield coolant pumps (0.2 MWe). The total auxiliary power required, allowing an efficiency of 95% is 208 MWe. This only amounts to 12% of the gross electrical output and ~14% of the net electrical output.

I-G Electrical Equipment

The generator electrical output is fed to the main transformer and thence to transmission lines. However, a portion of the generated power is used for operation of auxiliary equipment, i.e., pumps, ventilation systems, lighting, etc.

The auxiliary power is taken from the generator leads through a current limiting reactor in order to allow use of conventional oil circuit breakers in the auxiliary power substation. The use of generator switches will allow the plant to be started up backfeeding power from the transmission system through the main power transformer.

Table I-6

Major Energy Consuming Equipment in UWMAK-I

<u>System</u>	<u>Motor Size</u>	<u>Quantity</u>	<u>Required Horse Power</u>
1.) <u>Liquid Metal Pumps</u>			
Main Lithium Pumps	8300 Hp	12	99,600
Main Sodium Pumps	3750 Hp	12	45,000
Divertor Lithium Pump	675	1	675
Divertor Na Pump	575	1	575
480 Volt Transformer	(1000 KVA)	2/3(13 total)	10,460
2.) <u>Water System</u>			
Condensate Pumps	600 Hp	6 + 2 spares	3,600
Condensate Booster Pumps	1400 Hp	6 + 2 spares	8,400
Heater Drain Pump	1000 Hp	6 + 2 spares	4,000
Cooling Water Pump	6000 Hp	3	18,000
Service Water Pump	1750 Hp	2	3,500
Auxillary Feed Pump	500 Hp	2	1,000
Service Water Pump	900 Hp	2	1,800
Component Cooling Water Pump	500 Hp	2	1,000
480 Volt Transformer	(1000 KVA)	2/3(13 total)	10,460
3.) <u>Shield Cooling</u>			
Helium Pump	2 Hp	12	24
4.) <u>Fans (includes Cooling Tower)</u>			
Main Cooling Tower	200 Hp	42	8,400
Helium Coolant Cooling Tower	200 Hp	2 + spare	400
Building Exhaust Fan	300 Hp	2	600
Cooling	(7.5 MW)	1	10,000
5.) <u>Vacuum Pumps</u>			
Torus Vacuum Pumps	3000 Hp	1	3,000
Inner Bldg. Vacuum Pump	1500 Hp	1	1,500
6.) <u>Cryogenerators</u>			
Refrigerators	4.5 MW _e		6,100
7.) <u>Heaters</u>			
Lithium Cleanup Heaters	348 kW _e	13	6,000
Sodium Cleanup Heaters	388 kW _e	13	6,700
Sodium Hot Storage & Dump Tank	164 kW _e	13	2,750
Li Cleanup Pump	77 kW _e	13	1,340
Na Cleanup Pumps	63 kW _e	13	1,100
8.) <u>Divertor and Transformer Power Supply</u>			
Supply	6 MW _e	1	8,000
9.) <u>Other</u>			
Tritium Purification System	1 kW _e	22	30
Fueling	2.4 MW _e		3,250
Neutral Beam Injectors	15 MW _e (20 sec out of 5790)		69
10.) <u>Miscellaneous Plant Equipment</u> (Heating, A/C, Lighting, etc.)	10% of total		<u>26,743</u>
Total			294,173 Horse Power
Auxillary Power	$\frac{294173 \times 0.746 \times 0.9}{0.9 \times 0.95}$	= 231,003 KVA	
	$231,003 \times 0.9$	= 207,903 kW _e	

Table I-7

Summary of Auxillary Power Requirements - UWMAK-I

<u>System</u>	<u>Power Required (MWe)*</u>	<u>% of Total</u>	<u>% of Gross Plant Output</u>
Liquid Metal Pumps	110.47	53.1	6.6
Water System	36.58	17.6	2.4
Shield Cooling	0.17	0.1	0.01
Fans	13.71	6.6	0.8
Vacuum Pumps	3.18	1.5	0.2
Refrigerators	4.31	2.1	0.3
Heaters	12.73	6.1	0.8
Divertor and Transformer Power Supply	6	2.9	0.4
Other	2.37	1.1	0.1
Miscellaneous	<u>18.90</u>	9.1	<u>1.1</u>
	208		12.7

By using a cryogenic inductive storage unit and two inverters, the large amount of energy required to energize the divertor and transformer coils can be built up at a slow rate (6 MW) and transferred into and out of the coils rapidly (at a maximum rate of approximately 580 MW). Since this large transfer will be between the storage coil and the divertor and transformer coils, the power drawn from the power system will only be 6 MW to make up losses. The inverters will generate harmonic currents which are not allowable on the power system and therefore, harmonic filters are included in the design. It is not known whether a second off-site power supply will be required for a fusion reactor as it is for a fission reactor; therefore, only one off-site supply is included. However, four diesel engine-driven generators (one spare) are included for safe operation of all systems, and for keeping the liquid metals in a liquid state when off-site power is not available.

Single Line Diagram, Figure I-11 shows the principal features of the plant electrical system.

I-H Conclusions

The cycle net heat rate for the UWMAK-I reactor turbine generator unit is estimated to be 9,356 BTU/KW-HR and the conversion efficiency is estimated to be 32%. The calculated overall efficiency from the UWMAK-I reactor power plant is, however, based on preliminary estimates of the auxiliary power requirements which are in the range of 12% of the total generator electrical power output. For the UWMAK-I fusion reactor, the auxiliary power requirements for "conventional" power plant equipment is approximately 2.6%. The balance of the auxiliary power will be used to operate the intermediate systems inherent to the fusion reactor design, i.e., lithium and sodium pumps, cleanup systems, etc. Once a more detailed accounting is made of the auxiliary power needs, a more realistic estimate of the overall plant efficiency can be obtained. Nevertheless, it would not be expected to vary substantially from the 32% value unless significant improvements are made in the primary and secondary coolant loop designs.

I-I Recommendations

1. Although the heat balance presented is a workable one, improved efficiencies may be accomplished by optimization of main steam and feedwater design operating temperatures and pressures.

Consideration should also be given to cycle design alterations which may become necessary once manufacturers are actually confronted with the task of designing and fabricating the turbine generator units.

2. An additional aspect of the equipment design for the UWMAK-I fusion reactor which will require further attention is that of the power supply for the divertor and transformer coils. Since the design of this power supply has been given only rudimentary consideration, supplementary work is needed to determine a more reasonable (lower) cost for the equipment.

3. With regard to the reactor power supply requirements, it is noted that, if the divertor coils and the inductive storage coil remain aircore inductors as presently contemplated, they will produce magnetic fields that will make conventional mechanical and electrical equipment generally inoperative throughout the plant. It will, therefore, be necessary to develop some means of controlling these fields.

II. Overall Layout

II-A. Overview of Layout

The UWMAK-I nuclear power plant will resemble light water fission nuclear plants in its overall appearance. There will be a large reactor building as well as turbine, auxiliary, and service buildings, and cooling towers for the heat sink. Unique to this fusion plant will be the large hot cells required to replace the inner wall of the torus-magnet modules and the energy storage building to house the inductive coils for supplying power to the transformer and divertor coils during the charging time. While the large electrical switch yard is also conventional, the inverter and harmonic filter areas are provided due to special requirements associated with the magnetic energy storage system. The other major building, housing the diesel-generators and diesel oil tanks, contains the emergency power supply for the equipment that is felt to be essential for maintaining the safety of the plant. A smaller helium storage building for the helium gas cylinders is also required.

The location of all these buildings and structures that comprise the complete plant are shown on the property plat, Figure II-I. The source of make up water, lake or river, is not shown, but is assumed to be in the direction of the main cooling towers. A more detailed description of the plant is found in the general arrangement drawings, Figures II-2 thru II-5.

II-B. Reactor Building

The reactor building will be a large cylindrical building approximately 120 meters in diameter and 102 meters high. It comprises four floors: the main floor containing the primary containment and access tunnel; the lithium and sodium floors containing the processing equipment for these respective coolant loops; and the fourth floor for HVAC and miscellaneous equipment. The specific location of the major balance-of-plant equipment is shown on the general arrangement drawings, Figures II-2 thru II-4. The reactor and magnet components that are located inside the primary containment are shown in Figure 3 of the Overview Section of Volume I, and have been described in detail in Chapters I, III, IV, and VII of that report.

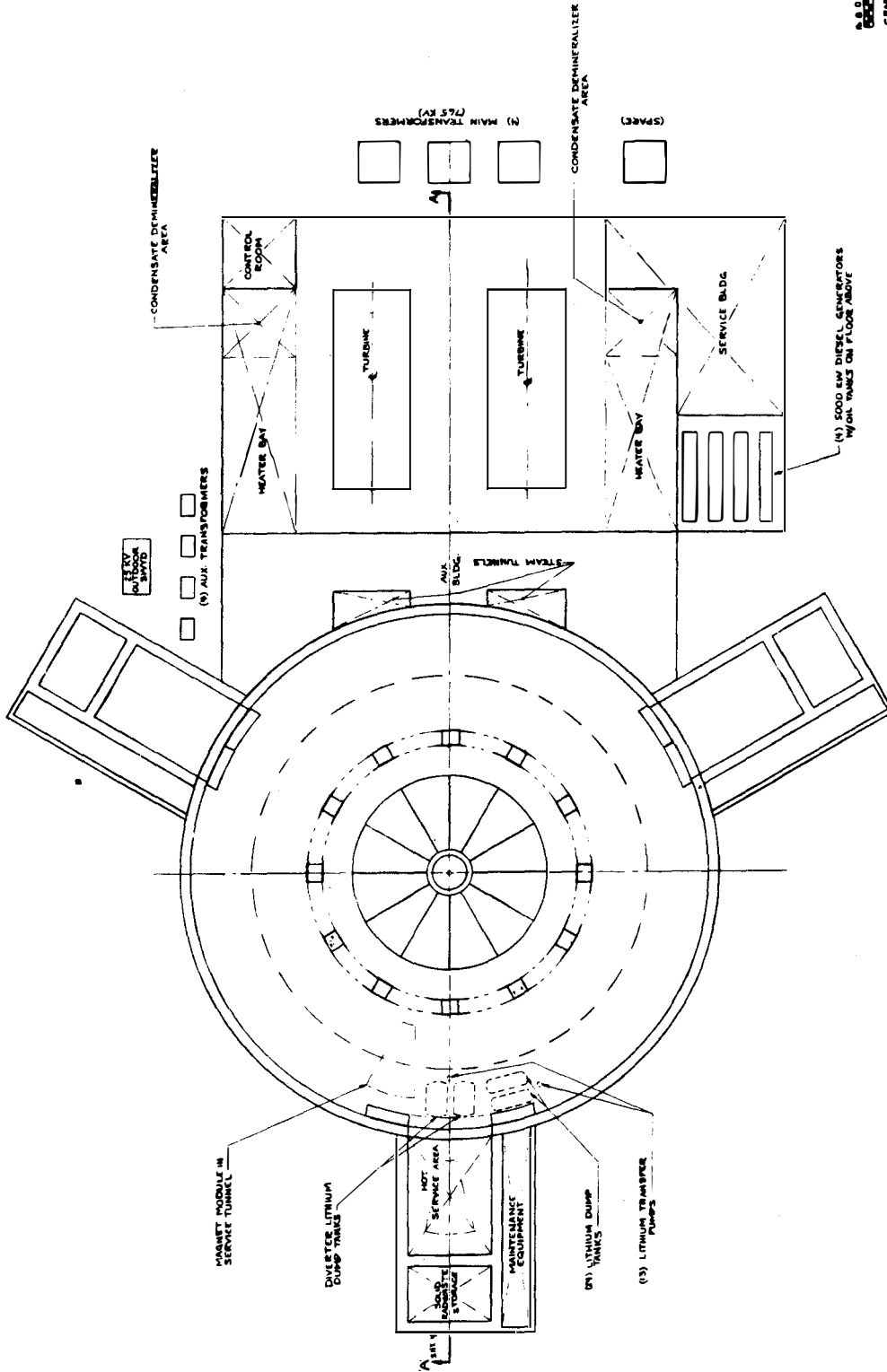


Figure II-2

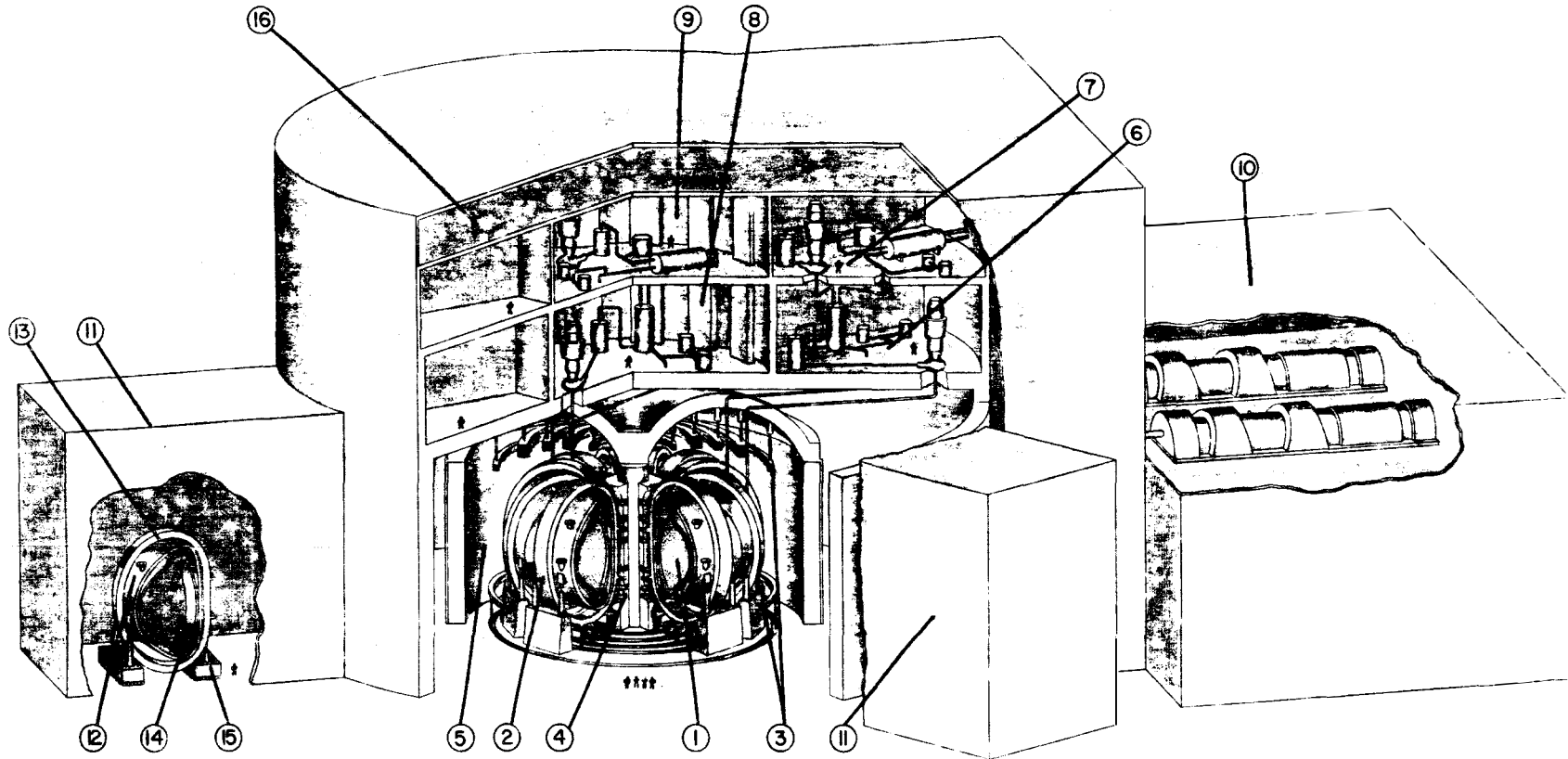
ASB:BRM
GRAPHIC SCALE

GRADE FLOOR PLAN
UNWPK I

PROJECT NO.	1374
DATE	1/17/68
DESIGNED BY	ASB:BRM
CHECKED BY	ASB:BRM
APPROVED BY	ASB:BRM
SCALE	AS SHOWN
STUDY A SHEET OF	176

Figure II-5

Wisconsin Tokamak Fusion Reactor, UWMAK-1



- 1. PLASMA
- 2. TOROIDAL FIELD COIL (12)
- 3. RETRACTABLE DIVERTOR COIL (8)
- 4. TRANSFORMER COIL (10)
- 5. EVACUATED PRIMARY CONTAINMENT BUILDING

- 6. Li PRIMARY SYSTEM (ONE FOR EACH OF 12 MODULES)
- 7. Na SECONDARY SYSTEM (" " " " " ")
- 8. DIVERTOR Li PRIMARY SYSTEM
- 9. DIVERTOR Na SECONDARY SYSTEM
- 10. TURBINE-GENERATOR BUILDING

- 11. HOT CELL REPAIR AREA
- 12. MAGNET SHIELD
- 13. BLANKET
- 14. DIVERTOR COLLECTION AREA
- 15. MOTORIZED MODULE SUPPORT VEHICLE
- 16. AUXILIARY EQUIPMENT AREA

1. Primary Containment

The reactor will be completely enclosed by the primary containment, which will have a reinforced concrete toroidal roof supported by twelve peripheral columns and one center column. The shell will be 244cm thick lined with a 0.32cm steel plate to provide leak-tightness. The wall of the primary containment will be a free-standing right circular steel cylinder supported on a track to allow the complete wall to revolve.

There will be a removable hatch in the steel cylinder large enough to allow the removal of one torus-magnet module. The radius of the containment is about 30.7 meters. The base of the primary containment will be a circular reinforced concrete mat which will serve as a common base mat for both primary and secondary containment buildings.

The primary containment will be designed for a maximum negative pressure of 15 psig (vacuum) and a maximum positive pressure of 10 psig (lithium fire). It will also be designed to support the lithium, sodium, and HVAC equipment floors above the primary containment.

2. Secondary Containment

The secondary containment will be a right circular reinforced concrete cylinder which will surround the primary containment. Three floors will be enclosed with the secondary containment:

- (1) The main floor used for movement of segments of the reactor for servicing;
- (2) The lithium floor;
- (3) The sodium floor.

The containment will consist of the outer concrete walls and the ceiling of the sodium floor all of which will be lined by steel plate to provide a vaportight barrier. The thickness of the concrete wall surrounding the liner will vary from floor to floor. The volume enclosed by the secondary containment liner will be designed for a maximum negative pressure of -8 psig and a maximum positive pressure of 10 psig (-5.52 to $6.89 \times 10^3 \text{ kg/m}^2$ respectively).

The radius of the entire building will be about 58.3 meters with 2.44 meter thick walls required for shielding the radiation emanating from the operating reactor on the lower level. The lithium floor is also a 2.44 meter thick reinforced concrete slab which is supported by the secondary containment walls and also rests on the toroidal roof of the primary containment. The cylindrical wall around the lithium floor has been reduced to 1.23 meter and all shielding walls on that level which are arranged in a radial rib-like configuration, are also 1.23 meters of concrete to shield against the radiation emitted from corrosion products from the stainless steel inner wall carried by the lithium. In addition, there will be some concrete columns in the central, circular portion of the floor to help support the floor above.

The sodium floor is a 1.23 meter thick reinforced concrete slab supported by the radial shield walls and columns below, and by the cylindrical secondary containment wall. The wall arrangement of the sodium floor is the same as for the lithium floor except that the concrete thickness is only 0.61 meters.

The loads considered in the design of both secondary and primary containments are dead and live loads in the structures along with the temperatures and pressures resulting from operating and accident conditions. In addition, any environmental and special loadings associated with current nuclear plant design such as seismic, flooding, missiles, pipe break etc. would be considered. The design criteria would be that those generally required for current nuclear plant design.

3. Lithium Floor

The lithium floor contains the equipment needed to extract the heat carried by the reactor primary lithium coolant and to process it. The major components of this loop are displayed in the piping diagram shown in Figure I-2. The relevant operating parameters are tabulated in the corresponding system flow chart in Table I-2.

There are two distinct lithium loops, one for the reactor coolant (which is duplicated 12 times on a "per module" basis) and one for the tritium-enriched divertor coolant. The divertor loop components are located in the center of the floor, while those for each module are located in the pie-shaped segments shown in Figure II-3 and II-5.

The main components are the intermediate heat exchanger (IHX) which transfers the heat to sodium, the lithium circulation pump, the lithium cleanup system and the lithium tritium extraction system. Since the lithium flow rate in the divertor loop is nearly the same as that in each modular loop (although the temperature is much lower), the size of the components for these two loops are about the same. The lithium tritium extraction system is an exception, however, since the divertor coolant lithium will be bearing a much larger tritium inventory than the reactor coolant. The extraction bed is therefore considerably larger for the divertor lithium. The height of the floor is largely dictated by the requirements of the long circulation pumps that will have a capacity of approximately 25,000 gpm (2.7×10^6 kg/hr).

The lithium floor will be inaccessible during reactor operation because of the large quantity of radioisotopes from the corrosion and sputtering of the reactor blanket stainless steel inner wall. Based on 500 kg of stainless steel being deposited in the reactor coolant per year, the shield walls have been nominally designed as 1.23 meter of concrete to maintain a protected area at the 1-2 mrem/hr level.

4. Sodium Floor

The sodium floor contains the equipment needed to transfer the heat picked up by the sodium and to process (i.e., cleanup and tritium extraction) the sodium. The major components of this loop are displayed in the piping diagram shown in Figure I-5. The relevant operating parameters are tabulated in the corresponding system flow chart in Figure I-3.

There are two distinct sodium loops in direct analogy to the lithium loops. One is for the reactor coolant (which is duplicated 12 times on a "per module" basis) and one for the tritium enriched divertor coolant. Components of the divertor coolant loop are located in the center of the floor, while those for each module are located in the pie-shaped segments.

The main components are the steam generator designed (see Section I-B-3) to produce superheated steam for utilization in the power cycle, the sodium circulation pump, the sodium cleanup system, the sodium tritium extraction system, and the thermal "flywheel" system of two large storage tanks. The tanks are utilized to maintain the sodium flow (and resultant steam generation) during the 6.5 minutes (out of 96.5 min. total) the plasma is down for recharging. This is done by bleeding off a small flow to the hot storage tank during the 90 minutes the reactor is in operation. During the 6.5 minutes of recharging, the sodium flow from the IHX is closed and a large flow is opened up from the hot storage tank, through the steam generator, and to the dump tank. During the subsequent 90 minute operating period, the same amount of flow routed to the hot storage tank is returned to the main stream from the dump tank.

In addition to components of the divertor coolant sodium loop, the inner, circular section of the floor contains the tritium production system and the vacuum pumps to maintain the primary containment at its design evacuation condition. The tritium production system consists of three major components: tritium purification equipment (cryogenic distillation columns to separate the hydrogen isotopes), tritium storage cylinders and a pelletizer to prepare the fuel for injection into the plasma.

The sodium floor is connected to the lithium floor below by a stairway and elevator in the inner, circular section and by a stairway at the outer perimeter of each modular section. Steam lines from each of the steam generators will feed into two header systems (one for each turbine-generator unit) that will enter the two main steam tunnels and then the two turbine systems. The height of this floor is also largely dictated by the requirements of the long sodium circulation pumps which will have a capacity of approximately 53,000 gpm (9.8×10^6 kg/hr).

5. HVAC Equipment Floor

The floor above the sodium floor will house the fans, blowers, chillers, filters, distribution ducts, and associated equipment required for the heating, ventilating and air conditioning (HVAC) systems of the reactor plant. It will also contain other miscellaneous equipment needed for the efficient functioning of the plant.

II-C. Hot Cells

The secondary containment is provided with three hot cells, each located 120° apart (Figures II-1,2,4,5). Each cell is for refabricating one-third of the 12 toroidal sections during each biennial refueling. Each cell will be a reinforced concrete structure, with a minimum of 2.44 meter thick walls and roof for shielding. The inner face of the cell will be lined with steel plate to provide a leaktight barrier which will form part of the secondary containment. A bridge crane will be provided to assist in handling the module.

The cell will consist of three main sections as seen in the general arrangement drawing Figure II-2. These are: the work area for the module, the manipulator and control area, and the high-level radwaste storage area. During refueling, the inner reactor coolant blanket will be remotely disassembled, a small section at a time, with the remote manipulators, and a new section installed. The highly radioactive dismantled sections will be compacted and then stored in the radwaste storage area.

II-D. Auxiliary Building

The auxiliary building is located between the reactor building and the turbine building. It will contain the majority of the cryogenic equipment, the main steam tunnels, the three helium-water heat exchangers, and the switchgear and cable spreading areas as seen in the general arrangement drawings, Figures II-2,3.

The cryogenic equipment consists of the five cryogenerators, and the large storage tanks containing the liquid helium and liquid nitrogen.

The helium-water heat exchangers transfer the heat from the gaseous helium shield coolant to water, which, in turn, transfers it to the air via the waste cooling towers. The heat exchangers, like the associated cooling towers, are considered essential so they are separated from one another. Two will operate during normal operation, but three 50% heat exchangers have been provided.

II-E. Turbine Building

The turbine building will house the two sets of turbine-generator units and their associated equipment. This associated equipment has been described in some detail in Chapter I. Basically a set consists of the condenser, reheaters, feedwater heaters, condensate demineralizer, condensate and condensate booster pumps and the feedwater pumps. The broad categories of the equipment has been shown on the general arrangement drawings, Figures I-7 and 8.

II-F. Service Building

The service building will mainly contain offices, repair shops and store-rooms. The offices will fulfill the needs of plant supervisors, meeting rooms, general offices and training rooms. The shops will include a dismantling room, machine shop, electrical shop, tool room and welding area among others. Because of the special nature of the superconducting magnets, some of the shops are likely to be more elaborate than those in conventional plants.

II-G. Additional Buildings

1. Diesel-Generator Building

The diesel-generator building is located off one side of the turbine building as shown in Figure II-2. It will house four sets of four main components: the four diesel-generators and their associated diesel oil tanks (located on the floor below), diesel fuel oil day tanks, and the diesel-generator exhaust silencers (located on the building roof).

Three diesel 33%-sized units are included along with one 33% spare. Each unit is rated at 5000 KW based on preliminary essential electrical loads. The two components that will require the bulk of the on-site diesel power are the helium cryogenerators and the vacuum pumps.

2. Helium Gas Storage Building

The helium storage tanks are housed in the helium gas storage building. As seen in the property plan, Figure II-1, it is located some distance from the reactor building to preclude any consequences from potential tank failures. The building has only minimal structural requirements, i.e., siding for the walls and roof.

3. Energy Storage Building

The energy storage building will provide the energy for charging the divertor magnetic coils during the current risetime, and for recharging the transformer coils during the downtime. In the discharge cycle of these coils, energy will flow back to the superconducting inductive ring. Only the energy loss in the circuit elements need be replenished from the power system. The heart of the storage system is a superconducting dipole **storage magnet**. The building will be in the shape of a torus approximately 50 meters in major diameter and 6 meters in minor diameter. The design of the working system is based on that developed by the Energy Storage Study, University of Wisconsin Engineering Project. The building will be located at some distance from the reactor building to minimize interferences from its magnetic fringing field.

II-H. Electrical Areas.

Three outside electrical areas are depicted on the property plan, Figure II-1. These are the conventional switch-yard, and the harmonic filter and inverter areas which are unique for a power plant. The inverter and harmonic filter equipment are needed to enable the energy storage unit to function without interfering with the electrical transmission system of the plant. They are described more fully in Chapter I, Section F.

II-I. Cooling Towers

The main cooling towers and waste heat cooling tower are both shown in the property plan, Figure II-1. There are four main cooling towers, two for each turbine-generator unit. Two of the four have 10 cells each, and the other two have 11 cells. The 134 meter length of each tower is at the upper limit of tower lengths for efficient operation.

The 307 meter separation distance between towers follows manufacturer's recommended practice to minimize airwake interference between towers.

II-J. Recommendations

1. There may be several advantages to reducing the number of coolant loops (e.g., 3 or 4 sections per coolant loop) for the twelve torus-magnet sections. The number of pumps, cleanup equipment and tritium extraction equipment would be also reduced at the expense of increased and more complex pipe and valve arrangements. It would also allow for an easier incorporation of some redundancy in the coolant loops. A more detailed economic and layout study would be required.

2. If the temperature of the lithium divertor coolant can be increased, this heat could be utilized more advantageously than in the current design. Similarly, the heat of the helium shield coolant might be utilized for some kind of process heat rather than dumping it through the waste heat cooling towers.

3. The thermal "flywheel" system employed could possibly be improved upon as the current system requires large inventories of sodium.

4. The piping, valving, and pumping arrangements underlying the current layout could be optimized and improved.

5. The operation of the service cells ought to be more carefully considered, particularly with regard to the disassembling and storing of the compacted inner wall sections. The waste storage area is one where several alternatives appear likely: buried vaults versus above ground storage, air-cooled versus forced convection systems, off-site shipment versus on-site storage. Details would have to be worked out before choices can be made.

6. As noted in Chapter III, confinement of the magnetic fringing field associated with the toroidal magnet concept will be necessary to minimize effects on plant components, personnel and the general site. If this goal cannot be achieved, it may be necessary to consider relocation of the auxiliary and turbine buildings from the reactor building.

III. Environmental Impact

III-A. Introduction and General Environmental Considerations

The objective of this chapter is to assess the impact on the environment resulting from the operation of UWMAK-I Fusion Reactor. It should be clearly understood that the specific numbers in this chapter refer only to UWMAK-I and therefore cannot be generalized to other types.

A distinction is made in this chapter between the environmental impact resulting from radiological effects and the environmental impact resulting from other effects, such as waste heat rejection and siting. The distinction was made because it was concluded that the major concern with the operation of the fusion reactor would be with radiological effects. Therefore, these effects are treated in more detail.

There are three principle radiological effects which have been considered: (1) radiological releases to the environment during normal operation; (2) radiological releases which might result from plant accidents; and (3) problems associated with the long term storage of radioactive wastes generated while the plant is operating. A possible fourth category is the transportation of radioactive wastes; however, this subject has been included under the heading of long term storage of radioactive wastes. There is one section in the chapter for each of these three effects.

The remainder of this section serves as a scoping study of general environmental effects. It is an attempt to identify the effects which must be considered and whether or not special problems result because the UWMAK-I is a fusion reactor system. No attempt is made to perform a detailed environmental assessment of these effects; rather, each effect is discussed in general terms.

III-A-1 Siting Considerations

Siting considerations focus on land despoilment and aesthetic effects. The concern with land despoilment is the impact that the construction of the plant will have on the terrestrial biology, and whether or not there may be unexpected and undesirable secondary effects of any kind, such as the elimination of any endangered species. It does not appear that the construction of a fusion reactor presents any special problem in this regard. Typical concerns which would be considered when any power plant is constructed would have to be evaluated. Aesthetic effects refers to the environmental impact of such things as plant noise and the general appearance of the plant facility. It would appear that building size would be a special consideration in the construction of a fusion reactor plant. For the UWMAK-I, the building is 102 m tall by 120 m in diameter. When the turbo-generator unit is added, the building is about 300m long.

The result is that the building is very large; it would be comparable to the Houston Astrodome. In addition to building size, the UWMAK-I incorporates four mechanical draft evaporative cooling towers which are 135 m long, 18.4 m high, and 16 m wide. Public opposition to some nuclear fission plants currently under construction has centered on the cooling tower size as the focal point for resistance.. However, these designs generally have incorporated the much larger natural draft type cooling towers. Since the UWMAK-I incorporates the mechanical draft design, the reactor building will be larger than the cooling towers and the addition of the cooling towers will not appreciably alter the aesthetics of the site.

Plant noise is not a serious environmental consideration for the UWMAK-I design as presently conceived. Normal precautions would certainly be required around high speed turbine equipment and pumps.

A reasonable question at this point is: What criteria would apply to siting a facility like UWMAK-I? The only available criteria that define the requirements for siting a fusion reactor are contained in present Federal Regulations, principally 10CFR20, 10CFR50, and 10CFR100; plus radiological safety publications such as those of the ICRP and FPC. The same regulations and safety guides determine the siting (and operation) of fission reactors and of chemical processing plants.

For example, the site boundary dimension for a fission reactor (exclusion radius) is related to the design basis accident (DBA). For this most serious accident conceived for the plant, the radiological whole body dose to an individual located at the site boundary must not exceed 25 rem. It must be assumed that UWMAK-I would have to meet the same requirement for some, yet to be defined, major accident. This consideration will be discussed in the section on Plant Accidents.

In general, the UWMAK-I site must have the capacity for safe operation of a 5000 MW_{th} (~1500 MW_e) power plant, consistent with presently defined requirements for a comparable fission reactor site.

At various times, some consideration has been given to underground siting of fission reactors. These considerations have always been rejected, and to date, all U.S. fission reactors have been built on the surface. Location of the UWMAK-I building underground does not appear to offer a net advantage in environmental impact either. The disadvantages are the difficulty in monitoring the building exterior for leaks; the more difficult accessibility for maintenance, transportation, etc., and in the event of a major tritium release, the greater likelihood of ground water contamination by tritium. Further study of this latter point is warranted.

III-A-2 Magnetic Fields

Because the operation of UWMAK-I requires large magnetic fields to confine the plasma, special environmental considerations

must be given to whether or not the large magnetic fields could effect the environment in any way. The presence of the magnetic field will certainly effect the plant operation and, specifically, the instrumentation and control system design. However, the concern here is whether or not the magnetic field, which is very high and will extend past the plant exclusion radius, will have a deleterious effect on the environment. The principal concerns would be whether or not the magnetic field would affect local airplane navigation, radio and television transmission, or the health of people in the local community.

It is not expected that any such effects would occur. As a point of reference, the local magnetic field in Wisconsin, due to the earth's magnetic field, is about one gauss. The maximum magnetic field in the UWMAK-I reactor is about 8.7×10^4 gauss.

The extent of the magnetic field around the plant has been calculated⁽¹⁾ and the results are shown in Figure III-1. These calculations show that 500 meters from the reactor center the local magnetic field is less than one gauss. The magnetic field is a minimum directly over the reactor due to the dipole nature of the field, and the magnetic field 500 meters above the reactor is also less than one gauss.

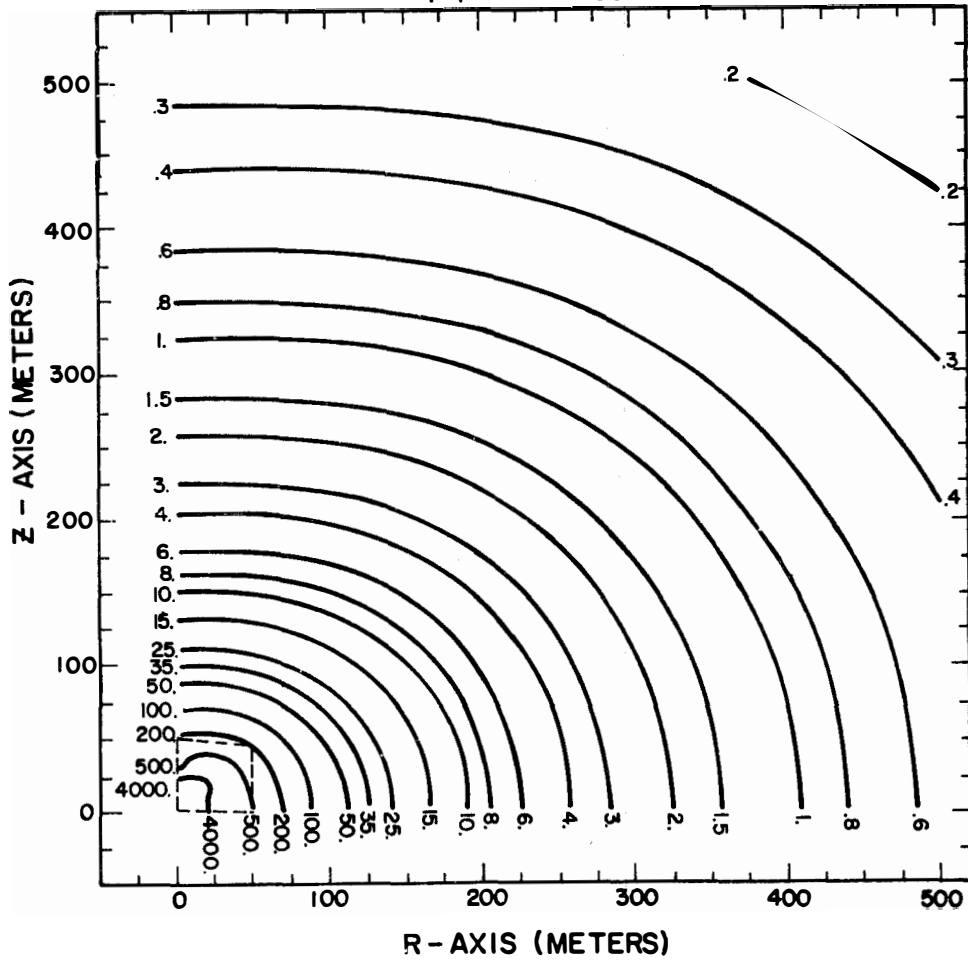
The biological effects of magnetic fields have been studied in various small scale efforts. While these studies indicate that the biological effects of magnetic fields, such as those which would be expected at the exclusion radius of the UWMAK-I, are negligible, further studies will be required. Some personnel limits which have been discussed are about 100-200 gauss for the Stanford Linear Accelerator with a maximum limit of 2000 gauss.

III-A-3 Resources

In addition to the environmental impact of the reactor itself, an environmental assessment must consider the impact on the environment that will result from supplying and disposing of the materials required to build and operate the plant. Each material used in the reactor power plant must be studied in terms of its environmental impact throughout its life cycle. This would include the impact of siting and operating materials processing plants (such as steel mills to supply materials), and disposal of the materials when the plants are decommissioned. It should also include comparisons of the postulated resource requirements with the availability of reserves. This is done in chapter IV of this report.

One unique problem presented by a fusion reactor like UWMAK-I results from the requirement for large quantities of material for the first wall. The blanket in the UWMAK-I is made with 316 stainless steel and the first 20 cm is designed to be replaced every two years. This requires that about 250,000 kg of stainless steel be supplied each year. Furthermore, the rest of the blanket must be replaced at ~10 year intervals generating 7,300,000 kg each time. Since the steel that is removed

|B| PLOT ON R-Z, VERTICAL PLANE
|B| IN GAUSS



is highly radioactive, it must be stored at a waste disposal site. While chemical reprocessing can separate different elements in the stainless steel, isotopic separation processes would be required to remove the radioactive isotopes (i.e. Fe55) from those that are not radioactive. This would probably not be economical, and therefore, new steel must be supplied to replace the radioactive steel removed from the first wall. In addition all of the structural steel in the blanket and shield becomes radioactive and must be disposed of when the plant is decommissioned. The total structural steel used for replacement is roughly equivalent to twice times the original quantity of steel required for the construction of the original blanket. A complete environmental impact assessment must consider the effect of this supply problem. Other materials have been considered for the first wall, such as niobium, molybdenum and vanadium alloys. The environmental impact of supplying these alloys must be considered in the same way.

Chapter IV of this report compares resource requirements with availability for fusion reactor systems. The material resources that must be available in the year 2000 to supply 10^6 MWe from fusion reactors in the year 2020 are summarized in Tables III-1 and III-2. The requirements indicated are based on the reactor concept which is most demanding on the particular resource (see footnotes). The resources available in the United States are shown in Table III-1 and those from sources outside the United States in Table III-2. The resource availability includes speculated discoveries of new reserves. In the past such speculations have been typically conservative.

A resource requirement which could present additional difficulties is the required use of large quantities of liquid helium (about 1,150,000 liters) to cool the magnets. There is a limitation on the world's supply of helium which could be recovered from underground. This problem is studied in Reference 2. There are four principal conclusions drawn: (1) superconducting magnets are essential to TOKAMAK fusion power; (2) in today's technology, these superconducting magnets will require liquid helium cooling to achieve the necessary low temperatures; (3) when fusion reactors become commercial, the necessary helium will have to be extracted from the atmosphere; and (4) though this may be expensive, fusion reactor economics are not significantly affected by the cost of helium -- increasing the cost of helium by a factor of 100 over today's prices will change the cost of fusion power by less than ten percent.

III-A-4 Thermal Effects

All power plants reject heat to the environment. The question here is whether or not the UWMAK-I rejects more heat than other power plants. The net efficiency (excluding auxiliary power requirements) of the UWMAK-I has been calculated to be ~32%. This compares with efficiencies of 33% for the typical LWR, 38% for HTGR's and estimated efficiencies of about 40% for LMFBR's. Thus, in the present design, about the same heat is rejected to the environment as LWR's but slightly more than from HTGR's and LMFBR's.

Table III-1AVAILABILITY OF METALS FROM USA RESOURCES - YEAR 2000

Metric Megatons

<u>Metal</u>	<u>Requirement for 10⁶ MWe</u>	<u>Possible USA Reserves</u>		
		<u>USA Reserves at Present Prices</u>	<u>At 3X Present Prices</u>	<u>At 10X Present Prices</u>
Nb (1)	0.7	.0054	.069	.1
Be (2)	0.12	.018	.018	.25?
Cr (3)	10.3	~0	1.2	>11
Ni (3)	7.2	.14	14.4	>20
Li (3)	1.1	.8	2.7	?
Cu (3)	7.1	20?	>100	Insufficient Data
Pb (3)	13.4	35	>100	Insufficient Data
Al (4)	0.6	~0	>1000	Very Large
V (5)	0.4	.1	>1	>10
Mo (3)	0.6	2.5	>6	Insufficient Data
Sn (2)	0.2	~0	.1	Very Small
Fe (3)	83	8,500	>100,000	Very Large
Zr (1)	0.002	.06	2.5	Insufficient Data
Ti (1)	0.8	>24	>33	>150

(1) - ORNL Fusion Reactor Concept (ORNL-TM-3096)

(2) - Princeton Concept (PPPL)

(3) - UWMAK-I (UWFDM-68)

(4) - Los Alamos THETA-Pinch (LA-DC-72-234A)

(5) - ORNL Concept with V substituted for Nb

Table III-2

AVAILABILITY OF METALS FROM SOURCESOUTSIDE THE UNITED STATES

Year 2000 - Metric Megatons

<u>Metal</u>	<u>Requirement for 10⁶MWe</u>	<u>Ex-USA Reserves at present prices</u>	<u>At 3X present prices</u>	<u>At 10X present prices</u>
Nb ⁽¹⁾	0.7	7.8	17.2	
Be ⁽²⁾	0.12	?	.03	
Cr ⁽³⁾	10.6	370	890	1180
Ni ⁽³⁾	8.0	24	922*	
Li ⁽³⁾	1.2	.2	.2	
Cu ⁽³⁾	7.4	>100	320	
Pb ⁽³⁾	13.9	50	>500	
Al ^(3,4)	0.7	>1500	>1600	Very Large
V ⁽⁵⁾	0.4	26	>100	
Mo ⁽³⁾	0.6	>4	13	
Sn ⁽²⁾	0.2	6	11	
Fe ⁽³⁾	87	170 x 10 ³	Large	Very Large
Zr ⁽¹⁾	0.002	>.07	>4	
Ti ⁽¹⁾	0.8	133	1000	

*All but 60 x 10⁶ short tons is material in sea-floor nodules, for which information is very sketchy.

The reduced efficiency in the UWMAK-I results because maximum steam temperatures are low (~430°C) and steam pressures are slightly lower (2000 psi). The maximum temperature is limited because the primary lithium cannot be maintained at temperatures higher than 500°C due to corrosion. Recent data on lithium-stainless steel corrosion indicate that the 500°C limit may be conservative.⁽³⁾

Future studies will be necessary to investigate the technical feasibility of design alternatives which could achieve higher thermal efficiencies. It is recognized that the intent of designing and the UWMAK-I was to limit the system to existing technology. However, this review indicates that designing the fusion reactor to achieve high thermal efficiencies may require an alternative choice of structural materials and/or coolants.

The environmental effect of the rejected heat from this plant would be influenced by the fact that the design incorporates mechanical draft evaporative cooling towers. The use of a cooling tower minimizes the concentrated thermal discharge to a body of water and ultimately spreads it out over a much larger volume. However, large quantities of water are consumed by the cooling tower and rejected as water vapor into the atmosphere. About 38,000 GPM would be evaporated in the four cooling towers for UWMAK-I. The effect on local climate of adding this water vapor to the atmosphere must be considered. In addition this represents a significant consumption of water which, in some cases, is essentially a local resource. It is estimated that 36,000 GPM would supply a city of 600,000 people. Finally, as water is circulated in the cooling tower, concentrations of minerals and salts build up, and the effect of rejecting this brine to the local body of water must be considered.

It should be recognized that while these are impacts on the environment which must be evaluated, they are special to the fusion reactor concept only to the extent that it may reject more or less waste heat than other sources of power. As pointed out earlier, this is a consideration for UWMAK-I because, as designed, the thermal efficiency is somewhat low. If an application for waste heat could be found the subsequent environmental impact of the lower efficiency would be alleviated.

III-B. Plant Effluents During Normal Operation

While the UWMAK-I is operating, certain radioactive isotopes from the plant system could be released through various boundaries of the system to the environment. The objective of this section is to identify the radioactive materials that might be released, determine the quantity of the materials that could be released and determine the dose and effect on the environment resulting from a release. In the UWMAK-I there are principally two sources of radioisotopes. The first is tritium which would be released while the plant is operating, and the second is radwaste such as corrosion products which could be accumulated and perhaps released to the environment during plant clean-up and maintenance operations. Of these two, by far the major concern is the tritium release. Releases of radwaste resulting from

clean-up and maintenance are of second order consequence and at this time would be difficult to estimate.

Tritium is one of the principal fuel components in the operation of the UWMAK-I and is a normal product of plant operation. In addition, an important function of the UWMAK-I, and purpose of using lithium as the primary coolant, is to generate tritium while the plant is operating. The result is that there are large inventories of tritium in the plant while it is operating. The tritium inventories in the plant are itemized in Table III-3 which shows the total inventory to be about 13.5 kilograms. This does not consider any tritium in an auxiliary storage system to accommodate malfunctions, such as fluctuations in the output of the tritium extraction system, nor does it include the amount of tritium which would be required for plant reserve if the entire tritium extraction system were to break down. Note also that the largest inventory of tritium is in the primary lithium circuit where there are 9.7 kilograms.

Tritium flow paths are shown schematically in Figure III-2. From there it can be seen that there are fundamentally two tritium flow paths to the environment. The first is through the liquid metal heat exchangers to the steam system where some tritium would be lost to the environment as part of the blowdown of the steam-water system. The second path is by diffusion through the containment system boundaries so that the tritium is ultimately dispersed in the air around the plant.

Of these tritium release paths the principal concern is with tritium released through the main heat transfer circuit to the secondary coolant system and then through the steam generator to the steam-water system. It is expected that virtually all of the tritium diffused through the steam generator would be present as tritiated water in the steam-water system. This is consistent with BWR experience⁽⁵⁾, PWR experience⁽⁶⁾, and treatment of the problem in related systems⁽⁷⁾. Part of this tritiated water would be released to the environment in the water blowdown to circulating water.

The plant has been designed to minimize the tritium release through this flow path. This can be done by sizing the fuel extraction system which removes tritium from the primary lithium. The objective is to limit the tritium concentration in the primary lithium to a value such that releases through this path are at or less than the design objective.

A design objective of between 1 and 10 curies of tritium release per day was chosen. Based on this objective, a fuel extraction system was sized and tritium concentrations in the primary lithium were determined. Calculations were then conducted to determine the diffusion of tritium from the primary lithium to the secondary sodium through the Intermediate Heat Exchanger (IHX), and then from the secondary sodium through the steam generator. These calculations indicate that the tritium loss will be about 10 curies per day via this path. (See chapter 9 in volume I)

Table III-3

Summary of Tritium Extraction System Characteristics^(a)

<u>Coolant System</u>	<u>Temp. Range °C</u>	<u>Extraction Method</u>	<u>Tritium Accumulation Per Day (kg)</u>	<u>Tritium Leakage Ci/day</u>	<u>Total Na or Li(kg)</u>	<u>Tritium Concentration in Li or Na ppm (wt.)</u>	<u>Tritium Inventory (kg)</u>
Primary Lithium	283-489	Yttrium Metal Bed	1.05(b)	10.1	1.73×10^6	5	in Li 8.7 in beds 1.0
Secondary Sodium	261-411	Yttrium Metal Bed	~0		7.6×10^5	8.7×10^{-5}	in Na 6.7×10^{-5} in beds ~0
Divertor Lithium Sodium	200-325 190-265	Yttrium Metal Bed	7.4 T + 5.0 D	2×10^{-4}	3.4×10^4 6×10^4	0.24 3×10^{-4}	in Li 8×10^{-3} in beds 3.5 in Na 6×10^{-6}
Divertor vacuum	25	Charcoal-cooled with liq. He	0.3 T + 0.2 D	1×10^{-4}		Not applicable	0.3
Helium	50-200	Metal getter	1.1×10^{-6}	low		Not applicable	low
			Total	10.1		Total	13.5

(a) Based upon thermodynamic calculations; no kinetic considerations

(b) At maximum breeding ratio of 1.49

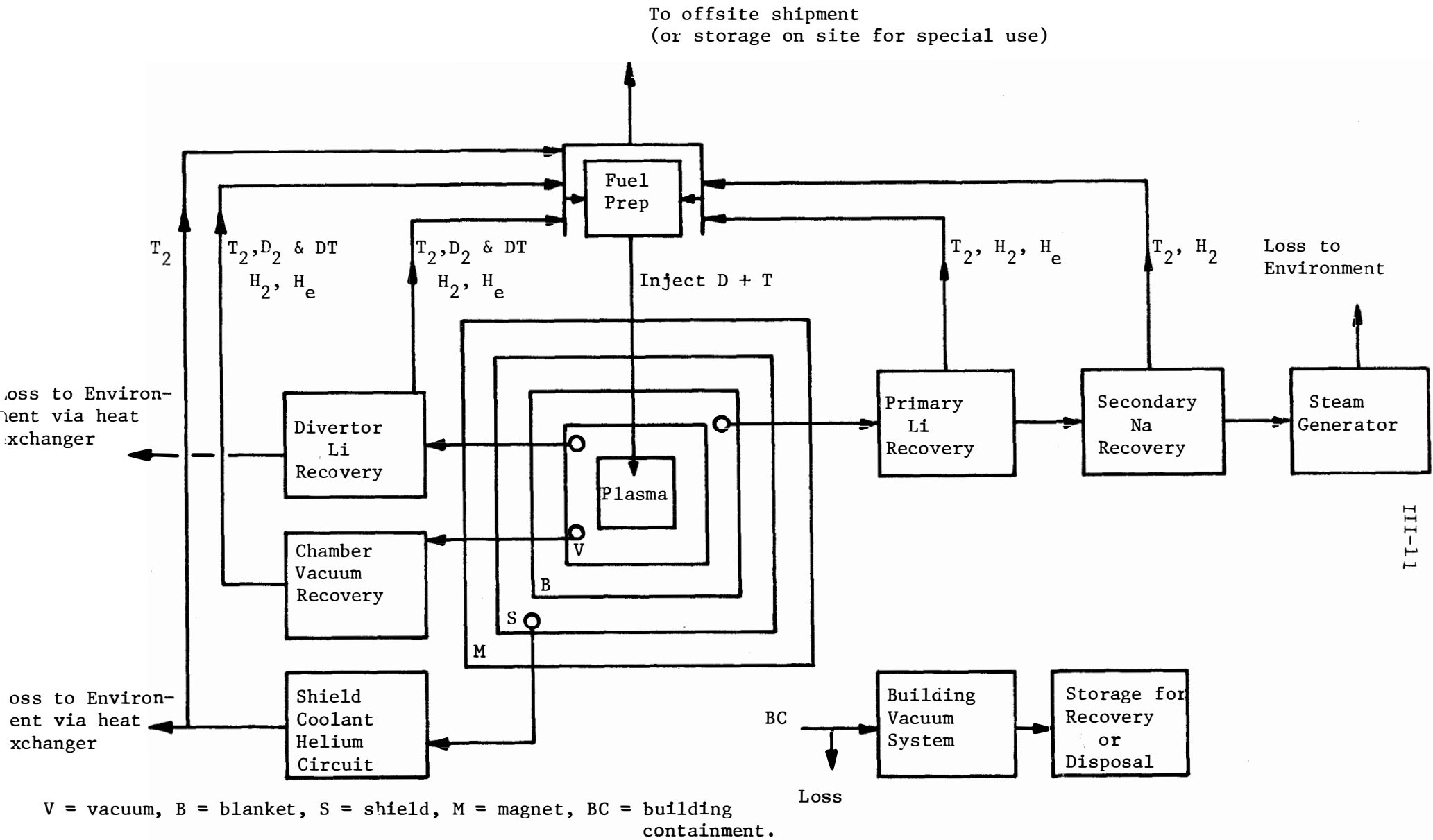


FIGURE III-2. Tritium Flow in UWMAK-I

The 10.1 curies per day is diluted in the 12,000 gpm blowdown water from the condenser cooling water discharge which would ultimately be deposited into some undefined body of water. The resulting tritium concentration in this discharge would be about $15 \times 10^{-5} \mu\text{Ci}/\text{cm}^3$. The regulatory limit on concentrations of radioactive material in water released to uncontrolled areas are described in Table II, Column 2, Appendix B, 10CFR20. These limits are the concentrations which would result in a dose of 1×10^{-2} rem/week to an individual who obtains his entire daily intake of water from the source. Thus, the release from UWMAK-I is about 6% of the regulatory limit and would result in a dose of 6×10^{-4} rem/week to a person obtaining his entire daily intake of water from this source.

By comparison, the lowest practicable limit from 10CFR50, Section II, is $5 \times 10^{-6} \mu\text{Ci}/\text{cm}^3$. This limit is established for LWR's and is based on LWR operating experience. It is the limit which LWR's must be designed to meet. Whether or not the same limit would be imposed on a fusion reactor system remains to be seen. If this limit were to be imposed, further dilution prior to discharge, by about a factor of ten, would be required.

It may be that fusion reactors will not be required to meet the same limits for tritium release that have been established for LWR's because tritium is only of many isotopes that must be considered in a LWR. Further, these radionuclide releases must be controlled not only during reactor operation but during transportation, reprocessing, and fabrication as well. Since tritium release during reactor operation plays an entirely different and more significant role in the fusion reactor system, it is possible that different limits may be set for its release which are higher than those employed for LWR's currently. On the other hand, the present momentum in the direction of lower releases for all radionuclides may be impossible to reverse.

Calculations of the dose from this discharge are difficult to determine without reference to a particular site. Some further dilution would result as the discharge is dumped. For example, the Clinch River, which is the discharge body of water for the Clinch River Breeder reactor, has a flow rate of about 2 million gallons per minute.⁽⁸⁾ If the concentration of tritium from the UWMAK-I were dumped into this body of water, the resulting dose would be reduced by two orders of magnitude, from 0.06 rem/year to 0.0006 rem/year.*

It should be noted that relative to other radionuclides, tritium has a low radiotoxicity which mitigates the hazard to the environment.⁽⁹⁾ It has a short biological half-life of about 12 days in the human body. It has shown no tendency to concentrate in vegetation, particular food cycles, or organs in the human body, and finally, it decays by the emission of a low energy beta-ray (18 keV).

*Workers at Battelle Northwest Laboratories have suggested that the release levels can be reduced to essentially zero by reducing water losses to a minimum by incorporating the blow down water into concrete and storing the concrete until the tritium decays. The half life of tritium is 12.40 years.

In summary, this section has focused on the release of tritium to fresh water systems. The releases of tritium to the air through the containment, and releases of tritium from the on-site storage are yet to be determined. In addition, effluents which would be released as a result of maintenance and cleaning of radioactive components must also be determined. However, the release through the major release path has been estimated to result in doses that would be well within the regulatory limit in 10CFR20.

III-C. Plant Accidents

In reviewing plant accidents for the UWMAK-I it is perhaps appropriate to follow a parallel path and approach the problem in the same way that plant accidents are considered for fission plants. This approach has the virtue of, first, helping to identify potential safety problems with the fusion reactor, and second, providing some insight as to the analysis, design, and testing which ultimately will be required to license the operation of such a plant. Therefore, the first part of this section will be devoted to a discussion of the fundamental accident analysis philosophy and approach which is typically used in the safety analysis of a fission reactor. The second section will then attempt to show how this philosophy might be applied to the safety analysis of a fusion reactor.

III-C-1. Safety Analysis and Design Philosophy

The underlying concept for the safe design of a fission reactor is that there are three "levels" of safety which provide "defense-in-depth" against any non-normal release of radioactivity to the environment.

At the first level accidents are prevented by intrinsic features of the design of the plant and the quality, redundancy, testability, inspectability, and fail-safe features of its components. The design is such that it should be unquestionably safe in all phases of operation and have a maximum tolerance for errors, off-normal operation and component malfunction. Analyses are made and test programs conducted to find those types of malfunctions or faults that could affect reliability of operation so that they can be guarded against by design, quality assurance, or fail-safe features as appropriate. Thus, the emphasis at the first level is upon inherently safe design features and quality controlled construction.

At the second level failures are assumed to occur in spite of the care taken above and protection is provided against the consequences of such failures. Typical examples of such failures are operator error, reactivity insertions, (in fission reactors) or failure of parts of the control system. Reliable protection devices and systems are then designed to assure that such incidents will be arrested or accommodated safely. Conservative design and safety margins, inspectability, and redundant detecting and actuating equipment are incorporated in the protection systems to assure both the effectiveness and reliability

of this second level of defense. In addition, these systems are designed to be routinely monitored and tested so that there is full assurance that they will operate reliably if required.

The third level of safety supplements the first two by considering extremely unlikely and unforeseen circumstances. The purpose of considering such events is to add margin in the plant design as an additional assurance of public safety. The result of analyzing such low probability events and implementing the third level of safety is to set containment building design pressure and design leak rates and to incorporate additional engineering safety features (such as the Emergency Core Cooling System in PWR's).

The purpose of performing a plant accident analysis is to identify the protection systems that will be required (second level) and to assure that there is an adequate plant safety margin for hypothetical low probability events (third level). The method of performing such an analysis begins by preparing a list of all possible accidents which could occur. The accidents are typically classified as Anticipated Operational Occurrences or Postulated Accidents. The single failure of any active component or a single wrong operator action are examples of accidents in the first category. Multiple single failures would be Postulated Accidents. Safety criteria must be generated to, first, determine what consequences are acceptable for each class of accident, and second, the degree of protection required to assure that acceptable consequences are not exceeded (are independent, redundant protective systems required?, etc.). Each accident is then analyzed and the consequence is compared with the acceptable criteria to determine what protection is required.

In addition to preparing a list of accidents, however, the safety analysis must focus on the potential hazards of plant operation thereby providing protection for hypothetical low probability events. The criteria for fission reactor siting in 10CFR100 require that an exclusion area be defined such that an assumed fission product release will result in whole body exposures of less than 25 rem and thyroid doses less than 300 rem. In the footnote to §100-11, the code says that the fission product release "should be based upon a major accident, hypothesized for purposes of site analysis or postulated from considerations of possible accidental events, that would result in potential hazards not exceeded by those from any accident considered credible." Thus, it is necessary to evaluate what might be called the "potential hazards" of operating the plant as well. Once "potential hazards" are quantified, the job of the safety analyst is to limit (i.e., reduce) the "potential hazards" by demonstrating a thorough understanding of credible accidents and placing a bound on what is "credible".

In this respect it should be noted that there is a difference in approach to the analysis of accidents for safety analysis reports and environmental reports. Analyses for safety purposes necessarily

consider "worst case" kinds of events and the analyses typically use conservative assumptions. On the other hand the focus in environmental reports is on the more realistic consequences of accidents and typically nominal conditions are assumed.

Once a list of accidents has been generated, an important part of the safety analysis is to develop the logical path between initiating events and ultimate consequences. This is important for several reasons, some are: (1) to understand mechanistically what must happen for the consequence to occur and thereby to identify technically sound reasons why it would not occur (i.e., "lines of defense") (2) to better understand the potential severity of the ultimate consequence; (3) to identify uncertainties and "lines of defense: which will require verification through analysis and testing; and (4) to identify engineered safety features or protective instrumentation which will prevent the progression of the sequence to the ultimate consequence. A convenient tool for developing this logical path is the safety assurance diagram (SAD). A sample SAD for a nuclear fission reactor is shown in Figure III-3. Once the initiating event is identified, the potential result of the event can be determined by following the lines from the first box. A double line indicates the more probable path. The lines are sometimes intersected by "lines of defense". These represent technical reasons why that path would not be followed. Each line of defense must be verified by analysis, experiment, testing, etc.

Thus, one can see that generating a complete safety analysis is a complex, comprehensive task. Obviously, such an analysis could not be incorporated herein. However, an attempt has been made to apply in a preliminary way the accident analysis philosophy for fission reactors to the UWMAK-I. The result of this effort is produced in the remaining portions of this section.

III-C-2. Safety Analysis of UWMAK-I.

The first step in the safety analysis is to prepare a list of events. A list is given in Table III-4 and is preliminary in the sense that a more complete list would require more design definition and detailed familiarity with the design. In addition, it is a list which typically requires iteration and is limited only by inventiveness, ingenuity, and experience. But it is the fundamental starting point for any safety analysis and, as such, should be given much thought. Initiating mechanisms for the accidents are also identified for some cases. These are not intended to be complete lists of initiating mechanisms, but rather to provide some ideas of how these accidents might occur.

Once the list of accidents is generated, the primary safety problem is to develop the mechanistic consequences of the postulated accidents in order to identify what potential pathways exist and how they might

Table III-4
List of Accidents

<u>Accidents External to Plant</u>	<u>Initiating Mechanism</u>
1. Earthquake	
2. Tornado	
3. Flood	
4. Airplane "collision" event	
5. Sabotage	
6. Loss of off-site power	
<u>Plant Malfunctions</u>	
1. Loss of primary cooling	. Primary pipe rupture
a) with reactor on	. Primary system blockage
. shutdown	. Pump failure
. failure to shutdown	. Loss of site power
b) with reactor off	
2. Lithium Fire	. Primary pipe rupture
	. Lithium spill
3. Sodium Fire	. Secondary pipe rupture
4. Loss of Secondary Cooling	. Same as (1)
5. Steam Generator Tube Failures (sodium/water reactions)	
6. IHX Tube Failures	
7. Magnet Failures	. Conductor breakage
	. Helium warm-up
8. Helium Warm-up Accidents	. Super-normal transition
9. Overpower Accidents	. Failure of He containment boundary
	. Increase in rate of fuel injection
	. Failure of Plasma Control System
10. Tritium Handling Accident and Fuel Preparation System Accidents	. Pipe failure in tritium extraction system
11. Release of Tritium from On-Site Storage	. Container leak
12. Rupture, melting, or other failure of the First Wall	. Misdirection of neutral beam
	. Loss of Cooling
	. Overpower accident
	. Magnet failure with "arcing"
13. Missile Accidents	. Missiles generated from He vaporization accident
	. Heavy component dropped on reactor while performing maintenance
14. Loss of Plasma Confinement	. Coil failure
	. Excitation of plasma instabilities
15. Electron Runaway	. Electric field too high
16. Loss of Lithium Flow to Divertor Plate	
17. Failure of Vacuum System	
18. Pipe Rupture in Divertor Cooling System	

lead to an "ultimate hazard"; to identify alternate pathways that may be more realistic, or alternatively, how realistic the pathway in question is; where "lines of defense" exist to interrupt the pathway; where engineered safety features should be provided; and where protective system instrumentation is required.

The second step is to determine the "potential hazards" of the plant operation. While the UWMAK-I is operating at power there are large quantities of stored energy in the system:

- 1) The stored energy in the superconducting magnets (212,000 MJ);
- 2) The kinetic energy of the plasma (3,000 MJ); and
- 3) The stored energy in the liquified helium (84,000 MJ).

Conceptually, the liquid helium is an energy sink; however, because it is capable of converting all forms of stored energy (i.e., anything at a temperature greater than $\sim 4^{\circ}\text{K}$) very effectively into mechanical work with a significant damage potential, it must be treated in the same manner as other forms of stored energy.

In addition to these quantities of stored energy there is a relatively large inventory of radioactive material:

- 1) The tritium inventory;
- 2) The structural materials with induced radioactivity; and
- 3) corrosion products; principally in the primary lithium.

The combination of a large quantity of stored energy and a relatively large inventory of radioactive materials poses the threat that the stored energy could accidentally be released in such a way that the radioactive materials are released to the environment.

Clearly, a hazard of great concern is a large release of tritium. If one has a lithium fire in which the fumes are released to the environment, the tritium will also be released and the accident has occurred. In this respect it represents a greater concern than typical accidents in a fission reactor which frequently require a postulated sequence of events which is tenuous and highly impregnated with conservative assumptions to generate an airborne aerosol of radioactive fission products. Once the lithium fire has been postulated, the airborne tritium is a natural consequence. On the other hand, as will be discussed in Section IV, the Biological Hazard Potential (BHP) of the tritium is significantly less than that of the fission products from a fission reactor.

To provide an estimate of the hazard involved, Atomic International has performed some radiological calculations to determine the consequences of releases to the environment of large amounts of tritium. Earlier it was noted that 10CFR100 specifies that whole body exposures should be less than 25 rem and thyroid doses less than 300 rem. However, the code also specifies that these doses are not to be considered acceptable but are to be used as "guides..... which can be used in the evaluation of reactor sites with respect to potential reactor accidents

of exceedingly low probability of occurrence, and low risk of public exposure to radiation". These criteria should be kept in mind as the following results are interpreted

The first calculation arbitrarily assumed a ground release of 10^6 curies (~100 grams) to the environment. This represents about 1% of the tritium inventory in the primary lithium system. The skin absorption and inhalation doses were then calculated at 600 meters (the exclusion radius for the Clinch River Breeder Reactor Plant) assuming a short-term (less than 8 hours), ground level release under worst-case meteorological conditions. The criteria from AEC Safety Guide no. 3⁽¹⁰⁾ were used for the calculations.

On the basis of Figure 3A in Safety Guide No. 3, the X/Q value for this case is 1.5×10^{-3} sec/m³, so that, for a release of 10^6 Ci, the time integrated concentration at 600 meters is 1.5×10^3 Ci - sec/m³. Assuming a breathing rate of 3.5×10^{-4} m³/sec (ICRP-2) and an intake dose of 1.7×10^{-4} rem/ μ Ci (ICRP-10), the inhalation dose at 600 meters is 87 rem. The principal authority on the toxicology of tritium, Langham and Pinsons work, (11) reported in the Journal of Applied Physiology, January 1957, indicates that the skin absorption dose from exposure to a tritium atmosphere is approximately equal to the inhalation dose. The cloud immersion dose is evaluated to be 2 rem if an average beta particle energy of 5.7×10^{-3} Mev is used in the equation appearing on Page 3.2 of AEC Safety Guide No. 3. Thus, the resulting whole body dose is about 176 rem at the exclusion radius. To reduce the whole body dose to 25 rem, the exclusion radius would have to be increased to about 2100 meters.

A second calculation was made to determine the whole body dose at the exclusion radius (600 meters) for the same release at an effective height of 100 meters. Such a release would more accurately simulate the release from a lithium fire. In the case of elevated release, the worst-case meteorological conditions are not the same for all distances from the point of release. Under certain meteorological conditions the ground level concentrations at 2100 meters from the point of release may be greater than the concentration at 600 meters, due to the fact that the cloud or plume does not reach ground level until it has moved downwind for considerable distances. For this reason, elevated releases are best evaluated on the basis of the envelope of the entire range of meteorological conditions. Figure 1A, AEC Safety Guide No. 3, evaluates the consequences of an elevated release by drawing a line through the peak ground level concentrations for Pasquill* Types A through F. On the basis of that figure, the X/Q values for a release height of 100 meters are 1.9×10^{-5} sec/m³ for a downwind distance of 600 meters.

*Pasquill types are weather conditions which have been classified in stability categories ranging from A through F in order of increasing stability. All categories are considered in this analysis since Pasquill Type A may result in peak doses at one location while Pasquill Type F may result in peak doses at another.

These X/Q values would result in a reduction of the whole body dose at the 600 meter exclusion radius to about 2 rem which is within the 25 rem guideline.

The 10^6 curie release was somewhat arbitrarily chosen to provide order of magnitude estimates. It is highly improbable that as much as 1% (~12 tonnes) Li could be completely consumed in a fire because of the vacuum around the reactor and inert gas in the Li Floor of the reactor building. Furthermore even if that much Li were to be burned, all of the tritium in that amount would have to escape to the atmosphere, requiring the complete breaching of 3 containment shells. However, It is clear from these calculations that potentially serious radiological hazards do exist even though they are, at this point, only hypothetical and they appear to be very low probability events. Subsequent analysis will be required to quantify the potential hazards and determine meaningful exclusion boundaries that would be required for fusion reactors of the UWMAK-I design.

III-C-3 Specific Accident Considerations for the UWMAK-I

While the analysis of specific accidents has not been carried out in detail, some consideration can be given to selected accidents. In particular the following accidents will be discussed:

- 1) Lithium Fires
- 2) Loss of Cooling Accidents
- 3) Magnet Failures
- 4) Helium Release Accidents.

III-C-3-a Lithium Fires

The possibility of lithium fires create the greatest hazard for a reactor like UWMAK-I. The primary concern is that they represent a potential mechanism for releasing large quantities of tritium to the environment. The potential for a lithium fire in UWMAK-I is minimized by evacuating the reactor building to a vacuum of ~1 torr (see Chapter II of this volume). Thus, some breach of the containment structure is required in addition to the initial failure (for example, a primary pipe rupture) to expose the lithium to oxygen and thereby create the environment for a lithium fire.

A secondary concern is the release of corrosion products. Most of the corrosion products are non-volatile and would be expected to plate-out on the components and piping in the reactor building. But it is possible that small quantities could be released to the atmosphere in a lithium fire. It should be noted that the corrosion products of some elements, such as NbO and MoO₃, are volatile and may be released in a lithium fire. The potential for releasing corrosion products in this manner should be evaluated.

III-C-3-b Loss of Cooling Accidents

The concern with loss of cooling accidents is assuring that the first wall is adequately cooled. Initial calculations indicate that if there is a complete loss of forced flow, during a burn, the wall will reach 600°C in about 10 seconds.

The ultimate concern is, of course, failure of the first wall. Failure could occur as a result of the thermal stresses which are induced in a radiation embrittled wall by a thermal transient. (Heating the wall to temperatures of $>650^{\circ}\text{C}$ will result in precipitation of helium atoms into bubbles which in turn will embrittle the metal.)

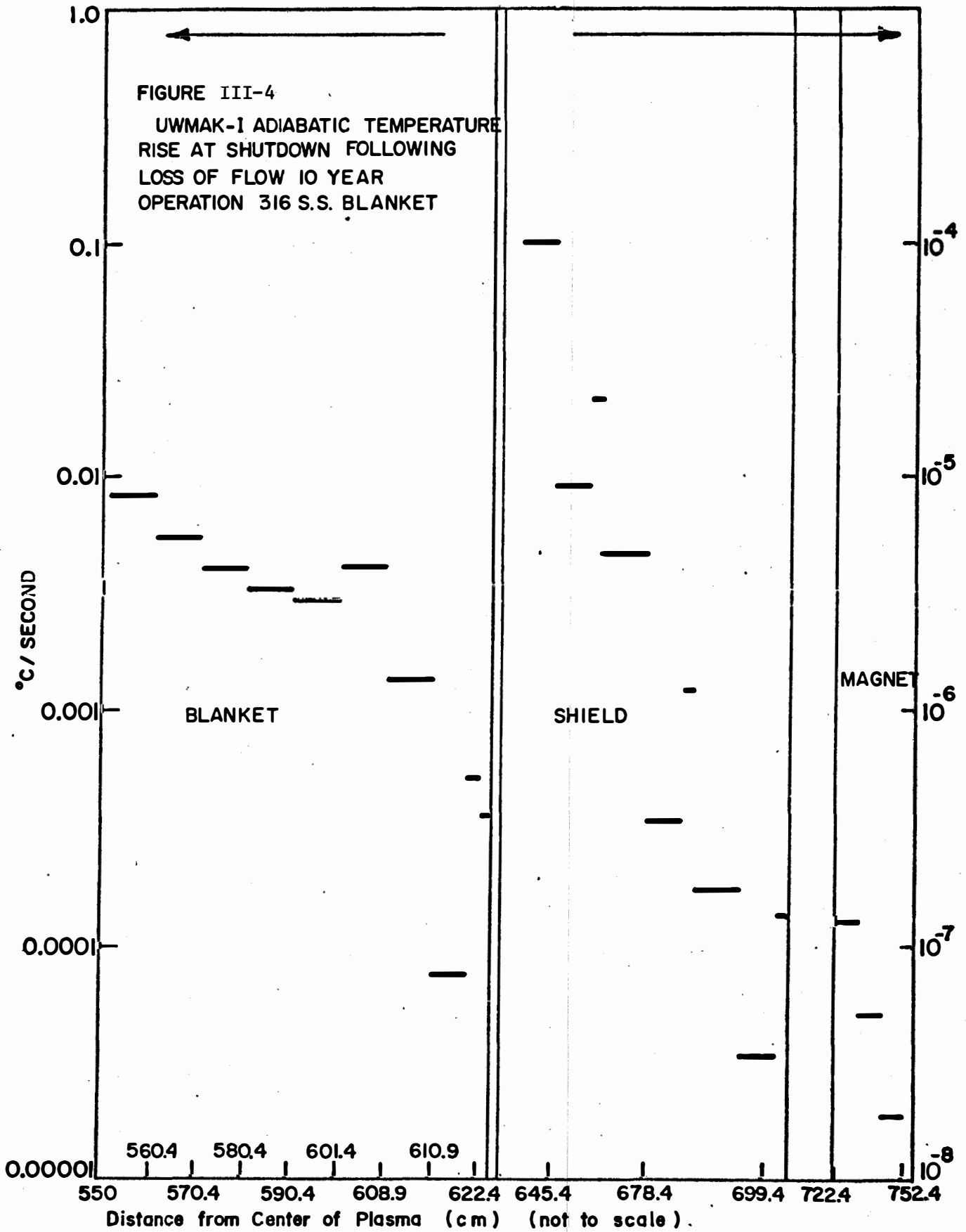
Any failure of the first wall would result in release of Li into the vacuum chamber and quenching of the plasma. There are 3×10^9 joules of stored kinetic energy in the plasma which must be dissipated in the first wall. If this energy is dissipated nonuniformly and concentrated on a local portion of the wall, there is a potential for rapid heating and vaporization of the wall. This would result in great difficulties for the plant operation and would require expensive (and extensive) cleanup procedures in a highly radioactive environment. However, this accident should not represent a severe hazard for the general public as all of the remaining containment devices would still be intact.

Some discussion of the general afterheat problem would be appropriate since the problem of removing afterheat after a loss of cooling accident is such a focal point in the design of LWR's. The adiabatic temperature rise from afterheat generation has been calculated⁽¹²⁾ and the results are shown in Figure II-4. The temperature rise in the region of maximum afterheat generation is only $0.1^{\circ}\text{C}/\text{sec}$. These results, which are based on very conservative assumptions of adiabatic heating, indicate that afterheat removal following a loss of coolant will not present serious problems.

III-C-3-c Magnet Failures

The principal concern with magnet failures is that some local mechanical failure might sever a coil element which could cause internal arcing. This in turn could cause a rapid release of part of the stored energy (the inductive coupling of a failed coil to the other coils reduces the amount of energy dissipation to about 50% of its original stored energy) and perhaps result in melting of some of the magnet material. Other than this, the magnets are to be designed to assure that even an extensive loss of superconductivity would not result in such a non-uniform rapid reduction of stored energy. The total magnetic energy stored in the entire toroidal field magnets would simply increase the overall magnet temperature to roughly 100°K when it is released uniformly inside the magnets and if complete cooling capabilities were lost.

Detectors will be placed throughout the magnets so that local malfunctions can be detected. When a serious malfunction is detected such that total shut-down is required, the following safeguard procedures can be exploited: 1) rapidly dumping liquid helium or a simple lowering of the helium level below the top part of the magnets; 2) energizing heaters; 3) swinging the fixing angle of the ac/dc reversible power convertor Graetz bridge such that maximum power flows back to the ac line at the maximum allowable voltage. The first two schemes would result in uniform loss of superconductivity thereby assuring that the stored energy is released throughout the magnet. The third scheme would reduce the amount of energy dissipated inside the magnets, rather than reduce the refrigeration power required to cool the magnets later. A combination of the first and third schemes is most interesting if their feasibility can be demonstrated.



III-C-3-d Helium Release Accidents

A second category of accidents associated with the use of superconducting magnets is the helium release accident. In this accident it is assumed that the helium containing boundary fails and liquid helium is released to the environment rapidly vaporizing and pressurizing the system. Typically, the helium release accident can be protected against by incorporating rupture disks or other pressure release mechanisms in the design. In UWMAK-I the building is designed for a 10 psi overpressure to accommodate helium release.

III-C-3-e Summary

This section has discussed in qualitative terms the apparent hazards of some specific accidents. While large quantities of stored energy have been identified as representing a potential hazard, realistic considerations of the accidents associated with those quantities of stored energy indicate that they can be dissipated reasonably without resulting in major releases of radioactive materials. The energy stored as kinetic energy in the plasma can be dissipated by expansion of the plasma, and quenching the plasma against the first wall. The stored energy in the magnets can be released either uniformly within the magnet or through the use of external resistors. The stored energy, or the effective stored energy, in the liquid helium can be released by the use of rupture disks or other pressure relieving mechanisms.

On the other hand, the calculations reported herein do show that the potential consequences of a tritium release can be quite serious. The logical potential consequences of the various initiating events must be investigated to quantify the potential hazards of operating the plant and to identify engineered safety features which may be required to minimize such a release.

In assessing the risk of a tritium release, it is important to recognize that four barriers must be penetrated before the tritium can be released to the environment. The first barrier is the primary coolant pressure boundary. This is completely enclosed by a second barrier, the primary containment. The primary containment is a reinforced concrete toroidal roof with a shell that is eight feet thick, lined with a one-eighth inch steel plate to provide leak tightness. The third barrier is the secondary containment -- a right circular steel-lined, reinforced concrete cylinder which encloses the main floor, the lithium floor, and the sodium floor. The last barrier is the outer building wall itself. These barriers will effectively tend to mitigate against any significant accidental tritium release.

III-D Long Term Storage of Radioactive Waste and Transportation Problems

III-D-1 Radioactive Waste Storage

The first wall of the UWMAK-I is exposed to a neutron loading of 1.25 Mw/m². These neutrons will interact with the first wall, as well as the structural materials which contain the lithium, resulting in transmutations

and induced radioactivity. Thus, as the UWMAK-I is operated, radioactive materials are generated which must ultimately be disposed. This section of the report will focus on that disposal problem and compare it with similar problems for fission reactor systems.

The waste management problem typically depends on the kind of waste that is generated. The wastes from a fission reactor fall into one of three categories: low level wastes, intermediate level wastes, and high level wastes. High level wastes must be stored and contained so that they are isolated from the biosphere permanently. It is these wastes that create the long term disposal problems and we will concentrate on them in this section.

The classification of wastes into these three categories is not universally based on any given set of criteria; however, a typical criteria from Reference 13 would be that low level wastes are wastes with radionuclide concentrations that are from 10^1 to 10^4 times the maximum permissible concentration (MPC) as taken from 10CFR20. Intermediate level wastes would be those where concentration was from 10^4 to 10^6 times the MPC. High level wastes would be those wastes with concentrations greater than 10^6 times the MPC.

The concentration of radionuclides in the 316 SS of the first wall of the UWMAK-I, assuming 2 years of continuous operation, are listed in Table III-5. These data show that the ratio of specific activity to MPC is on the order of 10^{15} or 10^{16} . Therefore, these wastes must be categorized as high level wastes and be contained and isolated from the biosphere.

In comparing the engineering problems associated with the long term storage of these wastes, it is necessary to compare the total volume of material that is generated, the amount of heat generated, and the radioactivity of the materials as a function of time. The quantities of radioactive materials removed annually from the UWMAK-I are listed in Table III-6 and compared with the volume of wastes generated during the reprocessing of fission reactor fuels (from Reference 9). These materials total about 736,000 kilograms per year. The resulting volume is about 94m^3 , based on the theoretical density which assumes that the waste is 100% compacted. This compares with a value of about $\sim 4\text{m}^3$ for a 1500 MWe LWR.

The large volume for UWMAK-I results because the radioactive isotopes cannot be chemically concentrated as they are in fission reactors. However, because the majority of the waste here is iron, and Fe-55 is one of the radionuclides, an isotope separation process would be required for any meaningful concentration of the waste. Therefore, concentration of these wastes would be impractical.

The radioactivity and the internal heat generated as a function of time by these wastes are shown in Figures III-5 and III-6. Comparable quantities for an LMFBR are also shown. These results would seem to indicate that the activity of the wastes from the UWMAK-I are ~ 7 times lower than wastes from an LMFBR. However, after 1 year of shutdown the activities are roughly comparable. A major concern with the disposal wastes from a fission reactor is the hazard resulting from the actinides which have much longer half-lives. An example

Table III-5
 Radionuclide Concentrations in 316 SS
 After 2 Years of Operation

<u>Isotope</u>	<u>Specific Activity Ci/cm³</u>	<u>MPC Ci/cm³</u>	<u>Approximate Ratio</u>
V-49	0.246	1×10^{-16}	2×10^{15}
Mn-54	8.28	1×10^{-15}	8×10^{16}
Mn-56	18.9	2×10^{-14}	10^{15}
Fe-55	27.9	3×10^{-14}	10^{15}
Co-58	13	2×10^{-15}	6×10^{15}
Co-60	.663	3×10^{-16}	2×10^{15}
Ni-57	.50	1×10^{-16}	5×10^{15}

Table III-6

Solid Wastes from UWMAK-I (1500 MWe) and a 1500 MWe LWRUWMAK-I (with 316 SS First Wall) (Volume I, UWFDM-68)

First Wall	245,000 kg/yr
Reflector	488,000
Corrosion Products	2,500
Sputtering	<u>250</u>
Total Volume (7.8 gm/cm ³) - 94 m ³	~736,000

Low Level Solid from Power Plant (Reference 9)*

Cubic Feet/yr	3,000-6,000
Kilograms/yr	90,000-150,000
Number 55 gal. Drums/yr	400-800
Burial Ground Area Used Square Feet/yr	2,700-5,400

Produced at Reprocessing Plant Site (Reference 9)*High Level Solid

Cubic Feet/yr	135
Kilograms/yr	7,250
Number 6" x 10' Containers/yr	90
Repository Space Required, Square Feet/yr	18,000

Cladding Hulls

Cubic Feet/yr	90
Kilograms/yr	11,400
Number 30 gal. Drums/yr	22
Area/yr	

Depends on whether storage is required at a commercial burial ground or Federal Repository

Low-Level Solids

Cubic Feet/yr	900-6,000
Kilograms/yr	45,000-100,000
Number 55 gal. Drums/yr	120-800
Burial Ground Square Feet/yr	1,500-7,250

*Values from Reference 9 were based on a 1000 MWe LWR and were linearly scaled for comparison with a 1500 MWe UWMAK reactor.

III-27
Figure III-5

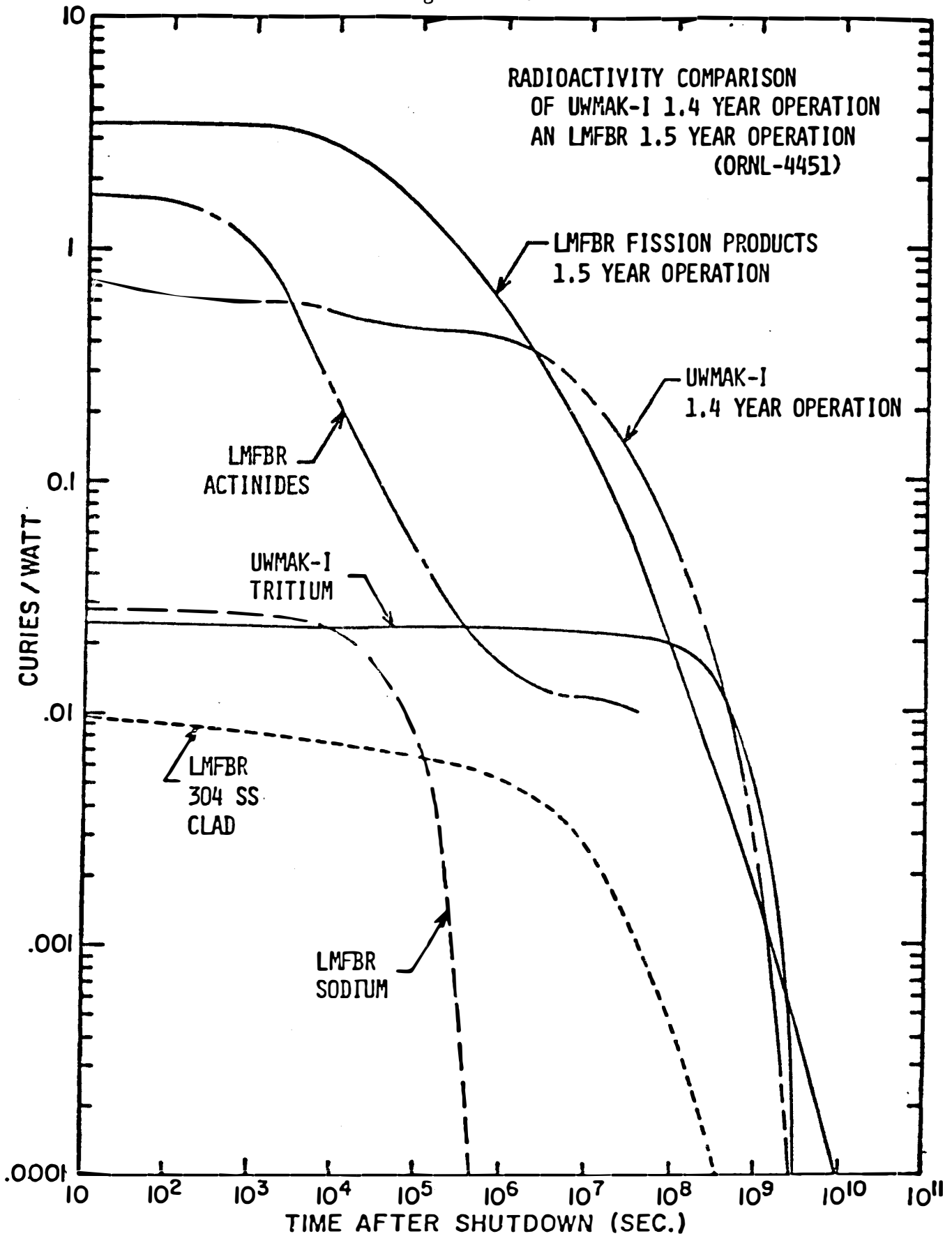
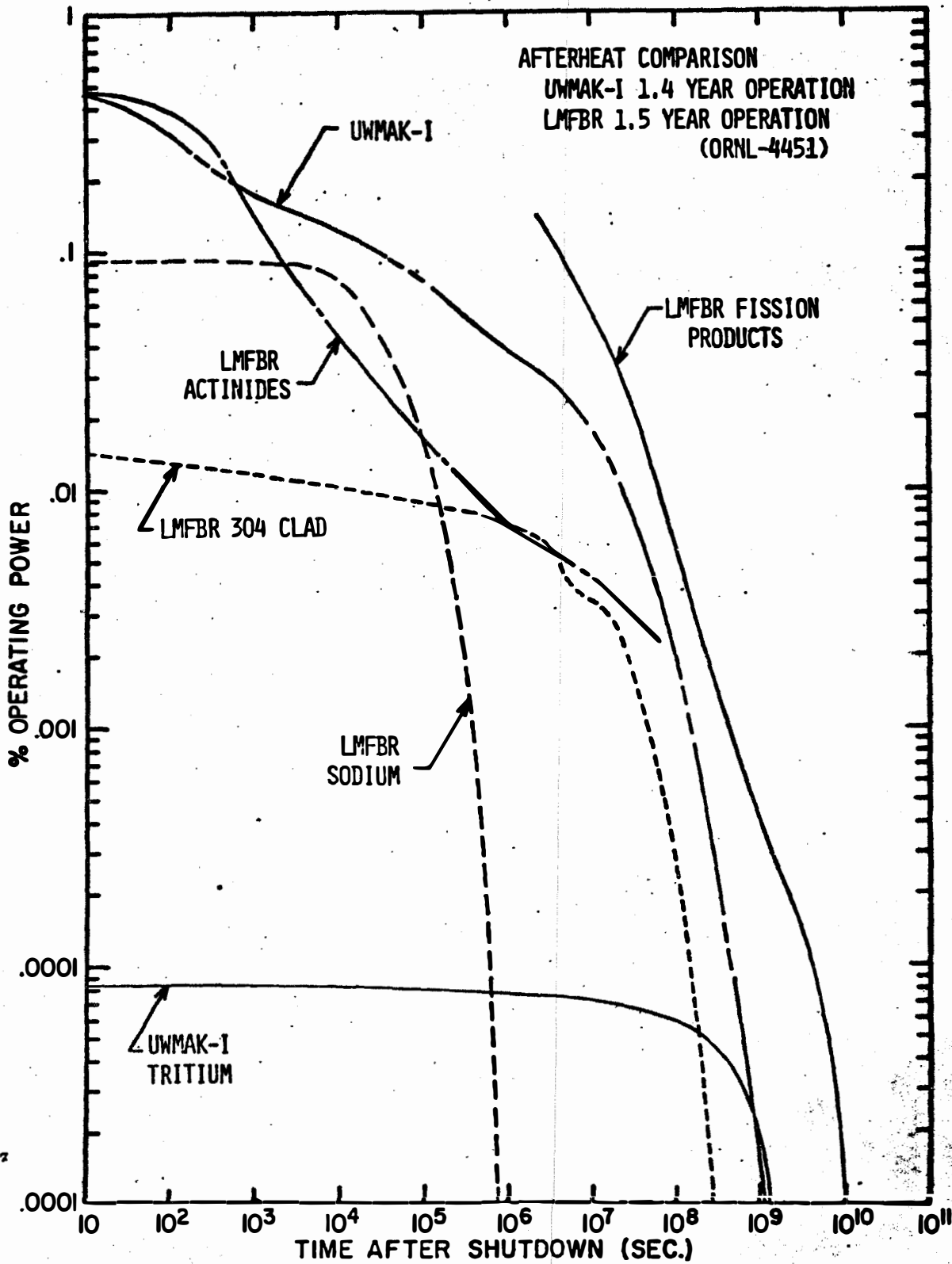


Figure III-6



is Pu²³⁹ which has a half-life of about 24,000 years. Though these wastes are only present in small concentrations, they present a disposal problem of a different magnitude. It is significant that the wastes from UWMAK-I do not contain such long-lived radionuclides.

Finally, it is important to consider the potential hazard associated with these wastes. A convenient tool for such a comparison is the biological hazard potential (BHP). The BHP is the ratio of the activity in Ci/kwt to the MPC as taken from 10CFR20. The BHP is thus equivalent to the volume of air required to dilute the activity per thermal kilowatt down to MPC levels. It provides a convenient means for comparing the relative biological hazards of different kinds of materials. While it is true (1) that the BHP does not account for mitigating factors and assumes complete release of all of the radioactive materials, and (2) that an evaluation of actual hazards would require a detailed analysis of the system design and the mechanisms for the release of the radioactive materials, the BHP does provide a more useful means for comparing given quantities of radioactive materials than does the activity alone.

Values of the BHP for fusion reactors of the UWMAK-I design with different blanket structural materials are shown in Table III-7 (Reference 14) and are compared to the values of the BHP from advanced fission reactor systems (LMFBR's). It is clear from this table that the BHP from materials generated in fusion reactors of the UWMAK-I design is significantly less than the BHP from the radioactive materials generated in a fission reactor. Furthermore, only values for I-131 and Pu-239 are shown in the Table. Many other hazardous radionuclides are generated in the fission reactor fuel cycle (e.g., Sr-90, Cs-137, Kr, etc.). It should be noted that the values of BHP in Table III-7 only reflect the relative hazards of the wastes at the time of shutdown. Figure III-7 shows how the BHP varies with time for fission products and UWMAK-I wastes.

These data can be summarized as follows: (1) the UWMAK-I generates larger waste volumes of high level radioactive wastes than a typical fission reactor; (2) the biological hazard potential of these wastes is significantly less; and (3) the hazards are further mitigated by the fact that no long-lived radionuclides comparable to the actinides from a fission reactor are present.

One might ask: how do these differences effect the engineering problem of storing such wastes. It is clear that the wastes from UWMAK-I are highly radioactive and must be stored for periods of time greater than a few hundred years. It is also clear that the storage problem will be complicated by the fact that more wastes (volume) must be stored. On the other hand, the results indicate that the wastes produced are relatively less hazardous.

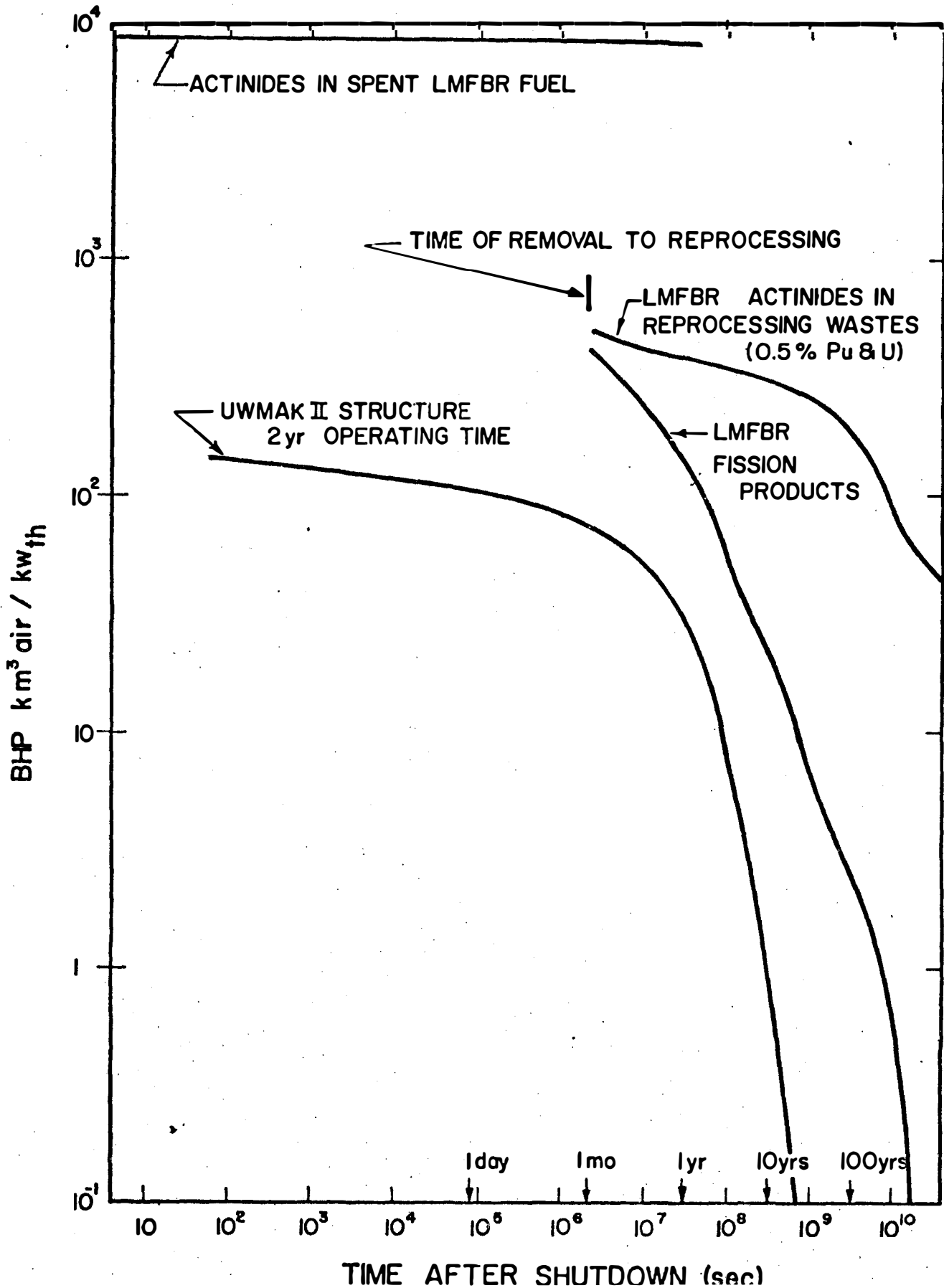
The significance of the lower BHP and the absence of actinides in the waste is two-fold. First, the criteria for a storage facility could perhaps be less rigid. For example, concerns over geological problems that may occur in thousands of years (which have plagued those seeking solutions to the engineering storage problems for fission reactor wastes) could be almost brushed aside. Second, the general public concerns over the permanent nature and potential biological hazards of the wastes generated by fission reactors could be somewhat mitigated.

Table III-7
 First Wall Radioactive Inventory at
 Shutdown After 10 Years of Operation

Isotope	Specific Activity dps/cm ³	Activity ci/kwth	MPC	"Biological Hazard Potential" km ³ of air/kwth	t _{1/2}
			μci/ml		
<u>316 SS</u>					
V-49	1.1 x 10(6)	0.67	1 x 10(-10)	6.7	331 days
Mn-54	4.0 x 10(10)	24	1 x 10(-9)	24	313 days
Mn-56	6.9 x 10(11)	42	2 x 10(-8)	2.1	2.58 hours
Fe-55	2.3 x 10(12)	140	3 x 10(-8)	4.6	2.7 years
Co-58	4.7 x 10(11)	29	2 x 10(-9)	14.5	71.4 years
Co-60	7.7 x 10(10)	4.7	3 x 10(-10)	15.6	5.26 years
Ni-57	1.8 x 10(10)	<u>1.1</u>	1 x 10(-10)	<u>11</u>	36.1 hours
Total (a)		~310		~80	
<u>Nb-1Zr</u>					
Nb-92m	2.5 x 10(13)	1520	1 x 10(-10)	15200	10.1 days
Nb-95m	8.1 x 10(11)	49.6	1 x 10(-10)	500	87 hours
Nb-95	6.8 x 10(11)	4.15	3 x 10(-9)	14	35.1 days
Zr-89	1.7 x 19(10)	1.02	1 x 10(-10)	10	78.4 days
Sr-89	6.20 x 10(11)	<u>37.9</u>	3 x 10(-10)	<u>126</u>	50.8 days
Total (a)		~1900		~16000	
<u>V-20Ti</u>					
Ca-45	4.2 x 10(10)	2.58	1 x 10(-9)	2.6	165 days
Sc-46	3.1 x 10(10)	1.87	8 x 10(-10)	2.3	83.8 days
Sc-48	2.99 x 19(10)	12.1	5 x 10(-9)	2.5	1.82 days
Ti-45	1.90 x 10(9)	<u>0.12</u>	1 x 10(-10)	<u>1.9</u>	3.08 hours
Total (a)		~56		~9	
<u>Advanced Fission Reactor</u>					
I-131		31.6		330	8 days
I-131 (milk pathway)		31.6		230,000	
Pu-239		0.06		1,000	24,400 years
Total Plutonium Isotopes		18.2		8,300	

(a) Including those isotopes not listed here

BHP vs TIME AFTER SHUTDOWN FOR AN LMFBR WITH
1.5yrs OPERATING TIME (ORNL-4451) and
UWMAK II



In addition to the lower BHP and the absence of actinides, the wastes produced in UWMAK-I are comparatively less hazardous for another reason. While some radioactive isotopes in the stainless steel waste could be leached out in ground water, the radioactive materials in the stainless steel are comparatively less mobile than those produced in the fission reactor fuel cycle. Therefore, when stored and contained, the wastes from UWMAK-I are less likely to contaminate the biosphere.

III-D-2 Transportation of Fuels and Radioactive Materials

Initially tritium shipments will be required to supply fuel for the UWMAK-I. As excess tritium bred over tritium burned begins to accumulate, the excess tritium must be shipped from the site or the breeding ratio reduced. In addition, the 736,000 kg of stainless steel from the blanket and corrosion products must be transported from the site to the irradiated materials storage location yr^{-1} .

The major shipping requirement is clearly the 736,000 kg/yr of stainless steel. By way of comparison a 1000 Mwe LWR is projected to ship 32,000 kg of irradiated fuel each year⁽¹¹⁾. This scales to 48,000 kg/yr for a 1500 Mwe LWR. Typical irradiated fuel shipment requirements for LWR's are listed in Table III-8 (Reference 9). According to these data about 15 rail shipments per year are required from the reactor plant to the fuel reprocessing facility. After separation, concentration, and storage at that facility, the waste must be shipped to its final storage location. Because the wastes have been concentrated, the solid wastes can be accommodated with 1-2 rail shipments per year.

TABLE III-8

Typical Irradiated Fuel Shipment Conditions 1000 Mwe LWR (Reference 9)

0.5	MT irradiated fuel per cask for truck
3.2	MT irradiated fuel per cask for rail
1	Cask per truck or rail car
60	truck shipments per 1000 Mwe reactor-year
10	rail shipments per 1000 Mwe reactor-year
1000	miles shipping distance from power plant to fuel recovery plant

It should be noted that the transportation of reactor fuels from the plant to the processing facility is affected by fuel cycle economics which are not present in the fusion reactor system. If the fuel is stored on site for long periods of time, the useful uranium and plutonium which would be recovered during reprocessing are idle and not being used. Thus, there is an economic incentive to move the irradiated fuel from the nuclear reactor site to a reprocessing facility as soon as the radiation levels have reached an acceptable level. These incentives are not present in the fusion reactor system and there is, therefore, considerably more flexibility in planning the transportation of the wastes to the ultimate disposal site.

The casks for the shipment of irradiated fuels could readily accommodate the thermal power and shielding requirements of the first-wall steel. By comparing the volume of first-wall steel to the volume of solid waste and noting that 1-2 rail shipments per year are required for the solid waste, it is probable that 15-30 rail shipments per year are required for the discarded UWMAK steel. The number of shipments will depend upon whether or not the steel is compressed. This number is comparable to the required 15 rail shipments per year for a 1500 Mwe LWR, from the reactor plant to the fuel reprocessing facility. It may also be possible to bury the steel on site but such an alternative needs more study.

III-E Conclusions

This report has reviewed the potential impact that operation of the UWMAK-I fusion reactor would have on the environment. In addition, it has outlined the general methods for conducting an accident analysis of the UWMAK-I and other fusion reactors. In general it has been a scoping study of environmental effects. However, specific emphasis has been placed on radiological effects. Viewed in its entirety, it would seem that the following conclusions can be drawn:

- 1) The building size (102m tall by 120m in diameter) is very large and when coupled with the balance of the facility, which includes cooling towers, could result in some siting problems.
- 2) The thermal efficiency of the UWMAK-I is comparable to LWRs but somewhat less than other power plants. This results primarily because the design was based on a lithium-stainless steel corrosion problem at temperatures in excess of 500°C.
- 3) A preliminary examination of the resource requirements indicates that: a) the virtual consumption of 736,000 kg of steel each year is a potentially significant environmental impact; b) if materials other than stainless steel are used, resource limitations become more significant; and c) the use of large quantities of helium for superconducting magnets creates a resource requirement which can be met by atmospheric extraction without severe economic penalties in tokamak reactor designs.

- 4) Plant effluent releases, primarily tritium in the discharge water, though not less than "low as practicable" limits for LWR's, are well below the limits in 10CFR20.
- 5) Though potential doses from a large scale tritium release can be hazardous, a preliminary review of potential accidents did not identify credible accidents which would be expected to result in such a hazardous release. This review, however, was preliminary and more work will be required to develop potential consequences of several initiating events.
- 6) Large volumes of high level radioactive waste are generated in the UWMAK-I design. A consideration of the waste disposal problem related to the accumulation of these wastes results in the following conclusions:
 - a. It seems clear that if the UWMAK-I is designed with a 316 SS wall which must be removed every two years, and the entire blanket every 10 years, the volume of high level wastes generated by UWMAK-I is significantly greater than the quantity of radioactive waste resulting from the reprocessing of fission reactor fuel.
 - b. The problem of waste generation can be mitigated by design alternatives employing both structural and first-wall materials which have low levels of induced long term radioactivity. (i.e. V or Al).
 - c. The wastes themselves are relatively less hazardous because, a) they do not contain long-lived actinides; b) the BHP of the materials is significantly less; and c) the materials are relatively more stable and less mobile and, therefore, less likely to escape into the biosphere.

III-F References

1. T. F. Yang, R. W. Conn, C. W. Maynard, "Stray Fields of the Conceptual Tokamak Fusion Reactor, UWMAK-I," UWFD-64, Feb. 25, 1974.
2. G. L. Kulcinski, "Potential CTR Requirements for Helium up to the Year 2020," FDM-38, University of Wisconsin, Nuclear Engineering Department, August 28, 1973.
3. I. Nihei, I. Sumiya, Y. Fukaya and Y. Yamazaki, "Corrosion Resistance of Austenitic Stainless Steel in Liquid Lithium," to be published.
4. E. Smith and M. Larinoff, "Power Plant Siting, Performance, and Economics with Dry Cooling Tower Systems," Proceedings, American Power Conference, Vol. 32, p. 544, 1970.
5. James M. Smith, et al., "Tritium Experience in Boiling Water Reactors," Trans. Am. Nucl. Soc., 14(1), 160, June 1971.
6. J. Locante, "Tritium in Pressurized Water Reactors," Trans. Am. Nucl. Soc., 14(1), 161, June 1971.
7. R. B. Briggs, "Tritium in Molten Salt Reactors," Reactor Technology, Vol. 14, No. 4, 335, Winter 1971-72.
8. D. G. Jacobs, "Sources of Tritium and its Behavior Upon Release to the Environment," TID-24635, 1968.
9. "The Safety of Nuclear Power Reactors and Related Facilities," WASH-1250, July 1973.
10. Safety Guide 3, "Assumptions used for Evaluating the Potential Radiological Consequences of a loss of Coolant Accident for Boiling Water Reactors," Safety Guides for Water Cooled Nuclear Power Plants, Division of Reactor Standards, U.S. AEC, December 1, 1970.
11. C. Y. Langham and T. K. Pinson, J. Appl. Physiology, Ja. 1957.
12. D. K. Sze, "Emergency Cooling and Afterheating Effects of a CTR Blanket," in Proc. 1st Int. Tech. Conf. Nuclear Fusion, CONF-740402-P1, 1974.
13. "Siting of Fuel Reprocessing Plants and Waste Management Facilities," ORNL-4451, July 1970.
14. "Transmutations, Radioactivity and Afterheat in a 5000 Mwt Tokamak Fusion Reactor," preliminary draft of paper to be published in Nuclear Technology. A summary is in Trans. Am. Nucl. Soc., Vol. 17, p.138, November 1973.

IV- Materials Resource Considerations

IV-A -1 Introduction

The construction of large scale Tokamak fusion power plants will place severe demands on critical elements. This stems from two basic features of tokamak fusion power plants.

1. Low power density (i.e. 1 MW/m^3 vs $10\text{-}100 \text{ MW/m}^3$ for fission reactors)
2. Use of relatively scarce materials (i.e. Nb, Cr, Mn, Sn, Be, etc.)

Therefore, it is important at this stage of reactor design to estimate the materials required for each reactor concept to make sure that such systems do not overstrain the materials reserves of a particular country, block of countries, or even the world.

We have attempted to estimate the materials requirements for the UWMAK-I "nuclear island" and, as much as possible, for the balance of the plant (heat exchangers, liners, etc.). The numbers quoted in this section are probably underestimates and do not take into account losses during fabrication or processing. However, the values should be within 50% of the ultimate amount and therefore represent minimum requirements.

The first section in this chapter outlines the needs of a plant like UWMAK-I while the following 9 sections go into the specific reserves and resources for Li, Cr, Ni, Cu, Ti, Al, V, Mo and Nb. The availability of these elements inside and outside the U.S. is evaluated as well as the availability at present prices, 3 times present prices and 10 times present prices. It should be understood that estimates of resources at 3X and 10X prices are based on limited data subject to many uncertainties. Their principal value is as indicators of the orders of magnitude of resources that might become available at the higher prices. The last section of this chapter tries to compare the materials requirements to generate 10^6 MWe of electricity with ~670 UWMAK type plants in the year 2020 which corresponds to ~30% of the projected U.S. needs at that time.

IV- A-2 Materials Requirements for UWMAK-I

IV- A-2-a Nuclear Island Requirements

The results of a thorough analysis of the design presented in Volume I of this report are given in Table I. The nuclear island is defined here as including all the material within the toroidal field magnets plus the divertor and vertical field coils and injectors. The coolant requirements include only that within the primary circuits (i.e. Li and He) and the liquid helium requirements include all the inventory in the magnets, liquifiers, transfer lines, and storage. Separate considerations will be given to the balance of plant.

The first thing to note is that the number of blanket, shield and toroidal field sets is not 12 but rather 15. This is one to include the spare cells needed outside the reactor in the event of failure and to allow 3 modules to be replaced every 6 months and restored within the next 6 months while the reactor is running.

TABLE I
Materials Requirements - UWMAK-I Nuclear Island
Metric Tonnes

Element	Blanket - 316 SS			Shield Structure & Absorbers	Magnets			Vacuum Pumps (c)	Misc.	Total	Tonnes MWe (1475 MWe)	
	Initial Structure (a)	1st wall replacement 14 times (b)	Reflector & Header replac. Twice		Toroidal Field Coils	T. F. Bracing (c)	Vertical Field Coils Incl. Dewar					Vertical Field Coil Support (c)
Al	79	69	146	26	123		118			562	0.38	
B				1580						1580	1.07	
C				446						446	0.30	
Cr	1406	1236	2636	457	1221	91	2126	181	9	9363	6.35	
Nb					86		15			101	0.07	
Cu	79	69	146	26	6163		1198			7681	5.21	
He				1	13		19			58	0.04	
Fe	4844	4258	9081	1573	4206	299	7322	599	29	(storage) 32211	21.84	
Pb				20500						20500	13.90	
Li	1159									541 (in pipes) 1700	1.15	
Mn	156	137	293	51	136	9	236	18	1	1037	0.70	
Hg									3	3	0.002	
Mo	156	137	293	51	136	236				1009	0.68	
Ni	1094	962	2051	355	950	54	1653	109	5	7233	4.90	
Ti					44		8			52	0.04	
Total Weight-	8973	6868	14647	25066	13078	453	12931	907	47	566	83534	56.63
Component Wt												
316SS	7814	6868	14647	2539	6895		11809				51122	
Li	1159									541	1700	
B ₄ C				2026							2026	
Pb				20500							20500	
He				1	13		19			25	58	
Cu Stabilizer					6040		1080				7120	
Nb-Ti					130		23				153	
Hg									3		3	
304SS						453		907	44		1404	

(a) 12 regular modules plus 3 spare units
(b) first 20 cm only, 491 MT each time
(c) 304 SS

Secondly, the amount of material required to replace the first 20 cm every two years (or 14 times during the 30 year lifetime) is calculated. Finally, numbers are also given for the replacement of the rest of the blanket (reflector and headers included) every 10 years, or twice during the plant lifetime.

The composition of the stainless steel used for these inventory numbers are as follows:

		<u>wt. %</u>	
	<u>304 SS</u>		<u>316 SS</u>
Fe	66		62
Cr	20		18
Ni	12		14
Mn	2		2
Mo	-		2
Al	-		1
Cu	-		1

The first point to note from table I is that the replacement of the first wall every two years and the rest of the blanket every 10 years increases the blanket requirements for 316 stainless steel by more than a factor of two. The total weight of 316 SS in the initial blanket is 7814 metric tonnes while replacing of the first 20 cm every two years (14 times in all) would require another 6868 tonnes. The replacement of the rest of the blanket is dominated by the 316 SS reflector and requires another 11523 tonnes over the 30 year lifetime.

The shield in UWMAK-I weighs ~2.8 times the blanket and is dominated by the weight of Pb (20,500 tonnes). There is also 2026 tonnes of B_4C required for neutron absorption in this component.

The magnets in UWMAK-I require over 27,000 metric tonnes of material most of which is 316 SS and 304 SS (22,548 tonnes). The amount of Cu stabilizer is 7243 tonnes while 153 tonnes of superconductor and 32 tonnes of liquid helium are also required.

We have included the vacuum pumps to highlight the need for mercury (3 metric tonnes) and 304 SS. Finally, there is 21 tonnes of liquid helium in storage and 541 tonnes of lithium in the rest of the primary coolant circuit. We have not included the materials in the fueling and heating injectors, the mobile transport vehicles nor has any attempt been made to tabulate all the miscellaneous equipment in the reactor enclosure.

The total mass of material required for the UWMAK-I nuclear island, over a 30 year life is 80,410 tonnes made up of 59% steel, 26% lead, 9% copper, 3% B_4C , 2% Li, 0.2% helium, 0.1% Nb-Ti superconductor, and 0.004% Hg. Put another way, the blanket accounts for 35%* of the total weight of the nuclear island, the shield for 31% and the magnets for 34%. Finally, the

*during the anticipated 30 year life

amount of materials required per MW_e for UWMAK-I is given in the last column of Table I. The values range from 21.8 tonne per MW_e for Fe to 13.9 for Pb, 6.35 for Cr, 5.2 for Cu, 4.90 for Ni, 1.07 for boron to 0.002 for Hg.

IV-A-2-b Materials Requirements for Balance of Plant

Many of the materials requirements for UWMAK-I are common to conventional nuclear generating plants with a three notable exceptions.

- 1) The number of loops is much larger in UWMAK-I (12 vs ~ 3-4 in a fission reactor)
- 2) The inclusion of an energy storage building and unit is not required for any current power plant.
- 3) The use of thermal fly wheels to level out the load to the turbine in a characteristic of the pulsed operation of a tokamak reactor.

Table II lists, as completely as possible, the materials resource demands outside the nuclear island. It should be noted that there are 14 loops in UWMAK-I (12 regular, 1 for the divertor and one spare). The mass requirements for the heat exchanges and regenerators were also included. The construction material for the Li-Na heat exchangers was 304 SS while Croloy-2 1/4 Cr was used for the main steam generators. Piping was assumed to be 316 SS in the primary circuit and 304 SS in the secondary loop. Croloy-2 1/4 Cr was used for the steam loop. It was impossible to calculate the total length of piping for this plant so we estimated the total weight and the basis of Sargent and Lundy's experience in the fast reactor field. The piping numbers for this plant probably only good to within a factor of two.

Estimates were also made of the building liner material (304 SS) and reinforcing rod. The later was estimated on the basis of 2% by volume of reinforcing rod for every m^3 of concrete. The dimensions of the liner were given in chapter I-C of this volume. The materials involved in the 14 liquid lithium and 14 liquid sodium pumps (12 for each loop, 1 for the divertor and one spare) were assumed to be all 304 SS.

It was not possible to make estimates of the material requirements for the turbine, reheaters, control room, and cooling towers. We also did not include the material requirements for the electrical switching gear. The materials involved in the tritium extraction equipment were not sufficiently defined at this time to make any reasonable estimates. However, we did include the Y requirements under the miscellaneous column.

The first thing to note from table II is that the total amount of metals identified in the balance of plant sections is ~50% higher than the amount required for the nuclear island. The second point to note is more than half the materials requirement outside the nuclear island result from the need for reinforcing rod for some 340,000 m^3 of concrete. We have used high carbon steel for the reinforcing rod and structural steel. This results in rather large amounts of iron for the balance of plant, in fact,

Table II
Materials Requirements for Balance of Plant-UWMAK-I
Metric Tonnes

Element	Heat Exchanger			Piping			Thermal	Dump	Pumps	Building	Reinforcing	Turbine	Energy	Misc.	Total	(1475 MWe) Tonnes Mwe
	Li-Na (a)	Na-Steam (b)	Regener- ative(c)	Li 316 SS	Na 304 SS	Steam (Croloy)	Flywheel Na Tanks(a)	Tanks Na+Li(a)	Na+Li(a)	Liner & Revol. Door	Rod & Struc Steel(d)	Generator Unit(e)	Storage Unit			
Al													445		445	0.30
Cr	762	181	8	82	184	4	1608	1305	1080	487		43	455		6199	4.20
Nb													39		39	0.03
Cu				5								454	2800		3259	2.21
He													80		80	0.05
Fe	2514	4912	27	283	607	150	5306	4306	3565	1606	66957	4149	1502		95924	65.03
Mn	76	9	1	9	18	1	161	130	108	49			46		608	0.41
Mo		11		9		2									22	0.01
Ni	457	811	5	64	110		965	783	648	292		86	273		4494	3.05
Na														17826(f)	17826	11.99
Ti													20		20	0.01
Y														5 - (g)	5	0.003
Zr														100 - (h)	100	0.07
Total	3809	5923	41	457	919	157	8040	6524	5401	2434	66957	4731	5660	17929	128982	87.4*

Components

304SS	3809				919		8040	6524	5401	2434			2276		29403
316SS			41	457											498
Croloy-2 1/4	1045				157										1202
Nb-Ti													59		59
Cu Stabilizer											454	2800			3254
Al												445			445
He												80			80
Na													17826		17826
Y													5		5
Carbon Steel	3833										66957				70790
Inconel-600	1045														1045
Low Alloy Steel												4277			4277
Concrete-m ³											(340000)				

- (a) 14 units (12 regular, 1 divertor, 1 spare)
 - (b) 17.6% Croloy-2 1/4; (Fe-96.25%; Cr-2.25%; Mo-1.0%; Mn-0.5%), 17.6% Inconel-600 (77.65% Ni, 15% Cu, 7% Fe, 0.35% Mn), 64.7% carbon steel
 - (c) 28 units
 - (d) 1% Mn Steel
 - (e) Low Alloy Steel-2% Ni, 1% Cr
 - (f) Secondary Loop
 - (g) Tritium Extraction Bed
 - (h) Liquid metal clean up system
- *approximate number due to roundoff

~80% of the metals requirement is for iron. There is also a rather large amount of Na required (17826 tonnes) for the secondary loop.

The demand for alloying elements such as Cr, Ni and Mn is also quite substantial. In fact, they are of the same order of magnitude as for the nuclear island (see Table I). A rather large amount of copper is required for the magnets in the energy storage unit and for the electrical generating units. Finally the unique demand for Y in the tritium separation units amounts to ~ 5 tonnes for UWMAK-I.

A summary of the requirements for the total plant is given in Table III. There are 4 points worth noting.

- . Sixty three (60) percent of the metals requirements is for iron (128,135 tonnes).
- . There are five other elements which are in large demand and represent the following percentages and weights in the UWMAK-I reactor.

Pb (10%)	20,500 tonnes
Na (8%)	17,826 tonnes
Cr (7%)	15,562 tonnes
Ni (6%)	11,727 tonnes
Cu (5%)	10,940 tonnes
- . There are also rather large requirements of critical elements such as He (138 tonnes) lithium (1700 tonnes), Hg (3 tonnes) and yttrium (5 tonnes), and Zr (100 tonnes).
- . Approximately 144 tonnes of metal is required for each MW_e in UWMAK-I.

The impact of such requirements on U.S. and the world resources will be addressed in section IV-L of this chapter and the economic problems will be addressed in Chapter V of this volume. However, it is clear at this point that even at an average price of 4-5\$/kg of finished product (~2 dollars per pound) the capital cost will approach ~600\$/kW_e.

Table IV summarizes the need for various alloys and compounds in the UWMAK-I system. The largest single type of material used is the high carbon steel for reinforcing rod and structural steel. However, there are also substantial requirements for 316SS (53,095 tonnes) and 304SS (29,403 tonnes). The demand for low alloy steel (for turbine constructions) is low by comparison to the austenite alloys as is the need for Croloy (1202 tonnes) for the steam system.

The boron carbide requirements of over 2000 tonnes (per plant) represents a rather large increase over the present manufacturing capacity of that compound and the 212 tonnes of Nb-Ti is 38 times the U.S. output of that compound in 1973.

Table III
Summary of Elemental Requirements for UWMAK-I

<u>Element</u>	<u>Metric Tonnes</u>			<u>Tonnes</u>
	<u>Nuclear Island</u>	<u>Balance of Plant</u>	<u>Total</u>	<u>MWe</u> <u>(1475 MWe)</u>
Al	562	445	1,007	0.68
B	1,580	---	1,580	1.07
C	446	---	446	0.30
Cr	9,363	6,199	15,562	10.55
Nb	101	39	140	0.09
Cu	7,681	3,259	10,940	7.42
He	58	80	138	0.09
Fe	32,211	95,924	128,135	86.87
Pb	20,500	----	20,500	13.90
Li	1,700	----	1,700	1.15
Mn	1,037	608	1,645	1.13
Hg	----	3	3	0.002
Mo	1,009	22	1,031	0.70
Ni	7,233	4,484	11,727	7.95
Na	---	17,826	17,826	12.13
Ti	52	20	72	0.05
Y	----	5	5	0.003
Zr	----	100	100	0.07
	<hr/>	<hr/>	<hr/>	<hr/>
	83,534	128,982	212,516	144.2

Table IV
Summary of Alloy Requirements for UWMAK-I
Metric Tonnes

<u>Alloy or Compound</u>	<u>Nuclear Island</u>	<u>Balance of Plant</u>	<u>Total</u>	<u>Tonne MWe (1475 MWe)</u>
316 SS	51,122	498	53,095	36.0
304 SS	1,404	29,403	30,807	20.89
Low Alloy Steel	---	4,277	4,227	2.90
Carbon Steel	---	70,790	66,957	47.99
Croloy - 2 1/4	---	1,202	197	0.81
Nb-Ti	153	59	212	0.14
B ₄ C	2,026	---	2,026	1.37
Inconel-600		1,045	1,045	0.71
Concrete - m ³	---	(340,000)	(340,000)	

A little better perspective on the sources of material demand for a toroidal fusion reactor like UWMAK-I is given in Table V. Here we examine the critical elements, Cr, Nb, Mn, and Ni.

The case for Nb is fairly clear, the demand is all associated with the magnetic confinement approach and roughly 3/4 comes from the magnets close to the reactor and 1/4 comes from the stored energy unit. The only way one could reduce the Nb requirements in UWMAK-I would be to redesign the toroidal and divertor magnets (an option to be explored in UWMAK-II).

Finally, it is worth noting that roughly 25% of all the Cr and Ni requirements stem from the recycling of the blanket material. Table V also shows that ~25% of the Mn, Cr and Ni requirements come from the reinforcing steel for the reactor magnets. Hence even if one were able to find a blanket material which would last for the entire reactor lifetime, we could not reduce the total Cr, Ni and Mn requirements by more than 1/4 of the values indicated in Table III. Another way to look at this is that even if we replaced the 316SS in the blanket with another metal, such as Al or V, the total Cr, Ni and Mn required for a system like the UWMAK reactor would not be reduced by more than 50% even allowing for different shield, piping and coolant loop materials.

Table V
Source of the Need for Critical Elements in the UWMAK-I
Reactor Facility*
% of Total Requirements

Element	Nuclear Island			Components Peculiar to UWMAK-I					
	Initial Structure	1st wall Repl.	Balance of Blanket Repl.	Shield	Magnets	Energy Storage Unit	Thermal Fly- Wheel Tanks	Liner + Rev. Door	Balance of Plant
Cr	9	8	17	3	23	3	10	3	24
Nb	-	-	--	-	72	28	-	--	--
Mn	9	8	18	3	24	2	10	3	22
Ni	10	8	17	3	24	2	8	2	27

*As compared to a Liquid metal cooled fission reactor

IV-B Lithium Reserves and Resources

If lithium is to be used as the tritium breeder in nuclear fusion, as a coolant, or both, availability in adequate amounts is of critical importance. This report summarizes data for lithium reserves and resources and discusses factors that may influence the availability of lithium in adequate amounts during the period 2000-2020.

IV-B-1 Types of Lithium Deposits

There are two major classes of productive lithium deposits: pegmatite deposits and brine deposits. In pegmatite deposits, lithium is present largely in one or more of three silicates: spodumene, petalite, and lepidolite, and one phosphate, amblygonite. Spodumene is by far the most important lithium mineral. Li contents of the minerals are as follows:

Spodumene - $(\text{Li,Na}) \text{Al Si}_3\text{O}_8$; Li 3.2 to 3.7%

Petalite - $(\text{Li,Na}) \text{AlSi}_4\text{O}_{10}$; Li 1.5 to 2.4%

Lepidolite - $\text{K}_2\text{Li}_3\text{Al}_4\text{Si}_7\text{O}_{21} (\text{OH,F})_3$; Li commonly 3 to 4%

Amblygonite - LiAlFPO_4 ; Li 3.5 to 4%

Pegmatite deposits are mined in open pit or underground. The rock is crushed, and spodumene is concentrated by flotation, or flotation plus heavy media separation. Brine deposits consist of brines trapped in voids in the salt or other deposits of saline lake basins (Searles Lake, Silver Peak) or the actual waters of salt lakes (Great Salt Lake). Li contents of brines of interest range from 35 ppm to 300 ppm. Fractional crystallization, with or without prior evaporation, and precipitation as carbonate are used to recover the Li.

IV-B-1-a Pegmatite Deposits

Lithium-bearing pegmatites are known on every continent of the world except Antarctica, but Free World reserves of Li in pegmatite are concentrated in Canada, the United States, Zaire, and Rhodesia. Available data on resources are given in the accompanying table. Data for the U.S., and in part for Canada, are good. Substantial additions to reserves in pegmatites are possible in Canada. Reserves in two pegmatites near Manono, Zaire, may be very large (Kesler, 1960). No data on reserves in U.S.S.R. or China are available; reserves could be large.

A large share of U.S. lithium reserves is in the pegmatites of the Kings Mountain District, North Carolina, and this is the only pegmatite district in the United States from which there has been significant production in recent years.

IV-B-1-b Brine Deposits

Production of lithium from brine deposits is largely a development of the period since World War II. It is now evident that this class of deposits contains more than half of the total U.S. reserves and resources. Furthermore,

since exploration of brine deposits for lithium is far less advanced than exploration of pegmatites, it seems likely that large new reserves will be developed in the future.

The most productive brine deposit, and perhaps the largest of known deposits, is in Clayton Valley (Silver Peak), Nevada. The brine (300 ppm Li) is pumped from wells into evaporating pans, where it is concentrated by solar evaporation. Soda ash is then added to precipitate Li_2CO_3 . There are various estimates of reserves. The latest (Kunasz, 1974) is given in the table. It covers brines in place to a depth of 1,000 feet. According to Kunasz, only a portion of this amount can be recovered with today's technology and economic parameters. The reserves at 3X present prices are taken from Norton (1973, p. 372) and correspond to his figures for "conditional" reserves.

Lithium reserves in the brines of Searles Lake (60-150 ppm) are decidedly smaller than those of Clayton Valley. Estimates, however, are only for Li that would be recovered as a byproduct of mining for potash and other salts from the upper salt body (Kunasz, 1974). The brine in this unit averages 150 ppm Li. No estimate of reserves of Li in the brines (60 ppm Li) of the lower salt body is available. Information on this point should be sought from the operating company. The reserves at 3X or 10X present prices could be very large.

A very large deposit of Li-bearing brine has been recognized through drilling for geothermal energy in the Salton Sea Basin. The volume of brine has been estimated at more than 5 km³, underlying an area of 50 km². Analyses show 210 to 215 ppm Li. Li content has been estimated by White (1968) at approximately 10⁶ m.t.

The waters of Great Salt Lake contain 35-70 ppm of Li, with total Li content estimated as 525,000 m.t. (Eardley, 1970) to 640,000 m.t. (Cummings, 1970). Plans by Gulf Resources to recover Li from the brines have recently been abandoned (Luckenbach, 1974).

It should be emphasized (cf. Norton, 1973) that known reserves of lithium in the U.S. are so large relative to conceivable requirements for non-nuclear uses that for many years there has been little incentive to exploration for lithium deposits. The potential for discovery of additional major deposits is very high, particularly in the saline basins of the Basin Range Province (Nevada, California, Utah, Arizona, New Mexico) that are sinks for drainage of areas of Tertiary or Recent volcanism.

Outside the United States, little is known of lithium in brines. Yet saline lakes in the volcanic belt of eastern Africa and in the Cordilleran belt from Mexico to Chile seem likely locales of occurrence of brine deposits. There is one report (Mining Journal, 1970) of a brine deposit in the Solar de Atacama, northern Chile, containing 0.2 percent Li. Reserves are estimated

at 1,200,000 short tons Li. The content of Li is extraordinarily high, and Norton (1973) points out that verification of estimates is needed.

IV-B-2 Size of Reserves Relative to Fusion Reactor Requirements

U.S. reserves of lithium at present prices may or may not be adequate to supply requirements for a reactor capacity of 10^6 MWe. Reserves at 3X present prices should be more than ample, particularly since further discoveries are to be expected once the economic incentive of large increase in demand comes into play.

References

1. Cummings, A. M., 1970, Lithium. Mineral Facts and Problems; Bull. 650, U.S. Bur. Mines, 1073-1081.
2. Eardley, A. J., 1970, Salt Economy of the Great Salt Lake; Third Symposium on Salt, Vol. 1, Northern Ohio Geological Society, Inc. Cleveland, 78-105.
3. Kesler, T. L., 1971, Lithium raw materials; Industrial Minerals and Rocks, 3rd ed., AIME, New York 521-531.
4. Kunasz, T. A., 1975 Lithium Raw Materials; AIME, Industrial Minerals and Rocks, rev. ed.,
5. Luckenbach, W. F., 1974, Lithium - Burgeoning demand will require new production; Eng. and Min. Jour., Vol. 175, 96-117.
6. Mining Journal, 1970, Chilean lithium-potassium, p. 597; Anonymous article.
7. Norton, J. J., 1973, Lithium, cesium, and rubidium--the rare earth alkali metals; In U.S. Mineral Resources, U.S.G.S. Prof. Paper 820, 365-378.
8. White, D. E., 1968, Environments of deposition of some base-metal ore deposits; Econ. Geol., 63, 301-335.

L I T H I U M R E S E R V E S

<u>Mine or District</u>	<u>Type of Deposit</u>	<u>Reserves at Present Prices</u>		<u>Additional Reserves at at 3X Present Prices</u>	
		<u>Li Content of Ore or Brine</u>	<u>Li Metal m.t. x 10⁶</u>	<u>Li Content of Ore or Brine</u>	<u>Li Metal m.t. x 10⁶</u>
U.S.A.					
Kings Mountain, N.C.	Pegmatite	0.60 to 0.70%	.44	>	.50
Silver Peak, Nevada	Brine	300 ppm	.49 (3)	300 ppm	1.81
Great Salt Lake, Utah	Brine	-----	-----	30 - 70	.55
Searles Lake, Calif.	Brine	150 ppm	.10 ^{1/}	150 ppm	.03
Salton Sea Basin, Calif.	Brine	-----	-----	210-215 ppm	1.00
Totals for U.S.A.			1.03 (3)		3.89
IV-14 World - Ex - U.S.A.					
Canada					
Barraute, Que.	Pegmatite	.55%	.076		
Bernic Lake, Man.	Pegmatite	2.01 to 2.24%	.040		
Georgia Lake, Ont.	Pegmatite	-----	-----	.52%	.055
Other Areas				-----	.080
Rhodesia, Bikita Area	Pegmatite	1.03%	.082		
Chile, Salar de Atacama ^{2/}	Brine	2,000 ppm	1.10		
Totals for World - Ex - U.S.A.			1.298		.135

Notes: 1/ Data for Searles Lake are for upper salt body only.

2/ Data for brines of Salar de Atacama need verification.

3/ More recent information (J. D. Vine, personal communication) indicates that reserves at Silver Peak are only 44,500 tons, hence total U. S. reserves are only .500 x 10⁶ m.t.

IV-C Chromium Reserves and Resources

Chromium, an essential component of stainless steel (18-33% Cr), has only one commercial source, the mineral chromite. Chromite ores are unevenly distributed about the world. The eastern hemisphere holds about 99 percent of world chromite reserves and resources. More than 90 percent of the total is contained in the Bushveld and Great Dyke layered complexes in South Africa and Rhodesia.

IV-C-1 Geologic Occurrence

Most of the world's resources of chromite are in primary deposits thought to be derived from materials of the earth's mantle. The materials have risen into the crust along deep crustal fractures, as liquids in stable continental interiors or as solids squeezed into overlying rocks in areas of mountain building. Each mode of origin leads to a characteristic occurrence of the chromite that is reflected in the grades and sizes of the resulting deposits. The two occurrences are:

- 1) Stratiform (layered) complexes
- 2) Alpine type (pod-like) deposits

Layered complexes form in stable continental areas and are the result of slow cooling of rock melts which contain chromium. Complexes range up to thousands of square miles in surface area. Under favorable conditions chromite crystals form and accumulate by gravity settling. This type of deposit contains the great reserves of chromium found in Rhodesia and South Africa. Chromite in such deposits is mostly lower in chromium and higher in iron than chromite in podiform deposits, but deposits in layered complexes are many times larger in tonnage.

Pod-like chromite deposits occur in mountain belts around the world and may have originally been formed in the same manner as chromite in layered complexes; however, during or after crystallization, upward squeezing has deformed the layers. Chromite layers are discontinuous, with the result that these deposits are groups of bands or pods, sometimes surrounded by zones of disseminated chromite. Size is highly variable, from several tons to several million tons, the chromite generally being higher in Cr and Al content than the chromite of layered complexes.

Besides the primary deposits, there are two classes of secondary deposits: (1) lateritic and (2) placer. Large tonnages of chromite exist in lateritic iron ores, but they present difficult problems of extraction and are low in grade. Placer deposits of chromite are known in Oregon and New Caledonia. So far as known, tonnages of chromite in such deposits are not large.

IV-C-2 Reserve and Resource Data

Table IV-C-1 contains published reserve and resource figures; Thayer's (1973) estimates from USGS Prof. Paper 820 are considered the best available for world chromite. He has presented figures for thousands of long tons of shipping ores and concentrates. Standard industry chromite grades are based on Cr, Fe, and Al content of ores; these vary over a small range of Cr content. High Fe content lowers the desirability of the ore. Industry demand for chromite with certain specifications will affect development of chromite deposits less and less, however, as these "specialty" ores are depleted.

To calculate tonnages of chromium in ores and concentrates, the following relations were used:

Grade	Cr/Fe ratio	%Cr ₂ O ₃	Ave. %Cr ₂ O ₃	%Cr
A	> 2:1	> 46	46	31
B	1.5-2:1	40-46	43	29
B-	≥ 1.5:1	> 40		
C	Cr:Al=3:1	~ 40	35	24

"B" grade deposits may be overestimated by this method. Insufficient breakdown of "B" grades did not allow separate calculations in this category.

Where possible, reserves and resources for individual deposits in the U.S. were tabulated; these figures are the best estimates available, although confidence is lowered by the highly variable nature of the pod-like deposits. Estimates of useable tonnage in the one large domestic stratiform complex in the Stillwater Range, Montana, are complicated by the great amount of faulting which has occurred and the relatively high Fe content of the chromite ore, which presently makes it more costly to utilize in place of higher Cr ores from abroad.

World reserves and known resources are highly concentrated in Southern Africa, where the 26,000 mi² Bushveld Complex and the 16,500 mi² Great Dyke complexes occur. Each is of the layered type, and chromite deposits in the bodies have been only partly evaluated. Bushveld reserve estimates are considered assured, whereas resource estimates are conservative. Great Dyke estimates are based on projections only to 500 feet below the outcrop, although they are known to extend to greater depths. (Thayer, 1973, p. 114, 119)

IV-C-3 Other Sources

Thayer (1973) is of the opinion that the probability of finding major new chromite districts is falling off rapidly, based on the rate of discovery of new deposits in recent years. It is difficult, however,

to assess the magnitude of undiscovered deposits simply because chromite is a difficult mineral to prospect for, either geophysically or geochemically. The search for new deposits, at least within the U.S., would be exceedingly expensive.

Possible world resources at 10X present price levels include the laterite deposits, which contain .5-3% Cr. These deposits range into billions of tons but present formidable extractive problems. Thayer (1973, p. 120) also points out that stainless steel scrap is a significant resource, which in 1968 provided the equivalent of about 12% of the chromium imported in cre.

In the United States, the only chance of increasing available resources lies in the peridotite bodies in the Appalachians, from Vermont to Alabama, in the Sierra Nevada, and in the Coast Ranges of California, Oregon and Washington, and in Alaska. Deposits of chromite occur in many of these bodies. They have been known for more than a century and have been worked intermittently, especially during World War II and the Korean emergency. They are Alpine-type deposits, in which chromite is found as high-grade pods and lenses, as chromite-rich layers interlayered with dunite, and as crystals disseminated in dunite and present to the extent of one or two percent. Chromite thus far produced has come partly from the high-grade lenses, partly from the interlayered material. Mining has been restricted to portions of the dunite bodies containing these two types of materials.

Thayer estimates "conditional resources" of high chromium ore in podiform deposits at 350,000 tons, stating that this figure is "postulated entirely on extensive exploration of known podiform ore bodies or new ore bodies in known districts under the stimulus of very high prices" (Thayer, 1973, p. 117). These ore bodies would include lenses of massive ore and the richer interlayered material (perhaps 10% Cr₂O₃ or better). The estimate is certainly the best possible one in the light of present information and in terms of the economic conditions that have determined U.S. production and consumption of chromite in the past. Under these conditions mining has necessarily been selective, and tonnages of "ore" are correspondingly restricted.

Under markedly different conditions, however, the restrictions might not apply. At price levels above 3X present prices, it might be possible to consider mass mining of a dunite body, taking not only pods and interlayered material but the disseminated chromite in between. This would have the advantage that many lenses of massive ore and bodies of interlayered material could be taken that would be too small for selective mining and, furthermore, would not even be discovered by chromite exploration of the kind conducted in the past. A dunite body of the right type can be likened to a plum pudding, in which the plums are of various sizes. The mining of the past has been restricted to the plums at or near the top of the pudding and mostly to the larger plums. It has not been economically feasible to find all the plums, nor has it been ordinarily possible to predict their locations on the basis of geological study.

It would appear that the one chance of developing resources of chromite in the United States capable of meeting the requirements for 10⁶ MWe lies in mass mining of a dunite body (or more than one) that contains enough high-grade and intermediate-grade bodies so that the average content of chromite

would be, say, 3% or above. At 3%, 18,000,000 tons of Cr metal in chromite (average 50% Cr_2O_3), would require about 600,000,000 tons of ore. The ore requirement is very large, but it may not be beyond reach, particularly if the requirement can be divided among two or three dunite bodies.

One such body may be that of the Flagstaff Hill area, El Dorado County, California. A total of 120×10^6 tons of ore available by open pit mining is a possibility. Red Mountain, Kenai Peninsula, Alaska, is another.

Low grade ores present problems in that the chromite is generally high in iron and difficult to liberate from the silicate matrix. Attempts to beneficiate such ores (Thayer, 1973) have not been encouraging, but the problem could yield to additional research.

References

- 1) Minerals Yearbook, 1971 (1972), p.
- 2) Thayer, T. P., 1973, Chromium, in United States Mineral Resources, USGS Prof. Paper 820, p. 111-121.

Footnotes to Chromium Resources, Table I

1. Stratiform deposits are formed in stable continental areas when chromium-bearing rock melts emplaced deep in the crust slowly cool. Chromite collects in layers in these complexes by gravity settling in extensive, continuous sheets.
2. Podiform deposits may originate much like stratiform deposits originally, but since they develop in areas of crustal deformation, they tend also to be deformed to a greater or lesser degree. Ores associated with these deposits tend to be linear or pod-shaped in form, small and discontinuous in nature.
3. Stillwater complex resource estimates vary widely, with one total resource estimate by Holliday (1965) of 14×10^6 tons, leaving about 10×10^6 tons Cr_2O_3 in a "hypothetical and speculative resources" category (i.e., undiscovered deposits in unknown districts, respectively) which are mainly applicable to Stillwater ores; the range here is between .6 and 2×10^6 tons Cr.
4. Large, low grade (1-2% Cr) chromite-bearing rocks near Red Mountain, Kenai Peninsula, Alaska could add significantly to total chromium resources, using surface mining techniques, if a method of concentrating the dispersed chromite could be found. This deposit is a marginal resource at 10X prices, but may contain more than 20×10^6 tons Cr metal.
5. U.S. total chromium resources are $\sim 1.5 \times 10^6$ tons Cr metal known; upwards of 1×10^6 tons Cr metal may be minable at high Cr prices, from other less well-explored deposits. Thayer's (1973) U.S. chromium resource estimate is 2.65×10^6 tons Cr.
6. World 10X resources here are derived from Thayer's "hypothetical and speculative" resource estimates, meaning no actual figures for chromium resources are available, due to lack of exploration. The figures for Bushveld Complex ores are a conservative estimate of deep chromite resources, presently unexplored.
7. Does not include estimates of reserves or resources from Selukwe, one of the world's major sources of metallurgical chromite.

CHROMIUM RESOURCES
TABLE I

COUNTRY DEPOSIT NAME	GEOL. TYPE	RESERVES			IDENTIFIED RESOURCES						COMMENTS
		PRESENT PRICES			3X PRICES			10X PRICES			
		TONS ORE x10 ⁶	GRADE %Cr	TONS METAL x10 ⁶	TONS ORE x10 ⁶	GRADE %Cr	TONS METAL x10 ⁶	TONS ORE x10 ⁶	GRADE %Cr	TONS METAL x10 ⁶	
United States											
1) Stillwater Complex, Mont.	Stratiform ¹ (B)				4.6	29	1.2	LARGE ³	15-25		See footnote
2) Chromites, Penn. & Maryland	Podiform ²				ND	ND	ND				
3) Chromite, Alaska	" (A,B)				.27	29	.07	LARGE ⁴	1-2		See footnote
4) Chromite, Grant Co., Ore.	" (B-)				.30	16	.05				
5) Massive Chromite, CA	" (A)				.23	31	.07				
6) Dissem. Chromite, Eldorado, Cal.	" (B-)				.7	3	.02				
7) Dissem. Chromite, Mountainview, Cal.	" (B-)				.3	5	.02				
8) Placers, Penn. & Maryland	Sedimentary				.1	29	.02				
9) Placers, Oregon	"				2.	4	.08	1.2	3-5	.04	
. S. Total *5							1.53			*	
World											
1) Bird R. Complex, Canada	Stratiform(B-)				3	29	.8	3	29	.8	
2) Magpie Mts., Canada	Magmatic(B-)				100	1.6	1.6				
3) Kemi, Finland	Stratiform (B)	11.3	29	3.3	5.6	29	1.6				
4) Bushveld Complex, S. Africa	Stratiform(A) (B)	56 1130	31 29	17.4 330	56 2260	31 29	17.3 660	3400	29	990	
5) Great Dyke, Rhodesia ⁷	Stratiform(A) (B)				560 56	31 29	174 16.2	560 56	31 29	174 16.2	
6) Philippines	Podiform(A) " (C)	.7 4.5	31 24	.2 1.1	.6 2.3	31 24	.2 .6				
7) Turkey	" (A)	5.6	31	1.7	5.6	31	1.7				

IV-20

8) India	" (A)	5.6	31	1.7	4.5	31	1.2		
	" (B)	2.3	29	.7	2.3	29	.7		
9) Greece	" (A)	.1	31	.03	.1	31	.03		
	" (C)	.1	24	.02					
0) Malagasy Republic	" (A)	4.5	31	1.4	3.4	3.	1.1		
	" (B)	1.1	29	.3	2.3	29	.7		
1) Iran	" (A)	1.7	31	.5	1.1	31	.3		
<hr/>									
2) Bahia, Brazil	Stratiform (A)	2.8	31	.9	3.4	31	1.1		
	" (B)	4.0	29	1.2	2.3	29	.7		
3) USSR	Podiform (A)	11 ?	31	3.5	11 ?	31	3.5		
	" (B)	1 ?	29	.3	2 ?	29	.7		
	" (C)	11 ?	24	2.7	11 ?	24	2.7		
4) Fiskenaesset, Greenland	Stratiform (B-)				11	15	1.7		
5) World laterite resources								.5-3	200+
<hr/>									
Total ~2640 x 10 ⁶ tons Cr				~370			~890 ³		1180 ⁶

IV-D Nickel Resources

Nickel is vital to all industrialized nations and is consumed in large quantities in the steel industry. Geologically, nickel tends to associate with rocks rich in Mg, low in Fe and Si. These rocks are most prominent along the juncture of large crustal blocks or in volcanic island terranes. In these rocks, nickel is dispersed as sulfides, or contained within the lattice of associated silicate minerals. Nickel sulfide deposits are also associated with certain mafic layered complexes. The U.S. is poor in nickel reserves, although Canada has large reserves.

IV-D-1 Occurrence of Nickel

Nickel deposits are divisible into 3 groups:

- 1) Nickel sulfide deposits
- 2) Nickel silicate deposits
- 3) Sea floor nodules

Nickel sulfide deposits were for many years the preferred source of nickel, because beneficiation of the ores and extraction of nickel from concentrates by smelting are relatively simple. Most nickel sulfide deposits are small, a million tons or less, but groups of deposits in the Sudbury district, Ontario, and in the Thompson district of Manitoba, have hundreds of millions of tons of ore. Mining of sulfide deposits is done almost entirely in underground mines. The ore-bodies have formed either during the crystallization of the associated rocks from magma, or by the later reaction of sulfur with nickel-bearing silicates. This latter process may occur when nickel-bearing silicate rocks are reheated in the presence of sulfur-bearing fluids, which extract nickel from the silicates. Segregation deposits tend to lie at the base of the associated igneous body, whereas deposits formed by sulfuration tend to lie along the margins of the nickel-bearing host rocks.

Nickel silicate deposits are those in which most of the Ni is held within the lattices of the associated silicate minerals. In this state the nickel is highly dispersed, averaging .2 to .4%, and is difficult and expensive to extract. The volume of such nickel-bearing rock is, however, enormous. Economic methods of extracting nickel from the silicates have ^{not} been developed, but richer deposits form by weathering of such rocks. Some of these are minable and are rapidly approaching equality with sulfide deposits as sources of nickel. Such deposits carry 1 to 5% Ni, contain tens to hundreds of millions of tons of ore, and are amenable to large-scale surface mining. A laterite development boom in Indonesia, New Caledonia, Australia and Central America has been in progress since 1970, and about 5×10^5 tons Ni/year in new capacity from nickel laterite deposits in these areas will be in development or planning by 1975. That amount will be 75-80% of total world nickel output (Engineering Mining Journal, March, 1971).

Laterites are more difficult and expensive than sulfides to refine, as the Ni must first be dissolved chemically from the ores and then extracted from solution before refining can proceed. In large-scale operations where grades exceed 1-1.5% recoverable Ni (all Ni in silicates cannot be extracted) these ores are competitive with sulfide ores at present prices. Laterite resources are very large.

Sea floor nodules are also becoming of interest to mining companies, as initially formidable extractive problems are worked out and methods of undersea mining are researched. The legal problem of who owns the sea floors has yet to be resolved, although several companies have been pushing for some basic guidelines in this area, with the intent of initiating development. Grades in nodules average ~1% Ni for sizeable tonnages, and significant amounts of Cu, Mn and Co are present. Estimates of total tonnage vary widely. These nodules form on the deep sea floor or on the flanks of oceanic ridges, apparently from ions that are in solution in sea water and are absorbed onto manganese oxides, scavenged by organisms, or drawn out of bottom sediments chemically during compaction (Ericson and Mollin, 1973).

IV-D-2 Reserves and Resources of Nickel

Data for reserves and resources of nickel are given in Table IV-D-1. Where available, reserve or identified resource figures from industry publications are used for the estimate; in countries for which little or no information is available, estimates from USGS Professional Paper 820 were used. These figures are considered conservative. Published industry estimates are subject to revision but are traditionally conservative also.

To divide the deposits into the listed categories, the following criteria were used. Reserves consist of ore in those deposits presently being mined. Undeveloped deposits of minable grade (~1.5% Ni in sulfide ores, or a like amount of recoverable Ni in laterites, which may grade higher in total Ni) have not been included. This hopefully weeds out deposits with good grade but unknown transportation, financing, mining or extraction problems. "3X resources" include deposits with grades greater than .5 Ni which have been identified but are not presently in development. The true effect of a 3X price cannot be seen simply as a reduction of minable grade to one third of that at present; the low concentration of Ni in minable deposits may mean greatly increased extraction costs. If this is the case, such low grade ore, at least in laterities, may need more than 3X prices. Some low grade disseminated sulfide deposits may require less than 3X prices to become reserves. Deposits with known mining or extractive difficulties are also included in this category, if of sufficiently high Ni content. Resources at 10X present prices are even more difficult to assess. If such price increases did occur, primary nickel-bearing rocks might be usable, raising nickel reserves almost infinitely; the increased power cost, however, may prevent mining of such materials.

IV-D-3 Comments on U.S. and World Resources

The nickel reserves of the United States are small, although modest additional reserves may have been developed by the Anaconda Company in the Stillwater Complex in Montana. The prospects of developing large reserves at present prices are dim. There are belts of ultramafic rocks both in the eastern and western United States, but deposits of the type found in the Thompson district have not been detected. At 3X present prices, however, the large resources of nickel (with copper) in the Duluth Complex might come into production, and at any rate they constitute an important strategic reserve. Mining in this area, however, is under attack on environmental grounds.

IV-D-4 Selected References

Cornwall, Henry R., 1973, "Nickel," in Brobst, Donald A., and Pratt, Walden P., eds., United States Mineral Resources, USGS Professional Paper 820, Washington, D.C., pp. 437-442.

Ericson, David B., and Wollin, Goesta, 1973, "Precipitation of Manganese oxide in deep sea sediments," in Interuniversity Program of Research on Ferromanganese Deposits of the Ocean Floor, Phase 1 Report: NSF Seabed Assessment Program, Washington, D.C., pp. 99-103 (unpublished).

Merritt, Paul C., 1971, "Nickel," Annual Survey and Outlook, Engineering Mining Journal, March, 1971, p. 148.

Nickel Resources

Footnotes

¹Duluth Complex ores are actually copper-nickel ores, with nickel the by-product. The estimate given is generous, in that only certain volumes of the mineralized rock are likely to be minable.

²Sudbury, Ontario, ores are extensive, but require deep underground mining; large resources of unknown amount are found in deeper or lower grade zones.

³Large potential exists in Australia for laterites. This is a preliminary figure representing only the last seven years' discoveries. Sulfide ores likewise are still being discovered.

⁴⁻⁹Laterite tonnages in these countries probably exceed the listed totals by several multiples; active exploration is continuing. These totals given come either from published industry sources or from USGS Professional Paper 820, where no other source was available.

¹⁰No 10X total estimate could be made; at this price, however, silicate nickel deposits might prove minable, boosting nickel reserves enormously.

¹¹Sea floor nodules are poorly known, and estimates of tonnage are speculative. The estimate given is a more conservative speculation as to minable tonnages of nodules; several companies are already actively test-dredging such nodules. A liberal estimate is included in the 10X column.

¹²The 3X estimate includes 18×10^6 tons Ni in deposits still in development stages or deposits minable at only slight price increases.

Nickel Reserves and Resources

Table IV-D-1

Country	Geol. Type	Reserves			Identified Resources						Comments
Deposit Name		Present Prices			3X Prices			10X Prices			
		Tons orex10 ⁶	Grade %Ni	Tons Metalx10 ⁶	Tons orex10 ⁶	Grade %Ni	Tons Metalx10 ⁶	Tons orex10 ⁶	Grade %Ni	Tons Metalx10 ⁶	
United States											
Union, Maine	sulfide	7.1	1	.07							
Stillwater, Mont.	magmatic				150-300	.25	.8				
Duluth, Minn.	byproduct				6500 ¹	.21	13.7				
Brady Glacier, Alaska								200	.25	.5	
Other Alaska	sulfide							21	.30	.06	
Missouri	byproduct				10	.5	.5				
Other sulfide ores	sulfide				1	.7	.07				
Riddle, Oregon	laterite	10	1.5	.15							
Washington	"				30	.5	.15				
North Carolina	"				5	1.0	.05				
Other Calif. & Ore.	"				55	.75	.41				
laterites											
U.S. Totals				0.2			.16			.6	
World											
Canada-sulfide deposits											
Thompson, Manit.		150	3	4.5	800	4-1.0	6.2				
Sudbury, Ont.		400 ²	1.5	6.0							
Other Canadian		6?	1.5	1.0	100	1.5	1.5	4200	.2	13.4	
Australia											
sulfide deposits		75		2.3	275	.6	1.6				
laterites ³							5.4				
Burma	sulfide							25	.3	.1	
Cuba	laterite				2000	1	20.				
Dominican Republic	"	72	1.6	1.2							
Greece	sulfide	2	1.7	.03							
India	sulfide				50	1.	.5				
Indonesia ⁴	laterite				500	1	5.				
Malagasy Republic	sulfide				2	2	.04				
New Caledonia ⁵	laterite	200	2.	4.5	300	1.8	4.5				
Philippines ⁶	"	150	1.3	~2.0	850	.8	6.8				

Table IV-¹ cont.

Country	Geol. Type	Reserves			Identified Resources						Comments
Deposit Name		Present Prices			3X Prices			10X Prices			
		Tons orex10 ⁶	Grade %Ni	Tons Metalx10 ⁶	Tons ores10 ⁶	Grade %Ni	Tons Metalx10 ⁶	Tons orex10 ⁶	Grade %Ni	Tons Metalx10 ⁶	
World, cont.											
Puerto Rico	laterite				100	.9	.9				
Colombia ⁷	"	40	2.6	.1							
Guatemala ⁸	"	50	1.3	.7	50	1.3	.8				
Brazil	"	23	1.7	.4	55	1.4-2.	.9				
Venezuela ⁹	"	60	1.6	~1.							
Yugoslavia					60	1.3	.8				
Botswana					40	1.0	ND				
Solomon Is.					100	1.2	1.2				
USSR											
sulfide					100	.6	.6				
laterite					100	1.5	1.5				
subtotal				~24.0			~62.0				
Sea Floor Nodules ¹¹					90,000	.8-1.1	860.0		.2	3.400 ¹⁰	very tentative
World totals				~24.0		?	922.0 ¹²				

IV-E Copper Resources

Copper, although one of the less abundant metals in the earth's crust, is relatively common in deposits of mineable concentration. It shows a marked association with igneous intrusive rocks common to regions of mountain building. Although copper is concentrated in several types of deposits, those of greatest individual size and recoverable copper content are either "porphyry" copper deposits or "stratabound" copper deposits. "Porphyry" copper deposits, in which the copper is associated with intrusive rocks, are found in most ocean-bordering mountain systems, and are especially abundant in the southwestern US, Chile and Peru. "Stratabound" deposits, which occur in sedimentary rocks, occur most frequently in former continental or continental margin areas. The largest known deposits are in Silesia and the African countries of Zaire and Zambia, but the deposit of White Pine, Michigan, is an important representative of the class.

IV-E-1 Geological Occurrence

Five major types of copper deposits are known:

- 1) Porphyry deposits
- 2) Stratabound deposits in sedimentary rocks
- 3) Volcanogenic deposits
- 4) Replacement deposits
- 5) Seafloor nodule deposits

Porphyry deposits are the leading source of copper worldwide, and are estimated to contain about half the world reserves of ~370 million tons of contained copper. The deposits range in grade from .1 to >1% Cu. Later weathering events have enriched primary ore in some deposits. Deposits with grades as low as .5% are economic at this time. Deposits range in size from several 100 million tons to several billion tons; most of the larger, high-grade deposits are found in Central and North America and the South American Andes. The ores occur as fine veinlets and disseminations in the intrusives and surrounding sediments and often are surrounded by characteristic mineral haloes which aid in location of such deposits.

IV-E-2 Stratabound Deposits in Sedimentary Rocks

The most important copper ores in sedimentary rocks are in Silesia and associated with Precambrian rocks in the African countries of Zambia and Zaire, where the copper minerals are thought to be the result of precipitation at the time of sedimentation or soon after. These deposits tend to be higher in grade than porphyries, from about 1 to 3+% cu. The ores lie in layers and may extend for tens of miles. Mineable volumes range from tens to hundreds of millions of tons of ore. There are several variations of the basic "stratabound" type.

IV-E-3 Volcanogenic Deposits

These deposits, often called "massive sulfide" ores, are associated with suboceanic volcanic centers. Volcanic-derived fluids deposit copper and other metals as sulfides in volcanic rocks near these volcanic centers. The deposits may be restricted to a particular horizon. Grade is variable, from trace to several percent Cu, and size is small, generally less than 10-20 million tons. A few deposits contain 50 million to more than 100 million tons of ore.

IV-E-4 Replacement Deposits

Replacement copper ores are the least predictable of all copper deposits, and may occur in veins, lenses, pipes and a host of other geometries. These deposits are common near the margins of intrusives rich in K, Na and Si, especially in rocks containing CaCO_3 . Locally they are found, however, with no apparent relation to associated igneous rocks and in areas lacking igneous activity altogether. Size is highly variable, from thin, tabular veins to large sheets or mantles in favorable rocks. Ore tonnages are less than 10 million tons, but grades tend to be high (5 - 10% + Cu). Most of these deposits are small; they are often associated with porphyry-type mineralization.

IV-E-5 Seafloor Nodules

Sea-floor nodules are aggregates of metal oxides which apparently derive their constituents from sea water. They are most abundant in parts of the ocean basins which receive little sediment from continental sources and unfortunately often lie at some depth. This is a newly recognized resource, but potentially a very great source of Mn, Co, Ni and Cu. Between 200 and 5,000 million tons of mineable nodules have been estimated to be present on the ocean floors, with copper contents around 1-1.5%; these estimates are based on minimal information, but a resource of $40-60 \times 10^6$ tons of Cu has been included in the USGS estimate of world copper, and a similar estimate has been given more recently (National Academy of Science).

Before these deposits can become mineable, international legal decisions on the administration of the sea floor will have to be made, as well as new developments in undersea mining and extractive techniques. Some shallower deposits may be presently mineable; the rate at which this resource will develop is not known.

IV-E-6 Reserves and Resources

Published information on tonnages and grades of individual U.S. copper deposits is meagre, and the following discussion draws heavily on data in USGS Prof. Paper 820. Where possible, the data are compared with available published figures. Copper reserves of the United States are currently estimated by the U.S. Bureau of Mines at 90,000,000 tons (Commodity Data Summaries, 1975).

In 10 producing and 12 non-producing porphyry deposits for which information is available, about 61×10^6 tons Cu metal is indicated.* If the other 20 producing porphyry deposits were added, it seems probable that the Bureau's figure of 90×10^6 tons would be reached. Total U.S. copper reserve figures are primarily in porphyry deposits, since production from most non-porphyry copper deposits except the White Pine deposit is small. Published figures do not give an accurate picture of potential reserves, since the limits of ore-grade rock are seldom known for years after a porphyry deposit has been put into production. Numerous operating porphyry deposits initially considered moderate in size have had long lifespans. The quoted porphyry reserve figures may differ from ultimate reserves by a factor of 2 or more.

Resources in U.S. deposits other than known low grade porphyry deposits are difficult to assess, because the full extent of low grade ore in known deposits is not known. Drilling to define this uneconomic material is simply not done until ore grade material begins to be depleted. Cox, et.al. (1973), estimated that 20 million tons of Cu are present in subeconomic porphyry ores and deposits in the development stage for which information was available.

Sedimentary Cu deposits in the U.S. are incompletely evaluated. Those being mined at White Pine, Michigan, presently supply about 5% of U.S. production, and the area has an appreciable potential for low grade ore. Other sedimentary copper occurrences are in the Belt Series rocks of Montana and Idaho, in the Kona Dolomite of Michigan and Wisconsin, and in the "red bed" deposits of southwestern and central U.S. Work is presently being done on the deposits in the Belt Series; however, no mining ventures have been begun to date. Cox et.al., (1973), estimate 1 billion tons of copper-bearing rock, averaging .5 to 1% Cu. The estimate could not be checked; most pertinent data are withheld by mining companies doing exploration in the area.

Deposits in Upper Michigan in the Kona dolomite were drilled several years ago. The deposits are known to be of ore grade but lie too deep and are too heavily broken up by faulting to be mineable.

"Red Bed" copper ores occur in terrestrial sediments. One such deposit, the Nacimiento, in New Mexico, has proved to be commercial, although only a fraction of the copper-bearing material can be mined economically at present. Several hundred million tons of this disseminated copper-bearing sandstone is the speculative estimate of Cox et.al. (1973) for the magnitude of the resource. Only information on the workings at Nacimiento is available, and some rise in the price of Cu is necessary before serious development can be expected.

* This includes an order of magnitude estimate of copper resources in the Butte, Montana district, equal to the tonnage of copper mined from the district to date. This tonnage is included in the reserve category, although all the mineralized rock may not be mineable at present Cu prices. It surely could be mined at 1.5-2X prices.

Similar deposits in the Flowerpot Shale of Kansas and Oklahoma are persistent over large areas but are thin. These deposits are presently being mined. Reserves mineable by open pit methods under less than 40 feet of overburden are estimated at ~ 100,000 tons Cu (Ham and Johnson, 1963). The main horizon is only 9 inches thick but averages about 2% Cu. The deposit is exposed for 3 to 6 miles along strike, but no effort has been made to determine its total extent here, or the limits of mineralized shale in the similar surrounding rocks (Johnson and Ham, 1972).

Another major copper resource is associated with nickel mineralization at the base of the Duluth Complex in Minnesota. Here copper minerals are disseminated. Locally there are concentrations carrying about 1% copper. Cox, et. al. (1973), estimate the total resource at 60 million tons of copper at a .25% cutoff. Environmental problems and the fact that mineable concentrations are irregularly distributed will seriously hamper development of these deposits.

IV-E-7 World Resources

Data for world resources and reserves of copper are given in Table IV-E-1. Only reserve estimates and a fraction of resources could be checked through the literature. In general, various estimates were comparable. African copper reserves were only checked for the main producers. Large resources of sedimentary copper remain unevaluated in Zambia and Zaire. No resource figures could be checked. USGS Professional Paper 820 was the source of data for the table, except that the world total given is a revised figure furnished by the USGS (National Academy of Sciences, 1975). Resources are known to be great in the Andean countries of South America and in the far East.

Major recent discoveries of copper deposits, porphyry deposits in particular, have been promoted by the concepts of plate tectonics, which imply that zones of crustal plate collisions are foci where favorable igneous rock melts originate. Identification of such collision zones in Pacific volcanic island regions, Central America and Iran have led to the discovery of large new copper deposits such as Bougainville (4 million tons Cu), Cerro Colorado (~ 19 million ton Cu) and Cheshmeh (~ 10 million tons Cu) respectively. Some 80-100 million tons of copper may ultimately be derived from these recently recognized areas. Exploration for sedimentary copper deposits in Precambrian shield areas of continents is likely also to be successful in locating large new deposits, as will undersea exploration for nodule deposits on the ocean floors.

Breakthroughs in mining and extraction technology would also add important "new" reserves and resources. In-place leaching is now allowing recovery of copper from "waste rock" of 10 years ago, and the minimum mineable grade of ore is predicted to drop from .5% to .25% Cu by the year 2000 (USGS Professional Paper 820, 1973).

Copper Resources

Table I

Footnotes

- 1) This category includes some conditional porphyry deposits (deposits evaluated but not economic at present) in addition to economic deposits in the development stage.
- 2) The "redbed" sedimentary copper deposits in the Flower Pot shale are poorly known; this is a preliminary estimate. Total reserves are probably low.
- 3) This figure is that of the U.S. Bureau of Mines (Commodity Data Summaries, 1974, p. 45)
- 4) Massive sulfide deposits are numerous in the Canadian shield, and contribute a significant percentage to Canadian copper production each year. The total listed here includes only the five largest deposits known.
- 5) Conditional resources include deposits the extent and grade of which are known but which are presently uneconomic. A price increase less than 3X would bring some of these into the reserve category.
- 6) Between 26×10^6 and 36×10^6 was the estimate from published sources, for Zambian copper reserves. An additional 10×10^6 tons Cu is assumed valid.
- 7) World reserve total is a new figure calculated by the U.S.G.S. (National Academy of Sciences, Mineral Resources and the Environment, Washington, 1975, p. 136). A breakdown of this total by countries is not available; the data given above in the table are older figures, some incomplete, and will not add up to the world total.
- 8) The estimates are based on estimates of conditional resources published in USGS Professional Paper 820. These figures are the best available but are low. Since no grade information is available no breakdown into price categories is possible.
- 9) No estimates are available for resources at this level.

- 10) Estimates of nodule resources are as follows: grade is the average of about 200 nodules, while tonnage is a rough calculation based on analysis of 101 photos, cores and grab samples of the World's ocean bottoms, i.e., mostly speculative.

One estimate gave $1,700,000 \times 10^6$ tons of nodules, or $6,800 \times 10^6$ tons cu, an estimate cited by McKelvey on a preliminary ocean resource map (McKelvey, 1969). A lower estimate used in conjunction with nickel resource evaluation gave $90,000 \times 10^6$ tons ore or $\sim 400 \times 10^6$ tons cu; although no justification can be offered except that initially mineable deposits are likely to be of much smaller size, the Professional Paper 820 estimate of $\sim 125 \times 10^6$ tons Cu is used. Other unforeseen factors involved in mining may further restrict the mining of nodule deposits.

References

- 1.) McKelvey, V. E., Stoertz, F. E., and Vedder, J. G., 1961, Subsea physiographic provinces and their mineral potential, USGS Circular 619.
- 2.) Mero, J. L., 1965, The Mineral Resources of the Sea, Elsevier Publ. Co., N.Y., 312 p.
- 3.) Moore, J. Robert and Cruickshank, Michael J., 1973, Identification of technologic gaps in exploration of marine ferromanganese deposits, in Inter-University Program of Research on Ferromanganese Deposits of the Ocean Floor, Phase 1 Report. NSF Seabed Assessment Program, Washington, D.C., pp 279-335 (unpub).
- 4.) Engineering Mining Journal, Various Issues, 1970 - 1973.
- 5.) Mining Engineering, Various issues, 1970 - 1973.
- 6.) National Academy of Sciences, 1975. Mineral Resources and the Environment, Resources of Copper, 127-183.
- 7.) U.S. Bureau of Mines, Commodity Data Summaries, 1975, 193 p.
- 8.) Cox et al., 1973, Copper. U.S. Geol. Survey, Prof. Paper 820, 163-190.
- 9.) Ham, W. E., and Johnson, R. S., 1963, Copper in the Flowerpot shale (Permian) of the Creta area, Jackson County, Oklahoma. Okla. Geol. Survey 64, 32 p.
- 10.) Johnson, K. S., and Ham, W. E., 1972, Permian copper-shale deposits of southwestern Oklahoma (abs.). Geol. Soc. Amer., Abstr. with Programs, 4, no. 7, 555.
- 11.) U.S. Bureau of Mines, 1975, Commodity Data Summaries.
- 12.) National Academy of Sciences, 1975, Resources of Copper. In Mineral Resources and the Environment, 127-183d.

Copper Reserves and Resources
Table IV-E-1

Country Deposit Name	Geol. Type	Reserves			Identified Resources						Comments
		Present Prices			3X Prices			10X Prices			
		Tons ore x 10 ⁶	Grade % Cu	Tons Metal x 10 ⁶	Tons ore x 10 ⁶	Grade % Cu	Tons Metals x 10 ⁶	Tons ore x 10 ⁶	Grade %Cu	Tons Metal x 10 ⁶	
United States											
Producing Porphyry deposits (10 of 29)	Porphyry		.4+	38							
Non Producing Porphyry	Porphyry		.4+	23 ¹⁾							
Sedimentary											
White Pine, Mich.	Sedimentary	~225	1.	2.2	900	~1	11				
Belt Group, Mont.	Sedimentary				ND	1-2	20?				
Flowerpot Shale, Okla & Kansas	Sedimentary		~2	.1 ²⁾	ND	ND	ND				
Nacimiento Deposits, N. Mex. + Ariz.	Sedimentary	10	1.5		ND	ND	ND				
Kona Dolomite, Mich.	"				"	1?	ND				
Aluth Gabbro							60				
Stillwater, Mont.	Magmatic				300	.25	1				
Conditional Porphyry	Magmatic						25				
US Total ³⁾				83			117				
World											
Canadian Porphyry	Porphyry			18							
Canadian Massive Sulfide ⁴⁾ Conditional resources ⁵⁾	Volcanogenic			5			20				
Mexico	Porphyry			16							
Central America	Porphyry			22							
Antilles	Porphyry			2							
South America											
Published	Porphyry			95			100				
Europe	Porphyry			25							
Lower Silesia	Sedimentary	3000	2	60							
Conditional Sedimentary	Sedimentary				billions	1-2	15-60?				
Africa											
Published ⁶⁾				53			ND				
Conditional							50				
Middle East - South Asia Incl India	Porphyry			10							

Copper Reserves and Resources
Table IV-F

Country Deposit Name	Geol. Type	Reserves			Identified Resources						Comments
		Present Prices			3X Prices			10X Prices			
		Tons ore x 10 ⁶	Grade % Cu	Tons Metal x 10 ⁶	Tons ore x 10 ⁶	Grade % Cu	Tons Metals x 10 ⁶	Tons ore x 10 ⁶	Grade %Cu	Tons Metal x 10 ⁶	
China				ND			ND				
USSR				39			50				
Oceania				19			ND				
World Totals ⁷⁾				<u>370</u>			<u>~270</u> ⁸⁾			<u>-</u> ⁹⁾	
Sea floor nodules					12,500	.4	<u>~ 50</u> 320				

IV-F Titanium

Titanium is an abundant component of the earth's crust, averaging 5700 ppm. It occurs in a variety of minerals, including titanium oxides (rutile, anatase, brookite), iron titanium oxides (ilmenite, hem-ilmenite, and titanomagnetite), and a number of silicate minerals. The source minerals of titanium at present are the titanium and iron-titanium oxides. Of these, rutile, ilmenite (FeTiO_3) and hemoilmenite ($\text{Fe}_2\text{O}_3 \cdot \text{FeTiO}_3$) are the most important. Rutile is the preferred raw material for titanium. Most of the titanium minerals commercially produced in the world at present (over 4,000,000 tons annually) are used as a source of TiO_2 for paint pigment. Total world production of titanium metal is probably less than 50,000 tons annually.

IV-F-1 Types of titanium deposits

The titanium-bearing deposits currently being mined are of two general types, magmatic deposits and sedimentary (placer deposits). Sedimentary deposits have thus far yielded the bulk of titanium mineral production, but magmatic deposits are of growing importance. A third class of deposits, residual deposits, is known but not a source of titanium at present.

Magmatic deposits are associated with coarse-grained igneous rocks derived from basaltic magmas. The deposits are accumulations of ilmenite, ilmenite-hematite (in microscopic intergrowth), or ilmenite and titanomagnetite. Concentrates from these deposits range from less than 10 percent to 32 percent Ti. Methods of treatment vary with the nature of the ore, involving chemical or metallurgical processes, or both. The ilmenite and ilmenite-hematite ores are currently worked for TiO_2 for paint pigment. Ilmenite-titanomagnetite ores are worked as a source of TiO_2 at Lake Sanford, Adirondacks, but in Finland and South Africa, vanadium present is the most important product.

Sedimentary deposits form as Ti-bearing minerals are moved from their source areas by erosion to collection points such as beaches or river channels. Along coastlines, sand-sized grains are reconcentrated by wave action into discontinuous ribbons of titaniferous heavy minerals, which may extend for miles along favorable coastlines and contain enormous tonnages of material. The deposits, however, are low-grade (1.5 - 10% combined Ti) and consist of rutile and ilmenite with numerous other minerals from which the titanium minerals must be separated. The deposits may be unconsolidated or consolidated; consolidated deposits are generally uneconomic at present.

The only large resources of residual origin are titanium-bearing bauxites. During the weathering of parent rocks, both aluminum and titanium are concentrated in the residual soil. When the bauxite is processed to obtain alumina, titaniferous sludge remains from which Ti could conceivably be recovered as a by-product. There is no production from such deposits at the present time.

IV-F-2 Sources of Data and Limitations

Most of the resource data used here are taken from Klemic and others (1973). Knowledge of United States and world resources of titanium is very incomplete, and current estimates of resources are certainly on the conservative side. The lower-grade deposits, in particular, have not been explored enough to determine resources, simply because economic incentive has been lacking.

IV-F-3 Availability of Titanium at 3X and 10X Present Price Levels

The estimated quantity of titanium available at various price levels is recorded in Table I. The titaniferous magnetite deposit at Lake Sanford, New York, was used as a model for magmatic deposits. This deposit is presently being mined for titanium; its grade is 12% Ti. Resources available at the 3X price level group then are deposits with Ti concentrations of 8-12%. Resources at the 10X price level are deposits containing from 4-8% Ti, with other modifying factors such as location, size and type of occurrence of Ti as qualifiers. On this basis, most magmatic deposits fall into the 3X category.

Unconsolidated beach deposits, of sufficient size, can be mined at 1% Ti content; the Ti content of Trial Ridge, Florida deposits (.84% Ti) was used as a lower limit for reserves in this category. Consolidated fossil beach deposits, common in the western states, are of comparable grades, but due to higher mining and processing costs must be considered resources available only at 10X present prices.

Most of the deposits falling in the "identified resources" category would yield titanium as a by-product of iron ore production; in some, such as Iron Mt., Wyoming or the Southeastern Alaska deposits, Ti is a deterrent to mining these ores for iron. A greatly increased price or heightened demand for titanium products would be required to make these ores Ti reserves. Low grade resources of titanium are very large, however.

IV-F-4 World Identified Resources

World identified resources are very large and are dominantly in magmatic deposits. (see Table I). In the table "reserves" are not distinguished from "resources", except for deposits for which definite reserve figures are quoted. The lump sum of "reserves" and "resources" is compiled by country, mostly from data by Klemec and others (1973). Total world "reserve" and "resource" figures are also included. It must be realized that the figures given are rather rough. They serve principally to indicate the order of magnitude of world titanium resources.

Total world potential titanium resources are very great, with processes for concentrating low grade magmatic ores already tested (CIM Bull. V. 66, 1973). Large additional resources of various grades are probably present in the beach sand deposits of the world.

IV-F-5 Environmental Considerations

Magmatic ores have been and will be dominantly mined by open pit methods; most of these deposits are of limited surface extent and far from population centers. Sedimentary ores, however, require dredging or large scale surface operations; their linear nature (extending for 10's of miles) means disturbance of ground over long distances. Owing to their occurrence considerable land use conflicts are involved and some of the resources of the Atlantic Coast of the United States will probably never be mined.

References

1. Klemic, Harry, Marsh, Sherman P., and Cooper, Margaret, 1973, "Titanium" in United States Mineral Resources, USGS Prof. Paper 820, p. 653-665.
2. Peterson, E. C., 1966, Titanium Resources of the United States, U.S. Bur. Mines Inf. Circ. 8290, 65 p.
3. Sparks, B. D., and Wong, R. H. T., 1973, Selective Spherical Agglomeration of Ilmenite Concentrates, Can. Inst. Mining Bull., V. 66, p. 73.
4. Stamper, J. W., 1970, Titanium in Mineral Facts and Problems, 1970; U. S. Bur. Mines Bull. 650, pp. 773-794.

TABLE I

TITANIUM RESOURCES

COUNTRY & DEPOSIT NAME	GEOL. TYPE	RESERVES			IDENTIFIED RESOURCES						COMMENTS
		TONS ORE X10 ⁶	GRADE % Ti	TONS METAL X10 ⁶	3X PRICES			10X PRICES			
					TONS ORE X10 ⁶	GRADE %Ti	TONS METAL X10 ⁶	TONS ORE X10 ⁶	GRADE %Ti	TONS METAL X10 ⁶	
UNITED STATES											
(1) Lake Sanford, N.Y.	Magmatic	121.5	12.0	14.5							
(2) Iron Mt., Wy.	"				30.0	9.0	2.70	148.0	5.8	8.6	
(3) Magnet Cove, Ark.	"				ND	3-6	.25				
(4) Duluth Gabbro, Minn.	"							94.6	13.8	13.0	bodies <10 ⁵ tons ea
(5) Round Lake, Wis.	"							81.6	8.4	6.9	bodies <10 ⁶ tons ea
(6) Nelson & Amherst Co.'s, Va.	"				120	3.6	4.3				
(7) Iron Hill, R.I.	Contact Meta.				46.0	4-10	3.8				
(8) San Gabriel Co., Ca.	Magmatic							7.0	6	.4	
(9) S.E. Alaska Deposits	"				12.0	5-10	.5				
(10) Trail Ridge, Fla.	Beach Deposit	1,500.	.84	12.4				ND	2-5	76.	
(11) Ocean Co., N.J.	"	380	1.8	6.8							
(12) Beach Deposits, S.C.	"				13.5	ND	1.6				
(13) Beach Deposits, Okla.	"							382.	1-4	4.8	fossil Shorelines
(14) Beach Deposits, Rocky Mts.	"							28.	4	1.0	minimum est.
(15) Oregon Bauxites	Residual ¹							40.	3.9	1.6	
(16) Hawaii Bauxites	"							ND	ND	30.8	
(17) Bauxites Residues	"							ND	ND	ND	large but uneval.
U. S. Total: 186 x 10 ⁶ tons Ti										~143	

IV-39

TABLE I cont'd
TITANIUM RESOURCES

COUNTRY & DEPOSIT NAME	GEOL. TYPE	RESERVES			IDENTIFIED RESOURCES						COMMENTS
		TONS ORE X10 ⁶	GRADE % Ti	TONS METAL X10 ⁶	3X PRICES			10X PRICES			
					TONS ORE X10 ⁶	GRADE %Ti	TONS METAL X10 ⁶	TONS ORE X10 ⁶	GRADE % Ti	TONS METAL X10 ⁶	
World Resources											
(1) St. Urban, Canada	Magmatic				22.	2.6	.57				
(2) Lac Allard, Canada	"	58.	20.4	11.83	25.	16.5	4.12	very large	1-2	ND	
(3) Lac Morin, Canada	"							230	6	13.8	
(4) Lac Dore, Canada	"				72.	6.5	4.68				
(5) Magpie Mts, Canada					100.+	10.6	10.6				
(6) Bushveld, S. A.					2000.+	7.8+	156.				
(7) All Canada (less #'s 2-5)							193.				
(8) All Europe							91.				
(9) All Oceania							34.				
(10) All S. America							16.				
(11) South Africa (less # 6)							270.				
(12) Africa (less #'s 6 & 11)							32.				
(13) India							118.				
(14) Asia (less # 13)							11.				
(15) World rutile resources							13.-41.				
Totals: ~1.1 x 10 ⁹ tons Ti				147 ³			965.-			* ⁴	
							1000.				

IV-40

1. Residual deposits are developed through the weathering of a pre-existing rock, bearing the metal(s) in question, these metals being concentrated at or near the surface.
2. Tons Ti at 3X prices are anomalously low; this is a result of the data available, not the scarcity of Ti-bearing deposits of the appropriate grade. For instance, large lower grade titanium deposits exist at Lake Sanford, but tonnage estimates are unavailable.
3. Total world reserves from Klemic, et al., 1973.
4. No total, insufficient information.

IV-G Aluminum Reserves

IV-G-1 Introduction

Aluminum is a high-use metal which is gaining in importance worldwide. It is presently extracted from bauxites, essentially Al-rich soils formed during the weathering of Al-bearing parent rocks. These deposits are most favorably developed in sub-tropical regions, which hold most of present-day reserves. It has been estimated that 67% of known bauxite reserves have been discovered in the last 25 years and bauxite-alumina reduction complexes are being developed worldwide at a rapid rate, especially in Africa and Australia. U.S. reserves are only a small fraction of world reserves, and several other sources of Al have been considered by the United States for future supply. Bauxites ($\text{Al}_2\text{O}_3 \cdot x \text{H}_2\text{O}$) are favored over other aluminous materials owing to their high content of Al_2O_3 , 45 percent or better, and simple composition, the latter lending itself to simple methods of extraction of the Al_2O_3 from which Al is recovered.

Geologic Occurrence

Bauxite development is favored by conditions which promote chemical leaching of rock materials, to the extent that all but the least soluble elements (mostly Al, Fe, and some Ti) are carried away in solution. Some of these physical conditions include: warm climate (but not necessarily tropical), abundant rainfall, high permeability of parent Al-bearing rocks favoring movement of large volumes of groundwater, and stable surface conditions which allow long periods of weathering and the preservation of the bauxitic weathering products. Most of the large bauxite deposits of the world can be related to recent or ancient combinations of these physical conditions acting on Al-bearing rocks.

IV-G-2 Other Sources of Aluminum

Although of lesser world consequence, because of the great size of world bauxite reserves, possible alternate sources of Al are important to the U.S. because of dwindling bauxite reserves and the less than encouraging chances of finding any more important domestic bauxite deposits (Patterson and Dyni, 1973). Interest in these sources has been greatly heightened during the past year by increases in the cost of imported bauxite.

High-alumina clays constitute an enormous resource of aluminum, in the billions of tons, and have been under study as sources of aluminum for many years. Much research has been done, and processes of extraction of alumina have already been developed. The problems are (1) dollar cost in comparison with cost of alumina from bauxite, and (2) energy costs. It is reported, however, that increase in the price of imported bauxite has brought extraction of alumina from high-alumina clays and shales near the break-even point (Committee on Government Operations, 1974). Further research is in progress. In November, 1974 (Engineering and Mining Journal), it was announced that the U.S. Bureau of Mines and eight domestic aluminum producers have joined in a project to explore recovery of alumina from clays, anorthosite, alunite, and other domestically available raw materials. The large kaolin deposits of Georgia are a particular object of interest, and the economics of aluminum production from these clays has been intensively studied in recent years (Ward and Husted, 1974).

Another potential source of aluminum is the mineral alunite $[KAl_3(SO_4)_2(OH)_6]$. As a result of recent exploration, reserves of alunite-bearing material, in Utah, containing 7 to 9 percent Al are now estimated at 680×10^6 tons. Russia is already extracting Al from alunite, and an American concern is developing the Utah deposits and is building a pilot plant preparatory to commercial-scale production.

Besides the above, enormous resources of Al are present in the mineral dawsonite $[NaAl(OH)_2CO_3]$, in the great oil shale deposits of Colorado, Wyoming, and Utah, and in bodies of anorthosite (chiefly plagioclase, Ca-Na aluminosilicate). Extraction technology is available; the problems are cost, and (for dawsonite) environmental problems and the feasibility of extracting dawsonite as a byproduct of oil recovery.

Reserves and Resources

Reserve and resource figures for the United States and the world are recorded in Table 1. Except for data on U.S. resources mentioned above, only reserve or identified resource information on bauxite deposits is included. Published tonnages and grades for deposits are included where known. Deposits actually producing are classed in the reserve category, while identified deposits in development stage are included in the adjacent column. So little data on resources for producing countries was available that no reasonable estimate for the 3X category could be made. Tons of metal was calculated using published grade information, or, if no published grade was available, a figure of 45% Al_2O_3 was arbitrarily assigned as an average figure for commercial deposits.

IV-G-3 Other Problems

Although world resources of bauxite are sufficient for many decades, several problems which may be of great import in future bauxite developments have already appeared. Bauxite is a low value, high volume commodity in the unprocessed state, and as such is mined by large scale surface operations which affect thousands of acres. Alumina plants generate large volumes of waste mud which accumulates and may cause large scale pollution as this fine material enters surface waters.

The development proposal for the 150 million ton Chittering deposit in Western Australia, some 30 miles from Perth, was recently rejected on environmental grounds, and operators will have to study the environmental impact of operations as a necessary step in development. Costs of environmental protection and reclamation will contribute significantly to total costs.

Large scale power requirements for aluminum production also will be a factor to consider. Droughts have affected both mining and reduction of bauxite and alumina by not allowing milling, which requires large water volumes, or by reducing hydroelectric output. 20,000 kwh of power (equivalent to 1300 pounds of coal) is required to reduce 2 tons of alumina (Al_2O_3) to 1 ton of Al metal. Some new aluminum reduction plants handle 100,000²₃ tons of alumina per year, and would require almost 1 billion kwh power in their operation. A new smelting process developed by Alcoa is reported to require 30% less power per ton Al than the present process. If these claims are borne out in commercial operations, a significant reduction of the power requirement can be made in new plants (EMJ, February 1973). Whether these levels of power use

can be sustained in producing areas becomes another concern. Hydropower or fossil fuel supplies in developing countries may not be great enough to supply their growing power needs and those of the aluminum plants; even as the shipping of ores to places where the power is available wanes as governments seek to control their resources more closely. This affects U.S. plants, since some 90% of their input is presently imported from outside sources. U.S. aluminum needs will be increasingly met by importing Al metal, unless alternative aluminous materials prove to be economic.

References

1. Patterson, Sam H. and Dyni, John R., 1973, "Aluminum," and Bauxite in Brobst, Donald A. and Pratt, Walden P., eds., United States Mineral Resources, USGS Professional Paper 820, Washington, D.C., pp. 35-43.
2. Mining Engineering, Engineering Mining Journal, Industry News Sections.
3. U.S. Bureau of Mines, 1967, Potential Sources of Aluminum, USBM Inf. Circ. 8335, 148 p.
4. U.S. Senate, Committee on Government Operations, Permanent Subcommittee on Investigations, 1974, Aluminum, 46 p.
5. Ward, W.C., Jr., and Husted, John E., 1974, Alumina from kaolin, Georgia Institute of Technology, Engineering Experiment Station, 45 p.

Table I
Aluminum Reserves and Resources

Country Deposit Name	Geol. Type	Reserves			Identified Resources						Comments
		Present Prices			Non Producing			3X Prices			
		Tons Ore x 10 ⁶	Grade %Al Metal	Tons x 10 ⁶	Tons Ore x 10 ⁶	Grade %Al	Tons Metal x 10 ⁶	Tons Ore x 10 ⁶	Grade %Al	Tons Metal x 10 ⁶	
United States											
1) Arkansas bauxite		40	20-40	~1.8							
2) Oregon & Wash. bauxite					100	18	18				
3) Hawaii bauxite					200	13	26				
4) Other bauxites		5	20-40	.2							
5) Western Alunite					680	8	54				
6) High Aluminum Clays					5000	18-20	950	5000	6+	350	
7) Dawsonite in Oil Shale	by product							4000	2	80(1)	
8) Al Phosphate rock	"							800	6	50	
9) Al-rich igneous rocks								>500	10	50(2)	
Total		45		~2			~1030			530(3)	
World											
1) Jamaica		800	26	210							
2) Costa Rica		165	22	36							
South America											
3) Brazil		500	22	110.	1300	22	286				
4) Onverdacht, Surinam		ND	ND								
5) British Guiana		700	22	154							
6) Caw Mts, Fr. Guiana		42	22	9							
Europe											
7) Hungary		ND	ND								
8) Vlesenica, Yugoslavia		100	22	2.2							
9) Titograd, "		ND	ND								
10) Helicon, Greece		100	22	2.2	200	22	44				
Oceania											
11) Cape York Peninsula, Aust.		2500	25	62.5	850	20	170				
12) Darling Range, "		500	16	80	850	16	136				
13) Mitchell Plateau, "					200	24	48				
14) Vana Levu, Fiji					ND	ND					
15) SW Borneo, Indonesia		10+	22	2							
16) Solomon Islands					80	23	18	70	23	16	
Asia											
17) All India					260	25	65				
18) Kattha, Punjab, W. Pak.					ND	ND					
19) United Arab Republic					60	22	13				
20) All China		500	22	110							

Aluminum Reserves and Resources

Country	Geol. Type	Reserves			Identified Resources						Comments
		Present Prices			Non Producing			3X Prices (5)			
		Tons Ore x 10 ⁶	Grade %Al Metal	Tons x10 ⁶	Tons Ore x 10 ⁶	Grade %Al Metal	Tons x10 ⁶	Tons Ore x 10 ⁶	Grade %Al Metal	Tons x10 ⁶	
Africa											
21) Guinea		2000	28	560	2030	22	450				
22) Ghana					270	22	59				
23) Minim Martap, Camerouns					1500	22	330				
24) Mt. Mange, Malawi		60	21	13							
25) Manatinina, Malagasy		70	22	15							
Total		7550		~2000	5800		~1600				(4)

Footnotes

1. Dawsonite, an aluminum sulfate, could only be utilized at a rate commensurate with oil shale production, or about .8 x 10⁶ tons Al/yr at full Oil Shale capacity of 10⁹ barrels/year.
2. No real estimates of potential from Al-rich igneous rocks have been made; tonnages, with no constraints on grade of content of impurities, are in the billions of tons.
3. This estimate is a conservative minimum.
4. No estimate of world aluminum resources can be made.
5. NOTE: No 10X resource estimate is included in this table.

IV-H Vanadium

IV-H-1 Introduction

Vanadium is a moderately abundant element, averaging about 135 ppm in the crust as a whole (Krauskopf, 1967). Its concentration into deposits of minable grade is unfortunately quite uncommon; it usually occurs as a minor element in other minerals, such as iron oxides, or in organic-rich sediments and residues. It has generally been recovered as a by-product of operations for iron, uranium, phosphorus, or petroleum. Most deposits thus far exploited were limited in size but relatively high in grade. The Colorado Plateau deposits, in which high concentrations of vanadium oxides [3% V_2O_5] occur as secondary accumulations in sandstone bodies, are a good example. A rare high-grade organic accumulation was the vanadium-rich asphaltite deposit at Minas Ragra, in Peru, which supplied much of the world's vanadium for many years. This deposit, like most of the high grade reserves in the Colorado Plateau, has been mined out.

IV-H-2 Sources of Data, Limitations and Definitions

The resource data included with this report are derived from numerous sources and differ in quality. The deposits listed have been classified either as "reserves" or "identified resources" (U.S.G.S., Prof. Paper 820, 1973). Reserve figures are given for deposits which are presently minable or are being mined. For these deposits size and mineral content of the ore-bearing rock are known to a degree such that the economics of extraction can be evaluated with some degree of certainty. Reserve figures are the result of extensive drilling to define limits and grades of ore bodies, geological mapping and evaluation, and possibly test mining of the ore. These figures, by necessity, are conservative. Identified resources, as the term is used here, are mostly deposits for which rough data on grade and tonnage have been obtained either by drilling or trenching, and for which there are at least some chemical analyses. The actual extent and grade of resources, however, are much less certain than for reserves.

IV-H-3 Types of Vanadium Deposits

Known deposits of vanadium fall mostly into 3 major categories:
A) magmatic deposits of vanadium-bearing iron-titanium oxides, which are generally mined for Fe or Ti, or both; B) deposits of the Colorado Plateau type, in sandstones, mined for both uranium and vanadium; C) sedimentary deposits in marine shales or phosphate rock; D) contact metamorphic deposits, at contacts of igneous rocks and sedimentary rocks, and E) in organic accumulation, especially in certain petroleum deposits. Of these, A), B), and E) have thus far been the principal sources of vanadium.

IV-H-4 Resources of Vanadium

Vanadium reserves at present prices, 3X present prices, and 10X present prices are given in Table IV-H-1. The classification of reserves is somewhat arbitrary. Vanadium-bearing magnetites in the Bushveld Complex of

South Africa are currently being mined for vanadium; the V content is about 1 percent. Similar deposits with comparable V content are classified in Table IV-H-1 as reserves at present prices. Deposits with more than 0.3% V and less than 1.0% V are classified as reserves at 3X present prices. Certain resources with less than 0.3% V are classified as reserves at 10X present prices. This system in effect assumes that the cost of vanadium would be inversely and linearly proportional to grade of ore. This may not be the case. Deposits other than magmatic Fe-Ti oxide deposits have been similarly grouped according to grade. This is done for lack of information; problems of extraction could require higher costs for vanadium from these sources, the shale deposits in particular.

The fact is that both resource and metallurgical (extractive) data for vanadium are very limited. With a world consumption that has not exceeded 40,000 tons annually, there has been no incentive, except in times of stress like World War II, to fully develop either resource data or metallurgical technology for lower-grade vanadium resources. Table IV-H-1 serves chiefly to indicate the order of magnitude of U.S. and world vanadium resources so far as these are known at the present time. Ultimate resources are undoubtedly much larger.

Some comments on U.S. resources are desirable. Estimates of vanadium available in the Duluth Gabbro are based on limited analyses and little quantitative analysis of mining potential, and it is unsure whether tonnage and grade are under- or overestimated. The deposits at Round Lake, Wisconsin are only partly explored. Some contact metamorphic iron deposits in Nevada and California contain significant quantities of vanadium, but chemical analyses for vanadium are available only for those listed. Total low-grade iron ore reserves are larger by a factor of 10 than those listed, and may represent additional V resources (Moore, 1971).

Surface areas of magmatic deposits in the United States generally are limited. The 1.5 mi² extent of the Lake Sanford deposits is probably typical, but masses of disseminated ore might involve much larger areas. Open pit methods of extraction would be favored for the mining of most of these large, low-grade deposits.

Estimating resources in sedimentary black shale deposits is especially difficult. Known evaluated and/or analyzed vanadium-enriched black shales in Idaho and Wyoming contain between 0.4% and 0.9% V and are generally associated with members of the Phosphoria formation. The phosphate-bearing section of the Phosphoria is presently yielding some vanadium as a by-product of the manufacturing of elemental phosphorus, but available analytical data indicate that most of the phosphate rock is rather low in V (~.07% - .1% V), although tonnage is enormous. Estimates of tonnage of V in phosphate rock are very rough and are based on the assumption that 1/5 of the 5 billion tons of present phosphate rock resources holds the concentrations of V listed; large errors are possible. Data on the shale occurrences are fragmentary; only one unit in one area has been evaluated (Love, 1961), and only 3 of the several identified vanadium-rich shale beds have been included in the given estimate. Others which may be potentially valuable are listed in the table. Potential vanadium resources in shales are considered very large, but the prospects of utilization must be tempered by the possibility of extractive problems, the fact that these deposits would have to be mined largely for their V content alone, and the large areas that might be disturbed

by mining. Their grade is such, however, that they have been placed in the 3X category.

Other possible sources which may provide large resources of V are:

1) Sedimentary Fe ores with .02 to .12 V. The best known are the minette iron ores of northern France, western Germany, and central England. Vanadium was recovered from this type of ore by Germany during World War II. Resources are large, and other large resources of V-bearing iron ore are known in Russia.

2) V occurs in oils (.02%) and coal beds (up to .3%) and can be recovered from ash as these fuels are burned. No quantitative estimates reflecting the importance of these sources are known.

IV-H-5 World Reserves and Resources

World identified reserves and resources are roughly 29×10^6 tons V; about 60% of this total is in ores in the Bushveld Complex in South Africa. Potential resources (deposits of known types predictable as occurring in geologically favorable, but presently undeveloped, districts) of magmatic ores are considered very great, as are resources occurring in black shale deposits. The resources in higher grade Colorado Plateau-type deposits are considered to be small.

IV-H-6 References

1. Balsley, J.B., Jr., 1943, Vanadium-bearing magnetite-ilmenite deposits near Lake Sanford, Essex Co., New York. U.S.G.S. Bull. 940-D, 99-123.
2. Davidson, D.F., and Lakin, H.W., 1961, Metal content of some black shales of the western conterminous United States. U.S.G.S. Prof. Paper 424C, p. 329-331.
3. Diemer, R.A., 1941, Titaniferous magnetite deposits of the Laramie Range, Wyoming. Geol. Survey Wyoming, Bull. 45, 215 p.
4. Fischer, R. P., 1973, Vanadium. U.S.G.S., Prof. Paper 820, 679-688.
5. Fischer, R. P., 1961, Resources of Vanadium in the U.S. In Vanadium, a materials survey, U.S.B.M. Inf. Circ. 8060, 33-41.
6. Gulbrandsen, R. A., 1960, Petrology of the Meade Peak phosphatic shale member of the Phosphoria formation at Coal Canyon, Wyoming, U.S.G.S. Bull. 1111C, p. 71-46.
7. Hollingsworth, J.S., 1967, Geology of the Wilson Springs vanadium deposits, Garland County, Arkansas. Geol. Soc. Amer. Guidebook Field conference, Central Arkansas: Ark. Geol. Comm., p. 22-28.
8. Jones, W. R., 1965, Vanadium deposits of Western Australia. Geology of Australian Ore Deposits, 2nd ed., vol. 1, 154-155.
9. Kish, L., 1972, Vanadium in the titaniferous magnetites of Quebec, Can. Inst. of Min. and Met., Bull., 65, 117-123.

10. Lister, G. F., 1966, The composition and origin of selected Fe-titanium oxide deposits. *Econ. Geol.*, 61, 275-310.
11. Lore, J. D., 1961, Vanadium and associated elements in the Phosphoria formation in the Afton Area, Western Wyoming. U.S.G.S. Prof. Paper 424C, 279-282.
12. Moore, Lyman, 1971, Economic evaluation of California-Nevada iron resources and iron ore markets. U.S.B.M., Inf. Circ. 8517, 206 p.
13. Rose, E. R., 1969, Geology of titanium and titaniferous deposits of Canada. *Geol. Surv. Canada, Econ. Geol. Rept. #25*, 177 p.
14. Rose, E. R., 1970, The ferride element content of titaniferous magnetites in Canada. *Can. Geol. Survey Paper 69-54*, 9 p.

TABLE IV-H-1
VANADIUM RESOURCES

COUNTRY & DEPOSIT NAME	GEOL. TYPE	RESERVES			IDENTIFIED RESOURCES						COMMENTS
		TONS ORE X10 ⁶	GRADE %V	TONS METAL X10 ⁶	3X PRICES			10X PRICES			
					TONS ORE X10 ⁶	GRADE %V	TONS METAL X10 ⁶	TONS ORE X10 ⁶	GRADE %V	TONS METAL X10 ⁶	
<u>UNITED STATES</u>											
(1) Lake Sanford, N.Y.	Magmatic ¹				100.0	.25	2.50				
(2) Iron Mt, Wy.	"				30.0	.36	1.08	148.0	.10	1.48	
(3) Buena Vista Hills, Nev.	Contact Meta. ²				35.5	.17	.60	28.0	.17	.47	Possibly high
(4) Segerstrom, Nev.	"							35.0	.14	.49	Limited data
(5) Round Lake, Wis.	Magmatic				120.0	.36	4.00				Incomplete data
(6) Duluth Gabbro, Minn.	"							90.0+	.11	1.00	Limited data
(7) Williams Springs, Ark.	"	5.00	.56	.28							
(8) Iron Mine Hill, R.I.	Contact Meta.										
(9) Colorado Plateau	Sandstone ³	10.00	.84	.84				7.0+	.17	.12	
(10) Potential Uranium Dep.	Sandstone					.078	.38				
(11) Phosphoria fm.											
-phosphatic units	Sedimentary ⁴							1000.0+	.07	7.00	Limited data
(12) Phosphoria fm shales	"										
-Afton, Wy.					45.0	.54	2.25				
-Sublette Ridge, Wy.						.45	.75				
-Paris, Ida.					ND	ND	ND				
-Coal Canyon, Wy.					3.5' zone	.40	ND				
(13) Other Shales	"										
-Comus fm, Nev.						.30	ND				
-Eureka, Nev.						.02-.2	ND				
-Chainman sh., Nev.						.10	ND				
-Minnelusa fm, S.Dak.						.15-.30	ND				
(14) Earth Sciences, Inc., Idaho ?					20	.8	1.7				
TOTALS	2.5 x 10 ⁶ Tons V			1.1			~13.3			~10.6	

IV-50

TABLE IV-H-1 cont'd
VANDIUM RESOURCES

COUNTRY & DEPOSIT NAME	GEOL. TYPE	RESERVES		IDENTIFIED RESOURCES							COMMENTS
		TONS ORE X10 ⁶	GRADE %V	TONS METAL X10 ⁵	TONS ORE X10 ⁶	GRADE %V	TONS METAL X10 ⁵	TONS ORE X10 ⁶	GRADE %V	TONS METAL X10 ⁵	
<u>WORLD</u>											
(1) Bushveld, S.A.	Magmatic	2,000.0	.90	180.00			100				
(2) Otanmaki, Finland	"	19.0	.28	.53							
(3) Mustavaara, Finland	"	40.0	.10	.40							
(4) Lac Dore, Canada	"				72.0	.28	2.16				
(5) Magpie Mts., Canada	"				100.0	.17	1.70				
(6) Swedish Deposits	"				ND	~.21	ND				Large resources
(7) Australian Deposits	"					.3-.73	15.0+				Low estimate
(8) El Romeral, Chile	"	80.0	.17-.22	1.50							
(9) Mt. Kachkanar, USSR	"	13,500.0	.56-.066	80.0							
(10) Blacksands, N. Z.	Sedimentary						hundreds	.1-.20	2.-4.0		
(11) Oil Residues, etc. Shales, Coals	"							.02-.30	ND		
TOTALS		~28 x 10 ⁶ Tons V		262.4			*5			*6	

IV-51

1. Refers to deposits whose contained mineral ores formed at the same time as, or immediately after the crystallization of the surrounding rock, and from the same molten material.
2. Mineral deposits which are located at the intersection of formerly molten rocks and any other kind of rock, usually sedimentary, in which transfer of metals from molten rocks to surrounding rocks has occurred.
3. Deposits of Colorado Plateau type, in which ore minerals occur in Sandstones, but were deposited after the sandstone was formed, rather than at the same time.
4. Deposits of metals accumulated at the same time as the surrounding sediments.
5. Deposits mineable at 3X prices worldwide are large, but little quantitative information is available, making the evaluated resource estimate in this column anomalously low.
6. Deposits mineable at 10X prices worldwide are considered very large, but no data on true magnitude are available, again making the evaluated resource estimate anomalously low.

IV-I Molybdenum

Molybdenum is a comparatively rare metal but has become very important in the steel and special alloy industries. It imparts hardness, toughness and corrosion resistance to steels used at high temperatures. Deposits of molybdenite (MoS_2), the most common ore mineral of molybdenum, occur in the western U.S. in porphyry-type intrusives, and this source supplies almost 70% of free world Mo production.

IV-I-1 Geology

Molybdenum occurs in four types of deposits:

- 1) "porphyry" deposits in which molybdenum is the principal valuable metal
- 2) "porphyry" deposits with copper
- 3) in vein deposits
- 4) in sedimentary rocks rich in organic material

Porphyry molybdenite deposits are the major source of molybdenum in the world today, primarily due to deposits found at intervals along the Cordilleras of North and South America. The mineral molybdenite occurs in tiny veins and fractures which cut across the intrusive rocks with which the ores are associated. Porphyry-type deposits contain several tens to several hundred million tons of ore, with grades ranging from .1% Mo to .3% Mo (.2 to .5% MoS_2). These deposits tend to occur in clusters, associated with intrusive rocks rich in Si, Na, and K, in areas of persistent crustal stress. This stress is expressed near the known deposits by abundant crustal fracturing and geologically recent volcanic activity.

Porphyry Cu-Mo deposits show many similarities to porphyry Mo deposits, except that Mo content is an order of magnitude lower (.01 - .05% Mo), with Cu the major ore metal. Size is comparable. No systematic explanation for the occurrence of these porphyry metal content variations is available, although Kestler (1973) has suggested Mo is more characteristically associated with continental land masses.

Vein deposits have produced significant Mo in a few areas, especially Quebec. These deposits are high in grade (as much as several percent MoS_2) but low in tonnage; production of over 500 tons Mo metal from such a deposits is rare. Of perhaps greater importance is their association with larger porphyry-type deposits, which may underlie the richer vein-type mineralization. Vein deposits may occur in any rock type, but are most common in igneous rocks of composition close to that of porphyry deposits, or at contacts between other rocks and such intrusives.

Sedimentary occurrences of Mo are common especially in black organic-rich shales and coals. Certain layers of the Phosphoria formation hold 50 to 500 ppm Mo (.005 - .05% Mo) which might be recovered as a by-product of phosphate mining. Sampled portions of the Minnelusa formation in South Dakota carry 70-3000 ppm Mo; the higher value is of ore grade (.3% Mo). If extractive techniques can be devised to recover Mo from sedimentary accumulations, and if

sufficient volumes of higher grade shales can be outlined, large increases in molybdenum resources could result. No information on tonnage in known Mo-bearing shales exists.

IV-I-2 Reserves and Resources

Reserve and resource figures are compiled in Table IV-I-1. Presently operating deposits are included in the "reserve" column, all others in the 3X category. The chart reflects the incompleteness of information, both in the United States and the world, on molybdenum reserves and resources. Published U.S. data are quite conservative, and may be low by a factor of two or more (King, et al., 1973). USGS Professional Paper 820 was used as the source of most data in the table, since other sources were essentially lacking. The author's methods of estimation were not discussed, hence the accuracy of these estimates cannot be appraised. King's estimate of Mo resources in the U.S. is 18×10^6 tons molybdenum metal. Estimates of Mo resources in porphyry Cu-Mo and other porphyry Mo deposits are derived from King, et al. (1973) also. Mo by-product reserves are calculated from incomplete tonnage and grade figures for producing U.S. porphyry deposits and may also be low by a factor of two.

World resource figures are from King, et al. (1973), with minor additions from industry publications. Their accuracy is unknown, except where definite tonnage and/or grade figures are given. Future exploration will undoubtedly add significantly to known world reserves and resources.

IV-I-3 References

- Kestler, Steven E., 1973, Copper, Molybdenum and Gold abundances in Porphyry Copper Deposits, Econ. Geol., 68, 106-112.
- King, R. U., Shawe, D. R., and Mackevett, E. M., Jr., 1973, "Molybdenum" in Brobst, Donald A., and Pratt, Walden P., eds., United States Mineral Resources, USGS Prof. Paper 820, Washington, D.C., 425-435.

Table IV-I-1

Footnotes

¹The estimate of total reserves for the U.S. is conservative, based on published figures. True magnitude of reserves is probably closer to King, et al's. (1973) estimate of $\sim 10 \times 10^6$ tons Mo metal.

²3X resources of molybdenum may be underestimated.

³By-product Mo reserves were calculated from available producing porphyry deposits and published grade information; data are incomplete. 3X column figure is modified from King, et al., (1973).

⁴World reserve and resource figures are from King, et al. (1973) except where specific information on tonnage and/or grade is included.

⁵World 3X resource figures include an unknown tonnage of ore that could be classed as reserves; no more detailed breakdown of world occurrences is available.

Table IV-I-1
Molybdenum Reserves () Resources

Country Deposit Name	Geol. Type	Reserves			Identified Resources						Comments
		Present Prices			3X Prices			10X Prices			
		Tons ore x 10 ⁶	Grade %Mo	Tons Metal x 10 ⁶	Tons ore x 10 ⁶	Grade %Mo	Tons Metal x 10 ⁶	Tons ore x 10 ⁶	Grade %Mo	Tons Metal x 10 ⁶	
United States											
Climax, Colo.	Porphyry Mo	1000?	.2	2.							
Urad-Henderson, Colo.	"	330	.25	.8							
Questa, N. Mexico	"	560	.11	.6							
Others	"				ND	ND	1.6				
Byproduct Mo ³	" Cu-Mo		.01-.05	2.	large	.01-.05	1.8				
Black Shales	Sedimentary				ND	.05-.3	ND				
Lignites, S. Dakota	"				ND	ND	.5				
U.S. Totals				5.41			3.9				
World ⁴											
Adanac, BC	Porphyry Mo				100	.14	.14				
Endako, BC	" "	600	.1	.24							
BC Moly, BC	" "				200	.12	.6				
Boss Mt., BC	" "				ND	.15	ND				
Byproduct Mo deposits, BC	" Cu-Mo		.01-.05	.5							
Other Deposits, BC	Porphyry				ND	ND	2.0				
Quebec, deposits	Vein						1.0				
S. American deposits	Porphyry Cu-Mo		.02-.05	2.4			3.3				
Australia	?						.05				
Africa	?						.05				
Asia	?						3.				
Central America	Porphyry Cu-Mo	2,200	.02	.5			.5				
China	?						.5				
Europe	?						.5				
Greenland	?						.1				
Japan	Vein						.1				
Mexico	Porphyry	ND	ND	.1			.5				
Norway	?										
Oceania	Porphyry Cu-Mo						.1				
Puerto Rico	Porphyry Cu-Mo						.2				
World Totals ⁵				~4			~13				

IV-J Niobium Reserves and Resources

IV-J-1 Introduction

Niobium is a metal that has grown rapidly in its applications during the period since World War II. Annual production and consumption have grown from about 5 million pounds in the late 1940's and early 1950's to more than 23 million pounds in 1974. Its uses in stainless steel and high-strength steel alloys are especially important. The growth in use, together with the recognition of an entirely new and important class of niobium deposits, led to an intensive search for niobium deposits in the 1950's and early 1960's. Numerous deposits were identified, and it became evident that world reserves and resources are very large relative to current or foreseeable demand for industrial purposes. The search for new deposits therefore slackened, although there has been intermittent exploration for niobium deposits in the intervening years.

IV-J-2 Geologic Occurrence

Most of the world's niobium resources are in deposits of three geologic types:

- 1) Placer (sedimentary) deposits
- 2) Pegmatite deposits
- 3) Deposits in alkaline igneous rock complexes

Placer deposits are mostly concentrations of columbite-tantalite $(\text{Fe, Mn})(\text{Nb, Ta})_2\text{O}_6$ along the channels of past or present river systems that drain areas in which weathering has released columbite-tantalite from the bedrock deposits in which it occurs. Deposits of this class on the Jos Plateau of Nigeria were for many years the world's principal source of niobium and still yield about nearly 10 percent of world annual production. Deposits of this type in Bear Valley, Idaho, containing the complex niobate euxenite, were worked during the 1960's, and placer deposits of columbite-tantalite, mostly small, are found in many countries of the world.

Pegmatite deposits have been sources of niobium minerals for many decades. Most are small, but two unusually large pegmatites in Zaire have contributed significantly to world supply and are still considered to have substantial reserves.

The great bulk of world reserves of niobium is in deposits associated with alkalic igneous complexes that are now known to exist on every continent, except possibly Australia. It was recognition of the presence of significant concentrations of pyrochlore $[(\text{Na, Ca})_2\text{Nb}_2(\text{O, OH, F})_7]$ and related minerals in these bodies, in the late 1940's and early 1950's, that led to intensive prospecting and exploration in the ensuing decade. Many economic or near-economic deposits were discovered, and reserves which were established are enormous relative to present or foreseeable normal industrial needs. When this had been established, interest in further exploration waned. There has been little incentive to explore these deposits fully, and published figures

on reserves and resources are unquestionably conservative.

In the United States, alkalic igneous complexes are known at a number of localities scattered over the country, but substantial niobium resources have been discovered thus far only in the Powderhorn Complex of western Colorado. Figures in the table are those of Temple and Grogan (1965). These authors, however, state that this reserve has been substantially increased by underground work and additional drilling. Furthermore, niobium is known to be present in substantial amounts in the mineral loparite $[(\text{Ce}, \text{Na}, \text{Ca})_2(\text{Ti}, \text{Nb})_2\text{O}_6]$ in rocks of the complex. There is thus the possibility of significant resources over and above those indicated by the published data. At what price level niobium from these resources would become available is not known.

Niobium deposits in alkalic igneous complexes are often referred to as carbonatite deposits, because pyrochlore and related minerals are most commonly concentrated in bodies of carbonate rock that are integral components of the complexes. Pyrochlore also occurs, however, in silicate rocks in certain complexes. Furthermore, whereas some of the world's deposits are in bedrock, some, including the world's largest and richest known deposit, at Araxá, Brazil, are deposits of residual soil accumulated as a consequence of deep weathering of pyrochlore-bearing carbonatites. Pyrochlore is concentrated as more soluble materials are removed during weathering.

IV-J-3 Reserves and Resources

Reserve and resource data are presented in Table IV-J-1. Those deposits now in production are placed in the reserve category, those of similar grade but not in production are placed in the 3X category and those of low or questionable grade are placed in the 10X category.

Much of the tonnage and grade data were previously compiled in USGS Prof. Paper 820, pp. 450-51, but under a slightly different set of headings. Additional unlisted or unevaluated deposits were located by literature search and the deposits at least noted, if unevaluated.

Information available is incomplete. For many deposits, data cover only proved reserves. No firm estimates of future consumption or processing losses are available. The quality of estimates of reserves is probably good, although conservative; deposits mineable at higher prices or demand levels have been estimated to contain about 10×10^6 tons Nb by Parker and Adams (1973), this amount in addition to their similar estimate of presently "economically" extractable Nb. In this report the "reserve" category is not as loosely defined, being limited to the tonnages in deposits presently producing niobium, rather than including deposits of similar size and grade which are not presently producers.

As indicated previously, the real abundance of Nb cannot be fully inferred from Table I; the number of discoveries of Nb-bearing deposits in the 1950's together with the limited market for Nb dampened the development of such ores.

Total reserves in most deposits have not been defined, nor is the extent of associated low grade material known. For some deposits, published reserve figures have been increased on the basis of personal experience of the writer of this report.

Resources in the United States are low, but there is some hope of new discoveries in favorable alkalic rocks in the eastern Rocky Mountains, where three of the known U.S. carbonatites are located.

Alkalic rocks in general contain small amounts of niobium; some carry up to several pounds per ton (Parker and Adams, 1973, p. 448). Recoverable concentrations of niobium might be found in soils derived from rocks of this type, as has been the case in Nigeria in the Jos Plateau.

Residues from processing bauxite from Arkansas contain Nb, and they constitute a domestic resource. Recovery processes, however, have not been developed.

Large potential resources present in alkaline complexes in Malawi and adjacent Mozambique cannot be evaluated due to lack of recent information. Several deposits in this region are known to contain niobium.

IV-J-4 Selected References

- Barton, W. R., 1962, Columbium and tantalum, a materials survey. U.S. Bur. Mines, Inf. Circ. 8120, 110 p.
- DeKun, N., 1962, The economic geology of columbium (niobium) and of tantalum Econ. Geol., 57, 377-404.
- Heinrich, E. W., 1966, The geology of carbonatites. Rand McNally, Chicago, 555 p.
- Mackay, R. A., Greenwood, R., and Rockingham, J. E., 1949, Geology of the Jos tin fields-- resurvey 1945-48, Nigeria Geol. Surv., Bull. 19, 80 p.
- Parker, R. L., and Adams, J. W., 1973, Niobium (columbium) and tantalum: U.S. Geol. Survey, Prof. Paper 820, 443-454.
- Temple, A. R., and Grogan, R. M., 1965, Carbonatite and related alkalic rocks at Powderhorn, Colorado, Econ. Geol., 60, 672-692.

Niobium (Columbium) Resources
Table J-1

Country Deposit Name	Geol. Type	Reserves			Identified Resources						Comments	
		Present Prices			3X Prices			10X Prices				
		Tons Ore x10 ⁶	Grade %Nb	Tons Metal x10 ⁵	Tons Ore x10 ⁶	Grade %Nb	Tons Metal x10 ⁵	Tons Ore x10 ⁶	Grade %Nb	Tons Metal x10 ⁵		
United States												
1) Iron Hill, Colo.	Carbonatite ¹				40	.175	.7					
2) Gem Park, Colo.	"							ND	.035	ND	Possible deeper ores	
3) Rocky Boy, Mont.	"							ND	ND	ND		
4) Potash Sulfur Spgs., Ark.	"							ND	ND	ND		
5) Magnet Cove, Ark.	"							12	.06	.1		
6) Bear Valley, Idaho	Sedimentary ²	200.0 yds ³	ND	.06								
7) Elmore Co., Idaho	"	ND	ND	ND								
8) Bauxite deposits, Ark	By product ³							54	.05-.15	.4		
Totals ~.13 x 10 ⁶ tons Nb				.06			.7			.5		
World												
1) Lake Nipissing, Ont	Carbonatite				5	.49	.2					
2) Lackner Lake, Ont.	"							50	.18	.9		
3) Manitou, Ont.	"				ND	.56	.6				Uncertain	
4) Chapleau, Ont.	"				35	.28	1.					
5) James Bay, Ont.	"				40	.35	1.4					
6) St. Honoré, Que.	"				100	.35	3.5					
7) Oka, Que.	"	225.0	.24	5.40								
8) Prairie Lake, Ont.	"				ND	ND	ND				"Abundant pyrochlore"	
9) Bugaboo Crk, B. C.	Sedimentary				65 yds ³	.071b/ yd ³	.04					
10) Fen, Norway	Carbonatite	ND	.1-.35	ND								
11) Save, Finland	"				ND	ND	.6					
12) Araxá, Brazil	"	300.0	2.10	63.00	1000	1.65	165					
13) Tapira, Brazil	"				10	.35	.4					
14) Lueshe, Congo	"				30	.94	2.8					
15) Bingo, Congo	"				7.1	1.7-2.5	1.4					
16) Placers, Congo	Sedimentary				ND	ND	.4					
17) Mrima Hill, Kenya	Carbonatite				56	.47	5.1					
18) Kaffo Valley, Nigeria	"				140	.18	2.5					
19) Jos Plateau, Nigeria	Alkali Granite ⁴							200+	ND	.7	Uncertain	
20) Sukulu, Uganda	Carbonatite	400	.25	10.0	200	.15	3.0					
21) Oldonyo, Tanzania	"				ND	.24	ND					
22) Panda Hill, Tanzania	"				ND	.2-.5	ND					
TOTALS ~16x10 ⁶ tons Nb				~78			~190			*6		

IV-59

IV-K. Summary Report on the Availability of Metals for the UWMAK-I Reactor

IV-K-1. Introduction

Five factors will govern the availability of metals for a Tokamak Reactor of the U.W. type in the year 2000 A.D.

- 1) The size of known reserves of metals and ores
- 2) Mine production capacity
- 3) The ability of the United States to compete in world markets for those metals that must be imported.
- 4) Smelting and refining capacities
- 5) Manufacturing capacity for alloy production and production of final shapes

The availability of each metal listed in the bill of materials for the U.W. Tokamak Reactor must be evaluated separately in terms of these factors. This section is a preliminary evaluation. It serves to indicate that each metal on the list will present its own peculiar problems of procurement.

In Table K-1, metal requirements for the construction of 10^6 MWe Tokamak* capacity are listed, together with estimated U.S. reserves at present and 3X present prices, U.S. consumption and production of each metal in 1973, world reserves at present and 3X present prices, and world production of each metal in 1973. In any one year, world production is approximately the same as world consumption.

IV-K-2. 316 SS

Metals required for 316 SS are iron, chromium, nickel molybdenum and manganese.

a) Iron: U.S. iron ore reserves at present prices are ample to sustain normal consumption plus reactor requirements well beyond the year 2000. The total requirement of 10^6 MWe, even if produced in a single year, would require only a 95% increase in U.S. iron ore production of 1973, not a serious matter. Unless steel mills happened to be operating at full capacity for normal requirements, there would be no major problem there.

b) Chromium: There are no U.S. reserves of chromium at present prices. At 3X present prices, domestic production of chromium to attain approximately 10% of the 10^6 MWe target would require tapping the chromite deposits of the Stillwater Complex, Montana. The mine and mill would have to be restored, and there would have to be adjustment of American metallurgical practice to permit use of the low grade concentrates that would be produced. Satisfactory procedures for controlling mine and mill waste would have to be developed. The proposed copper-nickel mining operation, by Anaconda Copper Corp., at the same site has met strong opposition from environmental groups. A lead time of 3-5 years would probably be needed, and, for economy, production should be spread over a 15 to 20-year period.

Supply of chromium from sources abroad is a much simpler problem, provided that access to these supplies can be had when they are needed. World reserves are ample to supply the target amount, even allowing for consumption between now and 2020 A.D., but an increase in mine production capacity over and above normal capacity would be required. If spread over the period 2000 to 2020, however, the increase necessary would not be large. Corresponding increases

*This is the amount of electricity that would represent 1/3 of the projected U.S. installed capacity in the year 2020. (UWFD-82, Aug. 1973).

TABLE K-1-U. W. TOKAMAK REACTOR

Data Relating to Metal Availability (All Quantities in 10⁶ m.t.)

Metal	Req. For 10 ⁶ MWe	U.S. Reserves		U.S. 1974 Production ^{3/}	U.S. 1974 Consumption ^{3/}	World - Ex - U.S.A. Reserves		1974 Prod.
		1X ^{1/}	3X ^{2/}			1X ^{1/}	3X ^{2/}	
304 & 316SS ^{4/}	56.89							
Fe	86.87	2000	>10,000	91.49	ca 91.0	246,000.0		413.0
Fe Ore (1973)				88.0	142.0			725.0
Cr	10.55	---	1.53	0.0	0.48	370.0	890.0	~2.0
Ni	7.95	0.2	~16.0	0.015	0.20	~24.0	?906.0	.67
Mo	0.70	5.4	>2.08	0.06	0.027	~4.0	~13.0	.021
Mn	1.13	0.0	>10.0	0.0	ca 0.81			~9.0
Pb	13.90	59.0		0.68	0.82	160.0	>500.0	2.81
Cu	7.42	>90.0	>100.0	1.70	1.79	>300.0	>500.0	5.75
Li	1.15	0.50	3.9	0.003	0.003	1.3 ^{7/}	0.2	.002
B	1.07	10.1	Large	~0.18	0.15	10.1		>0.15
Nb	0.09	.0054	.069	0.0	0.001	7.00	17.2	~.006 ^{6/}
Ti	0.05	>34.0	~ 29.0	ca 0.29 ^{8/}	0.200 ^{8/}	147.0		~.028 ^{6/}
Al	0.68	~2.0	>1000.0	0.40 ^{5/}	4.86	2000.0		13.4

^{1/} Reserves at present prices

^{2/} Reserves at 3X present prices.

^{3/} Primary metal only.

^{4/} 316 SS taken as Cr - 18%; Ni - 14%; Mo - 2%; Mn - 2%; Si - 1.0%; Cu-1.0%; Fe-62%; 304SS as Cr-20%;

^{5/} Primary metal from domestic bauxite. Ni-12%; Mn-2% and Fe-66%.

^{6/} Free World only. Ti metals only.

^{7/} Of this amount 1.1 x 10⁶ tons is Li estimated in brines of the Salar de Atacama; the validity of this estimate is in question.

^{8/} Titanium content of titanium minerals produced and consumed.

T9-AI

in smelting and alloy production capacities would be required. I should point out here that all major sources of chromium ores known in the world today are, to some extent, politically unreliable, particularly over the long term. The countries are Soviet Russia, Turkey, Rhodesia, and South Africa. Between to and 70% of the world's known reserves of chromite are in South Africa or Rhodesia. Both face difficult racial and political problems during the remainder of the century.

c) Nickel: U.S. reserves of nickel at present prices are very small and will be largely depleted by mining between now and the end of the century. Reserves of nickel at 3X present prices are largely in the Duluth Gabbro Complex in Minnesota. There are no mines operating in the Complex at the present time. There is only a very small domestic smelting and refining capacity. Inasmuch as the target amount is 40 times U.S. annual consumption of nickel in 1974 at least a 200% increase in alloy production and fabrication facilities per year will be required during the period 2000 to 2020.

World reserves of nickel at present prices are very large relative to the target amount, and new reserves are being developed. The sources of nickel are now spread fairly widely over the world, and this provides some assurance of future availability. In addition, the rapid progress of research and development of the deep sea nodule deposits gives promise of availability of very large amounts of nickel from that source. U.S. organizations are active in this work.

d) Molybdenum: The U.S. reserve position for molybdenum is very good. It is likely that reserves remaining toward the end of the century will be adequate to supply the target requirement at present prices, or certainly at 3X present prices. The target requirement is 5X present annual U.S. production of molybdenum. The U.S. is currently exporting 30 to 40 percent of annual production. There should be no great difficulty in meeting the 10^6 MWe requirement, if necessary increase in production capacity is planned properly in advance.

e) Manganese: The U.S. has no reserves of manganese at present prices, being totally dependent on sources abroad for its manganese supply. At 3X present prices, however, the target requirement could be met from domestic resources. It should be emphasized, however, that a 5-10 years lead time would be required to achieve significant U.S. production from these resources, since every one of them presents difficult metallurgical problems. In the smelting process, some increase in capacity would be required.

Summary for 316 SS: From the above it is evident that the most serious raw metal procurement problems are those for chromium and nickel. There could be an additional problem of creating additional capacity for the manufacture of 316 SS.

IV-K-3 Lead

Lead presents one of the most serious problems of metal procurement for the U.W. Tokamak Reactor. The target requirement is equal to nearly 4 times the 1973 world annual production of lead, and it is 24 times U.S. annual production. The latter, in turn, is only 67% of U.S. normal annual consumption. Both world and U.S. reserves of lead at present prices are large, but major increases in mine, mill, smelter, refinery and manufacturing capacities would be necessary in order to meet the 10^6 MWe requirement by the year 2020. These increases would be over and above those needed to meet the predicted 1.7 percent per year increase in world consumption for non-nuclear purposes. To the extent that

international competition for lead supply restricts the availability of lead to the U.S., large increases in U.S. mining, smelting, and refining capacity would be required. This could be a major problem. The U.S. lead industry presently is beset with serious environmental problems. Overcoming these is requiring large capital investments. The development of world and U.S. lead-producing industries should be watched carefully between now and the end of the century. It is possible that availability of lead could set a limit on the rate of development of generating capacity in fission reactors.

IV-K-4 Copper

Copper presents essentially the same problems as lead. It is difficult at this point to judge their potential severity. U.S. and world reserves of copper are extremely large relative to present rates of production. On the other hand, demand for copper is rising, and there is a great deal of concern over the ability of the U.S. copper mining industry to maintain even the present mining rates. Like lead, the copper industry is plagued with environmental problems and with the problem of restricted access to areas that offer promise of discovery of new deposits. Access to such areas is absolutely essential if even the present production rate from U.S. mines is to be maintained to the end of the century.

IV-K-5 Lithium

The problem for lithium is not one of reserves. A very large proportion of world reserves, at present prices and 3X present prices, is in the U.S. The problem here is one of mine production capacity. The target amount for 10^6 MWe is more than 200X present annual U.S. production. It is very difficult to see how more than a ten-fold increase in mine output can be achieved by the recovery methods currently in use. Inasmuch as large amounts of lithium are essential for the operation of any D-T reactor. I would strongly recommend that the matter of scale lithium production be explored with the lithium mining industry well before the end of the century. The available reserves of lithium are impressive, but their size gives no assurance that lithium can be produced at the necessary rates.

IV-K-6 Niobium

U.S. niobium reserves at present prices are less than 5% of the target requirement and, allowing for incomplete recovery of the metal from ores, not even adequate at 3X present prices. There is no niobium mining industry in the United States, and the alloy-producing industry has an annual capacity that is only about 1/60 of the target requirement. Total world production of niobium at the present time is only about 1/15 of the target requirement. World reserves are ample, but a very large increase in mining, smelting, alloy production, and fabricating capacities would have to be achieved. A substantial lead time is indicated.

IV-K-7 Titanium

Titanium is no problem from the standpoint of reserves available. The target amount is not large--it is approximately equal to current annual production of titanium metal. Some increase in metal producing and fabricating capacity would be required.

IV-K-8 Boron

The United States has about half of the world reserves of boron. These are large relative to present production and consumption, and the U.S. is currently an important exporting nation. Even against the target requirements for 10^6 MWe, reserves are large, but there is a problem of rate of production if the target amount is to be achieved. This is approximately five times current annual rate of production, so that boron presents the same problem as lithium on a reduced scale.

World reserves of boron are large, and U.S. and world reserves at 3X present prices are unquestionably enormous.

IV-K-9 Aluminum

U.S. reserves of aluminum ore are small at present prices, but it appears likely that by the end of the century the industry will be at least partly converted to use of clays, shales, and other lower grade metals available in enormous amounts in domestic deposits. The target amount is small relative to present metal production and fabricating capacities. Aluminum should, therefore, present no serious problems.

IV-K-10 Summary

From the above discussion it is evident that the most severe problems of metal availability are presented by chromium, lead, copper, boron, lithium and niobium; but nickel may also be somewhat difficult to procure in adequate amounts, especially from domestic sources. The general conclusion that one can draw from this appraisal is that in order to insure availability of the metals needed, the necessary increases in production capacity at all levels must be initiated well in advance of reactor construction. It is most essential that as soon as firm choices of reactor designs have been made, target amounts of metals be made known to the producing industries, and that they be encouraged to undertake promptly the development of necessary production capacity.

From the standpoint of industry, the continuing level of demand for metals for use in nuclear reactors is a matter of critical importance, since it governs the rate at which capital investments in mining, smelting, refining, and fabricating facilities must be amortized. It is therefore important that we arrive at figures for the amounts of the metals that will be required at various stages of development of the nuclear fusion energy industry. Estimates must be made of the amounts of metal that will be required both for construction and for maintenance of generating capacity. This will have an important bearing on industry plans.

V. Economics

A. Introduction

The primary measures of the practicality of a power plant design are the reliability and cost of the electricity produced. Reliability is primarily a function of the plant design and the dependability of the fuel supply but will not be discussed in detail here because the design and operating details of UWMAK-I are not known well enough. We can only assume that the plant will be designed, built and operated such that it has adequate reliability. The reliability of the fuel supply is essentially 100 percent since it depends on purchase of relatively small amounts of readily-available deuterium and proper design and operation of the tritium recovery systems within the plant. The environmental costs were discussed in Section III. The purpose of the remainder of this section is to describe the economics of UWMAK-I and estimate the cost of the electricity produced.

The cost of electricity produced in a power plant is determined primarily by the operating costs, the fueling costs, the capital costs, the amount of electricity generated, and the financial conditions for the utility operating the plant. Each of these primary factors is addressed below.

First, the plant operating cycle is described. Because Tokamak reactors have a unique operating cycle in comparison to conventional power plants, it is important that the operating cycle is understood well enough that the plant factor and operating costs can be estimated. The second section then determines the plant factors that appear attainable. It is desirable to have the plant factor as large as possible since the electricity production is essentially proportional to the plant factor, and the unit cost of electricity generally decreases as the plant factor increases. In addition, the plant factor should be high enough that the plant can be considered a reliable source of electricity during the seasonal peak periods of electricity consumption. In any case, the plant factor must be known before the electricity production and unit cost can be estimated.

The third section describes the UWMAK-I capital costs and presents the philosophy and basic assumptions used during development of the capital costs. The fourth and fifth sections estimate the electricity unit costs. First, the annual operations, maintenance, and fueling costs are estimated. These costs are then combined with the annual return on capital to determine the annual electricity cost and resultant electricity unit cost. All costs in this paper are on the basis of 1974 dollars.

V-B. The UWMAK-I Operating Cycle

The UWMAK-I has a three phase operating cycle consisting of

1. The initial loading and heating to ignition and operating conditions;
2. The fuel burning period;
3. The plasma shutdown, reactor evacuation, and transformer reset period.

During operating periods* this cycle is repeated at about 95 minute intervals as shown on Figure V-1. The operating conditions for each of the major equipment items throughout the operating cycle are shown on Figure V-2.

The equipment conditions listed at the upper left of Figure V-2 are the base conditions created during the startup preparation period at the end of an outage. At that time, the reactor divertor system is at its normal operating temperatures with all coolant and most vacuum systems operating. The cryogenic systems are holding the magnet coils at about 4°K. The Li and Na systems associated with the divertor are at the normal operating temperatures because of heating by use of the startup heaters. The core has been evacuated to 1×10^{-5} torr by the vacuum system, and the currents in the transformer have been reversed in preparation for startup of the next cycle.

These initial operating conditions are repeated at the beginning of each cycle. However, after the first operating cycle following an outage, the Li and He systems are maintained at the normal operating temperatures by heat due to the fusion reaction. The startup heaters are shut off as soon as ignition occurs in the first operating cycle following an outage. They remain off during the rest of the operating period.

At the beginning of an operating cycle, the transformer current is reversed into the normal operating mode, and the core is loaded with a fuel mixture of 50% D and 50% T until the pressure reaches 2.3×10^{-3} torr. During the next 100 seconds, as the plasma current increases, the currents in the vertical field (or divertor) coils are increased at the same rate as the plasma current. The plasma temperature rises during this period as a result of ohmic heating.

At 100 seconds, the neutral beams are turned on for a 20 second period to heat the plasma to ignition and then to the equilibrium operating conditions. Ohmic heating alone will not provide sufficient heating. The ignition occurs 10 seconds after the beams are turned on but the beams continue operating for another 10 seconds until the stable operating conditions for the plasma burn are achieved. During this latter 10 second period, fuel injection begins and raises the average ion density from $4 \times 10^{13} \text{cm}^{-3}$ to the operating value of $8 \times 10^{13} \text{cm}^{-3}$.

At the beginning of the burn period, the neutral beams are turned off but fuel injection continues for the entire burn period. The fuel is assumed to be injected as solid (D+T) pellets. The cryopumps are valved into the vacuum system during the initial operation to assist in maintaining the desired vacuum.

* An operating period is defined as a period of time in which the operating cycle is repeated without interruption or pause between operating cycles,

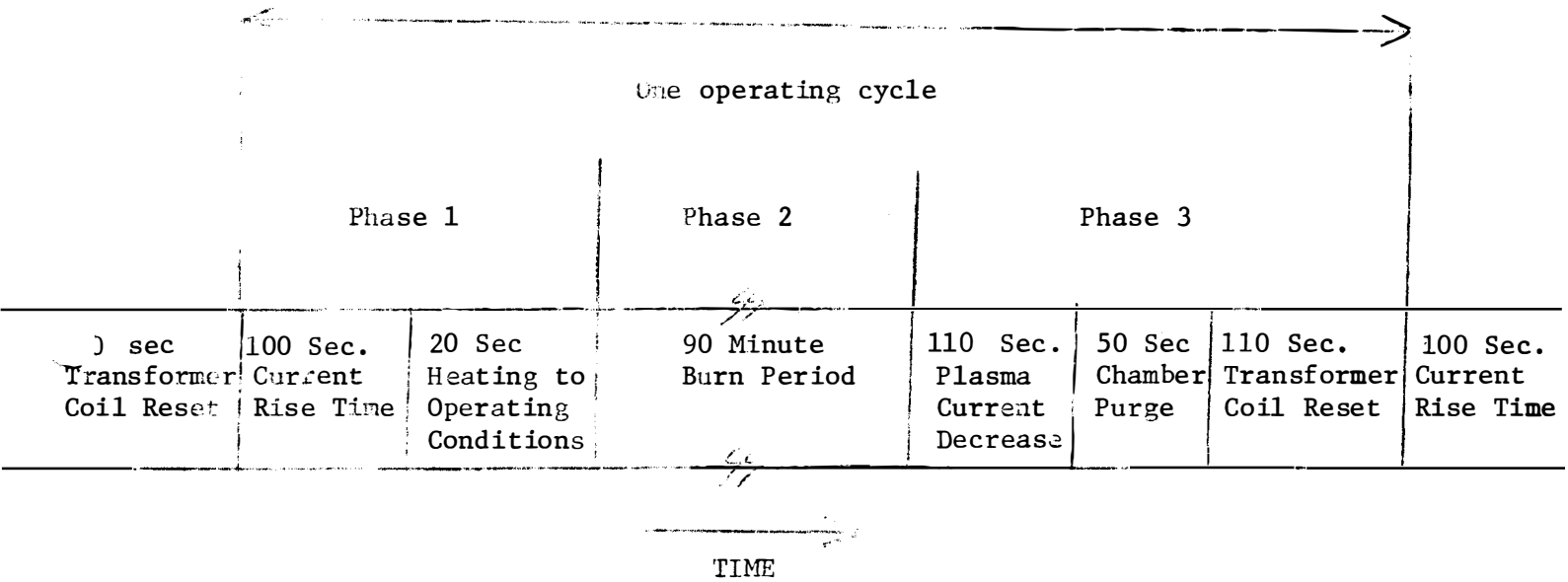


Fig. V-1 The UWMak-I Operating Cycle

At end of prestart-up period:

1. Lithium and sodium systems near operating temperatures by use of startup heaters.
2. All lithium and sodium and helium systems operating.
3. All vacuum systems operating, but cryopumps are valved off.
4. Reaction chamber at 10^{-5} torr.
5. All magnets at 4.2K.
6. Divertor current off.
7. Transformer reset to startup current.
8. Neutral beams off.
9. Fuel injectors off.

Core Loaded with 50% D-T mixture to 23×10^{-3} torr.

Transformer current reversed.

Divertor current turned on and gradually increased for 10 sec.

Entire cycle repeated numerous times without use of startup heaters.

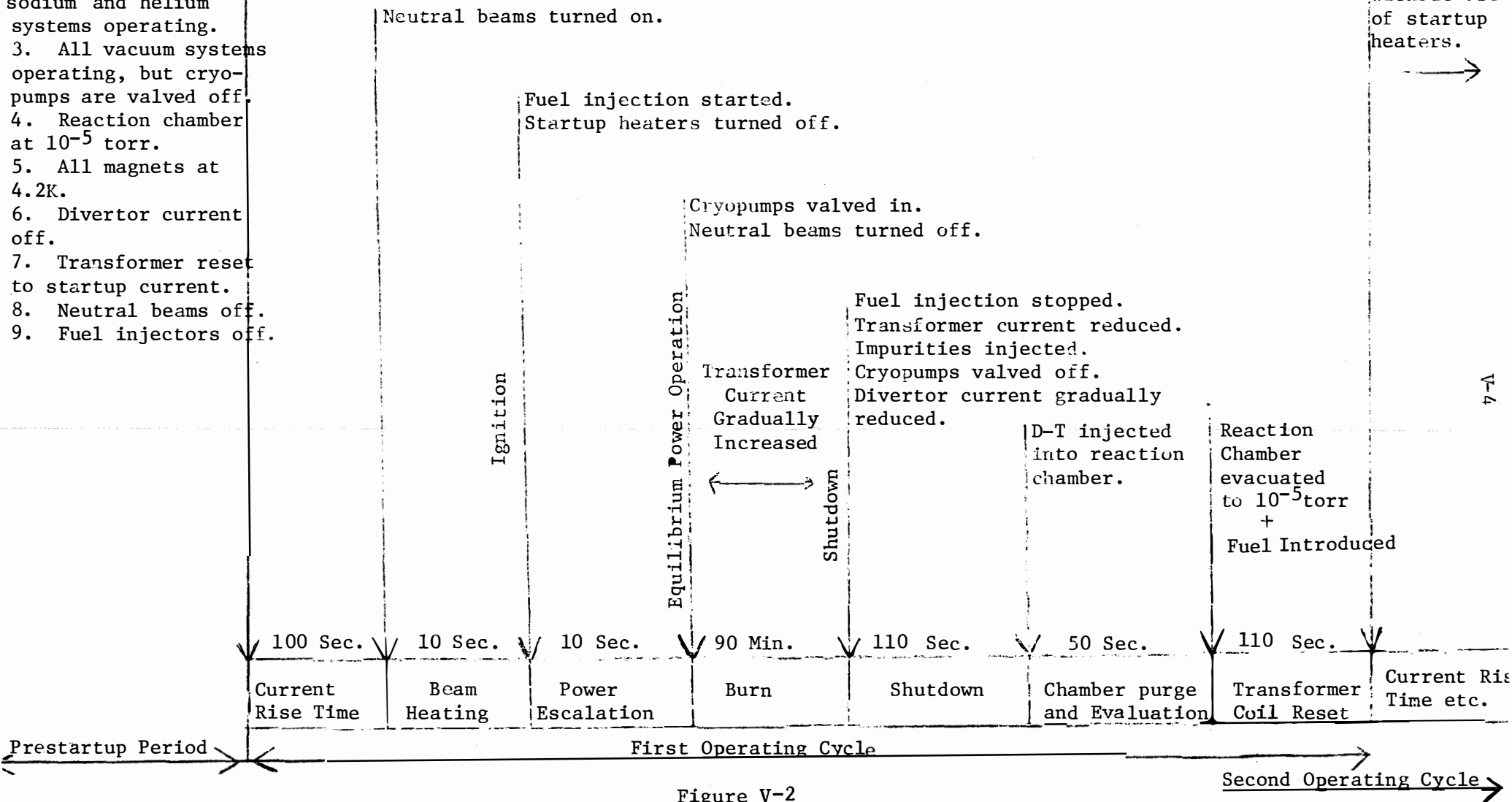


Figure V-2

Equipment Operation During Operating Period

The reactor system is designed to have about a ninety minute burn period. The transformer coils are designed to have adequate current capacity to maintain the plasma current during the burn phase.

The burn is terminated by cooling the plasma below the ignition temperature. This is done by shutting off the fuel injectors and injecting impurities which increase the heat transfer to the wall by radiation. At the same time, the cryopumps are isolated from the reaction chamber to avoid swamping them with impurities. The transformer and divertor currents are reduced to zero over a 110 second period.

The reaction chamber then is purged with deuterium gas to reduce the concentration of impurities low enough that the subsequent evacuation to 1×10^{-5} torr will reduce the quantity of impurities to the desired amount at the beginning of the next burn period. The transformer coils are then reset over 110 seconds to the desired currents at the start of the next operating cycle.

V-C. Fusion Reactor Plant Factor

The plant factor for a power plant is defined as the ratio between the actual power generation and the power generation that would occur if the plant operated 100 percent of the time at the design power level. The plant factor is always less than 100 percent because of (1) outage time for maintenance (and refueling, in some cases) and (2) operation at less than the design level during startup periods and periods of time when there is not a need for all the electricity which could be generated.

The plant factor for the UWMAK-I will be determined primarily by four factors:

1. The time required for wall replacement outages,
2. The amount of unscheduled outage time due to miscellaneous equipment failures and transmission system abnormal conditions,
3. The average length of the plasma burn, and
4. The length of the reactor rejuvenation time between plasma burns.

Each of these four factors will be briefly discussed and then a general correlation between these factors and the plant factor will be made.

V-C-1. The Biennial Wall Replacements

The inner wall is designed to last two years before replacement is necessary to prevent failure. During each two year period, the inner wall in each of the twelve reactor segments will be replaced as described in Chapter IV.

The optimum schedule for replacing the wall segments is determined by making an economic balance of (1) the costs for keeping spare wall segments in inventory, (2) the costs for replacement of the segments, and (3) loss

of income from sale of electricity during the outage periods. The cost for keeping spare segments in inventory is quite large and is directly proportional to the number replaced per outage. This cost decreases as the interval between outages decreases. Both the costs due to replacement of the segments and the loss of income from sale of electricity increase as the interval between outages decreases because the amount of outage time increases. (More time is required to prepare for the replacement and to prepare the reactor for operation after the replacements are completed.)

An economic balance for UWMAK-I shows that the optimum wall replacement interval is between 4 and 6 months. (See Table V-1) This interval would result in an outage during the spring and fall of each year when most utilities have minimum demand for electricity. Therefore, a 6 month replacement time was chosen for UWMAK-I.

During the wall replacement outages, all routine major outage maintenance would be done. This includes such items as periodic inspection and maintenance of the turbine-generators, inspection and maintenance of large motors and pumps, etc. Also major equipment modifications would be done.

V-C-2. Unscheduled Outage Time

All power plants are plagued by numerous outages due to minor equipment failures, loss of transmission system, etc. In addition, it is probable that a segment of the fusion reactor will occasionally have to be replaced because of a failure in one of the heat transfer walls, the inner wall, the divertor system, or the magnets. If such a replacement is necessary, it probably could be done rapidly (in less than a week) because a spare segment would be kept ready for installation.* The failed segment would be simply moved to a storage cell, and the spare put in its place. The failed segment then would be repaired during the subsequent reactor operating period.

An exact estimate of the amount of miscellaneous outage time cannot be made because the design of some of the equipment is not known at present. However, based on initial operating experience at nuclear power plants, a total miscellaneous outage time of four weeks per year appears reasonable. It should be noted that this four weeks per year of outage time represents the average conditions for a debugged reactor system. The initial operating period for large nuclear reactors has required more than four weeks per year of miscellaneous outage time (or equivalent loss of time due to operations at less than design power level.)

V-C-3. The Length of the Burn Period

The current design burn period is expected to be 90 minutes. If the burn is for a shorter time period, the plant factor is reduced because a larger fraction of the available reactor time is used for rejuvenation periods (which are relatively insensitive to burn time).

* A total of four complete spare segments would be kept in inventory. During each wall segment replacement outage, three would be installed on the reactor.

TABLE V-1
Wall Replacement Costs for UWMAK-I

Intervals Between Replacement Outages	Number Segments Replaced Per outage*	Annual Outage Time (days)	Annual Costs - millions of dollars			
			Segment Inventory Costs	Outage Costs	Loss of Income	Total
2 yrs.	12	20.5	37	0.58	7.4	45
1 yr.	6	23	18	0.66	8.3	27
6 mo.	3	28	9	0.8	10	19.8
4 mo.	2	33	6	0.94	11.9	18.8
3 mo.	1	38	3	1.09	17.3	21.7

Basis: Outage time (days) = (3) (No. segments replaced) + (5) (No. outages)
 Inventory cost (\$) = (20,300,000) (No. segments replaced/outage) (0.15)
 Outage labor costs = (Annual outage time) x (\$28,500/day)

Loss of income is 10 mills/kWh. or \$360,000 per day

* Equals number segments in inventory in order to perform outages.
 Does not include one additional segment in inventory to cover failures
 immediately following a replacement outage.

It is assumed that during the burn period, the average thermal power will equal the design power level of 5000 MW_t. This is a reasonable assumption because the life of the inner wall is determined primarily by the total number of neutrons passing through the wall not by the flux. Minor fluctuations of the thermal power level around the design level should not have a significant effect on the wall life as long as the average power level is 5000 MW_t.

V-C-4. The Length of the Rejuvenation Period

The rejuvenation period is essentially a non-productive time for heat generation. Any fusion reactions occurring during that period represent a minute fraction of the total heat generation. As explained in Section V-B the rejuvenation period is estimated to last approximately 390 seconds. During the time when the fusion reaction is shut off, the reactor is evacuated, the reactor is refueled, and the fusion reaction is re-established. The various actions during this period will have to be controlled by automatic control systems because of the numerous sophisticated actions that are necessary in a short time period.

Experience or detailed design may demonstrate that the rejuvenation would require a different time period. However, a change in the length of the rejuvenation period will not have a significant effect on the plant factor if the burn period is as long as 90 minutes and the rejuvenation period does not increase significantly. (See Figure V-3).

V-C-5. The General Plant Factor Correlation

The plant factor is defined as:

$$\frac{H_a}{H_t}, \text{ where}$$

H_a is the actual heat production during a time period, and H_t is the maximum possible heat production during the same time period. If it is assumed that UWMAK-I operates at the design power level throughout its burn periods, the annual heat production can be stated as:

$$H_a = (P_d) \left(\frac{T_b}{T_b + T_r} \right) (W_y - W_{uot} - W_{sot})$$

where

P_d is the design power level (MW_t)

T_b is the average burn time (seconds)

T_r is the average rejuvenation time (seconds)

W_y is the number of weeks in a year,

W_{uot} is the number of weeks of unscheduled outage time in a year,

and W_{sot} is the number of weeks of scheduled outage time in a year.

BASIS 90 MINUTE BURN
4 WEEKS UNSCHEDULED
OUTAGE TIME PER YEAR

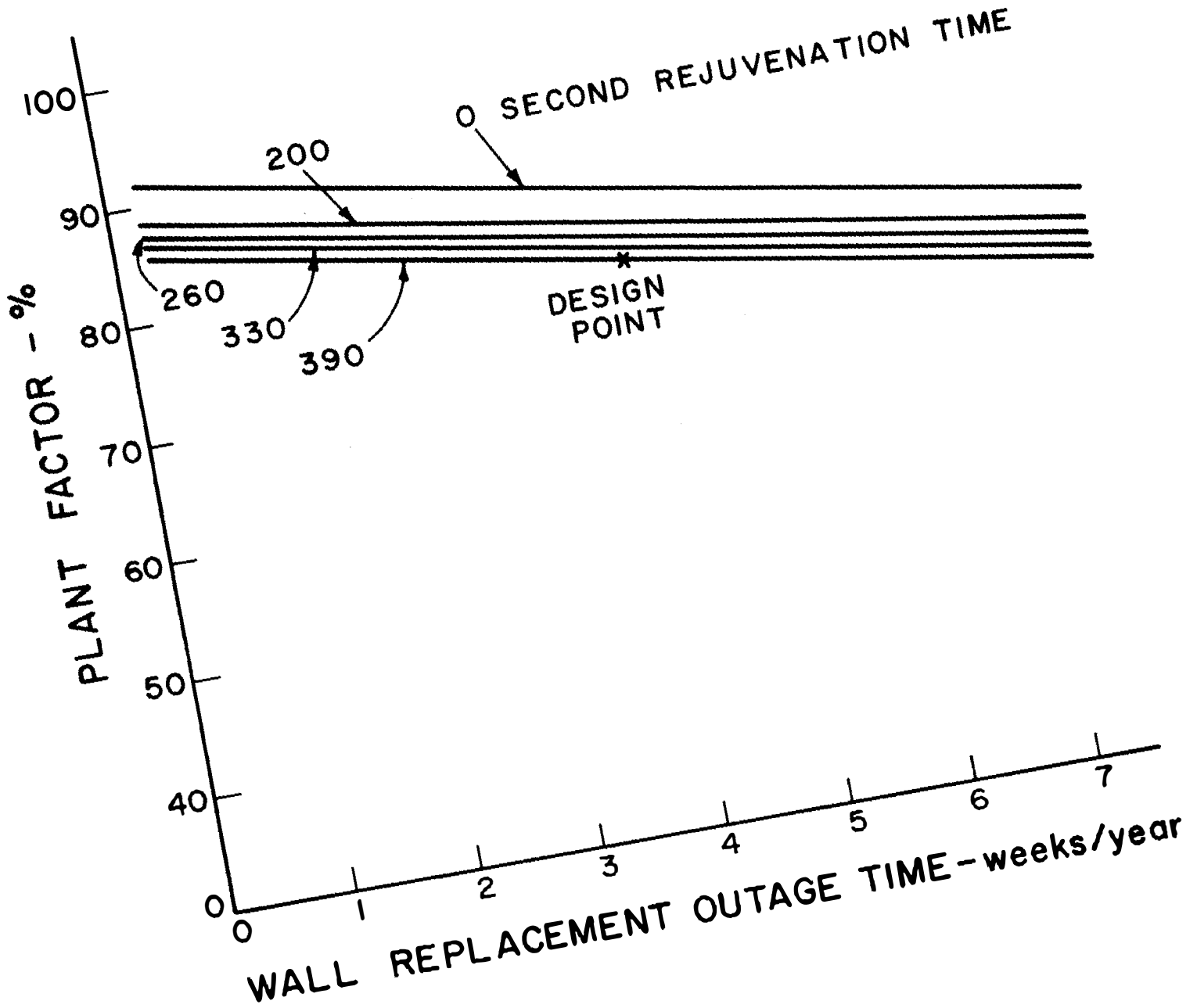


FIGURE V-3
UWMAK -I PLANT FACTORS

The maximum possible heat generation is the amount of heat that would be generated if the reactor operated in the burn mode throughout the year. Therefore:

$$H_t = (P_d)(W_y)$$

The plant factor is then given by

$$\frac{H_a}{H_t} = \left(\frac{T_b}{T_b + T_r} \right) \left(\frac{W_y - W_{uot} - W_{sot}}{W_y} \right)$$

Figures V-3 to V-5 present general correlations between the plant factor, the length of the burn, the length of the rejuvenation period and the length of the wall replacement outages. The star represents the design conditions.

In general, the correlations show that a plant factor of about 80% can be achieved with reasonable values of the design parameters. To achieve 80% plant factor, the permissible values for each of the design parameters are about:

1. an outage time of 4 weeks each year for wall replacement
2. an outage time of 4 weeks each year for unscheduled maintenance
3. a 90 minute burn time, and
4. a rejuvenation period length of about 390 seconds.

Throughout this analysis of plant factors, it has been assumed that the total electricity production will be proportional to the heat generation. This assumption is correct only if the design of the heat storage system is adjusted whenever the lengths of the burn and rejuvenation periods change so that the inlet steam conditions to the turbine generator are the same for all operating schedules. If the heat storage system design is not adjusted, a correction factor must be added to the plant factor equation to compensate for the changes in thermal efficiency as the lengths of the burn and rejuvenation period changes.

V-C-6. Summary

A plant factor of about 80% can be achieved for UWMAK-I with reasonable values of design parameters. To achieve this plant factor, it is necessary that the total outage time per year be no more than eight weeks when the rejuvenation time is about 7 percent of the total time for the reactor burn and rejuvenation. These conditions are satisfied by the design conditions of a 90 minute burn, a 390 second rejuvenation time, four weeks of unscheduled outage time per year, and four weeks of scheduled outage time per year for wall replacements.

BASIC 390 SECOND
REJUVENATION TIME
4 WEEKS UNSCHEDULED
OUTAGE TIME PER YEAR

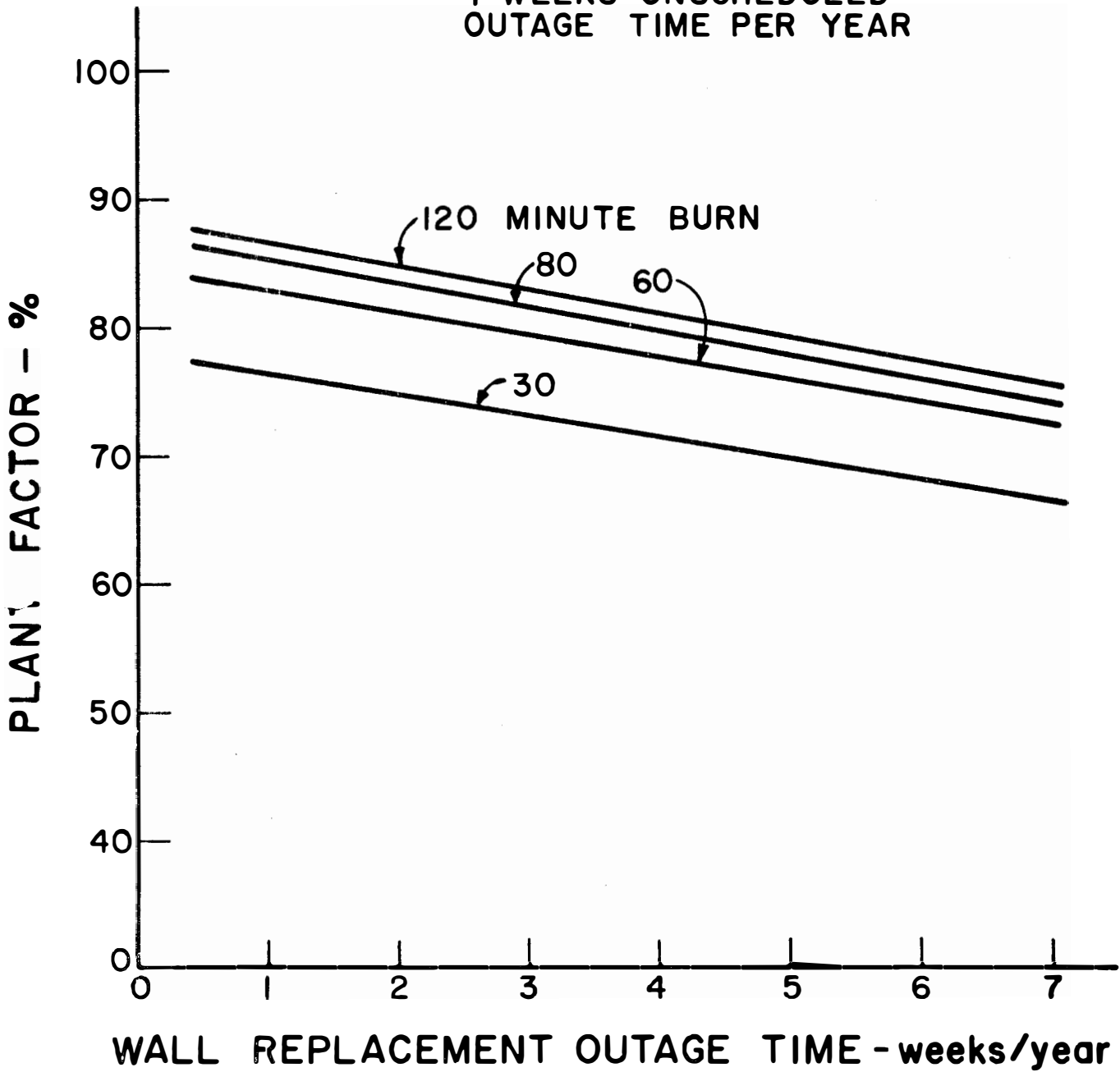


FIGURE V - 4
UWMAK - I PLANT FACTORS

PERMISSIBLE WALL REPLACEMENT OUTAGE TIME -

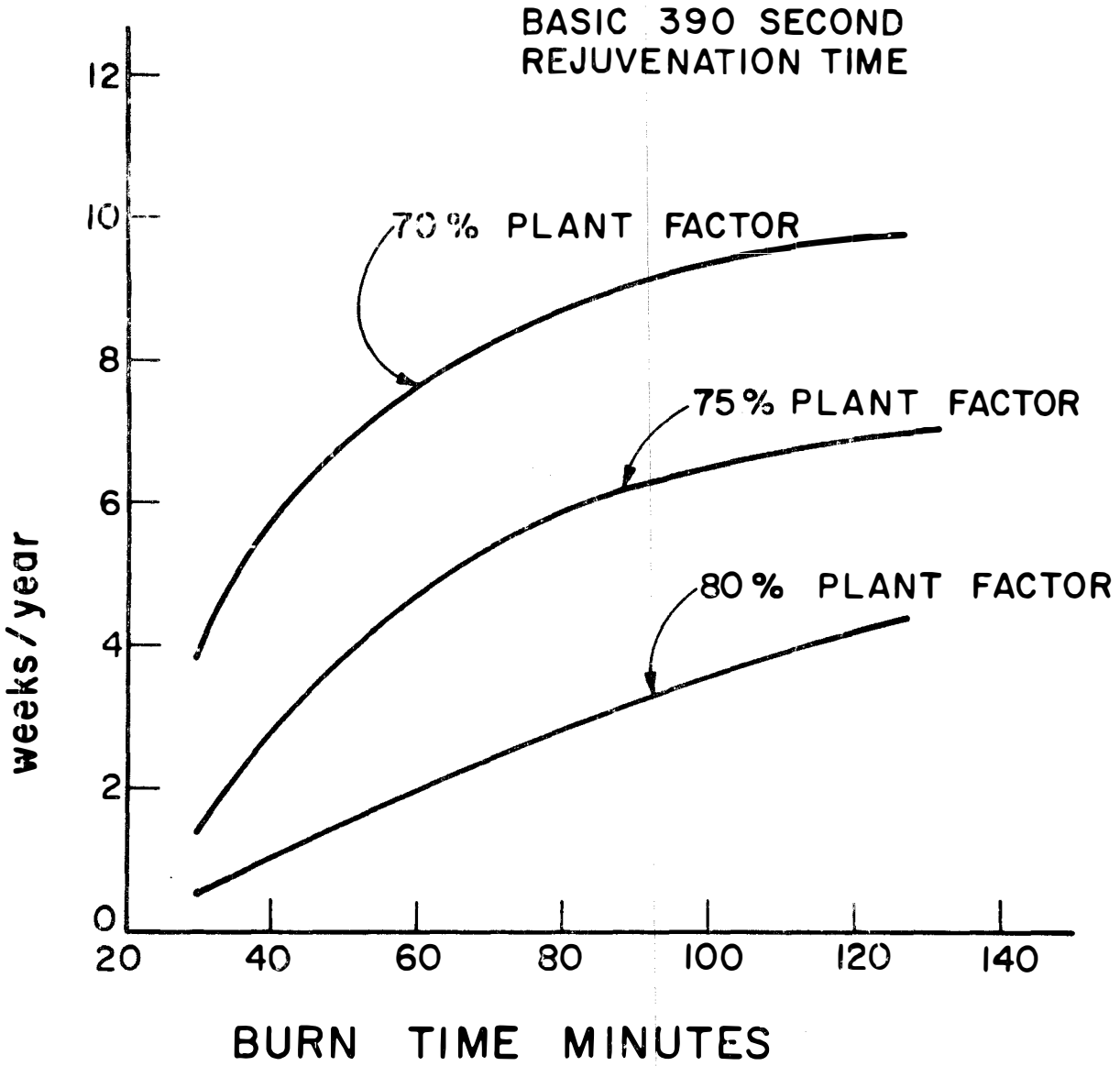


FIGURE V - 5
UWMAK-I PERMISSIBLE WALL REPLACEMENT
OUTAGE LENGTHS.

V-D. Capital Costs

The capital costs for UWMAK-I were estimated by use of standard preliminary capital cost estimating procedures. The primary guide for estimation of the capital cost was the document NUS-531 "Guide for Economic Evaluation of Nuclear Reactor Plant Design."⁽¹⁾ That document presents the general philosophy, procedures, and record tables for estimating all costs for a power plant.

A conservative approach was used in estimating the capital costs. Past experience has demonstrated that advocates of new facilities frequently underestimate the capital costs because of optimism in design and failure to include sufficient contingency for unforeseen difficulties. In this analysis, the construction costs were deliberately overestimated whenever uncertainties existed. As an example, current maximum equipment sizes were used whenever there was any doubt that larger equipment could be produced. This eliminated the economies-of-scale that might be realized by use of larger equipment or by increases in quantities manufactured.

No attempt was made to develop detailed designs for the numerous small support systems. It became apparent early in the effort that order-of-magnitude costs for such items would be adequate. Large errors in these costs would have no significant effect on the total capital costs because they cause a small fraction of the total costs.

Most of the costs were estimated by use of standard costs per unit of material. After development of a general design for a facility, the quantities of material needed for construction of that facility were estimated and then multiplied by the standard cost per unit of material to obtain the installed cost. The standard unit costs are presented in Table V-2.

The estimated capital costs are presented in Tables V-3 and V-4. Table V-3 presents the summarized costs by major plant components. Table V-4 presents a breakdown of the costs in the greater detail developed during the cost estimating. The basis for each of the costs is presented in Appendix A.

Several reference documents were used to obtain quantity requirements and unit costs. These costs were adjusted as appropriate for differences in size and for cost escalation. The primary source of information was WASH 1230 (Vol. 1).⁽²⁾

References

1. NUS-531, "Guide for Economic Evaluation of Nuclear Reactor Plant Designs," NUS Corporation, January, 1969.
2. WASH-1230 (Vol.1), "Pressurized Water Reactor Plant, 1000-MW_e Central Station Power Plants - Investment Cost Study," United Engineers and Contractors, June, 1971.

TABLE V-2
Standard Material Unit Costs

<u>Material</u>	<u>Purchase Cost</u>	<u>Installed Cost</u>
Argon	\$0.80/kg	-----
Deuterium	\$440/kg	-----
Helium	\$1.22/l.	-----
Lithium	\$10/kg	-----
Nitrogen	\$0.25/l	-----
Sodium	\$0.55/kg	-----
Tritium	No cost*	-----
B ₄ C	-----	\$3/kg
Stainless Steel		
Sheet or bulk usage	\$6.60/kg	\$8.80/kg
Special shapes	-----	\$17.60/kg
Lead	-----	\$0.60/kg
Zirconium getter	-----	\$45/kg
Yttrium getter	-----	\$330/kg
Concrete	-----	\$206/m ³
Alloy Steel		
Structural	-----	\$4.40/kg
Special shapes	-----	up to \$13.20/kg
Nb-Ti	\$33.00/kg	-----
Copper	\$1.10/kg	-----
Copper matrix	\$2.20/kg	-----
Copper stabilizer	\$3.30/kg	-----
Copper conductor	-----	\$4.29/kg
Aluminum	-----	\$1.10/kg
Aluminum conductor	-----	\$5.50/kg

*Mature industry assumed with a surplus of tritium

Table V-3
Cost data

(Prices are Present Day and Based on a 40 Hour Work Week)

Account Number	<u>Account Title</u>	<u>Total</u>
<u>DIRECT COSTS:</u>		
Nondepreciating Assets:		
20	Land and Land Rights	\$1,200,000
Depreciating Assets:		
26	Special Materials	28,290,000
Physical Plant		
21	Structures and Site Facilities	139,807,000
22	Reactor Plant Equipment	573,636,000
23	Turbine Plant Equipment	170,580,000
24	Electric Plant Equipment	142,859,000
25	Miscellaneous Plant Equipment	9,410,000
	SUB-TOTAL Physical Plant	1,036,292,000
<u>INDIRECT COSTS (All Depreciating Assets):</u>		
91	Construction Facilities, Equipment	24,300,000
92	Engineering Services	48,500,000
93	Other Costs	76,600,000
94	Interest During Construction	218,618,000
	SUB-TOTAL	367,018,000
	SUB-TOTAL (Total Depreciating Assets)	1,431,600,000
	TOTAL PLANT CAPITAL INVESTMENT:	1,432,800,000
	COST PER KILOWATT GENERATED	971

TABLE V-4
COST DATA

(Prices are Present Day and Based on a 40 Hour Work Week)

<u>Account Number</u>	<u>Account Title</u>	<u>Total*</u>
20	<u>Land and Land Rights</u>	
201	Land and Privilege Acquisition)	
202	Relocation of Buildings, Utilities, Etc.)	\$1,200,000
	TOTAL - ACCOUNT 20	<u>\$1,200,000</u>
21	<u>Structures & Site Facilities</u>	
211	Site Improvements and Facilities)	
.1	General Yard Improvements)	
.11	Grading, General Excavation and/or Fill and Landscaping)	
.12	Roads, Sidewalks & Parking Areas)	
.13	Retaining Walls)	
.14	Fences, Railings, and Gateways)	
.15	Sanitary Sewer System:)	
.151	Connection to Existing System)	See Page 3
.152	Septic Tank)	
.153	Distribution Box)	
.154	Tile Field (Drainage))	
.155	Piping, Conduits, & Manholes)	
.16	Yard Drainage & Storm Sewer System:)	
.161	Connection to Existing System)	
.162	Manholes, Catch Basins & Inlets)	
.163	Outfall Structure)	
.164	Piping, Conduits, Open Ditches)	
.17	Roadway & General Yard Lighting)	
.18	Cathodic Protection)	
.2	Waterfront Improvements)	
.21	Revetments)	
.22	Levees)	
.23	Breakwaters)	
.3	Highway Access)	
.31	Grading)	
.32	Surfacing)	

*Cost data as of January 1974

<u>Account Number</u>	<u>Account Title</u>	<u>Total</u>
21	Structures & Site Facilities (Cont'd)	
211	Site Improvements and Facilities (Cont'd)	
.3	Highway Access (Cont'd)	
.33	Culverts)	
.34	Bridges, Trestles, and Causeways)	
.35	Guards and Signs)	
.36	Lighting)	
)	\$8,000,000
.4	Railway Access)	
.41	Grading)	
.42	Bridges, Culverts & Trestles)	
.43	Ballast, Ties, Rails & Accessories)	
.44	Signals & Interlocks)	
.45	Switches, Crossovers & Bumpers)	
)	
.5	Waterway Access Facilities)	
.51	Dredging)	
.52	Piers, Barge Docks, Etc.)	
	TOTAL ACCOUNT 211	<u>\$8,000,000</u>
	Reactor Building Incl. Radwaste & Fuel Handling Areas	
.1	Basic Building Structures	
.11	Earth Work Including Dewatering, Walers)	
	Steel Sheeting)	
.13	Substructure Up to Grade Incl. Concrete,)	
	Reinforcing, Forms)	
.14	Superstructure)	
)	
.141	Concrete Work Incl. Floors, Exterior)	
	Walls, Interior Walls Piers, Col's.)	\$65,000,000
	Reactor Area Concrete, Etc.)	
.142	Structural & Gallery Steel)	
.143	Exterior Metal Siding Walls)	
.144	Roof Slabs, Roofing, Flashing Etc.)	
.147	Doors & Windows & Wall Lauvers)	
.148	Floor Finishes)	
.149	Painting Incl. Special Coating)	
.16	Structural Steel Stack	
	TOTAL .1	<u>\$65,000,000</u>

<u>Account Number</u>	<u>Account Title</u>	<u>Total</u>
21	<u>Structures & Site Facilities (Cont'd)</u>	
212	Reactor Building Incl. Radwaste & Fuel Handling Areas (Con'td)	
.2	Building Service	
.21	Plumbing Below & Above Grade	\$200,000
.22	Heating, Ventilation, Air-Conditioning	5,800,000
.23	Fire Protection System	150,000
.24	Electrical & Lighting	Incl. Acct. 24
.25	Elevator	100,000
	TOTAL .2	<u>\$6,250,000</u>
.3	Containment Structures	
.31	Primary Containment Liners at Reactor Area)	
.32	Secondary Liner Plate Work for Walls,) Floors, Roof)	18,667,000
.33	Penetrations (Mechanical & Electrical)	2,250,000
.34	Revolving Containment Door, Complete	<u>11,000,000</u>
	TOTAL .3	31,917,000
	TOTAL - ACCOUNT 212	\$103,167,000
213	Turbine Building Incl. Control Room, Heater Bay, Diesel Generator Area	
.1	Basic Building Structures	
.11	Earth Work)	
.13	Substructure)	17,000,000
.14	Superstructure Incl. Structural &) Gallery Steel)	
.2	Building Services	
.21	Plumbing	Incl. -.1
.22	Heating, Ventilation Air-Conditioning	1,300,000
.23	Fire Protection System	300,000
.24	Electrical & Lighting	Incl. Acct. 24
.25	Elevator	50,000
	TOTAL .2	<u>\$ 1,650,000</u>
	TOTAL ACCOUNT 213	\$18,650,000

<u>Account Number</u>	<u>Account Title</u>	<u>Total</u>
21	Structures & Site Facilities (Cont'd)	
214	Intake & Discharge Structures (Cooling Tower Building Work)	
.1	Circulating Water Cooling Tower Concrete Basins Incl. Outlet Structures	Incl. Acct. 232.3
.2	Earth Work	
.21	Circulating Water Pipe Excavation,) Backfill, Disposal & Dewatering)	
.22	Blow-down Pipe Excavation Backfill,) Disposal & Dewatering)	Incl. Acct. 232.0
.23	Make-up Pipe Excavation Backfill,) Disposal & Dewatering)	
.3	Make-up Pump House	
.31	Dredging River & Forebay Construction)	
.32	Substructure)	
.33	Superstructure)	\$1,000,000
.34	Structural Steel)	
.35	Building Services)	
.4	Retention Basin & Drain Line for Blow-Down	100,000
.5	Waste Heat Cooling Tower Building Work	
.51	Substructure	
.52	Superstructure	Incl. Acct. 232.3
.53	Structural Steel	
.54	Earth Work for Waste Heat Pipe	Incl. Acct. 232.0
.6	Protection Relief Slabs for Circulating Water, Blow-Down & Make-Up Pipe Lines	200,000
.7	Circulating Water Blow-Down Make-Up & Waste Heat Cooling Piping, Valves, Fittings, Etc.	Incl. Acct. 232.2
	TOTAL ACCOUNT 214	<u>\$1,300,000</u>

<u>Account Number</u>	<u>Account Title</u>	<u>Total</u>
21	<u>Structures & Site Facilities (Cont'd)</u>	
215	Reactor Auxiliaries Building Including Switchgear Bay	54,626,000
.1	Basic Building Structures)	
.11	Earth Work)	
.13	Substructure)	
.14	Superstructure Including Gallery Steel)	
.2	Building Services	
.21	Plumbing	75,000
.22	Heating Ventilation & Air-Conditioning	1,100,000
.23	Fire Protection System	100,000
.24	Electrical & Lighting	Incl. Acct. 24
.25	Elevator	100,000
	TOTAL .2	<u>\$1,375,000</u>
	TOTAL ACCOUNT 215	56,001,000
216	Radioactive Waste Building	
.1	Basic Building Structures)	Incl. Acct. 215
.2	Building Services)	
217	Fuel Storage Building	
.1	Basic Building Structures)	Incl. Acct. 215
.2	Building Services)	
218	Miscellaneous Buildings	
A	Service Building	
.1	Basic Building Structures)	
.11	Earth Work)	
.13	Substructure)	4,500,000
.14	Superstructure Including Structural Steel)	
	TOTAL .1	<u>\$4,500,000</u>

<u>Account Number</u>	<u>Account Title</u>	<u>Total</u>
21	<u>Structures & Site Facilities</u> (Cont'd)	
218	Miscellaneous Buildings (Cont'd)	
A	Service Building (Cont'd)	
.2	Building Services	
.21	Plumbing	Incl. .1
.22	Heating, Ventilation & Air-Conditioning	\$900,000
.23	Fire Protection System	50,000
.24	Electrical & Lighting	Incl. Acct. 24
.25	Elevators	100,000
	TOTAL .2	\$1,050,000
	TOTAL ACCOUNT 218-A	\$5,550,000
B	Harmonic Filter Area	
.1	Basic Building Structures)	
.11	Earth Work)	
.13	Substructure)	
.14)	
	TOTAL .1)	Incl. Acct. 24
.2	Services)	
.23	Fire Protection System)	
.124	Electrical & Lighting)	
	TOTAL .2)	Incl. Acct. 24
	TOTAL ACCOUNT 218-B	Incl. Acct. 24
C	Inverter Area	
.1	Basic Structures)	
.11	Earth Work)	
.13	Substructure)	
.14	Structural Steel)	
)	Incl. Acct. 24
.2	Services)	
.23	Fire Protection System)	
.24	Electrical & Lighting)	
	TOTAL .2)	Incl. Acct. 24
	TOTAL ACCOUNT	Incl. Acct. 24

<u>Account Number</u>	<u>Account Title</u>	<u>Total</u>
21	<u>Structures & Site Facilities (Cont'd)</u>	
218	Miscellaneous Buildings (Cont'd)	
D	Inductive Coil Storage Building	
.1	Basic Building Structures)
.11	Earth Work)
.13	Substructure)
.14	Superstructure Incl. Structural Steel)
.2	Building Services)
.21	Plumbing) \$790,000
.22	Heating Ventilation & Air-Conditioning)
.23	Fire Protection System)
.24	Electrical & Lighting)
	TOTAL ACCOUNT 218-D	<u>\$790,000</u>
E	Helium Storage Building	
.1	Basic Building Structures)
.11	Earth Work)
.13	Substructure)
.14	Superstructure Incl. Structural Steel)
.2	Building Services)
.21	Plumbing) \$100,000
.23	Fire Protection System)
.24	Electrical & Lighting)
	TOTAL ACCOUNT 218-E	<u>\$100,000</u>
F	Miscellaneous Structures & Building Work	
.1	Gate House (Permanent)	25,000
.2	Visitor Center Building	Not Incl.
.3	Electrical Yard Foundations & Structures	Incl. Acct. 24
.4	Heating Boiler House	\$200,000
.5	Hypochlorination Solution Tank Foundation	15,000
.6	Oil Separator Under-ground Vault	Incl. Acct. 24
.7	Foundation for Tanks (Water Storage)	150,000
.8	Berm & Foundation for Oil Storage Tanks	10,000

<u>Account Number</u>	<u>Account Title</u>	<u>Total</u>
21	<u>Structures & Site Facilities</u> (Cont'd)	
218	Miscellaneous Buildings (Cont'd)	
F	Miscellaneous Structures & Building Work (Cont'd)	
.9	Test Borings	\$200,000
.11	Laboratory Material Testing & Structural Steel Inspection (Not Incl. Quality Control & Assurance)	75,000
.12	Temporary Construction Buildings, Field Office Building, Toilet & Wash Building for Construction Employees	Not Incl.
.13	Maintenance & Services for Various Contractors Scope of Work	
.131	Maintenance of Roads & Track)
.132	Maintenance & Servicing of Sewage Plant & Lift Station))
.133	Maintenance & Servicing Construction Employees Wash & Toilet Buildings))
.134	Snow & Ice Removal Maintenance) Incl.
.135	Guards Service) in Acct. 91
.136	Switching & Handling of Railroad Cars on Station Property Incl. Necessary Yard Mobile Switching Equipment)))
.137	Traffic Flagman)
.138	Miscellaneous Other Provisions)
.14	Miscellaneous Yard Structures & Building Work	200,000
	TOTAL F	<u>\$875,000</u>
	TOTAL ACCOUNT 218	\$ 7,315,000
219	Ventilation Stack	Incl. Acct. 212.2
	TOTAL ACCOUNTS 211 to 219 Inclusive	<u>139,807,000</u>
	Contingency	Incl. Above
	TOTAL ACCOUNT 21 STRUCTURES & SITE FACILITIES	<u>139,807,000</u>

<u>Account Number</u>	<u>Account Title</u>	<u>Total</u>
22	Reactor Plant Equipment	
221	Reactor Equipment	
.1	Magnets	\$189,900,000
.2	Shield	41,333,000
.3	Blanket	74,160,000
0.4	Neutral Beam Injectors	6,000,000
0.5	Equipment Foundation	250,000
0.6	Reactor Seals	1,400,000
	TOTAL ACCOUNT 221	313,043,000
222	Main Heat Transfer & Transport Systems	
.1	Primary Lithium Coolant System	
.11	Pumps & Motor Drives Modular & Non Modular	16,625,000
.12	Piping	40,000,000
.13	Heat Exchangers (IHX and Clean-up Regenerative	37,800,000
.14	Tanks)	
.141	Dump Tanks	
.142	Make-Up Tanks	
.143	Clean-Up Tanks	9,700,000
.144	Tritium Extraction	
.15	Clean-Up System (Tank Including .14)	6,500,000
.16	Thermal Insulation Piping & Equipment	5,000,000
.17	Tritium Extraction	60,000
.2	Divertor Lithium System	
.21	Pumping	Incl. .11
.22	Piping	Incl. .12
.23	Heat Exchangers	2,550,000
.24	Tanks	Incl. .14
.25	Clean-Up	760,000
.26	Tritium Extraction	460,000
.3	Intermediate Sodium Loop System	
.31	Pumps & Motor Drives Modular & Non modular	31,300,000
.32	Piping	15,000,000
.33	Heat Exchangers (Steam Gen. & Clean-Up Regenerative)	25,300,000

<u>Account Number</u>	<u>Account Title</u>	<u>Total</u>
22	Reactor Plant Equipment (Cont'd)	
222	Main Heat Transfer & Transport Systems	
.3	Intermediate Sodium Loop Systems	
.34	Clean-Up System	\$700,000
.36	Tanks	
.361	Sodium Dump Tanks	\$20,000,000
.362	Hot Storage Tanks	
.363	Make-Up Tanks	
.364	Clean-Up Tanks	
.365	Tritium Extraction Tanks	
.37	Thermal Insulation Piping and Equipment	2,900,000
.38	Tritium Extraction	230,000
	TOTAL ACCOUNT 222	<u>\$214,885,000</u>
223	Auxiliary Heating Systems	
.1	Shield Cooling (He)	
.11	Pumping	372,000
.12	Piping	212,000
.13	Heat Exchangers	492,000
.14	Purification	36,000
.15	Tritium Extraction	30,000
.2	Magnet Cooling System	
.21	Cryogenic System	8,750,000
.22	Piping	250,000
.23	Transport System	250,000
.24	Tanks	50,000
	TOTAL ACCOUNT 223	<u>10,442,000</u>
224	Radioactive Waste Treatment & Disposal	
.1	Liquid Waste Processing & Equipment	180,000
.2	Gaseous Wastes and Off-Gas Processing System	0
.3	Solid Wastes Processing Equipment	90,000
.4	Wall Liner Disposal Equipment	60,000
	TOTAL ACCOUNT 224	<u>\$330,000</u>

<u>Account Number</u>	<u>Account Title</u>	<u>Total</u>
22	<u>Reactor Plant Equipment</u> (Cont'd)	
225	Nuclear Fuel Handling & Storage Systems (Fuel Injection)	
.1	Tritium Purification System	60,000
.2	Liquefaction	100,000
.3	Pellet Fabrication	180,000
.4	Pellet Injection	1,480,000
.5	Storage Equipment	50,000
	TOTAL ACCOUNT 225	<u>\$1,870,000</u>
226	Other Reactor Plant Equipment	
.1	Gas Systems	321,000
.2	Special Heating Systems	2,200,000
.3	Coolant Receiving, Storage & Make-up Systems	73,000
.4	Fluid Leak Detection	200,000
.5	Auxiliary Cooling Systems	2,300,000
.6	Maintenance Equipment	9,352,000
.7	Building Vacuum Systems	360,000
.8	Core Vacuum System	6,560,000
	TOTAL ACCOUNT 226	<u>\$21,366,000</u>
227	Instrumentation & Control	
.1	Reactor & Process I&C Equipment	
.2	Automatic Monitoring & Computation Equipment	
.3	Radiation Monitoring Systems	11,700,000
.4	Isolated Indicating & Recording Gauges, Etc.	
.5	Control & Instrument Piping, Tubing, & Wiring	
	TOTAL	<u>\$11,700,000</u>

<u>Account Number</u>	<u>Account Title</u>	<u>Total</u>
22	<u>Reactor Plant Equipment</u> (Cont'd)	
228	Fossil-Fueled Boilers & Superheaters	
.1	Boiler and/or Superheaters)	
.2	Draft Systems)	Not Req'd.
.3	Fuel Handling Systems)	
.4	Ash Handling Systems)	
	TOTAL FOR ACCOUNT 22	<u>\$573,636,000</u>
23	<u>Turbine Plant Equipment</u>	
231	Turbine-Generators	
.1	Turbine-Generators & Accessories	
	Including:	
.11	Two(2) 840.7 MW 1800 RPM Tandem Compound)	
	Four(4) Flow Nuclear Steam Turbines)	
	with 38" Last Stage Blades)	
.12	Two(2) 934.0 MVA Generators @ .90P.F.)	57,400,000
	and .50 SCR)	
.13	Non Standard Accessories)	
.14	Steam By-Pass System)	
.15	Live Steam Reheaters)	
.16	Piping, Valves & Hangers for By-Pass)	
	System	300,000
.17	Thermal Insulation	300,000
.2	Foundations	3,350,000
.3	Standby Exciters	
.4	Lubricating System	
.41	Oil Conditioning Equipment)	
.42	Clean & Dirty Oil Storage Tanks)	95,000
.43	Turbine Oil Transfer Pumps & Motors)	

<u>Account Number</u>	<u>Account Title</u>	<u>Total</u>
23	<u>Turbine Plant Equipment</u> (Cont'd)	
231	Turbine Generators (Cont'd)	
.5	Gas Systems	60,000
.6	Reheaters	Incl. .1
.7	Shielding	-
.8	Weather-Proof Housing	-
	TOTAL ACCOUNT 231	\$61,505,000
232	Heat Rejection Systems	
.1	Water Intake Common Facilities	
.11	Traveling Screens)	
.12	Screen Wash Pumps)	200,000
.14	Piping)	
.15	Chlorination)	
.2	Circulating Water Systems	
.21	Circulating Water Pumps & Motor Drives	1,125,000
.22	Circulating Water Piping, Valves & Fittings from Pumps to Condensers and to the Cooling Towers	10,500,000
.23	Waste Heat Cooling Tower Circulating Water Piping	10,000
.24	Cooling Tower Make-up Pipe Lines	Not Incl.
.25	Cooling Tower Blow-Down Pipe Lines	125,000
.26	Trench Work for Circulating Water Piping Systems	1,150,000
.3	Cooling Towers	
.31	Foundations & Basins	
.311	Mechanical Draft Towers	1,050,000
.312	Waste Heat Tower Structure	4,000,000
.313	Waste Heat Tower Circulating Water Pumps	110,000
.33	Four(4) Mechanical Draft Cooling Towers	5,300,000
.34	Mechanical Draft Waste Heat Cooling Tower	500,000
.35	Waste Heat System Heat Exchanger	775,000
.4	Other Systems Which Reject Heat to the Atmosphere	
	TOTAL ACCOUNT 232	\$24,845,000

<u>Account Number</u>	<u>Account Title</u>	<u>Total</u>
23	<u>Turbine Plant Equipment</u> (Cont'd)	
233	Condensing Systems	
.1	Condensers)	
.11	Condensers Complete Including Shells,)	
	Tube Plates, Water Boxes, Hot Wells, Etc.)	\$6,300,000
.12	Condenser Tubes)	
.13	Expansion Joints & Exhaust Stack Extensions)	
.14	Supervision of Erection)	
.16	Foundations)	100,000
.2	Condensate System	
.21	Condensate Pumps Suction Piping, Valves, Etc.	Incl. 235
.22	Condensate Pumping Units Consisting of:	
.221	Condensate Pumps & Motor Drives)	550,000
.222	Condensate Booster Pumps & Motor Drives)	
.3	Gas Removal System	
.31	Vacuum Pumps & Motor Drives)	
.32	Air Ejector Equipment)	115,000
33	Priming Ejectors)	
	TOTAL ACCOUNT 233	\$7,065,000
.4	Turbine By-Pass System	Incl. 231
234	Feed Heating System	
.1	Regenerative Heat Exchangers	
.11	Four(4) Strings of H.P. Closed Feedwater)	
	Heaters)	3,775,000
.12	Four(4) Strings of L.P. Closed Feed-)	
	water Heaters)	
.2	Pumps	
.21	Four(4) Turbine Driven Reactor Feed)	
	Pumps, Bedplates, Complete with)	
	Appurtenances)	
.22	Two(2) Motor Driven Reactor Feed Pumps Bed-)	
	Plates complete with Motor Drives)	3,870,000
.23	Four(4) Turbine Drives, for Reactor Feed)	
	Pumps)	
.24	Exhaust Ducts & Appurtenances to Main)	
	Condenser)	

<u>Account Number</u>	<u>Account Title</u>	<u>Total</u>
23	<u>Turbine Plant Equipment (Cont'd)</u>	
234	<u>Feed Heating System (Cont'd)</u>	
.2	Pumps (Cont'd)	
.25	Heater Drain Pumps & Motor Drives	\$435,000
.26	All Other Miscellaneous Pumps & Motors	1,300,000
.27	Foundations	50,000
.3	Piping & Tanks	
.31	Piping Systems	Incl. 235
.33	Tanks	
.331	Condensate)	
.332	Chemicals)	1,100,000
.333	Oil)	
	TOTAL ACCOUNT 234	<u>\$10,530,000</u>
235	<u>Other Turbine Plant Equipment</u>	
.1	Main Steam (or Other Vapor) Piping and Valves	
.11	Main Steam)	
.12	Extraction)	
.13	Condensate)	53,000,000
.14	Feedwater)	
.15	All Other Miscellaneous Systems, Drips, Drains and Vents)	
.16	Thermal Insulation	6,500,000
.2	Turbine Auxiliaries	Incl. 231.1 & 235.1
.3	Auxiliaries Cooling System	Incl. 212.2
.4	Make-Up Treatment System	Incl. 235.5
.5	Chemical Treatment & Condensate Purification Systems)	
.51	Filtration Equipment, Including Sand Filters, Aerators, Retention Tanks, Pumps, Etc.)	
.52	Demineralizing Equipment, Including Anion & Cation Units, Decarbonator, Mixed Bed Units, Pumps Regeneration Units)	4,900,000
.53	Condensate Polishing Equipment Including Polishers, Anion & Cation Regeneration Equipment, Resin Mixing & Storage Vessels, Pumps, Tanks, Instruments, Controls)	
.54	Chemical Feed Equipment Including Mixing Tanks, Pumps	

<u>Account Number</u>	<u>Account Title</u>	<u>Total</u>
23	<u>Turbine Plant Equipment</u> (Cont'd)	
235	Other Turbine Plant Equipment (Cont'd)	
.6	Central Lubrication Service System	
.61	Clean Oil Tank)	
.62	Dirty Oil Tank)	
.63	Turbine Oil Conditioning Equipment)	\$85,000
	Including Pumps)	
.64	Turbine Oil Transfer Pumps & Motors)	
.65	Portable Oil Centrifuge & Filters)	
.66	Miscellaneous)	
	TOTAL ACCOUNT 235	<u>\$64,485,000</u>
236	Instrumentation & Control	
.1	Process I&C Equipment)	
.2	Automatic Monitoring & Control Equipment)	2,000,000
.3	Isolated Indicating & Recording Gauges,)	
	Meters, and Instruments)	
.4	Control & Instrument Piping, Tubing,)	
	& Wiring	Incl. 235.1
	TOTAL ACCOUNT 236	<u>\$2,000,000</u>
	TOTAL FOR ACCOUNT 23	\$170,430,000
	Contingency	Incl. above
	Spare Parts	150,000
	TOTAL FOR ACCOUNT 23	<u>\$170,580,000</u>
24	<u>Electric Plant Equipment</u>	
241	Switchgear	
.1	Generator Circuits	536,000
.2	Station Service	3,756,000
	TOTAL FOR ACCOUNT 241	<u>\$4,292,000</u>
242	Station Service Equipment	
.1	Station Service &	549,000
.2	Low Voltage Unit Substations & Lighting	
	Transformers	1,246,000
.3	Auxiliary Power Sources (Incl. Four(4) 5000KW Diesels)	3,370,000
.4	Main Power Transformers	3,362,000
	TOTAL FOR ACCOUNT 242	<u>\$8,527,000</u>

<u>Account Number</u>	<u>Account Title</u>	<u>Total</u>
24	<u>Electric Plant Equipment</u> (Cont'd)	
243	Switchboards (Incl. Heat Tracing)	\$2,786,000
244	Protective Equipment	*95,000
245	Electrical Structures & Wiring Containers	1,150,000
246	Power and Control Wiring	
.1	Generator Circuits Wiring	677,000
.2	Station Service Power Wiring)	7,941,000
.3	Control Wiring)	
	TOTAL FOR ACCOUNT 246	<u>\$8,618,000</u>
247	Diverter Coil Power Supply System	64,600,000
248	Poloidal Magnet Rectifiers	700,000
249	Electrical Installation	
.1	Contractor Furnished Material-Conduits, Lighting Fixtures, Etc.	3,276,000
.2	Construction & Erection Labor	48,815,000
	TOTAL FOR ACCOUNT 249	<u>\$52,091,000</u>
	TOTAL FOR ACCOUNT 24	\$142,859,000
	Contingency	Incl. Above
	Spare Parts	<u>Incl. Above</u>
	TOTAL FOR ACCOUNT 24	\$142,859,000
25	<u>Miscellaneous Plant Equipment</u>	
251	Transportation & Lifting Equipment	
.1	Cranes, Hoists, Monorails & Conveyors	
.11	Two(2) 175 Ton/25 Ton Capacity Turbine Room Cranes	525,000
.12	Hot Cell Cranes	1,000,000
.13	Miscellaneous Hoists Cranes, Jibs & Trolleys for Equipment Maintenance	575,000
.14	One(1) 150 Ton/10 Ton Inductive Coil Storage Building Crane	300,000
.15	He Storage Building Crane	100,000
.16	Reactor Hall Crane	500,000
.2-.6	Railway & Roadway Equipment, Watercraft Aircraft, & Vehicle Maintenance Equipment	<u>50,000</u>
	TOTAL ACCOUNT 251	\$3,050,000

<u>Account Number</u>	<u>Account Title</u>	<u>Total</u>
25	<u>Miscellaneous Plant Equipment (Cont'd)</u>	
252	Air and Water Service Systems	
.1	Air Systems	
.11	Service Air Compressors & Motor Drives)	
.12	Service Air Receivers)	\$460,000
.13	Instrument Air Compressors & Motor Drives)	
.14	Instrument Air Receivers)	
.15	Instrument Air Dryers)	
.2	Water Systems	3,400,000
.3	Auxiliary Heating Boilers	<u>1,800,000</u>
	TOTAL ACCOUNT 252	\$5,660,000
253	Communications Equipment	220,000
254	Furnishings & Fixtures	<u>480,000</u>
	TOTAL FOR ACCOUNT 25	\$9,410,000
	Contingency	
	Spare Parts	
	TOTAL FOR ACCOUNT 25	<u>9,410,000</u>
26	<u>Special Materials</u>	
261	Moderator	0
262	Reflector	0
263	Reactor Coolant	\$17,000,000
264	Intermediate Coolant (Sodium)	9,804,000
265	Turbine Cycle Working Fluids	0
266	Other Materials	<u>1,486,000</u>
	TOTAL FOR ACCOUNT 26	28,290,000

<u>Account Number</u>	<u>Account Title</u>	<u>Total</u>
91	<u>Construction Facilities, Equipment and Services</u>	
911	Temporary Facilities)	\$7,300,000
912	Construction Equipment)	12,200,000
913	Construction Services)	4,800,000
	TOTAL)	<u>\$24,300,000</u>
	Contingency)	
	TOTAL FOR ACCOUNT 91)	
92	Engineering Services)	
921	Design Engineering)	23,100,000
922	Other)	25,400,000
	TOTAL FOR ACCOUNT 92)	<u>\$48,500,000</u>
93	<u>Other Costs</u>)	
931	Taxes and Insurance)	69,300,000
932	Staff Training and Plant Startup)	900,000
933	Owner's G&A)	4,900,000
	TOTAL FOR ACCOUNT 93)	<u>75,100,000</u>
94	<u>Interest During Construction (@8%)</u>)	
941	Physical Plant and Associated (5yrs) Indirect Costs)	215,614,000
942	Land and Land Rights (6yrs))	704,000
943	Special Materials (1yr))	<u>2,300,000</u>
	TOTAL FOR ACCOUNT 94)	218,618,000

NOTES:

1. See detailed estimate for scope of work included.
2. The cost of construction labor included in the estimate is based on the following:
 - a. Current labor rates and fringe benefits as now apply in the state of Wisconsin.
 - b. Manhours, & efficiency of work as has occurred in similar work area.
 - c. Manhour costs - as required to attract labor to man the job.
3. Prices for equipment and materials are present day and 40 hour week.
4. Allowances for future escalation of materials and construction labor are not included.

V-E. The Electricity Production Cost

The electricity cost for a power plant normally is determined by calculating three general types of costs:

1. The operation and maintenance cost,
2. The fuel cost, and
3. The annual return on capital.

V-E-1. The Operations and Maintenance Costs

The operations and maintenance (O & M) cost consists of the routine day-to-day expenditures for salaries, supplies, maintenance materials, process chemicals, etc. As a general rule, these costs are essentially constant from year to year.

Because the exact design for many of the UWMAK-I components is not known, an exact estimate of the O & M costs is not possible. However, a reasonable estimate can be made by use of known design features and experience at fission power plants.

The potential components of the O & M cost are:

- a. Salaries,
 - b. Miscellaneous supplies and equipment,
 - c. Outside support services,
 - d. Miscellaneous costs,
 - e. General & Administrative,
 - f. Replacement inner walls,
 - g. Coolant make-up,
- and h. Working capital requirements.

Each of these items is briefly described and estimated below, and then the total O & M cost is determined.

V-E-1-a. Salaries

The size of the operating crew needed for a power plant depends on many factors such as the number of power plants at the site, the utility's personnel policies, the amount of automation, etc. Consequently, a set of operation conditions and policies must be assumed in order to permit estimation of the size of the operating crew. The following assumptions were used for UWMAK-I:

1. It is the only power plant at the site,
2. The design and operation has been debugged so that only routine technical assistance is needed,
3. The plant operates 24 hours per day, 365 days per year,

4. Five complete operating crews are used to provide full operating plus day crew and relief coverage,
5. The additional maintenance personnel needed for the wall replacement outages are provided by an outside independent maintenance contractor,
6. General and administrative services are provided by the utility's central administrative organization,
7. The plant operations are highly automated and computer controlled from the central control room,
8. Specialty services such as non-routine analysis, film badge processing, etc., are provided by outside contractors.
9. A special crew rebuilds the inner wall segments and assists in performance of wall replacement outages.

The plant is expected to have a typical utility organization as described in NUS-531, and on Figure V-6. Each of the four functional groups - operations, maintenance, technical and clerical & services - is headed by a supervisor with full responsibility for his function. These four supervisors, in turn, report to an assistant superintendent and plant superintendent, who are responsible for overall plant safety and efficient operations.

The total normal operating staff for the plant is estimated to be 112 persons as shown in Table V.5.* This staff varies from that in NUS-531 primarily in the operations and maintenance activities, where additional personnel are included because of the more numerous and more sophisticated equipment and instrumentation systems.

Based on an assumed average personnel cost of \$12,000 per year, the total salary cost including fringe benefits is estimated to be \$1,350,000 per year.

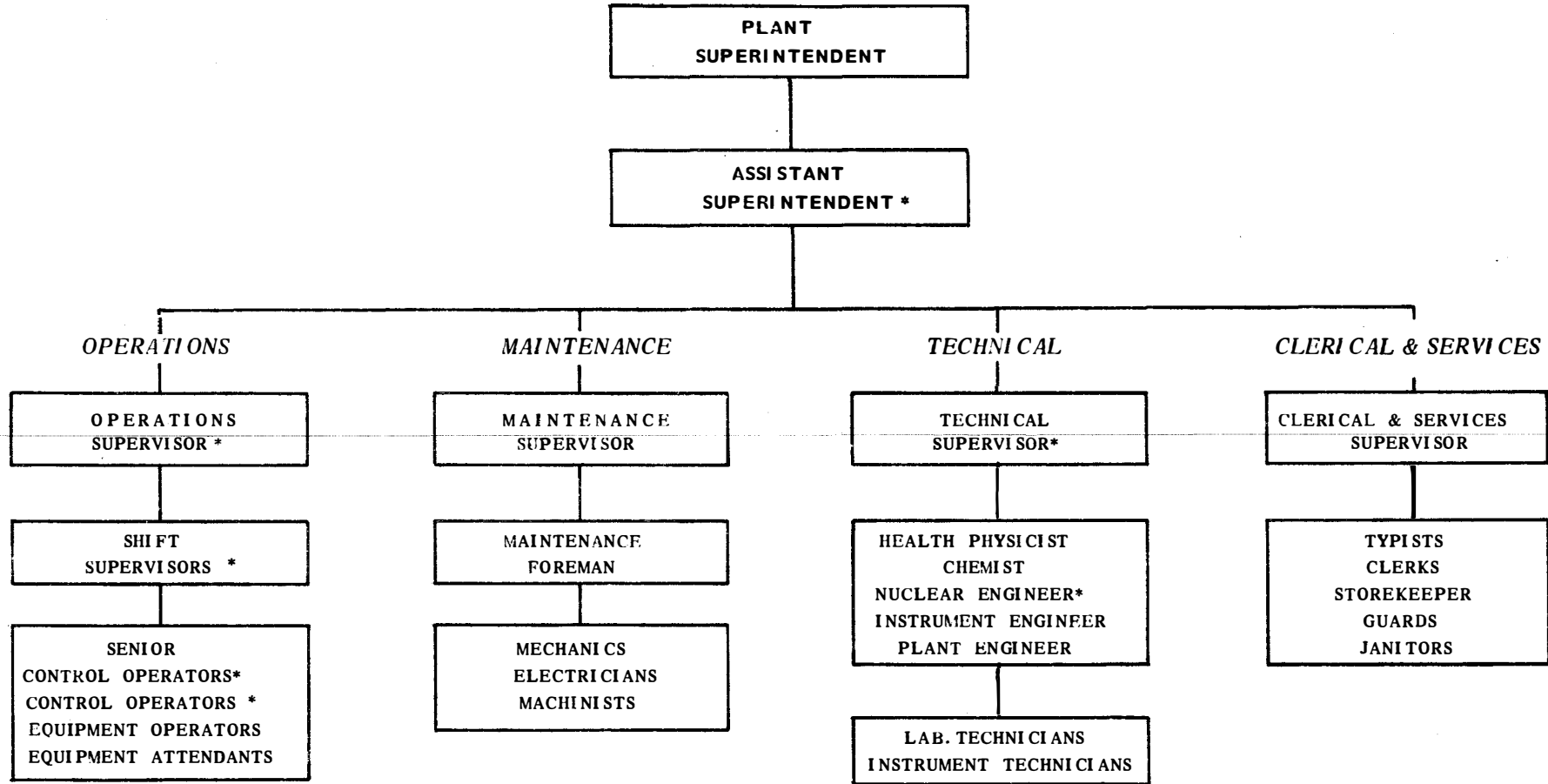
V-E-1-b. Miscellaneous Supplies and Equipment

This cost center includes such items as ion-exchange chemicals, biocides for fouling protection, gases, routine maintenance materials, waste containers, etc. - the multitude of material items used by the personnel during routine day-to-day operations. Because of the larger operating staff and more sophisticated equipment systems, it is estimated that this cost would be about 50% higher than for a fission reactor or about \$1,000,000 per year.

*The normal operating staff performs all activities except rebuilding the inner wall segments. A special crew, described below, is responsible for rebuilding the segments and assisting in replacement of those segments.

FIG. V - 6

TYPICAL PLANT STAFF



* A E C - LICENSED OPERATORS

TABLE V-5

UWMAK-I Personnel

<u>Position</u>	<u>Number persons Per Crew</u>	<u>Total Persons</u>
<u>Superintendents office</u>		
Plant superintendent	---	1
Assistant	---	1
Secretary	---	1
<u>Operations</u>		
Operations supervisor	---	1
Shift supervisors	1	5
Senior control room operator	1	5
Control room operator	2	10
Equipment operator	1	5
Equipment attendant	1	4
<u>Maintenance</u>		
Maintenance supervisor	---	1
Mechanical Foreman	---	1
Electrical foreman	---	1
Instrument foreman	1	5
Mechanic	1	5
Mechanics helper	1	5
Welder	---	4
Machinist	---	4
Electrician	---	3
Electrician helper	---	3
Instrument mechanic	2	10
Instrument helper	1	5
<u>Technical</u>		
Technical supervisor	---	1
Plant Engineer	---	1
Instrument Engineer	---	1
Nuclear Engineer	---	1
Health Physicist	---	1
Chemist	---	1
Technicians	---	8
<u>Clerical and Services</u>		
Clerical & services supervisor	---	1
Typist	---	2
Storekeeper	---	1
Clerk	---	2
Yardman	---	1
Janitor	1	5
Messenger and handyman	---	1
Guard	1	5
	<hr/>	<hr/>
Total	14	112

V-E-1-c. Outside Support Services

Two general types of outside support services probably will be needed for UWMAK-I . The first is the routine speciality services such as radioactive waste disposal, laundry, film-badge processing, etc. for which installation and staffing of facilities generally is more costly than use of outside help. Included in this category are personnel borrowed from other power plants. The total cost for the first type of outside services is estimated to be about \$350,000 per year, based on fission reactor experience.

The second type of outside support is the special maintenance force that is needed for replacing the inner wall. This requires a special crew trained to disassemble the reactor, move the irradiated segments to the storage cells, move rebuilt segments back to the reactor hall and then reassemble the reactor. It is expected that this will require 24 hours/day effort for four weeks per year with the associated higher costs for premium pay.

A crew of 96 men working each shift would expend about 16 man years of effort during each outage. If these men cost about 50% more than the average maintenance craftsmen because of special training, shift premiums, living expenses, and extra administrative costs, the total annual labor costs for these outages would be about \$800,000. This includes miscellaneous outage material costs.

V-E-1-d. Miscellaneous Costs

The miscellaneous costs are the numerous relatively small costs that do not fit into the other cost centers listed here. It includes such items as office supplies, vehicle maintenance, public relations expenses, travel, rent, training, etc. Assuming that these costs would be about 50 percent larger than for a fission reactor of the same capacity, yields an annual cost of about \$200,000.

V-E-1-e. General and Administrative Costs

General and administrative costs are the charges for activities such as fringe benefit administration, purchasing, division level management, etc. These usually average about 15 percent of the cost for salaries, supplies, and equipment, outside support services, and miscellaneous costs. This cost is calculated below on Table V-6.

V-E-1-f. Replacement Inner Walls

This cost is shown as a separate item because it is unique for fusion reactors and because of its magnitude. The stainless steel inner wall is replaced each two years. The total amount of stainless steel in that wall is 491,000 kg, costing approximately \$8,640,000 at the current typical unit cost for specialty S. S. shapes. One half of this cost would be charged against the electricity produced each year. In addition to the first wall, the rest of the blanket must be replaced every 10 years. The total material here amounts to 384,100 kg/year and an annual cost of \$3,380,000. The total annual cost for replacing the blanket is \$7,700,000.

TABLE V-6UWMAK-I Operations & Maintenance Costs

<u>Cost Item</u>	<u>Annual Cost</u>
Salaries, including fringe benefits	\$1,350,000
Miscellaneous supplies and equipment	1,000,000
Outside support services	1,150,000
Miscellaneous costs	200,000
	<hr/>
Sub total	\$3,700,000
General and Administrative (15% of above)	560,000
Replacement inner walls (annual share)	7,700,000
Coolant makeup (Li, Na, He(liq) He(gas))	38,000
	<hr/>
Total annual cost	\$11,998,000

V-E-1-g. Coolant Makeup

The two coolants of importance for this cost center are lithium and helium.

Lithium is lost due to reaction with neutrons, leakage, and adherence to components when they are removed or opened for maintenance. Because of the dangers resulting from leakage, losses will be kept as low as is economically possible and generally can be considered to have negligible impact. Losses due to neutron reactions cannot be avoided and result in destruction of about 400 kg per year. At a cost of \$10/kg, this is a cost of only \$4,000/yr. However, by definition that cost is a fuel cost and is not included in the coolant cost account.

Helium on the other hand is difficult to contain - continuous effort is necessary to prevent high leakage rates. The total inventory (cryogenic + shield cooling + energy storage unit) is about 621,000 liters (liquid) costing \$760,000. A typical loss of 5% per year would cost \$38,000/yr.

The cost for loss of nitrogen used to cool the shield is low enough that the cost can be considered to be included in the miscellaneous supplies and equipment costs.

Because sodium costs only \$0.25/lb and because leakage is kept to a low level for safety reasons the annual cost due to loss of sodium is considered to be negligible.

V-E-1-h. Working Capital Requirements

The working capital is the amount of money that must be on hand to pay day-to-day expenses or has been expended to purchase inventories of materials and supplies. The interest payment on the working capital generally is paid for in the annual return on capital and is not included in the O & M costs. Consequently, it will not be included in the O & M costs for UWMAK-I.

V-E-1-i. Total Operations and Maintenance Costs

The total O & M costs are summarized on Table V-6. The general and administrative costs were calculated during preparation of that table.

V-E-2. The Fuel Costs

The UWMAK-I operates on a mixture of 50% D₂ and 50% T₂. Because of the high breeding ratio and short doubling time, a surplus of T₂ will exist within six months of start of routine operation. The excess T₂ will have to be disposed of by sale to other fusion reactors which are just starting to operate, by storage, or by burial as solid waste. In this study, it is assumed that a surplus of T₂ will exist so that it has essentially zero value. In that case, there is no fuel purchase cost for the T₂.

The D₂, on the other hand, will have to be purchased at the current market price of about \$440 per kg. (\$200 per lb). The quantity of D₂ burned per year is about 140 kg. If a fifty percent loss occurs during the numerous recycles through the reactor, divertors, and fuel fabrications, the annual cost would be about \$123,000.

Because the fuel pellets are fabricated on site, the cost for fabrication is included in the O & M costs. The fuel cost normally includes only the cost of the fuel as delivered to the site.

Part of the lithium coolant is converted to tritium by absorption of neutrons. By definition, the cost of that lithium is a fuel cost because the tritium is recovered and used as fuel in the plasma. This loss of lithium is about 400 kgs per year. At a value of \$10/kg, this lithium costs about \$4,000/yr.

The total fuel cost is about \$127,000/year, consisting of about \$123,000 for D₂ and \$4,000 for lithium.

V-E-3. The Annual Return on Capital

Many of the costs for producing electricity can be related directly to the total capital costs for the plant. Examples are the real estate taxes, the interest on bonds, the dividends on stocks, insurance and unusual maintenance costs. Normal financial practice is to sum all such costs for a utility and then calculate a percent annual return on capital that will pay for these costs.

The annual return on capital depends primarily on the financial structure of the utility and on the amount of taxes that it must pay. The normal range is from 12 to 18 percent for private utilities and from 6 to 9 percent for public utilities.

Assuming a typical 15 percent annual return on the capital cost of 1,432,809,000 for a private utility (see Table V-3) results in an annual cost of approximately 214,920,000 for UWMAK-I.

V-E-4. The Total Electricity Cost

If the UWMAK-I operates at an eighty percent plant factor, the annual electricity production would be about 1.07×10^{10} kWh/yr. Summing the costs for that reactor results in the following total costs and unit cost for the electricity production. It is found that electricity from UWMAK-I should cost in the neighborhood of 21 mills per kW-hr.

Table V-7

UWMAK-I Electricity Costs

<u>Cost Item</u>	<u>Annual Cost</u>	<u>Unit Cost</u> (mills/kwh)
Operations & Maintenance	\$12,000,000	1.1
Fuel	127,000	0.01
Return on Capital	<u>212,865,000</u>	<u>19.9</u>
Total	224,992,000	21.0

VI. Conclusions

There is a great deal that could be said about the results of this study, but in order not to double the volume of this report we will reiterate, in one sentence or so, some of the major conclusions of each chapter. The reader is cautioned that it is very difficult to summarize, in a few words, the results of many calculations and conceptual design considerations. It is important to read both Vol. I and II to appreciate this fact, and it should be restated that the following conclusions apply to only UWMAK-I and cannot be blindly applied to other reactor concepts.

VI-A. Power Cycle

. The use of 12 separate reactor loops on the UWMAK-I reactor will reduce the leakage of tritium in the event of a catastrophic accident as well as to reduce the number of welds that need to be broken during a first wall replacement.

. The use of a secondary sodium loop accomplishes several objectives, including the reduction of tritium leakage, isolation of radioactive corrosion products from the steam cycle and the ability to provide a constant electrical power output, even during the period between burns.

. The Li primary coolant ($T_{\max} = 489^{\circ}\text{C}$) is used to produce 404°C steam at 2000 psia ($1.4 \times 10^6 \text{ kg/m}^2$) via a secondary sodium loop. This temperature and pressure requires the use of special, but readily attainable turbine-generator units.

. The Na "thermal flywheel" concept can even out the power generation of a pulsed reactor like UWMAK-I.

. The use of a sodium "thermal flywheel" requires large amounts of Na (~15,000 tonnes) not normally required for heat transfer. The associated storage tanks also place considerable demands on metal resources.

. A unique steam generator design utilizing helium gas doped with oxygen can be used to reduce tritium leakage into the steam cycle.

. The gross electrical output of the UWMAK-I reactor is 1681 MWe and the net constant output is 1473 MWe.

. Approximately 208 MWe of auxiliary power is required within the plant and this amounts to ~13% of gross output.

. Fifty three (53) percent of the auxiliary power is required for the liquid metal pumps and another 18% is required for the pumping of water.

. The energy conversion efficiency for UWMAK-I is 34% of the instantaneous power output and 32% of the average power output.

VI-B. Plant Layout

. Tokamak reactor buildings will be very large and may require special atmospheres (or lack of such) to prevent liquid metal fires, reduce tritium

leakage and to reduce vacuum pumping requirements.

. Attempts to completely contain tritium may require large amounts of steel liner on the inside of the large reactor buildings. This steel should be nonmagnetic in tokamak reactors and may amount to several thousand tonnes.

. Very thick concrete shielding (2.44 meters) is required to reduce the radiation levels due to neutron leakage from the UWMAK-I shield. This is required because the shield was only designed to reduce the nuclear heating and radiation damage in the magnets, not to provide protection for operating personnel.

. The repair of damaged UWMAK-I modules will require at least 3 large hot cells which have minimum dimensions of 35-40 meters high, 20 meters wide and 25 meters deep. The design and construction of such large hot cells will certainly be challenge to the current state of the art.

. The problem of on-site storage of discarded first wall segments must be addressed more fully before the total extent of building requirements can be estimated.

VI-C. Environmental Impact

. Siting of the UWMAK-I reactor and associated buildings may be hindered by the large building size (102 m tall, 120 m in diameter and up to 300 m long when the turbine building is attached).

. No serious problems are expected from the standpoint of magnetic field leakage, noise, air pollution or thermal pollution from UWMAK-I.

. By far the most serious operational release of radioactivity is the leakage of tritium through the power cycle. Calculations show that this can be kept to ~10 curies per day (or less) which is ~6% of the regulatory limit on such releases.

. Attempts to clearly identify the worst possible fusion plant accidents are hampered by the lack of operating experience with large reactor systems. However if some, as of yet undefined, accident could release as much as 1% of the total tritium inventory, then an exclusion radius of ~2100 meters would be required to keep the radiation dose to 25 rem to a person at the edge of the exclusion radius. Release of this tritium through a 100 m stack would greatly reduce these problems (i.e. to 2 rem at a 600 m exclusion radius).

. Preliminary considerations of lithium fires, loss of cooling accidents, helium gas pressurization, and magnet failures reveal that while such accidents have the potential to do great damage to the reactor, protection of the population around the reactor can be readily achieved.

. The generation of large amounts of high level radioactive waste in UWMAK-I (an average of ~736 metric tonnes per year) is more than a factor of 10 greater than that associated amount with a similar sized fission plant. On-site storage versus offsite storage requires that a complete assessment be made of the transportation problems.

. The biological hazard potentials of UWMAK-I radioactive wastes are considerably less than for those emanating from a similar sized fission reactor. This is mainly due to the lack of actinides, lack of extremely long-lived isotopes, and the more stable chemical nature of the isotopes.

VI-D. Materials Resources

. The construction of a large number of UWMAK-I reactors will place severe demands on critical elements because of (1) the low power density and (2) the use of relatively scarce materials (Nb, Cr, Mn, etc.) in UWMAK-I.

. The amount of metal required in UWMAK-I is 144 tonnes per MWe.

. The nuclear island accounts for 40% of all the metallic resource requirements and the balance of plant for the other 60%.

. Sixty (60) percent of the metals requirement is for Fe, 10% for Pb, 8% for Na, 7% for Cr, 6% for Ni and 5% for Cu.

. The total helium requirement is 138 tonnes (~1,100,000 liquid liters).

. Approximately 25% of all the Cr and Ni requirements results from replacing blanket materials due to radiation damage and another 25% is associated with the reinforcing for the superconducting magnets.

. Replacement of the 316 SS in the blanket with another metal such as V or Al would only reduce the Cr, Ni or Mn requirements by ~25%.

. Complete assessments of the availability of Li, Cr, Ni, Cu, Ti, Al, V, Mo and Nb at present, 3 times present, and 10 times present prices show that there are severe resource problems for some elements if a large amount of electricity (~ 10^6 MWe) were to be provided by UWMAK-I type reactors in the 21st century.

. There are reasonable U. S. reserves and production capabilities for the Fe, Mo, Cu, Ti and Al requirements of a large number (~680) of UWMAK-I type reactors.

. The U. S. has ample reserves at present, or 3 times present, prices for Ni, Mn, Pb, Li, Nb and B but significant increases in mine and mill production would be required to satisfy the UWMAK-I requirements to generate 10^6 MWe.

. The U. S. has neither the reserves, resources, or production capability for the Cr required by a large (~ 10^6 MWe) electrical generating capacity from UWMAK type reactors. There are ample world reserves but the question of reliance on foreign sources for critical materials must be assessed.

VI-E. Economics

. A complete analysis of the burn cycle, scheduled outage and unscheduled maintenance for UWMAK-I shows that a plant factor of ~80% is reasonable but probably a maximum value for UWMAK-I.

. The capital cost for the UWMAK-I reactor is \$971.

. Approximately 51% of the capital costs is associated with the nuclear island and 49% is associated with the balance of plant.

. The high capital costs of UWMAK-I reactors could be lowered by reducing the number of power loops from 12 to 3 or 4, and reducing the costs associated with the superconducting stored energy building.

. Interest during construction contributes 15% to the total plant costs.

. The electricity production cost for UWMAK-I is 21 mills per kwh. Most of this (95%) is associated with a 15% return on capital and essentially the rest of the costs are associated with the operation and maintenance costs. The fuel costs are only 0.01 mill per kwh.

. The cost of UWMAK-I and its electricity is felt to be quite reasonable considering the state-of-the-art assessment and conservative approach taken in this design.

Appendix ABasis for Capital Cost Estimates for UWMAK-I

<u>Account Number</u>	<u>Account Title and Estimating Philosophy</u>	<u>Quantity</u>	<u>Unit Cost</u>	<u>Total Cost</u>	<u>Reference Document</u>
20	<u>Land and Land Rights</u> Same as for a PWR	500 acres	\$2400	\$1,200,000	WASH 1230(Vol.1.1)
21	<u>Structures & Site Facilities</u>				
211	Site Improvements and Facilities		*		
212	Reactor Building		*		
213	Turbine Building		*		
214	Intake & Discharge Structures		*		
215	Reactor Auxiliaries Building		*		
218	Miscellaneous Building		*		
22	<u>Reactor Plant Equipment</u>				
221	Reactor Equipment (4 spare reflector elements included)				
221.1	Magnets (see Table V-4)			\$189,900,000	
221.2	Shield				
	316 S.S.	2539 MT	8.80	\$22,343,000	
	B ₄ C	2029 MT	3.00	\$ 6,690,000	
	Pb	20,500 MT	0.60	\$12,300,000	
				\$41,333,000	
221.3	Blanket (316 SS)	610 MT	17.60	\$10,740,000	
		7210 MT	8.80	\$63,420,000	
221.4	Neutral Beam Injectors	15 MW	\$0.40/watt	\$6,000,000	
221.5	Equipment Foundations and Supports	60 MT	\$4.40/kg	\$ 250,000	
221.6	Reactor Seals	470 meters	\$3000/m	\$1,400,000	
222	<u>Main Heat Transfer be Transport System</u>				
222.1 to 222.14			*		
222.15	Cleanup System				
	Zr	100 MT	\$45/kg	\$4,500,000	
	Filtration System (design unknown)			\$2,000,000	
222.16	Thermal insulation piping & equipment.*				
222.17	Tritium Extraction	180 kg	\$330/kg	\$ 60,000	

* means information must be provided by others

222.21 to 222.24			*	
222.25	Clean-up			
	Zr.	8,000 kg	\$45/kg	\$ 360,000
	Filtration System	(design unknown)		<u>400,000</u>
				\$760,000
222.26	Tritium Extraction	1,400 kg	\$330/kg	460,000
222.31 to 222.33			*	
222.34	Clean-up Systems			
	Zr	10 ⁴ kg	\$45/kg	\$450,000
	Filtration system			<u>250,000</u>
				\$700,000
222.35 to 222.37			*	
222.38	Tritium Extraction	700 kg	\$330/kg	\$230,000
223	<u>Auxiliary Heating Systems</u>			
223.1	Shield Cooling			
223.11	Pumping	12 pumps	\$31,000	\$372,000
223.12	Piping (Estimated pipe length and size)			\$212,000
223.13	Heat Exchangers	12 units	\$42,000	\$492,000
223.14	Purifications (filter systems, tanks)			\$ 36,000
223.15	Lithium extraction yttrium cost	80kg	\$330/kg	30,000
223.2	Magnet Cooling Systems			
223.21	Cryogenic System	15 kW	\$583,000/kW	\$ 8,750,000
223.22	Piping (Estimated pipe length and size)			250,000
223.23	Transport systems (cryogenic pump costs)			250,000
223.24	Tanks	200,000 liter tank		50,000
224	<u>Radioactive Waste Treatment & Disposed</u>			WASH 1230 (Vol. 1)
224.1	Liquid Radwaste System			
	Waste Holdup Tank			\$33,000
	Sump tank			4,000
	Sump pump and motor			8,000
	Disposal pumps and motors			3,000
	Waste evaporator			<u>132,000</u>
				\$180,000

224.2	Caseous Radwaste System - No special equipment required			
	Tritium extraction equipment and filters indicated in room ventilation costs.			
224.3	Solid Radwaste System (same as for PWR)	\$90,000		Wash 1230(Vo1.1)
224.4	Wall liner disposal equipment 3 crushers	\$20,000		\$60,000
225	<u>Fuel Handling & Storage Systems</u>			
225.1	Used Fuel Purification system 2-50kg/day Cryogenic stills	\$30,000		\$60,000
225.2	Liquefaction Heat exchange systems (50 kg/day)			\$100,000
225.3	Pellet Fabrication 20kg/day capacity			\$180,000
225.4	Pellet Injection (design unknown)			1,480,000
225.5	Storage equipment 200 kgs gas and 200 kgs liquid			50,000
226	<u>Other Reactor Plant Equipment</u>			
226.1	Inert gas systems - nitrogen only			
	Same capacity as PWR	\$71,000		WASH 1230 - Vo1. 1
	Argon (3 months supply)	50,000		
	Helium (3 months supply)	90,000		
	Piping and Pumps	110,000		
226.2	Special heating systems			
	Estimated pipe lengths, electric and steam capacity	\$2,200,000		
226.3	Cooling receiving, storage and makeup systems			
	Lithium 10,000 gallon tank		41,000	
	Sodium 5,000 gallon tank		32,000	
226.4	Fluid leak detectors	500	\$400	200,000
226.5	Auxiliary Cooling Systems	150% of PWR cost	2,300,000	"
226.6	Maintenance equipment			
	Segment Transporters	6	\$250,000	\$1,500,000
	Segment impact wrenches	12	1,000	12,000
	Maintenance and Inspection Cab			20,000
	Segment Radiation Shields	12	150,000	1,800,000
	Remote TV Equipment	5	4,000	20,000
	Hot Cell Maintenance Cabs	3	2,000,000	6,000,000
226.7	Building vacuum systems			
	1000 cfm vacuum system (1 torr)			120,000
	Cryogenic Condensation Equipment			240,000
226.8	Core vacuum system			
	Cryopumps	192	\$14,000	\$2,690,000
	Hg diffusion pumps	96	\$8,500	820,000
	Roots blowers	384	\$5,443	2,090,000
	Forepumps	96	\$3,780	360,000
	Piping			600,000

227	<u>Instrumentations & Control</u>	200% of PWR costs	\$11,700,000	WASH 1230(Vol.1
228	<u>Fossil-Fueled boilers & superheaters</u>	none required		
23	<u>Turbine Plant Equipment</u>	*		
24	<u>Electric Plant Equipment</u>	See Appendix B for Energy Storage Unit		
25	<u>Miscellaneous Plant Equipment</u>			
251.11	Turbine Hall 175/25 ton cranes	2	\$262,000	\$525,000
251.12	Hot Cell Cranes (200 ton)	3	\$332,000	\$1,000,000 WASH 1230-Vol. 1
251.13	Miscellaneous Equipment		\$575,000	
251.14	Stored Energy Building Crane (150/10 ton)		\$300,000	
251.15	He Storage Building Crane (20 ton)		\$100,000	
251.16	Reactor Hall Crane (175/35 ton)		\$500,000	
251.2-.6	Mobile Equipment (cars, trucks, etc.)		\$ 50,000	
252	<u>Air and water service systems</u>			
252.1	Air systems	150% of PWR	\$ 460,000	
252.2	Water systems	150% of PWR	3,400,000	
252.3	Auxiliary heating boilers	150% of PWR	1,800,000	
253	Communications Equipment	125% of PWR	220,000	
254	Furnishings & Fittings	150% of PWR	480,000	
26	<u>Special Materials</u>			
261	Moderator	none required		
262	Reflector	none required		
263	<u>Reactor Coolant and cryogenic systems</u>			
	Lithium	1,700,000	10/kg	17,000,000
264	<u>Intermediate coolant (sodium)</u>	17.826 x 10 ⁶ kg	\$0.55/kg	9,804,000
265	<u>Turbine Cycle working fluids</u>	no	special fluids	
266	<u>Other Materials</u>			
	Helium	1,102,000 liters	1.22/1	1,344,000
	Deuterium	40 kg	\$440/kg	17,600
	Nitrogen	500,000 liters	0.25/1	125,000
	Argon	1000 kg	0.80/kg	800
91	<u>Construction facilities, equipment and services</u>			
911	Design engineering	150% of PWR cost	\$24,300,000	
92	<u>Engineering Services</u>			
921	Design engineering	200% of PWR cost	\$23,100,000	
922	Other	150% of PWR cost	\$25,400,000	

93	<u>Other Costs</u>		
931	Taxes and Insurance	10% of material costs	75,000,000
932	Staff Training & Plant Startup	150% of PWR costs \$900,000	WASH 1230 (vol.1)
933	Owners G & A	150% of PWR costs	\$4,900,000
94	<u>Interest During Construction</u>		
941	Physical Plant	8% for 5 years	215,614,000
942	Land and Land Rights	8% for 6 years	704,000
943	Special Materials	8% for 1 year	2,300,000

Appendix BCost Data for 15 MWh Energy Storage Unit

	Material (MT)	Unit Cost (\$ kg)	Total Cost \$10 ⁶
A. Storage Magnet			
1. TiNb superconductor	59.7	33.00	1.97
2. Copper stabilizer	2,800	3.30	9.24
3. Fabrication of the above conductor	(2859.7)	1.10	3.15
4. Reinforcing stainless steel	1016	4.40	4.47
5. Mylar insulator	44	4.40	0.19
6. Micarta spacer	176	4.40	0.77
7. Stainless steel cryostat support	1260	4.40	5.54
8. Aluminum shield	445 MT	3.30	1.47
9. Assembly and installation	(5800)	1.10	6.38
B. Refrigeration Systems			
1. Refrigerator for S.C. magnet	5.3 kw @ 4.2 K	\$720/W	3.84
2. Refrigerator for Al-shield	184 kw @ 40 K	\$76.70/W	3.07
C. Vacuum System			0.87
D. Converter-Inverter System			
1. dc-ac-dc bridge	560 MW	\$15.00/kW	8.10
2. Shield compensating power supply	367.5 kW	\$40.00/kW	0.015
E. Conventional Facilities (building, site work, electricity, etc.)			<u>6.01</u>
Total energy storage and bridge cost			\$54.6 x 10 ⁶
an ac/dc bridge directly from utility line of 500 MW (\$20/MW)			\$10.0 x 10 ⁶
Total power supply system cost for UWMAK-I poloidal coils			= \$64.6 x 10 ⁶